Christophe Donnet
Ali Erdemir
Editors

Foreword by John Robertson

Tribology of Diamond-Like Carbon Films

Fundamentals and Applications

Springer

Tribology of Diamond-Like Carbon Films

Christophe Donnet • Ali Erdemir
Editors

Tribology of Diamond-Like Carbon Films

Fundamentals and Applications

Springer

Christophe Donnet
University Institute of France and
University Jean Monnet
Laboratoire Hubert Curien UMR 5513
18 avenue Professeur Benoît Lauras
42000 Saint-Etienne, France
Christophe.Donnet@univ-st-etienne.fr

Ali Erdemir
Argonne National Laboratory
Energy Systems Division
9700 South Cass Avenue
Argonne, IL 60439, USA
erdemir@anl.gov

ISBN 978-0-387-30264-5 e-ISBN 978-0-387-49891-1

Library of Congress Control Number: 2007930611

Printed on acid-free paper.

9 8 7 6 5 4 3 2 1

springer.com

Foreword

Diamonds have a very powerful image with both the public and the scientific community, because of their beauty and the historic difficulty in first synthesising it. Diamond-like carbon (DLC) is much less famous, but it has a similar importance in economic terms. DLC coatings are used on razor blades, in magnetic hard-disk drives, on bar-code scanners, on PET bottles, and on some car parts. But how did we develop the underlying technology? This book gives the detailed scientific and technological answer to this question.

The historical overview describes how DLC has a much shorter history than diamond itself, from the 1970s with Aisenberg and Chabot and then Holland using plasma deposition to first grow hard, amorphous carbon films. A great deal of early work was carried out by the group of Koidl in the 1980s. Meanwhile, Russian groups invented the cathodic arc and used it on carbon, and this allowed growth of a second type of hydrogen-free DLC. This material came to be known as tetrahedral amorphous carbon, which is abbreviated as ta-C or TAC, or various similar ways.

This range of growth techniques allowed us to understand the range of DLCs, as I summarise in Chapter 1. The thin film growth techniques are of critical importance, because DLC is only possible as a thin film material, not as a bulk glassy solid. However, historically, proving that someone had and had not grown diamond synthetically was at least as important as the growth itself. The same applies to DLC. A specific range of characterisation techniques are employed to measure the properties and bonding of DLC, as is described in Chapter 2.

Diamond is known to possess the most extreme properties of any real three-dimensional solid, such as highest atomic density, highest hardness, highest Young's modulus, highest room temperature thermal conductivity, etc. But diamond is inconvenient as a coating material, because its growth temperature is high. DLC has the huge advantage over diamond of having room temperature, rather low cost, large-area vacuum deposition methods. DLC is also amorphous which allows it to be the smoothest material known. These advantages are what gives DLC its wide range of applications noted above.

DLC does however have two drawbacks; one is that its thin films tend to have a large compressive stress, and the second that it is not mechanically tough.

Nevertheless the amorphous character of DLC means that it can be alloyed with metals and other elements like silicon which goes some way to solving these problems. These issues are described in Chapters 4 and 12.

The main applications of DLC are as a mechanical and protective coating. This is the focus of most chapters of the book, mainly in Chapter 3 and Sections B and C. Some years ago, there were many studies of DLC trying to develop the electronic properties of DLC, as field emission or doping, but these turned out to be unsuccessful or uncompetitive with other materials. Thus the focus of DLC research now continues in the area of mechanical properties.

The applications in magnetic hard-disk drives and on razors have existed for 10–25 years. The applications as coatings on tool tips and on car components are more recent, and have followed more recent advances in our understanding of tribology, thin film adhesion, and alloying. These topics are less easily found in the journal literature. This book for the first time brings together all these areas in a convenient form. This book will thereby provide an extremely useful reference for the economic developments in these areas.

John Robertson

Engineering Department,
University of Cambridge,
Cambridge CB2 1PZ, UK.
E-mail: jr214@hermes.cam.ac.uk

Acknowledgments

The strength of this book primarily lies in its very comprehensive and up-to-date nature. It provides an excellent overview of the state of the art in DLC films, in general, and their tribology, in particular. It also offers an exhaustive survey of the recent developments from a fundamental and industrial point of view. We thank our colleagues in the field for their invaluable contributions to this book. Without their time and effort, it would not have been possible to publish this book, which we hope will help us in furthering our quest to develop even better coatings in the near future. We also acknowledge the support of our institutions (Argonne National Laboratory, USA, the University Jean Monnet, France, and the University Institute of France) and funding agencies (the United States Department of Energy, Office of Energy Efficiency and Renewable Energy, Freedom Car and Vehicle Technologies Program; and Centre National de la Recherche Scientifique de France). Last but not least, we thank our families for their unwavering support and understanding during the preparation of this book.

Contents

Contributors

Koshi Adachi
Tribology Laboratory, Graduate School of Engineering, Tohoku University, Sendai 980–8579, Japan, koshi@tribo.mech.tohoku.ac.jp

Maria-Isabel De Barros Bouchet
Ecole Centrale de Lyon, Laboratoire de Tribologie et Dynamique des Systèmes UMR 5513, 36 avenue Guy de Collongue 69134 Ecully, France, Maria-Isabel.De-Barros@ec-lyon.fr

Bharat Bhushan
Nanotribology Laboratory for Information Storage and MEMS/NEMS, 201 W. 19th Avenue, Ohio State University, Columbus, OH 43210–1142, U.S.A, bhushan.2@osu.edu

Feodor M. Borodich
School of Engineering, Cardiff University, Queen's Buildings, Cardiff CF24 3AA, UK, borodichfm@Cardiff.ac.uk

Esteban Broitman
Department of Chemical Engineering, Carnegie Mellon University, Pittsburgh, PA 15213, USA, broitman@andrew.cmu.edu

Yip-Wah Chung
Center for Surface Engineering and Tribology, Robert R. McCormick School of Engineering and Applied Science, Northwestern University, Evanston, IL 60208, USA, ywchung@mail.mccormick.northwestern.edu

Christophe Donnet
University Institute of France and University Jean Monnet, Laboratoire Hubert Curien UMR 5513, 18 avenue Professeur Benoît Lauras, 42000 Saint-Etienne, France, christophe.Donnet@univ-st-etienne.fr

Gabriel Dumitru
University of Applied Sciences Northwestern Switzerland, School of Engineering Institute for Product and Production Engineering (IPPE), Steinackerstrasse 5 5210 Windisch, Switzerland, gabriel.dumitru@fhnw.ch

Ali Erdemir
Argonne National Laboratory, Energy Systems Division,
9700 South Cass Avenue Argonne, IL 60439, USA, erdemir@anl.gov

Asuncion Fernández
Instituto de Ciencia de Materiales de Sevilla (CSIC-Universidad de Sevilla)
Avda. Américo Vespucio 49, 41092 Sevilla, Spain, asuncion@icmse.csic.es

Andrea Ferrari
Engineering Department, University of Cambridge, Cambridge CB2 1PZ, UK,
acf26@hermes.cam.ac.uk

Julien Fontaine
Ecole Centrale de Lyon, Laboratoire de Tribologie et Dynamique
des Systèmes UMR 5513, 36 avenue Guy de Collongue, 69134 Ecully,
France. Julien.Fontaine@ec-lyon.fr

Martin Frank
CemeCon AG, Adenauerstrasse 20 A 4, 52146 Würselen, Germany,
Martin, Frank@CemeCon.de

Hans-Gerd Fuß
CemeCon AG, Adenauerstrasse 20 A 4, 52146 Würselen, Germany,
HansGerd, Fuss@CemeCon.de

Roland Hauert
Swiss Federal Laboratories for Materials Testing and Research,
Ueberlandstrasse 129, 8600 Dübendorf, Switzerland, Roland.Hauert@empa.ch

Christophe Heau
HEF Group, Rue Benoît Fourneyron, 42166 Andrézieux-Bouthéon, France,
cheau.hefrd@hef.fr

Kenneth Holmberg
VTT Technical Research Centre of Finland, Metallimiehenkuja 6, Espoo,
PL 1000, FIN-02044 VTT, Finland, kenneth.holmberg@vtt.fi

Lars Hultman
Thin Film Physics Division, Department of Physics, Chemistry and Biology
(IFM) Linköping University, 58183 Linköping, Sweden, larhu@ifm.liu.se

Koji Kato
Tribology Laboratory, Graduate School of Engineering, Tohoku University,
Sendai 980–8579, Japan, koji@tribo.mech.tohoku.ac.jp

Leon M. Keer
Center for Surface Engineering and Tribology, Robert R. McCormick
School of Engineering and Applied Science, Northwestern University,
Evanston, IL 60208, USA, l-keer@northwestern.edu

Dieter Klaffke
Federal Institute for Materials Research and Testing (BAM), 12200 Berlin, Germany, dieter.klaffke@bam.de

Patrick Lemoine
Nanotechnology Research Institute, University of Ulster at Jordanstown Shore road, Newtownabbey, BT37OQN, County Antrim, Northern Ireland, United Kingdom, p.lemoine@ulster.ac.uk

James A. McLaughlin
Nanotechnology Research Institute, University of Ulster at Jordanstown Shore road, Newtownabbey, BT37OQN, County Antrim, Northern Ireland, United Kingdom, jad.mclaughlin@ulster.ac.uk

Paul D. Maguire
Nanotechnology Research Institute, University of Ulster at Jordanstown Shore road, Newtownabbey, BT37OQN, County Antrim, Northern Ireland, United Kingdom, pd.maguire@ulster.ac.uk

Charles-Alix Manier
Federal Institute for Materials Research and Testing (BAM) 12200 Berlin, Germany, charles-alix.manier@bam.de

Jean-Michel Martin
University Institute of France and Ecole Centrale de Lyon, Laboratoire de Tribologie et Dynamique des Systèmes UMR 5513, 36 avenue Guy de Collongue, 69134 Ecully, France, Jean-Michel.Martin@ec-lyon.fr

Keiji Nakayama
National Institute of Advanced Industrial Science and Technology (AIST), Namiki 1–2, Tsukuba, Ibaraki 305–8564, Japan, k.nakayama@aist.go.jp

Jörg Neidhardt
Christian Doppler Laboratory for Advanced Hard Coatings, Department of Physical Metallurgy and Materials Testing, University of Leoben, 8700 Leoben, Austria and Thin Film Physics Division, Department of Physics, Chemistry and Biology (IFM), Linköping University, 58183 Linköping, Sweden, joerg.neidhardt@unileoben.ac.at

Yves Pauleau
National Polytechnic Institute of Grenoble, Centre National de la Recherche Scientifique CNRS-LEMD, B.P. 166, 38042 Grenoble 9, France, yves.pauleau@grenoble.cnrs.fr

Bojan Podgornik
University of Ljubljana, Centre for Tribology and Technical Diagnostics Ljubljana, Bogisiceva 8, SI-1000 Ljubljana, Slovenia, bojan.podgornik@ctd.uni-lj.si

John P. Quinn
Nanotechnology Research Institute, University of Ulster at Jordanstown,
Shore road, Newtownabbey, BT37OQN, County Antrim, Northern Ireland,
United Kingdom, jp.quinn@nibec.ulster.ac.uk

John Robertson
Engineering Department, University of Cambridge, Cambridge CB2 1PZ, UK,
jr214@hermes.cam.ac.uk

Helena Ronkainen
VTT Technical Research Centre of Finland, Metallimiehenkuja 6, Espoo
PL 1000, FIN-02044 VTT, Finland, helena.ronkainen@vtt.fi

Juan Carlos Sánchez-López
Instituto de Ciencia de Materiales de Sevilla (CSIC-Universidad de Sevilla)
Avda. Américo Vespucio 49, 41092 Sevilla, Spain. jcslopez@icmse.csic.es

Thomas W. Scharf
The University of North Texas, Department of Materials Science
and Engineering, Denton, TX 76203–5310, USA, scharf@unt.edu

Irwin L. Singer
US Naval Research Laboratory, Code 6176, Washington, DC 20375–5342, USA,
irwin.singer@nrl.navy.mil

Dirk Spaltmann
Federal Institute for Materials Research and Testing (BAM), 12200 Berlin,
Germany, dirk.spaltmann@bam.de

Gerry Van Der Kolk
Ionbond Netherlands b.v., Groethofstraat 22b, NL 5916 PB Venlo,
The Netherlands, gerry.van.der.kolk@ionbond.com

Andrey A. Voevodin
Materials and Manufacturing Directorate, Air Force Research Laboratory,
Wright-Patterson Air Force Base, Ohio, USA. Andrey.Voevodin@wpafb.af.mil

Rolf Wäesche
Federal Institute for Materials Research and Testing (BAM) 12200 Berlin,
Germany, rolf.waesche@bam.de

Mathias Woydt
Federal Institute for Materials Research and Testing (BAM) 12200 BERLIN,
Germany, mathias.woydt@bam.de

Diamond-like Carbon Films: A Historical Overview

C. Donnet[1] and A. Erdemir[2]

1 Introduction

Carbon is one of the most remarkable elements among all others in the periodic table. It exists in more than 90% of all known chemical substances and has the largest number of allotropes. Carbon-based solid materials exhibit exceptional properties such as super-high hardness and thermal conductivity, like in diamond, or unusual softness and lubricity, like in graphite. Besides these, carbon is the building block of carbon-based allotropes including white carbon (or ceraphite), nanotubes, buckyballs, other fullerenes, carbon–carbon composites, glassy carbons, and carbon nanofibers.

During the last three decades or so, carbon has also been the key element in the synthesis of thin coatings of diamond, diamond-like carbon (DLC), carbon nitride, boron carbide, and a myriad of transition metal carbide, and carbo-nitride coatings. Because of their exceptional mechanical and tribological properties, these coatings are now used in a wide range of engineering applications to control friction and wear. Figure 1 is a ternary diagram (proposed by Robertson and Ferrari) that illustrates the specific domains of various carbon-based coatings with respect to their sp^2- and sp^3-type bonding characteristics and hydrogen contents. A more comprehensive overview of these and other DLC films is provided by Robertson in Chapter 1. The fullerene-type allotropes of carbon represent a new class of materials and their usefulness is being explored in novel nano- to microscale devices.

The family of DLC coatings is perhaps the largest and represents one of most-studied among all other coatings. These coatings were first discovered in the early 1950s by Schmellenmeier [1] but did not attract much attention until the work of Eisenberg and Chabot almost two decades later [2]. During the 1980s, a few more researchers developed interest in these films, while during the 1990s, the research on DLC films gained momentum [3,4]. As can be deduced from Figs 2–4, almost

[1]University Jean Monnet, Saint-Etienne, France, Member of the University Institute of France, Paris, France

[2]Argonne National Laboratory, Argonne, IL, USA

C. Donnet and A. Erdemir (eds.), *Tribology of Diamond-Like Carbon Films: Fundamentals and Applications*.

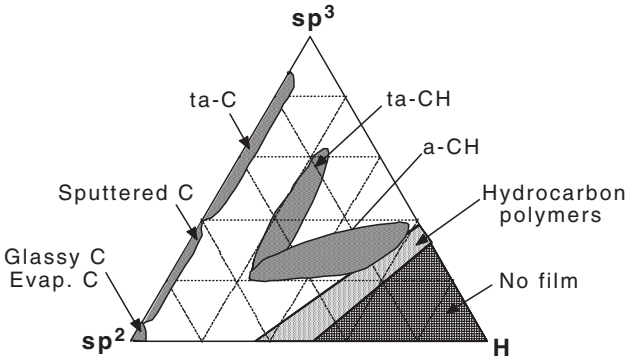

Fig. 1 Ternary phase diagram for various DLC films with respect to their sp^2, sp^3, and hydrogen contents. (After Robertson, [35].)

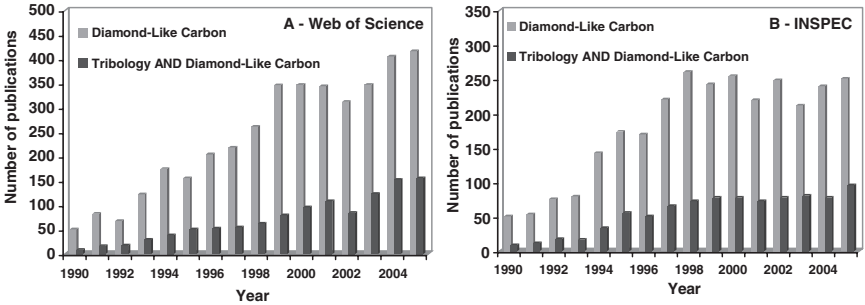

Fig. 2 Number of publications per year on DLC coatings (black bar) and on tribology of DLC coatings (grey bar), deduced from (a) the Web of Science and (b) the INSPEC data bases

every year since the early 1990s, numerous papers and patents have been devoted to DLC films. Since 2000, these films have attracted even more interest, and they are still the subject of numerous scientific studies. In the following sections, we will provide a brief overview of recent developments in the field of DLC films, in general, and some of the major milestones, in particular. We will also summarize the current status and future trends in these films.

More comprehensive overviews of DLC films are provided in Section A of this book. In this section, Chapter 1 reviews various forms and compositions of DLC films, while Chapter 2 tackles the challenging subject of characterization. These films are metastable forms of carbon combining both sp^2 and sp^3 hybridizations, including hydrogen when a hydrocarbon precursor is used during deposition. These two chapters do not deal with tribology, but understanding the tribological behavior of DLC films requires a solid background on the chemical and structural nature of these films, which, in turn, depends on the deposition process and/or parameters. The chemical

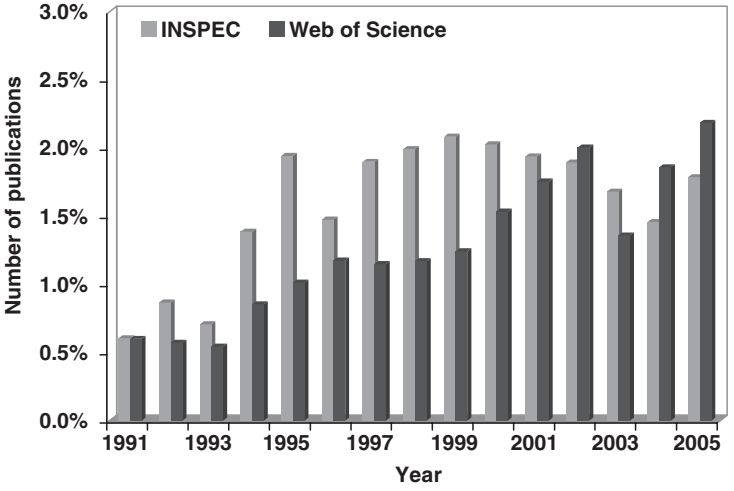

Fig. 3 Variation of the percentage of publications related to the tribology of DLC films within all other tribology-related publications, as deduced from the Web of Science and INSPEC data bases

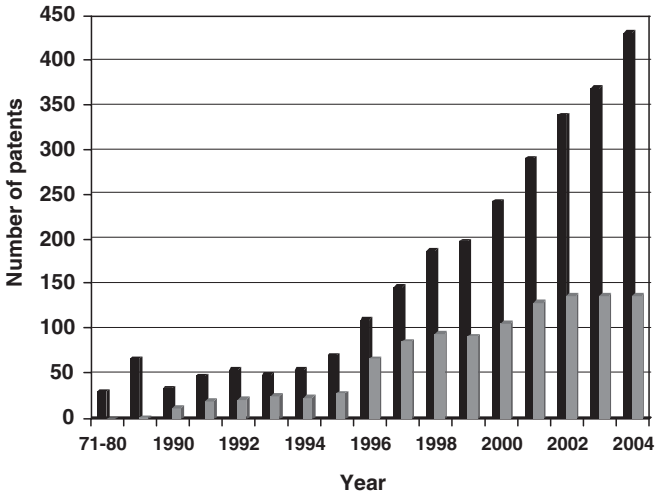

Fig. 4 Number of US patents issued per year on DLC coatings (black bar) and on their tribology (grey bar)

composition, such as the hydrogen and/or nitrogen content or the presence of other alloying elements, controls the mechanical and tribological properties of a sliding pair consisting of DLC on one or both sliding surfaces. Among the many properties of an engineering material, hardness and stiffness play the most important roles in its ability to carry the load and, hence, in its wear resistance. Chapter 3 reviews the mechanical

properties of DLC films extending from organic polymers for highly hydrogenated DLC films to diamonds for tetrahedral unhydrogenated DLC films. Whatever the nature of the DLC, one should keep in mind that the industrial success of DLC films in tribological contacts is strongly dependent on their adhesion properties. Basically, DLC films adhere well on substrates containing elements forming carbides, such as silicon or titanium. In most cases, intermediate layers need to be deposited in situ on the substrate before the deposition of the DLC films. This practice is detailed in the chapters of this book dedicated to industrial applications. Nevertheless, one of the most critical aspects of DLC films is the presence of stress, mainly resulting from the quenching of the impinging species during film growth. Chapter 4 reviews the various mechanisms responsible for stress in DLC films.

2 Inception and Early Studies

Historically, the earliest attempts to produce DLC films can be traced back to 1953 when Heinz Schmellenmeier reported a black carbon film derived from C_2H_2 gas in glow-discharge plasma. His film exhibited great hardness and, hence, was very resistant to scratching by other hard objects. Later work by Eisenberg and Chabot in the early 1970s produced such films on negatively biased metallic substrates by using an ion beam deposition system [2]. Their films were very hard and hence resistant to scratching and also possessed a high dielectric constant, high index of refraction, excellent optical transparency, and high resistance to corrosion in strongly acidic solutions. Because DLC films are typically amorphous and dense, they were less prone to pin-hole defects. During the mid-1970s, Holland et al. and a few other researchers were also able to synthesize DLC films from other hydrocarbon sources by simply applying a radio frequency (RF) bias to the substrate materials and thus creating a glow-discharge plasma [3–5]. Because of the impressive mechanical properties of these films, some researchers had speculated that they were perhaps composed of crystalline diamond, but systematic microscopic studies by Weissmantel et al. during the late 1970s dispelled these speculations by confirming that the DLC films had an amorphous structure [5].

During the 1980s, there were a few other reported papers on DLC films. In a 1985 review paper, Arnoldussen and Rossi from IBM predicted and discussed in detail the potential usefulness of thin DLC films for magnetic recording media [6]. Such a possibility had already been explored in 1981 by King, who was able to demonstrate far superior performance and efficiency for the DLC-coated disk media than the other types of overcoat materials used in hard disks at that time [7]. Based on his experimental findings, King concluded that the use of these films in magnetic recording media may lead to some major advances in the hard disk industry, and obviously his predictions were right. During the 1980s, only a few other tribological studies were performed on DLC [8–10]. In 1986, Robertson published a comprehensive review paper on amorphous carbons, including DLC films, and summarized the details of the main characteristics of such materials [11].

Since the early 1990s, the popularity of DLC films has gained momentum. We have witnessed an explosion in DLC-related research activities, including the number of publications and granted patents (see Figs 2–4). During these years, many novel types of DLC films were formulated; DLC films were produced on an industrial scale and systematic tribological studies were carried out. As a result of such increased industrial and scientific activities, our knowledge base on DLC films increased tremendously. Numerous key publications that appeared in books and journals focused on the synthesis, characterization, and industrial application of DLC films. In particular, papers published by Grill et al. [12], Miyoshi and his coworkers [13], Ronkainen et al. [14], Erdemir et al. [15], and Donnet et al. [16] provided the foundation for more in-depth studies and reinforced the notion that DLC films deserve more scientific and industrial attention. During the 1990s, systematic studies were also carried out to elucidate the effect of incorporation of hydrogen and other heteroatoms (F, N, Si, etc.) on the friction and wear properties of these films [17–28]. Since the beginning of 2000, several review articles have been published that provided more detailed insight into the unique structural, mechanical, and tribological properties of these films [18, 29–34]. In particular, a recent comprehensive review article by Professor Robertson is an excellent source for further information on DLC films and their properties [35].

3 State of the Art

Owing to their very unique structures and attractive properties and performance characteristics, DLC films continue to draw significant attention from both the scientific and industrial communities. As can be seen from Figs 2 and 3, the number of scientific papers published in recent years increased steadily, while the number of granted patents (see Fig. 4) reached record numbers during the same period, thus reinforcing the notion that these films are industrially useful and relevant. They are currently used in numerous industrial applications where high resistance to wear, scuffing, corrosion, and erosion is paramount. Some of the chapters in Section C of this book treat recent industrial applications, as does the next section in the current chapter.

Dedicated scientific studies on DLC films in recent years have led to the development of more exotic versions consisting of unique nanophases and/or structures. Specifically, with recent advances in deposition processes (hybrid arc-magnetron systems, femtosecond pulse laser deposition, etc.) it has now become rather easy to control the properties of DLC films and tailor them to meet the ever-increasing performance and durability requirements of industrial applications. Some of the latest films, based on nanoscale multilayers, provide excellent toughness and much improved tribological properties [36–37], while others are extremely hard and resilient, and hence well-suited for protection against wear under severe sliding conditions [38–40]. Another class of recent DLC films is not as hard but can provide what may be the lowest friction coefficients on any known material [41].

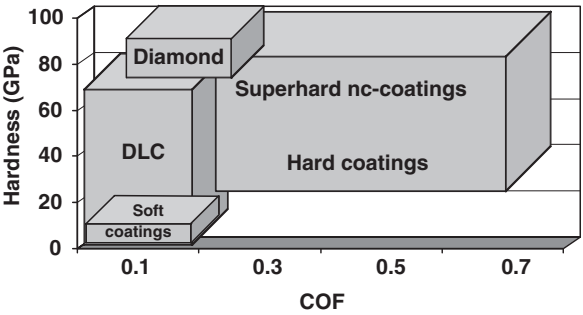

Fig. 5 A schematic representation of hardness and coefficients of friction (COF) of carbon-based and other coatings

DLC is the only material or coating that can provide both high hardness and low friction under dry sliding conditions. Most of the DLC films identified in Fig. 1 are inherently hard and lubricious under typical sliding conditions. Figure 5 illustrates this point better by categorizing various classes of tribological coatings with respect to their typical hardness and friction values. There is neither direct nor universal correlation between hardness and friction coefficients of engineering materials. This observation is especially true for DLC and other hard coatings, as shown in Fig. 5. Nonetheless, most DLC films available today are capable of providing not only high hardness but also low friction. Materials with high hardness and stiffness have, in general, high wear resistance. Diamond represents a prime example for this point. It has the highest known hardness and thus provides superior wear resistance when used as a bulk material or a thin coating.

As will be further realized from the other chapters of this book, DLC films have come a long way. They now represent some of the most interesting and important tribological materials that have ever been developed and have found numerous practical applications. Section B of the book provides an excellent overview of the fundamental tribological aspects of the DLC films that have been studied during the last 15 years. The chapters of this section cover almost all of the relevant topics, ranging from the role of hydrogen and carbon hybridization in friction and wear to the influence of incorporated heteroatoms as dopants or alloying elements in the carbonaceous network. The effects of third bodies on the tribology of DLC films are also covered, as are other important topics like environmental and thermal effects, super lubricity, and triboemission, as well as specific physical and chemical phenomena observed on sliding DLC surfaces under dry and lubricated sliding conditions.

4 Practical Applications

Since their initial discovery in the early 1950s, DLC films have emerged as one of the most valuable engineering materials for various industrial applications, including microelectronics, optics, manufacturing, transportation, and biomedical fields.

In fact, during the last two decades or so, DLC films have found uses in everyday devices ranging from razor blades to magnetic storage media [29]. For example, the thickness of the carbon overcoats used on magnetic hard disks has decreased almost linearly with time since the mid-1980s, and the DLC films used today are only a few nanometers thick, yet their durability and efficiency are much better than their predecessors. Moreover, these days most of us also appreciate the comfort and longevity of DLC-coated razor blades offered by several manufacturers.

Until the mid- to late 1990s, few industrial applications took advantage of the unique properties of DLC films. In fact, except for magnetic storage media, DLC films were not used in large volumes by industry. A few companies tried DLC films on eyeglasses and laser barcode scanners to improve their resistance to abrasion and/or scratching. Over the last decade, however, several new versions of DLC films (such as W-, Ti-, and Cr-doped films) have been synthesized, and with the introduction of industrial-scale, more robust coating systems, the production of high-quality DLC films has become rather easy and inexpensive. Over the past few years, researchers have made great strides in controlling the chemistry and hence the properties and performance of DLC films in actual applications. Current DLC films thus have the capacity to meet the increasingly stringent application requirements of advanced mechanical systems [29,42–44].

As a consequence, DLC films have made a significant positive impact on the manufacturing and transportation industries. These films are used in large volumes in various manufacturing industries to prevent wear and material transfer during drawing, stamping, molding, and rolling operations. In the transportation industry, many fuel injectors in high-performance diesel engines are now coated with DLC, as are a variety of other engine parts employed in race cars. In coming years, there is no doubt that DLC films will be found on several other critical engine components since future engine systems are expected to be much more compact, yet far more robust and efficient, than their predecessors. Downsizing with no compromise in performance and efficiency is likely to continue at an accelerated pace in the coming years and necessitate greater use of hard and low friction coatings like DLC.

We certainly owe much of the progress in the production and uses of DLC films to a very strong and progressive technology base acquired over the last two decades in the field of surface engineering. The current knowledge base and expertise in these fields are at a point where a coating specialist can produce a DLC coating tailored to meet or exceed the multifunctional property and performance demands of a given application. In particular, recent developments in magnetron sputtering, plasma-enhanced chemical vapor deposition, pulse-laser deposition, and cathodic arc technologies provide the kinds of flexibility that a specialist needs in designing and developing multifunctional DLC coatings having a multilayered or nanostructured/nanocomposite architecture that can provide excellent hardness, friction, toughness, and corrosion resistance. In fact, some nanocomposite films are quite hard, moisture insensitive, and self-lubricating, thus raising the prospect for truly “chameleon” coatings that can adapt their superior tribological properties to the surrounding environmental and thermal conditions [45]. When combined with duplex/multiplex surface

treatments, DLC coatings can enjoy additional functionalities that can meet the ever-increasing performance demands of more severe applications. Near-frictionless and near-wearless DLC films have also been synthesized in recent years and are currently being evaluated for a wide range of applications [46–48]. Several other forms of DLC films have greatly improved the performance, durability, and efficiency of numerous advanced mechanical systems.

Section C of this book is devoted to the industrial applications and future trends in DLC films. Although some of the applications are well-established and routine, others are still emerging. In the automotive field, as already mentioned, the use of DLC films in fuel injectors has become a routine operation. The other high-volume applications that are currently being explored for automobiles include tappets, valve lifters, and wrist pins. Even the door hinges and locking systems of some passenger cars are being coated with DLC rather than a thick layer of grease. Another rapidly growing practical application for DLC is in the textile industry, where various needles and components are coated with DLC. Computer hard disks have been using DLC for more than two decades, and their applications in other nano- to microscale devices (like MEMS) are being explored. Another emerging application for DLC films is in invasive and implantable medical devices. These films are currently being evaluated for their durability and performance characteristics in certain biomedical implants including hip and knee joints and coronary stents.

At present, high-quality DLC films are readily available from various commercial sources (such as CemeCon, Hauzer, Balzers, Ion Bond, HEF). Some of these DLC coatings are extremely hard and resilient, while others are relatively soft but capable of very low friction and wear coefficients. Films that contain unique crystalline nanostructures and/or nanophases are also available and have the ability to meet the increasingly stringent application conditions of advanced mechanical devices. These multifunctional nanocomposite DLC films are now routinely produced by both chemical and physical vapor deposition. These nanocomposite DLC films can also provide very impressive mechanical and tribological properties, while most of the recently developed nanocomposite coatings are able to provide superhardness but lack lubricity or low friction [49].

5 Future Directions

The field of carbon-based materials and coatings has enjoyed strong and growing interest from all kinds of scientific disciplines and industries during the last two decades. In particular, DLC coatings have attracted the most attention in recent years, mainly because they are cheap and easy to produce and offer exceptional properties for demanding engineering applications. Accordingly, in this book, we attempt to highlight some of the most important developments in the field of DLC films, in general, and their tribological properties, in particular. From the survey of the state of the art in scientific research and industrial practices that involve DLC

films, some chapters in the last section of this book discuss a range of future developments related to friction and wear of DLC films. Large-scale and low-cost manufacturing of DLC films will certainly lead to much broader applications in the near future. The present levels of industrial production of DLC films are probably still not reflective of their future potential, especially in the high-volume, large-scale production sectors (such as microelectronics, transportation, and manufacturing). There is a critical need to further reduce the coating costs and also improve process reliability to fulfill the quality and consistency requirements of these industrial sectors. More robust, low-temperature (<200°C) processes, with reduced sensitivity to unexpected changes in process parameters, are still needed for the deposition of DLC coatings in large-volume applications. There is also a need for processes that can produce high-quality coatings on a large number of different substrates, including not only low and high alloy steels, but also metallic (Al, Cu, Mg, etc.), ceramic, and polymeric (or rubber-like) materials.

For the last two decades, solid lubrication by thin coatings has mainly been used to stretch the limits of classical oils and/or fluid-based lubricants. An increasing demand to develop environment-friendly lubricants is leading to the development of new additives that are compatible with thin coatings, especially with the DLC films. In a related attempt to further improve the performance and durability of DLC films under lubricated sliding conditions, researchers have lately been creating special textures on their sliding surfaces. In particular, high-precision patterns created on DLC surfaces by excimer or femtosecond lasers have been shown to improve the tribological properties of these films under boundary-lubricated sliding conditions. Among the classical forms of DLC films, frontier research will also be devoted to the investigation of new forms of carbon-based solid lubricants, including multicomponent, nanotube, fullerene-like, and other composite carbon-based films.

References

1. Schmellenmeier H, 1953, Experimentelle Technik der Physik 1, 49.
2. Eisenberg S and Chabot R, 1971, J. Appl. Phys. 42, 2953.
3. Holland L and Ojha S M, 1976, Thin Solid Films 38, L17.
4. Spencer E G, Schmidt P H, Joy D C, and Sansalone F J, 1976, Appl. Phys. Lett. 29, 118.
5. Weissmantel C, Bewilogua K, Schurer C, Breuer K, and Zscheile H, 1979, Thin Solid Films 61, L1.
6. Arnoldussen T C and Rossi E M, 1985, Ann. Rev. Mater. Sci. 15, 379.
7. King F K, 1981, IEEE Trans. Magn. 17, 1376.
8. Enke K, Dimigen H, and Hubsch H, 1980, Appl. Phys. Lett. 36, 291.
9. Imamura A, Tsukamoto T, Shibuki K, and Takatsu S, 1988, Surf. Coat. Technol. 36, 161.
10. Andersson L P, 1981, Thin Solid Films 86, 193.
11. Robertson J, 1986, Adv. Phys. 35, 317.
12. Grill A, Patel V, and Meyerson B, 1991, Surf. Coat. Technol. 49, 530.
13. Miyoshi K, Wu R L C, and Garscadden A, 1992, Diam. Relat. Mater. 1, 639.
14. Ronkainen H, Koskinen J, Anttila A, Holmberg K, and Hirvonen J -P, 1992, Surf. Coat. Technol. 55, 428.

15. Erdemir A, Switala M, Wei R, and Wilbur P, 1991, Surf. Coat. Technol. 50, 17.
16. Donnet C, Belin M, Augé J C, Martin J M, Grill A, and Patel V, 1994, Surf. Coat. Technol. 68–69, 626.
17. Donnet C and Grill A., 1997, Surf. Coat. Technol. 94–95, 456.
18. Donnet C, 1998, Surf. Coat. Technol. 100–101, 180.
19. Donnet C, Le Mogne T, Ponsonnet L, Belin M, Grill A, and Patel V, 1998, Trib. Lett. 4, 259.
20. Donnet C, Fontaine J, Le Mogne T, Belin M, Heau C, Terrat J P, Vaux F, and Pont G, 1999, Surf. Coat. Technol. 120–121, 548.
21. Sanchez-Lopez J C, Donnet C, Fontaine J, Belin M, Grill A, Patel V, and Jahnes C, 2000, Diamond Relat. Mater. 9, 638.
22. Donnet C, Fontaine J, Grill A, and Le Mogne T, 2001, Trib. Lett. 9, 137.
23. Sanchez-Lopez J C, Donnet C, Loubet J L, Belin M, Grill A, Patel V, and Jahnes C, 2001, Diamond Relat. Mater. 10, 1063.
24. Fontaine J, Donnet C, Grill A, and Le Mogne T, 2001, Surf. Coat. Technol. 14 6–147, 286.
25. Sanchez-Lopez J C, Donnet C, Le Mogne T, 2002, Vacuum 64, 191.
26. Fernandez-Ramos C, Sanchez-Lopez J C, Belin M, Donnet C, Ponsonnet L, and Fernandez A, 2002, Diamond Relat. Mater. 11, 169.
27. Sanchez-Lopez J C, Belin M, Donnet C, Quiros C, and Elizalde E, 2002, Surf. Coat. Technol. 160, 138.
28. Sanchez-Lopez J C, Erdemir A, Donnet C, and Rojas T.C., 2003, Surf. Coat. Technol. 163–164, 444.
29. Erdemir A and Donnet C, 2000, Modern Tribology Handbook, B. Bhushan (ed.) CRC Press, Boca Raton, FL, pp. 871–908.
30. Erdemir A, 2002, J. Eng. Tribol. 216, 387.
31. Grill A, 1997, Surf. Coat. Technol. 94, 507.
32. Grill A, 1993, Wear 168, 143.
33. Tsai H C and Bogy D B, 1987, J. Vac. Sci. Technol. 5, 3287.
34. A. Erdemir and C. Donnet, 2006, J. Phys. D. 39, R311–327.
35. Robertson J, 2002, Mat. Sci. Eng. 37, 129.
36. Ban M, Ryoji M, Fujii S, and Fujioka J, 2002, Wear 253, 331.
37. Barriga J, Kalin M, Van Acker K, Vercammen K, Ortega A, and Leiaristi L, 2006, Wear 261, 9–14.
38. Ronkainen H, Koskinen J, Anttila A, Holmberg K, and Hirvinen J –P, 1992, Diam. Rel. Mater. 1, 639.
39. Horsfall R H, 1998, Proceedings of the 41st Annual Technical Conference, Society of Vacuum Coaters, Boston, MA, p. 60.
40. Sullivan J P, Friedmann T A, and Hjort K, 2001, MRS Bull. 26, 309.
41. Erdemir A, Eryilmaz O L, and Fenske G, 2000, J. Vac. Sci. Technol. A18, 1987.
42. Erdemir A and Donnet C, 2006, Wear: Materials, Mechanisms and Practice G. W. Stachowiak (ed.), Wiley, New York, pp. 191–209.
43. Lettington A H, 1998, Carbon 36, 555.
44. Hauert R, 2003, Diam. Rel. Mater. 12, 583.
45. Voevodin A A, Fitz T A, Hu J J, and Zabinski J S, 2002, J. Vac. Sci. Technol. 20, 1434–1444.
46. Zhou B, Wang L, Mehta N, Morshed S, Erdemir A, Eryilmaz O, Prorok BC, 2006, J. Micromech. Microeng. 16, 1374–1381.
47. Ajayi O O, Soppet M J, Erdemir A, Fenske G R, Shi B, Liang H, 2005, Tribol. Lubr. Technol. 61, 40–48.
48. Eryilmaz O L, Johnson J A, Ajayi O O, and Erdemir A, 2006, J. Phys.: Condens. Matter 18, S1751–S1762.
49. Erdemir A, Eryilmaz O L, Urgen Mm Kazmanli K, Mehta N, and Prorok B, 2006, Nanomaterials Handbook, Y. Gogotsi (ed.), CRC Press, Boca Raton, FL, p. 685.

Section A
General Overview on DLC Coatings

Classification of Diamond-like Carbons

J. Robertson

Abstract Diamond-like carbon (DLC) is an amorphous carbon (a-C) or hydrogenated amorphous carbon (a-C:H) thin film material with a high fraction of sp^3 carbon bonding. It is generally prepared by a deposition process which involves energetic ions. The sp^3 bonding is metastable compared to sp^2 bonding, unless it is stabilised by C–H bonds. The various types can be classified according to their fraction of sp^3 bonding and hydrogen (H). DLC variants alloyed with other elements such as Si, metals or B, N and F are also found.

Keywords sp^3, hydrogen content, density, ion beam, deposition, a-C:H, ta-C, alloys

1 Introduction

Diamond-like carbon (DLC) is an amorphous carbon (a-C) or hydrogenated amorphous carbon (a-C:H) thin film material with a high fraction of metastable sp^3 carbon bonding [1,2]. It is generally prepared by a deposition process which involves energetic ions. These ions give rise to the sp^3 bonding, which is metastable compared to sp^2 bonding, unless it is stabilised by C–H bonds. The ion-induced process is distinct from plasma polymerisation, where the C sp^3 bonding arises from a condensation of C–H groups with the evolution of molecular H_2. DLC can be alloyed with other elements such as Si, metals or B, N and F. This chapter focuses first on the unalloyed material and then mentions the alloyed varieties.

2 Phase Diagram

The types of DLC can be displayed on a ternary phase diagram, as shown in Fig. 1. This shows the fraction of sites in the alloy that are C sp^3, C sp^2 or hydrogen (H). The diagram was first derived by Jacob and Moller [3]. Note that here the total

Engineering Department, Cambridge University, Cambridge CB2 1PZ, UK

C. Donnet and A. Erdemir (eds.), *Tribology of Diamond-Like Carbon Films: Fundamentals and Applications*.

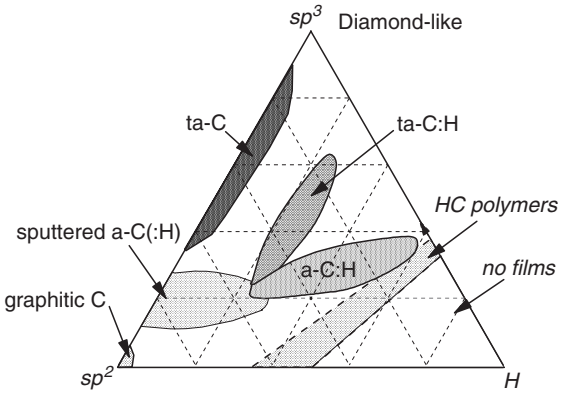

Fig. 1 Ternary phase diagram of the C, H system [2]

fraction of atoms adds up to 1. One should be careful with cases quoting the sp^3 fraction (of C only), or the H/C ratio instead of the H/(C + H) ratio.

The phase diagram consists of three main regions. The first region is H-free a-C along the left axis. The sp^2 a-C is typically glassy carbon, or a-C made by pyrolysis of hydrocarbon polymers or by evaporation, and is not DLC. An a-C of higher sp^3 content, but still without H, is typically made by sputtering, and is a DLC. The modern variants of sputtering, including unbalanced magnetron sputtering can create DLCs with quite large sp^3 contents. At even higher sp^3 content, there is a specific type of a-C designated as tetrahedral amorphous carbon or ta-C. This is made from ion or plasma beams with a high ion fraction and a narrowly defined ion energy. These methods include mass selected ion beam (MSIB) deposition, filtered cathodic vacuum arc (FCVA) and pulsed laser ablation deposition (PLD) [4–7]. Deposition occurs at room temperature.

The second region of the phase diagram is the bottom right of the figure, where the H content is so large that the material cannot form a fully connected network, but only gas molecules [3]. The boundary line of this region is defined by the compositions of C_2H_2 on the sp^2-H axis and $(CH_2)_n$ on the sp^3-H axis.

In between these regions lies the region of a-C:H materials. a-C:H is produced typically by plasma-enhanced chemical vapour deposition (PECVD) of hydrocarbon molecules, or by the reactive sputtering of graphite in an atmosphere including H or by ion beam deposition from a hydrocarbon gas precursor [8–13]. The typical PECVD or sputtering process will produce an a-C:H which lies in the region indicated as a-C:H. This can range from the material with only 20–25% H content up to those with very high H contents of ~60% of the total number of atoms.

As PECVD has advanced, it is possible to create the so-called high-density plasmas, such as by electron cyclotron resonance (ECR), inductively coupled plasma (ICP), the plasma beam source (PBS) or electron cyclotron wave resonance

(ECWR). These methods produce more dense a-C:Hs which we call highly tetrahedral hydrogenated amorphous carbon or 'ta-C:H' [14,15]. The high-density plasmas are achieved by operating at a pressure lower than the usual PECVD and by using magnetic fields to give long electron path lengths, which encourages a high plasma ionisation. As conventional PECVD processes improve, the zones of a-C:H and ta-C:H begin to merge.

3 Diamond-like Character

The 'diamond-like' character of DLC films obviously arises from its C–C sp^3 bonds. The DLC is an amorphous phase and atomically, it is a random network [2,16]. The mechanical properties of this network can be considered as an alloy of different bonding components, C–C sp^3, C–C sp^2 and C–H bonds. The Young's modulus, hardness and general diamond-like quality arise from the C–C sp^3 bonds. The C-C sp^2 bonds do not contribute much. The C–H bonds do not link up the network, so mechanically they are just like a dangling bond, and contribute nothing to mechanical properties [16]. Thus, the Young's modulus is found to depend monotonically on the mean C–C coordination number, or in other words, the C–C sp^3 fraction [17]. It is found that the density of a-C varies linearly on the C–C sp^3 fraction [18] (see Fig. 9).

It is found that the Young's modulus varies with the ion energy involved in deposition in a standard way. For H-free a-C, the modulus and sp^3 content pass through a maximum at an ion energy of about 100 eV, as in Fig. 2(a). For lower and

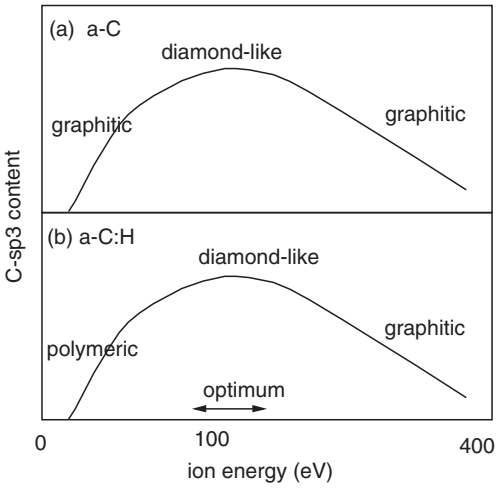

Fig. 2 Schematic variation of fractional diamond-like character of (a) a-C and (b) a-C:H with deposition ion energy

higher ion energies, the sp^3 content is less, the sp^2 content is larger and the films are more graphitic. For a-C:H films, the variation is similar. The maximum generally occurs at an ion energy of about 100 eV (Fig. 2(b)). At the optimum, the C sp^3 fraction is a maximum (but not necessarily so high). But at lower ion energies, the films contain many C(sp^3)–H bonds and they are more 'polymeric'. At higher ion energies, the sp^2 fraction increases and the films are more graphitic. Thus there is a difference in structure at low ion energies, between a-C and a-C:H. The actual sp^3 and H contents were determined by nuclear magnetic resonance (NMR) in a-C:H films [12,13].

4 Deposition Process

The sp^3 bonding which characterises DLC arises from the ion-assisted nature of the deposition process. This means that, to zeroth order, the resulting a-C or a-C:H depends primarily on this ion energy [8]. Strictly, it depends on the energy per incident C ion [19]. Thus, for a-C:H, it also depends somewhat on the precursor hydrocarbon molecule, C_nH_m.

There are two aspects to this. Firstly, the sp^3 content in pure a-C arises from the subplantation process, which depends on the ion energy [20]. Secondly, the H content of the a-C:H is lower than that of the precursor hydrocarbon species. H is lost due to ion bombardment, and this depends primarily on the ion energy.

The subplantation process creating sp^3 sites in a-C occurs as follows [19,20] (Fig. 3). Normally, when atoms are added to a solid, they add to the surface, and may diffuse about on the surface to find the lowest energy position. In subplantation, the incoming C ion has enough energy to pass through the outer layer of the film, enter

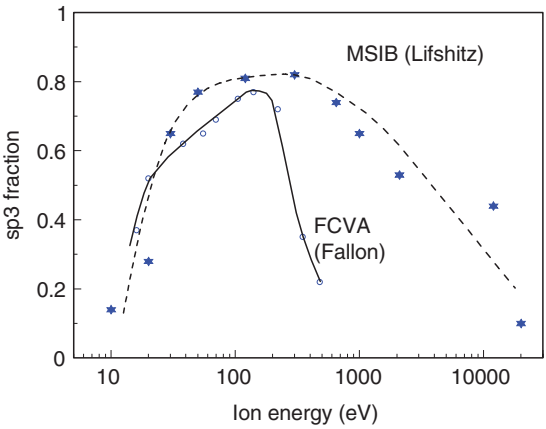

Fig. 3 The subplantation process of an energetic carbon ion into a C film. Subplantation of a diatomic C species into the film, with the breaking of the C_2 species

the film and cause subsurface growth. This gives rise to a local densification. Now DLC, like diamond, is metastable. The density of sp^3 diamond is ~50% higher than that of sp^2-bonded graphite. By analogy, the coordination of atoms in a-C follows the local coordination. Any surface growth of a-C will be unconstrained, normal to the film surface and will be in the lowest energy state, which is sp^2. But, subplantation will give rise to more dense, metastable zones, where the bonding will convert into sp^3. The mean coordination will be similar to that in bulk ta-C.

The sp^3 content and thus density depends in a standard way on the ion energy [19]. The maximum sp^3 content occurs at an ion energy per C ion of 100 eV. A lower ion energy results in a greater fraction not subplanting, but sticking to the other surface as sp^2. A higher ion energy also results in a lower sp^3 content. This occurs because the excess ion energy allows atomic relaxation around the implanted atom and a reversion of some sp^3 sites to the sp^2 ground state. The exact nature of this process is still debated. Roughly, it involves a thermal spike, which results in diffusion of the excess C atoms to the surface [19]. However, molecular dynamics simulations show that the real process is more complex than this simple, continuum description [21].

A similar process will occur in the formation of a-C:H and ta-C:H [14]. In addition, the ion bombardment will cause the loss of H, primarily by the displacement of H from C–H bonds to form H_2 molecules, which then leave the network [22,23]. This happens within the ion range of the incident CH_x^+ ion. Now, H loss in a-C:H involves a different process than in a-Si:H. a-Si:H with a lower H content is promoted by using a H-diluted silane plasma [24]. Atomic H from this plasma abstracts H from Si-H bonds [25], which leaves as H_2. The reduced H content eventually leads to the formation of microcrystalline Si which contains only ~1% H, compared to the typically 10% H in a-Si:H [24].

The opposite situation seems to occur in a-C:H, which when grown in H-diluted plasmas seems to have similar or higher H content than a-C:H grown from pure hydrocarbons [26,27]. H abstraction can occur, but it does not seem to lead to a lower H content. Presumably, as atomic H abstracts an H, it also adds an H to the resulting C dangling bond, as shown in Fig. 4, on the right. Thus the main process remains the displacement of H from C–H bonds by incident ions, shown in Fig. 4, on the left.

The overall result is that for a-C:H, the H content and sp^3 content decline monotonically with increasing hydrocarbon ion energy [2,8,12], as shown in Fig. 5. Displacement yields increase with ion energy. The hardness and diamond-like nature of the a-C:H go through a maximum, but this is a maximum of C–C bonded content, not that of a simple C sp^3. This is because at 0 eV, the C sp^3 content is at a maximum. However, it is all bonded to H atoms. As the ion energy increases, the H content decreases. The sp^3 content does not decrease as fast. Thus, there comes an ion energy where the C–C bonded fraction, excluding the C–H bonds, reaches a maximum. This is the composition of maximum modulus and hardness. For even higher ion energies, the sp^3 content decreases too much, and the C–C content and modulus now decreases. This is summarised in Fig. 6.

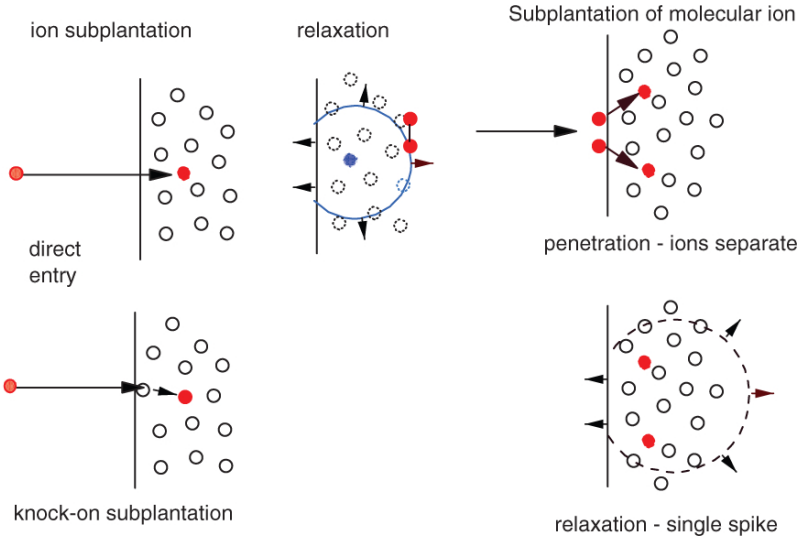

Fig. 4 Processes leading to loss and gain of hydrogen in a-C:H films

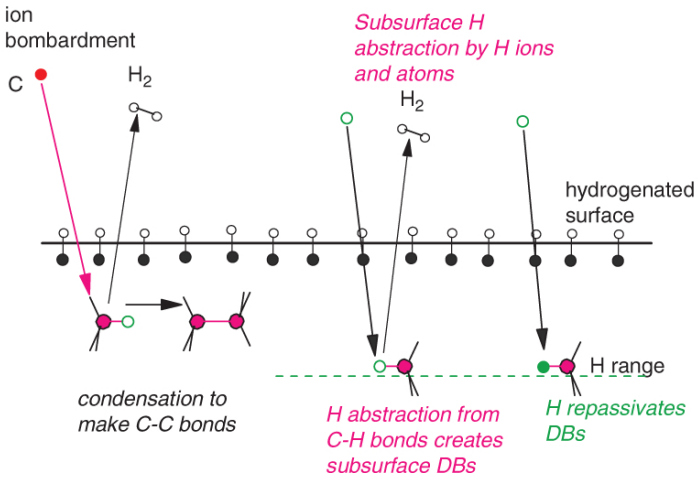

Fig. 5 Experimental dependence on sp^3 content, H content, mass density and optical band gap on the bias voltage for PECVD a-C:H films, deposited from methane or benzene

Generally, many applications would desire films with the maximum modulus or hardness. Thus, these would use ion energies around 100 eV. There are other cases though. For ta-C, in the FCVA method, ions leave the cathode with an ion energy of about 30 eV, unless an explicit bias voltage is attached to the substrate. This so-called floating potential is enough to give a high sp^3 content, and is often used.

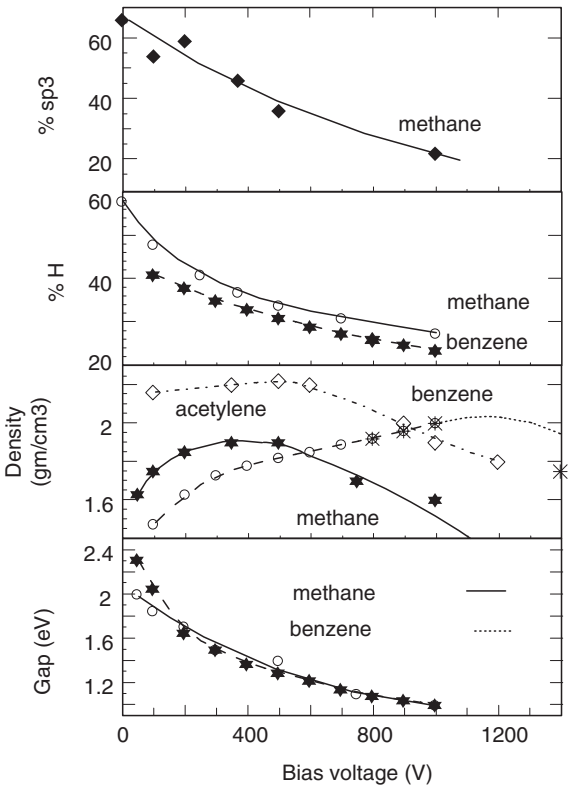

Fig. 6 Variation of the sp^3 fraction with the ion energy for ta-C deposited by an early cathodic arc [4] and by mass-selected ion beam deposition [6]

5 Growth Rates in PECVD

The precursor molecule for a-C:H growth is generally chosen with regard to the film growth rate. The growth rate is found to be strongly correlated to the ionisation potential of the molecule [8], as seen in Fig. 7. Unsaturated molecules with low ionisation potentials such as acetylene give much higher growth rates than methane.

Acetylene is also favoured by many workers because it has the lowest H content (along with benzene) of the usual precursor molecules, and thus the H content of the resulting a-C:H film also tends to be lower [19]. This gives the densest films (see Fig. 8). As the Young's modulus is related to the fraction of C–C bonding, lowering the H content tends to raise modulus, and thus hardness, for a given sp^3 content.

A disadvantage of acetylene as source gas is that it is impure, with about 1% impurity, compared to the highly pure availability of electronic grade methane.

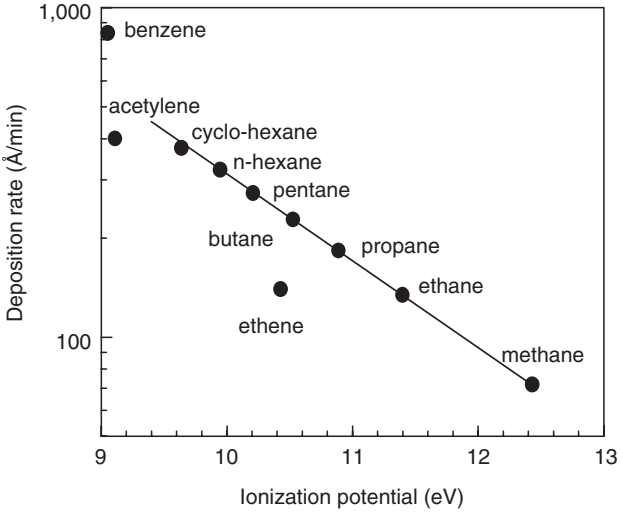

Fig. 7 Variation of PECVD growth rates of a-C:H on the ionisation potential of the precursor species

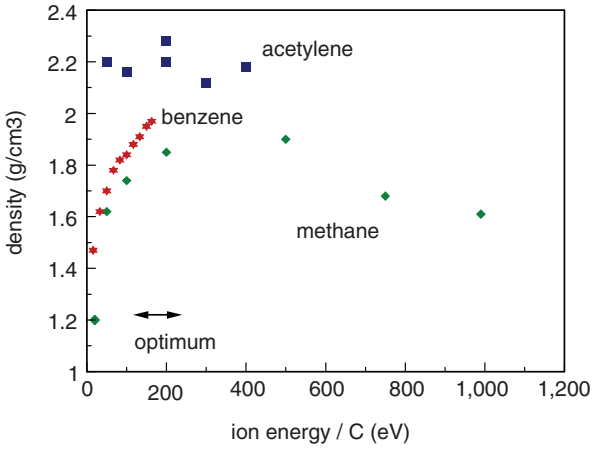

Fig. 8 Variation of a-C:H density with ion energy per C ion, for various precursor molecules

A second reason not to use acetylene is to access high ion energies. It is the ion energy per C atom that matters. Thus, one might want to deposit at a high ion energy of say 500 eV per C in order to reduce stress. An ion energy per C atom requires 500 eV for methane but 1,000 eV for acetylene. The former is experimentally easier, cheaper and safer.

An unusual combination is to deposit a-C:H from methane at a high ion energy (600–1,200 eV). This situation leads to the so-called superlow friction films of a-C:H which have been widely studied by Erdemir et al. [28–33]. The high ion energy may allow thicker films, due to stress relaxation, as discussed shortly. For methane, the ion energy per C atom is the same as the nominal value. Thus the ion energy is well over the optimum of value of 100 eV corresponding to maximum sp^3 content. Thus the C bonding is partly graphitic. But the high ion energy also leads to an implantation of much of the H atoms of the incident methane, so that the film has an unusually higher H content, for a-C:H films of this sp^2 content. This combination of high H content and higher sp^2 content is unique to methane as precursor. This also leads to be high surface H content, which appears to lead to very low friction coefficients. The friction processes of a-C:H and of diamond have been modelled by Harrison [34,35].

6 Stress

A second situation is the desire for thick films. The main disadvantage of DLC and ion beam methods is that they lead to films with a large intrinsic compressive stress. This stress causes delamination in thicker films. There is a maximum thickness of the film before it delaminates [2].

There are a number of methods to minimise this effect, such as using an adhesion layer of Si, a graded adhesion layer, multi-layered or metal alloying. Another method is to use high-energy pulsed deposition as in the plasma ion implantation immersion (PIII) process. In this case, the film is deposited with a mean ion of say 100 eV, but it is also subjected to short (~10 μs) pulses of much higher bias voltage of 1,000 eV or more. The high-energy ions cause a stress relaxation [36,37]. It appears that the high-energy ions allow some atomic relaxation which relieves the stress. A small amount of the sp^3 sites convert to sp^2, but not too many, so the overall diamond-like character remains. This process will work for both ta-C and a-C:H, in principle.

7 Density: sp^3 Plot

There are two typical variations of density with sp^3 content. The first, for H-free a-C, is a linear variation [18], expected from Vegard's law for an alloy. The second is for a-C:H. If it is ta-C:H prepared only from high-density plasma sources, the density increases monotonically with sp^3 content up to considerable sp^3 contents. Often, the density reaches a maximum, then the H content rises too rapidly and the large molecular size of C–H groups causes the density, which passes through a maximum, to fall at high sp^3 values (Fig. 9).

Raman has recently been found to be able to follow these trends in local bonding [38,39]. This is described in detail in Chapter 2. It was found that the width of the

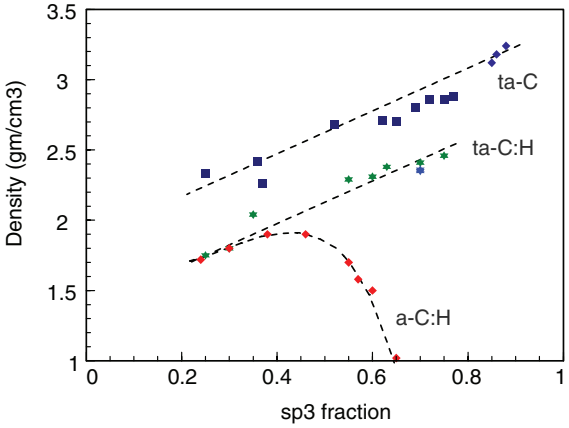

Fig. 9 Variation of the mass density derived from XRR or EELS with the total C sp^3 fraction, for ta-C, ta-C:H and a-C:H films

Raman G peak (FWHM of G) was proportional to the density, for most a-C's. It was also found that the dispersion of the wave number of the G peak with varying excitation energy (G dispersion) was proportional to the sp^3 content. Thus, a plot of G width versus G dispersion mirrors the dependence of density on sp^3 content shown in Fig. 9.

8 Alloyed DLCs

The properties of DLCs have been of sufficient interest that groups have naturally extended the range of materials by alloying with various other elements [40–45] (see Chapters 9, 12, 13, 19 and 24 for further details). The motivation for this is varied and the problem of compressive stress has been a major limitation. This led to the study on the effect of alloying with various transition metals, such as Ti, Cr and Al. Al in particular was found to reduce the stress, and thus allow growth of thicker films. These can be referred to as a-C:Me or a-C:H:Me, respectively. Graded layers have been employed. Alloying with transition metals is also motivated by a need to increase the mechanical toughness of the films. DLC is a rather brittle ceramic. Alloying with carbide-forming metals make it tougher due to the formation of nanosized carbide inclusions. Addition of Si to a-C:H is also found to lower stress and reduce the friction coefficient in humid conditions [44].

The second motivation for alloying with other elements is to modify the surface energy. Addition of F lowers the surface energy considerably. Si, N and B modify it. These can be referred to as a-C:X or a-C:H:X, respectively [42]. Films, with the addition of N in particular, have been extensively studied due to the interest in the hypothetical compound C_3N_4 in which C is sp^3 bonded and N is sp^2 bonded [43].

However, this effort is now declining, as it appears that this material cannot be prepared in the desired state.

9 Conclusions

The various forms of DLC is an amorphous carbon (a-C) or hydrogenated amorphous carbon (a-C:H) have been classified. They are materials with a high fraction of sp^3 carbon bonding [1,2]. They are prepared by a deposition process which involves energetic ions. These ions give rise to the sp^3 bonding. The ion-induced process is distinct from plasma polymerisation, where the C sp^3 bonding arises from a condensation of C–H groups with the evolution of molecular H_2. DLC can also be alloyed with other elements such as Si, metals or B, N and F, in which case they are referred to as a-C:Me, a-C:H:Me, a-C:X or a-C:H:X, respectively.

References

1. J. Robertson, Adv. Phys. 35, 317 (1986).
2. J. Robertson, Mat. Sci. Eng. R. 37, 129 (2002).
3. W. Jacob and W. Moller, App. Phys. Lett. 63, 1771 (1993).
4. P. J. Fallon, V. S. Veerasamy, C. A. Davis, J. Robertson, G. A. J. Amaratunga, W. I. Milne and J. Koskinen, Phys. Rev. B 48, 4777 (1993).
5. M. C. Polo, J. L. Andujar, J. Robertson and W. I. Milne, Diam. Relat. Mater. 9, 663 (2000).
6. Y. Lifshitz, G. D. Lempert, E. Grossman, I. Avigal, C. Uzan-Saguy, R. Kalish, J. Kulik, D. Marton and J. W. Rabalais, Diam. Relat. Mater. 4, 318 (1995).
7. V. I. Merkulov, D. H. Lowndes, G. E. Jellison, A. A. Puretzky and D. B. Geohegan, App. Phys. Lett. 73, 1228 (1999).
8. P. Koidl, C. Wagner, B. Dischler, J. Wagner and M. Ramsteiner, Mat. Sci. Forum 52, 41 (1990).
9. J. W. Zou, K. Reichelt, K. Schmidt and B. Dischler, J. App. Phys. 65, 3914 (1989).
10. W. M. M. Kessels, J. W. A. M. Gielen, M. C. M. van de Sanden, L. J. van Ijzendoorn and D. C. Schram, Surf. Coat. Technol. 98, 1584 (1998).
11. T. Schwarz-Selinger, A. von Keudell and W. Jacob, J. App. Phys. 86, 3968 (1999).
12. M. A. Tamor, W. C. Vassell and K. R. Carduner, App. Phys. Lett. 58, 592 (1991).
13. C. Donnet, J. Fontaine, F. Lefevre, A. Grill, V. Patel and C. Jahnes, J. App. Phys. 85, 3264 (1999).
14. M. Weiler, S. Sattel, T. Giessen, K. Jung, H. Ehrhardt, V. S. Veerasamy and J. Robertson, Phys. Rev. B. 53, 1594 (1996).
15. M. Weiler, K. Lang, E. Li and J. Robertson, App. Phys. Lett. 72, 1314 (1998).
16. J. Robertson, Phys. Rev. Lett. 68, 220 (1992).
17. A. C. Ferrari, J. Robertson, M. G. Beghi, C. E. Bottani, R. Ferulano and R. Pastorelli, App. Phys. Lett. 75, 1893 (1999).
18. A. C. Ferrari, A. LiBassi, B. K. Tanner, V. Stolojan, J. Yuan, L. M. Brown, S. E. Rodil, B. Kleinsorge and J. Robertson, Phys. Rev. B. 62, 11089 (2000).
19. J. Robertson, Diam. Relat. Mater. 3, 361 (1994).
20. Y. Lifshitz, S. R. Kasi and J. W. Rabalais, Phys. Rev. Lett. 68, 620 (1989).
21. N. A. Marks, App. Phys. Lett 89131924 (2006).

22. D. Boutard, W. Moller and J. B. M. U. Scherzer, Phys. Rev. B. 38, 2988 (1988).
23. C. Hopf, A. von Keudell and W. Jacob, J. App. Phys. 93, 3352 (2003).
24. U. Kroll, J. Meier, A. Shah, S. Mikhailov and J. Weber, J. App. Phys. 80, 4971 (1996).
25. J. Robertson, J. App. Phys. 87, 2608 (2000).
26. A. vonKeudell, T. Schwarz-Sellinger and W. Jacob, J. App. Phys. 89, 2979 (2001).
27. C. Hopf, W. Jacob and A. von Keudell, J. App. Phys. 97, 094904 (2005).
28. A. Erdemir, I. B. Nilufer, O. L. Eryilmaz, M. Beschliesser and G. R. Fenske, Surf. Coat. Technol. 120, 589 (1999).
29. A. Erdemir, O. L. Eryilmaz, I. B. Nilufer and G. R. Fenske, Surf. Coat. Technol. 133, 448 (2000).
30. A. Erdemir, Trib. Int. 37, 1005 (2004).
31. J. A. Johnson, J. B. Woodford, X. Chen, J. Andersson, A. Erdemir and G. R. Fenske, J. Appl. Phys. 95, 7765 (2004).
32. J. C. Sanchez-lopez, A. Erdemir, C. Donnet and T. C. Rojas, Surf. Coat. Technol. 163, 444 (2003).
33. C. Donnet and J. Fontaine, A. Grill, T. LeMonge, Trib. Letts. 9, 137 (2000).
34. G. T. Gao, P. T. Mikulski and J. A. Harrison, J. Am. Chem. Soc. 124, 7202 (2002).
35. G. T. Gao, P. T. Mikulski, G. M. Chateauneuf and J. A. Harrison, J. Phys. Chem. B. 107, 11082 (2003).
36. M. M. M. Bilek, D. R. McKenzie and W. Moeller, Surf. Coat. Technol. 186, 21 (2004).
37. M. M. Bilek et al., Thin Solid Films 482, 69 (2005).
38. A. C. Ferrari and J. Robertson, Phys. Rev. B. 61, 14095 (2000).
39. C. Casiraghi, A. C. Ferrari and J. Robertson, Phys. Rev. B. 72, 085401 (2005).
40. R. Memming, H. J. Tolle and P. E. Wierenga, Thin Solid Films 143, 31 (1986).
41. C. P. Klages and R. Memming, Mater. Sci. Forum. 52, 609 (1989).
42. http://www.ist.fraunhofer.de/english/c-products/tab/complete.html
43. S. Muhl and J. M. Mendez, Diam. Relat. Mater. 8, 1809 (1999).
44. K. Oguri and T. Arai, Surf. Coat. Technol. 47, 710 (1991).
45. S. Zhang, X. L. Bui, X. T. Zeng and X. M. Li, Thin Solid Films 482, 138 (2005).

Non-destructive Characterisation of Carbon Films

Andrea C. Ferrari

Abstract The availability of reliable characterisation tools for carbon films down to a few atomic layers' thickness is one of the most decisive factors for technology development and production. In particular, non-destructive techniques are preferred. This chapter reviews the use of x-ray reflectivity, surface acoustic waves, and Raman spectroscopy to characterise carbon films in terms of density, thickness, layering, elastic constants, roughness, structure, and chemical composition. Raman spectroscopy, in particular, allows to probe of most of the materials properties, even if indirectly. The use of atomic force microscopy (AFM) will be considered to assess the basic growth mechanism of carbon films. The measurement of thermal conductivity of carbon films will also be reviewed.

Keywords diamond-like carbon, structure, Raman spectroscopy, characterization

1 Introduction

The availability of reliable characterisation tools for carbon films down to a few atomic layers' thickness is one of the most decisive factors for technology development and production. In particular, non-destructive techniques are preferred.

Rather than reviewing all possible methods suitable to assess carbon films, here I focus on x-ray reflectivity, surface acoustic waves, and Raman spectroscopy. For carbon films, the combination of these methods allows a full structural characterisation in terms of density, thickness, layering, elastic constants, roughness, structure, and chemical composition. Raman spectroscopy, in particular, allows the assessment of most of the materials' properties, even if indirectly. I will also show how atomic force microscopy (AFM) can be used to study the basic growth mechanism of carbon films. Finally, I will review the thermal conductivity of carbon films.

Many other techniques are utilised in literature, for example, EELS, NMR, XANES, and XPS/X-AES. These are either destructive, or require isotope enhancement

Department of Engineering, University of Cambridge, Cambridge, CB3 OFA, UK
email:acf26@eng.cam.ac.uk

C. Donnet and A. Erdemir (eds.), *Tribology of Diamond-Like Carbon Films: Fundamentals and Applications*.

or preferentially probe the samples surface. As such they will not be considered in detail here. However, the calibration of some of the correlations presented is done with EELS, NMR, or XPS, as highlighted in the text.

2 Properties of Carbon Films

The great versatility of carbon materials arises from the strong dependence of their physical properties on the ratio of sp^2 (graphite-like) to sp^3 (diamond-like) bonds. There are many forms of sp^2-bonded carbons with various degrees of graphitic ordering, ranging from microcrystalline graphite to glassy carbon. In general, an amorphous carbon can have any mixture of sp^3, sp^2 and even sp^1 sites, with the possible presence of hydrogen and nitrogen. The compositions of nitrogen-free carbon films are conveniently shown on the ternary phase diagram (Fig. 1a).

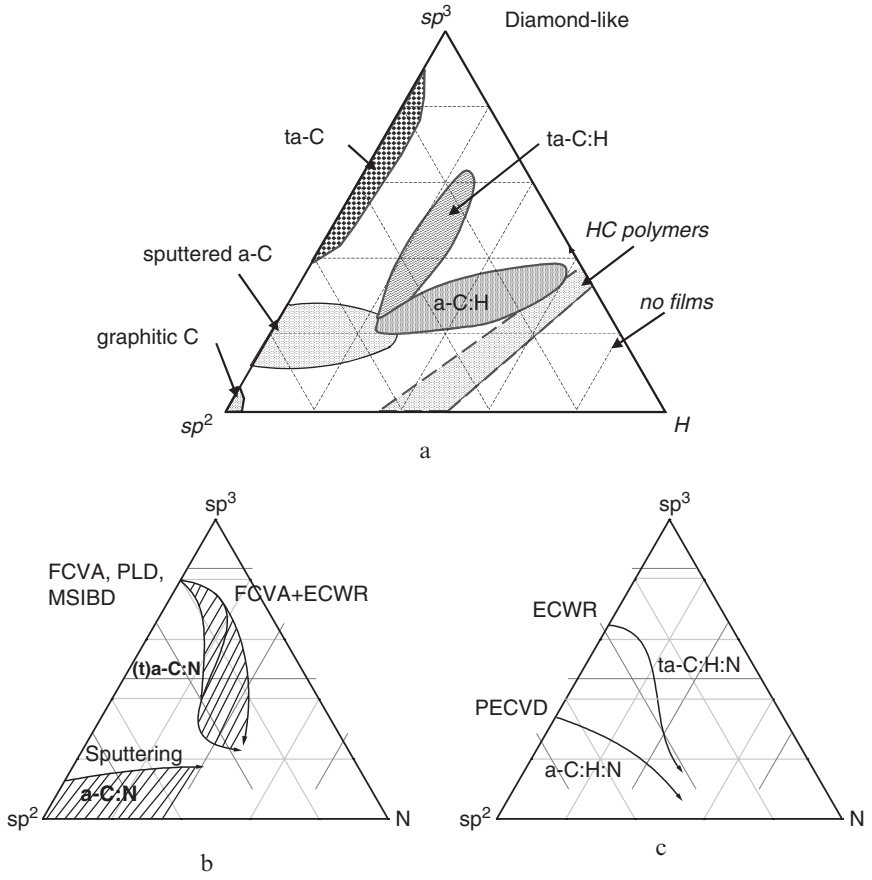

Fig. 1 (a) Ternary phase diagram of amorphous carbons. The three corners correspond to diamond, graphite and hydrocarbons respectively. (b,c) Ternary phase diagrams of amorphous carbon nitride alloys, without hydrogen (b) or with hydrogen (c), showing sp^2 C, sp^3 C and N

The key parameters are: (1) the sp^3 content; (2) the clustering of the sp^2 phase; (3) the orientation of the sp^2 phase; (4) the cross-sectional nanostructure; 5) the H or N content.

Tetrahedral amorphous carbon (ta-C) is the diamond-like carbon (DLC) with the maximum C–C sp^3 content. This material can be grown with deposition techniques involving energetic ions such as filtered cathodic vacuum arc (FCVA), mass selected ion beam deposition (MSIBD), and pulsed laser deposition [1–7]. The sp^3 content alone mainly controls the elastic constants [8], but films with the same sp^3 and H content but different sp^2 clustering, sp^2 orientation, or cross-sectional nanostructure can have different optical and electronic properties [9]. As we move from ordered graphite to nanocrystalline graphite, to amorphous carbon, and finally to sp^3-bonded ta-C, the sp^2 groups first become smaller, then disordered, and finally change from ring to chain configurations [9–11]. The evolution of the sp^2 phase clustering can be represented by the *amorphisation* trajectory [9–11] (Fig. 2) consisting of three stages from graphite to ta-C: (1) graphite→nanocrystalline graphite (nc-G); (2) nanocrystalline graphite→ sp^2 a-C; (3) a-C→ta-C. Note how the sp^2 clustering evolution and the sp^3 content evolution follow two distinct paths (Fig. 2b).

We classify hydrogenated amorphous carbons into four types [12]:

1. a-C:H films with the highest H content (40–60 at. %). These films can have up to 70% sp^3. However, most of the sp^3 bonds are hydrogen terminated and this material is soft and has low density. We call these films polymer-like a-C:H (PLCH). Their band gap ranges from 2 to 4 eV. They are usually deposited by plasma-enhanced chemical vapour deposition (PECVD) at low bias voltage [13–15].

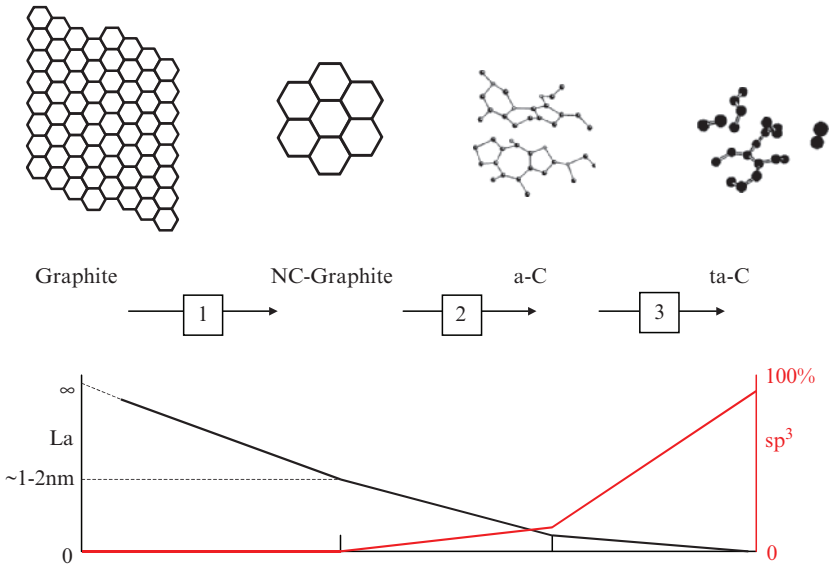

Fig. 2 (a) Variation of the sp^2 configuration along the three amorphization stages. (b) Schematic comparison of the evolution of the sp^2 cluster size (L_a) and sp^3 content. Note that in stages 1–2 to a strong sp^2 cluster size decrease corresponds a relatively small sp^3 increase, whilst the opposite is seen in stage 3

2. a-C:H films with intermediate H content (20–40 at. %). Even if these films have lower overall sp^3 content, they have more C–C sp^3 bonds than PLCH. Thus, they have better mechanical properties. Their optical gap is between 1 and 2 eV. We call them diamond-like a-C:H (DLCH). They are usually deposited by PECVD [12–14], or electron cyclotron resonance (ECR), or reactive sputtering at moderate bias voltage [12,14–18].
3. Hydrogenated tetrahedral amorphous carbon films (ta-C:H). ta-C:H films are a class of DLCH in which the CC sp^3 content can be increased whilst keeping a fixed H content, as in Fig. 1a. Many films defined in literature as ta-C:H are just DLCHs. However, due to the highest sp^3 content (~70%) and 25–30 at. % H, ta-C:Hs are really a different category as indicated by their Raman spectra, their higher density (up to 2.4 g/cm^3) and Young's modulus (up to 300 GPa) [1,8,19]. Their optical gap can reach 2.4 eV [20]. These films are deposited by high-density plasma sources such as electron cyclotron wave resonance (ECWR) [20,21] and plasma beams (PBS) [22,23].
4. a-C:H with low H content (less than 20 at. %). They have a high sp^2 content and sp^2 clustering. The gap is under 1 eV. We call them graphite-like a-C:H (GLCH). They are usually deposited by PECVD at high bias [13,14] or by magnetron sputtering [18].

Carbon nitrides are another important class of carbons often used for tribological applications. As for hydrogenated amorphous carbons, it is possible to classify the bonding in carbon nitrides into four types, based on the bonding in the corresponding N-free film [24]. The changes in the properties of carbon nitrides N content is increased should be compared with the corresponding N-free films. Thus, the variation of mechanical and electronic properties when N is added to a sp^2-bonded carbon differs from when N is added to a high sp^3 film. This is true whether H is present or not. There are four basic types of carbon nitrides, derived from sp^2 a-C, tetrahedral amorphous carbon (ta-C), a-C:H (from polymeric to diamond-like) and ta-C:H. Figure 1b and c shows the ternary phase diagrams which summarise the compositions of carbon nitrides with increasing N content [24]:

1. a-C:N. Here N is introduced in amorphous carbons with a high fraction of sp^2 bonds. An unusual aspect of these films is that a-C:N deposited above 200°C can become nanostructured, with a strong cross-linking between graphitic planes, which gives an increase in mechanical hardness and large elastic recovery [25–28]. However, this does not require an increase of the sp^3 fraction (see Fig. 1b,c) but can rather be seen as an increase in disorder [26–28]. This beneficial effect is exploited in carbon nitrides used in magnetic storage, since the deposition of the carbon layer on the disk is performed at ~200°C, the process temperature resulting from the magnetic layer deposition.
2. ta-C:N. This group includes films deposited by MSIBD [29], PLD [30], or FCVA [31–34], either under N_2 atmospheres or by nitrogen-assisted beams. Low pressure deposition and high ionisation ensure that film growth is controlled by ions. Resistivity and optical gap decrease when compared to the pure ta-C films

[24]. Generally, the sp^3 content of ta-C remains high at 80–90% up to about 10% N, and then the sp^3 content and density fall rapidly [24]. This sharp decrease is due to the high deposition pressure [35]. The sp^2 sites begin to clustering at low N contents (1%), before the sp^3 to sp^2 transition and this decreases the band gap [24]. Note that, although a general decrease of sp^3 content with N is observed, the trends are different according to the deposition systems [24]. This implies that the evolution of the sp^3 fraction and the degree of clustering of the sp^2 phase can be different for films of the same N/C ratio [24].

3. a-C:H:N. These are usually grown by PECVD [36–38]. a-C:H:N films have been deposited using a mixture of an hydrocarbon gas, such as methane, acetylene, benzene, and N_2 or NH_3. N incorporation is hindered if a high fraction of N_2 or a high substrate temperature is used. The best conditions for nitrogen incorporation correspond to the lowest H content in the gas phase. In contrast to a-C:N, the hardness in a-C:H:N decreases with N, due to the formation of more terminating groups, such as NH_2 and nitrile [24]. Higher substrate temperatures and bias decrease the overall N and H content, giving a more graphite-like material. In principle each a-C:H:N can be further classified as DLCHN, PLCHN. GLCHN, by considering the properties of the pristine a-C:Hs and their classifications, as described above.
4. ta-C:H:N. These are prepared by high-density plasma sources, such as electron cyclotron wave resonance (ECWR) [39,40], ECR [41,42], or helicon sources [43]. Introducing nitrogen into ta-C:H induces clustering of the sp^2 phase, without an appreciable sp^3 to sp^2 conversion, up to ~20% at N, with a corresponding increase in conductivity and decrease of optical gap. Higher N contents cause a transition to a lower sp^3 fraction and give softer films similar to PLCHN [24].

There are then many other carbon films studied in literature, which evolve from the pattern presented so far. Here we will not deal with them in detail. The discussed characterisation techniques can be extended to their case. For instance, their Raman spectra can be easily understood by considering the effect on the sp^2 clustering of the heteroatoms and using the rules for the interpretation of the spectra we will present in Section 5. Clearly, if carbides are formed, they will also show their Raman signature.

It is worth mentioning: (1) fluorinated DLCs, which can be used as low dielectric constant insulators to improve the switching performances of circuits (see, e.g. Ref. [44]). (2) Amorphous carbon–silicon alloys (a-C_{1-x}:Si_x:H_y) and hydrogenated carbon–silicon alloys (a-C_{1-x}:Si_x:H_y). They are studied both in the Si-rich and C-rich composition range [45]. The Si-rich alloys have a wider band gap than a-Si:H and are widely used as p-type window layers in a-Si:H-based solar cells [46]. The C-rich alloys are of interest as luminescent materials and as mechanical coating materials. The addition of Si to a-C:H has the beneficial effect of reducing the grown-in compressive stress, improving the thermal stability, and maintaining the low friction coefficient of a-C:H to a higher relative humidity [45,47,48]. (3) Metal incorporated films to reduce stress, wear and lower friction (see, e.g. [49]). (4) Nanostructured sp^2 carbons [50]. These are interesting in their own right. They

are particularly attractive for electrochemical applications, for supercapacitors, sensors, or fuel cells. Nanostructured carbon films can be produced by cathodic arc or magnetron sputtering in the presence of a relatively high gas pressure to favour the aggregation of sp^2 prior to their incorporation in the films. Supersonic cluster beam deposition can also be used to grow nanostructured thin films, where the impinging carbon cluster structure is substantially maintained in the deposited film [50]. These films are characterised by a "memory effect", i.e. they are partially reminiscent of the precursor clusters. Small carbon clusters may have chain or ring structures, whereas larger clusters have the tendency to form three-dimensional cage-like structures characterised by sp^2 coordination. Peculiar to these films is often the presence of carbon sp^1 chains [50].

Figure 3(a) plots the relation between density and sp^3 content for ta-C, ta-C:H, and a-C:H [1,19]. In ta-C many properties, such as Young's modulus, hardness, density, and smoothness correlate directly with the C–C sp^3 fraction. An sp^3 increase is found to correspond linearly to a density increase according to [1]:

$$\rho(\mathrm{g/cm^3}) = 1.92 + 1.37F \tag{1}$$

where F is the sp^3 fraction between 0 and 1. It is also found that the Young's modulus, E, scales with the sp^3 fraction as [1]

$$E(\mathrm{GPa}) = 478.5\ (F + 0.4)^{1.5} \tag{2}$$

From Eqs (1) and (2) we can derive a general density versus Young's modulus relation for ta-C:

$$\rho(\mathrm{g/cm^3}) = 1.37 + [E(\mathrm{GPa})]^{2/3}/44.65 \tag{3}$$

3 X-Ray Reflectivity

X-ray reflectivity (XRR) is a fast and non-destructive technique for the characterisation of density, thickness, roughness, and layering of thin films, especially for single or multiple layers on good quality substrates [51–61].

For x-rays the refractive index in solids is slightly smaller than unity, so that total external reflection occurs at low angles of incidence (Fig. 4). As the incidence angle θ_i increases above a critical angle θ_c, x-rays start to penetrate into the film [51,52]. For an ideally smooth surface the reflected intensity falls off as $(2\theta)^{-4}$, as predicted by the Fresnel's equations. For a real sample, the decrease is more rapid, because of the surface roughness, which scatters x-rays out of the specular beam. For a layer, of refractive index n_1, deposited onto a bulk substrate, of refractive index n_2, reflections at the different interfaces will cause interference. There will be constructive interference when the path difference between the reflected beams is

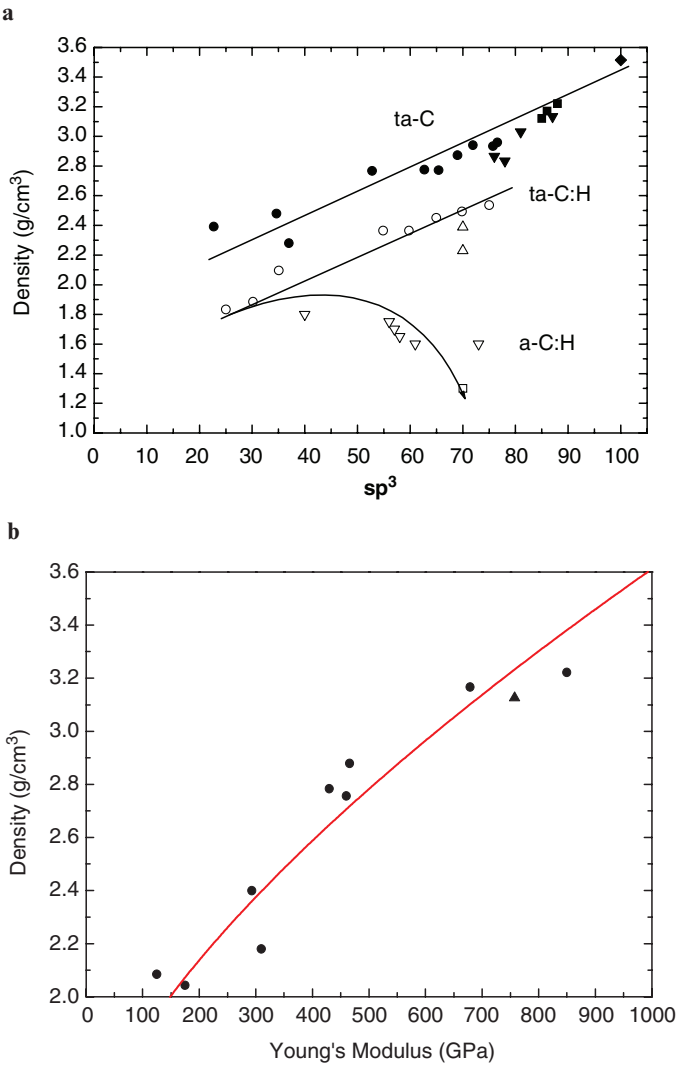

Fig. 3 (a) Density vs sp^3 fraction for N-free carbon films. Note the similar trends for ta-C and ta-C:H, but the opposite trend for a-C:H of increasing H content [19]. (b) Density versus Young's modulus for ta-C films. The experimental trend can be well described by Eq. (3), line in the plot

$\delta = (m + 1/2)\lambda$ or $\delta = m\lambda$, where m is an integer, for $n_1 < n_2$ and $n_1 > n_2$, respectively. The period $\Delta\theta$ of the fringes gives the layer thickness; for $\theta_i >> \theta_c$:

$$d \approx \frac{\lambda}{2\Delta\theta} \tag{4}$$

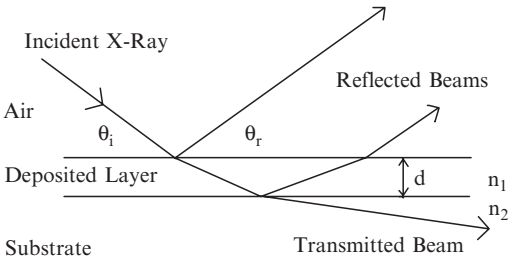

Fig. 4 Specular reflection of x-rays under grazing incidence from a single layer of refractive index n_1 and thickness d on a substrate of refractive index n_2.θ_i is the grazing incidence angle; θ_r is the reflectance angle

In the case of a multilayer, the structural periodicity results in the presence of Bragg peaks in the reflectivity curve.

As the intensity, rather than the amplitude, of the reflected beam is measured, it is not possible to determine directly all the material parameters of complex multiple layer systems. To do this, the reflectivity is simulated from a model structure [59] and the results compared with experiments until a good match is achieved. This process is automated and commercial routines are available [60]. In addition to layer thickness and density, the interface width can be determined by using these fitting procedures. However, the specular reflectivity does not distinguish between true roughness and compositional grading. To achieve this, the diffuse scatter has to be measured. Fitting both the specular and diffuse scatter from a single model structure one can generate independent measures of these parameters [61,62].

A number of papers report XRR studies of pure and hydrogenated carbon films (e.g. [19, 62–72]). Most are devoted to density determination. Few also consider thickness or roughness determination.

Figure 5a plots typical specular reflectivity curves for ta-C, deposited by single and S-bend FCVA and for ta-C:Hs. The S-bend FCVA ta-C and the ta-C:H films have only one dominant fringe period, which implies that they are essentially single layers. The interference fringe period gives a direct measure of the film thickness, the thinner films having longer period fringes. The single bend FCVA ta-C also shows a second set of longer period fringes, which indicate the presence of a surface layer. Indeed, to a closer inspection, the S-bend FCVA ta-C also presents a faint second set of fringes with an even bigger period, indicating a much smaller, but non-negligible, surface layer.

XRR is thus also a powerful tool to check the cross-sectional layering. Analysing a wide variety of films grown under different conditions it was found that extremely uniform or layered films could result even from the same deposition system [19]. As an example, Figure 5a plots XRR curves of various carbon films showing a surface layer (ta-C −80 V, thin S-bend FCVA ta-C, ta-C:H:Si) or heavy internal layering (PLD ta-C, ta-C −290 V, and +10 V) [19].

The density of amorphous carbon films is obtained from the critical angle. We consider carbon films containing four elements: C, N, H, and Si. If we express the

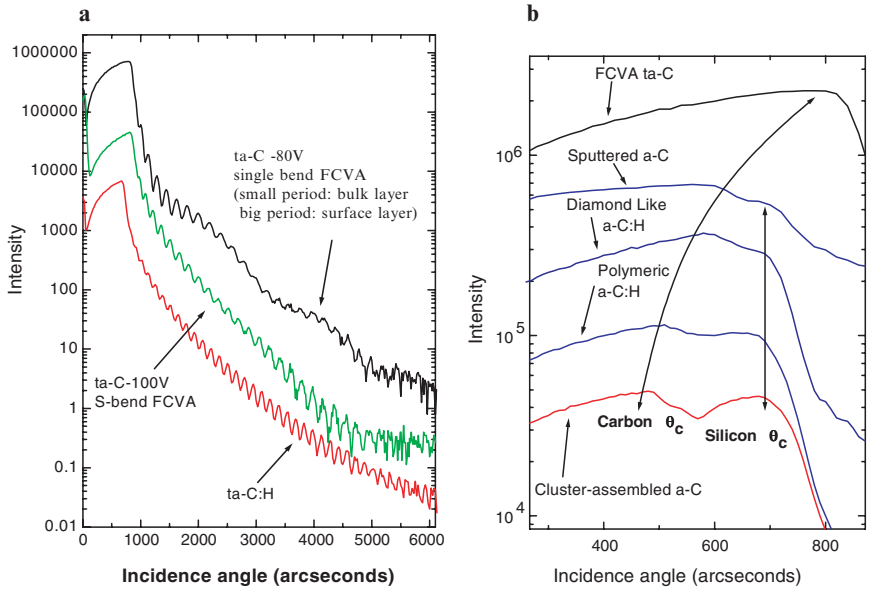

Fig. 5 (a) X-ray reflectivity profiles of single bend and S bend-FCVA ta-C films and for a representative ta-C:H film grown by ECWR. The clear double fringe period in the single bend FCVA film indicates layering. (b) X-ray reflectivity profiles of carbon films with density ranging from lower to higher than the Si substrate density. The film critical angle moves with increasing density. For films denser than Si, such as ta-Cs, only the film critical angle is detected

H atomic fraction as $X_H = 1 - X_C - X_N - X_{Si}$, with X_C, X_N, and X_{Si}, the C, N, and Si atomic fractions, then the density is related to the critical angle by [19,44,71]:

$$\rho = \frac{\pi^2 c^2 \varepsilon_0}{3\lambda^2 N_A e^2} M_C m_e \theta_c^{\,2} \frac{11X_C + 13X_N + 27.1X_{Si} + 1}{5X_C + 6X_N + 13.3X_{Si} + 1} \tag{5}$$

Where e is the electron charge, m_e is the electron mass, N_A is the Avogadro number, c is the velocity of light, ε_0 is the dielectric permittivity of vacuum, λ the x-ray wavelength and M_C the carbon molar mass. Note that the dependence on the H content is quite weak in the usual range X_H = 10–50%. (e.g. ρ = 2.3 g/cm^3 if X_H = 0.1 and 2.16 g/cm^3 if X_H = 0.5, with $X_N = X_{Si} = 0$, $\theta_c = 720°$ and λ = 1.3926 Å), so an approximate density evaluation can be obtained by neglecting the H content. Similarly, an estimate of the density can also be performed considering the films as made of carbon only, even if N is present. However, only by knowing the film composition the most accurate results can be derived.

The use of the critical angle for density measurement is exemplified in Fig. 5b for carbon films a few tens nanometer thick on a Si substrate. Some films, such as ta-C:Hs, have a density (and therefore a critical angle) similar to or just smaller than the Si substrate density (2.33 g/cm^3), so that the Si critical angle is seen, and not that of the film. The presence of the film only acts as a perturbation on the shape of the

critical angle, and a simulation of the reflectivity curve is needed to extract the density. In the case of films with very low density (e.g. porous carbons, or some a-C:Hs and a-Cs) a double critical angle is distinguishable (Fig. 5b). This allows a direct determination of the density from the reflectivity curve. Finally, if the film consists of a bulk layer denser than the Si, the critical angle is determined by the film. This is typically the case for ta-C films (Fig. 5b). Here, a single critical angle is observed and densities up to 3.26 g/cm^3 are obtained for a 70 nm thick 88% sp^3 film grown by S-bend FCVA [19]. The general density/sp^3 relation for carbon films presented in Section 2 (Eq. (1) and Fig. 3) was derived by XRR [19].

As remarked earlier, the reflectivity curves can show multiple periodicities (Fig. 6), which indicate significant internal layering (not just 1–2 nm at the surface or at the substrate interface). These XRR profiles can be simulated taking into account three, or more, layers with different densities. The density deduced from the critical angle

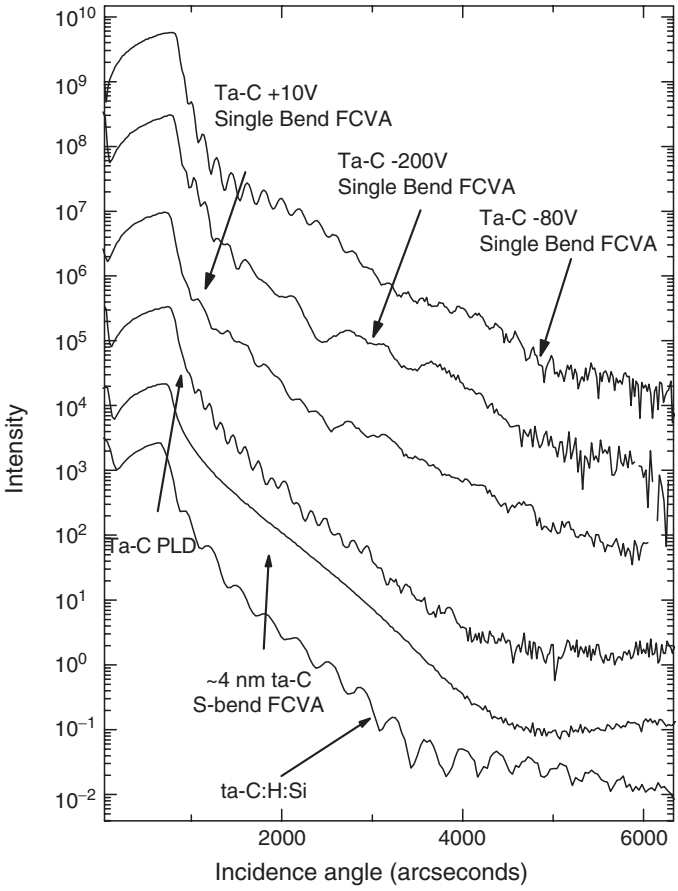

Fig. 6 XRR curves of various carbon films showing a surface layer (ta-C −80 V, thin S-bend FCVA ta-C, ta-C:H:Si) or heavy internal layering (PLD ta-C, ta-C −290 V and +10 V)

is that of the bulk, densest layer. The density of the other layers can be estimated with less accuracy from the fit parameters, but it is usually smaller, in the range 1.5–2.5 g/cm^3. For heavily layered films such as those in Fig. 6, coupling XRR with cross-sectional HRTEM, giving information on the structure of the films, could be a better starting point for fitting reflectivity curves, leading to an improved determination of the density of the layers.

XRR should be the method of choice to measure the mass density in amorphous carbons. Electron Energy Loss Spectroscopy is the standard method for measurement of the sp^3 fraction and provides the plasmon energy at the same time [19,73–80]. NMR would be the best method to measure the sp^3 content, however, the amount of sample required for NMR makes it unpractical for a day-to-day characterisation and it is definitely a destructive technique. Examples of NMR measurements can be found in refs [14,27,28,81–89]. EELS requires the removal of the sample from the substrate by chemical etch and, as such, it cannot be considered non-destructive, even if the sample itself, once removed from the substrate, is not damaged by the electron beam. Other ways to prepare EELS samples require ion milling or the deposition of the samples on an ad hoc NaCl substrate to be removed later. For this reason EELS is not described in details here. A comparative study of XRR and EELS can be found in Ref. [19]. However, since the plasmon energy derived by EELS has been widely used in the past to derive the density of carbons it is important to note the following. XRR directly measures the total electron density. The plasmon energy derived by EELS just measures the valence electron density. This is related to the total electron density by an average effective electron mass, m^*, which in principle is unknown. By comparing EELS and XRR data a common $m^* = 0.87\,m_e$ for most carbons was derived [19]. This was the basis to get the general density versus sp^3 relation of Fig. 3a. However, for polymeric a-C:H samples, the effective mass tends to be lower than the above number, down to $0.7\,m_e$ [19]. This cautions again on the use of EELS to estimate the mass density.

Figure 7 shows XRR data on ultra-thin ta-Cs, indicating the ability of XRR to measure films in the sub-10 nm range. Indeed, ta-C films have been measured down to a thickness of about 1 nm [51,90–92]. Unlike the case of thicker films, for ultra-thin carbons the critical angle is not strongly influenced by the film density. This is because the evanescent wave reaches the silicon substrate below the critical angle and the substrate density determines the critical angle. Only for ta-C films on silicon over about 20 nm thickness the critical angle can be used reliably to measure the near-surface density. Although the density influences the fringe contrast, the film interface width also influences the contrast. On the other hand, the film density does affect the position of the fringe maximum. So an overall fit of the reflectivity profile is necessary to derive the film properties. A degree of uncertainty thus remains in the determination of the film density for these ultra-thin layers, whilst the thickness is precise to 0.1 nm [92]. A density of ~2.6 g/cm^3 is measured even for ultra-thin ta-C films [92]. Note as well that the cross-sectional structure of the ultra-thin ta-Cs resembles that of the thicker ones, with a scaling of the bulk layer thickness, but not of the surface and interface layers (which are in the sub-nanometer range both in thick and thin films) [1].

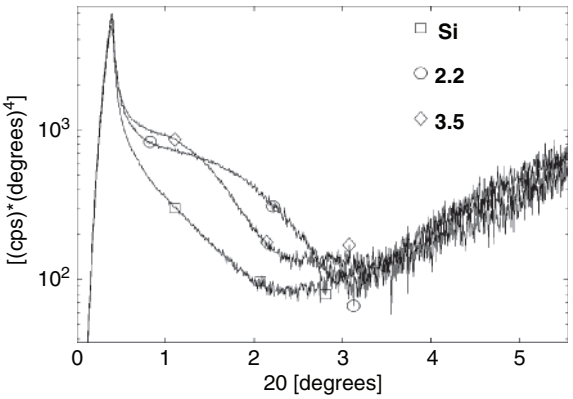

Fig. 7 X-ray reflectivity profiles for ultra-thin ta-C films on Si compared to the bare Si substrate, showing how XRR can discriminate between film and substrate even for extremely small films' thickness

XRR can also be used to estimate the film roughness. In the Born wave approximation the ratio of the integrated diffuse intensity to the integrated specular intensity only depends on the scattering vector and the roughness of the interface [55,56]:

$$\frac{I_{diff}}{I_{spec}} = \exp(q_z^2\sigma^2) - 1 \tag{6}$$

where q_z is the component of the scattering vector normal to the surface, and σ is the rms roughness. By measuring the integrated intensity of the diffuse and specular scatter scanning the sample angle (Fig. 8), genuine surface roughness can be separated from compositional grading [55]. When using XRR the top-surface rms roughness is usually found to be in the range 5–10 Å for all ta-C films [91,71]. However, the most direct way to measure and study the surface roughness evolution in carbon films is AFM (see Section 6).

4 Surface Acoustic Waves

A reliable measurement of the elastic constants of carbons is essential for many applications. However, when the film thickness is much lower than 1 μm and the substrate is softer than the film, standard experimental procedures, as well as nanoindentation, are unable to reliably determine the elastic constants. The difficulties of nanoindentation arise from the need to use an indentation depth less than 10% of the film thickness and from its high sensitivity to the substrate when measuring hard films on a soft substrate. In fact, nanoindentation just measures the hardness, and the reduced Young's modulus $E' = E/(1 - \nu^2)$ is then derived from an Oliver–Pharr [93,94] analysis of the indentation curve, so that E itself can be found only if a value for the Poisson's ratio, υ, is assumed.

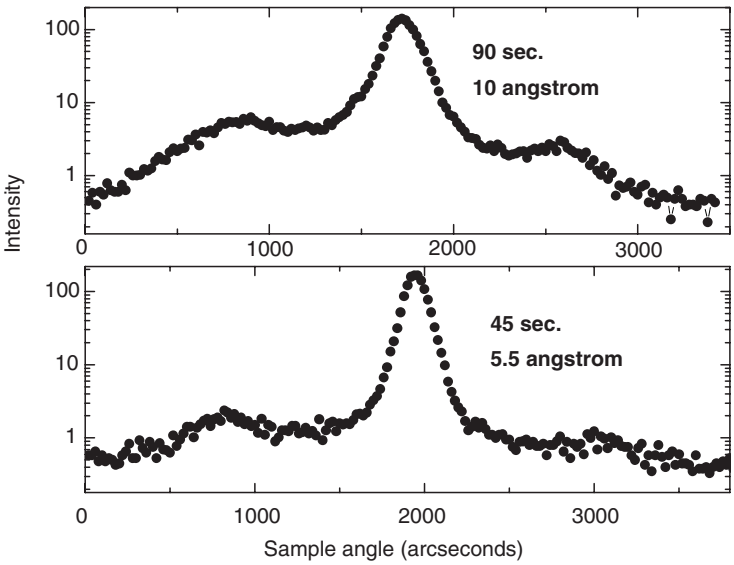

Fig. 8 Diffuse scattering curves of two ta-C films grown with different deposition times [51]. The detector angle (i.e. the scattering angle) is fixed, while the sample is rocked though the specular condition. The maximum intensity occurs for the specular reflection. The diffusely scattered intensity is greater in the thicker film, where the roughness is higher

The difficulties of this method are clear in that while the hardness values of ta-C are found to be between 60 GPa [94,95] and 90 GPa [96], the E' values vary more widely, from 400 GPa [84,95] to 1,100 GPa [96]. Various strategies have been proposed to improve the Oliver-Pharr analysis of the nanoindentation data [96]; however, it is very unlikely that they can work down to a thickness of 1 nm. A reliable alternative is to measure resonant frequencies of cantilevers, but this requires a complex sample preparation [97–99], and is also unsuitable for ultrathin films.

More convenient approaches are based on laser spectroscopic methods probing the propagation of long wavelength acoustic phonons (surface acoustic waves, SAWs): surface Brillouin scattering (SBS), exploiting thermally activated SAWs [8,100–102], and laser-induced SAW (LAW), exploiting SAWs excited by laser irradiation [103,104]. Both SAW-based methods offer the possibility of non-destructive determination of the elastic constants: they measure the velocity of SAWs, and derive from it the film properties. There are, however, significant differences in the way they operate. While SBS relies on thermally excited SAWs, LAW induces them by laser pulses, and allows significantly faster measurements. LAW analyses pulse propagation in the time domain, while SBS is a spectroscopic technique. LAW measures propagation in the MHz to hundreds of MHz frequency range, while SBS operates in the tens of GHz range, and is therefore intrinsically more sensitive to perturbations by thin films. On the other hand, velocity measurements by LAW are more precise, and these two features tend to compensate.

A homogeneous medium, with density ρ and elastic constants (EC) tensor $C_{i,j}$, supports longitudinal and transverse bulk acoustic waves (BAWs). These are non-dispersive, i.e. their velocity does not depend on frequency or wavelength.

The EC of isotropic media, such as nanocrystalline and amorphous media, are fully characterised by any couple among C_{11}, C_{44}, Young's modulus E, shear modulus G, bulk modulus B, Poisson's ratio ν. The relations between them are well known: $C_{44} = G$, $C_{11} = B + 4G/3$, $E = 9BG/(3B + G)$, $\nu = (1/2)(3B - 2G)/(3B + G) = (E/2G) - 1$. The velocities of longitudinal and transverse BAW are respectively [105]:

$$v_l = \sqrt{C_{11}/\rho} \text{ and } v_t = \sqrt{C_{44}/\rho} \quad (7)$$

Films thicker than ~1 μm can be considered semi-infinite media in BS because this thickness is sufficiently larger than the wavelength, allowing the existence of bulk waves. Furthermore, the displacement field of SAW decays almost completely before reaching the substrate for such thickness, so SAW become insensitive to substrate properties.

The measured BAW and SAW dispersion relations can be used to measure the EC, if the mass density is independently known. Since the BAW velocities are simple functions of the EC, they allow the direct determination of the EC from Eq. (7). On the other hand, SAW in thin films on a substrate depend in a complex way on the density of film and substrate, the thickness and the angle between the incident laser and the substrate [106,107]. In this case, densities and thickness must be independently measured, e.g. by XRR. If the substrate properties are known, the only unknowns are the film EC, and these are determined fitting the computed dispersion relations to the measured ones [108–110].

In the past few years BS and LAW have been used to analyse various kinds of carbons and the main results are reviewed here. Table 1 summarises literature data from SBS and LAW on the various carbon systems. Some of the results in Table 1 are derived with an approximate use of SBS, and comments are given in the table caption.

The ability of SBS and LAW to measure thin and ultra-thin ta-C films was assessed by performing a round-robin test. The results of the test show a good correlation between Young's moduli measured by SBS and LAW. This confirms the ability of SAW-based techniques to assess Young's modulus in a thickness range not attainable by conventional techniques. Also, this allows a validation of the LAW data by the more precise SBS measurements. This is crucial since SBS requires an average of a week to do the measurements necessary to extract a film's elastic constants, whilst LAW can perform the same analysis in a few minutes. Even though a value for the Poisson's ratio has to be guessed for LAW, this does not significantly affect the final E values.

Figure 9 plots the evolution of Young's moduli of ta-C films deposited by HCA as a function of thickness. The evolution of films properties with thickness will be discussed in more details in Section 6.

Table 1 Summary of EC derived from BS and LAW for the various carbon systems

	ρ (g/cm^3)	sp^3	t (nm)	H (at. %)	E (GPa)	G (GPa)	B (GPa)	ν	C_{ij} (GPa)	Reference
D	3.515	100		0	*1,053[d1]		444.8		C_{11} = 1,080	[111,112]
					*1,708[d2]				C_{12} = 127	[113]
									C_{44} = 576.6	
									C_{11} = 1,064	
									C_{44} = 541	
µC-D	3.5[d5]	100	Up to 400 µm	0	*1,037[d1]		435		C_{11} = 1,062	[113][d3]
	3.515[d5]		400 µm	0	*1,460[d2]				C_{12} = 122	[114][d4]
	3.50		2–13 µm	0	800–1,140				C_{44} = 541	[115][d6]
									C_{11} = 1,025 ÷ 1,150	
									C_{44} = 500 ÷ 540	
D (VRH)	3.515	100		0	1,144.6	534.3	444.8	0.07		[8][a]
G	2.267	0		0					C_{44} = 5.05	[116,117]
	2.267	0		0					C_{44} = 3.25	[118]
a-C:H	1.6→2.11	0→70	560–1,440	15→35	30→160	10→60		0.2→0.4		[119][b]
				28→15		30→90	135		C_{11} = 147→51	[119][b1]
	2.05→2.28	70→50	1,200	28→37	90→220	25→50		0.4→0.2		[120][b2]
			100–1,500							[121][g1]
	1.65→1.85									
	1.7									
a-C:N	1.8				*390	185.7	*144.5	*0.05	C_{11} = 392.1	[122][f]
									C_{44} = 185.7	
Ta-C:H	2.35	70	70	30	300	115	248	0.3		[8]
a-C→ta-C	1.8→3.3	20→80	50–5,600	0	150→800					[115][e1]
									C_{11} = 32 ÷ 91	[115][e2]
			5→30		539→659				C_{13} = 28 ÷ 117	[123]
			83–180							
									C_{33} = 35 ÷ 195	
									C_{44} = 4 ÷ 22	

(continued)

Table 1 (continued)

	σ (g/cm^3)	sp^3	t (nm)	H (at. %)	E (GPa)	G (GPa)	B (GPa)	ν	C_{ij} (GPa)	Reference
Ta-C	3.26	88	76	0	758	338	334	0.12	C_{11} = 785	[8,124]
	2.7		7	0	200–300	70–150	>67	0–0.43	C_{11} = 614	[8][c1]
	2.8		320	0		*244	*289		C_{44} = 244	[125]
	2.8		8		*571	200			C_{11} = 529→1,036	[100][c2]
	2.7→3.2				500					[121][g2]
C_{60}	1.7		1,500		10		11.3		C_{11} = 16.2 C_{12} = 8.8 C_{33} = 35 ÷ 195 C_{44} = 5.3	[127]
NAC	1 ÷ 1.3	10 ÷ 20	20–1,000		4.6 ÷ 8.8	2.5 ÷ 4	2 ÷ 3.7	0.1		[126]

*Data derived on the basis of the information given in the original references

[a]Voigt-Reuss-Hill isotropic average reported for comparison

[b]The data from [,119,113] have to be taken with caution for the following reasons: SBS was used in combination with nanoindentation, a constant $\nu = 0.3$ was assumed, and the sp^3 fraction was estimated by FTIR. These data summarise the range of EC derived for PECVD a-C:H by CH_4 for various bias voltages, pressures, post-deposition annealing temperatures and C ion implantation

[b1] a-C:H PECVD from C_2H_2 with varying pressure

[b2]From an Ar diluted CH_4 plasma, with varying RF power

[c1]Surface layer on the top of a 63 nm ta-C [c2]S-bend FCVA, ta-C 8 nm thick

[d1] Along <100> [d2]Along <111>

[d3]Hot-filament-assisted CVD polycrystalline diamond films with a preferential (110) texture

[d4]CVD polycrystalline diamond films deposited by an H_2 diluted CH_4 plasma

[d5]Assumed, not measured, value

[d6]CVD diamond films

[e,f,g]EC from LAW

[e1]Data a on a series of a-C to ta-C films deposited by FCVA, PLD, laser-arc, MSIB with various substrate temperatures

[e2]Thin films from a pulsed FCVA

[f]Magnetron sputtered a-C:N

[g1]PECVD a-C:H from cyclo-hexane, CH_4 and CH_4/Ar

[g2]ta-C samples from PLD, FCVA and ion-beam sputter deposition

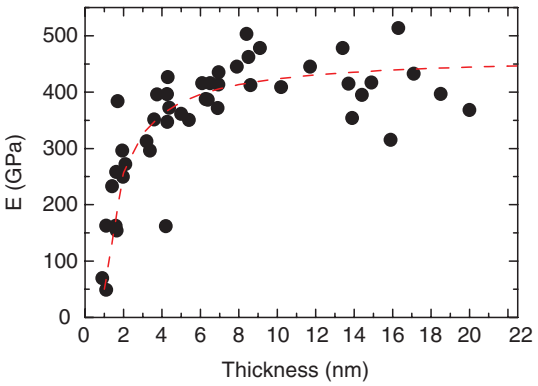

Fig. 9 Density versus Young's modulus for ta-C films. The experimental trend can be well described by Eq. (17), line in the plot

5 Resonant Raman Spectroscopy

5.1 Background

Raman spectroscopy is a fast and non-destructive method for the characterisation of carbon materials [10]. All carbons show common features in their Raman spectra in the 800–2,000 cm^{-1} region, the so-called G and D peaks, which lie at around 1,560 and 1,360 cm^{-1}, respectively for visible excitation, and the T peak at around 1,060 cm^{-1}, which is only seen for UV excitation [9–11,131–135]. The G peak is due to the bond stretching of all pairs of sp^2 atoms in both rings and chains. The D peak is due to the breathing modes of sp^2 atoms in rings [9,131–134]. The T peak is due to the C–C sp^3 vibrations [11,128–130]. Figure 10 shows as an example the multi-wavelength Raman spectra of ta-C, ta-C:H, a-C and polymeric a-C:H samples [11].

The G peak is always present for any carbon at any excitation energy and it is the best-defined peak. It is thus essential to derive the maximum information from this peak alone, before analysing in details the other peaks. The position of the G peak increases as the excitation wavelength decreases, from IR to UV, as show in Fig. 11. We define *G peak dispersion* the rate of change of the G peak position as a function of the excitation wavelength. Figure 11 shows a linear variation of the G peak with excitation wavelength. Thus, we can empirically define the G peak dispersion as:

$$Disp(G)\left(\frac{cm^{-1}}{nm}\right) = \frac{Pos(G)@244 - Pos(G)@514.5}{(514.5-244)nm} \tag{8}$$

Where, Pos(G)@wavelength indicates the G peak position measured at the specified wavelength. The dispersion increases with disorder. The G peak does not disperse in

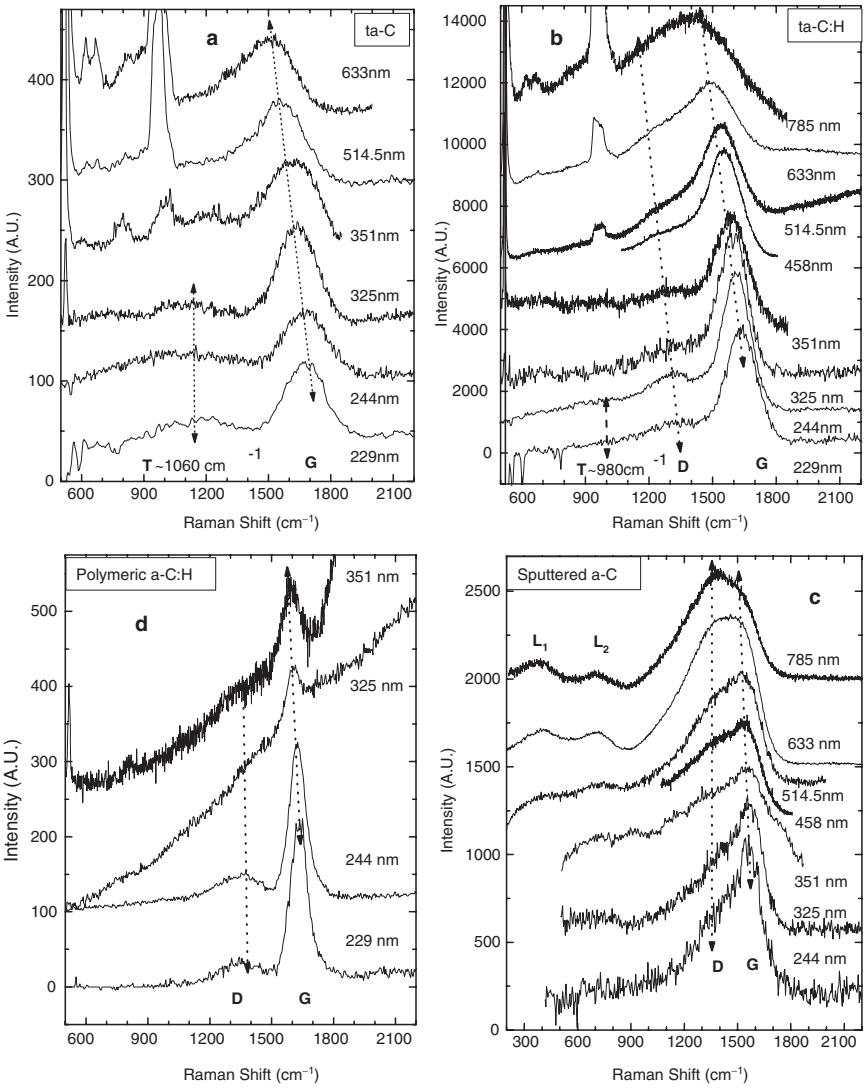

Fig. 10 Multi-wavelength Raman spectra of (a) ta-C, (b) ta-C:H, (c) sputtered a-C and (d) polymeric a-C:H. The peaks' trends and labels are indicated

graphene, graphite, nanocrystalline graphite, or glassy carbon. The G peak disperses only in more disordered carbons, where the dispersion is proportional to the degree of disorder. The G peak dispersion separates the materials into two types. In those with only sp^2 rings, the G peak dispersion saturates at a maximum of ~1,600 cm^{-1}, the G position in nc-graphite. In contrast, in those materials also containing sp^2 chains, particularly ta-C and ta-C:H, the G peak continues to rise past 1,600 cm^{-1} and can reach 1,690 cm^{-1} at 229 nm excitation in ta-C. Thus, ta-C has the largest dispersion.

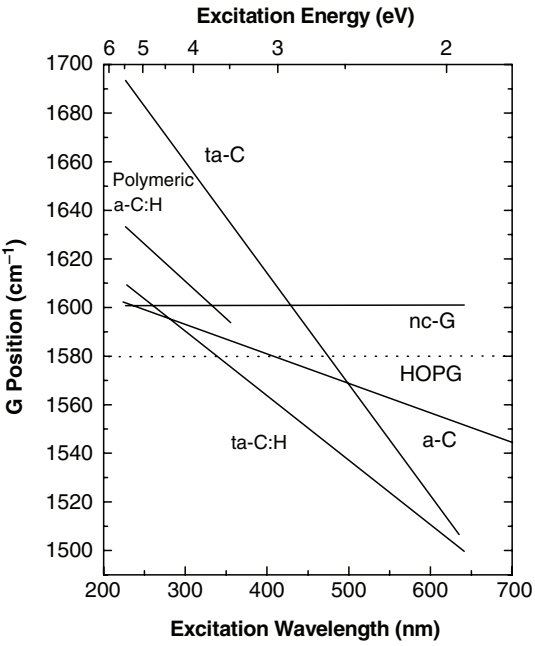

Fig. 11 Schematic dispersion of G peak position with excitation wavelength (*bottom scale*) and excitation energy (*upper scale*), for HOPG, nc-G, ta-C, ta-C:H sp^2 a-C and polymeric a-C:H

The other two key Raman parameters to monitor carbon bonding are the intensity ratio of the D and G peaks, I(D)/I(G), and the Full Width at Half Maximum of the G peak, FWHM(G). In amorphous carbons I(D)/I(G) is a measure of the size of the sp^2 phase organised in rings [9]. If I(D)/I(G) is negligible, then the sp^2 phase is mainly organised in chains, or, even if rings are present, the π-bonds are not fully delocalised on the rings [9].

Note that FWHM(G) and Disp(G) both probe disorder, *however, FWHM(G) is mainly sensitive to structural disorder, whilst Disp(G) is mainly a measure of topological disorder* [12]. Structural disorder arises from bond angle and bond length distortions. Topological disorder arises from the size and shape distribution of sp^2 clusters. Samples with an sp^2 phase entirely constituted of fully π-delocalised rings do not show any G peak dispersion [12]. The G peak is due to the resonant selection of sp^2 chains of different sizes at different excitation energies [11,133]. By size of the sp^2 chain we mean the effective chain conjugation length. In this framework, a long, strained sp^2 chain, with defects interrupting the π-delocalisation, is equivalent to a set of smaller chains. Thus, the G peak dispersion is mainly a measure of topological disorder. In contrast, the G peak width is a single wavelength parameter. It probes those sp^2 clusters resonant for a particular excitation energy. Clusters probed at a given excitation energy have roughly similar size. FWHM(G) would be small if the clusters were defect-free, unstrained, or "molecular". For a given cluster size, a

higher bond length and bond angle disorder lead to a higher FWHM(G). This implies that FWHM(G) is mainly a probe of structural disorder. Higher excitation energies are resonant with smaller clusters. This allows smaller differences between configurations and so FWHM(G) decreases with excitation energy [11,24].

Ideally, one would like to use Raman spectroscopy to extract bonding parameters of DLCs, such as density, sp^3 fraction, or H content. However, Raman spectroscopy is mainly sensitive to the configuration of sp^2 sites because of their higher cross section. The way to derive these properties is a model that relates sp^2 site disorder to the overall bonding, the so-called three-stage model.

The three-stage model [9,11] describes the evolution of the Raman spectra of carbons in terms of an amorphisation trajectory, starting from perfect graphite. Figure 12(a) plots the variation of G position as a function of the *amorphisation* trajectory. Following the reverse, *ordering* trajectory, from ta-C to graphite there can be non-uniqueness. This means that there can be sp^2 clustering or π-electron delocalisation without a corresponding $sp^2 \rightarrow sp^3$ conversion. For visible excitation, sp^2 clustering and ordering will always *raise* the G peak in stages 2 and 3 (Fig. 12(b)). In contrast, in UV excitation, increasing clustering *lowers* the G position. This is shown schematically in Fig. 12(c). Comparing visible to UV excitation, there is an *inversion* of the trends. This allows us to discriminate samples, which, although with different structures, may accidentally show very similar Raman spectra at a certain wavelength, as shown by the various crossing lines in Fig. 11. Indeed, if the G peak positions of two carbon samples are similar at 514.5 nm but differ in the UV, then the sp^2 clustering is higher for the sample with the lower G peak dispersion. Thus, for *any* set of carbon samples, a lower G peak dispersion *always* means ordering and, vice versa, an increase of G peak dispersion *always* means disordering. The G peak dispersion is thus a simple, direct way to characterise amorphous carbons in terms of gap, sp^2, or sp^3 content, or hardness and density.

Figure 13(a–d) show the significant examples of the use and meaning of the G peak dispersion. Figure 13(a) plots the dispersion of the G peak for ta-C:H samples annealed at increasing temperatures. The drop of the G peak dispersion corresponds to the onset of the clustering of the sp^2 phase, just before the onset of sp^3 to sp^2 conversion and H effusion [136,137]. Figure 13(b,c) plots the G peak dispersion as a function of Young's modulus for ta-C films of increasing thickness [1]. A linear relation is found, as expected from the above discussion. A final interesting example is shown Fig. 13(d). This plots the G peak position and dispersion as a function of the Si/(Si + C) ratio for a series of (t)a-$C_{1-x}Si_x$:H_y alloys [45]. In this case, for both green and UV excitations, the G peak linearly downshifts with the Si/(Si+C) ratio, thus the dispersion of the G peak is constant with Si/(Si + C). This is expected, since an increase in the Si content does not induce further clustering of the sp^2 phase. Si can only be sp^3 bonded and behaves differently from N, giving no hysteresis. Thus, in this case, the Si content can be directly derived from the G position in either green or UV Raman spectra [45].

The first UV Raman studies [129,130] found a new peak at ~1,060 cm^{-1} labelled T. This peak is due to a resonant enhancement of the σ states, and it directly probes the sp^3 bonding. It corresponds to the peak in the CC sp^3 vibration density of states

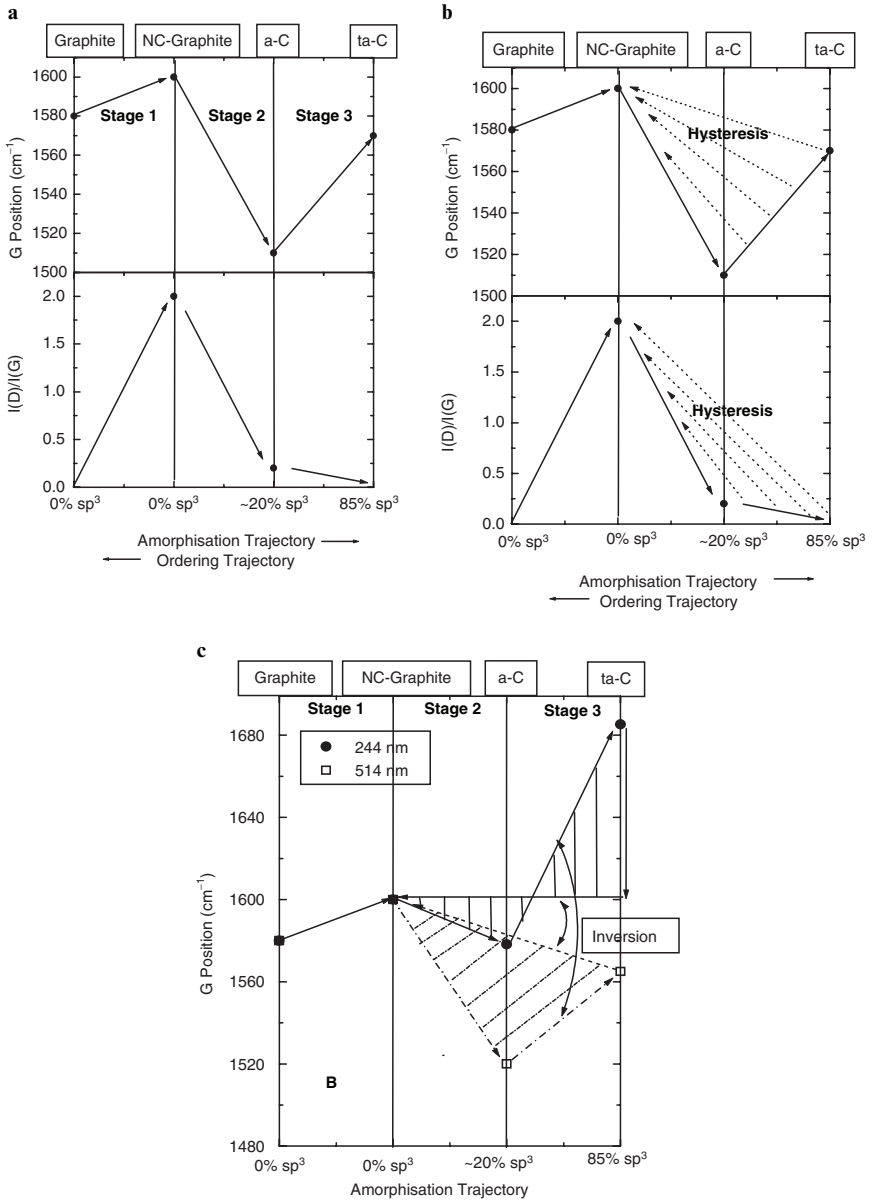

Fig. 12 Three-stage model of the variation of the Raman G position and, I(D)/I(G), with increasing disorder, for visible excitation (a,b) and for multi-wavelength excitation (c). The dotted left-pointing arrows in (b) mark the non-uniqueness (hysteresis) region in the ordering trajectory. (c) Amorphization trajectory, showing the possibility of non-uniqueness in stages 2 and 3 for two typical wavelengths (514.5 and 244 nm). The regions span by hysteresis at 514.5 nm and 244 nm are evidenced by lines. Note the trend inversion, with the highest shift Vis->UV for samples having the least ordered sp^2 phase

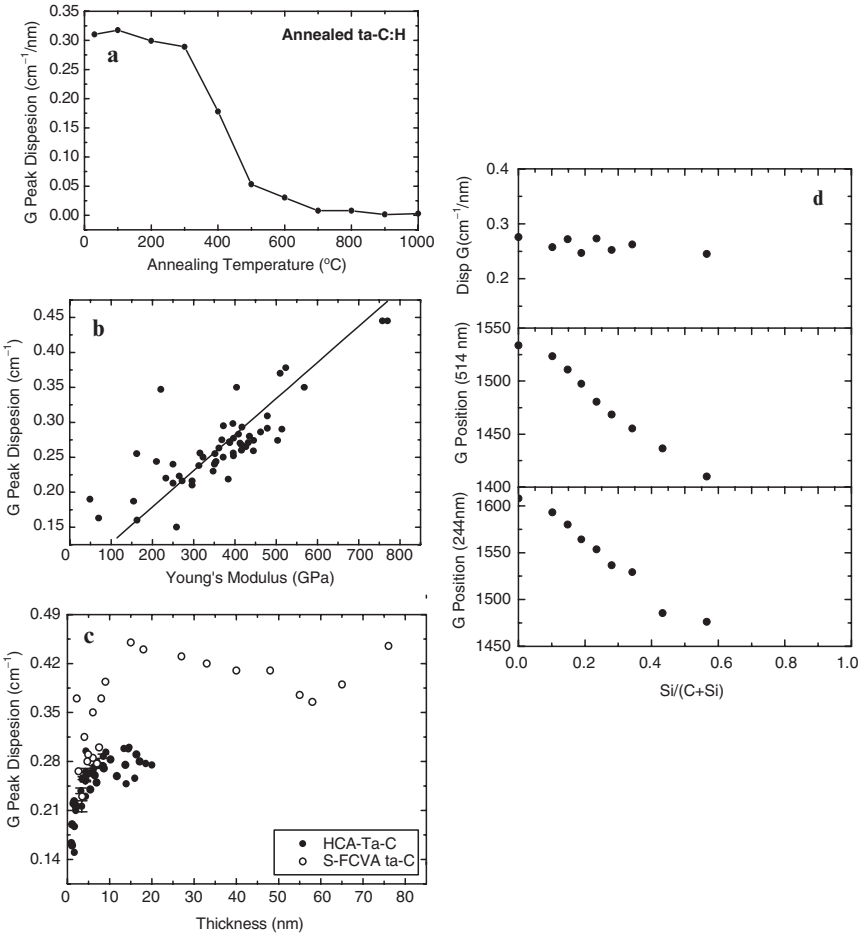

Fig. 13 (a) G peak dispersion for annealed ta-C:H samples. (b,c) G peak dispersion as a function of Young's modulus for ta-C films. (d) Variation of G peak dispersion, 514.5 nm G position and 244 nm G position for a series of (t)a-C_{1-x}:Si_x:H alloys as a function of Si/(C + Si)

(VDOS) of ta-C in simulations [138,139] and EELS data [140]. Figure 14 gives some empirical relations between the I(T)/I(G) ratio, the T peak position, and the sp^3 content [11,129].

The variation of I(T)/I(G) with the sp^3 content is quite non-linear for 60–90% sp^3 contents (Fig. 14(a)). This can be explained as follows. The UV Raman spectra always show a large G peak (Fig. 10). If this is subtracted, this leaves the T peak, which arises from a peak in the sp^3 VDOS. As the sp^3 content falls, the VDOS peak at 1,060 cm^{-1} shifts upwards to that of a sp^2 network at 1,400 cm^{-1} [140]. Alternatively, the changes could be represented as a reduction of the T peak at 1,060 cm^{-1} and the rise of a peak around 1,400 cm^{-1}, a D-like peak. Thus, as the sp^2 content of ta-C rises, the T peak intensity (corresponding to the CC sp^3

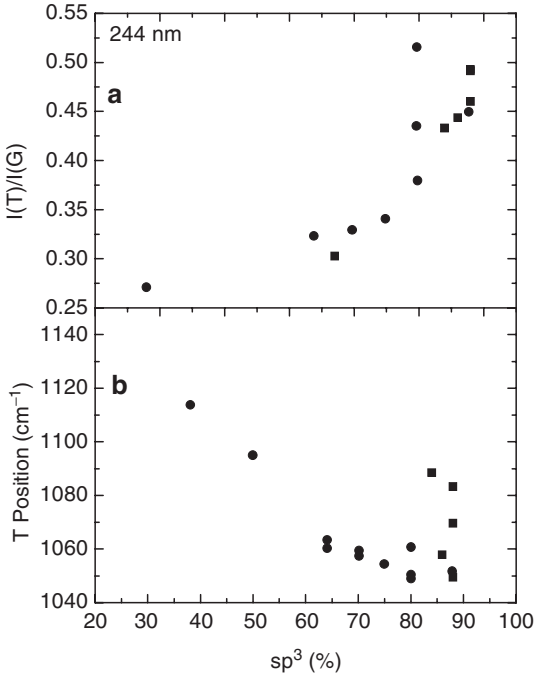

Fig. 14 (a) I(T)/I(G) and (b) T peak position versus sp^3 fraction for non-hydrogenated carbon films

VDOS) is reduced, with a corresponding increase of a D peak. A complication is that the intensity of the D peak depends not only on the sp^2 fraction, but also on its order. If the sp^2 sites have graphitic order, the D peak is absent in UV, if the sp^2 sites are in chains the D peak is absent, only if the sp^2 sites are in disordered rings does a residual D peak survive in UV [11]. This makes the T peak much less useful as a practical characterisation tool than originally thought [129,130], especially if compared to the G peak dispersion. However, we can give some qualitative rules on its use.

A T peak around 1,060 cm^{-1} and an I(T)/I(G) ratio of about ~0.4–0.42 in H-free samples is a sufficient condition to estimate an sp^3 content of ~80%. An I(T)/I(G) ratio of 0.3–0.4 still indicates a sp^3 content of 60–80%, but sp^2 clustering makes it difficult to give a precise figure. Finally, I(T)/I(G) < 0.2 indicates a sp^3 content lower than 20–30%. Thus the presence of a T peak provides yet another means to resolve non-uniqueness. Indeed, a sample with high sp^3 fraction and high clustering of the sp^2 phase will always show a T peak, even if smaller than a similar sp^3 content sample, but with limited clustering of the sp^2 phase. On the other hand, a sample with low sp^3 fraction, but with a similar sp^2 phase clustering and, thus, similar I(D)/I(G) in visible excitation, will not show any T peak. This empirical use of the T peak extends to hydrogenated samples. Figure 10(b) shows that the T peak in ta-C:H or a-C:H is around 980 cm^{-1}, lower than in ta-C. This is consistent with the simulations of the C–C sp^3 VDOS in ta-C:H [141]. The presence of the

residual D peak must be taken into account when fitting. For hydrogenated samples, EELS gives the total amount of sp^3-bonded C atoms, both as C–C and C–H sp^3 bonds, but the T peak is sensitive only to C–C sp^3 bonds. Indeed, comparing the UV Raman spectra of ta-C:H and polymeric a-C:H (Figs 10(b,d)), it is clear that most C sp^3 atoms are bonded to H in polymeric a-C:H, due to the absence of a clear T peak, whilst in ta-C:H there is a sizeable amount of C–C sp^3 bonds. Empirically, $I(T)/I(G)$~0.1–0.2 in (t)a-C:H indicates an overall sp^3 content of ~70%. Again, as sp^2 clustering also contributes of a D peak, this can make things more difficult.

5.2 Hydrogenated Amorphous Carbons

In hydrogen-free carbons, the structural and topological disorder vary in parallel along the amorphisation trajectory [9,11]. FWHM(G) and Disp(G) both increase as disorder increases, for all excitation energies [9,24]. The increase of disorder is linked to higher sp^3 content, density and mechanical properties, which causes the correlation between multi-wavelength Raman spectra and mechanical properties [11,142,143]. This still holds for a-C:Hs with H contents under 20–30 at. %, such as ta-C:H, DLCH and GLCH. By further increasing the amount of hydrogen over 25 at. %, the overall sp^3 content can still increase, but not the C–C sp^3 content. Indeed, PLCHs have the smallest defect density of any carbon films, together with the smallest mass density and stress. Structural disorder now decreases with H content, while topological disorder continues to increase [144] so that FWHM(G) and Disp(G) will have opposite trends.

Hydrogen has a further important effect, which helps the analysis of the Raman spectra. Contrary to nitrogen [24] or to annealing [11,145], the introduction of hydrogen into an amorphous carbon links the amount and configuration of the sp^2 phase with the overall sp^3 content (C–C + C–H sp^3). In principle this is quite fortunate, as it implies that for a-C:H a single wavelength Raman study could be enough to quantify the H and sp^3 content, the optical and mechanical properties. However, we urge extreme caution when doing a single wavelength analysis, since there are some deposition processes that can introduce sp^2 rings even in samples with high H content. In these cases, multi-wavelength Raman spectroscopy is necessary to extract reliable information.

5.2.1 0<H<20 at. %

In this region the H content is too low to decouple the evolution of structural and topological disorder. The Raman parameters can be interpreted as in H-free films.

1. If H is introduced in an otherwise nanocrystalline graphitic carbon, it breaks bonds and increases the bond angle and bond length disorder. This is reflected in an increase of both Disp(G) and FWHM(G)@244 (Fig. 15(a,b)). Thus, the

size of the sp^2 clusters decreases so that $I(D)/I(G)$ decreases as in Fig. 16(b). GLCH samples can be seen as the result of H incorporation in nc-G. The ideal trajectories, describing the modification of the Raman parameters with H incorporation in an otherwise nc-G, are indicated by a line in Figs 15 and 16.

2. If H is introduced in ta-C, this increases the order and clustering in the structure [146]. Thus, Disp(G) and FWHM(G) decrease, whilst $I(D)/I(G)$ increases (Figs 16(b), 15(a,b)).
3. If H is introduced in a mainly sp^2 amorphous carbon, it can produce both disordering and ordering effects, and they tend to compensate.

Generally speaking, for low H contents, the non-hydrogenated sp^2 phase can easily display all the non-uniqueness effects typical of low sp^3 carbons, as indicated by the shadowed regions in Figs. 15 and 16.

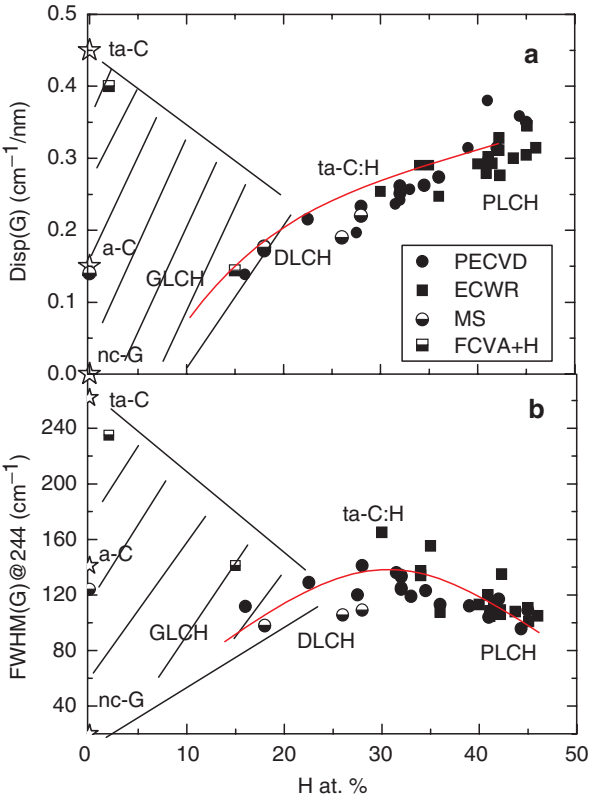

Fig. 15 (a) Disp(G) and (b) FWHM(G)@244 as a function of H content. The ideal trajectories of the Raman parameters with H incorporation from nc-G are marked by a line. The shaded regions represent the non-uniqueness at low H contents

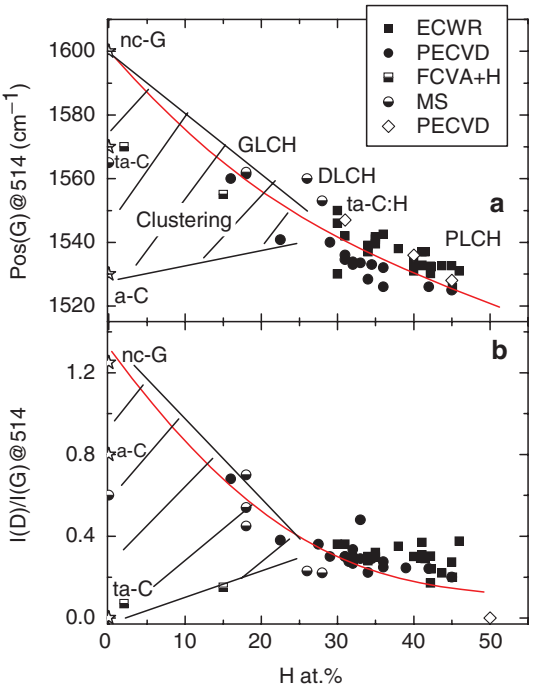

Fig. 16 (a) Pos(G)@514.5 and (b) I(D)/I(G)@514.5 nm as a function of H content. The ideal trajectories of the Raman parameters with H incorporation from nc-G are marked by a line. The shaded regions represent the non-uniqueness at low H contents

5.2.2 H>20 at. %

For higher H contents, however, the situation is different. Although the increase in H drastically reduces the size of ring-like sp^2 structures, it steadily reduces the density and strain in the samples. The sp^2 phase is still topologically disordered, but the structural disorder is lowered. Furthermore, as-deposited samples tend to evolve in a unique way as a function of H content, thus minimising hysteresis.

In this region, Pos(G)@514 and I(D)/I(G) decrease with H as in Fig. 16(a,b). Disp(G) continues to increase with H, but FWHM(G) reaches a maximum for ta-C:H and then decreases for PLCH (Fig. 15(a,b)). Similarly, Pos(G)@514 in PLCHs decreases to ~1,520 cm^{-1}, before being overshadowed by the photoluminescence (PL) background [12]. In contrast, in ta-C Pos(G)@514 reaches ~1,570 cm^{-1} (Fig. 15(a)). PLCHs also show an higher Disp(G) than ta-C:H (Fig. 15(a)). Within hydrogenated carbon films, ta-C:H shows the highest FWHM(G), and ta-C has the highest FWHM(G) of all carbons, for a given excitation energy.

As expected, I(D)/I(G) goes to zero for both PLCH and ta-C and is small for ta-C:H (Fig. 16(b)), since it is a measure of sp^2 rings and no rings are present in ta-C or PLCH.

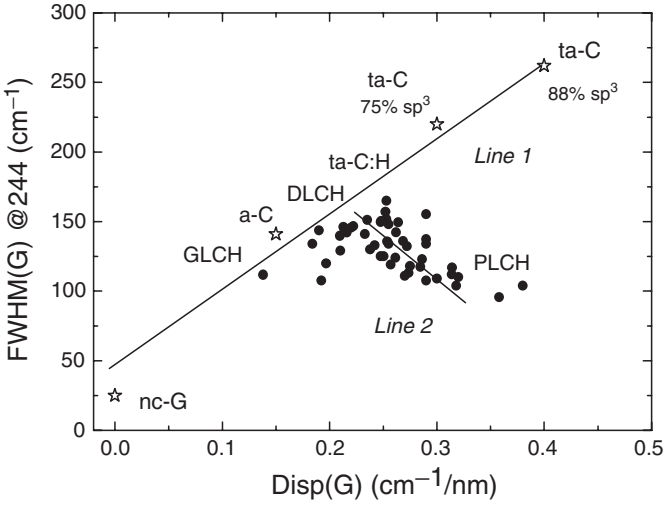

Fig. 17 Correlation between Disp(G) and FWHM(G)@244 for carbon films. The lines are guide to the eye

Thus, Disp(G) and FWHM(G) do not follow the same trends as a function of H content. This differs from the behaviour in H-free carbons where an increase of Disp(G) is always accompanied by a higher FWHM(G), but it reflects the decoupling of structural disorder from topological disorder. These effects are summarised in Fig. 17 [12].

For H-free carbons Disp(G) and FWHM(G) are always proportional and have the same trend as a function of the sp^3 content in Fig. 17 (Line 1). ta-C:H and GLCH also lie on Line 1. In contrast, all the samples with H >25–30 at. %, from DLCH to PLCH, follow the opposite trend (Line 2) in Fig. 17. Thus, in general, the same FWHM(G)@244, if lower than ~170 cm^{-1}, is associated to two different Disp(G), depending on the H content. In contrast, the same Disp(G), if over 0.2 cm^{-1}/nm, is associated with two different FWHM(G)@244 values. However, if we perform a multi-wavelength investigation and combine Disp(G) *and* FWHM(G)@244, we can uniquely characterise the carbon films.

We now relate the parameters FWMH(G) and Disp(G) to the underlying bonding properties. Since FWHM(G) is influenced by the structural disorder, we expect this to be the key parameter to uniquely measure the structural and mechanical properties, which ultimately depend on the amount of C–C sp^3 bonds for any a-C:H film. On the other hand, we expect Disp(G) to be very sensitive to the evolution of the sp^2 phase in any hydrogenated carbon film, and to be uniquely related to the optical properties and hydrogen content.

Since for low H contents Disp(G) and FWHM(G) have the same trends, and for high H contents Disp(G) uniquely evolves with H, and thus with the amount of C–H sp^3 bonds, we expect a relation between Disp(G) and the total sp^3 content in a-C:H (C–C sp^3 +C–H sp^3) [12]. However, since density or Young' modulus mainly

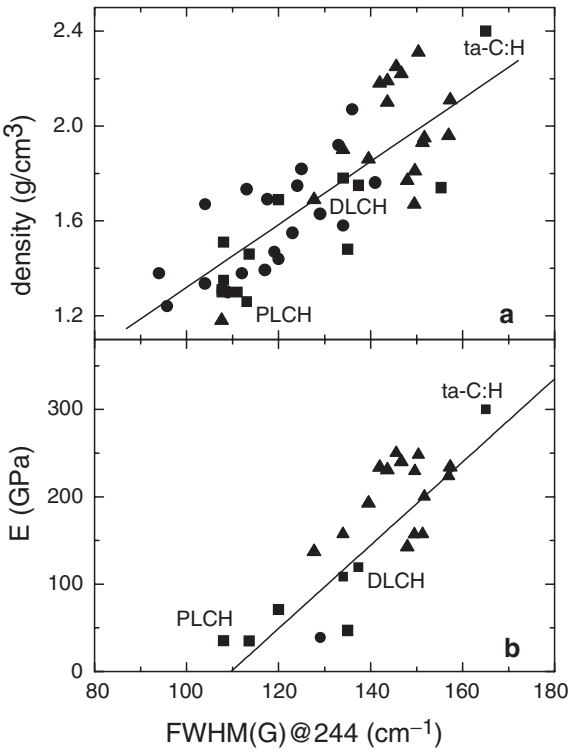

Fig. 18 (a) Density and (b) Young's modulus as a function of FWHM(G)@244. The linear fits are shown

depend on the C–C sp^3 content, in hydrogenated carbons they cannot be measured by Disp(G), but by FWHM(G) (Fig. 18 (a,b)).

From a linear fit of the data in Fig. 17(a,b), we get the following simple relations for H >20 at. %:

$$\rho[\mathrm{g/cm^3}] = 0.257 + 0.011\ W\ [\mathrm{cm^{-1}}] \tag{9}$$

$$E\ [\mathrm{GPa}] = -511 + 4.66\ W\ [\mathrm{cm^{-1}}] \tag{10}$$

where W = FWHM(G)@244.

Figure 3a shows the variation of mass density with sp^3 fraction for the different carbon films [19]. For H-free carbons, the density increases monotonically and linearly with sp^3 fraction. A similar behaviour is found for GLCH and DLCH up to a certain density. Then the ta-C:Hs continue to increase monotonically, whereas the PLCHs turn over and the density decreases for higher sp^3 values. The similar trends in Figs 3a and 17 again confirm that FWHM(G) and Disp(G) are related with density and total sp^3 content, respectively.

Disp(G), being a measure of topological disorder, is also a good measure of the band gap in hydrogenated carbons, as shown in Fig. 19. Given also that the Urbach energy, E_U, varies roughly linearly with gap, we expect Disp(G) and E_U to be linearly related. Thus, Fig. 18 is also the equivalent of the E_U versus optical gap relation found for hydrogenated amorphous carbons [12,144]. E_U is defined as the inverse of the slope of $\ln[\alpha(E)]$ at the E_{03} energy, where $\alpha(E)$ is the optical absorption and E_{03} is the photon energy at which the absorption coefficient reaches 10^3 cm^{-1} [12,144,147]. In fully sp^3 semiconductors, E_U increases with the amount of disorder and the spin density [147], but for PLCH E_U increases for decreasing spin density [144]. From Fig. 20, we see that E_U and Disp(G) have the same trends, thus similar physical meaning. Figure 20 demonstrates that E_U is a measure of structural disorder, as in a-Si:H, *only* in low or no hydrogen content samples. On the other hand, for high H content samples, E_U is a measure of topological disorder, as suggested in [144].

If we restrict ourselves to a-C:Hs with high hydrogen content (i.e. on line 2, Fig. 17), we can get other useful relations, valid *only in this regime*.

Figure 21 plots the square of the refractive index measured as a function of the density. By fitting Fig. 21 we find:

$$n^2 = -1 + 3.38\rho[\mathrm{g/cm^3}] \tag{11}$$

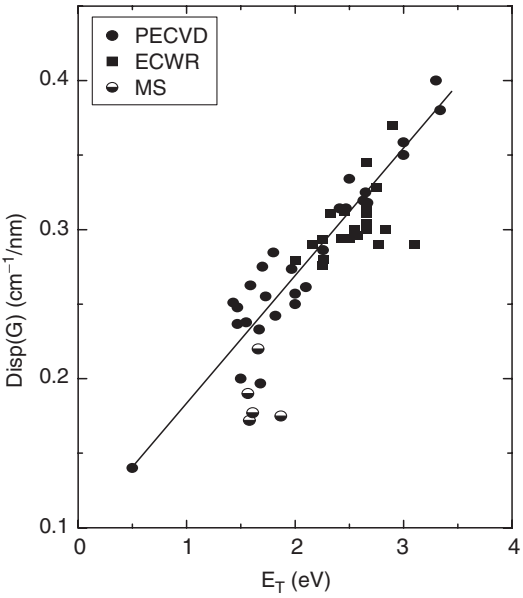

Fig. 19 Disp(G) as a function of Tauc Gap. The linear fit is shown

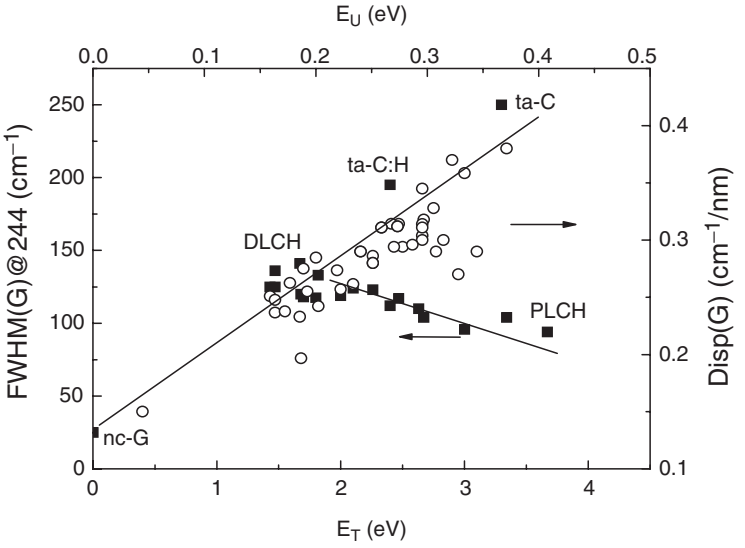

Fig. 20 Correlation between Raman parameters, Urbach energy and Tauc gap. The lines are guide to the eye

By combining Eqs (9–11), we also get:

$$n^2 = -0.13 + 3.7 \cdot 10^{-2}\ W\ [\mathrm{cm}^{-1}] \tag{12}$$

From Eq. (12), the relation between optical gap and density:

$$\mathrm{E_T(eV)} = 4.6 - 1.6\rho[\mathrm{g/cm^3}] \tag{13}$$

By combining Eqs (10–13), we get:

$$\mathrm{E_T(eV)} = 4.2 - 1.6 \cdot 10^{-2}\mathrm{W}[\mathrm{cm}^{-1}] \tag{14}$$

It is interesting to note that the linear relation between n^2 and density of Fig. 21 confirms that in hydrogenated amorphous carbons the product $E_G m^*$~constant, where m^* is the interband effective electron mass and E_G is the Penn Gap, i.e. the average bonding anti-bonding splitting [19]. A similar linear trend is reported in Ref. [72].

5.2.3 H>20 at. % and sp² phase clustered in rings

This case corresponds to PLCHs containing sp^2 rings or to highly hydrogenated GLCHs. We call this class of materials GLCHHs. This seems to be a very peculiar

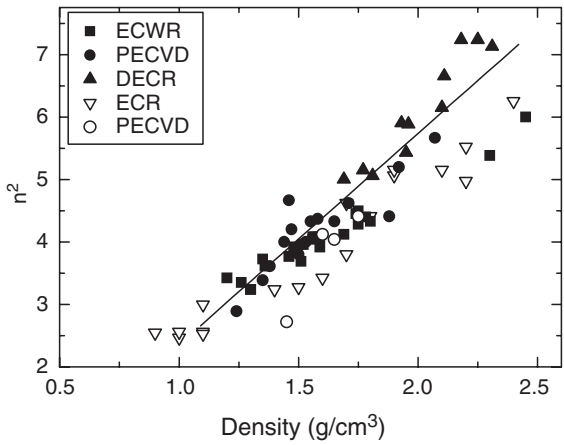

Fig. 21 Square of the refractive measured at 633 nm (with some data at 600 nm) as a function of density

case, but is sometimes found in literature and is quite important for tribology [148,149]. GLCHH is typically produced by PECVD from a mixture of CH_4 and H_2 and very high bias voltage [148,149]. Typical Raman spectra of GLCHH measured at 244 and 514 nm are plotted in Fig. 22 and compared with GLCH and PLCH samples. Figure 22 upgrades Fig. 15 to include GLCHHs. The Raman parameters are very close to GLCH, as expected from the more ring-like sp^2 configuration, which reduces Disp(G) with respect to PLCHs. However, the visible Raman spectrum shows a higher PL background than standard GLCH. Typically *m/I*(G) for GLCHH is ~5 µm, where m is the slope of the Raman spectrum between 1,050 and 1,800 cm^{-1} [12]. Indeed, the H content is 30–40 at. % [150] (Fig. 22 (a,b)). The density of these samples can be as low as 1.3 g/cm^3, below the density of typical GLCH (~1.6. g/cm^3). Thus, in order to identify GLCHH films we need to combine the analysis of Disp(G) and FWHM(G) with the PL background.

GLCHH films have interesting technological applications. Even though the mechanical properties of these samples can be very poor, they can show excellent friction behaviour in vacuum or dry nitrogen [148,149,151]. Thus, H content per se is not the only parameter controlling the friction in a-C:Hs, in agreement with Refs. [152–155]. Indeed, PLCH films do not show a friction coefficient as low as GLCHH with the same H content [152–155]. It is the optimal combination of high H content *and* sp^2 configuration, which gives the best frictional properties [12]. Disp(G) decreases for increasing sp^2 clustering [11] and is zero if the sp^2 phase is ordered in rings. Thus, for GLCHH this parameter cannot be related to the H content, as shown in Fig. 22(a). Disp(G) is in any case related the optical gap, since the optical gap is uniquely defined by the sp^2 phase clustering.

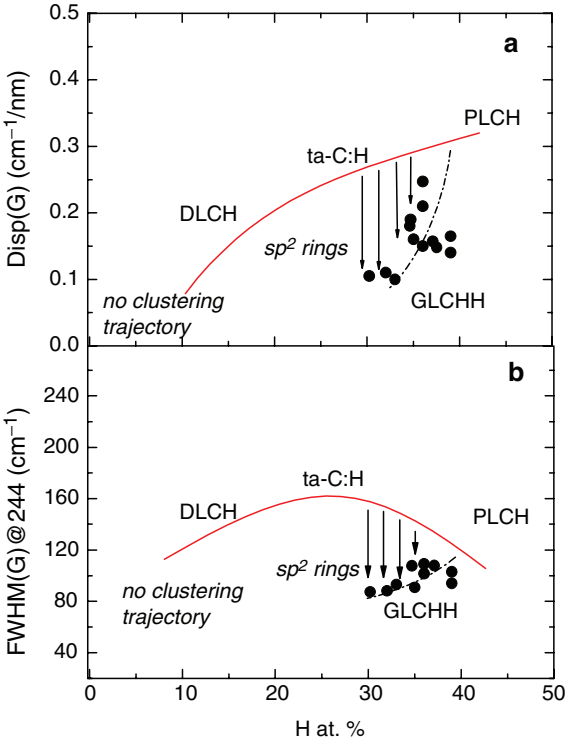

Fig. 22 (a) Disp(G) and (b) FWHM(G)@244 as a function of the H content for amorphous carbons, including GLCHH

5.3 *Carbon Nitrides*

We now consider the effect of nitrogen on the Raman spectra. For a review of the infrared spectra of carbon nitrides see Ref. [24]. The vibration frequencies of solid carbon nitrides are expected to lie close to the modes of the analogous unsaturated CN molecules, which are 1,500–1,600 cm^{-1} for chain-like molecules and 1,300–1,600 cm^{-1} for ring-like molecules [156,157]. This means that there is little distinction in the G-D region between modes due to C or N atoms. For example, the frequency of bond-stretching skeletal and ring modes is very similar in benzene, pyridine and pyrrole, so it is difficult to assess if an aromatic ring contains nitrogen or not. The modes in amorphous carbon nitrides are also delocalised over both carbon and nitrogen sites because of the nitrogen tendency to sp^2 clustering. There is, therefore, little difference between the Raman spectra of carbon nitrides and N-free carbon films in the 1,000–2,000 cm^{-1} region.

The similar frequencies of C–C and C–N vibrations could make the interpretation of the skeletal modes quite difficult, if one is hoping to single out C–N and N–N peaks, as often done in previous works (see, e.g. Refs. [158–161]). However, there

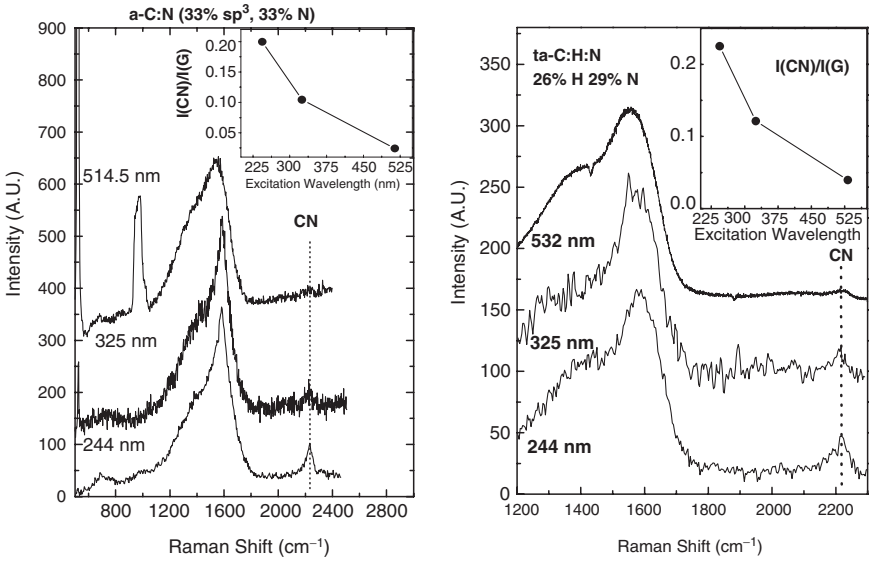

Fig. 23 (a) Multi-wavelength Raman spectra of a 33% sp^3, 33% N a-C:N. For 514.5 nm and, to a lesser extent, 325 nm excitations the contributions of the substrate Si Raman peaks at ~521 and 970 cm^{-1} are also seen. (b) Multi-wavelength Raman spectra of a ta-C:H:N film with ~26% H and 29% N

is no proof that the direct contribution of these modes in the 1,000–2,000 cm^{-1} region can be detected [24]. Instead, we analyse the trends in the G and D positions in the same way as in N-free samples. This enables us to explain in a simple way the observed spectra in the 1,000–2,000 cm^{-1} region, without the need to invoke specific contributions of heteropolar bonds. Figure 23(a,b) shows examples of Raman spectra of a cathodic arc deposited (t)a-C:N and (t)a-C:H:N films.

The three-stage model can be simply extended to explain the trends in the Raman parameters in any carbon nitride measured at any excitation wavelength. In particular, we consider the trends in the G peak position.

Figure 12(c) can be easily modified to explain carbon nitrides by recalling that, in general, adding N causes an independent evolution of sp^3 fraction and sp^2 clustering. This causes a non-uniqueness of the sp^2 configuration for a given sp^3 content. This means that the ordering trajectory induced by adding N to ta-C or ta-C:H is not equivalent to the reverse of the amorphisation trajectory leading from a-C to ta-C. Thus, for a certain sp^3 content, we can have various G peak positions, both in visible and UV-excitation. This effect is summarised for N free carbons in Fig. 12(c), by the regions defined by the dotted arrows pointing in the ordering direction. These indicate the various G peak positions that could correspond to a given sp^3 content. Figure 12(c) can be simply updated to predict the trends of G peak position in carbon nitrides, as shown in Fig. 24. This plots the schematic variation of Pos(G) for 244 and 514 nm excitations in carbon nitrides. Figure 24 is the

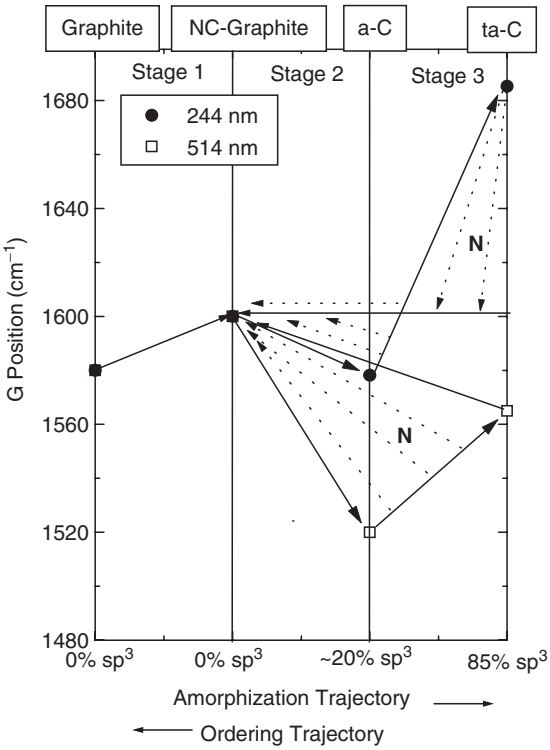

Fig. 24 Three-stage model of the variation of the G peak position versus disorder for visible and UV excitation in amorphous carbon nitrides. The bold right-pointing arrows represent the amorphisation trajectory in stages 2 and 3. The "bow-tie" and triangular-shaped regions defined by the dotted and continuous left-pointing arrows indicate the non-uniqueness regions for UV and visible excitations respectively. N generally induces non-uniqueness in stage 3, as indicated by the letter N in the graph

same as Fig. 12(c), with the only difference that now we consider the non-uniqueness regions as triggered by N introduction in high sp^3 samples (as further stressed by the letter N used in Fig. 24 to define these regions).

Figures 25–27 plot the trends in G peak position and dispersion for (t)a-C:N, (t)a-C:H:N and sputtered a-C:N films. Figure 24 immediately allows us to understand the trends of Figs 25–27. Clustering in UV Raman causes a G peak downshift with increasing N content for stage 3 carbons. Clustering is synonymous of ordering trajectory in Fig. 24. The possible downshift is larger for higher initial G peak positions above 1,600 cm^{-1}. On the contrary, clustering increases the G peak position for visible excitation. This upshift is larger, the lower the initial G peak position. Thus, following the ordering trajectory, the G peak trends for UV and visible excitation are *opposite* for stage 3 carbons. This is what is seen in Figs 25(a) and 26(a). Furthermore, the *trend inversion*, between visible and UV Raman, causes a higher G peak dispersion for lower sp^2 clustering, i.e. for lower

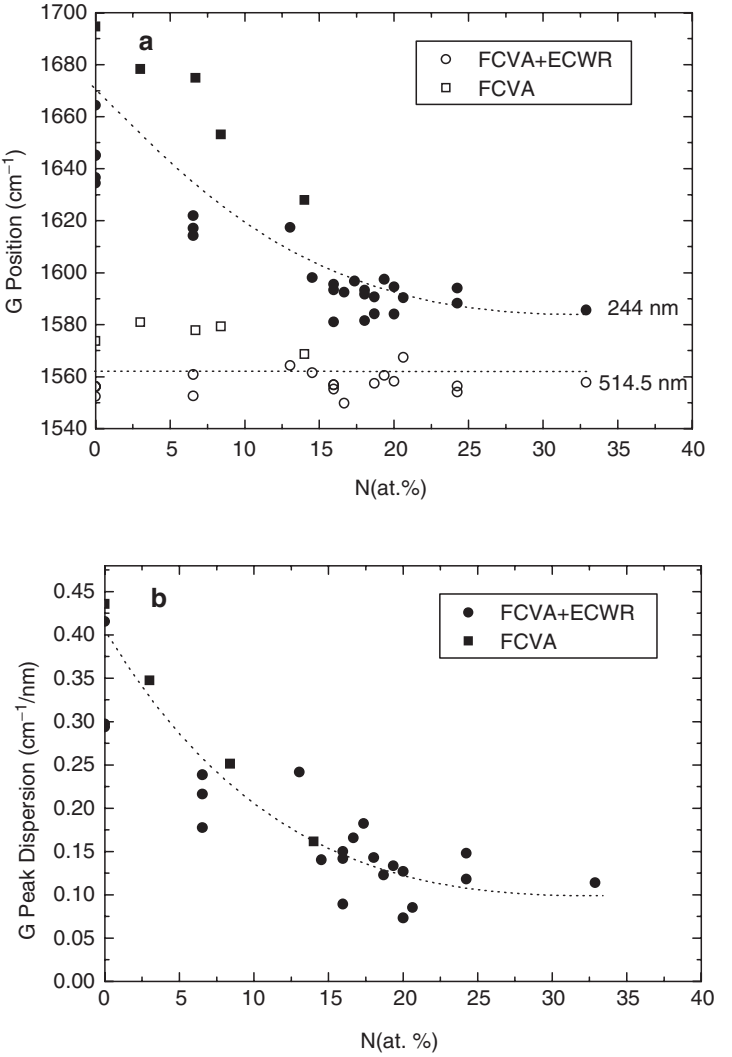

Fig. 25 (a) G peak position versus N content for 244 and 514 nm excitation for (t)a-C:N films. (b) Dispersion of G peak versus N content. The lines are guides to the eye

N content. This is seen experimentally in Figs 25(b) and 26(b). The G peak dispersion proves again to be a crucial parameter to resolve the ambiguity that non-uniqueness can cause for single excitation energy measurements.

In Section II we stressed that N addition in a-C may increase its hardness and elastic recovery, especially at temperatures higher than 200°C. In this case, N does not cause more clustering of sp^2 sites, but more cross-linking and thus increases disorder, even though not necessarily through an sp^3 increase [26–28]. These a-C:N

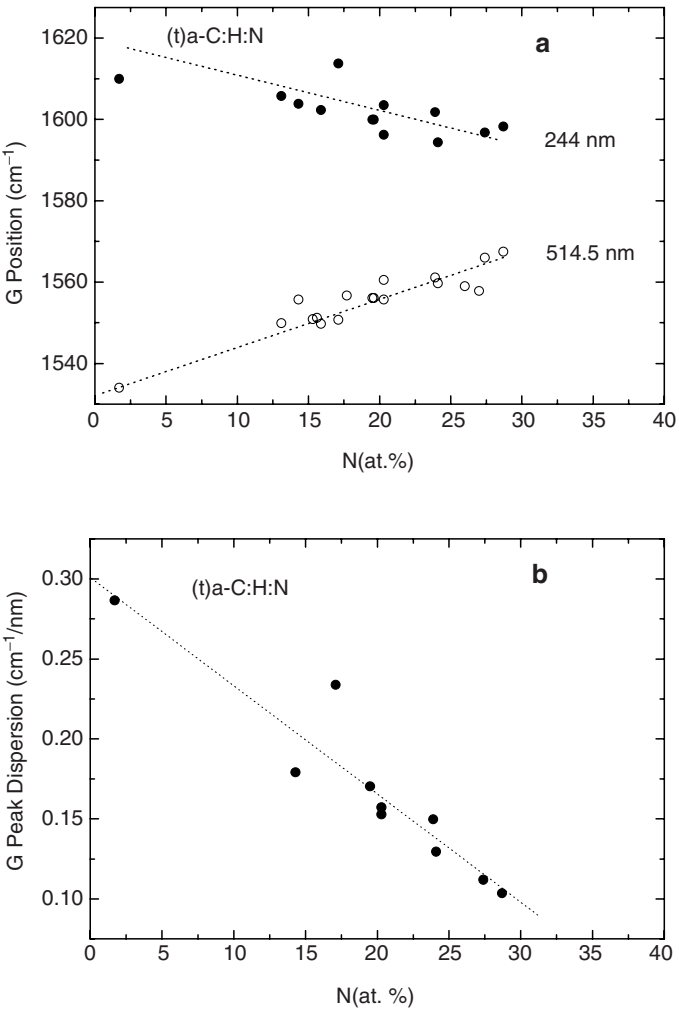

Fig. 26 (a) Variation of G peak position with N content at 244 and 514 nm excitation for (t)a-C:H:N films. (b) variation of G peak dispersion with N content. The lines are guides to the eye

can thus be classified as stage 2 carbons with increasing amorphisation. From Fig. 24, we see that the amorphisation trajectory for stage 2 carbons gives a decrease of G peak position for both visible and UV Raman spectra (bold right-pointing arrows). Figure 24 also predicts a larger decrease for 514 nm excitation. This implies that the G peak dispersion must increase for increasing N content. This is precisely what is seen experimentally in Fig. 27 (a,b). In general, it can also happen that N increases sp^2 clustering even for stage 2 carbons, e.g. for samples deposited at room temperature. In this case, Fig. 24 predicts a rise of G position in visible and *also* in UV excitation (dotted right-pointing arrows), but without the trend inversion

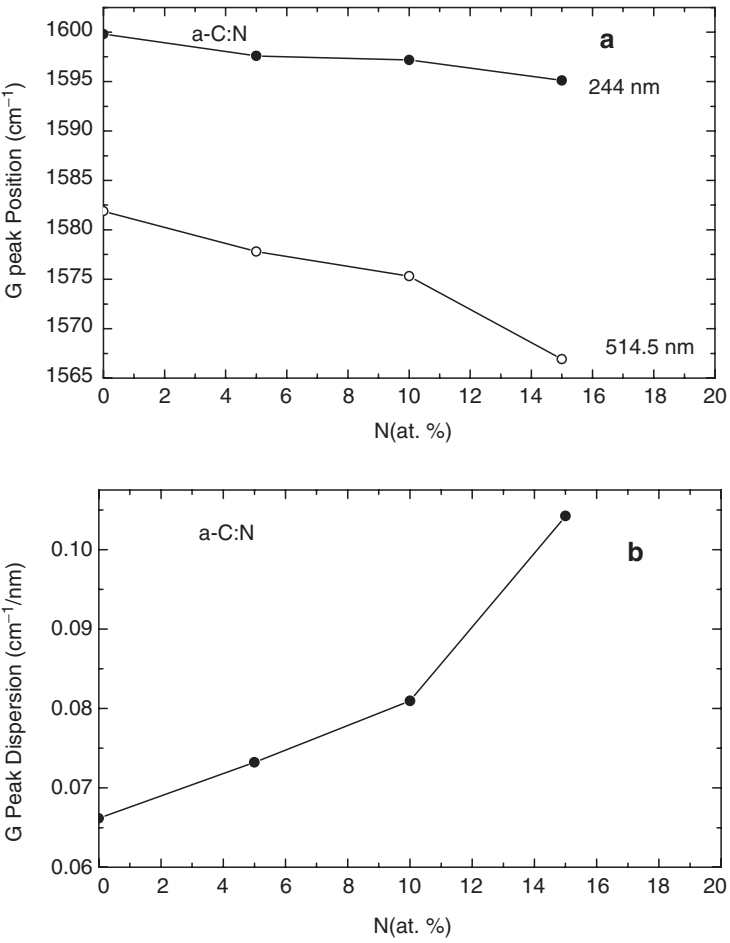

Fig. 27 (a) Variation of G peak position with N content for 244 and 514 nm excitation for high temperature deposited sputtered a-C:N films. (b) Variation of G peak dispersion with N content

typical of stage 3 carbons. However, the increase of G position with N for UV excitation is lower than the corresponding upshift for visible excitation. Thus, even without trend inversion, this again results in a lower G peak dispersion with increasing N content. Thus, as for *any* carbon, also for carbon nitrides a lower G peak dispersion *always* means ordering and vice-versa an increase of G peak dispersion *always* means disordering. A clear example of this is plotted in Fig. 28, where a wide collection of G peak dispersions and density data on various carbon nitrides produces an unambiguous relation.

The scratch resistance is a method used in the hard disk industry to assess the mechanical properties of ultra-thin carbon overcoats. It is performed by using an AFM with diamond tips [162,163]. Using image subtraction, scratches down to a residual depth of 0.1 nm can be evaluated, hence enabling the study of the very

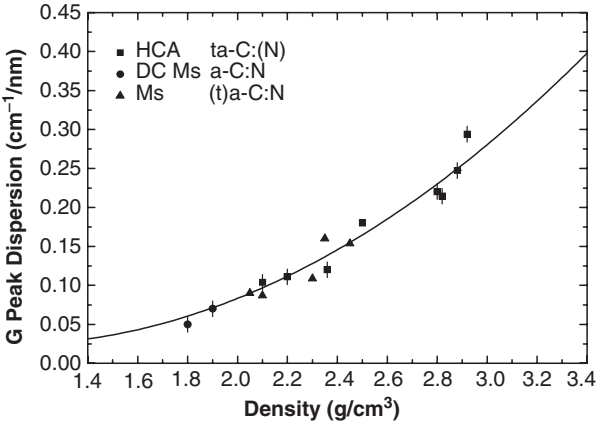

Fig. 28 G peak dispersion as function of the mass density for different carbon nitride films deposited by cathodic arc and sputtering. A clear correlation over a large density region is seen

beginning of plastic deformation. The scratch resistance is defined by the ratio of the applied loading force and the cross-sectional area of the scratches. It directly relates to the shear modulus and hardness of the carbon overcoats. The elastic constants of amorphous carbons scale with the sp^3 fraction and thus with the density, Section 2, Eqs (1–3). The G peak dispersion should thus directly correlate with the scratching resistance. This is clearly shown in Fig. 29(a,b), where a linear relation between G peak dispersion and scratching resistance of two sets of magnetron sputtered a-C:Ns and arc deposited ta-C:Ns is shown. Note how for the a-C:Ns the scratching resistance increases with the N content, whilst for ta-C:Ns it decreases, as we expect from the general trends described in Section 2.

In a similar way, we can easily extend to carbon nitrides the interpretation of the T peak as due to C–C sp^3 vibrations. An example of this is shown in Fig. 30 where the $I(T)/I(G)$ ratio is plotted as a function of sp^3 content and N content for a series of (t)a-C:N films. It is interesting to note that the trend in both the upper and lower axes is very similar. This again shows that N introduction in high sp^3 carbons induces an increase in the sp^2 phase clustering and decrease of the sp^3 content.

5.4 Non-Carbon Atoms Detection by Raman Spectroscopy

As explained in Section II, carbon films often contain H, N, Si or other elements. We discuss here the signatures of non-carbon atoms in the Raman spectra.

Visible Raman spectra can provide information on the H content via the PL slope [12,164]. Note that if samples have Tauc gaps bigger than the laser excitation wavelength, visible Raman measurements only probe the PL of sub-band gap clusters.

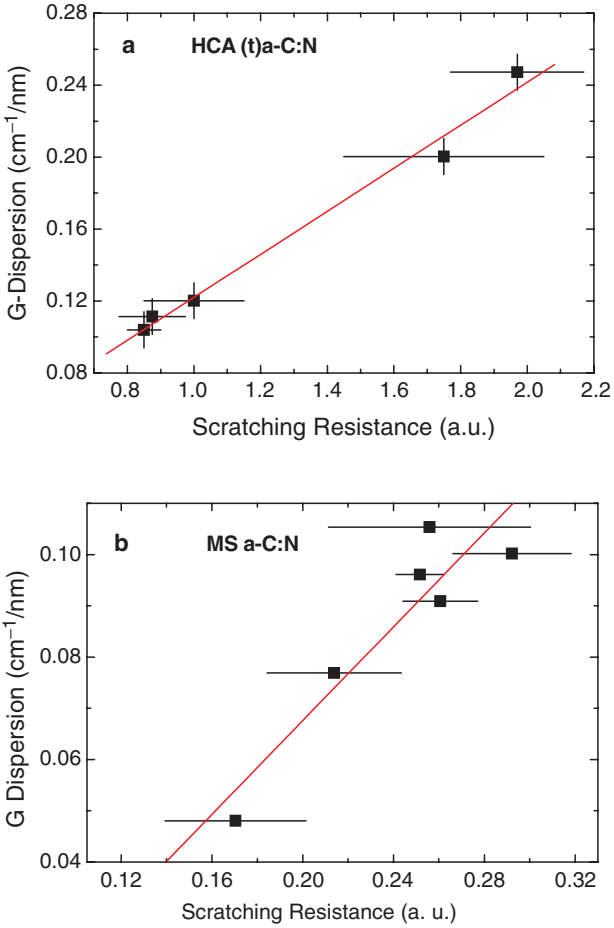

Fig. 29 G peak dispersion versus scratching resistance for MS sputtered and HCA (t)a-C:N films used for hard disk coating

This nevertheless allows an estimate of the H content, because the recombination efficiency of sub-band gap clusters also increases with H content [165–167]. This is demonstrated in Fig. 31(a) where we plot the average PL peak position as a function of the optical gap for various films [12]. The PL peak position is seen to saturate when the optical gap exceeds the excitation energy. On the other hand, Fig. 31(b) shows that, by normalising to the Raman intensity, the PL intensity continues to increase with H content, even for sub-gap excitation. Normalising to the G peak intensity is reasonable since, if we neglect the possible variation of 514 nm Raman cross section across the different a-C:H samples, the Raman and PL intensity both have a similar dependence on sample thickness, absorption coefficient and laser penetration depth. Thus, for practical purposes, it is not necessary to measure PL over a wide spectral range, but we can take the PL background under the D and

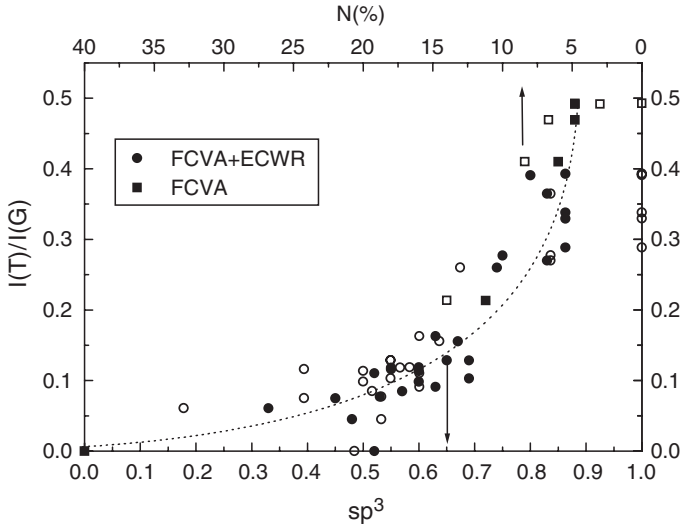

Fig. 30 Variation of T to G peak intensity ratio, I(T)/I(G), with sp^3 content, lower scale, and N content, upper scale and open symbols for (t)a-C:N films. The lines are guides to the eye

G peak spectral region. Note that PL has sometimes been seen in some H-free carbons [12,168]. However, the PL intensity in H-free samples is at least four times lower than that of PLCH, see Fig. 31(b). Also note that, for low density and porous carbons such as in [168], the PL may be associated with adsorbed water during deposition in poor vacuum or after exposure to air [169,170].

Figure 32(a) shows that the normalised PL slope, m/I(G), increases exponentially with the hydrogen content, for all films examined. The data of Fig. 32(a) give a simple formula for the hydrogen content [12]:

$$\mathrm{H\ [at.\ \%]} = 21.7 + 16.6 \log\left\{\frac{m}{I(\mathrm{G})}[\mu m]\right\} \tag{15}$$

Figure 32(b) shows that m/I(G) also increases exponentially with the Tauc gap for H >20 at. %.

UV Raman spectra can detect the C–C σ-bonds, due to the increase of their cross section with respect to the π-bonds. This is more general, in that any σ-bonds between heteroatoms can be seen for UV excitation. This implies that UV Raman spectroscopy can be a useful complementary tool to IR spectroscopy for elemental detection.

UV Raman thus allows the direct detection of C–H bonds. This is shown in Fig. 33, where a broad peak due to CH_x stretching is seen at 2,920–2,970 cm^{-1}. The other band at ~3,220 cm^{-1} is the second order G peak, as demonstrated by H-D isotopic substitution experiments [11]. ta-C:H has a very broad and small second order G peak compared to PLCH. The CH_x band is quite broad and it is difficult to properly

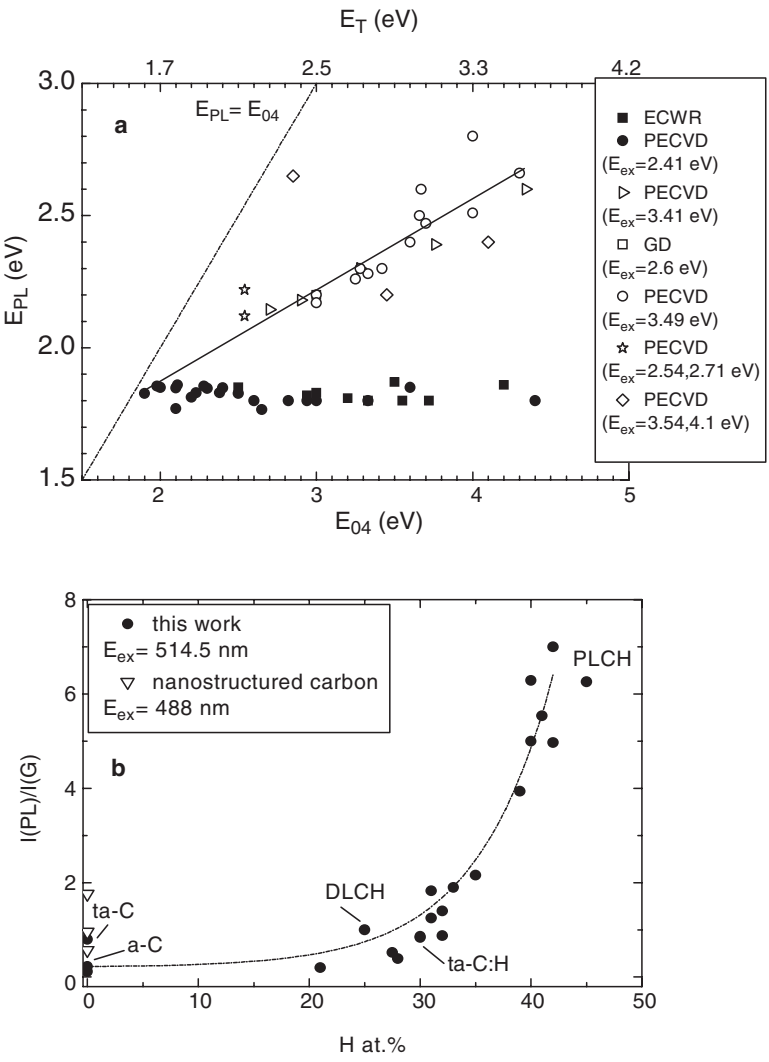

Fig. 31 (a) Variation of the PL energy with E_{04}. (b) I(PL)/I(G) as a function of H content. Note that a-C, DLCH with H <25 at. % and ta-C:H show a very weak PL, compared with PLCH. The lines are guide to the eye

deconvolute the separate contributions of sp^3 CH_x ($x = 2,3$) and CH sp^2 aromatic and olefinic vibrations [156]. Infrared spectroscopy is certainly preferable for quantitative analysis of CH_x stretching modes [171,172]. On the other hand, Raman measurements can be performed on any substrate or shape, such as metal-cutting tools, which are not suitable for IR. It is thus useful to analyse the CH-related UV Raman features. If the broad CH_x peak is fitted with a single Gaussian, its average position shifts from 2,920 cm^{-1} for PLCH and GLCH to 2,960 cm^{-1} in ta-C:H. This shift can be

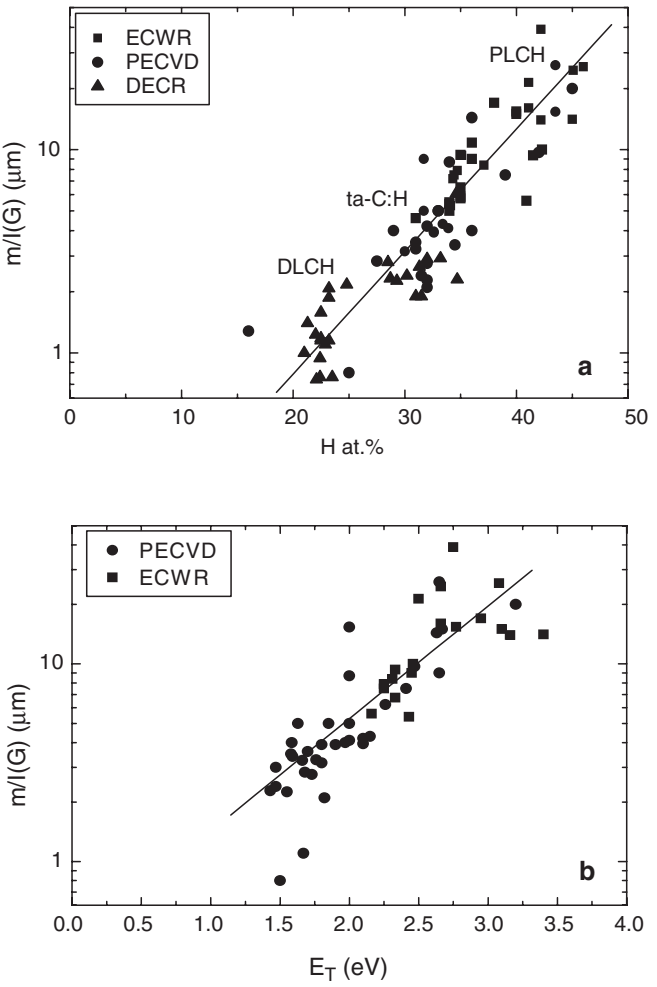

Fig. 32 m/*I*(G) as a function of (a) H content and (b) Tauc gap. The linear fits to the data are shown

interpreted as a lower CH sp^3 content or a higher sp^2 olefinic or aromatic contribution in ta-C:H compared to PLCH or GLCH [156,171,172].

Figure 23 shows that the intensity ratio of the sp^1 CN peak to the G peak, *I*(CN)/*I*(G), increases almost one order of magnitude moving from 514.5 to 244 nm excitation. Indeed, whilst it can be difficult to get a precise trend of *I*(CN)/*I*(G) for 514.5 excitation, the use of UV Raman spectra allows us to get a linear correlation between *I*(CN)/*I*(G) and the N content (Fig. 34). The enhancement of the sp^1 CN groups in UV excitation occurs because they have a π–π^* gap of 5–6 eV. A similar trend is observed for all carbon nitrides [24]. However, this trend is stronger and better defined for hydrogenated carbon nitride films

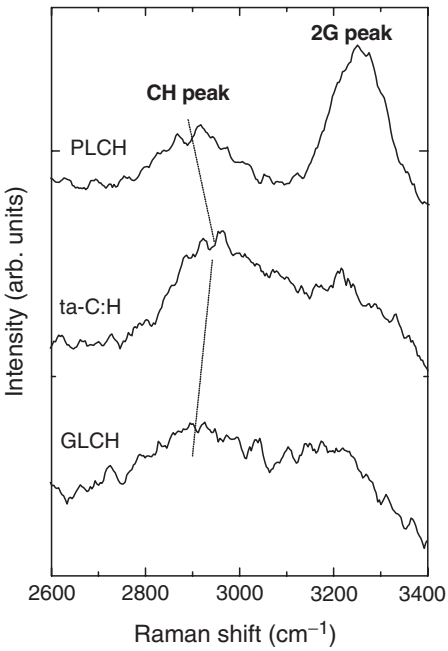

Fig. 33 UV Raman spectra showing the CH peak and second order of the G peak for template PLCH, ta-C:H and GLCH films

(Fig. 34(b)). This shows that N is less likely to form sp^1 sites in ta-C:N than in the softer materials [173,174].

Figure 35(a) plots the Raman spectra of an amorphous carbon silicon alloy with Si/(C + Si) = 0.35 taken at different excitation energy. The UV Raman spectra show two extra features at ~760 and 960 cm^{-1}, corresponding to the peaks in the VDOS of SiC, as expected for an amorphous silicon carbide [174]. These are almost never detected in visible Raman spectra of a-SiC alloys, due to the small cross section of Si–C vibrations. Figure 35(b) compares the IR and the UV Raman spectra of one a-Si:H film deposited at room temperature. In this case, the band at ~2,100 cm^{-1} is due to Si–H_2 stretching [45,176], and it is also seen in UV Raman spectra of the (t)a-$C_{0.65}$:$Si_{0.35}$:H alloy of Fig. 34(a). The band at ~650 cm^{-1} is due to SiH_n bending [45,176].

6 Roughness Evolution

Roughness evolution studies by AFM can be used to determine the minimum thickness for which a carbon film can be grown continuous and pinhole free. This parallels the direct testing performed by chemical, mechanical and spectroscopic methods to assess the coverage and corrosion protection of the overcoats [177,179]. The knowledge of the surface evolution mechanism of a certain class of carbon films, allows one to know if the loss of continuity in ultra-thin films is an intrinsic and

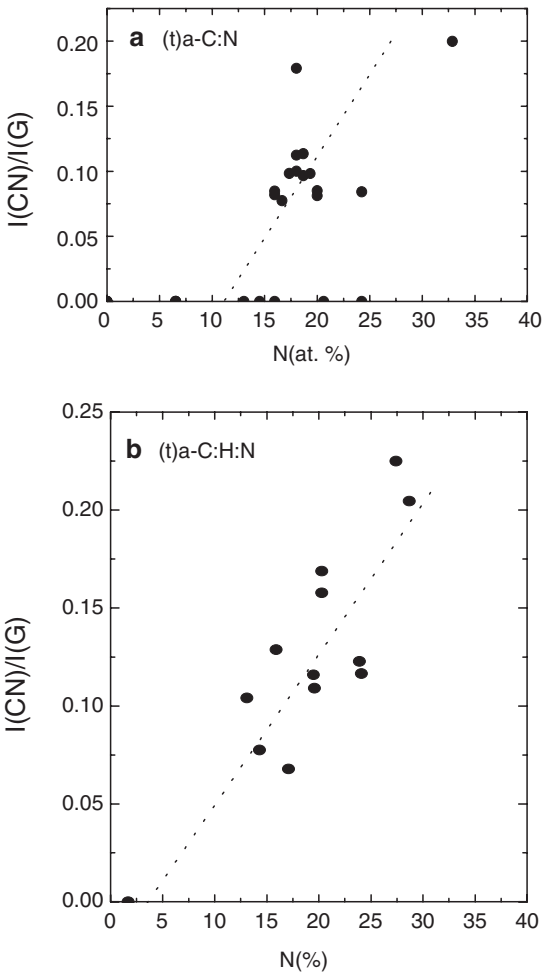

Fig. 34 Variation of $I(\mathrm{CN})/I(\mathrm{G})$ as a function of N content for (a) (t)a-C:N samples and (b) (t)a-C:H:N samples

unavoidable problem related to the nature of the deposited film, or if it is a technical problem, which could be improved with better process conditions [180–184].

If h is the film thickness and R the roughness, the film is continuous if h-R remains sizeable as h decreases. The roughness evolution of a film can generally be described by the fractal scaling laws [181], in which R scales as

$$R \sim \ell^{\alpha} f(t/\ell^{\alpha/\beta}) \tag{16}$$

Here t is the deposition time (assuming a constant deposition rate), ℓ is the length scale i.e. $\ell \times \ell$ is the window size where R is measured, with $\ell \leq L$ the size of the

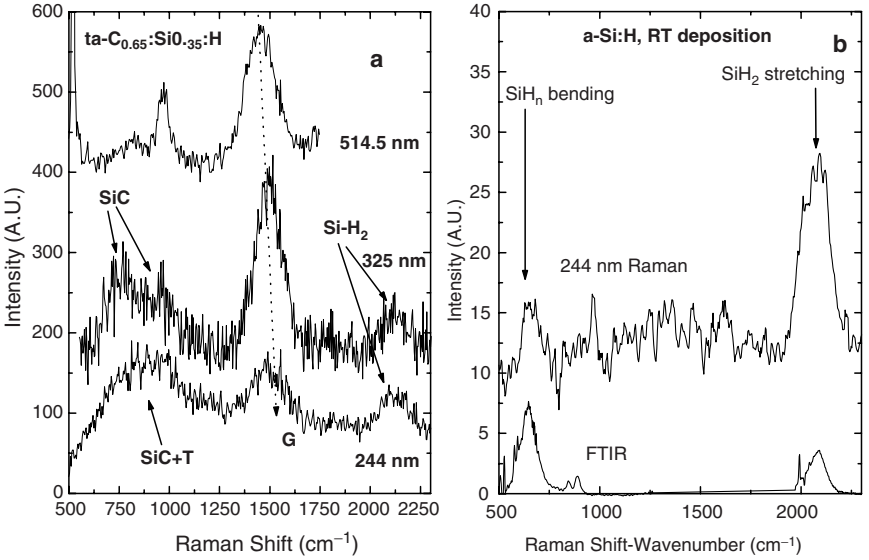

Fig. 35 (a) Multi-wavelength Raman spectra of a ta-$C_{0.65}$:$Si_{0.35}$:H sample. For UV excitation the SiC modes and the Si-H_2 stretching are seen. (b) Comparison of 244 nm Raman and infrared spectra of an a-Si:H sample deposited at room temperature, 30 at. % H

sample. $f(u)$ is a scaling function of the argument u = t/$\ell^{\alpha/\beta}$. For small times, that is $u << 1$, then $R \sim t^{\beta}$ and the heights at different surface sites are independent. As time increases, the heights at different sites become correlated. When the correlations are significant, the roughness saturates at a constant value R_{sat}. α is called the roughness exponent ($0 \leq \alpha \leq 1$). β is called the growth exponent [181]. The exponents α and β uniquely characterise how the surface evolves with the length scale ℓ and the time t. Their values define different growth mechanism universality classes [181,186]. For example, in random deposition the particles stick immediately where they land on a surface and β is 0.5, while α is undefined. In random deposition with surface diffusion, the particles do not stick immediately, and they can diffuse to a nearby valley site with lower height. This gives $\beta = 1/3$ and $\alpha = 1$. For ballistic deposition (with no diffusion), lateral sticking is also allowed, creating overhangs, in contrast to the random deposition model. This gives fractal exponents of $\beta = 0.5$ and $\alpha = 2/3$ [181].

Figure 36(a) shows the AFM pictures of 1 nm thick ta-C films. The surface is continuous and is characterised by uniformly distributed features [180]. Figure 36(b) plots the roughness as a function of film thickness for two sets of ta-C films, deposited on a laboratory scale S-Bend FCVA [187] and a production near process HCA source [188]. The roughness is constant (R ~0.12 nm) for every sample [180]. The roughness values are in agreement with previous reported data on thicker films [189]. The roughness is thus always much lower than the film thickness, so that h-R is positive even for 1 nm films and no pinholes are expected.

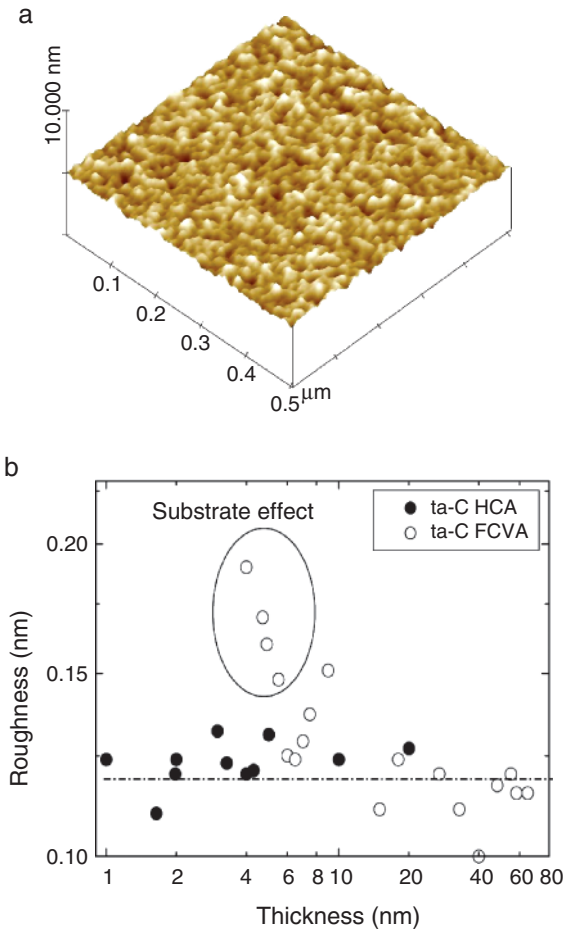

Fig. 36 (a) AFM picture of a ta-C film 0.9 nm thick. The scan size is 500 × 500 nm and the vertical scale is 10 nm. (b) Roughness as a function of the thickness for ta-Cs, deposited with two different cathodic arc systems (HCA, and FCVA). In the case of the ta-Cs deposited by FCVA, an exponential smoothing of the initial rougher substrate is observed

Note that the apparent roughness increase for low thickness in the FCVA films is due to the higher roughness of the Si substrate (~0.2 nm) used for these films with respect to the lower roughness substrate (~0.1 nm) used for the HCA films. This shows the smoothening effect of ta-C films even on an already smooth substrate, such as the Si used for the FCVA films.

Figure 36(b) shows that ta-C has ultra-low roughness (rms roughness ~0.12 nm) and that is independent on the film's thickness, thus providing films equally smooth when 1 or 100 nm thick [180]. These are unique properties since films usually form through a series of stages of nucleation, coalescence and possible roughening which, in general, lead to island formation for the thinnest films. For ta-C, we

found α ~0 and β ~0–0.1 [180,182]. This is consistent with the Edward-Wilkinson (EW) growth model [182,190]. Here, the smoothening mechanism is diffusion driven by local surface curvature [182,190]. Quantum and classical molecular simulations have shown that an efficient damping of surface fluctuations is achieved through impact-induced downhill currents, eroding hills on the film surface, in agreement with EW model [182]. This smoothing mechanism is able to explain several experimentally observed properties of ta-C growth [182]. For example, it accounts for the smoothing of initially rough substrates. Starting from a sine-shaped film surface in Fig. 37(a), the evolution of the surface was studied with classical molecular dynamics during the impact of 4000 atoms. Figure 37(b) shows the complete smoothing of the initial rough film, in agreement with the experiments [180,182]. This also explains why other carbon films, deposited at low ion energies, do not reach the ultra-smoothness of ta-C [180,182].

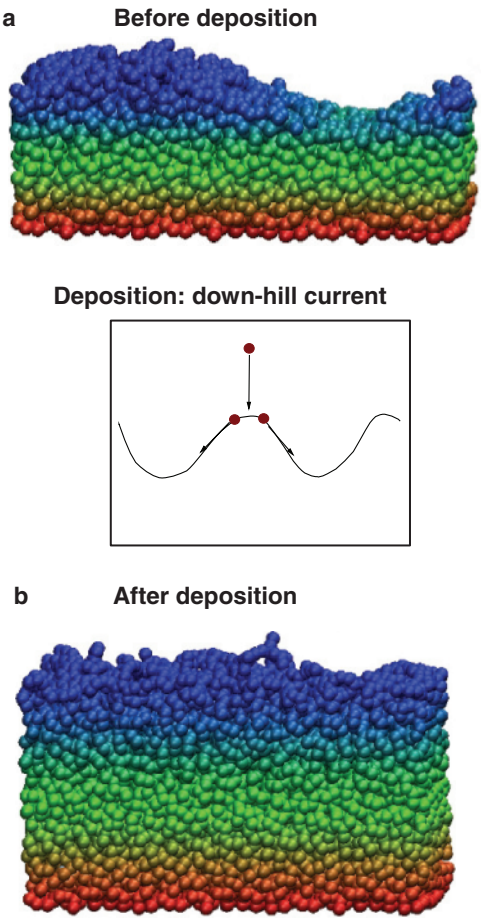

Fig. 37 Starting from a sine-shaped substrate surface (a), the evolution of the surface was studied with classical molecular dynamics during the impact of 4,000 atoms. (b) Shows the complete smoothing of the initial rough substrate, after the deposition [182]. The colour coding represents the height of the atoms

The surface roughness evolution for ta-C:H was also extensively analysed [191]. A very similar behaviour to ta-C was found, with the ta-C:H roughness slightly higher than the ta-C one for any given thickness. Also in this case the smoothening can be assigned to impact-induced downhill currents during growth. This indicates that ta-C:H, similar to ta-C, benefits from the energetic ion bombardment during deposition that produces extremely smooth films [191].

7 Evolution of ta-C Properties with Thickness

Figures 9 and 13(c) allow some interesting conclusions on the thickness evolution of ta-C properties. The density, sp^3 fraction and Young's modulus all decrease for films below 8 nm thickness [1]. However, there are distinct trends. The XRR density of a 2.2 nm ta-C film, 2.8 g/cm^3, corresponds, by using Eq. (1), to ~60% sp^3 content, similar to that found by direct electron energy loss spectroscopy measurements (~45%) [1]. In contrast, its Young's modulus (~100 GPa) would correspond to a much lower density of 1.9 g/cm^3 and an sp^3 fraction of ~0, if Eqs (1–3) are applied. This is general. The sp^3-density correlation of bulk ta-C of Eq. 1 still holds for ultra-thin films. However, ultra-thin films are softer than bulk films (60–70 nm thick) of the same density, so Eqs (2–3) do not hold. This conclusion bears fundamental implications for the magnetic disc coating applications of DLCs. It explains why ta-C films can maintain their corrosion protection properties down to 1 nm thickness, even if their mechanical properties are much softer than bulk (>10 nm) films. The softening of the mechanical properties of ultra-thin films is a size effect, and implies neither a strong density and sp^3 decrease, nor a change in the surface smoothness. Indeed, Section 6 pointed out that the roughness is constant for decreasing film thickness.

Thus, the first thickness reduction effect is that, for a given density and sp^3 content, the mechanical properties of an ultra-thin film are softer than what expected for the same film if is was thick.

The second effect is that the density and sp^3 fraction of ultra-thin films are, however, smaller than the maximum reported for bulk films. This is can be understood if one considers the cross-sectional structure of ta-C films [19]. The films consist of three layers, an outer layer, a middle "bulk" layer and an interfacial layer. The outer surface layer is about 0.5 nm thick and more sp^2. Its thickness corresponds to the carbon ion range. There is also an interfacial layer between the C and the Si substrate, where ion mixing creates C–Si bonding. Since the deposition conditions are constant during film growth, the thickness of the surface and interface layers is roughly independent of the total film thickness [19]. Thus, for thinner films, the thickness of the middle "bulk" layer decreases, but the nature of the surface layer (and thus the roughness) should not change much with thickness, for a given ion energy. The surface layer is also softer than the bulk film. This is also true for the interface layer, as C–Si bonds are softer than C–C bonds. This explains the quick decrease of the mechanical properties once the width of the bulk layer becomes similar to (or smaller than) the interface and surface layers, as observed in Fig. 9.

A simple expression can be derived to describe the evolution of E versus thickness:

$$E(z) = E_{\text{bulk}} - (E_{\text{bulk}} - E_{\text{csi}})\, z_{\text{csi}}/z \tag{17}$$

Where $E(z)$ is Young's modulus at a thickness z, E_{bulk} is Young's modulus of the bulk phase (which can be approximated with E for $z > 10$ nm) and z_{csi} is the total thickness of the surface and interface layers. For the HCA films in Fig. 9, z_{csi} ~1 nm, whilst E_{bulk}~ 450 GPa and E_{csi}~50 GPa. The line in Fig. 9 is a plot of Eq. (17) and is in excellent agreement with the experimental data, thus confirming this model. A similar equation with E replaced by Disp(G) fits the data in Fig. 13(c).

In any case, a 2 nm ta-C film still has a Young's modulus of ~100 GPa, sp^3 content of ~50% and a 2.8 g/cm^3 density. The smoothness and absence of pinholes give excellent corrosion resistance down to ~1 nm thickness, as confirmed by direct corrosion tests [178].

8 Thermal Conductivity

The thermal properties and, in particular, the thermal conductivity (K), of DLCs are very important for thermal engineering of micro-devices [192–197].

A convenient technique to measure thermal conductivity is the so-called 3ω method. This was initially developed for bulk materials [198] and later extended to thin films and nanostructures [199–201]. The measurements are performed by placing a thin conductor directly on the surface of the material of interest. An alternating current at frequency 1ω heats the conductor. This produces a resistance change at frequency 3ω. The amplitude of the temperature oscillation depends on the power per unit length, on the frequency (f) and on the physical properties of the material, such as ρ, K and heat capacity C_{p} [202]. In case of thin films on a substrate the temperature drop over the film needs to be separated from that over the Si substrate. This can be done by ensuring that the modulated thermal diffusion length $\Lambda_{\text{th}} \approx [K/(2\pi f C_{\text{p}})^{1/2}]$ is much smaller than the substrate thickness. This can be checked by determining K for the Si substrate [192].

Figure 38 shows the measured K temperature dependence for different types of DLCs: one PLCH, one GLCH, one DLCH, one ta-C:H and two ta-Cs of different densities [192]. It shows that K increases with T. This trend is typical of amorphous materials [202].

Figure 38 also shows (lines) the result of K calculation for two samples using the "minimum thermal conductivity" approach [192]. This is based on the assumption of random walks between localised excitations in an amorphous material with K given as [202]:

$$K_{\min} = (\pi/6)^{1/3} k_B (n_A)^{2/3} \sum_i \upsilon_i (T/\theta_i)^2 \int_0^{\theta_i/T} x^3 e^x (e^x - 1)^{-2} dx \tag{18}$$

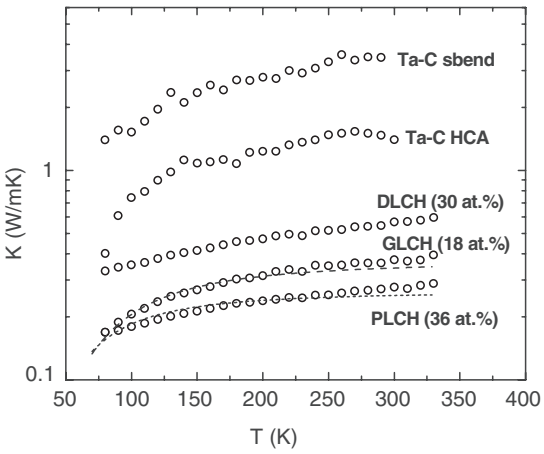

Fig. 38 K vs. T for representative samples

Here the sum is over three phonon polarisation branches ($i = L$ for longitudinal, $i = T_1$ and $i = T_2$ for transverse), k_B is the Boltzmann constant, $n_A = N_A\rho/M$ is the number of atoms per unit volume (N_A is Avogadro number, M is atomic mass), v_i is phonon group velocity of the ith branch and θ_i is the cutoff temperature. Distinguishing separate θ_i for the polarisation branches is not very well justified for disordered material system. At the same time, since Young's modulus and Poisson's ratio ν are known (see Section 4), one can consider separate phonon group velocities given by $v_L = (E/\rho)^{1/2}$ and $(v_T/v_L)^2 = 2(1-\nu)/(1-2\upsilon)$. ν = 0.12 for ta-C and ~0.3 for a-C:H (see Section 4). Note that there is no well-defined procedure for computing Debye temperature (θ_D) in disordered solids [203]. The heterogeneous nature of the material, with sp^2 clusters and sp^3 regions, makes it even more challenging to define Debye temperature theoretically. Thus, θ_D is considered an adjustable parameter and used instead of separate θ_I [193].

The calculated dependence, shown in Fig. 38, reproduces the measured T dependence of K very well. The extracted values for the effective θ_D are between 310–1,300 K, depending on the film structure. In particular, θ_D scales with ρ. Indeed, a linear extrapolation gives θ_D ~1,900 K for $\rho = 3.5$ g/cm^3, very close to that of diamond (~1,880 K) [204]. For comparison, the planar θ_D in graphite is ~2,280 K [205], while the perpendicular θ_D is ~760 K [206].

Fig. 39(a) plots K, measured at room T, as a function of ρ [1,206]. Figure 39(a) shows that K scales linearly with ρ and that the H content per se plays a minor role. For $\rho > 1.6$ g/cm^3, a linear fit of the data gives:

$$K\ [\mathrm{W/mK}] = 1.77\rho[\mathrm{g/cm^3}] - 2.82 \tag{19}$$

Since in amorphous and diamond-like carbons ρ scales with C–C sp^3 content, Eq. (1), Fig. 39(a) implies that K scales as well with this. Indeed, amongst hydrogenated carbon films, ta-C:H has the highest K because it has the highest C–C sp^3 content. The highest thermal conductivity amongst all DLCs is reached for ta-C (~3.5 W/mK).

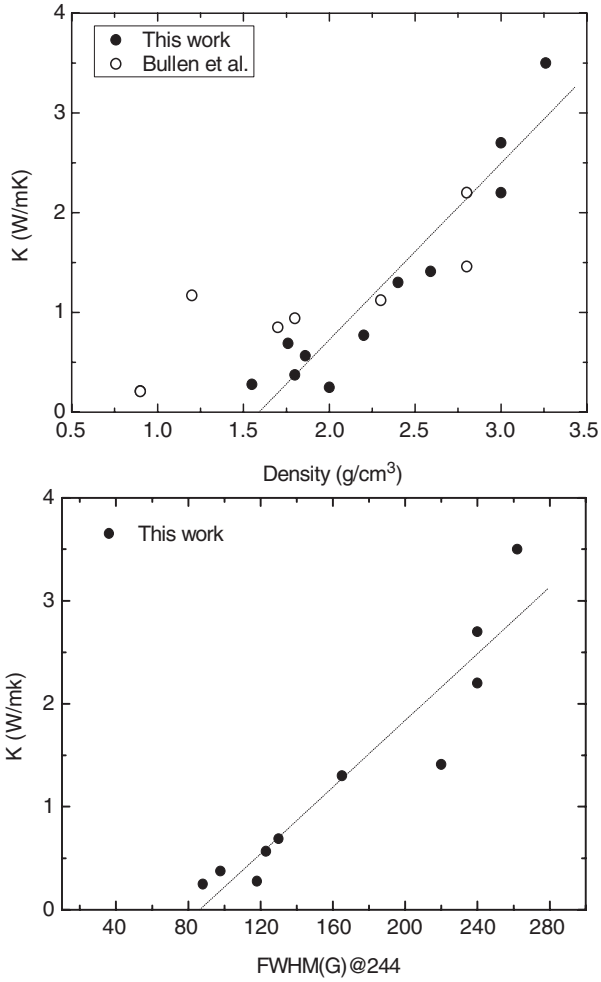

Fig. 39 (a) K at room T as a function of ρ (b) K as a function of FWHM(G)

Raman spectroscopy further confirms the correlation between film structure and thermal properties. Figure 39(b) plots FWHM(G)@244 as a function of *K*. Since FWHM(G) is proportional to the structural disorder, and this increases for increasing sp^3 content for as deposited samples (see Section 5), Fig. 39(b) confirms that *K* is linked to the sp^3 C–C content for as deposited samples. We can also get a simple relation between FWHM(G)@244 nm and thermal conductivity, for FWHM(G)@244 > 80 cm^{-1}:

$$K[\mathrm{W/mK}] = -1.397 + 0.0168\ \mathrm{FWHM(G)@244}\ [\mathrm{cm}^{-1}] \tag{20}$$

Note that, if we just scale *K* of a-Si [207] to that of an ideal fully sp^3-bonded amorphous carbon film [8,208] we would get *K* ~3 W/mK. On the other hand, the

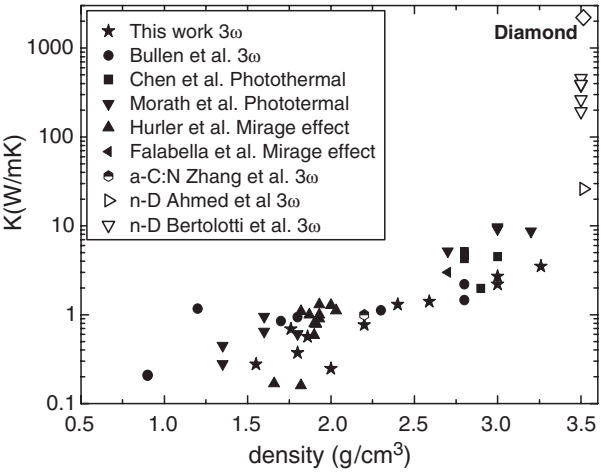

Fig. 40 K at RT measured by 3ω and other literature data as a function of ρ for a variety of DLC, n-D and diamond [190, 208–213]

minimum thermal conductivity [202] of such ideal material can be estimated to be ~1.5 W/mK. These simple estimates are in excellent agreement with the measured K for the highest sp^3 ta-C, which sets the upper limit for K. On the other hand, some literature reports show much higher values. Reference [209] has K for ta-C of 4–5 W/mK and Ref. [210] between 8 and 10 W/mK. They both used photo-thermal techniques, which require assumptions on the heat capacitance. Thus these values might be overestimated [192].

Note as well that K of diamond [211] is much higher than the maximum extrapolated for a fully amorphous sp^3 material. This means that K is also extremely sensitive to the *ordering* of the sp^3 phase, unlike any of the other common structural parameters used to characterise carbon films (such as density, Young's modulus, etc.), which depend on the *amount* of sp^3, but not in any significant way on this being amorphous or (nano)-crystalline. This is demonstrated in Fig. 40, which plots K as a function ρ for all DLCs reported in literature and for diamond and nano-diamond [192]. Figure 40 shows that K of n-D, which has sp^3 content and E just marginally higher than ta-C, is significantly bigger than that of ta-C. This is due to the presence of a crystalline, rather than amorphous, sp^3 phase. Similarly, for very low sp^2 contents, the ordering of the sp^2 phase in graphitic regions would significantly increase the thermal conductivity [205].

9 Conclusions

This chapter reviewed x-ray reflectivity, surface acoustic waves, Raman spectroscopy, AFM and 3ω method for the determination of the main structural properties of carbon films. The combination of these methods allows a full structural characterisation

in terms of density, thickness, layering, elastic constants, roughness, structure, chemical composition and thermal conductivity. Raman spectroscopy, in particular, allows the assessment of most of the materials properties, even if indirectly.

Acknowledgements The author wishes to thank all the people who contributed to the work reviewed in this chapter: C. Casiraghi, S. E. Rodil, B. Kleinsorge, M. Moseler, F. Piazza, R. Ohr, M. Von Gradowsky, C. Shug, H. Hilgers, D. Schneider, M. G. Beghi, C. E. Bottani, A. Libassi, B. K. Tanner, M. Shamsa, W.L. Liu, A. A. Balandin, V. Stolojan, L. M. Brown, D. Batchelder, I. R. R. Mendieta, B. Popescu, A. Champi, A. Erdermir, J. Fontaine, D. Grambole, J. Robertson. The author acknowledges financial support from the Royal Society and The Leverhulme Trust.

References

1. A. C. Ferrari, Surf. Coat. Technol. 180–181, 190 (2004).
2. Y. Lifshitz, G. D. Lempert, E. Grossman, Phys. Rev. Lett. 72, 2753 (1994).
3. A. Voevodin, M. S. Donley, J. S. Zabinski, Surf. Coat. Technol. 52, 42 (1997).
4. J. Schwan, S. Ulrich, H. Roth, et al., J. Appl. Phys. 79, 1416 (1996).
5. D. R. McKenzie, Rep. Prog. Phys. 59, 1611 (1996).
6. S. Anders, J. Diaz, J. W. Ager, R. Y. Lo, D. B. Bogy, Appl. Phys. Lett. 71, 3367 (1997).
7. P. J. Fallon, V. S. Veerasamy, C. A. Davis, J. Robertson, G. A. J. Amaratunga, W. I. Milne, J. Koskinen, Phys. Rev. B, 48, 4777 (1993).
8. A. C. Ferrari, J. Robertson, M. Beghi, C. E. Bottani, R. Ferulano, R. Pastorelli, Appl. Phys. Lett., 75, 1893 (1999).
9. A. C. Ferrari, J. Robertson, Phys. Rev. B, 61, 14095 (2000).
10. A. C. Ferrari, J. Robertson, Phil. Trans. R. Soc. London A, 362, 2477 (2004).
11. A. C. Ferrari, J. Robertson, Phys. Rev. B, 64, 075414 (2001).
12. C. Casiraghi, A. C. Ferrari, J. Robertson, Phys. Rev. B, 72, 085401 (2005).
13. P. Koidl, C. Wagner, B. Discheler, J. Wagner, M. Ramsteiner, Mater. Sci. Forum, 52, 41 (1990).
14. M. A. Tamor, W. C. Vassell, K. R. Karduner, Appl. Phys. Lett., 58, 592 (1991).
15. S. F. Yoon, K. H. Tan, Rusli, J. Ahn, J. Appl. Phys. 91, 1634 (2002).
16. O. Durand-Drouhin, M. Lejeune, M. Benlahsen, J. Appl. Phys., 91, 867 (2002).
17. T. Schwarz-Sellinger, A. von Keudell, W. Jacob, J. Appl. Phys., 86, 3988 (1999).
18. B. Popescu, A. Tagliaferro, F. De Zan, E. A Davis, J. Non Cryst. Solids, 266–269, 803 (2000).
19. A. C. Ferrari, A. Libassi, B. K. Tanner, V. Stolojan, J. Yuan, L. M. Brown, S. E. Rodil, B. Kleinsorge, J. Robertson, Phys. Rev. B, 62, 11089 (2000).
20. N. A. Morrison, S. E. Rodil, A. C. Ferrari, J. Robertson, W. I. Milne, Thin Solid Films, 337, 71 (1999).
21. M. Weiler, K. Lang, E. Li, J. Robertson. Appl. Phys. Lett., 1314, 72 (1998).
22. M. Weiler, S. Sattel, T. Giessen, K. Jung, H. Ehrhardt, V. S. Veerasamy, J. Robertson. Phys. Rev. B, 53, 1594 (1996).
23. M. Weiler, S. Sattel, K. Jung, H. Ehrhardt, V. S. Veerasamy, J. Robertson, Appl. Phys. Lett., 64, 2797 (1994).
24. C. Ferrari, S. E. Rodil, J. Robertson, Phys. Rev. B, 67, 155306 (2003).
25. Hellgren N., Johansson M. P., Broitman E., Hultman L., Sundgren J. E., Phys. Rev. B, 59, 5162 (1999).
26. Jimenez I., Gago R., Albella J. M., Caceres D., Vergara I., Phys. Rev B, 62, 4261 (2000).
27. Gammon W. J., Malyarenko D. I., Kraft O., Hoatson G. L., Reilly A. C., Holloway B.C., Phys. Rev. B, 66, 153402 (2002).

28. Gammon W. J., Hoatson G. L., Holloway B. C., Vold R. L., Reilly A. C., Phys. Rev. B, 68, 195401 (2003).
29. K. J. Boyd, D. Marton, S. S. Todorov, A. H. Al-Bayati, J. Kulok, R. A. Zuhr J. W. Rabalais, J. Vac. Sci. Technol. A 13, 2110 (1995).
30. J. Hu, P. Yang, C. M. Lieber, Phys. Rev. B 57, 3185 (1998).
31. C. A. Davis, D. R. McKenzie, Y. Yin, Kravtchinskaia, G. A. J. Amaratunga, V.J. Veerasamy, Phil. Mag. B 69, 1133 (1994).
32. V. S. Veerasamy, J. Yuan, G. A. J. Amaratunga, W. I. Milne, K. W. R. Gilkes, M. Weiler, L. M. Brown, Phys. Rev. B 48, 17954 (1993).
33. C. Spaeth, M. Kuhn, U. Kreissig, F. Richter, Diam. Relat. Mater. 6, 626 (1997).
34. B. Kleinsorge, A. C. Ferrari, J. Robertson, W. I. Milne, J. Appl. Phys. 88, 1149 (2000).
35. S. E. Rodil, W. I. Milne, J. Robertson, L.M. Brown, Appl. Phys. Lett. 77, 1458 (2000).
36. P. Hammer, N. M. Victoria, F. Alvarez, J. Vac. Sci. Technol. A 16, 2941 (1998).
37. S. R. P. Silva, J. Robertson, G. A. J. Amaratunga, B. Rafferty, L. M. Brown, D. F. Franceschini, G. Mariotto, J. Appl. Phys. 81, 2626 (1997).
38. J. Schwan, V. Batori, S. Ulrich, H. Ehrhardt, S. R. P. Silva, J. Appl. Phys. 84, 2071 (1998).
39. S. E. Rodil, A. C. Ferrari, J. Robertson, W. I. Milne, J. Appl. Phys. 89, 5425 (2001).
40. S. E. Rodil, N. A. Morrison, J. Roberston, W. I. Milne, Phys. Stat. Solidi A 175, 25 (1999).
41. M. Zhang, L. Pan, T. Miyazaki, Y. Nakayama, Jpn. J. Appl. Phys. 36, 4897 (1997).
42. S. Bhattacharyya, C. Cardinaud, G. Turban, J. Appl. Phys. 83, 4491 (1998); S. Bhattacharyya, M. Hietschold, F. Richter, Diam. Relat. Mater. 9, 544 (2000).
43. J. Q. Zhang, Y. Setsuhara, S. Miyake, B. Kyoh, Jpn J. Appl. Phys. 36, 6894 (1997).
44. Grill A., 2001, Diam. Relat. Mater. 10, 234.
45. Racine B., Ferrari A. C., Morrison N. A., Hutchings I., Milne W. I., Robertson J., 2001, J. Appl. Phys. 90, 5002.
46. Matsuda A., Tanaka K., 1987, J. Non-Cryst. Solids 97, 1367.
47. Oguri K., Arai T., 1992, Thin Solid Films 208, 158.
48. Gangopadhyay A. K., Willermet P. A., Tamor M. A., Vassel W. C., 1997, Tribol. Int. 30, 9.
49. Voevodin A. A., Schneider J. M., Rebholz C., Matthews A., 1996, Tribol. Int. 29, 559 (1996).
50. Milani P., Ferretti M, Piseri P., Bottani C. E., Ferrari A. C., LiBassi A., Guizzetti G., Patrini M., J. Appl. Phys. 82, 5793 (1997).
51. A. Libassi, B. K. Tanner, A.C. Ferrari, X-ray reflectivity from amorphous carbon. In; Properties of Amorphous Carbon, IEE-EIMS datareview series 29, INSPEC, p. 179 (2003).
52. B. Lengeler, X-ray absorption and reflection in the hard x-ray range. In: M. Campagna and K.Rosei (eds) North Holland, Amsterdam, The Netherlands (1990).
53. V Holy, U. Pietsch, T Baumbach, High-Resolution X-ray Scattering from Thin Films and Multilayers. Springer, New York (1999).
54. V. Holy, T. Baumbach, Phys. Rev. B 49, 10668 (1994).
55. D.E. Savage et al. J. Appl. Phys. 69, 1411 (1991).
56. D.E. Savage, N. Schimke, Y.H. Pang, M.G. Legally, J. Appl. Phys. 71, 3283 (1992).
57. I. Pape, T.P.A.Hase, B.K.Tanner, M. Wormington, Physica B. 253, 278 (1998).
58. B.L. Henke, E.M. Gullikson, J.C. Davis, Atom. Data Nucl. Data. 54, 181 (1993).
59. L.G. Parrat, Phys. Rev. 95, 359 (1954).
60. M. Wormington et al., Phil. Trans. Roy. Soc. A 357, 2827 (1999).
61. M. Wormington et al., Phil. Mag. Lett. 74, 211 (1996).
62. E. Kondrashov et al., Diam. Relat. Mater. 6, 1784 (1997).
63. S. Logothetidis, G. Stergioudis, Appl. Phys. Lett. 71, 2463 (1997).
64. A. Lucas, T.D. Nguyen, J.B. Kortright, Appl. Phys. Lett. 59, 2100 (1991).
65. M.J. Grundy et al., Thin Solid Films 172, 269 (1989).
66. E. Findeisen et al., J. Appl. Phys. 76, 4636 (1994).
67. F. Toney, S. Brennan, J. Appl. Phys. 66, 1861 (1989).
68. Y. Huai et al., Appl. Phys. Lett. 65, 830 (1994).
69. Q. Zhang, S.F. Yoon, Rusli, J. Ahn, H. Yang, D. Bahr, J. Appl. Phys. 86, 289 (1999).

70. J. Martinez-Miranda, et al., Mat. Res. Soc. Symp. Proc. 498, 55 (1998).
71. A. Libassi et al., Diam. Relat. Mater. 9, 771 (2000).
72. P. Patsalas, S. Logothedids, P. C. Kelires, Diam. Relat. Mater. 14, 1241 (2005).
73. E. Egerton, Electron Energy Loss Spectroscopy in the Electron Microscope. Plenum Press, New York (1986).
74. J. Fink, T. Muller-Heinzerling, A. Bubenzer, P. Koidl, G. Cercelius, Solid State Comm. 47, 687 (1983).
75. J. Fink, T. Muller-Heinzerling, J. Pfuger, B. Scheerer, B. Dishler, P. Koidl, A. Bubenzer, R. E. Sath, Phys. Rev. B 30, 4713 (1984).
76. S. D. Berger, D. R. McKenzie, P. J. Martin, Phil. Mag. Lett. 57, 285 (1988).
77. P. J. Fallon, L. M. Brown, Diam. Relat. Mater. 2, 1004 (1993).
78. J. Kulik, Y. Lifshitz, G. D. Lempert, I. W. Rabalais, D. Marton, J. Appl. Phys. 76, 5063 (1998).
79. C. A. Davis, K. M. Knowles, G. A.J. Amaratunga, Phys. Rev. Lett. 80, 3280 (1998).
80. S. Waidman, M. Knupfer, J. Fink, B. Kleisorge, J. Robertson, J. Appl. Phys. 89, 3783 (2001).
81. H. Pan, M. Pruski, B. C. Gerstein, F. Li, J. S. Lannin, Phys. Rev. B 44, 6741 (1991).
82. M. M. Golzan, D. R. McKenzie, P. B. Lukins, J. Hanna, A. M. Vassallo, Chem. Phys. 193, 167 (1995).
83. S. Kaplan, F. Jansen, M. Machonkin, Appl. Phys. Lett. 47, 750 (1985).
84. R. H. Jarman, G. J. Ray, R. W. Stadley, Appl. Phys. Lett. 49, 1065 (1986).
85. A. Grill, B. S. Meyerson, V. V. Patel, J. A. Reimer, M. A. Petrich, J. Appl. Phys. 61, 2874 (1987).
86. T. M. Alam, T. A. Friedmann, P. A. Schultz, D. Sebastiani. Phys. Rev. B 67, 245309 (2003).
87. C. Jager, J. Gottwald, H. W. Spiess, R. J. Newport, Phys. Rev. B 50, 846 (1994).
88. T. Blinc, D. Arcon, P. Cevc, I. Pocsik, M. Koos, Z. Trontelj, Z. Jaglicic, J. Phys. C. 10, 6813 (1998)
89. R. Kleber, K. Jung, H. Ehrhardt, I. Muhling, K. Breuer, H. Metz, F. Engelke, Thin Solid Films 205, 274 (1991).
90. C. Donnet, J. Fontaine, F. Lefebre, A. Grill, V. Patel, C. Jahnes, J. Appl. Phys. 85, 3264 (1999); R. Ohr, C. Shug, M. Wahl, et al., Anal. Bioanal. Chem. 375, 43 (2003).
91. B.K. Tanner, A. LiBassi, A.C. Ferrari, J. Robertson, Mater. Res. Soc. Symp. Proc. 675, W11.4 (2001).
92. R. Ohr, B. Jacoby, M.V. Gradowski, C. Schug, H. Hilgers, Surf. Coat. Technol. 173, 111 (2003).
93. W. C. Oliver, G. M. Pharr, J. Mat. Res. 7, 1564 (1992)
94. G.M. Pharr, D.L. Callahan, S.D. McAdams, T.Y. Tsui, S. Anders, J.W. Ager, I.G. Brown, C.S. Bhatia, S.R.P. Silva, J.Robertson, Appl. Phys. Lett., 68, 779 (1996).
95. S. Xu, D. Flynn, B.K. Tay, S. Prawer, K.W. Nugent, S.R.P. Silva Y. Lifshitz, W.I. Milne, Phil. Mag. B 76, 351 (1997).
96. T.A. Friedman, J.P. Sullivan, J.A. Knapp, D.R. Tallant, D.M. Follstaedt, D.L. Medlin, P.B. Mirkarimi, Appl. Phys. Lett. 71, 3820 (1997).
97. D. A. LaVan, R. J. Hohlfelder, J. P. Sullivan, T. A. Friedmann, M. Mitchell,C. I. H. Ashby, Mater. Res. Soc. Symp. Proc. 594, 295 (2000).
98. S. Cho, I. Chasiotis, T. A. Friedmann, J. P. Sullivan, J. Micromech. Microeng. 15, 728, (2005).
99. D. A. Czaplewski, J. P. Sullivan, T. A. Friedmann, J. R. Wendt, Appl. Phys. Lett. 87, 161915 (2005).
100. M.G. Beghi, A.C. Ferrari, K.B.K. Teo, et al., Appl. Phys. Lett. 81, 3804 (2002).
101. F. Nizzoli, J.R.Sandercock, Dynamical properties of solids. In: G. Horton and A. Maradudin (eds) North-Holland, Amsterdam, The Netherlands, p. 281 (1990).
102. M. G. Beghi, C. E. Bottani, A. C. Ferrari, Properties of Amorphous Carbon, In: S. R. P. Silva (ed.) EMIS Data Review Series No. 29, INSPEC (2003).

103. D. Schneider, P. Siemroth, T. Schulke, et al., Surf. Coat. Technol. 153, 252 (2002).
104. D. Schneider, Th. Witke, Th. Schwarz, B. Schneich, B. Schultrich, Surf. Coat. Technol. 126, 136 (2000).
105. J. D. Achenbach, Wave Propagation in Elastic Solids. North Holland, Amsterdam, The Netherlands (1990).
106. G. W. Farnell, E. L. Adler, Physical Acoustics, Vol. 9. In: W. P. Mason and R. N. Thurston (eds) Academic, New York, p. 35 (1972).
107. M. G. Cottam, A. A. Maradudin, Surface Excitations. In: V. M. Agranovitch, R. Loudon (eds) Elsevier Science, Amsterdam, The Netherlands, p. 1 (1984).
108. J. D. Comins, in Handbook of elastic properties of solids, liquids and gases, Vol. 1. In: M. Levy et al. (eds) Academic Press, Sidcup, UK (2000).
109. M. G. Beghi et al., J. Appl. Phys. 81, 672 (1997).
110. S. Makarov et al., J. Appl. Phys. 78, 5028 (1995).
111. R. Vogelgesang R. et al., Phys. Rev. B 54, 3989 (1996).
112. E. S. Zouboulis et al., Phys. Rev. B 57, 2889 (1998).
113. X. Jiang et al., Appl. Phys. Lett. 59, 1055 (1991).
114. J. K. Krüger et al., J. Appl. Phys. 87, 74 (2000).
115. D. Schneider et al., Thin Solid Films 295, 107–16 (1997); 332, 157–63 (1998); Diam. Relat. Mater. 7, 973–80 (1998).
116. M. Grimsditch, J. Phys. C: Solid State Phys. 16, L143 (1983).
117. M. Grimsditch, Phys. Stat. Sol. B 193, K9 (1996).
118. S. A. Lee, S. M. Lindsay, Phys. Stat. Sol. B 157, K83 (1990).
119. X. Jiang et al., J. Appl. Phys. 66, 4729 (1989); 68, 1018 (1990); Phys. Rev. B 43, 2372 (1991).
120. L. Valentini et al., J. Appl. Phys. 89, 1003 (2001).
121. Morath et al., J. Appl. Phys. 76, 2636 (1994).
122. Y. Kim et al., J. Vac. Sci. Technol. A 18, 1993 (2000).
123. T. Wittkowski et al., Thin Solid Films 368, 216 (2000).
124. R.Pastorelli et al., Diam. Relat. Mater. 9, 825 (2000).
125. M. Chirita et al., Phys. Rev. B 60, R5153 (1999).
126. C. E. Bottani et al., Europhys. Lett. 42, 431 (1998); C. Casari et al., Phys. Rev. B 64, 085417 (2001).
127. D. Fioretto et al., Phys. Rev. B 52, R8707 (1995).
128. S. Piscanec, F. Mauri, A. C. Ferrari, M. Lazzeri, J. Robertson, Diam. Relat. Mater. 14, 1078 (2005).
129. K. W. R. Gilkes, S. Prawer, K. W. Nugent, J. Robertson, H. S. Sands, Y. Lifshitz, X. Shi, J. Appl. Phys. 87, 7283 (2000).
130. V. I. Merkulov, J. S. Lannin, C. H. Munro, S. A. Asher, V. S. Veerasamy, W. I. Milne, Phys. Rev. Lett. 78, 4869 (1997).
131. F. Tuinstra, J. L. Koenig, J. Chem. Phys. 53, 1126 (1970).
132. C. Castiglioni, E. Di Donato, M. Tommasini, F. Negri, G. Zerbi, Synth. Metals 139, 885 (2003).
133. S. Piscanec, M. Lazzeri, F. Mauri, A. C. Ferrari, J. Robertson, Phys. Rev. Lett. 93, 185503 (2004).
134. C. Mapelli, C. Castiglioni, G. Zerbi, K. Mullen, Phys. Rev. B 60, 12710 (2000).
135. A. C. Ferrari, J. C. Meyer, V. Scardaci, C. Casirgahi, M. Lazzeri, F. Mauri, S. Piscanec, D. Jiang, K. S. Novoselov, S. Roth, A. K. Geim, Phys Rev. Lett. 97, 187401 (2006).
136. Conway N. M. J., Ferrari A. C., Flewitt A. J., Robertson J., Milne W. I., Tagliaferro A., Beyer W., Diam. Relat. Mater. 9, 765 (2000).
137. Ilie A., Ferrari A. C., Yagi T., Robertson J., Appl. Phys. Lett. 76, 2627 (2000).
138. Kohler T., Frauenheim T., Jungnickel G., Phys. Rev. B 52, 11837 (1995).
139. Drabold D. A., Fedders P. A., Strumm P., Phys. Rev. B 49, 16415 (1994).
140. Lopinski G. P., Merkulov V. I., Lannin J. S., Appl. Phys. Lett. 69, 3348 (1996).
141. Mauri F., Del Corso A., Appl. Phys. Lett. 75, 644 (1999).

142. C. Casiraghi, A. C. Ferrari, J. Robertson, R. Ohr, M. v. Gradowski, D. Schneider, Diam. Relat. Mater. 13, 1480 (2004).
143. M. V. Gradowski, A. C. Ferrari, R. Ohr, B. Jacoby, H. Hilgers, H.H. Schneider, H. Adrian, Surf. Coat. Technol. 174–175, 246 (2003).
144. G. Fanchini, A. Tagliaferro, Appl. Phys. Lett. 85, 730 (2004).
145. A. C. Ferrari, B. Kleinsorge, N. A. Morrison, A. Hart, V. Stolojan, J. Robertson, J. Appl. Phys. 85, 7191 (1999).
146. B. Kleinsorge, S. E. Rodil, G. Adamopoulos, J. Robertson, D. Grambole, W. Fukarek, Diam. Relat. Mater. 10, 965 (2001).
147. R. A. Street, Hydrogenated Amorphous Silicon, Cambridge University Press, New York (1991).
148. A. Erdemir, O. L. Eryilmaz, I. B. Nilufer, G. R. Fenske, Diam. Relat. Mater. 9, 632 (2000).
149. A. Erdemir, O. L. Eryilmaz, G. R. Fenske, J. Vac. Sci. Technol. A 18, 1987 (2000).
150. J. A. Johnson, J. B. Woodford, X. Chen, J. Andersson, A. Erdemir, G. R. Fenske, J. Appl. Phys. 95, 7765 (2004).
151. A. Erdemir, O. L. Eryilmaz, I. B. Nilufer, G. R. Fenske, Surf. Coat. Technol. 133–134, 448 (2000).
152. J. Fontaine, J. L. Loubet, T. Le Mogne, A. Grill, Tribol. Lett. 17, 709 (2004).
153. J. Fontaine, T. Le Mogne, J. L. Loubet, M. Belin, Thin Solid Films 482, 99 (2005).
154. A. Erdemir, Surf. Coat. Technol. 146–147, 292 (2001).
155. A. Erdemir, Tribol. Int. 37, 577 (2004).
156. Dollish F. R., W. G. Fateley, Bentley F. F., Characteristic Raman Frequencies of Organic Molecules. Wiley, New York, (1974).
157. Katkritzki A. R. (ed.),Physical Methods in Heterocycle Chemistry. Academic Press, New York, Vol II (1963), Vol IV (1971).
158. Wixom M. R., J. Am. Ceram. Soc. 73, 1973 (1990).
159. Chowdhury A. K. M. S., Cameron D. C., Hashimi M. S. J., Thin Solid Films 332, 62 (1998).
160. Fung M. K., Chan W. C., Gao Z. Q., Bello I., Lee S. T., Diam. Relat. Mater. 8, 472 (1999).
161. Yap Y. K., Kida S., Aoyama T., Mori Y., Sasaki T., App. Phys. Lett. 73, 915 (1998).
162. A. Wienss, G. Persch-Schuy, R. Hartmann, P. Joeris, U. Hartmann, J. Vac. Sci. Technol. A18, 2023 (2000); Appl. Phys. Lett. 75, 1077 (1999).
163. J. Windeln, C. Bram, H. L. Eckes, D. Hammel, J. Huth, J. Marien, H. Rohl, C. Shug, M. Wahl, A. Wienss, Appl. Surf. Sci. 179, 167 (2001).
164. Marchon B., Gui J., Grannen K., Rauch G. C., Ager J. W., Silva S. R. P., Robertson J., IEEE Trans. Mag. 33, 3148 (1997).
165. J. Robertson, Phys. Rev. B 53, 16302 (1996).
166. Rusli, J. Robertson, G. A. J. Amaratunga, J. Appl. Phys. 80, 2998 (1996).
167. T. Heitz, C. Godet, J. E. Bouree, B. Drevillon, J. P. Conde, Phys. Rev. B 60, 6045 (1999).
168. S. J. Henley, J. D. Carey, S. R. P. Silva, Appl. Phys. Lett. 85, 6236 (2004).
169. S. E. Rodil, S. Muhl, S. Maca, A. C. Ferrari, Thin Solid Films 433, 119 (2003).
170. G. Fanchini, S. C. Ray, A. Tagliaferro, Diam. Relat. Mater. 12, 1084 (2003).
171. B. Dischler, A. Bubenzer, P. Koidl, Solid State Commun. 48, 105 (1983).
172. J. Ristein, R. T. Stief, L. Ley, W. Beyer, J. Appl. Phys. 84, 3836 (1998).
173. Weich F., Widany J., Frauenheim T., Phys. Rev. Lett. 78, 3326 (1997).
174. Frauenheim T., Jungnickel G., Sitch P., Kaukonen M., Weich F., Widany J., Porezag D., Diam. Relat. Mater. 7, 348 (1998).
175. Karch K., Pavone P., Windl W., Shutt O., Strauch D., Phys. Rev. B 50, 17045 (1994).
176. Lucovsky G., Nemanich R. J., Knights J., Phys. Rev. B 19, 2064 (1979).
177. C. S. Bathia, C. Y. Chen, W. Fong, D. B. Bogy, Mat. Res. Soc. Symp. Proc. 593, 397 (2000).
178. . Bernhard, C. Ziethen, R. Ohr, H. Hilgers, G. Schonhense, Surf. Coat. Technol. 180–181, 621 (2004).
179. C. Casiraghi, J. Robertson, A. C. Ferrari, Mater. Today 10, 42 (2007)

180. C. Casiraghi, A. C. Ferrari, R. Ohr, A. J. Flewitt, D. P. Chu, J. Robertson, Phys. Rev. Lett. 91, 226104 (2003).
181. A.L. Barabasi, H. E. Stanley. Fractal Concepts in Surface Growth. Cambridge University Press, Cambridge (1995).
182. M. Moseler, P. Gumbsch, C. Casiraghi, A. C. Ferrari, J. Robertson, Science 309, 1545 (2005).
183. J. G. Buijnster, M. Camero, L. Vazquez, Phys. Rev. B. 74, 155417 (2006).
184. G. Capote, L. Prioli, F. L. Freire, J. Vac. Sci. Technol. 24, 2212 (2006).
185. I. Y. Kim, S. H. Hong, A. Consoli, J. Benedikt, A. Von Keudell, J. Appl. Phys. 100, 053302 (2006).
186. F. Family, J. Phys. A 18 L75 (1985).
187. K. B. K. Teo, S. E. Rodil, J. H. Tsai, A. C. Ferrari, S. E. Rodil, W. I. Milne, J. Appl. Phys. 89, 3707 (2001).
188. T. Witke, P. Siemroth, IEEE Trans. Plasma Sci. 27, 1039 (1999).
189. X. Shi, L. Cheah, J. R. Shi, S. Zun, B. K. Tay, J. Phys.: Condens. Matter. 11, 185 (1999).
190. S. Edwards, D. Wilkinson. Proc. R. Soc. London A 44, 1039 (1966).
191. S. Pisana, C. Casiraghi, A. C. Ferrari, J. Robertson, Diam. Relat. Mater. 15, 898 (2006).
192. M. Shamsa, W.L. Liu, A. A. Balandin, C. Casiraghi, W. I. Milne, A.C. Ferrari, Appl. Phys. Lett. 89, 161921 (2006).
193. J.P. Sulllivan, T.A. Friedmann, K. Hjort, MRS Bull. 26, 309 (2001).
194. J.K. Luo, A.J. Flewitt, S.M. Spearing, N.A. Fleck, W.I. Milne, Appl. Phys. Lett. 85, 5748 (2004); J.K. Luo, J.H. He, Y.Q. Fu, A.J. Flewitt, S.M. Spearing, N.A. Fleck, W.I. Milne, J. Micromech. Microeng. 15, 1406 (2005).
195. E. Marotta, N. Bakhru, A. Grill, V. Patel, B. Meyerson, Thin Solid Films 206, 188 (1991).
196. C.D. Wright, M. Armand, M.M. Aziz, IEEE Trans. Nanotech. 5, 50 (2006).
197. D.A. Czaplewski, J.P. Sullivan, T.A. Friedmann, J.R. Wendt, Diam. Relat. Mater. 15, 309 (2006).
198. D. G. Cahill, Rev. Sci. Instrum. 61, 802 (1990).
199. S. Ahmed, R. Liske, T. Wunderer, M. Leonhardt, R. Ziervogel, C. Fansler, T. Grotjohn, J. Asmussen, T. Schuelke., Diam. Relat. Mater. 15, 389 (2006).
200. W. L. Liu, A. A. Balandin, Appl. Phys. Lett. 85, 5230 (2004); J. Appl. Phys., 97, 073710 (2005).
201. M. Shamsa, W.L. Liu, A. A. Balandin, J.L. Liu, Appl. Phys. Lett. 87, 202105 (2005).
202. D.G. Cahill, R.O. Pohl, Solid State Commun. 70, 927 (1989).
203. J.J. Freeman, A.C. Anderson, Phys. Rev. B 34, 5684 (1986).
204. A. C. Victor, J. Chem. Phys. 36, 1903 (1962).
205. B.T. Kelly, Physics of Graphite. Applied Science Publisher, London (1981).
206. A.J. Bullen, K.E. O'Hara, D.G. Cahill, O. Monteiro, A. von Keudell, J. Appl. Phys. 88, 6317 (2000).
207. J.L. Feldman, M.D. Kluge, Phys. Rev. B 48, 12589 (1993).
208. P. C. Kelires, Phys. Rev. Lett. 73, 2460 (1994).
209. G. Chen, P. Hui, S. Xu, Thin Solid Films 366, 95 (2000).
210. W. Hurler, M. Pietralla, A. Hammerschmidt, Diam. Relat. Mater. 4, 954 (1995).
211. D.T. Morelli, T.A. Perry, J.W. Vandersande, J.W. Vandersande, Phys. Rev. B 48, 3037 (1993).

Mechanical Characterisation and Properties of DLC Films

P. Lemoine, J. P. Quinn, P. D. Maguire and J. A. McLaughlin

Abstract This chapter reviews the mechanical characteristics of diamond-like carbon (DLC) materials. It examines the motivations behind such studies, presents the experimental methods used to characterise them and discusses the main findings. DLC usually present wide-ranging mechanical properties, with the best specimen being tetrahedrally bonded in some cases approaching the performances of diamond. The chapter also discusses the effect of internal stress, doping and layering. However, we note a number of remaining issues, which concern mainly the nanoindentation protocols for ultra-thin layers, a significant aspect of the problem being the simultaneous effect of substrate deformations and tip blunting. To that end, a new analytical method was designed which extracts the intrinsic film's hardness H_F. Surveying a variety of DLC layers, we find that the H_F value tends to increase with thickness, at least up to 50 nm. This result is supported by complementary non-mechanical analysis. It is also observed elsewhere and is consistent with current growth models. Such independent correlation of the intrinsic characteristics of very thin DLC layers is a difficult task. It is, however, of importance to improve our understanding of the growth and bonding structure of DLC.

Keywords nanoindentation, amorphous carbon, hardness, Young's modulus

1 Introduction

The hybridisation of carbon bonds in diamond-like carbon (DLC) gives rise to a range of mechanical behaviours, which are of interest for essentially three reasons. Firstly, in tribological applications, DLC is applied to protect structures against potentially damaging contacts (tools, gears, data storage systems) and, as such,

Nanotechnology Research Institute, University of Ulster at Jordanstown, Shore road, Newtownabbey, BT37OQN, County Antrim, Northern Ireland, UK

C. Donnet and A. Erdemir (eds.), *Tribology of Diamond-Like Carbon Films: Fundamentals and Applications*.

must have excellent mechanical properties. Secondly, DLC exists almost exclusively in the form of thin films and, regardless of its primary role, the DLC layer must be able to sustain internal stresses and resist delaminations. Finally, these mechanical characteristics also link up to physical, electronic and thermal properties, which are difficult to measure for very thin disordered specimen; henceforth, this mechanical data provides useful complementary information. Indeed, this last motivation has always represented a major incentive for pursuing mechanical studies on DLC, in many cases to relate hardness (H) and Young's modulus (E) to density, sp^3 fraction and other parameters obtained from spectroscopic analysis. However, as DLC investigators work on very thin specimen, they also came to question and, in some cases, to refine, the experimental protocols, namely depth sensing indentation, hereafter called nanoindentation. Therefore, this chapter is organised in three sections: Section 2 deals with experimental protocols, Section 3 reviews mechanical data and emerging issues, Section 4 describes the intrinsic film's hardness and link to other properties. This is followed by concluding remarks.

2 Experimental Protocols

2.1 Nanoindentation Basics

Indentation techniques use a hard protuberance, the tip, to push and pull against the surface of the sample. The term hardness (H) is used to describe the ratio of the applied load (L) to the projected plastically deformed area (A).

$$H = \frac{L}{A} \tag{1}$$

This elasto-plastic property is directly linked to the material's yield strength (Y). Y is a fundamental property which relates to the bonding characteristics of the material, hence an important parameter used for modelling the mechanical response of carbon scaffolds. Although the precise link between H and Y is not universally accepted, nanoindentation is still the technique of choice to extract Y as tensile techniques are difficult to apply to small bulk volumes or thin-film specimen. In the past, indentation tests were done with mN–N loads and the corresponding 'microhardness' was calculated by a variety of protocols such as Rockwell, Brinnell, Vickers indentation, etc. Obviously, these methodologies rely on having an accurate microscopic measurement, a condition difficult to fulfil for very shallow indents (few 10 nm), even with transmission electron microscopy (TEM) analysis, as the image contrast is a material-dependent parameter. Another difficulty is that the deformations are not measured; hence, the elastic behaviour of the sample is not monitored.

Nanoindentation addresses both these issues. The operating principle is as follows. An apparatus applies the load and measures the displacement, and using

an indenter tip with a calibrated area function (shape), one can then link the load–displacement curves (*L–h* curves) to both the *H* and *E* values. A typical *L–h* curve is shown in Fig. 1. Many instruments are constructed around a stiff (~10^6 N/m) indenter column fitted with both load application coils and a capacitive displacement-sensing device. The load can also be applied electrostatically, which reduces thermal drift. A diamond tip is mounted on the bottom end of the column, usually a three-sided Berkovitch pyramidal diamond indenter. This diamond tip approaches, contacts, compresses and, on reversing the load, retracts from the sample. The surface contact is detected usually by monitoring the measured stiffness S (load/displacement) which, in this case, is the sum of the leaf spring (~100 N/m) and contact stiffness. The latter can be estimated using Hertz contact mechanics [1]

$$S = 2.a.E_{\mathrm{r}} \tag{2}$$

$$E_{\mathrm{r}} = \left(\frac{1 - v_{\mathrm{tip}}^2}{E_{\mathrm{tip}}} + \frac{1 - v^2}{E} \right)^{-1} \tag{3}$$

$$a = \left[\frac{3F\,R}{4E_{\mathrm{r}}} \right]^{1/3} \tag{4}$$

$$h = \frac{a^2}{R} \tag{5}$$

where E_{r} is the reduced modulus, a is the contact radius, R is the tip radius, resulting from its imperfect rounded end (R ~50 nm), F is the applied load and h is the

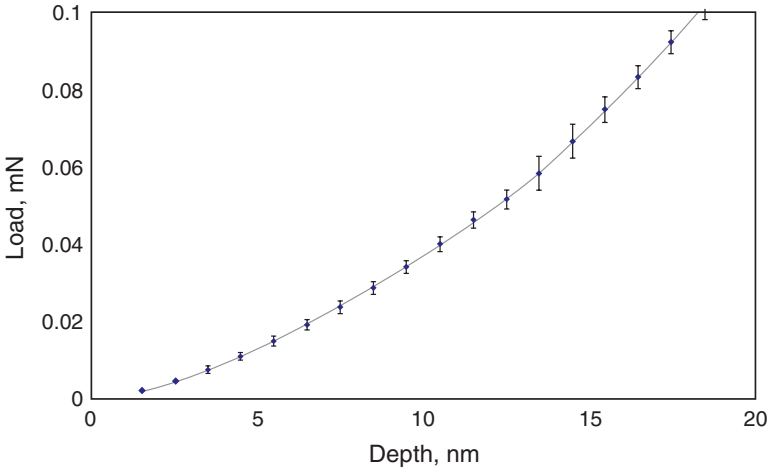

Fig. 1 Typical load–displacement curve

displacement into the surface. Taking $L = 1\,\mu N$ and $E_r = 200\,GPa$, we find $a = 5.7\,nm$, $S = 2294\,N/m$ and a displacement $h = a^2/R = 0.65\,nm$. Hence applying a micro-Newton load, the contact on a fairly stiff sample such as DLC should be detected with minimal compression of the surface.

With this contact point established, the L–h curve is obtained from the readings of the load on sample (L, μN). Usually, the E and H values are extracted from this L–h curve using the Oliver and Pharr method [1], which will be presented here while its shortcomings will be discussed later in the chapter.

At the maximum load (L, h) the sample surface follows the tip sides, from the apex to the contact depth h_c. As soon as the indenter starts unloading, the surface under the tip elastically retracts.

An important point to note is that, under fully plastic conditions, the area of contact under loading and the final indented area have the same projection over the surface plane. This is shown schematically in Fig. 2. This projection is called the contact area (A). Its relationship to the contact depth h_c depends on the indenter tip geometry. For a Berkovitch tip, we have:

$$h_c = h - \left(0.75\frac{L}{S}\right) \tag{6}$$

where S is the measured stiffness (in N/m) at the unloading point (h, L). S can be measured by a graphical method using a mathematical algorithm which fits the unloading segment. The contact depth is linked to A by carrying out indentations into a smooth, inert and isotropic material of known Young's modulus, usually fused silica ($E = 72\,GPa$) and using;

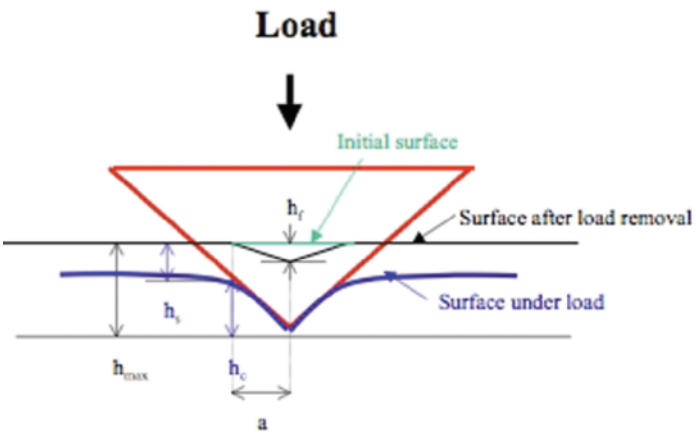

Fig. 2 Section through the indent. At the maximum load, the walls of the tip are in contact with the sample surface from the tip apex to the height *hc*; the contact depth. Also, the projected area of contact is also the projected final area. Also shown on the figure are the final depth (*hf*), maximale depth (h_{max}) and contact radius (a)

$$E_{\mathrm{r}} = \sqrt{\frac{\pi}{2}} \cdot \frac{S}{\sqrt{A}} \tag{7}$$

The validity of Eq. 7, which is based on elastic theory will be discussed later. This means that, having measured S and extracted h_{c} from Eq 6, with knowledge of E_{r}, one can access A and, using a fitting routine, build the indenter area function; typically

$$A = 24.5h_{\mathrm{c}}^2 + \mathrm{C}_1 h_{\mathrm{c}}^1 + \mathrm{C}_2 h_{\mathrm{c}}^{1/2} + \ldots + \mathrm{C}_8 h_{\mathrm{c}}^{1/128} \tag{8}$$

The lead term represents the area function of a perfectly sharp tip, the remaining terms account for tip blunting, which cannot be ignored for shallow indentations. The assumption of the method is that the contact area is not material dependent. Hence, using this calibration, it is now possible to use the (L, h, S) triplet, obtained on an unknown sample, to extract, in turn, h_{c}, A, E and H.

This method can be used for thin film samples, noting however, two spurious effects. The stiffness S will be influenced by the deformation of the substrate. An added complication stems from the pressure distribution under the indenter tip; with a blunt tip the maximal shear is below the surface, possibly within the substrate. These effects, which will be discussed later, can nonetheless be addressed by the continuous stiffness measurement (CSM) technique [2]. This protocol permits to measure S for each point of the loading segment. A small AC load is superimposed onto the ramping DC load, meaning that 'microscopic' loading–unloading cycles are effected continuously while loading. These small oscillations cause only elastic deformations in the sample. The stiffness on unloading (AC unloading!) is measured using a dynamical model, which includes the characteristics of the instruments (stiffness and damping constants), E and H are then extracted in the usual manner. The obvious advantages of this method are that (i) it gives E and H for each data point of the loading segment *for only one indentation experiment* and (ii) the measurement is dynamical; E and H are calculated *for a given frequency*, hence giving storage (E') and loss (E'') moduli, a nanoscopic equivalent of the classical dynamical mechanical analysis (DMA).

2.2 Other Methods

Some alternative methods are also used. In the bulge test [3] a given area of the thin film is free standing. Compressing the coated system and monitoring its deflection, one can use the pressure–deflection curve to calculate the Young's modulus of the thin film. This method has the advantage of deforming typically an area of a few square millimetres, hence, effectively sampling a larger fraction of the thin film than nanoindentation. Moreover, the bulge test also gives the internal stress within the film, a significant advantage for DLC materials which are often internally stressed. This method, however, requires to machine away a specific area of the substrate, which

may be difficult. Moreover, the hardness of the film is not accessible. The second class of techniques is based on surface acoustic waves (SAW), usually excited thermally with a laser source [4,5]. Obtaining the dispersion relation of the sound wave, one can extract the elastic constants, hence the Young's modulus of the thin film. The real advantage of the technique is its great surface sensitivity, allowing the characterisation of nanometric layers. Again, this technique does not measure the hardness, although some authors use the phenomenological relationship $E/H = 10$ to estimate the H value, a usage whose validity will be discussed later.

3 Review of Mechanical Data and Emerging Issues

3.1 Mechanical Properties of Elemental Carbon Materials

What can be expected of the mechanical properties of DLC, in its many forms, considering the hugely contrasting mechanical properties of graphite and diamond? In diamond, the carbon atoms are tetrahedrally coordinated to their first nearest neighbour by four sp^3 bonds. This results in a high bond energy per unit volume in all three directions of space. In graphite, the carbon atoms are bound in a planar hexagonal array, the graphene sheet, by trigonal sp^2 bonds. In addition, vertical π orbitals, which overlap along horizontal directions, consolidate these graphene sheets. However, these layers can easily slip past one another as this only requires breaking weak van der Waals bonds joining the sheets (~ few 0.01 eV). The graphite sheets can easily shear past one another and graphite is, overall a soft and compliant material. This describes the relationship between bonding and mechanical properties for diamond and graphite. In DLC, the atomic arrangements are different (see Chapter 1). However, to a large extend, the same relationship remains valid; i.e. the higher the sp^3 fraction the stronger

Table 1 The mechanical properties of various elemental carbon materials

Material	Form	Density (g/cm^3)	Covalent bonds	Young's modulus (GPa)	Hardness (GPa)	Tensile strength (GPa)
C60	Films	~1.7	Almost all sp^2	?	~0.2	–
C fibres	Fibres	1.7–1.9	Almost all sp^2	200–600	?	3.8–6.4
Graphite	Bulk	~2	100% sp^2	10	0.2–2	–
CNT	Fibres	~2	Almost all sp^2	1000	?	1
CNT	Film	<2?	Almost all sp^2	0.013	?	–
FLC	Films	~2.2	Almost all sp^2	480	45	–
a-C	Films	~2.2	sp^2-rich	100–200	10–20	–
a-C:H	Films	~2.2	Intermediate sp^3	100–300	10–30	–
t-aC	Films	3–3.2	sp^3-rich	300–500	50–80	–
Diamond	Bulk, films	~3.5	100% sp^3	1000	100	–

is the DLC. Indeed, the data presented in Table 1 shows that the E value (100–500 GPa) and H value (10–80 GPa) of DLC materials, in bold, are intermediate between those of graphite and diamond. However, the defects present in numerous forms in DLC (network terminations, bond angle disorder, impurities, etc.) and in other carbon materials will also influence the mechanical behaviour. Indeed, the table shows, that, whether the material is organised at the micro-scale or nanoscale, whether it forms fibres or thin films, the sp^3 fraction in carbons, high or low, is not the sole perquisite for superior mechanical properties.

3.2 Mechanical Properties of DLC Thin Films

There is a large body of data on the mechanical characteristics of DLC materials which cannot be reviewed in its entirety within this chapter. Instead, we have selected a number of specific issues which tend to outline the major milestones of this much-studied area. These are the effect of the sp^3 fraction, the link between internal stress and hardness, the nitrogen doping of the films and the production of multilayer systems.

B. Bhushan has initiated many such studies, developing new experimental protocols such as experiments on nanotoughness [6] and nanofatigue [7]. Some of his early studies [8] have been conducted for a wide range of DLC deposition conditions. The corresponding E and H values increase in the following order; amorphous carbon, a-C (RF sputtering), hydrogenated amorphous carbon, a-C:H (PECVD), tetrahedral hydrogenated amorphous carbon, t-aC:H (ECR-CVD) and tetrahedral amorphous carbon, t-aC (FCVA, PLD). This tends to support the above-mentioned hypothesis that the mechanical properties improve with the increasing sp^3 fraction, although his co-worker Sundanarayan [9] found differently when examining ultra-thin films. In many of the subsequent investigations, the discussion is usually conducted with the same held belief; the sp^3 fraction increases the E and H values. For instance, in t-aC films, optimizing the substrate negative bias in FCVA around −100 V gives concomitant maxima in density, sp^3 fraction and E and H value [10]. It is usually justified by the network-forming ability of the tetrahedrally coordinated sp^3 bonds. The constraint-counting model [11], for instance, derives the elasticity of the amorphous network from the bending and stretching of the covalent bonds, emphasising the crucial role played by the bond coordination number; i.e. highly coordinated networks (i.e. sp^3) show more elastic constraints. Robertson, who included the effect of sp^2 clustering in the model, presents this theoretical framework as the main tool of analysis for describing the mechanical properties of amorphous carbon. It fits reasonably well the Young's modulus data for tetrahedrally amorphous carbon (ta-C), the hardest form of DLC produced so far, but less so for hydrogenated amorphous carbon (a-C:H) [10].

However, the identification between high sp^3 fraction and high E and H values is at odds with a class of hard sp^2-carbon network structures discovered by various authors [12,13]. Alexandrou prepared a material, with curved nanoscale graphene sheets, at least 95% sp^2 bonded and displaying a hardness of 45 GPa, usually

referred as fullerene-like carbon (FLC). Others invoke the presence of pentagonal and heptagonal rings and, hence curvature, to explain the relatively high hardness of sp^2-rich carbon and carbon nitride films [14]. It may be that the disorder present in most DLC could bend the sp^2 regions, even for materials with intermediate or low sp^2 content. For these materials, two strengthening effects could be at play, the interlocking of curved graphitic shells and the network-forming ability of the sp^3 regions. The two processes have yet to be incorporated into a single mechanical model. One should note that the sp^3 bonds discussed in this model are the network-forming C–C bonds and not the C–H bonds. This is an important distinction that a spectroscopic technique like x-ray photoelectron spectroscopy (XPS) analysis is not capable of doing. For instance, Si doping of a-C:H often leads to a substantial hydrogenation of the film [15,16], which result in an increase of the sp^3 fraction, as detected from XPS analysis, and a smaller hardness and density values. This hydrogen-softening effect has also been discussed by others [17].

Another important aspect of the mechanical properties of DLC films is the internal compressive stress. Usually, the films with the best mechanical properties are also highly stressed and this has obvious technological implications for thick DLC films, particularly for t-aC materials. This codependence is justified by the growth models which indicate that such a stress is necessary to stabilise the dense sp^3 phase. However, it was later suggested [18], and demonstrated using pulse biasing [19], that this stress is only necessary in the initial stage of growth and can be reduced subsequently without compromising the E and H values too much.

Nitrogen doping of DLC has also became a major issue, as cubic carbon nitride [20] should have a higher strength than diamond. Unfortunately, the synthesis of this compound, or its amorphous equivalent, has proved difficult, mainly because of the natural tendency of carbon and nitrogen to form multiple bonds [21]. Nonetheless, films as hard as 33 GPa, measured by nanoindentation with the Oliver and Pharr method, have been produced [22].

Finally, there is now much effort being directed at producing DLC multilayers. The idea is that interfaces have the ability to stop the propagation of cracks and, in so doing, toughen the material, as studies on nanostructured materials have shown. In the case of DLC, the multilayer can be an alternance of sp^2 and sp^3 layers, prepared by varying bias conditions [23,24] or a sandwich of two different materials (aC and aCN for instance) [25]. As for other nanostructured materials, the thinnest alternance of layers gives the best strengthening effect [26]. In some case, the layering also permits to dissipate the internal compressive stress [24].

3.3 Emerging Issues

The primary issue regarding the mechanical properties of DLC films is the refinement of existing experimental techniques essentially because many DLC applications require sub-50 nm layers. As new experimental protocols will be devised, it may be necessary to revisit our understanding of the link between mechanical properties and

other characteristics. As regards current practice, a number of potential problems can be identified; the use of elastic theory, the influence of pile-up, the effect of the deforming surface on the geometry of loading, the substrate effect and an adequate accounting of the non-replicating geometry of the blunt indenter tip.

Elastic theory is invoked at two crucial stages of the nanoindentation protocol, firstly, to describe the initial surface contact and secondly, to calculate the unloading stiffness. Regarding contact, the CSM scheme used to measure the contact stiffness is relatively accurate (few 10 N/m) and corresponds to extremely small indentation depths (sub-nm, as seen in Section 2–1), hence the elastic approximation is likely to be justified in this case. By contrast, the unloading proceeds in an elasto-plastic region often schematised as a plastic core surrounded by an elastic region. Fully elasto-plastic treatments have been developed [27, 28]. However, it seems that, here again, the elastic approximation is adequate to describe the unloading stiffness [29].

Pile-up occurs when the indented materials are soft and do not work-harden [30]. Moreover, soft films on hard substrates tend to show more pile-up as the plastic flow is somehow redirected towards the surface. Imaging the indents by atomic force microscopy (AFM) has shown that these effects can seriously affect the measurement of hardness by the Oliver and Pharr method as the contact area is underestimated in this case [31]. The general consensus, however, is that pile-up occurs for relatively ductile load–displacement curves, when the final depth is at least 70% of the maximal depth [30]. This applies only to soft carbon films.

The second difficulty arises from the changing geometry of contact. Equations 6 and 7 use a theory that considers the contact between a solid of revolution, the indenter and a flat surface (the sample). However, on unloading, the deformed surface is clearly not flat. This has been treated using the concept of the effective indenter shape [32,33]. However, the problem is treated in isolation without considering the other issues discussed here (pile-up, substrate effect, etc.).

The substrate effect is the simple observation that the hardness of a coated system is influenced by the proximity of the substrate and, nowadays, the CSM technique is widely used to detect the onset of this effect. Alternatively, a rule of thumb has been used to estimate the depth at which hardness is not influenced by the substrate [34]. This method relies on keeping the depth at 10% of the film's thickness (t/10). This is problematic for ultra-thin films. Moreover, both experimental and finite element modelling (FEM) studies show that the substrate effect is also influenced by the mechanical properties of the substrate [35–37].

The final problem is the blunted geometry of the diamond indenter tip. Hertz contact mechanics shows that the H value increases with the depth (h) in an asymptotic manner ($H \sim h^{1/2}$) until it reaches a value indicative of that measured with a perfectly sharp tip. Moreover, as the depth of maximal shear lies somewhat below the surface, the hardness depends on the tip radius. This is confirmed by both FEM modelling and experimental studies; the hardness of a hard film on soft substrate decreases when the tip radius increases [38]. One should note that this rising trend of the blunting effect runs contrary to that of the indentation size effect, mostly encountered in polycrystalline materials. An additional difficulty emerges when indenting, particularly, stiff and hard samples, like tetrahedral amorphous carbon (t-aC) films. In this case, one may

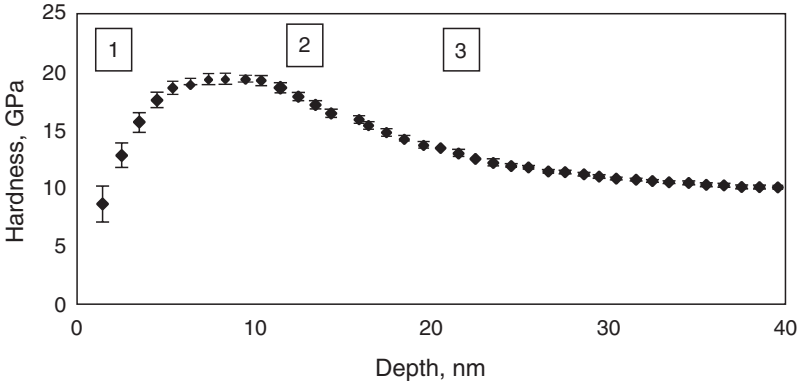

Fig. 3 Hardness (H) versus depth (h) curve for a 15 nm t-aC film on a sputtered alumina substrate

consider the deformation of the indenter tip and, indeed tip damage can be observed [39,40]. The Oliver and Pharr method only considers the tip's deformation when calculating the Young's modulus E from the reduced modulus E_R, but does not consider the tip area function $A(h_c)$ to be material-dependent. This inconsistency of the method may become a significant source of error for shallow indentations on very hard films. A more general problem is the combined influence of the substrate effect and tip blunting. This means that, for a hard coating on a soft substrate, like DLC on Si, the H value rises and then decreases with depth. Some researchers [41,42] choose an intermediate depth region, where the hardness is less influenced by the tip shape and substrate. This approach is not fully satisfactory; the chosen hardness value may still be influenced by these effects. This problem is illustrated on Fig. 3 which displays the hardness curve of a 15 nm thick t-aC film on a sputtered alumina substrate This film is very thin and also very hard (deposited with optimised bias). The three depth ranges labelled 1, 2 and 3 represent, respectively, the regions predominantly influenced by the blunted tip, the thin film and the substrate. Hence, according to that protocol, the tip blunting, region 1, would only extend up to approximately 6 nm depth. This is unrealistic considering most tip radii are between 40 and 200 nm. This is a major difficulty which is partly responsible for the large data scatter encountered in the literature with, for instance, hardness values for t-aC materials varying from 50 to 80 GPa.

4 Intrinsic Film's Hardness and Link to Other Properties

4.1 Measuring the Film's Hardness

The film's hardness can be extracted from the nanoindentation data, firstly, using numerical modelling [43,44]. This is time consuming and one must assume a relationship between yield and hardness, known for metals [45], but not necessarily so for DLC materials.

Another way to tackle the problem is to develop an analytical equation which gives an asymptotic description of the substrate effect, defining the measured hardness H as a function of the substrate's hardness H_S and the film's hardness H_F. Considering the variations of the contact depth (h_c) over thickness (t) ratio; i.e. $\beta_c = h_c/t$; H tends towards H_F for $\beta_c = 0$ and H tends towards H_S for $\beta_c = \infty$. Two such approaches have been devised, one by Bhattachraya [34], the other by Korsunsky [46]. The former is purely phenomenological, the latter partly relates to the mechanics of deformation. We will, however, focus on the Bhattachraya formalism which has been used by most DLC researchers [47,48]. The corresponding equations are, for a hard film on a soft substrate;

$$H = H_S + \left(H_F - H_S\right).\exp\left(-k_1.\beta_c\right) \tag{9}$$

and for a soft film on a hard substrate;

$$H = H_S + \left(H_F - H_S\right).\exp\left(-k_2.\beta_c^2\right) \tag{10}$$

This model assumes perfectly sharp tips. In practice, users of the Bhattacharnya model only fit the post-blunting region of the hardness curve [47,48]. This means that this protocol cannot be used for films thinner than the tip radius, typically around 40–200 nm for most nanoindentation studies.

This presents a serious limitation for which a new protocol has been designed [49]. This novel approach is based on the observation that the blunting effect is similar on coated and bulk systems and, therefore can be obtained while indenting a fused silica sample. Moreover, considering that real tips vary in shape, there is no single formula for $H(h_c)$. Hence, we use an empirical formula to fit the $H(h_c)$ curve to the fused silica data.

$$H_{SiO_2}\left(h_c\right) = a + \left(b.\exp\left(-c.h_c\right)\right) \tag{11}$$

The constants a, b and c relate to the tip geometry and to the hardness of fused silica at large depths (9–9.5 GPa). We then use the same function, with a hardness normalisation factor, to describe the H_S and H_F parameters, now a function of the variable h_c. H_S (h_c) is the hardness curve of the bulk substrate and H_F (h_c) is the theoretical 'bulk' film sample, experimentally unobtainable by thin-film deposition techniques. It is thus possible to modify Eqs [9] and [10] into;

$$H = H_S\left(h_c\right) + \left[H_F\left(h_c\right) - H_S\left(h_c\right)\right].\exp\left(-k_1.b_c\right) \tag{12}$$

$$H = H_S\left(h_c\right) + \left[H_F\left(h_c\right) - H_S\left(h_c\right)\right].\exp\left(-k_2.\beta_c^2\right) \tag{13}$$

Fitting these $H(\beta_c)$ functions to the experimental data, it is possible to extract the H_F value. Figure 4 shows that with smaller c values (blunter tips), the film's hardening

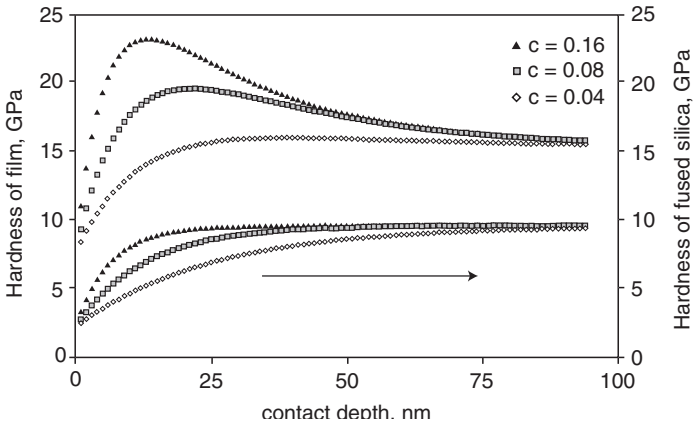

Fig. 4 Theoretical hardness curves for a hard film (H_F ~33 GPa) on a soft substrate (H_S ~15 GPa) for various blunting parameter c (Eq. 11). The corresponding hardness curves of fused silica from which the parameter c is determined, (the three curves below 10 GPa), are also shown in the figure

effect becomes less prominent, showing that the raw nanoindentation data is not sufficient for determining the intrinsic hardness of the film.

4.2 Intrinsic Film Hardness and Correlated Properties

In the following, this new method will be applied to two batches of carbon films analysed in two published studies, thereof labelled batch 1 [41] and batch 2 [39], allowing us to refine our previous observations. These films were prepared onto silicon wafers and hard Al_2O_3–TiC ceramic wafers, the base material used in magnetic head devices, thereafter called ALTIC. Batch 1 is a series of hydrogenated amorphous carbon (a-C:H) films prepared by plasma-enhanced vapour deposition (PECVD) [41]. Batch 2 comprises two sets, a-C:H films also deposited by PECVD and tetrahedral amorphous carbon (t-aC) films, prepared by filtered cathodic vacuum arc (FCVA) [39]. Within each batch of samples, the control of film thickness was achieved solely by varying the deposition time, keeping all other deposition parameters constant. The t-aC films were prepared with the substrate held at a floating potential, hence they were not optimised for density and hardness. The film thickness was measured by AFM microscopy. In what follows, the batch 1 samples are identified by their thickness and substrate type whereas the batch 2 samples are labelled 10P (10 nm thick a-C:H by PECVD), 10F (10 nm thick t-aC by FCVA), 50P (50 nm thick a-C:H by PECVD) and 50F (50 nm thick t-aC by FCVA).

Figure 5 shows the experimental hardness curve of a 47 nm thick a-C:H film on silicon from batch 1. Equation 12 gives a better fit to the data than the original Bhattacharnya equation. This difference is even more pronounced for thinner films, as can be seen in Table 2. The average value and error on H_F have been determined by considering the experimental errors on the measured hardness values. To date,

Table 2 Results from the fit to the Bhattacharya equation (Ref. [34]) and the new method presented here (Eq. 12 and 13); the statistical parameters refer to this last protocol

Batch 1/Si	HF,Bhattacharya	*HF*, Lemoine	X^2	R^2
9 nm	17 ± 1.0	22.4 ± 2.0	0.047	0.981
19 nm	19.8 ± 1.0	30.44 ± 2.0	0.061	0.98
27 nm	22.4 ± 1.0	32.1 ± 1.5	0.04	0.992
37 nm	25.8 ± 1.0	32.86 ± 1.0	0.074	0.996
47 nm	26.4 ± 1.0	32.9 ± 1.0	0.064	0.995
100 nm	25.8	27.3 ± 1.0	0.72	0.961
Batch	**H_F, Eq. 1**	**H_F, Eq. 8**	**X^2**	**R^2**
10P	13.6±1.0	26 ± 2.5	0.047	0.993
50P	14.9±1.0	30.8 ± 2.5	0.03	0.997
10F	12.1±1.0	29.2 ± 3.0	0.034	0.992
50F	39.2±1.0	38.1 ± 1.0	0.431	0.977
Batch	**H_F, Eq. 1**	**H_F, Eq. 8**	**X2**	**R^2**
10 nm	37 ± 1.0	18.7 ± 2.0	0.608	0.98
24 nm	33 ± 1.0	23.8 ± 1.0	0.262	0.99
37 nm	30 ± 1.0	26.5 ± 1.0	0.44	0.979
42 nm	30 ± 1.0	27.2 ± 1.0	0.618	0.973
Batch	**H_F, Eq. 1**	**H_F, Eq. 8**	**X^2**	**R^2**
10P	21 ± 1.0	21.8 ± 4.0	0.18	0.997
50P	12 ± 1.0	16.3 ± 4.0	0.71	0.974
10F	37 ± 1.0	42.7 ± 10.0	0.62	0.991
50F	50 ± 1.0	114 ± 20.0	4.6	0.953

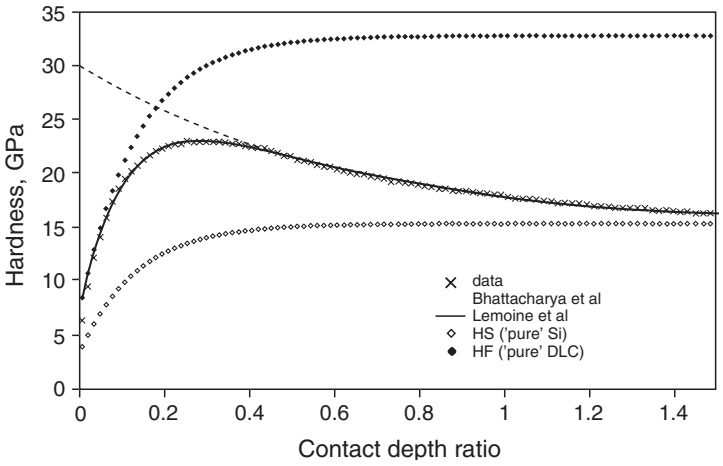

Fig. 5 Hardness curves versus contact depth ratio for a 47 nm thick a-C:H film on Si. The sample is from batch 1 [41]

the main limitation of this new method of analysis is that the assumption of $H = H_S$ for large depth is not necessarily correct. For hard coatings, a small hardening effect may persist at great depth; it is not possible to completely squeeze out the film.

Comparing films of equal thickness, we note, not surprisingly, that the taC films exhibit higher H_F values than the a-C:H films of both batches. Moreover, for both batch 1 and 2, the H_F values of the a-C:H films on Si are higher than those of the same films deposited on the ceramic substrate. This is not an incomplete accounting of the said substrate effect, which would give a larger H_F for the hard ALTIC substrate. By the same account, the H_F values of the t-aC films on Si are lower than those of the same films deposited on the ceramic substrate. Recalling our previous determination of critical loads L_C by nanoscratch testing [41]; we found that the substrate which corresponds to the largest critical load (Si for a-C:H and ALTIC for t-aC) also results in a high H_F value. It may be noted that, in this instance, the mechanical and adhesive properties of these a-C:H and t-aC films are triggered by the same growth mechanisms. Obviously, that situation may change at higher FCVA substrate negative bias.

One also notes a suspiciously high H_F value for the 50F film on the ceramic substrate. This may be due to the blunting of the tip while indenting this particularly hard sample [39]. Such an irreversible change in tip geometry would lead to an underestimation of the area function, hence an inflated H_F value. Nonetheless, the real H_F value of this sample must be higher than any of the others as it did blunt the tip. Examining the effect of thickness, we find that, in most cases, H_F increases with thickness at least up to 50 nm. The only exception to that rule is the case of the batch 2 a-C:H samples on the ceramic substrate; the H_F value of the 10P on ALTIC is larger than that of the 50P on ALTIC.

These thickness trends were compared to supplementary analysis carried out on the batch 2 samples on Si substrates by Raman, XRR and optical profilometry (OP) analysis [50]. Firstly, analysis of the Raman spectra indicates that the 50P sample has a higher G peak position ($1519.4 \pm 0.9\,cm^{-1}$) than the 10P one ($1509.5 \pm 1.8\,cm^{-1}$), although their intensity ratios I_D/I_G are similar (0.60 ± 0.1 and 0.58 ± 0.1, respectively). We did not measure any significant difference in background slope. Therefore, nothing can be concluded regarding either the graphitic content or hydrogen content of the two films. One also notes that the 50F sample has both a higher G peak position and a more negative skewness ($1559.9 \pm 1.8\,cm^{-1}$ and -3.3 ± 0.3) than the 10F sample ($1552.5 \pm 3.2\,cm^{-1}$ and -2.4 ± 0.0), indicative of a denser and more sp^3-rich carbon network for the 50F film [39]. One notes the relatively small skewness values, probably due to the FCVA floating potential conditions. The density, as measured by XRR analysis is larger for the t-aC films and increases with film thickness ($\rho_{10F} = 3.00 \pm 0.134$, $\rho_{50F} = 3.36 \pm 0.024$, $\rho_{10P} = 2.24 \pm 0.07$ and ($\rho_{50P} = 2.41 \pm 0.01$). Finally, the OP analysis gives the following refractive index values; $n_{10F} = 2.05 \pm 0.10$, $n_{50F} = 2.44 \pm 0.01$, $n_{10P} = 1.91 \pm 0.06$ and $n_{50P} = 2.32 \pm 0.01$. Hence, the thicker films also have a larger refractive index. The refractive index of the 50P is larger than that of the 10F, although, for equal thickness the t-aC also have a larger n_F than the a-C:H films. In all, it can be said that for this batch of samples, H_F, n_F and ρ all increase with film thickness.

Indeed, others have shown how the properties of an amorphous carbon film may change with its thickness. McCann and Ahmed [51,52] have shown how the density

and sp^3 fraction of t-aC and t-aC:N films increase with thickness, using Raman, XRR and XPS analysis. Patsalas [52] also used XRR analysis and elipsometry to monitor the properties of amorphous carbon films of various thicknesses prepared by magnetron sputtering. In bias conditions, the density increases with the film's thickness. Beghi et al. examined t-aC film with thickness varying from 2.2 to 8 nm [53]. The Young's modulus values, measured by the SBS technique, increase with the film thickness. Our mechanical results concur with this general trend; amorphous carbon films on Si get stronger (denser, stiffer and harder) as they get thicker. This is puzzling as the growth mechanisms for a-C:H and ta-C differ and could also be influenced by the nature of the substrate. However, surprisingly, it can be justified on account of the growth models which have been developed to explain the formation of both materials. The a-C:H film grows from a polymeric precursor which is gradually dehydrogenated by the plasma, hence densified [54]. Instead, the t-aC film is formed by an energetic subplantation into the growing layer, again a densification process [10], as seen in atomistic simulations [55] and conductive AFM experiments [56] which clearly show a 1 nm thick sp^2-rich layer residing on top of the t-aC films.

A final consideration, of interest to many researchers, is the relationship between the various properties, mechanical and others. Raman and nanoindentation measurements have often been compared to each other in the literature; however, for hydrogenated films comparisons are not meaningful as shown here. Similarly, the relationship between the density, stiffness and hardness of ultra-thin amorphous carbon films is not clearly understood, to date. Studies on thicker amorphous carbon films often assume a constant E/H ratio 10. Our results on ultra-thin films do not concur with this. Indeed E and H measure very different attributes of the material. H is an elasto-plastic property, nonetheless mainly dependent on the plastic behaviour of the material; i.e. the yield stress Y. The relationship $H = 3Y$ is often used [1], for instance, in finite elemental modelling of nanoindentation. However, one should note that this relationship was originally developed for metals and might not be valid for other materials like DLC. What is certain, however, is that, H relates to irreversible changes in the bonding structure of the carbon network, bond-breaking events and/or creation of dislocations. E, on the other hand, describes the elasticity of the material, hence is essentially a measure of bond and network stiffness. At one level, the two quantities are linked, for instance, network termination such as hydrogenated groups, weaken both the overall stiffness and strength of the network, as described in the constraint-counting model [11]. However, this linkage does not necessarily imply proportionality. H being a plastic property is more likely to be influenced by defects than E, an elastic characteristic and, in theory at least, E/H is not necessarily constant. A study by Beghi also indicates that ρ and E are not linearly correlated. Ultimately, to elucidate the dependences of ρ, E and H requires the development of bonding models taking into account the various defects of the amorphous carbon network (bond angle and bond length disorders, interruptions in the carbon network, localised hydrogenated groups, aromatic or oleofinic clusters and van der Waals bonds between adjacent molecular groups).

5 Concluding Remarks

The mechanical properties of DLC have been studied for some time, to elaborate better protective coatings, to improve film's adhesion and, more generally, to supply complementary information on the bonding structure of this disordered material. The main approach has been to use nanoindentation data and the Oliver and Pharr method to give the hardness and Young's modulus of the coated system although techniques based on SAW have also proved very useful. These studies have shown wide-ranging mechanical properties for DLC with H values from 10 to 80 GPa and E values from 100 to 500 GPa. Generally, carbon networks with good tetrahedral coordination (high sp^3 fraction) yield the harder and stiffer materials. They also tend to include a large internal compressive stress, although this stress can be relieved by pulse biasing with a minimal loss of hardness. Other strengthening strategies include nitrogenating, a mitigated success to date and layering, a convenient way of bringing stress relief again or toughening the layer. Nonetheless, there remain a number of outstanding issues, mainly concerned with the experimental protocols for studying ultra-thin films. The most crucial concerns are the piled-up material, for the softest types of DLC, the effect of the deforming geometry of the surface on the unloading mechanics, the deformation of the substrate and the blunting of the tip. Yet, there is no concomitant treatment which includes all these effects. We present, however, a novel method which tackles both substrate and tip-blunting effects. This protocol is based on a modified Bhattacharya equation and gives the intrinsic film's hardness value H_F. We have used it on a series of a-C:H and t-aC films from 10 to 50 nm thickness. We find that the fit to the hardness curves is good and, not surprisingly, the H_F of the t-aC layers is higher. We also find that, through growth mechanisms, the nature of the substrate can influence H_F and that, generally, the H_F value increases with the film thickness. This result was confirmed by complementary analysis techniques which found that both the density and refractive index of the layers also increase with the film thickness. Similar results were obtained elsewhere and are consistent with established growth models for both the a-C:H and t-aC materials. There is, however, no well-understood relationship between the various properties of ultra-thin DLC films. This would require the formulation of a bonding model including the various defects of the amorphous carbon network.

References

1. K. Johnson, Contact Mechanics. Cambridge University Press, New York, 1985, p.177.
2. W. C. Oliver and G. M. Pharr, An improved technique for determining hardness and Young modulus using load and displacement sensing indentation experiments. J. Mater. Res. 7, 1564–1582 (1992).
3. O. R. Shojaei and A. Karimi, Mechanical properties of tin thin films measured using nanoindentation and the bulge test, in N. R. Moody, W. W. Gerberich, N. Burnham and S. P. Baker

(eds) Fundamentals of Nanoindentation and Nanotribology, MRS vol 522, Warrendale, Pennsylvania, 1998, p. 245.
4. D. Schneider, P. Siemrotha, T. Schulke, J. Berthold, B. Schultrich, H. H. Schneider, R. Ohr, B. Petereit and H. Hillgers, Quality control of ultra-thin and super-hard coatings by laser-acoustics, Surf. Coat. Technol. 153, 252–260 (2002).
5. M. G. Beghi, A. C. Ferrari, K. B. K. Teo, J. Robertson, C. E. Bottani, A. Libassi and B. K. Tanner, Bonding and mechanical properties of ultrathin diamond-like carbon films, Appl. Phys. Lett. 81, 3804–3806 (2002).
6. X. Li and B. Bhushan, Evaluation of fracture toughness of ultra-thin amorphous carbon coatings deposited by different deposition techniques, Thin Solid Films 355–356, 330–336 (1999).
7. X. Li and B. Bhushan, Development of a nanoscale fatigue measurement technique and its application to ultrathin amorphous carbon coatings, Script. Mater. 47(7), 473–479 (1995).
8. S. Sundararajan and B. Bhushan, Micro/nanotribology of ultra-thin hard amorphous carbon coatings using atomic force friction force microscopy, Wear 229, 678–689 (1999).
9. J. Robertson, Diamond-like carbon, Mater. Sci. Eng. B 37, 129 (2002).
10. H. He and Thorper M. F., Elastic properties of glasses, Phys. Rev. Lett. 54, 2107 (1985).
11. I. Alexandrou, H.-J. Scheibe, C. J. Kiely, A. J. Papworth, G. A. J. Amaratunga and B. Schultrich, Carbon films with an sp^2 network structure, Phys. Rev. B. 60, 10903 (1999).
12. V. Blank, M. Popov, G. Pivovarov, N. Lvova, K. Gogolinsky and V. Reshetov, Ultrahard and superhard phases of fullerite C60: comparison with diamond on hardness and wear, Diam. Relat. Mater. 7, 427–431 (1998).
13. R. Gago, I. Jiménez, J. M. Albella, A. Climent-Font, D. Caceres, I. Vergara, J. C. Banks, B. L. Doyle and L. J. Terminello, Bonding and hardness in nonhydrogenated carbon films with moderate sp^3 content, J. Appl. Phys. 87, 8174 (2000).
14. J. F. Zhao, P. Lemoine, Z. H. Liu, J. P. Quinn, P. Maguire and J. A. McLaughlin, A study of microstructure and nanomechanical properties of silicon incorporated DLC films deposited on silicon substrates, Diam. Relat. Mater. 10(3–7), 1070–1075 (2001).
15. G. A. Abbas, P. Papakonstantinou, J. A. McLaughlin, T. D. M. Weijers-Dall, R. G. Elliman and J. Filik, J. Appl. Phys. 98(10), 103505–103511 (2005).
16. P. Bruno, G. Cicala, A. M. Losacco and P. Decuzzi, Mechanical properties of PECVD hydrogenated amorphous carbon coatings via nanoindentation and nanoscratching techniques, Surf. Coat. Technol. 180–181, 259–264 (2004).
17. A. C. Ferrari, S. E. Rodil, J. Robertson and W. I. Milne, Is stress necessary to stabilise sp^3 bonding in diamond-like carbon? Diam. Relat. Mater. 11, 994–999 (2002).
18. Y. B. Zhang, S. P. Lau, D. Sheeja and B. K. Tay, Study of mechanical properties and stress of tetrahedral amorphous carbon films prepared by pulse biasing, Surf. Coat. Technol. 195, 338–343 (2005).
19. A. Y. Liu and M. L. Cohen, Prediction of new low compressibility solids, Science 245, 841–842 (1989).
20. P. Papakonstantinou and P. Lemoine, Influence of nitrogen on the structure and nanomechanical properties of pulsed laser deposited tetrahedral amorphous carbon, J. Phys.: Condens. Matter 13, 2971–2987 (2001).
21. S. S. Roy, R. McCann, P. Papakonstantinou, P. Maguire and J. A. McLaughlin, The structure of amorphous carbon nitride films using a combined study of NEXAFS, XPS and Raman spectroscopies, Thin Solid Films 482, 145–150 (2005).
22. P. Patsalas,T. S. Logothetidis and P. C. Kelires, Surface and interface morphology and structure of amorphous carbon thin and multilayer films, Diam. Relat. Mater. 14, 1241–1254 (2005).
23. D. Sheeja, B. K. Tay, S. P. Lau, X. Shi and X. Ding, Structural and tribological characterization of multilayer ta-C films prepared by filtered cathodic vacuum arc with substrate pulse biasing, Surf. Coat. Technol. 132, 228–232 (2000).
24. K. H. Lee, R. Ohta, H. Sugimura, Y. Inoue, O. Takai and H. Sugimura, Amorphous carbon and carbon nitride multilayered films prepared by shielded arc ion plating, Thin Solid Films 475, 308–312 (2005).

25. S. Logothetidis, S. Kassavetis, C. Charitidis, Y. Panayiotatos and A. Laskarakis, Nanoindentation studies of multilayer amorphous carbon films, Carbon 42, 1133–1136 (2004).
26. L. Kogut and K. Komvopoulos, Analysis of spherical indentation cycle of elastic-perfectly plastic solids, J. Mater. Res. 19, 3641–3653 (2004).
27. R. L. Jackson and L. Kogut, A comparison of flattening and indentation approaches for contact mechanics modeling of single asperity contacts, ASME J. Tribol. 128(1), 209–212 (2005).
28. C. M. Cheng and Y. T. Cheng, On the initial unloading slope in indentation of elastic-plastic solids by an indenter with an axisymetrical smoth profile, Appl. Phys. Lett. 71(8), 2623–2625 (1997).
29. W. C. Oliver and G. M. Pharr, Measurement of hardness and elastic modulus by instrumented indentation: advances in understanding and refinements to methodology, J. Mater. Res. 7, 3 (2004).
30. Y. Y. Lim, M. M. Chaudhri and Y. Enomoto, Accurate determination of the mechanical properties of thin aluminium films deposited on sapphire flats using nanoindentation, J. Mater. Res. 14, 2314 (1999).
31. G. M. Pharr and A. Bolshakov, Understanding nanoindentation unloading curves, J. Mater. Es., 17(10), 2660–2671 (2002).
32. N. Schwarzer, T. Chudoba and F. Richterutf, Investigation of ultra thin coatings using nanoindentation, Surf. Coat. Technol. 200(18–19), 5566–5580 (2006).
33. S. Bec, A. Tonck, J. M. Georges, E. Georges and J. L. Loubet, Improvements in the indentation method with a surface force apparatus, Phil. Mag. A 74, 1061 (1996).
34. Z. Xu and D. Rowcliffe, Finite element analysis of substrate effects on indfentation behaviour of thin films, Thin Solid Films 447, 399 (2004).
35. R. Saha and W. D. Nix, Effects of the substrate on the determination of thin film mechanical properties by nanoindentation, Acta. Mater. 50, 23 (2002).
36. A. K. Bhattacharya and W. D. Nix, Analysis of elastic and plastic deformation associated with indentation testing of thin films on substrates, Int. J. Sol. Struct. 24, 1287 (1988).
37. C. Lu and D. B. Bogy, The effect of tip radius on nanoindentation hardness tests, Int J. Sol. Struct. 32, 1759 (1995).
38. P. Lemoine, J. P. Quinn, P. Maguire and J. A. McLaughlin, Comparing hardness and wear data for tetrahedral amorphous carbon and hydrogenated amorphous carbon thin films, Wear 257, 509 (2004).
39. R. Y. Lo, D. B. Bogy, Compensating for elastic deformation of the indenter in hardness tests of very hard materials, J. Mater. Res. 14, 2276 (1999).
40. P. Lemoine, J. F. Zhao, J. P. Quinn, J. A. McLaughlin and P. Maguire, Hardness measurements at shallow depths on ultra-thin amorphous carbon films deposited onto silicon and Al2O3-TiC substrates. Thin Solid Films 379, 166 (2000).
41. E. Martínez, J. L. Andújar, M. C. Polo, J. Esteve, J. Robertson and W. I. Milne, Study of the mechanical properties of tetrahedral amorphous carbon films by nanoindentation and nanowear measurements. Diam. Relat. Mater. 10, 145 (2001).
42. J. A. Knapp, D. M. Follstaedt, S. M. Myers, J. C. Barbour and T. A. Friedman, Finite-element modeling of nanoindentation, J. Appl. Phys. 85, 1460 (1999).
43. B. Bhushan and S. Venkatesan, Effective mechanical properties of layered rough surfaces. Thin Solid Films 473, 278, (2005).
44. K. Johnson, Contact mechanics, Cambridge University Press, New York, 1985, p. 177.
45. A. M. Korsunsky, M. R. McGurk, S. J. Bull, T. F. Page, On the hardness of coated systems. Surf. Coat. Technol. 99, 171 (1998).
46. X. G. Ma, K. Komvopoulos, D. Wan, D. B. Bogy and Y.-S. Kim, Effects of film thickness and contact load on nanotribological properties of sputtered amorphous carbon thin films.Wear 254, 1010 (2004).
47. S. Logothetidis, Surface and interface properties of amorphous carbon layers on rigid and flexible substrates. Thin Solid Films 482, 9 (2005).
48. P. Lemoine, J. P. Quinn, P. D. Maguire, J. F. Zhao and J. A. McLaughlin, Intrinsic mechanical properties of ultra-thin amorphous carbon layers, Appl. Surf. 253, 6165 (2007).

49. P. Lemoine, J. P. Quinn, P. D. Maguire and J. A. D. McLaughlin, Measuring the thickness of ultra-thin diamond-like carbon films, Carbon 44, 2617 (2006).
50. R. McCann, S. S. Roy, P. Papakonstantinou, G. Abbas and J. A. McLaughlin, The effect of thickness and arc current on the structural properties of FCVA synthesised ta-C and ta-C:N films. Diam. Relat. Mater. 14, 983 (2004).
51. I. Ahmad, P. D. Maguire, P. Lemoine, S. S. Roy and J. A. McLaughlin, Deposition of carbon films onto metal and silicon substrates by filtered cathodic vacuum arc, plasma enhanced CVD and unbalanced magnetron sputtering. Diam. Relat. Mater. 13, 1346 (2004).
52. P. Patsalas, T. S. Logothetidis and P. C. Kelires, Surface and interface morphology and structure of amorphous carbon thin and multilayer films. Diam. Relat. Mater. 14, 1241 (2005).
53. M. G. Beghi, A. C. Ferrari, C. E. Bottani, A. Libassi, B. K. Tanner, K. B. K. Teo and J. Robertson, Elastic constants and structural properties of nanometre-thick diamondlike carbon films. Diam. Relat. Mater. 11, 1062 (2002).
54. W. Jakob, Surface reactions during growth and erosion of hydrocarbon films. Thin Solid Films 326, 1 (1998).
55. P. C. Kelires, Surface properties of diamond-like amorphous carbon. J. Non Cryst. Sol. 227, 597 (1998).
56. D. Liu, G. Benstetter and W. Frammelsberger, The effect of the surface layer of tetrahedral amorphous carbon films on their tribological and electron emission properties investigated by atomic force microscopy. Appl. Phys. Lett. 82, 3898 (2003).

Residual Stresses in DLC Films and Adhesion to Various Substrates

Y. Pauleau

Abstract The origin of residual stresses in thin films and various models invoked to explain the development of such stresses are reviewed in the first part the chapter. Compressive intrinsic stresses develop in fully dense films such as diamond-like carbon (DLC) films produced at room temperature by energetic deposition techniques. Fundamental aspects related to residual stresses and adhesion of films, as well as the determination of the stress magnitude and adhesion strength of DLC films are presented in the second part. The effects of deposition parameters on the intrinsic stress level are analyzed in detail. The reduction of the stress level and improvement of film adhesion can be achieved via various approaches described in the last part of the chapter.

Keywords stress modeling, magnitude of stresses, adhesion strength, effect of process parameters, reduction of the stress level, improvement of the film adhesion

1 Introduction

Many forms of amorphous carbon films can be prepared by physical or chemical vapor deposition (PVD or CVD) techniques such as direct current (DC) or radio frequency (RF) sputtering, ion beam sputtering, direct ion beam deposition, cathodic arc deposition, pulsed laser deposition, and plasma-enhanced chemical vapor deposition. Carbon atoms can exhibit three types of hybridization, namely sp^3, sp^2, and sp^1 states. In general, an amorphous carbon film is a mixture of sp^3, sp^2, and even sp^1 sites, with the possible presence of hydrogen atoms up to 60 at. %. The composition of films can be conveniently represented in a ternary phase

National Polytechnic Institute of Grenoble, Centre National de la Recherche Scientifique, CNRS-LEMD, B.P. 166, 38042 Grenoble 9, France

C. Donnet and A. Erdemir (eds.), *Tribology of Diamond-Like Carbon Films: Fundamentals and Applications*.

diagram with the three corners corresponding to diamond (sp^3 configuration), graphite (sp^2 configuration), and hydrogen [1].

A diamond-like carbon (DLC) films is defined as an amorphous carbon (a-C) or a hydrogenated amorphous carbon (a-C:H) film containing a significant fraction of sp^3-bonded carbon atoms [2]. The content of sp^3-hybridized carbon atoms is often rather small in a-C:H films. Tetrahedral amorphous carbon (ta-C) film and its hydrogenated analog (ta-C:H) film correspond to DLC films with highest sp^3 content. Hydrogen-free DLC films with a high sp^3 content can be produced essentially by UV pulsed laser deposition, filtered vacuum cathodic arc deposition, and mass selected ion beam deposition [3]. The physical properties of amorphous carbon films are strongly dependent on the ratio of sp^2 (graphite-like) to sp^3 (diamond-like) bonded carbon atom concentrations. These films extensively studied for more than a decade exhibit a unique combination of chemical inertness, mechanical, tribological, and optical properties very promising for various applications.

Two major components are required for deposition of DLC films with a high sp^3 content, namely (i) a carbon source, and (ii) an energy source. The kinetic energy can be supplied to carbon species contributing to the growth of DLC films by momentum transfer during collision with energetic projectiles (sputter deposition), bombardment with energetic particles (ion-assisted deposition), electrostatic acceleration of carbon ions (direct ion beam deposition), or energy transfer during pulsed laser ablation or arc discharge. Carbon species having kinetic energies ranging from 2.5 to 25 eV can be produced by these energetic deposition processes. By contrast, carbon species generated by thermal processes such as thermal evaporation under vacuum possess much smaller kinetic energies, i.e., of the order of magnitude of kT, approximately 0.025 eV at ambient temperature [4,5]. Relatively high kinetic energies are needed to promote the electron transition from 2s to 2p orbital in carbon atoms and produce carbon films with a high content of sp^3-hybridized carbon atoms.

In general, compressive intrinsic stresses develop in thin films produced from energetic particles or by energetic deposition processes. The magnitude of intrinsic stresses is dependent on the impact energy per atom, which is the total kinetic energy of species colliding with the film surface per atom condensed and incorporated in the film [6,7]. Excessive compressive residual stresses in DLC films may cause mechanical damage, i.e., adhesion failures and delamination of films from the substrate surface. On a less catastrophic scale, large stresses can affect the physical properties of films. The elimination and release of residual stresses may also be the cause of undesirable changes of morphology and microstructure of films. As a result, there is a considerable interest in the determination and control of residual stresses developed in DLC films deposited under various experimental conditions.

The goal of this chapter is to review the origin of residual stresses in DLC films produced by various techniques. The basic aspects related to residual stresses in thin films and adhesion of films to substrates are presented in the first section of the chapter. The determination of the magnitude of residual stresses in DLC films, and adhesion strength of DLC films to various substrates is discussed in the second section.

Then, the relationships between the deposition parameters and the magnitude of residual stresses, that is, essentially the effects of process or physical parameters on the intrinsic stress level are analyzed in detail. The major approaches susceptible to be adopted for the reduction of residual stresses in DLC films and improvement of the film adhesion are described in the last two sections of the chapter.

2 Basic Aspects

2.1 Residual Stresses in Thin Films

Residual stresses exist in the bulk of polycrystalline materials not subjected to external forces. The residual stress system developed in these materials has zero resultant force since the materials are at equilibrium. According to the distance required for achieving this balance, three types of stresses can be distinguished, namely macroscopic stress or stress of order I, structural microstress or stress of order II, and internal stress or stress of order III [7]. The major stress, which can be determined in disordered materials such as amorphous carbon is the macroscopic stress. This stress develops in continuous films, that is, much thicker than films resulting from the coalescence of islands grown on flat substrate surfaces. The average value of the macroscopic stress is found to be independent of the film thickness in continuous films deposited onto non-epitaxial substrates inducing an island mode of growth with no crystallographic relationship between the orientation of the islands and the substrate. The magnitude of residual stresses, σ, developed in thin films, for example, amorphous carbon films depends on three different contributions, namely thermal stress, σ_{th}, intrinsic stress, σ_i, and extrinsic stress, σ_e. As a result, the magnitude of residual stresses can be expressed as follows:

$$\sigma = \sigma_{th} + \sigma_i + \sigma_e \tag{1}$$

2.1.1 Thermal Stresses

Thermal stresses, σ_{th}, arise from the difference of thermal expansion coefficients, α, of the substrate and film, $(\alpha_s - \alpha_f)$, combined with the difference between the temperature of samples during determination of stresses (currently performed at room temperature, T_r) and the deposition temperature, $(T_r - T_d)$. The magnitude of the thermal stress is given by:

$$\sigma_{th} = \left(\frac{E_f}{1 - \upsilon_f} \right) (\alpha_s - \alpha_f)(T_r - T_d) \tag{2}$$

where E_f and ν_f are Young's modulus and Poisson's ratio of the film, respectively. The contribution of the thermal stress is nil at room temperature for DLC films deposited either at room temperature or on substrates with a thermal expansion coefficient equal to that of DLC films. The major difficulty encountered in the calculation of the thermal stress from Eq. (2) arises from the determination of the biaxial modulus, $E_f/(1 - \nu_f)$, and thermal expansion coefficient, α_f, of the film. The values of $E_f/(1 - \nu_f)$ and α_f for films, in particular DLC films, can be very different from the values of the bulk material (diamond or graphite) given in the literature. Various experimental approaches can be adopted to determine the biaxial modulus and thermal expansion coefficient of films values [6].

2.1.2 Intrinsic Stresses

Intrinsic stresses, σ_i, are introduced in films during deposition. The magnitude of the intrinsic stress can be related to the microstructure or morphology of films, which depends on various deposition parameters [6]. The intrinsic stress value depends on the impact energy per atom, i.e., on the kinetic energy of particles striking the film surface during deposition (Fig. 1).

These incident particles can be atoms, molecules, ions, and radicals, either condensed on the film surface and incorporated in the film, or simply reflected at the film surface and backscattered to the gas phase. The considerations on intrinsic stresses developed in thin films produced via nonenergetic particles (average kinetic energy below 0.5 eV) can be separated conveniently from those developed

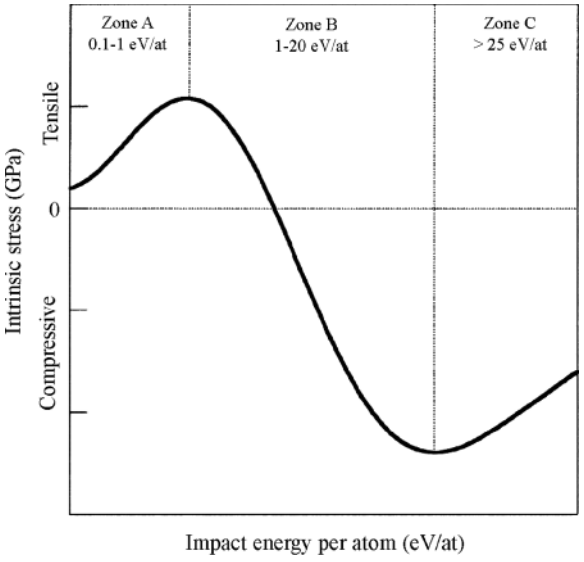

Fig. 1 Idealized intrinsic stress versus impact energy per atom

in films deposited by condensation of energetic species and/or under energetic particle bombardment with kinetic energies ranging from a few electron volts to a few hundreds of electron volts [8].

Tensile intrinsic stresses develop in films produced from nonenergetic particles (Fig. 1). The model most often used to explain the origin of tensile intrinsic stresses is the grain boundary relaxation (GBR) model established for polycrystalline films [6,7]. The GBR model is based on various hypotheses and physical arguments. As the film grows from isolated atomic clusters, interatomic attractive forces acting across grain boundaries, gaps between grains, or intercolumnar spaces cause an elastic deformation (or relaxation) of the grain walls. These attractive forces are counterbalanced by the intragrain or intracolumn tensile forces imposed by the constraint caused by the adhesion of the film to the substrate surface. The adhesion forces exceed the tensile forces developed between adjacent grains or columns. The intragrain tensile forces are prone to reduce the volume of the film as the film is detached from the substrate. The induced stress is tensile since the film is trying to contract. This model is adaptable to amorphous films exhibiting a columnar or fibrous microstructure or morphology.

Compressive intrinsic stresses develop in films produced from energetic particles (Fig. 1). The surface diffusion of atoms adsorbed on the film surface (adatoms) is promoted by energetic particle bombardment of the film surface during deposition. The microstructure of the films is modified progressively. The volume reduction of voids, grain boundaries, and intercolumnar spaces removes the origin of the tensile intrinsic stress. As a result, the magnitude of the tensile intrinsic stress decreases and tends to be equal to zero even though the yield strength of the deposited material is greater than zero. Beyond the sudden drop in tensile intrinsic stress, a transition between tensile and compressive intrinsic stress occurs as the impact energy per atom increases. Then, the magnitude of the compressive intrinsic stress increases progressively up to a maximum value with increasing impact energy per atom (Fig. 1, zone B). Two major models have been proposed to account for the generation of compressive intrinsic stresses in films produced from energetic particles [9–11].

The forward sputtering model established by Windischmann is based on three major assumptions: (i) energetic bombardment of the film surface causes displacements of atoms in the film from their equilibrium positions through a series of primary and recoil collisions, producing a volume distortion; (ii) for films deposited at low substrate temperatures, i.e., with the normalized growth temperature (T_d/T_m) or ratio between the absolute substrate temperature or deposition temperature (T_d) and the absolute melting point of the deposited material (T_m) below 0.25, mass transport and defect mobility are sufficiently low to freeze the volumetric distortion in place; and (iii) the relative volumetric distortion (d), which corresponds to a strain is proportional to the fractional number of atoms (n/N) displaced from equilibrium positions, i.e., $d = K\,(n/N)$, where K is the proportionality factor and N is the atom number per unit volume or atomic number density in the deposited material. The calculation developed on the basis of this model [9,10] leads to the expression of the volumetric distortion or elastic strain as a function of the flux and kinetic

energy of particles impinging on the film surface during deposition. The compressive intrinsic stress (σ_i), is related to the volumetric distortion by Hooke's law:

$$\sigma_i = \left(\frac{E_f}{1 - v_f} \right) d \tag{3}$$

The magnitude of the compressive intrinsic stress is given by:

$$\sigma_i = \left[\frac{E_f M_t}{(1 - v_f) D_f} \right] 4.79 \left(\frac{K \phi_p}{N_{Av}} \right) \delta \sqrt{E_p} = K \phi_p \sqrt{E_p} Q \tag{4}$$

where N_{Av} is the Avogadro's number, D_f the mass density of the film, and M_t the mass of film atoms (target atoms); ϕ_p and E_p are the flux and kinetic energy of energetic particles (projectiles), respectively. The constant k equal to$(4.79 K\ \delta/N_{Av}$ is related to the factor δ, which depends on the cohesi9ve energy (U_0), of atoms in the film, masses (M_p and M_t) and atomic numbers (Z_p and Z_t) of incident particles (projectiles) and film atoms (targets), respectively:

$$\delta = \left[\frac{M_t^{1/2} \left(Z_p Z_t \right)^{1/2}}{U_0 \left(M_p + M_t \right)^{1/2} \left(Z_p^{2/3} + Z_t^{2/3} \right)^{3/4}} \right] \tag{5}$$

The term Q corresponding to the stored elastic energy per mole is given by:

$$Q = \left(\frac{E_f}{1 - v_f} \right) \left(\frac{M_t}{D_f} \right) \tag{6}$$

The units for Q are erg/mol, for E_f given in dyn/cm^2, M_t in amu and D_f in g/cm^3. To convert erg/mol to eV/atom, the value of Q is divided by 10^{12}.

According to this model, the compressive intrinsic stress depends on the atomic volume of the film material (M_t/D_f). This dependence means that the interactions between the energetic particles (projectiles) and the atoms (targets) of the deposited material give rise to a variable strain depending upon the atomic arrangement in the film. The linear relationship between the compressive intrinsic stress and the factor Q has been observed for films deposited by various techniques [9,10]. However, the forward sputtering model exhibits various limits of validity. The model is not applicable for films with very light energetic particle bombardment, i.e., for $Z_p/Z_t << 1$, since the assumptions involved in the sputtering theory of Sigmund are not valid [12]. In addition, the model cannot be invoked to explain the intrinsic stress when the film surface senses particles having very low or very high kinetic energies. The lower energy limit of applicability corresponds approximately to the energy for atomic displacement in the films, which is about 18–30 eV for most materials [13,14]. With low energy projectiles, the assumption of isotropic cascades in the

target (film) involved in the sputtering theory is no longer valid. Bombardment of growing films by ions with a normalized energy (E_n) of less than a few electron volt per atom condensed on the film surface leads to films containing a significant fraction of voids resulting in tensile intrinsic stress developed in the films rather than a compressive intrinsic stress [15]. The upper energy limit of applicability is related to resputtering of the deposited material and possible mechanical damage of the film such as void formation and plastic flow [16]. Moreover, the magnitude of the compressive intrinsic stress predicted by this model increases continuously with increasing projectile energy (E_p). However, the maximum compressive stress observed in thin films is usually less than the yield strength. Beyond this maximum, the compressive intrinsic stress is found to decrease with increasing impact energy per atom (Fig. 1, zone C). The forward sputtering model does not predict this decrease.

The model proposed by Davis was established to explain the origin of compressive intrinsic stresses in relatively dense films [11]. This model is based on two major assumptions. The compressive intrinsic stress is assumed to be caused by film atoms implanted below the surface of the film by knock-on processes in accordance with the forward sputtering model. In addition, thermal spikes are assumed to reduce the stress by causing displacement of the implanted atoms. The implanted atoms in metastable position, which acquire more than some excitation energy (E_d), will escape from their metastable position to the surface of the film. Intense local heating resulting from the energy of bombarding particles transferred to film atoms in the very small area of the impact, i.e., thermal spike is supposed to provide the energy required for releasing implanted atoms from their metastable position within the film [17]. Assuming that there is a balance between implantation and relaxation processes, the density (n) of implanted atoms (or atoms displaced by energetic particle bombardment) is constant with time. On the basis of these assumptions, the ratio (n/N) and the relative volumetric distortion ($d = K\,(n/N)$) can be expressed as a function of the flux (ϕ_p) and kinetic energy of incident energetic species (E_p) in particular [11]. The compressive intrinsic stress (σ_i) related to the volumetric distortion by Hooke's law is given by:

$$\sigma_i = \left(\frac{E_f}{1-\nu_f}\right)\left(\frac{Kn}{N}\right) = \left[\left(\frac{13.36\,K}{U_0}\right)\left(\frac{E_f}{1-\nu_f}\right)\right]\left[\frac{\left(E_p\right)^{1/2}}{\frac{\phi_c}{\phi_p} + k_a\left(E_p\right)^{5/3}}\right] \tag{7}$$

or

$$\sigma_i = k\left[\frac{\left(E_p\right)^{1/2}}{\frac{\phi_c}{\phi_p} + k_a\left(E_p\right)^{5/3}}\right] \tag{8}$$

where U_0 is the sublimation energy of the deposited material and ϕ_c the flux of atoms condensed on the film surface and incorporated in the growing film. The factor k_a is equal to $(0.016\ \rho\ (E_d)^{-5/3})$ where ρ is a material-dependent parameter, which is of the order of unity [11]. The parameters κ and k_a in Eq. (8) are generally unknown. One method for determining these parameters is to use them as fitting parameters for a least-squares fit to data for which the kinetic energy (E_p), ion flux (ϕ_p), and deposition rate of films (ϕ_c), are known. With a low normalized flux (ϕ_p/ϕ_c) the ratio ϕ_c/ϕ_p in Eq. (7) is large with respect to the term $(k_a\ (E_p)^{5/3})$ and the compressive intrinsic stress can be approximated to:

$$\sigma_i = \left(\frac{E_f}{1-\nu_f}\right)\left(\frac{13.36\,K}{U_0}\right)\left[\frac{\phi_p\left(E_p\right)^{1/2}}{\phi_c}\right] \tag{9}$$

This expression is comparable with Eq. (4) which gives the compressive intrinsic stress predicted from the forward sputtering model. In the theory developed by Davis, the compressive intrinsic stress is found to be proportional to ϕ_p/ϕ_c, whereas the forward sputtering model leads to compressive intrinsic stress intensity linearly depending on ϕ_p only. For a very large normalized flux, ϕ_p/ϕ_c, Eq. (7) can be approximated to:

$$\sigma_i = \left(\frac{E_f}{1-\nu_f}\right)\left(\frac{13.36\,K}{U_0}\right)\left[\frac{1}{k_a\left(E_p\right)^{7/6}}\right] \tag{10}$$

Two different strategies can be adopted to reduce the magnitude of compressive intrinsic stresses in thin films. The first possibility is to produce films with low normalized fluxes, ϕ_p/ϕ_c, i.e., at high deposition rates and low energetic particle fluxes. The compressive intrinsic stress predicted by Eq. (9) is also reduced with decreasing kinetic energy of incident particles. However, in this case, the benefits of energetic deposition techniques may be considerably diminished. The alternative approach is to prepare films with high normalized fluxes (ϕ_p/ϕ_c), or at low deposition rates with high ion fluxes. The magnitude of compressive intrinsic stress expressed by Eq. (10) is reduced with increasing ion energy. However, too high-ion energies may lead to resputtering phenomena and significant damage with void formation in the films. Eventually, films produced under these conditions exhibit reduced mass densities and tensile intrinsic stress.

2.1.3 Extrinsic Stresses

The third component of residual stresses expressed by Eq. (1) is the extrinsic stress (σ_e) induced by external factors, i.e., interactions between the deposited material and environment. A lattice distortion may originate from various sources such as

incorporation of impurity (oxygen, hydrogen) atoms in the film, reaction producing a new phase with a different molar volume, and grain surface energy reduction. In general, these phase transformations lead to volume expansion and compressive stresses can be developed [18]. Consequently, for not fully dense films exhibiting tensile intrinsic stress, an impurity-induced compensating compressive stress may develop during deposition. This compressive stress originating from impurity incorporation may reduce the tensile stress in a non-overtly manner or produce a net compressive stress if the tensile intrinsic stress is totally compensated and overwhelmed even though the atomic peening mechanism is ineffective [19]. Therefore, the interpretation of stress data must be performed cautiously for films with compositions or impurity contents, which vary with process parameters as well as for films produced by reactive deposition processes, which may involve the formation of a new phase with a different molar volume by surface reactions such as oxidation, nitridation, or hydrogenation.

Furthermore, various molecules can penetrate open voids or pores present in not fully dense films and adsorb on pore walls thereby interaction forces between adsorbed species, in particular, between polar species such as water molecules can act to modify residual stresses. These interaction forces may be responsible for extrinsic stress generation in porous films, which were exposed to room air or chemical agents contained in various environments. Depending on the relative orientation of adsorbed polar molecules, nature of adsorbed species and composition of pore walls, attractive or repellent interaction forces may develop, and the resulting extrinsic stress in the films can be tensile or compressive. A model was proposed to explain the origin of extrinsic stress based on the adsorption of polar species on pore walls [6,20]. This model is not of great numerical precision; however, dipole interactions between adsorbed molecules are demonstrated to be responsible for the observed forces and stresses produced by realistic amounts of adsorbate. The model is based on two major assumptions: (i) the adsorbed molecular dipoles are arranged on the cylindrical pore wall with their axes normal to the surface and with charges of the same sign pointing inwards and outwards, respectively, and (ii) the circumference of the adsorbing surface is assumed to remain at the constant value of $2\pi a$ (where a is the radius of cylindrical pores), irrespective of the amount of material adsorbed on the pore walls. The interaction force between two dipoles was calculated from elementary electrostatic theory, and total interaction force acting on the cross-section of the film per unit width was expressed as follows [20]:

$$F_{\text{total}} = \frac{1.74 \times 10^9 n^2 \alpha^2 t_{\text{f}}}{5\pi\varepsilon a} \tag{11}$$

where n is the number of dipoles per unit area, α the dipole moment, t_{f} the film thickness, and ε the dielectric constant of the free space.

According to Eq. (11), for very porous films with relatively large pore radii (a) the extrinsic stress resulting from adsorption of molar molecules would be rather low. In these films, the distance between adsorbed polar molecules on opposite

pore walls is too large for efficient attractive or repellent interactions. For dense films such as DLC films, the pore radii (a) tend to be nil and the interaction force would be infinite. This situation is unrealistic since for too low pore sizes, the coverage of the pore walls by adsorbed polar molecules is expected to be nonuniform, or eventually molecules cannot be adsorbed if the pore diameter is less than the polar molecule diameter. As the pore diameter decreases, the number of dipoles per unit area (n) adsorbed on the pore walls decreases concomitantly, and the interaction force tends to be negligible. The magnitude of extrinsic stress originating from adsorption of polar molecules in not fully dense films would reach a maximum value for pore sizes comparable to the diameter of polar molecules.

2.2 *Mechanical Damage and Adhesion of Residually Stressed Films*

The mechanical resistance of the substrate only sustains elastic stresses in thin films. For films produced by energetic deposition techniques exhibiting compressive residual stresses such as DLC films, an excessive stress level may cause film buckling above an intrinsic defect at the film–substrate interface. The compressive stress is partially released by the film buckling. The released elastic strain energy is then available to drive the delamination of the film from the substrate [21,22]. No external loads are involved in the modes of failure of systems consisting of a residually stressed thin film deposited on a rigid substrate. In fact, the crack-driving force or strain-energy release rate can be defined as: $G = (\partial U/\partial A)$ where U is the elastic energy stored in the film and A the crack area. The criterion for crack advance is that G exceeds the toughness or the fracture resistance, which is the energy needed to advance the crack by a unit area [23].

The fracture and the delamination of films are governed by the elastic energy stored in the film initially adherent firmly to the substrate surface. This elastic energy depends on the film thickness and the magnitude of residual stresses in the film. For residual stresses (σ) assumed to be biaxial and isotropic in the plane of films, the elastic energy (U) stored in the film of unit surface area is given by [24]:

$$U = \left(\frac{1 - \nu_{\mathrm{f}}}{E_{\mathrm{f}}} \right) t_{\mathrm{f}} \sigma^2 \tag{12}$$

where t_{f} is the film thickness and the term in brackets is the reciprocal biaxial modulus of the film. The stress value is often found to be independent of the film thickness. As a result, the elastic energy (U), indicated by the shaded section in Fig. 2, increases linearly with increasing film thickness. This available energy can be consumed to produce mechanical failure of the film–substrate system. In particular, the mechanical instability of film–substrate structures can be observed when the elastic energy (U)

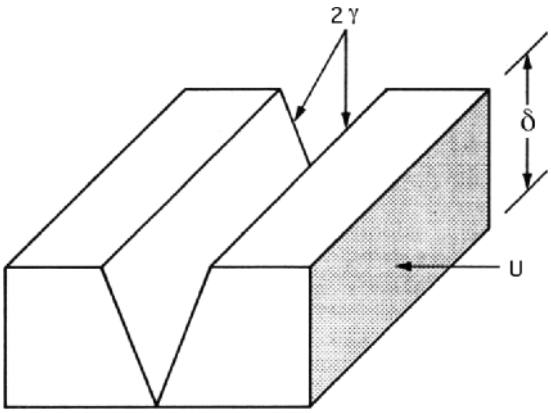

Fig. 2 A section of film of section δ and of unit surface area, i.e., of unit length and width

exceeds a critical value (U_c), which is determined by the surface free energy (γ), required for film failure. As illustrated in Fig. 2, the two new surfaces formed by the fracture correspond to an increase of 2 γ in the total surface free energy of the film–substrate system.

For a perfect film–substrate interface having maximum film–substrate adhesion, the increase in surface free energy upon delamination of the film from the substrate surface is given by [25]:

$$\gamma_d = \gamma_f + \gamma \tag{13}$$

where the subscripts f and s refer to film and substrate, respectively. In fact, γ_d is the work of adhesion for a given film–substrate system in which the film–substrate interface is perfect, i.e., the film and the substrate form a contiguous and perfect joint at the interface. For a film and a substrate totally disjointed or separated, the work of adhesion (γ_d) is equal to zero.

For not perfect film–substrate adhesion, a free energy (γ_i), is already expended and it corresponds to a measure of the degree of adhesion [25]. This free energy (γ_i) is nil for a perfect adhesion between the film and the substrate. For a film totally separated from the substrate, the work of adhesion (γ_d) is equal to zero and the free energy (γ_i), is given by the sum ($\gamma_f + \gamma_s$).

As a result, for the intermediate case in which an imperfect adhesion exists between the film and the substrate, the work of adhesion is given by [26]:

$$\gamma_d = \gamma_f + \gamma_s - \gamma_i \tag{14}$$

The surface free energies (γ_f and γ_s) are essentially known quantities while γ_i, the free energy of the formed interface as illustrated in Fig. 3, is an unknown quantity.

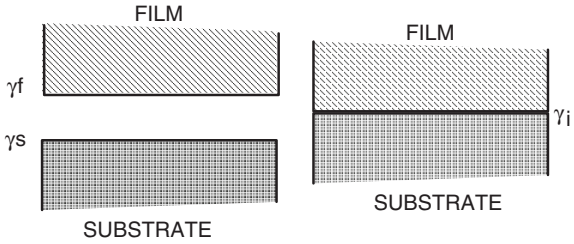

Fig. 3 Free-energy change when materials F and S are joined

In practice, γ_i depends not only upon the chemistry of the interface, but also upon its morphology and structural integrity. However, by minimizing γ_i, the work of adhesion (γ_d) may increase significantly for many systems.

2.2.1 Fracture of Films

Tensile residual stresses in a film bonded to a substrate may lead to crack formation in the film or fracture of the film. The crack is perpendicular to the film plane. In addition, the crack does not penetrate the substrate, and the film is not separated from the substrate at the intersection of the crack and the substrate. For this type of crack caused by a tensile fracture of the film, the Griffith fracture theory can be used, and the critical stress (σ_c) for fracture of the film, which is normal to the crack plane can be approximated to [27]:

$$\sigma_c = \left(\frac{2 E_f \gamma}{h} \right)^2 \tag{15}$$

where E_f is the Young's modulus of the film, γ is the surface free energy for the film fracture, and h is Griffith crack length. For simplicity, Poisson's ratio (v_f) of the film was omitted. This ratio can be neglected without significantly affecting the results [25]. The increase in total surface energy caused by the fracture of the film equal to 2γ (Fig. 2) can be considered as the critical energy for crack formation in the film (U_c):

$$2\gamma = U_c = \frac{\sigma_c^2 t_{fc}}{E_f} \tag{16}$$

where t_{fc} is the critical film thickness at which the elastic energy stored in the film exceeds the critical energy (U_c) for film fracture. This critical film thickness was assumed to be equal to the Griffith crack length (h). The fracture of the film may occur when the elastic energy (U) given by Eq. (12) exceeds U_c:

$$U = \frac{\sigma_c^2 t_{fc}}{E_f} > U_c \tag{17}$$

The value of U_c is governed by the magnitude of the surface energy (γ) for film fracture while the elastic energy (U) stored in the film depends on the product ($\sigma^2\ t_f$). For a given tensile residual stress value (σ) independent of the film thickness, the condition for film fracture U is approximately equal to U_c. As a result, the critical film thickness (t_{fc}) for film fracture is given by:

$$t_{fc} = \frac{2E_f\gamma}{\sigma^2} \tag{18}$$

2.2.2 Delamination of Films

For films with compressive residual stresses such as DLC films, a common mechanical instability is the delamination of films from the substrate and the blister formation at the film–substrate interface. The separation of the film from the substrate is also a fracture phenomenon. The planar fracture model proposed by Barenblatt [28] is more appropriate than the Griffith fracture theory for modeling this type of instability [25]. The basic parameter in the Barenblatt model is a modulus of cohesion (K) defined by the energy (U_k) required for the separation of the two surfaces, that is, for delamination of the film from the substrate surface or the crack formation at the film–substrate interface. The energy U_k is given by:

$$U_k = \left(\frac{1-\nu_f}{E_f}\right)\frac{K^2}{\pi} \tag{19}$$

The modulus of cohesion (K) can be approximated to [28]:

$$K^2 = \left(\frac{E_f}{1-\nu_f^2}\right)\pi\gamma \tag{20}$$

By neglecting Poisson's ratio (ν_f), in Eqs (19) and (20), the energy (U_k) is approximately equal to the surface free energy (γ) for film fracture. Furthermore, for delamination of the film from the substrate, the surface free energy (γ) can be equated to the work of adhesion (γ_d) and the critical energy for delamination of the film is given by:

$$U_{cd} = \gamma_d \tag{21}$$

This condition for film delamination is quite similar to that for film fracture given by Eq. (16). Thus, the condition for delamination of the film in terms of elastic energy (U) stored in the film can be expressed as follows:

$$U = \frac{\sigma^2 t_f}{E_f} > U_{cd} \tag{22}$$

Eq. (22) for film delamination is similar to Eq. (17) valid for film fracture. The critical film thickness for delamination (t_{fc}) can be deduced from Eqs (21) and (22):

$$t_{fcd} = \frac{E_f \gamma_d}{\sigma^2} \tag{23}$$

Hence, the critical compressive residual stress value for delamination of the film can be expressed as follows:

$$\sigma_{cd} = \left(\frac{E_f \gamma_d}{t_f} \right)^{1/2} \tag{24}$$

Finally, from the simplest aspects of fracture theory, it can demonstrated that the condition for mechanical stability of film–substrate structures is governed by four major parameters, namely surface free energy for film fracture (γ), surface free energy for delamination (γ_d), magnitude of residual stresses (σ), and film thickness (t_f). In addition, Eqs (17) and (18) describing the criteria for film fracture exhibit the same form as Eqs. (22) and (23) corresponding to the criteria for delamination of a film from the substrate surface. Catastrophic film failure can be avoided by minimizing elastic energy (U) stored in the film, i.e., by reducing the product (σ^2 t_f). Various aspects or requirements for a given application usually determine the minimum value of the film thickness. Therefore, the mechanical stability of film–substrate structures may be insured essentially via the reduction of the magnitude of residual stresses (σ). A significant reduction of residual stresses in thin films for a given film–substrate structure is not always possible for practical reasons. When fracture or delamination of films cannot be avoided, substitute materials for the film and/or the substrate or alternative deposition techniques must be considered for production of mechanically stable film–substrate structures.

3 Determination of the Magnitude of Residual Stresses and Adhesion Performance

Although the magnitude of residual stresses and the adhesion strength of thin films deposited on various substrates are intimately connected, that is, the adhesion strength of DLC films deposited on stainless steel substrates has been found to be

inversely proportional to the magnitude of residual stresses [29], the determination of residual stresses and adhesion strength values are performed using very distinct measurement techniques.

3.1 Determination of the Magnitude of Residual Stresses

The most common methods used for the determination of residual stresses in thin films are based on measurements of the deformation of film–substrate structures. These methods are well adapted to structures with amorphous or polycrystalline films for which the adhesion of films on the substrate surface depends on the magnitude of the macroscopic stress. With films tightly adherent to thin substrates such as Si wafers, a biaxial stress in the films of a sufficiently high intensity causes the substrates to bend elastically. A tensile stress (with a positive conventional sign) bends the film–substrate structure so that the film surface is concave, whereas a compressive stress (with a negative conventional sign) bends the structure so that the film surface is convex. The substrates can be in the form of either thin-cantilevered beams, or disks. The equations for stress calculation can be derived from the fundamentals of the theory of elasticity and elementary considerations of beam theory [30].

The magnitude of residual stresses (σ) is deduced from measurements of the radius of curvature (R_1) of the initial substrate and the radius of curvature (R_2) of the substrate covered with the film or radius of curvature of the film–substrate structure (beam) using the equation derived by Stoney [31]:

$$\sigma = \frac{1}{6}\left(\frac{E_s}{1-\nu_s}\right)\left(\frac{t_s^2}{t_f}\right)\left(\frac{1}{R_2}-\frac{1}{R_1}\right) \tag{25}$$

where E_s and ν_s are the Young's modulus and Poisson's ratio of the substrate, respectively; t_s is the substrate thickness and t_f the film thickness. Using totally flat substrates, the initial radius of curvature, R_1, tends to be infinity and the value of $1/R_1$ is negligible. The radius of curvature of film–substrate structures can be calculated from the deflection of the free end of the beam or the displacement of the center of the beam or a circular disk-type substrate [7]. The curvature radii of film–silicon structures in consequence of the existence of residual stresses in the films can be measured by various techniques. For DLC films deposited on silicon substrates, the curvature radii were determined by surface profilometer measurements and two-beam interferometer measurements [32].

The residual stresses in thin films deposited on single crystal substrates such as Si wafers cause a change of the interplanar distance of the (hkl) crystal planes. This change is revealed by the shift of the (hkl) diffraction peak in the x-ray diffraction (XRD) pattern to higher or lower diffraction angles depending on the nature of the residual stresses (compressive or tensile stresses). The magnitude of residual stresses (σ) is calculated from Hooke's law [33]:

$$\sigma = -\left(\frac{E_s}{1-\nu_s}\right)\left(\frac{d-d_0}{d_0}\right) \tag{26}$$

where d and d_0 are the interplanar distances of the crystal planes under stresses and in the absence of stresses, respectively. For DLC films deposited on (100)-oriented single crystal Si wafers by sputtering from a graphite target, the (311) diffraction peak of silicon appearing in the XRD pattern at a diffraction angle of 55° was selected as the "strain gauge" [34]. A peak shift towards higher diffraction angles was observed after deposition of DLC films. The shift ($\Delta 2\theta$) increases with increasing sputtering power and can be higher than 1°. The compressive residual stresses in DLC films deposited at a sputtering power of 3.9 W/cm^2 can be in the range 1–2 GPa depending on the substrate bias voltage.

The magnitude of residual stresses (σ) in DLC films can also be determined by visible Raman spectroscopy [35]. If a material is subjected to mechanical compression, the interatomic distances and bond lengths decrease, the interatomic force constants increase, and the atomic vibrational frequencies increase. As a result, the G-peak shift in Raman spectra of DLC films can be correlated with the magnitude of residual stresses as follows [36]:

$$\sigma = 2G_f\left(\frac{1+\nu_f}{1-\nu_f}\right)\left(\frac{\Delta\omega}{\omega_0}\right) \tag{27}$$

where G_f and ν_f are the shear modulus and Poisson's ratio of the film, respectively; $\Delta\omega$ is the shift in Raman wave number, and ω_0 the wave number of reference.

3.2 Determination of the Adhesion Performance

The principles of standard methods used to determine the adhesion performance of films to various substrates have been presented and discussed by Baglin [26,37]. In the "peel test," a narrow strip of the film is gripped and pulled slowly away from the substrate. The "peel strength" is defined as the force per unit strip width needed to detach the strip. This test simulates many practical situations. The test instrument must provide not only the delamination energy (U_d) but also the energy for plastic deformation of the strip ($U_{plastic}$), so that:

$$U_{test} = U_{plastic} - U_{stored} + U_d \tag{28}$$

where U_{test} and U_{stored} are the energy transferred to the film by the testing instrument, and the elastic energy stored in the film and available for release, respectively.

The adhesion of DLC films to polymer substrates was evaluated by peel tests using a cellophane adhesive tape carefully attached to the film at room temperature

[38–40]. An X-cut was made in the films with the angle between the cuts equal to 30° (X-cut method). After adhesion for 1–2 min, the tape was pulled off rapidly (not jerked) back upon itself at as close to an angle of 180° as possible. The peeling of the film at the X-cut area was then examined by optical microscopy. According to ASTM D 3359–97 [41], the film adhesion can be rated in six levels. The adhesion level is 5A if no peeling or removal occurs at all (absence of peeling); 4A if trace peeling or removal occurs along incisions (no peeling occurs at the intersect and little peeling observed at the X-cut); 3A if jagged removal along incisions occurs within 1.5 mm in either direction from the intersect of the X-cut; 2A if jagged removal along incisions occurs up to 3.0 mm in either direction from the intersect of the X-cut; 1A if most of the X-cut area peeled off with the adhesive tape; and 0A if the removal beyond the X-cut area occurs.

The scratch test is appropriate to evaluate the adhesion performance of films designed to resist damage by abrasion. For this test, a loaded diamond-tipped stylus is drawn across the film surface, with the load steadily increasing. At subcritical load, a smooth groove is formed in the film. Above a critical load, a ragged tear indicates detachment of the film from the substrate surface. The critical load (L_c) is defined as the load at which spalling or flaking of films occurs. This test depends critically on the elastic properties of the film and substrate, the nature of the stylus, the thickness of the films, etc., and does not work correctly for soft, thin films or strong adhesion. However, since fracture involves appreciable interface shear, the scratch performance has a parameter dependence different from that of the peel test. Therefore, these tests are of interest and can be combined for a complete evaluation of the adhesion performance of films.

The adhesion of DLC films was evaluated by means of a scratch-test method using various equipments commercially available [42–47]. During the scratch test, acoustic emissions and friction forces can be continuously monitored. The microstructure of the scratch track in the films is examined by optical microscopy. The scratch tests of DLC films were performed using diamond or sapphire tips with a radius of curvature in the range (50–200) μm. The normal load was increased up to 50 N at a loading rate of 100 N/min. The scratching speed may vary from 5 to 25 mm/min.

The adhesion strength may also be evaluated using the pin-pull test. A metal pin with a flat circular head (of surface area, A) is attached by epoxy or solder to the film under test. A load tester is used to find the threshold force (F) needed to pull off the pin (and attached film). The interface failure is assumed to have occurred simultaneously at all points of the area A, and the adhesion is quantified as F/A. Various difficulties arise in this test. One of them is the assumption of concurrent failure of the bond. In fact, the fracture nucleates usually at a single point near the edge of the pin (perhaps an irregularity of the meniscus of the epoxy). After that, the propagation of the fracture over the rest of the area occurs as fast and catastrophic. The threshold force measured is that required for crack initiation, whose dependence on the area A is indirect at best. As a result, the quantity F/A may not mean very much. The reproducibility of the test depends heavily on the perfection of the pin bound to the film.

The pull-off adhesion strength of DLC films was determined using the Sebastian II stud pull test [29]. The flat face of the solid cylinder (the stud or pin) of 3.6 mm in diameter was attached perpendicularly to the DLC-coated surface using Sebastian 5-epoxy glue. The sample and stud fixture were heated at 150°C for 1 h, and then cooled to room temperature. A gradually increasing downward force was applied to the stud while holding the sample stationary. The instrument recorded the highest value of force applied before failure.

Another measure of the adhesion strength of DLC films can be made by the Rockwell-C adhesion test [46,48]. This test was developed in Germany and is standardized in the VDI guidelines 3198 (1991) [49]. A standard Rockwell-C hardness tester is used to indent the films on the substrates. An optical microscope with a magnification of 100:1 is then used to evaluate the damage of films adjacent to the rim or boundary of the indentation pattern. The rate of adhesion strength is obtained by comparing the damage profiles of films with those given as references [49].

4 Effect of Deposition Parameters on the Magnitude of Residual Stresses

The intrinsic stress (σ_i) in DLC films is the major component of residual stresses (σ) given by Eq. (1). Indeed, DLC films are usually deposited on substrates at room temperature. Therefore, the contribution of thermal stress (σ_{th}) is nil. In addition, since the residual stresses developed in DLC films are found to be essentially compressive, the microstructure or morphology of films is sufficiently dense to keep any polar molecule (H_2O) adsorption off; thereby the development of extrinsic stress can be assumed to be negligible. The magnitude of residual (intrinsic) stresses in DLC films produced by various deposition techniques was investigated as a function of the major deposition or process parameters such as pressure in the deposition chamber, substrate bias voltage, and power density and composition of the gas precursor. However, very few attempts were made to explain the origin of stresses or the explanations remain at a very qualitative level.

The pressure effect on the residual stresses was investigated for DLC films deposited using a neutral beam saddle field source (Microvac 1200 DB, Ion tech Ltd.) from pure acetylene or C_2H_2-argon mixtures [29,50]. Compressive residual stresses were observed to vary in the range 0.8–1.6 GPa depending on the source current and pressure in the deposition chamber. For DLC films deposited at a source current of 0.6 A, the magnitude of residual stresses increased as the gas precursor pressure increased from 0.15 to 0.48 Pa. Using a source current of 1 A, the residual stresses reached a maximum value of 0.13 GPa at a deposition pressure of 0.28 Pa.

The magnitude of residual stresses was found to be dependent on the negative substrate bias voltage for DLC films deposited on quartz glass plates using a hybrid process, which combines plasma-based ion implantation and plasma-enhanced

chemical vapor deposition [51]. The compressive residual stresses in DLC films prepared from acetylene was approximately 0.4 GPa without the negative pulsed voltage required for ion implantation. The magnitude of residual stresses decreased considerably with increasing negative pulsed voltage during deposition, and was reduced to approximately 0.16 GPa at the negative pulsed voltage of −20 kV. The compressive residual stresses in DLC films produced from toluene were reduced to several MPa at a negative pulsed voltage in the range (5–7) kV. This reduction of residual stresses was attributed to the thermal spike effect caused by ion implantation. However, for a negative pulsed voltage exceeding −10 kV, the reduction of residual stresses was not observed because of the generation of the glow discharge by the negative pulsed voltage.

The power density used for deposition of DLC films is another process parameter, which can affect the magnitude of residual stresses. A capacitively coupled asymmetric plasma-enhanced CVD reactor was used to deposit DLC films from methane, acetylene, and benzene [52]. The pulsed power was applied to the cathode using a RF power supply, which can generate both continuous wave (cw) and amplitude modulated RF pulses. For the same amount of applied power density, the stress value can be reduced from 4.6 to 0.126 GPa by using pulsed discharges instead of continuous discharge. The results were analyzed qualitatively on the basis of the model proposed by Davis [11]. For DLC films deposited on biased substrates by unbalanced magnetron sputtering from a graphite target in Ar-H_2 discharges, the magnitude of residual stresses increased as the substrate bias voltage increased [34]. In addition, higher sputtering powers result in greater stress levels. The results were discussed qualitatively on the basis of the atomic peening mechanism [19].

Moreover, the magnitude of residual stresses was found to be dependent on the composition of the gas precursor [34,53]. In fact, the composition of the gas precursor affects not only the stress level but also the plasma and film composition. The effect of the gas precursor on the properties of DLC films was thoroughly studied for films deposited by electron beam excited plasma-enhanced CVD from CH_4 and C_6H_6 [53]. Film properties such as hardness, residual stresses, mass density, hydrogen content, and fraction of sp^3 bound carbon atoms were correlated to various deposition or process parameters, namely negative substrate bias voltage, distance from the electron beam, and pressure. The magnitude of compressive residual stresses was correlated to structural properties of DLC films. The stress intensity was found to be dependent on the mass density, total hydrogen atom content, and fraction of unbound hydrogen atom content to total hydrogen atom content. The compressive stresses in these a-C:H films decreased with increasing the sp^3 ratio in C–H bonds. This result is contrary to that for hydrogen-free a-C films where the magnitude of compressive residual stresses increased with increasing fraction of sp^3 bound carbon atoms [54,55]. For a-C:H films, an increase in the sp^3 ratio of C–H bonds was accompanied along with an increase in hydrogen atoms bound to carbon atoms. As a result, the network in the films is segmented by the termination with hydrogen atoms so that the compressive residual stresses can release. Furthermore, hydrogen-free a-C film exhibit a more rigid structure by forming a

larger number of C–C single bonds than C=C double bonds. In fact, major findings were derived from the correlations between compressive residual stresses and structural properties of a-C:H films. For DLC films deposited from methane, the fraction of unbound hydrogen atom content to total hydrogen atom content was the most influential factor for the compressive residual stresses. The mass density and total hydrogen content had little effect on the stress level. Moreover, DLC films containing graphite crystallites with the largest size, which involves a decrease in the sp^3 ratio in C–H bonds, exhibited higher compressive residual stresses. It was proposed that the unbound hydrogen atoms are trapped into the disordered microstructure of graphite crystallites. The insertion of unbound hydrogen atoms can contribute to an increase in volume and the strains resulting from the volume expansion induce compressive residual stresses. For DLC films produced from benzene as well as for films deposited from methane, the insertion of unbound hydrogen atoms is suggested to give a contribution to the compressive residual stresses. In addition, it was found that the compressive residual stress level increased with increasing mass density of films, and decreasing the contents of total hydrogen atoms and bound hydrogen atoms. This increase in stress level was accompanied along with a decrease in the size of graphite crystallites and sp^3 ratio in C–H bonds. From these results, it was assumed that the compressive residual stress increment arises from the proportion of cross-linking between graphite crystallites embedded into the three-dimensional network. Moreover, it was considered that the change of sp^2 sites into sp^3 C–C bonds by the cross-linking induces the volume expansion in DLC films in accordance with an increase in bond length, which results in an increase in the magnitude of compressive residual stresses.

Furthermore, it is well recognized that the magnitude of compressive intrinsic (residual) stresses developed in films produced from energetic particles such as DLC films depends on the impact energy per atom (Fig. 1). In fact, the stress level depends more specifically on the normalized momentum, P_n [6]:

$$P_n = \frac{\phi_p}{\phi_c}\sqrt{2 M_p \gamma E_p} \tag{29}$$

where ϕ_p and ϕ_c are the fluxes of incident energetic particles and condensing atoms on the film surface, respectively; M_p and E_p are the mass and kinetic energy of energetic particles, respectively. The term γ is the energy transfer coefficient expressed as follows:

$$\gamma = \frac{4 M_p M_t}{\left(M_p + M_t\right)^2} \tag{30}$$

where M_t is the atomic mass of target atoms, i.e., carbon atoms for DLC films. This expression of γ is derived from equations corresponding to the kinetic energy and momentum conservation laws for elastic collisions assuming that an elastic

head-on collision occurs between the incident energetic species and the film atoms, that is, the direction of the energetic species velocity after collision is reverse to the incident direction and the knocked atom moves after collision in the incident direction. For DLC films, the normalized momentum (Eq. (29)), which is the relevant physical factor is related to: (i) the kinetic energy and mass of carbon species condensed on the substrate surface and other species striking the film surface during deposition; (ii) the flux of carbon species condensed on the substrate, which corresponds to the deposition rate of DLC films; and (iii) the flux of energetic particles (projectiles) impinging on the surface, reflected at the film surface, and backscattered to the gas phase. These physical parameters, namely kinetic energy and flux of various species affect the microstructure and morphology of films as well as the intrinsic stress level and other physical characteristics of films such as packing density and microhardness. The values of physical factors affecting the magnitude of intrinsic stress (σ_i) depend on various process parameters, in particular, pressure (P) in the deposition chamber, substrate temperature (T_s), and substrate bias voltage (V_B) [6].

Residual (intrinsic) stresses were thoroughly investigated in DLC films sputter-deposited from a graphite target in argon magnetron discharges. Experiments were designed to estimate the flux and kinetic energy of particles impinging on the surface of a-C films deposited on (100)-oriented single crystal Si substrates of (6 × 1) cm^2 at ambient temperature. In the first series of experiments, DLC films have been deposited by conventional magnetron sputtering on grounded substrates. The compressive residual stresses in these DLC films decreased with increasing argon pressure whereas a reverse trend was observed for the mass density of films [56]. The surface of films deposited by magnetron sputtering can be exposed to four types of energetic particles, namely (i) neutral target atoms sputtered from the target surface and condensed on the substrate, (ii) neutral sputtering gas atoms previously implanted in the target as sputtering ions which are ejected from the target surface together with neutral target atoms, (iii) ions of the sputtering gas coming from the discharge, and (iv) neutralized sputtering ions backscattered from the target surface by elastic collisions. The flux of the second type of energetic particles is negligible with respect to the flux of carbon atoms ejected from the target. The reflection coefficients (R_0 and γ_0) corresponding to the flux and energy of sputtering ions neutralized and backscattered from the target surface (fourth type of energetic particles) are dependent on the atomic mass ratio, M_C/M_{Ar} [57,58]. For the carbon–argon system, the atomic mass ratio is equal to 0.3; hence, the reflection coefficients R_0 and γ_0 are less than 10^{-3} and 0.1, respectively [6]. Therefore, for this system, the contribution of backscattered neutral argon atoms to the energy deposited on the surface of growing films is negligible with respect to the contribution of neutral carbon atoms and argon ions originating from the plasma.

The argon pressure effect on the compressive intrinsic stress developed in sputter-deposited a-C films was analyzed using the forward sputtering model [9,10]. The compressive intrinsic stress in a-C films is given by [56]:

$$\sigma_i = 4.79\left(\frac{E_f}{1-\nu_f}\right)\left(\frac{K}{N}\right)\left[2.79\left(E_{Ar}\right)^{1/2}\phi_{Ar} + 2.64\left(E_C\right)^{1/2}\phi_C\right] \quad (31)$$

where E_{Ar} and E_C are the argon ion and carbon atom energies on the surface of a-C films, respectively; ϕ_{Ar} and ϕ_C are the argon ion and carbon atom fluxes on the surface of growing films, respectively. K is a proportionality factor and N the atomic number density in the deposited material. The dependence of the compressive intrinsic stress on the energetics of the deposition process is in good agreement with the prediction of the model proposed by Windischmann (Fig. 4).

The contribution of argon ions to the energy deposited on the film surface is relatively small compared to that of neutral carbon atoms, in particular, at low argon pressures when the thermalization phenomena of sputtered carbon atoms are not very efficient. In other words, in Eq. (31), at low argon pressures, the term 2.79 $(E_{Ar})^{1/2}\,\phi_{Ar}$ is negligible with respect to the term 2.64 $(E_C)^{1/2}\,\phi_C$. These thermalization phenomena involving collisions between sputtered carbon atoms and sputtering gas atoms play a major role in the deposition process. The number of collisions of carbon atoms in the gas phase and the thermalization of sputtered carbon atoms depend on the product between the target–substrate distance (d) and the argon pressure (P). This product is a relevant factor affecting the development of the intrinsic stress and governing their magnitude in sputter-deposited films. The compressive intrinsic stress was found to remain at a constant value of −0.75 GPa in a-C films produced under various experimental conditions with the same value of the product ($d \times P$) [56].

In another series of experiments, DLC films have been deposited by conventional and unbalanced magnetron sputtering on biased substrates. The characteristics of the

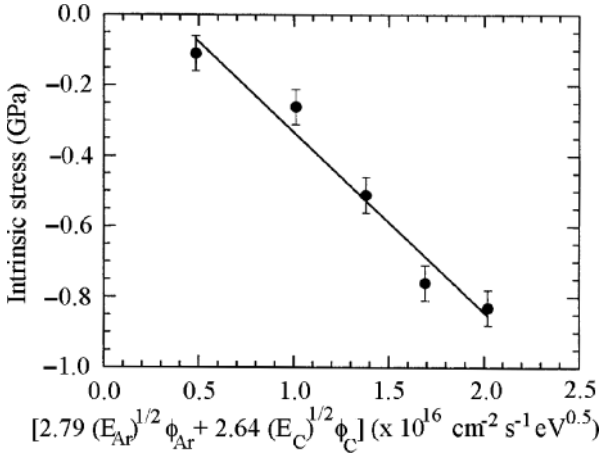

Fig. 4 Dependence of the intrinsic stress in a-C films on the energetics of the deposition process; the solid line was deduced from a least squares fit to the experimental data [56]

deposition process such as substrate temperature, ion flux (ϕ_{Ar}), and carbon atom flux (ϕ_C), on the film surface were determined as functions of the substrate bias voltage [56,59,60]. The compressive intrinsic stress in DLC films sputter-deposited by conventional magnetron mode at an argon pressure of 0.25 Pa and a sputtering power of 0.5 kW increased progressively up to a maximum value of −2.8 GPa with increasing bias voltage [61]. This maximum value is about three times higher than that obtained from films sputter-deposited on grounded substrates. The compressive intrinsic stress in DLC films produced by unbalanced magnetron sputtering also increased with increasing substrate bias voltage [61]. The films produced with a negative bias voltage higher than 50 V did not adhere to Si substrates since the compressive intrinsic stress in these films was probably higher than 2.5 GPa. The value of the compressive intrinsic stress in a-C films produced on grounded substrates using the unbalanced magnetron mode was of the same order of magnitude as that for a-C films deposited by conventional magnetron sputtering, i.e., between −0.8 and −1 GPa. The compressive intrinsic stress in a-C films produced by unbalanced magnetron mode increased more rapidly with increasing bias voltage than the compressive intrinsic stress in films deposited by conventional magnetron sputtering. The impact energy available on the film surface originates essentially from the kinetic energy of positive ions created in the argon discharge and accelerated by the negative substrate bias voltage. The maximum value of the average kinetic energy of neutral carbon atoms condensed on the substrate is about 10 eV, whereas the kinetic energy of positive ions is in the range 10–300 eV. The energy deposited on the growing films and resulting from the positive ion bombardment of the surface appears to be the relevant factor affecting the magnitude of the compressive intrinsic stress in a-C films deposited by conventional and unbalanced magnetron sputtering. Since the flux ratio (ϕ_{Ar}/ϕ_C) is also dependent on the negative substrate bias voltage or kinetic energy of positive ions impinging on the film surface, this flux ratio can be considered as an additional factor affecting the value of the intrinsic stress in a-C films produced under the experimental conditions investigated.

These results have been analyzed and discussed on the basis of models proposed by Windischmann and Davis. According to Windischmann's model, the compressive intrinsic stress is predicted to be proportional to the product of the particle flux (ϕ_p) and the square root of the particle energy (E_p, Eq.(4)), that is, to the product of the flux (ϕ_{Ar}) and square root of the kinetic energy (E_{Ar}) of argon ions striking the surface of growing a-C films. For a-C films sputter-deposited on Si substrates biased to a negative voltage in the range 20–300 V under an argon pressure of 0.25 Pa with a sputtering power of 0.5 kW, the intrinsic stress versus product $\phi_{Ar}\,(E_{Ar})^{1/2}$ is plotted in Fig. 5. The experimental values of the compressive intrinsic stress are in good agreement with the prediction of Windischmann's model as the product $\phi_{Ar}\,(E_{Ar})^{1/2}$ is less than 5×10^{15} ions $cm^{-2}\ s^{-1}\ eV^{1/2}$. Beyond this value, a large deviation between experimental and predicted results can be observed. As a result, additional phenomena resulting in stress relaxation must be considered for interpreting and modeling the effect of the ion flux and energy on the intrinsic stress in a-C films deposited by sputtering under intense energetic particle bombardment.

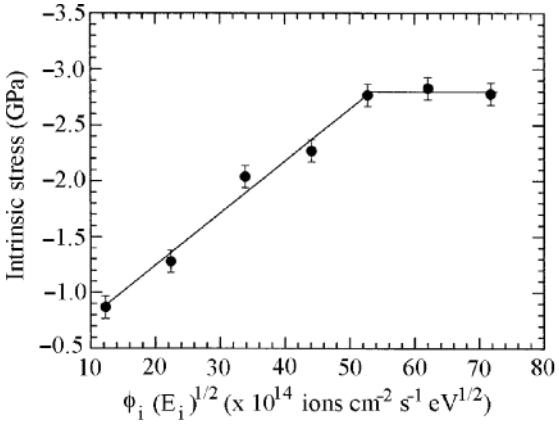

Fig. 5 Effect of the flux and energy of positive ions on the intrinsic stress in a-C films deposited with the conventional magnetron mode at a sputtering power of 0.5 kW under an argon pressure of 0.25 Pa; the substrate bias voltage for sputter-deposition of these films was between −20 and −300 V [61]

On the basis of the model proposed by Davis [11], the compressive intrinsic stress in films for which the film surface senses energetic particle bombardment during deposition can be calculated from Eq. (7). The flux ratio ϕ_C/ϕ_{Ar} was determined as a function of the kinetic energy (E_{Ar}) of Ar^+ ions striking the surface of negatively biased substrates for sputter-deposition of a-C films by conventional and unbalanced magnetron modes [61]. The magnitude of the compressive intrinsic stress in a-C films predicted by Davis's model is related to the kinetic energy of argon ions by the following equations:

$$\sigma_i = k\left[\frac{\left(E_{Ar}\right)^{1/2}}{\left(\frac{22.75}{2.4+0.1\left(E_{Ar}\right)^{1/2}}\right)+k_a\left(E_{Ar}\right)^{5/3}}\right] \tag{32}$$

$$\sigma_i = k\left[\frac{\left(E_{Ar}\right)^{1/2}}{\left(\frac{22.75}{26.6+5.72\left(E_{Ar}\right)^{1/2}}\right)+k_a\left(E_{Ar}\right)^{5/3}}\right] \tag{33}$$

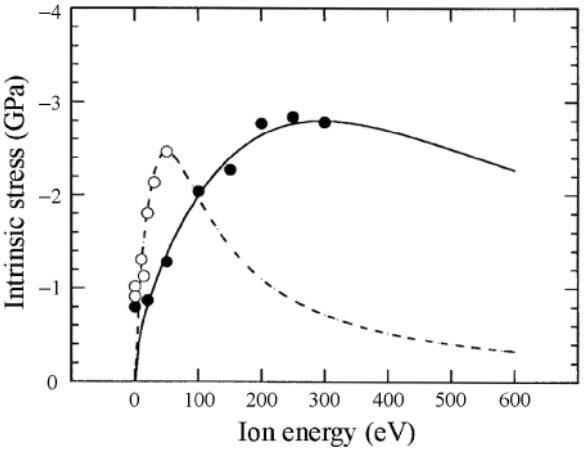

Fig. 6 Effect of the positive ion energy on the intrinsic stress in a-C films deposited at a sputtering power of 0.5 kW under an argon pressure of 0.25 Pa using: (●) the conventional magnetron sputtering mode, and (○) the unbalanced magnetron sputtering; the curves in solid and dashed lines represent the intrinsic stress values predicted by the model proposed by Davis [61]

Eqs (32) and (33) are valid for a-C films sputter-deposited by conventional and unbalanced magnetron modes, respectively.

Furthermore, these equations contain two undetermined parameters (κ and k_a), which were used as fitting parameters for a least-squares fit to experimental results. The theoretical curves and the experimental values of the compressive intrinsic stress in the a-C films sputter-deposited by conventional and unbalanced magnetron modes are represented in Fig. 6. The experimental results and predicted values of the compressive intrinsic stress are in very good agreement for a-C films sputter-deposited by conventional magnetron mode. For a-C films produced by unbalanced magnetron mode, the theoretical curve also fits the experimental values; however, these values correspond to relatively low ion energies since the films produced under more energetic ion fluxes were found to be not adherent to Si substrates.

5 Reduction of Residual Stresses

Various approaches have been adopted to reduce the residual stresses in DLC films, and thereby to improve the film adhesion. The effect of the incorporation of metallic or nonmetallic elements in DLC films on the residual stress level was thoroughly investigated.

Copper particles of 15–30 nm in size were embedded in DLC films prepared by a hybrid deposition technique combining plasma-enhanced CVD from

argon–acetylene (1:1) mixtures and magnetron sputtering of a copper target [62]. The films have been deposited on silicon and stainless steel substrates with an RF self-bias voltage of −450 eV. The copper content in the films was varied from 11 to 23 at. % as the sputtering power was increased from 280 to 320 W. The magnitude of compressive residual stresses in pure DLC films was found to be 2.9 GPa. The stress level was reduced to 0.7 and 1.2 GPa in films containing 11 and 23 at. % of copper, respectively. Depending on the composition, these metal/DLC films (or carbon-based nanostructured composite films) exhibit properties different from those of pure DLC films and can be considered as belonging to another class of films [63].

The residual stresses in nitrogen-doped DLC films deposited by RF plasma decomposition of mixtures of a hydrocarbon vapor and N_2 were reduced by nitrogen addition [64]. Recently, DLC films were grown by aspirating either acetylene or a mixture of acetylene and nitrogen into a saddle-field fast atom beam (FAB) source [65]. The variation of residual stress level per unit hardness for DLC films was investigated as a function of the power applied to the FAB source. The hardness and residual stresses increased with increasing applied power. A decrease in residual stress intensity was observed for DLC films produced from C_2H_2–N_2 mixtures while the film hardness was not significantly affected. A stress relief behavior was found for nitrogen-doped DLC films, which can exhibit a hardness of approximately 20 GPa. However, the nitrogen content in these "nitrogen-doped" DLC films was not reported. The reduction in average coordination number by nitrogen incorporation in the DLC films would be responsible for the stress reduction [66].

For films synthesized by RF plasma-enhanced CVD from trimethylsilane–methane (1:10) mixtures, the introduction of silicon into the DLC matrix can reduce the residual stresses to approximately 0.8 GPa, and the formation of a multilayered structure in addition to silicon can reduce the stresses to 0.68 GPa [67]. The silicon content in the films was in the range 16–23 at. %. The reduction of the stress level allowed the formation of free-standing thick (30 μm) DLC films and the fabrication of DLC rods (30 μm in length and 5 μm in diameter) by micromachining. The silicon incorporation to DLC films was also found to largely decrease the compressive residual stresses while the hardness was almost unchanged [68,69]. For Si-containing DLC films prepared by RF plasma-enhanced CVD from CH_4–SiH_4 mixtures, the magnitude of compressive residual stresses was found to be 30% lower than that of pure DLC films [70]. The stress reduction can reach 50% of Si containing DLC films deposited in a hybrid PVD-CVD equipment [71].

Very promising results have been reported for Si-containing DLC films deposited from CH_4–SiH_4 mixtures on Si substrates placed on the cathode of a conventional RF parallel-plate glow discharge reactor [72]. The residual stress level, Vickers hardness, and composition of films were investigated as functions of the self-bias voltage varying from −50 to −1,100 V. The compressive residual stress level was dependent on the cathode self-bias voltage (Fig. 7). In the low self-bias voltage range, the magnitude of residual stresses increased with increasing bias voltage, reached a maximum value, and then decreased monotonically for high values of the self-bias voltage. The stress level was reduced by

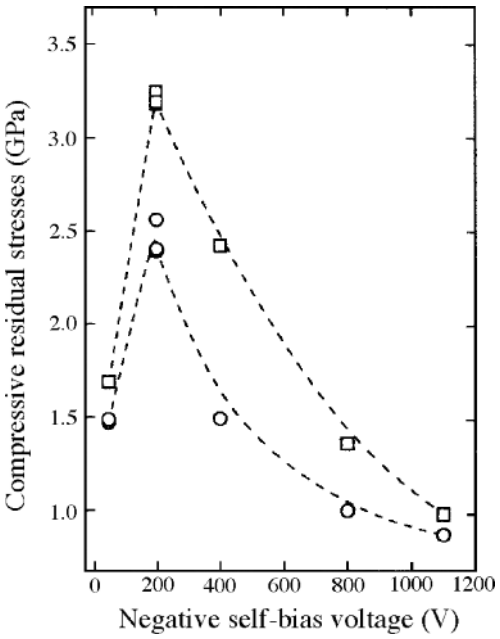

Fig. 7 Dependence of residual stresses on the self-bias voltage in Si containing DLC films deposited from SiH_4–CH_4 mixtures with a silane concentration of: (□) 0.2 vol. % and (○) 2.0 vol. % [72]

a factor of 3 for films deposited with 0.2 vol. % of silane as the self-bias voltage was varied from −200 to −1,100 V.

Furthermore, the increase in silane concentration in the reactor resulted in a reduction of the stress level in the films down to 1.0 GPa. A monotonic increase in film hardness was observed as the self-bias voltage was varied from −50 to −1,100 V (Fig. 8). Even for high values of the self-bias voltage, no reduction in the hardness values was noted, in contrast to what is generally observed for pure DLC (a-C:H) films. The hardness value of films deposited with 2.0 vol. % of silane was systematically higher than that of films prepared with lower silane concentrations in the gas phase. The carbon, hydrogen, and silicon contents in Si-containing DLC films deposited with 2.0 vol. % of silane in the discharge were determined by Rutherford backscattering spectroscopy (RBS) and energy recoil detection analyses (ERDA). The carbon content increased with increasing self-bias voltage, whereas the Si and H contents decreased (Fig. 9). An equivalent behavior was obtained for the composition of films deposited with 0.2 vol. % of silane in the gas phase, although in this case the silicon content in the films was approximately one order of magnitude smaller. These results demonstrated that Si/DLC composite films containing less than 5 at. % of silicon with high hardness (>20 GPa), low stress level (approximately 0.5 GPa), and high deposition rate (>40 nm/min) can be deposited by plasma-enhanced CVD.

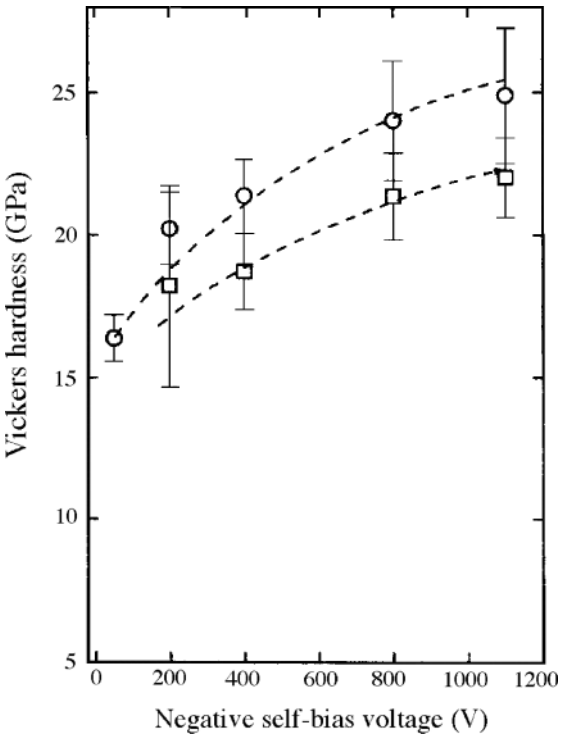

Fig. 8 Dependence of the Vickers hardness on the self-bias voltage in Si-containing DLC films deposited from SiH_4–CH_4 mixtures with a silane concentration of: (□) 0.2 vol. % and (○) 2.0 vol. % [72]

A reduction of residual stresses can result from energetic ion bombardment of DLC films. The residual stress level in DLC films deposited on Si substrates using an RF inductive plasma of Ar–C_2H_2 mixtures in a plasma immersion ion implantation chamber was monitored in situ during Xe^+, Ar^+, Ne^+, and C^+ energetic ion irradiation [73]. The magnitude of compressive residual stresses in DLC films was 9 GPa before the irradiation. A rapid decrease in stress level occurred as the irradiation dose was increased. The stress level saturated at a slightly tensile value of approximately 2.2 GPa for an irradiation dose of 5×10^{15} cm^{-2} using Xe^+, Ar^+, Ne^+, and C^+ ions of 230 keV, 100 keV, 56 keV, and 40 keV in kinetic energy, respectively. The stress change was modeled using bonding transformation between sp^3- and sp^2 carbon. For DLC films synthesized by a hybrid processing system of plasma-based ion implantation and deposition, the compressive residual stress level was found to be dependent on the pulse voltage [74]. The compressive residual stresses in DLC films deposited with no negative pulse voltage were approximately 1.55 GPa. The magnitude of residual stresses decreased considerably with increasing negative voltage during deposition and was reduced to approximately 0.2 GPa at a high

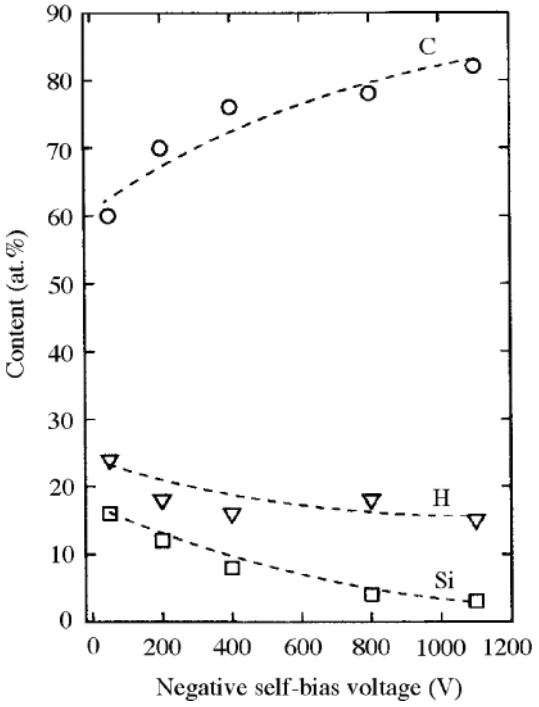

Fig. 9 Dependence of the carbon (○), hydrogen (▽), and silicon (□) content on the self-bias voltage in Si-containing DLC films deposited from SiH_4–CH_4 mixtures with a silane concentration of 2.0 vol. % [72]

voltage of −20 kV. This reduction in residual stresses may result from the local heating (thermal spike) of the substrate by deposition of ion beam energy [11,54].

Postdeposition annealing treatments of DLC films can also lead to a reduction of the magnitude of compressive residual (intrinsic) stresses. For DLC films produced by pulsed laser deposition, thermal annealing treatments were carried out to reduce the compressive residual stresses [75]. The magnitude of stresses was reduced from 3.3 to 1.5 GPa after annealing of DLC films at 300°C for 1 h. Several reports have been published in the literature concerning the growth of thick ta-C films through ta-C/a-C multilayered structures in order to reduce the residual stresses, and with the incorporation of thin Ti layers at the DLC–substrate interface to improve the film adhesion [76,77]. It has been possible to grow thick and hard ta-C films through total stress relaxation via postdeposition annealing at 600°C [78]. However, the introduction of multilayered structures creates additional complications for the deposition process, and postdeposition annealing discounts the ability to deposit the ta-C films on temperature-sensitive substrates.

6 Deposition of DLC Films with Improved Adhesion

Relatively thick DLC films are required for various applications, in particular, to improve the lifetime of films for tribological applications. According to Eq. (23), the critical thickness of stressed films for delamination can be increased by reducing the magnitude of residual stresses (σ) and/or by increasing the work of adhesion (γ_d). The adhesion of DLC films with a certain level of residual stresses can be improved using various approaches. The common practice is to use a glue layer interposed between the substrate surface and the DLC film. Intermediate metal or compound layers (Ti, Zr, W, Nb, Si, Cr, or WC) have demonstrated their potential in improving DLC film adhesion [79–92].

To improve the adhesion of DLC films on steel substrates, a Cr-substrate intermixing layer was obtained by ion bombardment of the substrate surface before depositing a Cr intermediate layer by magnetron sputtering [48]. Using W or WC interlayers on steel substrates, the adhesion of DLC films was found to be strongly dependent on the thickness of sputter-deposited W layers and CH_4 fraction in the gas phase during sputter-deposition of WC layers [43]. As the thickness of the W intermediate layer increased, the structure changed from small equiaxial grains to columnar ones, which became coarser with increasing thickness of the W layer. This microstructural change with a thicker W layer seems to result in the better adhesion of the DLC films. Furthermore, Ti interlayers, Ti/TiN multilayers, and Ti/TiN/TiCN transition layers were also investigated and deposited sequentially to create an interface between DLC films and steel substrates [45]. Ti interlayers alone fail to significantly improve DLC film adhesion. The Ti/TiN/TiCN transition layer was observed to lead to significant improvements of the adhesion of DLC films.

Gradient a-SiC_x intermediate layers have been deposited by RF plasma-enhanced CVD on glass substrates prior to deposition of DLC films [44]. The critical load determined by scratch tests was improved significantly. The improved adhesion may result from the fact that SiC is chemically more compatible to oxides due to the stability of SiO_x and their mixture with SiC materials. The atoms in two very small mixed regions between DLC films and carbon-rich a-SiC_x interlayers, and between silicon-rich a-SiC_x interlayers and glass substrates may form strong covalent bond network.

For surface acoustic wave (SAW) devices, DLC films have been deposited on top of $LiTaO_3$ substrates [93]. Using DLC films, the substrate surface can be stiffened so that the SAW velocity can be increased due to the high elastic constant and low mass density of DLC films. Introducing SiO_2 interlayers enhanced the adhesion strength between DLC films and $LiTaO_3$ substrates. As the thickness of SiO_2 interlayer increased, the critical load (L_c) and adhesion strength increased, i.e., L_c can reach a maximum value of 19.5 N using SiO_2 layers of 30 nm in thickness.

A number of substrate surface treatments performed prior to deposition of DLC films were also attempted to improve the film adhesion. The major role of these surface treatments is to activate the substrate surfaces. To improve the adhesion of DLC films on steel substrates, the activation process consisted of preliminary ion

nitriding followed by ion etching of the surface [46]. Very fine protuberances formed by the activation process provided large adhesion strength to the substrates. No intermediate layer was necessary. With Ti alloys, a simple in situ modification of the growth surface by 1 keV C^+ ion bombardment prior to the low energy (100 eV) deposition of ta-C films was demonstrated to improve the film adhesion considerably [94]. The initial high-energy ion bombardment creates a very thin interface layer, which allows the growth of ta-C films up to 6 μm in thickness. The compressive residual stresses were found to remain high (approximately 10 GPa) indicating that the very thin interface is able to anchor the very large compressive stresses.

The adhesion of DLC films on orthopedic biomaterials (stainless steel, CoCr, and Ti alloys) has been shown to be dependent on the length of the etching time of substrate surfaces by an argon atom beam [95]. It has been shown that there is an optimum etching time to maximize film adhesion regardless of the type of substrate metal alloy; hence, it is not a function of the details of the surface oxide layer. This variation of adhesion correlates with the film structure in terms of the sp^3 content. The optimum time for improved adhesion was related to the temperature of the substrate during etching and there appears to be a window centered at approximately 75°C to achieve best adhesion. The surface of Mg substrates has been pretreated mechanically by peening to ensure adequate adhesion of DLC films [96]. The peening treatments were carried out using air pressure type apparatus with SiC or graphite grits of approximately 20 μm in diameter as peening materials. To improve the DLC film adhesion, the peening treatment should perform three functions: (i) to clean the substrate surface, (ii) to increase the surface roughness, and (iii) to embed the peening material. The particles of SiC effective on all three points were able to improve the film adhesion. The particles of carbon were embedded in the substrate; however, these particles were not effective in improving film adhesion.

Obtaining a strong adhesion of DLC films on nonmetallic substrate surfaces is also very challenging. A combination of glue layer and surface treatment was attempted to improve DLC film adhesion on glass substrates [42]. First, a mixing layer was formed by ion beam-assisted deposition of carbon on glass substrates, which were attached to a sample holder cooled with water. The electron beam evaporation of a graphite source and the irradiation of the substrate surface by argon ion beam at 30 keV were carried out simultaneously in a vacuum chamber. In the second step, after forming the mixing layer, DLC films have been deposited on the layer by electron beam evaporation of the graphite source. The adhesion of DLC films on polycarbonate (PC) and polymethylmethacrylate (PMMA) substrates was investigated in detail [39]. An inductively coupled plasma (ICP) ion plating method was used to deposit hard DLC films from hexamethyldisiloxane (HMDSO) and oxygen reactants. Oxygen plasma was the most effective pretreatment method for improving the adhesion of DLC films on the polymer substrates by removing the contaminants and forming the polar functional groups on the surfaces. The adhesion of DLC films on PMMA substrates was always much worse than that on PC substrates. To improve the DLC film adhesion on PMMA substrates,

interfacial layers have been deposited by remote plasma polymerization to avoid the destruction of polyfunctional groups in the monomer precursors. Interfacial layers deposited using HMDSO/C_2H_5OH mixtures, methylmethacrylate and propylene oxide monomers were successful to improve the adhesion of DLC films on the PMMA substrates from 1A (with no interfacial layer) to 4A–5A, as measured by the X-cut method. The adhesion abilities of the interface layers were found to be strongly dependent on the gas phase reactions during deposition. Using polyethylene (PE) substrates, the adhesion of DLC films was shown to be strongly dependent on the substrate temperature [38]. The best result was achieved with a substrate temperature close to the PE melting point; the optimum temperature was in the range 80–100°C.

7 Conclusion

The residual stresses in DLC films produced at room temperature from energetic particles or using energetic deposition processes are essentially compressive. The major contribution in the magnitude of residual stresses corresponds to that of the intrinsic stress, which develops during the growth of films. The origin of the compressive intrinsic stress can be explained on the basis of models proposed by Windischmann and Davis. To assess the applicability of these models, numerous data regarding the plasma discharge, the flux, and kinetic energy of particles impinging on the film surface must be collected using more or less complex experimental techniques. The magnitude of residual stresses and the adhesion strength of DLC films deposited on various substrates can be evaluated independently using a variety of techniques. These quantities are intimately connected. The reduction of residual stress level is often required for improvement of the film adhesion.

Various approaches can be adopted to reduce the magnitude of residual stresses and/or to enhance the adhesion performance of films. The durability of DLC films, in particular, for tribological applications requires strong adhesion and high toughness. DLC films exhibiting extremely high hardness can be obtained without too much difficulty. Nevertheless, the production of relatively thick DLC films combining high hardness, strong adhesion, and high toughness is still a real challenge.

References

1. A. C. Ferrari, J. Robertson, Phys. Rev. B 61 (2000) 14095.
2. A. C. Ferrari, J. Robertson, Phys. Rev. B 64 (2001) 075414–075411.
3. M. Chhowalla, Y. Yin, G. A. J. Amaratunga, D. R. McKenzie, T. Frauenheim, Diam. Relat. Mater. 6 (1997) 207.
4. A. A. Voevodin, S. J. P. Laube, S. D. Walck, J. S. Solomon, M. S. Donley, J. S. Zabinski, J. Appl. Phys. 78 (1995) 4123.
5. A. A. Voevodin, M. S. Donley, Surf. Coat. Technol. 82 (1996) 199.

6. Y. Pauleau, Deposition and processing of thin films, in H. S. Nalwa (ed.) Handbook of Thin Film Materials, Vol. 1, Chap. 9, Academic Press, San Diego, CA, 2002, p. 455.
7. Y. Pauleau, Materials Surface Processing by Directed Energy Techniques, Elsevier, New York, 2006.
8. E. S. Machlin, Materials Science in Microelectronics, The Relationship between Thin Film Processing and Structure, Chap.VI, Giro Press, Croton-on-Hudson, NY, 1995, p. 157.
9. H. Windischmann, Crit. Rev. Solid State Mater. Sci. 17 (1992) 547.
10. H. Windischmann, J. Appl. Phys. 62 (1987) 1800.
11. C. A. Davis, Thin Solid Films 226 (1993) 30.
12. P. Sigmund, Sputtering by particle bombardment I, in R. Behrisch (ed.) Topics in Applied Physics, Vol. 47, Chap. 2, Springer, Berlin, 1981.
13. E. A. Kenick, T.E. Mitechell, Phil. Mag. 32 (1975) 815.
14. M. J. Makin, S. N. Buckley, G. P. Walters, J. Nucl. Mater. 68 (1977) 161.
15. J. E. Yehoda, B. Yang, K. Vedam, R. Messier, J. Vac. Sci. Technol. A, 6 (1988) 1631.
16. B. Window, K.-H. Müller, Thin Solid Films 171 (1989) 183.
17. K.-H. Müller, J. Vac. Sci. Technol. A, 40 (1986) 209.
18. E. S. Machlin, Materials Science in Microelectronics: The Relationship between Thin Film Processing and Structure, Chap. VI, Giro Press, Croton-on-Hudson, NY, 1995, p. 179.
19. F. M. D'Heurle, Metall. Trans. 1 (1970) 725.
20. E. H. Hirsch, J. Phys. D: Appl. Phys. 13 (1980) 2081.
21. G. Gille, in Current topics in materials science, in E. Kaldis (ed.), Mechanical Properties of Brittle Materials, Vol. 12, North-Holland, Amsterdam, The Netherlands, 1985, pp. 317–364.
22. M. S. Hu, A.G. Evans, Acta Metall. 37 (1989) 917.
23. M. D. Thouless, Thin Solid Films 181 (1989) 397.
24. J. J. Prescott, Applied Elasticity, Dover, New York, 1961, p.187.
25. E. Klokholm, IBM J. Res. Develop. 31 (1987) 585.
26. J. E. E. Baglin, Interface structure, adhesion and ion beam processing, in Y. Pauleau (ed.) Materials and Processes for Surface and Interface Engineering, Vol. 290, NATO-ASI Series, Series E: Applied Sciences, Kluwer Academic, Dordrecht, The Netherlands, 1995, p. 111.
27. A. Kelly, Strong Solids, Clarendon, Oxford, 1976.
28. G. I. Barenblatt, Adv. Appl. Mech. 7 (1962) 55.
29. M. M. Morshed, B. P. McNamara, D. C. Cameron, M. S. J. Hashmi, J. Mater. Proc. Technol. 143–144 (2003) 922.
30. A. Brenner, S. Senderoff, J. Res. Natl. Bur. Stand. 42 (1949) 105.
31. G. G. Stoney, Proc. Roy. Soc. London Ser. A 82 (1909) 172.
32. I. Ohlidal, M. Ohlidal, D. Franta, V. Cudek, V. Bursikova, P. Klapetek, K. Palenikova, Diam. Relat. Mater. 14 (2005) 1835.
33. B. D. Cullity, in Elements of X-ray Diffraction, M. Cohen, (ed.), Addison-Wesley, Reading, MA, 1978, p. 454.
34. S. Zhang, H. Xie, X. Zeng, P. Hing, Surf. Coat. Technol. 122 (1999) 219.
35. R. J. Narayan, Appl. Surf. Sci. 245 (2005) 420.
36. I. De Wolf, J. Raman Spectrosc. 30 (1999) 877.
37. J. E. E. Baglin, in Fundamentals of Adhesion, L.-H. Lee, (ed.), Chap. 13, Plenum Publishing, New York, 1990, p. 363.
38. I. Sh. Trakhtenberg, O. M. Bakunin, I. N. Korneyev, S. A. Plotnikov, A.P. Rubshtein, K. Uemura, Diam. Relat. Mater. 9 (2000) 711.
39. Y.-B. Guo, F. C.-N. Hong, Diam. Relat. Mater. 12 (2003) 946.
40. E. Alakoski, M. Kiuru, V.-M. Tiainen, Diam. Relat. Mater. 15 (2006) 34.
41. Standard Methods for Measuring Adhesion by Tape Test, ASTM Designation D 3359–83 668.
42. Y. Funada, K. Awazu, H. Yasui, T. Sugita, Surf. Coat. Technol. 128–129 (2000) 308.
43. K.-R. Lee, K. Y. Eun, I. Kim, J. Kim, Thin Solid Films 377–378 (2000) 261.
44. B. H. Lung, M. J. Chiang, M. H. Hon, Mater. Chem. Phys. 72 (2001) 163.
45. C.-L. Chang, D.-Y. Wang, Diam. Relat. Mater. 10 (2001) 1528.

46. H. Mori, H. Tachikawa, Surf. Coat. Technol. 149 (2002) 225.
47. T. Mikami, H. Nakazawa, M. Kudo, M. Mashita, Thin Solid Films 488 (2005) 87.
48. C.-C. Chen, F. C.-N. Hong, Appl. Surf. Sci. 243 (2005) 296.
49. W. Heinke, A. Leyland, A. Matthews, G. Berg, C. Friedrich, E. Broszeit, Thin Solid Films 270 (1995) 431.
50. M. M. Morshed, D. C. Cameron, B. P. McNamara, M. S. J. Hashmi, Surf. Coat. Technol. 169–170 (2003) 254.
51. Y. Oka, M. Kirinuki, Y. Nishimura, K. Azuma, E. Fujiwara, M. Yatsuzuka, Surf. Coat. Teechnol. 186 (2004) 141.
52. S. Kumar, D. Sarangi, P. N. Dixit, O. S. Panwar, R. Bhattacharyya, Thin Solid Films 346 (1999) 130.
53. M. Ban, T. Hasegawa, S. Fujii, J. Fujioka, Diam. Relat. Mater., 12 (2003) 47.
54. P. J. Fallon, V. S. Veerasamy, C. A. Davis, J. Robertson, G. A. J. Amaratunga, W. I. Milne, J. Koskinen, Phys. Rev. B 48 (1993) 4777.
55. S. Xu, D. Flynn, B. K. Tay, S. Prawer, K. W. Nugent, S. R. P. Silva, Y. Lifshitz, W.I. Milne, Philos. Mag. B 76 (1997) 351.
56. E. Mounier, Y. Pauleau, J. Vac. Sci. Technol. A 14 (1996) 2535.
57. J. Bottiger, J. A. Davies, P. Sigmund, K. B. Winterbon, Radiat. Effects 11 (1971) 69.
58. W. R. Gesang, H. Oechsner, H. Schoof, Nucl. Instrum. Methods 132 (1976) 687.
59. E. Mounier, E. Quesnel, Y. Pauleau, New diamond and diamond-like films, in P. Vincenzini (ed.), Proceedings of the Topical Symposium II on New Diamond and Diamond-Like Films of the 8th CIMTEC-World Ceramic Congress and Forum on New Materials, Advances in Science and Technology 6, Vol. 6, Techna srl, Faenza, Italy, 1995, p. 183.
60. Y. Pauleau, E. Mounier, P. Juliet, Protective Coatings and Thin Films: Synthesis, Characterization and Applications, NATO-ASI Series, Partnership Sub-Series 3: High Technology, Vol. 21, Y. Pauleau and P.B. Barna (eds), Kluwer Academic, Dordrecht, The Netherlands, 1997, p. 197.
61. E. Mounier, Y. Pauleau, Diam. Relat. Mater. 6 (1997) 1182.
62. C.-C. Chen, F. C.-N. Hong, Appl. Surf. Sci. 242 (2005) 261.
63. Y. Pauleau, F. Thièry, Surf. Coat. Technol. 180–181 (2004) 551.
64. P. Wood, T. Wydeven, O. Tsuji, Thin Solid Films 258 (1995) 151.
65. D. Sarangi, S. Kumar, R. Bhattacharyya, Diam. Relat. Mater. 13 (2004) 1844.
66. D. F. Franceschini, C. A. Achete, F. L. Freire, Appl. Phys. Lett. 60 (1992) 3229.
67. S. Takeuchi, A. Tanji, H. Miyazawa, M. Murakawa, Thin Solid Films 447–448 (2004) 208.
68. W. C. Vassell, A. K. Gangopadhyay, T. J. Potter, M. A. Tamor, M.J. Rokosz, JMEPEG 6 (1997) 426.
69. M. Ban, T. Hasegawa, Surf. Coat. Technol. 162 (2002) 1.
70. J. Meneve, E. Dekempeneer, J. Smeets, Diam. Films Technol. 4 (1994) 23.
71. L. Niederberger, H. Holleck, H. Leiste, M. Stüber, S. Ulrich, H. Baumann, Surf. Coat. Technol. 174–175 (2003) 708.
72. J. C. Damasceno, S. S. Camargo Jr., F. L. Freire Jr., R. Carius, Surf. Coat. Technol. 133–134 (2000) 247.
73. D. H. Lee, S. Fayeulle, K. C. Walter, M. Nastasi, Nucl. Instrum. Methods Phys. B 148 (1999) 216.
74. Y. Oka, M. Tao, Y. Nishimura, K. Azuma, E. Fujiwara, M. Yatsuzuka, Nucl. Instrum. Methods Phys. B 206 (2003) 700.
75. P. Mosaner, M. Bonelli, A. Miotello, Appl. Surf. Sci. 208–209 (2003) 561.
76. H. Ziegele, H. J. Schreibe, N. B. Schultrich, Surf. Coat. Technol. 97 (1997) 385.
77. J. P. Hirvonen, J. Koskinen, I. Koponen, J. Likonen, H. Kattelus, Nucl. Instrum Methods Phys. B 80 (1997) 1472.
78. T. A. Friedmann, J. P. Sullivan, J. A. Knapp, D. R. Tallant, D. M. Follstaedt, D. L. Medlin, P. B. Mirkarimi, Appl. Phys. Lett. 71 (1997) 3820.
79. S. Yang, D. Camino, A. H. S. Jones, D. G. Teer, Surf. Coat. Technol. 124 (2000) 110.
80. O. Wanstrand, M. Larsson, P. Hedenqvist, Surf. Coat. Technol. 111 (1999) 247.

81. V. V. Uglov, A. K. Kuleshov, D. P. Rusalsky, J. I. Onate, S. Z. Yang, Surf. Coat. Technol. 129 (2000) 150.
82. K. Bewilogua, C. V. Cooper, C. Specht, J. Schröder, R. Wittorf, M. Grischke, Surf. Coat. Technol. 132 (2000) 275.
83. A. A. Voevodin, J. P. O'Neill, J. S. Zabinski, Thin Solid Films 342 (1999) 194.
84. M. Stüber, S. Ulrich, H. Leiste, A. Kratzsch, H. Holleck, Surf. Coat. Technol. 116–119 (1999) 591.
85. J. S. Chen, S. P. Lau, Z. Sun, G. Y. Chen, Y. J. Li, B. K. Tay, J. W. Chai, Thin Solid Films 398–399 (2001) 110.
86. Q. Wei R.J. Narayan et al., J. Vac. Sci. Technol. A 17 (1999) 3406.
87. Y. Liu, A. Erdemir, E.I. Meletis, Surf. Coat. Technol. 82 (1996) 76.
88. J. G. Deng, M. Braun, Diam. Relat. Mater. 4 (1995) 936.
89. X. He, W. Li, H. Li, J. Vac. Sci. Technol. A, 14 (1996) 2039.
90. A. Erdemir, C. Bindal, G. R. Fenske, P. J. Wilbur, Tribology Trans.. 39 (1996) 735.
91. P. J. Wilbur, D. M. Weishaar, Diam. Relat. Mater. 8 (1999) 1648.
92. I. Sh. Trakhtenberg, A. B. Vladimirov, S. A. Plotnikov, A. P. Rubshtein, V. B. Vykhodets, O. M. Bakunin, Diam. Relat. Mater. 10 (2001) 1824.
93. J. Tian, Q. Zhang, Q. Zhou, R. Gruenwald, M. Huesgen, S. F. Yoon, J. Ahn, Surf. Coat. Technol. 198 (2005) 198.
94. M. Chhowalla, Diam. Relat. Mater. 10 (2001) 1011.
95. M. M. Morshed, D. C. Cameron, B. P. McNamara, M. S. J. Hashmi, Surf. Coat. Technol. 174–175 (2003) 579.
96. N. Yamauchi, K. Demizu, N. Ueda, T. Sone, M. Tsujikawa, Y. Hirose, Thin Solid Films 506–507 (2006) 378.

Section B
Tribology of DLC Coatings Fundamentals and Experimental Studies

Fundamentals of the Tribology of DLC Coatings

J. Fontaine[1], C. Donnet[2] and A. Erdemir[3]

Abstract This chapter provides an overview of the fundamental processes that may govern friction and wear of diamond-like carbon (DLC) coatings. First, the general cases of traditional and carbon-based solid lubricants in tribology are considered, since they exhibit low friction and high wear resistance. The emphasis is then shifted to DLC films and the specific contributions of three main phenomena – abrasion, adhesion, and interfacial shearing – are considered in detail in order to account for the very interesting tribological behavior of these films. Corresponding critical parameters are identified and their roles are evaluated with respect to the known structures and properties of most DLC films. Finally, the specific examples of adhesive phenomena controlling friction and wear during tests in ultrahigh vacuum (UHV) are discussed. Adhesion appears to be necessary for tribofilm buildup and hence friction reduction; however, continued occurrence of strong adhesive phenomena is detrimental to the superlow friction behavior of these films. Overall, the exceptional tribological behavior of DLC films appears to be due to a unique combination of surface chemical, physical, and mechanical interactions at their sliding interfaces.

Keywords adhesion, abrasion, shearing, vacuum, tribochemistry

1 Introduction

Increasing demands for higher power density, longer durability, and greater efficiency in future mechanical systems are pushing current materials and coatings to their limits. This trend represents a major challenge for tribologists and lubrication

[1]Laboratoire de Tribologie et Dynamique des Systèmes, UMR CNRS 5513, Ecole Centrale de Lyon, 36 avenue Guy de Collongue, 69134 Ecully, France

[2]University Institute of France and Laboratoire Hubert Curien, UMR CNRS 5516, Université Jean Monnet, 18 rue Professeur Benoît Lauras, 42000 Saint-Etienne, France

[3]Argonne National Laboratory, Energy Systems Division, 9700 South Cass Avenue, Argonne, IL 60439, USA

C. Donnet and A. Erdemir (eds.), *Tribology of Diamond-Like Carbon Films: Fundamentals and Applications*.

engineers. Modern moving mechanical assemblies often operate under boundary-lubricated sliding regimes where intimate asperity interactions can take place, as opposed to a thick fluid film separating the sliding surfaces and thus preventing direct contact. Some industrial applications even require sliding contact without any type of liquid lubrication, thus exacerbating the situation. To achieve and maintain higher efficiency and durability under such increasingly more severe sliding conditions, protective and/or solid lubricant coatings are becoming prevalent.

These coatings can generally be divided in two broad categories [1]: "soft coatings," which are usually good for solid lubrication and exhibit low friction coefficients, and "hard coatings," which are usually good for protection against wear, and exhibit low wear rates and hence longer durability (Fig. 1). Classical solid lubricant coatings include polymers, soft metals (e.g., lead, indium, silver, and gold) or lamellar solids (e.g., graphite, MoS_2), which are easily sheared. On the other hand, antiwear coatings are usually made of hard ceramics, like nitrides, carbides, borides, or oxides. The threshold between "hard" and "soft" coatings is roughly estimated to be around 10 GPa, not far from the hardness of ball bearing or tool steels, which are largely used as structural materials for most mechanical systems. The same observation holds for friction, with a threshold value of about 0.3 between solid lubricants and antiwear coatings, close to typical friction values of metals.

It would thus seem to be difficult to associate low friction and high wear resistance with all types of coatings in most tribological contacts. Some trade-offs can be found in combining both hard and soft materials in composite or multilayer coatings, which require complex procedures and further optimization of the deposition process. Nevertheless, a diverse family of carbon-based materials seems to "naturally" combine the desired set of tribological properties, providing not only low friction but also high wear resistance. These materials are widely known as

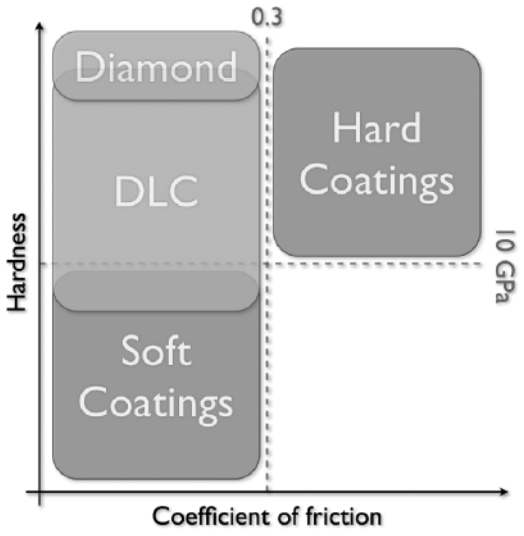

Fig. 1 Classification of coatings with respect to hardness and coefficient of friction, highlighting the special case of carbon-based coatings

the diamond and diamond-like carbon (DLC) coatings. They are usually harder than most metals and/or alloys, thus affording very high wear resistance and, at the same time, impressive friction coefficients generally in the range of 0.05–0.2 [2–4]. In some cases, friction values lower than 0.01 have been reported [5,6], a sliding regime often referred to as "superlubricity." These exceptional tribological abilities explain the increasing success of DLC coatings over the years, both in industrial applications and in the laboratory. Indeed, the evolution of DLC films studies over the last 25 years, as presented in the preface of this book, clearly demonstrates this trend.

2 Background on Tribological Coatings and their Friction and Wear Behavior

2.1 Coating Tribology

The original ideas for using "soft coatings" to reduce friction between unlubricated sliding surfaces were proposed by Bowden and Tabor back in the 1950s [7,8]. From their studies with a range of metals, they observed that friction was mainly controlled by adhesive phenomena resulting from the formation of micro-junctions between the sliding counterfaces. The tangential force F to break these junctions was thus the product of the real contact area A_r (total area of adhesive junctions) by the shear strength τ of the softest metallic counterpart, which is related to the friction coefficient μ:

$$\mu = \frac{F}{W} = \frac{A_r \tau}{W} = \frac{\tau}{P} \tag{1}$$

where W is normal force and P is contact pressure.

According to this theory, if we consider two hard and stiff counterfaces, the real area of contact will be small, but the shear strength will be high, leading to an intermediate increase in the coefficient of friction. Likewise, with one or two soft counterfaces in contact, the shear strength will be smaller, but the area of contact will be larger, leading to similar intermediate friction coefficients. However, considering two hard and stiff substrates separated by a thin soft metal film, the area of contact imposed by substrates will be small, while the shear strength of the interface imposed by the soft metal film will also be small. Thus, low friction coefficients could be achieved with soft metal films on hard and stiff substrates. This behavior has been observed experimentally, and not only for soft metals.

Nevertheless, the general case is much more complex, and at least three main contributions to the friction force have to be considered (Fig. 2). First is the abrasive component of friction, when asperities or entrapped debris on one counterface

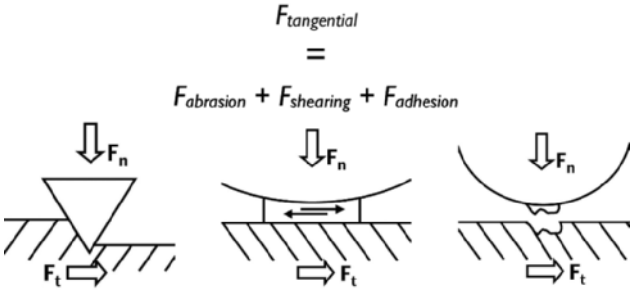

Fig. 2 Schematic of the three main fundamental contributions to friction (or tangential) force F_t with a normal force F_n

scratch the other. Second is the adhesive component, which occurs when adhesive junctions are formed between counterfaces, as described above. Third is the shearing component, which occurs when matter entrapped between sliding counterfaces (such as third bodies and transfer- or tribo-film) is flowing because of the shear forces. The lowest friction coefficients should thus be achieved by the application of very thin films that are also very easy to shear on hard and stiff substrates. This arrangement avoids abrasive phenomena as well as large shearing forces that would increase the friction.

Protective coatings to reduce wear have been based on Archard's law [9]:

$$V = \frac{k}{H} \cdot L \cdot F_n \tag{2}$$

Initially established for adhesive wear, involving shearing or breaking of adhesive junctions between counterfaces, this law also applies to abrasive wear involving scratching by asperities or entrapped debris. In both cases, the wear volume V is proportional to the sliding distance L and normal force F_n, and inversely proportional to the hardness H of the softest counterface. The wear coefficient k depends mainly on the materials and considered wear regime.

Equation 1 has been used as a guideline for the development of hard coatings as wear-resistant materials. Hardness is still at the center of research activities concerning protective coatings, with recent development of nanocomposite or superlattice films that are designed on the basis of the Hall-Petch effect, which predicts increased hardness with decreasing grain size. Nevertheless, with hard coatings, fracture and delamination wear could also occur. Furthermore, other properties are critical for the achievement of wear-resistant coatings, like the plastic work of indentation or the ratio of hardness to Young's modulus (H/E) [10]. The coating indeed needs to be hard to avoid abrasive or adhesive wear, but it also needs to be strain tolerant and tough to prevent crack propagation and to follow substrate deformations, especially when there are large differences in elastic modulus between the coating and its substrate.

2.2 Fundamentals of Frictional Interactions in Coatings

The causes of friction between solid surfaces are numerous and intricate. However, the work of Bowden and Tabor [7,8] helped tremendously in the identification of the main contributors to friction between metals. Their approach was later extended to coatings [11]. Although this approach does not allow full mathematical description of friction or the prediction of friction coefficients, it does provide qualitative understanding of the fundamental phenomena that govern friction in thin solid films.

The friction force can be seen as the consequence of three phenomena (see Fig. 2):

- *Abrasion*: plowing or scratching of surfaces by asperities or debris
- *Shearing*: plastic flow of asperities or interfacial material
- *Adhesion*: breaking of the adhesive junction between sliding counterfaces

The abrasive component is more predominant when asperities or moving particles inside the contact are harder than at least one of the counterfaces. The typical case is a hard and rough surface sliding against a soft one, or the presence of hard particles between softer sliding surfaces. The corresponding friction force results from the mechanical deformation leading to scratches and possibly loss of matter. The main controlling parameters will thus be the mechanical properties of the surface being scratched – mainly the hardness – and the geometry of the indenting asperity or particle.

The shearing component mainly corresponds to the dissipation resulting from plastic or viscous flow of matter confined between hard and stiff counterfaces. This matter can be a soft coating, such as a thin surface film, a contamination layer, or a "tribofilm," formed by tribochemistry and/or by a gathering of trapped wear debris particles. This contribution is mainly controlled by the covering ratio of this interfacial film, the rheological properties of this film, and the ratio t/l, where t is the film thickness and l the shearing length [12], i.e., the contact diameter.

The adhesive component results from the interactions between surfaces. The forces governing adhesion can have several origins, mainly electrostatic forces, capillary forces, polarization forces (van der Waals), and bonding forces (covalent, ionic, metallic, or hydrogen bonding). When these forces are involved in some areas of a contact, they may lead to the formation of an adhesive junction. The energy required to break it will affect friction, and the localization of the break (i.e., at the original interface or within one of the counterfaces) will control wear and also the morphological and chemical evolution of the sliding surfaces. Thus, the main parameters controlling the adhesive component of friction will indeed be the chemical reactivity of the sliding surfaces, which incidentally affects the nature of interactions. The roughness and mechanical properties of sliding surfaces are also important and can affect the processes involved in the making and breaking of the adhesive junctions.

In light of these three main contributions to the friction force, let us now consider how strongly they will be involved in the tribology of DLC films.

3 The Case of Diamond-like Carbon Films

To determine the relative importance of the three fundamental contributors to friction in the case of DLC films, one has to estimate several properties of these materials. As we have seen in the previous section, the mechanical properties of sliding surfaces control, to some extent, each of the three components of friction. Hardness and elastic modulus are also known to have a strong effect on friction and wear. Knowledge of these properties is thus paramount for gaining fundamental understanding of the tribological behavior.

In this section, we will first quickly review the mechanical properties of DLC films and then consider in detail the role of each fundamental contributor to friction, namely abrasion, shearing, and adhesion.

3.1 Mechanical Properties of DLC Films

Determination of the true mechanical properties of a material that exists only as a thin coating of less than a few micrometer thickness is a challenge. The recent development of instrumented indentation with nanometer-scale resolution allowed such measurements to be successfully performed, provided that some specific requirements are fulfilled, as explained in Chapter 4. Here, we will focus only on the general trends that have been observed with the DLC films and on specific, unusual mechanical behaviors that occur with some materials.

The great variety of DLC structures and compositions leads to a wide range of mechanical properties. Indeed, hardness varies from a few GPa up to more than 60 GPa, while the elastic modulus ranges from several tens of GPa up to several hundreds of GPa (Table 1). Increasing the hydrogen content has a tendency to reduce both the hardness and Young's modulus [13]. On the other hand, increasing the sp^3 fraction improves these mechanical properties [14]. Most DLC films are thus harder than most metallic materials; in particular, they are harder than steels.

All these materials also share a relatively uncommon property: they exhibit high *H/E* ratios, with values higher than 0.08 and up to 0.2 (see Table 1). For comparison, the highest value achievable with heat-treated tool steel is about 0.04; ceramics like Al_2O_3, ZrO_2, Si_3N_4, or SiC have values around 0.06; and nitride-based coatings

Table 1 Hardness (*H*), Young's modulus (*E*), and *H/E* ratio of the different families of DLC films (a = amorphous; ta = tetrahedral amorphous)

	a-C	a-C:H	ta-C	ta-C:H
Hardness (GPa)	12–18	7–30	28–65	28–60
Elastic modulus (GPa)	160–190	60–210	210–650	175–290
H/E ratio	0.08–0.1	0.1–0.16	0.1–0.2	0.16–0.21
References	[16,17]	[15,18–20]	[16,21,22]	[23]

(TiN, CrN) have values around 0.08. Moreover, such high *H/E* ratios mean that DLC films are relatively strain tolerant. DLC materials are known to exhibit high elastic recovery in nanoindentation experiments, meaning that accurate determination of their hardness with widespread Berkovich indenters is not easy compared to trigonal tips [15].

High strain tolerance is not the only unusual mechanical property of DLC films. Nanoindentation experiments were performed on a-C:H films by means of procedures developed for polymers [24,25]. By applying the load exponentially versus time, the strain rate was kept constant during indentation. The hardness measured at different strain rates was found to vary significantly, following a Norton-Hoff law, where $\dot{\varepsilon}$ is the strain rate and x is called the "viscoplastic exponent":

$$H = H_0 \cdot \dot{\varepsilon}^x \tag{3}$$

Viscoplastic exponents varied between 0.004 and 0.08 for a-C:H films with hydrogen contents from 24 to 42 at. % [13]. Such time-dependent mechanical behavior means that highly hydrogenated a-C:H films (more than ~25 at. %) have excellent relaxation abilities, probably thanks to some free volumes in their structures. Slow recovery of indents has been indeed observed and reported in the literature [15].

3.2 Fundamental Contributors to the Friction of DLC Films

Knowing the general mechanical properties of DLC films, we can now attempt to estimate the relative role of each of the three fundamental contributions to the friction force.

Abrasion

Abrasive phenomena on DLC surfaces are not very likely to occur under most tribological contacts, because of their high hardness and high strain tolerance. Abrasion could thus be observed mainly against hard and rough ceramics. Being harder than most metallic counterfaces, DLC films are used to protect them from abrasion. Moreover, the softest hydrogenated amorphous carbon films, a-C:H, are viscoplastic, meaning that they could exhibit some "healing" abilities for ductile scratches. Finally, if abrasion occurred with DLC films during sliding, it would mainly consist of abrasion of the counterface by DLC asperities, rather than DLC itself being scratched. Thus, the surface roughness of such carbon-based materials is critical. It is well known that DLC films usually present smooth surfaces, except maybe in the case of films formed by unfiltered cathodic vacuum arc deposition. Roughness of the films on industrial surfaces will then be mainly controlled by the substrate roughness and can therefore be minimized.

Shearing

Shearing involves the flow of matter within the contact zone. Once again, the high mechanical hardness of DLC films will minimize such phenomena inside the films. Nevertheless, the formation of transfer layers on counterfaces has long been reported for DLC films sliding against many types of counterfaces [3]. These transfer films, or rather "tribofilms" – since their composition and structure appear to be somewhat different from the original DLC film [26–28] – could be sheared during sliding and thus dissipate some energy. The question then arises as to whether we have "intrafilm" sliding (i.e., flow of the tribofilm itself) or "interfilm" sliding (i.e., shearing at the surface of the tribofilm) [11]. The answer will depend, of course, on the rheological properties of this tribofilm, but the film's composition and structure, let alone mechanical properties, are relatively unknown. Apparently, these tribofilms have an increased amount of sp^2 carbon and probably a reduced amount of hydrogen compared to the original DLC film [29]. However, this sp^2 carbon enrichment does not mean that there is some "graphitization" of the tribofilm – in the sense that large graphene sheets would form – that would result in some shearing within the tribofilm. Nonetheless, the tribofilms formed from DLC films are usually very thin, typically less than 100 nm, and relatively confined to the contact area – compared to soft coatings like MoS_2. We can expect the shearing to occur mainly at the surface of the tribofilm (interfilm sliding), provided that adhesion is not too strong between the growing tribofilm and the sliding DLC surface: the shearing component of friction for DLC films would then be involved if the adhesive component becomes large. Let us thus consider this last contribution.

Adhesion

To estimate the contribution of adhesion to the friction of DLC, one has to identify the nature of the interactions between surfaces. Of course, the nature of the counterface will be critical here, but eventually a carbonaceous transfer- or tribo-film is formed, resulting in a carbon-based film sliding against a carbon-based tribofilm.

These carbon-based materials adhere because of the strong covalent bonds. The strongest interactions we could expect are formation of covalent bonds between sliding surfaces through σ-orbitals. However, such bonds are highly oriented, hence difficult to neutralize within the solid/solid contacts; furthermore, they are very reactive and react readily with the environment (O, H, or OH) or form double bonds – creating π-orbitals, as reported to occur with DLC and tribofilm surfaces [26–28]. Adhesion with DLC films does not likely involve such covalent σ-bonds if O, H, or OH are available in the test environment.

The presence of π-orbitals from sp^2 carbon double bonds on the surface – which are out-of-plane, contrary to the in-plane σ-orbitals – may lead to relatively strong interactions when π-orbitals of both surfaces are close enough [30–33]. Nevertheless, molecules from the surface could easily shield these short-range interactions. This shielding accounts for the high friction of graphite under a vacuum as opposed to its

low friction in humid air [34]. These strong interactions between π-bonds, as well as the formation of σ-bonds between counterfaces, are more likely to occur under high vacuum or in ultrapure inert gas environments, explaining the high friction observed under such conditions with DLC films of low hydrogen content [35].

The effect of environment, especially water vapor, on the friction of DLC films appears to be complex, since it depends on the physical and/or chemical nature of the DLC films. For instance, the coefficient of friction increases with relative humidity for hydrogenated amorphous carbon (a-C:H) [36,37] while it decreases for pure amorphous carbon films (a-C or ta-C) [38]. However, the friction coefficients are in the intermediate to low range – 0.05 to 0.2 – in both cases. Several interactions could account for these values. Hydrogen bonds between hydrogenated carbonaceous surfaces and water molecules could be involved, but one has to keep in mind that such bonds are highly oriented. Capillary forces could also be involved, as observed in micro-tribological experiments, which show a concomitant increase in adhesion and friction forces as a function of surface coverage by water molecules [39]. In such a case, the surface roughness and real contact area would control these capillary forces (hence, friction) in a humid environment.

The weakest contributions to adhesion would be van der Waals forces between surfaces, which are active in inert environments (absence of water vapor) between "passivated" carbonaceous surfaces, typically hydrogenated carbon surfaces.

As a partial conclusion, we can infer that the main fundamental contribution to the friction of DLC films is adhesion, provided that the surfaces are relatively smooth. Of course, the extent of adhesion will be strongly affected by the surface, its topography, and its mechanical properties. Indeed, the strength of adhesive junctions will depend on the surface chemistry; their size will be affected by the roughness, even at small scales; and their release – or breaking – will depend on the relative strength of the adhesion and the mechanical properties of the surfaces. Moreover, these parameters are likely to evolve during sliding, since the surface can be affected either by tribochemical reactions with the environment or the counterface, or by breaking of the adhesive junctions inside the DLC film or the tribofilm. The next section will illustrate how these adhesive phenomena can be involved in the friction of DLC films, starting from a vacuum environment, which will emphasize the critical role of adhesion in friction.

4 Examples of Adhesive Phenomena

Hydrogenated amorphous carbon films with high hydrogen content can achieve extremely low friction coefficients – referred to as "superlubricity" or "superlow friction" – under vacuum or inert environments, as described in Chapter 8. Here we will demonstrate the prominent role of adhesion on tribofilm buildup and the achievement of superlow friction, and then on the loss of superlow friction [40,41].

4.1 Buildup of Tribofilms on Steel Counterfaces: A Case Study

In this section, to demonstrate the very critical role of tribofilm buildup in friction of DLC films, we will present a case study in which friction experiments were conducted in ultrahigh vacuum (UHV, $< 10^{-6}$ Pa) with a linear reciprocating tribometer. The average sliding speed was 0.5 mm/s, and the stroke length was 2 mm. These tests were run under a load of 3 N using hemispherical 52,100 bearing steel pins with a radius of curvature of 8 mm. Such contact conditions correspond to a maximum Hertzian pressure in the GPa range. The flat sample was a hydrogenated amorphous carbon film containing 42 at. % hydrogen. In this study, the effects of different surface preparation methods for the steel pins were compared. An in situ argon ion sputtering gun allowed easy manipulation of the near-surface chemistry of the sliding surfaces. Three types of pin were examined:

- *Raw pin* with native oxide layers and adventitious carbon contaminants
- *Oxidized pin* after a short etching to remove adventitious carbon
- *Etched pin* with no oxide layer and no adventitious carbon

The chemistry of the pin surfaces was checked by in situ Auger electron spectroscopy. All experimental details and results are further described in reference [40].

Figure 3a show typical coefficient of friction values for the three different pin surfaces. The running-in period clearly decreases as the adventitious carbon and oxide layers are removed by argon etching. Indeed, 34, 7, and 4 cycles are required to reach a friction coefficient of 0.01 for the raw, oxidized, and etched pins, respectively. Also, for the first cycle, the friction coefficient decreases from 0.22 for raw and oxidized pins down to only 0.05 for the etched pin. This finding suggests that the formation of a tribofilm, necessary to achieve low friction, is faster when oxide layers are largely removed.

These values concern only sliding friction. Figure 3b shows the tangential force as a function of motor position during the first cycle for each pin surface. Due to the relatively low stiffness of the tribometer, a linear increase is initially observed,

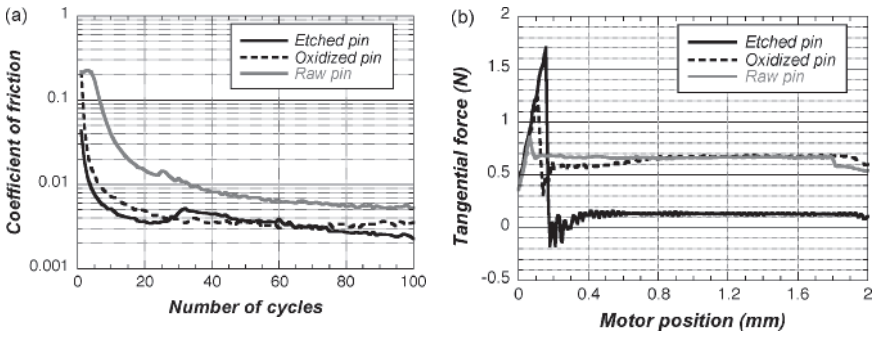

Fig. 3 (a) Friction coefficient during first 100 cycles and (b) tangential force during the first cycle for experiments performed on a-C:H film with different levels of surface preparation (see text for details)

corresponding to elastic bending of the tribometer. After reaching a maximum value, the tangential force drops suddenly to an almost constant value, meaning that full sliding started in the contact. This condition allows computation of the sliding friction coefficient (or dynamic friction coefficient). Moreover, from the maximum value reached before sliding for the tangential force, we can deduce the static friction coefficient. The computed values increase from 0.29 for the raw pin to 0.40 for the oxidized pin and finally to 0.56 for the etched pin.

Removal of the oxide layer leads to strong sticking, probably through the formation of adhesive junctions. We can assume that the rupture of these junctions takes place somehow within the DLC film, leading to much faster tribofilm buildup on the steel counterface. This behavior would explain the much lower initial sliding friction coefficient with the etched pin. The initial adhesion appears to be beneficial here, since it decreases the surface interactions during the continuation of the friction experiment. However, we will see in the next section how adhesion may become detrimental, and how it can be controlled thanks to environmental gases.

4.2 Tribochemical Interactions Controlling Adhesion

In another case study, the critical role of tribochemical interactions on adhesion (and hence, friction) is examined. Specifically, friction experiments were conducted in an UHV chamber on a linear reciprocating tribometer at a sliding speed of 0.5 mm/s, a stroke length of 2 mm, and a load of 3 N. The experiments were run with hemispherical 52,100 bearing steel pins having a radius of curvature of 8 mm. The flat sample was a hydrogenated amorphous carbon film containing 34 at. % hydrogen. Experiments were performed under UHV or under partial pressures of hydrogen [40,41] or oxygen [40] gas.

Figure 4 shows the friction coefficients for UHV and hydrogen gas up to 1,000 Pa. Under UHV, this DLC film initially exhibits a progressive decrease in friction, down to a superlow friction value of about 0.002, but after a few hundred cycles, the friction increases drastically, reaching values higher than 0.3. With a low pressure of hydrogen (50 Pa), the same behavior exists. However, at an intermediate pressure of 200 Pa, the superlow friction is intermittently lost, but the friction coefficient remains below 0.1 and decreases progressively to reach superlow friction again. At a much higher pressure of 1,000 Pa of hydrogen, the maximum friction coefficient remains below 0.01, the upper limit of superlubricity.

On this UHV tribometer, the values of the friction force are recorded by a data-logging system. Because the motion is performed at a constant speed, time-resolved measurements can be converted into spatially resolved ones. It is thus possible to present friction data in a two-dimensional diagram, one axis being devoted to cycle number, one axis being devoted to position along the wear track on the flat, and the color or grayscale reflecting the coefficient of friction (or any recorded signal during sliding). These charts are called “triboscopic images.” Figure 5 shows such images for the friction experiment under 200 and 1,000 Pa of hydrogen gas, focusing on the cycles affected by the friction increase.

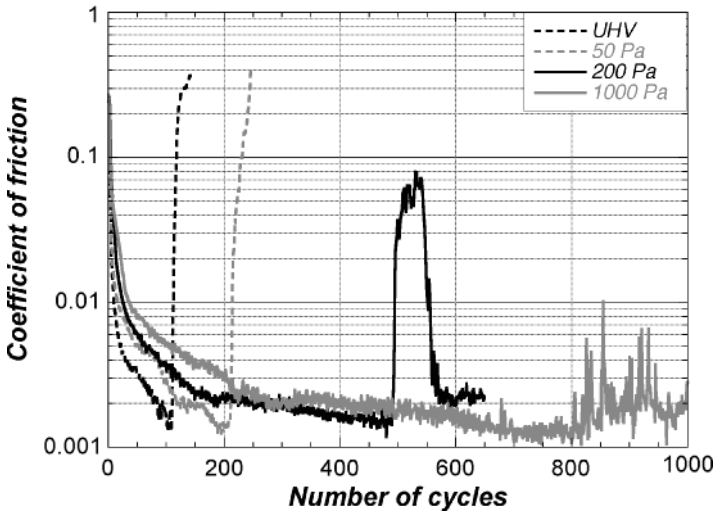

Fig. 4 Evolution of friction coefficient versus number of sliding cycles in various environments from ultrahigh vacuum (UHV) up to 1,000 Pa of hydrogen gas

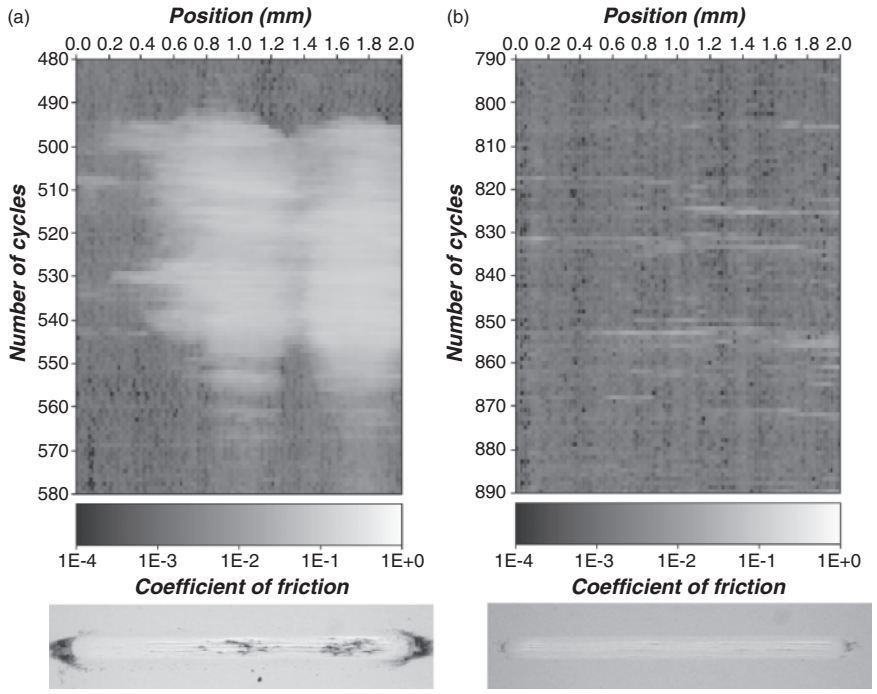

Fig. 5 Triboscopic images showing friction coefficient as a function of position along the wear track and number of cycles for experiments under 200 Pa of hydrogen (a) and 1,000 Pa of hydrogen (b). Corresponding optical micrographs of the wear tracks are shown below each triboscopic image for comparison

The triboscopic image obtained under 200 Pa of hydrogen (Fig. 5a), taken from Fig. 4, gives us some evidence that the friction increase starts only at very localized spots, spreading progressively albeit quickly to a great part of the wear track. Some parts of the track remain in the superlow friction regime, while others have an intermediate friction increase (note the logarithmic scale for the coefficient of friction). Moreover, degradations of the sliding track are well correlated with the high friction spots, with some deep grooves being observed. To account for such results, we may consider abrasive phenomena, but the friction would then be significantly affected for whole cycles, no matter the position along the wear track. Also, if the tribofilm was removed due to shearing or flow, friction would also be affected along the entire wear track. Hence, the friction increase can most likely be attributed to adhesive phenomena caused by strong interactions occurring at localized areas of the a-C:H coated flat, as explained in Section 3.2.

At a higher pressure of 1,000 Pa of hydrogen (Fig. 5b), the triboscopic image, taken from Fig. 4, shows that the friction increase occurs in a very scattered manner. High friction spots are indeed localized but last only one or very few cycles. Moreover, they occur at random positions. Adhesive phenomena thus seem to be partially prevented by the presence of hydrogen gas. The tendency to break C–H bonds and to form more sp^2 carbon is probably at the origin of the strong adhesion that occurs between sliding counterfaces. Since it seems possible to break C–H bonds on the sliding surfaces, H_2 molecules can probably also be broken during friction, allowing reactions with sp^2 carbon and thus production of new C–H bonds. As described in detail in Chapter 11 by Professor Nakayama, triboplasma generation between sliding DLC surfaces and the triboemission of electrons and even photons might help in the dissociation of H_2 into H. Hydrogen atoms can then react with the carbon to form C–H on the sliding surface. To confirm this hypothesis of hydrogen enrichment, new experiments were performed on the same sample in deuterium gas at a pressure of 1,000 Pa. The tribological behavior is similar to that observed in the same pressure of hydrogen. Being isotopes, hydrogen and deuterium are indeed chemically equivalent. The wear track on the flat obtained after 1,000 cycles has been analyzed by time-of-flight secondary ion mass spectroscopy (ToF-SIMS) [40]. The peak height of negative ions at a mass of 2 can be undoubtedly attributed to deuterium negatives ions, since the probability of obtaining H_2 negative ions is extremely low. This peak height was then divided by the height for negative ions at a mass of 1, corresponding to hydrogen negative ions. This ratio is the abundance of deuterium on the surface and can be compared to the natural abundance of deuterium (0.015%). Such measurements were performed inside and outside the wear track, before and after a very short and soft etching of the surface, whose purpose was to remove the few monolayers of physisorbed molecules. Outside the wear track, deuterium can be found 13 times more than its natural abundance, but it is almost fully removed after short etching, suggesting a weak bonding to the surface. In contrast, deuterium abundance is 240 times the natural one inside the wear track, and etching did not remove it completely, leaving 15 times the natural abundance. Thus, deuterium has a tendency to physisorb on the a-C:H surface, but it is strongly bonded to the surface inside the wear track, probably due to tribochemical reactions. The relative enrichment in hydrogen atoms inside the wear track will thus avoid or

limit the strong adhesion between the sp^2 carbon atoms, maintaining friction coefficients at lower values.

Surprisingly, such healing phenomenon can also be observed to a certain extent in oxygen [40]. However, oxygen is a much more reactive molecule, and hence, the tribochemical phenomena occur at much lower partial pressures. Figure 6 shows the evolution of the friction coefficient for our a-C:H sample under various pressures of oxygen gas. Even at 1 Pa, oxygen has a significant effect on the friction coefficient, since the minimum friction coefficient achieved is about 0.009 instead of less than 0.005 for all experiments performed under UHV. It is thus clear that oxygen will lead to different interactions between sliding surfaces. Nevertheless, the drastic friction increase under UHV mentioned previously also occurs after about 200 cycles, meaning that strong adhesive phenomena due to sp^2 carbon are still controlling the tribological behavior. At 10 Pa of oxygen, superlow friction cannot be achieved anymore, the friction coefficient remaining above 0.01. However, a transient friction increase is observed up to about 0.15, in a similar way to the intermediate hydrogen pressures of 200 Pa (Fig. 4). This friction increase is indeed similar to that observed with hydrogen gas: it also starts at localized spots on the flat wear track, extending to the entire wear track, and worn surfaces exhibit the same structural features as those found on surfaces rubbed in hydrogen. Then, the friction coefficient stabilizes at values between 0.01 and 0.02, even lower than that before the transient increase. Thus, oxygen probably also reacts with carbonaceous surfaces during sliding, allowing the tribofilm to "heal" and avoiding the predominance of sp^2 carbon on the surface. Finally, at 200 Pa of oxygen, the friction first decreases

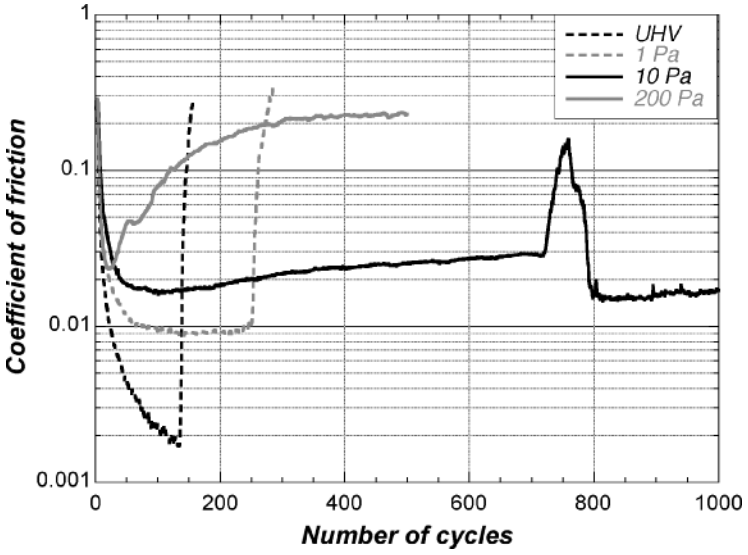

Fig. 6 Evolution of friction coefficient versus number of sliding cycles in various environments from ultrahigh vacuum (UHV) up to 200 Pa of oxygen gas

quickly, but then increases progressively, to reach values equivalent to the initial values, above 0.2. No features could be found on triboscopic images, the evolution of friction being the same whatever the position on the track length. Strong adhesive phenomena leading to significant surface degradations are not involved anymore.

5 Conclusion

The combination of extreme mechanical properties with weak surface interactions accounts for the low friction and high wear resistance of DLC films. These unique films have much to offer for a wide range of tribological applications. Over the years, scientists have made great strides in understanding their growth mechanisms, surface chemical/physical states, and tribological behaviors. This understanding has been used to design and customize various carbon-based coatings, such as doped or alloyed DLC and near-frictionless carbon, which can meet the multifunctional needs of future tribological applications. Unlike most other solids, DLC films enjoy a combination of low friction and high wear resistance under a wide range of sliding contact conditions. Detailed tribological studies show that test conditions and environmental species can dramatically affect the friction and wear performance of these films. Depending on the tribological and environmental constraints, tribo-oxidation and triboreaction with additives, graphitization, gaseous adsorption/desorption, and superlow friction can occur at the sliding contact interfaces of these films and control their friction and wear behavior. The next chapters will highlight some of these phenomena.

References

1. K. Holmberg, A. Matthews, Coatings Tribology – Properties, Techniques and Applications in Surface Engineering, Elsevier, Amsterdam, The Netherlands (1994).
2. A. Grill, Wear 168(1–2) (1993) 143.
3. A. Grill, Surf. Coat. Technol. 94–95(1–3) (1997) 507.
4. A. Erdemir, C. Donnet, in: Handbook of Modern Tribology, Vol. 2, B. Bushan (ed.), CRC Press, Boca Raton, FL (2000), Ch. 24.
5. C. Donnet, M. Belin, J. C. Augé, J. M. Martin, A. Grill, V. Patel, Surf. Coat. Technol. 68–69 (1994) 626.
6. A. Erdemir, O. L. Erylmaz, G. Fenske, J. Vac. Sci. Technol. A 18(4) (2000) 1987.
7. F. P. Bowden, D. Tabor, The Friction and Lubrication of Solids, Part I, Clarendon Press, Oxford (1950).
8. F. P. Bowden, D. Tabor, The Friction and Lubrication of Solids, Part II, Clarendon Press, Oxford (1964).
9. J. F. Archard, J. Appl. Phys. 24 (1953) 981.
10. A. Leyland, A. Matthews, Wear 246 (2000) 1.
11. I. L. Singer, Solid lubrication processes, in: Fundamentals of Friction: Macroscopic and Microscopic Processes, I. L. Singer and H. M. Pollock (eds), NATO ASI Series E Vol. 220, Kluwer Academic, Dordrecht, The Netherlands (1992).

12. R. Hill, The Mathematical Theory of Plasticity, Oxford University Press, Oxford (1950).
13. J. Fontaine, J. L. Loubet, T. Le Mogne, A. Grill, Tribol. Lett. 17(4) (2004) 709.
14. X. Shi, D. Flynn, B. K. Tay, S. Prawer, K. W. Nugent, S. R. P. Silva, Y. Lifshitz, W. I. Milne, Philos. Mag. B 76 (1997) 351.
15. S. Bec, A. Tonck, J. Fontaine, Philos. Mag. 86(33–35) (2006) 5465.
16. G. M. Pharr, D. L. Callahan, S. D. McAdams, T. Y. Tsui, S. Anders, A. Anders, J. W. Ager III, I. G. Brown, C. Singh Bhatia, S. R. P. Silva, J. Robertson, Appl. Phys. Lett. 68(6) (1996) 779.
17. S. Logothetidis, C. Charitidis, Thin Solid Films 353 (1999) 208.
18. N. Savvides, T. J. Bell, J. Appl. Phys. 72(7) (1992) 2791.
19. N. Maître, S. Camelio, A. Barranco, T. Girardeau, E. Breelle, J. Non-Cryst. Sol. 351 (2005) 877.
20. T. H. Fang, W. J. Chang, Appl. Surf. Sci. 252 (2006), 6243.
21. S. Sattel, J. Robertson, H. Ehrhardt, J. Appl. Phys. 82(9) (1997) 4566.
22. T. H. Zhang, Y. Huan, Comp. Sci. Technol. 65 (2005) 1409.
23. M. Weiler, S. Sattel, T. Giessen, K. Jung, H. Ehrhardt, V.S. Veerasamy, J. Robertson, Phys. Rev. B 53(3) (1996) 1594.
24. G. Hochstetter, A. Jimenez, J. L. Loubet, Macromol. Sci. Phys. B 38 (1999) 681.
25. P. Bertrand-Lambotte, J. L. Loubet, C. Verpy and S. Pavan, Thin Solid Films 398–399 (2001) 306.
26. T. Le Huu, H. Zaidi, D. Paulmier, P. Voumard, Thin Solid Films 290–291 (1996) 126.
27. A. Erdemir, C. Bindal, J. Pagan, P. Wilbur, Surf. Coat. Technol. 76–77 (1995) 559.
28. Y. Liu, A. Erdemir, E. Meletis, Surf. Coat. Technol. 86–87 (1996) 564.
29. B. Racine, M. Benlahsen, K. Zellama, M. Zarrabian, J. P. Villain, G. Turban, A. Grosman, ppl. Phys. Lett. 75(22) (1999) 3479.
30. M. S. Dresselhaus, G. Dresselhouse, Adv. Phys. 30(2) (1981) 139.
31. M. N. Gardos, in: Synthetic Diamond: Emerging CVD Science and Technology, K.E. Spear and J.P. Dismuke (eds), Wiley, New York (1994), p. 419.
32. M. N. Gardos, in: New Directions in Tribology, Proceedings of the Plenary and Invited Papers from the First World Tribology Congress (London, Sept. 8–12 1997), Mechanical Engineering Publications, London (1997), p. 229.
33. C. Donnet, A. Grill, J. Fontaine, T. Le Mogne, F. Lefebvre, V. Patel, C. Jahnes, in: Lubrication at the Frontier, D. Dowson et al. (eds), Elsevier, Amsterdam, The Netherlands (1999), p. 333.
34. D. H. Buckley, in: Surface Effects in Adhesion, Friction, Wear and Lubrication, Elsevier, New York (1981) p. 574.
35. C. Donnet, A. Grill, Surf. Coat. Technol. 94–95 (1997) 456.
36. K. Enke, Thin Solid Films 80 (1981) 227.
37. C. Donnet, T. Le Mogne, L. Ponsonnet, M. Belin, A. Grill, V. Patel, C. Jahnes, Tribol. Lett. 4 (1998) 259.
38. A. A. Voevodin, A. W. Phelps, J. S. Zabinsky, M. S. Donley, Diam. Relat. Mater. 5 (1996) 1264.
39. M. Tagawa, M. Ikemura, Y. Nakayama, N. Ohmae, Tribol. Lett. 17(3) (2004) 575.
40. J. Fontaine, T. Le Mogne, J. L. Loubet, M. Belin, Thin Solid Films 482 (2005) 99.
41. J. Fontaine, M. Belin, T. Le Mogne, A. Grill, Tribol. Int. 37 (2004) 869.

Environmental and Thermal Effects on the Tribological Performance of DLC Coatings

H. Ronkainen and K. Holmberg

Abstract Diamond-like carbon (DLC) coatings have low friction and high wear resistance compared to bulk materials and to other wear-resistant coated surfaces. The surrounding environment, gas atmosphere, humidity and temperature, affect the friction and wear performance of DLC films dramatically. In dry and inert atmospheres, the highly hydrogenated DLC films typically exhibit low friction performance, but the hydrogen-free DLC films have high friction accompanied with increased wear. In humid environment, the friction coefficient of both types of DLC films is similar varying in the range 0.05–0.2 and the best wear resistance can be achieved with hydrogen-free ta-C films. At elevated temperatures, the advantageous tribological properties of hydrogenated DLC films may be disturbed due to effusion of hydrogen and graphitization of the film structure in rather low temperatures. The hydrogen-free ta-C films on the other hand can survive in higher temperatures, even though the friction coefficient reaches higher values.

Keywords diamond-like carbon, DLC, hydrogenated, hydrogen-free, environment, humidity, temperature

1 Introduction

Diamond-like carbon (DLC) coatings have attracted great interest during the past decades due to their excellent mechanical, electrical and chemical properties. DLC is a metastable form of amorphous carbon with exceptional properties, like high hardness and chemical inertness providing favourable friction and wear properties.

DLC films cover a wide range of different types of coatings with similar, yet differing tribological properties. The two major categories of DLCs are the hydrogenated and hydrogen-free DLC films. The hydrogenated DLC films typically have hydrogen content from 20 to 40 at. % and the hydrogen-free DLC films have

VTT Technical Research Centre of Finland, Metallimiehenkuja 6, Espoo, P.O. Box 1000, 02044 VTT, Finland

C. Donnet and A. Erdemir (eds.), *Tribology of Diamond-Like Carbon Films: Fundamentals and Applications*.

only a small fraction of hydrogen as an impurity in the film structure. The composition of DLC films has been described in a ternary phase diagram of hydrogen content, sp^3 and sp^2 hybridization [112]. Using this classification, the major groups of DLC films that have been investigated mostly are hydrogenated amorphous carbon (a-C:H), amorphous carbon (a-C) and tetrahedral amorphous carbon (ta-C). A great interest has been addressed particularly to the tribological performance of a-C:H films deposited mostly with plasma-assisted chemical vapour deposition (PACVD) processes. Studies on the hydrogen-free a-C films, deposited with sputtering processes, and the hydrogen-free ta-C coatings, deposited by vacuum arc or laser ablation processes, have also been carried out, but to a lesser extent. The friction and wear performance of DLC films is greatly influenced by the intrinsic coating properties, the functional parameters applied and the environmental conditions. The environmental aspects affecting the tribological performance of DLC films will be reviewed in this chapter in respect of gas atmosphere, humidity and temperature.

2 Tribological Performance of DLC Coatings

The DLC coatings can be considered as low-friction coatings with high wear resistance compared to most bulk materials: for example, wear-resistant ceramic coatings, such as TiN. The TiN typically has a friction coefficient of about 0.5 against a steel counterpart, whereas DLC films exhibit friction coefficient less than 0.2 in normal atmosphere. In unlubricated contacts, the DLC coatings typically show similar friction values compared to boundary-lubricated steel against steel contacts. The wear resistance of DLC coatings also outperforms most wear-resistant materials and coatings in sliding contacts, since the wear rates of DLC films are two to three orders of magnitude lower compared to, e.g. TiN coating [115–117,120,139].

The DLC films cover a great variety of compositions and structures controlled by the deposition technique and deposition parameters. The film composition together with the test conditions (load and speed), test environment, temperature and counterface material influence the friction and wear performance of DLC films as reviewed in several publications [21,22,37,42,53,54]. Table 1 represents the typical friction and wear rate data of different types of DLC films.

3 Environmental Effects on Tribological Performance of DLC Films

The test environment has a dramatic influence on the friction and wear performance of hydrogenated and hydrogen-free DLC films. In dry air and in inert gasses the friction of hydrogenated DLC films is low, reaching superlow values in the range 0.001–0.02, when the films are highly hydrogenated. In humid air, the friction

Table 1 Friction coefficients values and wear rates from the literature for diamond, diamond-like carbon and doped DLC coatings

	Diamond coatings	Hydrogen free DLC	Hydrogenated DLC	Modified/ doped DLC	References used
Structure	CVD diamond	a-C ta-C	a-C:H ta-C:H	a-C:Me a-C:H:Me a-C:H:x Me=W,Ti…. x=Si,O,N, F,B...	[3,4,11,20,31,33,34, 37,42,45,48,51, 60,64,68,98,107, 118,119,122, 128,131,136,150]
Atomic structure	sp^3	sp^2 & sp^3	sp^2 & sp^3	sp^2 & sp^3	
Hydrogen content	-	> 1%	10–50 %		
μ in vacuum	0.02–1	0.3–0.8	0.007–0.05	0.03	
μ in dry N_2	0.03	0.6–0.7	0.001–0.15	0.007	
μ in dry air 5-15 % RH	0.08–0.1	0.6	0.025–0.22	0.03	
μ in humid air 15–95 %	0.05–0.15	0.05–0.23	0.02–0.5	0.03–0.4	
μ in water	0.002–0.08	0.07–0.1	0.01–0.7	0.06	
μ in oil		0.03	0.1	0.1	
K in vacuum	1–1000	60–400	0.0001		
K in dry N_2	0.1–0.2	0.1–0.7	0.00001–0.1		
K in dry air 5–15 % RH	1–5	0.3	0.01–0.4		
K in humid air 15–95 %	0.04–0.06	0.0001–400	0.01–1	0.1–1	
K in water	0.0001–1	–	0.002–0.2	0.15	
K in oil		–	–	(0.1)	

K refers to wear rate [$x10^{-6}mm^3(Nm)^{-1}$]

coefficient of hydrogenated DLC films increases to values 0.1–0.2. Similar values of friction coefficient are typically measured for the hydrogen-free DLC films in humid environment. However, the hydrogen-free DLC films have a high friction in dry conditions. The friction performance of hydrogenated and hydrogen-free DLC films is schematically represented in Fig. 1 indicating the high, low and superlow regimes of friction performance.

The superlow friction performance of hydrogenated DLC films in dry and inert environments has been attributed to the hydrogen-terminated dangling bonds with weak van der Waals forces acting in the contact between surfaces. In the humid oxygen-containing environment, this mechanism will be disturbed by water vapour molecules causing a tenfold increase in friction. Another mechanism affecting the tribological performance of the DLC films is the

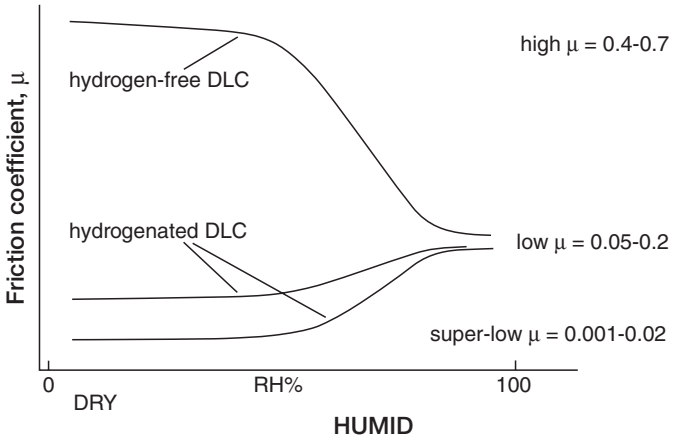

Fig. 1 The effect of humidity on the friction performance of hydrogenated and hydrogen-free DLC films as the relative humidity of the environment is increased

graphitization, which occurs on the contact surface of DLC films under tribological action. In the micrographitization process, the mechanical interactions between the sliding interfaces lead to graphitization at the micro-contact regions. In different atmospheres also material transfer will occur and the formation of transfer layer is evident, as reported by several authors. These layers have been shown to influence both the friction and wear performance of DLC films and counterparts.

The wear rates of DLC films are typically in the range 10^{-6} to 10^{-10} mm^3 (Nm)$^{-1}$ (see Table 1) and the wear resistance varies according to the structural features of the DLC films. Moreover, the environment can influence the wear behaviour, since a correlation has been found for the friction and wear performance of the DLC films. In general, the high friction is accompanied by high wear, as reported for the hydrogen-free films in an inert gas or in vacuum. Close correlation has also been shown between the friction and wear coefficients of hydrogenated DLC films in dry nitrogen, since the wear rates decrease with the decreasing friction coefficient as shown in Fig. 2 [22].

3.1 The Friction and Wear Performance of Hydrogenated DLC Films in Vacuum and Inert Environments

Hydrogenated DLC films have low friction coefficient in vacuum and in inert environments. Already in the pioneering work of Enke et al. [18], friction coefficient values of 0.005–0.02 were measured when the hydrogenated DLC

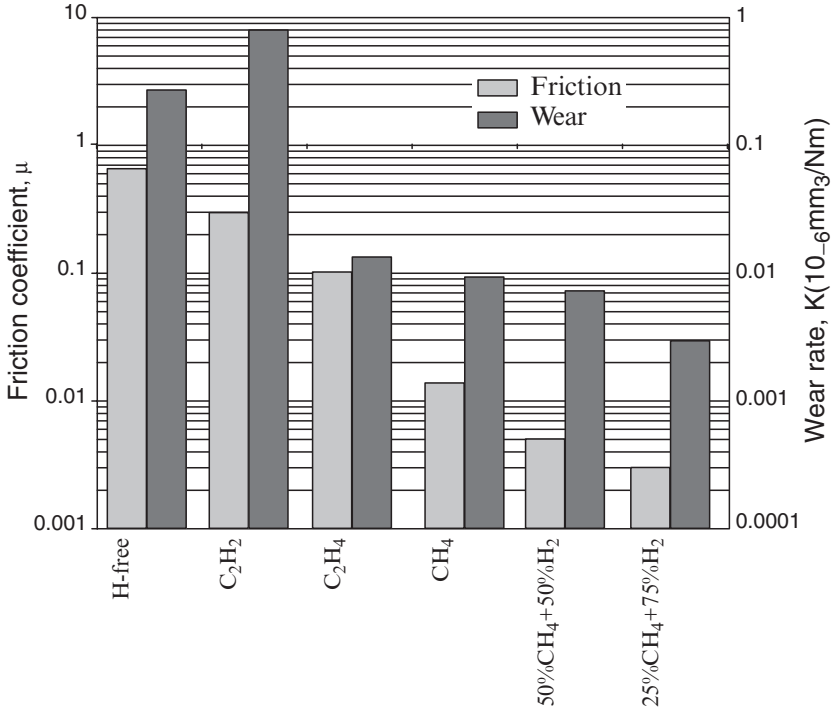

Fig. 2 The friction coefficients and wear rates of DLC films derived from different carbon sources and containing various hydrogen to carbon ratios. The tests were carried out in dry nitrogen. (After [22].)

films were sliding against steel in vacuum conditions ($p_{H_2O} = 10^{-8}$ Torr). As the partial pressure of water vapour increased (10^{-1} Torr), the friction increased to 0.19. A similar performance was also observed in nitrogen atmosphere as the relative humidity was increased [17,18]. Memming et al. [89] also measured friction values down to 0.02 in ultra-high vacuum (UHV), in dry nitrogen and in low humidity (<1% RH) conditions. However, in humid nitrogen and oxygen the friction coefficient values were about 0.25 and increased in dry oxygen up to 0.6. Similar observations have also been made by several other authors [13,24,61,98,108]. Examples of typical friction and wear rate values reported for hydrogenated DLC (a-C:H) films are represented in Table 2.

3.1.1 Hydrogenated DLC Films with Superlow Friction Performance in Inert Environment

The low friction performance of hydrogenated DLC films has been shown to reach superlow values in inert and dry environments. Donnet et al. [13] measured the friction coefficient values in the range 0.006–0.008 for steel balls sliding against

Table 2 The friction coefficient values and wear rates of the hydrogenated DLC coatings tested in different environments

DLC film		Tribological testing						
Film (substrate)	Deposition technique	Counter material	Load [N]/[GPa]	Speed [ms^{-1}]	Environment	Friction Coefficient	Wear rate [$x10^{-6}$ $mm^3(Nm)^{-1}$]	Reference Author year
a-C:H (Si)	PACVD	Steel	1 N	(1000 rpm)	Vacuum (p_{H2O}= $1.3x10^{-6}$ Pa)	0.005–0.02	–	[17,18]
					RH 100 %	0.19	–	
a-C:H (Si)	PACVD	Steel	0.8 N		UHV	0.02	–	[89]
					Dry N_2	0.02	–	
					Humid N_2	0.25	–	
					Dry O_2	0.6	–	
a-C:H (Si3N4)	PACVD	Si_3N_4	1–1.7 N/ 0.91 GPa	50–$133{\cdot}10^{-6}$	Air	0.2–0.3	–	[97]
					Nitrogen	0.01–0.15	–	[98]
					Vacuum +high temp	0.1–1.3	–	
a-C:H (SiC)	IB	Si_3N_4	1–20 N / 0.4–1.5 GPa	0.026	Ar	0.04	0.00046	[24]
					N_2	0.03	0.0009	
					Dry air	0.07	0.0192	
					Ambient air	0.15	0.0724	
a-C:H (steel)	d.c.CVD	Steel	2 N	0.03-0.09	Vacuum 10-6 Pa	0.08	–	[108]
a-C:H (Si)	PACVD	Stainless steel	4 N/ 1 GPa	0.0017	10^{-7}–10^{-1} Pa	0.006–0.008	–	[13]
					10 Pa–50 Pa	0.01–0.07	–	
					10^5 Pa (RH 40 %)	0.15	–	
					Dry N_2 (RH<2%)	0.02	–	

a-C:H (AISI 440B)	PACVD	Al_2O_3	5–40 N	0.1–3.0	Ambient air (50 % RH)	0.02–0.13	0.046–0.16	[118]
a-C:H	PACVD	AISI 52100	3.3-20 N/ 0.8–1.45 GPa	1-500 rpm	Vacuum ($2x10^{-4}$ Pa)	0.003–0.009	2.2–7.8	[134]
						0.006–0.015	0.026–0.091	
					Dry N_2	0.10–0.23	0.098–0.194	
					Amb. air (RH 50 %)			
a-C:H (steel)	PACVD	a-C:H (AISI M50)	10 N/ 1.04 GPa	0.5	Dry N_2	0.003–0.0005	0.00046–0.00015	[30]
a-C:H/ diff. at.% H (Si)	PACVD	Steel	1 GPa	0.0012	Vacuum ($<10^{-7}$ Pa)	0.004–0.068	-	[123]
						-	0.018–0.11	
					Ambient air (25-40 %RH)			
a-C:H (Si)	PACVD	SiC	1 N	0.1	Vacuum	0.17	0.0017	[149]
					N2	0.06	0.0022	
					O2	0.1	0.515	
					Dry air (RH 4-6 %)	0.07	0.113	
a-C:H (Si)	PACVD	AISI 440C	1.06–3.08 N/ 1.2–1.8 GPa	0.0042-0.025	High humidity (RH 90–95 %)	0.12–0.17	0.016–0.022	[150]
					Low humidity (RH 17–20 %)	0.05–0.22	0.022–0.025	
a-C:H (Si)	PACVD	AISI 440C	10 N/ 1.6 GPa	0.02	Ambient air (RH 25–45 %)	0.03–0.1	0.02–0.1	[127]
a-C:H (AISI 440C)	PACVD	AISI 440C	9.4 N	0.016	Ambient air (RH 40–60 %)	0.15–0.25	0.19–0.057	[104]
a-C:H (AISI 440C)	ECR–CVD	AISI 52100	1–10 N/ 0.7–1.5 GPa	0.02–0.15	Ambient air (RH 45–55 %)	0.18–0.22	0.03–0.08	[75,76]
a-C:H (Si)	PACVD	AISI 52100	2 N	2	N_2 RH<5 %	0.035	0.0125	[78]
					N_2 RH 100 %	0.2	0.1357	

a-C:H film in vacuum. In dry nitrogen (10^5 Pa, RH <1%), similar friction values were measured. Verkammen et al. [134] measured low friction values for the PACVD deposited a-C:H films sliding against steel in the range 0.003–0.009 in vacuum (2×10^{-6} mbar) and 0.006–0.015 in dry nitrogen. The film wear rates were in the range 2.2×10^{-6} to 7.8×10^{-6} $mm^3(Nm)^{-1}$ and 0.026×10^{-6} to 0.091×10^{-6} $mm^3(Nm)^{-1}$, respectively. Both the friction and wear could be reduced by using a-C:H coated pin sliding against the a-C:H coating reaching friction values in the range 0.002–0.09 in different atmospheres.

Extremely low friction values have been measured for the highly hydrogenated DLC films deposited by PACVD. The superlow friction values, 0.003–0.005, were measured by Erdemir et al. [30] when sliding DLC against DLC in dry nitrogen. The superlubricity is related to adhesive friction on a molecular scale and thus it is necessary to avoid friction occurring on the macro- and microscale. The ploughing friction can be avoided by using hard substrates, and the asperity collisions can be avoided by using nanosmooth surfaces, like polished Si wafers, sapphire or cleaved mica surfaces. The effect of surface roughness on friction was shown by Erdemir, as he reported the friction evolution for the same hydrogenated DLC film deposited on two substrates with different surface roughness. The rougher steel disc (R_a = 20 nm) performed higher friction in dry nitrogen (0.007) compared to the film deposited on smooth (R_a = 0.7 nm) sapphire disc (0.003) as represented in Fig. 3 [20].

According to Donnet et al. [14] the nanosmooth surfaces can be generated between two smooth DLC coatings or between the DLC film and the transfer layer formed on the sliding counter surface.

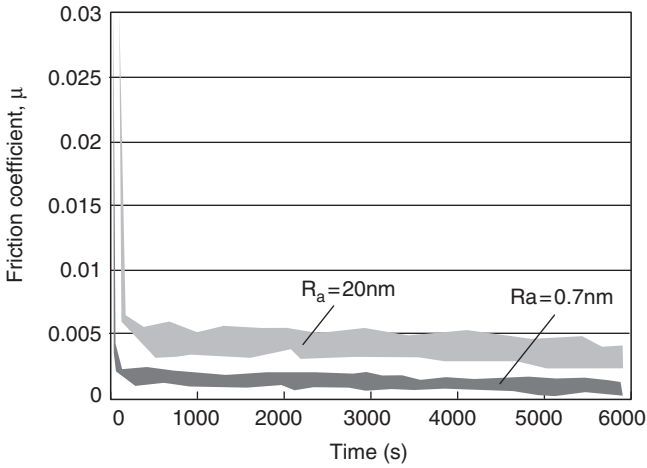

Fig. 3 Friction coefficient of highly hydrogenated DLC films deposited on steel (R_a = 0.020 μm) and on sapphire (R_a = 0.0007 μm) substrates. Tests were carried out in dry nitrogen, with load of 10 N and sliding velocity of 0.3 ms^{-1}. (After [20].)

Donnet and Grill reviewed the influence of coating properties on the friction performance of a-C:H films in UHV. Ultra-low friction ($\mu < 0.01$) was reached, when the hydrogen content of the film was high enough (about 40 at. %), the carbon network was sufficiently cross-linked and the film structure had a noticeable fraction of hydrogen unbonded to carbon [11]. The minimum hydrogen content required for the superlow friction performance in UHV was later explained to be dependant also on the deposition method employed by Sánchez-López et al. [123].

Erdemir et al. observed the tribological performance of hydrogenated a-C:H films deposited by PACVD technique to be changed according to the source gas composition used in deposition. The lowest friction performance in dry nitrogen atmosphere was measured for the DLC against DLC contact, when the films were obtained with gas compositions having high hydrogen to carbon ratio. The superlow friction values, in the range 0.003, were measured for the films derived from the gas mixture of 25% methane and 75% hydrogen. The coating was highly hydrogenated and it was named nearly frictionless carbon (NFC). With increasing amounts of hydrogen in the source gas mixture, the wear rate of the coating also decreased in dry nitrogen, accompanied by decreasing friction. In ambient humid environment (26–44% RH) similar friction coefficient values in the range 0.1–0.2 were measured for the films deposited with different source gas mixtures [28–30].

Sánchez-López et al. [123] suggested the viscoplastic behaviour of the coating being an indicator for predicting the friction performance of the coatings in UHV. The presence of unbonded hydrogen trapped in the structure of the coating increases the viscoplasticity of the coating and decreases the hardness of the coating. Fontaine et al. [33,34] determining the viscoplastic exponent for a-C:H coatings and established a correlation between superlow friction and viscoplasticity for the a-C:H films. The authors also suggested the possibility to control the viscoplaticity and hardness of the coating independently in order to obtain high hardness with superlow friction performance.

3.1.2 The Effect of Hydrogen in Inert Environment

Hydrogen has been shown to play a key role in the tribological performance of hydrogenated DLC films in an inert environment. Already Paulmier et al. [108] reported the reduction of friction caused by the adsorption of atomic hydrogen on the DLC surface as the adsorbed hydrogen decreased the chemical activity of DLC film. Further Zaidi et al. [145,146] and Le Huu et al. [72,73] observed that H^+ was desorbed while tribotesting the DLC film in vacuum, but a small quantity of water vapour stopped the desorption of H^+. The authors claimed the hydrogen to be weakly bonded in C–H bonds under vacuum conditions and desorption of hydrogen to occur at low temperatures due to frictional heating. Hydrogen was claimed to act as a lubricant reservoir reducing the friction, but at the same time increasing the wear.

Donnet et al. studied the friction performance of DLC coatings with hydrogen content of 34 at. % in UHV and noticed that the coating experienced a drastic increase of friction in vacuum after a short period of superlow (0.005) friction. This high friction in inert atmosphere could be reduced by introducing at least 1 kPa of hydrogen gas in the vacuum chamber as represented in Fig. 4. The low friction performance could be further enhanced by increasing the test temperature in order to enhance the diffusion of hydrogen species. The effect of hydrogen was attributed to the favourable friction process on the molecular scale due to systematic formation of a carbonaceous transfer film during the tribological test. The sliding was explained to occur between the two nanosmooth contact surfaces, namely the deposited films and the transfer film [14].

Fontaine et al. also used hydrogen to control the friction performance of a-C:H films in inert atmospheres. The intermediate and high hydrogen pressures (100–1,000 Pa) were observed to provide a healing effect on the transfer layer and the superlow friction performance of the a-C:H film with low intrinsic hydrogen content. The authors also noticed the effect of the oxide layer formed on the counter surface. This oxide layer had to be removed either by etching or by sliding action, in order to allow the favourable reaction between carbon and metallic iron to occur, leading to build-up of the transfer film [33–35].

The superlow friction performance of highly hydrogenated a-C:H films in dry nitrogen is explained to be governed by the presence of hydrogen. On the surface

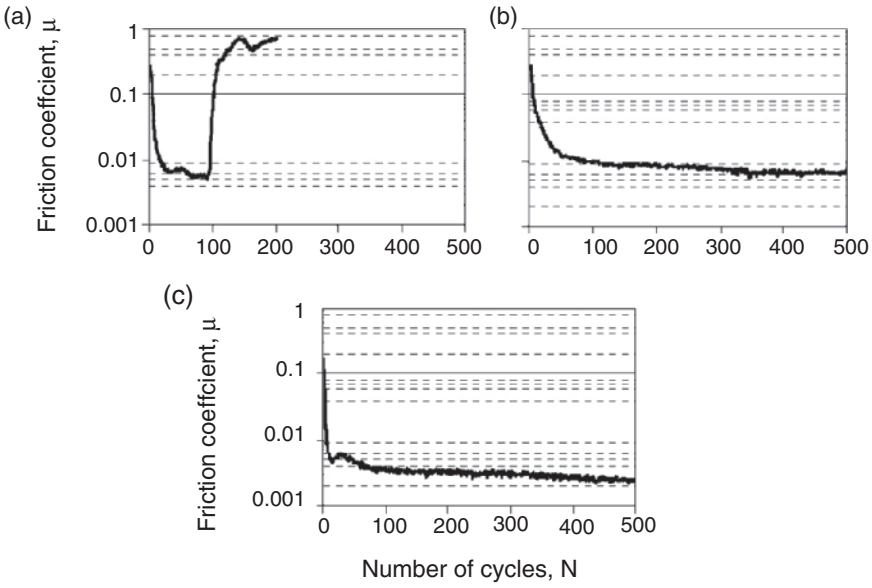

Fig. 4 Friction coefficient as a function of sliding cycles of hydrogenated (34 at. % H) DLC film tested (a) in UHV conditions at room temperature (25°C) and in atmosphere of pure hydrogen (1 kPa) (b) at room temperature (25°C) and (c) at 150°C. (After [14].)

of films prepared in highly hydrogenated plasmas, the carbon atoms are strongly bonded to hydrogen, eliminating the free σ-bonds on the surface. Some carbon atoms are also believed to be dihydrogenated (i.e. two hydrogen atoms bonded to one carbon atom), with sliding occurring between two hydrogen-terminated surfaces providing superlubricity in inert atmosphere, e.g. in dry nitrogen. Atomic and/or molecular hydrogen within the films can also serve as a reservoir that can continuously replenish and terminate the σ-bonds that can be exposed by mechanical wear or thermal desorption [19,20].

The superlow friction performance of hydrogenated DLC films in inert environments is thus attributed to the hydrogen-terminated surfaces interacting through weak van der Waals forces. According to Gardos, these hydrogen-terminated bonds have a low bonding strength of about 0.08 eV per bond. In the humid oxygen-containing environment, the coefficient of friction increases, which corresponds to an increase in bond strength from about 0.08 eV per bond to about 0.21 eV per bond, which is typical for hydrogen bonding of water molecules at C=O sites [39].

3.1.3 The Effect of Gas Adsorption in Inert Environment

The adsorption of gasses on hydrogenated DLC film surface has been observed to have an influence on the friction performance in an inert environment. In the tests performed in dry nitrogen, and in vacuum, against steel (AISI 52100), the friction coefficient of a-C:H film varied from 0.003 to 0.009 in vacuum (2×10^{-6} mbar) and from 0.006 to 0.015 in dry nitrogen. The dependence of dwell period and sliding speed was observed to have an influence on the friction performance in dry nitrogen and in vacuum. The steady-state friction was a function of sliding speed and decreased with increasing speed. The static friction was observed to be a function of the dwell period increasing with increasing dwell period, which was attributed to adsorption phenomena. The tests in ambient air did not show a similar effect [134].

The effect of gas adsorption on the highly hydrogenated DLC films was studied by tribotesting in dry nitrogen by Heimberg and co-authors. With sliding speeds 0.1 mms^{-1} and higher superlow friction coefficient values (0.003–0.008) were measured, but as the sliding speed reduced, the friction coefficient increased to values typically measured in ambient air (0.01–0.1). Tests with different time-delays between sliding cycles showed increasing friction coefficient as the exposure time was increased as shown in Fig. 5. The superlow friction could be sustained, suppressed and recovered as a function of exposure time. The rise in friction coefficient was found to be in good quantitative agreement with the adsorption kinetics predicted by Elcovich equation for gas adsorption onto carbon [49].

A model of fractional coverage based on the adsorption of environmental contaminants and their removal through the sliding contact was developed by Dickrell et al. [9]. The model was found to fit the experimental friction data

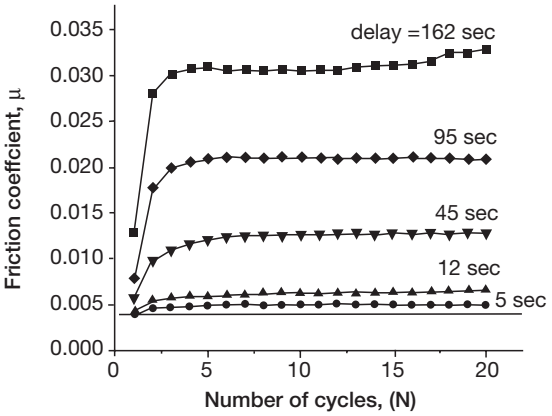

Fig. 5 The friction coefficient of highly hydrogenated DLC film is shown as a function of reinitialized cycle number for five different time delays. The solid line indicates the friction coefficient measured in the continuous high speed test ($\geq$1 mms^{-1}) with friction coefficient of 0.004. (After [49].)

with a constant deposition rate of adsorbates, if the removal fraction increased with increasing speed and decreasing dwell time. The computer simulations by Borodich and Keer also suggested microscopic processes, such as breaking and forming of interatomic bonds, to affect macroscopic phenomena, like friction. In addition, the initial roughness of the DLC surface was suggested to considerably influence the probability of breaking bonds during mechanical removal of adsorbates, and on the process of the gradual tribochemical wear of DLC films [6].

3.2 The Friction and Wear Performance of Hydrogenated DLC Films in Ambient Air and Humid Environments

The hydrogenated DLC films are known to be sensitive to the presence of oxidizing elements, like water vapour and oxygen, and the friction coefficient in ambient air is typically higher than in inert environments. The friction coefficient values of 0.005–0.02 measured for the hydrogenated DLC films sliding against steel in vacuum (p_{H_2O} = 10^{-8} Torr) increase up to values in the range 0.2 as the partial pressure of water vapour is increased as shown in Fig. 6.

A similar trend was also observed in nitrogen atmosphere when the relative humidity increased [17,18]. According to Donnet et al. [15] the friction is strongly influenced by water vapour at partial pressures higher than 0.05 kPa (2% RH) increasing the friction coefficient up to 0.15 accompanied by severe wear. The typical values of friction coefficient reported for hydrogenated DLC films

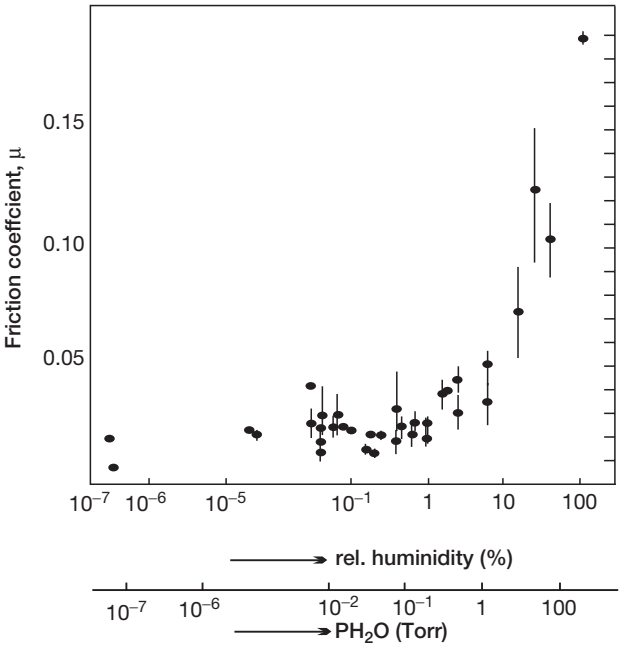

Fig. 6 The friction coefficient (μ) of hydrogenated DLC film sliding against steel pin as the relative humidity is increased. (After [18].)

sliding in ambient air against steel are in the range 0.1–0.3 and against ceramic materials in the range 0.02–0.15 (Table 2).

The friction coefficient values of highly hydrogenated DLC films tested against themselves in UHV also increased from superlow value 0.004, when H_2O or O_2 was introduced in the chamber. As described in Fig. 7 the friction coefficient started to increase with H_2O vapour pressure exceeding 0.01 Torr (1.3 Pa) and increased up to 0.07 with vapour pressure 10 Torr (1.3×10^3 Pa) representing about 50% RH. The O_2 pressure had an analogous effect on friction performance, but higher O_2 pressure was required in order to induce a similar increase in friction. The N_2 gas has hardly any effect on the friction. Under H_2O vapour pressure, the friction increase may be caused by the adsorbed layer of H_2O molecules covering the film surface and increasing the dipole-like interaction of the DLC film interfaces. The friction changes were reversible and no evidence on tribochemistry was observed by Auger Electron Spectroscopy (AES). In the case of hydrogenated DLC sliding against hydrogenated DLC, the friction changes are suggested to be dominated by weakly physisorbed gas molecules [3,4,20,62].

Similar increase in friction coefficient with increasing humidity and with the presence of oxygen has been observed by Li et al. [78] in tests carried out with steel balls (AISI 52100) against hydrogenated DLC. The tests carried out in humid

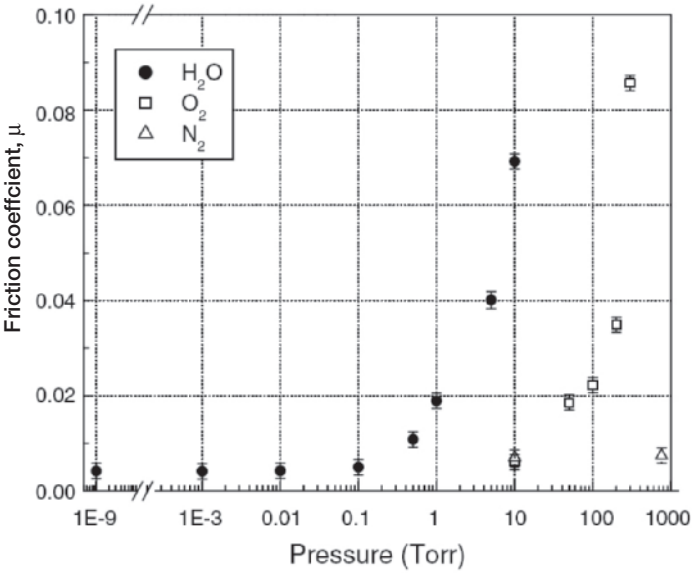

Fig. 7 Friction coefficient of a highly hydrogenated DLC films under varying pressures of H_2O, O_2 and N_2. (After [62].)

air (40% RH), humid nitrogen (40% and 100% RH), dry oxygen (<5% RH) and dry nitrogen (<5% RH) showed low friction coefficient in dry nitrogen, but increased friction for increased humidity. The highest friction was experienced in oxygen atmosphere. The increasing humidity was also observed to increase the wear rate of the DLC film as shown in Fig. 8 for the N_2 environment.

Under humid conditions water molecules are expected to cover the surface. The studies on the effect of water adsorption on DLC films carried out by Tagawa et al. [129] showed that the hydrogenated DLC films had a higher advancing contact angle of water (83–97°) compared to hydrogen-free DLC films (77°) measured by quartz crystal microbalance (QCM). The hydrogen termination of the dangling bonds on hydrogenated DLC film surface increases the contact angle of water, thus leading to decreased adhesion force and to lower friction. The adhesion force measured by an environment-controlled microtribometre reached the highest values for the W-tip sliding against hydrogenated DLC films deposited on Si, with relative humidity values of 40–60%, which represents water coverage of a few molecular layers between contacting surfaces.

In the case where the water molecules are weakly adsorbed on the hydrogenated DLC surface, they can be easily displaced by, e.g. the sliding counterpart. The effect of sliding speed on friction coefficient was observed to have a decreasing trend in tests carried out in humid air (50% RH) with hydrogenated DLC films sliding against steel (AISI 52100) or Al_2O_3 balls. The friction coefficient decreased from 0.42 to 0.10 against steel and from 0.10 to 0.02 against alumina, as the sliding speed increased from 0.1 to 3 ms^{-1} [114] The influence of sliding speed was also

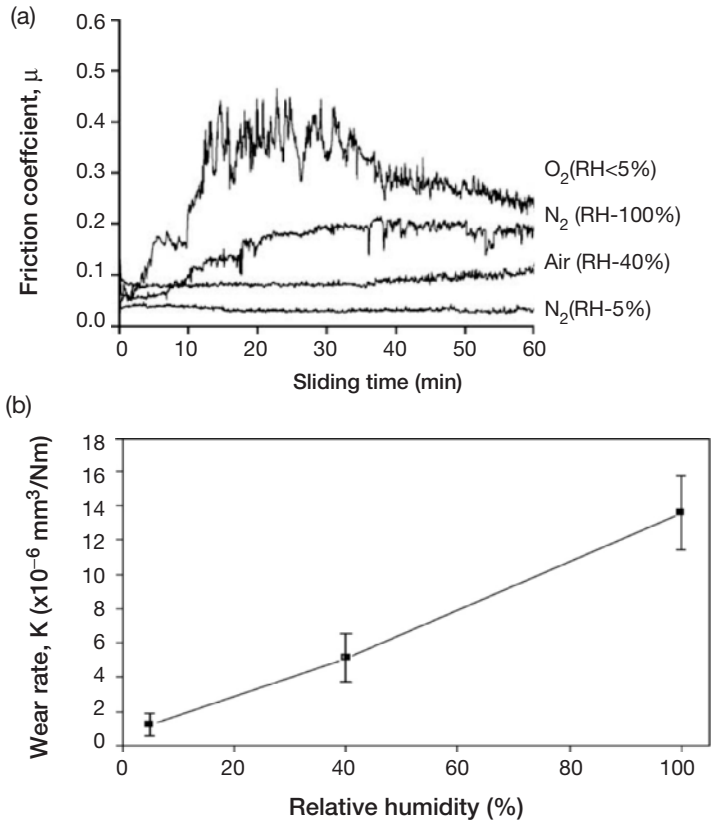

Fig. 8 (a) The friction coefficient of hydrogenated DLC film at different relative humidity in nitrogen environment (<5, 100% RH) and O_2 (<5% RH) environment and in humid air (40% RH), and (b) the wear rates of DLC film at different relative humidity in nitrogen environment. The steel pin was slid against the DLC film with a normal load of 2 N and the sliding velocity of 2 ms^{-1}. (After [75,77].)

verified in sliding tests carried out under different H_2O pressures. The results showed that higher H_2O pressure required higher sliding velocity to exhibit a similar decrease in friction compared to lower pressure conditions [62].

The tribological tests carried out in ambient air (25–40% RH) with reciprocating pin-on-flat test configuration by Sánchez-López et al. [123] showed that the wear resistance of hydrogenated DLC films is related to the intrinsic structural film properties that are controlled by the deposition conditions. It was observed that the best wear resistance of DLC films was related to higher hardness and higher Young's modulus accompanied with a lower amount of hydrogen in the structure. The hardness and Young's modulus is increased as the hydrogen content decreases combined with the higher cross-linking of the carbon network in the hydrogenated DLC film.

3.2.1 Formation of Transfer Layer

A frequently observed feature in tribological testing of DLC films is the formation of transfer layer. Formation of a transfer layer has been reported from the early days of DLC research by, e.g. Memming et al. [89], Miyoshi et al. [98], Sugimoto and Miyake [126] among the first authors. The formation of carbonous transfer layer on the sliding surface was observed to reduce the friction coefficient. A drastic decrease in friction was reported by Miyoshi [98] as a layer of reaction products was formed. In another case, the friction reduction was observed as the transfer of hydrocarbons with a specific orientation to the ball surface was generated [126]. The formation of transfer layer has been observed to be enhanced by the increased sliding distance (20–25 km) leading to friction reduction (from 0.16 to 0.05–0.07) [25,88]. Moreover, the sliding speed has been observed to enhance the layer formation as shown in Fig. 9, where the largest and most compact transfer layer was observed for high load and high sliding speed. The thick layer formation was also observed to decrease the wear rate of the hydrogenated DLC film and the steel pin sliding against the coated surface [117]. The transfer layer formation is typically observed in tests carried out in ambient air, but also in UHV when the DLC film was sliding against steel [13].

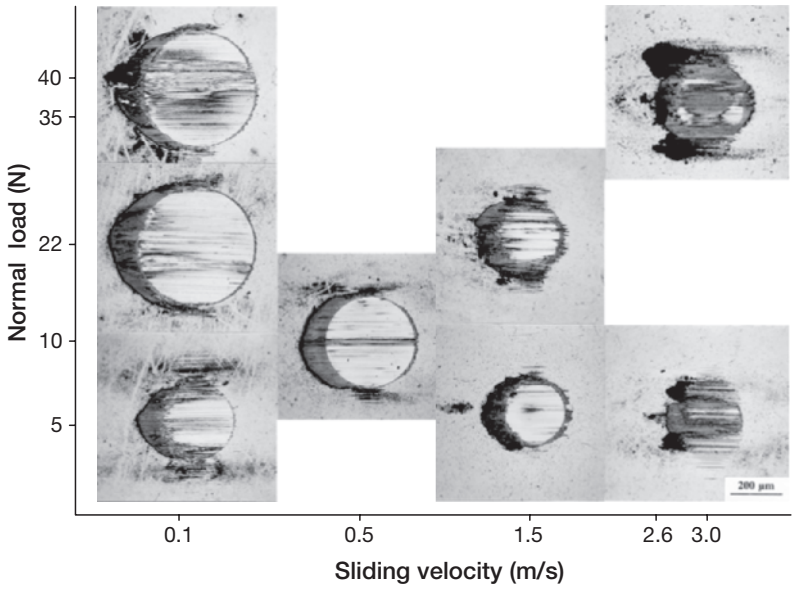

Fig. 9 The wear surfaces of the steel pins slid against the PACVD deposited hydrogenated a-C: H film. The sliding speed was varied in the range 0.1–3.0 ms^{-1} and the normal load in the range 5–40 N

3.2.2 The Graphitization of the Hydrogenated DLC Film Structure

The micrographitization was suggested to be responsible for the low friction performance of DLC films by [56]. In 1993, Wei et al. [140] observed, by Raman analyses, the formation of disordered graphite on the wear surface of the hydrogenated DLC film due to fatigue wear in lubricated rolling-contact fatigue tests. Erdemir and co-workers discovered in pin-on-disc sliding tests carried out in dry nitrogen atmosphere, a transfer layer formation on the wear surface of a steel pin. The layer was rich in carbon and had a disordered graphitic structure as verified by micro-laser Raman spectroscopy [26]. Later, graphitization was also detected to occur in ambient atmosphere [83]. The mechanism was explained to occur as the accumulation of sliding-induced heat causing the gradual destabilization of C–H bonds in the hydrogenated tetrahedral structure.

Since hydrogen atoms are expected to promote the sp^3 bonding of the hydrogenated DLC structure, the release of hydrogen will destabilize the tetrahedral bonding and enhance the transformation of tetrahedral sp^3 structure to graphite-like sp^2 structure. The removal of hydrogen can, thus, trigger the transformation of the sp^3 structure into a graphite-like sp^2 structure. The transformation of hydrogenated DLC structure to graphite is thus suggested to gradually proceed at asperities due to repeated tribological contacts that lead to graphitization resulting in microcrystalline graphite [23,82,84,85]. Besides this wear- and friction-induced annealing on local contact areas, the sliding-induced strain energy can also further assist the transformation process [84].

The graphitization has been detected by several analysis techniques. Micro-laser Raman was used by several authors evidencing the presence of disordered graphite structure in the carbonous transfer layer or in the debris particles at sliding interfaces [26,79,83,121,151]. In Fig. 10, the micro-laser Raman spectra of the transfer layer and the wear debris generated in the tests carried out with steel pin sliding against DLC film reveal a similar structural chemistry to the crystalline graphite. The two broad Raman bands, at 1,336 and 1,594 cm^{-1}, match the D and G bands of crystalline graphite. The signal peaks of the transfer layer are not as sharp as that of the graphite, which is probably due to the small particle size, high structural disorder in the transfer layer and to phonon-damping effects.

Besides Raman analysis, the electron diffraction pattern analysis, FTIR analysis and bright-field/dark-field imaging has evidenced the presence of graphite in the tribocontact of hydrogenated DLC films [82,83,85]. The nanoindentation analysis also revealed that the transfer layer with a graphitic nature was characterized by lower values of Young's modulus (E) and hardness (H) compared to original coating. [110].

A higher sliding velocity was observed to enhance the friction reduction during tribotesting suggesting transformation of DLC to a graphitic state to be a direct consequence of frictional heating [27,14]. By using a software program,

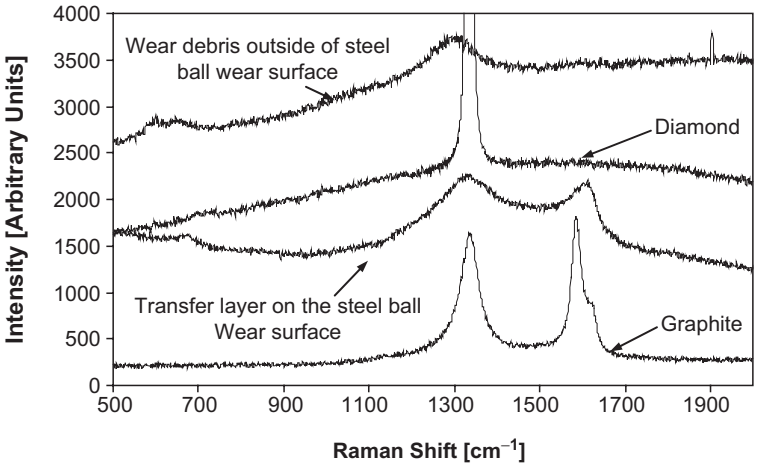

Fig. 10 Raman spectra of the transfer layer formed on the pin wear surface and the wear debris collected outside the wear surface of the steel pin. Raman spectra of the crystalline graphite is provided as a reference. (After [122].)

the flash temperatures generated at the contact asperities were estimated. When the steel pin was sliding against hydrogenated a-C:H with high load (up to 40 N) and sliding speed (up to 3 ms^{-1}), the flash temperature reached values in the range 350°C as calculated by Ronkainen and Varjus [27]. Other estimations carried out by using a simple model for asperity temperature rise, represented temperature values in the range 100–300°C for the metal pins and in the range 220–1,245°C for the ceramic pins sliding against hydrogenated DLC with an increasing trend for the repeated contacts [84]. The hydrogen effusion has been observed to occur in a-C:H films at elevated temperatures 300–600°C depending on the deposition parameters used for the coating deposition [141]. As the flash temperature on the surface asperities of DLC-coated surface is increased during repeated sliding, the hydrogen effusion is likely to occur and some of the DLC film structure will transform to graphite-like carbon.

The graphitization was observed to be sensitive to humidity effects. The low humidity level (0% RH) enhanced the graphitization rate due to reduction of the effect of water molecules, which could be observed as a shortening of the sliding distance required for the steady-state low friction performance and for the formation of graphitized tribolayer at low humidity conditions. Conversely, the graphitization rate decreased in high humidity (100% RH) and at lower temperature (−10°C) conditions [85].

3.2.3 Tribochemisty of Hydrogenated DLC Films

In humid environments and in ambient air, oxidizing species, like H_2O and O_2, are present, influencing the tribological performance of materials. The tests carried out at

water vapour partial pressures of 1 hPa (4% RH) showed friction coefficient of 0.15 accompanied by severe wear reported by Donnet and co-workers. The authors observed wear particles consisting of ferrous oxides (Fe_2O_3) embedded in an amorphous carbon structure [15]. The influence of atomic oxygen was observed to influence the friction performance of hydrogenated DLC films more than molecular oxygen, by increasing the friction value from 0.08 measured in inert environment, up to 0.22. This was attributed to the higher sticking coefficient of atomic oxygen compared to the molecular oxygen, leading to increased chemical activity of the diamond-like coating due to adsorbed oxygen [108].

During tribological testing of DLC films in ambient air, occurrence of material transfer has been observed by several authors [36,96,107,118,119]. The SIMS analyses and Auger elemental imaging, for example, showed that a transfer layer consisting of carbon, iron, chromium and oxygen was formed when a steel pin was slid against the DLC film in humid (50% RH) air. When Al_2O_3 pin against hydrogenated DLC film was used, aluminum and oxygen together with carbon species were detected after sliding in humid air as detected by Ronkainen et al. [118,119].

In humid conditions, the surface interaction of the steel ball with water vapour seems to accelerate the surface oxidation of the steel ball, resulting in high concentration of iron (Fe) in the wear debris. The Auger analyses showed that the wear debris contained large amount of iron when a-C:H film was slid against steel counter body (AISI 52100) in humid air or in dry oxygen. The friction coefficient increase from 0.025 to 0.2 accompanied with the increase of Fe concentration in wear debris was detected by Park and co-authors as the humidity of the surrounding air increased from 0% to 90% RH as shown in Fig. 11. Moreover, in dry oxygen environment, the friction against steel was high (0.2–1.0) accompanied by the Fe incorporation in the wear debris. However, for the sapphire balls slid against a-C: H film in dry oxygen, low friction values (0.02–0.07) were detected, even though aluminum was detected in the wear debris [107].

Kim et al. reported the effects of oxygen and humidity on friction and wear of highly hydrogenated (55 at. % H) a-C:H films produced by PACVD. When the films were slid against silicon nitride ball in air and argon atmosphere with dry (<3% RH), intermediate (50% RH) and saturated (95% RH) humidity conditions, the friction coefficient increased from 0.06 to 0.19 as the humidity increased. In humid and oxygen atmospheres, the tribochemical reaction with DLC was observed, and oxidized hydrocarbon species (C=O) were created forming polymer-like wear debris, as detected by FTIR microprobe. This was verified at higher loads (9.8 N) [67]. For the low loads (7.8 kPa), the creation of C–O bonds was reported by Olsen et al. [105]. According to Zaidi et al. [144] oxygen forms various types of oxygenated complexes on the carbon surface as the film is in contact with the atmosphere. The formation of oxygen complexes is strongly dependent on the relative humidity, which might be the reason for the negative effect of humidity on the friction and wear performance of the hydrogenated carbon films. Oxidation of the unstable polymer-like surface layer could, therefore, be the main reason for the degradation of the frictional behaviour of the coating.

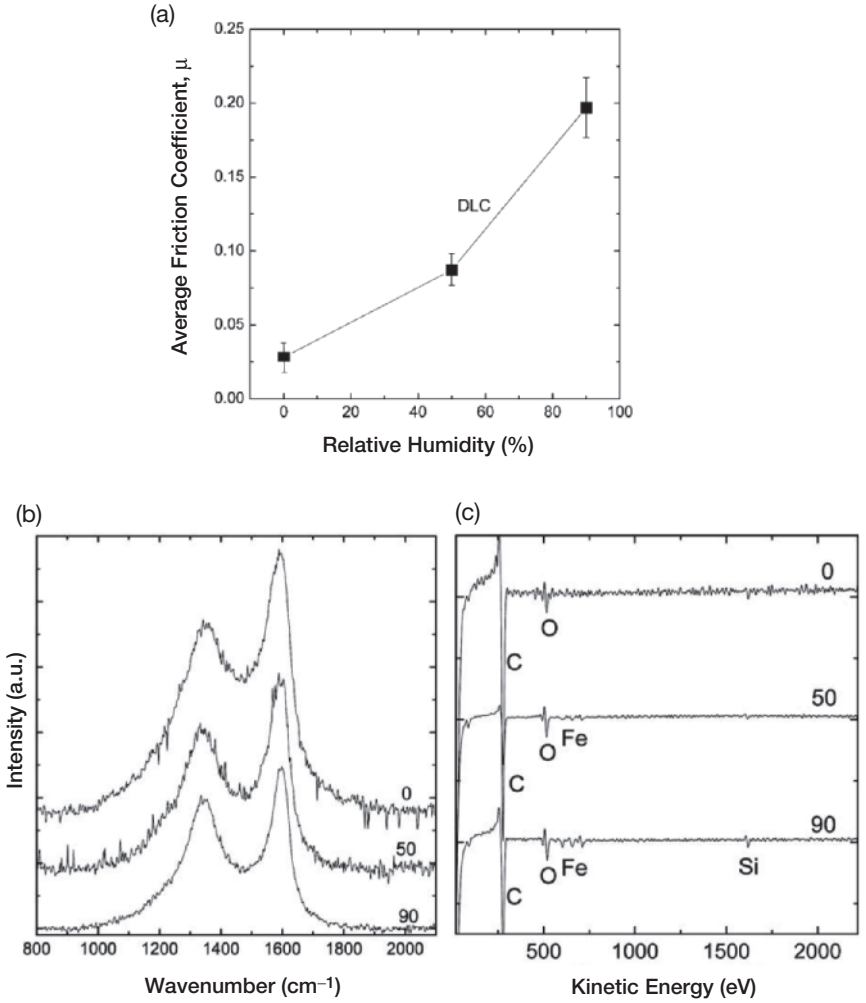

Fig. 11 (a) The dependence of the average friction coefficient of hydrogenated DLC film on relative humidity (0, 50 and 90% RH) in ambient air. (b) Raman spectra and (c) Auger spectra of the wear debris formed by sliding a steel ball against a DLC film in ambient air (0, 50 and 90% RH). (After [107].)

Fukui et al. [36] analysed the wear tracks and wear debris generated in the tribological tests carried out with a-C:H film sliding against steel pin in pin-on-disc tests in humid air (65% RH). According to the EDS spectra the wear debris contained carbon, oxygen and iron, and it was presumed that most of the powdery wear debris was generated by wear of the steel pin. According to the time-of-flight secondary ion mass spectroscopy (TOF-SIMS), high-order mass fragments were detected inside the wear track of the coating. The presence of mass numbers 42 (C_3H_6), 43 (C_2H_3O), 58 (C_4H_{10}), 84 (C_6H_{12}), 104 (C_7H_4O, C_8H_9), 138 ($C_6H_2O_4$), 149

($C_8H_5O_3$), 163 ($C_8H_{19}O_3$) and 219 ($C_{15}H_{23}O$) were found inside the wear track. These results differed from the original composition of the DLC film representing mass numbers 14 (CH_2) and 28 (C_2H_4). The presence of species with high-order mass numbers such as polymers (molecules of higher order hydrocarbons) inside the wear track assumes that polymerization occurs as the transfer layer is formed during tribotesting. These friction polymers contribute to the friction performance of hydrogenated DLC film in humid environment. Yoon et al. [143] also suggested the formation of a carboxylic acid soap when oxidized DLC films chemically reacted with ferrous oxide.

The tribological performance of DLC films in oxygen- and water-containing environments was explained to result from friction-induced physical and chemical interactions by Li and co-workers [76,77]. They carried out pin-on-disc tests with hydrogenated DLC films against steel in humid air (~40% RH), dry nitrogen (<5% RH), humid nitrogen (~100% RH) and dry oxygen (<5% RH). In dry nitrogen, the lowest friction coefficient was measured (0.035) with the formation of a carbon-rich transfer layer on the pin wear surface The worn DLC surface exhibits similar structure to the original film. However, in oxygen- and water-containing conditions, distinctive structural changes by x-ray photoelectron spectroscopy (XPS) was detected. On the worn surface, the concentration of oxygen was 3–4 times higher compared to the original film, and some traces of Fe species were also detected when oxygen or humidity were present. The XPS analysis of the wear surface of DLC film indicated the carbon 1s core level spectrum being shifted to a higher binding energy. The intensity of C–C (or C–H) decreased, while the intensity of C–O and C=O peaks increased and new peaks describing carboxylic acid (HO–C=O) groups were observed as shown in Fig. 12.

Li and co-workers further detected, by XPS analysis, Fe–C bonds on DLC wear surface after tribotesting DLC against steel in humid nitrogen and dry oxygen conditions, and Fe–O bonds after tests in dry oxygen. The concentration of oxygen elements and the intensity of C–O and C=O bonds indicated the cracking of the film chains and the oxidation of DLC film. The broken C–C and C–H bonds form macro-radicals, which in the presence of water or oxygen, would chemisorb water or oxygen molecules to form peroxide radicals (ROO*). The peroxide radicals could remove hydrogen atoms from water molecules or molecular chains of DLC film and form hydroperoxide groups (–COOH). Radicals could also react with water or oxygen molecules directly and generate peroxide radicals (R′OO*), which would react again. These processes, which are described in Fig. 13, will be repeated until the carbon network is terminated [75,77].

The friction-induced oxidation changes the surface chemical states from C–H bonds to oxygen-containing groups, which means an increase in the bonding strength from 0.08 eV per bond related to the van der Waals bonding, to about 0.21 eV per bond for the C–O and C=O sites. This results in increased friction values in humid environment [39]. The macro-radicals could also react with activated Fe atoms to form Fe–C bonds under frictional shearing action. The peroxide radicals could also react with Fe atoms to form ROO–Fe bonds. These interactions will lead to strong adhesive friction. Since the temperature at the

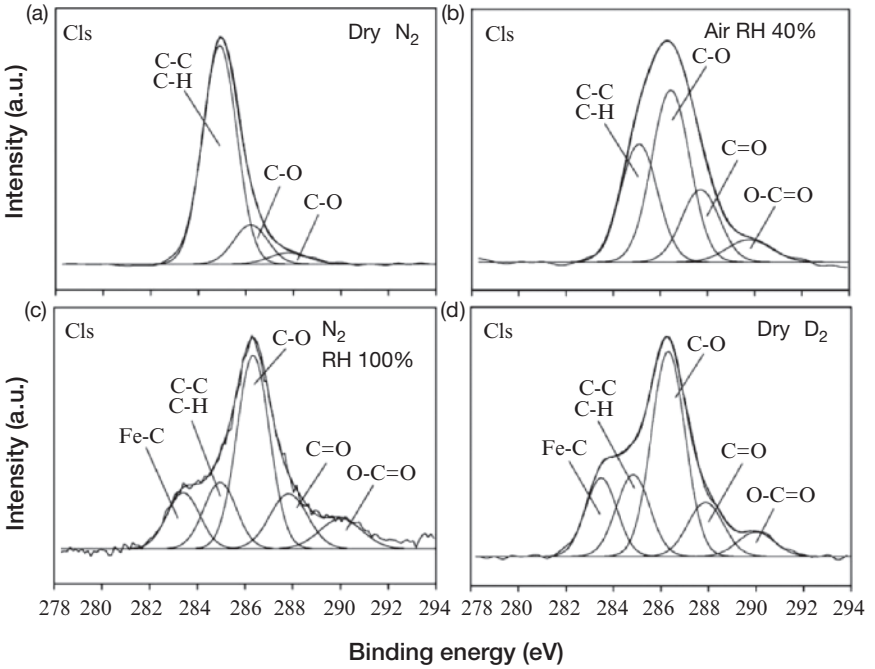

Fig. 12 The XPS spectra for carbon 1s states on the worn surface of hydrogenated DLC film tested in different environments, (a) in dry nitrogen (RH <5%), (b) in humid air (about 40% RH), (c) in humid nitrogen (about 100% RH) and (d) in dry oxygen (<5% RH). (After [75].)

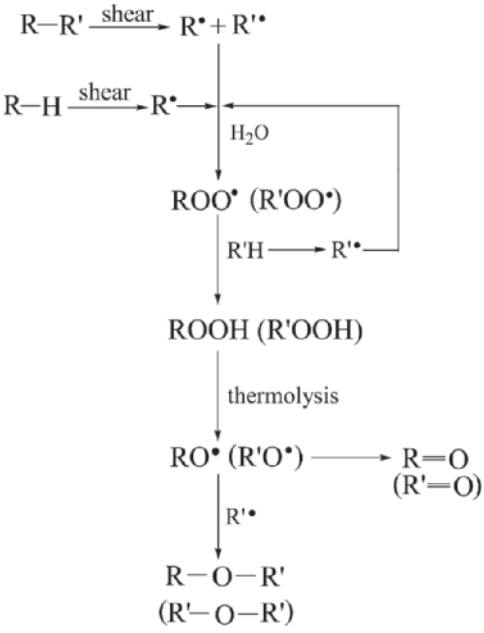

Fig. 13 Schematic diagram of the cracking and oxidation processes of DLC film during friction testing in humid environment. (After [77].)

surface asperities will increase during sliding action (about 100–300°C) Fe can react with water and oxygen forming Fe species, Fe_2O_3, Fe_3O_4 and FeOOH, in the tribocontact [77].

When DLC film is sliding against Si_3N_4, silica gel formation has been observed on the worn surface due to the oxidation and hydrolysis of the Si_3N_4 ball, which resulted in low friction (0.085) in humid nitrogen. The Al_2O_3 counter material, on the other hand, catalyzed the degradation of DLC causing high wear of DLC coating as detected by Li et al. [76]. The authors concluded that in oxygen- and/or water-containing environments the formation of the transferred carbon-rich layer on the steel ball was inhibited by the friction-induced chemical reaction and oxidation of the hydrogenated DLC film.

3.2.4 The Influence of Doping on the Tribological Performance of Hydrogenated DLC Films in Ambient Environment

Since the tribological performance of hydrogenated DLC films is greatly influenced by the environmental aspects, doping and alloying has been used to modify some of the surface-related properties, and to overcome the tribological limitations. Typical alloying elements used to influence the tribological performance, are silicon, fluorine, nitrogen and different metals.

Silicon incorporation in a-C:H structure affects most coating properties, including surface energy and internal stresses, and is therefore often used to stabilize the friction performance of a-C:H coating in humid atmosphere. The friction coefficient of Si-doped a-C:H film appears to be significantly reduced, below 0.1, compared to an undoped a-C:H film in ambient air as reported, e.g. by Oguri and Arai [103], Itoh et al. [55] and Miyake and Kaneko [92]. As Meneve and co-authors studied the behaviour of a-Si_{1-x}:C_xH films ($0.7 < x < 0.9$), they noticed that in humid conditions the potential applications will be limited to contact pressures below 1 GPa due to the lower wear resistance of the Si-doped coating [90].

Gilmore and Hauert received similar results, since the coating wear increased by a factor of 2–4 when the Si content increased from 1 to 6 at. %. Simultaneously, the Si doping reduced the friction in high humidity environment by a factor of three compared to undoped DLC. The friction coefficient of Si-doped DLC coating could be held approximately constant at 0.08 ± 0.01 over the humidity range 5–85% with a 4 at. % Si-doping [40]. The Auger spectroscopy of Si-doped DLC films revealed the formation of Si-rich oxide debris and the low and stable friction performance was related to sliding between hydrated silica debris on both coating and counterpart surfaces [63].

Multilayer coatings consisting of a stack of Si-doped nanocomposite DLC layers provide stress relief, enabling the deposition of thick layers without loss of adhesion. The multilayer films showed low friction (<0.1) regardless of the humidity also providing an improved abrasion resistance [8]. The nanocomposite DLC resulted in friction coefficients typically between 0.05 and 0.15 even in humid air [100,101].

Different gas species have also been used for doping DLC films. Fluorine incorporation in the a-C:H structure affects the surface properties and reduces the internal stresses. The combination of Si and F in a a-C:F:Si:H film structure can further improve the tribological performance of Si-doped coating [93]. On the other hand, F-incorporation was found to increase the friction against steel up to 0.9 in dry environment [41]. The friction performance of the Ar- and N-incorporated DLC films have shown low friction performance typically in the range 0.05–0.18 with low wear rate in different environments [148].

The DLC films have also been doped with several different metals, such as Ti, Nb, Ta, Cr, Mo, W, Ru, Fe, Co, Ni, Al, Cu and Ag. The compressive stresses are typically reduced to values below 1 GPa. The metal-alloyed a-C:H structures exhibit steady-state friction values in the range 0.10–0.20 with slight dependence on the humidity. The tribological behaviour of these metal-alloyed a-C:H films has been explained by a combination of ceramic-like properties (high hardness) and polymer-like properties (high elasticity, low surface energy) [11].

3.3 The Friction and Wear Performance of Hydrogen-Free DLC Coatings in Ambient Air and in Humid Environment

Hydrogen-free DLC films can be divided into two major groups according to the bond structure of the film. The tetrahedral amorphous carbon (ta-C) films are highly sp^3 bonded providing the film with diamond-like properties, such as high hardness and chemical inertness. The ta-C films can be deposited by different techniques, e.g. arc discharge or laser ablation. The amorphous hydrogen-free films (a-C) produced by magnetron sputtering are mostly sp^2 bonded, and therefore have different tribological performance compared to ta-C.

In humid environments, the ta-C films have a rather stable friction performance showing friction coefficient values typically in the range 0.1–0.2 against different counterface materials as shown in Table 3. The wear rates vary from 0.001×10^{-6} $mm^3(Nm)^{-1}$ to 0.1×10^{-6} $mm^3(Nm)^{-1}$ depending on the deposition method and deposition parameters used. The amorphous a-C films have similar friction performance to ta-C films, but the wear rates are higher for the a-C coatings compared to ta-C coatings.

Hirvonen and co-authors deposited ta-C films by an ion beam technique. The films had a steady-state friction coefficient of 0.14 against steel and 0.06 against silicon nitride in pin-on-disc tests carried out in ambient air [50]. The ta-C films deposited by arc-discharge method showed friction coefficient values in the range 0.12–0.2 against steel with an increasing trend as the sliding proceeded. The wear rate of ta-C coatings was in the range $0.07 \cdot \times 10^{-6}$ $mm^3(Nm)^{-1}$ against steel. Hirvonen et al. [51,52] reported the tribological performance of the ta-C film to be dominated by the formation of a carbon-rich transfer layer onto the counterface. The surface roughness of the films influenced the friction performance of ta-C coatings, since the films deposited by using a curved solenoid to filter the

Table 3 The friction coefficient values and the wear rates of the hydrogen-free DLC coatings tested in different environments

DLC film		Tribological testing						
Film (substrate)	Deposition technique	Countermaterial	Load (N)/(GPa)	Speed (ms^{-1})	Environment	Friction	Wear rate ($x10^{-6}$ $mm^3(Nm)^{-1}$)	Reference Author year
ta-C (WC-Co)	Ion beam deposition	Steel	0.95 GPa	0.13	Ambient air	0.13	–	[50]
		Si_3N_4	1.23 GPa			0.06		
ta-C (Tool steel)	Vacuum arc discharge	AISI52100	0.86 GPa	0.1	Ambient air (40% RH)	0.12–0.22	0.07	[51,52]
ta-C (Steel)	Vacuum arc discharge	ta-C (Steel)	10–80 N	0.1–6.0	Ambient air (10^5 Pa)	0.04–0.13	–	[2]
					Vacuum (10^{-5} Pa)	0.6		
ta-C (Si)	Pulsed arc discharge	Si_3N_4	1.54 N	0.1	Ambient air (72% RH)	0.07	0.15	[67]
ta-C (Si)	Pulsed arc discharge	AISI 52100	5–20 N	0.1	Ambient air (50% RH)	0.26–0.17	<0.01	[115]
		M50	10 N	0.1		0.22	<0.01	
		Al_2O_3	5 N	0.1		0.21	0.06	
ta-C (Si)	Pulsed arc discharge	AISI 52100	10 N	0.1	Amb. air (20% RH)	0.4	0.008	[116]
					Amb air (50% RH)	0.19	0.007	
					Amb.air (70% RH)	0.2	0.01	
		Al_2O_3	5 N	0.1	Amb. air (10% RH)	0.26	0.07	
					Amb air (50% RH)	0.17	0.04	
					Amb.air (70% RH)	0.2	0.09	
ta-C (AISI 440B)	Pulsed arc discharge	AISI 52100	5–35 N	0.1–3	Ambienta air (50% RH)	0.14–0.19	0.03–0.16	[118]
		Al_2O_3				0.1–0.14	0.04–0.11	
ta-C (AISI440C))	Pulsed laser deposition	AISI440C/ Sapphire	0.98 N/0.8–1.1 GPa	0.2	Air (50% RH)	0.12/0.09	0.001	[137]
					N_2 (<2% RH)	0.10/0.08		
					Vacuum (10^{-7} Pa)	-/0.5		

(continued)

Table 3 (continued)

DLC film		Tribological testing						
Film (substrate)	Deposition technique	Countermaterial	Load (N)/(GPa)	Speed (ms^{-1})	Environment	Friction	Wear rate ($x10^{-6}$ $mm^3(Nm)^{-1}$)	Reference Author year
ta-C (AISI 440B)	Pulsed arc discharge	AISI 52100	5N/0.8 GPa	0.02	Dry air (<3% RH) Dry N_2	0.66 0.61	–	[121]
ta-C (AISI 440B)	Pulsed arc discharge	AISI 52100	5N/0.8 GPa	0.02	Dry air (<3% RH)	0.72	–	[71]
ta-C (Steel)	Pulsed vacuum arc	AISI 52100	2.5	0.01	Ambient air	0.35–0.1	–	[1]
ta-C (AISI H13)	Arc-PVD	AISI 52100	10 N/1.04 GPa	0.1	Dry N_2 Dry air Amb. air (40% RH)	0.6–0.7 0.3–0.7 0.14	–	[124]
ta-C (AISI H13)	Cathodic arc evapora-tion	ta-C (M50)	1 N	0.07–0.03	Vacuum O_2 H_2 Humidity (50% RH)	0.65 0.25 0.15 0.07	–	[3,4]
ta-C (AISI 440C)	Pulsed laser deposition	AISI 440C/SiC	1 N	0.125–0.2	Amb. air (40% RH) Dry N_2	0.11/0.12 -/0.05–0.7	against SiC: 0.2 against SiC: 8	[138]
	Filt. cathodic vacuum arc	AISI 440C/SiC	1 N	0.125–0.2	Amb. air (40% RH) Dry N_2	0.1/0.11 -/0.09–0.7	against SiC: 0.1 against SiC: 9	
ta-C (Ti-alloy)	Arc discharge	AISI 52100	2 N	0.02	Vacuum ($<10^{-3}$ Pa) Amb. air (40%RH)	0.34–0.41 0.12–0.23		[91]
a-C (Tool steel)	Magnetron sputtering	WC	25 N	0.048–0.45	Dry air (about 7% RH)	–	0.04–0.14	[57]
a-C (AISI52100)	Sputtering	Steel	5 N	0.07	Ambient air (30–40% RH)	0.2	0.06	[102]
a-C (HSS)	Magnetron sputtering	WC-Co	40–80 N	0.4	Ambient air	≤0.1	0.021–0.043	[31]

macroparticles during the deposition, resulted in friction values down to 0.07 when slid against Si_3N_4 pin [67].

The ta-C coatings deposited by pulsed vacuum arc-discharge method, having a predominantly sp^3 (66%)-bonded structure and containing less than 1 at. % hydrogen, are hard (54 GPa) with a high Young's modulus (445 GPa). In ambient air (50% RH), the wear rates of the coatings varied from 10^{-9} to 10^{-10} mm^3 $(Nm)^{-1}$ [67, 70,115,122].

The friction performance of the ta-C films studied by Ronkainen and co-workers with different normal loads (5–35 N) and sliding velocities (0.1–3.0 ms^{-1}) was stable showing friction coefficient in the range 0.14–0.19 against steel pin and in the range 0.1–0.14 against Al_2O_3 in humid air (50% RH), as shown in Fig. 14. The highest friction value (0.23) was measured for the high load and high sliding speed combination (35 N, 2.6 ms^{-1}). This was caused by the high local temperature generated in the sliding contact, which was verified by flash temperature calculations to be around 700°C. The high temperature presumably reduced the amount of water vapour in the sliding contact causing an increase in friction [118].

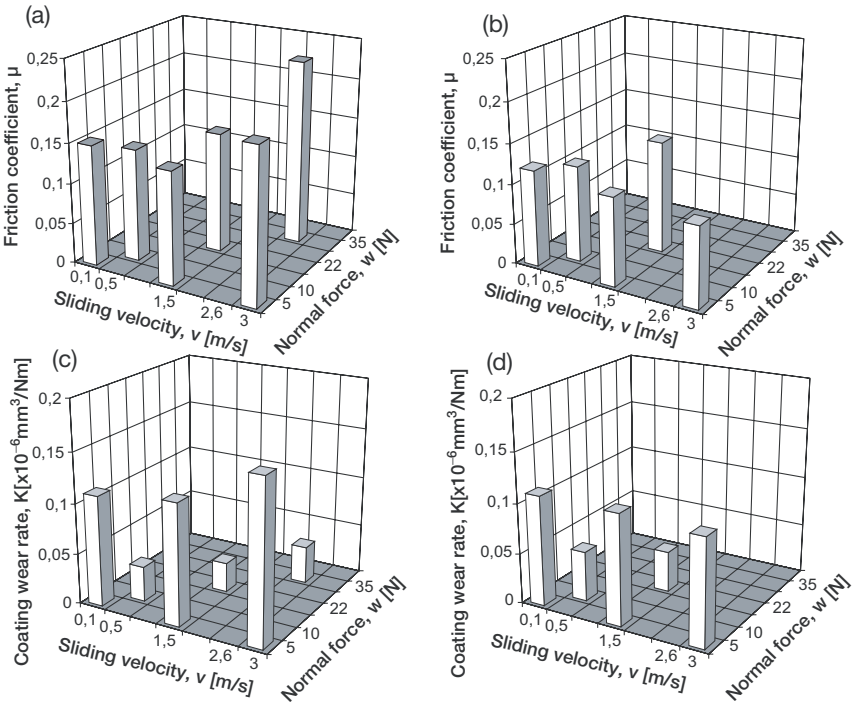

Fig. 14 The friction coefficient of ta-C film sliding against (a) steel and (b) Al_2O_3 balls and the coating wear rates against (c) steel and (d) Al_2O_3 balls in pin-on-disc tests with different normal loads (5–35 N) and sliding velocities (0.1–3 ms^{-1}). (After [118].)

The wear rates of ta-C films were typically lower than that of a-C:H films tested in similar test conditions. On the other hand, the wear rates of the counterparts were higher for the pins sliding against the ta-C coating due to slightly higher surface roughness of ta-C coating [115,117]. A transfer layer was formed on the steel pin (AISI 52100) wear surface that contained carbon and oxygen detected by secondary ion mass spectrometry (SIMS). On the wear surface of the coating, SIMS depth profiling and elemental imaging revealed a transfer of pin materials, iron and chromium. The amount of these species tended to increase as the sliding distance was increased up to 25 km accompanied with the increase in friction from 0.19 to 0.53 [116]. The micro-Raman analyses of worn surfaces of ta-C films indicated resemblance of graphite on the wear track of ta-C coating after a 5,400 m sliding against steel or Al_2O_3 [122]. In a similar way, the structure of ta-C film deposited by filtered cathodic vacuum arc was transformed to polycrystalline graphite, as detected by [125].

The hydrogen-free DLC films deposited by pulsed laser deposition (PLD) showed similar friction and wear properties compared to arc-discharge deposited ones. As determined by Voevodin et al. [135,137,139], the friction coefficient measured for the ta-C coatings against sapphire was in the range 0.07–0.10, and around 0.2 against steel due to chemical interaction of ta-C with steel. In the tests carried out in different atmospheres, namely ambient air (50% RH), dry nitrogen (<2% RH) and low vacuum (10 Pa of water vapour), the friction coefficient was observed to be nearly independent of the environment, since in all cases some water vapour was present in the test environment. The amount of humidity influenced the steady-state friction of ta-C films the most, showing a decreasing trend as the humidity was increased from 5% to 80% RH. The transfer film formed on the wear surface of hydrogen-free DLC film was suggested to be necessary for the low friction performance, and the graphite-like structure was detected in the transfer film after several thousands of sliding cycles. The Raman spectra showed the transformation of film structure from tetrahedral amorphous DLC to polycrystalline graphite as depicted in wear debris in Fig. 15 [137].

Due to high thermal stability (up to 400°C) of the PLD ta-C film, the thermally induced sp^3 to sp^2 transition was not possible according to Voevodin and co-workers. However, the high local pressures and the shear stresses acting on the coating surface during sliding could induce relaxation of the metastable sp^3 phase into sp^2 phase. The wear rates measured for the ta-C coatings were low, in the range 10^{-9} to 10^{-8} $mm^3(Nm)^{-1}$ [137]. The thin lubricating graphitic film on top of the hard supporting ta-C layer thus provides an ideal system to reduce friction and wear.

The surface acoustic wave (SAW) analysis showed that the elastic modulus of ta-C coatings was reduced about 5% due to sliding action against the Al_2O_3 pin [69,70]. In addition, the phase contrast imaging atomic force microscopy (AFM) showed a lower elasticity of wear surface compared to the original film. The thickness of this surface layer was the greatest at the asperity summits, where the local contact pressure was high and the temperature flash was

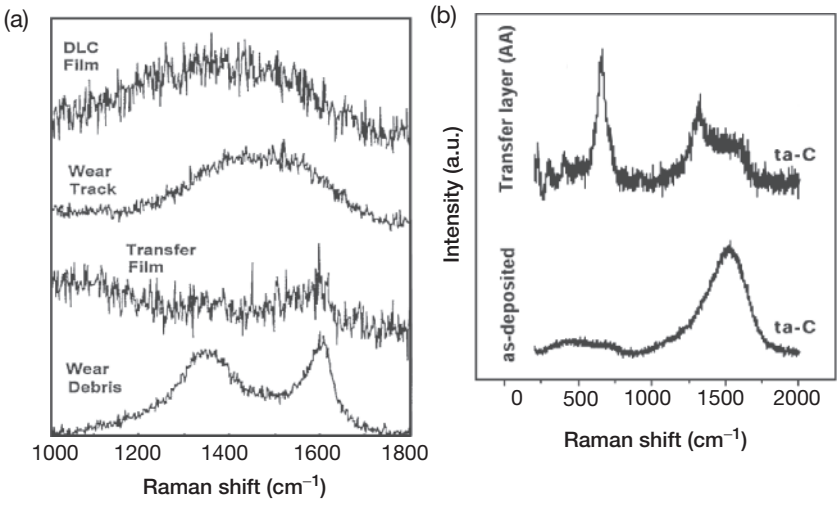

Fig. 15 (a) Comparison of Raman spectra recorded for as deposited hydrogen-free DLC film, wear track, wear debris and transfer film formed after 10^5 sliding cycles in pin-on-disc test in ambient air (50% RH). (From [137]). (b) Raman spectra of hydrogen-free ta-C film as deposited and the transfer layer generated in ambient air (30–40% RH). (After [124].)

most probable [1]. These phenomena can be related to the tribochemical changes occurring on the film surface during sliding action.

Sánchez-López and co-authors carried out Raman analyses on the samples of hydrogenated and hydrogen-free DLC films tested in ambient humid air (30–40% RH), dry air (RH <1%) and dry nitrogen (RH <1%). They detected the presence of a broad peek centred at 650–670 cm^{-1} in the transfer layer (Fig. 15). The presence of these peaks were more evident in the less-hydrogenated a-C:H or hydrogen-free ta-C coatings tested in ambient air. The peaks were attributed to the formation of iron oxide by tribochemical reaction of the uncoated steel ball in ambient air [124].

The ta-C films typically can have a high surface roughness, which increases friction in the beginning of sliding. This effect of surface roughness can be reduced by optimizing the process parameters favouring smoother surfaces [58]. Moreover, filtering of macroparticles can be used to reduce their effect in the vacuum arc deposition [46]. The steady-state friction values for the ta-C films deposited by filtered arc deposition have been measured in the range 0.08 [125].

The hydrogen-free amorphous carbon (a-C) films have similar friction performance to ta-C coatings showing reasonably low friction in humid environment. Friction coefficient values of 0.2 have been measured for the pure a-C film in sliding tests carried out in ambient air against steel with wear rate of 0.06×10^{-6} $mm^3(Nm)^{-1}$. The friction evolution of pure a-C film shows typically a fluctuating

trend, and therefore a-C films are in most cases doped with metallic species, like Cr and W. The metal-doped a-C films have typically lower and smoother evolution of friction compared to undoped a-C films.

The metal doping, on the other hand, increases the wear rate of the films compared to undoped ones as shown in Fig. 16 [102]. The Cr-doped films had a stable friction performance around 0.1–0.2 and the wear rate of 10^{-6} mm^3(Nm)$^{-1}$, when sliding against Ti and Al counterparts in humid air studied by Konca et al. [65,66]. Against WC counter material, friction coefficient values of 0.07–0.05 and wear rates of 0.043 $\times$ 10^{-6} mm^3 (Nm)$^{-1}$ to 0.021 $\times$ 10^{-6} mm^3 (Nm)$^{-1}$ were measured in ambient air as the load was increased from 40 N to 80 N [31].

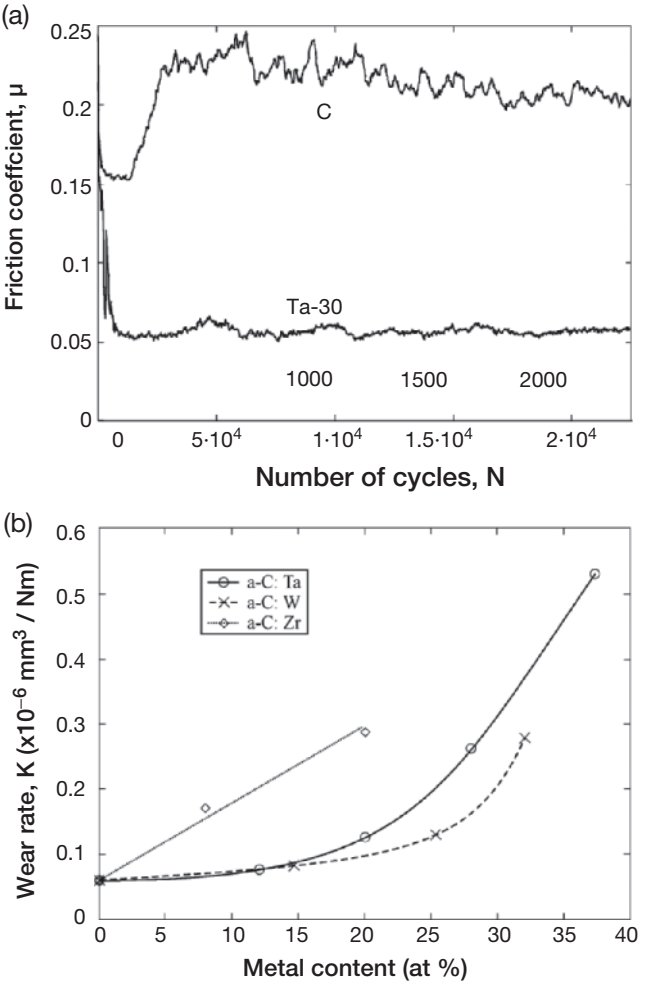

Fig. 16 (a) The friction performance of the pure a-C and Ta-doped a-C films and (b) the wear rates of a-C coatings doped with different metals from pin-on-disc tests. (After [102].)

The low friction performance of hydrogen-free DLC films in ambient air can be attributed to the presence of humidity. The H_2O molecules are adsorbed on the DLC film surface terminating the dangling bonds of the DLC film. By this mechanism the bond strength between the interacting surfaces is reduced to about 0.21 eV per bond, typical for the hydrogen bonding of water molecules at C=O sites [39], providing reasonable low friction performance. On the other hand, the a-C films are sp^2 bonded and a sp^2-bonded graphitic transfer layer is also formed on the contact surface of ta-C films. In humid conditions, these graphitic carbon species can assist in providing low friction performance.

3.4 The Friction and Wear Performance of Hydrogen-free DLC Films in Vacuum and Dry Environments

The hydrogen-free DLC coatings have a different behaviour in inert environments, compared to hydrogenated DLC films, since they represent high friction and wear performance in vacuum and in dry environment. For the ta-C coatings prepared by PLD technique the friction was increased from about 0.08 to 0.5 after several thousand sliding cycles in vacuum (10^{-7} Pa), as observed by Voevodin and co-workers (Fig. 17). The authors discovered surface graphitization to be responsible for the low friction in humid air, and high friction in vacuum for the hydrogen-free DLC coatings [135,137,139]. Meunier et al. [91] measured in vacuum (10^{-3} Pa) similar high friction values 0.5–0.7 for the ta-C films deposited by filtered cathodic arc. The friction behaviour is typically erratic in vacuum, but in ambient atmosphere steady friction is typically detected. In vacuum conditions the friction coefficient has also been observed to increase as the normal force is increased [2].

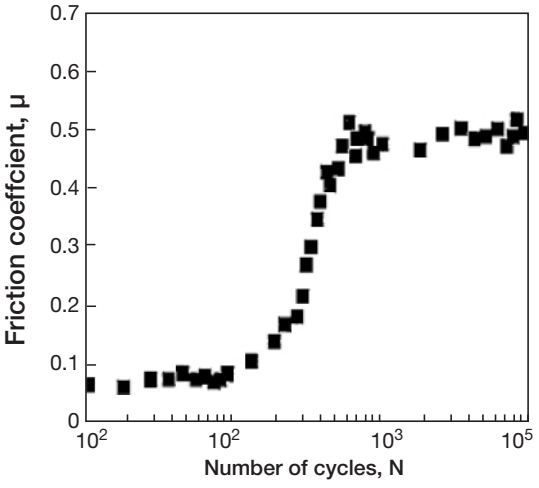

Fig. 17 The friction coefficient evolution for hydrogen-free DLC (ta-C) film sliding against sapphire ball in high vacuum conditions (10^{-7} Pa). (After [137].)

The influence of humidity on the friction performance of the vacuum arc-deposited ta-C coatings was studied by [3]. The ta-C coated steel balls were tested against the ta-C coated discs by pin-on-disc experiments conducted in a vacuum chamber. The tests were carried out under vacuum (10^{-6} Pa), as well as in an atmosphere of hydrogen, oxygen and water (1,300 Pa corresponding to 50% RH). In vacuum, ta-C coating performed high friction in the range 0.65 accompanied with high wear. After introduction of oxygen, hydrogen and water vapour into the chamber, the friction was reduced to approximately 0.25, 0.15 and 0.07, respectively, with a reduced wear of the coating. The ta-C coatings thus have a different friction performance in vacuum compared to a-C:H, but similar frictional response in humid environments close to the water condensation pressure as observed in the Fig. 18. Similar friction performance was also observed by [62].

The ta-C coatings deposited by pulsed vacuum arc technique, exhibited high friction coefficient values in dry nitrogen and dry air, when ta-C coated discs were slid against steel balls with low sliding speed. The friction values were in the range 0.6 in dry air and in the range 0.6–0.8 in dry nitrogen as presented in Fig. 19 [121]. However, the friction of the ta-C coating could be reduced when the ta-C coatings were doped with hydrogen by depositing the films with pulsed vacuum arc discharge in hydrogen (H_2) or methane (CH_4) atmospheres. The friction coefficient was decreased from 0.7 to 0.28 as the hydrogen content of the film increased from >1 at. % to 16 at. % hydrogen as shown in Fig. 20 [71]. The results clearly show the importance of the presence of water

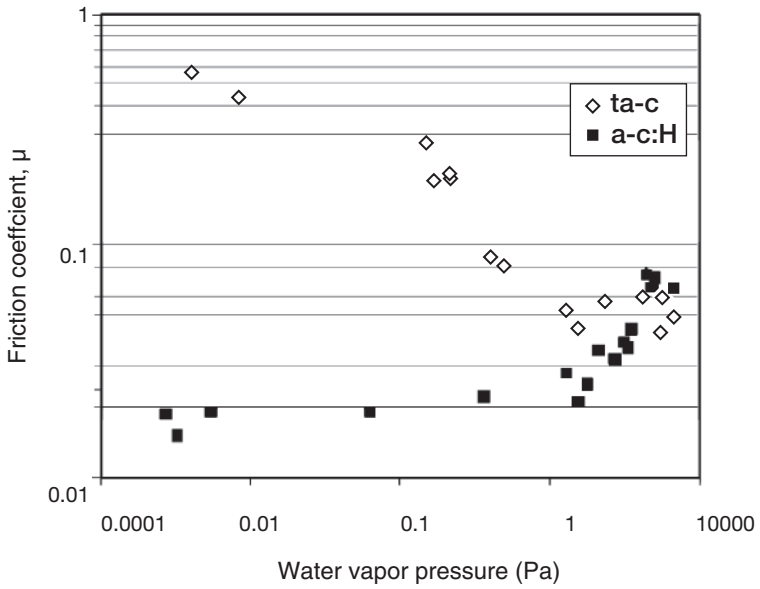

Fig. 18 Friction performance of hydrogen-free ta-C and hydrogenated a-C:H as a function of water vapour pressure. (After [4].)

vapour in the surrounding environment or presence of hydrogen in the coating in order to reach low friction performance of ta-C coatings.

The hydrogen-free amorphous carbon (a-C) films, deposited by magnetron sputtering technique, have similar high friction performance in dry and inert atmospheres to ta-C films. In argon, the a-C films have a friction coefficient of 0.63 against Al ($K = 1.28 \times 10^{-5}$ mm^3/m), 0.53 against Ti ($K = 1.39 \times 10^{-4}$ mm^3/m) and

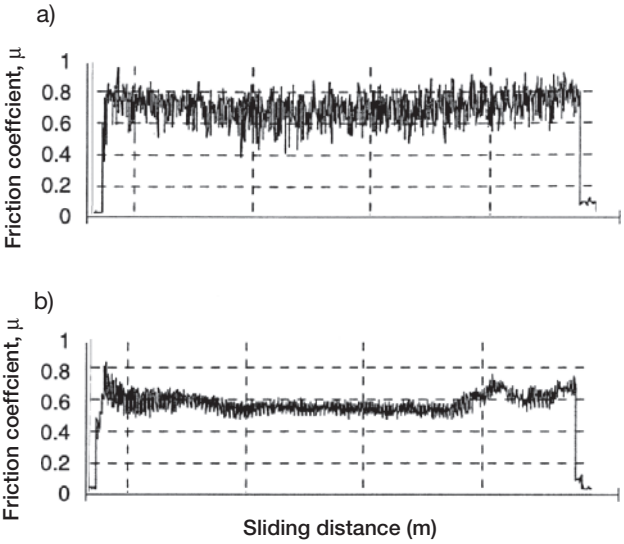

Fig. 19 The friction coefficient of ta-C coating sliding against steel pin (AISI 52100) in (a) dry nitrogen and (b) dry air. The normal force was 5 N, sliding velocity 0.02 ms^{-1} and sliding distance 24 m. (After [119].)

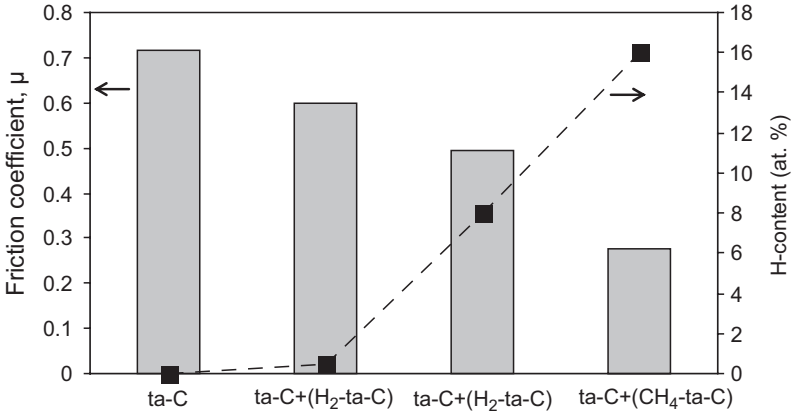

Fig. 20 The coefficient of friction for ta-C coatings with different hydrogen contents. The pin-on-disc tests were carried out with steel pins (AISI 52100) with 5 N normal force and sliding velocity of 0.02 ms^{-1} in dry synthetic air (about 0% RH). (After [121].)

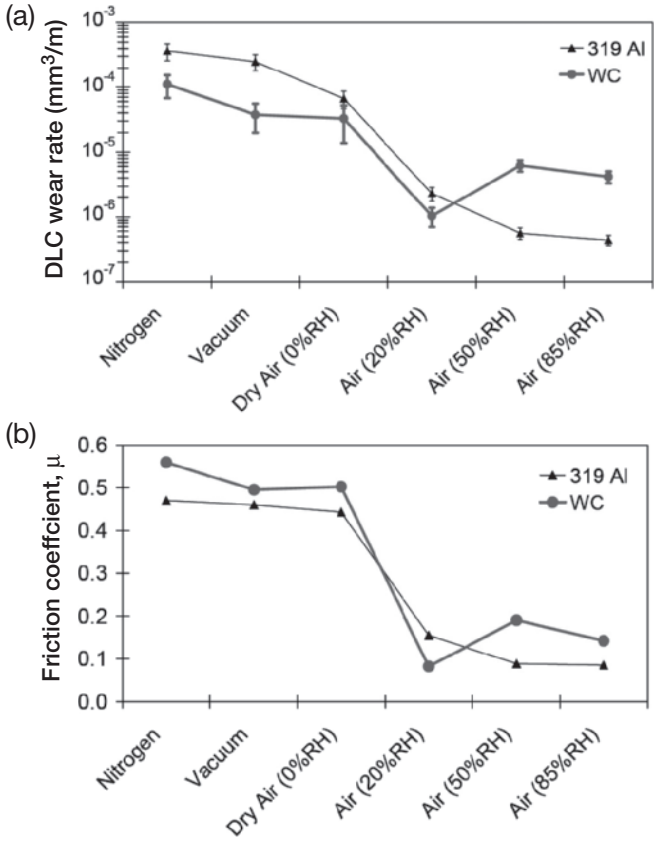

Fig. 21 (a) The wear rates and (b) the steady-state friction coefficient values of the hydrogen-free a-C coatings against Al and WC under various test environments. The normal force was 4.9 N and the sliding velocity 0.12 ms^{-1}. (After [64].)

0.48 against Cu (K = 1 × 10^{-9} mm^3/m). In humid air (22% RH) the friction coefficient values are considerably lower, against Al 0.18 (K = 7.87 × 10^{-7} mm^3/m), against Ti 0.09 (K = 7.34 × 10^{-7} mm^3/m) and against Cu 0.39 (K = 7.99 × 10^{-7} $mm^3/m)^{-1}$ [65,66].

In addition, the Cr doped a-C coatings had a high friction in vacuum, nitrogen and dry air (5% RH) as shown in Fig. 21. In humid air, the friction decreases as the humidity increased from 20% to 85% RH [64]. In hydrogen environment the friction coefficient is about 0.015 and a carbonous transfer layer is detected on the wear surface [109].

The importance of humidity for the low friction performance of hydrogen-free DLC films is evident from the experimental results. In ambient, humid air, low friction performance can be achieved for the ta-C and a-C coatings, but in vacuum and in dry environments high friction coefficient values combined with high wear have been observed. The friction performance of hydrogen-free ta-C films is influenced by

the highly sp^3-bonded hydrogen-free structure of the film. The surface carbon atoms of the ta-C are bonded to their neighbouring atoms with three σ-bonds, leaving the fourth bond free, dangling out of the surface. In open air these dangling bonds are terminated by adsorbates, like e.g. water molecules or hydrogen. In inert gas or in vacuum, the adsorbed atomic species will be removed due to mechanical action of thermal desorption. If the σ-bonds are exposed, the dangling bonds can establish strong covalent interactions with the atoms of the counterface material causing high adhesion between the surfaces indicated by high friction [4,19].

The AFM-based nanowear tests have shown that the a-C films deposited by DC magnetron sputtering, are covered with thin (1.5–2.0 nm) graphite-like surface layers [80]. Moreover, for ta-C coatings the surface atoms are found to reconstruct into sp^2 sites often bonded in graphitic rings. This reconstruction, by placing the dangling bonds on adjacent surface atoms lower the energy by π-bonding and creates lower surface energy [7]. Earlier, also McKenzie et al. [87] have detected the sp^2-enriched surface of ta-C coating. These results suggest that both the types of hydrogen-free DLC films have sp^2-bonded carbon structure at the surface. The phenomenon is enhanced by the graphitization taking place due to tribological action. This suggests that the friction performance of hydrogen-free DLC films is influenced by the graphitic nature of the film surface and the graphitic nature of the generated transfer layer. The graphitic species require contaminants, like water molecules or hydrocarbons, to be present in the tribocontact in order to provide low friction performance [55]. Since the water molecules and hydrocarbon species fairly readily desorb from the surface due to sliding action, the friction of hydrogen-free DLC films increases in dry and inert environments.

4 Thermal Effects on Tribological Performance of DLC Coatings

The performance of the DLC films at elevated temperatures is greatly influenced by the nature and structure of the films. The hydrogen and water vapour also play a key role in the high temperature performance of the DLC films. The dehydrogenation of the a-C:H film structure will change the coating structure and thus the performance of the coatings. On the other hand, for the hydrogen-free DLC films the desorption of water vapour is detrimental for the friction and wear performance at elevated temperatures.

4.1 The Thermal Effects on Hydrogenated DLC Films

The thermal stability of DLC films differ according to the film structure and composition. In the hydrogenated DLC films, the hydrogen plays an important role in the bonding configuration by stabilizing the tetrahedral coordination (sp^3

bond) and thus controlling the film properties. The existence of hydrogen in DLC film increases the proportion of sp^3 bonds. Annealing the hydrogenated DLC film at elevated temperatures causes hydrogen desorption in the film. Hydrogen effusion will occur in a-C:H films at elevated temperatures from 300°C to 600°C depending on the deposition parameters used for the coating deposition [141].

The polymeric DLC films will have lower hydrogen effusion temperature in the range 260–350°C compared to the harder films (deposited at higher bias voltage) in the range 550°C. The dense ta-C:H coatings have an even higher annealing temperature in the range 700°C. The conversion of film structure to nanocrystalline graphite can also start at lower temperature for polymer like films, in the range 300°C, when heated in air [112,130]. Gao and co-workers reported the heating of hydrogenated DLC structure up to temperature 420 K (147°C) to cause substantial amount of hydrogen desorption from the surface, detected by mass spectroscopy. This effect was accompanied with an increase in friction and wear [38]. According to Liu et al. [86], the structure of a-C:H showed no appreciable change after annealing up to 400°C, but at higher temperatures the dehydrogenation of the a-C:H structure occurred followed by precipitation of small graphite crystals. However, the hardness remained approximately constant after annealing at the temperature range 200–700°C.

Miyoshi et al. [97] reported thermal stability to higher temperatures, since the increase in friction was observed when the annealing temperature raised from 500°C to 600°C and remained high in the range 600–700°C. Memming et al. [89] observed the loss of hydrogen in DLC films when annealed above 550°C with strong increase in friction up to 0.68 in UHV and dry nitrogen. However, no significant change was observed in humid atmosphere. Similar effect has been observed by Grill [42].

The general trend at elevated temperatures is the increased wear [23,81, 132]. The evolution of hydrogen is followed by the phase transformation of sp^3 to sp^2 bond structure. The graphitization as well as oxidation of the hydrogenated DLC film will wear out the DLC structure rapidly at elevated temperatures. Erdemir and Donnet [22] reported an increasing wear rate for DLC at elevated temperatures from 100°C as observed in Fig. 22. Compared to the room temperature tests (0.000186×10^{-6} mm^3 $(Nm)^{-1}$) the wear rate increased dramatically for the a-C:H film in 250°C (1.39×10^{-6} $mm^3(Nm)^{-1}$). Liu et al. [81] reported a rather stable wear performance of a-C:H films sliding against Al_2O_3 in humid air at elevated temperatures up to 200°C, but in 300°C and above, the wear increased dramatically leading to total rupture of the coating due to graphitization. However, the friction was decreased from 0.15 down to 0.02 with increasing temperature, but the wear life of the film was short at high temperatures (Fig. 23).

When testing the annealed films in room temperature unchanged wear resistance for hydrogenated DLC films was detected up to an annealing temperature of 300°C [77,78] and 400°C [133]. It was also shown that the testing environment had a greater effect on wear performance compared to the annealing effect. Grill

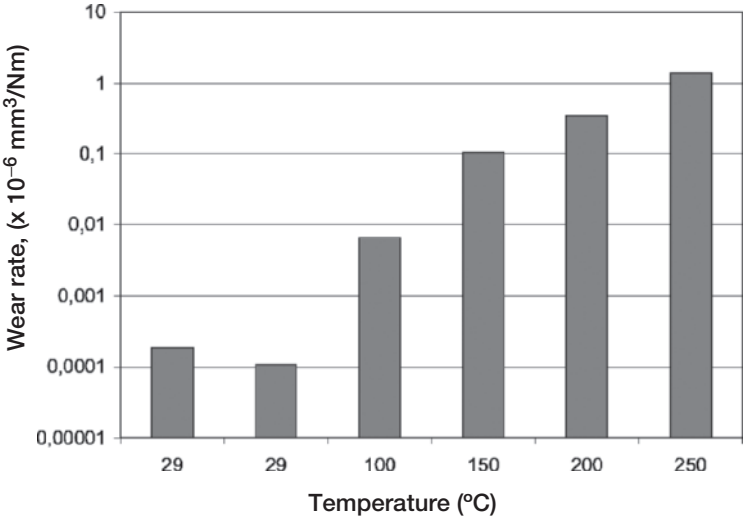

Fig. 22 Effect of temperature on wear performance of hydrogenated DLC film. (After [22].)

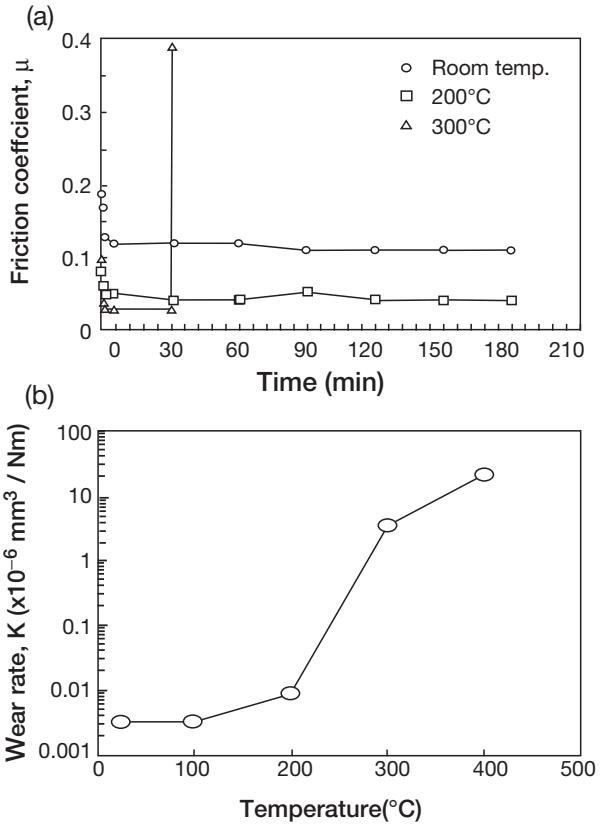

Fig. 23 (a) The friction coefficient evolution of DLC films sliding against Al_2O_3 at different temperatures. (b) The influence of temperature on wear rates of the hydrogenated DLC film. (After [81].)

et al. [47] have reported that the films deposited in higher temperature and with higher bias voltage are more stable at elevated temperatures and they remained wear-resistant even after annealing at a temperature of 590°C.

The thermal stability of a-C:H films can be enhanced by doping, e.g. with Si. The increased silicon content has been observed to stabilize the structure and the Si-doped film graphitize in a higher temperature compared to pure a-C:H. The integrated intensity ratio I_D/I_G of the Raman shift describing the change in the bonding structure was increased to 400°C for the Si-doped DLC compared to 300°C for the pure DLC. Only insignificant oxidation occurred for the Si-doped a-C:H films at 300°C and the remaining carbon was converted to the graphitic phase at 600°C compared to 500°C for the undoped DLC [142]. On the other hand, other doping species, like fluorine, were found to decrease the temperature stability [99].

4.2 Thermal Effects on Hydrogen-free DLC Films

The hydrogen-free DLC films resist oxidation or phase transformations to much higher temperatures compared to hydrogenated DLC films. The tetrahedral amorphous carbon ta-C contains hydrogen only as an impurity and the structure is a highly sp^3 hybridized. Due to their structure the ta-C films deposited by vacuum arc discharge are stable up to 1,000 K (727°C) when annealed in vacuum [87]. If heated in air, oxidation of the film is observed at 450–500°C [112]. However, annealing at 400°C (673 K) has been reported to influence the wear performance of ta-C by increasing the wear rate to some extent when sliding against stainless steel after the process [74].

Concerning the ta-C films deposited by pulsed laser ablation technique, the thermal stability has been shown to be related to the initial structure (sp^3/sp^2 ratio) and chemical properties of the coating. Changes in sp^3/sp^2 bonding ratio of the coating has been reported to occur at annealing in 300°C [59]. However, good thermal stability has been reported up to 900 K (627°C) in UHV for optimized coatings [119].

In cryogenic temperatures, the friction of ta-C coating was increased to values 0.3–0.6 in 77 K (−204°C) from the those measured against steel counterface in room temperature (about 0.2). The lowest friction coefficient (about 0.2) in 77 K was measured for the ta-C against ta-C sliding pair with a lower intrinsic hardness of the coating (40 GPa). Smoothening type of wear was observed for the ta-C coating in low temperatures [106].

The hydrogen-free amorphous carbon (a-C) films deposited by magnetron sputtering are reported to be thermally stable up to 300°C, after which the hardness drops drastically with temperature due to graphitization of the coating structure. The thermal stability can, however, be improved by using, e.g. nanocomposite structures [147]. The high temperature pin-on-disc tribometre tests with a-C coatings showed increased wear at temperature as low as 120°C due to loss of stability

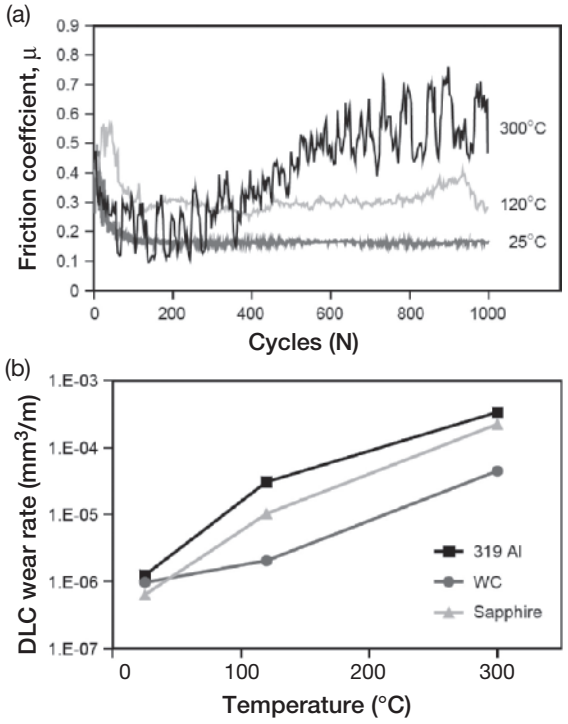

Fig. 24 (a) The friction coefficient of a-C coated discs and 319 Al pins sliding at temperatures 25°C, 120°C and 300°C. Tests were run for 60 m with a normal load of 4.9 N and sliding velocity of 0.12 ms^{-1}. (b) The variation of the wear rate of a-C coating with temperature when tested against 319 Al, WC and sapphire at temperatures 25°C, 120°C and 300°C. Test was run for 1,500 m at 25°C and for 69 m at 120°C and 300°C using 4.9 N applied load. (After [66].)

and significant oxidation of the coating in air at elevated temperatures. The wear of a-C coatings is increased dramatically when tested at elevated temperatures accompanied with the increase in friction as shown in Fig. 24 [66]. The increased friction performance is attributed to the absence of adsorbed water in the tribocontact, which is necessary for the low friction performance of the hydrogen-free coatings.

5 Concluding Remarks

The friction and wear performance of DLC films varies in different environments and according to changes in surrounding humidity. The friction performance and different mechanisms controlling the tribological interaction are represented schematically in Fig. 25.

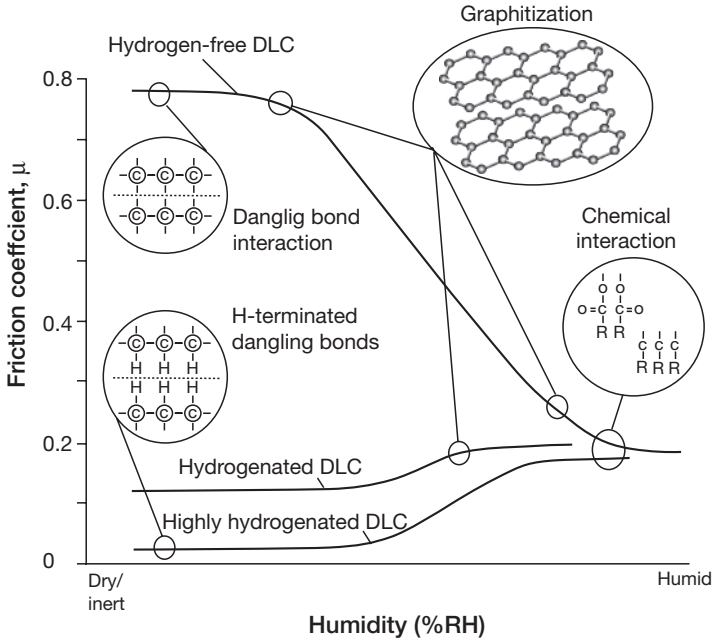

Fig. 25 Schematic picture of friction performance of DLC films as function of humidity and mechanics controlling the tribological performance

In dry and inert environments the amount of hydrogen in the coating structure determines the tribological performance of the DLC coating. The hydrogen-free DLC coatings experience high friction and wear in dry and inert environments. In inert environments the highly sp^3-bonded structure of hydrogen-free DLC film can partly explain the high friction performance. The surface carbon atoms of ta-C film are bonded to their neighbouring atoms with three σ-bonds, leaving the fourth bond free, dangling out of the surface. In ambient humid air, the dangling bonds are terminated or passivated by adsorbates, like water molecules, oxygen or hydrogen.

However, in a dry environment the adsorbates will be removed during sliding due to mechanical rubbing action or due to thermal effects leading to exposed σ-bonds establishing strong covalent interactions with the atoms of the counterface material. This causes high adhesion between the surfaces indicated by high friction. On the other hand, the outermost surface structure of the ta-C films as well as the a-C films has been reported to have a sp^2-hybridized structure. In addition, the graphitization of the hydrogen-free DLC structure has been observed to occur. The graphitic species on the coating surface can thus also contribute to high friction performance in dry environment, since graphite requires adsorbed water to provide easy shear between the densely packed atom sheets.

The highly hydrogenated DLC films exhibit superlow friction performance in dry and inert atmospheres. The tribological performance of highly hydrogenated DLC films in dry or inert environment is controlled by the interaction between hydrogen-terminated DLC structures or between hydrogen-terminated DLC structure and the transfer layer. The DLC surface with hydrogen-terminated dangling bonds experiences weak bond strength of about 0.08 eV per bond, typical for van der Waals bonding of hydrocarbons [39]. Besides high hydrogen content, great smoothness of the surface is an essential requirement for the contacting surfaces to reach the superlow friction level.

The hydrogenated DLC films that have a moderate amount of hydrogen in their structure can have a superlow friction coefficient in an inert or dry environment, but only for a limited period of time. The friction of such DLC films tends to increase to higher values, even close to values experienced by hydrogen-free DLC films after longer period of sliding in dry environment. This phenomenon occurs due to removal of hydrogen from the surface due to sliding action causing increased interaction of dangling bonds of contacting surfaces. However, this increased friction coefficient can be reduced to superlow level if hydrogen is provided from the environment. The depleted hydrogen on the surface also leads to graphitization of the outermost surface of the hydrogenated DLC structure, thus increasing the friction in dry environment. These phenomena verify the hydrogen-controlled tribological mechanism of hydrogenated DLC films acting in dry and inert environments.

The superlow friction performance of hydrogenated DLC films is destroyed in humid air due to adsorbed water vapour on the contacting surfaces leading the higher friction values. On the contrary the friction of hydrogen-free DLC films is reduced in humid air from the high values experienced in dry environment, due to dissociation and adsorbtion of water molecules on the DLC film surface and formation of C–OOH and C–H bonds that can passivate the dangling bonds of the coating surface. As the humidity is increased the friction performance of both hydrogenated and hydrogen-free DLC films will converge showing similar low friction coefficient in humid environment.

The friction values of DLC films vary generally in the range 0.1–0.2 when humidity and oxygen is present in the surrounding environment. In this case the tribological interaction is controlled by water vapour and gas adsorption on the contacting surfaces. Oxidation of the DLC film and the counter material will also occur in oxygen containing environments accompanied with the wear of the counterpart showing the importance of tribochemistry in humid environments. The wear resistance in humid environment is related to the hardness of the film and in most cases the hard hydrogen-free ta-C films exhibit the best wear performance.

In order to further understand the tribochemical reactions acting in the tribological contacts of DLC films, advanced analyses techniques, like phase contrast imaging AFM, XPS, EDS, Auger and Raman, are required for the study of friction- and wear-induced phenomena. It is also necessary to combine the knowledge of tribology, physics and chemistry in order to fully understand the controlling mechanisms of DLC films in tribological contacts.

The elevated temperatures tend to disturb the tribological performance of DLC films. The hydrogenated DLC films experience hydrogen effusion in elevated temperatures accompanied with graphitization of the film structure leading to increased wear with increased temperature. The hydrogen-free ta-C films have a more stable structure in high temperatures, but the friction is increased at elevated temperatures due to removal of water vapour from the surface. Thus high temperature has a similar effect on tribological performance of ta-C films compared to dry environment.

The dependence of the tribological performance of DLC films on the surrounding environment and the temperature, directs the use of the films in different applications. The hydrogen-free DLC films cannot be used in dry or inert atmosphere, since they require humidity for low friction performance. The hydrogenated DLC films, on the other hand, are sensitive to elevated temperatures causing degradation of the film performance. In normal atmosphere, both hydrogenated and hydrogen-free coatings have similar friction performance but the wear resistance is dependent on the film structure, the hydrogen-free ta-C film providing best wear resistance in normal atmosphere. These phenomena among other things need to be considered when DLC coatings are used in practical applications.

References

1. Ahn, H. -S., Chizhik, S. A., Dubravin, A. M., Kazachenko, V. P., Popov, V. V. (2001). Wear 249: 617–625.
2. Aksenov, I. I., Strelnitskij, V. E. (1990). Proceedings of the 2nd European Conference on Diamond, Diamond-like and Related Materials, Grans Montana, Switzerland, September, 1990, 6 pp.
3. Andersson, J., Erck, R. A., Erdemir, A. (2003a). Wear 254: 1070–1075.
4. Andersson, J., Erck, R. A., Erdemir, A. (2003b). Surf. Coat. Technol. 163–164: 535–540.
5. Buckley, D. H. (1981). Surface Effects in Adhesion, Friction, Wear and Lubrication. Tribology Series 5. Elsevier Scientific Publishing, Amsterdam, The Netherlands, 617 pp.
6. Borodich, F. M., Keer, L. M. (2005). Thin Solid Films 476: 108–117.
7. Chen, C. W., Roberts, J. (2006). Diam. Relat. Mater. 15: 936–938.
8. Dekampeneer, E., Van Acker, K., Verkammen, K., Meneve, J., Neerinck, D., Euflinger, S., Pappaert, W., Sercu, M., Smeets, J. (2001). Surf. Coat. Technol. 142–144: 669–673.
9. Dickrell, P. L., Sawyer, W. G., Erdemir, A. (2004). Journal of Tribology 126: 615–619.
10. Donnet, C. (1995). Condensed Matter News 4(6): 9–24.
11. Donnet, C. (1998). Surf. Coat. Technol. 100–101: 180–186.
12. Donnet, C., Grill, A. (1997). Surf. Coat. Technol. 94–95: 456–462.
13. Donnet, C., Belin, M., Auge. J. C., Martin, J. M., Grill, A., Patel, V. (1994). Surf. Coat. Technol. 68/69: 626–631.
14. Donnet, C., Fontaine, J., Grill, A., Le Mogne, T. (2000). Tribol. Lett. 9(3–4): 137–142.
15. Donnet, C., Le Mogne, T., Ponsonnet, L., Belin, M., Grill, A., Patel, V., Jahnes, C. (1998). Tribol. Lett. 4: 259–265.
16. Enke, K. (1980). Appl. Phys. Lett. 36(4): 291–292.
17. Enke, K. (1981). Thin Solid Films 80: 227–234.
18. Enke, K., Dimigen, H., Hübsh, H. (1980). Appl. Phys. Lett. 36(4): 291–292.
19. Erdemir, A. (2001). Surf. Coat. Technol. 146–147: 292–297.

20. Erdemir, A. (2004). Tribol. Int. 37: 1005–1012.
21. Erdemir, A., Donnet, C. (2001). Tribology of diamond, diamond-like carbon and related films. In: Bhushan, B. (ed.) Modern Tribology Handbook. Vol. 2, Materials, Coatings and Industrial Applications. CRC Press, Boca Raton, FL, pp. 871–908.
22. Erdemir, A., Donnet, C. (2005). Tribology of diamond and diamond-like carbon films: an overview. In: Stachowiak, G.W. (ed.) Wear – Materials, Mechanisms and Practice. Wiley, London.
23. Erdemir, A., Fenske, G. R. (1996). Tribol. Trans. 39(4): 787–794.
24. Erdemir, A., Switala, M., Wei, R., Wilbur, P. (1991). Surf. Coat. Technol. 50: 17–23.
25. Erdemir, A., Nichols, F. A., Pan, X. Z., Wei, R. Wilbur, P. (1993). Diam. Relat. Mater. 3: 119–125.
26. Erdemir, A., Bindal, C., Pagan, J., Wilbur, P. (1995).Surf. Coat. Technol. 76–77: 559–563.
27. Erdemir, A., Bindal, C., Fenske, G. R., Zuiker, C. Wilbur, P. (1996). Surf. Coat. Technol. 86–87: 692–697.
28. Erdemir, A., Fenske, G. R., Terry, J., Wilbur, P. (1997). Surf. Coat. Technol. 94–95: 525–530.
29. Erdemir, A., Nilufer, I. B., Eryilmaz, O. L. Beschliesser, M., Fenske, G. R. (1999). Surf. Coat. Technol. 120–121: 589–593.
30. Erdemir, A., Eryilmaz, O. L., Nilufer, I. B., Fenske, G.R. (2000). Surf. Coat. Technol. 133–134: 448–454.
31. Field, S. K., Jarratt, M., Teer, D. G. (2004). Tribol. Int. 37: 949–956.
32. Fontaine, J., Donnet, J., Grill, A., Le Mogne, T. (2001). Surf. Coat. Technol. 146–147: 286–291.
33. Fontaine, J., Belin, M., Le Mogne, T., Grill, A. (2004a). Tribol. Int. 37: 869–877.
34. Fontaine, J., Loubet, J. L., Le Mogne, T., Grill, A. (2004b). Tribol. Lett. 17: 709–714.
35. Fontaine, J., Le Mogne, T., Loubet, J. L., Belin, M. (2005). Thin Solid Films 482: 99–108.
36. Fukui, H., Irie, M., Utsumi, Y., Oda, K., Ohara, H. (2001). Surf. Coat. Technol. 146–147: 378–383.
37. Gangopadhyay, A. (1998). Tribol. Lett. 5: 25–39.
38. Gao, F., Erdemir, A., Tysoe, W. T. (2005). Tribol. Lett. 20(3–4): 221–227.
39. Gardos, M. N. (1994). Tribology and wear behaviour of diamond. In: Spear, K. E., Dismuke, J. P. (eds) Synthetic Diamond: Emerging CVD Science and Technology. Wiley, New York, pp. 419–502.
40. Gilmore, R., Hauert, R. (2000). Surf. Coat. Technol. 133–134: 437–442.
41. Gilmore, R., Hauert, R. (2001). Thin Solid Films 398–399: 199–204.
42. Grill A. (1997). Surf. Coat. Technol. 94–95: 507–513.
43. Grill, A. (1999). Diam. Relat. Mater. 8: 428–434.
44. Grill, A., Patel, V. (1993). Diam. Relat. Mater. 2: 597–605.
45. Grillo, S. E., Field, J. E. (2003). Wear 254: 945–949.
46. Hakovirta, M., Tiainen, V. -M., Pekko, P. (1999). Diam. Relat. Mater. 8: 1183–1192.
47. Grill, A., Patel, V., Meyerson, B. S. (1991). J. Electrochem. Soc. 138(8): 2362–2367.
48. Harris, S. J., Weiner, A. M., Meng, W. J. (1997). Wear 211: 208–217.
49. Heimberg, J. A., Wahl, K., Singer, I. L., Erdemir, A. (2001). Appl. Phys. Lett. 78(17): 2449–2451.
50. Hirvonen, J. -P., Koskinen, J., Lappalainen, R., Anttila, A. (1989). Mater. Sci. Forum 52&53: 197–216.
51. Hirvonen, J. -P., Koskinen, J., Anttila, A., Lappalainen, R., Toivonen, R., Arminen, E., Trkula, M. (1990a). Wear 141: 45–58.
52. Hirvonen, J. -P., Lappalainen, R., Koskinen, J., Anttila, A., Jervis, T. R., Trkula, M. (1990b). J. Mater. Res. 5(11): 2524–2530.
53. Holmberg, K., Matthews, A. (1994). Coatings Tribology – Properties, Techniques and Applications in Surface Engineering. Tribology Series, 28. Elsevier Science, Amsterdam, The Netherlands, 442 pp.
54. Holmberg, K., Koskinen, J., Ronkainen, H., Vihersalo, J., Hirvonen, J. -P., Likonen, J. (1994). Diam. Films Technol. 4(2): 113–129.

55. Itoh, Y., Hibi, S., Hioki, T., Kawamoto, J. (1991). J. Mater. Res. 6(4): 871–874.
56. Jahanmir, S., Deckman, D. E., Ives, L. K., Feldman, A., Farabaugh, E. (1989).Wear 133: 73–81.
57. Jiang, J., Arnell, R. D. (1998). Wear 218: 223–234.
58. Jun, Q., Jianbin, L., Jing, W., Wenzhi, L. (2000). Surf. Coat. Technol. 128–129: 324–328.
59. Jung, H. -S., Park, H. -H., Pang, S. S., Lee, S. Y. (1999). Thin Solid Films 355–356: 151–156.
60. Klafke, D., Brand, J., Brnad, C., Wittorf, R. (2005). J. Tribotest 11: 213–232.
61. Kim, D. S., Fisher, T. E., Gallois, B. (1991). Surf. Coat. Technol. 49: 537–542.
62. Kim, H. I., Lince, J. R., Eryilmaz, O. L., Erdemir, A. (2006). Tribol. Lett. 21(1): 53–58.
63. Kim, M. -G., Lee, K. -R., Eun, K. Y. (1999). Surf. Coat. Technol. 112: 204–209.
64. Konca, E., Cheng, Y. -T., Weiner, A. M., Dasch, J. M., Alpas, A. T. (2005). Surf. Coat. Technol. 200: 1783–1791.
65. Konca, E., Cheng, Y. -T., Alpas, A. T. (2006a). Diam. Relat. Mater. 15: 939–943.
66. Konca, E., Cheng, Y. -T., Weiner, A. M., Dasch, J. M., Alpas, A. T. (2006b). Surf. Coat. Technol. 200: 3996–4005.
67. Koskinen, J., Anttila, A., Hirvonen, J. -P. (1991). Hard carbon coatings by the pulsed arc-discharge method. In: Tzeng, Y., Yoshikawa, M., Murakawa, M., Feldman, A. (eds) Applications of Diamond Films and Related Materials. Material Science Monographs, 73. Elsevier Science, Amsterdam, The Netherlands, pp. 845–850.
68. Koskinen, J., Hirvonen, J. -P., Lappalainen, R., Anttila, A. (1994). Diam. Relat. Mater. 3(1–2): 52–55.
69. Koskinen, J., Hirvonen, J. -P., Keränen, J. (1998a). Relaxation of sp3 bonds in hydrogen-free carbon films during growth. In: Silva, S. R. P., Robertson, J., Milne, W., Amaratunga, G. A. J. (eds) Amorphous Carbon: State of the Art. Singapore. World Scientific Publishing Co. Ltd., Cambridge, UK, pp. 46–56.
70. Koskinen, J., Schneider, D., Ronkainen, H., Muukkonen, T., Varjus, S., Burck, P., Holmberg, K., Scheibe, H. -J. (1998b). Surf. Coat. Technol. 108–109: 385–390.
71. Koskinen, J., Ronkainen, H., Varjus, S., Muukkonen, T., Holmberg, K., Sajavaara, T. (2001). Diam. Relat. Mater. 10: 1030–1035.
72. Le Huu, Zaidi, H., Paulmier, D. (1995). Wear 181–183: 766–770.
73. Le Huu, Zaidi, H., Paulmier, D., Voumard, P. (1996). Thin Solid Films 290–291: 126–130.
74. Leng, Y. X., Chen, J. Y., Yang, P., Sun, H., Wan, G. J., Huang, N. (2003). Surf. Coat. Technol. 173: 67–73.
75. Li, H., Wang, C., Chen, J., Zhou, H., Liu, H. (2005a). Appl. Surf. Sci. 249: 257–265.
76. Li, H., Wang, C., Chen, J., Zhou, H., Liu, H. (2005b). Tribol. Lett. 19(3): 231–238.
77. Li, H., Xu, T., Wang, C., Chen, J., Zhou, H., Liu, H. (2006a). Diam. Relat. Mater. 15: 1228–1234.
78. Li, H., Xu, T., Wang, C., Chen, J., Zhou, H., Liu, H. (2006b). Thin Solid Films 515: 2153–2160.
79. Li, K. Y., Zhou, Z. F., Bello, I., Lee, C. S., Lee, S. T. (2005c). Wear 258: 1577–1588.
80. Liu, D., Zhang, S., Ong, S. -E., Benstetter, G., Du., H. (2006). Mater. Sci. Eng. A 426: 114–120.
81. Liu, H., Tanaka, A., Umeda, K. (1999). Thin Solid Films 346: 162–168.
82. Liu, Y., Meletis, E. I. (1997). J. Mater. Sci. 32: 3491–3495.
83. Liu, Y., Erdemir, A., Meletis, E. I. (1996a). Surf. Coat. Technol. 86–87: 564–568.
84. Liu, Y., Erdemir, A., Meletis, E. I. (1996b). Surf. Coat. Technol. 82: 48–56.
85. Liu, Y., Erdemir, A., Meletis, E. I. (1997). Surf. Coat. Technol. 94–95: 463–468.
86. Liu, Z. T., Xu, N. K., Geng, D. S., Zheng, X. L. (1993). Surf.Eng. 9(2): 148–150.
87. McKenzie, D. R., Yin, Y., Marks, N. A., Davis, C. A., Pailthorpe, B. A., Amaratunga, G. A. J., Veerasamy, V. S. (1994). Diam. Relat. Mater. 3: 353–360.
88. Meletis, E. I., Erdemir, A., Fenske, G. R. (1995). Surf. Coat. Technol. 73: 39–45.
89. Memming, R., Tolle, H. J., Wierenga, P. E. (1986). Thin Solid Films 143: 31–41.
90. Meneve, J., Dekampeneer, E., Smeets, J. (1994). Diam. Films Technol. 4(1): 23–27.

91. Meunier, C., Alers, P., Marot, L., Stauffer, J., Randal, N., Mikhailov, S. (2005). Surf. Coat. Technol. 200: 1976–1981.
92. Miyake, S., Kaneko, R. (1992). Thin Solid Films 212: 256–261.
93. Miyake, S., Kaneko, R., Kikuya, Y., Sugimoto, I. (1991). J. Tribol. 113: 384.
94. Miyake, S., Takahashi, S., Watanabe, I., Yoshihara, H. (1987). ASLE Trans. 30(1): 121–127.
95. Miyoshi, K. (1990). Surf. Coat. Technol. 43/44: 799–812.
96. Miyoshi, K. (2001). Wear 251: 1061–1067.
97. Miyoshi, K., Pouch, J. J., Alterovitz, A. (1989). Plasma-Deposited Amorphous Hydrogenated Carbon Films and Their Tribological Properties. NASA TM-102379. Cleveland, Ohio, 11 pp.
98. Miyoshi, K., Wu, R. L. C., Garscadden A. (1992). Surf. Coat. Technol. 54/55: 428–434.
99. Müller, U., Hauert, R., Oral, B., Tobler, M. (1995). Surf. Coat. Technol. 76–77: 367–371.
100. Neerinck, D., Persoone, P., Sercu, M., Goel, A., Kester, D., Bray, D. (1998a). Diam. Relat. Mater. 7: 468–471.
101. Neerinck, D., Persoone, P., Sercu, M., Goel, A., Verkatraman, C., Kester, D., Halter, C., Swab, P., Bray, D. (1998b). Thin Solid Films 317: 402–404.
102. Nilsson, D., Svahn, F., Wiklund, U., Hogmark, S. (2003). Wear 254: 1084–1091.
103. Oguri, K., Arai, T. (1990). J. Mater. Res. 5(11): 2567–2571.
104. Ohana, T., Nakamura, T., Suzuki, M., Tanaka, A., Koga, Y. (2004). Diamond and Related Materials 13: 1500–1504.
105. Olsen, J. E., Fisher, T. E., Gallois, B. (1996). Wear 200: 233–237.
106. Ostrovskaya, Y. L., Strel'nitskij, V. E., Kuleba, V. I., Gamulya, G. D. (2001). Tribol. Int. 34: 255–263.
107. Park, S. J., Lee, K. -R., Ko, D. -H. (2004). Tribol. Int. 37: 913–921.
108. Paulmier, D., Zaidi, H., Nery, H., Le Huu, T. (1993). Surf. Coat. Technol. 62: 570–576.
109. Qi, Y., Konca, E., Alpas, A.T. (2006). Surf. Coat. Technol. 600: 2955–2965.
110. Rabbani, F. (2004). Surf. Coat. Technol. 184: 194–207.
111. Rey, S., Prevot, B., Fogarassy, E., Arnault, J. C., Hommet, J., Le Normand, F., Boher, P. (2000). Appl. Phys. A 71: 433–439.
112. Robertson, J. (2002). Mater. Sci. Eng. R 37: 129–281.
113. Ronkainen, H. (2001). Tribological Properties of Hydrogenated and Hydrogen-free Diamond-like Carbon Coatings. VTT Publications 434. VTT Technical Research Centre of Finland, Espoo, Finland, 52 pp.
114. Ronkainen, H., Varjus, S. (1994). Tribology evaluation of diamond-like carbon films by pin-on-disc tests at a wide range of sliding speeds and loads. In: Hedenquist, P., Hogmark, S. (eds), Proceedings of the 6th Symposium on Tribology, Vol. I: 12–15 June 1994, Uppsala, Sweden, 49–56.
115. Ronkainen, H., Koskinen, J., Anttila, A., Holmberg, K., Hirvonen, J-P. (1992a). Diam. Relat. Mater. 1: 639–643.
116. Ronkainen, H., Likonen, J., Koskinen, J. (1992b). Surf. Coat. Technol. 54/55: 570–575.
117. Ronkainen, H., Varjus, S., Koskinen, J. (1992c). Tribologia 11(4): 133–141.
118. Ronkainen, H., Koskinen, J., Likonen, J., Varjus, S., Vihersalo, J. (1994). Diam. Relat. Mater. 3: 1329–1336.
119. Ronkainen, H., Likonen, J., Koskinen, J., Varjus, S. (1996). Surf. Coat. Technol. 79: 87–94.
120. Ronkainen, H., Varjus, S., Holmberg, K. (1998). Wear 222: 120–128.
121. Ronkainen, H., Koskinen, J., Varjus, S., Homberg, K. (1999). The friction behaviour of a-C: H and ta-C films in dry and humid conditions. In: Verkammen, K., Meneve, J. (eds) COST 516 Tribology Symposium. Antwerpen, Belgium, 20–21 May, pp. 140–149.
122. Ronkainen, H., Varjus, S., Koskinen, J., Holmberg, K. (2001). Wear 249: 260–266.
123. Sánchez-López, J. C., Donnet, C. Loubet, J. L., Belin, M., Grill, A., Patel, V., Jahnes, C. (2001). Diam. Relat. Mater. 10: 1063–1069.
124. Sánchez-López, J. C., Erdemir, A., Donnet, C., Rojas, T. C. (2003). Surf. Coat. Technol. 163–164: 444–450.
125. Sheeja, D., Tay, B. K., Yu, L., Lau, S. P. (2002). Surf. Coat. Technol. 154: 289–293.

126. Sugimoto, I., Miyake, S. (1990). Appl. Phys. Lett. 56(19): 1868–1870.
127. Suzuki, M., Ohana, T., Tanaka, A. (2004). Diam. Relat. Mater. 13: 2216–2220.
128. Svahan, F., Kassman-Rudolphi, Å., Wallén, E. (2003). Wear 254: 1092–1098.
129. Tagawa, M., Ikemura, M., Nakayama, Y., Ohmea, N. (2004). Tribol. Lett. 17(3): 575–580.
130. Tallant, D. R., Parmeter, J. E., Diegal, M. P., Simpson, R. L. (1995). Diam. Relat. Mater. 4: 191–199.
131. Tanaka, A., Nishibori, T., Suzuki, M., Maekawa, K. (2004). Wear 257: 297–303.
132. Vanhulsel, A., Blanpain, B., Celis, J-. P., Roos, J., Dekempeneer, E., Smeets, J. (1998). Surf. Coat. Technol. 98: 1047–1052.
133. Venkatraman, C., Brodbeck, C., Lei, R. (1999). Surf. Coat. Technol. 115: 215–221.
134. Verkammen, K., Meneve, J., Dekempeneer, E., Smeets, J., Roberts, E. W., Eiden, M.J. (1999). Surf. Coat. Technol. 120–121: 612–617.
135. Voevodin, A. A., Donley, M. S. (1996). Surf. Coat. Technol. 82: 199–213.
136. Voevodin, A. A., Zabinski, J. S. (2000). Thin Solid Films 370: 223–231.
137. Voevodin, A. A., Phelps, A. W., Zabinski, J. S. Donley, M. S. (1996). Diam. Relat. Mater. 5: 1264–1269.
138. Voevodin, A. A., Jones, J. G., Back, T. C., Zabinski, J. S., Strelnitzki, V. E., Aksenov, I. I. (2005). Surface and Coatings Technology 197: 116–125.
139. Voevodin, A. A., Donley, M. S., Zabinski, J. S. (1997). Surf. Coat. Technol. 92: 42–49.
140. Wei, R., Wilbur, P. J., Liston, M. J., Lux, G. (1993). Wear 162–164: 558–568.
141. Wild, C., Koidl, P. (1987). Network structure and thermal decomposition of plasma deposited a-C:H films studied by gas effusion spectroscopy. In: Koidl, P., Oelhafen, P. (eds) EMRS Symposia Proceedings, Volume XVII, Amorphous Hydrogenated Carbon Films. France. Les Éditions de Physique.
142. Wu, W. -J., Hon, M. -H. (1999). Surf. Coat. Technol. 111: 134–140.
143. Yoon, E. -S., Kong, H., Lee, K. -R. (1998). Wear 217: 262–270.
144. Zaidi, H., Frene, J., Senouci, A., Schmitt, M., Paulmier, D. (2000). Surf. Coat. Technol. 123: 185–191.
145. Zaidi, H., Le Huu, Paulmier, D. (1994). Diam. Relat. Mater. 3: 787–790.
146. Zaidi, H., Le Huu, Robert, F., Bedri, R., Kadiri, E. K., Paulmier, D. (1995). Surf. Coat. Technol. 76–77: 564–571.
147. Zhang, S., Bui, X. L., Li, X. (2006). Diamond and Related Materials 15: 972–976.
148. Zhang, W., Tanaka, A. (2004). Tribol. Int. 37: 975–982.
149. Zhang, W., Tanaka, A., Wazumi, K. K., Koga, Y. (2002). Thin Solid Films 413: 104–109.
150. Zhang, W., Tanaka, A., Wazumi, K. K., Koga, Y. (2003). Tribol. Lett. 14(2): 123–130.
151. Zhou, Z. F., Li, K. Y., Bello, I., Lee, C. S., Lee, S. T. (2005). Wear 258: 1589–1599.

Third Bodies and Tribochemistry of DLC Coatings

T. W. Scharf[1] and I. L. Singer[2]

Abstract Much of the literature on diamond-like carbon (DLC) tribological coatings emphasizes the processing–structure–tribological property interrelationships but often ignores or speculates on the mechanisms which control friction and wear. In reality, third-body processes, such as transfer films that form in the moving contact, are responsible for the long life of DLC coatings. In this chapter, the friction and wear behavior of amorphous diamond-like nanocomposite (DLN) coatings, Ti- and W-doped DLC, and hydrogenated DLC coatings in low speed, dry sliding contact have been investigated using a home-built *in situ* Raman tribometer. *In situ* optical microscopy identified how third-body processes controlled friction and wear behavior of these DLC coatings in reciprocating sliding against sapphire hemispheres in dry (~4% RH) and humid (~20–60% RH) air between contact stresses of 0.7 and 1.1 GPa. *In situ* visual observations monitored the health (e.g., formation, thickening, thinning, and loss) of transfer films at the sliding (buried) interface. For most of the coatings, interfacial sliding between the transfer film and underlying wear track was the dominant velocity accommodation mode (VAM) responsible for steady-state low friction coefficients between 0.03 and 0.2, with lower values obtained at high contact stress and lower RH percentage. Transfer film behavior with the W-doped DLC coating was also studied when lubrication changed from dry air to a perfluoropolyether (PFPE) lubricant.

In situ Raman spectroscopy was used to investigate the chemistry of DLC coatings and the tribochemically-formed transfer films. For the cases of DLN and some DLC coatings, Raman spectra in the C–C band region (1300–1700 cm^{-1}) evolved from that of the coating to the transfer film as the transfer film thickened; this shift in the graphite-like carbon (G band) peak was shown to correlate with the relative amount of transfer film. Raman spectroscopy and energy-dispersive x-ray analysis identified tribochemical phases such as TiO_2 and WO_3 in transfer films formed from Ti-DLC and W-DLC, respectively. In addition, *ex situ* Fourier

[1] The University of North Texas, Department of Materials Science and Engineering, Denton, TX 76203-5310, USA

[2] U.S. Naval Research Laboratory, Code 6176, Washington, DC 20375-5342, USA

C. Donnet and A. Erdemir (eds.), *Tribology of Diamond-Like Carbon Films: Fundamentals and Applications*.

transform infrared (FTIR) spectroscopy verified that these transfer films had different carbon–carbon and carbon–hydrogen chemistry than the coatings.

Keywords Friction, DLC, Solid Lubricants, Third bodies, Transfer films, Wear, Raman, FTIR, Spectroscopy, Energy-dispersive x-ray analysis, EDX, Velocity accommodation, Tribochemistry, Lubrication, Krytox, D-peak, G-peak, *in situ*, Surface Films/Coatings

1 Introduction

Diamond-like carbon (DLC) exhibits an unusual combination of tribological and mechanical properties not often found in tribological coatings such as low friction coefficients, low wear rates, relatively high hardness, high elastic modulus, and good adhesion [1,2]. Most of the research on DLC coatings has emphasized processing/property relationships, such as the role of processing parameters and alloying (e.g., with hydrogen or silicon) in achieving low friction and low wear; examples can be found in many of the accompanying chapters. While such studies are important for designing improved coatings, tribological studies are needed to explain the friction and wear behavior. In particular, there is an obvious contradiction between DLC's mechanical and tribological properties and the Bowden–Tabor model for low-friction coating [3] that associates low friction with low shear strength materials like MoS_2 and graphite, not with high hardness materials like DLC. Furthermore, traditional friction models cannot account for the fact that addition of Si and/or O into the coatings can lower the friction coefficient by a factor of two, from 0.1 to 0.05 without significantly changing the hardness of the coatings [2,4–9].

An alternative model of friction and wear, introduced by Godet and coworkers [10–12], involves third-body processes. Third bodies are formed by the relative motion of the two parent (first body) materials in the sliding contact. They often appear first as thin films transferred to the stationary counterface, and then evolve into wear particles [12–15]. By separating the two first bodies, third bodies take on the chore of transmitting stresses and accommodating the relative motion between the counterfaces (velocity accommodation mode, VAM). Thus, friction and wear behavior is controlled by the third-body processes, as opposed to the first-body properties.

Much of what we know about third-body processes has been inferred by *ex situ* analysis of sliding contacts. Typically, tests are run for a preselected number of cycles, the two first-body counterfaces are separated and the worn surfaces are analyzed. This *ex situ* approach has been used to study the role of transfer films in long-lived solid lubricant coatings like MoS_2 [16–18] and hard coatings based on DLC [9,19–26]. However, real-time, *in situ*, observation of the sliding interface during friction testing is a more direct method for identifying third-body processes. Years ago, Sliney [27] used *in situ* studies to show

debris accumulation and flow in solid lubricant contacts. More recently, Berthier [12] and Descartes et al. [28] reported *in situ* visualization studies of MoS_2 coatings and showed how third bodies "flow" in and out of the contact: particles detach from the first body, circulate in the contact, then leave either temporarily (and later recycled in the contact) or permanently (as wear debris ejected from the contact). The Naval Research Laboratory (NRL) group [29,30] has identified several third-body processes controlling friction and wear of Pb-alloyed MoS_2 and boric acid coatings. For the case of alloyed MoS_2 against sapphire counterfaces in dry air, transfer films generated during sliding reduced the friction coefficients by accommodating motion through interfacial sliding, the dominant VAM. However, in moist air friction coefficients increased, leading to small contributions of shearing, detachment, and recirculation of debris to the VAM. Other complementary methods for real-time monitoring of sliding interfaces are also being pursued: electrical contact resistance (ECR) mapping [31,32], Fourier transform infrared (FTIR) [33,34] and Raman [30,35–41] spectroscopies.

Raman spectroscopy is particularly useful for studying DLC for several reasons. First, the Raman C–C band intensities in the 1300–1700 cm^{-1} region are enhanced due to the resonant Raman effect [42]. Second, two particular bands in this region, the D (so-called disorder) and G (graphitic) bands, often show changes in their peak location and intensity depending on the structure of the carbon [43]. Third, Raman spectra can be acquired with high spatial resolution, which adds to its usefulness for investigating transfer films. An important, but not fully exploited, finding of Raman analysis is that transfer films and debris generated during sliding against DLC have distinctly different D and G features than the DLC coatings themselves [22,24]. For these reasons, *in situ* Raman can provide new insights into tribochemistry (chemistry induced by rubbing) and role of the transfer film in the friction and wear processes.

The goal of the research has been to demonstrate that third bodies control the sliding friction and wear behavior of DLC coatings. Optical microscopy has identified the third-body formation and attachment as transfer films; Raman spectroscopy, FTIR, and scanning electron microscope (SEM) with energy-dispersive x-ray (EDX) analysis have identified the thickness and chemistry of third bodies. Various DLC coatings have been investigated including: diamond-like nanocomposite (DLN, C-H:Si-O) [7–9,37–41]; metal-doped Ti-DLC (C-H:Ti), W-DLC (C-H:W), and Ti-C (C:Ti) [44,45]; and hydrogenated DLC [1,46]. Differences in their friction and wear behaviors in dry and moist air and at several loads are reported. *In situ* visualization of the interface during sliding contact was used to identify VAMs and to correlate third-body processes to friction and wear behavior. Another objective of this chapter is to demonstrate that *in situ* Raman can be used to quantify, as well as monitor, the thickness of transfer films. The influence of a liquid lubricant on the third-body processes will also be examined. Discussion will focus on the role of chemistry/tribochemistry in the formation and adhesion of transfer films and the role of velocity accommodation on friction and wear of DLC coatings.

2 Experimental

Three groups of DLC coatings were tested:

(a) Bekaert Advanced Coating Technologies' (Amherst, NY) amorphous DLN (C-H:Si-O) coatings prepared by plasma-enhanced chemical vapor deposition (PECVD) [7–9,37–41].
(b) Timken Company's (Canton, OH) amorphous Ti-DLC (C-H:Ti), W-DLC (C-H:W), and reference Ti-C (C:Ti) coatings prepared by reactive magnetron sputtering [44,45].
(c) IBM Corporation's (Yorktown Heights, NY) amorphous hydrogenated DLC coatings prepared by DC-biased plasma-assisted chemical vapor deposition (PACVD) [1]. The H–C bond fraction for the CY5 (cyclohexane gas precursor) coating was 1.0, i.e., all of H was bonded to C, whereas the fraction for the AC8 (acetylene gas precursor) coating was 0.57 [46].

The approximate nominal thickness, residual stress, hardness, and elastic modulus values of the coatings investigated are listed in Table 1.

Sliding tests were performed using a homebuilt *in situ* Raman tribometer shown in Fig. 1 [30,37–41]. The reciprocating stage was designed to fit directly underneath the optics of the microscope, enabling *in situ* optical/video imaging and Raman spectroscopy of the sliding contact region through a transparent hemisphere. A 6.35 mm diameter sapphire hemisphere (H = 21 GPa; E = 400 GPa) was loaded against the DLC coatings via a fixed weight at the end of the lever arm. A piezosensor housed below the sample stage measured the friction force. Occasionally, tests were also performed with hardened AISI 52100 steel hemispheres. Normal loads were 6.4 N and 23.9 N, which corresponded to initial mean Hertzian contact stresses, P_m, of 0.5–1.3 GPa. Tests were performed in either dry (~2–4% RH) or humid (~20–60% RH) air at room temperature. At least three tests were run at each condition, and each test was run at a sliding speed of 1 mm/s between 300 and 5000 cycles. The track length was 6 mm for the first 300 cycles then cut back to 4 mm for the remaining cycles, as in stripe testing [17]. Computer-aided data acquisition recorded both average and spatially resolved friction forces at 300 total points (20 µm intervals) along a 6 mm

Table 1 Nominal DLC coating thicknesses and mechanical properties. (From [9,44,46].)

Coating	Thickness (µm)	Residual stress (GPa)	Hardness (GPa)	Elastic modulus (GPa)
DLN-1	2.3	–0.5	12	88
DLN-2	1.9	–1.4	17	128
Ti-DLC	2	–1.4	11	125
W-DLC	2.8	–1.5	12	156
Ti-C	1	–1.2	8	110
AC8 ($CH_{0.34}$)	1	–0.77	14	95
CY5 ($CH_{0.42}$)	1	–0.33	4	20

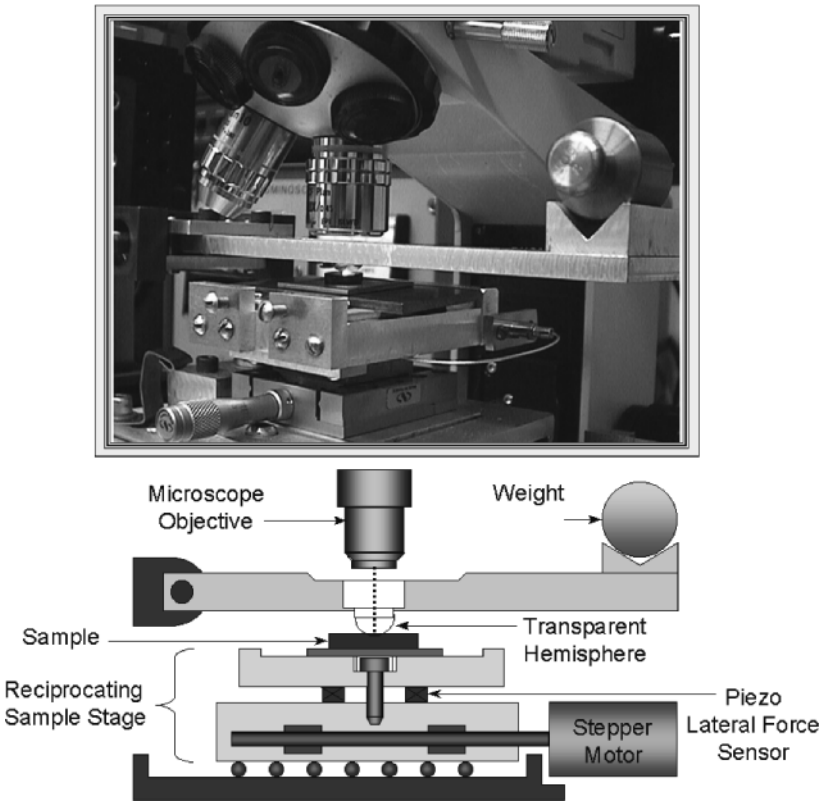

Fig. 1 Photo and schematic representation of the *in situ* Raman tribometer. Micro-Raman spectroscopy and optical microscopy at the sliding point contact can be performed through the objective lens positioned above the transparent hemisphere. (Reprinted from [30,36]. With permission.)

track length and 200 total points along a 4 mm track length. The friction coefficient, μ, was obtained by dividing the mean value of the spatially resolved friction force from 10% to 90% along the track by the normal load. We refer to the friction coefficient as being in steady state when it remains constant and without spikes.

During a test, the optical microscope could be used either to observe the sliding contact or to perform micro-Raman spectroscopy. Optical images were acquired using a video camera and recorded on VHS tape at 30 frames/s. Still images were obtained either from the videotape or by image capture software. Optical interference between the transparent hemisphere and flat produced Newton's rings. These rings were used to determine the separation, h, of the hemisphere from the DLC surface as a function of distance from the center of the contact. Destructive interference (dark bands) occurred at separations $h = 0$ and $h = n\lambda/2$ where $\lambda/2 \sim 0.25\,\mu m$ and $n = 0, 1, 2,\ldots$

The Raman microprobe (System 1000, Renishaw, Gloucestershire, UK) consisted of a low power (25 mW) argon ion laser (514.5 nm) excitation source and a

holographic spectrometer; the resolutions were 2 μm for lateral and 1 cm^{-1} for the spectrometer. At this power density (~8 $mW/\mu m^2$), there were no changes in the spectra due to surface heating. The laser was focused at the center of the sliding contact in spot mode with either a 20X or 50X stand-off objective lens. Raman shifts were measured over a wavenumber range from 200 to 1800 cm^{-1} at an acquisition time of 20 s, which translated to roughly 6 sliding cycles. The C–C vibrations for the coatings were deconvoluted and fitted (mixed Gaussian/Lorentzian) into the well-known D and G peaks [43,47]. Baseline corrections were applied to all spectra to remove small fluorescent/luminescent background.

After a test, the counterfaces were separated and analyzed. Coating wear tracks and transfer films on hemispheres were analyzed *ex situ* by a combination of optical microscopy, Raman spectroscopy, stylus profilometry (Tencor P-10), and FTIR spectroscopy. Five profilometry traces were performed on each contact to obtain wear depths and transfer film thicknesses. For coating wear tracks, the wear factor was calculated as the wear track volume divided by the load and the total distance traveled by the hemisphere; in practice, it was computed by dividing the cross-sectional area of the wear track by the load and the number of cycles. For *ex situ* FTIR studies on the DLN coatings, identical friction tests were run with 6.35 mm diameter AISI 52100 steel hemispheres at a normal load of 8.6 N, which corresponded to mean Hertzian contact stress of 0.7 GPa. Steel hemispheres had to be used because sapphire showed a huge IR absorption, which obscured IR signals from transfer films. Reflectance IR spectra were taken with a NicPlan infrared microscope (Thermo Nicolet, Madison WI) interfaced to a Magna 760 FTIR spectrometer (Thermo Nicolet, Madison, WI). The infrared microscope contained an integrated narrow-band mercury–cadmium–telluride MCT detector ($D^* > 1 \times 10^{10}$) and had lateral resolution of 50 μm. Spectra of the transfer films on AISI 52100 steel hemispheres were obtained from a circular spot of ~100 μm defined by a circular aperture inserted into the IR beam. Spectra were collected at a resolution of 2 cm^{-1} using Happ-Genzel apodization, no zero filling, the Mertz phase correction, and a signal gain of 4. Background reflectance spectra were collected under the identical collection conditions on an area of the bare steel hemisphere next to the transfer film. The background spectra were used to calculate the IR spectra in a log [1/R] format with R being the ratio of reflectance of the transfer film versus the reflectance of the bare steel hemisphere.

3 Results

3.1 Diamond-like Nanocomposite Coatings

3.1.1 *In Situ* Analysis of Transfer Film Buildup during Steady-state Friction in Dry Air

Figure 2 shows a typical friction coefficient versus cycle curve obtained with a sapphire hemisphere against a DLN-1 coating in dry air (~4% RH) at a mean Hertz stress of 0.7 GPa [36,39,41]. The friction coefficient dropped rapidly from an

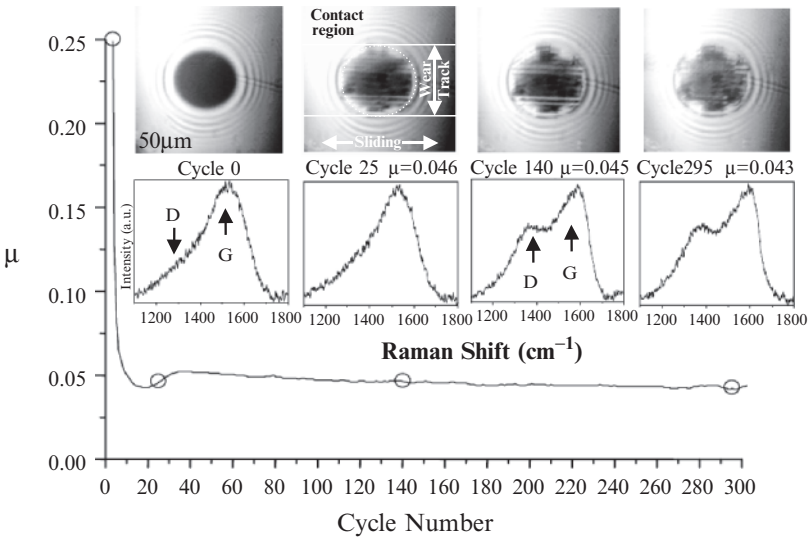

Fig. 2 Friction coefficient (μ) versus cycles for DLN-1 coating in dry air (~4% RH) at a mean Hertz stress of 0.7 GPa. Also shown are *in situ* images and Raman spectra taken at the cycles denoted by a circle on the curve. (Reprinted from [41]. With permission.)

initially high value of 0.25–0.05 and remained constant for 300 cycles. Figure 2 also shows four *in situ* optical images of the sapphire/DLN interface taken during sliding contact. The dark circle at cycle 0 is due to destructive interference of Newton's rings and confirms that the sapphire was in direct contact with the DLN coating; the diameter of the contact area was 104 μm, which compares favorably with the calculated Hertz diameter of 98 μm. Within a few sliding cycles, a transfer film accumulated across most of the contact area on the sapphire hemisphere (see image, cycle 25). With continued sliding, the transfer film thickened and became patchy; *ex situ* profilometry of this and similar transfer films gave film thicknesses from 100 to 200 nm. Direct measurement of the (apparent) area of contact, combined with the friction coefficient, gave values of interfacial shear strength ($\tau = \mu \bullet P_m$) of 28–30 MPa, which compare favorably with a value of 25 MPa from a different silicone-formed DLN coating [48]. Videotapes showed that the transfer film remained motionless during sliding, indicating that the VAM was interfacial sliding.

In situ Raman spectra, also shown in Fig. 2, were acquired in six cycles either before or after the images were taken. Only the bands in the C–C stretch region (1200–1700 cm^{-1}) are reported; these bands are found in many types of carbon films with nanoscale or amorphous structures, including DLC and graphitic and glassy carbons [47]. Initially (cycles 0 and 26–32), the peaks were identical to the *ex situ* peaks of the DLN coating. As the transfer film thickened, the peaks evolved to those characteristic of a graphite-like transfer film [36,39]; the latter, seen in the two rightmost spectra, showed a D-peak at 1385 cm^{-1} and a G-peak at 1585 cm^{-1} shifted ~50 cm^{-1} higher than the same peak in the DLN coating. This evolution occurs because the *in situ* Raman spectrum combines Raman signal from both the

thin layer of transfer film and the underlying DLN coating; deconvolution of the spectra provided another measure – along with Newton's rings – of the thickness of the transfer film [39,41]. This process will be described below.

3.1.2 *In Situ* Analysis During Friction Instability and Transfer Film Thinning in Dry Air

Figure 3 shows a friction coefficient versus cycle curve obtained later in sliding, when the transfer film began to thin and the friction coefficient started to fluctuate. The susceptibility of the transfer film to scratching, suggested by the faint horizontal lines in Fig. 2, is more apparent in the image at cycle 400 in Fig. 3. By cycle 450, *in situ* Raman spectra showed that the C–C bands had reverted to that of the coating, an indication that the transfer film was thinning. Some 60 cycles later, the friction began to climb, ultimately to 0.5, before falling to its steady-state value. The image at cycle 514 shows a dark ellipse at the center of the sliding contact; the ellipse is where the hemisphere was in contact with the wear track and indicates that a patch of the transfer film was lost. At the peak of the friction spike, the VAM changed from interfacial sliding to a mix of sliding and shearing (and extrusion) of debris in the interface. Most of the debris that entered the contact was smeared along the track; only a small amount attached to the hemisphere, but not as a continuous transfer film. Over the next 30 cycles, as the friction coefficient dropped to 0.05, a transfer film partially reformed on the hemisphere (see cycle 661 image) and the VAM returned to interfacial sliding. However, unlike the pre-spike stage of sliding, a thick transfer film never developed, as also seen in the two rightmost Raman spectra. Similar third-body processes (removal of transfer film, debris recirculation, and

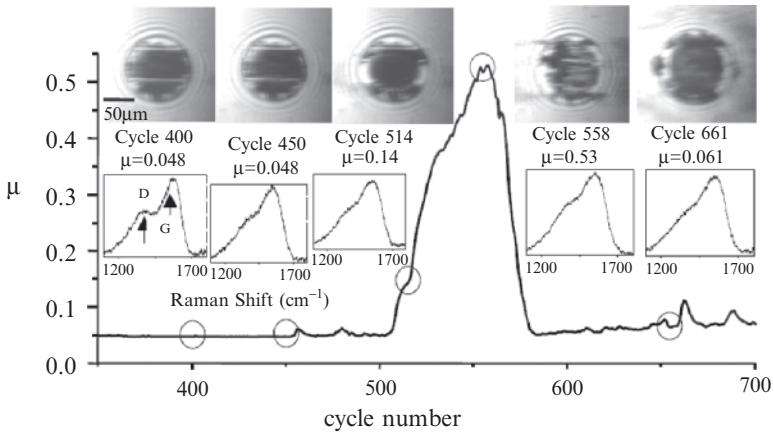

Fig. 3 Friction coefficient, *in situ* images and Raman spectra versus cycles; from the continuation of the test shown in Fig. 2. (Reprinted from [41]. With permission.)

reformation of a transfer film) were seen during each of the friction spikes throughout the remainder of the test. *Ex situ* profilometry of the wear scar on the hemisphere showed a patchy transfer film and an abraded sapphire surface [36].

3.1.3 *In Situ* Analysis of Transfer Film Buildup During Steady-state Friction in Humid Air

Figure 4a shows a typical friction coefficient versus cycle curve for DLN-1 coating taken at low contact stress (0.7 GPa) in ~40% RH air [37,39]. The friction coefficient slowly fell to values of ~0.06 by about cycle 130 and remained nearly constant to cycle 300. Figure 4a also shows five *in situ* optical images of the sapphire/DLN interface taken at the center of contact before and during various stages of sliding. Within 20 sliding cycles, as the friction coefficient dropped to <0.11, a transfer film accumulated across the contact area on the sapphire hemisphere similar to the dry air test. Over the next 280 cycles, the transfer film thickened as evident by the inward motion of the Newton's rings (cycle 50 image) and, later, by the gradual loss of focus of the DLN surface (cycles 170 and 295 images). Steady-state friction values ($\mu_{s.s.}$ ~0.06) and stable transfer film growth were observed during the remainder of the test, unlike the dry air test where friction fluctuations were observed with this contact stress.

Figure 4b shows six *in situ* Raman spectra of the C–C bands taken at various cycles during the test. At cycle 0, the spectrum was identical to that of the coating (i.e., taken *ex situ*) as expected. By cycles 23–28, the spectrum began to change: the G-band peak shifted from 1520 to 1555 cm^{-1} and the D band (1365 cm^{-1}) evolved from a shoulder to a distinct peak. With further sliding, the D-band peak continued to increase in intensity and the peak of the G-band shifted upward to 1600 cm^{-1}

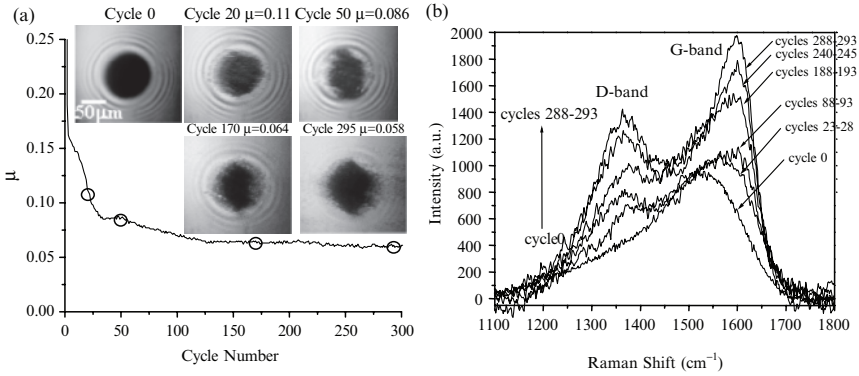

Fig. 4 (a) Friction coefficient and (b) *in situ* Raman spectra versus cycles for DLN-1 coating in humid air (~40% RH) at a mean Hertz stress of 0.7 GPa. Insets in (a) are *in situ* optical images taken during sliding. (Reprinted from [39]. With permission.)

(similar to the dry air test). No further shift in the G-band peak was exhibited past cycle 245, just a slight increase in both band intensities as shown by the spectrum at cycles 288–293.

3.1.4 *In Situ* Analysis During Friction Instability and Transfer Film Thinning in Humid Air

Figure 5a shows a friction coefficient versus cycle curve for DLN-2 coating also taken at ~40% RH air, but now at high contact stress (1.1 GPa) [37,39]. The friction coefficients were lower (μ ~0.035) than in the low contact stress test; however, the initial buildup and thickening of the transfer film (not shown) were similar. By cycle 1,300, a thick, compact transfer layer had developed. However, by cycle 1,605, the Newton's rings inside the contact area indicate that the transfer film was beginning to wear in the middle of the contact, even though the friction remained low; and since several rings can be seen, the transfer film was at least 0.5 μm thick. The first friction spike at cycle 1,668 coincided with the removal of a narrow "sliver" of transfer film inside the contact. With each additional cycle, an adjacent sliver was removed, widening the area over which the sapphire made contact with the coating. The image at cycle 1,674 shows the interface during the peak of a friction spike. The middle portion (the dark ellipse) of the transfer film, at least 0.5 μm thick, was removed, placing the hemisphere nominally in contact with the coating over an elliptical area approximately 200 × 60 μm. At the trailing edge of the friction spike, when the friction fell to 0.04, the cycle 1,730 image showed that the "hole" began to reaccumulate transfer film.

Figure 5b shows five *in situ* Raman spectra of the carbon D- and G-band peaks taken during the test. The spectrum taken during steady-state friction, at cycles 1,418–1,423, is similar to spectra taken after cycle 240 shown in Fig. 4b. By

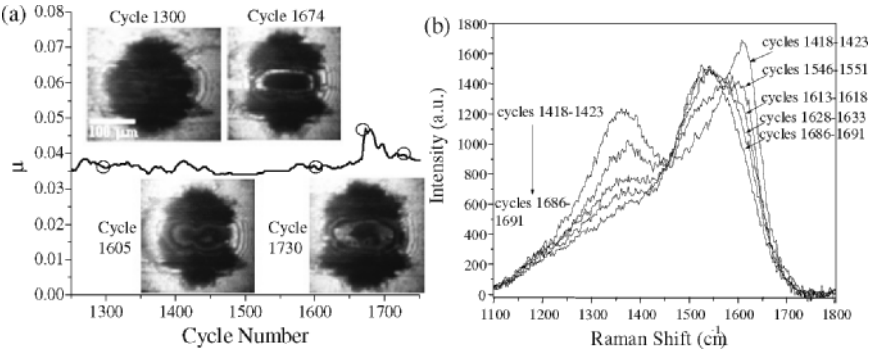

Fig. 5 (a) Friction coefficient and (b) *in situ* Raman spectra versus cycles for DLN-2 coating in humid air (~40% RH) at a mean Hertz stress of 1.1 GPa. Insets in (a) are *in situ* optical images taken during sliding. (Reprinted from Ref [39]. With permission.)

cycles 1,546–1,551, as the transfer film thinned, the spectrum began to change: the G-band peak shifted downward from 1605 to 1580 cm^{-1} and the intensity of the D band (1365 cm^{-1}) decreased. During the friction spike, cycles 1,686–1,691, the spectrum was that of the DLN coating, i.e., the peak of the G band was down to 1530 cm^{-1} and the D band dropped in intensity. No further changes in the spectra were exhibited in the center of the contact even though a new transfer film formed. This correlation of transfer film thickness and Raman spectra evolution suggests that the *in situ* spectra might be a composite of the DLN coating and the transfer film.

We have quantified the transfer film thickness by combining Raman spectra with stylus profilometry and a light-scattering model based on Beer's Law [40]. Since the *ex situ* and *in situ* Raman spectra of thick transfer films are identical, we postulate that *in situ* Raman spectra of the sliding interface can be represented as sums of two baseline spectra, those of the coating and the transfer film at a given frequency, e.g., 1605 cm^{-1}. The sum spectra for transfer film on coating as a function of Raman frequency (ν) and thickness (t) is given by:

$$I(t,\nu) = I_{\infty}{}^{C}(\nu)(\exp(-2t/\lambda_f)) + I_{\infty}{}^{f}(\nu)(1-\exp(-2t/\lambda_f)) \quad (1)$$

where $I_{\infty}{}^{C}$ is the measured Raman intensity at saturation for infinitely thick coating, $I_{\infty}{}^{f}$ is the measured Raman intensity at saturation for infinitely thick transfer film, and λ_f is the experimentally determined mean free path of the transfer film, ~500 nm [40]. The assumption made in deriving Eq. (1), that the thickness of the coating >> λ^{DLN}, is clearly justified for the present coatings, where the thickness is ~2 μm.

One can then invert Eq. (1) and solve for the thickness as a function of intensity at a given frequency,

$$t(\nu) = \left(\frac{\lambda_f}{2}\right)\ln\left[\frac{I\infty^{C}(\nu) - I\infty^{f}(\nu)}{I^{m}(\nu) - I\infty^{f}(\nu)}\right] \quad (2)$$

where $I^m(\nu)$ is the measured intensity from the experimental spectra. Equation (2) allows one to calculate the transfer film thickness directly from experimental spectra.

Figure 6 shows the *in situ* G-peak (ν= 1605 cm^{-1}) and D-peak (ν= 1365 cm^{-1}) intensities from Fig. 5b converted to transfer film thickness using Eq. (2) and plotted along with the friction coefficient versus cycles. A straight-line linear fit through the last four calculated thickness values intercepted a thickness of ~32 nm (G-peak) and ~23 nm (D-peak) at cycle 1,667, where the first friction spike initiated, and ~25 nm (G-peak) and ~16 nm (D-peak) at the peak of the friction spike. There is relatively good agreement between the D-peak and G-peak intensities in determining *in situ* transfer film thickness. This indicates that the friction coefficient remained in steady state until the transfer film thickness was less than 23–32 nm ± 13 nm, the latter indicating the error in the optical mean free path value, and reached a maximum value at a film thickness of 16–25 nm ± 13 nm.

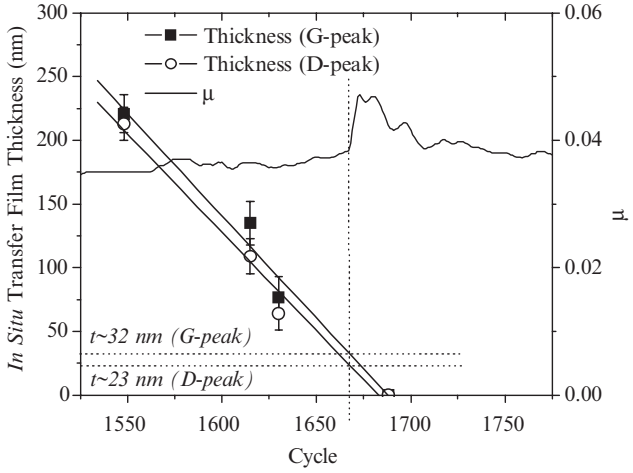

Fig. 6 *In situ* transfer film thickness values (calculated from D-peak and G-peak data in Fig. 5b) and friction coefficients for the ambient air/high contact stress test. (Reprinted from [40]. With permission.)

We interpret this result as evidence that the friction coefficient remained constant until the transfer film wore through (assuming linear wear). Although more work needs to be done on the accuracy of the quantification scheme, these results show that this procedure will be able to provide reasonably accurate approximations of transfer film thickness, hence extending the usefulness of *in situ* Raman tribometry.

3.1.5 *Ex Situ* Raman Spectroscopy and FTIR Spectroscopy of Transfer Films

Figure 7 shows *ex situ* Raman spectra of transfer film (after test in Fig. 4) and DLN-1 coating. The coating spectrum is clearly different from the transfer film. The coating and transfer film D-peaks are located at ~1365 cm^{-1}; however, the D-peak of the coating is less intense. The G-peak has shifted from ~1520 cm^{-1} (coating) to ~1600 cm^{-1} (transfer film). DLC coatings also show the same changes in Raman spectra between the parent DLC coating and transfer films [24,26]. Another difference is that the coating exhibited hydrocarbon stretching vibrations at ~2900 cm^{-1} not observed in the transfer film. In addition, the Raman spectrum of the transfer film taken *ex situ* for DLN-1 is identical to the one taken *in situ*, e.g., at 288–293 cycles (Fig. 4b). Moreover, the spectra of all transfer films had similar line shapes, even when generated under different test conditions: e.g., in ~40% RH air for 20 and 2000 cycles and in ~4% RH air for 1325 cycles [37,40].

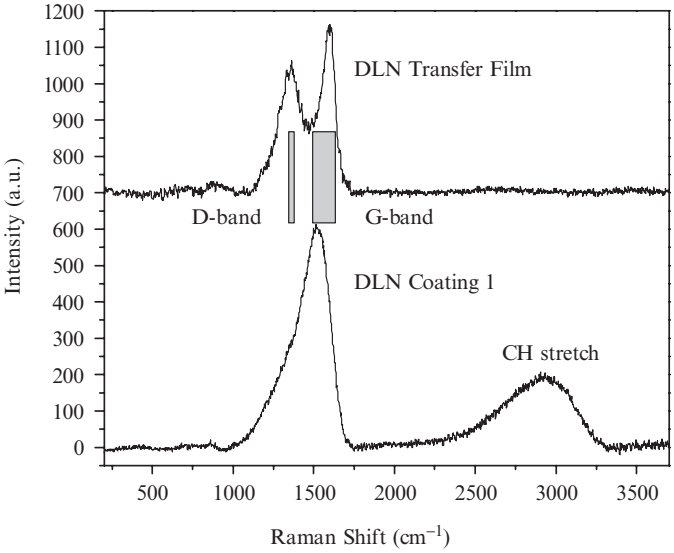

Fig. 7 *Ex situ* Raman spectra of DLN- 1 coating and its transfer film in humid air (2,000 cycle test). (Reprinted from [37]. With permission.)

Table 2 Steady-state friction coefficients (± 0.001) for DLN-1 coating against AISI 52100 steel hemispheres at 0.7 GPa mean Hertz stress under varying humidity and cycles (Reprinted from [37]. With permission.)

% RH	4	20	40	60
$\mu_{s.s.}$	0.042	0.046	0.052	0.056
Cycles	400	1,800	2,000	2,000

Figure 8 shows *ex situ* FTIR spectra of DLN-1 coating and transfer films on steel hemispheres from four different relative humidity tests [37]. The friction coefficients for these tests, summarized in Table 2, were similar to the values obtained against sapphire hemispheres. The spectrum of the DLN coating consisted of the major IR absorption (near 1000 cm^{-1}) attributed to Si–O stretches of silicon oxide species formed during DLN coating deposition. Additional IR bands are attributed to CH_2 and CH_3 deformations at ~1400 cm^{-1}, graphitic-type carbon at ~1580 cm^{-1}, C–H stretches (predominantly CH_2) at ~2900 cm^{-1}, and O–H stretches at ~3600 cm^{-1}.

The most striking difference between the coating and transfer film is the appearance of a broad band centered near 3350 cm^{-1}, which we attribute to inclusion of water into the transfer film. Another feature is the shift of the graphitic carbon/HOH wag band to higher wavenumber (1710 cm^{-1}) as the relative humidity increased. This we attribute to a –COOH group (carboxylic acid). There were also changes in the band profiles in the Si–O and Si–C spectral regions (1200–800 cm^{-1}) whose origin are not completely understood. Finally, the Si–H stretch near

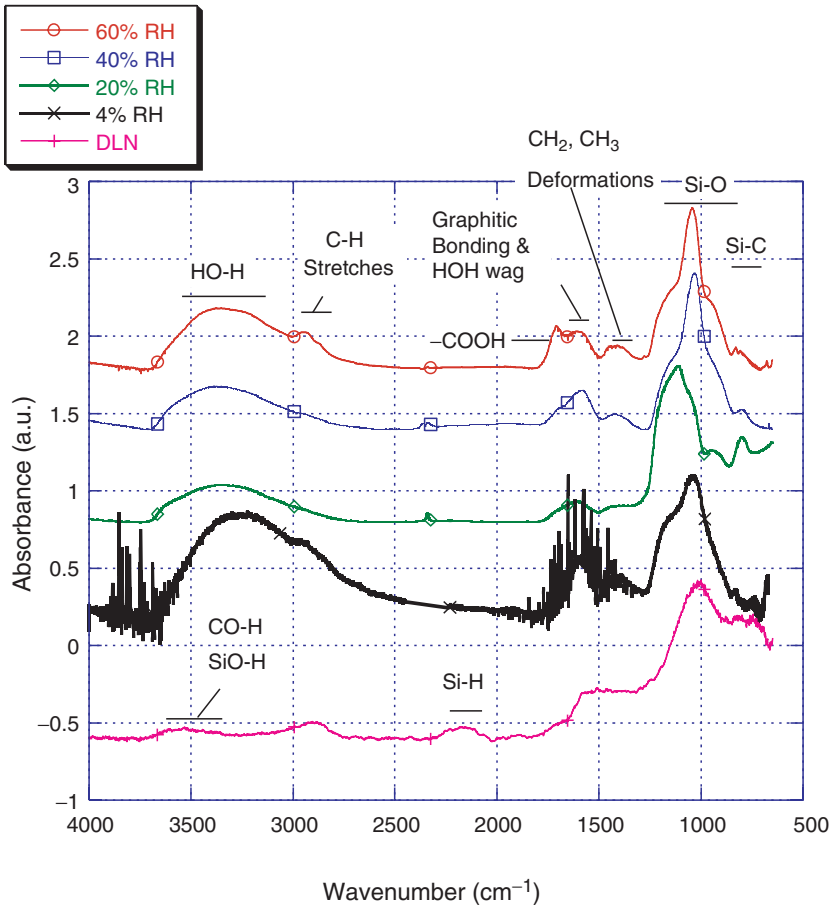

Fig. 8 *Ex-situ* infrared spectra of DLN-1 coating (Table 2) and transfer films at four different relative humidities. Assignments of the prominent IR features are given. (Reprinted from [37]. With permission.)

2200 cm^{-1}, which is clearly observable in the DLN coating, was not seen in the transfer film.

We can account for the changes in the IR spectra of the transfer film with respect to that of the coating by assuming that water and oxygen react with the DLN coating during the wear process and transfer film growth. The presence of IR absorption near 1600 cm^{-1} and 2900 cm^{-1} indicates that the coating contained C=C bonds and C–H bonds, respectively. Water can attack a terminal C=C bond resulting in the formation of a hydroxyl group on one of the carbon atoms and a free hydrogen ion. The hydrogen ion will attach to the other carbon of the double bond pair, i.e.,

$$-C{=}C-H_2 + H_2O \rightarrow -CH-CH_2(OH)$$

resulting in a terminal hydroxyl group (–CH_2OH). The alcohol, in turn, can be oxidized to an aldehyde (–CHO), which can undergo further oxidation to a carboxylic acid (–COOH) [20]. These reactions can account for the increasing absorbance of the band at 1710 cm^{-1} in the transfer film spectra as the RH increased from 20% to 60% (see Fig. 8); note that this peak, despite the spectrum high noise, was likely absent in the 4% RH spectra. Similarly, oxygen can attack the Si–H bond, which would account for its absence, near 2200 cm^{-1}, in the transfer film spectra.

The water reaction products can also account for the increase in friction coefficient with increasing humidity. In both dry and humid tests, steady-state sliding occurred between the transfer film and the surface of the DLN wear track. As just explained, in humid conditions, the transfer film (and likely the track surface) contained increasing concentrations of polar groups. In contrast, in dry conditions, neither the coating nor the transfer film contained significant concentrations of polar groups. Polar groups will contribute dipole–dipole interactions between the contacting surfaces. Specifically, as the surface concentration of the polar –OH and –COOH groups increases with humidity, a stronger interaction between the transfer film and the worn (and chemically modified) DLN surface would be expected. These interactions are stronger than those of pure CH_2 and CH_3 groups, the other constituents of DLN and dry transfer films. Hence, the more reactive species formed during sliding in humid air could explain the increase in friction with humidity.

3.1.6 Wear Behavior of DLN Coatings

Although the friction was more stable in moist air, the DLN coatings wore a factor of ten more in moist air than in dry air (see Table 3). Thus a DLN coating on a slide bearing could fail sooner in dry air than in moist air, not because it would wear out sooner, but rather because it could not sustain a stable transfer film. This shows that the simple notion of coating wear factor is not sufficient to predict the tribological performance.

The similarity in the friction and wear behavior of steel and sapphire hemispheres can be explained completely by third-body processes. Microscopy and profilometry showed that the transfer films on both hemispheres looked the same and had similar thickness. Since the wear factors of the coatings were independent of hemisphere material (see Table 3), it is likely that wear was controlled by the transfer film, and not the hemisphere, rubbing against the coating. Since sliding took place between

Table 3 Depths (nm) and wear factors (10^{-7} mm^3 $N^{-1}m^{-1}$) of wear tracks measured at 300 cycles on DLN coatings at 0.7 GPa contact stress (depth uncertainty is ± 2 nm) (Reprinted from [36]. With permission.)

Hemisphere		Sapphire			Steel	
Coating		DLN1		DLN2		DLN2
% RH	**Depth**	**Wear factor**	**Depth**	**Wear factor**	**Depth**	**Wear factor**
4	1.5	1.4	1	1.6	3	2.8
35–52	21	12	17	9.5	18	8.2

the transfer film and the coating, it is not surprising that the friction coefficients for steel and sapphire hemispheres were the same. The more subtle differences in friction behavior with the two hemispheres are probably due to differences in attachment and removal of transfer film from the two materials. The friction and wear behavior of MoS_2 coatings exhibited the same lack of sensitivity to ball materials [16,49,50]. Lastly, there were no strong correlations between the coating properties listed in Table 1 and the friction and wear behavior. Thus, third-body processes seem to be more responsible for the friction and wear behavior than the coating properties emphasized in studies reported in the literature.

3.2 Metal (Tungsten and Titanium) Doped DLC in Dry Sliding

3.2.1 Friction Behavior

Figure 9 shows typical friction coefficient versus cycle curves for the three coatings (Table 1) against sapphire in dry (9a) and ambient (9b) air, and against steel in dry (9c) and ambient (9d) air. For sapphire in dry air, the friction coefficients for the Ti-C

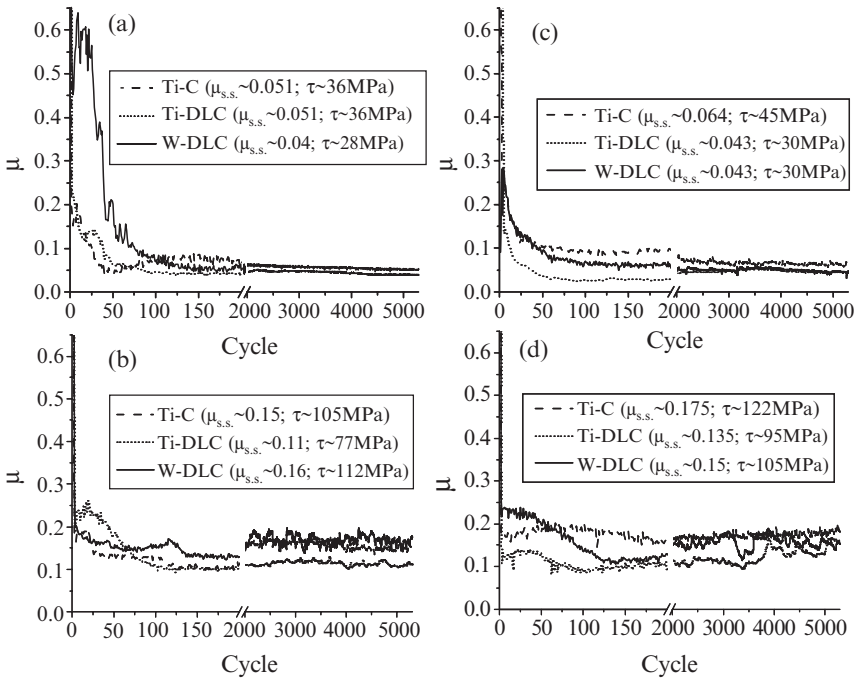

Fig. 9 Typical friction coefficient versus cycle curves for W-DLC, Ti-DLC and Ti-C coatings against sapphire in (a) dry and (b) ambient air, and against steel in (c) dry and (d) ambient air at 0.7 GPa mean Hertzian stress. Steady-state friction coefficients ($\mu_{s.s.}$) and interfacial shear strengths ($\tau = \mu \bullet P_m$) are also listed for each testing condition

and Ti-DLC coatings initially fell rapidly to steady-state values of ~0.04–0.06 after 50 cycles and remained constant for the remainder of the 5,300 cycles test. In contrast, friction coefficient for the W-DLC coating was much higher during the run-in period, ~0.6 from the start compared to ~0.2 for the Ti-C and Ti-DLC coatings. With increasing cycles, the friction coefficient of the W-DLC coating began to slowly drop until around 100 cycles when it reached steady-state friction coefficient ($\mu_{s.s.}$) of ~0.05. Thereafter, the friction behavior of all three coatings remained constant at ~0.05. The most obvious difference between the friction behavior of sapphire compared to steel (see Fig. 9c) occurred with the W-DLC coating; with steel, there was not the extended run-in period. With further sliding, the friction coefficients of all three coatings reached $\mu_{s.s.}$ of ~0.05–0.06, similar to sapphire $\mu_{s.s.}$ values.

In ambient air for sapphire (Fig. 9b) and steel (Fig. 9d), all three coatings exhibited similar friction behavior, although the $\mu_{s.s.}$ values were higher in ambient air, ~0.1–0.15, compared to dry air, ~0.05. The run-in behavior in ambient air was similar to the Ti-C and Ti-DLC coatings in dry air, with the exception of the W-DLC coating which did not exhibit the high friction run-in regime for the first 100 cycles. Figure 9 also lists the calculated interfacial shear strengths ($\tau = \mu \bullet P_m$) under steady-state sliding for each testing condition. The lower shear strengths are exhibited in dry air, in accordance to the friction coefficients, with little variation in values between the coatings. The differences between the μ and τ values in dry versus ambient air will be addressed in the discussion section.

3.2.2 Wear Behavior

Wear factor scatter plots for all three coatings sliding against sapphire and steel hemispheres in dry and ambient air are shown in Fig. 10. The wear factors are plotted at various cycles and in some cases there is more than one measurement for a given cycle. In all cases, the wear factor was higher during the first 300 cycles (run-in regime) than for the remainder of the test (steady-state regime). The Ti-C and Ti-DLC coatings exhibited lower wear in dry air than in ambient air, which also correlates with the lower friction coefficients in dry air. However, the W-DLC coating had higher wear in dry air against sapphire than in ambient air out to 300 cycles, which is in contrast when rubbing against steel. This wear behavior also correlated to the higher friction coefficient during run-in, but over time the friction coefficients reached steady-state and subsequently the wear factors were significantly lowered. With continued sliding out to 5,300 cycles, the wear factor in dry air decreased and equalled the wear factor in ambient air, which is also in good agreement with the steady-state friction coefficient. Of the three coatings tested, there is good agreement in ranking the wear factors in dry air with steel and sapphire hemispheres: the Ti-C coating had the lowest wear factor followed closely by the Ti-DLC coating; the W-DLC coating had the highest wear factor. In contrast, in ambient air, the wear was virtually identical during run-in amongst the three coatings. With continued sliding to the end of the tests, the wear trend followed the behavior seen in dry air, i.e., decreasing wear factor with cycles, but not as large of a difference.

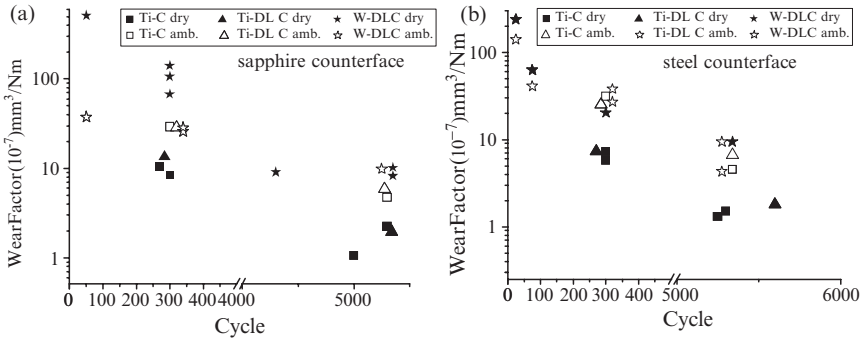

Fig. 10 Wear factor versus cycle curves for the three metal doped carbon coatings against (a) sapphire and (b) steel in dry and ambient air at 0.7 GPa mean Hertzian stress

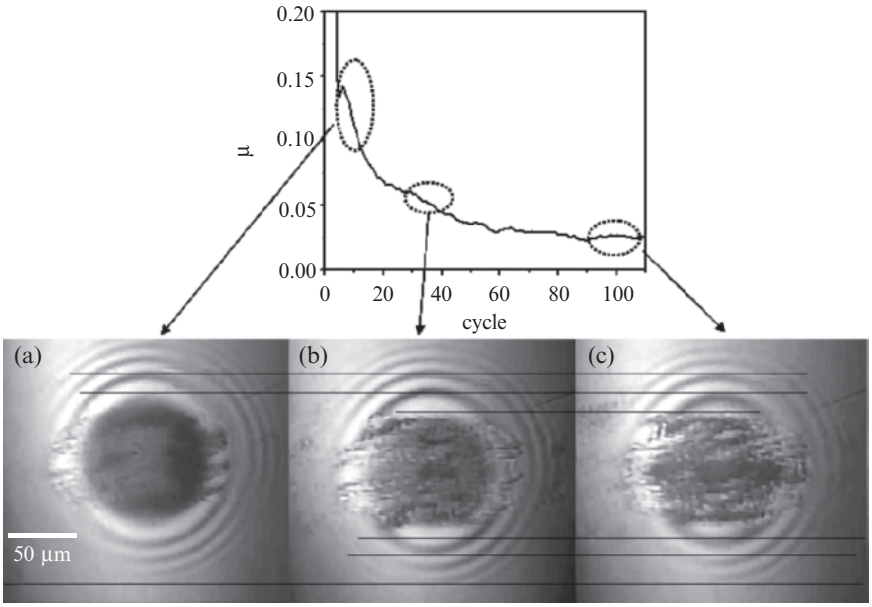

Fig. 11 Run-in friction behavior from the test shown in Fig. 9a with three accompanying *in situ* optical images of a sapphire/Ti-DLC coating interface taken during sliding contact in *dry air* at 0.7 GPa mean Hertzian stress. Parallel lines indicate change in coating thickness as shown by inward motion of Newton's rings

3.2.3 *In Situ* Transfer Film Observations

Figure 11 shows the run-in friction behavior from the test shown in Fig. 9a with three accompanying *in situ* optical images of sapphire versus Ti-DLC in dry air. The dark circle in Fig. 11a at cycle 10 is due to destructive interference of Newton's

rings and shows the area of contact made by the sapphire loaded against the Ti-DLC coating. The diameter of the contact area was 102 μm, which compares favorably with the calculated Hertz diameter of 98 μm. Within 10 sliding cycles, as the friction coefficients dropped to ~0.11, a transfer film accumulated across most of the contact area on the sapphire hemisphere. By cycle 36, shown in Fig. 11b, the transfer film thickened as evident by the inward shift of the Newton's rings (more at top of the contact area than in direction of sliding) and the friction coefficient dropped to ~0.06. Further thickening and friction reduction ($\mu_{s.s.}$ ~0.04) occurred out to cycle 100 (Fig. 11c) with more inward shifts in Newton's rings at the top than in the direction of sliding. As the transfer film continued to thicken, the interface lost focus and the Newton's rings gradually disappeared. Videotape analysis showed that the transfer film in the sliding contact remained motionless from the beginning to the end of test (5,300 cycles). Thus, the VAM was interfacial sliding between the transfer film and the underlying wear track during the entire test. The same transfer film behavior occurred for the Ti-C coating in dry air.

The W-DLC exhibited extremely different transfer film behavior under identical conditions in dry air. Figure 12 shows the run-in friction behavior from the test depicted in Fig. 9a. The three accompanying *in situ* optical images, taken at three different positions (1, 3, and 5 mm) across the wear track at cycle 10, showed wear debris in the interface. The positional arrows in Fig. 12 indicate that the debris was never stationary during a single pass; instead, debris sheared in and out of the

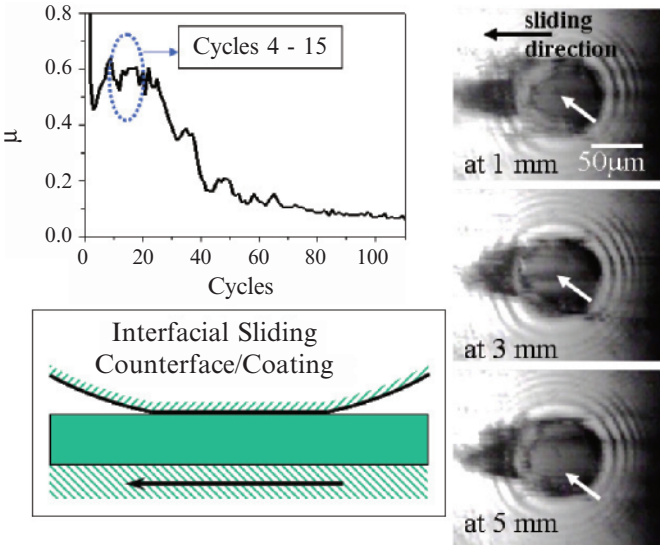

Fig. 12 Run-in friction behavior from the test shown in Fig. 9a with three accompanying *in situ* optical images of a sapphire/W-DLC coating interface taken during sliding *cycle 10* at three positions across the wear track in *dry air* at 0.7 GPa mean Hertzian stress. Arrows indicate that the wear debris was never stationary in the sliding contact. A schematic is shown of the velocity accommodation mode (VAM), interfacial sliding between sapphire counterface and coating

contact. The arrows point to color variations inside the contact area: lighter areas signify wear debris shearing and darker areas signify no debris present between the sapphire/coating interface. Furthermore, videotape analysis showed shearing of debris in and out of the contact. The VAM, depicted schematically in Fig. 12, was interfacial sliding between the hemisphere and the coating with no transfer film present. In addition, Newton's rings across the contact showed no height variations, evidence that no transfer film accumulated, as previously seen with the Ti-DLC and Ti-C coatings at cycle 10. The initially high friction coefficient, μ ~0.6, at cycle 10 was that of sapphire sliding directly against the W-DLC coating.

Figure 13 shows that from cycle 34 to cycle 43, as the friction dropped from $\mu \sim 0.35$ to $\mu < 0.20$, patches of stationary transfer film started to accumulate at the sides of the contact of the hemisphere (see thinner arrows in the three *in situ optical* images at cycle 36 for clarification). By cycle 43, the transfer film at the sides was stationary and did not shear in the contact. At the same time, third-body debris

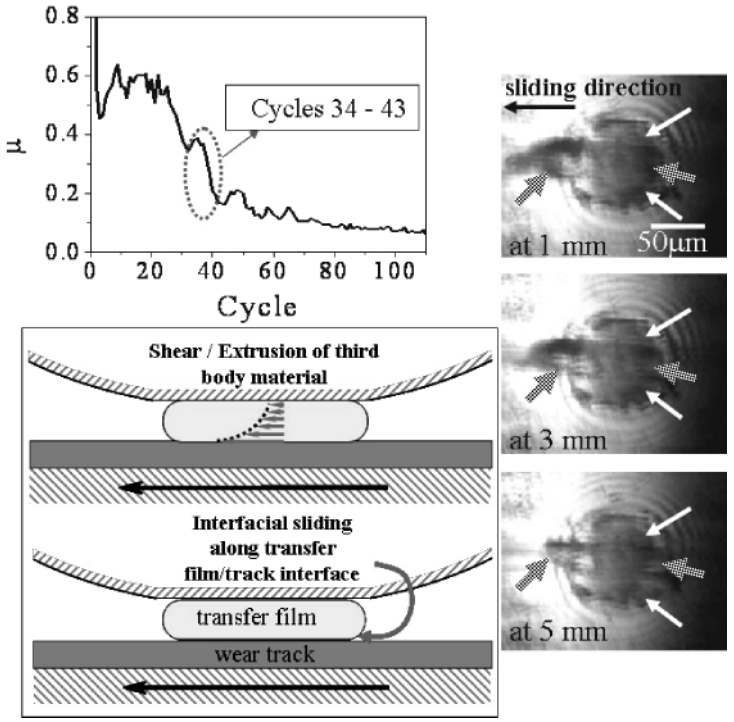

Fig. 13 Run-in friction behavior from the test shown in Fig. 9a with three accompanying *in situ* optical images of a sapphire/W-DLC coating interface taken during sliding *cycle 36* at three positions across the wear track in *dry air* at 0.7 GPa mean Hertzian stress. Thicker arrows in the center of the sliding indicate that the transfer film was never stationary; a schematic of this velocity accommodation mode (VAM), shearing, and extrusion of third body, is also shown. Thinner arrows in the top and bottom of the sliding contact indicate that the transfer was stationary and the VAM was interfacial sliding between transfer film and coating as shown by the schematic

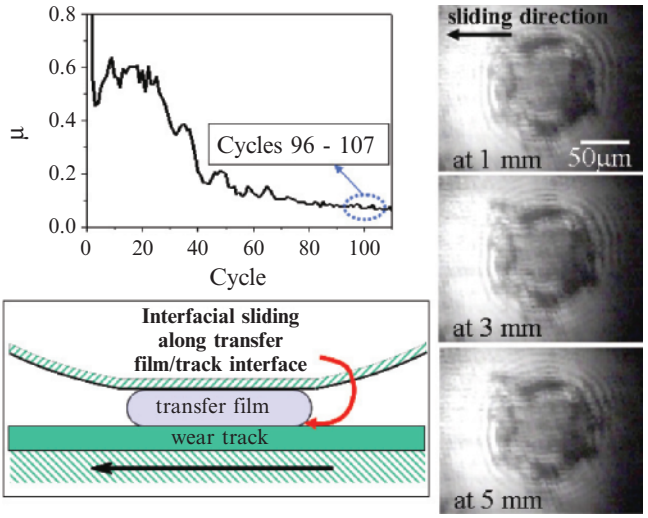

Fig. 14 Run-in friction behavior from the test shown in Fig. 9a with three accompanying *in situ* optical images of a sapphire/W-DLC coating interface taken during sliding *cycle 100* at three positions across the wear track in *dry air* at 0.7 GPa mean Hertzian stress. Transfer film was stationary and the velocity accommodation mode (VAM) was interfacial sliding between transfer film and coating as shown by the schematic

passing through the center of the contact sheared, extruded, and recirculated in and out of the center portion of the contact causing high friction. Thus, two VAMs were active: interfacial sliding at the sides and shearing and extrusion of third body (schematic in Fig. 13) in the center of the contact. Not until around cycle 100 (Fig. 14), when the friction coefficient reached a low value of ~0.07, did a stationary transfer film cover the entire hemisphere (see three identical images at cycle 100). Interfacial sliding between it and the underlying wear track, VAM depicted in Fig. 14, produced the low friction. For the remainder of the test, the transfer film remained stationary in the contact, without shearing or detaching, and the friction reached its steady-state value, μ ~0.05 by cycle 140. However, unlike the Ti-C and Ti-DLC transfer films in dry air, there was no thickening with increasing sliding cycles for the duration of the test.

Figure 15 shows three *in situ* optical images of a sapphire/W-DLC coating interface taken during sliding contact in ambient air, from the test shown in Fig. 9b. Unlike in dry air, a transfer film attached to and covered most of the contact area on the sapphire hemisphere by 10 cycles, and the friction coefficient fell to 0.18 vs 0.6 in dry air. Over the entire track length (optical images at 1, 3, and 5 mm in Fig. 15) there was no evidence of shearing of third bodies in and out of the contact, as seen in dry air. For the next several hundred cycles, as the friction coefficient dropped slightly to a steady-state value of ~0.12, the transfer film remained stationary in the contact area. The film also thickened slightly, as determined by the inward motion of the Newton's rings. During the entire test, the VAM was interfacial

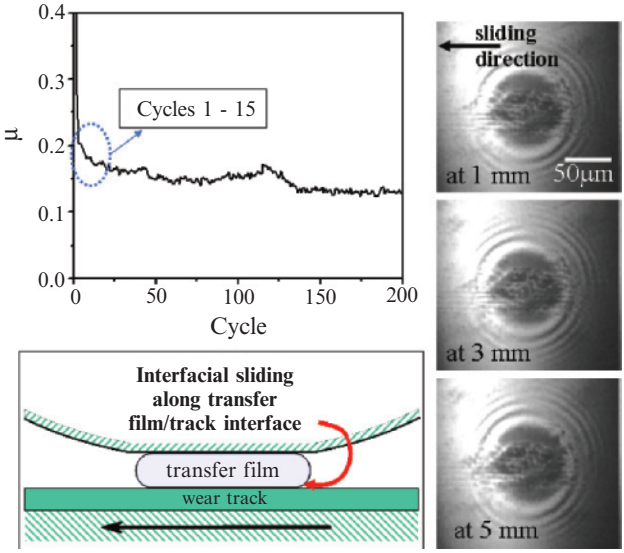

Fig. 15 Run-in friction behavior from the test shown in Fig. 9a with three accompanying *in situ* optical images of a sapphire/W-DLC coating interface taken during sliding *cycle 10* at three positions across the wear track in *ambient air* at 0.7 GPa mean Hertzian stress. Transfer film was stationary and the velocity accommodation mode (VAM) was interfacial sliding between transfer film and coating as shown by the schematic

sliding (Fig. 15 schematic). Similar transfer films and friction behavior were also observed for Ti-DLC and Ti-C coatings in ambient air (not shown).

3.2.4 SEM and Raman Spectroscopy of *Ex Situ* Transfer Films

Figure 16a shows an SEM image of a Ti-DLC wear scar on a sapphire hemisphere after 5300 cycles of sliding in ambient air from the test shown in Fig. 9b. A compact, ~100 μm diameter transfer film is visible. Figure 16a also shows *ex situ* Raman spectra of an unworn Ti-DLC coating, the transfer film, and a reference rutile (TiO_2) powder. The coating contained only the C–C bands: the G band at 1550 cm^{-1} and the D band at 1379 cm^{-1}, the same peaks seen on DLN coatings. The weak carbon D band was responsible for asymmetrically broadening the Raman spectra below the G band, as it did with DLN coatings. The transfer film spectrum also showed the carbon G and D bands, but shifted to 1598 cm^{-1} and 1351 cm^{-1}, respectively, again similar to the peaks in the DLN transfer films. Typically for transfer films, both bands sharpen, and the G band shifts to higher wavenumbers, while the D band shifts to lower wavenumbers. In addition, the transfer film spectrum contained low wavenumber peaks at 441 cm^{-1} and 611 cm^{-1} identified by rutile powder (peaks at 450 cm^{-1} and 614 cm^{-1}) to be titanium dioxide.

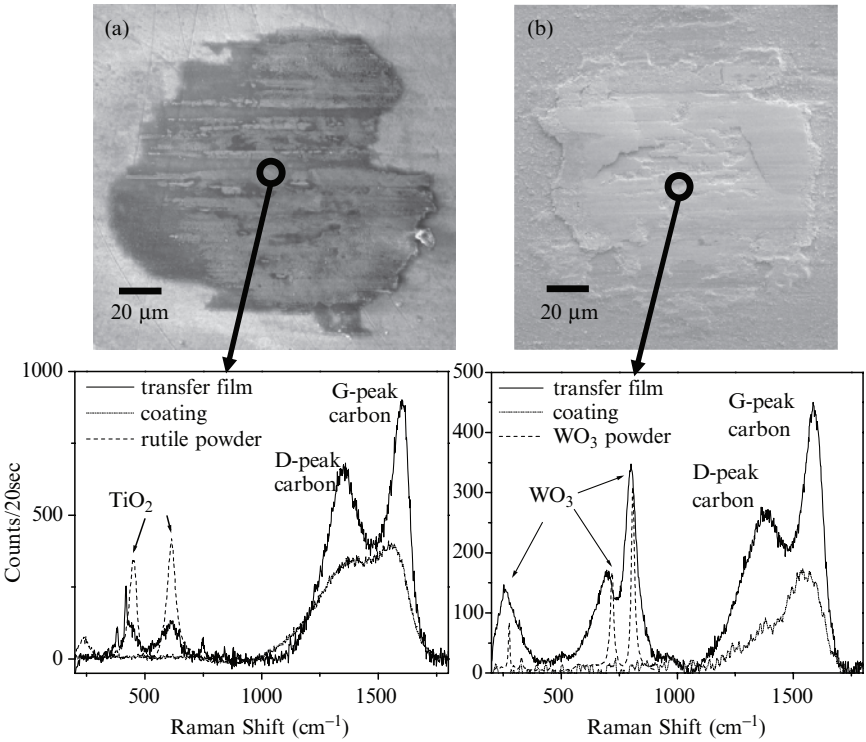

Fig. 16 SEM images of (a) Ti-DLC and (b) W-DLC wear scars on sapphire hemispheres after 5,300 cycles of sliding in ambient air from the test shown in 9b. Also shown are three Raman spectra of the transfer film, unworn (a) Ti-DLC or (b) W-DLC coating, and a reference (a) rutile (TiO_2) powder or (b) WO_3 powder

The two sharper peaks at lower wavenumbers are from the underlying sapphire hemisphere. EDX measurements (not shown) taken concurrent with SEM also showed Ti and higher oxygen to carbon peak ratios in the transfer film than in the unworn coating, further evidence that the metal in the coating oxidized during transfer film formation.

Figure 16b shows an SEM image of a W-DLC wear scar on a sapphire hemisphere after 5,300 cycles of sliding in ambient air from the test shown in Fig. 9b. Similar to the Ti-DLC coating, a compact, ~100 μm diameter transfer film was visible. Figure 16b also shows three Raman spectra of an unworn W-DLC coating, the transfer film, and a reference tungsten trioxide (WO_3) powder. The coating spectra, similar to that of Ti-DLC, contained only the G band at 1545 cm^{-1} and the D band at 1359 cm^{-1}. Again, the much weaker carbon D band was responsible for asymmetrically broadening the Raman spectra below the G band. Once again, the carbon G- and D-band spectrum of the transfer film sharpened and shifted to 1588 cm^{-1} and 1379 cm^{-1}, respectively. In addition, the transfer film spectrum

Table 4 Summary of whether or not transfer films initially formed in sliding with W-DLC, Ti-DLC, and Ti-C coatings at 0.7 GPa mean Hertz stress under dry and ambient air. Also listed are the compounds and elements found in transfer films by Raman spectroscopy and EDX

	Initial transfer film			
	Dry air	Ambient air	Raman spectroscopy	EDX
W-DLC	No	Yes	WO_3, C (D and G)	C, O, W
Ti-DLC	Yes	Yes	TiO_2, C (D and G)	C, O, Ti
Ti-C	Yes	Yes	TiO_2, C (D and G)	C, O, Ti

contained low wavenumber peaks at 260, 696, and 800 cm^{-1} identified by referenced tungsten trioxide powder (peaks at 277, 718, and 808 cm^{-1}) as tungsten oxide. Moreover, EDX measurements showed W and higher oxygen to carbon peak ratios in the transfer film than in the unworn coating. Hence, analysis of transfer films from Ti-DLC and W-DLC support our earlier contention that tribochemical processes – in this case against metal-doped DLC – readily oxidized third-body debris. Table 4 summarizes transfer film tribochemistry data collected from Raman and EDX spectroscopies for all three coatings.

3.3 W-DLC in Lubricated Sliding

The influence of a liquid lubricant on the friction coefficient and VAM of sapphire versus DLC was also investigated. The lubricant was Krytox (143 AZ, Lot 64), a perfluoropolyether (PFPE) fluid made by DuPont. Figure 17 shows three typical

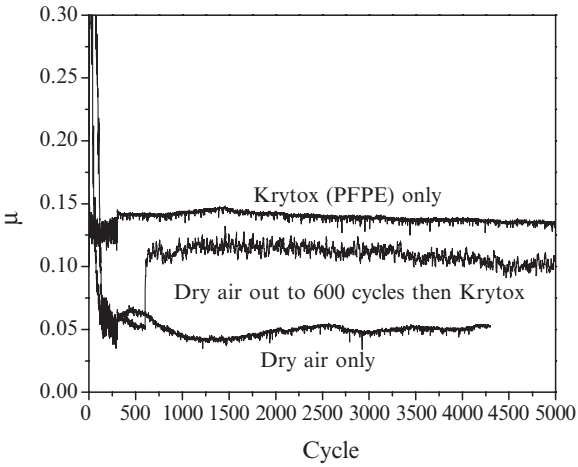

Fig. 17 Typical friction coefficient versus cycle curves for W-DLC coating against sapphire in dry air with Krytox in between, unlubricated out to 600 cycles then Krytox added, and previously shown (Fig. 9a) unlubricated at 0.7 GPa mean Hertzian stress

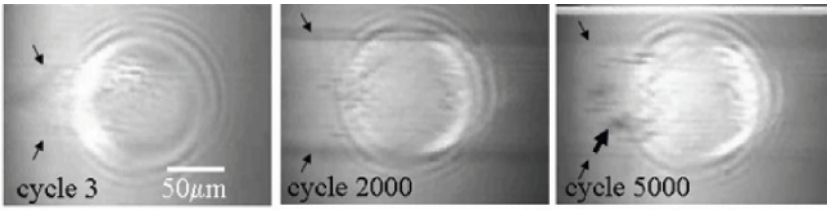

Fig. 18 *In situ* optical images of a sapphire/W-DLC coating interface taken during sliding with Krytox lubricant in dry air at 0.7 GPa mean Hertzian stress. Arrows indicate position of wear track and wear debris (see text for details)

friction coefficients versus cycle tests for sapphire sliding against a W-DLC coating. The upper curve was taken with Krytox present from the beginning of sliding and the lower curve, as in Fig. 9a, in dry air (unlubricated). With Krytox, the friction coefficient dropped immediately (by cycle 3) to 0.13; and as presented earlier, in dry air, the run-in friction coefficient remained high at ~0.6 for about 25 cycles. In steady state, the friction coefficient in Krytox was more than twice that in dry air, 0.13 vs 0.05, respectively; a friction coefficient of 0.13 is typical for a boundary lubricant with no antifriction additives [33]. The middle curve test was begun in dry air with the Krytox added at 600 cycles. When Krytox was added at cycle 600, the friction coefficient immediately jumped from 0.05 to ~0.11 and remained there out to 5,000 cycles.

In situ visual observations of these contacts offered new insights into the effect of a liquid lubricant on transfer films and friction behavior of a DLC coating in lubricated sliding contact. A careful viewing of the videos taken during the Krytox lubricated test was unable to detect any coating wear or transfer film formation during 5,000 cycles. Figure 18 shows representative *in situ* optical images at 3, 2,000, and 5,000 cycles from the videos. Cycle 3 is shown instead of cycle 0 (pre-sliding) since there were no detectable differences inside their contact areas, hence no initial third bodies. The oblique-pointing arrows in Fig. 18 show how the wear track width increased by 50% from cycle 3 to cycle 2,000, but hardly changed out to cycle 5,000. However, some wear debris, probably from the coating, were generated as shown by the thicker arrow in Fig. 18 at cycle 5,000. Sliding appears to have been sustained by the lubricant with separation distance less than that resolvable by the Newton's rings (≤25 nm). Thus, with Krytox the velocity accommodation relied on a thin lubrication film, whereas in dry air, the VAM was interfacial sliding between a transfer film and coating wear track.

Figure 19 shows a more detailed curve of the transition in friction coefficient, from the test shown in Fig. 17, when Krytox was added at cycle 600. The friction coefficient increased immediately from ~0.05 (cycle 600) to 0.11 (cycle 604), where it remained out to cycle 5,000. The accompanying *in situ* optical images at cycles 585, 615, and 4,500 in Fig. 19 show the evolution of the transfer film before and after Krytox was added. As seen more clearly in the videos, the transfer film

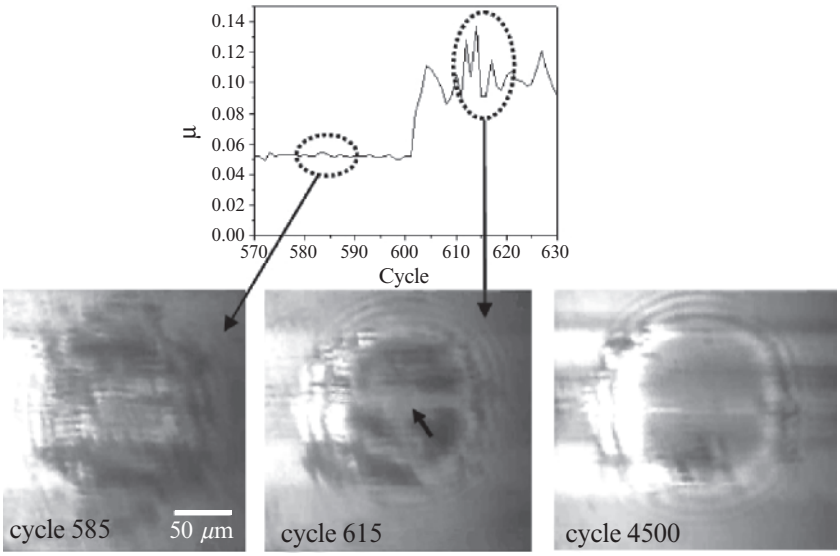

Fig. 19 Transition in friction coefficient from dry to lubricated (Krytox) sliding from the test shown in Fig. 17 with 3 accompanying *in situ* optical images of a sapphire/W-DLC coating interface taken during sliding in dry air at 0.7 GPa mean Hertzian stress

developed in dry air (cycle 585) began to fall off by cycle 615 (see arrow); and with further sliding out to 4,500 cycles, most of the transfer film was lost. It is likely that the Krytox, a low surface energy fluid, entered the film/sapphire interface, displaced the film, and then prevented third bodies from adhering to the sapphire surface thereafter. This suggests that liquid lubricants do not support low friction sliding by transfer films. However, more investigations are needed to understand the competition between transfer film formation and film wear under liquid lubrication.

3.4 Hydrogenated DLC Coatings

3.4.1 Friction Behavior

Figure 20 shows typical friction coefficients versus cycle curves in dry and moist air for AC8 and CY5 coatings listed in Table 1. For both sets of coatings the steady-state friction coefficients were lower in dry air than in ambient air, similar to DLN and Me-DLC coatings. In addition, the AC8 coatings had lower friction coefficients than CY5 coatings under the same humidity, and the CY5 coatings had longer run-in stages in both dry and ambient air.

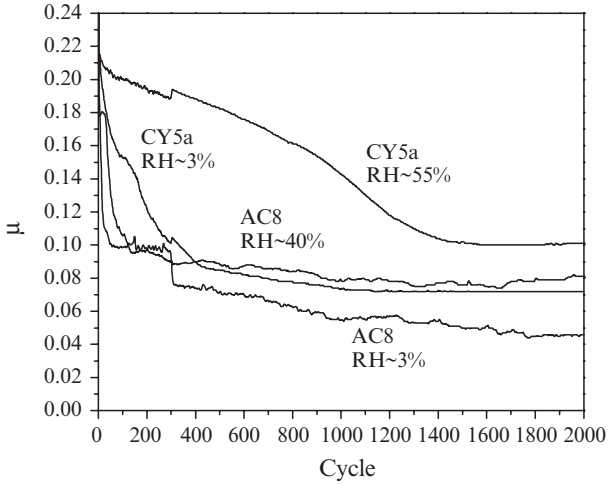

Fig. 20 Typical friction coefficient versus cycle curves for $CH_{0.34}$ (AC8) and $CH_{0.42}$ (CY5) coatings against sapphire in dry (~3% RH) and ambient (~40–55% RH) air at 1.1 GPa mean Hertzian stress

3.4.2 *In Situ* Transfer Film Observations and Raman Spectroscopy

The third-body contributions to friction were identified by examining videotapes and analyzing Raman spectra[1] of the sliding contact. Figures 21 and 22 show selected *in situ* images of the contacts and Raman spectra, respectively. In ambient air, coating AC8 had a short run-in regime, as a transfer film collected along the edges of the contact; one sees in Fig. 21b a doughnut-shaped buildup of transfer film, whose thickness is probably hundreds of nanometer, based on the slight distortion (inward motion) in Newton's rings. Although Raman spectra showed no measurable (25 nm or less) transfer film at the center of the contact at any time (Fig. 22a), the surrounding transfer film likely provided the lubrication (interfacial sliding between transfer film and coating) needed to reduce the friction coefficient to <0.10. In contrast, coating CY5 had a long run-in regime and high friction coefficient in ambient (~40% RH) air because no visible transfer film developed (Fig. 21c). Nonetheless, there was noticeable track wear and loose debris outside the contact area. In dry air, where friction coefficients were lower than in ambient air, similar to other DLC coatings, coating AC8 showed immediate transfer film formation and thickening, as evidenced by the image in Fig. 21d and the *in situ* Raman spectra of mixtures (coating and transfer film), similar to DLN, in Fig. 22b.

[1] *In situ* Raman spectra (at 514.5 cm^{-1}) of coating CY5 exhibited such a large fluorescence background that no distinct peaks could be seen.

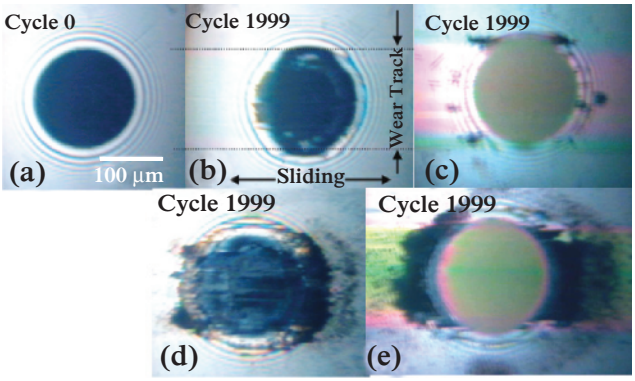

Fig. 21 *In situ* optical images of sapphire/CH_x coatings interfaces taken at (a) cycle 0, presliding and cycle 1,999 for (b) AC8 in ambient (~40% RH) air, (c) CY5 in ambient (~40% RH) air, (d) AC8 in dry (~3% RH) air, and (e) CY5 in dry (~3% RH) air at 1.1 GPa mean Hertzian stress

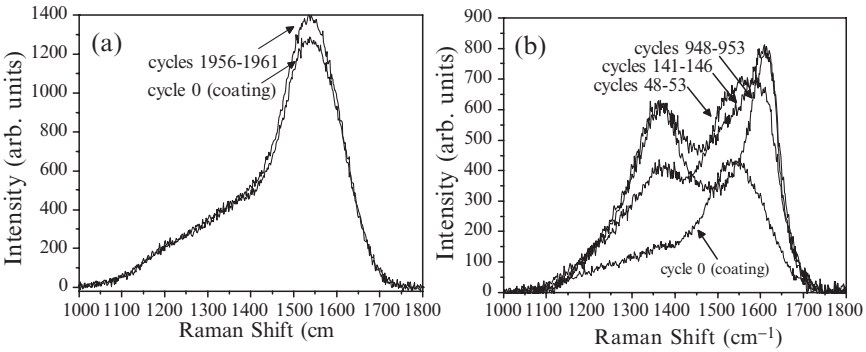

Fig. 22 *In situ* Raman spectra for $CH_{0.34}$ (AC8) coating in (a) humid air (~40% RH) and (b) dry (~3% RH) air for increasing sliding cycles at a mean Hertzian contact stress of 1.1 GPa

In contrast, coating CY5 had a slow run-in, during which time lots of wear debris were generated, but no measurable transfer film was seen (Fig. 21e). We suspect that some transfer occurred, perhaps only at the leading edges of the contact, to accommodate the velocity at a friction coefficient <0.1.

4 Discussion

In situ tribometry identified the buildup and attachment (or lack thereof) of third bodies at the buried interface of a sliding contact. It also revealed how third-body processes affected the friction behavior of DLN, W-DLC, Ti-DLC, and CH_x coatings

in dry and moist air. For most of the DLC coatings, under all test conditions, a transfer film began to form on the sapphire hemisphere during the first cycle. During buildup of the transfer film, the friction coefficient fell to <0.1. Video analysis showed that most of the sliding motion took place between the transfer film on the hemisphere and the coating, i.e., the velocity was accommodated by interfacial sliding. Thus the low friction attributed to the DLC coatings was really due to interfacial sliding between the transfer film and the worn DLC surface. A second VAM, shearing and extrusion of third bodies, was observed at higher friction coefficients (0.6–0.2). When the friction spikes occurred during low friction sliding, as they did with DLN coatings, they were accompanied by shearing of debris in the contacts. In all higher friction events, many VAMs were seen, including transfer film detachment and recirculation of debris between the hemisphere and the track.[2] Nonetheless, interfacial sliding was the dominant VAM mode for DLC coatings.

For the metal-doped DLC coatings, third bodies began to form during run-in. A transfer film began to collect on the sapphire hemisphere during the first cycle for all coatings except the W-DLC coating in dry air. In the latter case, the friction remained high during the first 100 cycles due to shearing and extrusion of third-body material in and out of the contact, but no transfer film adhered to the sapphire hemisphere. Then a transfer film began to partially adhere to the sapphire hemisphere, causing the friction coefficient to drop, and the VAMs were a mix of interfacial sliding and shearing of third bodies. Further reduction in the friction coefficient to steady-state values was a result of more transfer film accumulating across the sapphire hemisphere and only interfacial sliding; this was the dominant VAM for all other metal-doped DLC coatings during the steady-state friction regime.

These *in situ* results support two earlier inferences from past *ex situ* analyses: that (1) solid lubricant coatings like DLC [20–25, 51], MoS_2 [13–18,29,32,41,48,49], and H_3BO_3 [30,41] rely on transfer films to maintain low friction and (2) interfacial sliding is the dominant VAM. In the case of DLC, the transfer films have been identified by *in situ* and *ex situ* Raman spectrometry to be carbon based [23,26,40,41,51]. Even with interfacial sliding between the transfer film and the coating, friction coefficients exhibited two characteristic behaviors. For DLN coatings, they reached low steady values, then, at sufficiently high contact stresses, became unstable with periodic friction spikes. *In situ* optical images and video recordings of the sliding interface suggest how third bodies controlled this friction behavior. Low, steady friction was achieved when a transfer film built-up on the hemisphere, covered the contact area, and remained there. Loss of transfer film led to higher friction. The slow rise in friction before the first spike in dry and moist air was due to transfer film wear by localized thinning, then removal. Subsequent friction spikes also occurred because of transfer film wear.

[2] Although transfer film instabilities could be viewed, they could not be studied in detail with our low capture rate (30 frames per sec) and, therefore, will not be interpreted further.

Table 5 Calculated interfacial shear strengths, ($\tau = \mu \bullet P_m$), in MPa, in dry and moist air for DLC coatings

Hemisphere	Sapphire		Steel	Sapphire	Steel	Sapphire	Steel	Sapphire	Sapphire
Coating	DLN 1	DLN 2	DLN 2	Ti- DLC	Ti- DLC	W-DLC	W-DLC	AC8	CY5
p_m (GPa)	0.7	1.1	0.7	0.7	0.7	0.7	0.7	1.1	1.1
~% RH									
3–4	30	28	30	36	30	28	30	49	77
35–55	37	38	36	77	95	112	105	88	110

The high friction values, therefore, can be attributed to areas of bare sapphire sliding against the DLN wear track.

The friction coefficients of all DLC coatings studied were typically lower in dry air than in moist air; however, in moist air, the DLC coatings had more than twice the friction coefficient of the DLN coatings. We suggest that capillary forces can account for both the higher friction coefficient and more stable transfer film in moist air. We also suspect that the lower friction coefficient on DLN in moist air can be attributed to the Si–O surface layers in the DLN coatings and their transfer films; Si–O layers should have a lower surface energy and would therefore be less easily wetted than the C–H surface layers on DLC and its transfer films [52]. Adsorbed water could increase the interfacial shear stress required to slide the DLC transfer film along the DLC wear track. The calculated interfacial shear strengths for all DLC coatings are summarized in Table 5. The shear strengths were lower in dry air than moist air for all coatings with τ(DLN) ≈ τ(Me-DLC) < τ(hydrogenated DLC). In moist air, τ(DLN) << τ(Me-DLC) ≈ τ(hydrogenated DLC). Moreover, τ values for DLN coatings in moist air (36–38 MPa) were not much larger than in dry air (28–30 MPa).

Other groups [51,53–63], many included in this book, have also determined that adsorbates clearly impact friction behavior. For example, Heimberg et al. [54] and Dickrell et al. [58] studied the influence of adsorption rates and coverage on the friction behavior of DLC coatings. They found that superlow friction coefficients ~0.003–0.008 were exhibited in nominally dry nitrogen, so long as the exposure time between sliding contacts remained below about 5 s. Longer exposures caused the friction coefficient to increase to >0.1, typical of DLC coatings in ambient air, but the superlow friction coefficient was recovered by reducing the exposure time below the nominal value. Thus, the time-dependent friction behavior indicated that gas–surface interactions play a strong role in inhibiting superlow friction. In addition, Andersson et al. [56] determined water adsorption resulted in friction increases due to dipole-like interaction of the sliding interface. Recently, Kim et al. [60] determined that weakly physisorbed gas molecules influenced the friction behavior by physically separating the hydrogenated DLC interface. This effect was completely reversible when water was added (adsorbed) or removed (displaced).

Here we speculate on the role of transfer films and friction coefficients. Moisture likely enhanced both the agglomeration of particles forming third-body debris and the adhesion of the film transferred to the hemisphere. Moisture, known to bond

strongly to dangling bonds in carbons [63,64], would be the "glue" that holds carbon clusters together. FTIR suggested the oxidation pathways for third bodies formed from DLC coatings, like the breaking of the C=C graphitic bonds in DLN transfer films. Chemistry also played a role in the adhesion of transfer films from W-DLC coatings. In dry air, the transfer film took nearly 100 cycles to adhere. It is likely that some moisture in the nominally "dry" air promoted the eventual adherence of the W-DLC transfer film to sapphire. In moist air, organic acid entities in the transfer film, such as polar groups like –COOH, likely account for increased friction coefficient. Steady-state friction coefficients for metal-doped coatings were higher than for hydrogenated DLC; however, they were the same for both metal dopants and in both the hydrogenated and nonhydrogenated matrix in their respective environment. This suggests that the friction coefficient is controlled by both the tribochemically modified carbon in the transfer film sliding against tribochemically modified carbon on the wear track and the metal oxides in the transfer film. Also, since the friction coefficients are lower in dry air than in ambient air, as previously seen for DLC [21,51], there is likely some chemical reaction between carbons in the presence of water vapor/oxygen.

We also speculate on the relationship between higher shear strengths (Table 5) in moist air and the second VAM – shearing and extrusion of third bodies. As moisture caused the interfacial shear strength to increase, τ approached that of the transfer film. When this happened, the transfer film could begin to shear along its weakest plane. Shearing and extrusion could continue until the interfacial shear strength dropped below the shear strength of the transfer film, which happened in dry air.

The similarity in the friction behavior of DLC coatings using steel and sapphire hemispheres can be explained completely by third-body processes. Since the wear factors of the coatings were independent of hemisphere material (see Table 3), it is clear that friction and wear were controlled by the transfer film, and not by the hemisphere. The more subtle differences in friction behavior with the two hemispheres were attributed to differences in attachment and removal of transfer films from the two materials. The most striking example was the case of W-DLC and Ti-DLC coatings in dry air and in ambient air. To understand the chemical basis for attachment of third bodies to different hemispheres, thermochemistry calculations [65] were used to predict bonding between the materials involved. Equilibrium compositions were calculated for steel (Fe) and sapphire (Al_2O_3) hemispheres reacted with metal dopants (Ti and W) with and without O_2. The results, presented in Table 6, can account for the main observations: the nonattachment of W-DLC transfer films to sapphire hemispheres in dry air and the easier attachment in ambient air; the easier attachment to steel in dry and ambient air; and the easier attachment of both Ti-C and Ti-DLC transfer films to both hemispheres in dry and ambient air. The reaction products and whether bonding occurred between the hemispheres for all combinations are also summarized in Table 6. W does not form any reaction products with sapphire, with or without the presence of oxygen. On the other hand, Ti does bond to sapphire, forming TiAl whether or not oxygen is present. For the steel hemisphere, both Ti and W bond to it without oxygen forming

Table 6 Thermochemical equilibrium calculations of reaction products and whether bonding occurred between the hemispheres

Counterbodies		Reaction products		Bonding between counterbodies?
Hemisphere	Metal dopant	Without O_2	With O_2	
Al_2O_3	W	None	WO_3	No
Al_2O_3	Ti	TiAl + TiO	TiAl + TiO; Al_2O_3 + $Ti_2O_3/Ti_3O_5/Ti_4O_7$; $Al_2O_3{}^*TiO_2$ + TiO_2	Yes
Fe	Ti	FeAl + Fe_2Ti	TiO, Ti_2O_3; TiO_2; FeO^*TiO_2; TiO_2 + Fe_2O_3	Yes
Fe	W	Fe_3W_2	FeO^*WO_3 + WO_2; Fe_2O_3 + WO_3	Yes

FeTi and Fe_3W_2, respectively. These calculations agree with the previous *in situ* observations of whether a transfer film formed or not during run-in.

Lastly, transfer films also controlled the wear factors of the parent coatings. The highest wear factor was seen with W-DLC in dry air, when the transfer film did not attach readily to the hemisphere. After the transfer film attached, the wear factors (Fig. 10) always decreased. That is why most of the wear took place during the initial run-in. In comparing the coatings, there was no significant difference in wear factors between the Ti-C and Ti-DLC coatings in their respective environment. The very high wear factor of W-DLC in dry air, due to the sapphire rubbing against the coating, could be viewed *in situ*. Therefore, we can finally explain why there were no strong correlations between the coating mechanical properties listed in Table 1 and the friction and wear behavior: third-body processes, not the mechanical properties of the first body hemispheres, controlled friction, and wear during sliding contact with DLC coatings.

5 Summary and Conclusions

In situ optical and Raman spectroscopy were used to identify near surface chemistry and visualize dynamics at buried sliding interfaces. Third-body processes such as thickening, thinning, and loss of transfer films were identified during sliding of sapphire and steel against DLN, W-DLC, Ti-DLC, and hydrogenated DLC coatings; these processes were used to explain both steady-state friction and friction instabilities. Friction and wear differences with humidity and contact pressure were also correlated to the third-body processes as follows:

- For all DLC coatings, steady low friction coefficients, low interfacial shear strengths, and low wear factors occurred when well-adhered transfer films covered the contact area of the hemisphere.
- For all DLC coatings, the dominant VAM at low ($\mu \sim 0.05$) friction in dry air as well as higher ($0.1 \leq \mu \leq 0.2$) friction in ambient air was interfacial sliding between

the transfer film on the hemisphere and the coating. At the higher friction during run-in, shearing of the third bodies also contributed to velocity accommodation. The friction coefficient began to drop when a transfer film attached to the hemisphere and velocity was accommodated by interfacial sliding.

- For DLN coatings, friction instabilities were associated with loss of transfer film in the sliding contact. The low friction values in between these friction spikes and fluctuations occurred during periodic healing of the transfer film.
- Although DLN wore less in dry air than in moist air, and its friction coefficient was lower, its friction coefficient was less stable because it could not form a stable transfer film in dry air. Similarly, wear of W-DLC coatings in dry air was more severe during run-in since no transfer film formed; nonetheless, by the end of the tests, the wear factors in ambient and dry air were comparable.
- For W-DLC and Ti-DLC coatings, the adherence of the transfer film to the hemisphere during run-in depended on the metal dopant in the coating, consistent with bonding predicted by thermochemical equilibrium calculations.
- Lubrication of W-DLC coatings with Krytox was incompatible with transfer film retention and formation. Instead, sliding in Krytox was sustained by a lubricant film, whose friction coefficient (0.13) was more than twice that of dry air/unlubricated (0.05).
- For DLN coatings, *ex situ* FTIR spectroscopy identified changes in C–C, C–H, C–O bonding between transfer films and coating at different humidities, and suggested a chemical basis for the increase in friction with humidity.
- For DLN and AC8 ($CH_{0.34}$) coatings in dry air, the upward shift in the G-band peak position was shown to correlate with increased thickness of transfer film.
- A light scattering model based on Beer's Law was applied to *in situ* spectra taken during the thinning of a transfer film that led to spikes in the friction coefficient. At high load in ambient air, the thickness of DLN transfer film at the friction spike was estimated to be between 16 and 25 ± 13 nm, i.e., spiking occurred only when the transfer film was worn away. This methodology demonstrated that *in situ* Raman spectroscopy can be used to monitor transfer film thickness, hence friction stability, during solid lubricated sliding contact.

Acknowledgments The authors thank Chandra Venkatraman, Dan Kester, and Cyndi Brodbeck at Bekaert Advanced Coating Technologies for the DLN samples; Alfred Grill at IBM for the CH_x (AC8 and CY5) samples; Gary Doll and Ryan Evans at Timken Co. for the Ti- and W-doped DLC samples; and Robert Mowery for collaboration on FTIR analysis. We also thank Kathy Wahl for the numerous contributions, conversations, and for reading the manuscript, and the ONR for funding the research. One of the authors (TWS) thanks the ASEE for his Post-Doctoral Research Fellowship while at NRL.

References

1. A. Grill, Review of the tribology of diamond-like carbon. Wear, 1993, 168: 143–153.
2. C. Donnet, Recent progress on the tribology of doped diamond-like and carbon alloy coatings: a review. Surf. Coat. Tech., 1998, 100–101: 180–186.

3. F. P. Bowden and D. Tabor, The Friction and Lubrication of Solids, Part 1. 1986, Clarendon Press, Oxford, p. 112.
4. R. Gilmore and R. Hauert, Comparative study of the tribological moisture sensitivity of Si-free and Si-containing diamond-like carbon films. Surf. Coat Tech., 2000, 133–134: 437–442.
5. K. Oguri and T. Arai, Tribological properties and characterization of diamond-like carbon coatings with silicon prepared by plasma-assisted chemical vapor deposition. Surf. Coat. Tech., 1991, 47: 710–721.
6. K. Oguri and T. Arai, Two different low friction mechanisms of diamond-like carbon with silicon coatings formed by plasma-assisted chemical vapor deposition. J. Mater. Res., 1992, 7: 1313–1316.
7. V. F. Dorfman, Diamond-like nanocomposites (DLN). Thin Solid Films, 1992, 212: 267–273.
8. D. Neerinck, P. Persoone, M. Sercu, A. Goel, C. Venkatraman, D. J. Kester, C. Halter, P. Swab, and D. Bray, Diamond-like nanocomposite coatings for low-wear and low-friction applications in humid environments. Thin Solid Films, 1998, 317: 402–404.
9. D. J. Kester, C. L. Brodbeck, I. L.Singer, and A. Kyriakopoulos, Sliding wear behavior of diamond-like nanocomposite coatings. Surf. Coat. Tech., 1999, 113: 268–273.
10. M. Godet, The third-body approach: a mechanical view of wear. Wear, 1984, 100: 437–452.
11. Y. Bethier, M. Godet, and M. Brendle, Velocity accommodation in friction. Tribol. Tech., 1989, 32: 490–496.
12. Y. Berthier, Maurice Godet's third body. In: The Third Body Concept. 1996, Elsevier, Oxford, pp. 21–30.
13. I. L. Singer, A thermochemical model for analyzing low wear-rate materials. Surf. Coat. Tech., 1991, 49: 474–481.
14. I. L. Singer, Mechanics and chemistry of solids in sliding contact. Langmuir, 1996, 12: 4486–4491.
15. I. L. Singer, How third-body processes affect friction and wear. MRS Bulletin, 1998, 23(6): 37–40.
16. S. Fayeulle, I. L. Singer, and P. D. Ehni, Role of transfer films in wear of MoS_2 coatings. In: Mechanics of Coatings. Vol 17, 1990, Elsevier, Oxford, pp. 129–138.
17. K. J. Wahl and I. L. Singer, Quantification of a lubricant transfer process that enhances the sliding life of a MoS2 coating. Tribol. Lett., 1995, 1: 59–66.
18. K. J. Wahl, D. N. Dunn, and I. L. Singer, *Wear* behavior of pb-mo-s solid lubricating coatings. Wear, 1999, 230: 175–183.
19. I. Sugimoto and S. Miyake, Orienting hydrocarbons transferred from a high performance lubricative amorphous c:h:si film during sliding in a vacuum. Appl. Phys. Lett., 1990, 56: 1868–1870.
20. D. S. Kim, T. E. Fischer, and B. Gallois, The effects of oxygen and humidity on friction and wear of diamond-like carbon films. Surf. Coat. Tech., 1991, 49: 537–542.
21. K. Jia, Y. Q. Li, T. E. Fischer, and B. Gallois, Tribology of diamond-like carbon sliding against itself, silicon nitride, and steel. J. Mater. Res., 1995, 10: 1403–1410.
22. A. Erdemir, C. Bindal, J. Pagan, and P. Wilbur, Characterization of transfer layers on steel surfaces sliding against diamond-like hydrocarbon films in dry nitrogen. Surf. Coat. Tech., 1995, 76–77: 559–563.
23. Y. Liu, A. Erdemir, and E. I. Meletis, A study of the wear mechanism of diamond-like carbon films. Surf. Coat. Tech., 1996, 82: 48–56.
24. A. A. Voevodin, A. W. Phelps, J. S. Zabinski, and M. S. Donley, Friction induced phase transformation of pulsed laser deposited diamond-like carbon. Diam. Relat. Mater., 1996, 5: 1264–1269.
25. A. A. Voevodin, J. P. O'Neill, and J. S. Zabinski, Nanocomposite tribological coatings for aerospace applications. Surf. Coat. Tech., 1999, 116–119: 36–45.
26. A. Erdemir, O. L. Eryilmaz, I. B. Nilufer, and G. R. Fenske, Synthesis of superlow-friction carbon films from highly hydrogenated methane plasmas. Surf. Coat. Tech., 2000, 133–134: 448–454.

27. H. E. Sliney, Dynamic of solid lubrication as observed by optical microscopy. ASLE Trans., 1978, 21: 109–117.
28. S. Descartes, M. Cassard, Y. Berthier, A. Ginet, and A. Aubert, MoS_x, a solid lubricant: yes, but which scales of tribological interpretation should be used? In: The consequences on the friction of mechanisms sixth European space mechanisms and tribology symposium. 1997, University of Lyon, France.
29. I. L. Singer, S. D. Dvorak, and K. J. Wahl, Investigation of third body processes by in vivo Raman tribometry. In: NORTRIB 2000 Conference Proceedings, 9th Nordic Symposium on Tribology. Vol 1. 2000, VTT, Finland, pp. 31–41.
30. S. D. Dvorak, K. J. Wahl, and I. L. Singer, Friction behavior of boric acid and annealed boron carbide coatings studied by *in situ* Raman tribometry. Tribol. T., 2002, 45: 354–362.
31. M. Belin and J. M. Martin, Triboscopy, a new approach to surface degradations of thin films. Wear, 1992, 156: 151–160.
32. K. J. Wahl, M. Belin, and I. L. Singer, A triboscopic investigation of the wear and friction of MoS_2 in a reciprocating sliding contact. Wear, 1998, 214: 212–220.
33. P. M. Cann and H. A. Spikes, In Lubro Studies of lubricants in EHD contacts using FTIR absorption spectroscopy. Tribol. T., 1991, 34: 248–256.
34. E. Olsen, T. E. Fischer, and B. Gallois, *In situ* analysis of the tribochemical reactions of diamond-like carbon by internal reflection spectroscopy. Wear, 1996, 200: 233–237.
35. C. U. A. Cheong and P. C. Stair, *In situ* studies of the lubricant chemistry and frictional properties of perfluoropolyalkyl ethers at a sliding contact. Tribol. Lett., 2001, 10: 117–126.
36. T. W. Scharf and I. L. Singer, Role of third bodies in friction behavior of diamond-like nanocomposite coatings studied by *in situ* tribometry. Tribol. T., 2002, 45: 363–371.
37. T. W. Scharf, R. M. Mowery, and I.L. Singer, *In situ* Raman tribometry of diamond-like carbon coatings and transfer films in dry and lubricated contacts, symposium on rolling element bearings. 2002, ASTM, West Conshohocken, PA, pp. 7–16.
38. I. L. Singer, S. D. Dvorak, K. J. Wahl, and T. W. Scharf, Third body processes and friction of solid lubricants studied by *in situ* optical and Raman tribometry. In: D. Dowson, M. Priest, G. Dalmaz, A. A. Lubrecht (eds) Proceedings of the 28th Leeds-Lyon Symposium on Tribology. Vol 40, Tribology series, 2002, Elsevier Scientific Publishing, London, pp. 327–336.
39. T. W. Scharf and I. L. Singer, Monitoring transfer films and friction instabilities with *in situ* Raman tribometry. Tribol. Lett., 2003, 14: 3–8.
40. T. W. Scharf and I. L. Singer, Quantification of the thickness of carbon transfer films using Raman tribometry. Tribol. Lett., 2003, 14: 137–145.
41. I. L. Singer, S. D. Dvorak, K. J. Wahl, and T. W. Scharf, Role of third bodies in friction and wear of protective coatings. J. Vac. Sci. Technol. A, 2003, 21: S232–S240.
42. R. J. Nemanich and S. A. Solin, first- and second-order Raman scattering from finite-size crystals of graphite. Phys. Rev. B, 1979, 20: 392–401.
43. J. Robertson, Amorphous carbon. J. Adv. Phys., 1986, 35: 317–374.
44. R. D. Evans, E. P. Cooke, C. R. Ribaudo, and G. L. Doll, Nanocomposite tribological coatings for rolling element bearings. Mater. Res. Soc. Symp. Proc., 2003, 750: 407–417.
45. G. L. Doll, C. R. Ribaudo, and R. D. Evans, Engineered surfaces for steel rolling element bearings and gears. Vol 2, Materials Science and Technology Conference Proceedings, New Orleans, LA, Sept. 26–29, 2004, pp. 367–374.
46. C. Donnet and A. Grill, Friction control of diamond-like carbon coatings. Surf. Coat. Tech., 1997, 94–95: 156–462.
47. A. C. Ferrari and J. Robertson, Resonant Raman spectroscopy of disordered, amorphous, and diamondlike carbon. Phys. Rev. B, 2001, 64: 75414.
48. I. L. Singer, Solid lubrication processes. In: Fundamentals of Friction: Macroscopic and Microscopic Processes. 1992, Kluwer Academic, Dordrecht, The Netherlands, pp. 237–261.
49. I. L. Singer, R. N. Bolster, J. Wegand, S. Fayeulle, and B. C. Stupp, Hertzian stress contribution to low friction behavior of thin MoS_2 coatings. Appl. Phys. Lett., 1990, 57(10): 995–997.
50. I. L. Singer, S. Fayeulle, and P. D. Ehni, Wear behavior of triode-sputtered MoS_2 coatings in dry sliding contact with steel and ceramics. Wear, 1996, 195: 7–20.

51. J. C. Sánchez-López, A. Erdemir, C. Donnet, and T. C. Rojas, Friction-induced structural transformations of diamondlike carbon coatings under various atmospheres. Surf. Coat. Tech., 2003, 163–164: 444–450.
52. T. W. Scharf, J. A. Ohlhausen, D. A. Tallant, and S. V. Prasad, Mechanisms of friction in diamond-like nanocomposite coatings. J. Appl. Phys., 2007, 101: 63521–1–11.
53. C. Donnet, T. Le Mogne, L. Ponsonnet, M. Belin, A. Grill, V. Patel, and C. Jahnes, The respective role of oxygen and water vapor on the tribology of hydrogenated diamond-like carbon coatings. Tribol. Lett., 1998, 4: 259–265.
54. J. A. Heimberg, K. J. Wahl, I. L. Singer, and A. Erdemir, Superlow friction behavior of diamond-like carbon coatings: time and speed effects. Appl. Phys. Lett., 2001, 78: 2449–2451.
55. C. Donnet, J. Fontaine, A. Grill, and T. Le Mogne, The role of hydrogen on the friction mechanism of diamond-like carbon films. Tribol. Lett., 2001, 9: 137–142.
56. J. Andersson, R. A. Erck, and A. Erdemir, Frictional behavior of diamond-like carbon films in vacuum and under varying water vapor pressure. Surf. Coat. Tech., 2003, 163–164: 535–540.
57. J. Fontaine, M. Belin, T. Le Mogne, and A. Grill, How to restore superlow friction of DLC: the healing effect of hydrogen gas. Tribol. Int., 2004, 37: 869–877.
58. P. L. Dickrell, W. G. Sawyer, J. A. Heimberg, I. L. Singer, K. J. Wahl, A. Erdemir, A gas surface interaction model for spatial and time dependent friction coefficient in reciprocating contacts: applications to near frictionless carbon. J. Tribol. – T. ASME, 2005, 127: 82–88.
59. F. Gao, A. Erdemir, and W. T. Tysoe, The tribological properties of low-friction hydrogenated diamond-like carbon measured in ultrahigh vacuum. Tribol. Lett., 2005, 20: 221–227.
60. H. I. Kim, J. R. Lince, O. L. Eryilmaz, and A. Erdemir, Environmental effects on the friction of hydrogenated DLC films. Tribol. Lett., 2006, 21: 53–58.
61. E. Konca, Y. -T. Cheng, A. M. Weiner, J. M. Dasch and A. T. Alpas, vacuum tribological behavior of the non-hydrogenated diamond-like carbon coatings against aluminum: effect of running-in in ambient air. Wear, 2005, 259: 795–799.
62. E. Konca, Y. -T. Cheng, and A. T. Alpas, Dry sliding behaviour of non-hydrogenated DLC coatings against Al, Cu and Ti in ambient air and argon. Diam. Relat. Mater., 2006, 15: 939–943.
63. Y. Qi, E. Konca, and A. T. Alpas, Atmospheric effects on the adhesion and friction between non-hydrogenated diamond-like carbon (DLC) coating and aluminum – A first principles investigation. Surf. Sci., 2006, 600: 2955–2965.
64. J. K. Brennan, T. J. Bandosz, K. T. Thomson, and K. E. Gubbins, Water in porous carbons. Colloids Surf. A, 2001, 187: 539–568.
65. Poine, A, Outokumpu HSC Chemistry for Windows Version 4.1, 2002, Outokumpu Research Oy, Pori, Finland and ARSoftware, Landover, MD.

An Overview of Superlubricity in Diamond-like Carbon Films

A. Erdemir[1], J. Fontaine[2] and C. Donnet[3]

Abstract Diamond-like carbon (DLC) films have emerged as a class of very important tribological materials in recent years mainly because of their outstanding properties, such as high mechanical strength and hardness, excellent chemical inertness, and exceptional friction and wear performance under both dry and lubricated sliding conditions. Persistent and systematic research efforts during the last decade have resulted in the development of a new breed of DLC films providing superlubricity and near-wearless sliding even under very harsh contact and environmental conditions. In fact, the dry sliding friction and wear coefficients (i.e., as low as 0.001 and 10^{-11} mm^3/N.m, respectively) of these films are among the lowest reported to date, and such unusual tribological properties may have huge positive impacts on efficiency, durability, and performance characteristics of a wide range of mechanical systems, including magnetic hard disks, sliding and/or rolling contact bearings, gears, mechanical seals, scratch-resistant glasses, invasive and implantable medical devices, microelectromechanical systems (MEMS) and many more. In this chapter, we attempt to provide an up-to-date overview of these novel DLC films that can provide superlubricity and discuss in detail those factors that control their very unique lubrication mechanisms. Specifically, we concentrate on the state of the art in our understanding of their superlow friction and wear mechanisms, and how these mechanisms may relate to their structural chemistry, mechanical properties, and test and environmental conditions. In particular, various intrinsic (film-specific) and extrinsic (or test condition-specific) factors that play major roles in friction and wear of DLC films are discussed in detail and correlated with their friction and wear mechanisms.

Keywords superlubricity, diamond-like carbon, fundamental mechanisms, intrinsic and extrinsic factors

[1]Argonne National Laboratory, Energy Systems Division, 9700 South Cass Avenue, Argonne, IL 60439, USA

[2]Laboratoire de Tribologie et Dynamique des Systèmes, UMR CNRS 5513, Ecole Centrale de Lyon, 36 avenue Guy de Collongue, 69134 Ecully, France

[3]University Institute of France and Laboratoire Hubert Curien, UMR CNRS 5516, Université Jean Monnet, 18 rue Professeur Benoît Lauras, 42000 Saint-Etienne, France

C. Donnet and A. Erdemir (eds.), *Tribology of Diamond-Like Carbon Films: Fundamentals and Applications*.

1 Introduction

The word "superlubricity" in tribology refers to a new sliding regime in which friction or resistance to sliding nearly vanishes [1]. This means that those factors that normally contribute to friction do not exist any more, and the solid bodies that are in contact with each other slide over one another without creating much adhesion or friction. Achievement of such a sliding regime in real-world applications would be rather extraordinary mainly because friction is a major source of lost energy and a cause of hazardous emissions to our environment in a wide range of moving mechanical assemblies. At the moment, the annual cost of friction- and wear-related energy and material losses in these mechanical assemblies is estimated to be as much as 5% of the gross national products of most industrialized nations. Hence, the further reduction or elimination of friction and wear from these assemblies would be extremely beneficial to conserving our limited energy resources and protecting our environment.

In the early 1990s, the prospect of achieving superlubricity seemed quite possible on the atomically smooth-sliding surfaces of certain materials [1,2]. Specifically, Hirano and Sokoloff theoretically predicted that when such surfaces are brought into contact in an incommensurate or ideally misaligned/misfit fashion, the frictional forces generated between them should vanish during sliding. Their predictions were experimentally verified during the 1990s. Specifically, with the use of such advanced tools as scanning tunneling and atomic force microscopy (STM and AFM), measurement of superlow friction, and hence the observation of superlubricity on incommensurate sliding systems became feasible [3–5]. Since then, the interest in superlubricity research has grown considerably, and during the last decade or so, this effort has shifted towards the development of novel engineering materials and coatings, such as diamond-like carbon (DLC), that can provide superlubricity under industrially relevant sliding conditions of various mechanical systems [6,7].

DLC coatings have existed for more than half a century. Despite such a long existence, they did not attract much attention from scientific and industrial communities until the late 1980s. At that time, their unusual friction and wear properties were realized, and some unique application possibilities were envisioned [8,9]. Since then, many systematic studies have been carried out on DLC films, and over the years, their structure, properties, and performance characteristics have been greatly improved to the point where they are now considered as one of the most important coatings in the tribology field. As a result of numerous concerted efforts, more robust and durable versions of DLC films have been synthesized in recent years and further optimized to provide not only superhardness, but also superlubricity under a wide range of test conditions.

In this chapter, we aim to provide an up-to-date overview of these superlubricious films and to discuss those factors that control their lubrication mechanisms. In particular, we will present the state of the art in our understanding of the superlow friction and wear mechanisms of these films. We will also explain how these

mechanisms may relate to their structural chemistry, mechanical properties, and test and environmental conditions and/or parameters.

This chapter encompasses four main sections. In the first section, we briefly review the superlubricity in other solid materials and talk about their lubrication mechanisms. We feel that such a short review is essential for understanding what gives rise to superlubricity in crystalline solids and how it may relate to, or differ from, the superlubricious behavior of certain DLC films. In the second section, we will devote much of our attention to the root causes of friction and the lubrication mechanisms of DLC films. The third section is devoted to the experimental verification and/or observation of superlubricity in these films. The last section will concentrate on the fundamental lubrication mechanisms and the specific role of hydrogen and other elemental species in the superlubricity of DLC films.

2 Superlubricity in Crystalline Solids

During the 1990s, several researchers attained superlubricity or near-frictionless sliding regimes on the atomically smooth-sliding surfaces of a number of crystalline solids. The most important requirement for superlubricity was that the sliding surfaces had to be brought into contact in an incommensurate or ideally misaligned/misfit fashion [3–5,10–13]. Mechanistically, it was argued that such a sliding contact situation would favor a high degree of atomic-scale mismatch at the contact interface, and hence the extent of atomic-scale stick-slip will be insignificant. Apparently, under such sliding conditions, there is little or no direct registry between atoms of opposing surfaces; thus, the extent of atom–atom interactions is very low or essentially absent. For example, Hirano et al. [3] reported factors of up to four reductions in the amount of frictional force when two mica sheets were increasingly rotated out of registry and finally brought into an incommensurate state of sliding. Using an atomic force microscope, Mate et al. [14] reported friction coefficients as low as 0.005 for graphite, while Dienwiebel et al. [5] demonstrated zero friction on the same material under conditions of complete incommensurability using an AFM instrument called Tribolever [15]. Intercalation of graphite with C_{60} eliminated the incommensurability requirement for superlubricity in graphite [4,16]. Specifically, the existence of spherical C_{60} molecules between the graphene sheets of graphite was apparently able to overcome the incommensurability requirement for superlubricity. As for the tribological mechanisms, it was proposed that C_{60} significantly increases the interlamellar spacing and may also act as nanoscale ball bearings during sliding. In another study, Martin et al. confirmed that superlubricity is not limited to graphite. They showed that it might also exist between the sliding surfaces of atomically smooth and ultrathin films of MoS_2, provided that their surfaces are again in a state of incommensurability [10,12].

Besides the lamellar solids mentioned above, superlubricity was also achieved in a few other crystalline solids, including Si, Ag, NaCl [3,6,7,11,13], and a number of DLC films [17–20]. For the crystalline solids, incommensurability or a state of

very weak interatomic interactions was a major requirement. Specifically, in most of these solids, the transition from stick-slip to continuous sliding could only be achieved along certain crystallographic sliding directions or under some very light loading conditions (i.e., less than a nano-Newton) in ultrahigh vacuum (UHV). In summary, superlubricity in certain crystalline solids is now a reality but only feasible under specific test conditions (often involving light contact loads, specific sliding directions, high vacuum, and special AFM-type instruments). From a more practical point of view, we need new materials and/or coatings that can provide superlubricity across the scales and under industrially more relevant sliding conditions that may involve severe contact pressures, high sliding speeds, elevated temperatures, liquid lubricants, etc. Such an achievement would undoubtedly have an immediate benefit for a wide range of moving mechanical systems ranging in sizes from a few micrometers to several centimeters and beyond.

Thanks to the recent dedicated and more systematic studies, a number of novel carbon films can now provide superlow friction and wear to sliding tribological surfaces under more realistic sliding conditions. Specifically, researchers have developed a series of hydrogenated and nitrogen-containing DLC films that provide friction coefficients below 0.01 [17–24]. Furthermore, they have incorporated special additives into a range of liquid lubricants, enabling hydrogen-free DLC films to attain superlubric states under oil-lubricated sliding conditions [25]. Accordingly, in the following sections, we will concentrate on these films. We will also talk about their lubrication mechanisms in light of the recent fundamental studies carried out by these authors [17–24] and those reported by other researchers in the open literature. In particular, we will discuss in detail the pivotal role of hydrogen in the superlubricity of DLC films.

3 Lubrication Mechanisms of DLC Films

Unlike the above-mentioned crystalline solids whose superlubricity depends primarily on the degree of incommensurability between highly ordered surface atoms, DLC films are structurally amorphous, and hence, the mechanisms proposed for the crystalline solids may not be valid for these materials. One may argue that at an atomic scale, the sliding surfaces of DLC films will naturally be in an incommensurate state (since they are structurally amorphous), and from an atomistic point of view, these films do perhaps satisfy the incommensurability requirement for superlubricity. However, all kinds of DLC films are structurally amorphous, but only a few of them are able to provide friction coefficients down to the superlubric range.

Another possible scenario is that during dynamic sliding, the very top layers of DLC films may have been altered structurally or forced to assume an ideally ordered state (something similar to the graphene sheets in crystalline graphite), which then assumes an incommensurate contact interface and hence provides superlubricity, as in graphite. Such a possibility cannot be ruled out, considering that numerous scientists

[18,19,26–28] have in the past reported some degree of graphitization for rubbing surfaces of DLC films and for the debris particles that originate from such sliding interfaces. However, elucidation of this possibility is extremely difficult mainly because we do not yet have the powerful structural tools that can gauge the true structure of top layers that may have been a few Angstrom thick.

As will be discussed later, the DLC films have different structural and chemical forms. Overall, they exhibit attractive physical, chemical, electrical, optical, mechanical, and tribological properties. Because of their excellent chemical inertness, they are extremely resistant to corrosive and/or oxidative attacks, even in highly acidic or basic aqueous media. Some DLC films are superhard (as high as 90 GPa) and resilient, while others have hardness in the range 5–10-GPa. As mentioned above, certain DLC films are capable of providing superlubricity to sliding surfaces, while others exhibit friction coefficients as high as 0.7. Such a contrasting combination of so many outstanding properties in one material is uncommon in our engineering fields, but DLC has them all, and materials that provide superlow friction and wear are urgently needed to meet the increasingly more demanding sliding conditions of the numerous mechanical systems that are used extensively by industry or under development.

Some of the current and pending industrial applications for DLC films include various engine parts and components, manufacturing tools, magnetic hard disks, aerospace materials, mechanical face seals, medical implants, razor blades, and microelectromechanical systems (MEMS) [8,29,30]. In the following subsections, we will provide a brief overview of the different classes of DLC films and then concentrate on their structural and chemical natures. Subsequently, we will focus on their tribology and the factors that control their friction and wear mechanisms in relation to the test conditions and environments.

3.1 Classification of DLC Films

Since their initial discovery in the early 1950s [31], DLC films have gone through some major overhauls. In particular, the structural chemistry of these films has largely been refined in recent years, and as a result, their mechanical and tribological properties were significantly improved [8,9,17,32–34]. These films are now available over a broad range of structures and chemical compositions. Structurally, some are highly graphitic in nature and hence are soft, while others are very much diamond-like, possessing more than 80% sp^3-bonded carbon atoms in their structures and being very hard. Chemically, some DLC films are totally hydrogen-free [34], while others contain significant amounts of hydrogen and other elemental species, including N, F, Si, Ti, Cr, W, S, etc., in their amorphous structures [33,35,36]. The incorporation of these elements in DLC films made a huge positive impact on their mechanical, electrical, and tribological properties.

Almost all of the DLC films are produced by vacuum-based physical and chemical vapor deposition methods at temperatures ranging from sub-zero to 400°C.

The structural chemistry and, hence, the properties of these DLC films are strongly dependent on the type of deposition method, the presence or absence of alloying elements, and the precursor carbon sources used during their deposition. These films are mainly made up of sp^2- and sp^3-bonded carbon atoms. Over the years, scientists have made great strides in not only understanding but also controlling the structural chemistry of DLC films. The state of the art in designing and synthesizing these films has now reached the point where an experienced coating specialist can reliably formulate a novel DLC film that is most suited to meet the specific application conditions of a mechanical system – be it a gear, a roller bearing, a biomedical implant, or a computer hard disk. The broad knowledge bases accumulated over the years have further motivated scientists to look at things from a more fundamental point of view and design films that can provide extremely low friction and/or wear. Thanks to these concerted efforts, there now exists a series of DLC films providing superlow friction and wear under severe sliding conditions [17–24].

Regardless of the type, structurally, almost all DLC films available today are amorphous. It is sometimes possible to incorporate certain nanocrystalline phases (in nanocomposite or nanolayer-coating architectures [32,33,37]) into DLCs, but the bulk or the main matrix of these films is usually made of a highly disordered network of sp^2- and sp^3-bonded carbon atoms. Vacuum-based deposition processes currently used in the production of DLC films include cathodic-arc physical vapor deposition (PVD), pulse laser deposition (PLD), magnetron sputtering, ion-beam assisted deposition, and plasma-enhanced chemical vapor deposition. Depending on the deposition process and carbon sources used, the structural chemistry of DLC films may vary a great deal. Such differences in their structure and chemistry may in turn result in major differences in their mechanical and tribological properties.

In addition to sp^2- and sp^3-bonded carbon atoms, small amounts of sp^1 bonding are also feasible under certain deposition conditions, but in most cases, these do not account for more than 1 or 2 at. % [29,34,38]. The relative amounts of sp^2- versus sp^3-bonded carbon atoms in DLC films may vary a great deal and affect their properties immensely. For example, if a film is mostly made of sp^2-bonded carbon atoms, then their hardness values tend to be very low, and when tested in a tribological test machine, they may behave more like graphite. The friction coefficients of these films are low in humid test environments but become high in vacuum or inert test chambers. DLC films consisting of mostly sp^3-bonded carbons are very hard (like diamond), and their tribological behavior is claimed to be similar to that of diamond [23,39–41].

When DLC films are derived from a hydrocarbon source (such as acetylene or methane), besides the sp^2- and sp^3-bonded carbon atoms, there will be large amounts of hydrogen within their structures. Most of the hydrogen atoms will be bonded to carbon with strong sp^3 bonding, but others will be accommodated as atomic or molecular interstitials. Table 1 summarizes some of the basic properties of these carbon films (ta-C and a-CH) with respect to their sp^2, sp^3, and H contents. In addition to the ones shown in this table, several more DLC films may consist of additional alloying elements or discrete compound phases in a nanocomposite

Table 1 Structure, composition, and properties of two forms of DLC [8]

Composition and properties	ta-C	a-CH
Hydrogen content, at. %	<5	20–60
Sp^3 (%)	5–90	20–65
Density ($g \cdot cm^{-3}$)	1.9–3.0	0.9–2.2
Thermal stability (°C)	<600	<400
Optical gap (eV)	0.4–1.5	0.8–4.0
Electrical resistivity ($\Omega \cdot cm^{-1}$)	10^2–10^{16}	
Index of refraction	1.8–2.4	
Compressive stress (GPa)	0.5–5	
Hardness (GPa)	<80	<60
Young's modulus (GPa)	<900	<300

and/or superlattice or nanolayer architectures, which can dramatically influence their structural, mechanical, and tribological properties, as will be discussed later.

3.2 Tribology of DLC Films

DLC films have been the subject of numerous tribological investigations in past years. As highlighted in the Introductory Chapter of this book, hundreds of papers have so far been published on the tribology of DLC films. For a quick survey of the major findings, refer to the recently published review papers on this subject in Refs[8,30,35,42,43]. In general, previous studies have confirmed that DLC films are lubricious and at the same time resistant to wear. However, they also found that their friction and wear properties may be strongly affected by test conditions and environments, as well as their structural and chemical nature. For example, the friction coefficient of hydrogenated DLC films is much higher in humid air than in dry air or nitrogen, while the opposite is true for hydrogen-free DLC films [21,44–46].

Attaining ultra- to superlow friction in DLC films has proven to be very difficult. As mentioned before, these films are structurally and chemically diverse. They exist over a broad range of structures and compositions. Since friction is strongly affected by their structural and chemical nature, ascribing that a narrow range of friction coefficients for all DLCs (as a class) is almost impossible. Such is not the case for various types of metals and alloys, regardless of some variations in their chemical and/or structural nature. In most cases, the friction coefficients of various steels (regardless of their chemical and structural state and mechanical properties) lie between 0.6 and 0.8; but, for DLC films, such a situation does not exist.

Most solid lubricants (indium, lead, silver, graphite, MoS_2, etc.) provide lubricity to sliding surfaces by undergoing easy shear [47]. In the case of DLC films, shear deformation is not feasible because they are structurally amorphous and thus possess no crystallographic shear planes to enable easy shear. As a general rule,

bulk shear or plastic flow is not one of the mechanisms that control friction in DLC films. If so, what makes these films so lubricious? The quick answer is that they shear through a sharp interface that exists between the DLC film itself and the counterface material, which may be covered by a very thin third-body or transfer layer. The friction coefficient of DLC against those counterfaces that do not form a transfer layer tends to be high.

In most tribological tests, a relatively high friction occurs in the beginning, but a much lower friction prevails as sliding continues. Such a reduction in friction always coincides with the formation of a thin transfer layer on the sliding surface of the counterface material [18,19,22,27,48,49]. As a result, after the initial run-in period, the sliding essentially takes place between the parent or original DLC film on the disk side and the transferred layer on the counterface ball or pin side. This layer is mostly made of carbon migrating from the DLC side. Raman spectroscopy and transmission electron microscopy have revealed that significant structural ordering takes place among the carbon atoms of the transfer layers during sliding tests [27,49,50]. Depending on the type of counterface material used during the sliding, the transfer layers may also consist of small amounts of wear debris particles of the counterface materials. In the case of steel counterfaces, some finely ground iron oxides may also appear within the transfer layers.

Besides the transfer layer mechanism for low friction, the frictional behaviors of almost all DLC films are strongly influenced by a range of extrinsic (or test condition specific) and intrinsic (film specific) factors [30]. Some of the extrinsic factors include the relative humidity or chemical nature of the test environment, ambient temperature, contact pressure, sliding velocity, type of sliding motion, presence or absence of a liquid, and/or solid lubricant on sliding surfaces. The most important intrinsic factors are film composition, structural nature (including nanolayers and/or nanophases), thickness, surface roughness, and a range of mechanical properties, including hardness, elastic modulus, and viscoelasticity. As is well known in tribology, a smooth surface finish and a high degree of chemical inertness are always preferred for achieving low friction and wear in most sliding tribosystems.

In typical practical applications, liquid lubricants and/or greases are used to control friction and wear. Because of the active antifriction additives, these lubricants can form a protective and chemically passive boundary film that can provide easy shear during sliding. The solid DLC films work the same way. When applied on the sliding contact surfaces of a machine component, they can protect these surfaces against wear and provide easy shear during sliding contacts. As will be elaborated later, the chemical composition of the DLC films strongly affects their performance and protective nature during tribological uses. For example, the incorporation of alloying elements such as hydrogen, sulfur, nitrogen, fluorine, and boron was shown to have significant beneficial effects on the frictional behavior of DLC films [30,35,51–53]. In particular, boron was able to reduce the friction of highly hydrogenated DLC films in humid test environments by more than 60% [30].

In the following section, we will concentrate on those DLC films that can afford superlubricity to sliding surfaces. We will also discuss how superlubricity is attained

and measured on these films, and what factors influence their lubrication behavior. In particular, the effects of test conditions and environments are elaborated.

4 Experimental Verification of Superlubricity in DLC Films

Visually, all DLC films look alike. They have a shiny black color. However, as mentioned earlier, both structurally and chemically, they differ substantially from one another. As a result, their mechanical and tribological properties span a broad range. Furthermore, specific test conditions and/or environments established during sliding experiments can also play major roles in their friction and wear behavior. For example, depending on the test conditions, the reported friction values for various DLC films range from 0.001 to 0.7 [17–24,27,54], confirming the large disparity in the frictional performance of various DLC films. Their wear coefficients may also differ by several orders of magnitude. Unlike other crystalline solids whose superlubricity may depend on the degree of incommensurability, attaining superlubricity in DLC films is much more complicated and may be difficult to maintain over broad test conditions and/or film structure, and/or compositions. It can only be achieved by the control of not only test conditions and/or environments, but also film structure and/or composition.

4.1 Challenges in Measuring Superlow Friction

Measuring frictional forces in the millirange is rather difficult. It requires a reliable test unit equipped with robust and ultrasensitive force gauges. Even one degree of misalignment and very low levels of background noise can affect the measurement of the true frictional force. It is extremely important to demonstrate that superlow friction forces can effectively be recorded during the course of sliding tests, as realized by an UHV tribometer available at Ecole Centrale de Lyon [55]. This apparatus consists of a linear reciprocating pin-on-flat contact configuration, and the applied load on hemispherical pins is adjustable from 0.5 to 5 N. For the type of steel pins used, it is possible to achieve theoretical Hertzian contact pressures ranging from ≈0.3 to ≈1.8 GPa. The sliding speed in this test system can vary from 0.01 to 2 mm/s over a track length ranging from 0.5 to 5 mm. The vacuum level is usually about 10^{-7} Pa, but ultrapure and dry gases can be introduced in the chamber at pressures of about 10^{3} Pa. An analog–digital converter allows a minimal recorded force of 5×10^{-4} N. The electronic plus mechanical noises do not exceed a few milli-Newtons. Consequently, the minimum average friction force, which is detectable with the equipment at hand, is about 2×10^{-3} N, corresponding to a friction coefficient of about 2×10^{-3} for a 1 N normal force.

Figure 1a shows the typical evolution of the average friction coefficient, versus the number of sliding cycles, of a superlow-friction DLC film tested under UHV conditions. In this test, a normal load of 3 N was applied against an uncoated 8 mm radius

hemispherical pin made of AISI 52100 bearing steel. The corresponding maximum theoretical Hertzian contact pressure is about 550 MPa. The sliding speed was 0.5 mm/s with reciprocating amplitude of 1.5 mm. The residual pressure in the chamber was lower than 5×10^{-7} Pa. Figure 1b shows the unprocessed friction tangential force recorded over one cycle (two alternate passes of the ball against the DLC related to cycle number 400) during the superlow friction regime. As can be observed, the friction force change in direction (256 recorded data points for one-way pass on the track length) can hardly be detected during this cycle. The average tangential force during one pass is about 8 mN, corresponding to a friction coefficient of about 2.7×10^{-3}. However, due to mechanical and electronic noise, the standard deviation around this value is about 10 mN higher than the mean value. This highlights the difficulty of measuring such extremely low coefficients of friction, especially inside a vacuum chamber.

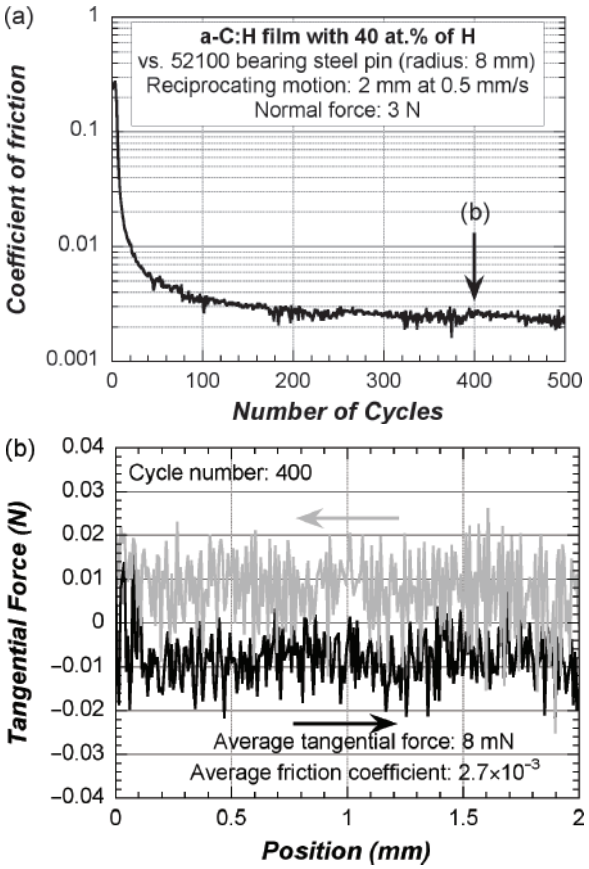

Fig. 1 (a) Coefficient of friction versus number of sliding cycles and (b) tangential force versus position along track during the friction loop of cycle #400 for a-C:H film sliding in ultrahigh vacuum (UHV)

In the case of a pin-on-disk machine with a unidirectional sliding contact configuration, one has to determine the lowest sensitivity limit of its force gauges (such as load cell, linear variable displacement transducer, and strain gage) to make sure that this machine is capable of reliably sensing loads that are 1/1,000 of the normal or dead weight loads that are normally applied on top of the pin specimens. Furthermore, one has to check the calibration of the machine's force gauge and make sure that the lateral and normal forces have a linear relationship down to the lowest load levels one can test. Argonne National Laboratory possesses a pin-on-disk machine with sensitivity well below 1 g force. If one uses 1 kg force in a sliding experiment, then being able to sense 1 g lateral force will enable measurement of friction in the millirange, which can translate into friction coefficients as low as 0.001. If the normal forces are in the range of a few grams, then measuring friction in the millirange with this system is difficult. In such a situation, one can reverse the direction of sliding and take the average of frictional forces from both directions to arrive at an approximate friction value. Furthermore, since friction is sensitive to vibrations, the system must be well isolated from outside vibrations, especially if very light loads are used during the friction experiments.

Another way to accurately measure very low frictional forces is described in Ref. [45]. Specifically, in a ball-on-disk machine with several strain gauges attached strategically to the tribometer's arm, one measures or monitors the normal and friction forces acting at the same time on the ball during sliding under load. The load can be increased at selected increments and kept constant for a long duration at each increment to collect enough data. The acquired friction force data at each step are then plotted against the corresponding loads, and the slope of this plot is taken as the friction coefficient of that sliding interface. Kim et al. found that this method yields a fairly accurate measurement of friction coefficients of DLC films capable of values less than 0.01 [45]. In addition, they claim that such a procedure ensures that the friction coefficient does not change with varying load. This should be the case provided all the other conditions remain the same.

4.2 Chemical and Structural Nature of Superlubricious DLC Films

Compared to some other solids, most carbon-based materials are inherently lubricious and hence can provide relatively low friction during most dry and lubricated sliding conditions. Diamond, glassy carbons, and graphite are prime examples of such materials, which exhibit friction coefficients as low as 0.1 [56]. As mentioned earlier, certain DLC films are capable of friction coefficients below 0.01 [21–24]. In particular, the friction coefficients of highly hydrogenated (containing ~40 at. % hydrogen) DLCs were reported to be as low as 0.001 in dry nitrogen and/or high vacuum environments [23]. Such superlow friction values are not attainable with hydrogen-free DLC films. In fact, when tested in high vacuum or inert gases, the friction coefficients of hydrogen-poor or -free DLC films can be rather high. For example,

Miyake et al. [54] and others [44–46] found that DLC films with little or no hydrogen reach friction values higher than 0.35. Erdemir et al. reported friction values as high as 0.7 for hydrogen-free DLC films [21–24]. Based on a systematic study, Erdemir et al. demonstrated a close correlation between the friction coefficients of various DLC films and the hydrogen content of the gas discharge plasmas from which these DLC films were derived [6,24]. This correlation is depicted in Fig. 2. In general, their results indicate that the higher the hydrogen content of the gas discharge plasma, the lower the friction coefficient. The DLC film that exhibited the lowest friction coefficient (i.e., 0.001) was derived from a gas discharge plasma of 25% methane and 75% hydrogen (corresponding to a hydrogen to carbon ratio of 10); while a hydrogen-free DLC (with more than 80% sp^3-bonded carbon atoms) provided friction coefficients higher than 0.5 [21,23]. The friction coefficients of DLC films derived from pure acetylene (with a hydrogen to carbon ratio of 1) were 0.3–0.4 in dry nitrogen.

Donnet et al. [55] reported similar results for certain DLC films (prepared by IBM) tested in high vacuum. Figure 3 shows the superlow friction behavior of a-C:H films containing 40 at. % hydrogen, tested in UHV conditions. The steady-state friction is near 0.002 with extremely low wear. As a result of their systematic studies, Donnet et al. confirmed that not all hydrogenated DLC films yield superlow friction. Specifically, they found that below 35 at. % hydrogen in DLC, the

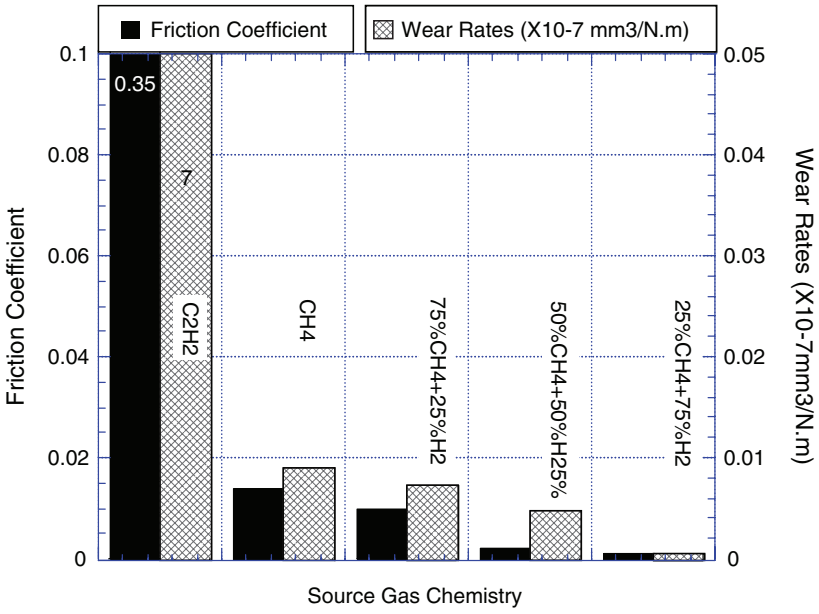

Fig. 2 Friction and wear coefficients of DLC films derived from various source gases in a plasma-enhanced chemical vapor deposition system. Note that the friction coefficient and wear rate of a pure acetylene-derived DLC film are among the highest, while those of a film derived from 75 vol. % hydrogen and 25 vol. % methane are the lowest. (Test conditions: load, 10 N; speed, 0.5 m/s; temperature, 22–23°C; test environment, dry N_2)

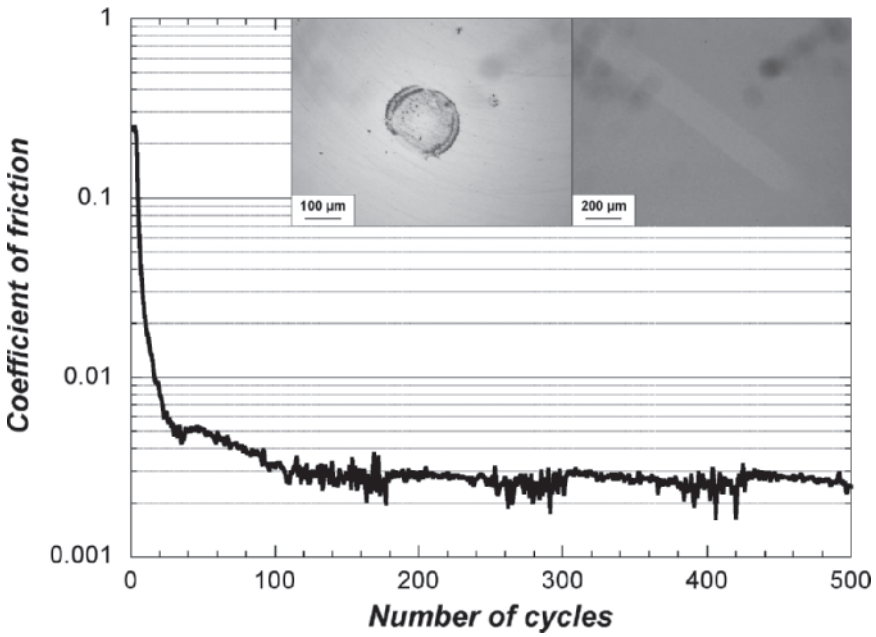

Fig. 3 Friction behavior of a superlow-friction a-C:H film (40 at. % hydrogen) tested in UHV conditions. Inset shows the wear scar and track formed on the ball and disk, respectively, at 500 cycles

friction coefficients are as high as 0.5, and at much higher concentrations, the friction coefficients are less than 0.01 in an UHV.

Hydrogen does not exclusively control the superlubricity of DLC films, as depicted in Fig. 4. Silicon incorporation into DLC films may also be responsible for superlow friction coefficients (as low as 0.007) when the film is rubbed with a steel ball in high vacuum [56]. The a-C:H:Si films are probably the first experimental evidence of superlow friction with DLC films. They were deposited in an electron cyclotron resonance plasma of ethylene and silane. Polarized infrared spectroscopy revealed that this superlow friction behavior can be attributed to hydrocarbon transferred from the rubbed film to the ball surface and oriented along the sliding direction.

Fluorine incorporations into a-C:H films may also be responsible for friction values less than 0.01. With an a-C:H:F film containing 18 at. % of fluorine and only 5 at. % of hydrogen, the stabilized coefficient of friction observed in UHV is only about 0.005 [57]. Fluorine incorporation in the covalent network, besides controlling the cross-linking by terminating some bonds, similar to hydrogen, will also probably favor the presence of free volumes in the structure and flexibility of the molecular chains during sliding. This observation is based on the much larger size and electronegativity of the fluorine atom compared to hydrogen. Such an a-C:F:H film with 23 at. % of monovalent atoms exhibits a superlow friction consistent with that of a-C:H films with much higher hydrogen content.

Freyman et al. report superlow friction in ambient air conditions for DLC with sulfur deposited by magnetron sputtering in a mixture of $Ar/H_2/H_2S$ [58]. The a-C:

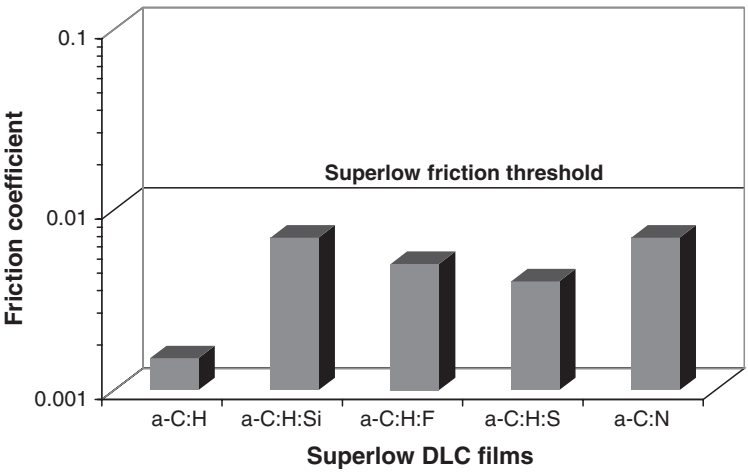

Fig. 4 Types of DLC films exhibiting superlow friction

H:S films contain 30 at. % hydrogen and 5 at. % sulfur. The films are thermally stable up to 300°C in air, and the hardness decreases from 13–8 GPa due to the sulfur incorporation. Evidence of C–S bonds is suggested by x-ray photoelectron spectroscopy investigations. Freyman et al. observed a steady-state superlow friction of 0.004 in ambient humid air, compared to 0.02 without sulfur incorporation. This superlow friction behavior is attributed to weaker binding between adsorbed water molecules and the C–S–H surface, resulting from the smaller dipole moment of S–H compared to C–H.

Nitrogen incorporation in DLC may also induce superlow friction. Sánchez-López et al. report that a-C:N films deposited by dual-ion-beam-assisted deposition exhibit a superlow friction coefficient of 0.007–0.008 in nitrogen gas whatever the nature of the counterface material [59]. The use of nitrogen gas at atmospheric pressure is presumably hindering the access of reactive species such as oxygen and water molecules, thus maintaining a gap between the counterface and preventing interaction between dangling bonds from contacting surfaces. The superlow friction coefficient is, therefore, achieved as a result of the highly passive nature of the sliding counterface. Kato and his coworkers also achieved ultralow friction (less than 0.01) by blowing nitrogen gas into the sliding interfaces of Si_3N_4 balls and ion-beam-deposited CN_x coatings [17]. Based on numerous other studies in dry nitrogen, vacuum, and elevated temperatures, they concluded that nitrogen–surface interactions (bolstered by mechanical action and tribochemical reaction) might have been the reason for the ultralow friction behavior of these CN_x films.

Overall, these and other dedicated studies suggest that the control of surface chemistry or chemical interactions at sliding DLC interfaces is extremely important for the friction and wear behavior of these films. Specifically, by controlling or effectively eliminating the intrinsic and extrinsic sources of friction in DLC films, one should be able to achieve ultra- and superlow friction coefficients under both dry and lubricated sliding conditions.

5 Mechanisms of Superlubricity in DLC Films

Ultralow friction coefficients can be achieved under conditions where contacting surfaces interact weakly or create very little or no adhesive forces during sliding. Such a condition is somewhat satisfied by the use of highly formulated engine oils, especially under mixed lubrication regimes where low-shear boundary films together with hydrodynamic lift ensure low friction. However, under dry sliding conditions, no such boundary films or hydrodynamic effects exist to overcome surface adhesive forces. Consequently, most solid materials, including metals and ceramics, create high adhesive forces and, hence, friction when sliding. As emphasized earlier, DLC films can also be considered as solid materials, but they naturally provide low friction regardless of oils and/or other lubricants. However, achieving superlow friction in these films is only feasible under specific conditions. Table 2 summarizes some of the key requirements that have to be fulfilled to achieve superlow friction (in the millirange) with DLC films. Note that each of these key requirements may be influenced by some other parameters, some of which are test-condition specific, while others are related to film structure and chemistry. Overall, superlow friction in DLC films can only be achieved by effectively controlling such parameters. In the following paragraphs, some of the key parameters (surface roughness, chemical and tribochemical interactions, transfer films, thermal effects, etc.) are discussed.

5.1 Intrinsic and Extrinsic Factors Affecting Friction in DLC Films

As mentioned above, many factors control the frictional behavior of DLC films, and the controlling factors may change a great deal from one type of DLC to another. We find it convenient to divide these factors into two broad categories: intrinsic and extrinsic.

Intrinsically, the degree of sp^2 versus sp^3 bonding, as well as the relative amounts of hydrogen and/or other alloying elements in the structure or on the sliding

Table 2 Key requirements for achieving superlow friction in DLC films

Key requirements from DLC film	Influencing key factors	Influencing deposition and experimental parameters
Tribofilm or transfer layer buildup	Surface condition and/or chemistry of counterface material	Native oxide and contaminant films
High chemical inertness and mechanical hardness	Surface topography/roughness	Generation of wear debris, formation of transfer layers
	High hydrogen content	Deposition process parameters
Thermal stability	Structural and/or chemical modification	Ambient and/or frictional heating
High viscoplasticity of contacting surfaces	Flexibility of the hydrocarbon network	Deposition process parameters
	Absence of chemically active gaseous contamination	Partial pressure of O_2, H_2O gases during sliding

surfaces of DLC films, can strongly affect their friction and wear behaviors. As discussed earlier, the presence or absence of certain alloying elements and/or nanoscale secondary phases in the film can also strongly affect friction and wear. Other intrinsic factors that may have minor effects on the frictional behavior include the nature of the substrate on which the DLC film is deposited; the mechanical, thermal, and electrical properties of the substrate; and the counterface materials.

Extrinsically, the frictional behavior of DLC films is primarily affected by the extent of chemical, physical, and mechanical interactions between the rubbing surfaces of the films and their surrounding atmosphere, which may consist of a large variety of gaseous, liquid, and solid species. The physical roughness of the sliding surfaces of DLC films is also important, and if this factor is not controlled effectively, it may adversely affect friction and wear. In general, rougher surfaces tend to cause higher friction. The specific test conditions and/or parameters (load, speed, type of motion, distance, etc.) employed during the sliding tests can also strongly affect the friction and wear of DLC films. In particular, extrinsic parameters such as contact pressure, loading mechanism, nature of sliding motion and speed, and ambient temperature need to be controlled during sliding tests to achieve superlow friction. The presence or absence of a transfer film on the sliding surfaces of counterface materials and the physical and/or chemical nature of such films can also influence friction. The following paragraphs briefly describe the most important intrinsic and extrinsic factors.

5.1.1 Physical Roughness

High physical roughness often leads to high friction between most sliding surfaces. On such rough surfaces, a high degree of mechanical interlocking occurs between surface asperities, and this condition often gives rise to high friction. In microcrystalline diamond films, the surface finish can be rather rough due to the highly faceted nature of diamond grains. Such a rough surface finish causes high friction and wear during sliding tests [60]. Unlike diamond, DLC films are structurally amorphous. As a result, their surface finish can be extremely smooth (especially when deposited on highly polished surfaces). When deposited on an originally rough or lapped surface, their surface roughness will obviously be high, and the friction coefficients of such surfaces will also be high. The DLC films deposited by PLD and/or arc-PVD methods may be relatively rough, mainly because during deposition some nano/microparticles and/or droplets are also ejected from the solid carbon targets and subsequently are deposited on the surface of the substrate materials along with the DLC films.

5.1.2 Chemical Interactions

The degree of chemical interactions between sliding DLC surfaces chiefly depends on the chemical nature of the surrounding environment as well as the counterface material. A high degree of interaction may adversely influence the friction and wear

properties. In hydrogen-free DLC films, certain chemical interactions may be beneficial and, in fact, key to achieving low friction; but for highly hydrogenated DLC films, strong chemical interaction is not needed and could cause high friction under certain conditions.

The most important cause of adhesive interactions in DLC films is covalent bonding, which may readily occur between the unoccupied or dangling σ-bonds of carbon atoms at sliding interfaces. In a UHV test condition, friction coefficients of 0.6–1 have been reported for diamond and hydrogen-free DLC films and are attributed largely to strong σ-bond interactions between surface carbon atoms [44–46,61,62]. Obviously, when tests are run in UHV, the surface adsorbates that normally pacify those strong σ-bonds are absent. Therefore, covalent bonding can easily take place between sliding diamond and/or DLC surfaces and gives rise to the high friction coefficients in UHV.

The other sources of adhesive interactions in DLC films are due to relatively weaker π-π* interactions and van der Waals forces. Since, during most sliding contacts, the DLC surfaces may undergo structural transformations and become somewhat graphitic, adhesive forces resulting from π-π* interactions become a possibility. Graphitization of sliding DLC surfaces at nano- to microscales is known to provide reasonably low friction coefficients, especially in humid test environments. However, in vacuum or dry test environments, these graphitized surfaces do not achieve low friction (since graphite is more lubricious in humid environments). In addition to σ-bond and π–π* interactions, van der Waals forces, capillary forces, and electrostatic attractions may be present at sliding DLC surfaces, and these can also influence their friction and wear. These forces are relatively weak and become more important under light loads and nanoscale contact situations as in MEMS.

5.1.3 Tribochemical Interactions

Most DLC films are chemically inert. They do not normally react with other chemical species in their surroundings. However, during sliding contacts, this situation changes, and DLC films become active chemically and react with the gaseous, liquid, or solid chemical species in their surroundings. The extent and nature of chemical interactions vary from one type of DLC film to another; as a consequence, their friction and wear coefficients also vary a great deal [42–44]. Among the many gaseous species, hydrogen has a very beneficial effect on the friction and wear behavior of hydrogen-free or hydrogen-poor DLC films. These films attain friction coefficients of less than 0.01 in inert gases or vacuum when hydrogen gas is supplied to their sliding surfaces from an external source [21,22,62,63]. Apparently, under the influence of dynamic sliding, hydrogen molecules dissociate into hydrogen atoms, then react with the surface carbon atoms of these DLC films and effectively passivate those dangling σ-bonds that otherwise cause high friction. As a result, the friction coefficients of these surfaces become very low. Highly hydrogenated DLC films do not need hydrogen for lubricity,

which is part of their compositions; hence, when and if needed, it is always available.

Regarding gaseous species like oxygen, water, and other reactive molecules, their presence in test chambers seems to be beneficial for hydrogen-free DLC films, but detrimental to the frictional behavior of highly hydrogenated DLC films. For example, upon introduction of water molecules in vacuum and/or inert gases, hydrogen-free DLC films enjoy up to 90% reductions in their friction coefficients, while the friction coefficients of highly hydrogenated DLC increase by factors of 8–10 [21,39,44–46]. Such a dramatic effect of environmental species on friction is primarily attributed to strong physical and chemical interactions that are triggered by dynamic sliding. Specifically, it is proposed that surface carbon atoms (especially those with dangling σ-bonds) react with hydrogen, oxygen, and/or water molecules and form a chemically bonded surface layer. These layers may be removed by mechanical wear, but they can re-form quickly and continue to affect the frictional behavior of these films. Recent systematic studies by Heimberg et al. [63] and Dickrell et al. [64] confirmed that the formation of such films is rapid due to the strong gas–surface interactions. In addition to chemical effects, under high humidity conditions, condensed water molecules can give rise to capillary forces, which can also increase friction.

When DLC films are tested in a liquid medium (such as water, oil, or fuel), the friction and wear may be controlled by the physical (such as viscosity) and chemical nature (such as polarity, chemical affinity, molecular size, and boundary film-forming tendency) of the liquid. If a low-shear tribochemical reaction product or boundary film is formed on the sliding surfaces, then low friction coefficients can be obtained in liquid media as well.

In the past, researchers have demonstrated that tribochemical interactions between sliding surfaces of tungsten-containing DLC films and the sulfur-bearing additives in oils have led to the formation of low-friction tribofilms (such as WS_x) [65]. Likewise, hydrogen-free DLC films were shown to attain superlow friction under lubricated sliding conditions if the base oil lubricant contains glycerol mono-oleate (GMO) as an additive [25,66]. It is thought that some H- and HO-containing radicals in GMO react preferentially with the surface carbon atoms of the hydrogen-free DLC films and eventually form monolayers of strongly bonded end groups on the sliding surfaces, which, in turn, prevent σ-bond interactions that can otherwise cause high friction in these hydrogen-free DLC films.

5.1.4 Thermal Effects

DLC films represent a structurally amorphous and thermodynamically metastable class of materials. As a result, when excited thermally, the DLC atoms will try to rearrange themselves and assume a more ordered and thermodynamically more stable bonding configuration. Graphite is one of the most stable forms of carbon. Under the influence of frictional or ambient heating, the sliding surfaces of amorphous DLC films may transform to a graphitic state [67,68]. Films with a high

degree of sp^3 bonding are known to be more resistant to graphitization than those with lower fractions of sp^3 bonding and higher fractions of hydrogen content. In the case of highly hydrogenated DLC films, upon heating, some hydrogen atoms (especially the ones that are not bonded to carbon) begin to diffuse out and leave a relatively porous and weak structure behind. Carbon atoms may also start rearranging and forming thermodynamically more stable structural configurations. As a result of such changes in chemical and structural morphology, DLC films lose their lubricity and wear resistance. Accordingly, DLC films are not meant for applications that involve very high temperatures. Intermittent or short exposures to elevated temperatures may be tolerable, but continuous and/or longer duration exposures should not be the case.

5.1.5 Third-body or Transfer Layers

When DLC films are rubbed against an uncoated counterface (regardless of the type of material), most often, a third body or transfer layer builds up [18,19,22,27, 48–50]. The formation of such layers on a counterface surface usually has a beneficial effect on the friction and wear behavior of these films as was shown in Fig. 5. Chemically, these layers consist mainly of carbon, but they can also contain oxygen, hydrogen, and the main ingredients of the counterface material [27]. The kinetics of transfer film formation on counterface materials are rather complex and have a lot to do with the test environment and/or conditions, as well as the chemical nature of the counterface surface. For example, transfer films form faster on chemically clean surfaces of steel pins than those that are covered by an oxide layer [69]. Oxide-based ceramics such as alumina, zirconia, etc. have much poorer tendency to form transfer layers on their sliding surfaces than their metallic forms.

Ambient temperature may also play a role in their formation kinetics. At elevated temperatures, transfer films tend to form faster and shorten the time required for reaching the low friction steady-state regime. The loading condition may also play a role in the formation of transfer films. Under heavier loads, transfer films form faster and over the entire contact spot of the pin or ball counterfaces.

For DLC films tested in UHV, Donnet et al. determined that the formation of a continuous carbon-rich transfer film on sliding pin surfaces was extremely important for achieving ultralow friction [55,69]. When sliding tests were performed under increasing partial pressures of water vapor, the transfer layers formed on the pin side became much thinner (as detected by Auger electron spectroscopy), and this condition led to significant increases in friction. Donnet et al. concluded that the kinetics of transfer film formation is closely related to the type of counterface material and test environment and conditions. Recent systematic studies by Scharf and Singer further confirmed that the formation and periodic loss of transfer films from sliding sapphire ball surfaces are the main causes of fluctuations in the friction behavior of DLC coatings [70].

After the formation of a transfer film on a counterface surface, the sliding essentially takes place between the original and transferred films. As mentioned above,

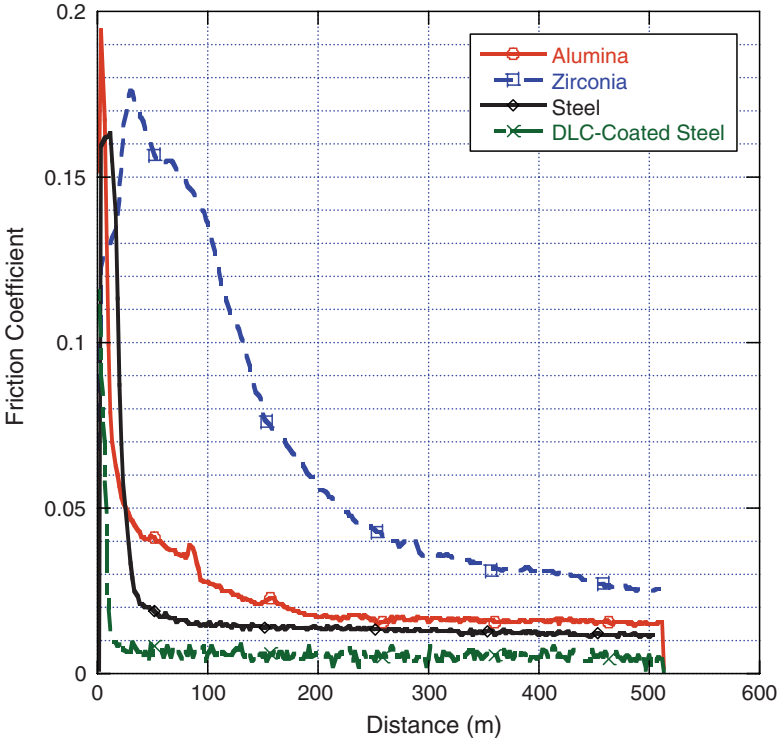

Fig. 5 Friction coefficient of a highly optimized hydrogenated DLC film against various counterface materials. Note that the lowest friction is achieved when sliding against the DLC-coated ball counterface. Relatively higher friction coefficients of ceramic balls (especially during the initial running-in period) may have been due to their inability to form a continuous transfer film on their rubbing surfaces. (Test conditions: load, 10 N; speed, 0.5 m/s; temperature, 22–23°C; test environment, dry N_2)

the structural chemistry of transferred films could be very different from that of the original film. In this respect, the term "tribofilm" seems more appropriate than "transfer film," since it forms under the influence of tribological rubbing action. Several authors have reported the friction-induced conversion of sp^3 to sp^2 sites and even "graphitization" [18,19,22,27,48–50] of the amorphous structure, as observed on the wear debris by electron energy loss spectroscopy and also on the transfer layer by Raman spectroscopy. Again, these tribochemical phenomena are strongly dependent on the nature of the environment surrounding the contact zone, mainly the pressure of oxygen and/or water vapor. In the case of a-C:H films, hydrogen may also be released from the film during friction [71]. Overall, these friction-induced structural and chemical modifications of the amorphous network of DLC have a strong influence on its tribological behavior.

5.1.6 Viscoplasticity and Mechanical Effects

We previously mentioned that a sufficient amount of hydrogen in the film is needed to achieve superlow friction. Since hydrogen is a monovalent atom, increasing its content will undoubtedly reduce the proportion of C–C bonds and, thus, decrease the degree of cross-linking within the amorphous carbon network. We can thus suppose that superlow friction in DLC films is somewhat related to the degree of such cross-linking. However, the amount of hydrogen required for reduced cross-linking will depend strongly on the deposition process and/or condition. Indeed, the structure of amorphous hydrogenated carbon films is more complex since they have a substantial amount of unbounded hydrogen [72] and aromatic clusters [73]. Differences in deposition techniques, precursors, and plasma conditions will obviously lead to considerable variations from the theoretical random covalent network model [74]. Thus, the cross-linking of the films cannot be deduced from the hydrogen content alone, except maybe for comparison between samples obtained with the same process. Mechanical properties appear then as an indirect means to evaluate the degree of cross-linking. Indeed, at high hydrogen contents, a-C:H coatings can be viscoplastic, i.e., their hardness increases with increasing strain rate [57]. This effect can be quantified by fitting the data from nanoindentation tests with the Norton-Hoff equation: $H = H_0 \cdot \dot{\varepsilon}^x$, where H is the hardness, H_0 a constant, $\dot{\varepsilon}$ the strain rate, and x the viscoplastic exponent [57]. The viscoplastic nature of these materials implies that the random carbon network could relax, probably through "free volumes," as happens in some polymers.

A good correlation has recently been demonstrated between the stabilized friction coefficient of DLC films in vacuum and the viscoplastic exponent x [57]. Indeed, all DLC films exhibiting very small values for the viscoplastic exponent – and that can thus be considered as plastic films – systematically exhibit high values of steady-state friction coefficients. In contrast, all the films with large values of the viscoplastic exponent exhibit superlow friction values. Since viscoplasticity is controlled by network relaxation, allowed by the presence of free volumes in the material, we can assume that the surfaces of a-C:H coatings and/or the transfer film are able to relax much easier and faster, permitting weaker interactions between asperities on the sliding surfaces. The control of these properties can thus be achieved either from the properties of the a-C:H film itself or through tribochemical reactions with the environment, as described in the previous sections.

5.2 Mechanistic Model for the Superlubricity of DLC Films

As is clear from the foregoing, the frictional behavior of DLC films is controlled by numerous extrinsic (test condition specific) and intrinsic (film specific) factors. Adhesive or chemical interactions play the greatest roles, provided the sliding

surfaces are extremely smooth and the effects of environmental species are minimal. Based on the results of many extensive studies we conducted in the past, we propose the following mechanistic model for the superlubricious nature of certain hydrogenated DLC films described in this chapter.

The carbon atoms that make up the bulk of DLC films have a very high affinity towards hydrogen and bond to it very strongly and hence become chemically very passive, since the unoccupied or free σ-bonds are totally satisfied. Passivation by other species in the test environment, such as oxygen, water molecules, and hydroxyl ions, is also possible, but the carbon atoms are already tied up to hydrogen during deposition; thus, there are no dangling or free σ-bonds left for occupation by these species. Once all the carbon atoms are passivated, such surfaces become chemically inert, causing very little adhesive interactions with counterface materials during sliding and yielding the superlow friction shown in Fig. 6 [27]. Because C–H bonding is covalent and extremely strong (stronger than C–C bonds), bonded hydrogen is difficult to remove from the carbon surface. In addition to bonded hydrogen, some free hydrogen may also be present within the DLC structures as interstitials. Free hydrogen within the films serves as a reservoir and can replenish or replace those hydrogen atoms that may be lost or removed from the surface by thermal heating and/or mechanical action during sliding.

When DLC films are prepared in highly hydrogenated gas discharge plasmas, some of the carbon atoms (at least those on the surface) could be dihydrated, that is, two hydrogen atoms become bonded to each carbon atom on the surface. This bonding can occur on the unreconstructed (100) surfaces of diamond structures under some special or supercritical conditions. It may also occur under the energetic

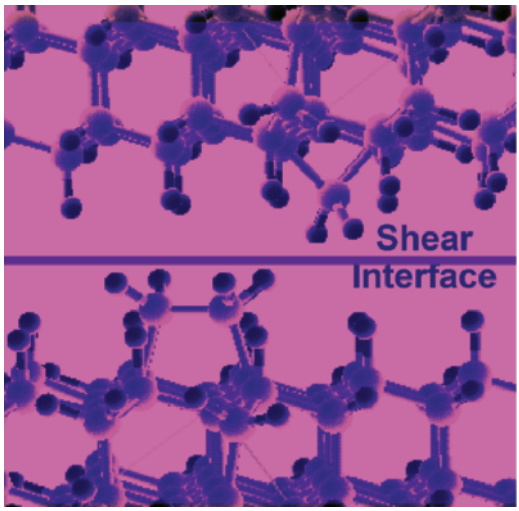

Fig. 6 An atomic scale representation of the sliding interfaces of highly hydrogenated DLC films. Note that all the carbon atoms at the shear interface are terminated by hydrogen

hydrogen bombardment in a highly hydrogenated gas discharge plasma consisting of ten hydrogen atoms per carbon atom. The existence of dihydrated carbon atoms on the surface will further increase the hydrogen density on the surface and will thus provide better shielding or passivation of carbon atoms. As a result, such DLC surfaces exhibit superlow friction. Such a friction model is presented in Fig. 6 for a partially dihydrated sliding DLC surface [27].

One more reason why these DLC films provide superlow friction is that, when the free electrons of hydrogen atoms pair with the dangling σ-bonds of surface carbon atoms, the electrical charge density is permanently shifted to the other side of the nucleus of the hydrogen atom and away from the surface. Such a shift in charge density allows the positively charged hydrogen proton in its nucleus to be closer to the surface than the electron, which is used up by the dangling σ-bond of a surface carbon atom. Therefore, the creation of such a dipole configuration at the sliding interface should give rise to repulsion rather than attraction between the hydrogen-terminated sliding surfaces of the DLC films.

6 Conclusion

Superlubricity is a fascinating and important subject in tribology. Achieving superlubricity in bulk materials or thin films is very challenging and requires numerous factors to be controlled and/or manipulated. As emphasized in the present chapter, it requires a close linkage between theoretical and experimental approaches in material science and tribology.

In DLC films, superlubric sliding regimes are only feasible with certain types and under some restrictive test and environmental conditions. Unlike other materials whose superlubricity has so far been demonstrated at nanoscales, DLC films are able to exhibit superlubricity in macroscopic scales and under industrially relevant test conditions. Their superlubricity under multi-asperity contact situations may not solely be explained on the basis of simple molecular interactions; close control of a number of intrinsic and extrinsic factors (surface chemistry and rheology, atomic-scale interactions at sliding interfaces, the chemistry and temperature of test environments, etc.) are extremely important and play major roles in their friction and wear behaviors. Specifically, by controlling or effectively eliminating the intrinsic and extrinsic sources of friction in DLC films, one should be able to achieve superlow friction coefficients.

We have highlighted the difficulty of measuring such extremely low coefficients of friction, especially inside a vacuum chamber of a macroscopic tribometer. The tribofilm buildup and the weak intermolecular interactions between flexible hydrocarbon chains are paramount factors to observe superlow friction. We have also discussed the various experimental factors influencing the previous key conditions to reach superlow friction, including the initial surface chemistry of contacting bodies, the composition and viscoplasticity of the DLC film, and the presence or absence of certain gaseous species during the friction process. Some of these factors

are also paramount to control the duration of the superlow friction level. At the present stage of investigations, the combination of factors responsible for superlow friction is far from the usual conditions of most contacts found in broader tribological technologies. Moreover, some of these factors may disappear during the sliding process; hence, the conditions that lead to superlubricity may change over the time, and thus, keeping a DCL film superlubricious indefinitely may be a difficult proposition.

From a practical point of view, research on superlubricity may lead to significant improvements in the performance, efficiency, and durability of mechanical devices lubricated with thin solid films. Indeed, most commercial solid lubricants exhibit friction coefficients in the range 0.1–0.3. Thus, the research activities on superlow friction with DLC films further motivate both theoretical and experimental investigations, which in the end may lead to a better understanding of the origins of friction, in general, and superlubricity, in particular. Such an understanding will undoubtedly benefit work on the design and production of novel bulk materials and thin solid films (like DLC) that can consistently provide friction coefficients in the 0.01–0.001 range.

References

1. M. Hirano and K. Shinjo, Wear, 168 (1993) 121.
2. J. B. Sokoloff, PRB, 42 (1990) 760.
3. M. Hirano, K. Shinjo, R. Kaneko, and Y. Murata, PRL,. 67 (1991) 2642.
4. K. Miura, D. Tsuda, and N. Sasaki, J. Surf. Sci. Nanotechnol., 3 (2005) 21.
5. M. Dienwiebel, G. S. Verhoeven, N. Pradeep, J. W. M. Frenken, J. A. Heimberg, and H. W. Zandbergen, PRL, 92 (2004) 126101.
6. A. Erdemir, O. L. Eryilmaz, and G. Fenske, J. Vac. Sci. Technol., A18 (2000) 1987.
7. C. Donnet, J. Fontaine, A. Grill, and T. Le Mogne, Trib. Lett., 9 (2000) 137.
8. A. Erdemir and C. Donnet, Tribology of diamond, diamond-like carbon and related films, in B. Bhushan (ed.) Handbook of Modern Tribology, CRC Press, Boca Raton, FL, 2001, pp. 871–899.
9. C. Donnet and A. Grill, Surf. Coat. Technol., 94–95 (1997) 456.
10. J. M. Martin, C. Donnet, Th. Le Mogne, and Th. Epicier, Phys. Rev. B, 48 (1993) 10583–10586.
11. A. Socoliuc, R. Bennewitz, E. Gnecco, and E. Meyer, Phys. Rev. Lett., 92 (2004) 134301.
12. J. M. Martin, H. Pascal, C. Donnet, Th. Le Mogne, J. L. Loubet, and Th. Epicier, Surf. Coat. Technol., 68 (1994) 427.
13. M. Goto and F. Honda, Wear, 256 (2004) 1062–1071.
14. C. M. Mate, G. M. McClelland, R. Erlandsson, and S. Chiang, PRL, 59 (1987) 1942.
15. M. Dienwiebel, E. de Kuyper, L. Crama, J. W. M. Frenken, J. A. Heimberg, D. -J. Spaanderman, D. Glastra van Loon, T. Zijlstra, and E. van der Drift, Rev. Sci. Inst., 76 (2005) 043704.
16. K. Miura S. Kamiya, and N. Sasaki, PRL, 90 (2003) 055509.
17. K. Kato, N. Umehara, and K. Adachi, Wear, 254 (2003) 1062.
18. J. Fontaine, C. Donnet, A. Grill, and T. LeMogne, Surf. Coat. Technol., 146 (2001) 286.
19. J. Fontaine, M. Belin, T. Le Mogne, and A. Grill, Tribol. Int., 37 (2004) 869.
20. A. Erdemir, O. L. Erylmaz, I. B. Nilufer, and G. R. Fenske, Surf. Coat. Technol., 133–134 (2000) 448.

21. A. Erdemir, Surf. Coat. Technol., 146 (2001) 292.
22. C. Donnet, T. Le Mogne, L. Ponsonnet, M. Belin, A. Grill, V. Patel, and C. Jahnes, Tribol. Lett., 4 (1998) 259.
23. A. Erdemir, Mat. Res. Soc. Symp. Proc., 697 (2002) 391.
24. A. Erdemir, O. L. Eryilmaz, I. B. Nilufer, and G. R. Fenske, Diam. Relat. Mater., 9 (2000) 632.
25. M. Kano, Y. Yasuda, Y. Okamoto, Y. Mabuchi, T. Hamada, T. Ueno, J. Ye, S. Konishi, S. Takeshima, J. M. Martin, M. I. D. Bouchet, and T. Le Mogne, Tribol. Lett., 18 (2005) 245.
26. A. Erdemir, C. Bindal, G. R. Fenske, and P. Wilbur, Tribol. Trans., 39 (1996) 735.
27. J. C. Sanchez-Lopez, A. Erdemir, C. Donnet, and T. C. Rojas, Surf. Coat. Technol., 163–164 (2003) 444.
28. T. W. Scharf and I. L. Singer, Tribol. Trans., 45 (2002) 363.
29. J. Robertson, Mat. Sci. Eng., 37 (2002) 129.
30. A. Erdemir and C. Donnet, J. Phys. D: Appl. Phys., 39 (2006) R311–327.
31. H. Schmellenmeier, Experimentelle Technik der Physik, 1 (1953) 49.
32. C. Strondl, G. J. van der Kolk, T. Hurkmans, W. Fleischer, T. Trinh, N. M. Carvalho, and J. T. M. de Hosson, Surf. Coat. Technol., 142 (2001) 707.
33. P. E. Hovsepian, Y. N. Kok, A. P. Ehiasarian, A. Erdemir, J. G. Wen, and I. Petrov, Thin Solid Films, 447 (2004) 7.
34. J. P. Sullivan, T. A. Friedmann, and K. Hjort, MRS Bull., 26 (2001) 309.
35. C. Donnet, Surf. Coat. Technol., 100/101 (1998) 180.
36. A. K. Gangopadhyay, P. A. Willermet, M. A. Tamor, and W. C. Vassel, Tribol. Int., 30 (1997) 9.
37. D. M. Cao, B. Feng, W. J. Meng, L. E. Rehn, P. M. Baldo, and M. M. Khonsari. Appl. Phys. Lett., 79 (2001) 329.
38. A. C. Ferrari and J. Robertson, Phys. Rev. B., 61 (2000) 14095.
39. C. Su and J. C. Lin, Surf. Sci. 406 (1998) 149.
40. A. Erdemir, J. Eng. Tribol., 216 (2002) 387.
41. A. Erdemir, Tribol. Int., 37 (2004) 1005.
42. C. Donnet and A. Grill, Surf. Coat. Technol., 94–95 (1997) 456.
43. A. Grill, Surf. Coat. Technol. 94 (1997) 507.
44. J. Andersson, R. A. Erck, and A. Erdemir, Surf. Coat. Technol. 163 (2003) 535.
45. H. I. Kim, J. R. Lince, O. L. Eryilmaz, and A. Erdemir, Trib. Lett., 21 (2006) 53–58.
46. J. Andersson, R. A. Erck, and A. Erdemir, 2003, Wear, 254 (2003) 1070.
47. A. Erdemir, Solid lubricants and self-lubricating films, in B. Bhushan (ed.) Handbook of Modern Tribology, CRC Press, Boca Raton, FL., 2001, pp. 787–818.
48. A. Erdemir, C. Bindal, J. Pagan, and P. Wilbur, Surf. Coat. Technol., 76–77 (1995) 559.
49. Y. Liu, A. Erdemir, and E. I. Meletis, Surf. Coat. Technol., 82 (1996) 48.
50. Y. Liu and E. I Meletis, J. Mat. Sci., 32 (2004) 3491.
51. F. Qian, V. Craciun, R. K. Singh, S. D. Dutta, and P. P. Pronko, J. Appl. Phys., 86 (1999) 2281.
52. F. Garrelie, A. S. Loir, C. Donnet, F. Rogemond, R. Le Harzic, M. Belin, E. Audouard, and P. Laporte, Surf. Coat. Tech. 163–164 (2003) 306.
53. T. Le Mogne, J. M. Martin, and C. Grossiord, in: Lubrication at the frontier, D. Dowson et al. (eds), Elsevier, Amsterdam, The Netherlands., 1999, pp. 413–421.
54. S. Miyake, S. Takahashi, I. Watanabe, and H. Yoshihara, ASLE Trans., 30(1) (1987) 21.
55. C. Donnet, M. Belin, J. C. Augé, J. M. Martin, A. Grill, and V. Patel, Surf. Coat. Technol., 68/69 (1994) 626.
56. I. Sugimoto and S. Miyake, Appl. Phys. Lett. 56(19) (1990) 1868.
57. J. Fontaine, J. L. Loubet, T. Le Mogne, and A. Grill, Tribol. Lett. 17(4) (2004) 709.
58. C. A. Freyman, Y. Chen, and Y. W. Chung, Surf. Coat. Technol., 201 (2006) 164.
59. J. C. Sánchez-López, M. Belin, C. Donnet, C. Quiros, and E. Elizalde, Surf. Coat. Technol., 160 (2002) 138.
60. B. K. Gupta, A. Malshe, B. Bhushan, and V. V. Subramaniam, J. Tribol., 116 (1994) 445.
61. S. Chandrasekar and B. Bhushan, Wear, 153 (1992) 79.
62. K. Miyoshi, R. L. C. Wu, A. Garscadden, P. N. Barnes, and H. E. Jackson, J. Appl. Phys., 74 (1993) 4446.

63. J. A. Heimberg, K. J. Wahl, I. L. Singer, and A. Erdemir, Appl. Phys. Lett., 78 (2001) 2449.
64. P. L. Dickrell, W. G. Sawyer, J. A. Heimberg, I. L. Singer, K. J. Wahl, and A. Erdemir, J. Tribol., 127 (2005) 82.
65. B. Podgornik, D. Hren, and J. Vizintin, Thin Solid Films, 476 (2005) 92–100.
66. M. I. de Barros-Bouchet, J. M. Martin, T. Le-Mogne, and B. Vacher, Tribol. Int., 38 (2005) 257.
67. A. Erdemir and G. R. Fenske, Tribol. Trans., 39 (1996) 787.
68. R Kalish, Y Lifshitz, K Nugent, and S Prawer, Appl. Phys. Lett., 74 (1999) 2936.
69. J. Fontaine, T. Le Mogne, J. L. Loubet, and M. Belin, Thin Solid Films, 482 (2005) 99.
70. T. W. Scharf and I. L. Singer, Tribol. Trans., 45 (2002) 363.
71. B. Racine, M. Benlahsen, K. Zellama, M. Zarrabian, J. P. Villain, G. Turban, and A. Grosman, Appl. Phys. Lett., 75(22) (1999) 3479.
72. C. Donnet, J. Fontaine, F. Lefebvre, A. Grill, V. Patel, and C. Jahnes, J. Appl. Phys., 85(6) (1999) 3264.
73. M. A. Tamor and W. C. Vassel, J. Appl. Phys., 76 (1994) 3823.
74. J. C. Angus, Y. Wang, in: Diamond and Diamond-Like Films and Coatings, R.E. Clausing (ed.), Plenum Press, New York, 1991, p. 173.

Hard DLC Growth and Inclusion in Nanostructured Wear-protective Coatings

A. A. Voevodin

Abstract Wear-resistant coatings using hard hydrogen-free and tetrahedral bonded ta-DLC offer a unique combination of high hardness, low friction, and extremely low wear rates. The related coating deposition techniques of such wear-protective coatings are reviewed, including filtered vacuum arc and pulsed laser deposition (PLD), where process parameters and plasma characteristics are correlated to ta-DLC bonding and mechanical characteristics. Advancements in hybrid plasma-deposition methods and process-control arrangements allow production of hard ta-DLC with high adhesion and fracture resistance through the development of graded and multilayer coating architectures. Further enhancement came with nanocrystalline carbide/amorphous DLC compositions, where high toughness is achieved by using grain boundary sliding for strain accommodation without brittle fracture. Multiple crystalline/amorphous interfaces help to divert and split nanocracks, avoiding coating macro-cracking even when relatively softer substrates experience a high degree of deformations. Since ta-DLC is exceptionally good in ambient conditions, adaptive "chameleon" composites were developed to use this tribological benefit of ta-DLC, while introducing additional solid lubricant phases for other environments and/or protecting DLC material from degradation in extreme environments, including dry air or inert gas, high vacuum, and elevated temperatures in air. DLC is an important part of today's tribological coating applications, where a high wear resistance and the absence of lubricating fluids are critical, e.g., aerospace, dry machining, and MEMS. The coatings with hard DLC phases can provide friction reduction and wear-life extension without the need of lubrication systems, reducing mechanism complexity, costs, weight, and environmental impact.

Keywords diamond-like carbon, hydrogen-free, hard, tribology, multilayer, composite, coating, pulsed laser deposition, vacuum arc deposition

Materials and Manufacturing Directorate, Air Force Research Laboratory, Wright-Patterson Air Force Base, Ohio, USA

C. Donnet and A. Erdemir (eds.), *Tribology of Diamond-Like Carbon Films: Fundamentals and Applications*.

1 Introduction

This chapter discusses wear-resistant coatings which have hard diamond-like carbon (DLC) as one of their main components. In general, carbon films with high values of density, hardness, electrical resistivity, chemical inertness, IR transparency, and the lack of detectable long-range structural order are typically defined as DLC materials. The unique combination of properties of DLC films with a special focus on tribological and wear-protective applications are discussed in a number of reviews [1–6]. These properties critically depend on a ratio of sp^3 and sp^2 electron hybridization of carbon atoms in DLC amorphous structure. In addition, a large group of DLC materials involves hydrogenated carbon structures, produced from hydrocarbon gas precursors. Together, the variation of sp^3/sp^2 ratio and hydrogen content produce a large spread in obtained DLC structures and properties, which were classified by Robertson [1] on a ternary (sp^3, sp^2, H content) diagram. This classification can be found in Chapter 1, and Chapters 5 and 6 are specifically devoted to the hydrogenated DLC materials. The hardest and closest to diamond is a hydrogen-free DLC with approaching 100% of sp^3-type tetragonal coordinated bonding. These are known as ta-DLC and typically produced by physical vapor deposition methods from solid graphite targets in the absence of hydrogen. This chapter discusses various types of wear-protective coatings containing hard hydrogen-free ta-DLC for applications in sliding and rolling contacts. These hard wear-resistant DLC materials are highly inert and typically posses a considerable compressive stress. Different approaches for adhesion and stress management of ta-DLC wear-protective coatings are reviewed, including functionally gradient, multilayered, and nanocomposite architectures.

2 Conditions for Preparation of Hard Wear-resistant ta-DLC Coatings

Successful ta-DLC deposition processes have two distinctive features. First, films are deposited at a relatively low substrate temperature (25–100°C). Second, the deposition process characteristically involves high-energy carbon ions, atoms, or clusters, which have arrival energies of at least 50–70 eV. These two conditions, when the energy of arriving atoms is sufficient to initiate strong sp^3 interatomic bonds and when adatom mobility is reduced due to a low substrate temperature, result in the formation of amorphous ta-DLC. There is also an upper limit for the energy of deposited carbon atoms at about 150 eV, above which the intensification of displacement damage and surface heating begin interfering with ta-DLC growth. This establishes a fairly narrow energy window for ta-DLC production with an optimum at about 100 eV, as it was experimentally and theoretically confirmed [1,7]. The energy ranges of deposited carbon atoms in the most commonly used processes of DLC growth are shown in Fig. 1

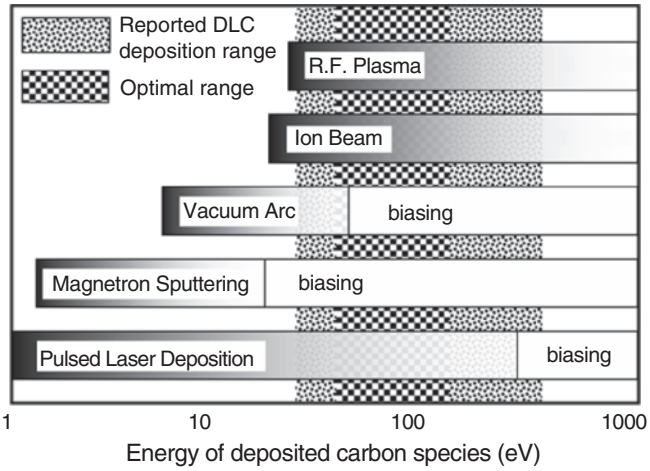

Fig. 1 Comparison of energy ranges of carbon species in DLC growth using selected physical vapor deposition techniques. Energy regions corresponding to DLC formation are shown [6]

together with the energy ranges which are typically reported for hard ta-DLC production [6].

Data presented in Fig. 1 are from different physical vapor deposition techniques. Each of them allows varying degrees of regulation of the deposition energy ranging from several to several hundred electron volts. Out of these deposition process, the filtered cathodic vacuum arc (FCVA) and pulsed laser deposition (PLD) are leading in terms of producing films with a highest sp^3 ratio, density, and hardness as summarized in Table 1. Both these processes are characterized by the presence of highly energetic and dense carbon ion fluxes in the produced plasma, which is a key for the production of ta-DLC as it was mentioned earlier.

A typical schematic for PLD growth is shown in Fig. 2a, where an excimer laser was used to produce 25 ns, 248 nm laser beam pulses of 900 mJ energy at 10 Hz. The beam was focused to the pulse energy density of 7 J/cm^2 and randomly scanned across a graphite target. The substrate holder was located above the target surface and rotated, which permitted uniform deposition simultaneously on multiple substrates. About 10 nm/min growth rate was realized with such arrangements. A detailed review of PLD processes for DLC growth can be found in Ref. [6]. Scaled-up PLD arrangements may include multiple lasers and laser beam scanning along cylindrical graphite targets for large area growth [8,9]. In FCVA growth (Fig. 2b), a filtered cathodic arc assembly is typically attached to the vacuum chamber to deliver carbon ions filtered of neutral atoms, clusters, and macroscopic particulates. One widely used design is a 90° bend filter, following the original work by Aksenov et al. [10,11]. In this design, a graphite cathode is evaporated with about 100–130 A arc direct current, generating a carbon plasma. Carbon ions are guided by an electromagnetic field to the substrate location through a 90° turn, while droplet emission from arc spots is prevented from reaching the substrate. The design and operation of possible FCVA sources are

Table 1 Some properties of natural diamond and selected DLC films [6]

Material	Preparation technique	Density, (gm/cm^{-3})	% sp^3	Hardness, (GPa)	Young's modulus, (GPa)	Friction coefficient against metals*	References
Diamond	Naturally occuring	3.52	100	100	1,050	0.02–0.10	20–22
DLC	Sputtering	1.9–2.4	2–5	11–24	140	0.20–1.20	23–26
Me doped H:DLC	Reactive sputtering	–	–	10–20	100–200	0.10–0.20	27–30
H:DLC	r.f plasma	1.57–1.69	–	16–40	145	0.02–0.47	16–18,31–33
H:DLC, DLC	Ion beam	1.8–3.5	–	32–75	–	0.06–0.19	41–44
ta-DLC	Vacuum arc	2.8–3.0	85–95	40–100	500	0.04–0.14	34–40
ta-DLC	PLD	2.4	70–95	30–60	200–500	0.03–0.12	15,45–50

*The variation of friction coefficient is due to it strong dependence on test environments.

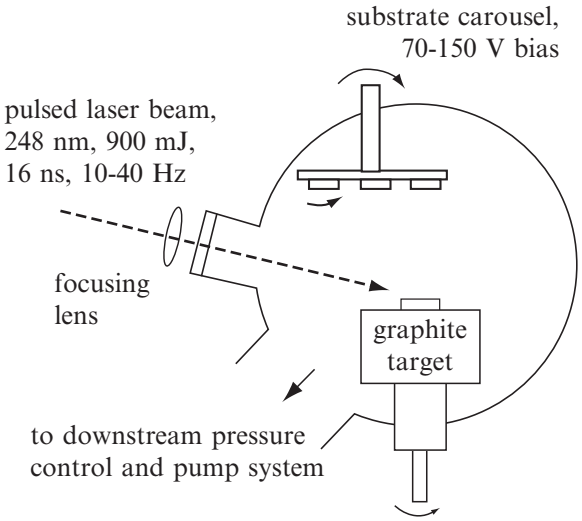

Fig. 2a Schematics of (a) pulsed laser deposition and (b) filtered cathodic vacuum arc processes for ta-DLC growth

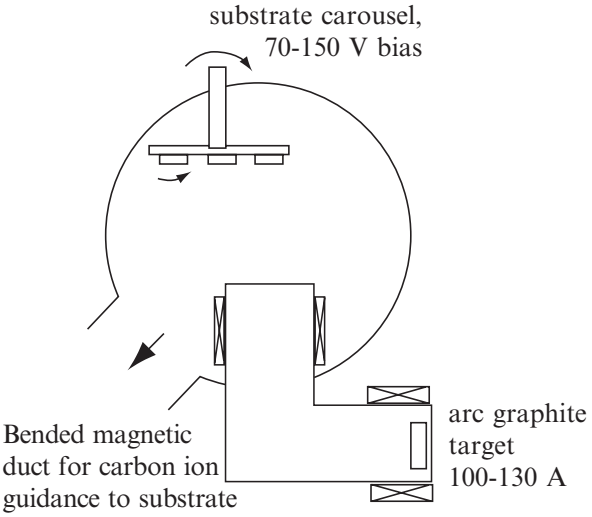

Fig. 2b Schematics of (a) pulsed laser deposition and (b) filtered cathodic vacuum arc processes for ta-DLC growth

discussed in a number of reviews [12–15]. The FCVA sources are easily scaled-up for the large industrial applications of wear-protective coatings [16].

DLC films produced with PLD [6,17] or FCVA [12,15,18–20] have predominantly sp^3 interatomic bonding, hardness of 50–60 GPa, elastic modulus of 400–600 GPa, coefficients of friction (c.o.f.) about 0.05–0.1, and wear rates of about 10^{-9} mm^3/Nm

(several orders of magnitude lower than that of rival ceramics, hard metals, or H: DLC) for un-lubricated sliding against steel counterparts at ambient conditions [1,3,4,8,9,21,22]. This makes them mechanically superior for wear-protective applications, but this typically comes with a price of a large, close to 1 GPa, level of compressive stress stored in such films.

Thermal stress annealing with interrupted growth process is possible [23], which however, can elongate process time for coating large substrates due to the inserted heating and cooling cycles. Other ways of the stress management include DLC doping with metals, where about 10 at. % addition of carbide-forming metals (Ti, W, Ta, Cr, Si, etc.) was found to significantly reduce stress and increase coating reactivity for a promoted adhesion to metal substrates [1,3,24,25]. Such doping, typically leads to a reduction of DLC hardness, since carbide bond forming competes with sp^3 bond forming required for a highest hardness. However, the hardness reduction is well compensated by the improved adhesion and contact toughness of such metal doped DLC coatings. More details on doping and alloying DLC coatings can be found in Chapters 12 and 13.

In production, metal doping is easily achieved in PVD processes by using metal targets in combination with graphite targets. A most efficient way is perhaps hybrid processes combining FCVA or PLD for ta-DLC growth and magnetron sputtering for metal atoms [26,27]. One such process is shown in Fig. 3 with intersection of plasma derived from a laser ablation of graphite and magnetron sputtering of Ti. Other hybrid PVD processes and mixed targets can be also used. Gradient interfaces and multilayer coating structures are discussed next as the means of improving adhesion and managing stress of ta-DLC coatings, while keeping their high hardness.

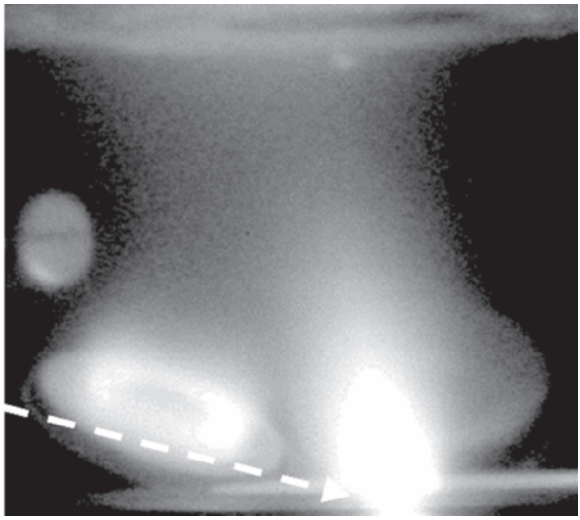

Fig. 3 Photograph of the hybrid magnetron sputtering and pulsed laser ablation process, showing intersection of plasma fluxes from a Ti magnetron (*left*) and graphite laser ablation (*bottom*) on a substrate holder above

3 Functional Gradient and Multilayer Coatings with ta-DLC Coatings

One approach to improve adhesion of hard and highly stressed ta-DLC coatings for wear-protective applications is to use multilayer coating architectures, where DLC layers are separated with metal layers and incorporated in a functionally gradient coating to accommodate stresses and reduce micro-cracking [28–30]. Such coatings have a gradual transition of chemistry, structure, and properties from substrate material to DLC without sharp interfaces, which are potential places for crack initialization. The concept architecture typically includes a deposition of a thin (50–100 nm) metal underlayer, transition to a load supporting carbide layer, then to metal-doped DLC layer, and subsequent transition to multiple pairs of metal/DLC layers [30,31].

Examples of effective gradient compositions are Ti-TiN-TiCN-TiC-H:DLC for hydrogenated DLC [32,33] and Ti-TiC-DLC for hydrogen-free ta-DLC [30]. In the development of the later composition, the importance of graded elastic modulus through the substrate coating/interface was highlighted as shown in Fig. 4.

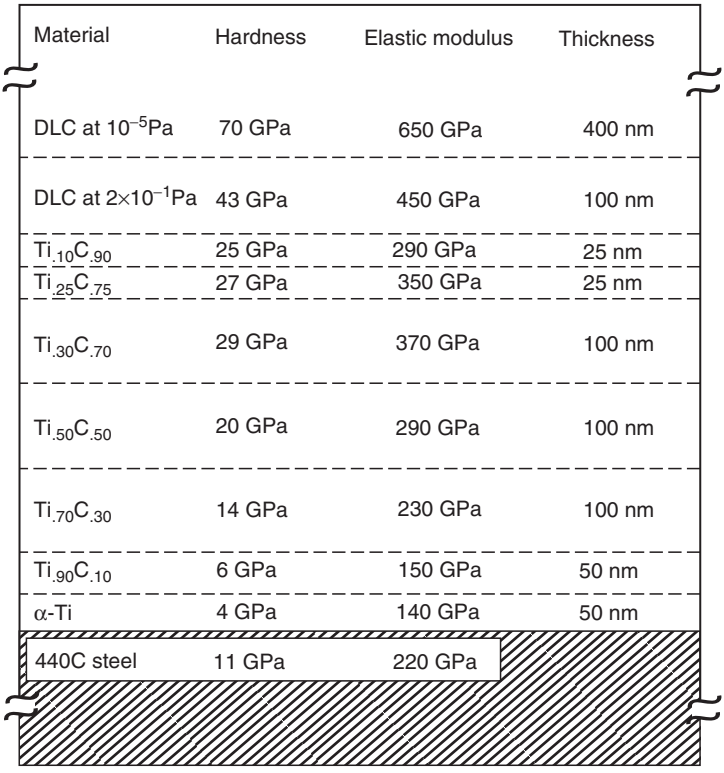

Fig. 4 Design of a functionally gradient Ti-TiC_x-DLC coating, where chemistry and elastic modules are transitioned from metallic substrate to hard DLC top layer [30]

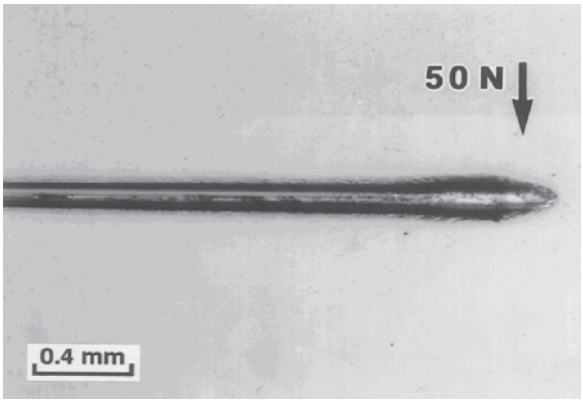

Fig. 5 Scratch produced on the surface of a functionally gradient Ti-TiC$_x$-DLC coating by a diamond stylus under 50 N load. The absence of cracks demonstrates that the coating has excellent toughness [30]

The gradual buildup of material stiffness from the substrate with E = 220 GPa to the DLC layer with E = 650 GPa avoids sharp interfaces that can provide places for crack initiation, good chemical continuity, and creates load support for the hard DLC top-coat. The graded coating shown in Fig. 5 does not exhibit any signs of brittle fracture in scratch tests with a 50 N load, which is at least five times higher than similar coatings without functionally graded interfaces [30]. The graded approach can be combined with multilayer and nanocomposite architectures to further enhance tribological properties.

An effective route for improving toughness in multilayers is the introduction of ductile, low elastic modulus layers into the coating structure to relieve stress and allow crack energy dissipation by plastic deformation in the crack tip. This approach results in a decreased overall coating hardness, but the gain in the fracture toughness improvement is far more important in most of the tribological applications. Figure 6a shows a schematic of a multilayer [Ti/DLC]$_n$ coating on a graded load-support foundation, where the ductile Ti layers in the multilayer stack were graded at every DLC interface to avoid brittle fracture [31]. A cross-sectional photograph of this coating with 20 [Ti/DLC] pairs is shown in Fig. 6b. The ductile Ti layers reduced the composite coating hardness to 20 GPa as compared to a single layer DLC coating, which has a hardness of about 60 GPa. However, due to dramatic improvements in toughness, the multilayer coating design permitted operation during sliding friction at contact pressures as high as 2 GPa without fracture failure compared to 0.6–0.8 GPa for single layer DLC. Figure 7 shows an example of rolling element thrust bearings where races were coated with a multilayer coating shown in Fig. 6. This thrust bearing withstood contact loads in excess of 1 GPa while considerably decreasing friction torque and noise of high-speed rotating mechanisms of aerospace systems.

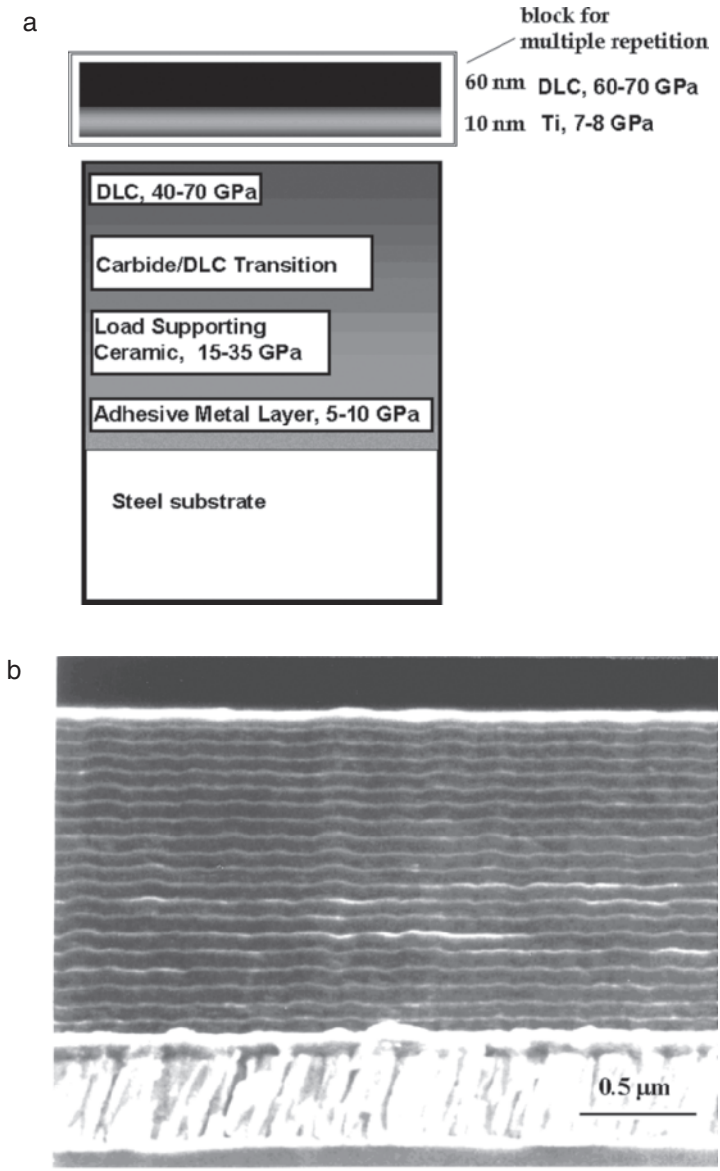

Fig. 6 A multilayer coating with multiple Ti/DLC pairs on top of a functionally gradient layer for an optimum combination of cohesive and adhesive toughness: (a) design schematic; (b) cross-sectional photograph of the coating produced with 20 Ti/DLC pairs [31]

In general, the combination of multilayer and functionally gradient approaches in the design of DLC wear-protective coatings produces exceptionally tough wear-protective coatings for engineering applications. One drawback, slowing the widespread use of new multilayer coatings, was the need for reliable process

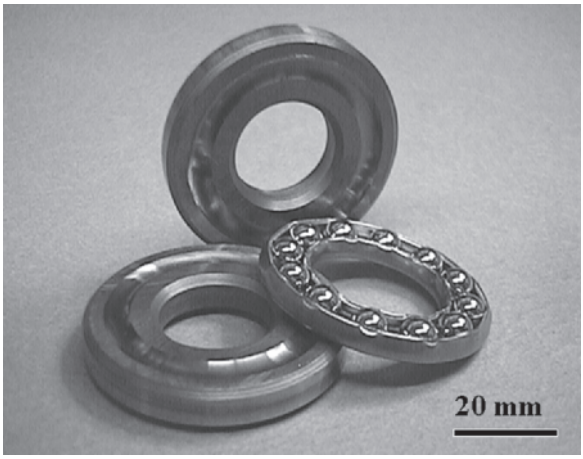

Fig. 7 Thrust rolling element bearings which races were coated with a multilayered Ti/DLC coating shown in Fig. 6 for reduction of torque, noise, and increase of service life

controls to ensure that the correct compositions, structures, and properties are implemented during complex coating architecture growth. However, modern process instrumentation and control technologies are able to meet this challenge and permit successful scale-up and commercialization, for example, see Ref. [34] for a review of reactive sputtering control methods during growth of coatings with DLC layers. Functional gradient and multiplayer designs are now commonly utilized in the production of modern tribological coatings. More examples can be found in Chapters 17, 18, and 19, discussing industrial applications of DLC coatings.

4 Tough Nanocrystalline Carbide/Amorphous DLC Coatings

An alternative to employing multilayers to toughen DLC coatings is embedding grains of nanocrystalline hard phases (such as carbides) into an amorphous ta-DLC matrix. These types of composites contain a high volume of grain boundaries with crystalline/amorphous transitions across grain/matrix interfaces, limiting initial crack sizes and helping to deflect and terminate crack growth. In the course of the development of tough nanocomposite coatings [35–39] several design concepts were formulated, which are applicable to nanocrystalline carbide/amorphous DLC coatings:

1. A graded interface layer is applied between the substrate and crystalline/amorphous composite coating to enhance adhesion strength and relieve interface stresses (combination of functional gradient and nanocomposite design) [30,31].
2. Encapsulation of 3–10 nm sized hard crystalline grains in an amorphous matrix restricts dislocation activity, diverts and arrests macro-crack development, and maintains a high level of hardness similar to superhard coating designs [40,41].

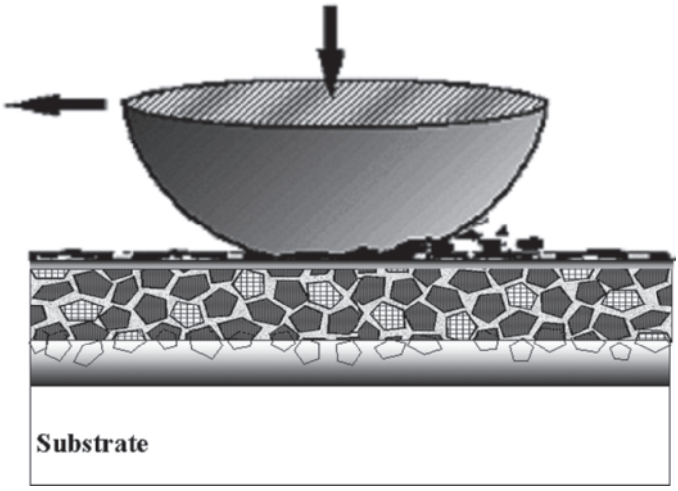

Fig. 8 Schematic of a tough nanocomposite coating, featuring a noncrystalline/amorphous design in the main coating layer for cohesive toughness and a functionally gradient interface layer for adhesive toughness. DLC is used as an amorphous phase in this design together with nanocrystalline carbide phases [52]

3. A large volume fraction of grain boundaries provides ductility through grain boundary sliding and nanocracking along grain/matrix interfaces [36,38,42,43].

Combination of the nanocrystalline/amorphous DLC designs with a functionally graded interface, as shown Fig. 8, provides high cohesive toughness and high interface (adhesive) toughness in a single coating. Several examples of tough wear-resistant composite coatings have been reported, and produced by both PLD and FCVA techniques [36,37,44]. They combined nanocrystalline TiC and WC carbides with an amorphous ta-DLC matrix and designated as TiC/DLC and WC/DLC composites. Figure 9 provides an example of a transmission electron microscopy (TEM) image from a TiC/DLC nanocomposite, where nanocrystalline TiC grains were embedded in amorphous hydrogen-free DLC matrix [35]. This material was obtained by a hybrid deposition process shown in Fig. 3.

The hardness of these coatings was about 32 GPa for TiC/DLC and 27 GPa for WC/DLC with correspondingly high elastic modulus, producing a hardness to modulus ratio of about 0.1 [36,37]. Single-phase materials with such high hardness would typically experience a brittle fracture once the load exceeded their elastic limit. The behavior of the TiC/DLC and WC/DLC composites was contradictory to this expectation. Under high contact loads, both coatings exhibited surface deformations, which visually appear to be plastic (Fig. 10). This plasticity at high contact stress is a result of TiC and WC grain boundary sliding in the DLC matrix. Figure 11 shows a high magnification image taken from a TiC/DLC nanocomposite during in situ TEM tensile strain experiments (A. A. Voevodin, C. D. Smith, I. Robertson, I. Petrov, unpublished, 2003). This image clearly shows a network of nanovoids

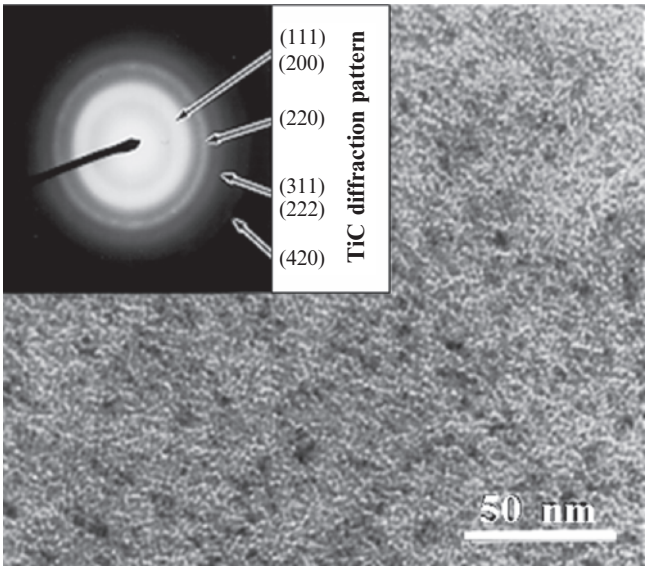

Fig. 9 TEM image of an TiC/DLC nanocrystalline/amorphous composite coating with improved toughness characteristics. SAD pattern shows presence of crystalline TiC and amorphous carbon [38]

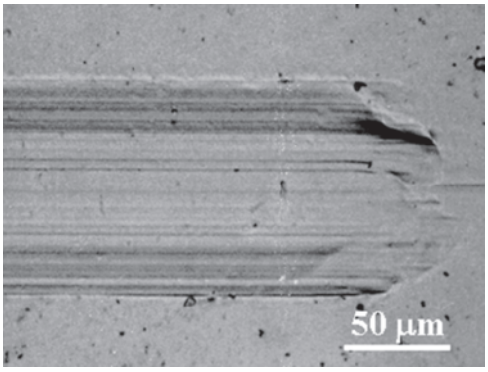

Fig. 10 Appearance of a plastic deformation inside scratch path on the surface of 32 GPa hard TiC/DLC nanocomposite coating obtained with diamond needle of 0.2 mm radius under 50 N normal load [38]

appearing around nanosized grains under applied external stress in result of grain boundary sliding. Some of these nanovoids are connected to form nanocracks, which have multiple splits and diversions due to the presence of multiple amorphous/crystalline boundary interfaces.

The grain boundary sliding and crack termination mechanisms eliminate brittle fracture and provide macroscopic ductility and toughness to TiC/DLC and WC/DLC composites, resulting in a dramatic improvement of scratch toughness

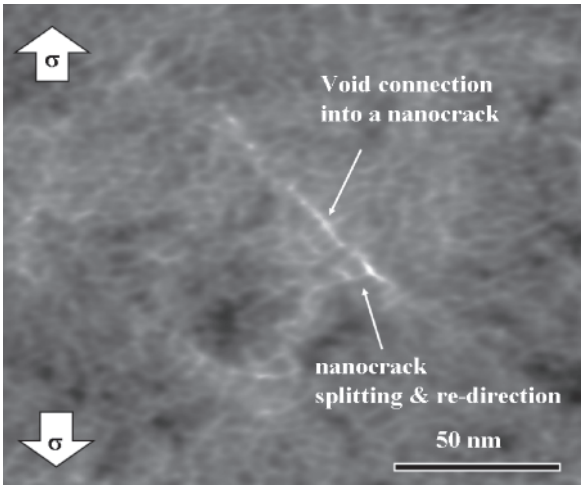

Fig. 11 TEM image of a TiC/DLC nanocomposite from in situ tension strain experiments, showing formation of nanovoids in result of the grain boundary sliding and nano-crack splitting and termination

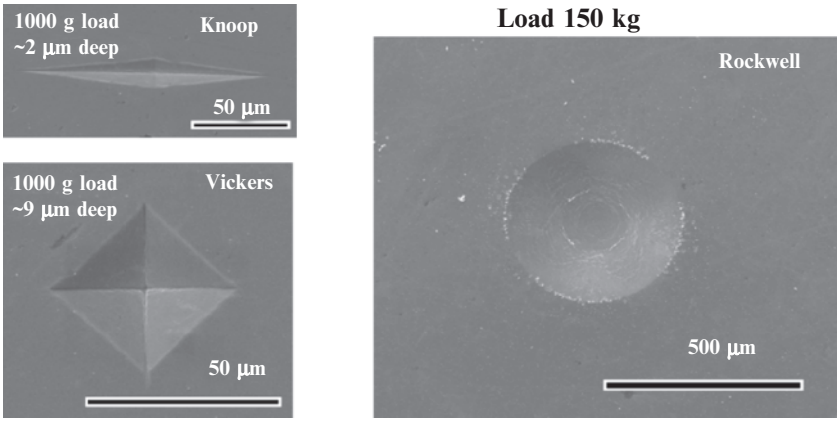

Fig. 12 Knoop, Vickers, and Rockwell indentation marks on the surface of 1 μm thick hard TiC/DLC nanocomposite coatings applied to steel substrates, demonstrating their exceptional resistance to brittle fracture at high degrees of deformations [52]

characteristics. Scratch toughness estimates were at least 3–4 times more than that of single-phase nanocrystalline TiC and WC coatings deposited on the same substrates, with the same interlayers, and the same thicknesses [36,37]. This encouraging result justified the proposed DLC-toughing concept. Another confirmation is presented in Fig. 12, which compares indentations made at the highest loads in Knoop, Vickers, and Rockwell C indentations into the surface of a TiC/DLC coating on steel substrates. There are no observable cracks in these coatings, even

after significant substrate plastic compliance. This is very unique for DLC-based coatings with hardness at about 30 GPa.

Thus, novel nanocomposite designs for tough DLC-based tribological coatings are very promising and provide a very attractive alternative to multilayer architectures. Nanocomposite coatings are easily applied to different substrate geometries and sizes, since they do not require a precise control of the individual layer thickness and frequent cycling of the deposition parameters, as it is required for fabrication of multilayer coatings. Suitable scale-up of deposition techniques are currently under intense study, for example, in applications to heavily loaded gears and bearings [45,46].

5 Adaptive Low Friction "Chameleon" Nanocomposites with DLC Phases

Tough TiC/DLC and WC/DLC composites discussed above demonstrated low friction and wear in ambient environment tests [36,47]. In these composites, a hydrogen-free DLC matrix was used to encapsulate carbide nanocrystals. The use of a DLC matrix in long-duration aerospace applications may create a problem due to the graphitization of DLC in friction contacts and an associated increase in friction coefficient in space environment [48,49]. This can be counteracted with hydrogenated DLC coatings discussed in Chapters 5 and 6, which however will have a considerably reduced wear resistance at high contact loads and speeds. Another alternative approach is to incorporate dichalcogenide space lubricants, such as MoS_2 or WS_2, into the composite coatings with ta-DLC. This approach leads to environmentally adaptive tribological materials, which were termed "chameleon" for their ability to resist friction and wear by changing surface chemistry and microstructure in response to environmental and loading variations, much like a chameleon changes its skin color to avoid predators. The following design concepts were developed to combine with the concepts of tough nanocomposites described above [38,50,51]:

1. Solid lubricant reservoirs are introduced as amorphous or poorly crystalline inclusions to minimize reduction in composite hardness and elastic modulus, since crystalline solid lubricants are typically very soft.
2. Friction forces and surface reactions with the environment are used to generate a lubricious transfer film or "skin" at the tribological contact, which can self-adjust with each environmental change; that is, coating components serve as reservoirs to supply material for the "tribo-skin," where formation of a lubricating film with the required chemistry and structure reduces friction.

Figure 13 presents a schematic of a nanocomposite coating design that exhibits "chameleon" behavior. This design was implemented in the fabrication of WC/DLC/WS_2 [52], YSZ/Au/DLC/MoS_2 [50], and Al_2O_3/Au/DLC/MoS_2 [53] "chameleon" coatings where an amorphous DLC component and nanocrystalline phases (e.g., YSZ, WC, Au) were used to produce optimum mechanical performance and

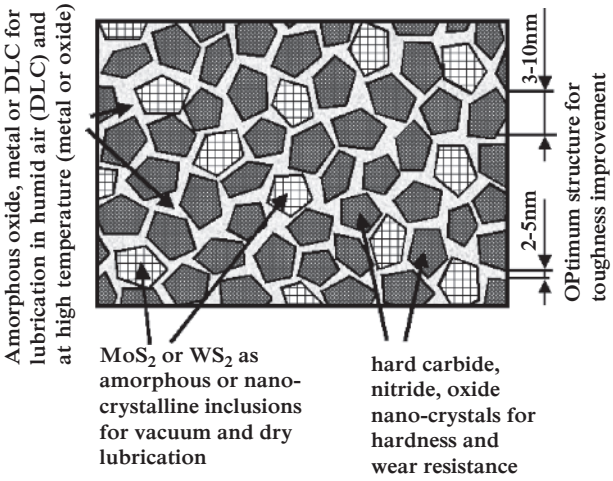

Fig. 13 Schematic of a conceptual design for a nanocomposite tribological coating with chameleon-like surface adaptive behavior [52]

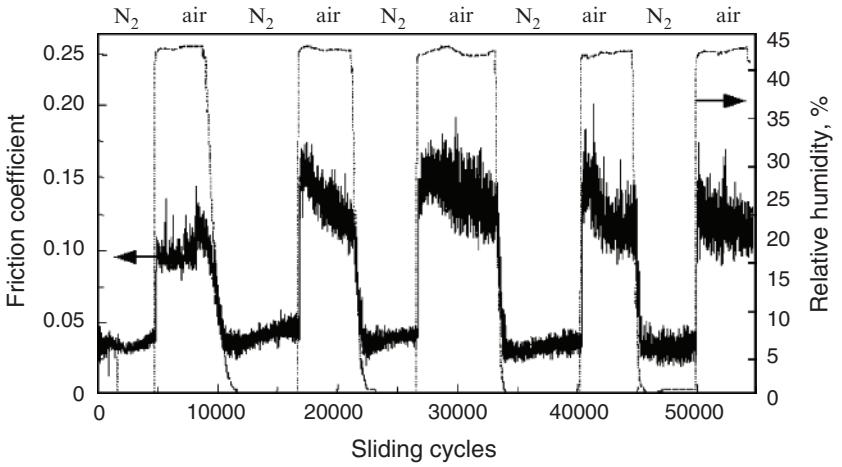

Fig. 14 Friction coefficient variation of a "chameleon" YSZ/Au/MoS_2/DLC coating in a test with cycled relative humidity. Friction response is repeatedly switching from lubrication provided by MoS_2 in dry environments to lubrication provided by DLC in moist conditions [52]

load support. In low-temperature humid environments, a graphitic-like transfer layer is formed by an $sp^3 \rightarrow sp^2$ phase transition of the DLC component, which eventually leads to the formation of some crystalline graphite. This layer provides a low friction coefficient (i.e., 0.1–0.15) and significantly reduces further wear. In humid environments, formation of MoS_2 or WS_2 transfer layers is not favorable due to their oxidation and higher friction. When the environment changes to dry (N_2 or air)

or vacuum and the temperature remains low, a WS_2 or MoS_2 transfer layer is formed by an amorphous → crystalline transformation of dichalcogenide inclusions. Rubbing orients the crystalline material such that the low-friction basal plane is parallel to the surface. This provides friction coefficients as low as 0.01, reducing further wear of the composite coating. The process then repeats itself with each environment cycling. An example of adaptive performance in cycling humidity tests is shown in Fig. 14 using a YSZ/Au/DLC/MoS_2 composite coating, where a switch of tribofilm friction response between that of DLC in humid and that of MoS_2 in dry conditions was observed [50].

Investigations are ongoing to characterize transfer film change dynamics in cycled environments using in situ analyses methods [54,55]. The considerable progress was also made to extend a high temperature composite operation boundary to above 500°C due to the incorporation of noble- and oxide-forming metals into the composite coating architecture [50,53,56], in addition to the DLC phase.

6 Conclusions

Hard hydrogen-free ta-DLC materials offer unique tribological performance due to their high hardness, low friction, and extremely low wear rates. Currently, these materials are synthesized by PLD and FCVA techniques, and both methods are progressing fast towards industrial scale-up and broad commercialization. Problems of ta-DLC with low adhesion and high level of compressive stress were effectively solved through the development of graded and multilayer coating architectures, which was supported by the development of hybrid plasma deposition methods and process-control arrangements. Further enhancement came with nanocrystalline carbide/amorphous DLC compositions, where high contact toughness is achieved by using grain boundary sliding for strain accommodation without brittle fracture. Multiple crystalline/amorphous interfaces help to divert and split nanocracks, avoiding coating macro-cracking even when relatively softer substrates experience a high degree of deformations. Since ta-DLC is exceptionally good in ambient conditions, adaptive “chameleon” composites were developed to use this tribological benefit of ta-DLC, while introducing additional solid lubricant phases for other environments, e.g., dry, high vacuum, and elevated temperature.

Multiple examples show that a significant practical benefit can be obtained when incorporating hard DLC together with other metallic or ceramic materials in different types of gradient, multilayer, or composite coating architectures. In general, DLC is an important part of tribological coatings for applications, where a high wear resistance and the absence of lubricating fluids are critical, e.g., aerospace, dry machining, MEMS. It can also find its way to applications, where oils and greases are traditionally used. The coatings with hard DLC phases can provide friction reduction and wear-life extension without the need of lubrication systems, reducing mechanism complexity, costs, weight, and environmental impact.

References

1. J. Robertson, Diamond-like amorphous carbon, Mater. Sci. Eng. R: Reports R37 (2002) 129–281.
2. Q. Wei, J. Narayan, Superhard diamondlike carbon: preparation, theory, and properties, Int. Mater. Rev. 45 (2000) 133–164.
3. C. Donnet, Recent progress on the tribology of doped diamond-like and carbon alloy coatings: a review, Surf. Coat. Technol. 100–101 (1998) 180–186.
4. A. Grill, Tribology of diamondlike carbon and related materials: an updated review, Surf. Coat. Technol. 94–95 (1997) 507–513.
5. J. Robertson, Properties of diamond-like carbon, Surf. Coat. Technol. 50 (1992) 185–203.
6. A. A. Voevodin, M. S. Donley, Preparation of amorphous diamond-like carbon by pulsed laser deposition: critical review, Surf. Coat. Technol. 82 (1996) 199–213.
7. J. Robertson, Mechanism of sp^3 bond formation in the growth of diamond-like carbon, Diam. Relat. Mater. 14 (2005) 942–948.
8. J. M. Lackner, C. Stotter, W. Waldhauser, R. Ebner, W. Lenz, M. Beutl, Pulsed laser deposition of diamond-like carbon coatings for industrial tribological applications, Surf. Coat. Technol. 174–175 (2003) 402–407.
9. R. Dietsch, T. Holz, D. Weibbach, R. Scholz, Large area PLD of nanometer-multilayers, Appl. Surf. Sci. 197–198 (2002) 169–174.
10. I. I. Aksenov, V. A. Belous, V. G. Padalka, V. M. Khoroshikh, Apparatus to rid the plasma of a vacuum arc of macroparticles, Instrum. Exp. Tech. 21 (1978) 1416–1418.
11. I. I. Aksenov, V. A. Belous, V. G. Padalka, V. M. Khoroshikh, Transport of plasma streams in a curvilinear plasma-optics system, Soviet J. Plasma Phys. 4 (1978) 425–428.
12. R. L. Boxman, V. Zhitomirsky, B. Alterkop, E. Gidalevich, I. I. Beilis, M. Keidar, S. Goldsmith, Recent progress in filtered vacuum arc deposition, Surf. Coat. Technol. 86–87 (1996) 243–253.
13. D. A. Karpov, Cathodic arc sources and macroparticle filtering, Surf. Coat. Technol. 96 (1997) 22–23.
14. A. Anders, Approaches to rid cathodic arc plasmas of macro- and nanoparticles: a review, Surf. Coat. Technol. 120–121 (1999) 319–330.
15. P. J. Martin, A. Bendavid, Review of the filtered vacuum arc process and materials deposition, Thin Solid Films 394 (2001) 1–15.
16. V. I. Gorokhovsky, R. Bhattacharya, D. G. Bhat, Characterization of large area filtered arc deposition technology. Part I – plasma processing parameters, Surf. Coat. Technol. 140 (2001) 82–92.
17. D. L. Pappas, K. L. Saenger, J. Bruley, W. Krakow, J. J. Cuomo, T. Gu, R. W. Collins, Pulsed laser deposition of diamond-like carbon films, J. Appl. Phys. 71 (1992) 5675–5684.
18. I. I. Aksenov, V. E. Strel'nitskij, Properties of diamond-like coatings prepared by vacuum arc deposition, Surf. Coat. Technol. 47 (1991) 98–105.
19. M. Hakovirta, V. -M. Tiainen, P. Pekko, Techniques for filtering graphite macroparticles in the cathodic vacuum arc deposition of tetrahedral amorphous carbon films, Diam. Relat. Mater. 8 (1999) 1183–1192.
20. H. Takikawa, K. Izumi, R. Miyano, T. Sakakibara, DLC thin film preparation by cathodic arc deposition with a super droplet-free system, Surf. Coat. Technol. 163–164 (2003) 368–373.
21. H. Ronkainen, J. Likonen, J. Koskinen, Tribological properties of hard carbon films produced by the pulsed vacuum arc discharge method, Surf. Coat. Technol. 54/55 (1992) 570–575.
22. A. A. Voevodin, M. S. Donley, J. S. Zabinski, J. E. Bultman, Mechanical and tribological properties of diamond like coatings prepared by pulsed laser deposition, Surf. Coat. Technol. 76–77 (1995) 534–539.
23. T. A. Friedmann, J. P. Sulliva, J. A. Knapp, D. R. Tallant, D. M. Follstaedt, D. L. Medlin, P. B. Mirkarimi, Thick stress-free amorphous-tetrahedral carbon films with hardness near that of diamond, Appl. Phys. Lett. 71 (1997) 3820–3822.

24. Q. Wei, R. J. Narayan, J. Narayan, J. Sankar, A. K. Sharma, Improvement of wear resistance of pulsed laser deposited diamond-like carbon films through incorporation of metals, Mater. Sci. Eng. B 53 (1998) 262–266.
25. C. Bauer, H. Leiste, M. Stuber, S. Ulrich, H. Holleck, Mechanical properties and performance of magnetron-sputtered graded diamond-like carbon films with and without metal additions, Diam. Relat. Mater. 11 (2002) 1139–1142.
26. A. A. Voevodin, M. A. Capano, A. J. Safriet, M. S. Donley, J. S. Zabinski, Combined magnetron sputtering and pulsed laser deposition of carbides and diamond-like carbon films, Appl. Phys. Lett. 69 (1996) 188–190.
27. A. A. Voevodin, J. S. Zabinski, Hybrid plasma deposition methods for synthesis of nanostructured materials, in: A. A. Voevodin, D. V. Shtansky, E. A. Levashov, J. J. Moore (eds), Nanostructured Thin Films and Nanodispersion Strengthened Coatings, Kluwer Academic, Dordrecht, The Netherlands, 2004, pp. 103–111.
28. D. P. Monaghan, D. G. Teer, P. A. Logan, I. Efeoglu, R. D. Arnell, Deposition of wear resistant coatings based on diamond like carbon by unbalanced magnetron sputtering, Surf. Coat. Technol. 60 (1993) 525–530.
29. M. Stuber, S. Ulrich, H. Leiste, A. Kratzsch, H. Holleck, Graded layer design for stress-reduced and strongly adherent superhard amorphous carbon films, Surf. Coat. Technol. 116–119 (1999) 591–598.
30. A. A. Voevodin, M. A. Capano, S. J. P. Laube, M. S. Donley, J. S. Zabinski, Design of a Ti/TiC/DLC functionally gradient coating based on studies of structural transitions in Ti-C films, Thin Solid Films 298 (1997) 107–115.
31. A. A. Voevodin, S. D. Walck, J. S. Zabinski, Architecture of multilayer nanocomposite coatings with super-hard diamond-like carbon layers for wear protection at high contact loads, Wear 203–204 (1997) 516–527.
32. D. P. Monaghan, D. G. Teer, R. D. Arnell, I. Efeoglu, W. Ahmed, Ion-assisted CVD of graded diamond like carbon (DLC) based coatings, J. de Physique IV 3 (1993) 579–587.
33. A. A. Voevodin, J. M. Schneider, C. Rebholz, A. Matthews, Multilayer composite ceramic-metal-DLC coatings for sliding wear applications, Tribol. Int. 29 (1996) 559–570.
34. A. A. Voevodin, P. Stevenson, J. M. Schneider, A. Matthews, Active process control of reactive sputter deposition, Vacuum 46 (1995) 723–729.
35. A. A. Voevodin, S. V. Prasad, J. S. Zabinski, Nanocrystalline carbide/amorphous carbon composites, J. Appl. Phys. 82 (1997) 855–858.
36. A. A. Voevodin, J. S. Zabinski, Load-adaptive crystalline/amorphous nanocomposites, J. Mater. Sci. 33 (1998) 319–327.
37. A. A. Voevodin, J. P. O'Neill, S. V. Prasad, J. S. Zabinski, Nanocrystalline WC and WC/a-C composite coatings produced from intersected plasma fluxes at low deposition temperature, J. Vac. Sci. Technol. A 17 (1999) 986–992.
38. A. A. Voevodin, J. S. Zabinski, Supertough wear resistant coatings with 'chameleon' surface adaptation, Thin Solid Films 370 (2000) 223–231.
39. A. A. Voevodin, J. G. Jones, J. J. Hu, T. A. Fitz, J. S. Zabinski, Growth and structural characterization of yttria stabilized zirconia – gold nanocomposite films with improved toughness, Thin Solid Films 401 (2001) 187–195.
40. S. Veprek, A. S. Argon, Towards the understanding of mechanical properties of super- and ultrahard nanocomposites, J. Vacuum Sci. Technol. B 20 (2002) 650–664.
41. J. Musil, Hard and superhard nanocomposite coatings, Surf. Coat. Technol. 125 (2000) 322–330.
42. C. Mitterer, P. H. Mayrhofer, M. Beschliesser, P. Losbichler, P. Warbichler, F. Hofer, P. N. Gibson, W. Gissler, H. Hruby, J. Musil, J. Vlcek, Microstructure and properties of nanocomposite Ti-B-N and Ti-B-C coatings, Surf. Coat. Technol. 120–121 (1999) 405–411.
43. S. Veprek, The search for novel, superhard materials, J. Vac. Sci. Technol. A 17 (1999) 2401–2420.

44. O. R. Monteiro, M.-P. Delplancke-Ogletree, R. Winand, R. Y. Lo, I. Brown, Synthesis and characterization of thin films of WCx produced by mixing W and C plasma streams, Surf. Coat. Technol. 94–95 (1997) 220–225.
45. V. I. Gorokhovsky, C. Bowman, P. Gannon, D. VanVorous, A. A. Voevodin, A. Rutkowski, C. Muratore, R. J. Smith, A. Kayani, D. Gelles, V. Shutthanandan, B. G. Trusov, Tribological performance of hybrid filtered arc-magnetron coatings. Part I: Coating deposition process and basic coating properties characterization, Surf. Coat. Technol. 201 (2006) 3732–3747.
46. V. I. Gorokhovsky, C. Bowman, P. Gannon, D. VanVorous, A. A. Voevodin, A. Rutkowski, Tribological performance of hybrid filtered arc-magnetron coatings. Part II: Tribological properties characterization, Surf. Coat. Technol. 201 (2007) 6228–6238.
47. A. A. Voevodin, J. P. O'Neill, J. S. Zabinski, Tribological performance and tribochemistry of nanocrystalline WC/amorphous diamond-like carbon composites, Thin Solid Films 342 (1999) 194–200.
48. H. Zaidi, Le Huu, D. Paulmier, Influence of hydrogen contained in hard carbon coatings on their tribological behaviour, Diam. Relat. Mater. 3 (1994) 787–790.
49. A. A. Voevodin, A. W. Phelps, M. S. Donley, J. S. Zabinski, Friction induced phase transformation of pulsed laser deposited diamond-like carbon, Diam. Relat. Mater. 5 (1996) 1264–1269.
50. A. A. Voevodin, J. J. Hu, T. A. Fitz, J. S. Zabinski, Nanocomposite tribological coatings with "chameleon" friction surface adaptation, J. Vac. Sci. Technol. A 20 (2002) 1434–1444.
51. A. A. Voevodin, J. S. Zabinski, Nanocomposite and nanostructured tribological materials for space applications, Comp. Sci. Technol. 65 (2005) 741–748.
52. A. A. Voevodin, J. P. O'Neill, J. S. Zabinski, WC/DLC/WS2 nanocomposite coatings for aerospace tribology, Tribol. Lett. 6 (1999) 75–78.
53. C. C. Baker, J. J. Hu, A. A. Voevodin, Preparation of Al_2O_3/DLC/Au/MoS_2 chameleon coatings for space and ambient environments, Surf. Coat. Technol. 201 (2006) 4224–4229.
54. J. -H. Wu, D. A. Rigney, M. L. Falk, J. H. Sanders, A. A. Voevodin, J. S. Zabinski, Tribological behavior of WC/DLC/WS_2 nanocomposite coatings, Surf. Coat. Technol. 188–189 (2004) 605–611.
55. R. R. Chromik, C. C. Baker, A. A. Voevodin, K. J. Wahl, In situ optical tribometry studies of nanocomposite coatings, Mater. Res. Soc. Symp. Proc. 890 (2006) 275–280.
56. C. Muratore, A. A. Voevodin, J. J. Hu, J. S. Zabinski, Tribology of adaptive nanocomposite yttria-stabilized zirconia coatings containing silver and molybdenum from 25–700°C, Wear 261 (2006) 797–805.

Environmental and Surface Chemical Effects on Tribological Properties of Carbon-based Coatings

F. M. Borodich[1], Y. -W. Chung[2] and L. M. Keer[2]

Abstract During the past several decades, diamond-like carbon (DLC) and various carbon-based coatings were developed with a wide range of chemical, mechanical, and physical properties. Because of the difference in synthesis techniques and tribotesting conditions explored in these studies, many experimental results appeared to contradict one another. This chapter presents an overview of the effects of the environment and surface chemistry on friction and wear performance of several carbon-based coatings: silicon carbide, boron carbide, DLC, and amorphous carbon nitride. In addition, we present a model to explain time-dependent effects on the friction behavior of hydrogenated DLC coatings based on the combined effects of ambient gas adsorption and mechanical removal.

Keywords carbon-based films, dry friction, chemical reactions, adsorption, water vapor

1 Introduction

Recent advances in coating science and technology have led to the introduction of hard and lubricious carbon-based coatings, such as carbon nitride (CN_x), diamond-like carbon (DLC), boron carbide (nominally B_4C), and nanostructured DLC-based nanocomposites. These coatings have been investigated for various tribological applications, e.g., powertrain tribocomponents, dry machining, solid lubrication, and computer disk drives. Literature studies demonstrated that friction and wear properties of these carbon-based coatings depend strongly on the environment. For example, during dry sliding between two hydrogenated DLC-coated surfaces in a nominally dry nitrogen ambient, the friction coefficient depends sensitively on the presence of water

[1]School of Engineering, Cardiff University, Queen's Buildings, Cardiff, CF24 3AA, UK

[2]Center for Surface Engineering and Tribology, Robert R. McCormick School of Engineering and Applied Science, Northwestern University, Evanston, IL 60208, USA

C. Donnet and A. Erdemir (eds.), *Tribology of Diamond-Like Carbon Films: Fundamentals and Applications*.

vapor [9] and increases with time delay between sequential sliding experiments [18]. On the other hand, in the presence of oxygen, acceleration of graphitization (i.e., conversion of sp^3- to sp^2-bonded carbon atoms) and oxidation of carbon may occur, leading to increased friction and wear, as observed by Marchon et al. [21] and more recently by Kato et al. [20]. In some instances, counterface materials react with the carbon coating, forming softer components and resulting in wear of a nominally harder surface by a softer counterface, as illustrated by the work of Harris et al. [16, 17]. The objective of this chapter is to review and discuss how the environment and surface chemistry affect friction and wear of several carbon-based coatings.

2 Silicon Carbide

Sugimoto and Miyake [25] reported that the lubricating performance of amorphous silicon carbide films synthesized by plasma methods is greatly improved by annealing at 800°C. Infrared spectroscopy studies showed that both as-deposited films and films annealed at <600°C contain considerable amounts of hydrogen arising from the incomplete decomposition of hydrogenated gas sources. When annealed at 800°C, all remaining hydrogen was liberated from the film. It is reasonable to hypothesize that the dehydrogenation process results in the formation of graphite-like structures, leading to lower friction. The low friction (friction coefficient ~0.01) was maintained until the film was worn out.

3 Boron Carbide

Most boron carbide (B_4C) films reported in the literature are amorphous, with hardness ranging from 25 to 45 GPa. Its physical properties were discussed in detail by Thevenot [26]. When an uncoated steel ball runs against a surface coated with B_4C film, polishing of the harder B_4C surface occurred (Fig. 1). Given that steel is much softer than B_4C, physical processes such as mechanical ploughing cannot explain the wear of B_4C. Instead, certain tribochemical reaction(s) between Fe and B_4C must be responsible for the observed wear [15, 17]:

(a) As-prepared
(b) After 500 cycles rubbing against steel

Interestingly, the wear process can be described remarkably well by a power law [16, 17]:

$$\overline{A(n)} = A_1 n^{\beta} \tag{1}$$

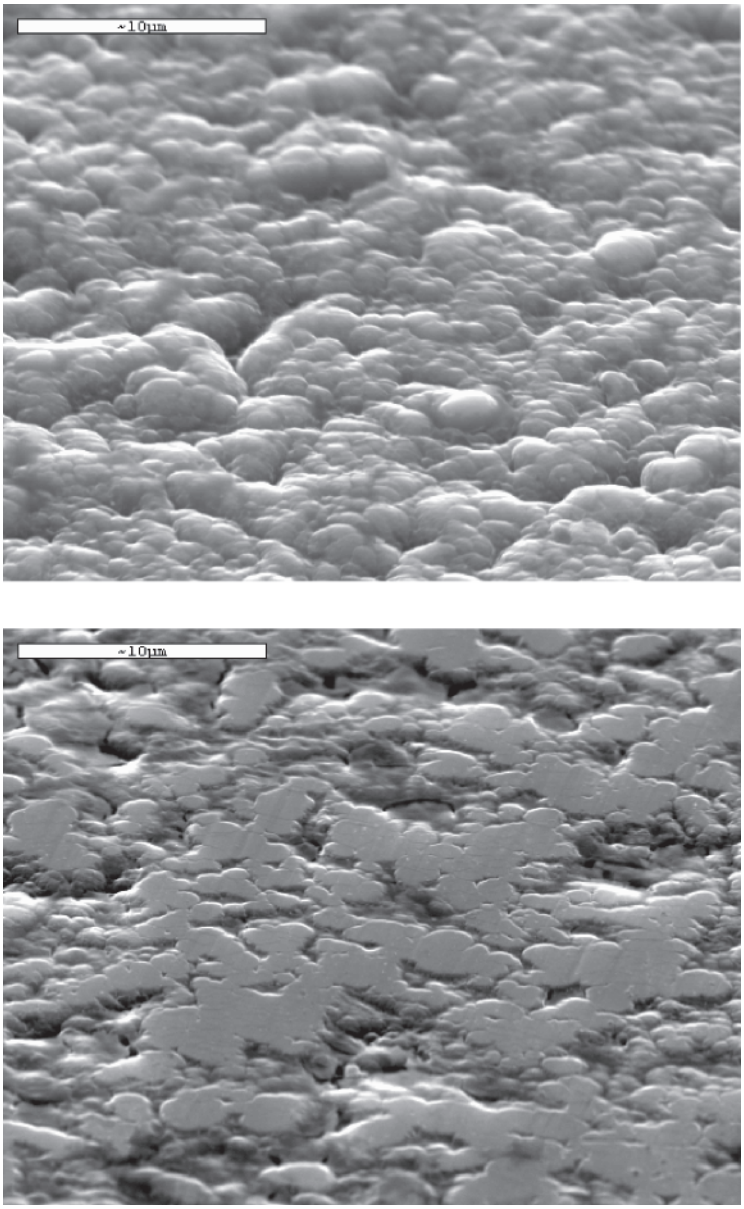

Fig. 1 SEM images of a B_4C film (30 × 30 µm) [2]

where $\overline{A(n)}$ is the average abrasion rate for the nth cycle, and A_1 the abrasion rate for the first cycle. β must lie between 0 (the abrasion rate is constant) and −1 (the abrasion rate drops to zero in the 2nd and subsequent cycles). A typical value for β is −0.8. This power law relationship was observed to be valid for up to 4 orders of magnitude of n.

It was further observed that boron carbide surfaces give friction coefficient values ~0.03–0.05 under ambient conditions [8]. An explanation for this relatively low friction behavior is the formation of boric acid (H_3BO_3) on the surface of boron carbide in the presence of oxygen and water vapor. Boric acid has a layer structure similar to graphite and is believed to behave like a solid lubricant. Prioli et al. [23] prepared samples of pure boric acid and showed that the coefficient of friction for boric acid is in the range 0.05–0.2, with an average value of 0.1. This is 2–3 times greater than the observed values for boron carbide under similar ambient testing conditions. Hence, the explanation of the low-friction behavior of boron carbide is still an open question.

4 Hydrogenated Diamond-like Carbon

Hydrogenated DLC is not a unique substance. Its properties depend on the hydrogen concentration and the synthesis methods, which affect the film density and the sp^3/sp^2 ratio. Generally, increased hydrogen concentration breaks up the C–C sp^3 network, reducing the elastic modulus and hardness. Numerous studies demonstrated that friction and wear properties of these hydrogenated DLC films depend strongly on the environment and the hydrogen content [1, 7, 9, 10, 17, 18, 21, 22, 24, 28, 29]. For example, Erdemir [9] reported that the friction coefficient of hydrogen-free DLC in dry nitrogen was approximately 0.65 and dropped to 0.25 after moist laboratory air was introduced. The same test for the highly hydrogenated DLC showed that the friction coefficient increased from 0.003 to 0.06. Marchon et al. [21] reported that the friction coefficient of a head/disk pair (DLC film in contact with either a Mn/Zn ferrite or $CaTiO_3$ ceramic slider) in pure nitrogen was 0.2 and increased to 1.2 when oxygen was introduced into the system. They attributed this behavior to the oxidation of the carbon film when exposed to oxygen, with the formation of CO or CO_2. Donnet et al. [6] noted that under their testing conditions in ultrahigh vacuum, addition of oxygen did not affect the low-friction behavior of hydrogenated DLC, but addition of water vapor increased the friction coefficient from about 0.01 to 0.1.

Such sensitivity of the friction behavior of hydrogenated DLC towards water vapor may be the source of many contradictory results reported in the literature. To overcome this sensitivity, researchers introduced various metal dopants to the DLC, e.g., tungsten, and titanium. These metal dopants are only moderately successful in reducing the water vapor effects (see, e.g., [14, 27]) with friction coefficients exceeding 0.05 in humid environments. In some recent experiments, it was demonstrated that introduction of 5 at. % sulfur is sufficient to suppress deleterious effects due to water vapor [12, 13]. Figure 2 shows that the friction coefficient of self-mated hydrogenated DLC doped with 5 at. % sulfur is below 0.01, both in dry air and in air with 50% relative humidity.

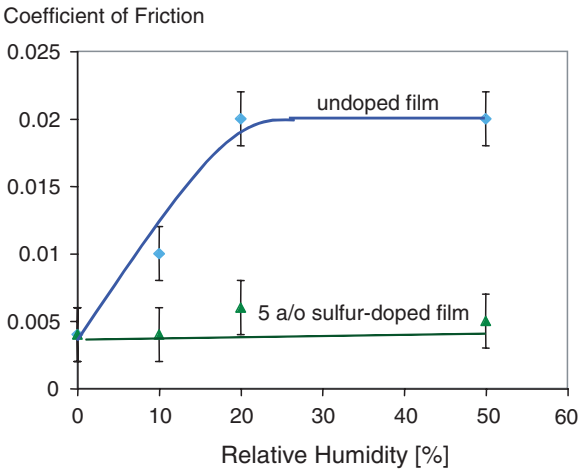

Fig. 2 Coefficient of friction versus relative humidity for self-mated hydrogenated DLC films with and without 5 at. % sulfur

5 Modeling Friction Behavior of Hydrogenated DLC in Humid Air

Heimberg et al. [18] showed that the friction coefficient depends on the time delay between successive contacts on the self-mated hydrogenated DLC surfaces. This suggests that friction is related to the amount of water vapor adsorbed on the DLC surface during friction experiments. Assume that the coefficient of friction has three contributions, that is,

$$\mu = \mu_{\text{mech}} + \mu_{\text{w}} + \mu_{\text{mol}}, \tag{2}$$

where μ_{mech} is the part of friction due to mechanical deformation and asperity interactions, μ_{w} is the part of friction caused by the presence of water vapor, and μ_{mol} is the part caused by all other molecular effects. Therefore, we can write:

$$\mu = \mu_{\text{c}} + \mu_{\text{w}}, \tag{3}$$

where $\mu_{\text{c}} = \mu_{\text{mech}} + \mu_{\text{mol}}$. If we assume that μ_{w} is proportional to the amount of water adsorbed on the surface, then we can calculate time-dependent effects as observed by Heimberg et al. [18] once the rate of adsorption is known. The Elovich equation was used to describe the rate of thermally activated adsorption of molecules on surfaces, that is,

$$\frac{\mathrm{d}\theta}{\mathrm{d}t} = Be^{-\alpha\theta}, \tag{4}$$

where θ is the fractional coverage of water vapor, t is the time, and B some empirical constant. In the reciprocating ball-on-flat tribotesting conducted by Heimler et al. [18], one can assume that during the ith cycle and at the kth point along the track, the ball mechanically removes a certain amount of adsorbed water vapor from the surface. The same point has been reexposed to the atmosphere for a certain amount of time between cycles. The water coverage at the kth point and the ith cycle, $\theta(k,i)$, increases continuously due to adsorption and decreases abruptly when the ball passes over the kth point at time t, that is,

$$\left[\theta(k,i)\right]^{\pm} = \theta(k,i)\big|_{t+0-} - \theta(k,i)\big|_{t+0+}, \tag{5}$$

where $[\theta(k,i)]^{\pm}$ is the change in water coverage during ball passage. It is assumed that the change is proportional to $\theta(k,i)\big|_{t+0-}$ via the following relationship:

$$\left[\theta(k,i)\right]^{\pm} = p\theta(k,i) \tag{6}$$

where p $(0 \le p \le 1)$ defines the probability of mechanical removal of adsorbed water. Integrating Eq. (4) and substituting Eq. (6), we obtain:

$$\theta(k,i)\big|_{t+\Delta t(k,i)+0+} = \ln\left[\exp\left(\alpha\theta(k,i)(1-p)\right) + \alpha B\Delta t(k,i)\right]/\alpha, \tag{7}$$

where $\Delta t(k,i)$ is the time between ball passes.

In the experiments of Heimberg et al. [18], the DLC coatings were deposited on steel flats and either on 6.35 mm sapphire balls or 12.7 mm diameter steels balls. Reciprocating pin-on-disk tests were performed in a nominally dry nitrogen environment with an oxygen level of 0.7%. The track length was 5 mm. Each track was initially run-in for 1,000 cycles at high sliding speeds (1–5 mm/s). The speed-dependent test began with 100 cycles at high speed (1–5 mm/s) followed by 20 cycles at a lower speed. The ball was in continuous sliding contact with the disk. The experimental sequence and results are shown in Fig. 3. Using the above theoretical approach, Borodich and Keer [3] and Borodich et al. [4] successfully simulated these reciprocating tribotesting experiments, as shown in Fig. 3. The simplified assumption that μ_w is proportional to the water coverage appears justified.

6 Amorphous Carbon Nitride

More than a decade ago, amorphous CN_x was suggested as a superhard solid lubricant [5]. It was found that the friction coefficient of the steel-CN_x pair in unlubricated conditions was about 0.16. Amorphous CN_x coatings can be prepared using various techniques such as reactive magnetron sputtering and ion-beam-assisted deposition (IBAD). The hardness of these coatings typically varies between 15 and 30 GPa (see, e.g., [19, 20]). Similar to hydrogenated DLC,

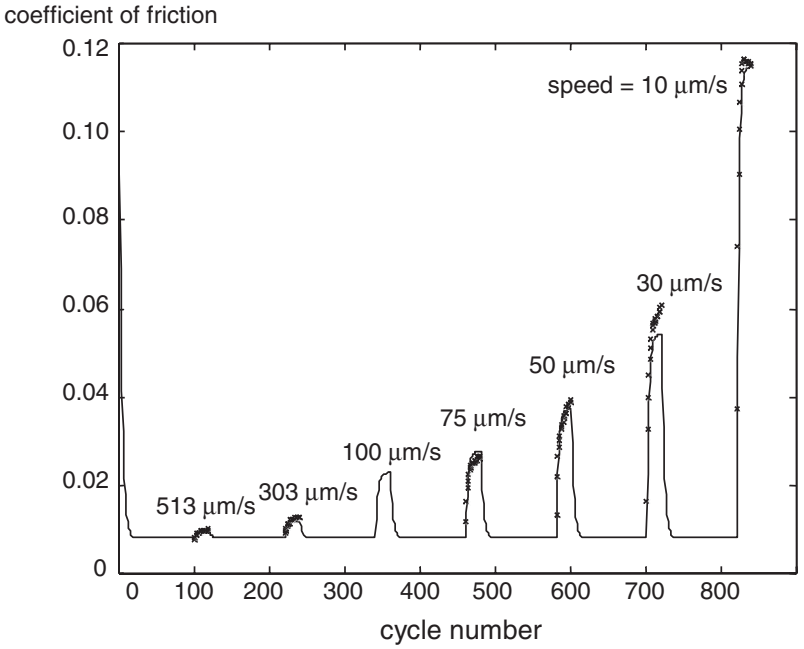

Fig. 3 Experimental (*) and simulated (continuous lines) coefficient of friction versus cycle number for self-mated hydrogenated DLC films tested in nominally dry nitrogen

friction and wear properties of CN_x coatings are dependent on the atmospheric conditions, degrading with increased humidity in the testing environment [11, 20, 24]. In pure nitrogen (without oxygen and water vapor), friction coefficients <0.01 were obtained with smooth surfaces and when both surfaces were coated with amorphous CN_x, either initially or through the formation of transfer films. Apparently, initially rough surfaces can be smoothed by performing friction measurements in oxygen. When this was followed by testing in pure nitrogen, low friction coefficients (<0.01) were obtained [1]. Given its stability, molecular nitrogen is not likely to be the species passivating the film surface; rather, some sort of plasma discharge might have occurred at the tribocontact that resulted in the formation of atomic or excited molecular nitrogen, which then passivated the surfaces.

7 Conclusion

The above brief review indicates that when one performs tribological studies of a given system, one must consider the potential interfacial chemical reactions and ambient gas adsorption (physisorption and chemisorption) that may occur. As illustrated here, these effects can have dominating effects on friction and wear.

Acknowledgments We thank the support of the Center for Surface Engineering and Tribology at Northwestern University.

References

1. Adachi K., Wakabayashi T. and Kato K. (2005) The effect of sliding history on the steady state friction coefficient between CN_x coatings and N_2 lubrication. In: Life Cycle Tribology, Proc. 31st Leeds-Lyon Symposium on Tribology, Leeds 2004, Tribology and Interface Engineering Series, Elsevier, Amsterdam, The Netherlands, pp. 673–677.
2. Borodich F. M., Harris S. J. and Keer L. M. (2002) Self-similarity in abrasion of metals by nano-sharp asperities of hard carbon containing films. Appl. Phys. Lett., 81, 3476–3478.
3. Borodich F. M. and Keer L. M. (2005) Modeling effects of gas adsorption and removal on friction during sliding along diamand-like carbon films. Thin Solid Films, 476, 108–117.
4. Borodich F. M., Korach C. J. and Keer L. M. (2007) Modeling the tribochemical aspects of friction and gradual wear of DLC films. J. Appl. Mech. ASME, 74(1) 23–30.
5. Chen M. Y., Lin X., Dravid V. P., Chung Y. W., Wong M. S. and Sproul W. D. (1993) Synthesis and tribological properties of carbon nitride as a novel superhard coating and solid lubricant. Trib. Trans., 36, 491–495.
6. Donnet C., Le Mogne T., Ponsonnet L., Belin M., Grill A., Patel V. and Jahnes C. (1998) The respective role of oxygen and water vapour on the tribology of hydrogenated diamond-like carbon coatings. Tribol. Lett., 4, 259–265.
7. Dugger M. T., Wahl K. J., Chung Y. -W., Bhushan B. and Rothschild W. (1991) An investigation of environmental effects on the wear and surface composition of thin film magnetic discs. STLE, SP31, 43–53.
8. Erdemir A., Bindal C. and Fenske G. R. (1996) Formation of ultralow friction surface films on boron carbide. Appl. Phys. Lett., 68, 1637–1639.
9. Erdemir A. (2001) The role of hydrogen in tribological properties of diamond-like carbon films. Surf. Coat. Technol, 146, 292–297.
10. Erdemir A. and Donnet C. (2001) Tribology of diamond, diamond-like carbon, and related films. In: B. Bhushan (ed.) Modern Tribology Handbook. Vol 2, CRC Press, Boca Raton, FL, pp. 871–908
11. Fernandez A., Fernandez-Ramos C. and Sánchez-López J. C. (2003) Preparation, microstructural characterization and tribological behaviour CN_x coatings. Surf. Coat. Technol, 163–164, 527–534.
12. Freyman C. A., Zhao B., Chen Y. F. and Chung, Y. W. (2006a) Water adsorption and desorption on ultra-low friction sulfur-doped hydrogenated carbon films. J. Phys. Condens. Matter, 18, S1721–1726.
13. Freyman C. A., Chen Y. F. and Chung Y. W. (2006b) Synthesis of carbon films with ultra-low friction in dry and humid air. Surf. Coat. Technol., 201, 164–167.
14. Gilmore R. and Hauert R. (2000) Comparative study of the tribological moisture sensitivity of Si-free and Si-containing diamond-like carbon films. Surf. Coat. Technol., 133–134, 437–442.
15. Gogotsi Yu.G., Koval'chenko A. M. and Kossko I. A. (1992) Tribochemical interactions of boron carbides against steel. Wear, 154, 133–140.
16. Harris S. J. and Weiner A. M. (1998) Scaling relationships for the abrasion of steel by diamondlike carbon coatings. Wear, 223, 31–36.
17. Harris S. J., Krauss G. G., Simko S. J., Baird R. J., Gebremariam S. A. and Doll G. (2002) Abrasion and chemical-mechanical polishing between steel and a sputtered boron carbide coating. Wear, 252, 161–169.
18. Heimberg J. A., Wahl K. J., Singer I. L. and Erdemir A. (2001) Superlow friction behavior of diamond-like carbon coatings: time and speed effects. Appl. Phys. Lett., 78, 2449–2451.

19. Kato K., Koide H. and Umehara N. (2000) Micro-wear properties of carbon nitride coatings. Wear, 238, 40–44.
20. Kato K., Umehara N. and Adachi K. (2003) Friction, wear and N_2-lubrication of carbon nitride coatings: a review. Wear, 254, 1062–1069.
21. Marchon B., Heiman N. and Khan M. R. (1990) Evidence for tribochemical wear of amorphous carbon thin films. IEEE Trans. Magnet., 26, 168–170.
22. McGuiggan P. M., Hsu S. M., Fong W., Bogy D. and Bhatia C. S. (2002) Friction measurements of ultra-thin carbon overcoats in air. J. Tribology. ASME, 124, 239–244.
23. Prioli R., Ponciano C. R. and Freire F. L. (2000) Nanoscale interaction mechanism between a solid tip and a layered material while in relative motion: the boric acid case. Appl. Phys. A., 71, 233–236.
24. Sánchez-López J. C., Belin M., Donnet C., Quiros C. and Elizalde E. (2002) Friction mechanisms of amorphous carbon nitride films under variable environments: a triboscopic study. Surf. Coat. Technol, 160, 138–144.
25. Sugimoto I. and Miyake S. (1989) Lubricating performance enhancement of amorphous silicon carbide film by annealing effects and microbeam analyses of the tribological interface. J. Appl. Phys., 66, 596–604.
26. Thevenot F. (1990) Boron carbide – a comprehensive review. J. Europ. Ceram. Soc., 6, 205–225.
27. Voevodin A. A. and Zabinski J. S. (2000) Supertough wear-resistant coatings with 'chameleon' surface adaptation. Thin Solid Films, 370, 223–231.
28. Voevodin A. A., O'Neill J. P. and Zabinski J. S. (1999) Nanocomposite tribological coatings for aerospace applications. Surf. Coat. Technol., 119, 36–45.
29. Zaïdi H., Paulmier D. and Lepage J. (1990) The influence of the environment on the friction and wear of graphitic carbons. II. Gas coverage of wear debris. Appl. Surf. Sci., 44, 221–233.

Triboemission and Triboplasma Generation with DLC Films

K. Nakayama

Abstract This chapter first describes the general features of triboemission and triboplasma generation as the basic knowledge to understand the phenomena in regard to diamond-like carbon (DLC) films. Next, the electrical properties and structure of DLC films are described, which are essential for an understanding of the triboemission phenomena in DLC films. This is followed by a description and discussion on triboemission on amorphous carbon (a-C), hydrogenated amorphous carbon (a-C:H), and nitrogenated amorphous carbon (a-C:N) films in connection with triboplasma generation, in addition to a presentation of the triboplasma distribution on tetrahedral hydrogen-free amorphous carbon (ta-C) film. In regard to a-C and a-C:H films, the characteristics of triboemission of electrons, ions, and photons, and plasma generation are also described and discussed in relation to the friction coefficient, hydrogen content, and the electric resistivity of the films under the circumstances of vacuum, ambient air, and oil lubrication. For a-C:N films, triboemission phenomena are described in comparison with those of a-C:H films. With respect to ta-C film, the chapter also presents the distribution of triboplasma generation with two-dimensional photons emitted from the vicinity of sliding contact

Keywords triboemission, electrons, ions, photons, triboplasma, tribocharging, hydrogenated carbon films, nitrogenated carbon films, tetrahedral hydrogen-free amorphous carbon film, DLC film, dry sliding, oil lubrication

1 Introduction

Various kinds of particles are emitted from a sliding contact and its vicinity [1,2]. These particles are electrons [2], negative and positive ions, photons, radicals, and molecules [1]. From systematic work, the particle emission phenomena are

National Institute of Advanced Industrial Science and Technology (AIST), Namiki 1-2, Tsukuba, Ibaraki 305-8564, Japan

C. Donnet and A. Erdemir (eds.), *Tribology of Diamond-Like Carbon Films: Fundamentals and Applications*.

currently classified into three broad categories: (1) triboemission from the inside of the contact; (2) triboemission from the triboplasma generated in the rear outside gap of the sliding contact; and (3) postemission from the outside of the contact [3–5]. Most of these particle emission phenomena are deeply connected with the tribocharging phenomena [5]. So *the phenomena embracing tribocharging, triboemission, and postemission are termed triboelectromagnetic phenomena* [5–8]. Figure 1 shows the most recent model of triboelectromagnetic phenomena [5], which has been modified from the first version [9] and following recent models [3,8]. At the sliding contact, the frictional temperature rises and wear of the sliding solid occurs. *Thermoelectrons* and *thermally stimulated electrons* are emitted at and the vicinity of the sliding contact depending on the frictional temperature levels [10], while *chemically induced electrons* are emitted by the interaction between the freshly worn surface and the surrounding active molecules [2]. These electrons and straying electrons, which are produced by such phenomena as cosmic rays, are accelerated by an intense *tribocharging-induced electric field*, which cause discharging of ambient gas molecules. By this gas discharge, triboplasma is generated through an *electron avalanche process* [5]. The plasma emits electrons, ions, and photons. Photons are also emitted from the inside of the sliding contact (in addition to electrons) [4–5]. One of the postemission electrons is the chemically induced emission electrons, while that of the photons is thought to originate from the attack on solid surfaces by charged particles, either electrons or ions produced in the triboplasma [5].

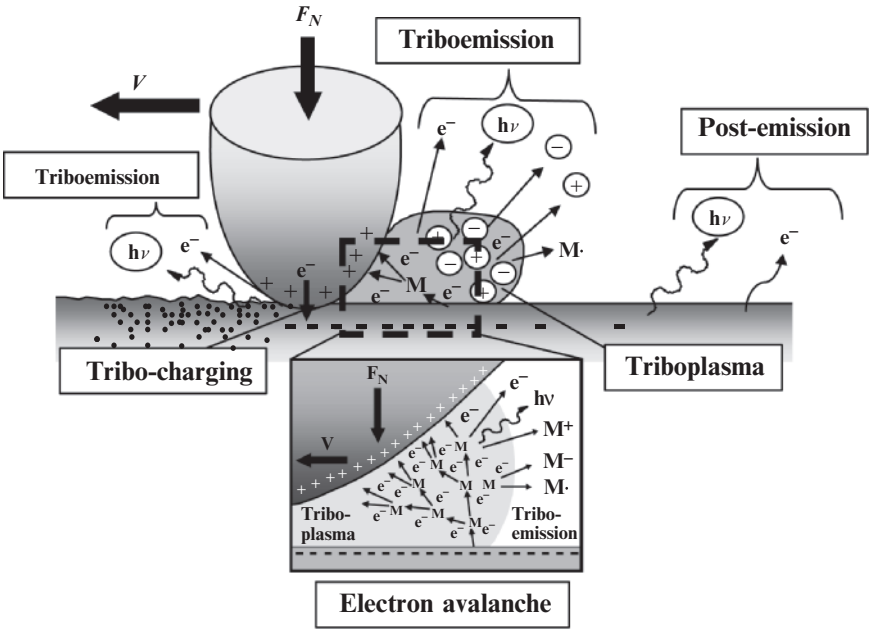

Fig. 1 Conceptual model of triboelectromagnetic phenomena

These kinds of triboemission and triboplasma phenomena cause various kinds of tribophysical and tribochemical events having beneficial or harmful effects on the tribosystem [11, 12]. In the following sections, the general features of the phenomena of triboemission and triboplasma generation will first be described, and then the characteristics and the mechanisms of the phenomena with aC-, aC:H-, aC:N- and taC-films of diamond-like carbon (DLC) films will be presented and discussed.

2 General Features of Triboemission and Triboplasma Generation

Figure 2 shows the emission intensity of negatively charged particles as a function of the electric resistivity of various solids scratched by a diamond stylus in ambient air [13]. Negatively charged particles mean electrons and negative ions, while positively charged particles are positive ions. As most of the emitted electrons immediately become attached to air molecules to form negative ions [14], the charges detected are the same charges as electrons emitted from sliding contacts. As seen in Fig. 2, the charge intensity increases sharply with the resistivity (ρ) of a solid (note the ordinate is on a logarithmic scale). Two kinds of electron emission mechanisms have been proposed: (1) chemically induced emission from metals [2]; and (2) triboemission from insulators [14]. The number of the electrons that result from chemically induced emissions from metals [2] is very small and their energy is quite low, varying from 0.1 to 2 eV [15–17]. On the other hand, in insulators, enormous

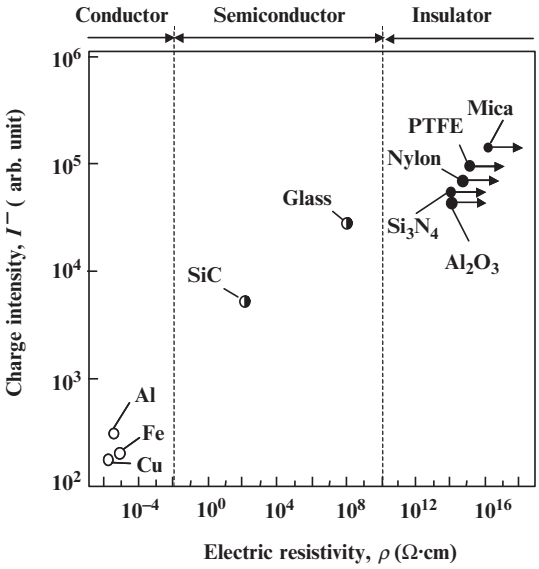

Fig. 2 Relation between negative charge emission intensity, I^-, and electric resistivity, ρ

numbers of high-energy electrons varying from a few electron volts to kilo electron volts are emitted [12]. In the case of semiconductors, the tribocharging-induced electric field increases from the negligible electric field of metals to the extremely intense electric field of insulators with an electric resistivity of solids. Therefore, the number of electrons increases greatly in the region of semiconductors with an increase in the electric resistivity of solids; the electric resistivity, which causes tribocharging, is the strongest influencing factor of both the number and energy of triboemission particles. In the past, several mechanisms of tribocharging have been proposed [18]. These include: (1) work function difference, in which electrons transfer from a contacting solid with a lower work function to a mating solid with higher work function [18]; (2) asymmetric rubbing [19]; (3) removal of neutralized surface layers to reveal intrinsic charged surfaces [20]; (4) transfer of protons and hydroxide ions [21]; and (5) due to pyroelectricity and piezoelectricity [22]. Under oil lubrication, two additional kinds of tribocharging mechanisms have been proposed. They are the oil–solid contact mechanism [23] and the double-layer mechanism [24].

As stated above, positive ions are emitted from the sliding contact together with the electrons. Figure 3 shows the relation between the ratio of the emission intensity of negative particles against positive particles (charge ratio, I^-/I^+) and the electric resistivity (ρ) measured under the same experimental condition of Fig. 2 [13]. With an increase in ρ, the value of I^-/I^+ decreases in the region of semiconductors, approaching the value of $I^-/I^+ = 1$ for insulators. The values of I^-/I^+ in the insulator are a little bit higher than $I^-/I^+ = 1$. This is because the mobility ratio of the negative ions is higher than that of the positive ions [14]. So *the same number of electrons and positive ions are emitted from the plasma generated in insulators*. The tribophoton intensity emitted from triboplasma has a linear relationship with the electron emission intensity [1]. These photons consist of UV, visible, and IR photons [25]. The photon spectrum in the UV region emitted from the sliding contact completely

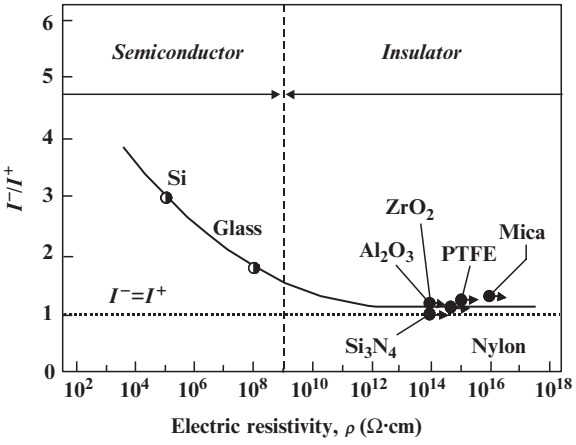

Fig. 3 Relation between ratio of negative to positive charge emission intensity, I^-/I^+, and electric resistivity, ρ.

coincides with that of the gas discharge plasma. This result demonstrated that *the triboplasma generation originates from the discharging of the surrounding gas molecules due to the intense tribocharging-induced electric field* [25]. By the success of obtaining two-dimensional photon images emitted from the vicinity of the sliding contact, the predicted plasma has already been discovered both under dry [4] and oil-lubricated conditions [5]. The measured side plasma image had a shape very similar to the predicted plasma image shown in Fig. 1 [5].

The triboemission intensity depends on the ambient gas pressure (p), hardness of the solid, sliding velocity (V), and the normal force applied (F_N) [25]. The plasma intensity increases with decreasing the gas pressure, reaches a maximum at $p_{max} = 3 \times 10^3$ Pa and then ceases at $p \leq 10^1$ Pa in an air atmosphere [26]. The gas pressure, where triboemission or triboplasma generation becomes a maximum, depends on the gas species [26,27]. It has been shown that this plasma decomposes the organic gas molecules to form high molecular weight products on the frictional surface to reduce friction and wear [11]. Furthermore, it decomposes the oil molecules under oil-lubricated sliding contact forming degraded oil and evolving volatile molecules [12].

3 Electric Nature and Structure of DLC Films

As described above, triboemission is a function of the tribocharging-induced electric field and triboemission intensity is deeply connected with the insulating nature of sliding materials. So, first the insulating nature of DLC film is described.

Figure 4 shows electric resistivity (ρ) as a function of the hydrogen and nitrogen content, C_H and C_N of the a-C:H and a-C:N films, respectively [8]. These films were

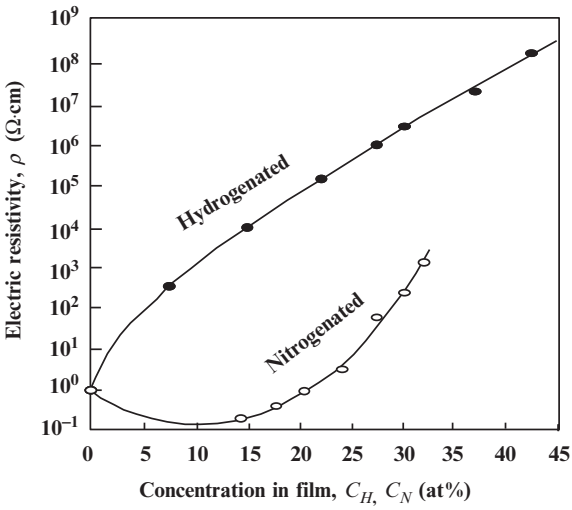

Fig. 4 Relation between electric resistivity, ρ, and hydrogen and nitrogen content in amorphous carbon films, C_H, C_N

coated by the DC-magnetron sputtering method on a K^+ ion-exchanged soda lime glass substrate. The values of C_H and ρ were determined using the hydrogen forward-scattering technique and a four-point probe, respectively. The ρ_H of a-C:H increases almost linearly in the region of $C_H > 5$ at. % in the semilogarithmic graph with C_H, while the ρ_N of the nitrogenated carbon film is 3–5 orders of magnitude lower than that of hydrogenated carbon film. It decreases first, and then increases, reaching a minimum with C_N [8]. The electric resistivity of various kinds of DLC films has been reported in a review article in Ref. [28].

It is known that the Raman spectrum of aC:H films gives two kinds of peaks called the *D(disorder)-band* and *G(graphite)-band* [29]. Figure 5 shows the peak position of the G band and the peak intensity ratio of the D band against the G band (I_D/I_G)as a function of C_H (K. Nakayama and H. Ikeda, unpublished data).The peak position of the G band shifts to the lower frequency and the I_D/I_G ratio decreases with C_H. The shift of the G band peak position to the lower frequency is an indication of the decrease of the sp^2 character and the decrease of the I_D/I_G ratio indicates the decrease of the number and size of the *carbon microcrystallite* [28]. As the sp^2 graphite bonds act as the localized conduction state and it is hard for the sp^3 bonding structure to conduct electrons, the electric resistivity of the a-C:H film increases with C_H. The carbon film at $C_H = 0$ at. % has a soft graphite-like structure with a conductive nature due to the sp^2 bonding, and this graphitic structure changes to sp^2-bonded graphitic clusters (or graphitic islands) of fused sixfold rings embedded in an sp^3-bonded matrix with an increase in C_H [30]. The sp^2 cluster size decreases and the percentage of the $–CH_2$ group having more sp^3 bonding increases, giving a less conductive and hard diamond-like nature with a further increase in C_H. However, at excess hydrogen content, this structure leads to polymer-like structures having decreased hardness by further formation of $–CH_2$. These structural changes from sp^2 to sp^3 with the increase of hydrogen content (C_H) in the film causes the above increase of electric resistivity in Fig. 4, the increase of the contact angle,

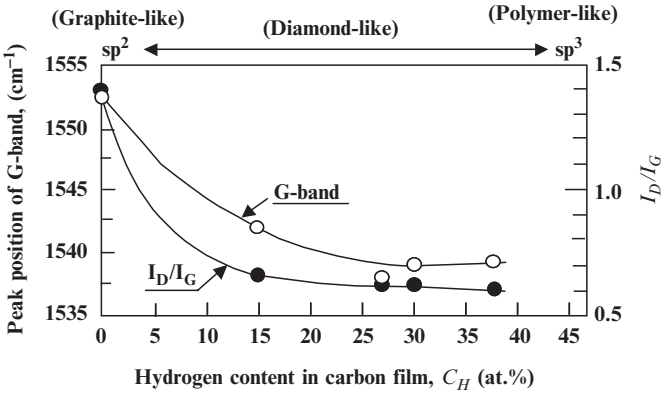

Fig. 5 *D*ependent nature of peak position of G band and ratio of intensity of D band to that of G band, I_D/I_G, on hydrogen content in film, C_H

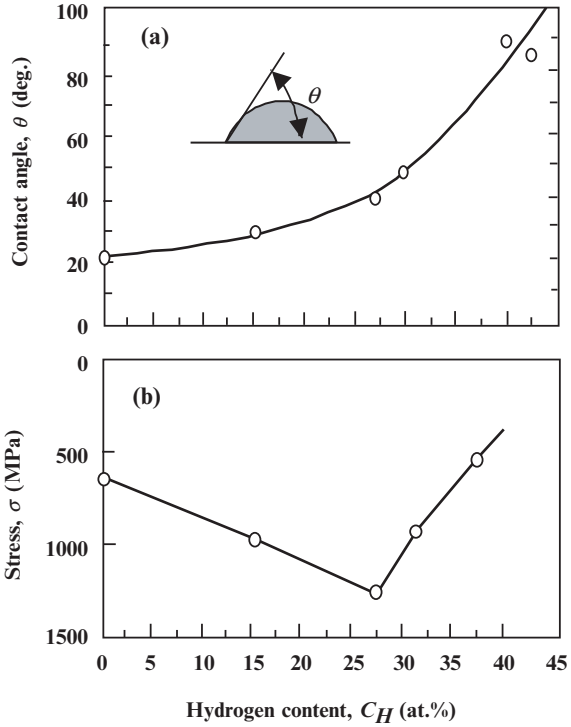

Fig. 6 Dependence of contact angle, θ (a), and internal stress, σ (b), on hydrogen content, C_H, in carbon film

i.e., the decrease of surface energy in Fig. 6a, the change in the internal stress shown in Fig. 6b, and the adhesion strength of the carbon films to the substrate.

In a-C:N films, the carbon is replaced by nitrogen without changing the amorphous network and morphology of the films [31]. The structure of the a-C:N films have sp bonding of C≡N and sp^2 bonding of C=N, together with sp^3 bonding of NH_2 [31]. The very low electric conductivity of the a-C:N film compared to that of a-C:H film must be connected with such things as the existence of the conductive nature of the sp^2 bonding of C=N. The ta-C films were shown to have an insulating nature. For detail of Raman spectroscopy on a-C:H and a-C:N films, comprehensive and outstanding reviews are given by Ferrari et al. [32] and Abrasonis et al. [33], respectively.

4 Triboemission from a-C:H Films in Vacuum

In this section, triboelectron emission is described and discussed from the point of view of friction, wear of a-C:H films in vacuum. The triboelectron emission from the a-C:H films were measured by a pipe-shaped channeling electron multiplier

during sliding of a normal sintered alumina (Al_2O_3) ball ($\phi = 4$ mm, $H_V = 11.5$ GPa) on a-C and a-C:H films in a low vacuum (during a flow of dry air at a gas pressure of $p = 5 \times 10^{-3}$ Pa) under a normal force of $F_N = 0.44$ N and a sliding velocity of $V = 22$ mm/s. This is a simulation of the Al_2O_3/TiC of the head material sliding on a-C:H film coated on the magnetic recording disk in the hard disk drive (HDD).

4.1 Triboelectron Emission and Friction

Figure 7 shows the intensity of the triboelectron emission (I^-) and friction coefficient (f) as a function of the sliding distance (l) in the sliding contacts of the Al_2O_3 ball on the glass substrate (Fig. 7a) and that on a-C:H film with $C_H = 37$ at. % (Fig. 7b) [34]. It is seen that glass emits only a negligibly small number of electrons in spite of such a high friction coefficient (average 0.7), while a-C:H film with $C_H = 37$ at. % intensely

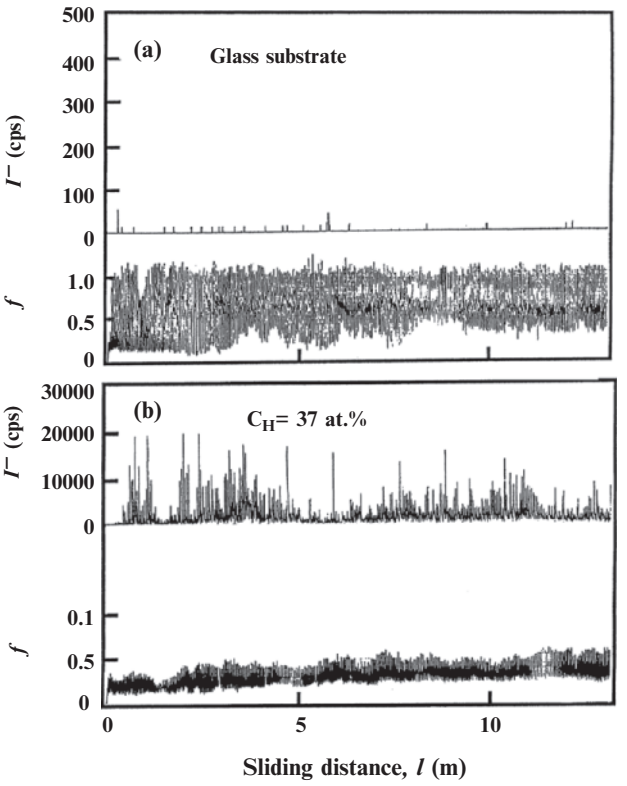

Fig. 7 Dependence of electron emission, I^-, and friction coefficient, f, on sliding distance in glass substrate (*above*) and hydrogenated carbon film with hydrogen content $C_H = 37$ at. % (*below*) under dry sliding in vacuum

emits electrons in bursts in spite of a much lower friction coefficient than that of glass (friction is not the direct controlling factor of triboelectron emission).

Figure 8 shows the dependent nature of electron emission (I^-) and the friction coefficient (f) on the hydrogen content (C_H) in the carbon film [35]. The I^- and the f slightly decreased in the region of $0 < C_H < 20$ at. % (Regime I) increased steeply in the region of 20 at. % $< C_H <$ 32 at. % (Transition regime) and decreased gradually at 32 at. % $< C_H$ (Regime II) with an increase in C_H. It is noted that I^- and f strongly depend on C_H and that both transit from low values to high values at almost the same C_H value, and f increased by double, but I^- increased by 10^2–10^4 times in the transition from regime I to regime II. However, when we carefully compare the two curves of I^- and f, we will find that no good correlation between them exists, especially in regime II, where f is kept constant but I^- decreases with C_H. Further, in the transition region, it was observed that I^- suddenly increased at a certain sliding distance, though f is kept almost constant (the figure is not shown here) [36]. This is because, I^- is concerned with the fresh worn surface and the electric resistivity (ρ), while f originates from the shearing of the real area of contact. However, f indirectly affects I^- through affecting the wear mode change, as seen below.

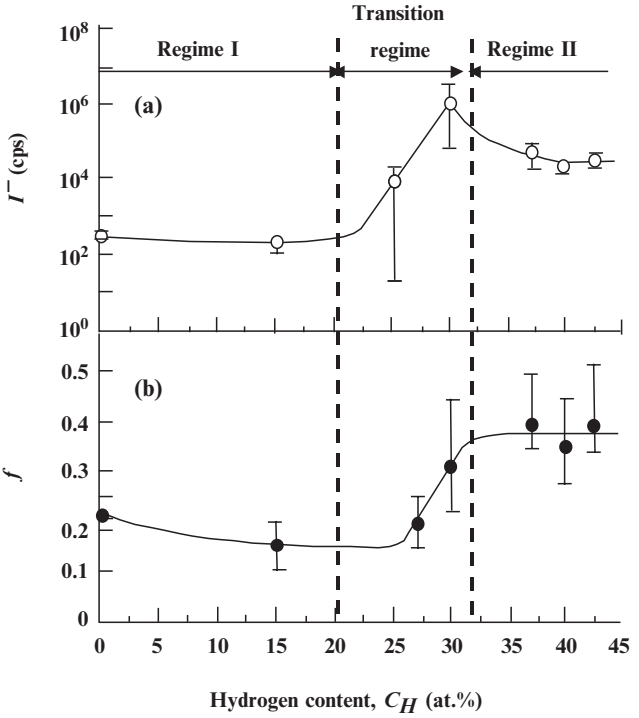

Fig. 8 Dependence of electron emission intensity, I^- (a), and friction coefficient, f (b), on hydrogen content in carbon film, C_H, under dry sliding in vacuum

4.2 Triboelectron Emission and Wear

To determine the reason for the transition of the triboelectron emission from low to high values, the wear mechanism of the a-C:H films was investigated by observing the wear track surfaces using atomic force microscope and secondary electron microscope at various C_H at. % in the carbon films after the sliding experiments (Fig. 9) [37].

At C_H = 0 at. % in regime I, straight cracks are formed parallel to the sliding direction together with film flaking (or delamination) and flaking away as indicated by arrows "a" and "b," and "c," respectively, but the surfaces between the cracks were very smooth, as if there was no wear, as seen in Fig. 9a. However, the atomic force microscopy (AFM) image showed small, straight, grooved wear having depths of several to tens of nanometers, as seen in Fig. 9b. This extremely low wear was attributed to the lubricious film formed by adsorption of the surrounding gas molecules such as residual H_2O in a vacuum chamber, since the film had the highest surface energy (the lowest contact angle), as shown in Fig. 6a. A fatigue process due to the combined effect of the cyclic normal and tangential stresses produced the cracking, flaking, and breaking of the carbon films. Internal tensile stress initiated normal cracks "a" and "b," while internal compressive stress generated wrinkles due to film flaking, as described below. These wrinkles are due to: (1) the formation of microdelamination cracks initiated at the film/substrate interface, (2) growth to

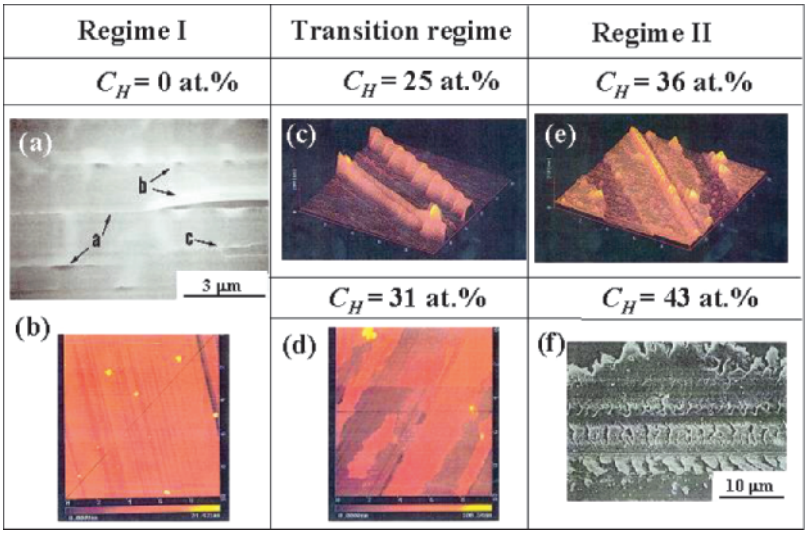

Fig. 9 Secondary electron microscope (a) and AFM (b) images at hydrogen content in carbon film C_H = 0 at. % in regime (I), AFM images at C_H = 25 at. % (c) and C_H = 31 at. % (d) in transition regime, and AFM images at C_H = 36 at. % (e) and C_H = 43 at. % (f) in regime (II) under dry sliding in vacuum

larger delamination cracks through coalescence, (3) delamination of the film from the substrate, and finally (4) being rubbed off as wear debris. In the films with tensile stress, a similar delamination process takes place following the formation of normal cracks [32]. The low electron emission in regime I has been attributed to low wear.

At C_H = 25 at. % in the transition regime, the aC:H film is flaked, forming wavy wrinkles having heights ranging from 100 to 250 nm, as seen in Fig. 9c. As the film at C_H = 25 at. % has the highest internal compressive stress (see Fig. 6b), the relief of the compressive stress flaked the film producing the high wrinkles. These wrinkles were all worn away at and above C_H = 31 at. %, revealing the underlying surface, as seen in Fig. 9d. This increased breaking of the wrinkles at and above C_H = 31 at. % was caused by the increased friction, which resulted from the more weekly bound film due to the decreased surface energy (the increased electron emissions originated from the increased formation of freshly worn surfaces).

The films in regime II have lower internal compressive stress due to a softer polymeric structure and higher friction caused by increased adhesion between two sliding surfaces due to lower surface energy than that at C_H = 31 at. %. In regime II, two kinds of typical wear modes were observed, as seen in Figs 9e and f. One is heavy flaking film and the subsequent breakdown of the flaked film, and the other is crack formation perpendicular to the sliding direction accompanying plastic deformation. In the first wear mode, most of the wavy wrinkles are worn away, but some wrinkles remain without wearing away at C_H = 36 at. %. The lower internal compressive stress plays a major role in retaining the wrinkles without wear. This results in lower triboemission intensities in regime II than those at C_H = 31 at. %. The second wear mode is shown in Fig. 9f (C_H = 43 at. %), which has parallel cracks perpendicular to the sliding direction and plastic deformation. The cracks and the plastic deformation must be caused by the same process as in brittle materials, and the soft polymeric nature at high C_H in regime II, respectively.

Two kinds of triboelectron emission mechanisms of chemically induced emission and triboplasma exist, both of which are concerned with gas, as stated above. A gas pressure level of 5 mPa is too weak to emit electrons by chemical means and triboplasma. Therefore, only noise-level electron emission is observed in the glass substrate in spite of the high friction shown in Fig. 7a. On the other hand, triboelectron emission from a-C and a-C:H films was definitely and intensely detected even in such vacuum, as shown above. The reason of the intense electron emission from the a-C and a-C:H films in vacuum is not clear. One plausible mechanism is giving off some gases or gaseous products during crack formation, flaking and breaking off of the films, and the subsequent plasma generation due to discharging of the evolved gas, though it is unlikely that substantial amounts of gasses are stored interstitially in a hard coating process. Otherwise, it is difficult to explain the increased electron emission phenomena in a-CH films with higher C_H having higher electric resistivity.

5 Triboemission from A-C:H Films in Ambient Air

A specially invented charge detector measured tribocharged particles in ambient air [6], while tribophotons were detected by a photomultiplier (PMT), which is sensitive to the wavelengths of 399–650 nm. Triboemission of negative and positive particles was measured during sliding a diamond hemispherical pin with a radius of $r = 300\,\mu m$ on a-C and a-C:H films under $F_N = 0.2\,N$ and $V = 5.2\,cm/s$ in ambient air with a relative humidity of 52–53%, while the tribophotons were measured in a tribosystem of a diamond pin having an included angle of 90° and a tip radius of $r = 100\,\mu m$ in a dry air atmosphere with a gas pressure of 1×10^5 Pa under $F_N = 0.2\,N$ and $V = 4.4\,cm/s$. These particles were sampled every 100 µm.

5.1 Triboemission and Hydrogen Content

The tribocharging-induced surface potential (tribopotential, U) was too weak to be observed at low hydrogen content in a region of $C_H \leq 15$ at. %, while it was definitely detected in a region of 12 at. % $< C_H$. The value of U increased with C_H, since the electric resistivity increases with C_H (see Fig. 4). On the other hand, the emissions of both the negative and positive particles were clearly observed for all a-C and a-C:H films. However, photons were detected only in the region of $C_H > 15$ at. %.

Figure 10 shows the charge intensity of the negative and positive particles and photons accumulated for 1,000 ms, I^-, I^+, and I_{hv} (a), the charge ratio of the emission intensity of the negative particles against the positive particles, I^-/I^+ (b), and the friction coefficient f (c) as a function of C_H in the carbon film [6,8]. The value of I^- is almost a low constant in the region of $C_H = 0$–15 at. %. But it increases steeply to higher values in the regime of 15 at. % $< C_H <$ 37 at. % and then is saturated in the region of 37 at. % $< C_H$. The value of I^+ is one order of magnitude weaker than that of I^- at $C_H = 0$ at. %. It increases slowly in the region of $0 < C_H <$ 15 at. %, sharply increases in the region of 15 at. % $< C_H <$ 37 at. %, and is then saturated at $C_H >$ 37 at. %. The value of I^- is much higher than that of the positive particles at $C_H = 0$, as seen in Fig. 10a. However, the difference between the two curves of the negative and positive particles becomes smaller and smaller with C_H (Fig. 10a), that is, the charge ratio, decreases from $I^-/I^+ = 12$ to $I^-/I^+ \approx 1$ with the increase of C_H (Fig. 10b). On the other hand, photon emission was only observed above $C_H = 15$ at. % and the photon emission intensity (I_{hv}) increases sharply with C_H as in the charged particles. So, transition from low to higher values occurs in the region of 15 at. % $< C_H <$ 37 at. % in both the charged particles and the photons. A similar transition of the friction coefficient occurs from low to high in almost the same transition region as that of the triboemission phenomena. Tribocharging-induced surface potential was also generated and increased in the same C_H region.

The triboemission increase with C_H in Fig. 10a is caused by the generation of triboplasma due to discharge in ambient air with an increase in the electric resistivity of a-C:H films with C_H, as discussed below. So these features in Fig 10a and c are similar to those in Fig 8a and b.

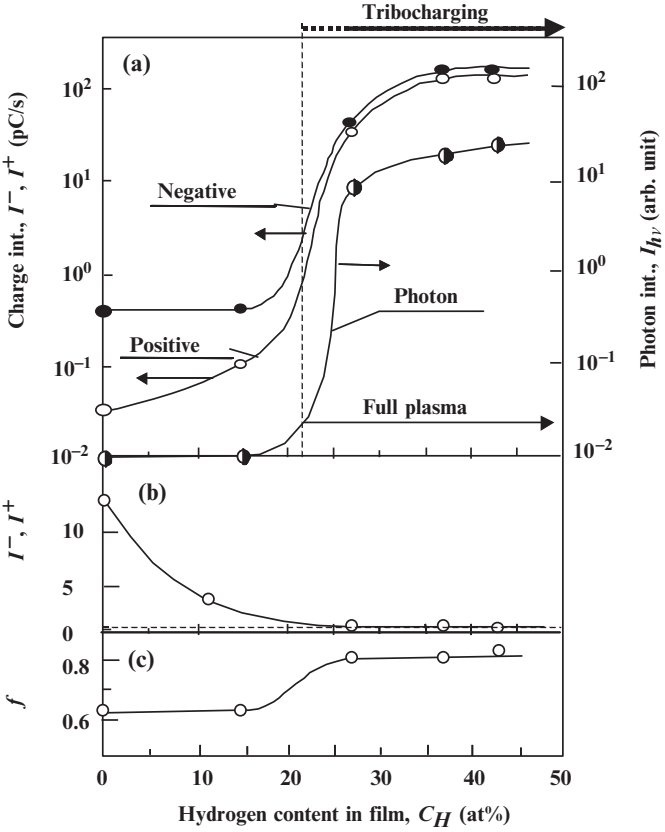

Fig. 10 Relations among negative and positive charges and photon emission intensity, I^-, I^+, I_{hv} (a), ratio of negative to positive charge emission intensity, I^-/I^+ (b), and friction coefficient, f (c), in regard to hydrogen content in carbon film C_H under dry sliding in ambient air

5.2 Triboemission and Electric Resistivity

Figure 11a shows I^-, I^+, and I_{hv}, against electric resistivity ρ, while Fig. 11b shows I^-/I^+ against ρ. Both the graphs in Figure 11a and b are very similar to those of Figs 2 and 3, respectively [6,8]. This clearly demonstrates that the sharp increase in these particle emissions and the decrease in the charge ratio with C_H in Figs 9a and 10b are due to the tribopotential caused by the increase in the electric resistivity with C_H. In the region of $\rho > \sim 10^5$ Ω cm (C_H = 23 at. %), electrons are highly accelerated to cause the plasma in air, emitting photons together with the charged particles (*spark discharge*). In this region, *full plasma* is generated, having the same number of electrons and positive ions. On the other hand, in the region $\rho < 10^5$ Ω cm, the tribopotential is not enough to accelerate the electrons to cause the spark discharge, so no photons are observed, i.e., a *dark emission* occurs.

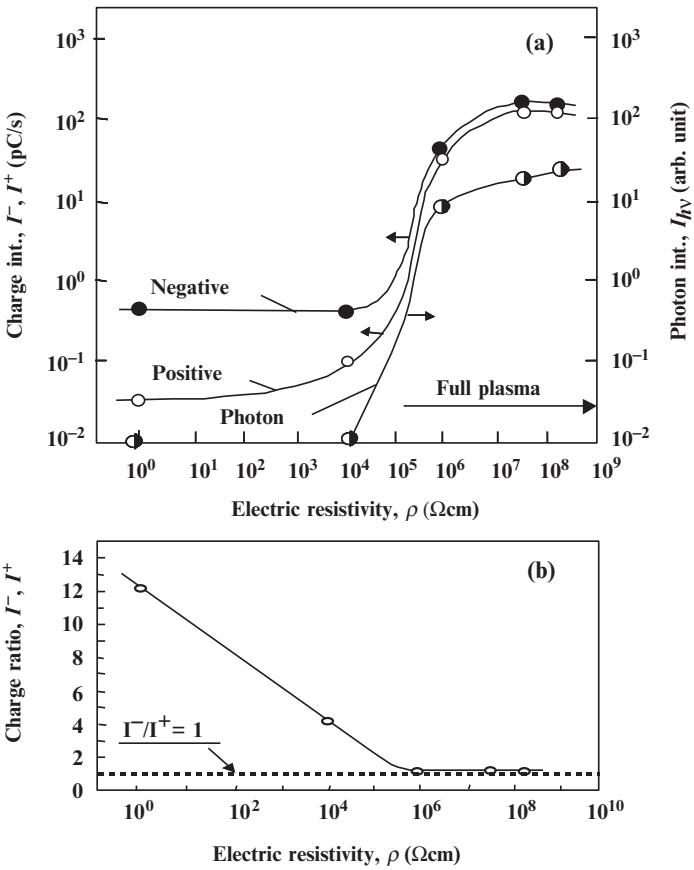

Fig. 11 Relations among negative and positive charges and photon emission intensity, I^-, I^+, I_{hv} (a) and ratio of negative to positive charge emission intensity, I^-/I^+ (b) in regard to electric resistivity of hydrogenated carbon film, ρ_H, under dry sliding in ambient air

The shape of the curve in Fig. 11a is very similar to that of Fig. 10a. This is because the relation between ρ_H and C_H is almost linear on a semilogarithmic scale in the region of 5 at. %, < C_H as described above in Fig. 4.

6 Triboemission Under Oil Lubrication

Triboemission of negative and positive particles, surface tribopotential, and friction were measured in a tribosystem of a diamond hemispherical pin having an included angle of 90° and a tip radius of 300 μm sliding on aC:H films under perfluoropolyether (PFPE) oil lubrication, under $F_N = 0.2$ N and $V = 5.2$ cm/s. The PFPE (market

name: *Z-dol*) molecules have the structure $HO–CH_2–(CF_2CF_2O)_m–(CF_2O)_n–CH_2–OH$ and a molecular weight of 2,000.

Figure 12 shows the effect of the C_H values on (a) the I^- and I^+ values, (b) the I^-/I^+ values, and (c) f, under PFPE oil-lubricated conditions [8]. For comparison, those of dry sliding are also plotted in the same figure. It is clearly seen that the features of I^- and I^+ under PFPE oil lubrication are similar to those in dry sliding, though the values of I^- and I^+ under PFPE oil lubrication are 1 ~ 2 orders of magnitude lower than those in dry sliding. Both the I^- and I^+ values first increase slowly after passing a small minimum, then increase steeply in the region of 15 at. % < C_H < 37 at. % and saturate or decrease after reaching a maximum in the region of 37 at. % ≤ C_H, respectively. The arrows in PFPE oil lubrication at C_H = 43 at. % show that the number of the charged particles increases with repeated sliding. It is also seen that the I^- values are always greater than the I^+ values under PFPE lubrication, as observed in dry sliding.

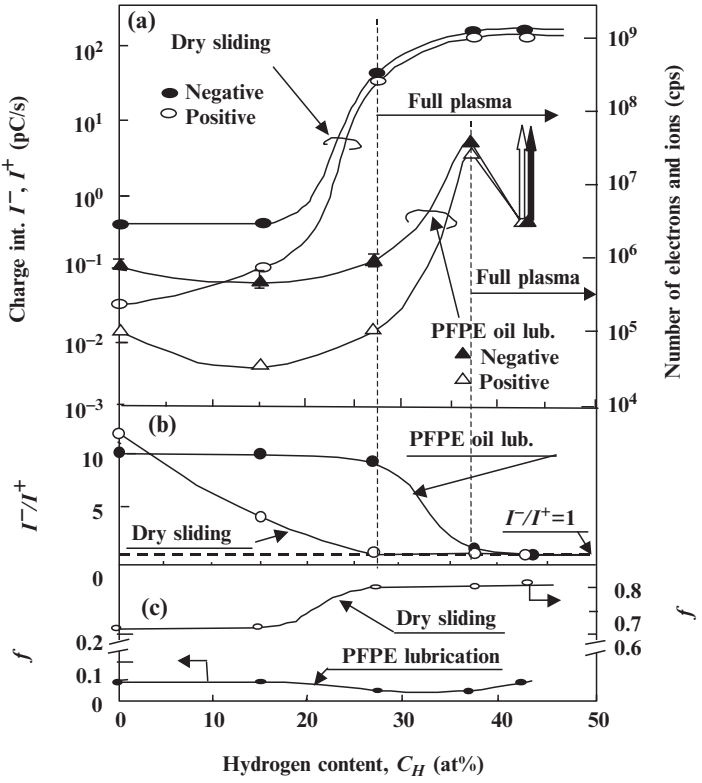

Fig. 12 Relations among negative and positive charge emission intensity, I^-, I^+ (a), ratio of negative to positive charge emission intensity, I^-/I^+ (b), and friction coefficient, f (c), in regard to hydrogen content in carbon film, C_H, under dry sliding in ambient air and PFPE oil lubrication

The charge ratio (I^-/I^+) under PFPE oil lubrication is initially almost constant in the region of $0 < C_H < 27$ at. % and then decreases to approach $I^-/I^+ = 1$ with increasing C_H, as in dry sliding.

The friction coefficient (f) under PFPE oil lubrication was much lower than that of dry sliding. However, the most interesting feature under oil lubrication is that friction decreases to a minimum and then increases [7], while triboemission increases to the maximum and then decreases in the region of 15 at. % $< C_H <$ 43 at. %. This feature is completely different from that in dry sliding, where both triboemission and friction transit from low to high values with C_H. This result demonstrates again that the main cause of triboplasma is not due to friction force. From the point of view of frictional energy loss, the hydrogen content around $C_H = 30$ at. % is ideal, but this hydrogen content is undesirable for protecting lubricating oil degradation by triboplasma [12]. The dependent nature of I^-, I^+, and I^-/I^+ on ρ_H under PFPE oil lubrication was similar to that under dry sliding [8], i.e., I^- and I^+ increase and I^-/I^+ decreases, approaching $I^-/I^+ = 1$ with ρ_H.

7 Triboemission in a-C:N Films

It has been observed that full plasma is generated at $C_N > 25$ at. % and $C_H > 13$ at. % for a-C:N and a-C:H films, respectively, and that triboelectron emission intensity (I_N^-) of a-C:N film is much lower than that of a-C:H film in the plasma region [15–18]. This is because a-C:N film has much lower electric resistivity than a-C:H film to generate triboplasma, as seen in Fig. 4. As plasma generation is a function of surface tribopotential and, in turn, of electric resistivity, the I_N^- and I_H^- values in the plasma regions are plotted against ρ_N and ρ_H values in Fig. 13. The I_N^- and I_H^- values increase roughly linearly in a single line with electric resistivity ρ_H and ρ_N, even in different kinds of DLC films. From the point of view of the triboplasma degradation of the lubrication oil molecules, nitrogenated amorphous carbon films are recommended for use in tribology.

8 Triboplasma Generation in ta-C Films

In the above sections, it has been described and discussed that triboplasma is generated in a-C:H and a-C:N films with high electric resistivity. As ta-C film has an insulating nature, triboplasma is also generated. Figure 14 shows the two-dimensional plane images of the total (UV, visible, and IR) photons emitted from a tribosystem of ta-C film coated with a thickness of 100 nm on a ruby ball (diameter = 6 mm) sliding on a sapphire disk in a dry air atmosphere with a gas pressure of 1,000 mBar under $F_N = 0.5$ N and $V = 25$ cm/s (K. Nakayama, C. Matta and J. M. Martin, unpublished

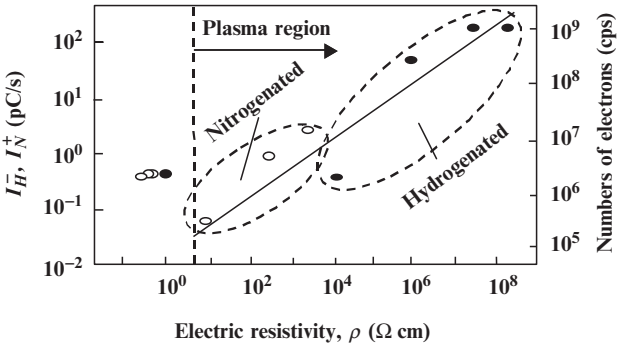

Fig. 13 Relation between negative charge emission intensity from hydrogenated and nitrogenated carbon films, C_H, C_N, and electric resistivity of carbon film ρ_H, ρ_N under same experimental condition as that in Fig. 14

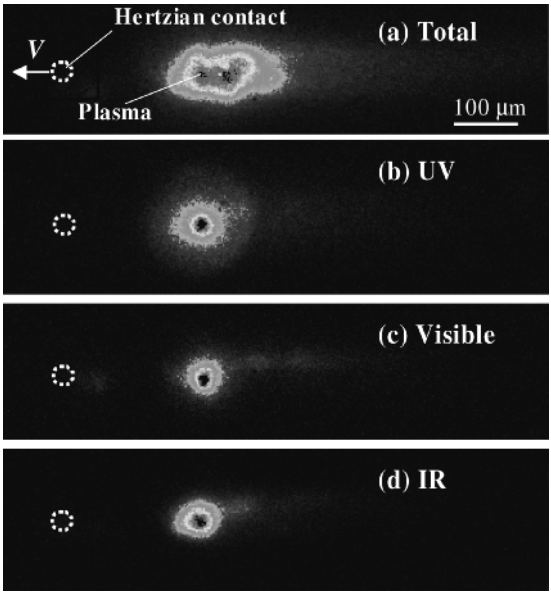

Fig. 14 Two-dimensional plane images of total (a), UV (b), visible (c), and IR (d) photons emitted from sliding contact of ta-C film coated on ruby ball and sapphire disk under dry sliding in dry air atmosphere

data). The UV, visible, and IR plasma images were measured by inserting the UV, visible, and infrared IR transmittance filters between the optical microscope and the intensified charge coupled device (ICCD) camera. The details of the experimental procedure are described in a previous paper [4,5]. You can see the clear plasma image

generated in the rear part of the sliding contact, separated about 200 μm from the contact, and emitting UV, visible, and IR photons.

9 Concluding Remarks

The characteristics of triboemission and triboplasma generation with DLC films have been reviewed. Electrons and ions are emitted from the sliding contact when DLC film was used as a sliding partner with and without accompanying photon emission at films having lower and higher electric resistivity, respectively. The triboemission intensity increases with hydrogen content. This is because with an increase in the hydrogen content the electric resistivity increases. The high electric resistivity in turn causes greater tribocharging, which generates more intense triboelectric fields in the gap of sliding contact to cause more intense triboplasma, which emits electrons, ions, and photons. Triboemission occurs in a vacuum, in ambient air, and under oil lubrication in DLC films. Under dry sliding both triboemission and friction increase with an increase in the hydrogen content, but under oil lubrication, triboemission becomes maximum when friction becomes minimum. Nitrogenated carbon film has a lower electric resistivity and in turn lower triboemission and lower plasma generation compared to hydrogenated carbon films. So from the point of view of triboplasma oil degradation, nitrogenated amorphous carbon film is preferable. Tetrahedral amorphous hydrogen-free carbon film also generates triboplasma because of its insulating nature.

As the high energetic triboplasma forms beneficial lubricious tribochemical films or causes harmful degradation of lubricant molecules, respectively, depending on the tribosystem in various machines and processing under dry and oil lubricated sliding, it is essential to control the plasma generation in developing new advanced triboplasma technologies. For the plasma control, coating by DLC film is clearly a useful method, since the plasma generation depends greatly on the composition of the DLC film as described above. So the DLC coating will play an important role in the development of new advanced tribology technology from the point of triboelectromagnetic phenomena.

References

1. K. Nakayama, N. Suzuki, H. Hashimoto, Triboemission of charged particles and photons from solid surfaces during frictional damage, J. Phys. D: Appl. Phys. 25, 303–308 (1992).
2. K. Nakayama, J. A. Leiva, Y. Enomoto, Chemi-emission of electrons from metal surfaces in the cutting process due to metal/gas interactions, Tribo. Int., 28, 507–515 (1995).
3. K. Nakayama, Microplasma generation in polymers and ceramics in different atmospheres, Proc. Asiatrib. JAST, Kanazawa, Japan 2, 767–768 (2006).
4. K. Nakayama, R. A. Nevshupa, Plasma generation in a gap around a sliding contact, J. Phys. D.: Appl. Phys. 35, L53–L56 (2002).

5. K. Nakayama, Plasma generated and photons emitted in an oil lubricated sliding, J. Phys. D. Appl. Phys. (Submitted).
6. K. Nakayama, B. Bou-Said, H. Ikeda, Triboelectromagnetic phenomena of hydrogenated carbon films – triboelectrons, -ions, -photon, and –charging, ASME J. Tribol. 119, 764–768 (1997).
7. K. Nakayama, S. Nguyen, Triboelectromagnetic phenomena in a diamond/hydrogenated-carbon-film tribosystem under perfluoropolyether fluid lubrication, Appl. Surf. Sci. 158, 229–235 (2000).
8. K. Nakayama, Triboemission of electrons, ions, and photons from diamondlike carbon films and generation of tribomicroplasma, Surf. Coat. Technol. 188–189, 599–604 (2004).
9. K. Nakayama, Tribophysical phenomena and tribochemical reaction, Jpn J. Tribo. 42, 1077–1084 (1997).
10. K. Nakayama, H. Matamura, Mater. Res. Symp. Proc. 872 J18.24.1–J18.24.6 (2005).
11. K. Nakayama, H. Hashimoto, Triboemission, tribochemical reaction, and friction and wear in ceramics under various n-butane gas pressure, Tribo. Int. 29, 385–393 (1996).
12. K. Nakayama, Verification of the decomposition of perfluoropolyether fluid due to tribomicroplasma, 49, pp.17–25 (2006).
13. K. Nakayama, Triboemission of charged particles and resistivity of solids, Tribo. Lett. 6, 37–40 (1999).
14. K. Nakayama, H. Hashimoto, Triboemission of charged particles and photons from wearing ceramic surfaces in various gases, Tribo. Trans. 35, 643–650 (1992).
15. K. Nakayama, T. Fujimoto, The energy of electrons emitted from wearing solid surfaces, Tribo. Lett. 17, 75–81 (2004).
16. V. S. Kortov, R. I. Mints, I. E. Myasnikov, P. Gaprindoshvily, Energy distribution of exo-electron emission in the dark at low temperature, Phys. Sta. So. A3, K13–K15 (1970).
17. J. Loff, Die Energieverteilung der Elekronenemission mechanisch bearbeiteter Metaloberflaechen, Z. Naturforschg. 12a, 267–268 (1957).
18. W. R. Harper, Contact and frictional electrification, Clarendon Press, Oxford, pp. 50–75 (1967).
19. J. Latham, Electrification produced by the asymmetric rubbing of ice on ice, J. Appl. Phys., 14, 488–490 (1963).
20. M. I. Kornfeld, Frictional electrification, J. Phys. D: Appl. Phys. 9, 1183–1192 (1976).
21. T. Oguchi, M. Tamatani, Contact electrification in inorganic binary compounds, J. Electrochem. Soc. 133, 841–847 (1986).
22. A. J. P. Martin, Triboelectricity in wool and hair, Proc. Phys. Soc. 53, 186–189 (1941).
23. B. Phair, L. Bensch, J. Duchowsky, M. Khazan, V. Tsalyuk, Overcoming the electrostatic discharge in hydraulic, lubricating and fuel-filtration applications by incorporating novel synthetic filter media, Tribo. Int. 48, 343–351 (2005).
24. T. J. Harvey, R. J. K. Wood, G. Denuault, H. E. G. Powrie,Investigation of electrostatic charging mechanism in oil lubricated tribo-contacts, Tribo. Int. 35, 605–614 (2002).
25. K. Nakayama, R. A. Nevshupa, Characteristics and Pattern of Plasma generated at sliding contact, Trans. ASME: J. Tribo. 125, 780–787 (2003).
26. K. Nakayama, R. A. Nevshupa, Effect of dry air pressure on characteristics and patterns of triboplasma, Vacuum 74, 11–17 (2004).
27. K. Nakayama, H. Hashimoto, Effect of surrounding gas pressure on triboemission of charged particles and photons from wearing ceramic surfaces, Tribo. Trans. 35, 35–42 (1995).
28. H. Tsai, D. G. Bogy, Characterization of diamondlike carbon films and their application as overcoat on thin-film media for magnetic recording, J. Vac. Sci. Tech. A5, 3287–3312 (1987).
29. D. Beerman, J. Silverman, R. Lynds, M. R. Anderson, Modeling studies of amorphous carbon, Phys. Rev. B30, 870–875 (1984).
30. J. Robertson, E. P. O, Reilly, Electronic and aromatic structure of amorphous carbon, Phys. Rev. 35, 2946–2957 (1987).

31. J. H. Kaufman, S. Metin, Symmetry breaking in nitrogen-doped amorphous carbon: infrared observation of the Raman-active G and D bands, Phys. Rev. B 39, 13053–13060 (1989).
32. A. C. Ferrari, J. Robertson, Interpretation of Raman Spectra of disordered and amorphous carbon, Phys. Rev. B61, 14095–14107 (2000).
33. G. Abrasonis, R. Gago, Phys. Rev. B73, 125427-1–125427-13 (2006).
34. K. Nakayama, H. Ikeda, Triboemission characteristics of electrons during wear of amorphous carbon and hydrogenated amorphous carbon films in a dry air atmosphere, Wear 198, 71–76 (1996).
35. K. Nakayama, K. Yamanaka, H. Ikeda, T. Sato, Friction, wear, and triboelectrons emission of hydrogenated amorphous carbon films, Tribo. Trans. 40, 507–513 (1997).

Doping and Alloying Effects on DLC Coatings

J. C. Sánchez-López and A. Fernández

Abstract Doped or alloyed diamond-like carbon (DLC) coatings is an important category of DLC characterized by the incorporation of different elements in their structure to achieve multifunctionality and improved properties in respect to pure DLC films. By controlling the nature, content and distribution of the dopants, tailored synthesis of doped-DLC with properties adapted to a desired value for specific applications can be obtained. Common dopants are light elements (B, Si, N, O or F), metals and combinations thereof to modify properties such as hardness, tribological properties, internal stress, adhesion, electrical conductivity or biocompatibility. The purpose of this chapter is to provide an overview of the different alloyed-DLC and more novel nanostructured coatings reported in the literature in relation with the property of interest. The tribological properties will be discussed in light of their chemical composition and microstructure trying to obtain general trends or correlation between them when possible due to the high number of parameters influencing their practical tribological response.

Keywords diamond-like carbon, doped-DLC, alloyed-DLC, Me-DLC, CN_x, wear, friction, tribology, lubrication

1 Introduction

Diamond-like carbon films (DLC) have found a wide range of applications in recent years owing to their unique properties. High-quality DLC films can have hardness and coefficient of friction comparable to that of diamond, leading themselves to exciting applications pertaining to tribological surface coatings. Some interesting review articles have been published by Grill [47–49], Bull [10], Donnet [28], Lifshitz [82], Erdemir and Donnet [33], Robertson [108], Hauert and Müller [58]and Hauert [57]. Figure 1 presents schematically

Instituto de Ciencia de Materiales de Sevilla (CSIC-Universidad de Sevilla), Avda. Américo Vespucio 49, 41092 Sevilla, Spain.

C. Donnet and A. Erdemir (eds.), *Tribology of Diamond-Like Carbon Films: Fundamentals and Applications*.

different possibilities of doping DLC with different elements such as Si, F, N, O, and metals (and combinations thereof) to modify their nature and properties and still maintaining the amorphous phase of the coating. By this way, different film properties such as thermal stability, hardness, internal stress, tribological properties, electrical conductivity, surface energy and biocompatibility can be continuously adapted to a desired value for specific applications. In the last two decades several hundred papers have been published on the changes of different properties of a-C:H when alloyed or doped with different elements. The modified DLC films are deposited by the same techniques as the regular films by adding species containing the modifying elements to the environment and details can be found in Chapter 2. Although some general correlations between the basic parameters and the final performance of the coating are known there is still a lack of correlation between basic properties and microstructure and the real performance of the coating in a technical or biological application. Besides, it is usually difficult to predict the influence of an alloyed element on the final response, especially in the case of tribology where the final properties are controlled by a non-linear interaction of several different parameters.

The extremely low wear rates, in the order of 10^{-9} mm^3 Nm^{-1}, which can be found in DLC coatings, are generally attributed to the combination of high hardness and low friction coefficient. Unfortunately, there is a very large compressive stress

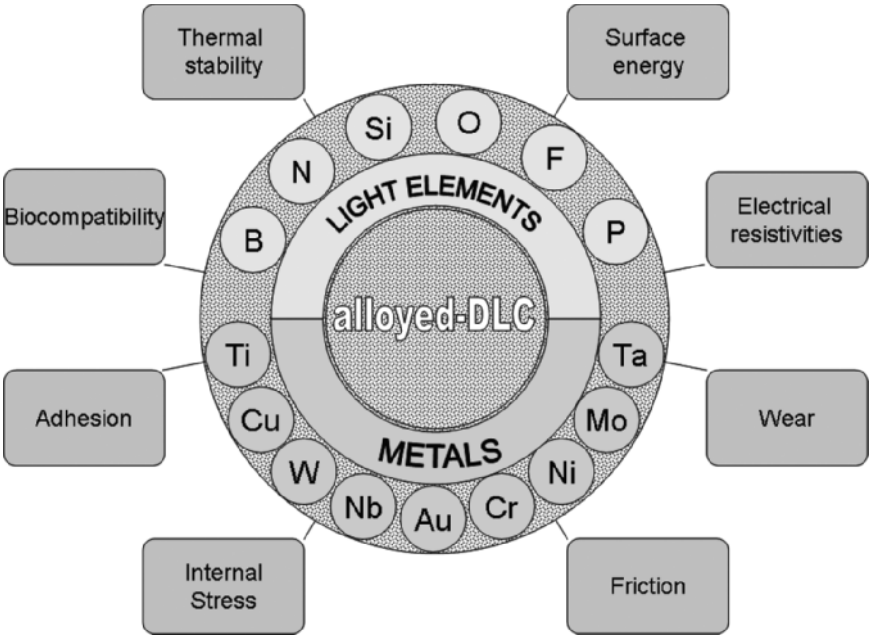

Fig. 1 Scheme of typical doping elements introduced into the DLC compositions for achieving improved properties

in DLC films that exists irrespective of thin film growth technique, such as magnetron sputtering, pulsed laser deposition, ion beam deposition, etc. This large compressive stress, when accumulates to a certain level, causes the film to bulge and peel off from the substrate, thus restricting the applications for thin DLC films. Therefore, elimination or minimization of compressive stresses in DLC films offers a major challenge for technological applications of DLC coatings. Traditional approaches to obtain DLC films with low internal stress involved increasing deposition temperature or decreasing the energies of carbon species arriving at the substrate surface. Unfortunately, all these are achieved at the expense of reducing sp^3/sp^2 ratio. Actually, the elimination or minimization of compressive stresses in DLC films by alloying with metals and the use of metallic interlayers between the film and the substrate have been currently extended to reduce the compressive stress in the DLC films. In other words, in many practical applications other requirements are imposed to the coating as anti-sticking properties or tailored surface energies; these are obtained by introducing light elements as Si, O, N or F.

The purpose of this chapter is to provide an overview of the different alloyed DLC coatings reported in the literature. It will also summarize those experimental studies which concentrated on the properties modified or applications foreseen for such DLC coatings. The chapter is divided into four main sections addressing the different nature and modulation of the alloying elements in these films. Specifically, Section 2 is devoted to the incorporation of light elements such as B, Si, N, O or F. Due to the special relevant numbers of publications related to N-containing C-based films, a special section is devoted to N-doped a-C:H films and alloyed CN_x coatings (Section 3). In Section 4, the main emphasis is placed on the contributions regarding metal-containing DLC films and the last part of our chapter presents some emerging advanced nanostructured systems that may be considered as modified DLC whose functionality is obtained through chemical and microstructural modulation at a nanometre scale (Section 5). For each chapter the description of the main results is grouped by a property of interest placing emphasis on the tribological properties.

2 Doping with Light Elements (F, O, N, Si)

2.1 Tribological Properties

F and Si containing DLC films can be prepared to be as wear-resistant as the pure hydrogenated DLC [50]. Furthermore, Si incorporation in DLC can render its friction against steel and the wear of the steel counterpart insensitive to moisture [43]. The combination of silicon and fluorine doping of DLC has been achieved by Miyake et al. [93]. The microtribological behaviour on an atomic scale of the Si-containing film was further improved by fluorination while the adhesion to the substrate and strength of the carbon is greatly improved by adding small quantities of silicon. For magnetic recording media,

the friction has to be further reduced by applying lubricants on the top surface of the protective DLC coating. It was shown that surface fluorination can reduce the friction and microwear of DLC [128]. Other works have used fluorinated hydrocarbons or their mixtures with hydrocarbons or hydrogen to deposit fluorine-containing DLC films by RF PACVD [21]. Nevertheless, whereas the addition of silicon introduces a high amount of hydrogenated carbon in the film composition, the deposition with fluorine increase the presence of $–CF_2$ and $–CF_3$ groups that reduce the density of the network structure [56]. This reduction in network cross-linking leads to a diminution in hardness and wear resistance, especially when increasing F concentration [52, 149]. Donnet et al. [29] has studied how to control the wear rate of F-DLC films by appropriate selection of the growing conditions (average impact energy of the ions, precursor, diluting gas). Wear rates comparable to those observed to non-fluorinated DLC films can be obtained for films up to 20 at. % and sufficient dilution with hydrogen at the highest deposition bias and lowest gas pressure. Highly fluorinated DLC [F/(F + C) > 0.4] appear to be soft with no wear resistance. Moderate fluorination [F/(F + C) < 0.2] can be controlled by deposition conditions to obtain films with a comparable wear resistance and friction level than conventional DLC films, but with a lower degree of stress and surface energy.

Miyake [92] has elucidated the complex frictional behaviour of the investigated F-DLC films in ambient air by ex situ infrared (IR) measurements. In the steady-state the friction stabilizes at 0.20. It was found that the halogenated carbon framework decomposed into carbonaceous chains of reduced molecular size and fluorinated C=C moieties, such as polydifluorinatedacetylene (PDFA), that were oriented in the sliding direction as seen by polarized IR probe. These films exhibited a more cross-linked structure with a lower fraction of unbound fluorine and higher compressive stresses, compared to less wear-resistant films. Contrary to wear, friction appears to be independent of the bias and gas pressure within the studied range, but depends very much on the contact pressure during friction.

Alternatively, the co-alloying of B and F with DLC to produce films with a combination of high hardness and hydrophobic properties has been proposed recently based on the suppressing effects on the sp^2 graphitic cluster formation and hydrogen incorporation of B and F dopants, respectively. He et al. (2005) deposited BF-DLC films by plasma immersion ion processing (PIIP) method on transparent polymer substrates. By maintaining the B concentration in the range 3.8–6.0 at. % and F content in the range 6.0–17.7%, coatings can exhibit hydrophobicity as high as Teflon (contact angles of ~83°) while maintaining a hardness of 15 GPa (only 3–5 GPa below unalloyed DLC film). Unfortunately, no tribological results were reported for the co-alloyed BF-doped DLC. The enhanced properties are attributed to the F–C and B–C hybridized bonds produced during PIIP synthesis of the FB-DLC films.

From a technological point of view, a low and stable coefficient of friction across a wide range of relative humidity is of particular relevance in some applications. Especially in the watch industry where a high-precision mechanical chronometre requires a constant friction value, independent of the ambient humidity, ensuring

accuracy of the time displayed. A major disadvantage of DLC is the deterioration of its lubricating properties at high relative humidity, limiting its use in certain tribological applications. The incorporation of silicon has been widely studied and reported as being effective in reducing friction coefficient in ambient humid air to below 0.1, with a limited deterioration of the wear resistance. This was first shown by Oguri and Arai [99] and later by Meneve et al. [88], Gangopadhyay et al. [43] and Wu et al. [145]. Friction appears to be significantly reduced ranging between 0.03 and 0.1 compared to conventional undoped DLC in ambient air conditions, with a comparable high wear resistance. Gilmore and Hauert [45] demonstrated the tailoring of a-C:H films by F and Si incorporation to yield a coating with a low and stable friction coefficient independent of the relative humidity. The dependence of coefficient of friction on the relative humidity can be changed from a positive correlation for pure DLC to a negative correlation if more than 6 at. % silicon is incorporated in the film. This is shown in Fig. 2 where the friction

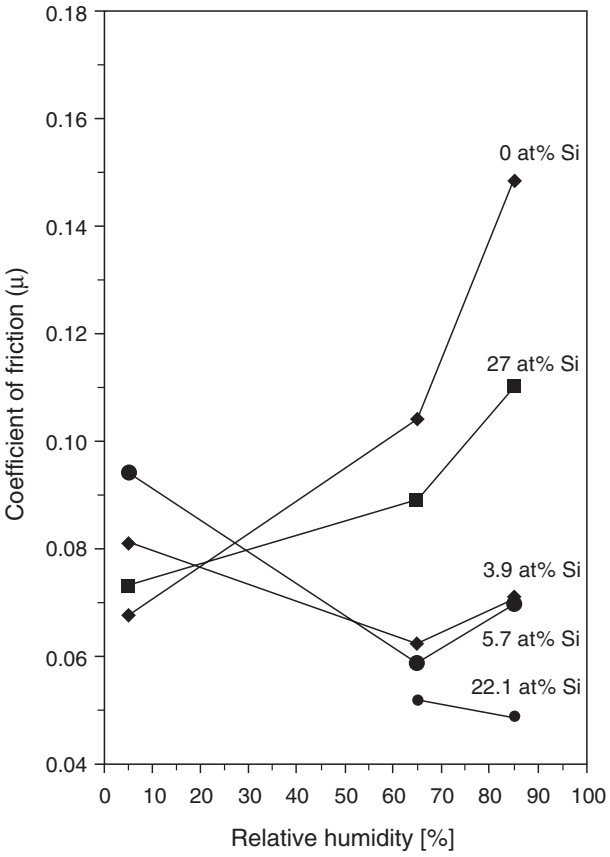

Fig. 2 Variation of the friction coefficients versus the relative humidity for different Si concentrations in a DLC coating. The counterface was a 100Cr6 ball. [44, 45]

coefficient is drawn versus relative humidity for different Si contents in DLC films. At approximately 4 at. % Si-content the friction coefficient is almost independent of the relative humidity, namely 0.072. As a result of the addition of Si the wear rate increased but at 4 at. % it is still low enough to be tolerated in most applications.

The tribological behaviour is attributed to the formation of SiO_2 wear particles and their interaction with the humid environment through tribochemical effects. SiO_2 nanodomains promote the absorption of water with formation of Si–O–OH groups. The formation of this hydrated silica phase at the frictional interface will be responsible for the low friction coefficient measured [90]. Miyamoto et al. [95] achieved ultralow friction (0.007) when the film was rubbed with a steel ball in a high vacuum. Polarized microIR spectroscopy revealed that such a very high lubrication performance was primarily attributed to hydrocarbons transferred from the rubbed film to the ball surface and oriented along the sliding direction [125]. Also, a systematic transfer film build-up was observed in C:Si:O films with a composition (0.8:0.1:0.1) and 10% of H by Hioki et al. [61]. Friction coefficients ranged between 0.04 and 0.07, at relative humidity levels varying from 20% to 70% in air or nitrogen. Ultralow friction values down to 0.02 or less were observed in dry nitrogen. However, this tribological behaviour seems to be observed when the contact pressure remains low enough, that is below 1 GPa. At higher contact pressures, conventional unhydrogenated and hydrogenated DLC films cannot be surpassed. Consequently, Si-doped DLCs may be used in applications requiring both low friction (<0.1) and high wear resistance ($<10^{-7}$ mm^3 Nm^{-1}) under moderate contact pressures and humid conditions, that is, for the protection of low stress aerospace or automotive components, precision ball bearings and gears, sliding bearings and magnetic recording media. For dry conditions, the friction and wear behaviours of pure DLC cannot be surpassed, whatever the contact pressure.

2.2 Surface Energy

Certain applications may require reducing the surface energy but maintaining the high wear resistance. In magnetic storage technology, for example, the incorporation of fluorine changes the surface energy of the a-C:H to prevent stiction of the read–write head in magnetic hard disks without losing the wear resistance [29]. Recently, research has shown that it is possible to prepare hydrophobic DLC films that are hard and have excellent optical properties [62]. [51] showed that incorporation of F, O, N and Si in DLC could modify water-wetting angles. F or Si incorporation increased the contact angle of water (more hydrophobic), while the opposite behaviour is observed with O, N and P (more hydrophilic). The effect of F and Si on the surface energy of DLC films was attributed to the reduction mainly of the polar part of the surface energy, due to the loss of sp^2 C hybridization and dangling bonds. Indeed, since F and Si are unable to form double bonds, it is supposed that these elements force carbon into a sp^3 bonding state. The incorporation of fluorine into DLC films

has so far been the most effective way to improve the hydrophobicity [52, 56], because it is able to reduce the dispersive component as well [51] due to the increment of $–CF_2$ and $–CF_3$ groups that reduce the density of the network structure [149]. It is thus possible to get fluorine-doped films with surface energies comparables (20 mN m^{-1}) to PTFE used for non-stick purposes (18 mN m^{-1}). The use of silicon can provide intermediate values (31 mN m^{-1}) although lower in respect to hydrogenated DLC (43 mN m^{-1}). Simultaneous incorporation of O and Si, especially from a Si-containing monomer, such as hexamethyldysiloxane, was found to have the same effect as F incorporation and reduced the surface energy from 43 to 22 mN m^{-1}.

2.3 Biocompatibility

Due to its bio-haemocompatible nature, there is growing interest in the application of DLC on orthopaedic and other implants [8, 12]. An up-to-date review is also proposed by Hauert in this book. Analogous to the tailoring of the tribological properties of DLC by alloying, the biological properties of DLC can also be altered. As an introduction, see the review article by Butter and Lettington [11]. Especially the manipulation of surface bioreactions by adding adequate elements such as titanium (Ti) or Si into the amorphous a-C:H matrix is expected to result in new fields of application. A desirable achievement is to obtain a bioreactive surface enhancing bone. For example, in the paper of Djouadi et al. [25] the addition of SiO to DLC resulting in a reduced inflammatory reaction on implanted stents is described. Further, Si-containing a-C:H coatings are under evaluation as a special coating for cardiovascular prostheses. In the case of artificial heart valves, the Si in the a-C:H matrix renders the surface antithrombogenicity by inhibiting the fibrinogen activation and phosphorus increases the blood compatibility [79].

3 N-Containing DLC Films

3.1 Doping of DLC with Nitrogen: a-C:N and a-C:H:N Films

3.1.1 General Considerations: Preparation Conditions

PVD methods have been demonstrated to be very effective in the incorporation of nitrogen to carbon films[14, 19, 73, 81, 110, 154]. In particular, standard magnetron sputtering at low sputtering pressures (~3–6 mTorr) of Ar/N_2 mixtures (~3–6% N_2 in Ar) and large substrate pulsed bias (–300 V), are now well-known processes [14, 19, 81] to produce thin nitrogenated carbon films (a-C:N) containing

6–8 at. % of nitrogen in carbon. These films are today used for surface protection of hard disk drivers. Also films prepared by a dual ion beam assisted deposition (DIBAD) system, have been reported for hard disk protection [73]. In this case, the films are prepared by Ar^+ bombardment of a carbon target and simultaneous N^+ bombardment of the growing film reaching nitrogen contents of 10 at. % in this case.

The doping of hydrogenated DLC coatings with nitrogen has been undertaken mainly by CVD methods by adding N_2 and other nitrogen-containing gases to the gas phase [1, 59, 121, 129, 147, 153]. In general, these methods produce low deposition rates due to the formation of volatile species likely of the type HCN and C_2N_2 [65, 67]. [59] showed that for up to 60 at. % nitrogen in the plasma, the incorporation probability of nitrogen is about 1/17 that of carbon. Further, increasing the amount of nitrogen in the plasma drops the nitrogen incorporation probability to 1/44. Even though this method is not suited for preparation of films with high nitrogen contents, they however yield well characterized N-doped films. Amorphous C:H:N films have also been investigated regarding their biocompatibility [147], optical [1] or electrical [121] properties.

3.1.2 Microstructural Characterization

Due to the amorphous character of the non-stoichiometric nitrogen-doped films, a combination of techniques must be used to achieve a full understanding of the microstructural characteristics of these complex films. X-ray photoelectron spectroscopy (XPS) [59] 5, and references therein), IR and Raman spectroscopies [71, 118] and nuclear magnetic resonance (NMR) [112] have been used, among other techniques [136] to analyse these films. Several species have been identified as the main components of the amorphous network: –C–N–; –C=N–; –C≡N–; –C–N= ; –C–NH–C; –C–NH_2; and –N–CH_3, a more detailed analysis of the assignment of major components will be reviewed in Section 3.2.2.

3.1.3 Tribological Behaviour

It is interesting to determine which benefits of N-doping of carbon coatings can offer for friction reduction and wear protection as compared to DLC coatings. The question is somewhat difficult to answer because properties of both DLC and a-C:N are strongly influenced by the preparation method, nitrogen content, chemical and microstructural aspects. Even for the same method, there are property deviations due to different configurations from one deposition system to another. In this section, we present carbon films with nitrogen contents below 10 at. % whilst the next one is

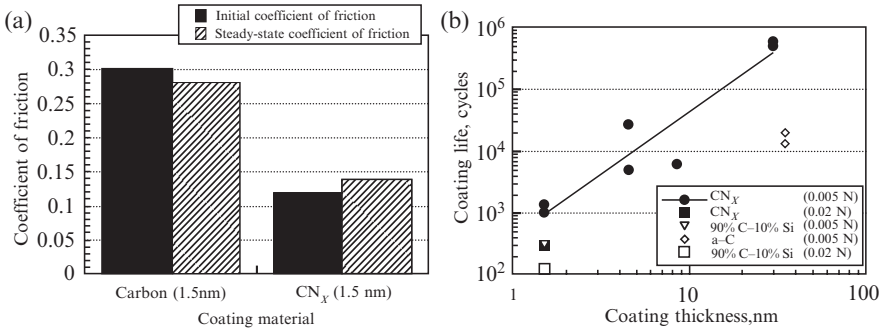

Fig. 3 (a) Friction coefficient of pure and nitrogen-doped carbon coatings sliding against a Si_3N_4 pin under a normal load of 0.02N. (b) Life cycles of pure and nitrogen-doped carbon coatings during sliding against a Si_3N_4 pin. (From [73].)

devoted to the tribology of alloyed C:N films with higher N contents. In the segment of low N contents, nitrogenated amorphous carbon are already replacing DLC as an overcoat for some magnetic disk applications because it provides a combination of good wear resistance and active bonding to surface lubricants [19, 73, 14, 81].

As an illustration of these improvements, Figs 3a and 3b show data on friction coefficient and coatings lifetime for pure and N-doped carbon films as reported by Khurshudov et al. [73]. Lower friction coefficients and about 3–10 times longer life have been found for N-doped ones in comparison to pure carbon coatings [73]. This has found an important niche of application in magnetic storage technology, e.g. hard disks. By adding nitrogen to the a-C:H matrix in the protective overcoat of magnetic thin film rigid disks resulted in improved performance (wear, start-stop cycles, stiction) compared to pure a-C:H [19]. A similar application for DLC coatings is the protection of VCR head drums against wear from the tape by dust and embedded Fe oxide particles [80]. Further development in improving the corrosion resistance may be obtained by filtered arc deposition of ta-C and ta-C:N coatings [109].

Doping with nitrogen has also been reported to reduce residual stress [39, 40] and to improve the thermal stability in carbon films [59]. These improvements are very important for certain technical applications of these films.

3.2 C-N Alloying: CN_X Films

3.2.1 General Considerations: Preparation Conditions

In a series of papers [16, 17, 83] based on some theoretical calculations, Cohen et al. proposed that a carbon nitride phase of the C_3N_4 composition with almost pure covalent C–N bonds (~7% ionicity) and C–N bond distances of 1.47 Å,

should exhibit hardness properties similar to those of diamond. Since this prediction, many works have been carried out to attempt the synthesis of polycrystalline carbon nitride coatings. In most of these works sub-stoichiometric and amorphous CN_x phases have been reported having a carbon nitride-like character with x values covering a wide range of values (from 0.01 to 1.2). Already in 1979 Cuomo et al. reported polymeric C–N films with N/C atomic ratios close to 1.0 as obtained by reactive magnetron sputtering (RF) of carbon targets in a N_2/Ar atmosphere. Since then, numerous studies [2, 6, 7, 46, 84, 98, 106, 107, 120] have been published describing different approaches to grow carbon nitride films using different experimental methods. Except for a few cases [87, 98, 150] which reported nanocrystallites embedded in an amorphous CN_x matrix, the deposits were in most of the cases amorphous (with a maximum nitrogen content of up to 45 at. %), and were always carbon-rich. The ion-assisted deposition methods were the most efficient in terms of nitrogen incorporation and deposition rate. We have discussed in the previous section about the behaviour of coatings with low nitrogen contents (at. % <10) used mainly for hard disk protection applications. In this section, we will discuss the amorphous CN_x coatings with x values higher than 0.10 and reaching values close to 1.0.

3.2.2 Microstructural Characterization

Due to the amorphous and polymeric-like character of the CN_x films, their microstructural and chemical characterization is very difficult. A quite detailed analysis of microstructure and bonding in these films has been reported by Koh and Nakajima [95], Hammer et al. [53], Jiménez et al. [68], Gago et al. [41], Sánchez-López et al. [113], Fernández et al. [35]. In these articles CN_x coatings prepared by magnetron sputtering and ion beam-assisted deposition under different experimental conditions (pure N_2 or N_2/Ar mixtures in the gas phase) have been characterized by ^{1}H-, ^{13}C- and ^{15}N-NMR (see Fig. 4), IR-, x-ray photoelectron-, electron energy-loss- and x-ray absorption spectroscopies.

A structure formed by graphitic CN_x basal planes cross-linked by N or C atoms has been demonstrated. For carbon nitride films grown with dominant nitrogen assistance, the linking sites are nitrogen atoms. For films with a very low nitrogen content grown with dominant Ar^+ ion assistance, the linking sites are carbon sp^3 hybrids. Promotion of both linking sites seems to be competitive and is not obtained simultaneously [41]. It has also been demonstrated that the double-peak structure, frequently observed in the N 1s photoelectron spectra of amorphous CN_x, mainly results from one N participating in aromatic structures (400.2 eV) (N_{arom}, N bonded to two sp^2-C atoms) and another 'non-aromatic' form (398.1 eV) connecting different aromatic microdomains (N_{bridge}, N bonded two three sp^2-C atoms or –NH– bonds) or as terminal groups ($–NH_2$, –C≡N) [35, 112].

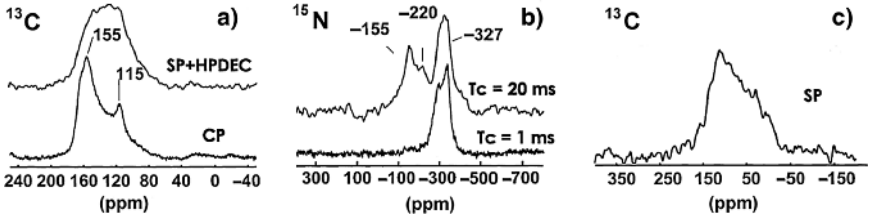

Fig. 4 (a and b) ^{13}C- and ^{13}N-NMR spectra of a CN_x sample prepared in pure N_2 plasma and (c) ^{13}C-NMR spectrum of a CN_x sample prepared in a N_2/Ar plasma. (From [35].)

3.2.3 Tribological Properties

In a similar case to what was observed in DLC coatings, there is a wide dispersion of data regarding tribological and mechanical behaviour of CN_x coatings depending on their stoichiometry, deposition parameters, methodology, etc. Koskinen et al., [76] found steady-state friction coefficient in the range 0.2–0.3 with a tendency to rise with increasing nitrogen content and almost no dependence of the wear rate. Friction coefficients between 0.18 and 0.25 were determined by Kusano et al. [78], the higher values corresponding to the more nitrogenated films. Meanwhile, Czyzniewski et al. [20] gave coefficients of friction of the order of 0.45 and independent of nitrogen content in the gas mixture. In the same way, Zou et al. [155] found that the films deposited at different nitrogen pressures have similar friction coefficients (~0.15) but their wear behaviour varied greatly. Conversely, [142] have reported a friction coefficient decrease from 0.14 to 0.07 for CN_x films when the N/C ratio increases from 0.2 to 0.45.

It is obvious from the previous data that the N/C atomic ratio is not the main factor controlling the tribological behaviour of coatings. In fact the type of bonding and microstructure may play an important role in determining the final properties [111, 115]. In Fig. 5, the variation of the tribological properties of a series of CN_x coatings is shown in ambient air in the order of decreasing N/C content as measured by quantitative EELS. Although an increase in the N/C ratio appears to improve the friction and wear properties, it is not the main factor controlling the tribological behaviour. Indeed, the π ratios parameters for the C (π_C) and N (π_N) defined as the relative ratio between the intensity of the π^* and σ^* transition for their respective K-edge electron energy-loss spectra appear to correlate well with the tribological behaviour (see Fig. 5). A good performance is thus associated with high values of (π_C) and low of (π_N) ratios. These trends suppose a higher participation of C in aromatic structures (more graphitic-like) and an increased cross-linking between these aromatic domains by N (N_{bridge}). Consequently, this would result in lower friction coefficients by easy shear of the sp^2-bonded C planes and improved wear resistance by higher interconnection between different aromatic domains. The compromise between these two factors is leading to the best tribological behaviour. This important conclusion highlights the importance

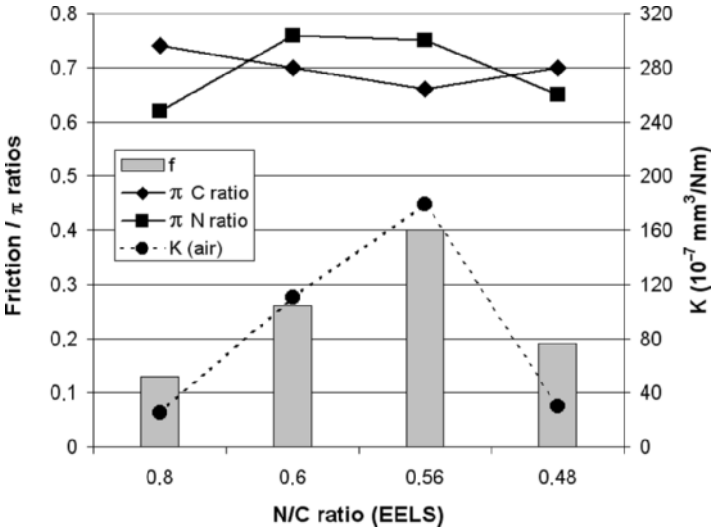

Fig. 5 EELS parameters and friction coefficient of CN_x coatings as obtained by magnetron sputtering. (From [115].)

of the number and position of the N atoms in the C–N structure more than the content itself in determining the tribological behaviour.

The tribological response of the CN_x films has been found to be very dependent on the type of environment used during the test as seen in the case of pure DLC. The friction coefficient can vary from typical values of around 0.1 in ambient air to 0.6 in ultra-high vacuum [30, 31, 113]. The sensitivity of the CN_x films to ambient moisture H_2O vapour has been demonstrated [76]. It was found that the friction coefficient increased with increasing nitrogen content, especially at lower values of relative humidity. However, its influence becomes less pronounced as the sp^2 character of the film structure increases [111]. The frictional properties of amorphous carbon nitride coatings appear to rely on transfer film processes controlled by the nature of the environment, as observed previously in other solid lubricants, such as DLC and MoS_2. The surface chemistry of this easy-shear transfer film was determined to be formed by C sp^2-bonding-rich structures after partial nitrogen release during friction [111]. The dramatic increase in UHV or dry conditions occurred when transferred material disappears from the point of contact, and friction coefficients rise – in the same range as values related to diamond, graphite or poorly hydrogenated DLC. Transfer of steel from the pin counterface instead of CN_x transfer to the opposite counterface, was evidenced by AES line-scan across the wear track [114]. In moist air, as long as the surface sites are saturated by H, O or H_2O, the friction decreased to the 0.1–0.2 range. It has been also reported a remarkable decrease in dry nitrogen below 0.01 [72, 113]. The use of nitrogen gas at atmospheric pressure

is presumably hindering the access of reactive species such as oxygen and water molecules, and maintaining a gap between the counterfaces, preventing interlocking by dangling bonds [114].

3.2.4 Fullerene-like CN_X Films

A very interesting type of CN_x coatings is the so called fullerene-like carbon nitride. This material was reported to have a unique resilient behaviour, providing both high hardness and flexibility [66]. The material was originally produced by heating the substrate during magnetron sputter deposition process [119] and has about 20 at. % N concentration, predominantly sp^2 interatomic bonding and is characterized by a high degree of graphite plane bending and cross-linking (fullerene-like character). Hardness values are around 10–20 GPa while elastic modulus vary between 40 and 120 GPa and friction coefficient is about 0.3 at ambient conditions [9, 66, 97]. Fullerene-like CN_x typically has better thermal stability than DLC, and the degree of stability depends on the preparation temperature and the type of nitrogen bonding in the coating [63]. Preparation by pulsed laser deposition and a detailed comparison to DLC coatings has also been reported [135].

3.2.5 Si-doped CN_X Films

In a similar way to Si-doped DLC coatings, CN_x have also been doped with Si to improve their thermal stability [38], hardness [116] or surface energy [15]. In particular several studies [36, 37] have been carried out to study the influence of Si-doping in CN_x coatings regarding friction coefficient and wear under different atmospheres. It has been found that doping of CN_x with Si (<3 at. %) improves the tribological behaviour of CN_x coatings considerably in humid air. The buffer effect of silicon-doped CN_x decreasing the moisture sensitivity of the friction coefficient was attributed to the adsorption of water molecules on SiO_2 domains formed in the Si-containing films. This adsorbed water may lubricate the contact in humid atmosphere allowing the shear strength to diminish.

4 Doping with Metals: Me-DLC

4.1 Tribological Properties

Alloying of DLC films has been done with many different metals including Ti, Nb, Ta, Cr, Mo, W, Ru, Fe, Co, Ni, Al, Cu, Au, Ag [5, 9, 66, 77, 85, 97, 138] mainly by magnetron sputtering of metallic targets in the presence of acetylene

or another hydrocarbon gas. Other PVD techniques, such as vacuum arc and pulsed laser deposition techniques have also been used. The structure of these films has not yet been systematically investigated, but in many cases, metals are in the form of small nanocrystallites of pure metal or metal carbide (depending on the nature and concentration of the metal) dispersed throughout the carbon network. The inclusion of fine metal carbides also has the advantage of reducing the chemical erosion by hydrogen bombardment, thus increasing the deposition rate.

Perhaps, the most known benefits of incorporating metals into DLC coating is the reduction of compressive internal stress and enhancement of adhesion. Thus, interesting optimum wear rates may be obtained for each type of metal dopant, with a concentration that seems to depend on its nature. Most of the previous tribological tests have been performed in ambient air conditions and exhibited steady-state friction in the range 0.10–0.25 with a slight dependence on humidity and load for metal contents below 30 at. %. Incorporation of higher concentration of metal atoms in DLC resulted in an increase in the friction coefficients up to 0.6 [151]. The tribological behaviours of the metal containing DLC films have been explained by a combination of ceramic-like properties (high elastiticity and hardness, E & H and low surface energy, S), thus leading to high H/E values and low S/H values. Nevertheless, the tribological performances of the Me-doped DLC coatings can differ sharply from one another. For instance, Harris et al. [54] found that the friction coefficients can differ by factors of two (0.13–0.30; WC balls) or more (0.09–0.4) for steel balls. Another example is the study of Ti and Cr-C:H films done by Su and Kao [124] both in dry and lubricated conditions using a SRV reciprocating sliding machine at 100 N of normal load and a constant 1 mm stroke. The tribological performance compared to hard ceramic coatings such a TiN, CrN, TiCN and CrCN resulted very variable depending on the machine configuration (point or line contact), nature of counterbody (Al or steel) and type of lubricant. When using Al as counterbody, the hard coatings showed better performance than Ti or Cr-DLC due to severe adhesion that pulls out the coating. Using steel cylinder in dry conditions, the Ti-DLC displayed lower friction coefficient, noise and wear resistance than Cr-DLC in dry conditions, however, for lubricated tests Ti-DLC coatings did not provide effective protection on contact surfaces under high contact stresses. These differences suggest that extreme caution should be exercized when giving general rules in the Me-DLC coatings.

The improvement of wear resistance of the DLC coatings through incorporation of metal is significant, especially during the initial stages of the sliding tests. Figure 6 taken from the reference of Wei et al. [148] showed that low addition of Cu (1.2%) or Ti (2.75%) improves significantly the wear resistance compared to the pure DLC coating measured by a ‘crater grinding method’. It is also observed that the effect of titanium is stronger than that of copper. Raman analysis indicated a shift of the G peak to shorter wavelength with the addition of metal, which means that the compressive stress has been reduced. XPS data provided evidences of Ti–C bonds which could justify the higher wear resistance compared Cu-doped DLC, because Ti is a strong carbide former whereas Cu is a very weak one. Wei also tried with Si

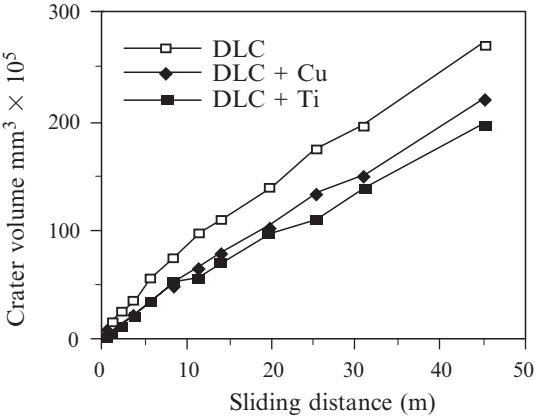

Fig. 6 Wear test results for pure DLC, Cu-DLC and Ti-DLC coatings as a function of the sliding distance. (From Wei et al. 1998.)

and DLC and found the same trend. This was in agreement with previous results shown by Monteiro et al. [96] using W and Ti-doped DLC films. Tungsten is another example of carbide former.

For Ta and W incorporation in DLC by reactive sputtering, friction coefficients of less than 0.1 have been achieved with much lower wear rates than TiN and TiAlN coatings under the same testing conditions [27]. Wang et al. [138] tested Cr-DLC against steel balls at 10 N and 0.3 m/s with friction coefficient below 0.3 for 3,000 m of sliding distance. The improved wear performance was attributed to the combined protection from a hard DLC coating and a converted graphite solid lubricant.

The wear life of steel gears and bearings has been enhanced by deposition of a thin DLC layer (approx. 1 μm), co-deposited with transition metals such as W and Cr. This performance improvement has been related to the ability of the Me-DLC to form a smooth surface during initial wear-in. Mercer et al. [89] proved W-DLC coated gears in a 'four-square' testing machine using a polyol ester oil. The material removal occurs by a gradual polishing mechanism at the most prominent ridges leaving the original valleys intact. Such smoothing has a beneficial effect on the hydrodynamic efficiency of the lubrication layer. It also increases the contact area and diminishes the ensuing wear rate. Conversely, delamination and spalling were observed in Cr-DLC. The difference has been attributed to a combination of residual stress and toughness [139]. Harris and Weiner [155] studied quantitatively the rate of abrasion of steel by various commercial W-DLC coatings. The results demonstrated that the volume of steel removed does not depend strongly on the average nominal contact stress but only on the abrasiveness of the Me-DLC coating. The importance of the abrasive or polishing action of wear-resistant coatings onto the counterpart is suggested in some papers [155] as the primary reason why hard coatings can improve the lifetime of bearings.

Another aspect exhibiting growing interest at present relates to the use of DLC with boundary or mixed lubrication in order to reduce the oil consumption and to ensure acceptable performance in periods of temporary or even permanently poor lubrication conditions. The possibilities for obtaining boundary lubrication with DLC coatings and the suitability of conventional base oils and additives are not clear. Some studies have investigated the doping of DLC (especially with metals) to make them more 'metal-like' providing actual boundary lubrication without steel in the contact [69]. The hypothesis is that by allowing with metallic or non-metallic element is possible to increase the surface activity that enables the use of conventional oils and additives. Thus, Kalin and Vižintin [70] showed that Si-DLC and Ti-DLC coatings combined with additives successfully prevent the adhesive wear and material transfer but in W-DLC coatings, a complete removal of the coating was always observed. Another study presented by Podgornik et al. [104] clearly explains that low-friction behaviour of boundary-lubricated W-DLC coatings is governed by formation of WS-containing tribofilms on the steel countersurface or exposed steel substrate, which reduce friction by up to 50%. Several other studies using doped DLC coatings and steel counterbodies [3, 94, 101, 148] have confirmed that their tribological behaviour is very dependent on a variety of selected conditions, as well as the physical and mechanical properties of the DLC coatings, the base oils (sometimes fully formulated oils) and the additives. Moreover, the non-doped DLC have provided effective prevention of adhesion and wear, comparable to steel/steel contacts, even without additives in the oil [70]. According to these facts, it is clear that specific optimization and tailoring of the coatings and lubricants is necessary for each boundary-lubrication coupled with further understanding of the mechanisms responsible for the observed friction and wear behaviour.

4.2 Adhesion

To use as tribological coatings, DLC films must adhere well to the substrate material, the adhesive forces having to overcome the high internal stresses that otherwise would cause film delamination. On many steels, good adhesion of DLC films has been found through the use of metallic interlayers, for example, titanium, chromium [127, 137] or silicon [90], and metal doping of DLC itself. The better adhesion of the Me-DLC coatings is the key issue to why these coatings have found more use in industrial applications than pure DLC films. Progress has been achieved by developing functionally graded coatings where chemical composition and mechanical properties are gradually evolving from steel substrate to the DLC through metal-to-metal carbide layers. Voevodin et al. [133] used Ti and TiC(H) graded underlayers to increase the wear resistance and toughness of DLC films. The gradient design has been extensively employed onto steels and tungsten carbide substrates due to the improvement

in load-support and adhesion properties [22, 30, 124]. This development combined with the possible incorporation of the same metal inside the DLC coating further improves the adhesion. For example, Wang et al. [138] determined that Cr inclusion by cathodic arc evaporation within the DLC aids the reduction of internal stress and ensures sufficient adhesion strength by developing a Cr/Cr_3C_2 interface.

4.3 Biocompatibility

There are many papers reporting on tribological experiments using a pin-on-disk set-up or a hip simulator to determine friction and wear of DLC-coated hip joint balls sliding against ultra-high molecular weight polyethylene (UHMWPE) or of metal/metal joints with one or both sides coated with DLC. An overview of different materials and surface treatments used in bearing surfaces in human joint replacements was published by Dearnley [24]. Several authors reported a decreased wear of the UHMWPE by coating the counterpart with DLC. The UHMWPE wear rate is one of the most important factors affecting life and performance of hip joints and knee implants, since the generated debris has been linked to complications as tissue inflammation, bone loss and implant loosening. Most of these experiments have been made using distilled water or 1 wt. % NaCl water. No tribological experiments in a biological environment using alloyed DLC as a coating are yet known to us.

Hauert et al. [60, 61] showed that the adsorption of different proteins could be altered as a function of the Ti content in the DLC film and an improved cell morphology was obtained by the addition of Ca–O [32]. The adsorbed proteins will subsequently influence cell attachment, cell proliferation and cell differentiation. Bone marrow cell culture experiments on these a-C:H/Ti coatings demonstrated that the differentiation of bone marrow cells into bone resorbing cells, that is, osteoclasts, is inhibited on all titanium-containing a-C:H coatings [117] making a-C:H/Ti a valuable coating for implants.

4.4 Electrical Resistivities and Optical Properties

Me-DLC films containing 15% Ta, W, Ti, Nb, having similar wear resistance as DLC and friction coefficients <0.2, but higher conductivities (up to 0.005 Ω cm), have been deposited by DC magnetron sputtering of the metals in acetylene [51]. Four-probe measurements showed that the resistance of the DLC films does not change linearly with dopant concentration, in agreement with what has been reported [26]. Amorphous semiconductors usually have all states localized, and their conduction exhibits hopping, especially variable-range hopping mechanisms. When the concentration of foreign atoms that can contribute to localized

states is increased, the distance that the electron will cross over one tunnelling event would be smaller, leading to a reduced resistivity. When the concentration of these atoms is increased to such a level that continuous channels might be formed for the transport of electrons, the material could essentially behave like metallic materials.

Wei et al. [144] have measured the *I-V* characteristics of pure DLC and those containing Ag, Cu and Ti dopants. All the coatings except the one containing Ti form a Schottky contact with the measuring probe. The Ti–DLC sample simply exhibits metallic conduction as a resistor, with its *I-V* curve following Ohm's law. This can, in part, be understood in connection with the XPS observation that Ti–C bonding is present in the film. Ti–C bonding is essentially metallic and its presence might greatly enhance the conduction of the film by increasing the density of states near the Fermi level. It was also observed that light has a strong effect on electrical conduction of the DLC coatings [143].

Since one of the applications of DLC is for protective coatings for IR windows, it should be important to study the effect of foreign atoms on the IR range optical properties. There are generally three contributions to the remittance of a semiconductor, i.e. band–band transitions, free carriers and phonons (lattice vibrations). When the specimen is doped, this contribution from free carriers can be enhanced significantly. The emittance of DLC containing a small fraction of metallic elements shows a significant increase in the whole range of measurement, while the transmittance in the IR range is considerably decreased so that the coating is almost opaque. The effect of titanium is much more profound in this respect. Ti-incorporated DLC coatings behave almost as a black body, where the transmittance just goes to zero. Free carriers suppress all contribution from band–band transitions, from localized states and phonons. In other words, the emitted radiation from other contribution might have been absorbed before it reaches the specimen surface. The optical properties of a-C:H coatings have been adapted by the introduction of W and Cr as nanosized carbide inclusions in the film. These coatings are applied, for example, as selective absorber coatings for thermal solar energy conversion [42].

5 Modulated Alloying at the Nanoscale: Multilayered and Nanocomposite Coatings

When alloying metals into a-C:H coating the additional elements can either be diluted in the matrix and a new single phase coating is produced or can be present as a second separate phase modulated in the nanometre scale. The multilayered and nanocomposite films belong to this new category of advanced nanostructured coatings that open new possibilities of property improvement by appropriate control of their composition and structure at the nanoscale. The major function of these structures is to significantly enhance hardness, fracture toughness and adhesion of the coatings, and thus to improve their wear resistance.

Today, multilayer coatings are intensively investigated as a means of improving the properties of DLC or to reduce unwanted properties of DLC without losing the beneficial properties of the pure films. In the previous section, we briefly reviewed the uses of functionally graded coatings and the assembly of several layers to enhance adhesion between substrate and DLC coatings. This has been carried out by Knoblauch et al. [74] for pure DLC and many others with alloyed DLC and/or alternating other hard coatings [22, 91, 124, 133]. In this part, we refer rather to superlatices where the layers are periodically repeated with individual thickness in the 5–50 nm range. It is known that multilayers, for example, can reduce grain growth and limit crack propagation and, thus increase the toughness of the coating [130]. One example of multilayered structure used in commercial gear applications is the WC/C coating exhibiting improved performances during mixed or boundary lubrication regimes. WC/C multilayer from Balzers (Balinit C) can increase 10–40% the load carrying capacity, reduce friction and gasoline consumption by up to 1% [57]. The periodicity of the multilayer structure controls the tribological properties. Short periods promote wear resistance, while long periods promote fatigue resistance [123].

Another way to improve properties of DLC coatings is to try to obtain a so-called nanocomposite film morphology essentially consisting of a high density of nanometre-sized crystals embedded in an amorphous matrix, for example, tungsten [123] or titanium carbide particles in an a-C:H matrix [102, 152]. In contrast to the ultrahard nanocomposites (i.e. TiN/Si_3N_4), this type contains of significantly larger grains of some tens of nanometres with a thicker separating amorphous phase between the nanocrystallites of about 5 nm. The crystallite size of 10 ± 50 nm is large enough to allow the formation of dislocations, but is too small for self-propagation of cracks. The larger grain separation permits adaptation of incoherency strains and enables formation of nanocracks between the crystallites to allow pseudoplastic behaviour. In this way, this material exhibits four times higher toughness than single-crystalline TiC and hardness values of about 32 GPa. These TiC/a-C films were therefore called ‘load-adaptive coatings’ [132].

The incorporation of carbide particles into amorphous carbon was already reported by Sundgren et al. [27] since the beginning of DLC as a low-friction hard coating. The later works by Dimigen and Klages [122] on doping of a-C:H films with metals like Ti, Ta, Nb and others, also supposed the presence of carbide nanocrystals in the amorphous a-C:H matrix. In fact, this new generation of multicomponent nanocomposite coatings can be regarded as further progress on the metal-doped DLC coatings described in the previous section. The current knowledge on the behaviour of nanostructured materials makes possible the development of new coatings with tailored properties by appropriate control of the microstructure and chemical composition at the nanoscale. Martínez-Martínez et al. [86] reported the relation structure–properties in nanocomposite films consisting of TiC crystallites in a hydrogen-free a-C matrix deposited by magnetron sputtering process. In Fig. 7, a sharp transition towards low friction and wear

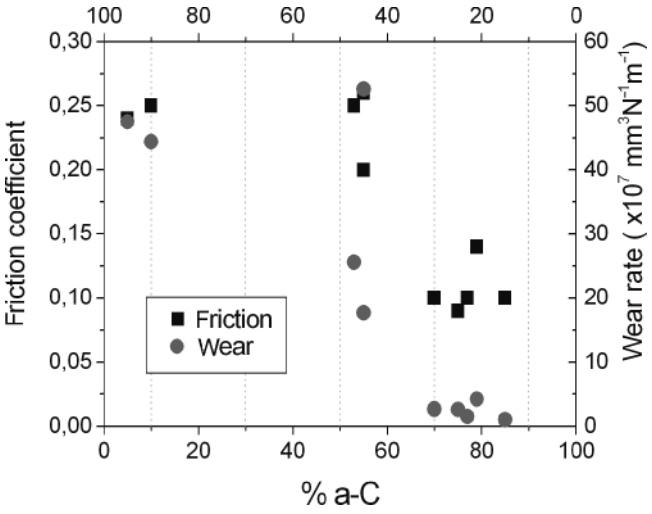

Fig. 7 Evolution of the tribological properties (friction and wear) for a nanocomposite TiC/a-C depending on the nanocrystalline/amorphous phase contents

rates is found when the amorphous carbon phase overpass the 55%, with an optimum of around 10–30% of nanocrystalline TiC. Previous publications also reported improved performance on a similar range of compositions [34, 102, 126]. In that case, the friction mechanism appears controlled by the transfer film build-up of a graphitic-like nature similar to classical DLC. However, when a high fraction of ceramic phase is present, the transfer film is not stable being partially removed by the hard TiC nanocrystals resulting in high and noisy friction curves [103]. On the other hand, comparing the tribological properties of WC/C in multilayered and nanocomposite forms, the more homogeneous dispersion of WC nanocrystallites throughout the W-C:H layer provides better abrasive wear resistance, but the multilayered form performs better in the impact fatigue tests. These results show that it is possible to tailor Me-C(H) coatings with different properties for specific applications, depending on the tribological requirements in the application.

Another type of adaptative nanocomposite coatings corresponds to the WC/DLC/WS_2 system [132, 146], consisted of 1–2 nm, WC and 5–10 nm WS_2 grains embedded in an amorphous DLC matrix. This nanocomposite exhibited self-adaptation to operating conditions that occur in aerospace application involving environmental changes from ambient air to vacuum. The DLC provides excellent tribological behaviour in ambient air ($f = 0.03$) while WS_2 does in vacuum ($f < 0.05$). Reversible regulation of the composition of the transfer film between WS_2 and graphite with environmental cycling, WS_2 crystallization and DLC graphitization have been identified as mechanisms responsible for such behaviour.

6 Conclusions

The incorporation of dopants in DLC films may lead to greater multifunctionality and much improved properties and, hence, performance in practical applications. Most modifications have been made to reduce their, typically high, internal compressive stresses, to increase the adhesion to the substrate (N, Si, metal incorporation), to modify surface energy (N, F, O, Si) or to increase their biocompatibility (Ti, Si, Ca). The nitrogen-doped DLC films have been proven to be very effective in magnetic storage technology as protective overcoats. It was demonstrated that the improvements in friction and wear are due to the increase in sp^2 character and higher interconnectivity of the aromatic domains by the N atoms. The doping DLC with metals increases the wear resistance of the resultant coatings while maintaining the friction coefficients in a range 0.1–0.2. It appears that this improvement most probably results from reduction in the internal compressive stresses, formation of metal–carbide bonds and enhancement of the adhesion although the hardness and Young's modulus can be slightly reduced. The incorporation of metal should be limited to 30–40 at. %. Higher concentrations produce an increment in hard carbide and metallic phases that cause increased abrasive and adhesive wear together with higher friction coefficients. The better adhesion and the fact that Me-DLC coatings have markedly lower compressive stress are key issues as to why these coatings have found more usage in industrial applications than pure DLC films. The use of a gradual transition from metal to ceramic and to DLC is presented as a well established way to improve load support and adhesion strength. The doping of DLC in order that they behave in a similar way to conventional metal-lubrication mechanisms is at a much younger state of comprehension and more investigations must be carried out to reach a maturity in understanding its properties under boundary-lubricated contacts.

The number of different material compositions and structures appears to be enormous when one starts to alloy different elements into DLC coatings. However, the real response of a coating in a specific application has to be determined by conducting field tests. In a tribological system many properties and parameters (the different material properties of the friction counterparts, environment-test conditions) interact with each other in a non-linear and locally different way. This can cause a coating that is optimized for a certain tribological application to perform worse under other tribological conditions. To overcome these variations in performance and to extend the applicability over a broader range of test conditions, researchers have been exploring novel coating architectures having multilayers, nanostructures or composites. Some of them have demonstrated to provide better performance and durability than their traditional counterparts in high load bearing, rolling and sliding contact applications. The combination of low friction and high toughness are key requirements which may be matched by nanocomposites or multilayers which also contains some lubricating solid phases.

In summary, the optimization of the material combination and deposition parameters is always a challenging subject for each element or combination of elements. When it is achieved, the doped-DLC films may exhibit promising tribological properties in terms of steady-state friction level and wear rates for many applications.

References

1. Adhikari A., Adhikari S., Omer A. M. M., Rusop M., Uchida H., Soga T., Umeno M. (2006) Optical and structural properties of amorphous carbon thin films deposited by microwave surface-wave plasma CVD. Diam. Relat. Mater. 15: 188–192.
2. Baker M. A., Hammer P. (1997) Study of the chemical composition and microstructure of ion beam-deposited CN_x films including an XPS C1s peak simulation. Surf. Int. Anal. 25: 301–314.
3. Ban M., Ryoji M., Fujii S., Fujioka J. (2002) Tribological characteristics of Si-containing diamond-like carbon films under oil-lubrication. Wear 253: 331–338.
4. Ban M., Hasegawa T. (2003) Internal stress reduction by incorporation of silicon in diamond-like carbon films. Surf. Coat. Technol. 62: 1–5.
5. Bauer C., Leiste H., Stuber M., Ulrich S., Holleck H. (2002) Mechanical properties and performance of magnetron-sputtered graded diamond-like carbon films with and without metal additions. Diam. Relat. Mater. 11: 1139–1142.
6. Bousetta A., Lu M., Bensaoula A. (1995) Physical-properties of thin carbon nitride films deposited by electron-cyclotron-resonance assisted vapour-deposition. J. Vac. Sci. Technol. A 13: 1639–1643.
7. Boyd K. J., Marton D., Todorov S. S., Albayati A. H., Kulik J., Zuhr R. A., Rabalais J. W. (1995) Formation of C-N thin-films by ion-beam deposition. J. Vac. Sci. Technol. A 13: 2110–2122.
8. Brizuela M., Garcia-Luis A., Viviente J. L., Braceras I., Oñate J. I. (2002) Tribological study of lubricious DLC biocompatible coatings. J. Mater. Sci. Med. 13: 1129–1133.
9. Broitman E., Hellgren N., Wanstrand O., Johansson M. P., Berlind T., Sjöstrom H., Sundgren J. E., Larsson M., Hultman L. (2001) Mechanical and tribological properties of CN_x films deposited by reactive magnetron sputtering. Wear 248: 55–64.
10. Bull S. J. (1995) Tribology of carbon coatings: DLC, diamond and beyond. Diam. Relat. Mater. 4: 827–836.
11. Butter R. S., Lettington A. H. (1995) Diamond-like carbon for biomedical applications. J. Chem. Vap. Depos. 3: 182–192.
12. Butter R., Allen M., Chandra L., Lettington A. H., Rushton R. (1995) In-vitro studies of DLC coatings with silicon intermediate layer. Diam. Relat. Mater. 4: 857–861.
13. Chang C. L., Jao J. Y., Chang T. C., Ho W. Y., Wang D. Y. (2005) Influences of bias voltage on properties of TiAl-doped DLC coatings synthesized by cathodic arc evaporation. Diam. Relat. Mater. 14: 2127–2132.
14. Chan W. Ch., Zhou B., Chung Y. W., Lee C. S., Lee S. T. (1998) Synthesis, composition, surface roughness and mechanical properties of thin nitrogenated carbon films. J.Vac.Sci. Technol. A 16: 1907–1911.
15. Chen L. Y, Hong F. C. N. (2003) Surface tension studies of (Si,N)-containing diamond-like carbon films deposited by hexamethyldisilizane. Diam. Relat. Mater. 12: 968–973.
16. Cohen M. L. (1985) Calculations of bulk moduli of diamond and zincblende solids. Phys. Rev. B 32: 7988–7991.
17. Cohen M. L. (1989) Novel materials from theory. Nature 338: 291–292.
18. Cuomo J. J., Leary P. A., Yu D., Reuter W., Frisch M. (1979) Reactive sputtering of carbon and carbide targets in nitrogen. J. Vac. Sci. Technol. 16: 299–302.
19. Cutiongco E. C., Li D., Chung Y. W., Bhatia C. S. (1996) Tribological behaviour of amorphous carbon nitride overcoats for magnetic thin-film rigid disks. J. Tribol. 118: 543–548.
20. Czyzniewski A., Precht W., Pancielejko M., Myslinski P., Walkowiak W. (1998) Structure, composition and tribological properties of carbon nitride films. Thin Solid Films 317: 384–387.
21. D'Agostino R., Lamendola R., Favia P., Giquel A. (1994) Fluorinated diamond-like carbon-films deposits from radiofrequency glow-discharge in a triode reactor. J. Vac. Sci. Technol. A 12: 308–313.

22. Dahan I., Admon U., Frage N., Sariel J., Dariel M. P., Moore J. J. (2001) The development of a functionally graded TiC-Ti multilayer hard coating. Surf. Coat. Technol. 137: 111–115.
23. Damasceno J. C., Camargo S. S., Freire F. L., Carins R. (2000) Deposition of Si-DLC films with high hardness, low stress and high deposition rates. Surf. Coat. Technol. 113: 247–252.
24. Dearnley P. A. (1999) A review of metallic, ceramic and surface-treated metals used for bearing surfaces in human joint replacements. Proc. Inst. Mech. Eng. Part H—J. Eng. Med. 213: 107–135.
25. Djouadi M. A., Beer P., Marchal R., Sokolowska A., Lambertin M., Precht W., Nouveau C. (1999) Antiabrasive coatings: application for wood processing. Surf. Coat. Technol. 116/119: 508–516.
26. Dikshit S. J., Lele P., Ogale S. B., Kshirsagar S. T. (1996) Influence of in-process copper incorporation on the quality of diamond-like carbon films deposited by pulsed laser deposition technique. J. Mater. Res. 11: 2236–2241.
27. Dimigen H., Klages C. P. (1991) Microstructure and wear behavior of metal-containing diamond-like coatings. Surf. Coat. Technol. 49: 543–547.
28. Donnet C. (1998) Recent progress on the tribology of doped diamond-like and carbon alloy coatings: a review. Surf. Coat. Technol. 100/101: 180–186.
29. Donnet C., Fontaine J., Grill A., Patel V., Jahnes C., Belin M. (1997) Wear-resistant fluorinated diamondlike carbon films. Surf. Coat. Technol. 94/95: 531–536.
30. Donnet C., Fontaine J., Le Mogne T., Belin M., Héau C., Terrat J. P., Vaux F., Pont G. (1999a) Diamond-like carbon-based functionally gradient coatings for space tribology. Surf. Coat. Technol. 120/121: 548–554.
31. Donnet C., Martin J. M., Fontaine J., Sánchez-López J. C., Quirós C., Elizalde E., Sanz J. M., Rojas T. C., Fernández A. (1999b) The role of CN chemical bonding on the tribological behaviour of CN_x coatings. Surf. Coat. Technol. 120–121: 594–600.
32. Dorner-Reisel A., Schurer C., Nischan C., Seidel O., Muller E. (2002) Diamond-like carbon: alteration of the biological acceptance due to Ca-O incorporation. Thin Solid Films 420/421: 263–268.
33. Erdemir A., Donnet C. (2001) Tribology of diamond, diamond-like carbon and related films. In: Bhushan B. (eds) Modern tribology handbook, Vol II. CRC Press, Boca Raton, FL, pp. 871–908.
34. Feng B., Cao D. M., Meng W. J., Rehn L. E., Baldo P. M., Doll G. L. (2001) Probing for mechanical and tribological anomalies in the TiC/amorphous hydrocarbon nanocomposite coating system. Thin Solid Films 398/399: 210–216.
35. Fernández A., Fernández-Ramos C., Sánchez-López J. C. (2003) Preparation, microstructural characterization and tribological behaviour of CN_x coatings. Surf. Coat. Technol. 163–164: 527–534.
36. Fernández-Ramos C., Sánchez-López J. C., Belin M., Donnet C., Pascaretti T., Fernández A. (2002a) Tribological and mechanical properties of CN_x- and $SiCN_x$-Ti-TiN multilayered systems grown onto steel. Vacuum 67: 441–448.
37. Fernández-Ramos C., Sánchez-López J. C., Belin M., Donnet C., Ponsonnet L., Fernández A. (2002b) Tribological behaviour and chemical characterization of Si-free and Si-containing carbon nitride coatings. Diam. Relat. Mater. 11: 169–175.
38. Fernández-Ramos C., Sánchez-López J. C., Rojas T. C., Fernández A. (2003) Structural modifications of silicon-doped carbon nitride films during post-deposition annealing. Diam. Relat. Mater. 12: 1055–1060.
39. Franceschini D. F., Achete C. A., Freire F. L. (1992) Internal-stress reduction by nitrogen incorporation in hard amorphous-carbon thin-films. Appl. Phys. Lett. 60: 3229–3231.
40. Franceschini D. F., Achete C. A., Freire F. L., Beyer W., Mariotto G. (1994) Structural modifications in a-C:H films doped and implanted with nitrogen. Diam. Relat. Mater. 3: 88–93.
41. Gago R., Jiménez I., Cáceres D., Agulló-Rueda F., Sajavaara T., Albella J. M., Climent-Font A., Vegara I., Raisanen J., Rauhala E. (2001) Hardening mechanism in graphitic carbon nitride films grown with N_2/Ar ion assistance. Chem. Mater. 13: 129–135.
42. Gampp R., Gantenbein P., Kuster Y., Reimann P., Steiner R., Oelhafen P., Brunold S., Frei U., Gombert A., Joerger R., Graf W., Köhl M. (1994) Characterization of a-C:H/W and a-C:H/Cr solar selective absorber coatings. In: Wittwer V., Granqvist C. G., Lampert C. M (eds.) Optical

Materials Technology for Energy Efficiency and Solar Energy Conversion XIII, Proc. SPIE 2255: 92–106.
43. Gangopadhyay A. K., Willermet P. A., Tamor M. A., Vassell W. C. (1997) Amorphous hydrogenated carbon films for tribological applications.1. Development of moisture insensitive films having reduced compressive stress. Tribol. Int. 30: 9–18.
44. Gilmore R., Hauert R. (2000) Comparative study of the tribological moisture sensitivity of Si-free and Si-containing diamond-like carbon films. Surf. Coat. Technol. 133/134: 437–442.
45. Gilmore R., Hauert R. (2001) Control of the tribological moisture sensitivity of diamond-like carbon films by alloying with F, Ti or Si. Thin Solid Films 398: 199–204.
46. Gouzman I., Brener R., Hoffman A. (1995) Nitridation of diamond and graphite surfaces by low-energy N_2^+ ion irradiation. Surf. Sci. 333: 283–288.
47. Grill A. (1993) Review of the tribology of diamond-like carbon. Wear, 168: 143–153.
48. Grill A. (1997) Tribology of diamondlike carbon and related materials: an updated review. Surf. Coat. Technol. 94–95: 505–513.
49. Grill A. (1999) Diamond-like carbon: state of the art. Diam. Rel. Mater. 8: 428–434.
50. Grill A., Patel V. (1996) Wear resistant fluorinated diamondlike carbon films. Diam. Films Tech. 6: 13–21.
51. Grischke M., Bewilogua K., Trojan K., Dimigen H. (1996) Application-oriented modifications of deposition processes for diamond-like-carbon-based coatings. Surf. Coat. Technol. 74/75: 739–745.
52. Hakovirta M., He, X. M., Nastasi J. (2000) Optical properties of fluorinated diamond-like carbon films produced by pulsed glow discharge plasma immersion ion processing. J. Appl. Phys. 88: 1456–1459.
53. Hammer P., Lacerda R. G., Dropper R., Alvarez F. (2000) Comparative study on the bonding structure of hydrogenated and hydrogen free carbon nitride films with high N content. Diam. Relat. Mater. 9: 577–581.
54. Harris S. J., Weiner A. M., Meng W. J. (1997) Tribology of metal-containing diamond-like carbon coatings. Wear. 211: 208–217.
55. Harris S. J., Weiner A. M. (1998) Scaling relationships for the abrasion of steel by diamond-like carbon coating. Wear. 233: 31–36.
56. Hatada R., Baba K. (1999) Preparation of hydrophobic diamond like carbon films by plasma source ion implantation. Nucl. Instrum. Methods B148: 655–658.
57. Hauert R. (2004) An overview on the tribological behaviour of diamond-like carbon in technical and medical applications. Tribol. Int. 37: 991–1003.
58. Hauert R., Müller U. (2003) An overview on tailored tribological and biological behaviour of diamond-like carbon. Diam. Relat. Mater. 12: 171–177.
59. Hauert R., Glisenti A., Metin S., Goitia J., Kaufman J. H., van Loosdrecht P. H. M., Kellock A. J., Hoffmann P., White R. L., Hermsmeier B. D. (1995) Influence of nitrogen doping on different properties of a-C:H. Thin Solid Films 268: 22–29.
60. Hauert R., Muller U., Francz G., Birchler F., Schroeder A., Mayer J., Wintermantel E. (1997) Surface analysis and bioreactions of F and Si containing a-C: H, Thin Solid Films 308/309: 191–194.
61. Hauert R., Knoblauch-Meyer L., Francz G., Schroeder A., Wintermantel E. (1999) Tailored a-C: H coatings by nanostructuring and alloying. Surf. Coat. Technol. 120/121: 291–296.
62. He X. M., Hakovirta M., Nastasi M. (2005) Hardness, hydrophobic and optical properties of fluorine and boron co-alloyed diamond-like carbon films. Mat. Lett. 59: 1417–1421.
63. Hellgren N., Lin N., Broitman E., Serin V., Grillo S. E., Twesten R., Petroy I., Colliex C., Hultman L., Sundgren J. E. (2001) Thermal stability of carbon nitride thin films. J. Mat. Res. 16: 3188–3201.
64. Hioki T., Itoh Y., Itoh A., Hibi S., Kawamoto J. (1991) Tribology of carbonaceous films formed by ion-beam-assisted deposition of organic material. Surf. Coat. Technol. 46: 233–243.
65. Hong J. G., Turban G. (1999) Etching process of hydrogenated amorphous carbon (a-C:H) thin films in a dual ECR-r.f. nitrogen plasma. Diam. Relat. Mater. 8: 572–576.
66. Hultman L., Neidhardt J., Hellgren N., Sjostrom H., Sundgren J. E. (2003) Fullerene-likecarbon nitride: A resilient coating material. MRS Bulletin 28: 194–202.

67. Ishikawa K., Yamaoka Y., Nakamura M., Yamazaki Y., Yamasaki S., Ishikawa Y., Samukawa S. (2006) Surface reactions during etching of organic low-k films by plasmas of N_2 and H_2. J. Appl. Phys. 99: 083305-1–083305-6.
68. Jiménez I., Gago R., Albella J. M., Cáceres D., Vergara I. (2000) Spectroscopy of π-bonding in hard grapitic carbon ntride films: Superstructure of basal planes and hardening mechanism. Phys. Rev. B 62: 4261–4264.
69. Kalin M., Vižintin J., Barriga J., Vercammen K., van Acker K., Arnšek A. (2004) The effect of doping elements and oil additives on the tribological performance of boundary-lubricated DLC/DLC contacts. Tribol. Lett. 17: 679–688.
70. Kalin M. and Vižintin J. (2006) Differences in the tribological mechanisms when using non-doped, metal-doped (Ti, WC), and non-metal-doped (Si) diamond-like carbon against steel under boundary lubrication, with and without oil additives. Thin Solid Films 515: 2734–2747.
71. Kaufman J. H., Metin S., Saperstein D. D. (1989) Symmetry-breaking in nitrogen-doped amorphous-carbon infrared observation of the Raman-active G-bands and D-bands. Phys. Rev. B 39: 13053–13060.
72. Kato K., Umehara N., Adachi K. (2003) Friction, wear and N_2-lubrication of carbon nitride coatings: a review 254: 1062–1069.
73. Khurshudov A., Kato K., Daisube S. (1996) Comparison of tribological properties of carbon and carbon nitride protective coatings over magnetic media. J. Vac. Sci. Technol. A 14: 2935–2939.
74. Knoblauch L., Hauert R., Savan A., Pfluger E., Tixier S., Simmonds M., van Swygenhoven H., Mikhailov S. et al. (1997) Tribological properties of bias voltage modulated a-C: H nano-scaled multilayers. Surf. Coat. Technol. 94/95: 521–524.
75. Koh M., Nakajima T. (2000) Adsorption of aromatic compounds on CxN-coated activated carbon. Carbon 38: 1947–1954.
76. Koskinen J., Hirvonen J. P., Levoska J., Torri P. (1996) Tribological characterization of carbon-nitrogen coatings deposited by using vacuum arc discharge. Diam. Relat. Mater. 5: 669–673.
77. Kukiełka S., Gulbiński W., Pauleau Y., Dub S. N., Grob J. J. (2006) Composition, mechanical properties and friction behavior of nickel/hydrogenated amorphous carbon composite films. Surf. Coat. Technol. 200: 6258–6262.
78. Kusano Y., Evetts J. E., Somekh R. E., Hutchings J. M. (1998) Properties of carbon nitride films deposited by magnetron sputtering. Thin Solid Films 33: 56–61.
79. Kwok S. C. H., Jin W., Chu P. K. (2005) Surface energy, wettability, and blood compatibility phosphorus doped diamond-like carbon films. Diam. Relat. Mater. 14: 78–85.
80. Lee K. R., Eun K. Y. (1996) Tribolgy of diamond-like carbon coated VCR head drums. Mater. Sci. Eng. A 209: 264–269.
81. Li D. J., Guruz M. U., Singh C., Bhatia C. S., Chung Y. W. (2002) Ultrathin CN_x overcoats for 1 Tb/in^2 hard disk drive systems. Appl. Phys. Lett. 81: 1113–1115.
82. Lifshitz Y. (1999) Diamond-like carbon—present status. Diam. Relat. Mater. 8: 1659–1676.
83. Liu A. Y. and Cohen M. L. (1989) Prediction of new low compressibility solids. Science 245: 841–842.
84. López S., Dunlop H. M., Benmalek M., Tourillon G., Wong M. S., Sproul W. D. (1997) XPS, XANES and ToF-SIMS characterization of reactively magnetron-sputtered carbon nitride films. Surf. Int. Anal. 25: 315–323.
85. Lungu C. P. (2005) Nanostructure influence on DLC-Ag tribological coatings. Surf. Coat. Technol. 200: 198–202.
86. Martínez-Martínez D., López-Cartes C., Justo A., Fernández A., Sánchez-López J. C., García-Luis A., Brizuela M., Oñate J. I. (2005) Tailored synthesis of TiC/a-C nanocomposite tribological coatings. J. Vac. Sci. Technol. A 23: 1732–1736.
87. Matsumoto O., Kotaki T., Shikano H., Takemura K., Tanaka S. (1994) Synthesis of carbon nitride in plasma arc. J. Electrochem. Soc. 141: L16–L18.
88. Meneve J., Jacobs R., Eersels L., Smeets J., Dekempeneer E. (1993) Friction and wear behavior of amorphous hydrogenated $Si_{1-x}C_x$ films. Surf. Coat. Technol. 62: 577–582.
89. Mercer C., Evans A. G., Yao N., Allmech S., Cooper A. V. (2003) Material removal on lubricated steel gears with W-DLC-coated surfaces. Surf. Coat. Technol. 173: 122–129.

90. Michler T., Grischke M., Bewilogna K., Hieke A. (1999) Continuosly deposited duplex coatings consisting of plasma nitriding and a-C:H:Si deposition. Surf. Coat. Technol. 111: 41–45.
91. Misra A., Kung H. (2001) Deformation behavior of nanostructured metallic multilayers. Adv. Eng. Mater. 3: 217–222.
92. Miyake S. (1993) Microtribology evaluation of carbonaceous films by FTIR and SPM. In: Miyoshi K., Chung Y. W. (eds) Surface diagnostics in tribology, Series in modern tribology, Vol 1, World Scientific, Singapore, pp. 183–204.
93. Miyake S., Kaneko R., Kikuya Y., Sugimoto I. (1991) Micro-tribological studies on fluorinated carbon-films, Transactions of the ASME, J. Tribol. 113: 384–389.
94. Miyake S., Saito T., Yasuda Y., Okamoto Y., Kano M. (2004) Improvement of boundary lubrication properties of diamond-like carbon (DLC)films due to metal addition. Tribol. Int. 37: 751–761.
95. Miyamoto T., Kaneko R., Miyake S. (1991) Tribological characteristics of amorphous-carbon films investigated by point contact microscopy. J. Vac Sci. Technol. B 9: 1336–1339.
96. Monteiro O. R., Delplancke-Ogletree M. P., Lo R. Y., Winand R., Brown I. G. (1997) Synthesis and characterization of thin films of WC_x produced by mixing W and C plasma streams. Surf. Coat. Technol. 94/95: 220–225.
97. Neidhart J., Czigany Z., Brunei I. F., Hultman L. (2003) Growth of fullerene-like carbon nitride thin solid films by reactive magnetron sputtering; role of low-energy ion irradiation in determining microstructure and mechanical properties. J. Appl. Phys. 93: 3002–3015.
98. Niu C. M., Lu Y. Z., Lieber C. M. (1993) Experimental realization of the covalent solid carbon nitride. Science 261: 334–337.
99. Oguri K., Arai T. (1990) Low friction coatings of diamond-like carbon with silicon prepared by plasma-assisted chemical vapor-deposition. J. Mater. Res. 5: 2567–2571.
100. Omer A. M. M., Adhikari S., Adhikary S., et al. Effects of iodine doping on optoelectronic properties of diamond-like carbon thin films deposited by microwave surface wave plasma CVD. Diam. Relat. Mater. 13: 2136–2139.
101. Ouyang J. H., Sasaki S. (2005) Friction and wear characteristics of a Ti-containing diamond-like carbon coating with an SRV tester at high contact load and elevated temperature. Surf. Coat. Technol. 195: 234–244.
102. Patscheider J., Zehnder T., Diserens M. (2001) Structure–performance relations in nanocomposite coatings. Surf. Coat. Technol. 146/147: 201–208.
103. Pei Y. T., Galvan D., De Hosson J. T. M., Cavaleiro A. (2005) Nanostructured TiC/a-C coatings for low friction and wear resistant applications. Surf. Coat. Technol. 198: 44–50.
104. Podgornik B., Hren D., Vižintin J. (2005) Low-friction behaviour of boundary-lubricated diamond-like carbon coatings containing tungsten. Thin Solid Films 476: 92–100.
105. Polonsky I. A., Chang T. P., Keer L. M., Sproul W. D. (1998) A study of rolling contact fatigue of bearing steel coated with PVD TiN films: coating response to cyclic contact stress and physical mechanisms underlying coating effect on the fatigue life. Wear 215: 191–204.
106. Ren Z. M., Du Y. C., Ying Z. F., Qiu Y. X., Xiong X. X., Wu J. D., Li F. H. (1994) Electronic and mechanical properties of carbon nitride films prepared by laser ablation graphite under nitrogen ion-beam bombardment. Appl. Phys. Lett. 65: 1361–1363.
107. Ricci M., Trinquecoste M., Auguste F., Canet R., Delhaes P., Guimon C., Pfisterguillouzo G., Nysten B., Issi J. P. (1993) Relationship between the structural organization and the physical-properties of PECVD nitrogenated carbons. J. Mater. Res. 8: 480–488.
108. Robertson J. (2002) Diamond-like amorphous carbon. Mater. Sci. Eng. R 27: 129–281.
109. Robertson J. (2003) Requirements of ultrathin carbon coatings for magnetic storage technology. Trib. Int. 36: 405.
110. Rusop M., Mominuzzaman S. M., Soga T., Jimbo T., Umeno M. (2005) Nitrogen doped n-type amorphous carbon films obtained by pulsed laser deposition with a natural camphor source target for solar-cell applications. J. Phys. -Cond. Mater. 17: 1929–1946.
111. Sánchez-López J. C., Donnet C., Belin M., Le Mogne T., Fernández-Ramos C., Sayagués M. J., Fernández A. (2000) Tribochemical effects on CN_x films. Surf. Coat. Technol. 133: 430–436.
112. Sánchez-López J. C., Donnet C., Lefebvre F., Fernández-Ramos C., Fernández A. (2001) Bonding structure in amorphous carbon nitride: A spectroscopic and nuclear magnetic resonance study. J. Appl. Phys. 9: 675–681.

113. Sánchez-López J. C., Belin M., Donnet C., Quiros C., Elizalde E. (2002a) Friction mechanisms of amorphous carbon nitride films under variable environments: a triboscopic study. Surf. Coat. Technol. 160: 138–144.
114. Sánchez-López J. C., Donnet C., Le Mogne T. (2002b) Tribological and surface characterisation in UHV of amorphous CN_x films. Vacuum 64: 191–198.
115. Sánchez-López J. C., Martínez-Martínez D., López-Cartes C., Fernández-Ramos C., Fernández A. (2005) A nanoscale approach for the characterization of amorphous carbon-based lubricant coatings. Surf. Coat. Technol. 200: 40–45.
116. Sarangi D., Sanjines R., Karimi A. (2004) Effect of silicon doping on the mechanical and optical properties of carbon nitride thin films. Thin Solid Films 447: 217–222.
117. Schroeder A., Francz G., Bruinink A., Hauert R., Mayer J., Wintermantel E. (2000) Titanium containing amorphous hydrogenated carbon films (a-C:H/Ti): surface analysis and evaluation of cellular reactions using bone marrow cell cultures in vitro. Biomaterials 21: 449–456.
118. Schwan J., Batori V., Ulrich S., Ehrhardt H., Silva S. R. P. (1998) Nitrogen doping of amorphous carbon films. J. Appl. Phys. 84: 2071–2081.
119. Sjöstrom H., Stafstrom S., Boman M., Sundgren J. E. (1995) Superhard and elastic carbon nitride thin-films having fullerene-like microstructure. Phys. Rev. Lett. 75: 1336–1339.
120. Sjöström H., Hultman L., Sundgren J. E., Hainsworth S. U., Page T. F., Theunissen G. S. A. M. (1996) Structural and mechanical properties of carbon nitride CN_x ($0.2 < x < 0.35$) film. J. Vac. Sci. Technol. A 14: 56–62.
121. Somani P. B., Yoshida A., Afre R. A., Adhikary S., Soga T., Umeno M. (2006) Nanostructured nitrogenated amorphous carbon films doped with nitrogen on p-silicon. Phys. Stat. Sol. A 203: 1982–1991.
122. Sundgren J. E., Johansson B. O., Karlsson S. E. (1983) Mechanisms of reactive sputtering of titanium nitride and titanium carbide I: Influence of process parameters on film composition. Thin Solid Films 105: 353–366.
123. Strondl C., van der Kolk C. G., Hurkmans T., Fleischer W., Trinh T., Carvalho N. M., de Hosson J. T. M. (2001) Properties and characterization of multilayers of carbides and diamond-like carbon. Surf. Coat. Technol. 142/144: 707–713.
124. Su Y. L., Kao W. H. (2000) Optimum Me-DLC coatings and hard coatings for tribological perfomance. J. Mater. Eng. Perform. 9: 38–50.
125. Sugimoto I., Miyake S. (1990) Oriented hydrocarbons transferred from a high-performance lubricative amorphous C:H:Si film during sliding in vacuum. Appl. Phys. Lett. 56: 1868–1870.
126. Stüber M., Leiste H., Ulrich S., Holleck H., Schild D. (2002) Microstructure and properties of low friction TiC–C nanocomposite coatings deposited by magnetron sputtering. Surf. Coat. Technol. 150: 218–226.
127. Taube K., Grischke M., Bewilogua K. (1994) Improvement of carbon-based coatings for use is the cold forming of nonferrous metals. Surf. Coat. Technol. 68/69: 662–668.
128. Trojan K., Grischke M., Dimigen H. (1994) Network modification of DLC coatings to adjust a defined surface-energy. Phys. Status Solid. A 145: 575–585.
129. Ulmeno M., Adhikary S. (2005) Diamond-like carbon thin films by microwave surface-wave plasma CVD aimed for the application of photovoltaic solar cells. Diam. Relat. Mater. 14: 1973–1979.
130. Vepřek S. (1999) The search for novel, superhard materials. J. Vac. Sci. Technol. A 17: 2041–2420.
131. Voevodin A. A., Zabinski J. S. (1998) Superhard, functionally gradient, nanolayered and nanocomposite diamond-like carbon coatings for wear protection. Diam. Relat. Mater. 7: 463–467.
132. Voevodin A. A., Zabinski J. S. (2000) Supertough wear-resistant coatings with "chameleon" surface adaptation. Thin Solid Films 370: 223–231.
133. Voevodin A. A., Rebholz C., Schneider J. M., Stevenson P., Matthews A. (1995) Wear-resistant composite coatings deposited by electron enhanced closed field unbalanced magnetron sputtering. Surf. Coat. Technol. 73: 185–197.
134. Voevodin A. A., Schneider J. M., Rebholz C., Matthews A. (1996) Multilayer composite ceramic-metal-DLC coatings for sliding wear applications. Tribol. Int. 29: 559–570.
135. Voevodin A. A., Jones J. G., Back T. C., Zabinski J. S., Strel'nitzki V. E., Aksenov I. I. (2005) Comparative study of wear-resistant DLC and fullerene-like CN_x coatings

produced by pulsed laser and filtered cathodic arc depositions. Surf. Coat. Technol. 197: 116–125.
136. Walters J. K., Pickup D. M., Newport R. J. (2005) Structure of a-C:N:H prepared from ammonia. J. Mat. Res. 20: 3338–3345.
137. Wang J. S., Sugimura Y., Evans A. G., Tredway W. K. (1998) The mechanical performance of DLC films on steel substrates. Thin Solid Films 325: 163–174.
138. Wang D. Y., Weng K. W., Chang Ch. L., Guo X. J. (2000) Tribological performance of metal doped diamond-like carbon films deposited by cathodic arc evaporation. Diam. Relat. Mater. 9: 831–837.
139. Wang R., Mercer C., Evans A. G., Cooper C. V., Yoon K. H. (2002) Delamination and spalling of diamond-like-carbon tribological surfaces. Diam. Relat. Mater. 11: 1797–1803.
140. Wei J., Hing P., Mo Z. Q. (1999) Structure and tribological behaviour of carbon nitride films. Wear 229: 1141–1147.
141. Wei Q., Narayan R. J., Narayan J., Sankar J., Sharma A. K. (1998) Improvement of wear resistance of pulsed laser deposited diamond-like carbon films through incorporation of metals. Mat. Sci. Eng. B 53: 262–266.
142. Wei Q., Narayan R. J., Sharma A. K., Sankar J., Narayan J. (1999) Preparation and mechanical properties of composite diamond-like carbon thin films. J. Vac. Sci. Technol. A 17: 3406–3414.
143. Wei Q., Sankar J., Sharma A. K., Oktyabrsky S., Narayan J., Narayan R. J. (2000) Atomic structure, electrical properties, and infrared range optical properties of diamondlike carbon films containing foreign atoms prepared by pulsed laser deposition. J. Mater. Res. 15: 633–641.
144. Wei Q., Sankar J., Narayan J. (2001) Structure and properties of novel functional diamond-like carbon coatings produced by laser ablation. Surf. Coat. Technol. 146/147: 250–257.
145. Wu W. J., Pai T. M., Hon M. H. (1998) Wear behavior of silicon-containing diamond-like carbon coatings. Diam. Relat. Mater. 7: 1478–1484.
146. Wu J. H., Sanghavi M., Sanders J. H., Voevodin A. A., Zabinski J. S., Rigney D. A. (2003) Sliding behaviour of multifunctional composite coatings based on diamond-like carbon. Wear 255: 859–868.
147. Yang P., Huang N., Leng Y. X., Yao Z. Q., Zhou H. F., Maitz M., Leng Y., Chu P. K. (2006) Wettability and biocompatibility of nitrogen-doped hydrogenated amorphous carbon films: Effect of nitrogen. Nucl. Inst. Meth. Phys. Res. B 242: 22–25.
148. Yao N., Evans A. G., Cooper C.V. (2004) Wear mechanism operating in W-DLC coatings in contact with machined steel surfaces. Surf. Coat. Technol. 179: 306–313.
149. Yokomichi H., Masuda A. (1999) Effect of sputtering with hydrogen dilution on fluorine concentration of low hydrogen content fluorinated amorphous carbon thin films with low dielectric constant. J. Appl. Phys. 86: 2468–2472.
150. Yu K. M., Cohen M. L., Haller E. E., Hansen W. L., Liu A. Y., Wu I. C. (1994) Observation of crystalline C_3N_4. Phys. Rev. B 49: 5034–5037.
151. Zehnder T., Patscheider J. (2000) Nanocomposite TiC/a-C:H hard coatings deposited by reactive PVD. Surf. Coat. Technol. 133–134: 138–144.
152. Zehnder T., Schwaller P., Munnik F., Mikhailov S., Patscheider J. (2004) Nanostructural and mechanical properties of nanocomposite nc-TiC/a-C:H films deposited by reactive unbalanced magnetron sputtering. J. Appl. Phys. 95: 4327–4334.
153. Zhang R. I., Ma H. T. (2006) Nano-mechanical properties and nano-tribological behaviors of nitrogen-doped diamond-like carbon (DLC) coatings. J. Mat. Sci. 41: 1705–1709.
154. Zhou Y. S., Wang O. M., Du H., Song G. H., Xiao J. O., Gong J., Sun C., Wen L. S. (2005) Structural characterization of nitrogen doped diamond-like carbon films deposited by arc ion plating. Appl. Surf. Sci. 241: 295–302.
155. Zou X. R., Xie J. Q., Feng J. Y. (1999) Structural and tribological characteristics of carbon nitride films deposited by the reactive ionized-cluster beam technique. Surf. Coat. Technol. 111: 119–122.

Tribology of Carbon Nitride Coatings

K. Adachi and K. Kato

Abstract Carbon nitride (CN_x) coatings exhibit a wide range of very attractive properties (such as low friction and wear, high hardness, good thermal and chemical stability, etc.) which make them very suitable for demending mechanical and tribological applications. During sliding against uncoated silicon nitride (Si_3N_4) and CN_x-coated Si_3N_4 in gaseous nitrogen atmosphere or in nitrogen gas flow, it provides superlow friction and wear. The beneficial effect of nitrogen on reducing friction and wear is much more pronounced if the portion of the running-in period is carried out in air or in oxygen before introducing nitrogen to the sliding interface. In this chapter, we will provide a comprehensive overview of the unique tribological properties of CN_x coatings in general and the effects of various gaseous environments on these properties in particular.

Keywords carbon nitride, gaseous nitrogen, low friction, low wear, tribolayer

1 Introduction

CN_x is theoretically expected to be harder than diamond if it has a metastable crystalline compound of the type of β-C_3N_4 [1,2]. However, practically produced CN_x coatings still do not have such ideal structure, and the hardness values reported by several research groups typically range from 15 to 50 GPa [3,4]. The specific carbon nitride coating to be discussed in this chapter is referred to as CN_x which contains 12–13% nitrogen in its amorphous structure [5] and has a hardness value of 30 GPa.

In dry nitrogen or in the flow of nitrogen gas, a contact combination of Si_3N_4/CN_x or CN_x/CN_x gives friction coefficients of 0.01–0.001 and the specific wear rates less than 10^{-7} mm^3/Nm [6]. The effect of nitrogen in reducing friction and

Tribology Laboratory, Graduate School of Engineering, Tohoku University, Sendai 980-8579, Japan.

C. Donnet and A. Erdemir (eds.), *Tribology of Diamond-Like Carbon Films: Fundamentals and Applications*.

wear is much more pronounced if we let the initial running-in period partially proceed in air before introducing the nitrogen gas to the sliding interface. The choice of proper running-in atmosphere is critically important for achieving marked reductions in friction and wear of CN_x when test environment is switched to dry nitrogen.

Recent results of the tribological properties of CN_x coatings are described in this chapter and their high potentials as good tribological materials are demonstrated.

2 Coating Procedure and Material Properties of CNx Coatings

CN_x coatings are typically produced on Si wafers or Si_3N_4 disks by the deposition of carbon from a carbon target (99.999% pure) together with the bombardment and mixing of carbon with the nitrogen ions generated simultaneously from an ion beam gun. The carbon for the coating on Si wafer is sputtered from the carbon target by argon ions, and in the case of Si_3N_4 disks, it is evaporated from a solid carbon material by heating with the electron beam. Figure 1 shows the schematic diagram of two types of coating methods that consist of the nitrogen ion gun for mixing, argon ion gun for sputtering, and electron beam source for evaporation. This figure also shows the carbon targets together with rotary disks where the substrates are attached.

The background and operating pressures in the vacuum chamber are lower than 2×10^{-4} Pa and 1.4×10^{-2} Pa, respectively. The acceleration voltage and the total ion current of argon ions for sputtering is 1 keV and 100 mA, respectively. The deposition rate of carbon is monitored via calibrated quartz crystal oscillators

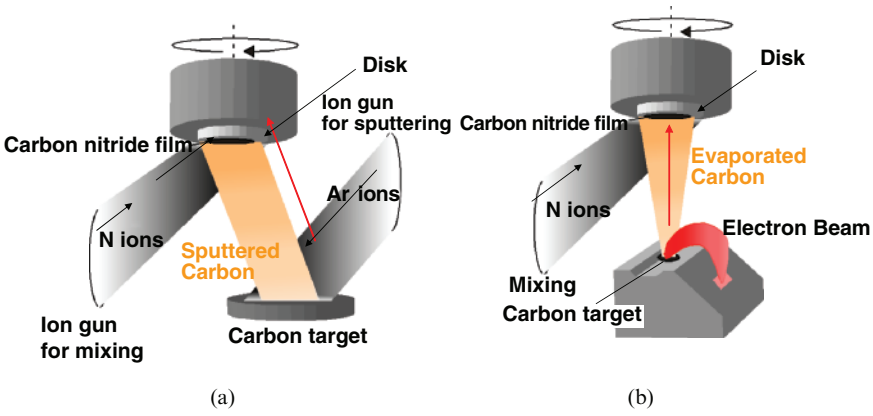

Fig. 1 Schematic illustration of two types of coating methods used in the deposition of CN_x coatings including nitrogen ion gun for mixing, argon ion gun for sputtering, electron beam source for evaporation, carbon target, and rotary substrate holder for the coating

and is varied in the range 1–50 nm/min. The energy and ion current density of beam-assisted nitrogen ions range from 0.5 to 10 keV and from 10 to 90 μA/cm^2, respectively. Substrates such as Si wafers and Si_3N_4 disks are sputter-cleaned prior to deposition by 5 min bombardment with argon ions of 1–3 kV acceleration voltage and 100 μA/cm^2 ion current density. Representative coating thickness of CN_x described in this chapter is 100 nm for Si-wafer substrate or 400 nm for Si_3N_4 disk, and its deposition rate is 0.2 nm/s or 2 nm/s, respectively.

Field emission–TEM images and electron diffraction patterns of the cross section of a typical CN_x coating on Si wafer in Fig. 2 clearly show that the CN_x coating is about 100 nm in thickness, has an amorphous structure, and the interlayer between CN_x coating and Si wafer is 5–10 nm thick. Figure 3 shows x-ray photoelectron spectroscopy (XPS) analysis of the surface of CN_x coatings on Si wafer. It is shown that the composition ratios of carbon, nitrogen, and oxygen are about 81%, 12%, and 7%, respectively. Composition ratios of carbon and nitrogen at 0.56 nm below the surface are about 88% and 12%, where oxygen is not detected. Raman analysis shows that the intensity ratio of D band and G band (Graphite) is about 2.0 [7].

Figure 4(a) shows the hardness of the CN_x coating on Si wafer and (100) surface of the bulk Si wafer observed with a nanohardness tester. The effect of deposition rate on coating hardness is shown in Fig. 4(b) for the case of CN_x on Si_3N_4 disk. The hardness of the CN_x coatings varies in the range from 15 to 40 GPa depending on the indentation depth and the coating deposition rate.

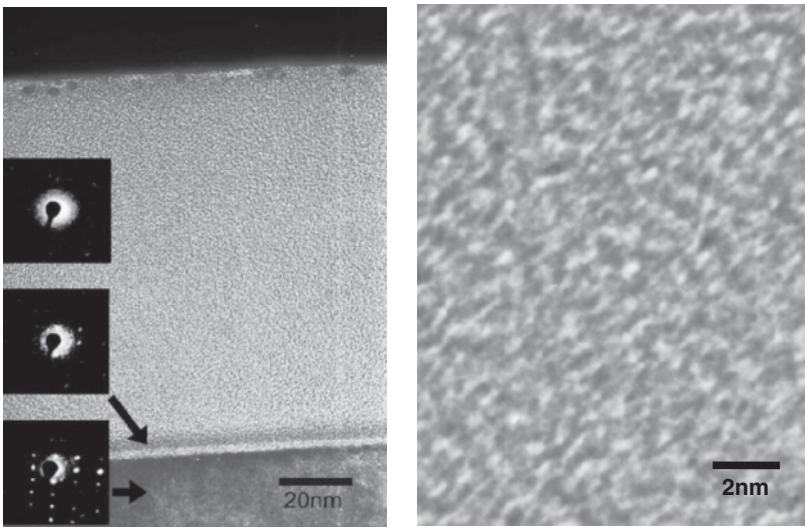

Fig. 2 Low- and high-resolution field-emission transmission electron micrographs of the cross-section of CN_x coated on Si wafer

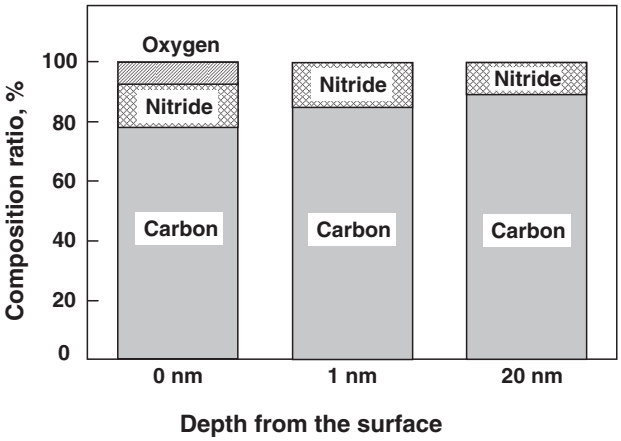

Fig. 3 Chemical composition of CN_x coating at various depths as determined by XPS. This film was produced on Si wafer

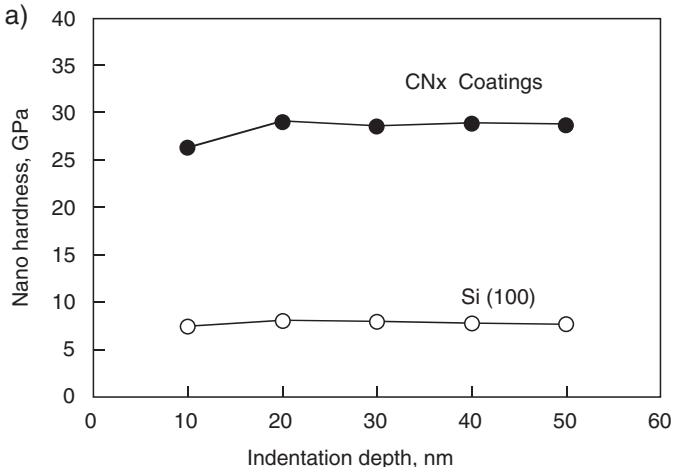

Fig. 4 (a) Hardness of CN_x coating of 100 nm thickness on Si wafer measured as a function of indentation depth

3 Friction of CN_x Coatings

3.1 Effect of Test Atmosphere on Friction of Si_3N_4 Ball/CN_x-coated Si Wafer

Figure 5 shows the effects of various gases (including nitrogen, carbon dioxide, and oxygen) and vacuum on friction coefficients of a pair of Si_3N_4 ball/CN_x-coated Si wafer [7]. Figure 6 shows the friction coefficients in steady state after 240 sliding

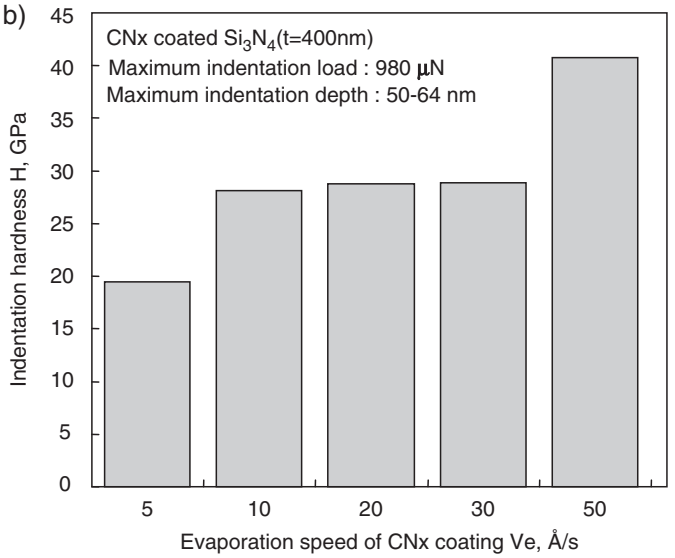

Fig. 4 (b) Effect of deposition rate on the hardness of CN_x coating of 400 nm thickness on Si_3N_4

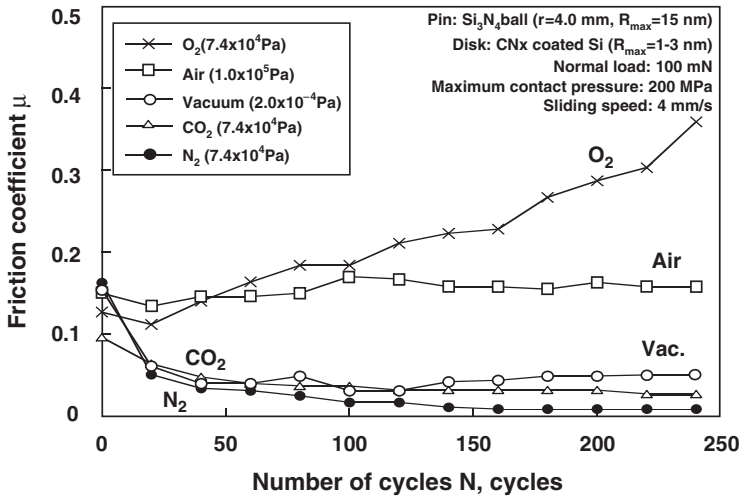

Fig. 5 Friction coefficient of Si_3N_4 /CN_x-coated Si wafer in air, O_2, CO_2, and N_2 of 7.4×10^4 Pa, and vacuum of 2×10^{-4} Pa

cycles for the same test results summarized in Fig. 5 [7]. As is clear, the friction coefficient becomes the lowest in dry nitrogen, where steady-state friction coefficient is less than 0.01. Carbon dioxide provides a similar effect as that of nitrogen in terms of reducing friction, but the steady-state friction coefficient is about three times larger than that in nitrogen. Oxygen results in a totally opposite effect.

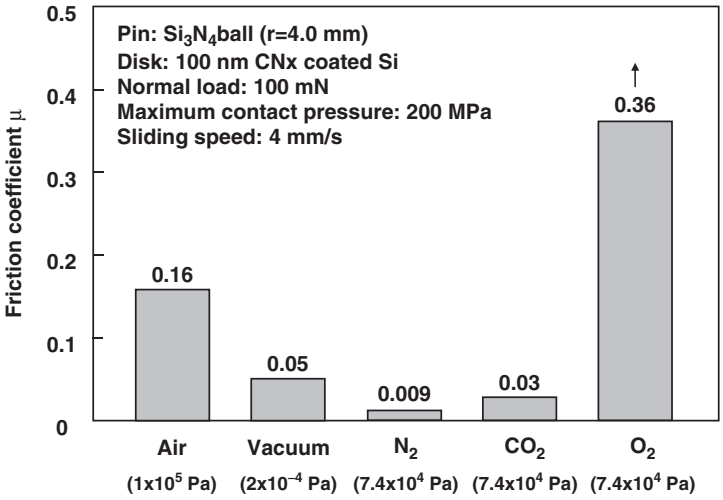

Fig. 6 Effects of surrounding gases or vacuum on friction coefficient at the 240th cycle in Fig. 5

Specifically, the friction coefficient in oxygen increases up to 0.36 after 240 sliding cycles. It is clearly shown from these test results that friction coefficient at Si_3N_4/CN_x contact is quite different depending on the kind of atmospheric gases present in the test chamber.

3.2 Effect of Humidity on Friction of Si_3N_4 Ball/CN_x-coated Si_3N_4 Disk and CN_x-coated Si_3N_4 Ball/CN_x-coated Si_3N_4 Disk

If water molecules are gradually introduced into the nitrogen gas of 1×10^5 Pa (containing ~100 ppm oxygen concentration) in order to change its relative humidity, friction coefficient increases from 0.01 to about 0.1 by increasing humidity from 2% to 60% RH as shown in Fig. 7 for Si_3N_4/CN_x on Si_3N_4 contact, and Fig. 8 for CN_x-coated Si_3N_4/CN_x-coated Si_3N_4 pairs [8]. The overall effects of humidity on their friction coefficients in nitrogen are summarized in Fig. 9. Proportion of friction coefficient to relative humidity at Si_3N_4/CN_x-coated Si_3N_4 contact is more than that at CN_x-coated Si_3N_4/CN_x-coated Si_3N_4 contact. In addition, sudden rises in friction coefficient occur over 5% RH due to the agglomeration of wear debris particles at sliding interface. These debris particles are generated mainly by the oxidation of Si_3N_4 at the contact interface. Their detrimental effects on friction become much more pronounced and frequent at humidity levels of more than 30% RH.

Figure 10 shows the effect of storage humidity of the CN_x coatings on friction properties in nitrogen. It shows that to guarantee low and stable friction coefficients

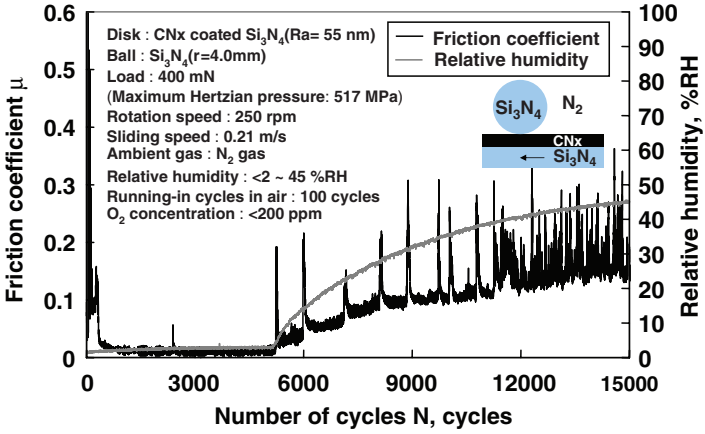

Fig. 7 Effect of relative humidity (RH %) in nitrogen of 1.03×10^5 Pa on friction coefficient of Si_3N_4/CN_x-coated Si_3N_4 test pair

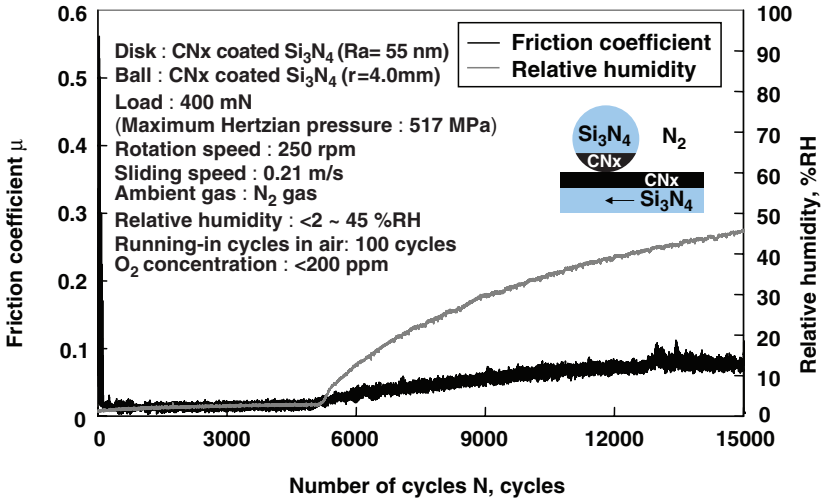

Fig. 8 Effect of relative humidity (RH %) in nitrogen of 1.03×10^5 Pa on friction coefficient of CN_x-coated Si_3N_4/CN_x-coated Si_3N_4 test pair

in the order of 0.001–0.01 when sliding CN_x-coated Si_3N_4 against CN_x-coated Si_3N_4 in nitrogen, the specimen must not be exposed to humidity higher than 20% RH.

It is also clearly shown from these results that those gases, which provide low friction coefficients for Si_3N_4/CN_x-coated Si_3N_4 and CN_x-coated Si_3N_4/CN_x-coated Si_3N_4 pairs mentioned above play an important role for avoiding water molecule adsorption on the sliding contact interfaces.

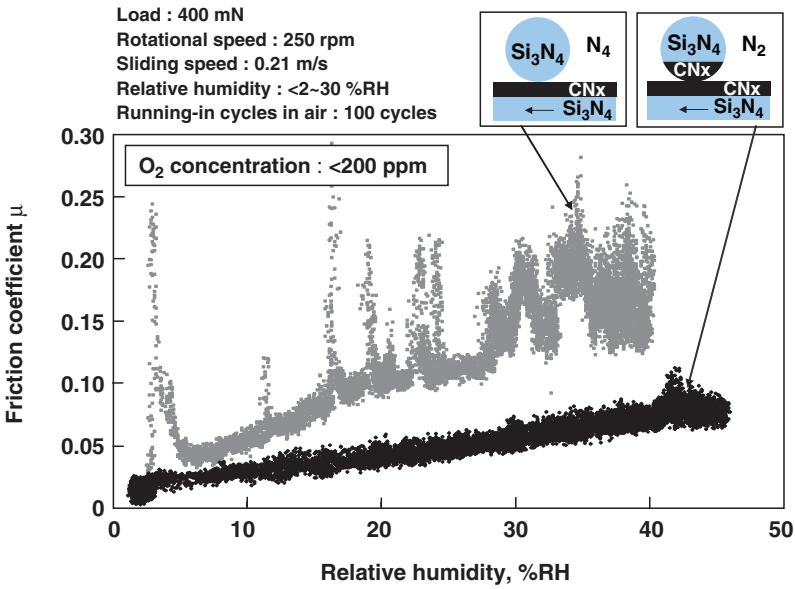

Fig. 9 Effect of relative humidity on friction coefficients of Si_3N_4/CN_x-coated Si_3N_4 and CN_x-coated Si_3N_4/CN_x-coated Si_3N_4 test pairs under 400 mN load at 0.21 m/s in nitrogen

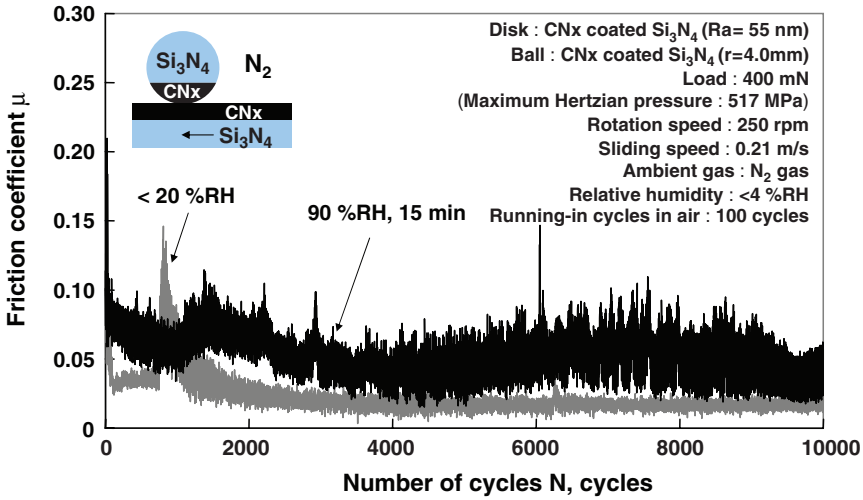

Fig. 10 Effect of storage humidity of CN_x coating on friction coefficients of CN_x-coated Si_3N_4/CN_x-coated Si_3N_4 test pair under 400 mN load at 0.21 m/s in nitrogen

4 Lubrication of CN_x Coatings with Nitrogen

4.1 Effect of Nitrogen Flow on Friction of Si_3N_4 Ball/CN_x-coated Si_3N_4 Disk and CN_x-coated Si_3N_4 Ball/CN_x-coated Si_3N_4 Disk

It is confirmed in the previous section that nitrogen is effective in reducing friction of both Si_3N_4/CN_x-coated Si_3N_4 and CN_x-coated Si_3N_4/CN_x-coated Si_3N_4 test pairs. This suggests a practical technology of lubrication with nitrogen. It is expected as a new type of promising lubrication for tribological contact in small and precise machines such as microelectro mechanical systems (MEMS), in which conventional lubrication methods with liquids, solids, and gases cannot work due to meniscus force, wear particle generation, and other structural problems.

The practical possibility of such a new lubrication technology is confirmed by gas flow system with pin-on-disk friction tester as shown in Fig. 11 [9]. A certain amount of gas was supplied to the sliding interface by blowing nitrogen at a constant flow rate of 2.0 L/min through a pipe at the distance of 10 mm from the contact spot between the pin and the disk. Figure 12 shows frictional response of Si_3N_4 ball against CN_x-coated Si_3N_4 disk to the flow of nitrogen to the contact interface. It is clearly shown that nitrogen flow has a beneficial effect on reducing friction.

Figures 13(a) and (b) show friction properties at four different ball/disk combinations of Si_3N_4/Si_3N_4, CN_x on Si_3N_4/Si_3N_4, Si_3N_4/CN_x on Si_3N_4, and CN_x on Si_3N_4/CN_x on Si_3N_4 in air and in nitrogen flow, respectively [6]. The beneficial effect of flowing nitrogen to the sliding interface is clearly shown in all of these pin/disk combinations in Figs 13(a) and (b). In sliding contact combinations of Si_3N_4/Si_3N_4, Si_3N_4/CN_x-coated Si_3N_4, and CN_x-coated Si_3N_4/CN_x-coated Si_3N_4, blowing nitrogen to the interface reduces friction coefficient by the amount of about 50% (from 0.80

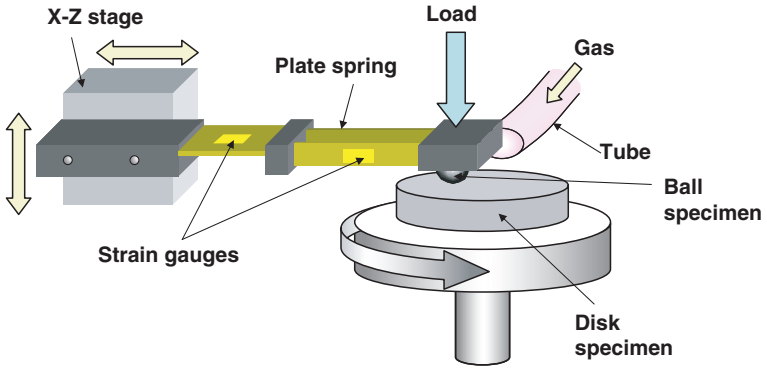

Fig. 11 Schematic illustration of friction tester retrofitted with a tube to enable gas flow to the sliding interface during tests in air. Tube diameter = 4 mm, gas flow rate = 2.1 cc/mm^{2}s (2 L/min), distance between ball center and tube end = 10 mm

to 0.40), 50% (from 0.30 to 0.15), and 77% (from 0.30 to 0.07), respectively. Especially, the sliding pair of CN_x-coated Si_3N_4/CN_x-coated Si_3N_4 provides very low and stable friction coefficient of 0.07 or less with the flow of nitrogen. In the case of CN_x-coated Si_3N_4/Si_3N_4, friction coefficient shows low and stable value of 0.05 at initial stage until 2,500 cycles, and it gradually increases to the similar value as that provided by the Si_3N_4/Si_3N_4 contact pair due to the removal of the CN_x coatings on the Si_3N_4 ball.

Figure 14 shows the effects of various gases on friction coefficients of CN_x-coated Si_3N_4/CN_x-coated Si_3N_4 contact [10], while Fig. 15 summarizes the friction coefficients of those test pairs in a bar chart in the steady-state sliding regime of Fig. 14 [10]. Friction coefficient, i.e., ~0.01, is the lowest in nitrogen while it is much higher, i.e., more than 0.15, when oxygen or air is blown to the sliding interface.

The beneficial effect of nitrogen on reducing friction of CN_x (see Fig. 13) is much more enhanced by the supply of nitrogen directly to the sliding interface after a certain number of sliding cycles in air. Specifically, as shown in Fig. 16(a) and (b), the friction coefficients of Si_3N_4/CN_x-coated Si_3N_4 and CN_x-coated Si_3N_4/CN_x-coated Si_3N_4 become much lower when nitrogen is introduced to the sliding interface following 1,000 running-in cycles in air. The arrows in the figure show the starting cycle of nitrogen flow [6]. When the nitrogen flow starts at the same time as starting of sliding, friction coefficient is rather unstable (Fig. 16(a)) and relatively high, i.e., 0.07 (Fig. 16(b)). The nitrogen flow to the sliding interface after 1,000 runnning-in cycles in air, however, reduces friction coefficients down to values as low as 0.01. This finding suggests the importance of the sliding history on friction prior to nitrogen gas flow and points out that nitrogen gas is essential for achieving low friction coefficients in CN_x coatings.

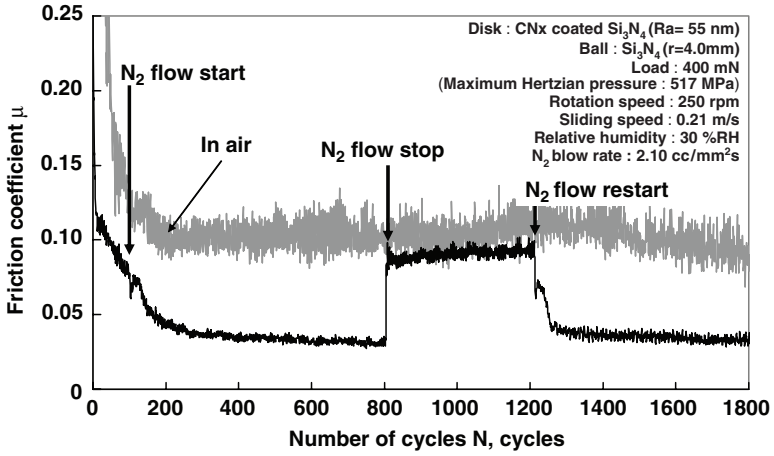

Fig. 12 Response to friction at Si_3N_4 /CN_x-coated Si_3N_4 contact by flowing of nitrogen

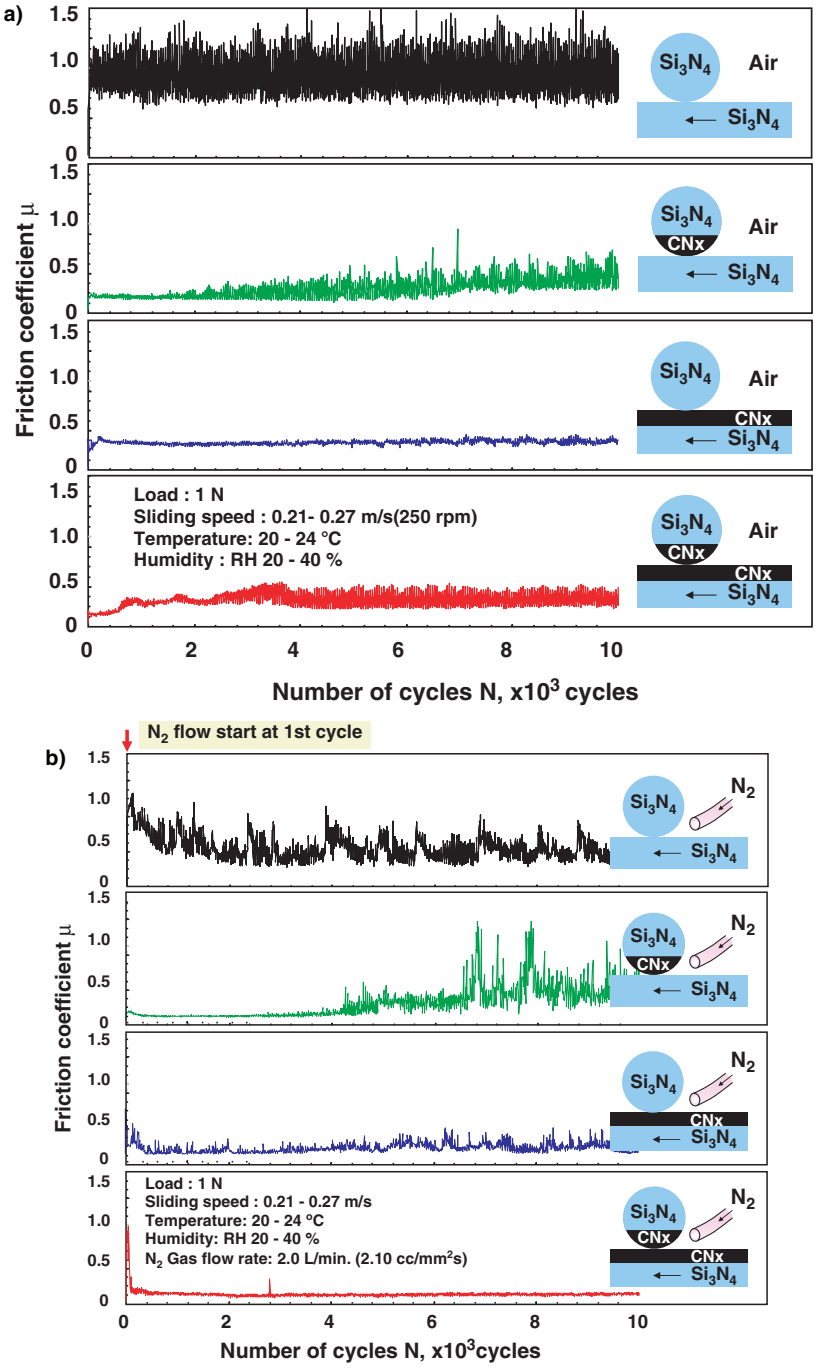

Fig. 13 Friction coefficients in 10^4 cycles in air (a) and in the flow of nitrogen (b) of the contact combination of Si_3N_4/ Si_3N_4, CN_x-coated Si_3N_4/Si_3N_4, Si_3N_4/CN_x-coated Si_3N_4 and CN_x-coated Si_3N_4 /CN_x-coated Si_3N_4

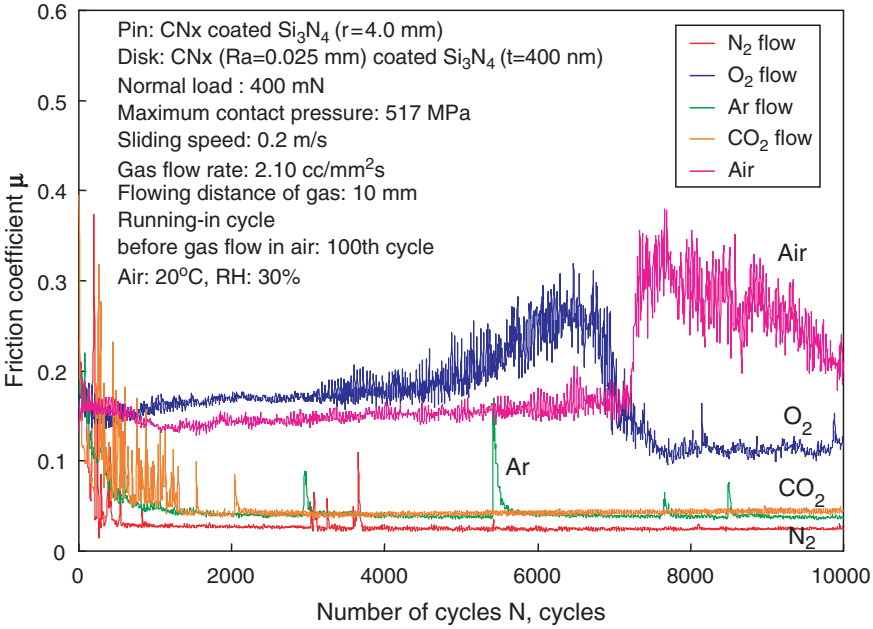

Fig. 14 Friction coefficient of CN_x-coated Si_3N_4 /CN_x-coated Si_3N_4 contact in air and in the flow of oxygen, carbon dioxide, argon, and nitrogen

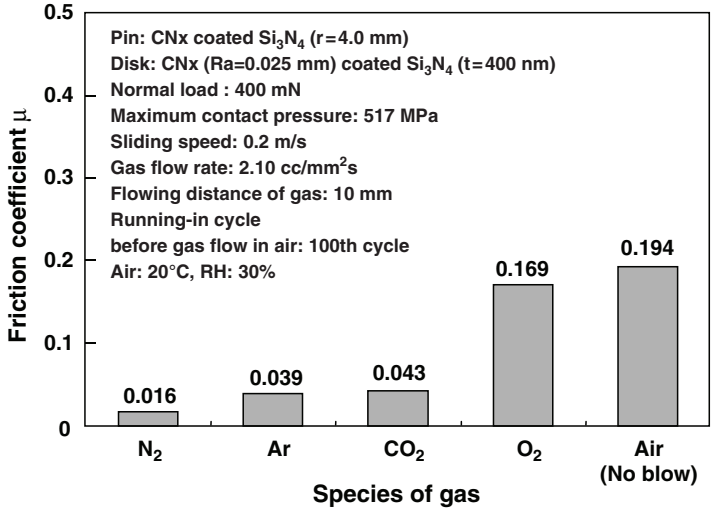

Fig. 15 Effect of gas species on friction coefficient of CN_x-coated Si_3N_4 /CN_x-coated Si_3N_4 test pair in air

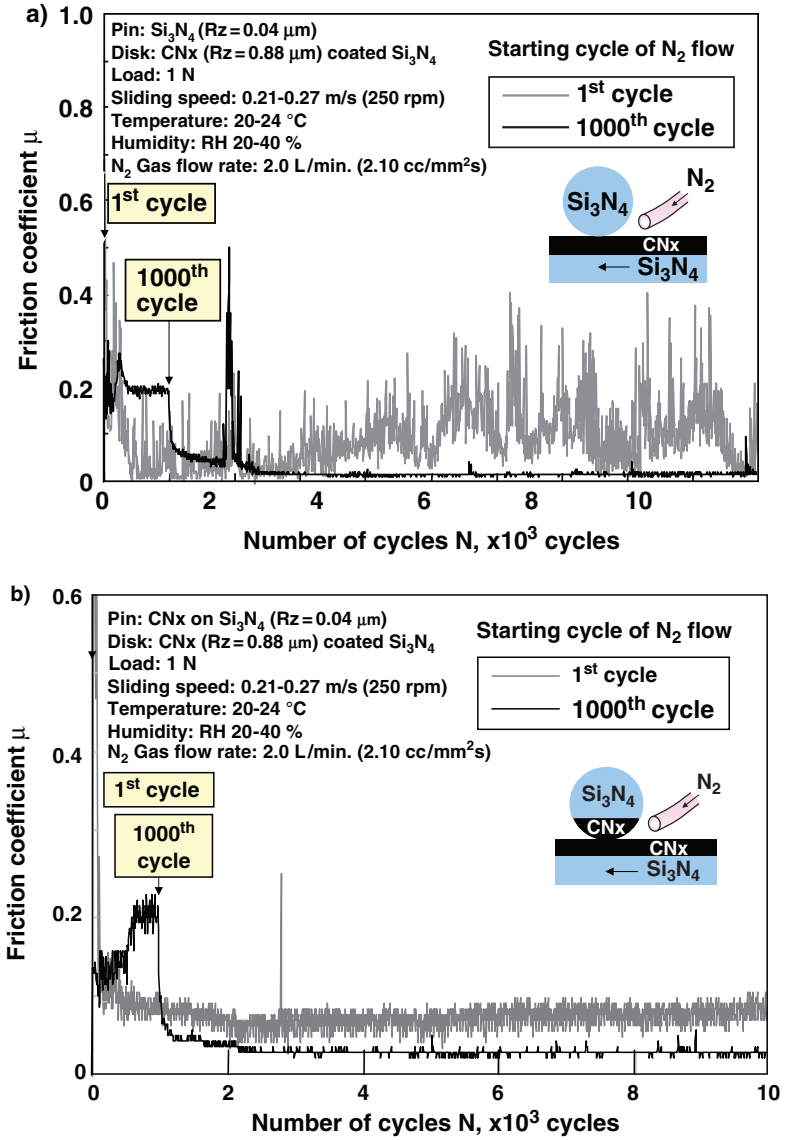

Fig. 16 Quick reduction in friction coefficient by having N_2 flow after 1,000 running-in cycles in air: (a) Si_3N_4 /CN_x-coated Si_3N_4; (b) CN_x-coated Si_3N_4/CN_x-coated Si_3N_4

This kind of running-in effect on friction of CN_x in nitrogen flow is much more pronounced when the atmosphere for running-in is oxygen for the initial 50 cycles as shown in Fig. 17 [6]. The steady-state friction coefficient in nitrogen flow is reduced from 0.1 to 0.005 by introducing test pairs subjected to 50 running-in cycles in oxygen flow first.

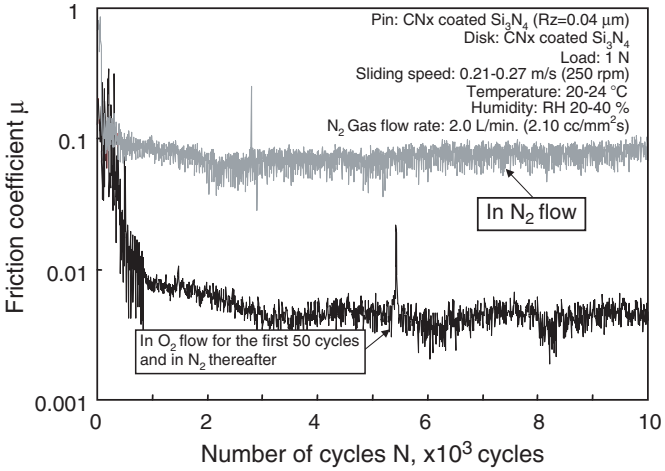

Fig. 17 Effect of running-in of initial 50 cycles in oxygen flow on friction coefficient of CN_x-coated Si_3N_4 /CN_x-coated Si_3N_4 test pair in nitrogen flow

4.2 Effect of Flow Gas on Friction at the Contact Combination of Si_3N_4 Ball/CN_x-coated Si_3N_4 Disk and CN_x-coated Si_3N_4 Ball/CN_x-coated Si_3N_4 Disk

Figure 18 shows the friction coefficients of CN_x-coated Si_3N_4/CN_x-coated Si_3N_4 test pairs in three different atmospheric conditions: air, oxygen flow, and nitrogen flow. As is clear, in the running-in period of these sliding tests, friction coefficient first gradually increases, and then decreases to relatively low and constant values [6]. In this figure, it is interesting to notice that the running-in periods are the shortest in air and oxygen or the steady-state regime is reached ten times faster in these gases than in nitrogen flow.

Figure 19 shows steady-state friction coefficient and specific wear rates of the CN_x coated balls slid against the CN_x-coated Si_3N_4 disks in air, oxygen flow, nitrogen flow; oxygen flow for the first 550 cycles and nitrogen flow in the following cycles; and air for the first 100 cycles and nitrogen flow in the following cycles. Here, specific wear rate was defined as a total wear volume at 10,000th cycle divided by the load and the sliding distance. Although the sliding at CN_x-coated Si_3N_4/CN_x-coated Si_3N_4 contact in nitrogen flow generates much lower friction coefficient at the steady-state sliding condition, friction at the initial stage of sliding is much higher than those in air and oxygen flow. Larger specific wear rate in case of the nitrogen flow is considered as caused by higher friction at the initial stage. It is considered the reason why running-in process in air and/or oxygen flow is useful to obtain the low friction coefficient quickly. It is therefore important to notice that the running-in in a proper atmosphere effectively reduces not only for friction, but also wear when rest of the sliding tests are conducted in nitrogen.

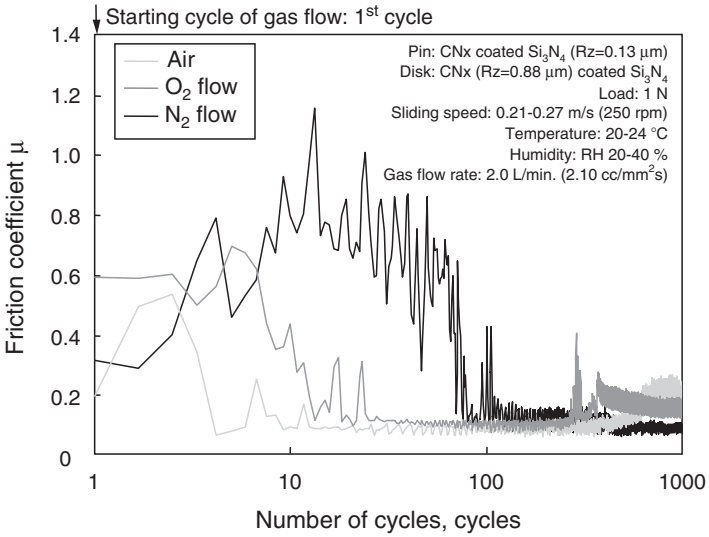

Fig. 18 Friction coefficient of CN_x-coated Si_3N_4/ CN_x-coated Si_3N_4 test pair in three different atmospheric conditions: air, oxygen flow, and nitrogen flow

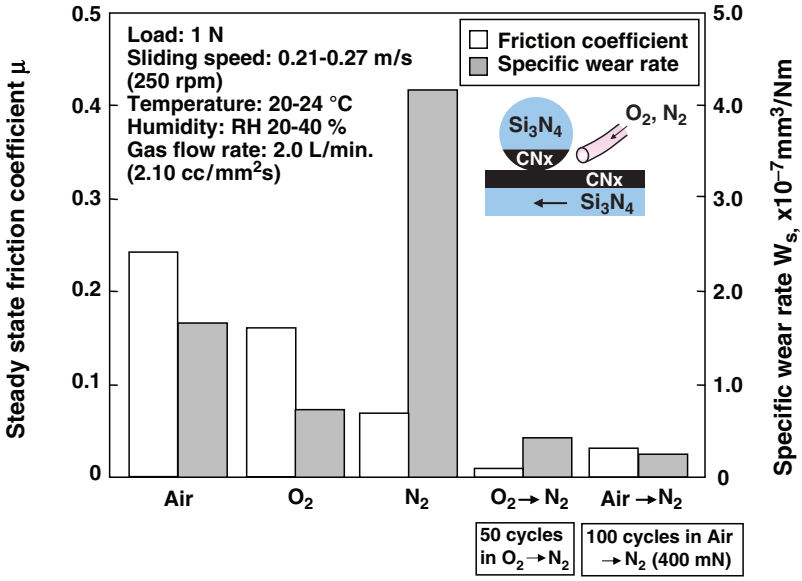

Fig. 19 Friction coefficients in steady state and specific wear rates observed at CN_x-coated Si_3N_4 /CN_x-coated Si_3N_4 under 1 N load at 0.21 m/s in air, in oxygen flow, in nitrogen flow supplied at the 1st friction cycle in air, the 100th after running in air, and 50th after running in oxygen flow

5 Mechanisms of Low Friction of CN_x Coatings in Nitrogen

It is well-confirmed in the previous section that initial running-in is a key issue for reducing friction of Si_3N_4/CN_x-coated Si_3N_4 and CN_x-coated Si_3N_4/CN_x-coated Si_3N_4 test pairs in nitrogen flow. Two aspects, therefore, which may have involved in the mechanisms of low friction in nitrogen during the running-in period are discussed in this section.

First of all, the mechanical interlocking of sharp asperities on rough surfaces cause high friction. Therefore, smoothing of these surfaces by wear during the running-in period should have a positive effect on steady-state friction as shown in Fig. 20, in which the linear relationship between the friction coefficient and worn surface roughness of CN_x coating after sliding observed in nitrogen is clearly shown [11]. It is confirmed from the figure that friction coefficients below 0.01 can be achieved only when the worn surface roughness is below 5 nm. At the same time it is also shown that the resultant roughness on the wear scar controls the thickness of the tribolayer.

Figure 21 confirms the effect of nitrogen in reducing friction at the contact combination of steel ball/CN_x-coated Si wafer [12]. Friction coefficient drops from 0.10 to 0.01 after about 50 cycles in dry nitrogen although it stays at about 0.8 in ultra-high vacuum. The optical photos in Fig. 22 confirm that the low friction coefficient of 0.01 is generated by having a tribolayer sticking on the contact spot of the steel ball in dry nitrogen [12]. Figure 23 shows that the optical photo of wear scar on a CN_x-coated Si_3N_4 ball after sliding against CN_x-coated Si_3N_4 disk gives low friction

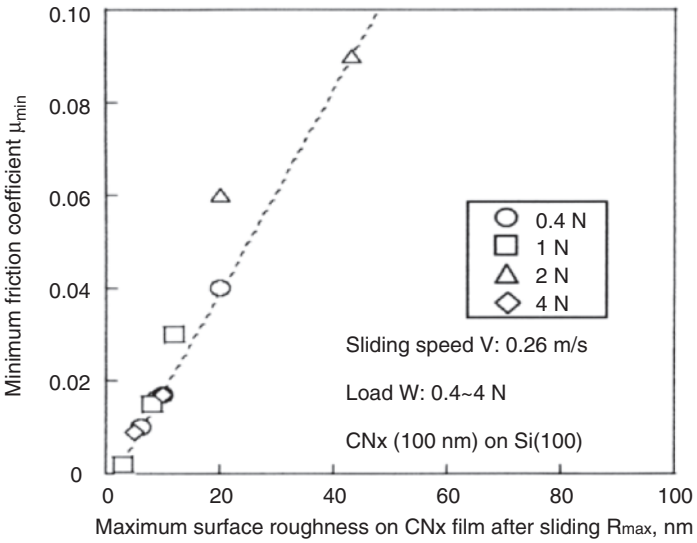

Fig. 20 Relationship between the minimum friction coefficient and the maximum surface roughness on wear scar of CN_x-coated Si wafer during sliding against Si_3N_4 ball in nitrogen atmosphere

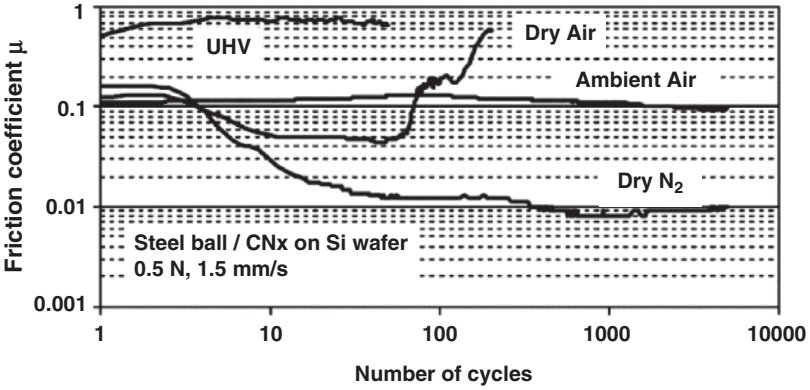

Fig. 21 Effect of dry nitrogen, ambient air, dry air, and vacuum on friction coefficient of steel ball sliding against CN_x-coated Si wafer

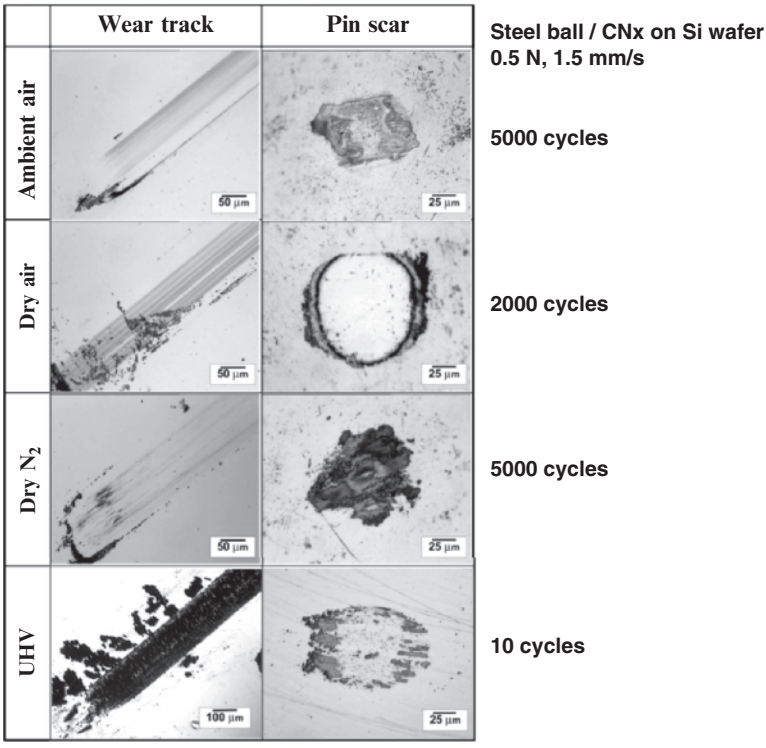

Fig. 22 Optical images of wear scars on the steel pins and CN_x coatings after sliding tests of the test pair as in Fig. 21

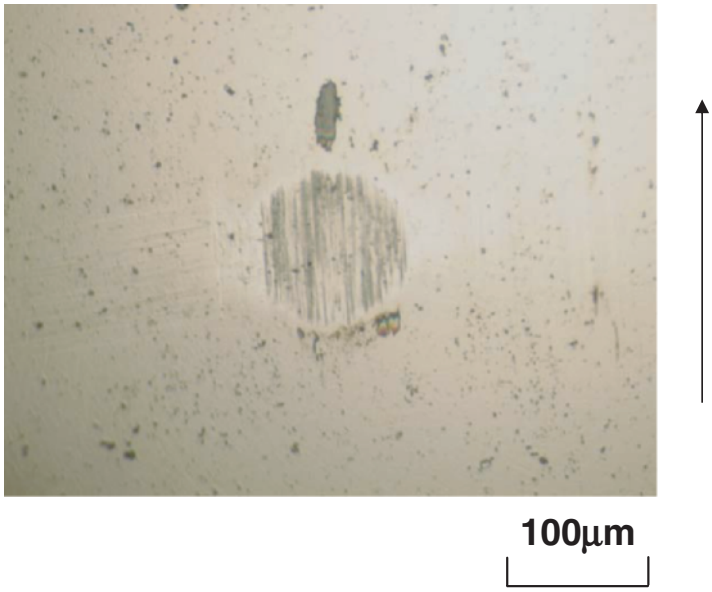

Fig. 23 An optical image of wear scar on a CN_x-coated Si_3N_4 ball after sliding against CN_x-coated Si_3N_4 disk in nitrogen flow

in the flow of nitrogen. A tribolayer formed on the ball shown in Fig. 23 gives such low friction. The analysis by Raman spectrum of the wear scar in Fig. 24 shows that a graphite-like structure is formed in the tribolayer. This observation gives some explanation about the mechanism of low friction observed in the chapter if the graphitic structure of the tribolayer behaves similarly as graphite does in the experiment by Zaidi et al. [13] as shown in Fig. 25, where the friction coefficients are about 0.2 in oxygen, 0.1 in water vapor, and 0.02 in helium or argon at the sliding contact between steel pin and graphite plate. The migration of helium or argon atoms into the lattice defects of graphite is supposed to reduce the friction coefficient down to 0.02 in their study. This kind of model may give one type of explanation of low friction coefficient of the order of 0.001 observed in nitrogen or in the flow of nitrogen at Si_3N_4/CN_x-coated Si_3N_4 contact and CN_x-coated Si_3N_4/CN_x-coated Si_3N_4 contact in this chapter.

6 Wear of CN_x Coatings

It is well confirmed in the previous section that initial running-in is a key issue for achieving superlow friction between sliding pairs of Si_3N_4/CN_x-coated Si_3N_4 and CN_x-coated Si_3N_4/CN_x-coated Si_3N_4 in nitrogen flow.

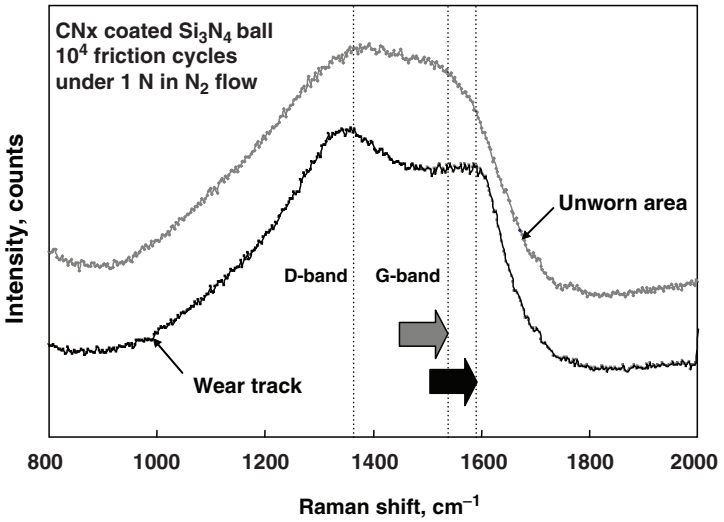

Fig. 24 Raman spectrum on wear scar of CN_x-coated Si_3N_4 ball after 10^4 friction cycles against CN_x-coated Si_3N_4 disk

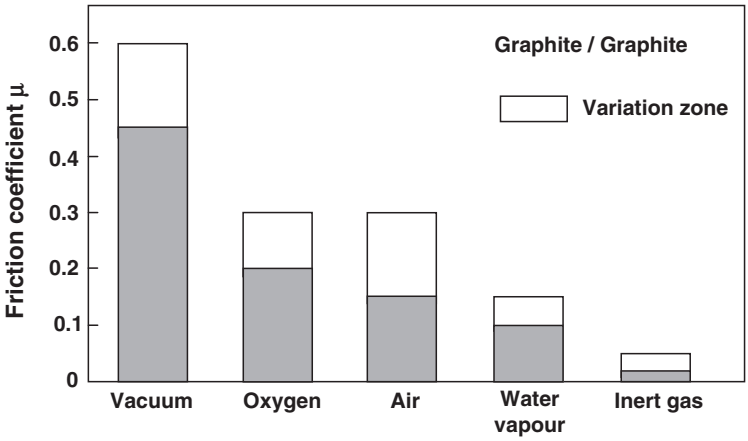

Fig. 25 Friction coefficient at graphite/graphite contact in different environments

On the other hand, tribolayer formed during running-in is also key to reducing friction. Wear particles, which form agglomerates, transfer layers, inclusions, mixing layer, or free particles, are therefore helpful for the formation of the low-friction lubricant films.

In the case of wear of CN_x coatings, the role of wear particles in friction is quite unclear at present, although fine wear debris particles were found on the surfaces of CN_x coatings and Si_3N_4 together with some agglomerates and transfer layers on ball surfaces after reaching the steady-state sliding regimes.

In this early stage of study of wear of CN_x coatings in relation to friction, it would be important to know the mechanical wear mechanism of CN_x coatings in nanometer scale as the first step to the understanding of friction mechanism of CN_x coatings against Si_3N_4 or CN_x coatings in nitrogen.

Figure 26 shows an atomic force microscopy (AFM) image and cross-profiles of a wear track on CN_x-coated Si wafer after 20 friction cycles in the E-SEM by a diamond pin [14]. Change of wear volume and specific wear rate as a function of number of friction cycles is shown in Fig. 27, where a fine wear debris particle is suddenly generated by delamination at the ninth cycle and wear volume increases suddenly [14]. Scanning electron microscopy (SEM) and AFM observations confirm that a wear particle generated at such a moment has a shape of a thin flake in nanometer scale. The critical friction cycle, N_c for generating such a thin flaky wear particle of CN_x is obtained under various normal load and pin tip radius and the

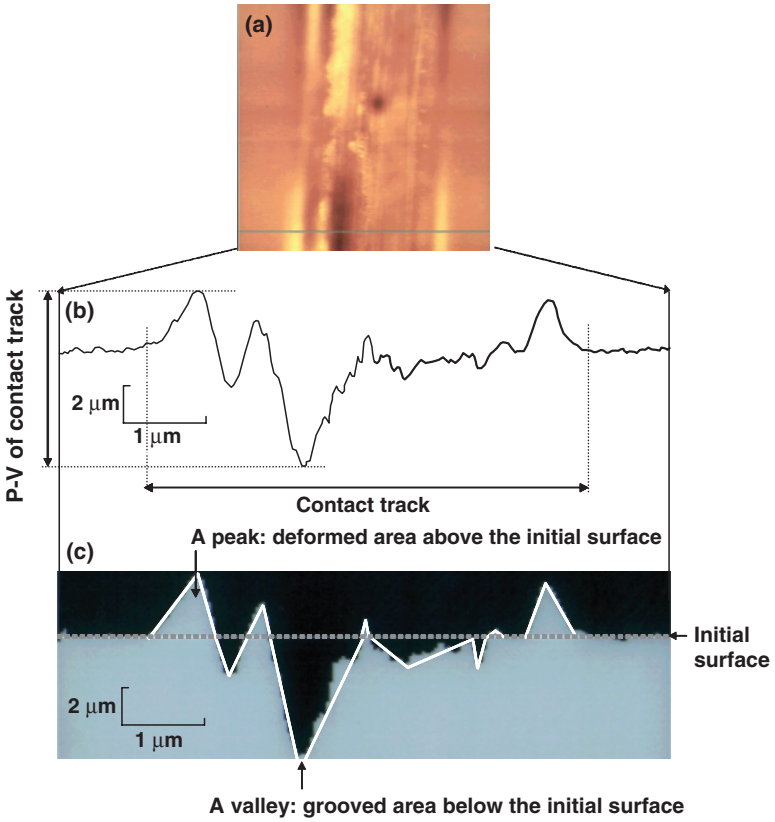

Fig. 26 AFM image and cross-profile of a wear track formed on CN_x coating that was deposited on Si wafer after 20 friction cycles by a diamond pin: (a) AFM image, (b) cross-profile, (c) simplified profile for wear volume calculation

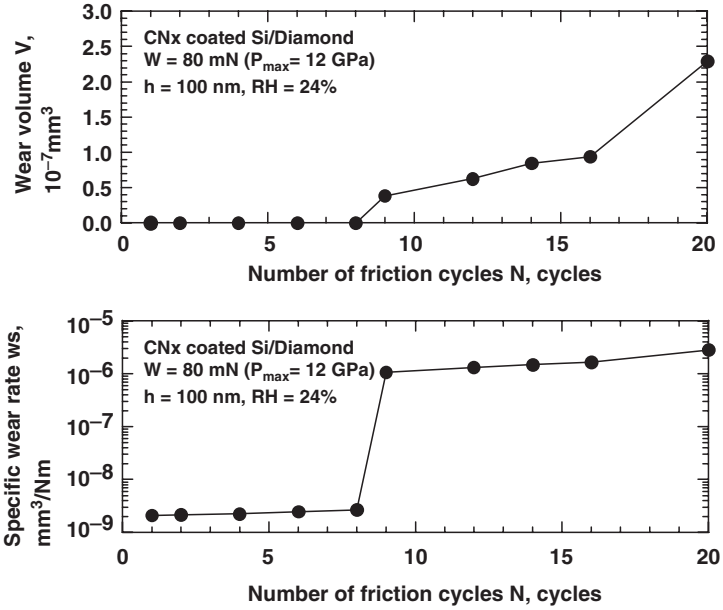

Fig. 27 Wear volume and specific wear rate of CN_x coating in 20 friction cycles by a diamond pin

representative plastic strain $\Delta\varepsilon_p$ around the contact of an asperity or a tip is calculated by measuring the depth of groove on a wear track.

Figure 28 shows the experimental relationship between the representative plastic strain $\Delta\varepsilon_p$ in the contact area of nanometer scale and the critical friction cycle, N_c when nanometer scale surface delamination of CN_x coating takes place to generate a thin flaky wear particle [14–16].

It is clear from the results of Figs 27 and 28 that thin and flaky wear particles are generated by the mechanism of low cycle fatigue at the abrasive contacts between CN_x coating and diamond pin tip or asperities on its surface. Wear mechanisms for the small wear rate in the range of 10^{-9} mm^3/Nm observed before having the low cycle fatigue wear in Fig. 27 are very unclear at this stage. However, the understanding of mechanical wear mechanism of CN_x coating in nanometer scale as shown in Figs 27 and 28 must be an introduction to the understanding of running-in mechanism which results in low friction coefficient below 0.01 at the contact combination of Si_3N_4/CN_x-coated Si_3N_4 contact and CN_x-coated Si_3N_4/CN_x-coated Si_3N_4 in nitrogen.

7 Concluding Remarks

Attractive friction and wear properties of CN_x coatings sliding against Si_3N_4, CN_x-coated Si wafer or CN_x-coated Si_3N_4 observed in recent results are summarized as follows;

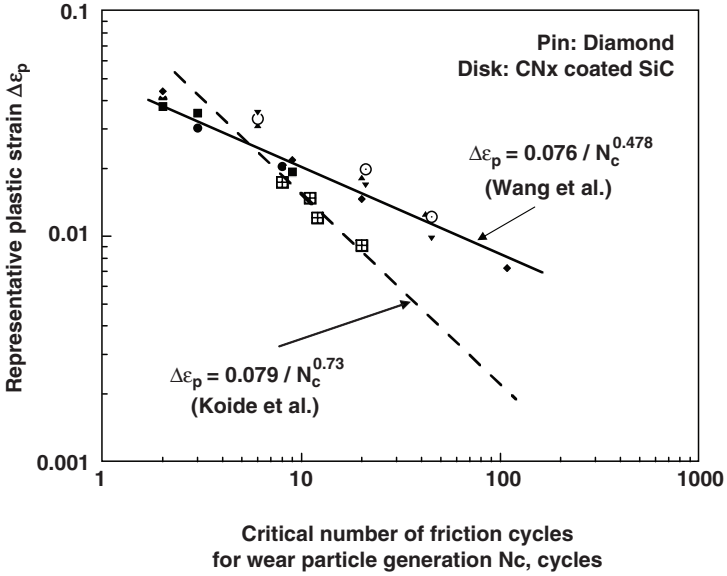

Fig. 28 Nanoscale wear law based on low cycle fatigue wear of CN_x coatings in repeated sliding against a diamond pin

1. The contact combinations of Si_3N_4/CN_x-coated Si wafer, Si_3N_4/CN_x-coated Si_3N_4 and CN_x-coated Si_3N_4/CN_x-coated Si_3N_4 are capable of providing friction coefficients below 0.01 in gaseous nitrogen.
2. Nitrogen flow to the contact interface in air effectively reduces sliding friction coefficient for the contact combinations of Si_3N_4/CN_x-coated Si_3N_4 and CN_x-coated Si_3N_4/CN_x-coated Si_3N_4 from 0.30 to 0.15 and from 0.30 to 0.07, respectively. This suggests that lubrication of CN_x coatings with gaseous nitrogen is practically useful.
3. The effect of nitrogen in reducing friction and wear is much more pronounced if the running-in sliding period is carried out in air or oxygen before introducing nitrogen to the sliding interface. By allowing 1,000 cycles of sliding to take place in air, the friction coefficient in nitrogen flow is reduced from about 0.1 to 0.02 for the contact combination of Si_3N_4/CN_x-coated Si_3N_4. By allowing 50 cycles of sliding in oxygen flow before nitrogen flow, the friction coefficient in nitrogen flow is reduced from 0.1 to 0.005 and specific wear rates of less than 10^{-7} mm^3/Nm is observed.
4. Surface sperities of CN_x coatings are worn away by a low cycle fatigue wear mechanism during the initial running in periods which range from less than 100 cycles to 1,000 cycles. We feel that this is an interesting finding which requires further in-depth studies that can help better understand the very unique friction and wear mechanisms of CN_x coatings.

References

1. A. I. Liu, M. L. Cohen, Prediction of new low compressibility solid, Science, 245 (1989), 841–842.
2. M. L. Cohen, Predicting useful materials, Science, 261 (1993), 307–308.
3. D. Li, E. Cutiongco, Y. -W. Chung, M. -S. Wong, W. D. Sproul, Composition, structure and tribological properties of amorphous carbon nitride coatings, Surf. Coat. Technol., 68/69 (1994), 611–615.
4. E. H. A Dekempeneer, J. Meneve, J. Smeets, S. Kuypers, L. Eersels, R. Jacobs, Structural, mechanical, and tribological properties of plasma-assisted chemically vapour deposited hydrogenated C_xN_{1-x}:H films, Surf. Coat. Technol., 68/69 (1994), 621–625.
5. A. Khurshudov, K. Kato, D. Sawada, Microtribological characteristics of carbon nitride coatings, Proc. Int. Tribol. Conf., Yokohama (1995), pp. 1931–1936.
6. K. Adachi, T. Wakabayashi and K. Kato, The effect of sliding history on the steady state friction coefficient between CN_x coatings under N_2–gas lubrication, Proceedings of the 31st Leeds-Lyon Symposium on Tribology, 2004, in Tribology, D. Dowson et al. (eds) Life Cycle, 2005, Elsevier Science, pp. 673–677.
7. N. Umehara, K. Kato, T. Sato, Tribological properties of carbon nitride coatings by ion beam assisted deposition, Proc. Int. Conf. Metal. Coat. Thin Films, (1998), p. 151.
8. K. Adachi, N. Sodeyama, K. Kato, Effect of humidity on friction of carbon nitride coatings under N_2 gas lubrication, Proc. of WTC 2005, (2005), WTC2005-64275.
9. K. Adachi, D. Ueno, K. Kato, Nitrogen gas lubrication of carbon nitride coatings, Proc. Annual Fall Meet. JAST, Oct. 8–10, (2002), pp. 83–84.
10. S. Toyokawa, K. Kato, K. Adachi, Friction and wear property of carbon nitride film with N_2 gas blow lubrication, Proc, 38th Annual Meet. Tohoku Branch Jpn. Soc. Mech. Eng., (2003), pp. 54–55.
11. Tokoroyama, N. Umehara, H. Tomita, Y. Takenoshita, Effect of surface roughness and transfer layer of mating ceramic parts for ultra low friction phenomena in sliding between CN_x and ceramics, Trans. Jpn. Soc. Mech. Eng. C, 69 (2003), 2824–2829.
12. J. C. Sánchez-López, M. Belin, C. Donnet, C. Quiros, E. Elizalde, Friction mechanisms of amorphous carbon nitride films under variable environments: a triboscopic study, Surf. Coat. Technol., 160 (2002), 138–144.
13. H. Zaidi, F. Robert, D. Paulmier, Influence of adsorbed gases on the surface energy of graphite: consequences on the friction behaviour, Thin Solid Films, 264 (1995), 46–51.
14. D. F. Wang, K. Kato, Nano-scale fatigue wear of carbon nitride coatings: Part I-Wear properties, Trans. of the ASME, J. Tribol., 125 (2003), 430–436.
15. K. Kato, H. Koide, N. Umehara, Micro-wear properties of carbon nitride coatings, Wear, 238 (2000), 40–44.
16. K. Kato, N. Umehara, K. Adachi, Friction, wear and N_2-lubrication of carbon nitride coatings: a review, Wear, 254 (2003), 1062–1069.

Tribology of DLC Films Under Fretting Conditions

R. Wäsche and D. Klaffke

Abstract The tribological behaviour of several diamond-like carbon (DLC) coatings of the type a-C:H has been investigated under gross-slip fretting conditions and the effects of the counterbody material, ambient atmosphere, ambient temperature and liquid lubricating medium were assessed. DLC films have a significant friction- and wear-reducing effect under fretting conditions. Specifically, with their uses as thin protective films on tribological surfaces, very low friction coefficients in the range 0.01–0.1 with wear coefficients of about $1 \cdot 10^{-7}$ mm^3/Nm were realized. This is not only valid for dry sliding in ambient air, but also under lubricated sliding conditions in both the aqueous (deionized water) and organic media (liquid lubricant). The presence of sodium chloride in aqueous test media does not show any significant effect on altering the friction and wear characteristics of these films. However, when increased ambient temperatures are imposed on DLC as one of the sliding partners, the coating structure begins to degrade. Up to 100°C, their friction coefficients are not affected (in fact, noticeable decreases in friction are observed with increasing temperature). However, transformation processes to graphitic carbon seem to be induced immediately with further increases in temperature leading to increased wear coefficients and a significant reduction of the coating lifetime. This reduction of coating lifetime itself depends on the material of the counterbody.

Keywords DLC, oscillating sliding, counterbody, relative humidity, temperature, lubrication

1 Introduction

DLC coatings are of great importance in many fields of application owing to their largely beneficial properties. As already outlined in other chapters of this book, the combination of high hardness, chemical inertness and low friction and wear properties makes them very attractive for use as protective coatings in a wide range of applications

Federal Institute for Materials Research and Testing (BAM), 12200 Berlin, Germany

C. Donnet and A. Erdemir (eds.), *Tribology of Diamond-Like Carbon Films: Fundamentals and Applications*.

that involve rolling, rotating or sliding conditions. Just as these properties depend largely upon the ratio of sp^2 to sp^3 hybridization of the carbon network and the amount of dopants including hydrogen, so does the tribological behaviour [1–8]. However, since oscillating sliding and fretting is generally characterized by rather low sliding velocities, nevertheless, there are significant differences in tribological behaviour due to different components of the tribosystem. Among the most important ones are the influence of the counterbody material and the composition of the environment, but the lubrication medium besides the composition of the DLC film itself also matters [9–17]. The ambient temperature also plays a crucial role with regard to the application limits and coating life time [18–20]. Therefore, in this chapter, the response of the DLC films under oscillating sliding and fretting conditions will be analysed in terms of counterbody material, environmental conditions like humidity of the air, in lubricated contacts and under increased operating temperatures.

2 Dry Sliding Against Different Counterbody Materials

2.1 Experimental

2.1.1 Tribotesting

Tests were performed on a test rig for oscillating motion with small amplitudes, described in more detail in Ref. [21]. The non-rotating ball is fixed at the top of a lever and is pressed against the surface of the disk as shown in Fig. 1. During each test, the coefficient of friction (COF) and the total linear wear are continuously recorded

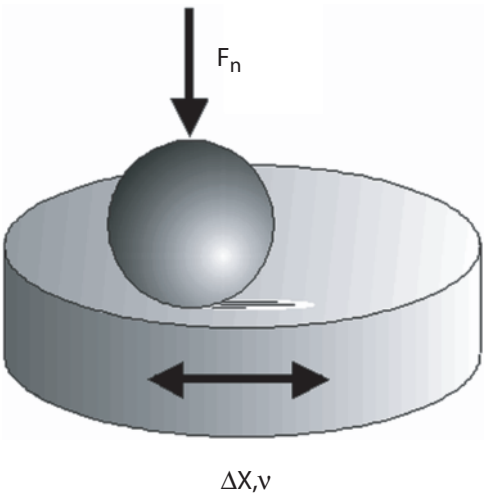

Fig. 1 Schematic of ball-on-disk contact geometry used in the experiments

by means of a PC data acquisition system with 1,000 data points for each quantity. The friction is described quantitatively by the COF. For comparison, the steady-state value of COF is used and calculated as the average of the last 500 data.

The wear is very small in most tests so that a continuous monitoring of the linear wear is at the limit of resolution. The wear therefore has to be determined at the end of each test. The wear of both bodies in contact is calculated separately from the diameter of the (circular) wear scar at the ball and the profile of the wear scar on the disk using equations compiled in Ref. [23]. The wear behaviour is described quantitatively by the coefficient of wear (k) according to Eq. (1). k is defined as the total wear volume (W_v), divided by the product of normal force (F_n) and total sliding distance s, with x = stroke and n = number of cycles:

$$k = W_v (F_n s)^{-1} = W_v (F_n 2\ x\ n)^{-1} \tag{1}$$

2.1.2 Materials

The coatings used in theses dry sliding experiments were deposited using a Balzers PA-CVD apparatus with radio frequencies (RFs) of 13.56 MHz. The RF glow discharge leads to reactive gaseous species and ions in an atmosphere of a hydrocarbon (normally acetylene)/argon gas mixture. These high-energy particles are necessary to build a hard carbon coating. With a typical growth rate of 2–3 µm/h the deposition temperature lies below 200°C. The coatings were deposited with constant process parameters. For better adhesion, a thin metal layer (about 400 nm) was first deposited on the substrates using a magnetron-sputtering process. Both deposition processes were done in the same coating machine. The coatings were deposited on the plain surface of steel rings (polished) with 42 mm diameter and 10 mm thickness. In order to evaluate possible effects of the counterbody material, four different metals and four different ceramics were selected (see Table 1 for details). All materials were used in the form of a ball with 10 mm diameter and a polished surface.

Table 1 Counterbody materials (ball) used in oscillating sliding tests against a-C:H coatings (disk)

Material	Young's modulus (GPa)	Hardness HV 10
100Cr6 (AISI 52100)	210	850
X40Cr13	210	250
X10CrNiMoNb18-10	210	180
Ti-6Al-4V	110	375
Al_2O_3 (htc-99.7)	390	1,900
SiC (EkaSiC D)	410	2,700
Si_3N_4	300	1,800
ZrO_2 (ZN40)	200	1,200

2.2 Results

2.2.1 Frictional Behaviour

When running against the metallic counterbody, the coatings behave in a similar fashion. The evolution of COF in dry, normal and moist air for three different steels (i.e., 100Cr6, X40Cr13, X10CrNiMoNb18-10) and a Ti alloy (i.e., Ti6Al4V) against a-C:H is shown in Fig. 2. There is a short running-in phase, followed by a stationary low and stable friction. The COF is lowest in moist air (0.06) and highest in dry air (0.14). In tests against stainless steel (X40Cr13), the friction is low on all levels of RH, while in dry air a short running-in peak occurs. The friction is again the highest (but still below 0.2) in dry air and the smallest (0.11) in moist air. In tests against the second stainless steel (X10CrNiMoNb18-10) also a short running-in peak occurs, and the friction here is smallest in dry air (0.10) and highest in normal air (0.15).

In tests against the titanium alloy the effect of humidity is the smallest. The stationary friction coefficient is between 0.05 and 0.07 for all values of RH. A very

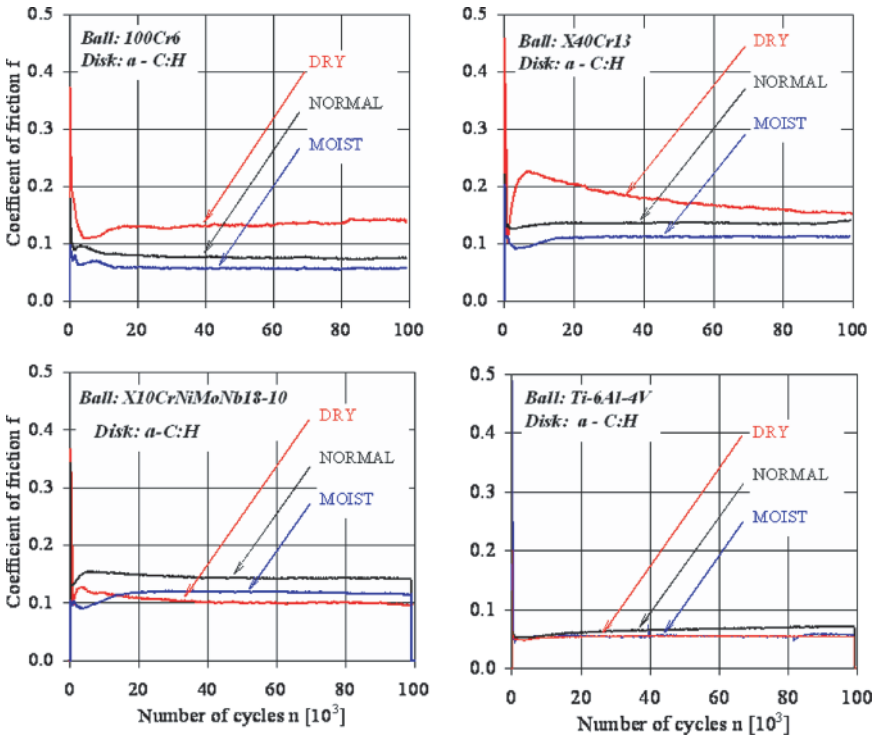

Fig. 2 Evolution of coefficient of friction (COF) in dry, normal and moist air for three different steels 100Cr6, X40Cr13, X10CrNiMoNb18-10 and Ti alloy Ti6Al4V against a-C:H

short running-in peak occurs in dry air and in moist air. The peak values are the highest in dry air for all four metals, but only last for a relatively short period of some 100 cycles. The stationary friction coefficient is rather low (<0.2) against all metals for all values of RH. The friction is the smallest in tests against Ti6Al4V, the values for 100Cr6 are slightly higher, while the stainless-steel balls produce the highest values, which are, however, still small (<0.17) for unlubricated conditions.

In tests against the four ceramic materials, much bigger differences are observed. Against α-alumina and zirconia, too, the friction behaviour is similar to that of the metals. However, both of the silicon ceramics show unstable high friction values in the dry test environment. Evolution of COF in dry, normal and moist air for four ceramic materials – Al_2O_3, ZrO_2, SiC and Si_3N_4 – against a-C:H is shown in Fig. 3. In tests against an alumina ball the lowest friction values are determined. Only in dry air a running-in peak occurs (0.28), followed by a very low stationary friction coefficient of 0.03. Against ZrO_2, no running-in occurs, the friction is the smallest in dry air and much higher in normal and in moist air, but of course rather low (0.10) for unlubricated tribocontacts.

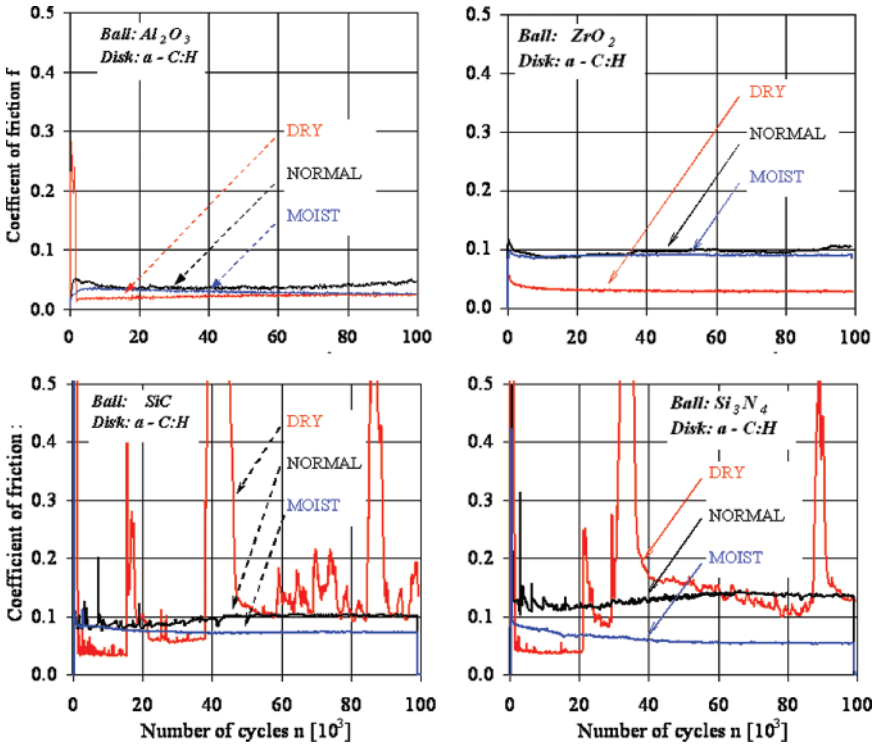

Fig. 3 Evolution of coefficient of friction (COF) in dry, normal and moist air for four ceramic materials Al2O3 (*upper left*), ZrO2 (*upper right*), SiC (*lower left*) and Si3N4 (*lower right*) against a-C:H

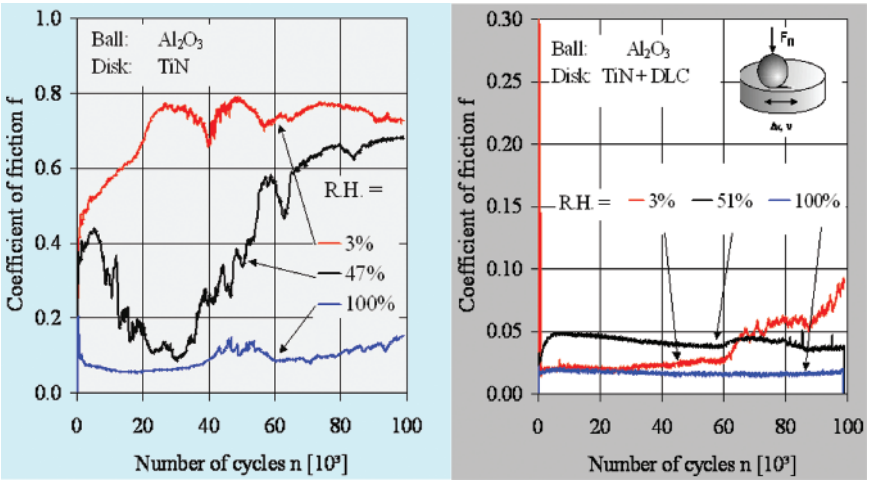

Fig. 4 Coefficient of friction (COF) for the system TiN against Al2O3 running in dry, normal and moist air (*left*), and COF for the system TiN coated with DLC against Al2O3 (*right*)

Quite a different friction behaviour is found in tests against SiC. In normal and in moist air the friction is rather constant and low (0.10 in normal and 0.08 in moist air). In dry air, however, a remarkable running-in with high friction (0.68) occurs, followed by a phase with very low friction (0.03). This phase, however, lasts only for <20,000 cycles, then shows some peaks and an irregular evolution. This behaviour can be attributed to the wearing-through occurring after 18,000 cycles.

The friction behaviour of Si_3N_4 against a-C:H shows the same characteristics as for SiC. The friction against Si_3N_4 in normal air is slightly higher than against SiC and slightly lower in moist air. The COF exhibits running-in peaks for SiC and Si_3N_4, and is the most pronounced in dry air. The friction values are the smallest and the least effected by humidity in tests against Al_2O_3. For both oxide ceramics the stationary friction is the smallest in dry air.

Figure 4 compares the friction behaviour of DLC coatings relative to titanium nitride (TiN). The left diagram shows TiN against Al_2O_3 ball as an example. Typically, systems with TiN as well as other hard coatings show relatively low friction coefficients in humid air, but much higher friction as relative humidity (RH) decreases. The diagram on the right side shows the friction when the same TiN coating is again coated by a a-C:H type DLC film. The friction coefficient under identical conditions is lower by more than one order of magnitude with a much smoother development with time.

2.2.2 Wear Behaviour

The wear is determined from the size of the wear scars. For example, Fig. 5 (in the upper half) shows optical micrographs of the wear scars formed on the a-C:H

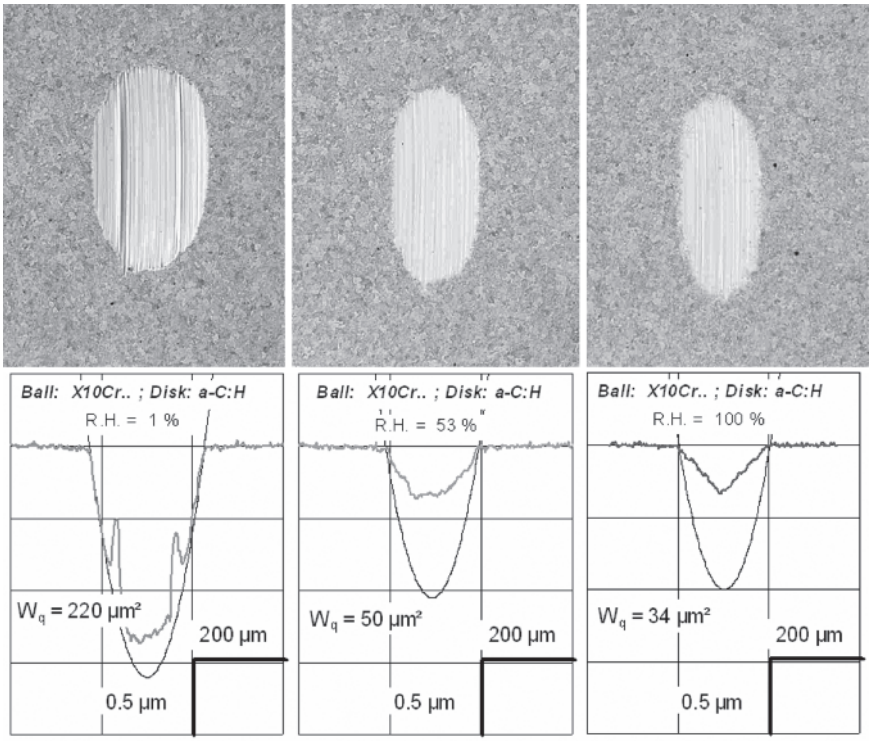

Fig. 5 Optical micrographs of the wear scars on the a-C:H coated disk and corresponding wear profiles at ball and disk after tests against steel 100Cr6 in dry (*left*), normal (*middle*) and moist (*right*) air

coated disk after tests against 100Cr6 steel (AISI 52100) in dry, normal and moist air. The lower half shows the line profiles across the wear scars which have been determined by surface probing using a diamond stylus. A second smoother line in parabolic form corresponds to the idealized hypothetical surface of the ball. The part of the line being below the surface profile line is considered to correspond to the volume of the ball which has been worn away. There is a scale in the lower right corner of each diagram, showing the scale horizontally with 200 µm and vertically with 0.5 µm. The wear scar shows the highest width and depth in dry air (see left picture and profile in Fig. 5), but the coating is not perforated even in dry air.

The total wear coefficient k is determined from the size and the depth of the wear scars. Figure 6 shows the coefficient of wear of the systems with the four metallic counterbodies for three different values of RH of the ambient air. 'Dry' refers to a RH of less than 5%, 'normal' is about 50% and 'moist' is more than 95% RH. It can be noted that all metallic counterbodies induce very similar results, but in dry air the wear coefficient is roughly a factor of five higher than in normal and moist air with values as low as 0.03×10^{-6} mm^3/Nm for Ti6Al4V.

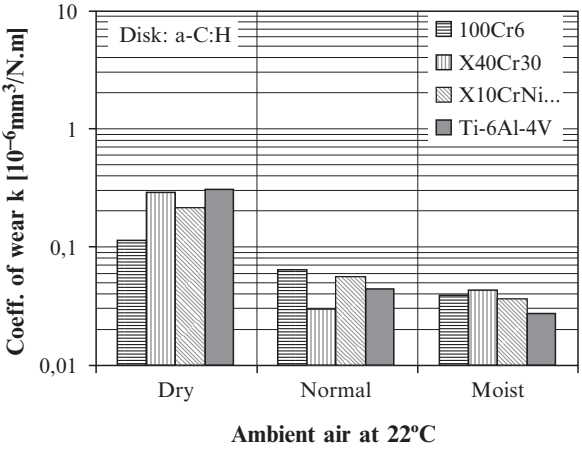

Fig. 6 Coefficient of wear of the systems with the four metallic counterbodies for three different values of relative humidity (RH) of the ambient air

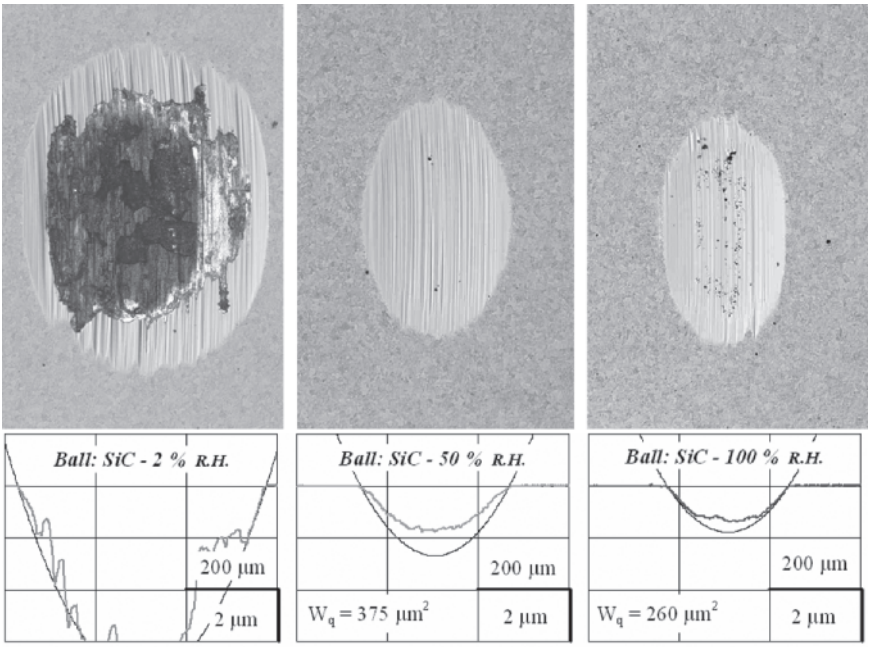

Fig. 7 Optical micrographs of the wear scars on the a-C:H disk and corresponding wear profiles at ball and disk after tests against SiC ball in dry (*left*), normal (*middle*) and moist (*right*) air

However, systems with ceramic balls show in all cases higher wear rates. For example, tests against SiC reveal a very strong effect of RH on wear. Figure 7 shows optical micrographs of the wear scars on the a-C:H disk after tests against SiC ball in dry, normal and moist air. After testing in normal and moist

air, the depth of the wear scar is less than the coating thickness, in dry air the coating is worn through in the central area and severe wear occurs on the substrate. This is also documented by the depth of the wear scar profiles below the micrographs.

Figure 8 shows the results of the wear coefficients for the ceramic counterbodies. Generally, as with the metallic balls, lacking humidity in the ambient is the harshest environment with wear coefficients about five times higher than in normal or moist air. However, there is a tendency that in dry and normal air the systems with the oxide ball materials show significantly lower system wear as the non-oxide materials like SiC and Si_3N_4. This is in agreement with the results in the optical micrographs of Fig. 7, and also with the unstable friction coefficients in the graphs with SiC and Si_3N_4 balls in Fig. 3. In fact, zirconia not only shows the lowest wear coefficients

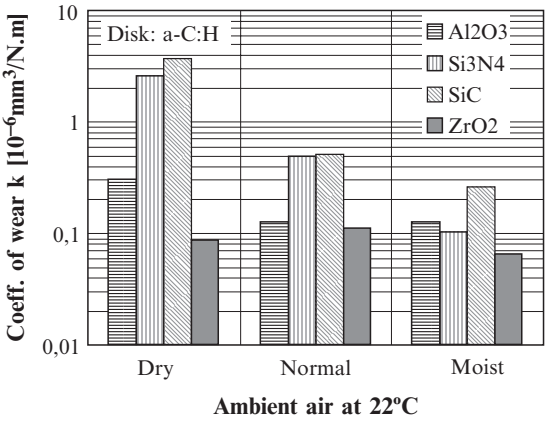

Fig. 8 Wear coefficients for four ceramic counterbodies for three different values of relative humidity (RH) of the ambient air

of 0.065×10^{-6}mm^3/Nm in moist air, but also the coefficients are almost equal over the whole range of RH. In moist air, the differences between the four systems disappear.

2.3 Discussion

The tribological behaviour of a-C:H coatings against different counterbody materials is dominated mainly by tribochemical processes acting in the contact zone. One of the main reasons for low friction and wear coefficients is seen in the formation of transfer layers. A transfer of carbon material from the coating to the ball surface leads to very low fiction values [13,24,25]. Metals and oxide

ceramics are protected against severe wear by this carbon transfer layer. In the case of silicon-based ceramics there is obviously a strong influence of a different mechanism, leading to a reduced lifetime of the coatings, especially in dry air. The reason for this is not clear but may be attributed to a reduced adhesion capability of the surface of Si-based ceramic materials, although this is somewhat contradictory to the earlier reports in the literature [25]. Another reason could be the higher hardness of SiC and Si_3N_4 which was reported to increase friction [16], especially in dry environment when the lack of water molecules leads to a subsequent removal of carbon atoms/molecules from the coating so that the wear rate is increased. However, looking at Fig. 3 and at the corresponding micrograph in Fig. 7, under conditions of dry air test, spalling or delamination seems to be part of the wear process at the DLC coating when sliding against SiC or Si_3N_4 ceramics. This indicates that the presence of fatigue phenomena in the coating may be due to the enhanced friction, which does not appear under conditions of normal or humid air tests.

Generally, the friction and wear behaviour of a-C:H coatings on steel substrates depends strongly on the material of the counterbody. The RH affects friction and wear to a different extent for different counterbody materials.

However, when the tribological behaviour of a-C:H coatings is compared with that of other hard coatings, the benefits are striking. In atmospheric conditions, including dry air, friction and wear can be reduced by as much as 1–2 orders of magnitude. Figure 9 shows a very interesting overview obtained in a study done on a number of metal-doped a-Me-C:H coatings on steel substrates, where Me was W, Ti and Si. The three diagrams show the coefficient of system wear drawn against the COF, separated for low (left), medium (middle) and high (right) RH, respectively. Each diagram contains not only the results for the DLC coatings, but also those for TiN and the uncoated 100Cr6 steel (AISI 52100) pairings. In this comparison, it becomes easily clear that only DLC coatings combine a low friction with a low wear coefficient. The difference being roughly an order of magnitude lower in value compared with TiN, and even much higher when compared with the uncoated steel.

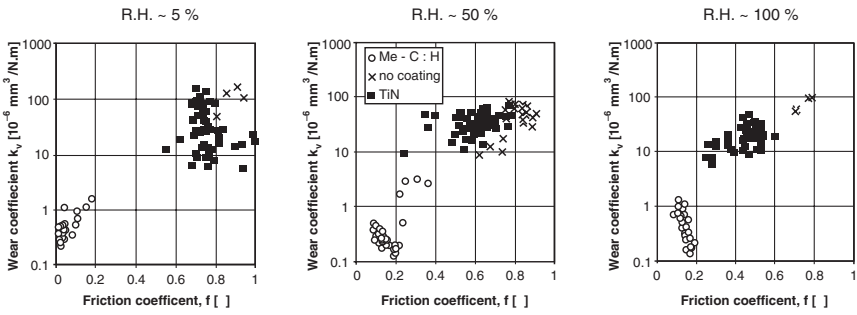

Fig. 9 Wear coefficient drawn against the friction coefficient of steel 100Cr6 (AISI52100) uncoated, coated with TiN and coated with Me-C:H, Me being W, Si and Ti; dry air (*left*), normal air (*middle*) and humid air (*right*)

3 Sliding under Media-lubricated Conditions

3.1 Experimental

3.1.1 Materials

The deposition of DLC coatings used in this section was carried out by pulsed arc evaporation of pure graphite under vacuum conditions. The deposition technology was described in more detail in Ref. [22]. Under these conditions hard amorphous carbon films (ta-C) with a high content of sp^3 bonds are formed.

As substrates, coin-like disks of Ti6Al4V were used with 35 mm diameter and 5 mm thickness with polished surface. Applying an optimized plasma-cleaning procedure in the vacuum chamber just before film deposition C-films with an excellent adhesion HF1 (Rockwell indentation) and a thickness of about 3 µm are deposited.

The Young's modulus (E) of the films, measured by means of laser-induced acoustic surface waves, was about 400 GPa. According to the one-tenth rule (H E/10), this corresponds to hardness values (H) above 40 GPa (= 4,000 HV) in the superhard range. In order to study the possibility of applying carbon coatings in water-lubricated systems, distilled water was used; additionally, isotonic sodium chloride solution (with 0.9% NaCl), as well as solutions with lower (0.25%) and with higher (4%) concentration of NaCl, were also used.

Organic media lubrication was investigated with hexadecane and paraffin oil as well as two synthetic oils used in automotive applications as engine oils (polyethylenglycol (PAG46/4) and polypropylenglycol (PPG32), two slightly different engine oils).

3.1.2 Tribotesting

All tests were performed in a gross-slip fretting tribometre with a ball-on-disk configuration, described in more detail in Ref. [23]. A ball of Al_2O_3 with 10 mm diameter was used as a counterbody, since in unlubricated tests against aluminium oxide this material suffers nearly no wear. The frequency of 20 Hz and the stroke of 0.2 mm lead to a mean sliding speed of 0.008 m/s, so that hydrodynamic effects may be excluded. The test conditions are compiled in Table 2. Friction and wear quantities, COF and wear coefficient k, are determined in the same way as described in Section 2.1.1.

3.2 Results

3.2.1 Friction

Figures 10 and 11 show the evolution of friction coefficients with the number of cycles. Generally, for all investigated media the friction coefficient is below 0.1.

Table 2 Test conditions for media-lubricated sliding tests

Ball	α-alumina
Disk	Ti-6Al-4V + ta-C
Motion	Oscillating sliding
Stroke	0.2 mm
Frequency	20 Hz
Load	10 N
Temperature	24°C
Lubricants	Distilled water
	Dist. water with 0.25% NaCl
	Dist. water with 0.9% NaCl
	Dist. water with 4% NaCl
	Hexadecane
	Paraffin oil
	Engine oil PAG 46/4
	Engine oil PPG 32

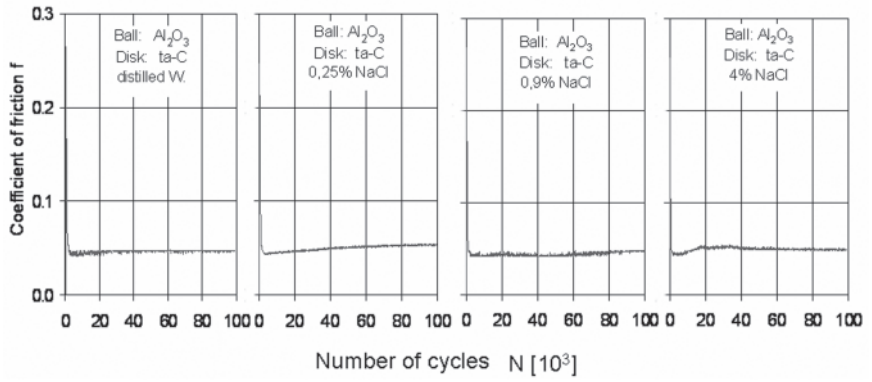

Fig. 10 Evolution of friction coefficients with the number of cycles in water-based media

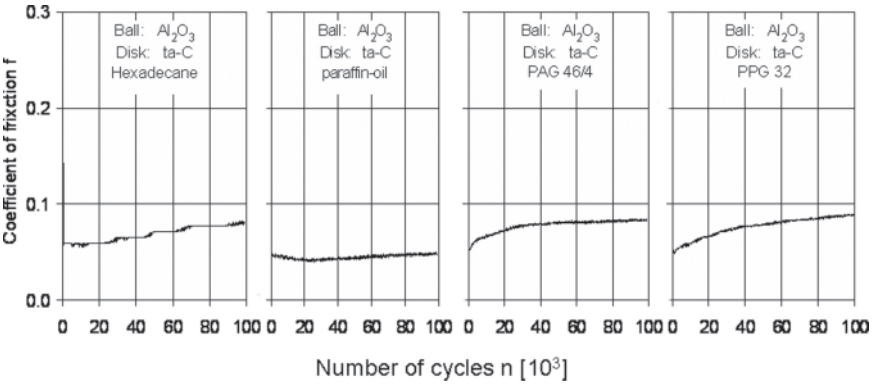

Fig. 11 Evolution of friction coefficients with the number of cycles in organic media

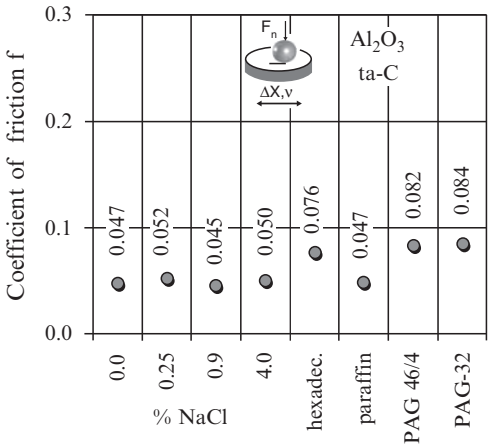

Fig. 12 Overview over all observed stationary coefficients of friction (COF) of media lubricated systems

When sliding in an aqueous environment, as exposed in Fig. 10, the friction practically does not change with time. For the non-aqueous lubricant media there is a slight increase of friction with time, with the exception of paraffin oil. In this case, too, the COF is low at 0.05 and stays at this value over the whole duration of the experiment. Figure 12 gives an overview of all observed stationary COF as measured at the end of the experiments.

3.2.2 Wear

Figure 13 shows the wear scars and the corresponding wear profiles at ball and disk (DLC coating) for the four systems running in aqueous environment. It can be seen from the wear scar profiles below the micrographs that the wear takes place mainly on the ball side, not on carbon coating. This can be deducted from relatively low values of planar wear W_q of the coatings and the dashed parabolic line below the surface profile representing the (relatively large) worn part of the ball. Analogous to the friction, the wear is very similar in the water-based media, so that the presence of sodium and chlorine ions practically makes no difference. The same is more or less valid for the non-aqueous lubricant media as shown in Fig. 14. The only exception is the system with paraffin oil lubrication. Although in this case the COF is rather low and not significantly different from the other systems, wear of the carbon coating is slightly higher then in the other systems.

Figure 15 shows a comparison of the wear coefficients, which are almost all in the range of $0.2–0.3 \times 10^{-6}$ mm³/Nm. The system lubricated with hexadecane shows the lowest value with 0.06×10^{-6} mm³/Nm.

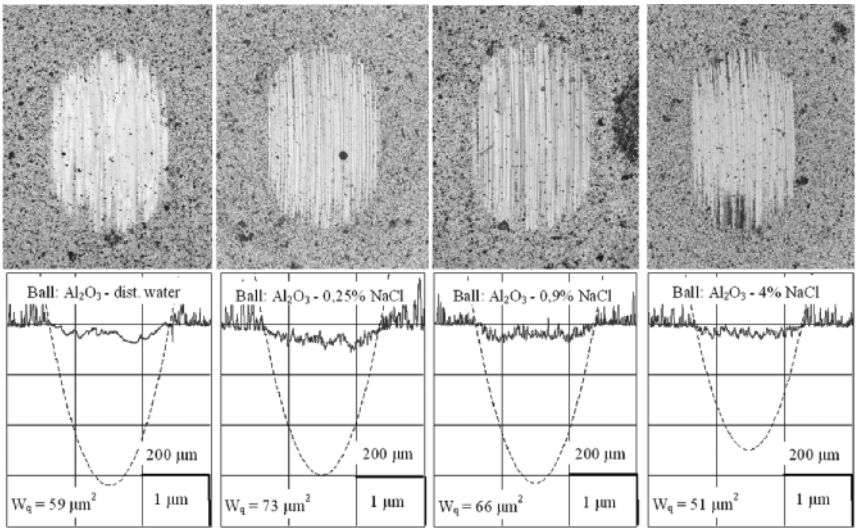

Fig. 13 Wear scars and the corresponding wear profiles at ball and disk (DLC coating) for the four systems running in aqueous environment against alumina ball. Sodium chloride concentration varies from 0% (*left*) to 4% (*right*)

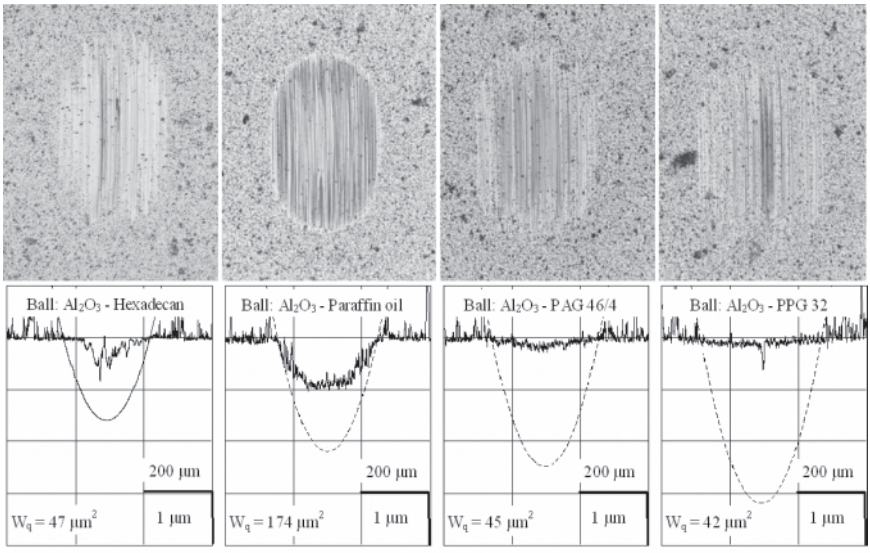

Fig. 14 Wear scars and the corresponding wear profiles at ball and disk (DLC coating) for the four systems running in organic media against alumina ball

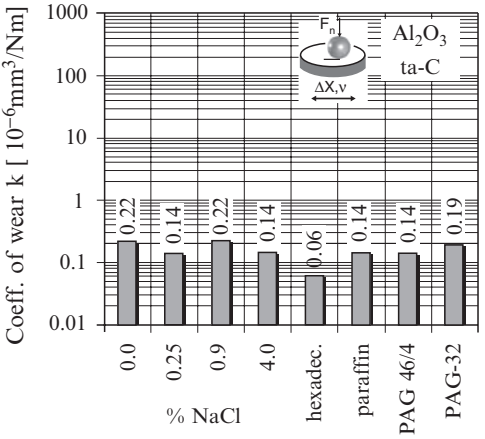

Fig. 15 Comparison of the wear coefficients of aqueous and non-aqueous media-lubricated systems

3.3 Discussion

An excellent tribological performance of DLC films when lubricated by water and organic media including mineral oils is well documented in the literature for hard hydrogen-free a:C coatings [26,27,32]. In the case of lubrication with water, friction was lower as with additive containing oil [26,28,29]. The experimental results presented here confirm these findings, and show that sodium and chlorine ions do not influence the tribological response. The surface roughness is important because it influences the wear of the alumina counterbody [27,32]. In almost all cases, including the organic media, the wear is found at the counterbody, not at the DLC layer. The wear resistance depends on the liquid and leads to very low specific wear rates of the same order of magnitude ($0.06–0.22 \times 10^{-6}$mm^3/Nm) for all liquids [30,31].

4 DLC Film Performance at Elevated Temperatures

4.1 Experimental

4.1.1 Materials and Coating Deposition Process

The investigated DLC coatings (a-C:H) with a constant, homogeneous property profile [33] used in this section were deposited with a high frequency PACVD Balzers coating apparatus, working at 13.56 MHz. The coating thickness was 2.5 µm.

The hydrogen content of the coating was controlled at 15 at. % during deposition. Temperature during the deposition was 200°C. The hardness of the coating was 25 GPa. Between coating and substrate, a 0.5 µm thick titanium layer was deposited prior to deposition of the DLC layer, in order to improve the adhesion to the substrate. This Ti layer was deposited in the same PACVD apparatus by magnetron sputtering. The substrate was polished HSS steel with roughness of $R_a < 0.01$ µm and $R_z < 0.06$ µm. The counterbodies were α-alumina and silicon nitride balls with a diameter of 10 mm and a polished surface.

4.1.2 Tribotesting

The tribological experiments were carried out in a SRV III oscillating tribometre with high temperature capabilities (Optimol instruments, Munich, Germany).

The tribological characterization comprises the determination of the COF and the coefficient of system wear k according to Eq. (1). The system wear is the sum of the wear at ball and disk. The system wear coefficient is the wear volume normalized to sliding distance and normal force. The wear volume is calculated from the wear scar at ball and disk, which is determined by profilometry with a diamond stylus tracing perpendicular to the sliding direction.

4.1.3 Test Program

The DLC coatings were tested in the temperature range 25–250°C against alumina and silicon nitride. All other test parameters were kept constant during the testing. Test duration was 100,000 cycles. Table 3 shows the test conditions for the tests carried out at different ambient temperatures.

4.2 Results

Against the alumina counterbody, the COF at room temperature was 0.103 ± 0.005 as determined from five different experiments. The RH was not controlled during the tests, but it may be assumed to be within the range of normal air. Figure 16 shows the evolution of friction with the number of cycles for the

Table 3 Test conditions for high temperature experiments

Tribosystem		Test parameters	
Ball	10 mm diameter, polished	Stroke Δx	0.2 mm
	Alumina, silicon nitride	Frequency ν	20 Hz
Disk	DLC on HSS steel	Normal force F_n	10 N
Lubricant	None	Number of cycles	100,000
Ambient	Air	Temperature	24°C up to 250°C

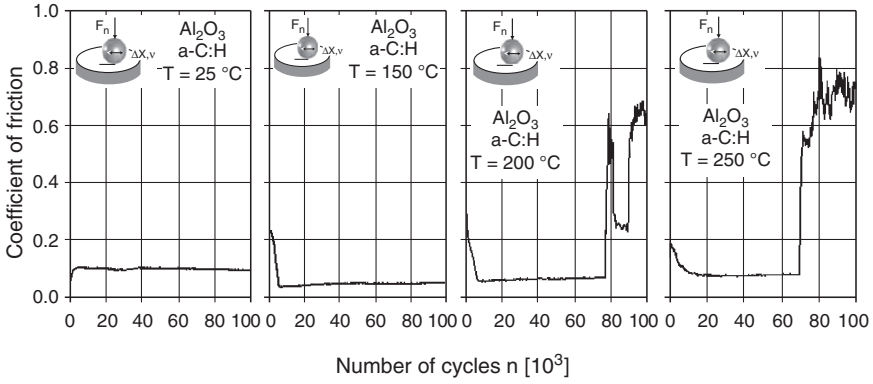

Fig. 16 Evolution of friction with the number of cycles for DLC coatings running against alumina ball at temperatures from 25°C to 250°C

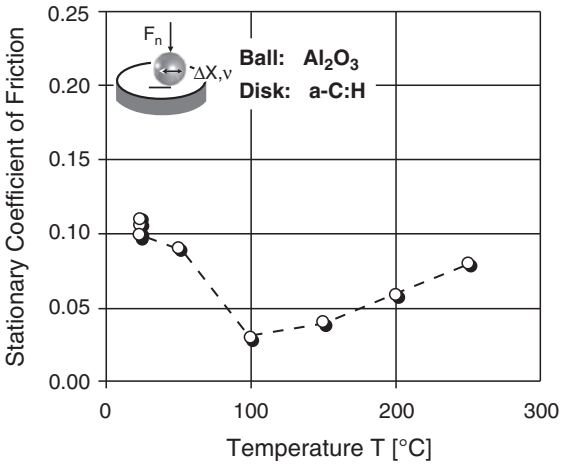

Fig. 17 Stationary coefficient of friction (COF) with increasing temperature for DLC coatings against alumina ball

corresponding temperatures from 25°C to 250°C. It may also be noticed, that with increasing temperatures at the beginning of the test, a friction peak with a COF of more than 0.2 occurs, followed by a period of low friction until the coating is worn through. At 200°C and 250°C the lifetime of the coating decreased drastically and the coating was worn through after about 78,000 at 200°C and 65,000 cycles at 250°C. When the coating was worn through, COF increased suddenly to values of 0.6 showing an increased scattering range at the same time. Figure 17 shows stationary COF with increasing temperature. Lowest values are observed at 100°C ambient temperature.

The evaluation of the wear scars revealed that alumina as the counterbody material is more wear-resistant than the DLC coating itself and that therefore wear occurs mainly at the DLC layer. This fact is more pronounced especially when the ambient temperature is increasing. Although the COF is the lowest around 100°C, the coefficient of wear increases with increasing temperature starting right from room temperature. Figure 18 shows the increase of the coefficient of wear by about a factor of 3 from room temperature to 250°C. However, with regard to the lifetime of the coating at different temperatures the wear coefficient is not an objective tool to use, since the number of cycles to failure may decrease dramatically due to some structural changes within the coating. This may already be seen in Fig. 16, when the coating is worn through and the friction increases suddenly to levels of 0.6 and above. Figure 19 shows the number of cycles to failure with increasing temperature.

When the counterbody material is changed to silicon nitride, the tribological behaviour of the tribocouple Si_3N_4/DLC is principally similar to that of the Al_2O_3/DLC, but more complex. The COF is generally higher against silicon nitride and hence in agreement with the results discussed in Section 2.2.2. With increasing temperatures, this finding translates also in a smaller number of cycles to failure of the coating. The coating is worn through at 150°C after a few cycles.

4.3 Discussion

Due to the fact that DLC is a metastable form of amorphous carbon, it consists of a mixture of sp^2 and sp^3 hybridized carbon atoms linked together in a three-dimensional

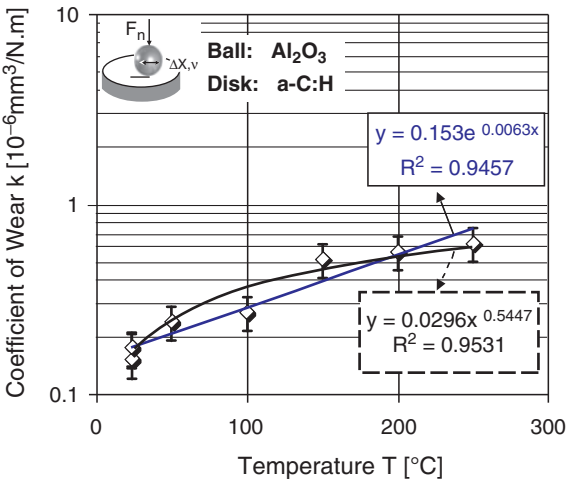

Fig. 18 Coefficient of wear from room temperature to 250°C for DLC sliding against alumina ball

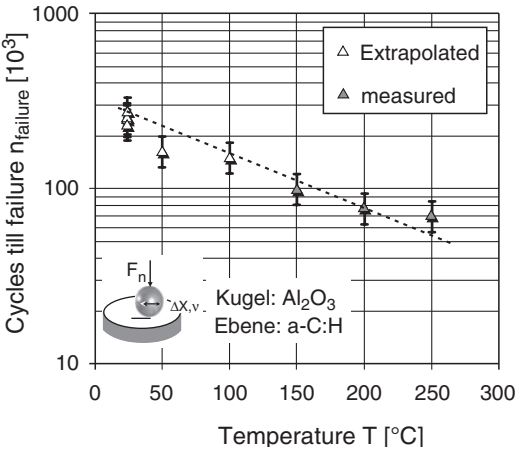

Fig. 19 Number of cycles to failure for DLC coatings sliding against alumina ball with increasing temperature

amorphous network. This network contains differing amounts of hydrogen and is prone to transformation by enhanced oscillations of the carbon–carbon bonds. It will eventually transform into the stable form of graphite when temperature is high enough [34]. As the experimental results show, when sliding under dry conditions, this process can occur at temperatures as low as 200°C [35], other transformation temperatures are reported to be significantly higher at about 300°C [20]. This is further confirmed by the results of this investigation which shows a significant increase in friction at 200°C for the alumina a-C:H pairing. Although the friction decreases with increasing temperatures up to 100°C and then increases with further increasing temperatures, interestingly the lifetime of the coating decreases continuously with rising temperatures from room temperature up. This points out that the transformation process as a tribochemical process going on in the tribointerface is induced by frictional heating at the asperity-level contacts. It seems that this transformation of the amorphous network into graphite, as experienced by an increasing friction coefficient, higher wear rate and, eventually, catastrophic coating failure, is somehow material-dependent. It seems further that with silicon nitride as counterbody material, the transformation rate is significantly higher than with alumina. It may also be expected that the coating composition will be of influence. Thus far, unfortunately, rather few experimental results in this regard are available, so that a more detailed understanding is not possible yet.

Overall, the use of DLC coatings may be limited to temperature ranges below 200°C, depending on the counterbody material. Silicon nitride produces significantly lower coating lifetimes than alumina. This is, however, already observed under room temperature conditions.

5 Summary and Conclusions

In agreement with the vast majority of publications on this subject, DLC films have a significant friction- and wear-reducing effect under fretting conditions. Very low friction coefficients in the range 0.01–0.1 with wear coefficients of about $1 \cdot 10^{-7}$ mm^3/Nm are feasible. This is valid for dry sliding in ambient air, but also under lubricated sliding conditions in both aqueous (neutral) and organic media. Sodium chloride did not show any significant influence on the friction and wear characteristics. However, at increased ambient temperatures imposed on the tribological pairing with DLC as a sliding partner, the coating structure is prone to degradation. Up to 100°C the COF is not affected, but transformation processes to graphitic carbon are induced immediately with rising temperatures leading to increased wear coefficients and a significant reduction of the coating lifetime. This reduction of coating lifetime itself depends on the material of the counterbody.

Acknowledgements The authors want to express their sincere gratitude to Manfred Hartelt, Christine Neumann and Andrea Krause for their help in carrying out the experimental work.

References

1. Ahmed S. I. -U, Bregliozzi G., Haefke H. (2003) Microfrictional properties of diamond-like carbon films sliding against silicon, sapphire and steel. Wear 254: 1076–1083.
2. Robertson J. (2003) Improving the properties of diamond-like carbon. Diam. Relat. Mater. 12(2): 79–84.
3. Hauert R., Müller U. (2003) An overview on tailored tribological and biological behavior of diamond-like carbon. Diam. Relat. Mater. 12(2): 171–177.
4. Bauer C., Leiste H., Stüber M., Ulrich S., Holleck H. (2002) Mechanical properties and performance of magnetron-sputtered graded diamond-like carbon films with and without metal additions. Diam. Relat. Mater. 11(3–6): 1139–1142.
5. Baba K., Hatada R. (2005) Preparation and properties of metal –containing diamond-like carbon films by magnetron plasma source ion implantation. Surf. Coat. Technol. 196(1–3): 207–210.
6. Ouyang J. H., Sasaki S. (2005) Friction and wear characteristics of a Ti-containing diamond-like carbon coating with SRV tester at high contact load and elevated temperature. Surf. Coat. Technol. 195(2–3): 234–244.
7. Erdemir A. (2004) Genesis of superlow friction and wear characteristics in diamond-like carbon films. Tribol. Int. 37(11–12): 1005–1012.
8. Robertson J. (2003) Improving the properties of diamond-like carbon. Diam. Relat. Mater. 12(2): 79–84.
9. Stallard J., Mercs D., Jarrat M., Teer D. G., Shipway P. H. (2004) A study of the tribological behavior of three carbon based coatings, tested in air, water and oil environments at high loads. Surf. Coat. Technol. 177–178: 545–551.
10. Ronkainen H., Varjus S., Holmberg K. (2001) Tribological performance of different DLC coatings in water lubricated conditions. Wear 249(3–4): 267–271.
11. Gilmore R., Hauert R. (2000) Comparative study of the tribological moisture sensitivity of Si-free and Si-containing diamond-like carbon films. Surf. Coat. Technol. 133–134: 437–442.
12. Tanaka A., Nishibori T., Suzuki M., Maekawa K. (2004) Characteristics of friction surfaces with DLC films in low and high humidity air. Wear 257(3–4): 297–303.

13. Jiang J., Zhang S., Arnell R. D. (2003) The effect of relative humidity on wear of a diamond-like carbon coating. Surf. Coat. Technol. 167(2–3): 221–225.
14. Anderson J., Erck R. A., Erdemir A. (2003) Frictional behavior of diamond-like carbon films in vacuum and under varying water vapor pressure. Surf. Coat. Technol. 163–164: 535–540.
15. Zhang W., Tanaka A., Wazumi K., Koga Y. (2002) Effect of environment on friction and wear properties of diamond-like carbon film. Thin Solid Films 413(1–2): 104–109.
16. Liu H., Tanaka A., Kumagai T. (1999) Influence of sliding materials on the tribological behavior of diamond-like carbon films. Thin Solid Films 352(1–2): 145–150.
17. Klaffke D., Brand J., Brand C., Wittorf R. (2004) Tribological characterization of a-C:H at room temperature; effect of counter body material. In: Bartz W. J. (ed.) Proceedings of 14th International Colloquium on Tribology, Vol 1, pp. 605–614.
18. Klaffke D., Wäsche R., Czichos H. (1992) Wear behavior of i-carbon coatings. Wear 153: 149–162.
19. Krumpiegl T., Meerkamm H., Fruth W., Schaufler C., Erkens G., Böhner H. (1999) Amorphous carbon coatings and their tribological behavior at high temperatures and in high vacuum. Surf. Coat. Technol. 120–121: 555–560.
20. Bremond F., Fournier P., Platon F. (2003) Test temperature effect on the tribological behavior of DLC coated 100Cr6 couples in dry friction. Wear 254(7–8): 774–783.
21. Klaffke D. (1995) On the influence of test parameters on friction and wear of ceramics in oscillating sliding contacts. Tribotest J. 1–4: 311–320.
22. Schultrich B. (1999) Film deposition by laser and arc technologies. Contr. Plasma Phys. 39: 463–472.
23. Klaffke D. (1989) Fretting wear of ceramics. Tribol. Int. 22(2): 89–101.
24. Erdemir A., Bindal C., Fenske G. R., Zuiker C., Wilbur P. (1996) Characterization of transfer layers forming on surfaces sliding against diamond-like carbon. Surf. Coat. Technol. 86–87: 692–697.
25. Grill A. (1997) Tribology of diamond like carbon and related materials: an updated review. Surf. Coat. Technol. 94–95: 507–513.
26. Ronkainen H., Varjus S., Holmberg K. (1998) Friction and wear properties in dry, water- and oil-lubricated DLC against alumina and DLC against steel contacts. Wear 222: 120–128.
27. Ronkainen H., Varjus S., Holmberg K. (2001) Tribological performance of different DLC coatings in water-lubricated conditions. Wear 249: 267–271.
28. Rabbani F., Vogelaar B. M. (2004) The importance of unbound hydrogen and increased aromatic structure on the friction and wear behaviour of amorphous hydrogenated carbon (a-C:H) coatings. Diam. Relat. Mater. 13: 170–179.
29. Sánchez-López J. C., Erdemir A., Donnet C., Rojas T. C. (2003) Friction-induced structural transformations of diamond-like carbon coatings under various atmospheres. Surf. Coat. Technol. 163–164: 444–450.
30. Miyake S., Saito T., Yasuda Y., Okamoto Y., Kano M. (2004) Improvement of boundary lubrication properties of diamond-like carbon (DLC) films due to metal addition. Tribol. Int. 37: 751–761.
31. Liu H., Tanaka A., Kumagai T. (1999) Influence of sliding materials on the tribological behaviour of diamond-like carbon films. Thin Solid Films 352: 145–150.
32. Podgornik B., Jacobson S., Hogmark S. (2003) DLC coating of boundary lubricated components – advantages of coating one of the contact surfaces rather than both or none. Tribol. Int. 36: 843–849.
33. Brand J., Brand C., Gäbler J. (2003) Die Vielfalt der Kohlenstoffschichten – ein Überblick. Tribologie und Schmierungstechnik 50: 18–22.
34. Robertson J. (2002) Diamond like amorphous carbon. Mater. Sci. Eng. R 37: 129–281.
35. Klaffke D., Wäsche R. (1989) Tribological behaviour of tungsten doped i-carbon layers deposited on silicon infiltrated silicon carbide (SiSiC) under sliding and fretting conditions up to 250°C. Proc. 5th Eurotrib, Helsinki 1989, Vol 3, Finnish Soc. Tribology (Ed.), Espoo.

Tribology of DLC Films Under Slip-Rolling Conditions

C. Manier, D. Spaltmann and M. Woydt

Abstract Today diamond-like carbon (DLC) coatings are used in many applications such as in medical tools, machine tools, computer devices like hard disks and many more. In the near future, the tribological properties of the coatings will allow replacing some of the common lubricant additives like extreme pressure and anti-wear additives. This would have a beneficial impact on the environment and on fuel consumption.

However, an extensive use of DLC coatings and a shift towards mass production volumes of DLC-coated parts submitted to slip-rolling conditions will only be possible, if the coated system is fully characterized. Due to the large variety of production processes and the resulting different properties of coatings, a market screening of today's available coatings has been performed. Layers of several different suppliers were tested under defined conditions on specified and comparable substrates. Investigations were carried out to elucidate underlying reasons for the behaviour of the coatings tested. The results of the tests and the respective investigations are summarized in this chapter.

Typically, the coated substrates were made of 52100 steel (60 HRC). They were tested on a twin disc tribometer of the Amsler type under mixed/boundary lubrication conditions. Pure paraffinic oil (ISO 46) and polyglycol (environmentally acceptable lubricants, ISO46) were used for lubrication. As a standard, the coated substrates were tested against a counter disc of the same material as the substrate under high initial average Hertzian contact pressure. Different factors such as layer thickness, counter disc roughness and material, nature of the bond layer were investigated. The lack of adherence and the presence of defects on the DLC coating before testing seem to be the most common failure causes. After the tests, Raman spectroscopy reveals that most of the coatings show a structural transformation, probably a graphitization. This can be due to possible local high stresses induced by the counter disc roughness.

Keywords DLC coating, diamond, steel, wear, friction, slip rolling, lubrication

Federal Institute for Materials Research and Testing (BAM), Division VI.2: Tribology and Wear Protection, D-12200 Berlin, Germany

C. Donnet and A. Erdemir (eds.), *Tribology of Diamond-Like Carbon Films: Fundamentals and Applications*.

1 Introduction

Diamond-like carbon (DLC) coatings enjoy more and more widespread industrial application. They are already used successfully as coatings on cutting tools for non-ferrous materials (coatings for the drilling of Al 6061) [1]. Even in medical tools, such as hand pieces in dental drills, the respective races of the bearings are coated with 'hydrogenated' diamond coatings. In the car industry, parts of the lock components are covered as well to increase the respective lifespan without 'noise'. However, the use of coatings on heavily stressed components is momentarily restricted to race and super sports cars. In the plastics manufacturing industry, DLC coatings are used in casting moulds as a non-sticking layer for easier removal of the injected pieces from the moulds, thus increasing the productivity of the whole moulding process. Diamond coatings even found their way into food industry, for example in the production of plastic bags. Here, the use of liquid lubrication is unlikely. DLC coatings are even introduced into everyday life since some razor blades are covered with DLC, to ensure better shaving.

The properties of certain types of DLC coatings such as their chemical inertness, their far higher hardness compared to steel, their exceptionally low wear rate and a low coefficient of friction (especially under unlubricated conditions), have originally initiated a more and more widespread use in all kinds of application.

However, there are still some barriers which have to be overcome for the use of DLC coatings to move from an economical niche position to the mass production market. Today, a large variety of production processes exist for creating DLC coatings. The type of process strongly influences the structures and properties of the final coatings. The effect of the process on the coating properties needs to be fully understood and the coatings have to be characterized metallurgically, in order to enhance the market share of the DLC coatings by assuring 'isoproperties' from batch to batch; a must for high volumes.

At the start, these processes required substrate temperatures sometimes higher than 450°C for the deposition of the coatings. Technological progress in chemical vapour deposition (CVD) and physical vapour deposition (PVD), in particular thanks to the plasma-assisted technology, now allows depositions at lower temperatures (e.g. below the tempering/annealing temperature of carbon steels), thus deteriorating the initial properties of the substrates less.

However, the large process variety leads to the production of a seemingly endless amount of different types of coatings with different sets of properties. Actually, there are various possible types of amorphous DLC layers:

- With a polymeric tendency called 'a-C' for 'amorphous Carbon' or 'a-C:H' for 'amorphous hydrogenated Carbon'
- With a diamond-like tendency called 'ta-C' for 'tetrahedral amorphous carbon' and nanocrystalline set with diamonds (th-C for tetrahedral Carbon)

The large variety of DLC coatings leads to the problem of finding a suitable coating for a certain application. As the DLC designation is very general and the exact

deposition conditions remain mostly secret, each layer type has thus to be investigated virtually down to the atomistic level in order to determine its respective properties. The lack of, and the difficulty in, metallurgical characterization form the biggest obstacle on the enlargement of the application of DLC coatings in certain areas, for example in highly loaded slip-rolling applications in mass production markets.

In order to determine the best trio 'process–type–properties' in terms of lifespan under a given, high Hertzian contact pressure, tribological tests under slip-rolling conditions with a slip of 10% were carried out on layers supplied by different manufacturers and original equipment manufactures (OEMs). It is intended to set a benchmark, demonstrating the performance of the state-of-the-art DLC coatings under very demanding conditions. The aim of these tests was also to elucidate any critical and relevant properties which are required of a DLC coating to be resistant to slip-rolling conditions. The results of this ongoing benchmarking are presented here in an anonymous manner.

2 Experimental Details

2.1 Parameters

The slip-rolling tribological tests were carried out in an Amsler-type twin disc tribometer. Figure 1 shows a sketch of the arrangement of the discs. The experimental parameters are summarized in Table 1.

The geometry of the discs with an outer diameter of 42 mm generates a contact of the ball–cylinder type. The top, ball-shaped counter discs were uncoated and only pre-polished or 'as-grinded', turning at a speed of 354 revolutions per minute (rpm). The lower, cylindrical discs were coated and rotating with 390 rpm, leading to a slippage of 10%. The force is applied to the system by means of a spring leading to an average Hertzian pressure P_{mean} from 1.0 to 1.5 GPa [2] (1.75 GPa in recent tests, which is equivalent to P_{max} = 2.62 GPa). For comparison, an average contact pressure of 1.25 GPa corresponds to a maximum Hertzian pressure of P_{max} = 1.875 GPa, which is equivalent to a load stage of 12 (P_{max} = 1.861 MPa) in the FZG test rigg (FZG: Forschungsstelle für Zahnräder und Getriebebau [Institute for Machine Elements Gear Research Centre]). This load stage is the most demanding test procedure for gears as described in the international standard ISO 14635-1. The test conditions for the DLC coatings applied here even exceed this demanding standard. The calculation of the contact pressures performed here does not take into account the coating, as its thickness is relatively thin (~2 µm). In order to gain practical advantages over additives containing, high-performance lubricants, it is obvious that the DLC coatings and nanocrystalline diamond (THC: tetrahedral carbon) layers have to withstand Hertzian contact pressures much larger than FZG load stage of 12.

The number of cycles is recorded by an optical sensor and is generally limited for practical reasons to 1 million (in endurance tests to 10 million) or until a critical damage of the layer occurs. The development of the coefficient of friction and the wear

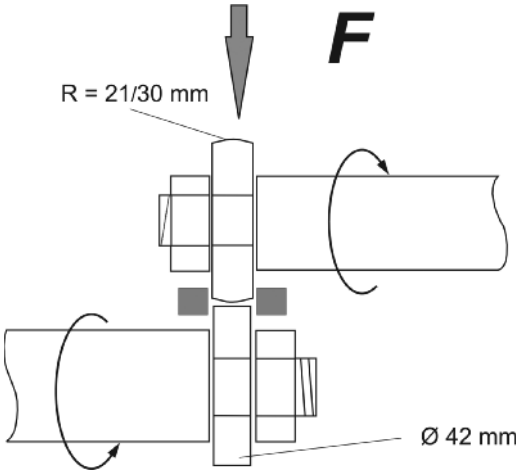

Fig. 1 Schematic diagram of the experimental tribometer. The lower disc turns at a speed of 390 rpm, the upper disc at 354 rpm

Table 1 Experimental conditions

Conditions	Parameters
Dimensions of the discs	Diameter: 42; Width: 10 mm
Contact	Grounded/polished curved disc (radius of curvature: 30 mm or 21 mm) against coated cylindrical disc.
Substrate	100Cr6H – Cronidur30 – SSiC – HIP-ZrO_2
Type of motion	Rolling with a 10% slip rate
Initial average Hertzian pressure P_{mean}	1.0–1.25–1.5 GPa (F_N = 338–660–1,140 N)
Rotation speed	390–354 rpm
Sliding speed v_{diff}	0.08 m/s
Cycles n_{tot}	Until 10^6 or rupture (damaged surface of 1 mm^2)
Sliding distance	Until 13.2 km
Surrounding temperature	Ambient temperature (≈22°C)
Lubricants	Paraffinic oil ($\eta_{40°C}$ = 44.2 mPa·s), polyglycol PAG 46-1, dry

volume cannot be as easily assessed as criterion of a critical damage. Tests have shown that a rise in the coefficient of friction (COF) is not necessarily followed by a failure of the coating. In some tests, the COF even dropped as the coating failed. Therefore, damage was arbitrarily defined as 'critical', if a single damaged surface area of 1 mm^2 could be observed. The size of such a damaged spot corresponds to 3 times the contact area at an initial, average Hertzian pressure of 1 GPa (or equals the contact area at 1.5 GPa). It might occur that a certain coating is damaged in several locations leading to a total damaged area larger than 1 mm^2. Such a coating would still count as 'resistant to slip-rolling', as long as none of the single damaged zones

exceeds an area of 1 mm^2. This definition has so far proven to be highly practical. The microscopic control of the layers is carried out at logarithmically increasing intervals. In order to optimize the detection of the damage while the tribological test is in progress, an acoustic emission sensor is placed close to the zone of contact. In short, an acoustic emission event 'informs' fairly early about the initiation of future damages on the microscale, before a macroscopic defect can be observed. The main results obtained with this detection method are accessible in reference [3].

The thickness h_0 of the lubricating film (see Fig. 2) is evaluated as a function of the load applied using the elasto-hydrodynamic (EHD) models of lubrication of Cheng, Hamrock and Archard [2]. For the respective calculations, all viscosimetric and thermo-physical properties were determined, including the pressure viscosities up to 150°C of the unadditivated paraffinic oil in ISO VG 46 [4]. The counter discs have a roughness of R_a ~0.6 µm. With paraffinic oil as lubricant and under the experimental conditions applied, the tribological tests were carried out in the regime of mixed or boundary lubrication since the parameter of Tallian $\lambda = h_{min} / (\sigma_A^2 + \sigma_B^2)$ [5,6] is definitely lower than $\lambda = 3$ ($\sigma_{A/B}$ RMS roughness of the discs). However, these calculations are only an estimate sufficient to determine the regime of lubrication. The calculation is carried out with the viscosity value at 22°C. The exact viscosity in the point of contact under such extreme conditions remains unknown.

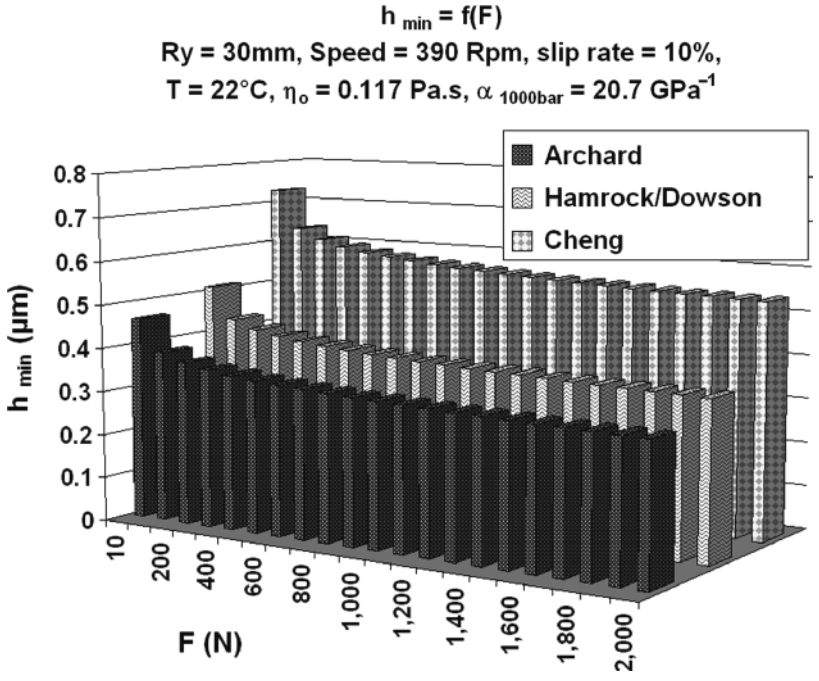

Fig. 2 Estimation of the paraffin oil film thickness as a function of the force applied according to the EHL contact model of Cheng, Hamrock and Archard

Fresh paraffinic oil is applied at ambient temperature of approximately 22°C. It limits the degradation of the surfaces subjected to the tribological, Hertzian contact strain and deformation, as the heat is dissipated by the fluid. This oil does not include any additives of the EP/AW type (EP: extreme pressure; AW: anti-wear). Avoiding such additives makes the tests simpler by eliminating possible effects of such additives. In addition, if it can be proved that such additives can be replaced by a combination of less or non-additivated base oils and coating without any undesirable effects on the lifetime, the ecological friendliness of tribosystems can be highly improved.

2.2 The Substrates

The substrates are mainly made of 100Cr6H steel (AISI 52100) with a hardness of 60 HRC (Rockwell hardness). In order to assess the influence of the hardness and of Young's modulus of the substrate on the slip-rolling behaviour of the respective coating, some tests were carried out with discs made of SSiC (sintered SiC) and of steel alloyed with 0.3–0.5 wt. % of nitrogen, X30CrMoN 15 1 (or Cronidur 30; 1.4108), of hardness 20 HRC, SSiC being the harder material than the alloyed steel (see Table 2). The characteristics of the hot isostatically pressed (HIP) ZrO_2 (ZTA: zirconia toughened alumina) are given as an indication, as only one test has been performed with this material. In this test the ZrO_2 disc was uncoated running against a toroid, coated disc made of SSiC. The steel substrates were standardized at the same polished roughness.

2.3 The Coatings

The layers and their characteristics are summarized in Table 3. All the layers were deposited on polished steel substrates. Their thickness ranges between 1 and 10 µm. Several types of a-C:H layers were tested, doped or undoped, with or without intermediate, adhesive transition layers. The doping agents used for the coatings are

Table 2 Properties of the substrates

Material	100Cr6H (52100 steel)	SSiC	HIP-ZrO_2	X30CrMoN 15 1
Density ρ (g/cm^3)	7.8	3.1	5.42	7.67
Young's modulus E (GPa)	210	410	256	224.3
Poisson ratio ν	0.30	0.17	0.23	0.3
Hardness, Vickers (GPa)	7.0 [HV10] ≡ 60 HRc	28 [HV0.5]	14.5 [HV0.5]	2.4 [HV10] ≡ 20 HRc
Tenacity K_{IC} (MPa·m$^{1/2}$)	20	3.2	13.9	>200
Bending strength σ_{4B} (MPa)	>2,000 (traction)	410	1,399	780 (traction)

Table 3 DLC-coating and THC-coating properties

Manufacturer	X	A	B	C	D	E	F	G	H	I
Type	THC	a-C:H:Si	a-C:H:Me	a-C:H ? n.a.	a-C:H	a-C:H:Me	a-C:H:Si	ta-C	THC	a-C:H (composed layer)
Process		PECVD	PEPVD/ CVD	PECVD	PECVD	PVD		PVD vacuum arc-assisted		PECVD
Interlayer	None	Si	None/Ti – W	Si	Ti	Cr	Si	Ti		Cr + W-C:H
Dopant(s)	No data	Si	Ta/Ti + W	No data	No	W	Si	None	No data	W in the interlayer
H content	0%	18–20%	3–15% /<5%	No data	15%	No data	No data	0%	No data	No data
Thickness (µm)	1–2	2/10	2–3	1	2/1	1–2	3–5	3	1.2	3 (total)
Young's Modulus (GPa)	<1,000	161	No data	118	256	150–170	251	500	No data	200
Hardness (GPa)	<120	16	<10	8	28	11–12	33	No data	No data	24 (20 mN)
R_a/R_z (µm) coating		0.02/0.2	0.1/1.4	0.01/0.12	0.02/0.1	0.02/0.3	0.02/0.1	0.3/1.6	0.01/0.14	0.01/0.12
R_a (µm) counter disc		0.05–0.6	0.6	0.6	0.6	0.6	0.6	0.6	0.3	0.24

of the type Si, Ti, W or Ti and W. The transition layers used are metal layers composed of silicon, chromium, titanium or Ti-W. The undoped ta-C-type coating with a titanium transition layer was also tested. The deoxidized SSiC substrate was coated with a nanocrystalline (THC) diamond layer for the respective slip-rolling tests. The manufacturers provided a batch of their standard coatings, i.e. without certain test specifications and metallurgical properties. Therefore, some modifications (variation of thickness, absence of adhesive interlayer) were required in a second batch for some coatings.

2.4 Analyses

Between each phase of the slip-rolling tests, the damages are identified by optical microscopy. The topography of the zone subjected to the tribological strain is also analysed with an atomic force microscopy. Furthermore, the respective zones are examined by EDX to identify the adhesive interlayers. In order to detect a possible structural change in the layer, the wear track on the coating is the subject of an analysis by Raman spectroscopy (using a Dilor XY Spectrometer with a CCD detector and an argon ion laser with an excitation wavelength of 514 nm). The power is limited to 10 mW (100 kW/cm^2) in order to avoid possible structural changes caused by an intense exposure to the radiation. Mechanical profilometry is applied to measure any change in the roughness of the surfaces tested.

3 Results and Discussion

All results of the slip-rolling tests with paraffinic oil are depicted in Fig. 3. The vertical lines represent the number of cycles reached. Their style indicates the initial, average Hertzian stress applied, i.e., 1.0 GPa (dotted line) or 1.25 GPa (dashed-dotted line) or 1.5 GPa (dashed line) or 1.75 GPa (solid) The numbers written under the figure are identification numbers of the tests and the Roman numerals ‘I’ and ‘II’ point out the batch of origin (‘II’ as batch of ‘modified’ layers). The number of cycles, at which the critical damage (1-mm^2 criterion) was reached, is marked by an ‘X’, a rise in the acoustic response by a rhombus. The detection of a rise in the acoustic activity always precedes the optical failure criterion (damaged area of 1 mm^2 in size). This method of monitoring permits the detection of a change in the system but its interpretation remains difficult.

According to Fig. 3, the coatings from suppliers ‘D’ and ‘G’ as well as ‘H’ and ‘I’ show by far the best results and seem to be the most successful candidates for further slip-rolling applications. Some of these coatings can exceed the million-cycles stage under 1.5 GPa of initial average Hertzian pressure (217 ksi) and sometimes over 10 million cycles like the samples ‘G3’ and ‘D5’. Some of the tests (D2 and D3 with lower initial Hertzian pressures of 1.25 GPa and 1.0 GPa, respectively)

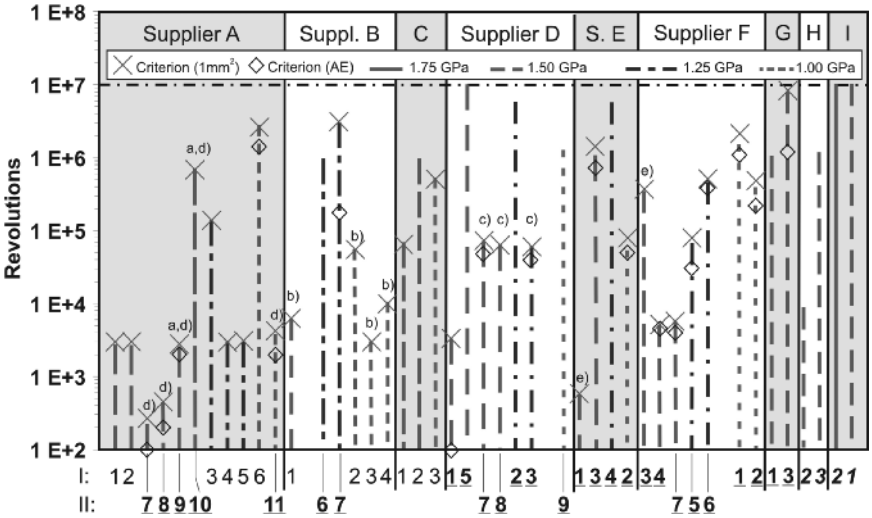

Fig. 3 Number of revolutions to failure of paraffin oil-lubricated DLC coatings: (a) counterbody polished, (b) without interlayer, (c) half thickness, (d) double thickness, and (e) acoustic emission overflow, (I and II) batch of coating; (1,…, *n*) number of coatings of the respective coater

have been stopped, if a sample has reached 10 million cycles at a higher pressure. Experience gained from the tests has shown that coatings enduring the first 500,000 cycles can withstand over 1 million cycles. It is perhaps due to the change in the lubrication regime. Profilometry shows that mainly the uncoated counter disc is polished during the tests, decreasing the global roughness of the system and thus enhancing the formation of the oil film. This in turn leads to an increase in the Tallian λ value, which indicates a shift towards the EHD lubrication mode. The EHD lubrication mode is less severe than the mixed/boundary mode, as the contact surface is loaded 'hydrostatically'. If the change in lubrication regime takes place after the first 500,000 cycles, this could explain the prolonged lifespan of over 1 million cycles up to 10 million cycles and more under high contact pressures.

However, the tribological tests have shown that some coatings failed before reaching 1 million cycles. Some did not even 'survive' 1,000 cycles! There are at least two possible explanations for this behaviour: the initial overall roughness is too high to be reduced quickly enough for a change of lubrication regime; or, the most likely explanation, the adhesion of the coating was not good enough, in combination with residual stresses, the slip enhancing a peeling effect. The test results presented in Fig. 3 show that the industrially produced coatings differ in quality even in the same batch of the very same supplier. This demonstrates that the reliability of the coating process, including the pretreatment of the substrate to be coated and the manufacturing machines, has to be improved to achieve a more homogeneous and reproducible distribution of the coating properties within batches. Figure 4 shows representative coatings and the respective counterbody after slip-rolling tests at initial, average Hertzian pressures of 1.5 GPa pointing out the sometimes poor adhesion of some coatings.

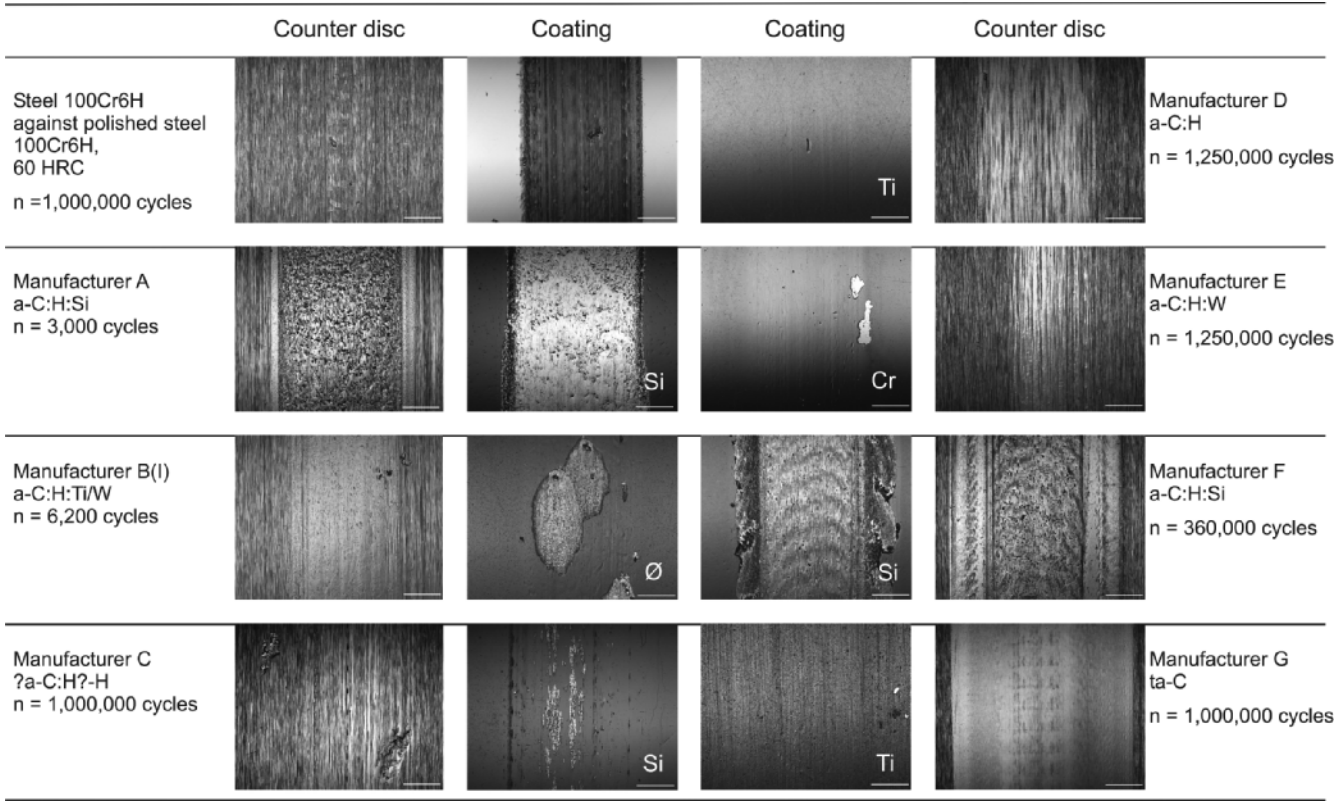

Fig. 4 Optical microscope images of the discs being tested at P_{mean} = 1.5 GPa with paraffin oil lubrication. The bond layer type is indicated on the bottom right hand corner of the pictures (scale: 500 µm)

Table 4 Influence of the thickness

	Type/interlayer	Thickness (µm)	Initial average Hertzian pressure P_{mean} (GPa)	Average lifespan (cycles)
A7, A8	a-C:H:Si/Si	10	1.5	500
Other A samples	a-C:H:Si/Si	2	1.5	3,000
D7, D8, D9	a-C:H/Ti	1	1.0–1.25–1.5	70,000
Other D samples	a-C:H/Ti	2	1.0–1.25–1.5	>1,000,000

3.1 Influence of the Coating Thickness (Manufacturers A and D)

In order to determine the influence of the coating thickness, the layers of the first batch of manufacturer A were supplied with a thickness of 2-µm thickness, those of the second with 10-µm thickness. For comparison, the layers of supplier D are 2-µm thick and 1-µm thick. The results are summarized in Table 4. According to the results, it is noteworthy that the thickness plays a role in the slip-rolling behaviour of DLC layers. In particular, the coating thickness seems to influence their lifespan [7]. An increase of the coating thickness leads to a drop of the lifespan for the a-C:H layers doped with Si on a sublayer of Si (manufacturer A). In addition, a reduction in thickness by 50% for the pure a-C:H layers on Ti of manufacturer D also gives poor results. It would thus seem that there is an optimal thickness of 2 µm for the layers of the a-C:H type. However, even if the coatings are of the same type, it is difficult to make a general statement, as the layers were produced differently and have different intermediate layers.

3.2 Influence of the Counter Disc Roughness (Results with Coatings of Manufacturer A)

The tests performed on samples A9 and A10 differ slightly from the others owing to the fact that the uncoated counter disc made of 100Cr6H has a polished, smooth surface ($R_a = 0.05$ µm), instead of being 'as-grinded' with $R_a = 0.6$ µm, as in all the other tests. In comparing samples A9 and A10 with samples A7 and A8, it is obvious that the starting roughness of the counter disc plays a part in the lifespan of the coating, especially in view of the thickness of the oil film.

The reduction of the starting roughness of the counter disc significantly increases the lifespan of coating A, up to 3 orders of magnitude. As can be seen from Table 5, even the worst performing sample with polished counterbody lasts 6 times longer than the best performing sample with a rough (as-grinded) counterbody.

Table 5 Influence of counterbody roughness

Sample	Type/interlayer	Initial average Hertzian pressure (GPa)	Roughness of counter disc R_z (µm)/R_a (µm)	Cycles till 1 mm² failure criterion
A7	a-C:H:Si/Si	1.5	3.42/0.62	270
A8	a-C:H:Si/Si	1.5	2.83/0.50	450
A9	a-C:H:Si/Si	1.5	0.30/0.05	2,800
A10	a-C:H:Si/Si	1.5	0.30/0.04	685,000

Table 6 Change of roughness values for sample G3 with cycles

G3	n = 0		n = 10,000	
	R_z (µm)	R_a (µm)	R_z (µm)	R_a (µm)
Coated disc	1.57	0.26	0.47	0.07
Counter disc	2.78	0.47	0.27	0.06

It should be noted that the steel counter disc undergoes a strong polishing process in the contact zone during the test. In the case of a-C:H coatings, the R_z and R_a values of the counterbody decrease by about 25% at the end of the first 3,000 cycles, without a change in the coating roughness (R_a = 0.01 µm; R_z = 0.15 µm). As the a-C:H coatings generally have an even surface, the roughness values are simply those of the substrate. Due to the production process, the ta-C coatings of supplier G exhibit higher roughness values. As can be seen from Table 6 both surfaces, i.e. even the coated surface, undergo a polishing process with a decrease of the roughness values of up to 90%.

This leads to a change in the lubrication regime, as indicated by Tallian's parameter λ now being equal to ~3 (using Archard's equation for the approximation of the minimal film thickness). The system lubrication now running closer to EHD conditions (without changes of further parameters, i.e. still about 400 rpm at initial average Hertzian contact pressures of 1.0–1.75 GPa) can explain the long lifespan of this sample (n_{max} ~10 million cycles).

A reduction in initial roughness prior to the tests leads to the less demanding EHD lubrication conditions right from the start (but increase finishing costs in production). It also avoids the formation of hard wear debris during the otherwise occurring polishing process, which can damage the coating. Although these fragments are immediately removed from the contact zone by the lubricant flow, they remain in suspension in the oil tub which has a volume of ~0.16 L. The formation of debris sediments in the oil tube has so far not been observed. The debris can thus be redirected into the zone of contact, attracted by the movement of the fluid, which is induced by the rotation of the lower disc.

However, it is more desirable to develop layers which resist a rough countersurface than to add a machining stage of polishing, in particular if these coatings have to be used on complex shaped mechanical components. In the short run, with the exception of coatings of suppliers D and G, it seems to be more likely, that the tribological performance of the coatings will be improved by polishing the countersurface, rather than by developing new coating systems.

3.3 Influence of Young's Modulus and Hardness of the Layers

The values of the modulus of elasticity and hardness of the layers supplied by the various manufacturers are very different, as can be seen in Table 3. As the respective data obtained from the coating supplier may differ considerably due to various techniques used, most modulus and hardness values were evaluated at the Federal Institute of Materials Research and Testing (BAM) using a nanoindenter. Although it might look fussy to exactly determine the hardness of a coating, it is still of some importance, as the harder coatings on the softer steel substrate are sometimes compared to an eggshell (see also the section concerning the substrate influence). Considering the modulus and hardness values in Table 3 and that the layers of supplier D and G are more resistant and behave better under slip-rolling conditions with respect to their competitors (see Fig. 3), it appears that the modulus of elasticity has to be at least similar or higher than that of the substrate. Nevertheless, the effect of the hardness of the layers remains difficult to interpret.

3.4 Influence of the Nature of the Intermediate Layer (or Adhesive Layer or Interlayer)

Comparing the results relating to the layers of manufacturer B (see Fig. 3), it is clear that the absence of an interlayer between the substrate and the DLC layer is prejudicial to its lifespan. Indeed, the samples not comprising this 'adapter of adhesion' deteriorate faster, even with lower initial contact pressures (samples B2, B3, B4 in Fig. 3). The intermediate or bond layer is therefore necessary in order to improve the interface between the DLC coating and the substrate. The goal is to obtain an intermediate layer which adheres to the substrate and on which adheres the functional DLC layer. Again, considering the properties of the coatings in Table 3 and the results in Fig. 3, an interlayer containing or made from titanium or chromium guarantees a longer lifespan. Indeed, the a-C:H pure layers of the manufacturer D are deposited on an interface containing titanium, like the ta-C layers of manufacturer G, and reach 10 million cycles under an initial, average Hertzian contact pressure of 1.5 GPa in the lubricating medium (in paraffinic oil) without any noticeable damage. The doped a-C:H layers with a Cr interfacial layer seem to be resistant to slip-rolling as well. Chromium and titanium, as interlayer materials, are thus adapted for a coating configuration 'steel/interlayer/DLC'.

3.5 Influence of the Hydrogen Content and Doping Agents

Hydrogen can be bound to the carbon atoms but it is also possible that it is present in dissolved form in the layers. Considering the data on the hydrogen amount (see

Table 3) and the results of the slip-rolling tests (see Fig. 3), there does not appear to be a correlation between the hydrogen content and the number of cycles without a critical damage. For example, ta-C layers, with nearly 100% sp^3 hybridized carbon and theoretically no C-H bonds can reach 10 million cycles, even having a very high elastic modulus. The undoped a-C:H layers of supplier D contain approximately 15% hydrogen also reach 10 million cycles at an initial average Hertzian contact pressure of 1.5 GPa (with paraffin oil lubrication). Furthermore, the THC coating of supplier 'H' exceeded 2 million cycles and the doped a-C:H coating of supplier 'I' also reached 10 million cycles. It is therefore difficult to assess the influence of the hydrogen content on the resistance of the layers in slip-rolling tests.

However, it is interesting to note that the two types of layers which resist best (supplied by manufacturers D, G and H) contain a large amount of sp^3 hybridized carbon. Therefore, a high sp^3 hybridization amount seems to be favourable for the lifespan. However, there may as well be an optimal value for the amount of sp^3-hybridization with a given proportion of C-C bonds and C-H bonds.

With the exception of the layers of manufacturer 'I', the non-doped layers of the manufacturers D and G are more successful in slip-rolling tests than the doped layers. Therefore, the dopants do not seem to play a dominating role in the slip-rolling behaviour under high Hertzian pressures.

3.6 Topography Influence

Topography has a lesser influence compared to the thickness or the interlayer nature. A topographic study with an AFM on the tested layers was carried out [8] (see also Fig. 5). This study reveals that the layers can roughly be classified into two categories: those with crater-shaped surfaces and those with bumpy surfaces, the latter showing, on average, a longer slip-rolling resistance (lifespan) and reaching 1 million cycles (layers of the manufacturer D).

3.7 Substrate Influence

According to Table 3, the Young's modulus and the hardness of the DLC coatings are much higher than the respective values of the standard 100Cr6H substrate. The idea is to use a substrate of higher stiffness and hardness to avoid an eggshell effect, i.e. to provide a better mechanical support for the DLC coatings in this respect. The sintered SiC (SSiC) substrate has a modulus of elasticity of 410 GPa that is to say twice that of the 100Cr6H steel modulus and should therefore constitute a good support. A layer of nanocrystalline diamond (THC) was deposited on this deoxidized substrate. A typical result of a typical test (an average pressure of 1.5 GPa with paraffinic oil) is presented in Fig. 6 (coated SSiC against coated SSiC). Four configurations were tested:

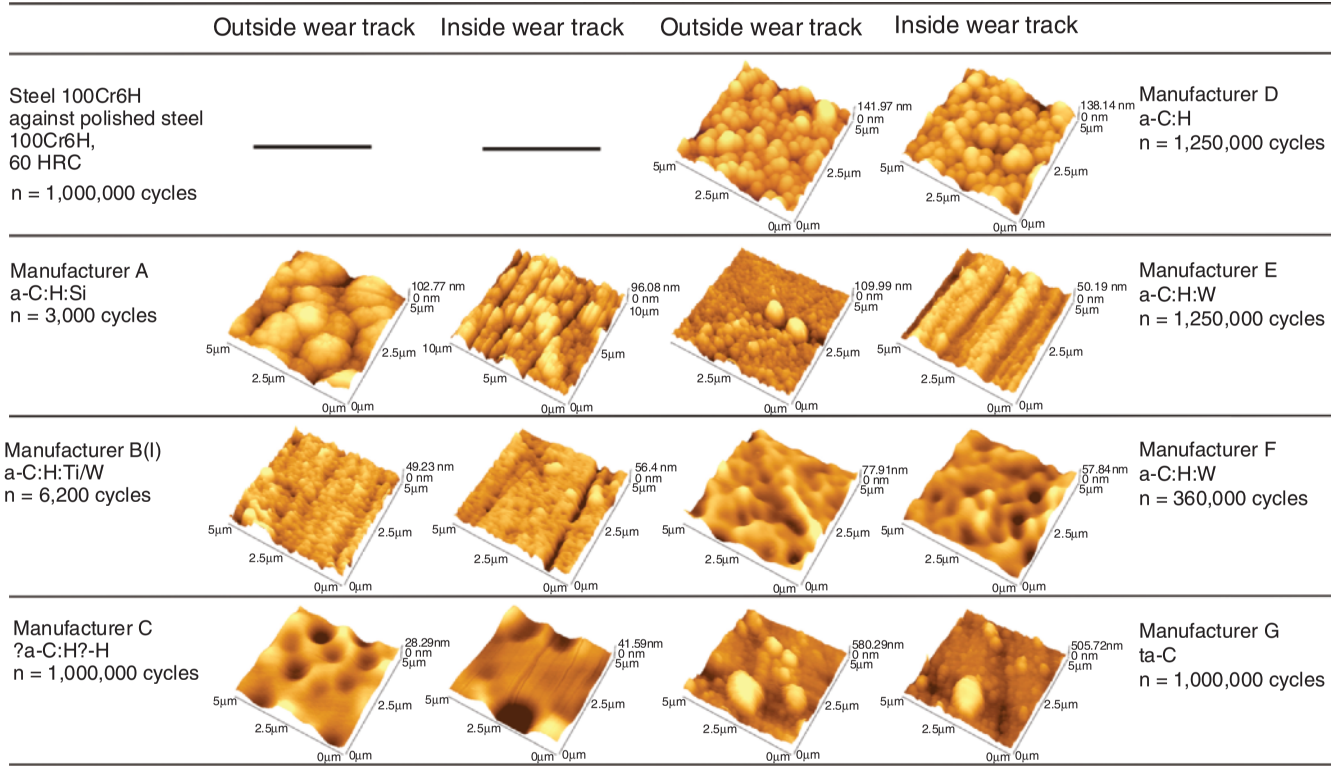

Fig. 5 AFM topography images of DLC surfaces inside and outside the wear track

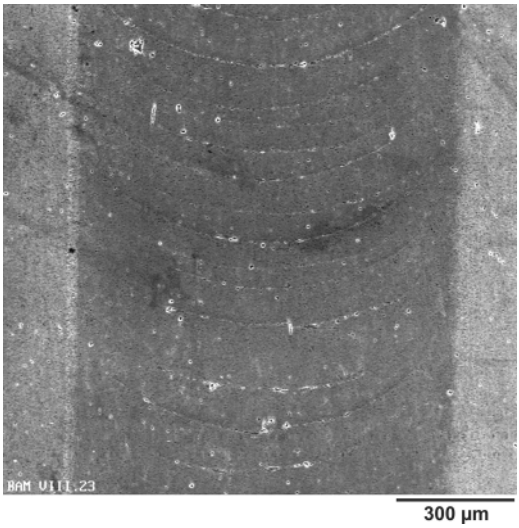

Fig. 6 SEM image of the surface of a SSiC disc in the state after slip-rolling at P_{mean} = 1.5 GPa

- Polished SSiC against polished SSiC (reference)
- Coated SSiC against uncoated 100Cr6H
- Coated SSiC against coated SSiC
- HIP ZrO_2 against coated SSiC

All the slip-rolling tests with SSiC substrate gave poor results [9]. All the layers deteriorated quickly and did not resist more than 10,000 revolutions under an initial average Hertzian contact pressure of 1.5 GPa, except in the case of HIP-ZrO_2 where the layer resisted up to 490,000 cycles. Multiple grooves of Hertz and cracks were formed in the SSiC substrate and propagated to the layers, which then disaggregated by flaking/spalling. In consequence, it cannot be stated that the coating failed. The SSiC substrate has quite low fracture toughness. However, the grade used here exhibited defects such as porosities and even cracks, leading to a premature damage of the layers. Moreover, the slip-rolling tests at an initial average Hertzian pressure of 1.5 GPa caused the formation of conical cracks, as can be seen in Fig. 6. Rather than supporting the layers due to its higher elastic modulus, the SSiC initiated the failure of the layers due to the formation of cracks inside the substrate. Therefore, SSiC does not seem to be a very suitable substrate for the nanocrystalline diamond layers because of a low fracture toughness or tenacity. However, it is known from literature [10] that self-mated SSiC couples can be quite slip-rolling resistant under the same test conditions at 1.5 GPa.

Instead of using a harder substrate to support hard layers, it is now intended to use softer substrates to adapt to the counterbody. Following the results obtained with the 100Cr6H steel substrates, ‘D’ coatings were deposited on nitrogen steel with a lower hardness, (Cronidur 30, 20 HRC) with a Ti interlayer. The counter disc was made of the same steel, but was left uncoated. After 1 million cycles under

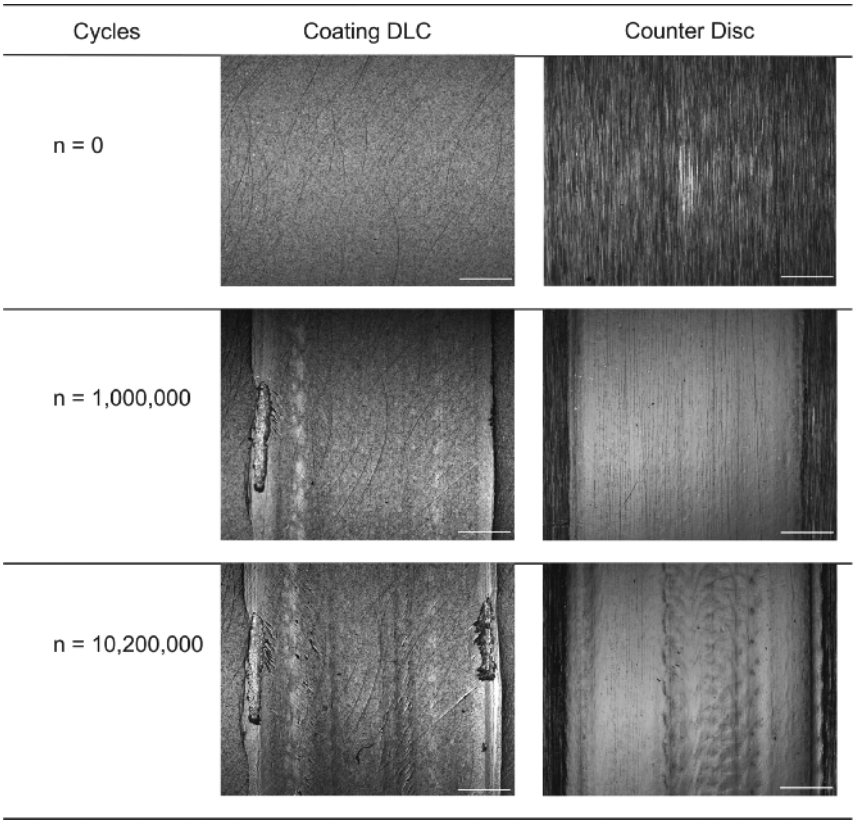

Fig. 7 Test with Cronidur 30 steel substrate (20 HRC); scale: 500 µm

slip-rolling conditions at an initial, average Hertzian contact pressure of 1.5 GPa, using mineral paraffinic oil as lubricant, the coating was still not pierced due to wear (see Fig. 7). The substrate being less hard, the rolling track is far broader. In order to demonstrate the protective influence of the coating, two uncoated discs have been tested under the very same conditions for an equal number of cycles, i.e. 1 million cycles. Figure 8 shows the counter disc at that stage, with many holes, cracks and cavitations in the middle of the wear track, due to rolling contact fatigue and three body abrasion.

The a-C:H coated Cronidur 30 discs were tested under slip-rolling conditions for more than 10 million cycles under the standard conditions listed in Table 1. The only defects which appeared in the layers are marks of juddering/stick slipping, bulgings which form on the sides of the track (Fig. 7) and some cracks oriented 45° away from the track. Very few significant flaked zones are visible. Those are especially visible on the top of the bulgings at the edge of the track. In a foreseeable way, the soft substrate gets deformed in the zone where the contact pressure is highest, i.e. the central track. Profilometry on the wear track reveals a

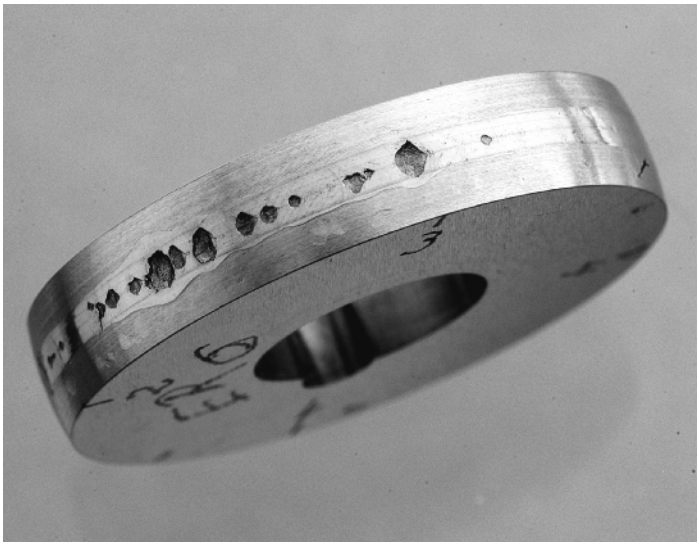

Fig. 8 Uncoated disc after 10^6 cycles slip-rolling against an other uncoated disc in paraffinic oil at 1.5 GPa, both made of Cronidur 30 steel (20 HRC)

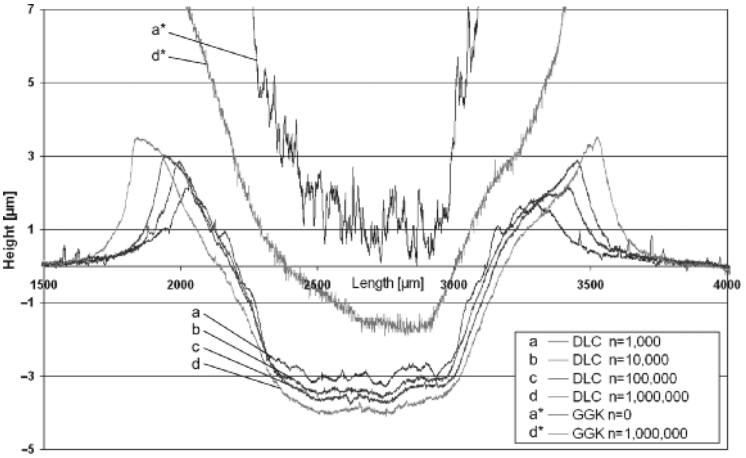

Fig. 9 Profiles of the groove of a D coating on Cronidur 30 (20 HRC) tested under 1.5 GPa with paraffin oil lubrication at different cycles

depth of deformation of 2.5–3 µm (see Fig. 9) just after a few turns. Much more surprisingly, however, the DLC layer does not deteriorate due to the subsidence of the substrate, but even follows its deformation. Raman analyses confirmed that the layer is still present in the central track. As can be seen from the profilometry graphs in Fig. 9, more than 90% of the deformation takes place during the first 100,000 cycles. The counter disc is at first polished during the start of the slip-rolling tests. Getting closer to 10 million cycles, the counter disc gets rough with

an irregular surface. This surface is corrugated with furrows which are formed in the centre of the track. The formation of wear continues but becomes critical for the uncoated counter disc.

Due to the deformation, it is even more difficult to evaluate the wear volume of the layer. The traditional profile measurement simply records the deformation. It cannot answer the question whether or not the layer has been thinned due to the testing. Especially, as there was no flake off, the edges of which could have been used for thickness measurement. Interestingly, despite a layer hardness of 28 GPa, this coating has a certain 'flexibility' or 'suppleness'. The lack of flaking also proves that titanium is a good interlayer, as the DLC layer is able to follow the deformations of the substrate.

It should be noted that in the contact zone, a work-hardening effect of the Cronidur30 substrate could be observed up to a depth of approximately 500 µm. The hardness of the substrate rose by up to 25% from 2.4 GPa to 3.0 GPa. A more detailed description of these experiments can be found in Ref. [11].

3.8 Lubricant Influence

Paraffinic oil without additives tends to level the coefficient of friction between 0.06 and 0.09 for all the layers whatever the applied force is. Depending on the layers, the friction coefficient increases or decreases during the tests.

Some tests were carried out by replacing the paraffinic lubricant with a fully formulated polyalkyleneglycol PAG 46-1 (diol). The tested coatings are a-C:H layers of the manufacturers A, B and C. The cylindrical disc is coated and the toric counter disc is not. The respective substrates were made of 100Cr6H. A ninth coating, H, of THC type, 2-µm thick and with a roughness R_a = 0.01 µm was also tested under these conditions (see Table 7). The maximum number of revolutions reached is relatively low and the first three coatings listed in Table 7 are quickly damaged heavily. The wear rate is higher with polyglycol as lubricant, in comparison to the results that were obtained with unadditivated paraffinic oil. A possible reason for the higher wear rate under polyglycol lubrication could be due to the

Table 7 Effect of the polyglycol on some coatings

				Cycles		Coefficient of friction at the test end	
Coating	Type	Thickness (µm)	Pm (GPa)	Glycol PAG 46-1	Paraffin oil	Glycol PAG 46-1	Paraffin oil
A	a-C:H:Si	2	1.5	3,000	3,000	0.070	0.085
B	a-C:H: Me	2–3	1.0	55,000	55,000	0.056	0.068
C	a-C:H ?	1–2	1.5	25,000	65,000	0.063	0.080
C	a-C:H ?	1–2	1.5	25,000	1,000,000	0.063	0.077
H	THC	1–2	1.5	900,000	800,000	0.054	0.076

lower pressure–viscosity coefficient of the PAG46-1. This leads to a calculated film thickness, which is ~25% smaller compared to the one of paraffinic oil. However, the defects observed under polyglycol lubrication are identical to those generated in paraffinic oil. Nevertheless a general decrease of the coefficient of friction of 15–20% is observed. The lubricant polyglycol decreases friction in the case of layers A, B and C, but led on the other hand to a higher wear rate. However, in the case of the coatings of manufacturer H, the coating reached a larger number of revolutions in slip-rolling tests with polyglycol lubrication as with paraffinic oil lubrication, while at the same time lowering the COF by about 30%. The lubricant applied therefore has an effect on the durability and performance of the DLC coatings in slip-rolling tests. This effect, however, seems to depend on the type of the coating.

In addition, the layers of suppliers A, B, D, E and G were tested in the absence of any lubrication. The results are listed in Table 8. For these tests, the respective discs rolled in direct contact with each other, creating a dry friction with an initial average Hertzian pressure of 1.0 GPa, i.e. 338 N. Investigating with an optical microscope in the differential interference contrast mode, the layers exhibited a deterioration of colour (see Fig. 10). Considering Table 8, the coefficient of friction is higher and the destruction of the coatings is faster, as compared to lubricated conditions. But among the layers there is an order of magnitude of difference in the number of life cycles before a notable damage occurs. The layers of the manufacturers D and E are distinguished particularly: the layers failed between 30,000 and 100,000 cycles, which is 3–10 times more than for the layers of supplier G and 10–30 times more than for the layers of supplier A and B. Curious is the fact that the coefficient of friction decreases in the case of the manufacturer E. This is possibly due to the effect of a transfer of part of the DLC coating onto the steel counter disc, thus creating a contact 'carbon against carbon'. This material transfer, however, reduces the thickness of the layer and in turn its lifetime. Admittedly, the transfer thus seems beneficial, as it reduces the COF, but at the cost of the thickness of the layer. Nevertheless, it is preferable that a partial transfer takes place rather than a sudden flaking. The fact that the counter disc is polished does not seem to have any positive effect under dry friction (G4). Polishing is not inevitably advantageous, as in the case of ceramics tested under rolling conditions [10].

Table 8 Tests carried out under 1.0 GPa without lubrication (dry)

Coating	Number of revolutions n	Coefficient of friction μ at the end of the test	μ average
A12	3,000–4,000	0.52–0.53	0.37
B11	3,000	0.17	0.2
D4	3,000–10,000–30,000–131,000	0.15–0.18–0.21–0.34	0.2
E5	30,000–102,000	0.21–0.13	0.18
G2	3,000–10,000	0.34–0.49	0.45
G4 (with counter disc polished)	3,000–10,000	0.41–0.49	0.42

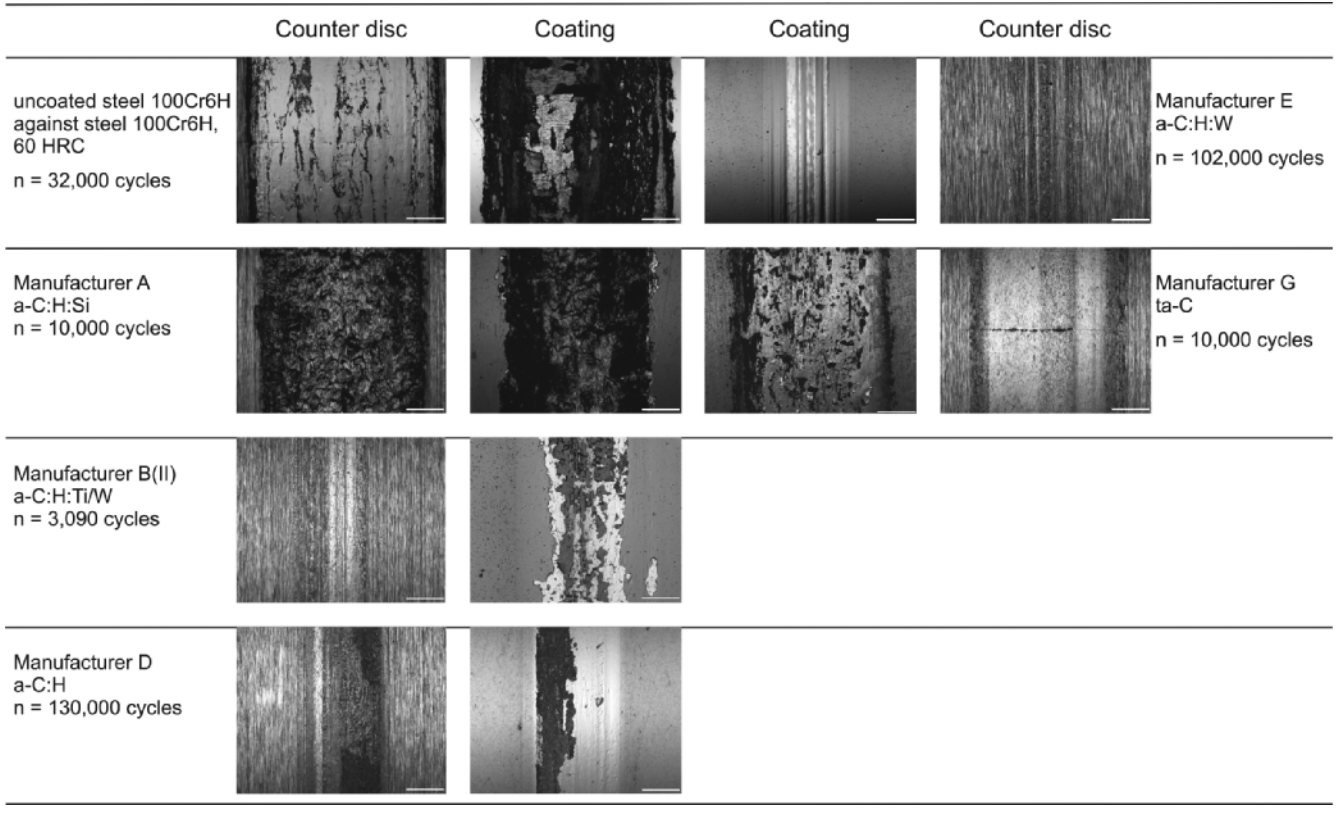

Fig. 10 Optical microscope images of DLC coatings and their respective counterbody, after dry slip-rolling tests at 1.0 GPa (the white bars represent a distance of 500 µm)

3.9 Raman Analysis of the Layers

3.9.1 Lubricated Coatings

Zones inside and outside the wear track of the tested samples A5, B1, C3, D1, E1, F4 and G3 (for the respective results of the slip-rolling tests see Fig. 3) were analysed with Raman spectroscopy (see Fig. 11, left). These investigations were carried out in order to determine the following properties of the respective samples:

- Rate of crystallinity and type of structure (evolution of the position of the peak G [12]);

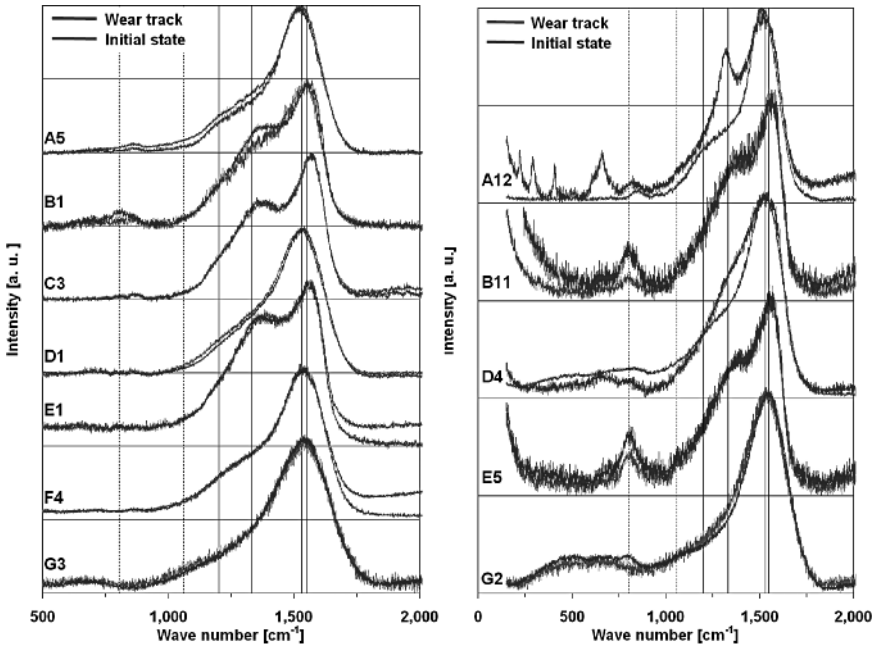

		P_{mean} (GPa)	Cycles
A5	a-C:H:Si	1.25	3,000
B1	a-C:H:Me	1.5	6,100
C3	a-C:H ?	1.0	400,000
D1	a-C:H	1.5	3,300
E1	a-C:H	1.5	570
F4	a-C:H:Si	1.5	5,000
G3	ta-C	1.5	4.400.000

		P_{mean} (GPa)	Cycles
A12	a-C:H:Si	1.0	4,000
B11	a-C:H:Me	1.0	3,000
D4	a-C:H ?	1.0	131,000
E5	a-C:H:Me	1.0	102,000
G2	ta-C	1.0	10,000

Fig. 11 (*Left*) Raman spectra of some coatings tested under paraffin oil lubrication; (*right*) Raman spectra of coatings tested without lubrication

- Factor of deconvolution Q [13] and ratio I(D)/I(G), with I(D), the intensity of the disordered graphite peak, and I(G), the intensity of the graphite peak, after a Breit–Wigner–Fano (BWF) deconvolution;
- Intensity ratio between the D peak at about 1,350 cm^{-1} and the G peak at about 1,550 cm^{-1}.

The peaks at 805 cm^{-1} and 1,060 cm^{-1} are due to excitations in the glass material of the microscope objectives.

All those coatings are termed DLC coatings, but the spectra are very different. This illustrates the inhomogeneity of the properties. Some present a more or less marked elbow. This difference is ascribable to the structure of the layers in particular to the carbon bonds. The layer G would be thus of ta-C type while B, C and E would be of a-C:H type. Obviously the layers C, E, F and G are not or nearly not affected by structural changes because of the slip-rolling tests, whereas the layers D and especially A and B, which rolled only very few rotations, undergo a structural transformation. The rise of the elbow is probably an indication of a graphitization of the layer under load.

The layers E1 and F4 are relatively quickly destroyed, no transformation is visible. A5, B1 and D1 are quickly destroyed but a transformation takes place. C3 rolls a long time, no transformation occurs but C3 was exposed to a lower pressure and can 'graphitize with difficulty' since its D peak is already very marked before starting the test.

G3 also rolls for a long time but a graphitic transformation takes place with its destruction (see Fig. 12). The transformation during rolling can be prejudicial for the behaviour of the ta-C coating G. On the other hand, the a-C:H layers, containing graphitic zones at the start, can as well be destroyed quickly (manufacturers A and F, Fig. 3) as well as rolling up to 10 million cycles (manufacturer D). It is difficult to

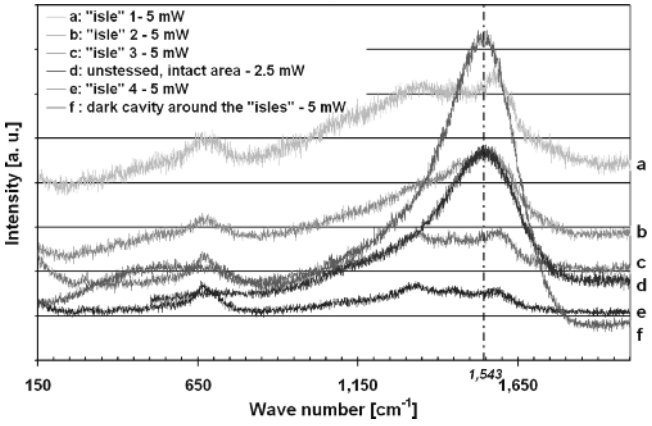

Fig. 12 Raman spectra taken outside and inside the groove of G3 after 9 millions cycles

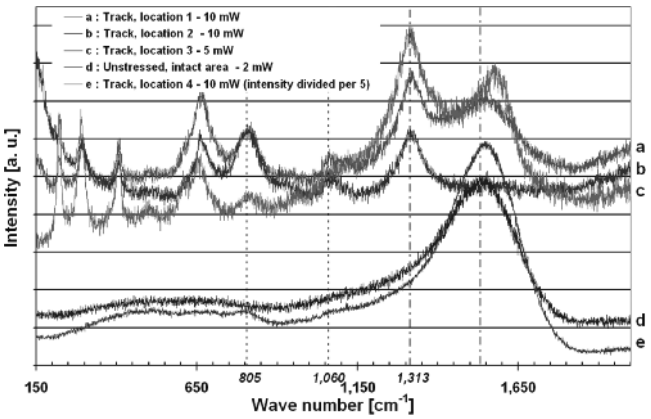

Fig. 13 Spectra of different areas on the dry tested G2 sample

affirm if the graphitization involves the destruction or if the destruction involves the graphitization, or, if the graphitization is really critical for the lifespan at all.

For the analysis of the track of the G3 layer after 9 million cycles with the damage criterion reached refer to Fig. 13. Various zones are visible: clear and rough 'islands' surrounded by dark hollows. The dark hollows present a spectrum identical to the layer at the initial, untested state, while the spectra of the 'islands' present peak characteristics for iron oxides (Fe_3O_4 at 670 cm^{-1}) [14,15] and a G peak, which has moved towards larger wave numbers with an increase in the intensity of the D peak. The latter can be partly overestimated, the presence of the peak Fe_3O_4 at 670 cm^{-1} indicating the presence of oxides, with the Fe_2O_3 oxide having a very near peak at 1,317 cm^{-1}. However, as the other peaks of Fe_2O_3 at 222, 298, 406 and 613 cm^{-1} [14,15] are not detected, graphitization is very likely. The analysis of the edge of the polished zone on the counter disc of the G3 sample (not presented) shows a blackish transfer of carbon with a spectrum strongly resembling E1, i.e., a more amorphous structure than the initial DLC layer and richer in carbon of the graphite type [16]. Then this structural transformation is a possible cause of the bad wear resistance under rolling.

3.9.2 Dry Tested Coatings

The layers of suppliers A, B, D, E and G were tested without lubrication. The respective unloaded zone and wear tracks were analysed in the same way by Raman spectroscopy (Fig. 11, right). The spectra of the zones subjected to the load are all different compared to those taken of the respective unloaded areas. A rise of the elbow due to the increase in the D peak is visible in all the cases, except the layer G, which presents places without changes in the track. The iron oxide forma-

tion of the Fe_3O_4 type (single peak at 670 cm^{-1}) and α-Fe_2O_3 type (which exhibits five peaks, one at 1,317 cm^{-1}) is also visible, attesting of a transfer of metal from the counter disc on the coating or attesting of a localized total wear of the layer (if the G peak is no more present).

The absolute intensities (not shown) of the zones analysed in the track decrease, compared to the intensities of the intact zones. This indicates a reduction in the thickness of the layer in the track (in particular samples B and D). In the case of E5, some zones do not present any more a spectrum of the DLC type (not represented). The peaks D and G disappeared, indicating a complete removal of the layer at these places, which is a proof for a bad adhesion of the DLC coating on the substrate.

The G2 coating was analysed in more detail. The respective spectra of Raman spectroscopy are shown in Fig. 13. In the dark zones of the track, oxides form (spectra a and c, in Fig. 13). At the edge of the track (spectrum b), no signal due to the last trace of layer is visible, so the layer was destroyed at this place. Clear zones (spectrum e) show a spectrum similar to the unstressed intact zone (spectrum d) with a G peak which moved towards higher wave numbers. It is possible that a part of the DLC layer was transferred on the counter disc then again on its original substrate during the test, giving, as a result, different spectra in the track with oxides and DLC peaks or just oxide peaks or just DLC peaks. The D peak is covered by the peak of Fe_2O_3 at 1,317 cm^{-1}, and an interpretation of its evolution is impossible. But, as in the case of G3, the G peak moves towards the largest wave numbers, making the supposition of a graphitization [13] and the formation of a graphitic transfer film credible. Then the lubricant would reach a higher graphitic carbon rate, perhaps improving its properties.

4 Summary and Conclusions

The applied force is not the only criterion influencing the lifespan under slip-rolling conditions. Certain layers are able to reach several million cycles under strong Hertzian stresses while others wear or flake more quickly at lower stresses. The presence of defects at the beginning is crucial. A layer prematurely damaged cannot resist for a long time, as the defects propagate. The interlayer has an important part and the optimal one is the layer containing titanium or chromium. An optimal thickness of approximately 2 µm under the conditions which were used (1.5 GPa–1.75 GPa initial average Hertzian pressure and paraffinic oil) seems to be the most effective. The substrate must have a good tenacity, but its hardness is less critical, certain layers being able to follow the deformation of a steel having a 20 HRC hardness and protecting really the steel. The lubricant polyalkyleneglycol PAG 46-1 decreases friction, but also the lifespan with the most of the coatings. The roughness takes a part in the lifespan. A rough counter disc will be polished during the firsts rotations. It could create a lubrication transition. It was seen that polished counterbodies at the starting point have a greater lifespan, probably due to less

severe contact at the beginning which avoids debris formation. The determination of the influence of the coating intrinsic properties, like the amount of hybridization, the hydrogen content and the mechanical properties, must go further. Nevertheless, at the destroyed state, the layers present a structural transformation compared to their original state, probably due to a graphitization during rolling with formation of a transfer film rich in graphitic carbon.

Acknowledgements The authors want to express their sincere gratitude to Manuel Löhr, Ute Effner, Klaus Wittke, Regina Pahl and Sigrid Binkowski for their help in carrying out the experimental work.

References

1. Schultrich B., Weihnacht V., Scheibe H.-J., Stucky T. and Bräunling S. (2005). Superharte amorphe Kohlenstoffschichten für Zerspannungs- und Umformwerkzeuge, 46. Tribologie-Fachtagung, GfT, Band I, 32/1–32/9.
2. Czichos H. and Habig K.-H. (2003). Tribologie Handbuch Reibung und Verschleiß 2. Auflage, Vieweg Verlag.
3. Löhr M., Spaltmann D., Binkowski S., Santner E., and Woydt M. (2006). In situ Acoustic Emission for wear life detection of DLC coatings during slip-rolling friction. Wear 260: 4–5, 469–478.
4. Schmidt R., Klingenberg G. and Woydt M. (2006). New lubrication concepts for environmentally friendly machines –Tribological, thermophysical and viscosimetric properties of lubricants interacting with triboactive materials, BAM Research Report 277, ISBN 3-86509-528-3 Wirtschaftsverlag NW, 27568 Bremerhaven, Germany.
5. Kalin M., Vižintin J., Vercammen K., Barriga J. and Arnšek A. (2006). The lubrication of DLC coatings with mineral and biodegradable oils having different polar and saturation characteristics. Surf. Coat. Technol., 200: 4515–4522.
6. Tallian T. E. (1967). ASLE Transactions, 10:418.
7. Wei R., Wilbur P. J. and Kustas F. M. (1992). A rolling contact fatigue study of hard carbon coated M-50 Steel. J. Tribol. 114: 298–303.
8. Spaltmann D., Löhr M., Binkowski S., and Woydt M. Einfluss der (2004). Topographie von DLC-Schichten auf deren Verhalten unter geschmierter Wälzbeanspruchung, Tribologie und Schmierungstechnick 6/2004: 18–24.
9. Löhr M., Spaltmann D., Effner U., and Woydt M. (2005). Einfluss des E-Moduls und des Grundöls auf das Wälzverhalten von DLC- und Diamantbeschichtungen. Tribologie und Schmierungstechnick 1/2005: 32–36.
10. Effner U.and Woydt M. (2003). Slip-Rolling and Machining of Engineering Ceramics. BAM research report Nr. 259, Wirtschaftsverlag NW, Bremerhaven, Germany, 3-89701-976-0;
Effner U. and Woydt M. (2000). Wälzverschleiß und Endbearbeitung von Ingenieurkeramiken - Einfluß der bearbeitungsbedingten Oberflächenausbildung auf das tribologische Verhalten unter Wälzreibung und deren Charakterisierung mittels Ultraschallmikroskopie, BAM research report 237, Wirtschaftsverlag NW, Bremerhaven, Germany, 3-89701-520-X.
11. Spaltmann D., Löhr M., Binkowski S., Kelling N., Soltwedel R., Woydt M. and Santner E. (2005).Damages of slip-rolling tested DLC coatings on steel substrates of different hardness. Materialwissenschaft u. Werkstofftechnik, 36(2): 62–68.
12. Ferrari A. C. and Robertson J. (2000). Interpretation of Raman spectra of disordered and amorphous carbon. Phys. Rev. B 61: 14095–14107.
13. Prawer S., Nugent K.W., Lifshitz Y., Lempert G. D., Grossmann E., Kulik J., Avigal I. and Kalish R. (1996). Systematic Variation of the Raman Spectra of DLC Films as a Function of sp2:sp3 composition. Diam. Relat. Mater. 5: 433–438.

14. Oh S. J., Cook D. C. and Townsend H. E. (1998). Characterization of Iron Oxides Commonly Formed as Corrosion Products on Steel. Hyperfine Interact. 112: 59–66.
15. Massey M. J., Baier U., Merlin R. and Weber W. H. (1990). Effects of pressure and isotopic substitution on the Raman spectrum of α-Fe_2O_3: Identification of two-magnon scattering. Phys. Rev. B 41: 7822–7827.
16. Scharf T. W. and Singer I. L. (2003). Quantification of the thickness of carbon transfer films using Raman tribometry. Tribol. Lett. 14(2): 137–145.

Tribological Behavior of DLC Films in Various Lubrication Regimes

B. Podgornik

Abstract Owing to their attractive properties, diamond-like carbon (DLC) coatings are becoming increasingly important in the field of machine components. The extreme hardness, high elastic modulus, excellent wear and corrosion resistance, high thermal and chemical stability, and the low-friction nature of these coatings open further possibilities in improving tribological performance and reliability of different components. Despite the low friction coefficients, normally observed for DLC-coated surfaces under dry sliding conditions, only few DLC-coated tribological components are likely to be operated completely without a lubricant. There are many reasons for that. First, tribological properties of unlubricated DLC coatings are very sensitive to the surrounding atmospheric conditions, notably the relative humidity. Further, it is not always possible or economically desirable to coat all surfaces in the system, while the lubricant also serves other functions, such as cooling, in mechanical systems. Thus, the majority of DLC-coated components will continue to be operated under lubricated conditions, mainly under boundary lubrication, and will initially use the same lubricants as originally developed for uncoated surfaces. Therefore, the knowledge about DLC coatings' tribological behavior under different lubrication conditions and influence of lubricants and their constituents is crucial, if the possibilities and benefits of the DLC coatings in mechanical systems are to be fully exploited.

Keywords diamond-like carbon, lubrication, lubrication regimes, additives, tribology, friction, wear, tribofilms

Centre for Tribology and Technical Diagnostics, University of Ljubljana, Ljubljana, Bogisiceva 8, SI-1000 Ljubljana, Slovenia

C. Donnet and A. Erdemir (eds.), *Tribology of Diamond-Like Carbon Films: Fundamentals and Applications*.

1 Introduction

During the past three decades or so, a wide range of hard, wear resistant coatings was developed and quite successfully used in different tribological applications. Hard coatings, which are mainly nitrides, carbides, and carbonitrides of transition metals (such as TiN, TiCN, TiAlN, CrN) have become essential in improving the performance of cutting and forming tools [1–5]. Analogously, hard low-friction coatings are now becoming more and more important in the field of machine components [6–9]. Today, the trends in the machine-component industry are towards higher performance, improved reliability and tolerances, more environment-friendly products, less lubrication, and reduced frictional losses [10,11]. Owing to their attractive tribological properties, diamond, diamond-like carbon (DLC) coatings and especially metal-doped DLC coatings represents one of the means to achieve these goals [6–9,11–15]. Extreme hardness, high elastic modulus, excellent wear and corrosion resistance, high thermal and chemical stability, chemical inertness, and the low-friction nature of DLC coatings make them good prospects for a wide range of machine component applications [8,16–18]. However, in many respects, the demands on coatings for machine components are very tough, much tougher than those on cutting tools [1]. The expected life-time is very long, the coating costs must normally be very low compared to component costs, the substrate hardness is rather low, failure or detachment of the coating can lead to a catastrophic failure of the whole system and usually the contact is lubricated. The majority of machine components are operating under lubricated conditions, either in mixed, boundary, elastohydrodynamic (EHD), or hydrodynamic (HD) regime (Fig. 1), where interactions between the contact surfaces and lubricant play a significant role. Especially under boundary lubrication

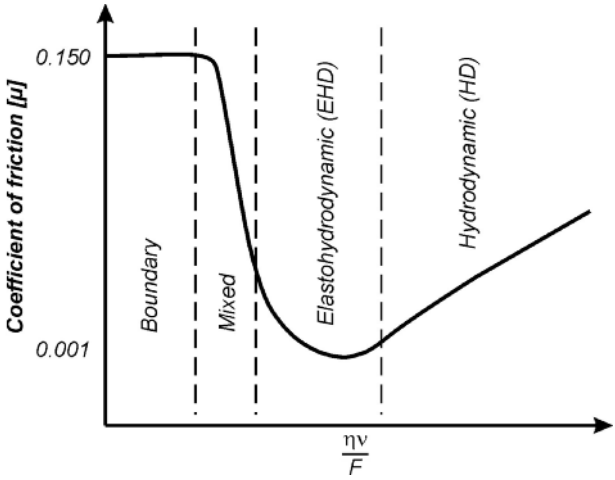

Fig. 1 Stribeck-curve and identification of main lubrication regimes [34]

conditions chemical interactions between the lubricant additives, oxygen in the ambient atmosphere, and the metallic surfaces dictate the tribological behavior of the contact [19].

Many types of DLC coatings have turned out to provide excellent low friction and wear protection properties under different contact conditions. Depending on the deposition method, the deposition parameters, and surrounding environment, the dry sliding friction of DLC coatings against different metallic or ceramic materials is typically reported to be in the range of 0.1–0.005 [2,17,20–24]. This is in the same range of, or lower than, the typical values of metallic surfaces operating under boundary lubrication conditions. Despite this favorable friction level, only few DLC-coated machine components are likely to be operated without a lubricant, at least for the near future. This has many reasons. First, tribological properties of unlubricated DLC coatings are greatly influenced by the surrounding atmospheric conditions, especially the relative humidity [8,15,25,26]. For example, amorphous hydrogenated carbon coatings (a-C:H) show extremely low friction in vacuum and dry atmospheres ($\mu = 0.04–0.006$), but humidity distinctively increases the friction coefficient of a-C:H films [20,23]. Second, the lubricant also serves to do other functions in the mechanical system, such as cooling and wear particles removal. And third, very often it is not economically viable and sometimes not even technically feasible to coat all components in the system. Thus, a majority of DLC-coated machine components will continue to be operated under lubricated conditions, and will initially use the same lubricants as originally developed for uncoated steel surfaces.

Although the usage of DLC coatings with environmentally friendly fluids (i.e., water) might provide the basis for new, environmentally more acceptable solutions compared to existing practice, for at least another decade DLC coatings will have to operate with today's lubricants, originally designed for uncoated metallic surfaces. With the introduction of DLC-coated surfaces in existing systems the major concern is the compatibility with existing lubricants and lubricant additives [27]. Therefore, the knowledge about DLC coatings' tribological behavior under different lubrication conditions and influence of lubricant and its constituents is crucial, if the possibilities and benefits of DLC coatings in mechanical systems are to be fully exploited.

2 Starved Lubrication

Majority of machine components are operating under boundary-lubricated sliding conditions. However, if there is a lack of lubricant or sudden failure in the lubrication system, conditions will gradually change into starved lubrication, where capability of the contact surfaces to resist scuffing and wear plays a very significant role. If lubricant is removed from the system, being base oil or fully formulated lubricant, uncoated steel surfaces show signs of failure within the first 1,000 sliding cycles, as shown in Fig. 2 [28]. On the other hand, application of DLC coatings

was found to prolong the lifetime of contact surfaces from 2 to 5 times, with the DLC–steel combination showing the very best results and sustaining more than 4,000 sliding cycles before failure occurred (Fig. 2). Furthermore, in the case of DLC-coated surfaces, the increase in friction was limited only to high loads, as compared to uncoated steel surfaces, where the friction increases rapidly over a wide load range, as shown in Fig. 3. These results clearly indicate the capability of DLC coatings to improve load-carrying capacity and prolong the life of contact surfaces in starved lubrication caused by lubricant loss or lubrication system malfunction [27–29].

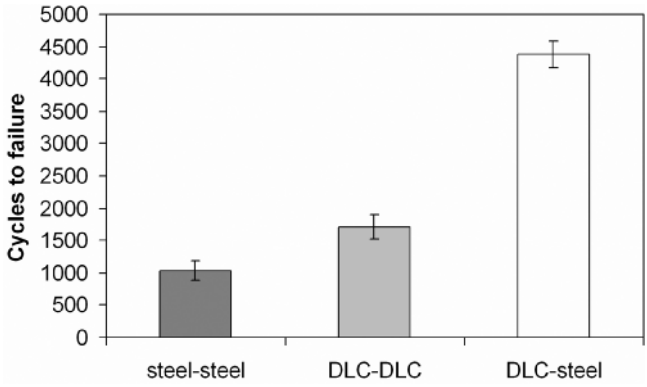

Fig. 2 Cycles to failure for DLC (WC/a-C:H)-coated and uncoated surfaces, investigated under starved lubrication condition and contact pressures ranging from 3 to 5.5 GPa [28]

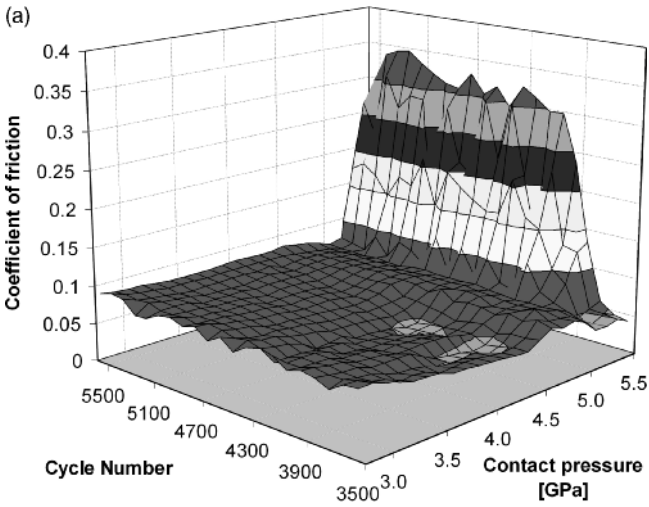

Fig. 3 Friction maps at the moment of failure for (a) DLC/steel (WC/a-C:H) and (b) steel/steel material combinations exposed to starved lubrication in pure poly-alpha-olefin (PAO) oil [28]

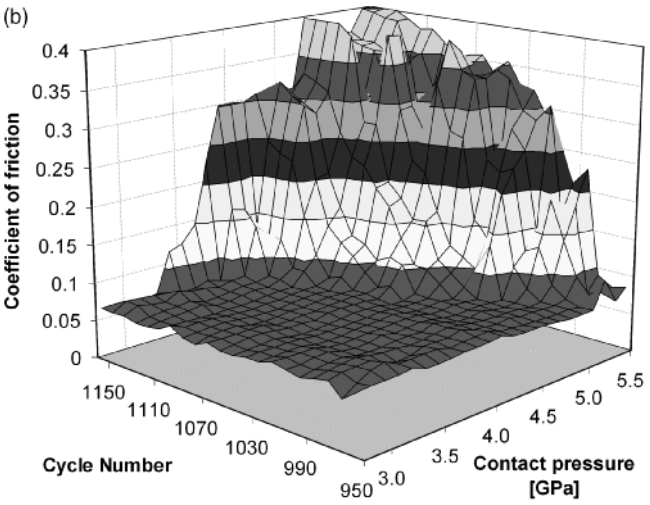

Fig. 3 (continued)

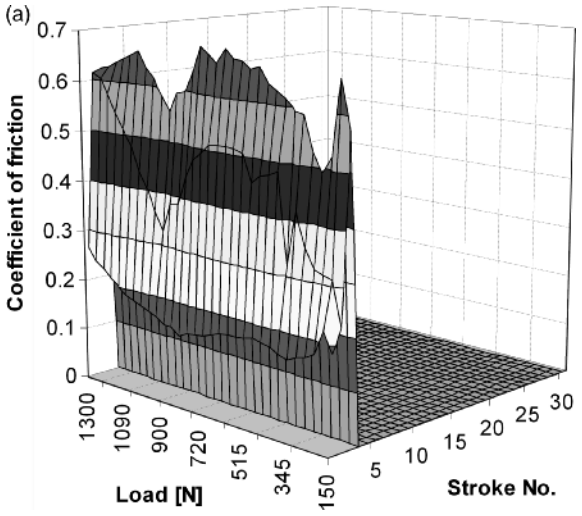

Fig. 4 Friction maps for cold work tool steel, sliding against austenitic stainless steel in (a) PAO and (b) fully formulated forming oil, and (c) for WC/a-C:H-coated tool steel operating in PAO oil [32]

On the other hand, starved lubrication conditions are very common in metal-forming applications [30]. In order to prevent transfer of work material to tool surface, tools have to be polished and special, highly chlorinated lubricants have to be applied [30–32]. In the case of base oils without any additives transfer of work material to tool surface and transfer from initial boundary regime towards starved lubrication happen at the very beginning of the operation. Change from base oil to fully formulated forming oil gives very uniform friction behavior of the tool and complete protection against transfer of work material in the wide load range, as shown in Figs. 4a and 4b. Coating of tool surface with DLC coating gives similar

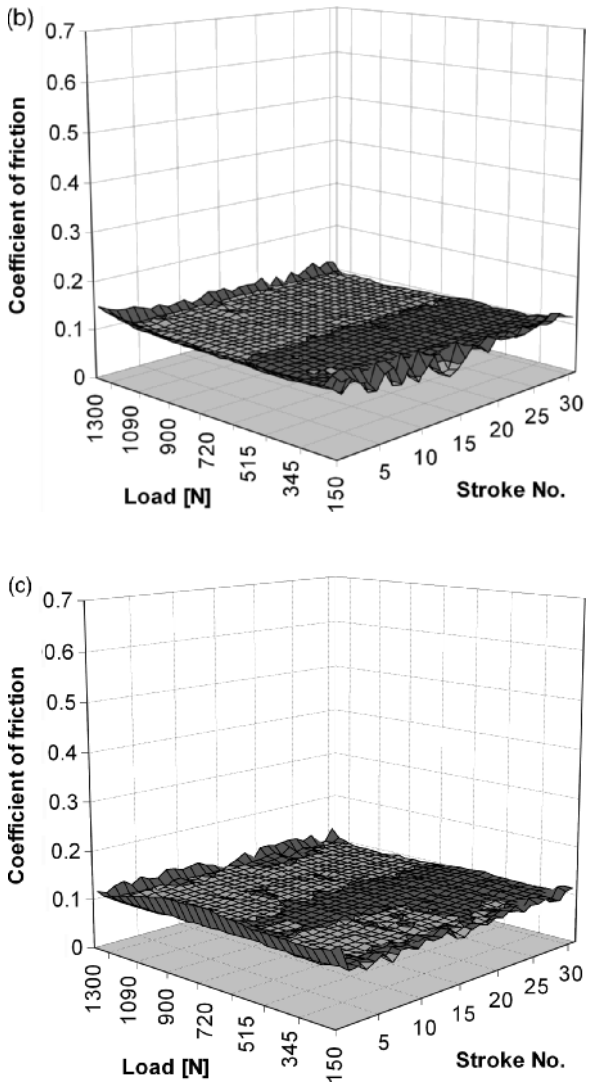

Fig. 4 (continued)

frictional properties and excellent protection against work material transfer to tool surface, as shown in Fig. 5. However, in contrast to uncoated tool steel, where surface polishing and use of fully formulated forming oil is required, DLC coatings can provide the required tribological properties of the tool as already in the case of base oil (Figs. 4c and 5) and with a reduced need for surface polishing [32,33]. Thus, DLC coatings show a great potential in making environmentally hostile forming lubricants more ecologically acceptable.

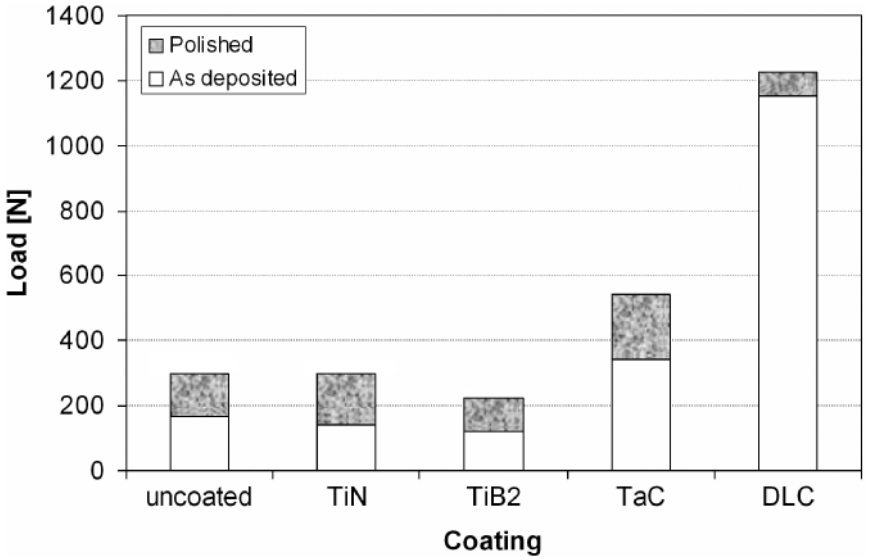

Fig. 5 Critical loads for the beginning of transfer of stainless steel to coated and uncoated cold work tool steel [32]

3 Boundary Lubrication

A vast majority of the machine components are operating under boundary lubrication conditions, where interactions between the lubricant, surrounding oxygen, and contact surfaces determine the tribological behavior of the contact [19,34,35]. In order to prevent metal to metal contact and to reduce friction and wear of the contact surfaces different oil additives are used under boundary lubrication [27,36,37]. From a tribological point of view, friction modifiers, anti-wear (AW) and extreme-pressure (EP) additives are the most important in terms of minimizing friction and wear, and protecting contact surfaces under severe sliding conditions. It is generally accepted and described in detail in the literature that the mechanism through which EP and AW additives reduce the friction and wear of metallic surfaces under boundary lubrication is related to the formation of tribochemical films, generated through tribologically activated reactions between oil additives and the metallic surface [19,35,38–40]. The efficiency of a tribochemical film, or the so-called tribofilm, is highly dependent on its chemical composition. While the AW action of oil additives is due to the formation of phosphates, friction reduction is controlled by the presence of sulfides [35,37–39].

Oil additives were originally developed to work with the uncoated surfaces of metal parts, i.e., typically iron oxides [19]. Now, if the metallic surface is coated by an inert low-friction coating, such as an extensive family of DLC coatings, the surface chemistry will be radically altered. In this way the mechanism of conventional AW and EP additives may be hindered or even prevented, in which case the coating

may even impair the tribological properties of the contact [41,42]. Furthermore, there are many parameters, which influence on the tribological behavior of the coated contact, including coating type and material combination, lubricant composition, contact conditions, etc.

3.1 Coating One or Both Contact Surfaces

In the case of uncoated steel surfaces AW and EP additives improve running-in performance of the contact surfaces by reducing the number of cycles needed for the running-in process to take place (Fig. 6). Furthermore, use of AW and EP additives also results in reduced wear and steady-state friction, as shown in Fig. 7* [37, 43, 44].

Application of DLC coatings on all surfaces in contact (i.e., DLC against DLC) reduces high initial friction, normally experienced in the steel/steel contact, and depending on the contact conditions, coefficient of friction can be even up to 50% lower, when compared to uncoated steel surfaces. However, the running-in process will require more cycles than in the case of steel/steel contact, especially at lower

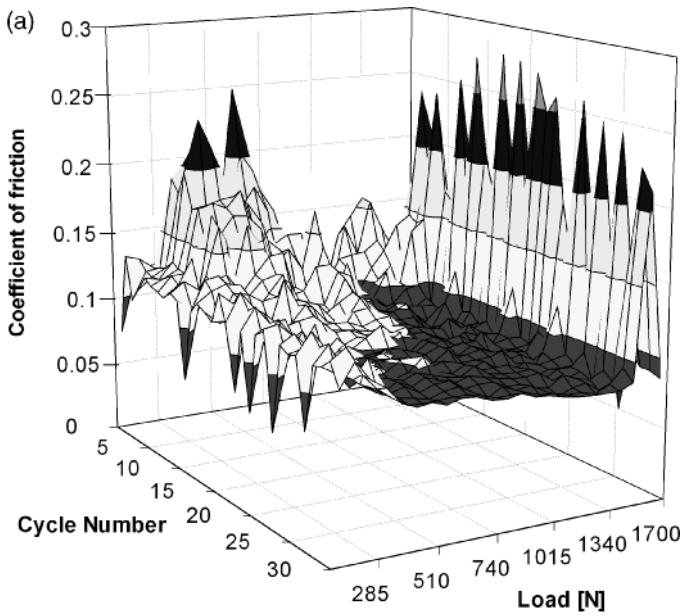

Fig. 6 Friction maps of the running-in sequence for uncoated steel surfaces running in (a) PAO oil, (b) PAO with sulfur-based EP additive and (c) PAO with phosphorous-based AW additive [44]

* Due to measuring software error, coefficient of friction values reported in [43,46 and 47] are too high, with the correction factor being of $\sqrt{2}$

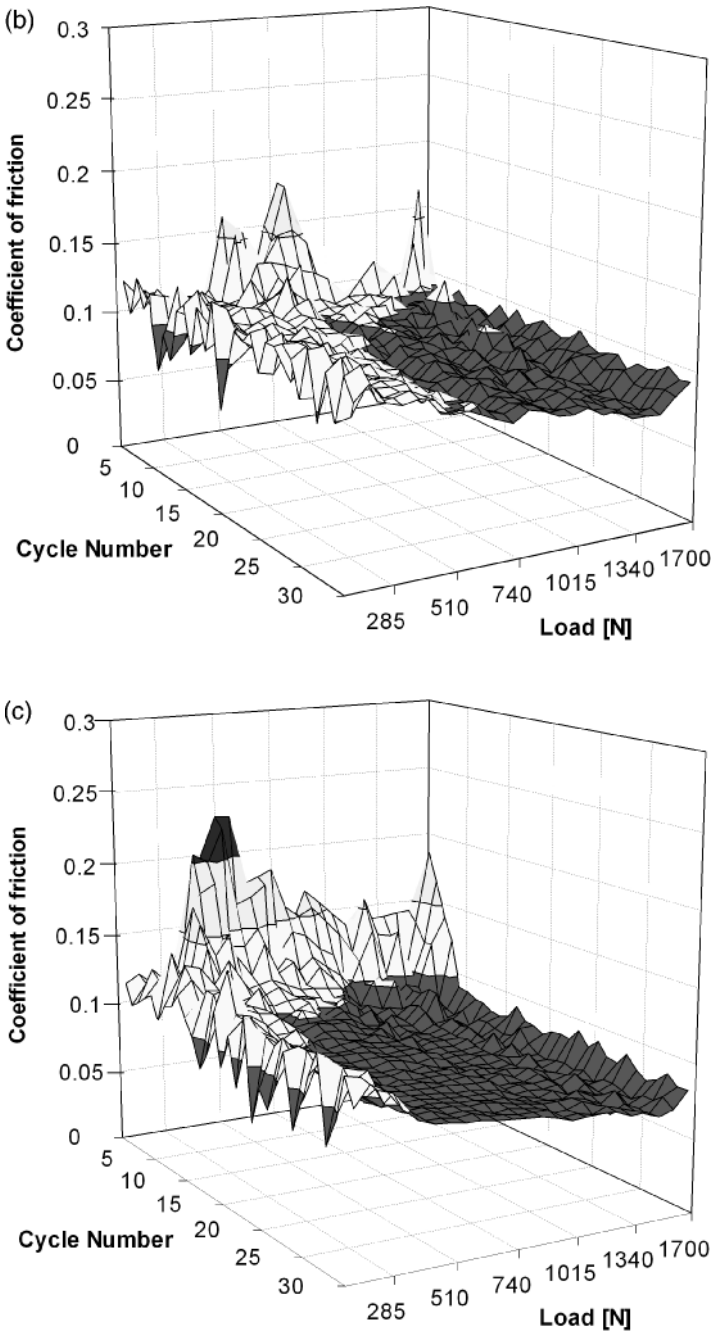

Fig. 6 (continued)

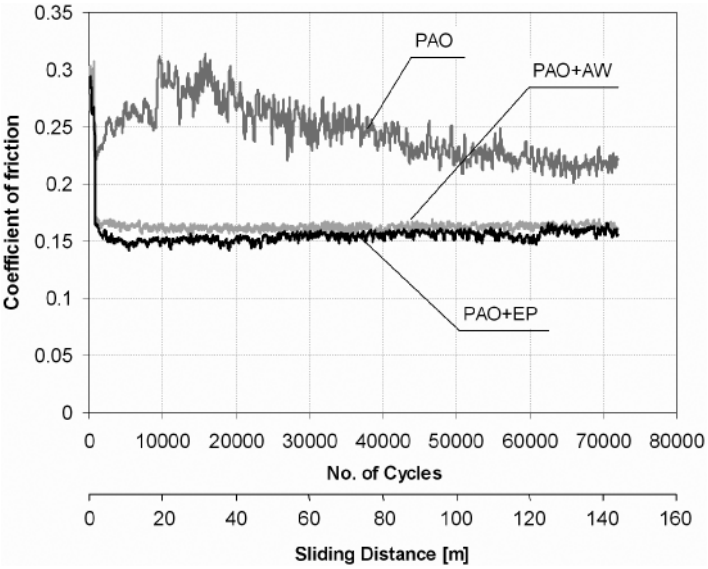

Fig. 7 Coefficient of friction curves for uncoated steel surfaces running under boundary-lubricated sliding conditions (p_H = 1.5 GPa, v_s = 0.02 m/s) [43]

loads, as shown in Fig. 8. In the non-run-in situation, severe asperity contact will occur through the lubricant film. In these contacts, the low-friction properties of the DLC coating help in keeping the friction level low [8,16]. However, due to high hardness, coated surfaces will need more contact cycles to smoothen down and to better accommodate each other. The DLC/DLC contact exhibits the same behavior, with low friction but a long running-in period, regardless of being lubricated with base oil or lubricant containing additives, as exemplified in Fig. 8. Furthermore, after running-in period, the DLC-coated surfaces do not show any discernable evidence of tribochemical layer formation, which would indicate tribologically activated chemical reaction between the oil additives and the coated surfaces [42,43,45–47].

On the other hand pairing of DLC-coated and DLC-uncoated steel surfaces shows the most rapid running-in process (Fig. 9) and the lowest coefficient of friction. As for the DLC/DLC combination, no influence of additives during the running-in period was reported [44]. The detailed mechanism behind this beneficial behavior of the DLC-coated/uncoated combination is not yet fully explored. However, transfer of coating material from coated to uncoated partner [43,46] and smoothening of the steel surface already against the harder coating during the first strokes are two important parts.

When sliding cycles are increased to several hundreds or thousands, the coefficient of friction reaches a steady-state value and the wear of contact surfaces will start. In general, deposition of DLC coatings on one or both contact surfaces gives

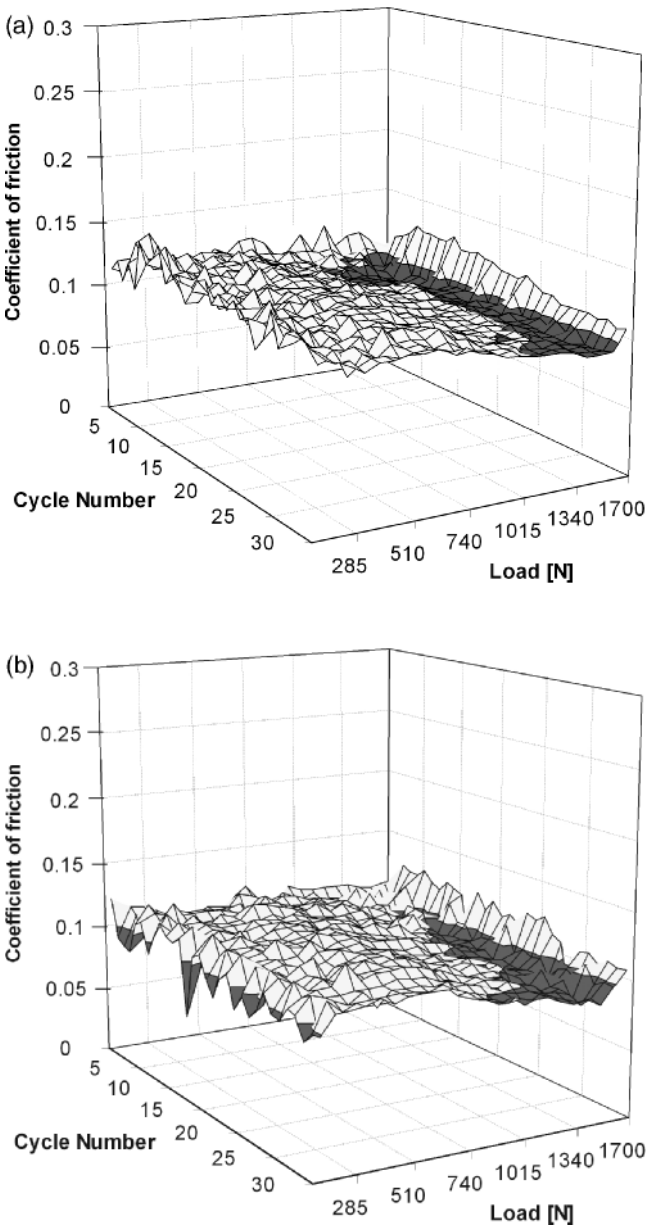

Fig. 8 Friction maps of the running-in sequence for DLC/DLC contact running in (a) PAO oil and (b) PAO with sulfur-based EP additive (DLC coating being of WC/a-C:H type) [44]

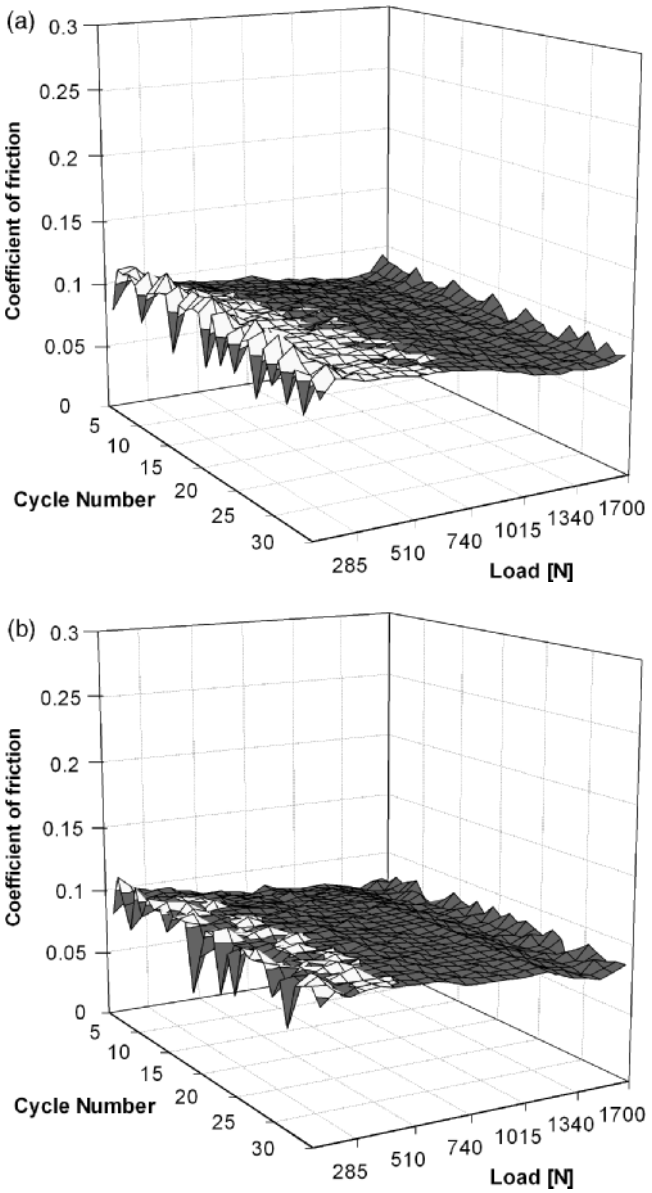

Fig. 9 Friction maps of the running-in sequence for DLC/steel contact running in (a) PAO oil and (b) PAO with sulfur-based EP additive (DLC coating being of WC/a-C:H type) [44]

reduced steady-state friction under boundary lubrication, especially when combining formulated oils and metal-doped DLC coatings running against uncoated steel surface [44,45], as shown in Fig. 10a. Coated/uncoated combinations also show the lowest wear rates, which was found for base as well as for formulated

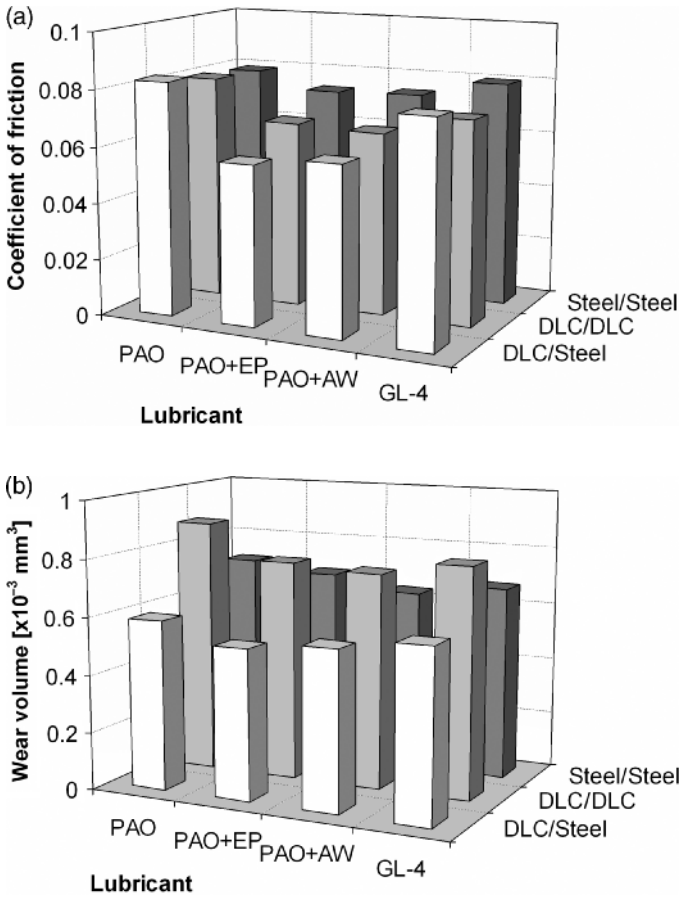

Fig. 10 (a) Steady-state friction and (b) wear volume after 8,000 sliding cycles for different material combinations running-in base and formulated lubricants under condition of boundary lubrication; DLC coating being of WC/a-C:H type ($p_H = 4$ GPa, $v_s = 0.1$ m/s) [45]

oils (Fig. 10b). In general coated partner shows one order of magnitude lower wear than uncoated counter-surface when operating under boundary-lubricated sliding conditions [43,47,48]. However, for certain contact conditions, the DLC-coated and mated uncoated steel surfaces may show similar level of wear [43–45], while for others, DLC coatings can substantially increase wear rate of the counter-surface [49]. On the other hand, combination of both contact surfaces coated with DLC coating will generally lead to the highest level of wear, experienced for base and formulated oils (Fig. 10b). This behavior can probably be explained by the harder surfaces of DLC causing more aggressive wear during the longer running-in process [44,45].

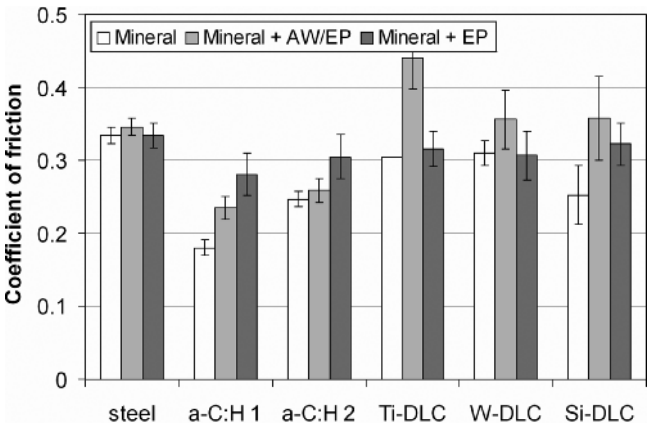

Fig. 11 Influence of coating type on the steady-state friction of boundary-lubricated DLC/DLC contact (p_H = 1 GPa, v_s = 0.1 m/s, T = 80°C) [51]

3.2 Influence of DLC Coating Type

Dry sliding tribological behavior of DLC coatings greatly depends on the coating type (i.e., a-C, ta-C, a-C:H, Me-C:H) and the surrounding atmosphere, especially relative humidity. While hydrogenated DLC coatings show drop in friction with reduced relative humidity, hydrogen-free DLC coatings have the opposite trend [21,22,50]. Also under boundary lubrication, the tribological response of DLC coatings depends on the coating type [43,44,47,48,51], as shown in Fig. 11. When self-mated, friction and wear of lubricated DLC coatings greatly depend on the DLC coating type, with nondoped or pure DLC coatings (a-C, ta-C, a-C:H) showing lower friction and wear than doped DLC coatings. With the presence of additives in the lubricant, a new layer which appears as a soft amorphous layer can be formed on the contact surface for some nondoped DLC coatings, but not for doped ones. However, no evidence of any reaction between additives and DLC coatings for DLC/DLC contact was reported [51]. On the other hand, for some hydrogenated carbon coatings (a-C:H) it was found that Molybdenum dithiocarbamate (MoDTC) and Zinc dithiophosphate (ZDDP) additives can react directly with the DLC surface, forming molybdenum disulfide (MoS_2) sheets and thus further improving friction and wear performance of these contacts [52,53]. Therefore, it is clear that tribological behavior of boundary-lubricated DLC-coated surfaces depends on the combined effect of coating type and lubricant composition, especially when in contact with uncoated steel surface.

In the case of pure DLC coatings running against uncoated steel, smooth running-in, low wear and friction similar to boundary-lubricated steel surfaces (~0.15) are already obtained in pure PAO oil, as shown in Fig. 12. On the other hand, EP and AW additives as well as use of fully formulated oils have very small effect on friction and wear of pure DLC coatings [54], especially at lower additive concentrations

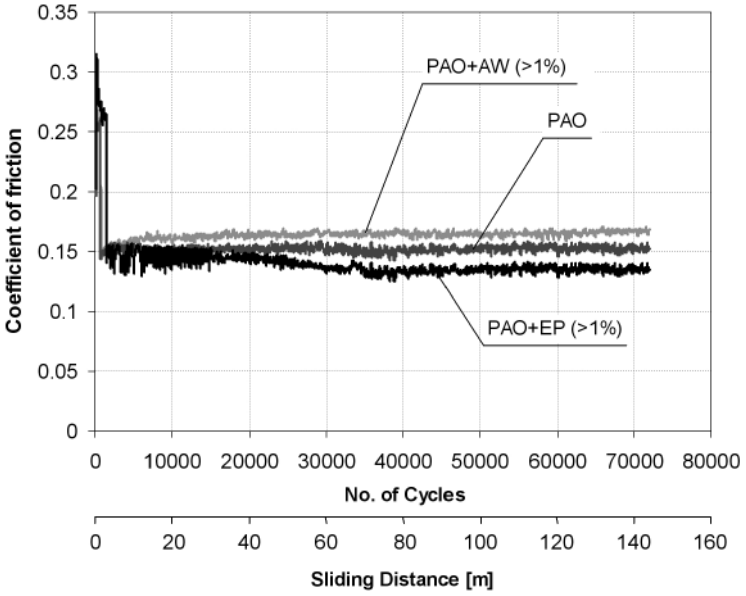

Fig. 12 Coefficient of friction curves for pure DLC coatings running against uncoated steel under boundary lubrication [43]

(Figs. 13 and 14). As in the case of both contact surfaces coated, no evidences of reaction products or tribofilm formation on the DLC-coated surface can be found [12,28,44,45], with a carbon transfer layer, responsible for low-friction behavior and low wear behavior of steel/DLC systems [55] being observed on steel counter-surfaces after sliding. At higher additive concentrations, additives start to react with the steel counter-surface in a similar way as for steel/steel combination [46], thus equalizing friction and wear performance of steel/DLC systems to uncoated steel surfaces [43,46].

Doped DLC coatings also show faster and smoother running-in (Fig. 9), and lower friction and wear as compared to uncoated steel surfaces, but generally give about 2 times higher wear rates than pure DLC coatings, as shown in Figs. 13 and 14. However, additives have a much more pronounced effect on the tribology of doped DLC coatings, especially metal-doped DLC coatings (Me-C:H) [53]. In the case of pure PAO oil, W-doped DLC coatings running against uncoated steel display friction of about 0.15. Friction level remains the same when using low AW additive concentrations, while high AW additive concentrations lead to similar friction values as observed for boundary-lubricated steel/steel contacts. On the other hand, EP additive concentration, greatly affect the tribology of W-doped DLC coatings, with optimum EP additive concentration leading to substantially reduced friction and wear of the contact [46,48].

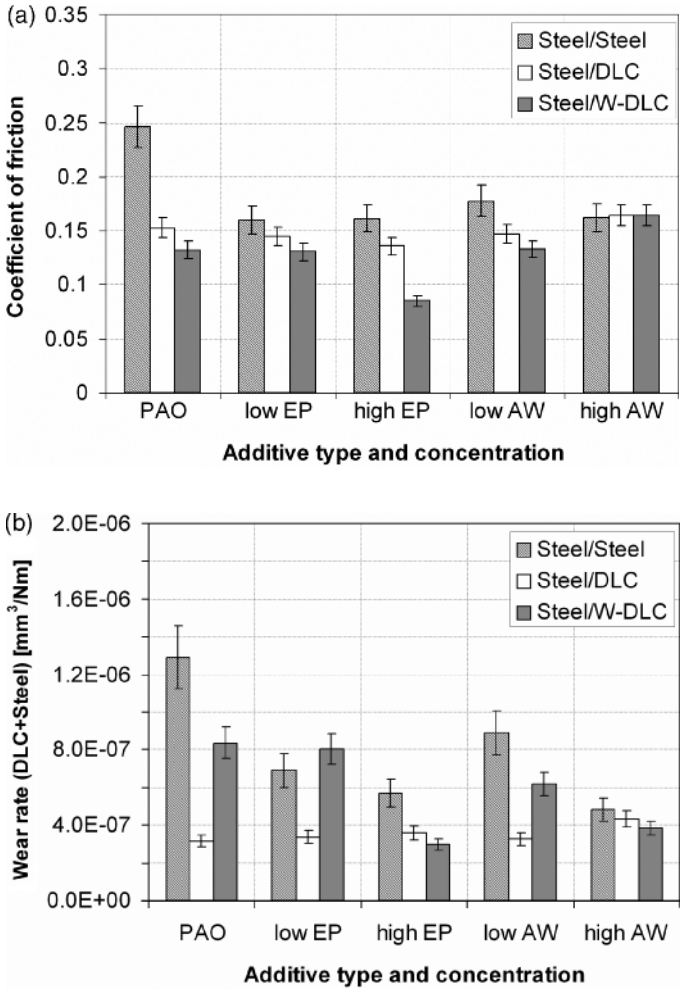

Fig. 13 (a) Steady-state friction and (b) wear rates for pure and W-doped DLC coatings when tested against uncoated steel surface under boundary lubrication, showing influence of additives [43]

In the case of metal-doped DLC coatings doped elements improve the boundary-lubricating effect of DLC coatings, most probably by providing a "metal-like" behavior [51,53]. And for metal-doped DLC coatings, tribofilms, being additive type and concentration-dependant, are normally formed on the steel counter-surface or on the exposed steel substrate, but not on the coating itself [43,44,46,47]. However, as already mentioned, for some Mo-based additives MoS_2 containing layers were also found on the coated surface [12,52,53].

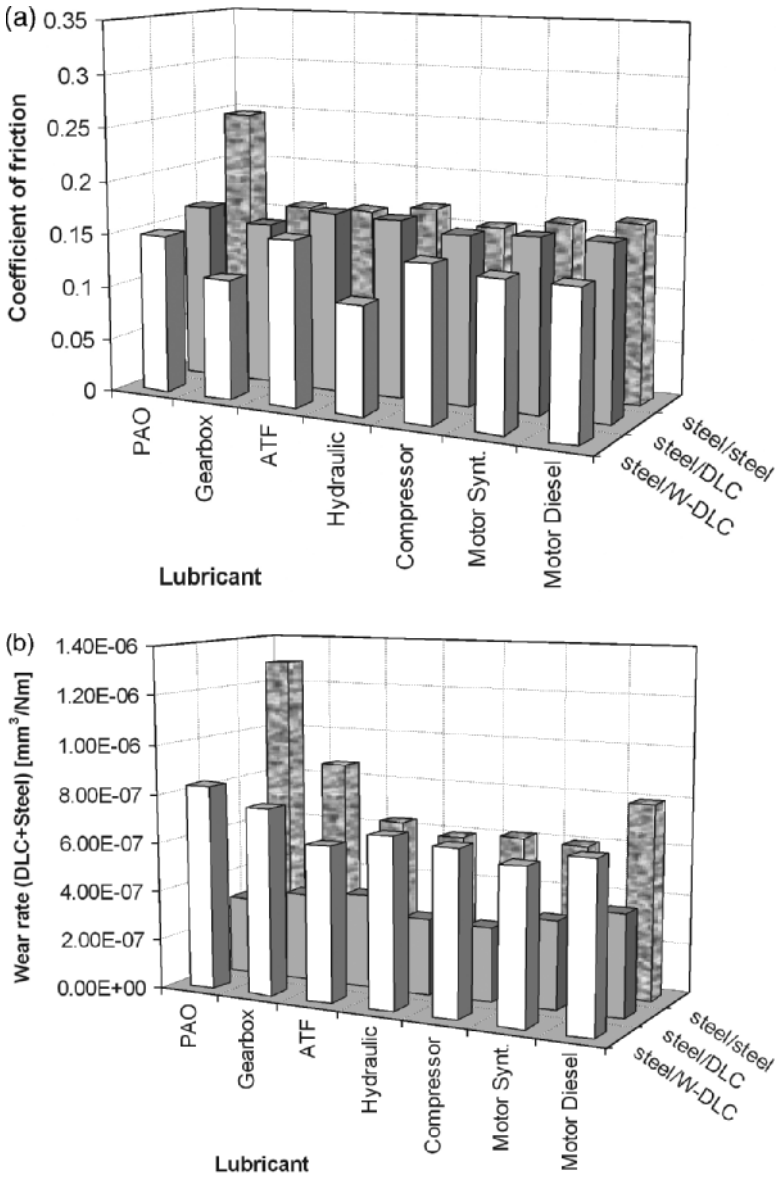

Fig. 14 (a) Steady-state friction and (b) wear rates for pure and W-doped DLC coatings when tested in fully formulated oils against uncoated steel surface under boundary lubrication [48]

When operating in fuels, pure DLC coatings again show superior wear resistance. As compared to steel and metal-doped DLC coatings, pure DLC coatings give not only the best surface protection (Fig. 15), but also relatively stable and low friction, especially for highly evaporating gasoline fuel, as shown in Fig. 16. On the

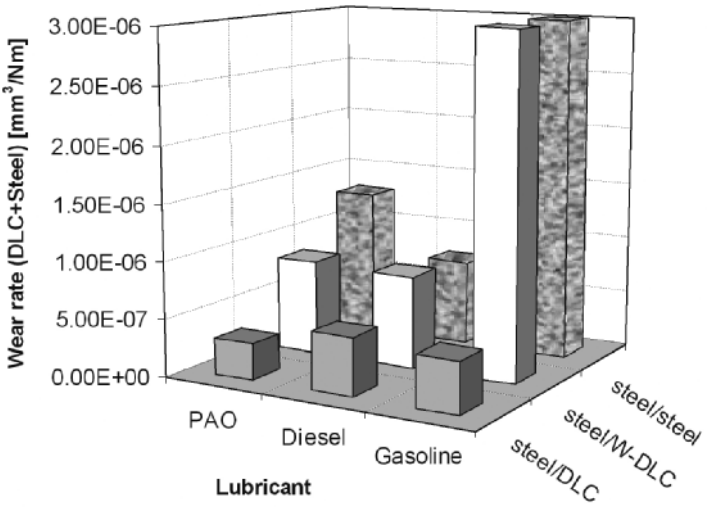

Fig. 15 Wear rates of DLC films when lubricated by fuels

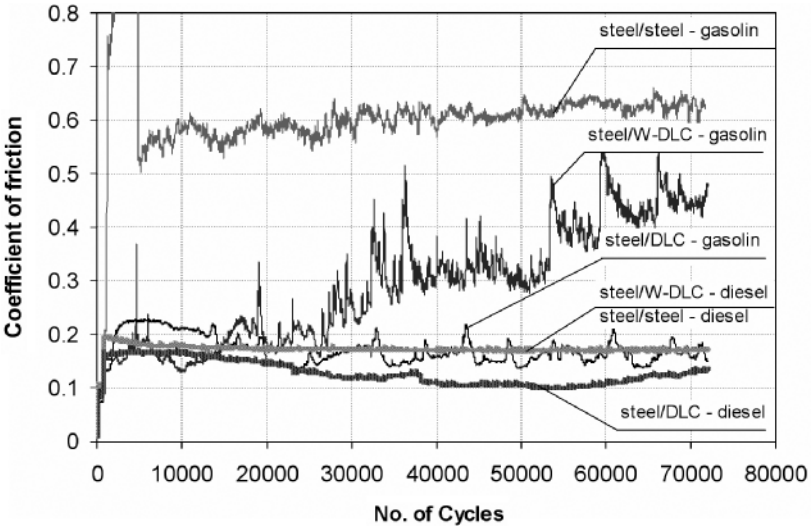

Fig. 16 Friction curves for DLC films when lubricated by fuels

other hand, W-doped DLC coatings show coefficient of friction and wear rates comparable to uncoated steel when operating with diesel fuel, but better surface protection and lower friction for gasoline fuel [48].

3.3 Influence of Additive Type and Concentration

As already described, the tribological behavior of pure DLC coatings is more or less independent of the additive type and concentration, even when operating under boundary lubrication and with fully formulated lubricants (Figs. 13 and 14). However, this is not the case for doped DLC coatings. Under boundary lubrication, friction and wear of doped DLC coatings, especially metal-doped may vary considerably depending on the additive type and concentration used [12,43,46]. Furthermore, large amounts of polar groups and unsaturated fatty acids, available in lubricants like sunflower oil, were found to substantially improve the efficiency of lubrication of inert DLC surfaces [56–57].

Influence of additive type and concentration for the case of W-doped DLC coatings running against steel surface under boundary lubrication is exemplified in Fig. 17, using contact pressure of 1.5 GPa and sliding speed of 0.02 m/s [46]. In the case of pure PAO oil and for very low S-based EP additive concentrations (< 0.01%), the coefficient of friction was found to be in the range between 0.12 and 0.15. Increasing the amount of EP additive to 0.1% resulted in reduction of friction, with the coefficient of friction dropping to a value of about 0.11. After some sliding cycles (15,000 cycles for the selected conditions), the coefficient of friction starts to rise again, shortly reaching values observed for pure PAO oil. Similar reductions in friction in the early stages of sliding were observed for 0.5% and 1% EP additive concentrations. However, after the initial 10,000–15,000 running-in cycles, the coefficient of friction is further reduced, attaining a value below 0.1. Concentrations

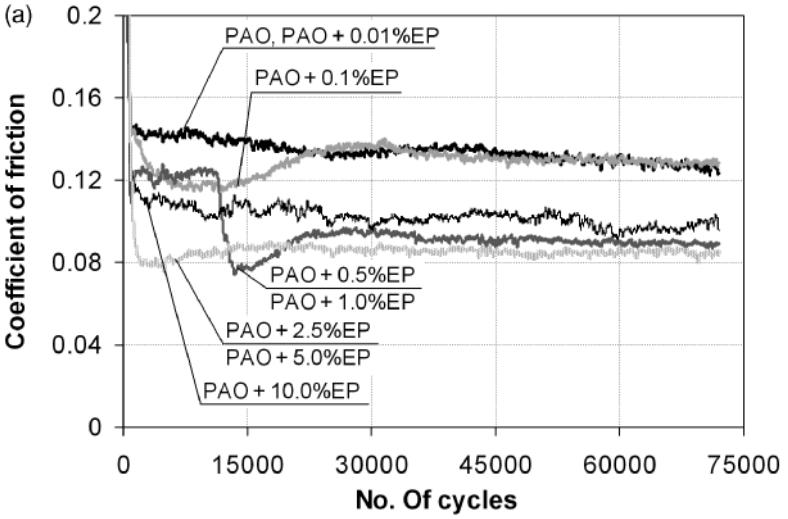

Fig. 17 Influence of (a) sulfurized olefin polysulfide EP additive and (b) diamine monohexyl and amine dihexyl phosphate AW additive on friction of the steel – WC/a-C:H combination (p_H = 1.5 GPa, v_s = 0.02 m/s) [47]

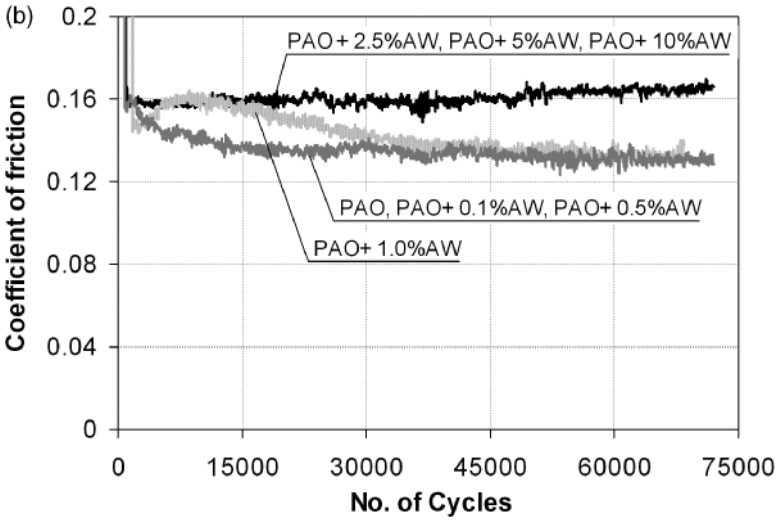

Fig. 17 (continued)

of 2.5% and 5% gave the smoothest and lowest friction coefficient of about 0.08, obtained from the very beginning of sliding and maintained for more than 6.10^6 sliding cycles [46]. Increasing the amount of EP additive over 5% did not result in any further reduction of friction. On the contrary, 10% of EP additive caused an increase in friction, with the coefficient of friction reaching a steady-state value above 0.1, as shown in Fig. 17a.

The influence of the P-based AW additive on frictional behavior of W-DLC coatings running against steel is not so pronounced as for the S-based EP additive. As shown in Fig. 17b AW additive concentrations below 0.5% gave the same friction as pure PAO oil. Increasing the AW additive concentration above 1% led to increase in friction, with the coefficient of friction being in the range between 0.15 and 0.18. However, in the case of 1% AW additive concentration, the coefficient of friction reached a steady-state value of pure PAO oil after some 40,000 cycles, as shown in Fig. 17b.

Similar influence of additives can also be observed when both contact surfaces are coated with W-doped DLC coatings. However, even for optimum additive concentrations certain number of sliding cycles is needed before low-friction behavior is obtained, as shown in Fig. 18. In contrast to coated/uncoated contact combination, no steel surface is accessible until the coating is worn through, if both contact surfaces are coated.

In general, metal-doped DLC coatings show faster response to additives in terms of friction reduction, and to much lower friction and wear of the contact when in particular the concentration of S-based EP additive is increased. At optimum EP additive concentrations, as much as 35% reduction in friction and more than 2 times

lower wear rates, with wear of the DLC-coated surface being almost eliminated, can be expected. However, further increase in EP additive concentration will also results in increased friction and wear rate of contact surfaces, in certain conditions even leading to coating removal [47]. While increase in P-based AW additive also shows reduction in wear when metal-doped DLC coatings are paired with steel counter-surface, friction is continuously increased with increased AW additive concentration until values typical for uncoated steel surfaces are reached (Fig. 19).

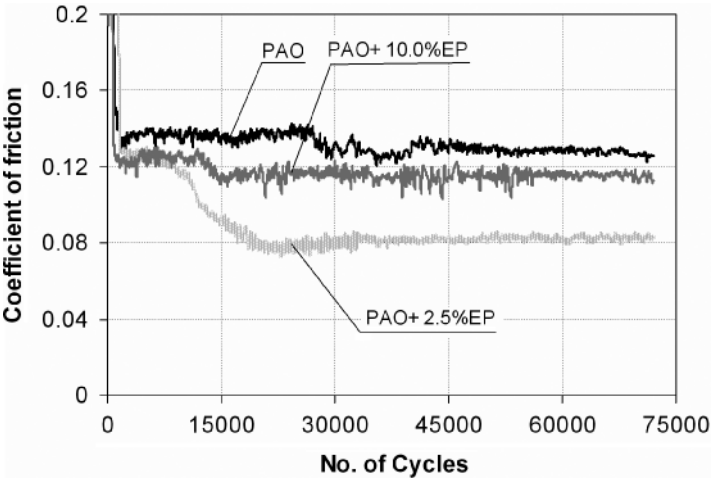

Fig. 18 Influence of S-based EP additive on the coefficient of friction of W-doped DLC coatings when self-mated (p_H = 1.5 GPa, v_s = 0.02 m/s) [47]

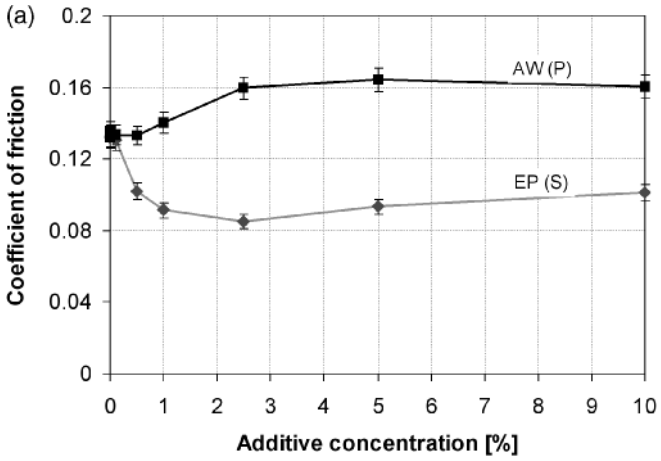

Fig. 19 Influence of additives on the (a) steady-state friction and wear rates of (b) W-doped DLC-coated and (c) uncoated steel surface when operating under boundary lubrication (p_H = 1.5 GPa, v_s = 0.02 m/s) [47]

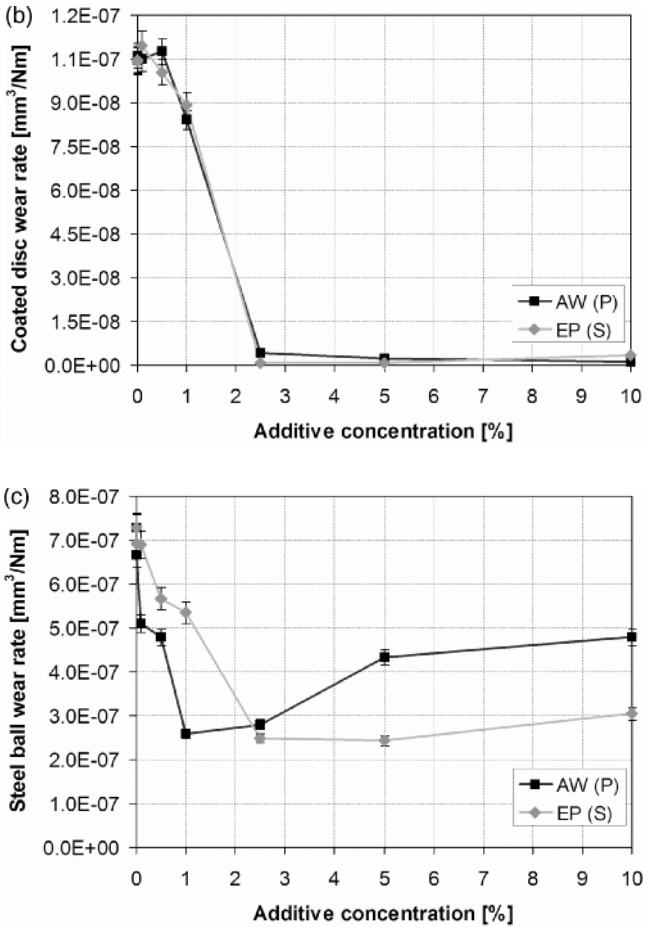

Fig. 19 (continued)

When using MoDTC and ZDDP additives, hydrogenated DLC coatings, being metal-doped or undoped (a-C:H, Me-C:H) show similar friction as observed for uncoated steel surfaces, which was found for DLC/steel and DLC/DLC combinations. Furthermore, as compared to base lubricants, addition of MoDTC and ZDDP additives gives reduced friction and up to 4 times lower wear rates for hydrogenated DLC coatings, especially when self-mated [52]. However, for hydrogen-free DLC coatings (a-C), friction and wear do not change with the presence of MoDTC and ZDDP additives, as already mentioned and shown in Fig. 20.

In formulated lubricants, additives are part of an additive package, whose complicated chemistry and composition are application and contact conditions-dependant. However, for fully formulated lubricants also, the tribological behavior

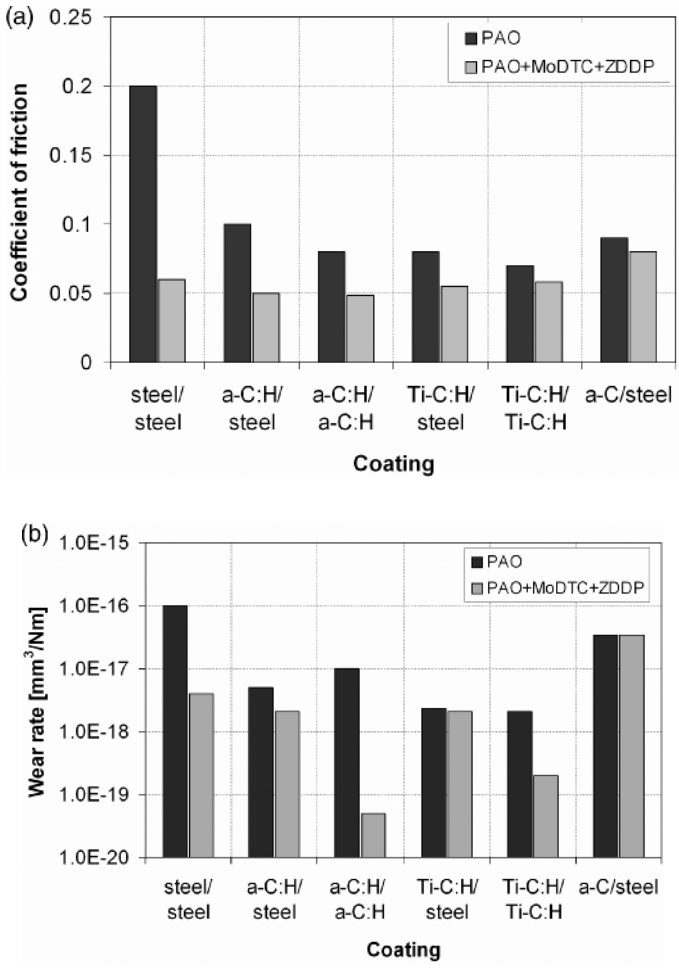

Fig. 20 (a) Steady-state friction and (b) wear rates of different DLC coatings when using MoDTC and ZDDP additives (p_H = 0.6 GPa, v_s = 0.2 m/s, T = 100°C) [52]

of boundary-lubricated metal-doped DLC coatings was found to be additive-dependant [48]. In the case of lubricants with higher amount of additives (i.e., gear-box and hydraulic oils), especially S-based additives, W-doped DLC coatings show faster reduction in friction as well as lower friction, as shown in Fig. 21. However, the reduction in friction is not as pronounced as observed for single additives, with different formulated lubricants also giving similar wear rates (Fig. 14). Hindered effect of additives when used as an additive package can be related to interactions between the additive package constituents, which then reduce the activity toward the coating [28,45].

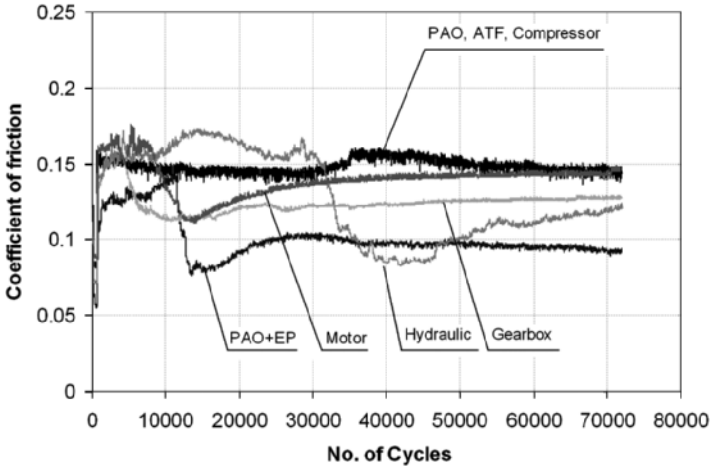

Fig. 21 Friction curves for steel – WC/a-C:H combination when lubricated with fully formulated oils (p_H = 1.5 GPa, v_s = 0.02 m/s) [48]

In the case of uncoated steel surfaces, AW action of additives is primarily due to the formation of poly(thio)phosphates on the contact surfaces and the ability of phosphate glasses to digest iron oxides during tribochemical reaction [58]. On the other hand, friction reduction is controlled by the presence of sulfides [39,40,52,58]. However, in the case of DLC-coated surfaces processes of tribofilm formation can be quite different. For metal-doped DLC coatings, tribofilms normally formed on the steel counter-surface or revealed steel substrate were found to be additive type and concentration-dependant [44,46–48].

Boundary-lubricated sliding in pure or low additive-containing lubricants results in transfer of coating material from coated to uncoated partner, as exemplified in Fig. 22 [44–46]. At increased AW additive concentrations, additive starts to react with the uncoated steel counter-surface, forming the same phosphorus-rich tribofilms and giving the same friction level as observed for the steel/steel combination. For MoDTC additives MoS_2-containing tribofilms, typical for uncoated steel surfaces, can also be found on the coated surface, even when both contact surfaces are coated [52,53]. However, interactions between MoS_2 and carbonaceous surfaces are not yet understood. The same behavior is observed for pure and metal-doped DLC coatings [46,48,52,59]. In the case of S-based EP additives and pure DLC coatings increase in additive concentration also leads to formation of typical iron–sulfur-based tribofilms on the steel counter-surface. However, this is not the case for metal-doped DLC coatings.

For W-doped DLC coatings, transfer of coating material (W and C) from coated to uncoated partner was followed by the formation of a new type of tribofilm, when

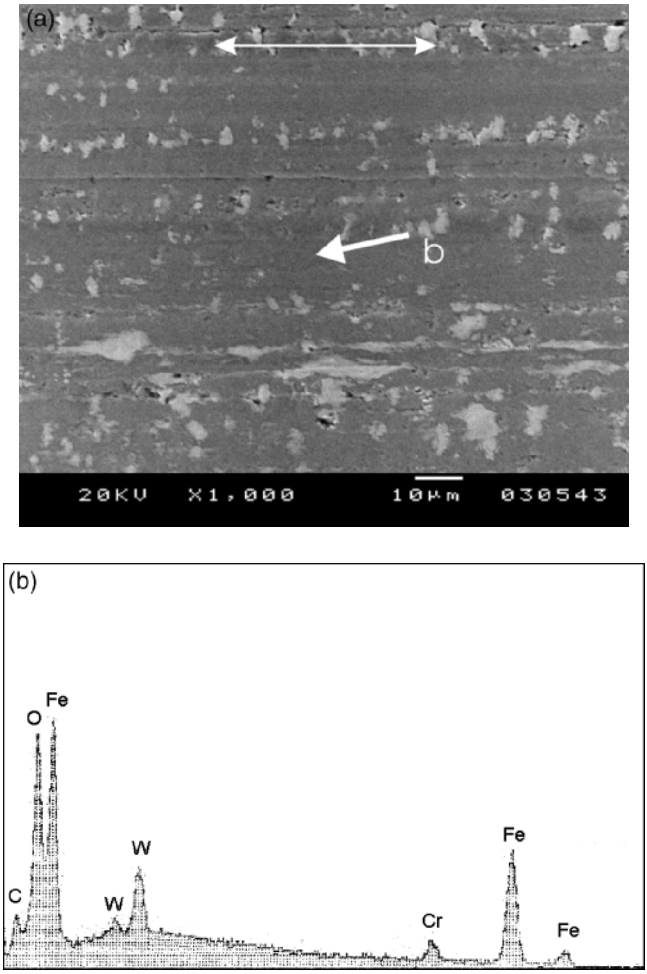

Fig. 22 (a) SEM micrograph and (b) EDS analysis of transfer film formed on the steel surface after sliding against W-doped DLC coating in pure PAO oil [47]

the EP additive concentration exceeded certain value (Fig. 23). Furthermore, formation of tribofilm consisting of transferred coating material (W and C) and reaction products from the additive (S) was found to coincide with the drop in friction [45,46]. However, for the low additive concentrations, of about 0.1% for a contact pressure of 1.5 GPa and a sliding speed of 0.02 m/s, W–S-type tribofilm and low friction can be maintained only for a short period of time (Fig. 18). On the other hand, for 0.5% and 1.0% EP additive concentrations an increase in the number of sliding cycles was found to lead to further reduction in friction, as shown in Fig. 18. Auger Electron Spectroscopy (AES) spectra of the tribofilms formed on the steel counter-surface in the region of high and low friction are shown in Fig. 24. At the

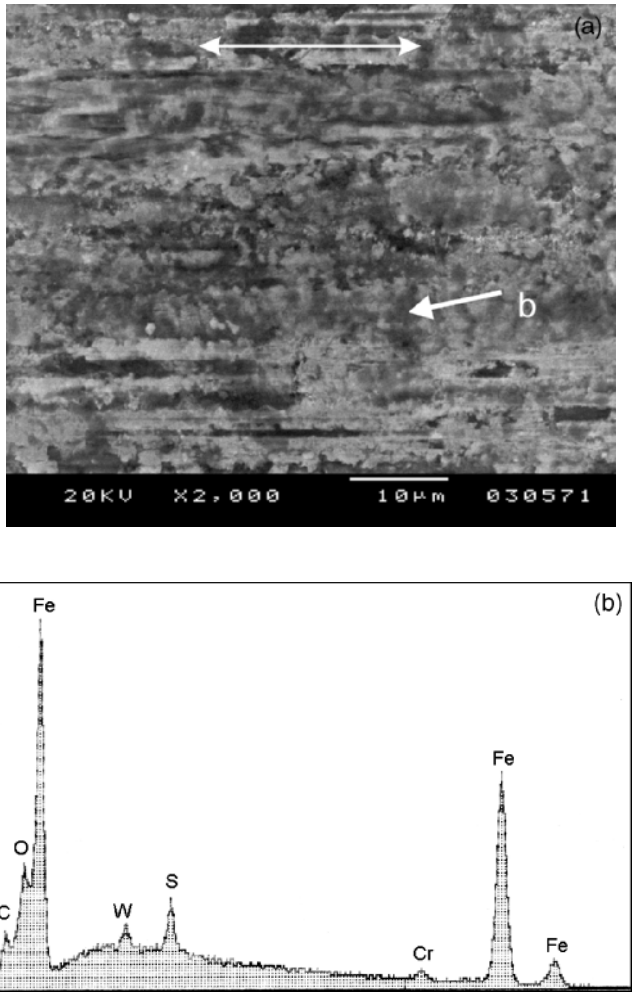

Fig. 23 (a) SEM micrograph and (b) EDS analysis of transfer film formed on the steel surface after 10,000 sliding cycles against W-doped DLC coating in PAO oil with 0.5% S-based EP additive [47]

beginning of sliding, AES analysis confirms the presence of oxygen, carbon, tungsten, sulfur, and iron in the tribofilm (Fig. 24a). Detailed analysis of the tribofilm revealed that it consists mostly of transferred W and C, with sulfur compounds being formed locally at the surface (light areas on Fig. 23a). At the end of the test, an approximately 15–20-nm thick reactive tribofilm showing more or less the W–S-type structure can be observed (Fig. 24b), which is also found in the case of fully formulated oils with higher amount of S-based additives [48]. The same but denser W–S-type tribofilms (Fig. 25), with their thickness increased up to 300 nm, are formed when using optimum EP additive concentrations (2.5% and 5% for the

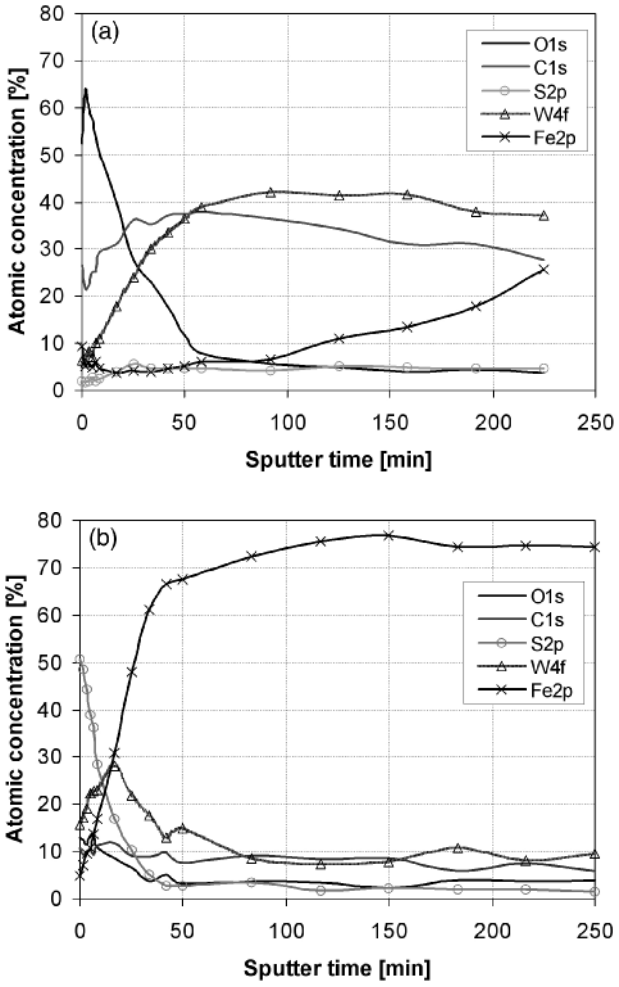

Fig. 24 AES spectra of the steel surface when sliding against W-doped DLC coating in PAO oil containing 0.5% S-based EP additive; (a) region of higher friction and (b) of low friction [47]

presented example), which give the most favorable tribological properties (Fig. 19). However, too high concentrations of the EP additive give increased friction and wear, with the tribofilms formed on the steel counter-surface showing the same iron–sulfur-rich composition, as normally observed for the steel/steel combination [46].

X-ray photoelectron spectroscopy (XPS) analysis of tribofilms formed in the area of low friction (0.08) when using W-doped DLC coatings and S-based EP additives indicates the presence of WS_2 compounds on the steel counter-surfaces (Fig. 26). The broad peak of S_{2p} from 160.5 to 165 eV is attributed to

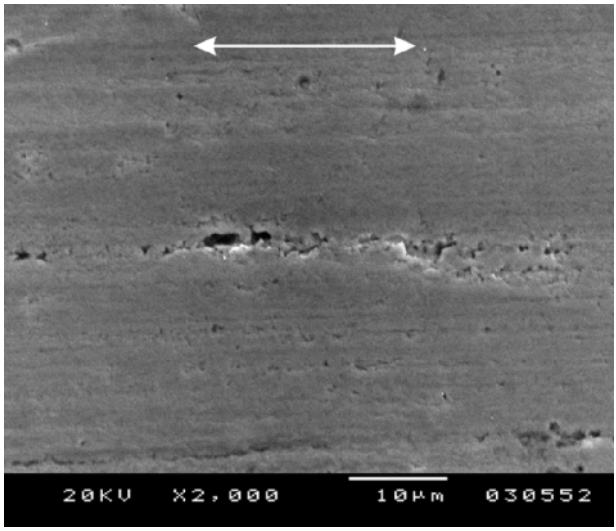

Fig. 25 SEM micrograph of transfer film formed on the steel surface after sliding against W-doped DLC coating in PAO oil containing 2.5% S-based EP additive [47]

FeS (161.4 eV), FeS_2 (162–163 eV) and WS_2 (162.4–163.6 eV) [60]. The existence of WS_2 can be mutually supported by the spectrum of W_{4f}, showing a peak at 32.6–34.8 eV.

The mechanism by which MoDTC reduces friction of boundary-lubricated steel surfaces, as well as hydrogenated DLC coatings [52, 53] is attributed to the formation of MoS_2. MoS_2 is generated in situ by the friction process, where even 2D crystal arrangements reduce friction [61, 62]. Molybdenum (Mo) and tungsten (W) have very similar atomic radii. Furthermore, both disulfides (MoS_2 and WS_2) show trigonal prism geometry [63], which has been recognized as fundamental for the low shear strength and efficient solid lubrication of MoS_2 [64]. WS_2, on the other hand, has also been recognized by Voevodin et al. [65] as a potential friction-reducing agent in solid lubrication coatings. Therefore, it can be concluded that, in combination with a S-based EP additive, tungsten transferred from the W-doped DLC coating to the steel counter-surface during sliding may form tribofilms containing WS_2 nanocrystals, which are similar and possess similar low-friction properties as MoS_2-containing tribofilms [46,60,65]. The tungsten transferred from the W-doped DLC coating can be in two forms: nanocrystaline elemental tungsten and tungsten carbide (WC). The reaction mechanism of both tungsten species to form WS_2 can be explained by Density Functional Theory (DFT) and the Hard-Soft Acid-Base Principle (HSAB) developed by Pearson and Parr [66]. Applying the HSAB principle for elemental tungsten nanocrystalites, with W(0) being a soft acid and sulfide a softer base than species containing oxygen (O_2), formation of WS_2 or even up to $WS_{x\,(x>2)}$ structures will prevail over WO_3. The reaction mechanism of other tungsten species in the form of WC material is not easily explained.

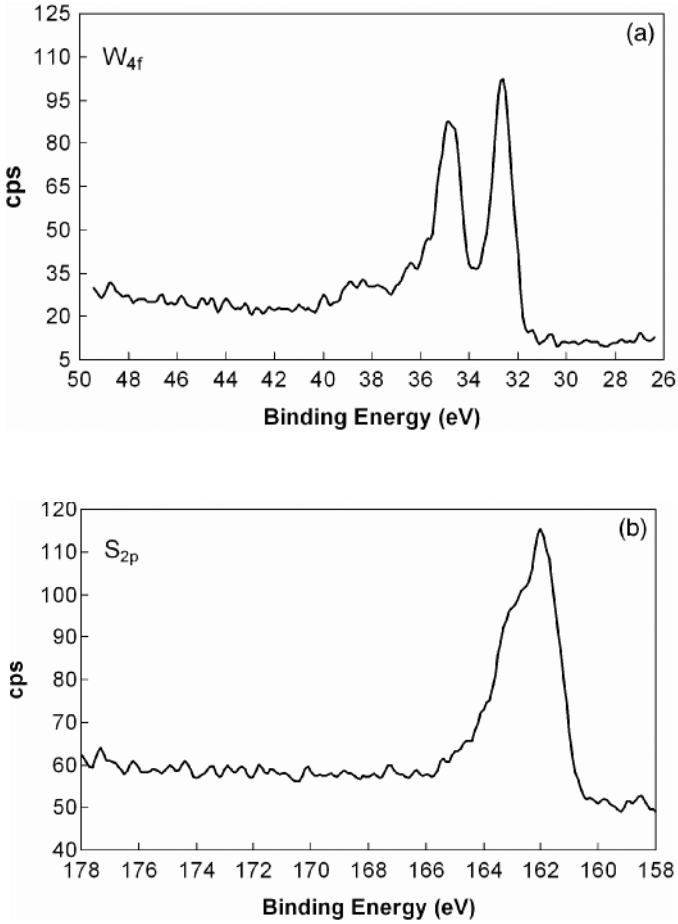

Fig. 26 XPS spectra of (a) W_{4f} and (b) S_{2p} for the tribofilm formed on the steel surface after sliding against W-doped DLC coating in PAO containing 0.5% S-based EP additive [47]

However, if during sliding tungsten carbides are ground to very small particles the high surface/volume ratio would favor the kinetic effect of sulfide formation over the thermodynamic stability of the carbide structure [46]. Therefore, in order to maintain WS_2-containing low-friction tribofilm, which only forms on the steel surface, supply of transferred coating material (W) and sulfur from the single additive or additive package in fully formulated oil [48] is required. Once the coating is worn off or if additive is consumed, the supply to the tribofilm is cut. This leads to the removal of the tribofilm and a climbing of friction, which reaches values typical for steel/steel contact or nonadditivated lubricants [47,48,59].

3.4 Influence of Contact Conditions

Depending on the application, contact surfaces are exposed to diverse contact conditions, which also determine the lubrication regime under which contact surfaces operate. And especially under boundary lubrication change in contact conditions, including contact pressure, sliding speed and temperature can have a considerable influence on the tribological behavior of contact surfaces, being metallic or DLC coated.

3.4.1 Contact Pressure

Influence of contact pressure on the coefficient of friction and wear rate for W-doped DLC coating running against uncoated steel in PAO oil with 1% S-based EP additive is shown in Fig. 27. In the case of a contact pressure of 1 GPa drop in friction during first 5,000 cycles was followed by an increase in the coefficient of friction, which reached steady-state value comparable to boundary-lubricated steel surfaces after about 15,000 cycles (Fig. 27a). Increase in contact pressure leads to change in friction behavior and increased wear rates of the coated contact. For a contact pressure of 1.5 GPa initial friction of about 0.13 was followed by additional drop below 0.1, which is similar to one caused by an increase in EP additive concentration (Fig. 18). Further increase in contact pressure gives similar tribological behavior, with low friction being obtained in shorter time. At the same time influence of additive concentration will escalate with increased contact pressure [47,59]. Higher contact pressure corresponds to higher frictional energy, which in the case of W-doped DLC

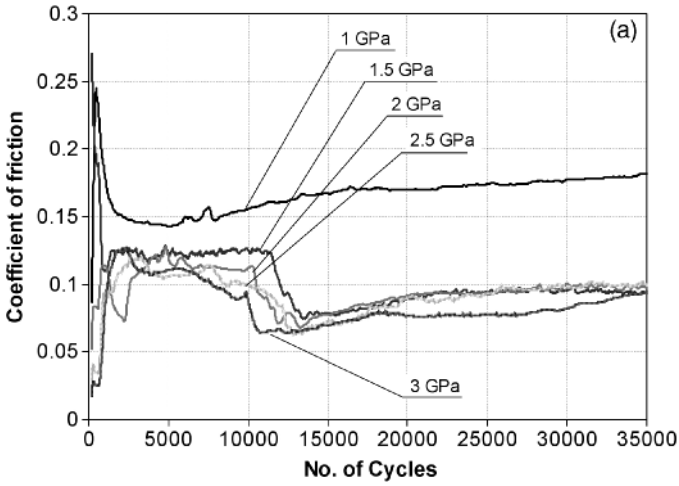

Fig. 27 Influence of contact pressure on (a) friction behavior, and (b) steady-state friction and wear rate of steel/W-doped DLC combination running in PAO oil with 1% S-based EP additive concentration (v_s = 0.02 m/s, T = 50°C)

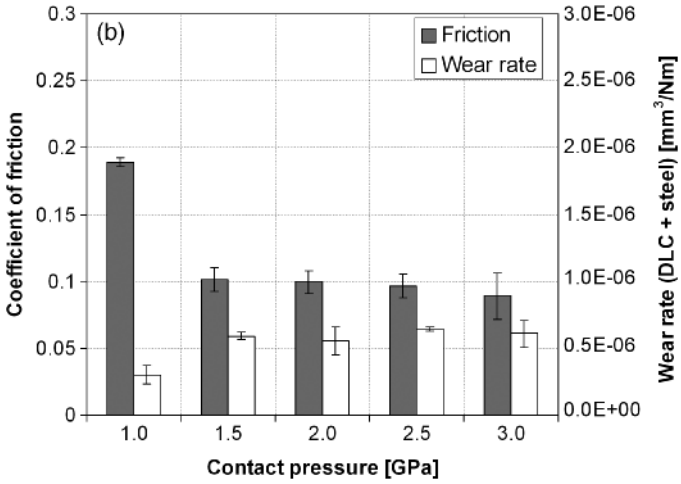

Fig. 27 (continued)

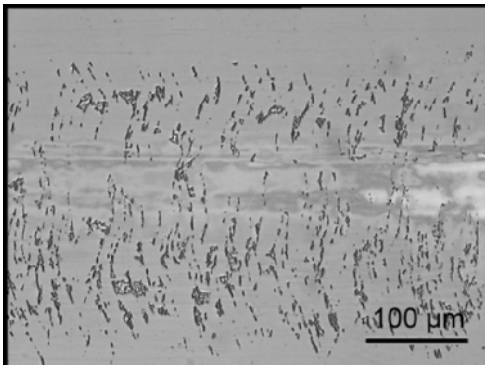

Fig. 28 Example of the coating failure when contact pressure exceeds load-carrying capacity of the system

coatings means higher potential for WS_2-containing tribofilm formation. However, if contact pressure exceeds load-carrying capacity of the coated surface, instantaneous failure of the coating in the form of cracking and spallation will occur (Fig. 28).

3.4.2 Sliding Speed

In contrast to contact pressure, increase in sliding speed results in increased steady-state friction and reduced wear rate of W-doped DLD coatings when running against uncoated steel in oils containing EP additives (Fig. 29). For contact pressure

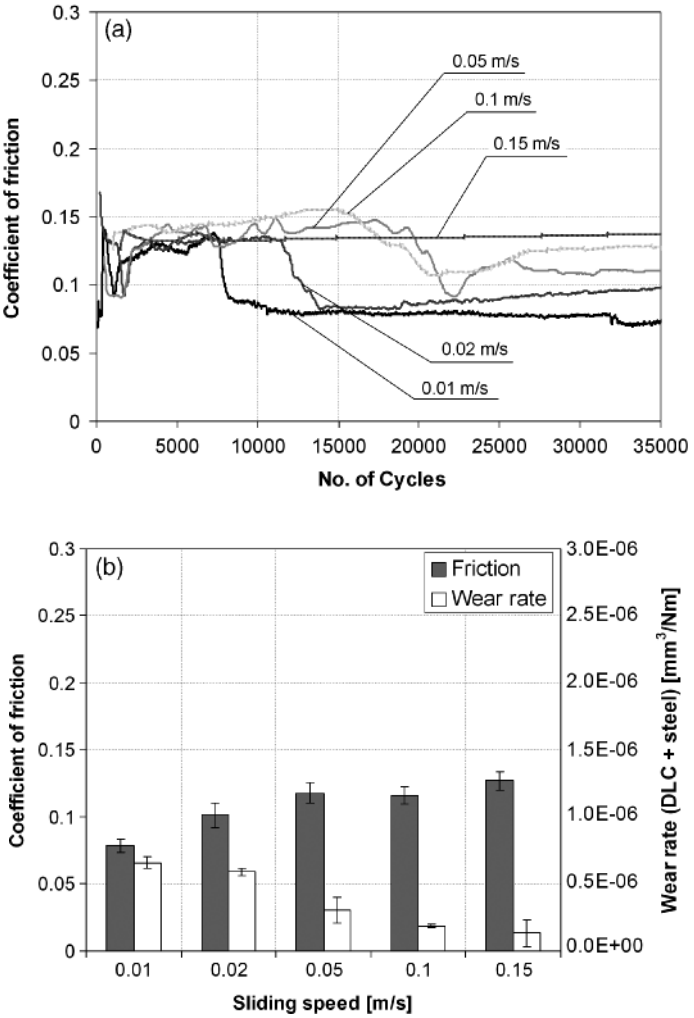

Fig. 29 Influence of sliding speed on (a) friction behavior and (b) steady-state friction and wear rate of steel/W-doped DLC combination running in PAO oil with 1% S-based EP additive concentration (p_H = 1.5 GPa, T = 50°C)

of 1.5 GPa and 1% S-based additive concentration, increase in sliding speed from 0.01 to 0.1 m/s, obtained by increasing frequency under reciprocating sliding, resulted in increased number of cycles needed for the coefficient of friction to reach low level (<0.1), as shown in Fig. 29. Furthermore, while for sliding speeds of up to 0.1 m/s distinctive drop in friction and presence of WS_2-containing tribofilms is reported whereas this is not the case for higher sliding speeds [67]. High sliding speeds (≥0.15 m/s) show friction level similar to pure PAO oil (Fig. 18) and no evidences of WS_2-type tribofilm formation. Compared to contact pressure, change in

sliding speed gives the opposite tribological response of W-doped DLC coatings when operating with S-based additives under boundary lubrication. Higher sliding speeds mean higher frequencies and increased possibility for effective removal of generated frictional heat, thus requiring larger number of sliding cycles before conditions for WS_2-tribofilm formation are reached.

3.4.3 Operating Temperature

With a change in contact pressure and sliding speed, operating temperature of boundary-lubricated contact surfaces will also change. Therefore, depending on the application, operating temperature can vary from room temperature to temperatures exceeding stability limit of the lubricant or the DLC coating. In general, coating of surfaces with DLC reduces contact temperatures [54]. However, when coated, surfaces will be exposed to different operating temperatures, which can change their tribological behavior, especially when using formulated oils [43]. In the case of pure DLC coatings, operating temperatures of up to 200°C have no influence on the friction and wear, neither for base nor for formulated lubricants, as shown in Fig. 30 [43]. Only when temperature exceeds 200°C, DLC coatings start to show signs of decomposition [43,68], which can lead to reduced friction but also to increased coating wear rate [43,69]. On the other hand, tribological behavior of metal-doped DLC coatings is much more dependant on the operating temperature.

Influence of operating temperature on the tribological behavior of boundary-lubricated W-doped DLC coatings is shown in Fig. 31. For pure PAO oil, the coefficient of friction and wear rates are almost independent of the operating temperature

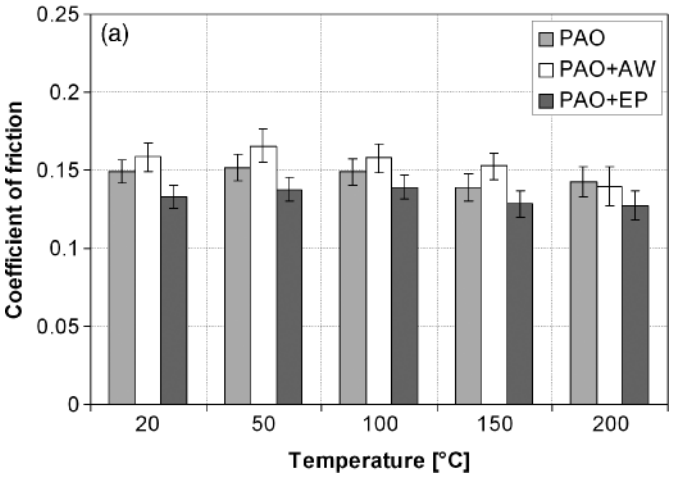

Fig. 30 Influence of operating temperature on (a) steady-state friction and (b) wear rate of undoped DLC coatings running against uncoated steel (p_H = 1.5 GPa, v_s = 0.02 m/s) [43]

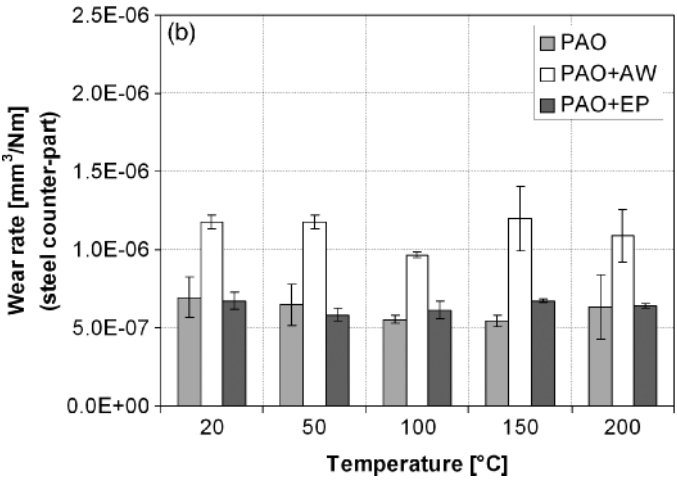

Fig. 30 (continued)

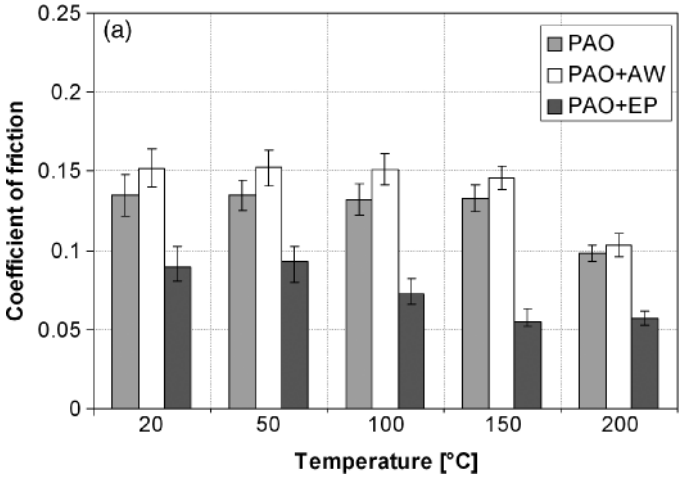

Fig. 31 Influence of operating temperature on (a) steady-state friction and (b) wear rate of steel/W-doped DLC combination (p_H = 1.5 GPa, v_s = 0.02 m/s) [43]

up to 200°C, similarly as observed for pure DLC coatings. The same behavior can also be observed when using PAO oil with P-based AW additives [43]. However, in the case of S-based EP additives increase in temperature was found to have similar effect on friction and wear of W-doped DLC coatings as increase in EP additive concentration (Fig. 18), with temperatures above 100°C giving up to 40% reduction in friction (Fig. 31). As shown in Fig. 32, increase in temperature also results in reduced number of cycles when drop in friction to values as low as 0.05 occurs. Surface analyses of tribofilms formed on the uncoated steel surfaces tested against

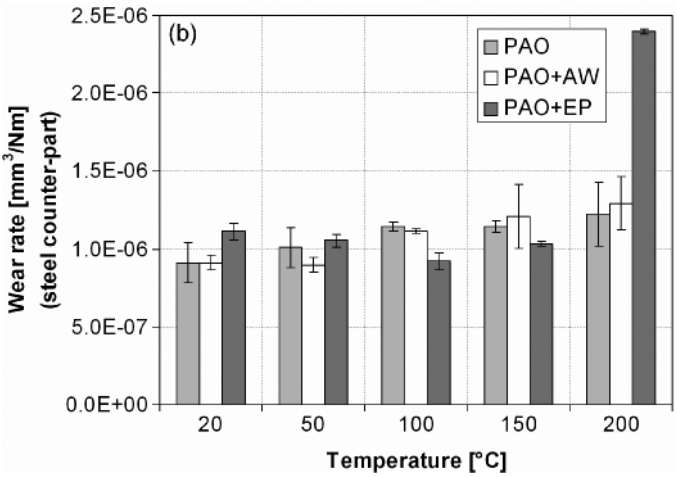

Fig. 31 (continued)

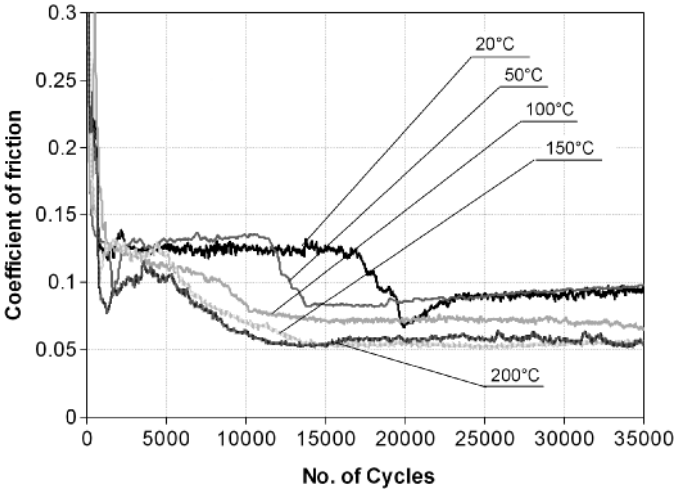

Fig. 32 Influence of operating temperature on friction behavior of W-doped DLC coating when running against uncoated steel in PAO oil with 1% S-based EP additive (p_H = 1.5 GPa, v_s = 0.02 m/s) [43]

W-doped DLC coatings at elevated temperatures showed similar WS_2-containing tribofilms as observed for boundary lubrication at room temperature. However, tribofilms formed at increased temperatures display higher sulfur content as shown in Fig. 33. Higher temperatures accelerate W–S reaction kinetics and increase activation energy [70], thus providing conditions for faster tribofilm formation and more pronounced response in terms of friction reduction.

4 EHD Lubrication

From the friction-and-wear point of view, the most critical conditions occur under boundary lubrication, which is also the region where the majority of surface failures originate. On the other hand, EHD-lubricated or HD-lubricated components will not show any signs of surface failure if properly designed and lubricated. Therefore, the main question when switching to DLC-coated surfaces is, do the DLC coatings provide the same conditions for EHD or HD film formation as uncoated steel surfaces.

Change of lubrication regime from boundary to EHD lubrication, caused by surface smoothening is exemplified in Fig. 34 [28]. For uncoated steel surfaces running in base PAO oil at a contact pressure of 1 GPa and sliding speed of 0.15 m/s, EHD conditions with the coefficient of friction of about 0.04 were obtained after about 1,500 m of sliding. As already described in Section 3.1 (Coating one or both contact

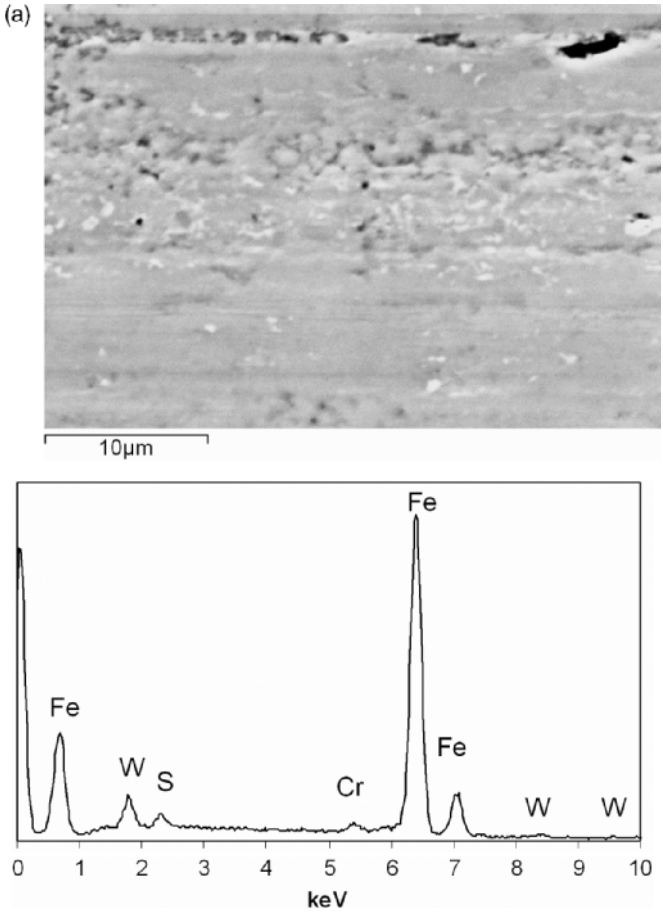

Fig. 33 SEM micrographs and corresponding EDS spectra of the steel counter-surface tested against W-doped DLC coating at (a) 20°C and (b) 150°C (p_H = 1.5 GPa, v_s = 0.02 m/s, PAO + 1%EP)

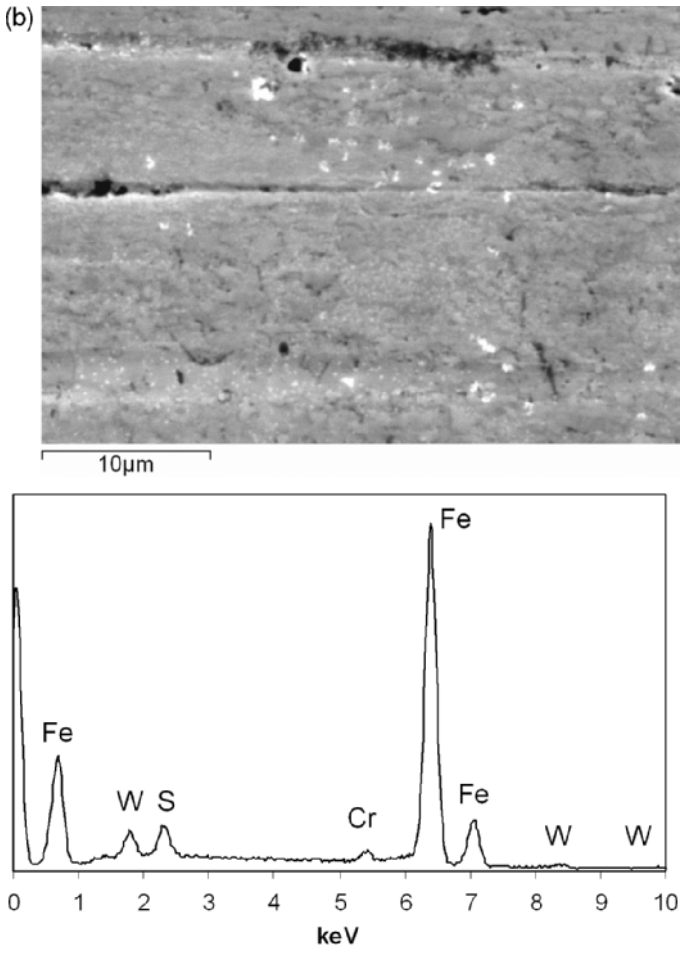

Fig. 33 (continued)

surfaces), DLC/steel combinations give faster running-in, with EHD conditions and the same level of friction reached after only 500 m of sliding (Fig. 34). However, when both contact surfaces are DLC-coated friction is up to 2 times higher as in the case when at least one contact surface is uncoated, and no transition from boundary to EHD lubrication regime can be observed (Fig. 34). Even when EP-formulated and AW-formulated lubricants are used, steel/steel and steel/DLC combinations show similar friction under EHD lubrication, while coating of both contact surfaces results in much higher friction, as shown in Fig. 35.

It is evident [28] that DLC coatings, not even metal-doped, do not provide the same conditions for EHD film formation as uncoated steel surfaces. In order to obtain an adequate EHD or HD film one of the contact surfaces have to be uncoated, which at the same time results in faster running-in and faster transition from boundary to EHD lubrication regime.

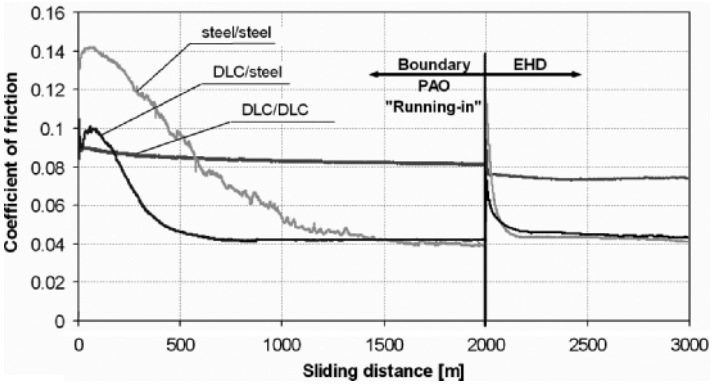

Fig. 34 Change from boundary to EHD lubrication regime for DLC-coated surfaces; DLC coating being of WC/a-C:H type [28]

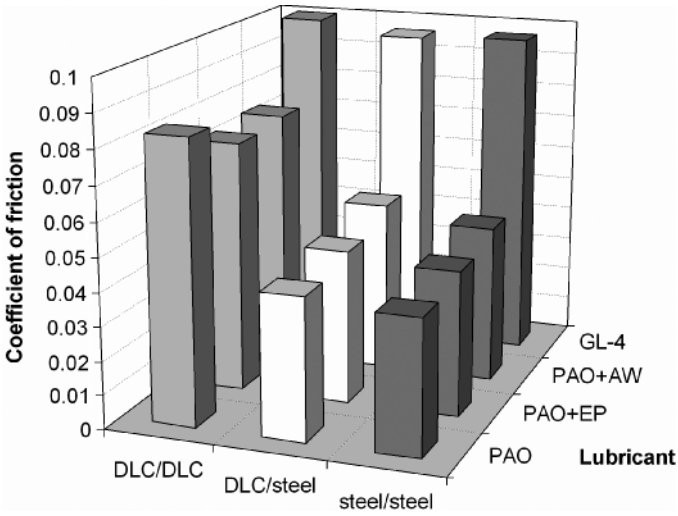

Fig. 35 Average coefficient of friction for EHD-lubricated contacts; DLC coating being of WC/a-C:H type [28]

5 Concluding Remarks

Possible improvements in the tribology of lubricated contacts due to DLC coating application are summarized in Fig. 36. This is a modified Striebeck diagram in which one can see the extent of improvements in different lubrication regimes. Obviously, the DLC-coated surfaces are more effective in lowering friction under starved and boundary-lubricated sliding conditions. They can also ensure a faster and smoother transition form boundary to EHD lubrication regime.

In general, DLC coatings give better friction and wear properties than uncoated steel surfaces under dry as well as lubricated sliding conditions. In the case of highly evaporating fluids, complete loss of lubricant, or lubricating system malfunction, DLC coatings provide improved protection against material transfer and failure of contact surfaces over a broad range of loads, speeds, and temperatures, extending the lifetime of the components for up to 5 times. Furthermore, deposition of DLC coatings reduce a relatively high initial coefficient of friction of boundary-lubricated steel surfaces, with DLC/steel contact leading to a more favorable and smoother running-in process and low friction obtained from the very beginning of sliding. On the other hand, for the contact of two DLC-coated surfaces running-in process seems to take long before steady-state conditions are reached, most probably due to a contact between two hard rough surfaces, which require longer time to accommodate to each other. Improved tribological properties of boundary-lubricated surfaces, obtained with DLC/steel combination can be explained by a faster and more efficient smoothening of the steel counter-surface and the inherent low-friction nature of the coating material transferred from the coated to the uncoated part.

Under boundary-lubricated sliding conditions involving a DLC and a steel counterface, contact is primarily governed by the transfer of coating material from coated to uncoated surface, which results in reduced friction. For pure DLC coatings, which show superior wear resistance, tribological behavior under boundary lubrication is more or less independent of the lubricant and additive type and concentration used. The exception is MoDTC additive which generates MoS_2 sheets and reduced friction of hydrogenated DLC coatings. However, in

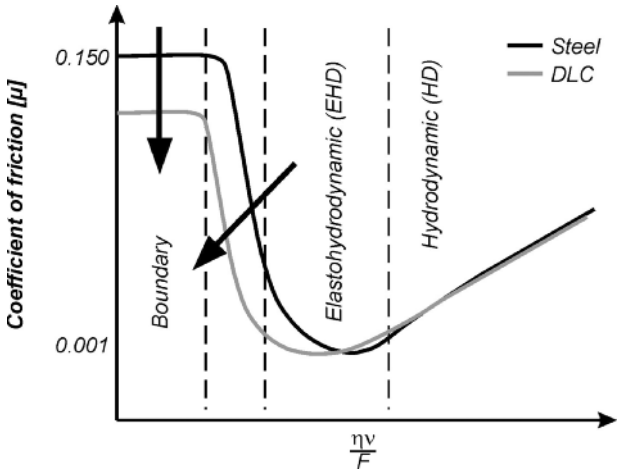

Fig. 36 Possible improvements in the tribology of lubricated contacts obtained by DLC coating application [71]

the case of metal-doped DLC coatings, tribological behavior can change quite significantly depending on the additive type and concentration, especially when single additives are used. For base or low levels of additive-containing lubricants, the frictional behavior of metal-doped DLC coatings is determined by the transfer of coating material to the uncoated steel counter-surface or exposed steel substrate. In the presence of S-based additives transferred coating material will start to react with the additive components, forming a new type of tribofilm, which in the case of W-doped DLC coatings consists of WS_2 nanocrystals. Depending on the additive concentration, WS_2-containing tribofilm, with similar tribological properties as MoS_2, will grow in thickness, thus providing conditions for further reduction in friction and wear. Increase in S-based additive concentration gives faster response not only in terms of friction reduction and lower friction, but also increased coating-removal rate, which escalates with increased load. Low concentrations, on the other hand, not only mean longer response times but also lower coating-removal rates and long-lasting low-friction periods. However, too low S-based additive concentrations do not support formation of such dense tribofilms. And too high additive concentrations (S-based and P-based) lead to increased friction, which is caused by immediate formation of sulfur-rich or phosphorous-rich tribofilms, as normally observed in boundary-lubricated steel/steel contacts. Therefore, optimum additive concentration, being application or contact conditions-dependant, is required in order to obtain fast formation of dense low-friction tribofilms, which can give up to 50% lower friction and wear as compared to base lubricants and/or steel/steel contact and can last for more than 1.10^7 sliding cycles. In order to form such low-friction tribofilm, revealed steel surface is necessary and to maintain it, supply of transferred coating material and additive is required. Once the coating is worn off or additive is consumed, the supply is cut. This leads to the wear out of the tribofilm and a climbing friction. The friction then reaches the levels typical of DLC surfaces operating in nonadditivated lubricants or uncoated steel surfaces operating in formulated oils.

In the case of metal-doped DLC coatings, increase in contact pressure, corresponding to higher frictional energy accelerates the process of low-friction tribofilm formation, thus resulting in lower friction. Increase in operating temperature has similar effect, with higher temperatures accelerating W–S reaction kinetics for the case of W-doped DLC coatings and S-based additives. On the other hand, increase in sliding speed has the opposite effect on the tribological behavior of DLC-coated surfaces, most probably due to more effective removal of generated frictional heat.

Although DLC coatings provide reduced friction and better surface protection under boundary lubrication, they do not provide the same conditions for EHD or HD film formation as uncoated steel surfaces. However, if paired with the steel counter-surface faster and smoother transition from boundary to EHD lubrication can be reached, with the coefficient of friction being comparable to steel/steel contact.

References

1. Hogmark S., Jacobson S., Larsson M., and Wiklund U. (2000). Mechanical and tribological requirements and evaluation of coating composites. In: Bhushan B. (ed.) Modern Tribology Handbook, CRC Press, Boca Raton, FL.
2. Holmberg K. and Matthews A. (1994). Coatings Tribology. Elsevier, Amsterdam.
3. Leffler B., Svensson M., and Lord L. (1998). Behaviour of Material in Machining. In: IOM Conference Proceedings, Stratford, p. 3.
4. Rutherford K. L., Bull S. J., Doyle E. D., and Hutchings I. M. (1996). Laboratory characterization of the wear behaviour of PVD-coated tool steels and correlation with cutting tool performance. Surface and Coatings Technology 80:176–180.
5. Stoiber M., Panzenbock M., Mitterer C., and Lugmair C. (2001). Fatigue properties of Ti-based hard coatings deposited onto tool steels. Surface and Coatings Technology 142–144, 117–124.
6. Podgornik B. (2001). Coated machine elements – fiction or reality? Surface and Coatings Technology 146–147, 318–323.
7. Rincon C., Zambrano G., Carvajal A., Prieto P., Galindo H., Martinez E., Lousa A., and Esteve J. (2001). Tungsten carbide/diamond-like carbon multilayer coatings on steel for tribological applications. Surface and Coatings Technology 148:277–283.
8. Ronkainen H., Varjus S., and Holmberg K. (1998). Friction and wear properties in dry, water- and oil-lubricated DLC against alumina and DLC against steel contacts. Wear 222:120–128.
9. Rosado L., Jain V. K., and Trivedi H. K.(1997). The effect of diamond-like carbon coatings on the rolling fatigue and wear of M50 steel. Wear 212:1–6.
10. Johnston S. V. and Hainsworth S. V. (2005). Effect of DLC coatings on wear in automotive applications. Surface Engineering 21:67–71.
11. Treutler C. P. O. (2005). Industrial use of plasma-deposited coatings for components of automotive fuel injection systems. Surface and Coatings Technology 200:1969–1975.
12. Ban M., Ryoji M., Fujii S., and Fujioka J. (2002). Tribological characteristics of Si-containing diamond-like carbon films under oil-lubrication. Wear 253:331–338.
13. Dimigen H. and Klages C. P. (1991). Microstructure and wear behavior of metal-containing diamond-like coatings, Surface and Coatings Technology 49:543–547.
14. Michler T., Grischke M., Bewilogua K., and Hieke A. (1999). Continuously deposited duplex coatings consisting of plasma nitriding and a-C:H:Si deposition. Surface and Coatings Technology 111:41–45.
15. Voevodin A. A., Rebholz C., and Matthews A. (1995). Comparative tribology studies of hard ceramic and composite metal-DLC coatings in sliding friction conditions. Tribology Transaction 38:829–836.
16. Erdemir A., Nichols F. A., Pan X. Z., Wei R., and Wilbur P. (1993). Friction and wear performance of ion-beam-deposited diamond-like carbon films on steel substrates. Diamond and Related Materials 3:119–125.
17. Grill A. (1997). Tribology of diamond-like carbon and related materials: an updated review. Surface and Coatings Technology 94–95:507–513.
18. Kodali P., Walter K. C., Nastasi M. (1997). Investigation of mechanical and tribological properties of amorphous diamond-like carbon coatings. Tribology International 30:591–598.
19. Bartz W. (1994). Additive fur Schmierstoffe. Expert verlag, Renningen.
20. Erdemir A. (2001). The role of hydrogen in tribological properties of diamond-like carbon films. Surface and Coatings Technology, 146–147, 292–297.
21. Erdemir A. (2004). Genesis of superlow friction and wear in diamond-like carbon films. Tribology International 37:1005–1012.
22. Liu Y., Erdemir A., and Meletis E. I. (1997). Influence of environmental parameters on the frictional behavior of DLC coatings. Surface and Coatings Technology 94–95, 463–468.

23. Erdemir A., Halter M., Fenske G. R., Zuiker C., Csencsits R., Krauss A. R., and Gruen D. M. (1997). Friction and wear mechanisms of smooth diamond films during sliding in air and dry nitrogen. Tribology Transaction 40:667–675.
24. Ronkainen H., Varjus S., Koskinen J., and Holmberg K. (1999). Friction and wear performance of a-C:H films in a wide normal load and sliding velocity range. Tribologia – Finish Journal of Tribology 18:3–13.
25. Liu Y., Erdemir A., and Meletis E. I. (1997) Influence of environmental parameters on the frictional behavior of DLC coatings. Surface and Coatings Technology 94–95, 463–468.
26. Ronkainen H., Varjus S., Koskinen J., and Holmberg K. (2001). Tribological performance of different DLC coatings in water-lubricated conditions. Wear 249:267–271.
27. Ajayi O. O., Kovalchenko A., Hersberger J. G., Erdemir A., and Fenske G. R. (2003). Surface damage and wear mechanisms of amorphous carbon coatings under boundary lubrication conditions. Surface Engineering 19:447–453.
28. Podgornik B., Vizintin J., Jacobson S., and Hogmark S. (2004). Tribological behaviour of WC/C coatings operating under different lubrication regimes. Surface and Coatings Technology 177–178, 558–565.
29. Persson K. and Gahlin R. (2003). Tribological performance of a DLC coating in combination with water-based lubricants. Tribology International 36:851–855.
30. Schey J. A. (1984). Tribology in Metalworking – Friction, Lubrication and Wear. ASM, Metals Park, Ohio.
31. Podgornik B., Hogmark S., and Sandberg O. (2002). Hard PVD coatings and their perspectives in forming tool applications. In: Proceedings of the 6th International Tooling Conference – The Use of Tool Steels: Experience and Research, Karlstad University, Karlstad, Sweden. pp 881–891.
32. Podgornik B., Hogmark S., and Sandberg O. (2004). Influence of surface roughness and coating type on the galling properties of coated forming tool steel. Surface and Coatings Technology 184:338–348.
33. Podgornik B. and Hogmark S. (2006). Surface modification to improve friction and galling properties of forming tools. Journal of Materials Processing Technology 174:334–341.
34. Czichos H. and Habig K. H. (1992). Tribologie Handbuch: Reibung und Verschleiss, Vieweg, Wiesbaden.
35. Stachowiak G. W. and Batchelor A. W. (1993). Engineering Tribology, Elsevier, Amsterdam.
36. Fein R. S. (1991). Boundary lubrication, Lubrication Engineering 47:1005–1008.
37. Vizintin J. (2003). Oil surface: Additive Reaction Mechanisms. In: Totten GE (ed.) Surface Modification and Mechanisms. Marcel Dekker, New York.
38. Barros M. I., Bouchet J., Raoult I., Le Mogne T., Martin J. M., Kasrai M., and Yamada Y. (2003). Friction reduction by metal sulfides in boundary lubrication studied by XPS and XANES analyses. Wear 254:863–870.
39. Martin J. M., Grossiord C., Le Mogne T., and Igarashi J. (2000). Transfer films and friction under boundary lubrication. Wear 245:107–115.
40. Willermet P. A., Dailey D. P., Carter R. O., Schmitz P. J., and Zhu W. (1995). Mechanism of formation of antiwear films from zinc dialkyldithiophosphates. Tribology International 28:177–187.
41. Ajayi O. O., Erdemir A., Fenske G. R., Nichols F. A., Sproul W. D., Graham M., and Rudnik P. J. (1992). Tribological behavior of oil-lubricated TiN-coated steel. Surface and Coatings Technology 54/55:496–501.
42. Bull S. J. and Chalker P. R. (1992). Lubricated sliding wear of physically vapour deposited titanium nitride. Surface and Coatings Technology 50:117–126.
43. Podgornik B. and Vizintin J. (2005). Tribological reactions between oil additives and DLC coatings for automotive applications. Surface and Coatings Technology 200:1982–1989.
44. Podgornik B., Jacobson S., and Hogmark S. (2003). DLC coating of boundary lubricated components – advantages of coating one of the contact surfaces rather than both or none. Tribology International 36:843–849.

45. Podgornik B., Jacobson S., and Hogmark S. (2003). Influence of EP and AW additives on the tribological behaviour of hard low friction coatings. Surface and Coatings Technology 165:168–175.
46. Podgornik B., Hren D., and Vizintin J. (2005). Low-friction behavior of boundary-lubricated diamond-like carbon coatings containing tungsten. Thin Solid Films 476:92–100.
47. Podgornik B., Hren D., Vizintin J., Jacobson S., Stavlid N., and Hogmark S. (2006). Combination of DLC coatings and EP additives for improved tribological behaviour of boundary lubricated surfaces. Wear 261: 32–40.
48. Podgornik B. and Vizintin J. (2006). Compatibility of DLC Coatings with Formulated Oils. In: Book of abstracts: International Conference on Metallurgical Coatings and Thin Films - ICMCTF 2006, AVS, San Diego, p 15.
49. Kalin M. and Vizintin J. (2005). The tribological performance of DLC-coated gears lubricated with biodegradable oil in various pinion/gear material combinations. Wear 259:1270–1280.
50. Park S. J., Kim J. K., Lee K. R., and Ko D. H. (2003). Humidity dependence of the tribological behavior of diamond-like carbon films against steel ball. Diamond and Related Materials 12:1517–1523.
51. Kalin M., Vizintin J., Barriga J., Vercammen K., Van Acker K., and Arnsek A. (2004). The effect of doping elements and oil additives on the tribological performance of boundary-lubricated DLC/DLC contacts. Tibology Letters 17:679–688.
52. Barros'Bouchet M. I., Martin J. M., Le Mogne T., and Vacher B. (2005). Boundary lubrication mechanisms of carbon coatings by MoDTC and ZDDP additives. Tribology International 38:257–264.
53. Miyake S., Saito T., Yasuda Y., Okamoto Y., and Kano M. (2004). Improvement of boundary lubrication properties of diamond-like carbon (DLC) films due to metal addition. Tribology International 37:751–761.
54. Vercammen K., Van Acker K., Vanhulsel A., Barriga J., Arnsek A., Kalin M., and Meneve J. (2004). Tribological behaviour of DLC coatings in combination with biodegradable lubricants. Tribology International 37:983–989.
55. Donnet C. and Grill A. (1997). Friction control of diamond-like carbon coatings, Surface and Coatings Technology 94–95:456–462.
56. Kalin M., Vizintin J., Vercammen K., Barriga J., and Arnsek A. (2006). The lubrication of DLC coatings with mineral and biodegradable oils having different polar and saturation characteristics. Surface and Coatings Technology 200:4515–4522.
57. Podgornik B., Vizintin J., Strnad S., and Stana-Kleinschek K. (2004). Influence of surface energy on the interactions between hard coatings and lubricants. In: Proceedings of COST 532 Conference: Triboscience and Tribotechnology, Ghent University, Ghent, Belgium. pp 52–61.
58. Martin J. M., Grossiord C., Varlot K., Vacher B., and Igarashi J. (2000). Synergistic effects in binary systems of lubricant additives: a chemical hardness approach. Tribollogy Letters 8:193–201.
59. Podgornik B., Jacobson S., and Hogmark S. (2004). Influence of EP additive concentration on the tribological behaviour of DLC-coated steel surfaces. Surface and Coatings Technology 191:357–366.
60. Martin I., Vinatier P., Levasseur A., Dupin J. C., and Gonbeau D. (1999). XPS analysis of the lithium intercalation in amorphous tungsten oxysulfide thin films. Journal of Power Sources 81–82:306–311.
61. Grossiord C., Varlot K., Martin J. M., Le Mogne T., Esnouf C., and Inoue K. (1998). MoS_2 single sheet lubrication by molybdenum dithiocarbamate. Tribology International 31:737–743.
62. Grossiord C., Martin J. M., Varlot K., Vacher B., Le Mogne T., and Yamada Y. (2000). Tribochemical interactions between ZnDTP, MoDTC and calcium borate. Tribology Letters 8:203–212.
63. Cotton F. A., Wilkinson G., Murillo C. A., and Bochmann M. (1999). Advanced Inorganic Chemistry. Wiley, New York.

64. Lansdown A. R. (1999). Molybdenum Disulphide Lubrication. Elsevier, Amsterdam.
65. Voevodin A. A., O'Neill J. P., and Zabinski J. S. (1999). WC/DLC/WS_2 nanocomposite coatings for aerospace tribology. Tribology Letters 6:75–78.
66. Pearson R. G. (1996). Chemical Hardness. Wiley–VCH Verlag, Weinheim, Germany.
67. Podgornik B. and Vizintin J. (2006). Influence of contact conditions on tribological behaviour of lubricated DLC coatings. In: Proceeding of 5th International Forum on Advanced Material Science and Technology, Xiangtan University, Xiangtan, China. p 21.
68. Bremond F., Fournier P., and Platon F. (2003). Test temperature effect on the tribological behavior of DLC-coated 100C6-steel couples in dry friction. Wear 254: 774–783.
69. Sedlacek M. (2005). Overview of DLC coatings and their tribological properties. Faculty of Mechanical Engineering, Ljubljana.
70. Atkins P. W. (1998). Physical Chemistry. Oxford University Press, Oxford.
71. Hogmark S. (2005). Progress report on WG3: Tribochemistry. COST 532 Triboscience and Tribotechnology, Workgroup meeting, Prague.

Section C
Applications and Future Trends in DLC's Tribology

Industrial Production of DLC Coatings

H.-G. Fuß and M. Frank

Abstract Hard DLC coatings combine unique mechanical, chemical, and electrical properties. The possibility to produce them at very low temperatures, compared to those of conventional hard coatings, makes them an excellent choice for wear parts being coated without loss in hardness. The lifetime of cutting tools, not necessarily coated at low temperatures, can significantly be improved by using hard DLC coatings in machining. Sophisticated industrial coating technology capable of combining PVD-sputtering and PACVD can be provided for that. Steadily increasing demands for the performance of wear parts and cutting tools in connection with the versatility of these technologies will lead to an increasing market and further diversification.

Keywords DLC, PVD, sputtering, PACVD, industrial coating technology, CC800/9-MLT, turn key solution

1 Introduction

There are a number of applications in, for example, the molding and automotive industry requiring reduction in frictional properties and the elimination of adhesive transfer of plastics to the tool. Despite the fact that coatings based on PTFE, $WS_{2,}$ or MoS_2 have shown very low affinity for adhering to the plastics or for the reduction of friction, their use is limited to only a few applications due to their low surface hardness and insufficient protection against abrasive wear.

In comparison, coatings generally described as diamond-like carbon (DLC) coatings exhibit good frictional properties and reduced material adhesion combined with a high surface hardness within one coating system. Additionally, these coatings offer elevated protection against abrasive wear in comparison to the many other friction-reducing coatings present in the market. Based on the outstanding frictional

CemeCon AG, Adenauerstrasse 20 A 4, 52146 Würselen, Germany

C. Donnet and A. Erdemir (eds.), *Tribology of Diamond-Like Carbon Films: Fundamentals and Applications*.

behavior, DLC coatings can be used on cutting tools in both lubricated and dry conditions. This makes DLC ideal for applications requiring lubricant-free processing as found in the production of food and medical technology. In addition, DLC coatings are inert, offering good protection against corrosion while reducing the tendency to adhesion of workpiece material.

Beside its useful properties, an important aspect is that DLC can be produced even at very low temperatures. This makes the coating process uniquely suited for mold materials and automotive wear parts, such as plain carbon and low alloyed steels, as temperature-sensitive materials lose their hardness at higher coating temperatures. Therefore, carefully developed low-temperature deposition processes need to be employed for coating production. In this case, there are virtually no limitations in the selection of the substrate materials to be coated.

2 Carbon Coatings and Coating Technology

Carbon is probably one of the most versatile materials in nature. Besides its enormous importance in the area of organic chemistry and biology, it becomes increasingly important in the area of material science and as a material for coatings. Graphite as the only thermodynamical stable phase of carbon has only minor importance in the area of technological coatings, while fullerenes and nanotube coatings are still undergoing research. DLC- and CVD-diamond films are however well established and see a steady growing market, especially in the area of coated cutting tools and protective coatings for wear parts.

The first approach for classification is a ternary sp^3-sp^2-H diagram [1–3], showing the contents of sp^3-bonded carbon, sp^2-bonded carbon and hydrogen, that is mostly included to a certain degree in DLC coatings.

The amount of tetrahedral-bonded, or in other words sp^3-bonded, carbon atoms is mainly responsible for the hardness and wear resistance while the other components tailor the coating in respect to lubrication, electrical conductivity, wetting behavior, etc. If the H content is increased, the characteristics develop toward polymer coatings. Moreover, the interconnectivity of the C sites and the size and the mixing of different structures are of equal importance. Although DLC coatings are amorphous there is a medium-range order of the domains that play an essential role in the coating properties. Ovid'ko reports average domain sizes of 3–10 nm in tungsten-doped DLCcoatings [4]. Dorfman claims astonishing properties of interpenetrating carbon networks in his patent application [5].

A huge increase in the characteristics and applications is achieved by doping the coating with nonmetallic and, mainly, metallic elements. Moreover, gradient layers and multilayers are possible. In most cases a physical vapor deposition (PVD) interlayer, e.g., CrN, is deposited to achieve sufficient adhesion between substrate and DLC coating. While diamond – whether nanostructured or not – is a well-defined crystalline material, DLC is a collective term for the very wide range of

amorphous carbon coatings with a confusing variety of names reflecting the wide range of characteristics and applications.

The Guideline VDI2840 "Carbon Coatings" (Verein Deutscher Ingenieure (VDI), Society of German Engineers) released in November 2005 made a commendable approach to classify and characterize DLC [6]. Instead of using the term DLC, the term amorphous carbon is favored, to avoid, for example, the mix-up with diamond coatings, which are by definition crystalline. These amorphous carbon coatings are classified into seven categories:

1. a-C hydrogen-free amorphous carbon
2. ta-C tetrahedral-bonded hydrogen-free amorphous carbon
3. a-C:Me metal-doped hydrogen-free amorphous carbon (Me = W,Ti)
4. a-C:H hydrogen-containing amorphous carbon
5. ta-C:H tetrahedral-bonded hydrogen-containing amorphous carbon
6. a-C:H:Me metal-doped hydrogen-containing amorphous carbon (Me = W,Ti)
7. a-C:H:X modified hydrogen-containing amorphous carbon (X = Si,O,N,F,B)

In the guideline all coatings can be produced by PVD, PACVD, or a combination of PVD and PACVD. Conventional CVD fails to produce DLC, because the impact of ions is necessary in any case to force a certain fraction of carbon atoms into the small sp^3 bond.

As a consequence, PVD-coating equipment with capabilities for PACVD should be the most appropriate device to produce the large variety of DLC coatings under industrial conditions. In that case, the necessary PVD interlayer can be produced within one batch as a monolayer or as a gradient layer. The interlayer, mostly CrN or TiAlN, provides outstanding adhesion and overload resistance. Also the doping of DLC is most easily done without the use of hazardous halogenides by sputtering simultaneously from a Ti-, WC-, Cr-, or Si-target. Such coatings contain small carbide particles in amorphous a-C:H matrix providing even better wear resistance than metal free a-C:H coatings. Silicon, oxygen, and fluorine are used to enhance the hydrophobic character of the coatings, but have a significantly lower wear resistance [7].

DLC can be produced by all kinds of PVD-coating technologies. Cathodic arc or electron beam techniques need high temperatures to evaporate the high melting carbon sources. It is complex in these cases to prevent high substrate temperatures and deterioration of the films by droplets or macroparticles.

Within PVD-coating technology magnetron sputter deposition using evaporation of carbon by bombardment of inert gas ions is favored. Glow discharges should be used for the generation of ions in industrial applications for coating large batches of tools and wear parts. Ion beam techniques seem too complex for these cases. This applies also to PACVD.

A negative voltage at the substrate table (bias) is used to reduce hydrogen content as well as the optical band gap and increases hardness and density of the coating [8] (Fig. 1). Low pressure and high ion energy will favor the ratio of sp^3-bonded carbon atoms.

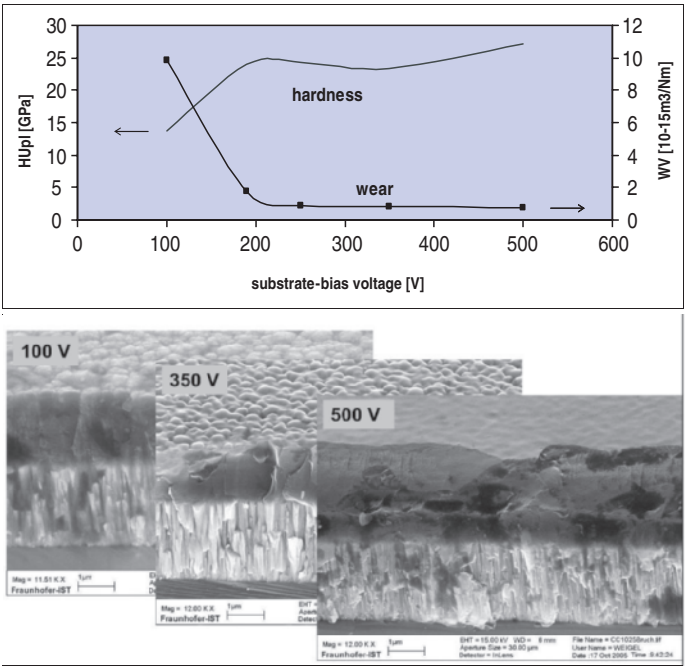

Fig. 1 Influence of bias voltage on morphology of a-C:H coatings, hardness (HUpl) and wear rate. (Coating equipment CC800/9-MLT, CemeCon) (SEM images courtesy by FhG-IST, Braunschweig, Germany)

In PVD-coating units the magnetrons are used for doping the carbon coating with a wide variety of metals. In the PACVD mode the magnetrons can be used as auxiliary electrodes for plasma generation. In this case, shutters shield the targets and prevent sputtering, but usually medium- or high-frequency power supplies are applied to generate the plasma at the substrate side.

To match the hydrogen content different carbon precursor gases like CH_4 or C_2H_2 can be used, or hydrogen itself is added separately. For hydrogen-free coatings like ta-C, carbon should be introduced by sputtering of graphite targets. In this case, the moderate sputter rate of carbon has to be considered.

3 Industrial Coating Systems

Although there are approaches to process simulation, profound knowledge and experience of the engineers are still the main factors of success. Trial-and-error methods are increasingly displaced by design of experiments (DoE) strategies. These DoE strategies are very specific and beyond the scope of this chapter.

An important point during upscaling is the assurance for a homogeneous distribution of plasma density and energy. If high plasma density and low substrate temperature are required, thermal management is a problem of comparable complexity. Using high power inputs, e.g., up to 80 kW, small inhomogeneities on the substrate surface or in the plasma density immediately lead to arcing, which can cause deterioration of the films or can damage the coating unit. In this respect innovative techniques for power supplies and for arc-suppressing circuits play an important role for safe and reliable production.

Modern coating equipment is built up in a modular manner and combines the preceding features in a highly efficient and industrial way. Moreover, it has the capability to produce standard and high-tech metal-nitrides, metal-carbides, metal-oxides, metal-borides, and mixtures thereof. For example, *CC800/9-MLT* is a specialized coating machine for carbon coatings and a broader range of parameters in the PACVD mode.

Using large-scale physical vapor deposition equipment with high pumping speed, DLC coatings can be produced by operating up to six cathodes simultaneously with or without shutter facilities in a common reactive-gas atmosphere. A large variety of different substrate tables and batching materials allow the running of small and large batches depending on the number or size of the substrates.

Figure 2 illustrates a typical process-flow diagram for the production of DLC. After pumping down the unit to high vacuum $<<10$ mPa ($<<1 \times 10^{-4}$ Torr), the substrates are heated up by a resistance heater to desorb humidity and adsorb gas species. Plasma etching prior to the coating step enables good adhesion of the coating by substantial surface modification by ion bombardment (sputter cleaning). However, due to the energy transfer from the bombarding gas ions the substrate temperature can increase rapidly during the etching step and therefore needs to be carefully controlled when temperature-sensitive materials are involved.

Low temperature-coating processes require lower cathode power and a carefully chosen bias voltage to control the maximum substrate temperature. Using pulsed power supplies is an alternative to reduce the temperature, where sputtering is achieved by asymmetric bipolar or unipolar pulsing of the target power at a frequency of up to 350 kHz. Pulsed bias voltage additionally opens up to sustain stable conditions and temperature when producing highly insulating a-C:H films with a typical electrical resistivity of $>10^6$ Ωcm compared to that of a-C:H:Me films (<1 Ωcm).

Two routes can be followed to produce metal-free and metal-doped a-C:H coatings:

1. Magnetron sputtering of carbon and metal targets with pulsed DC or DC in an Argon-C_2H_2-plasma
2. PACVD in an Argon-C_2H_2-hydrogen or CH_4-hydrogen atmosphere by radio-frequency-DC-plasma or pulsed-DC-plasma

In mode 1 graphite targets are used. Additionally, a carbon precursor gas can be added to match the H/C ratio in the resulting a-C:H coating. By a negative bias on the substrate table the sp^3/sp^2 ratio can be influenced. The temperatures are controlled

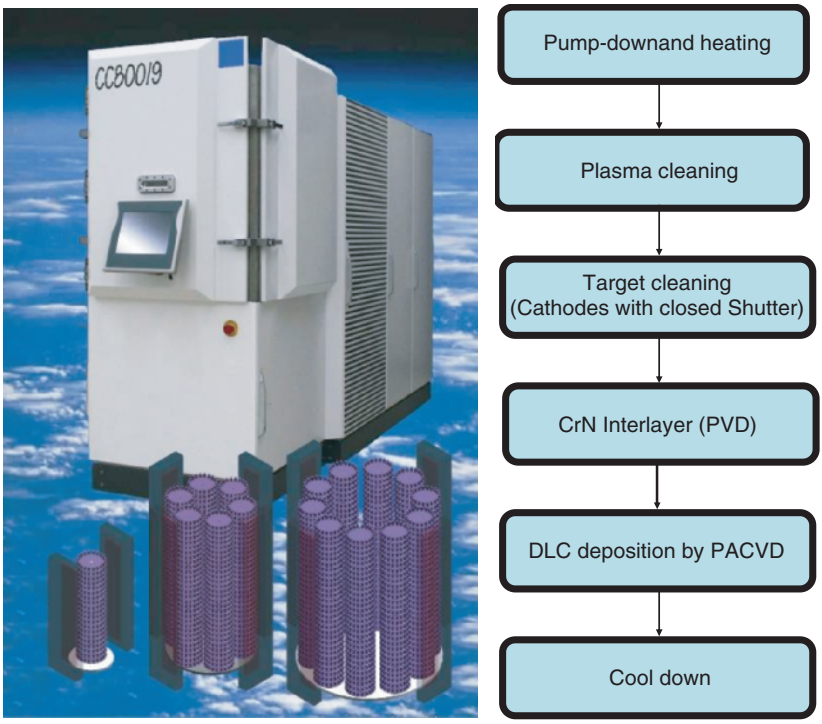

Fig. 2 (*Left*) Different batch sizes for cutting inserts for a CC800/9 coating unit and (*right*) process-flow diagram of a typical DLC process

by the applied cathode power and bias voltage in the range of about 180–300°C with appropriate process parameters, depending on the requirements of the tools and components to be coated. Higher coating temperatures will lead to graphitization of the coating due to outward diffusion of hydrogen during coating.

In a "CC800/9"-device mostly two carbon and two chromium magnetrons are used (Fig. 3). The chromium targets are for the deposition of a Cr-based interlayer with a thickness of 0.5 µm to several microns. In many cases this is CrN, but even more complex gradient layers are also used, e.g., Cr = >CrN = >CrCN = >DLC.

Wear parts are mostly coated in mode 1 by pulsed DC, the so-called high ionization pulsing (h.i.p.). This assures a high ionization and thickness distribution even on large areas. The latter has a thick CrCN gradient layer and DLC is deposited at a higher bias voltage resulting in a higher sp^3-content (Fig. 4a).

Especially for sharp cutting tools, mostly mode 1, running with cathodes in the DC mode, is used. The constant DC excitation of the plasma leads to lower ionization protecting the sharp cutting edges from too intensive ion bombardment. In most cases these coatings are deposited on a hard and comparably thick interlayer, which also contributes to the cutting process. One advantage of this process is an increased coating rate (Fig. 4b).

Fig. 3 Batching of a CC800/9 coating unit with cutting tools

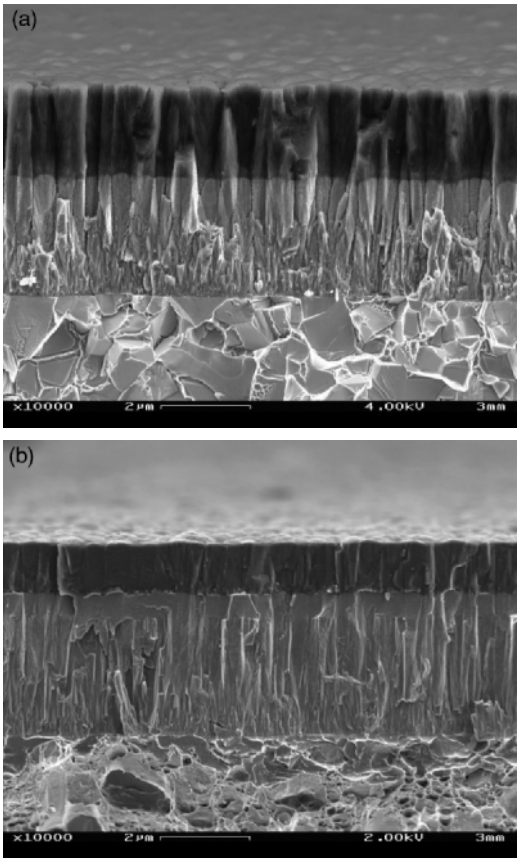

Fig. 4 DLC coatings produced (a) by pulsed DC and (b) by DC with thick CrN underlayers. (c) Low friction carbon coating (mode 2)

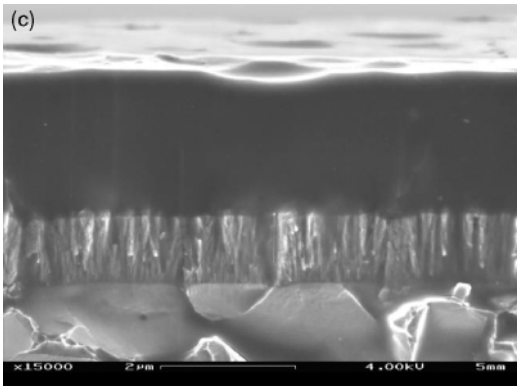

Fig. 4 (continued)

Mode 2, as a PACVD process, is especially for substrate temperatures below 200°C and for applications where low friction is focused (Fig. 4c). This process results in a-C:H coatings, called LFC coatings (low friction carbon), with coefficients of friction below $\mu = 0.1$. The hydrogen-carbon plasma has a high carbon content and high plasma density. Correct choice of all parameters, mainly the bias voltage, keeps the substrate temperature considerably below 200°C. To prevent electrical charging or arcing, the power is applied mainly by medium frequency pulsing.

H_2, CH_4, or C_2H_2 are used as precursor gases. The total pressure is higher than in mode 1 and can reach up to 5 Pa. The coating unit "CC800/9-MLT" can work in a considerably higher pressure range extending the features and applications for this kind of coating. In most cases, there is only a thin Cr or an understoichiometric CrN interlayer of, for example, 1.0 µm to assure a reliable adhesion.

It has to be kept in mind that the deposition process is only one step in the production of modern high-tech coatings: cleaning, conditioning, pretreatment before deposition, and polishing afterwards are indispensable steps and sometimes cause comparable costs. A coating unit is only one link of a chain and the reliable suppliers of coating technology offer complete "turnkey" solutions with all necessary peripheral equipment (Fig. 5).

4 Applications of DLC coatings

CCplusD, produced in mode 1, is a DLC coating with extreme hardness and elasticity, as well as with excellent coefficient of friction, especially for metal-cutting applications. This special DLC coating is combined with an adherent, extremely hard TiAlN-graduated interlayer, resulting in self-smoothing capabilities of the coating. This allows a considerable increase of service life, e.g., for critical applications like threading or milling nonferrous metals. Composite materials or glass-fiber and carbon-fiber reinforced

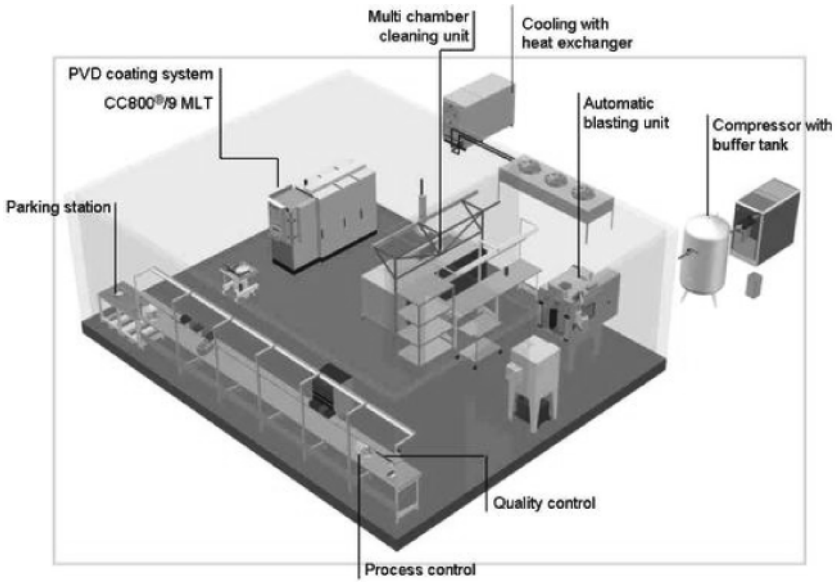

Fig. 5 Complete turnkey production line for DLC coatings (e.g., CemeCon AG)

materials are a severe challenge for tools. To economically machine these difficult-to-cut high-tech materials, including nonferrous metals, suppliers must act if they want to stay in the market. Compared to conventional DLC coatings, this kind of coating provides for considerably improved lubricious properties.

The CCplusD coating grinds or smoothes itself down as far as necessary and offers the suitable counterpart to the application at every point of the tool. This results in increased protection against abrasive wear on the cutting edge, and in the flute the collection of lubrication and sticking is prevented.

Round tools or cutting inserts, used dry or wet, show an excellent run-in process. In practice, this combination coating achieves an increase in the service life by around 15 times compared to uncoated carbide milling cutters when milling AlMgSi1 (Fig. 6).

Figure 7 shows an application of DLC4000. The lifetime of a slider for plastic injection for magnetic tapes made of polystyrol with dimensions of 145 × 130 × 30 mm was increased by a factor of 4 reducing the maintenance costs for 1 year by nearly €20,000.

It is a challenge to coat large-area components in order to meet all the technical requirements such as uniform coating thickness and good adhesion over the whole surface area. Figure 8 shows the batching of 5 fixture rings, each for three 10-inch wafers, to be coated with LFC. Major points to achieve uniform coating thickness are the total pressure and the bias voltage to get best plasma excitation over the whole area (Fig. 9).

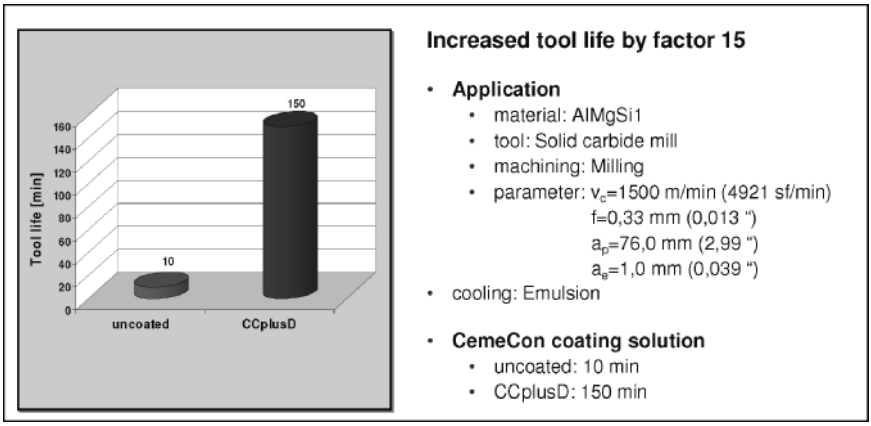

Fig. 6 CCplusD performance in milling AlMgSi1

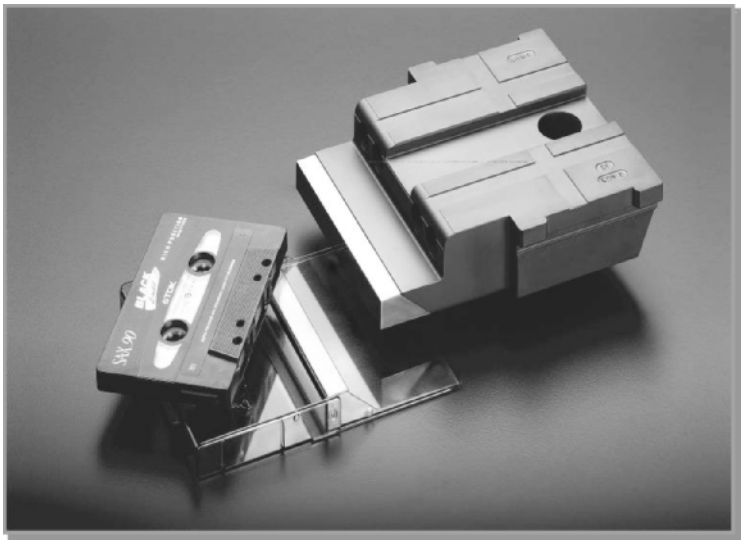

Fig. 7 DLC-coated plastic injection mold for manufacturing of polystyrene-covers for magnetic tapes; maximum coating temperature 200°C

5 Summary and Outlook

Hard DLC coatings combine unique mechanical, chemical, and electrical properties. The possibility to produce them at very low temperatures, compared to those of conventional hard coatings, e.g., TiAlN, makes them an excellent choice for wear parts being coated without loss in hardness. The lifetime of cutting tools, not

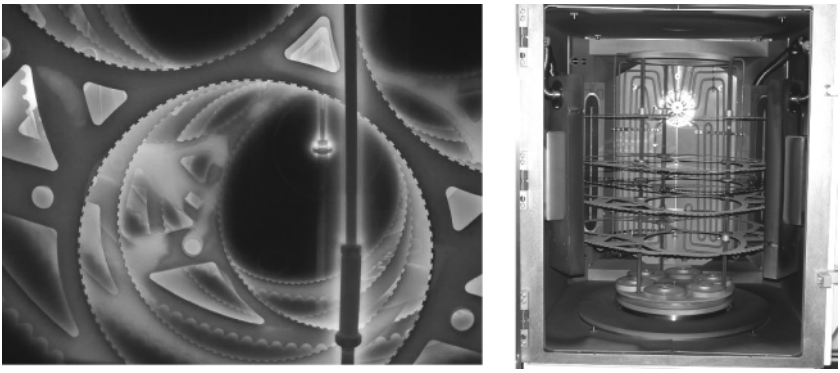

Fig. 8 Large-area coating of fixtures with LFC, used for manufacturing of Si-Wafer; total diameter 550 mm; coating temperature 150°C. (*Left*) Plasma excitation during coating step. (*Right*) Open chamber after batching

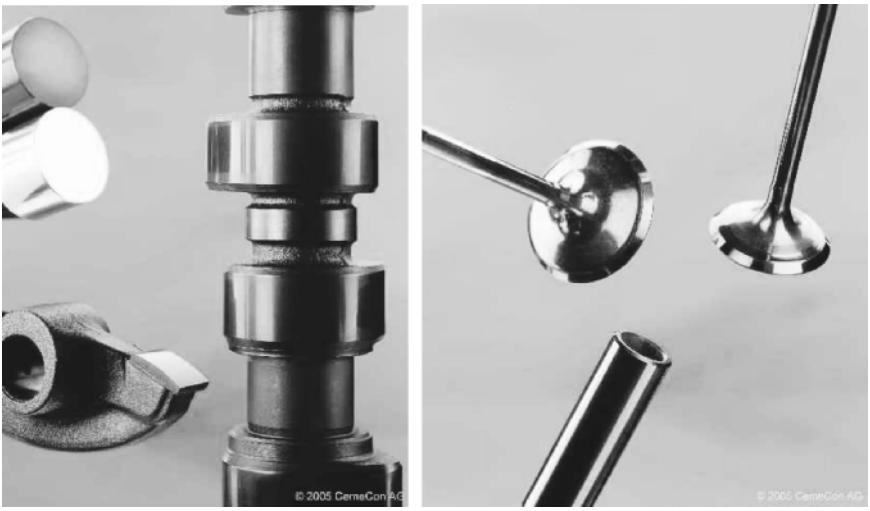

Fig. 9 Coating of wear parts for automotive industry with DLC4000. (*Left*) Camshafts and valve tappets, maximum temperature 180°C. (*Right*) Valves and wrist pins, maximum temperature 220°C

necessarily coated at low temperatures, can significantly be improved by using hard DLC coatings in machining nonferrous alloys.

Steadily increasing demands for the performance of wear parts and cutting tools in connection with the versatility of carbon will lead to an increasing market and further diversification. In consequence, this will also push the improvement and development of new coating technologies such as HPPMS.

For example, “high power pulse magnetron sputtering” (HPPMS) is emerging from the laboratory to the industrial scale. The high pulses create a considerably higher ionization of up to 100% in contrast to a much lower percentage with conventional magnetron sputtering or even pulsed magnetron sputtering. This efficient process means that the advantages of smooth layers, high gas ionization and high metal ionization can be combined – all without droplets. Additional parameters like pulse height and duration can further match the coatings to their specific application. Especially the combination of high ion densities and even lower substrate temperatures becomes possible.

References

1. P. Reinke, W. Jacob, and W. Möller, J. Appl. Phys. 74 (1993) 1354.
2. J. Robertson, Diamond Related Mat. 3 (1994) 361.
3. Ullmann’s Encyclopedia of Industrial Chemistry, Wiley-VCH Verlag GmbH and Co. KGaA, 2006.
4. I. A. Ovid’ko, Nanostructured Coating, ed. A. Cavaleiro and J.TH.M. De Hosson, Springer Science + Business Media LLC, 2006, p.78 ff.
5. European Patent EP1676306A1, published 08-17-2006.
6. Verein Deutscher Ingenieure, VDI 2840, Kohlenstoffschichten, Grundlagen, Schichttypen, und Eigenschaften, Beuth Verlag GmbH, 10772 Berlin, 2005.
7. Brand, J.; Bewilogua, K. DLC based coatings for tribological applications. Int. Workshop on Appl. Of Nanocryst. Diamond. 2006, Kolkata, India.
8. J. Robertson, Diamond Related Mat. 3 (1994) 361.

DLC Films in Mechanical and Manufacturing Industry

C. Héau

Abstract In this chapter, diamond-like carbon (DLC) films for the manufacturing industry are discussed. Section 2 is dedicated to the production of a-C:H coatings by PACVD technology and the difficulty of the control of the plasma when it is generated by biasing the parts to be coated. This section also describes how process parameters can be interconnected and how they can influence the coating properties. Section 3 is related to some functional characterisations of DLC-coated parts that allow checking of the coatings properties and quality. The combination of coatings allows improving the performances of DLC. This can be achieved in vacuum equipment that can do both PVD and PACVD processes. It is particularly interesting to combine a hard chromium nitride layer deposited by reactive magnetron sputtering and a DLC top layer. This process can be used to increase the scratch resistance of DLC. Some tribology characterisations are also discussed in Section 4. These tests are very important for the optimisation of a DLC coating as they can, in some case, simulate the real working conditions. The DLC hard coatings are used not only for wear resistance but also for friction reduction. This last aspect is very important as it can contribute not only to wear reduction but also to the reduction of energy consumption. Section 5 describes some mechanical parts corresponding to various sectors of industry, where DLC is used for friction reduction, wear reduction or both. Section 6 briefly describes new concepts of deposition equipment that are developed to increase the productivity of such coatings. This last point is particularly important as DLC represents an excellent technical solution for wide markets like automotive industry.

Keywords DLC, mechanical properties, mechanical applications, friction, wear, high productivity equipment.

HEF Group, rue Benoît Fourneyron, 42166 Andrézieux-Bouthéon, France

C. Donnet and A. Erdemir (eds.), *Tribology of Diamond-Like Carbon Films: Fundamentals and Applications*.

1 Introduction

The application of diamond-like carbon (DLC) for mechanical and manufacturing industry is submitted to a sustained growth since the mid-1990s. It was at this period that the adhesion of DLC coatings started to be sufficiently well controlled to allow reliable use of coated parts. The exceptional tribological properties of DLC have been known since a long time. It particularly concerns a wear resistance higher than classical PVD hard coatings, even those having similar hardness. But the most important difference of DLC with the classical hard coatings concerns the reduced value of friction coefficient against many kinds of materials [1], including those with a reputation of having a disastrous friction behavior like titanium or aluminum alloys.

2 PACVD DLC Technology

Most of the industrial processes for the deposition of DLC for mechanical applications are based on plasma-assisted chemical vapour deposition. In such processes, the principle is to introduce a carbon containing gas at a pressure allowing a glow discharge by applying a bias voltage on a substrate holder. From that point, many possibilities are available to make a process, leading to a large variety of DLC coatings. The carbon containing gas is generally a hydrocarbon.

The choice of the carbon precursor is based on criteria like the hydrogen to carbon ratio, the ease to manage the gas and safety considerations. Generally, precursors containing a low H/C ratio [2] are preferred to minimise the hydrogen content in the DLC film in order to optimise the hardness of the coating. The lowest H/C in hydrocarbon gas is 1 and is met in acetylene and benzene. Acetylene is available as a gas, and its main drawback concerns the purity, which in general is not accurately controlled. On the other hand, benzene is liquid at room temperature and has to be vaporised to be managed as a gas. With such precursors one also has to take care of condensation risks in cold places in the deposition equipment as well as in the primary pump. Despite being available with high purity, benzene, as major drawback, is known to be a carcinogen.

The way to generate the glow discharge is also a very important process parameter. For DLC processes, the glow discharge has two main functions. The first one is to activate the hydrocarbon precursor and produce radicals and atoms, which deposit and react on the surface of the growing coating. The second one concerns the production of positive ions. The biased substrate holder is negative with respect to the deposition chamber, which is generally grounded. Hence some positive ions in the bulk of the plasma can diffuse up to the cathode sheath where they are accelerated by the electric field of the surface of the parts. This phenomenon produces an intensive ion bombardment on the surface of the growing film, which modifies the properties of the DLC coating by changing the hydrogen content and the hybridisation state of carbon. Ion energy impinging on the surface of the coating is probably the most important parameter controlling the coating properties.

Ion energy can be tuned by the bias voltage and is influenced by the total working pressure. In such glow discharge, mean free path of ions can be small compared to the thickness of the cathode sheath. When ions are accelerated to the parts, they are submitted to collisions with gaseous species and lose part of their energy in the collision by electrical charge exchange or kinetic energy transfer. Increasing pressure reduces the mean free path, resulting in a decrease of ion energy at the substrate surface. Generating the plasma by biasing the parts is apparently simple, but in fact many parameters are interconnected, making the process rather complicated [3]. Ion energy plays a predominant role in the hydrogen amount and in the hybridisation state of carbon, which determine the characteristics of the coatings like hardness and friction [2,4].

The biasing of the substrate holder can be done by using radio frequency power supply or pulsed DC power supply. DLC coatings are poorly conductive material, for this reason alternative signals are necessary for biasing to prevent arcing or vanishing of the plasma when the thickness of the coating increases. For both technologies, the adjustment of the mean voltage allows to tune the ion energy. At a given pressure and bias voltage, the resulting power injected in the plasma increases with the cathode surface, i.e. with the surface of parts on the substrate holder. The power density in the plasma can change when the surface of biased part is changed. Particularly, electrostatic confinement can occur when the distance between the biased parts and their disposition is not appropriate. Electrostatic confinement tends to locally increase the power density, changing the dissociation and the ionisation in the plasma phase. Electrostatic confinement can result in the change of the coating properties. Positioning of parts on the substrate holder is then an important parameter for the homogeneity of coating properties.

In the particular case of radio frequency processes there are some constrains like the cathode to anode surface ratio [1] and the use of an impedance matchbox between the generator and the substrate holder. The cathode surface must be at least ten times smaller than the anode surface to keep the ratio nearly constant between the self-biasing voltage and the peak-to-peak amplitude of the RF signal. The cathode to anode surface ratio can be artificially increased by plasma confinement between parts. The surface ratio is not purely geometric. Working below a surface ratio of 10 changes the power density in the plasma, keeping the self-biasing constant. This results in some variation in the properties of DLC. The setting and tuning of the impedance matchbox can be a sensitive operation.

The gas activation by the plasma can also produce powder in the gas phase, which can alter the quality of the coating by introducing defects. When plasma density and gas precursor partial pressure are high enough, three body collisions can occur in the gas phase allowing the reaction between radicals and the nucleation of powders. Process parameters are adjusted to prevent such phenomena, but as mentioned earlier, plasma density is difficult to control as it depends on plasma confinement, which is related to the location of parts between each other on the substrate holder.

The gas distribution is also an important parameter as it controls the homogeneity of the coating spatial distribution. For the treatment of simple-shape parts like

silicon wafers for the MEMS industry, the reactor and gas distribution can be built around the silicon wafer, which is always located at the same position. For jobbing activity, the shape and size of parts vary from one batch to the next. In that case, it is no more possible to design the reactor around one-part geometry. Generally, the treatment homogeneity is obtained by combining the effect of gas distribution with the motion of parts in the vacuum chamber. The gas distribution is adjusted along the height of a cylindrical reactor using gas pipes, resulting in high homogeneity along the axis of the cylinder. This equipment's configuration results in a heterogeneous treatment in the volume of the reactor characterised by a decrease in the deposition rate with the distance to the gas injection. To overcome this problem, one solution would be to distribute gas pipes homogeneously on the periphery of the reactor. This solution is more complicated and heterogeneity would still appear, depending on the parts affecting the gas distribution. The best solution is to use a rotating substrate holder as in PVD technology. Such substrate holders can have from one to three rotations. Hence, all the parts in the chamber are submitted to the same heterogeneities, resulting in a homogeneous treatment on all of them.

3 Basic Characteristic Properties of Coatings

When speaking about coatings, the first important thing concerns the adhesion to the substrate. Basically, the adhesion is characterised using scratch test or Rockwell C indentation. When carrying out such tests, the observation of the indentation is particularly important to determine if the failure has an adhesive character or a cohesive one. Such tests allow localising the weakest point in the structure, and it can be at an interface or in a material. Adhesive failure, as illustrated in Fig. 1, is

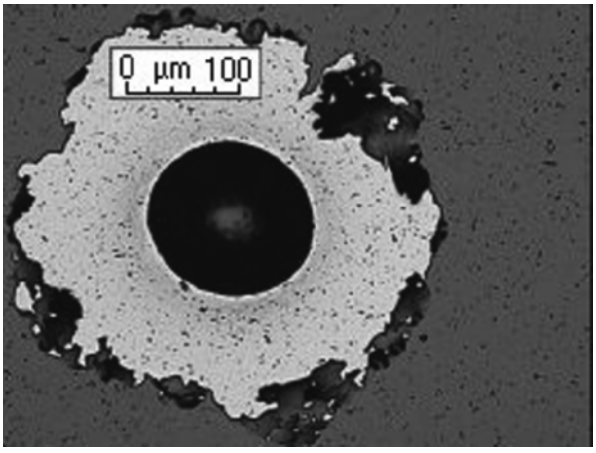

Fig. 1 Adhesive failure at 60 kg load

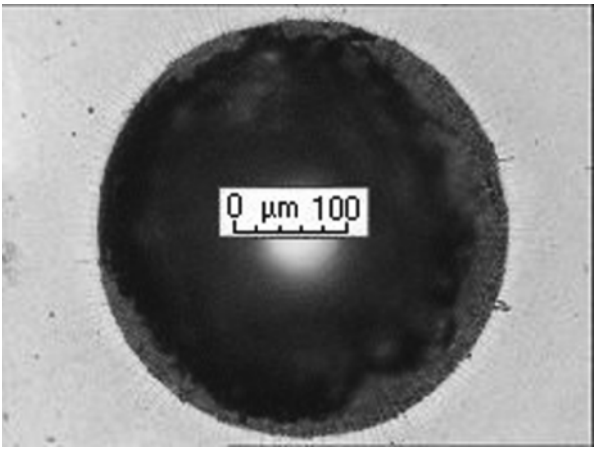

Fig. 2 Cohesive cracking at 150 kg load

observed when the cracking propagates at the interface between the substrate and the coating. Examinations of adhesive failures show large domains where the coating has been removed, revealing the substrate. The observation of the edges of flakes is also important. At the edges of the flakes, the fracture is strictly perpendicular to the coating. In most of the cases, lack of adhesion is attributed to some insufficient cleaning, insufficient degassing of parts or a lack of etching.

Cohesive failure, as shown in Fig. 2, is observed when cracks propagate inside the coatings, and radial cracking is visible around the indentation. Depending on the coating properties, the cracking can propagate up to the substrate, not necessarily signifying a lack of adhesion.

For a scratch test, the load at which the failure occurs can be measured. This failure load depends on some parameters, which are not directly linked to the coating. The increase of the substrate hardness produces the increase of the critical load. When the substrate hardness increases, it is necessary to increase the load to produce the necessary deformation of the substrate to induce cracking in the coating on the side of the scratch. Similarly, when testing coating with Rockwell indentation, the load to be applied must take into account the hardness of the substrate for comparable measurements.

The critical load of DLC coatings can vary from around 5 N on aluminium alloy substrate up to 30 N on hard steels. It is possible to further increase the critical load of DLC coating by duplex processes, for example by combining nitrided steel and DLC [5] or PVD hard coatings and DLC. It is particularly interesting to combine PVD hard coatings and DLC when both processes are carried out in the same deposition chamber. The combination of nitrides like CrN or TiN with DLC can increase the critical load of DLC by 30%. This is particularly interesting for applications where contact pressure is rather high. Anyway, the efficiency of a thin hard coating reveals its full potential when the part is designed using the appropriate substrate material.

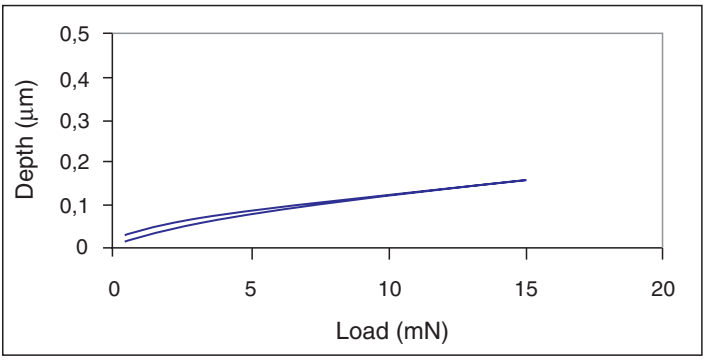

Fig. 3 Hardness and reduced Young's modulus measurement from indentation depth/load curves for a DLC coating

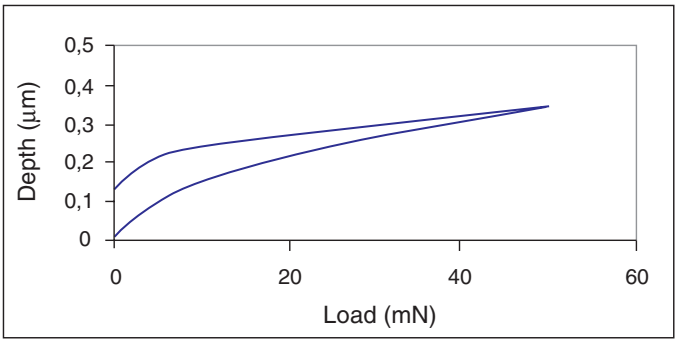

Fig. 4 Indentation curve of a CrN coating

DLC coatings are characterised by rather high hardness and a highly elastic behaviour, such that the indentation cannot be observed by microscopy. Hence, the determination of hardness necessitates using apparatus able to record the force versus displacement curve, from which hardness, Young's modulus and elastic to plastic deformation work ratio can be determined, as shown in Fig. 3.

Elastic deformation for DLC represents generally between 75% and 90% of the total deformation during indentation. This value is much higher than classical hard PVD coatings like CrN, TiN, where elastic deformation is generally around 50% of the total one. For comparison, Fig. 4 shows indentation curve on a CrN coating having nearly 50% of plastic deformation.

The hardness of a-C:H coatings for mechanical applications is in the range of 25–35 GPa, which is comparable to the hardness of classical hard coatings. Despite similar hardness, DLC coatings have higher abrasive wear resistance, which is weakly influenced by hardness. In Fig. 5, one can see the evolution of microhardness and reduced Young's modulus as a function of the deposition temperature. It is

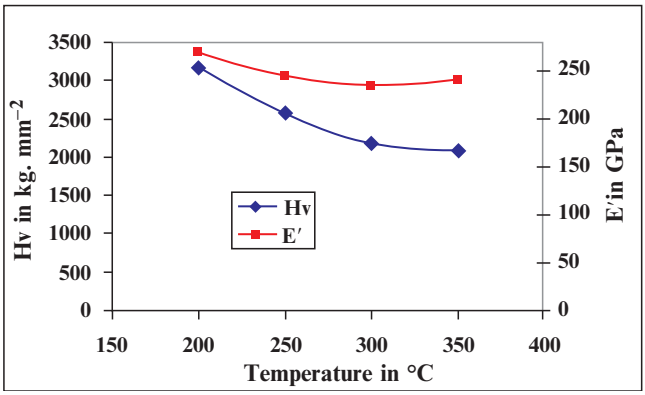

Fig. 5 Influence of deposition temperature on hardness and reduced Young's modulus

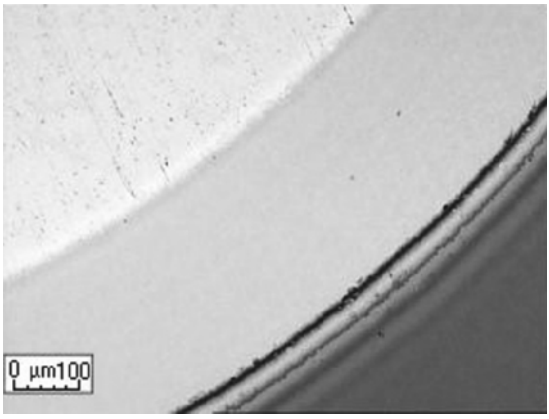

Fig. 6 Calotest on a CrN + DLC-coated high-speed steel sample

interesting to note that the hardness and reduced Young's modulus decrease when the deposition temperature is increased, indicating changes in the hybridisation state and hydrogen content. This effect is important to consider as the deposition of directly on substrate or after a PVD coating will start at different temperature.

The use of DLC coatings on high-precision mechanical parts necessitates an accurate control of the thickness. Thickness is generally measured using calotest. The test consists of wearing the coating using a steel ball covered with abrasive slurry. The measurement of the remaining wear crater diameter allows determining the thickness of the coating and of the layers constituting the coating. Figure 6 illustrates a crater obtained on a DLC coating. The crater shows the substrate in the top left corner, then the CrN coating, the adhesion layer and the DLC layer in the

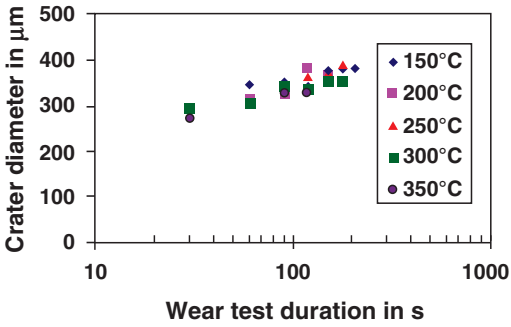

Fig. 7 Abrasive wear resistance of coatings deposited at various temperatures

bottom right corner. Interference fringes are visible in the adhesion and in the DLC layers, close to the interface with the PVD CrN layer.

Usually, thick DLC coatings are black. When the thickness of the DLC coating is less than 1 µm, some coloration superimposed to the black colour appears. As DLC coatings are partly transparent, the light can reflect at the substrate interface and make interferences with reflected light on the DLC surface. For low thickness coatings, the coloration results from the thickness and refractive index. The thickness of the DLC coatings can be increased up to a few micrometers. For general purpose, the thickness of DLC coatings is between 1 and 3 µm. Higher thickness can be detrimental for the roughness and brittleness of the coating.

When the load applied during the test, the diamond slurry and the run distance are well controlled, it becomes possible to determine abrasive wear resistance by calotest [6,7]. Of course, the worn crater must remain inside the coating; otherwise, the characterisation integrates the wear resistance of the substrate. By measuring the worn diameter as a function of test duration, it becomes possible to determine the abrasive wear resistance. In the case of DLC coatings, it appears that the abrasive wear resistance is much higher than that of hard nitride coatings with similar hardness.

Figure 7 illustrates the influence of deposition temperature on abrasive wear resistance by diamond slurry of 0.25 µm. It is observed that despite large hardness variation the abrasive wear resistance is the same for all the coatings. This result cannot be generalised when changing the properties of the DLC by the mean of the bias voltage or the total pressure; decrease in hardness is correlated to decrease in wear resistance.

4 Tribology Testing

DLC coatings are mainly used for their particular mechanical behaviour, which concerns the wear resistance and the friction coefficient. It is then interesting to characterise properties related to wear and friction. When applied on mechanical

parts, DLC coatings can also be degraded by other mechanism like surface fatigue. Mechanical parts can be submitted to conditions where load can vary with time inducing loading/unloading cycles on the surface resulting in fatigue of the coating which breaks even at loads far below the fracture limit.

The friction can be simply characterised by pin on disk test. This test is very particular as the solicitation is far from most of the conditions in service. However, it allows obtaining some tendencies related to friction and wear. With such a test, it is possible to coat with DLC the disk or the spherical pin or both of them.

When coating the disk, it is only possible to test friction. The dry friction coefficient depends on the nature of the counterpart. For example, friction coefficients between 0.1 and 0.2 are classical values observed when sliding DLC against steel in dry conditions. Such low friction coefficient is very specific to DLC. Nevertheless, the counterpart material has a great influence. For example, DLC does not improve friction against rubber parts where slip-stick phenomenon dominates. Friction against copper alloys, brass and bronze is not as low as against steel; despite this, such materials are used to make mechanical parts and reduce friction. It is noticeable that DLC coatings have particularly low friction against materials well known for their very poor friction ability like titanium and aluminium alloys. When testing the coating on the disk, an increase of friction with the cycle number can be observed. The pin wear results in the reduction of Hertz contact pressure with time. The wear on the coating cannot be measured.

Reversing the test configuration, i.e. applying the coating on the pin, is very interesting. It still allows measuring friction but the test becomes more severe for the DLC coating as it can show wear degradation generally as abrasion. In this configuration, the DLC on the spherical pin remains in contact all along the test. The friction coefficient is similar to the one of the previous test configuration.

The deposition of DLC on disk and pin results in a significant decrease of friction coefficient, which can drop below 0.05 in dry conditions. Such behaviour is not usual as, in general, the friction of a material against itself can result in poor friction and seizing. The DLC coating on the pin is still subjected to abrasion while no degradation is observed on the disk. When carrying out the test at high load, some fracture in the coating on the pin can occur. Figure 8 shows the evolution of dry friction coefficient of DLC-coated pins against a steel disc and a DLC-coated disk. The test was carried out at 50 rpm, at a relative speed of 0.04 m/s with a normal load of 5 N, enabling maximum contact pressure of 860 MPa.

It is interesting to carry out tribology characterisations using AMSLER test. This test configuration allows reaching contact pressure and speed, which are close to the conditions encountered on mechanical parts [8]. Moreover, this test is less sensitive than pin on disk to contact pressure variations because of wear. Two disks with a spherical section rotate against each other. This test allows characterising coatings in rolling conditions or in sliding condition, depending of the rotation direction of the two disks. Contact pressure in the range 1–3 GPa can be achieved as well as sliding speed between 0.08 and 1.50 m s^{-1}. Hence the rotation speed and the load can be adjusted in a manner that friction conditions are close to the one encountered in the mechanical parts like the camshaft/tappet. Such a test can be

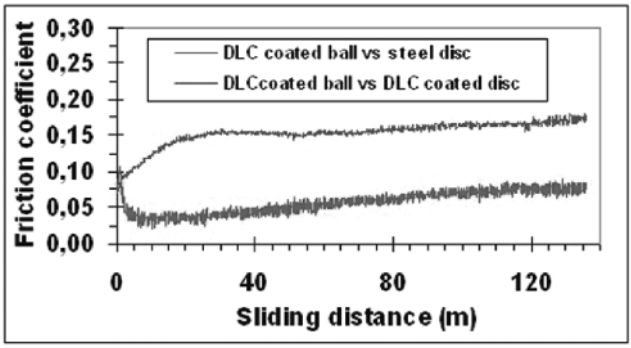

Fig. 8 Evolution of dry friction coefficient of DLC-coated pins against a steel disc and a DLC-coated disk

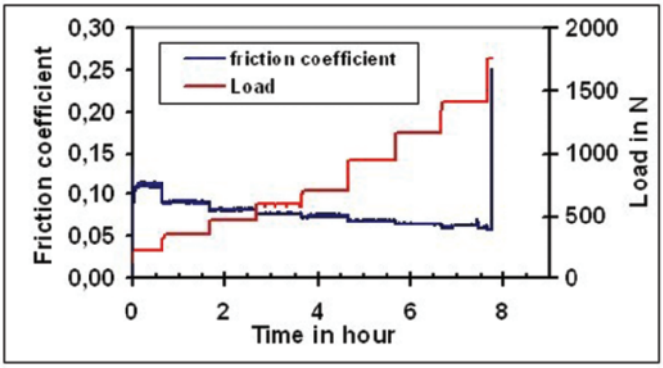

Fig. 9 Evolution of friction coefficient in an Amsler test under lubricated condition

carried out in dry or partly lubricated conditions. The relatively simple shape of the samples and the easiness to implement the test make it a powerful tool for the optimisation of a DLC coating before carrying out test-on-bench test. Increasing step by step the load, it is possible to test the load-bearing capacity of the coating. In Fig. 9, the friction curve is reported. The test was carried out using an engine lubricant. The relative speed between disks is 1.5 m s^{-1}. The load between the two 50-mm-diameter disks is 230 N at the beginning of the test and is maintained for 40 min. Then the load is increased by 120 N each hour up to the failure of the coating.

The degradation mode observed during such tests is generally cracking of the coating, which degenerates in flaking. The coatings are rarely worn by abrasion mechanism, thanks to the excellent abrasive wear resistance of DLC coatings. The DLC-coating performances can be improved by adding a hard PVD coating under the DLC coating. The hard-coating base layer allows greater crack resistance

of DLC, improving the load fracture by a factor of 2. The record of the friction coefficient allows detecting the initial cracking. When cracking and degradation of the coating occur, instabilities appear on the friction coefficient record.

5 Application of DLC on Mechanical Components

For mechanical applications, DLC coatings are generally deposited on steel parts. The steel material must be chosen so that its mechanical characteristics are compatible with the application. Steel parts can be divided into two categories. The high mechanical characteristics steel tempered below 250°C necessitates specific processes which are adapted to prevent the loss of bulk properties of parts. For high mechanical characteristics steel tempered over 420°C, a wider range of processes are applicable, especially the combination of hard PVD coatings deposited on the part prior to the deposition of DLC. Such a combination of coatings is particularly interesting when the parts are subjected to severe conditions of use like high load. Recently, DLC processes have been adapted for the treatment of aluminium and titanium alloys, especially used in aeronautic industry, for a matter of weight reduction and related energy consumption.

In general, the quality of the part is very important. Failure of the coated parts can often be attributed to inappropriate substrate. Machining of parts can create burrs on edges of mechanical parts. Such burrs must be removed before coating. The detachment of particles (coated burrs) from the part in service can cause severe degradations in the mechanical contact by indenting the coated surface. The roughness of the parts can also be the cause of failure of the mechanical system. The failure can be attributed to the coated part and/or to the counterpart. On the coated part, high roughness can induce the local fracture of the coating by concentration of stress. On the other hand, the hard DLC coating on a rough surface can produce high wear by scratching the counterpart.

The deposition of DLC on mechanical components covers a wide field of sectors including automotive industry, aeronautic, food transformation, textile industry and biomedical applications. In most cases, the reduction of friction is the most important property. It allows principally to reduce energy consumption and hence contributes to the reduction of emission of gases involved in global warming. In Fig. 10, one can see swash plates for air-cooling system coated with DLC. The reduction of friction allows reducing the energy consumption. A second effect of friction reduction concerns the reduction of wear as the energy dissipated in the mechanical contact is decreased.

Applications can be shared by two groups: components working in lubricated conditions and components working in other conditions. Concerning lubricated conditions, the use of DLC coatings is particularly interesting when limit conditions are met. In such conditions, the contact is partly lubricated and parts can come into contact. The DLC coating helps to keep a low friction when the lubricant film becomes discontinuous, hence limiting wear and friction. When contact pressure or

Fig. 10 Swash plates for air-cooling system in automotive application

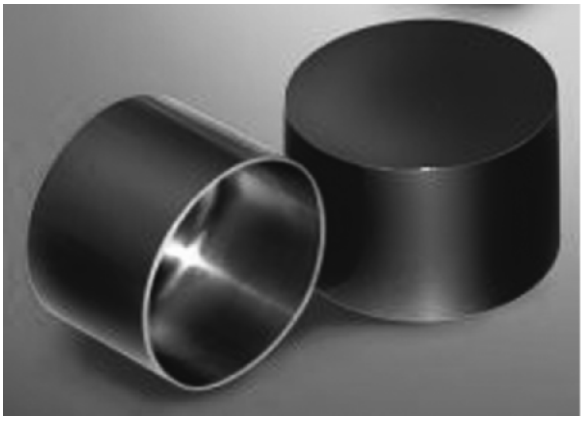

Fig. 11 Tappets coated with a PVD CrN and a DLC top layer

relative speed is increased, the thickness of the lubricant film increases sufficiently to separate the parts. The friction coefficient is no more related to the coating but to the viscosity of the lubricant. The roughness of parts is of course a crucial parameter as it determines the lubricant film thickness that can separate the parts, modifying the pressure and speed limits at which hydrodynamic regime appears. Figure 11 shows tappets coated with a chromium nitride layer deposited by PVD and a top layer of DLC deposited by PACVD in a single batch. Such parts necessitate a low-temperature process to keep the mechanical properties of steel. The DLC top layer brings a significant reduction of friction in lubricated conditions, allowing the reduction of pollutant emission.

The use of DLC is also interesting for the wear reduction, allowing increase in the lifetime of the component. In some cases, the use of DLC coatings has allowed

Fig. 12 Mould for compact disk injection coated with DLC

to design new generation of components working in particularly severe conditions. For example, the development of high pressure direct injection system has been possible, thanks to the extraordinary properties of DLC.

The friction of the textile fibre produces severe abrasion of steel parts used for guiding. High hardness coating reduces the wear but can damage the textile fibre when the friction coefficient is high. For these reasons, DLC coatings are particularly suitable. Figure 12 shows the mould for a compact disk. It is coated with DLC to improve the abrasive wear resistance of the surface. DLC is particularly adapted as it can respect the initial surface roughness with no defect.

A particular field of application of DLC concerns their unique ability of low friction against materials known to have very poor friction properties like titanium alloys and aluminium alloys. For example, DLC coatings have allowed the manufacture of moulds for injection of plastic. The moulds can be composed of several parts, which slide against each other at the aperture and closure of the mould. In this regard, aluminium is particularly interesting as it is easily machined and presents a high thermal conductivity that helps reducing the duration of the injection cycle. DLC is applied on movable parts made of aluminium. Without DLC, the movable parts are severely worn out and the mechanical system can be blocked by seizure.

Another field of application concerns the treatment of cutting tools used to machine aluminium. The use of DLC allows facilitating the chip evacuation and prevents the sticking on the tool. Due to the limitation in thermal stability of DLC, cutting tools working at low temperature are preferred, like taps. However, drills coated with DLC have good performances in aluminium alloys, as the cutting effort remains low, preventing an increase of temperature. Using DLC on taps for applications in copper alloys and brass also allows preventing the sticking of chips. For all these applications, roughness has an important role. A surface presenting grooves collects metal by transfer, which is mechanically bonded to the surface, resulting in increased adhesion.

6 Towards High Productivity Equipment

The surface deposition on mechanical parts concerns a large field of applications, from unique part to millions of pieces. The production cost and the productivity must be considered for each kind of application. For unique or a small amount of parts, batch equipment is suitable. In such production equipment all the process steps are carried out in a single chamber. It generally includes heating, etching, coating and cooling down prior to venting.

When considering the production of millions of pieces a year, other design of equipment must be considered. The simplest one is an air-to-air in-line machine. Such a machine is composed of a series of vacuum chambers linked by gate valves, which allow the transfer of the load from one chamber to the next. The first and last chambers are dedicated to the transfer of the load of parts between air and vacuum and vice versa. Hence the intermediate chambers remain under vacuum and do not require degassing in normal operating condition. The first chamber is dedicated to degassing of the parts to be coated, followed by a chamber for etching and another for coating. With such a configuration, one batch of coated parts comes out at a frequency corresponding to the longest step.

A further productivity improvement can be achieved with cluster equipment. The process chambers are connected around a central transfer chamber. In such architecture, a batch of parts does not necessarily pass through all the process chambers. For example, the machine can be equipped with several coating chambers if the coating step is the longest one, allowing increased productivity. The number of process chambers is limited by the size of the central transfer chamber.

The last improvement of productivity can be achieved by using a parallel architecture. In this case, each vacuum chamber is connected to a transfer chamber, both constituting a module. Each transfer chamber is then connected to the others. The equipment includes a loading and an unloading chamber. For the process steps, the number of chambers per step is designed according to the step duration. A long step necessitates several chambers in parallel. Hence, such equipment configuration allows getting one batch of coated parts at a frequency limited by the shortest step. In this case, the productivity is fully optimised. The concept of a module allows a high degree of flexibility to design a full equipment optimised for a specific application.

7 Conclusions

Thanks to the exceptional tribological properties of DLC, low dry friction and high abrasive wear resistance, the application of this coating material in mechanical and manufacturing industries is undergoing intensive development. It covers various applications like the deposition on engine components for friction reduction, even

in lubricated conditions, or like guiding parts in textile industry requiring abrasion resistance. Depending on the principal property required, the coating must be adapted. The harder coating is not necessarily the best as it is also often the most brittle.

The coating architecture needs to be adapted to the condition of use, particularly hardening of the substrate, or the deposition of a hard PVD coating prior to DLC can be necessary for high load applications.

The deposition technology and the equipment design must be considered to optimise the productivity, especially when considering large volume of parts, as is the case for the automotive industry.

References

1. H. Liu, A. Tanaka and T. Kumagai, Influence of sliding mating materials on the tribological behaviour of diamond-like carbon films, Thin solid Films 352 (1999) 145–150.
2. J. Robertson, Diamond-like amorphous carbon, Mater. Sci. Eng., R37 (2002) 129–281.
3. H. Ronkainen, J. Koskinen, S. Varjus and K. Holmberg, Experimental design and modelling in the investigation of process parameter effects on the tribological and mechanical properties of r.f.-plasma-deposited a-C:H films, Surf. Coat. Technol. 122 (1999) 150–160.
4. J. Fontaine, C. Donnet, T. Le Mogne, M. Belin, Y. Berthier, C. Héau, J. P. Terrat and G.Pont, Tribology of diamond-like carbon coatings for space mechanisms, Proceedings of the International Tribology Conference Nagasaki, 2000.
5. E. I. Meletis, A. Erdemir and G. R. Fenske,Triblogical characteristics of DLC films and duplex plasma nitriding/DLC coating treatments, Surf. Coat. Technol. 73 (1995) 39–45.
6. M. G. Gee and M. J. Wicks, Ball crater testing for the measurement of the unlubricated sliding wear of wear-resistant coatings, Surf. Coat. Technol. 133–134 (2000) 376–382.
7. T. Michler and C. Siebert, Abrasive wear testing of DLC coatings deposited on plane and cylindrical parts, Surf. Coat. Technol. 163–164 (2003) 546–551.
8. M. Löhr, D. Spaltmann, S. Binkowski, E. Santner and M. Woydt, In Situ acoustic emission of wear life detection of DLC coating during slip-rolling friction, Wear, 2006 260 (2006) 469–478.

Wear Resistance of Amorphous DLC and Metal Containing DLC in Industrial Applications

G. J. van der Kolk

Abstract Diamond-like carbon (DLC)-based coatings have found widespread applications during the last 10 years and further application possibilities are rapidly emerging. Over the years, the DLC coatings have been highly optimized and tailored to meet the increasingly stringent application requirements of numerous mechanical and/or tribological systems. In this chapter, a brief overview is given of the typical wear modes and mechanisms encountered in practical applications. Effective solutions currently available for the various wear modes are also provided. Finally, some of the industrially used deposition technologies and practical applications are presented.

Keywords wear mechanisms, load carrying capacity, industrial applications

1 Wear Mechanisms in Practical Applications

For a comprehensive overview of various wear mechanisms that dominate the wear behaviour of various materials and coatings, readers should refer to the book by Chattopadhyay [1]. In general, it was found that the great majority of the wear mechanisms identified so far is related to the contact interfaces between two solid bodies. However, in most industrial applications, e.g. for plastic injection moulding, and for various components like valves and cylinders, the main wear mechanism is related to the fluid-to-body interfaces. Some specific examples are provided later in this chapter.

Naturally, the specific wear mechanism depends on the contact mode. Contact modes for various body-to-body interactions can be due to:

- Purely sliding mode
- Purely rolling mode
- Mixed mode; a combination of rolling and sliding

Ionbond Netherlands b.v., Groethofstraat 22b, NL 5916 PB Venlo, The Netherlands

C. Donnet and A. Erdemir (eds.), *Tribology of Diamond-Like Carbon Films: Fundamentals and Applications*.

- Purely impact mode
- Mixed impact and sliding mode

The most dominant wear mechanisms occurring in well-designed coating systems are:

- Abrasive wear
- Adhesive wear
- Fatigue wear
- Erosive wear
- Corrosive wear
- Impact wear

For improperly designed coating systems, one of the key wear mechanisms is related to the *load-carrying capacity*. Overloading may result in cohesive failure, and thus delamination in the film, or adhesive failure due to flaking of the film from the substrates or components.

In Table 1 the various contact modes and wear mechanisms are grouped for 2-body interactions. Corrosive and erosive wear are not considered and will not be discussed further in this chapter.

For the majority of industrial applications, a combination of sliding and impact wear may occur, where the contact loads are as high as possible and very close to the yield point of base materials. Consequently, the near surface regions of these materials need to be designed and optimized in such a way as to counteract abrasive, impact, and fatigue wear by increasing the load-carrying capacity.

The various contact mechanisms existing for some practical applications are given in Table 2.

Table 1 Dominant wear mechanisms for various contact modes (see also [2])

	Abrasive wear	Adhesive wear	Fatigue wear
Sliding mode	v	v	
Rolling mode	v		v
Mixed mode	v	v	v
Impact mode			v
Impact + sliding	v		v

Table 2 Contact mechanisms for practical applications

	Sliding	Rolling	Sliding + rolling	Impact	Impact + sliding
Roller bearing		v	v		
Plunger	v			v	
Sliding bearing	v				
Piston pin	v				
Valve				v	v
Tappet	v				v
Gear			v		v
Camshaft	v				v
Ejector pin	v				

1.1 Abrasive Wear

For reduction of abrasive wear, it is well known that there is an inverse proportionality to the surface hardness of the product. Generally, the wear is described by:

$$V \sim K.\, F_n.\, D / H \tag{1}$$

were V = wear volume; K = material and surface state-dependent constant; F_n = normal force; D = sliding distance; H = hardness (or shear yield of the softer surface).

1.2 Fatigue Wear

For fatigue wear, there are various models, since this type of wear is related to the pre-existence or accumulation of point defects on or within the solid bodies. The microstructure and nanostructure of the surface layers also play a dominant role. For metallic surfaces, fatigue wear may result from the formation of dislocations and vacancies under the influence of cyclic loading/unloading. In the later stages of deformation, void formation may take place at specific defect sites, finally resulting in large voids and microcracking. Fatigue generally decreases with increasing ratio between hardness (H) and E-modulus (E) as reported by Oberle et al. [3]. Johnson [4] has shown that the critical load for plastic deformation can be described as follows:

$$P_c \sim H^3/E^2_{mod} \tag{2}$$

where P_c = critical pressure for plastic deformation; H = hardness; E_{mod} = elastic modulus.

An overview of the importance of the elastic modulus is given by Leyland and Matthews in Ref. [5].

1.3 Load-carrying Capacity

Regarding the load-carrying capacity of a solid, failure generally occurs when the von Mises stress becomes higher than the critical yield stress of that solid. Systematic calculations regarding the load-carrying capacity of solid surfaces have been carried out by Schwarzer and Chudoba [6,7,8]. An example of the von Mises stress for a 2.1-μm-thick DLC film on a steel substrate under an indenter with a spherical tip is shown in Fig. 1 (from [7]). A complicating factor for DLC is the build-up of compressive stress as a function of deposition conditions and of layer thickness. Generally, the calculated von Mises stress can be superimposed on the

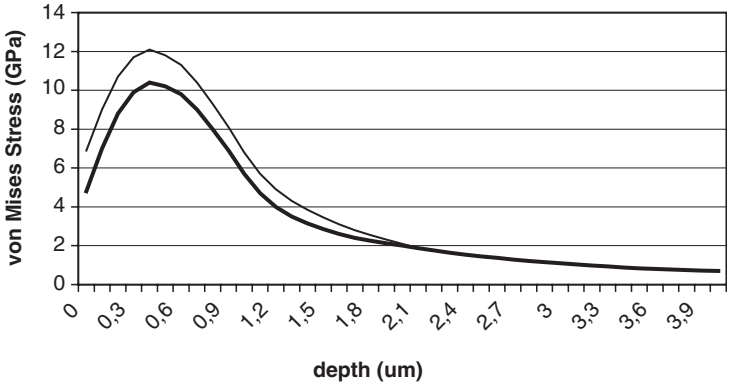

Fig. 1 Von Mises stress for 2.1-μm DLC on steel substrate with an indentation by a 4-μm sphere at a load of 19.7 mN (for details see [7]); the thin line is an assumed correction for compressive stress present in the DLC film

Table 3 Comparison of abrasive wear behaviour and load-carrying capacity of four different DLC-based coatings [9]

Coating type	a-C:H:Si/a-C:H	a-C:H:W	a-C:H:W/a-C:H	CrN/a-C:H
Deposition	RF PACVD	Magnetron	Magnetron/MF	Magnetron MF
a-C:H Thickness	1.5 μm		1.5 μm	1.5 μm
Nanohardness (GPa)	22	11	21	21
Vickers hardness (HV 0,02 g/mm2)	2,700	1,135	2,410	2,850
E-modulus (AFM, GPa)	200	120	187	185
Abrasive wear rate	0.7×10^{-15} m^{2}N	4×10^{-15} m^{2}N	0.7×10^{-15} m^{2}N	0.7×10^{-15} m^{2}N
Load-carrying capacity (arbitrary units)	66		130	180

compressive stress already existing within the material. Such a situation may result in the increase of the von Mises stress but lowering of the critical load at which the material yields.

In Figure 1 an assumed compressive stress of 1 GPa/μm is added to the calculated von Mises stress. Clearly the total stress is now 18% above the yield stress. Consequently the effective stress-absorbing capacity of the DLC coating compared with a zero-stress layer, like that calculated by Schwarzer, is reduced by 18%. For thicker DLC coatings the compressive stress reduces the effective stress-absorbing capacity. Therefore, in practical applications DLCs are grown as multilayers, with low stress-supporting films. As supporting layers, for example, nitrides, metal-containing DLC or Si-containing DLC are used, thereby limiting the thickness of the highly compressive DLC layer to 2–3 μm.

In a recent study by Hieke et al. [9], a number of DLC coatings with various support layers were produced using mid-frequency and radio-frequency power sources and their resistance to abrasion and load-carrying capacities was compared. The specific coatings used in their study are summarized in Table 3.

The abrasive wear of DLC coatings has been measured with a ball cratering system operating with an alumina suspension. To quantify the wear rate results, the volume of the coating removed by the cratering device was divided by the normal force and the track length of the rotating ball. A reasonable unit of wear is 10^{-15} m^2N. The reduction of abrasive wear with increasing hardness is clearly observed. Also noticeable in Table 3 is that the abrasive wear is only related to the hardness of the top DLC layer but the support layers do not play any significant role.

The load-carrying capacity of the DLC coatings was also determined by Hieke et al. [9] and compared under identical measurement conditions. Specifically, using a scratch tester they performed tests under increasing load (from 0 to 70 N), and the specific loads at which the film-substrate systems showed severe flaking were reported (see Table 3). A reference measurement was taken with a 1.5-μm a-C:H coating with Cr interface layer. As shown in the table, the load-carrying capacity of the a-C:H:W film that used a support layer was increased by 30%, and after using a base layer of CrN, it was further increased by 80%. Similar findings have been reported in Ref. [10].

1.4 Impact Wear

Impact wear of DLC-based coatings has been studied by a number of groups. Work by the group of de Hosson and Strondl [11,12,13] has indicated that a layered architecture can be very beneficial in delaying fatigue under impact loading. A stack of nanolayers of W-rich a-C:H:W and W-poor a-C:H:W can easily outperform a homogeneous a-C:H:W coating by a factor 2–3.

2 Examples of Industrial Application of DLC-based Coatings

In Fig. 2 the annual market value of coatings (in million euros) is shown for the tool and the component markets. The coatings can be done as part of the in-house operations or can be provided as a service. Although DLC-based coatings are used on tools like CD moulds, the mass volume application of DLC coatings is currently in the field of the component market. In fact, DLC-based coatings represent over 70% of component coatings at present.

2.1 Diesel Injection

The driving force for wide-scale application of DLC coatings has been the fuel injector systems used in diesel engines. Specifically, increasing injection pressures from 1,400 bar to well over 2,000 bar have forced diesel engine companies to apply

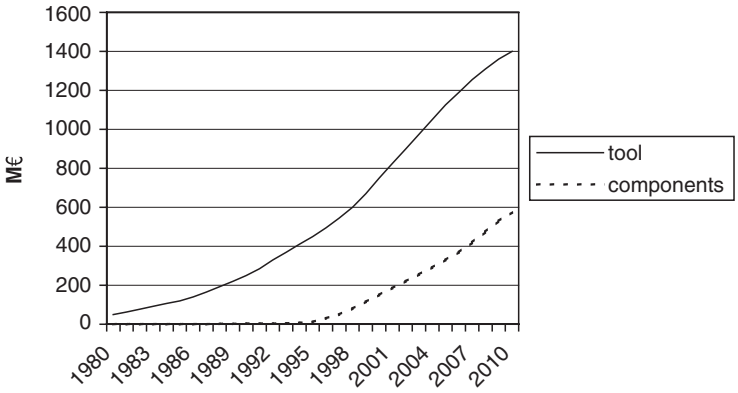

Fig. 2 Market value estimates (in million euros) for PVD and PACVD coatings for tools and components

Table 4 Worldwide introduction of DLC-based coatings on diesel injection systems

Europe	Patent	1983
initially a-C:H:W	Application development	1993
Now a-C:H:W/a-C:H	Large-volume application	1995 onwards
or CrN/a-C:H	Market penetration > 50%	~1998
Japan	Basic development	Late 1970s
Initially CrN	Application development	1990–1995
	Large-volume application	1995 onwards
	Market penetration >50%	
North America	Basic development	Late 1970s
Initially TiN	Application development	1990–1995
Now a-C:H:W/a-C:H	Large-volume application	1995 onwards
	Market penetration > 50%	

coatings on injector parts or plungers (see article by Treutler [14]). For diesel injection applications, initially coatings like TiN, CrN, and a-C:H:W have been used. Historic reasons have initially led to a preference per industrial zone for specific coatings (see Table 3). The tendency is now converging to multilayered coating systems, with a base layer of a-C:H:Me or a nitride and a top layer of a-C:H. In Table 4, the introduction speed of coatings on diesel injection pumps is shown.

2.2 Engine Parts

The high momentum occurring in present turbo diesel engines also results in excessive loads on parts in the valve train, like rocker arms and tappets, and on other parts in the engine like piston pins and crankshaft bearings (Figs 3 and 4). For tappets, the

Fig. 3 DLC-coated tappet

Fig. 4 DLC-coated piston pins

first mass volume applications started around 2002. Tappets are now routinely coated, the penetration is still limited (in the range of a small percentage) but is increasing stepwise. It is expected that a penetration of 10% will be reached by 2008.

For piston pins the driving factor for DLC coatings is based on cost-price reduction. The first mass volume coating of piston pins started only recently.

In Table 5, the penetration of DLC-based coatings for some mass volume applications is summarized.

Table 5 Uses of DLC coatings in various engine components

Application	Introduction	Penetration 2006 (%)	Coating
Diesel injection	1994	95	Multilayer a-C:H
Tappet	2002	2	Multilayer a-C:H, Cr_2N
Piston pin	2004	<1	Multilayer a-C:H
CD mould	Early 1990s	~100	a-C:H
Racing	Early 1990s	~100	Multilayer a-C:H
Gears	Early 1990s	~0	

2.3 Gears

For gears, numerous developments have taken place in recent years (see, e.g. [15–18]). However, these developments have not yet resulted in large volume applications. One of the key factors of coatings in gears is to reduce the friction coefficient; this will also result in lower failures due to micropitting. This is especially important when there is a compromise of lubrication conditions. It has been demonstrated by Murakawa et al. [15] that when a loss-of-lubrication situation occurs after a period of normal lubrication, surface improvements may extend the time period for running before catastrophic failure occurs. The two surface improvement methods they have investigated are:

- Micro shot-peening (MSP), which involves a mixture of metallic and ceramic powder with particle size 40–100 μm being shot-peened onto a grounded gear surface, resulting in a gear surface without grinding traces. The MSP treatment alone hardly increased the lifetime under dry running conditions.
- PVD coating: a-C:H:W coatings were used to coat both untreated gears and MSP-treated gears. The PVD coating prolonged the running time under loss-of-lubricant conditions by a factor of 2–3, relative to the uncoated gears. Further, the combination of an MSP and PVD coating prolonged the running time considerably.

Gears are coated in those applications where loss of lubrication may have catastrophic consequences (e.g. helicopters), or where maintenance is very expensive and hence the expenditure for coating is less relevant (e.g. gears for large windmills).

2.4 Other Industrial Applications

There are numerous other applications and here are some examples:

- Medical – screws to reduce friction and prevent metal ion release
- Moulding – ejectors, moulds; to reduce wear and friction
- Aerospace – various parts to reduce friction and fretting wear
- Textile needles – to reduce wear
- Compressors – to allow higher pressures and to reduce wear

3 Conclusions

The introduction of DLC-based coatings in industrial applications started some 10 years ago. Currently in some applications a penetration of nearly 100% has been achieved. In other applications, the penetration is still far below the maximum achievable. It is expected that within the next 5–10 years, the applications of DLC coatings will grow further.

The longer-term developments (10-year scale) will probably bring a reduction of DLC-based coatings in automotive applications. It is expected that when fuel cell technology is used for normal engines, the amount of surface-treated parts will be drastically reduced. The majority of DLC-coating applications in automotive industry is linked with sliding, rolling or rotating engine components, which will become obsolete as the future engines are powered by fuel cells (see Paatsch [19] for an overview). However, applications in other fields (such as manufacturing, medical, textile, aerospace) are expected to steadily increase.

References

1. R. Chattopadhyay, Surface wear, analysis, treatment and prevention, ASM International 2001, Materials Park, OH, ISBN 0-87170-702-0.
2. G. L Doll, R. D. Evans, and S. P. Johnson, 48th Annual Technical Conference Proceedings of the Society of Vacuum Coaters (2005) 595–598.
3. T. L. Oberle, J. of Met. (1951) 438.
4. K. L. Johnson, Contact Mechanics, Cambridge University Press, London UK, ISBN 0-521-34796-3.
5. A. Leyland and A. Matthews, Wear 246(2000) 1–11.
6. N. Schwarzer, Surf. Coat. Technol. 133–134(2000) 397.
7. T. Chudoba, N. Schwarzer, and F. Richter, Surf. Coat. Technol. 154 (2002) 140–151.
8. N. Schwarzer, T. Chudoba, D. Billep, and F. Richter, Surf. Coat. Technol. 116–119(1999) 244.
9. A. Hieke, T. Hurkmans, G. J. van der Kolk, M. Tobler, and R. Bonetti, 48th Annual Technical Conference Proceedings of the Society of Vacuum Coaters (2005) 556–561.
10. P. Maurin-Perrier, R. Riand, C. Heau, B. Engelric., and A. Sommer. Paper presented at International Conference on Metallurgical Coatings 2005.
11. N. J. M. Carvalho, J. T. M. de Hosson, Materials Research Society 697 (2002) 15–21.
12. C. Strondl, G. J. van der Kolk, T. Hurkmans, W. Fkeischer, T. Trinh, N. Carvalho, and J. T. M. de Hosson, Surf. Coat. Technol. 142 (2001) 707–713.
13. C. Strondl, G. J. van der Kolk, T. Hurkmans, W. Fleischer, N. M. Carvalho, and J. T. M. de Hosson. 44th Annual Technical Conference Proceedings of the Society of Vacuum Coaters (2001) 67–71.
14. C. P. O. Treutler, Surf. Coat. Technol. 200 (2005) 1969–1975.
15. M. Murakawa, T. Komori, S. Takeuchi, and K. Miyoshi. Surf. Coat. Technol., 120–121: (1999) 646–652.
16. O. Hurasky-Schönwerth and M. Weck. PVD-coatings and synthetic ester in the tribological system of gear contact (in German), Tagungsband 41, Arbeitstagung: Zahnrad und Getriebeuntersuchungen, WZL, RWTH Aachen 2000.
17. O. Hurasky-Schönwerth and M. Weck. Behavior of PVD-coatings in rolling contact (in German), Tagungsband 40, Arbeitstagung: Zahnrad und Getriebeuntersuchungen, WZL, RWTH Aachen 1999.

18. M. Weck and O. Hurasky-Schönwerth. Environmentally compatible tribo-systems in gearing. Proceedings of the 4th World congress on gearing and power transmission, Paris 1999, p. 2159–2172.
19. W. Paatsch, Surf. Coat. Technol. 169–170 (2003) 753–757.

DLC Films in Biomedical Applications

R. Hauert

Abstract Diamond-like carbon (DLC) has outstanding tribological properties and is, additionally, tolerated well by the body. Due to this advantageous combination of properties, research and development efforts have been made toward the use of DLC coatings in biomedical applications. It has been demonstrated that DLC coatings do not trigger any adverse effects on attached cells and that DLC can be considered to be biocompatible by in vivo and also many in vitro experiments. DLC surfaces also have an excellent haemocompatibility and DLC-coated cardiovascular implants such as artificial heart valves, blood pumps, and stents are already commercially available. The different studies presented demonstrate that DLC has the ability to reduce wear, more or less independently of the lubricant used, in load-bearing implants when sliding against metals or against DLC. However, it seems that when DLC slides against ultra high molecular weight polyethylene (UHMWPE) in the presence of body fluids, the good tribological properties that DLC shows in air could not be obtained. The in vitro experiments of DLC sliding against UHMWPE apparently showed different results, due to variations in experimental setups (ball-on-disk, hip or knee simulator, surface roughness) and especially the different liquids used as lubricants. In some medical applications such as guidewires, urinary tract catheters, and orthodontic archwires, the in vitro and in vivo experiments on DLC-coated parts showed an improved tribological performance. When implanting a DLC-coated material, it has to be considered that the reaction layer at the DLC/substrate interface has to have a high chemical durability under in vivo conditions to guarantee lifetime adhesion.

Keywords diamond-like carbon, DLC, amorphous hydrogenated carbon, biomedical application, load-bearing implant, hip joint, knee joint, interface, UHMWPE, lubricant

Swiss Federal Laboratories for Materials Testing and Research, Empa, Dübendorf, Switzerland

C. Donnet and A. Erdemir (eds.), *Tribology of Diamond-Like Carbon Films: Fundamentals and Applications*.

1 Introduction

Nowadays, due to overaging of the population as well as the increasing average weight of people, an increasing number of load-bearing joints have to be replaced by artificial implants, mainly hip joints and knee joints but also, to a lesser extent, other joints such as spinal disks. Additionally, diseases like arthritis can also require the replacement of joints.

Different materials for joints, with specific advantages and disadvantages, are implanted today. In prosthetic hip replacements the most commonly used implant materials are a steel femoral head articulating against an ultra high molecular weight polyethylene (UHMWPE) acetabular cup. The average wear rate of the polymer cup is in the range of 20–60 mm^3/year mainly in the form of micrometer-sized wear particles. The approximately 10^{10}–10^{11} polyethylene particles generated a year (or about 50,000/each single step) have been identified as the main factor limiting the lifetime of the implants. The large number of these particles, their size, as well as their ability to adsorb endotoxins [1] can induce inflammatory reactions causing bone resorption, which may lead to implant loosening (aseptic loosening). When a ceramic femoral head is used instead of a metallic one, according to clinical investigation, the wear rate of the UHMWPE cup can be further reduced, on average by 50% [2], which is still a large number of particles. Metal on metal hip joints have wear rates in the range of 1–5 mm^3/year, which amounts to around 10^9-µm-sized particles. Additionally, increased metal ion blood levels are observed, which can cause a delayed-type metal hypersensitivity. These metallic particles also may adsorb endotoxins supporting aseptic implant loosening. Additionally, we have to keep in mind that the number of allergies is increasing at a rate of about 10% each year. It is not known if, in the future, humans will also develop new allergies against implant metals or metallic particles. Ceramic on ceramic joints show very low wear in the range of 0.05 mm^3/year [2]; however, they may crack and release millions of hard particles which cannot all be removed surgically. The replacement joint can, therefore, only be a ceramic on ceramic type, since metals or UHMWPE would be worn out quickly by ceramic particles that migrate onto the articulating surfaces. An overview article of the different materials and surface treatments used in load-bearing surfaces in human joint replacements was published in 1999 by Dearnley [3]. A comparative study of the performance of metallic and ceramic femoral heads, and especially the importance of the surface finish, was published by Dowson [2].

To overcome the problem of particle generation in artificial implants, the use of a very low wear coating material which is additionally biocompatible is required. Since diamond-like carbon (DLC) coatings are known to be biocompatible and are also known to have extremely low wear rates in many applications, the biotribology of DLC coatings has been investigated in vitro. Several hundred DLC-coated artificial joints have already been implanted; however, these turned out to be rather problematic. Two main fields of biological applications of DLC have emerged. One application is the coating of implants that are in direct contact with blood.

Among these are heart valves, blood pumps, and stents. Another application is the use of DLC coatings to reduce wear in load-bearing joints. The different results published on experiments with DLC-coated femoral heads sliding against polyethylene cups revealed unexpected problems. However, joints where both sides are coated with DLC show promising results in laboratory tests. For an overview of DLC coatings in biological applications see Ref. [4].

In the following sections, the biocompatibility of DLC surfaces will be described and thereafter the biotribology of DLC and especially the crucial influence of lubricants will be addressed.

2 Biocompatible DLC and Alloyed DLC Surfaces

When a material is implanted into the body it has to be biocompatible. In vivo, the implant materials have to withstand the corrosive environment and not cause inflammatory or repulsive body reactions or any other undesirable effect. Additionally, the materials have to perform their desired function, such as low wear and fast bone ingrowths, over a long time.

Usually, the expected tissue reactions are first assessed by in vitro cell experiments. However, cell experiments cannot determine the in vivo biocompatibility of a certain material, but cell tests, if successful, can describe the principal biological in vitro response of a surface and are, therefore, an important step toward in vivo testing.

A number of research groups have investigated cell behavior by growing different cell types in vitro on DLC and studying the cell response. Macrophages, fibroblasts, human myeloblastic ML-1, human embryo kidney 293 cells, and other cell types have been grown on DLC under different conditions, and cell responses such as proliferation rate, viability, cell adhesion, differentiation, cell morphology, and cytoskeletal architecture have been monitored.

Fibroblast cells, for example, cultured on DLC- and N-containing DLC films, showed an excellent cytocompatibility (cell-compatibility) by means of proliferation rate and morphological behavior. In Fig. 1, a scanning electron microscope (SEM) image is shown of two mouse fibroblast cells (M3T3 cell line) immediately after mitosis, which illustrates the cell activity. Additionally, the cells keep intense contact with the underlying cell layer by their filopodiae and the cell surfaces show a high density of microvilli.

These in vitro experiments, as well as the in vivo reaction of DLC-coated CoCr cylinders implanted for 90 days in the lateral femoral cortex of sheep, showed that the DLC-coated surfaces are well tolerated by the body [5]. Mohanty et al. [6] confirmed the in vivo biocompatibility on DLC-coated Ti samples implanted in the skeletal muscle of rabbits for up to 1 year. An overview of the reaction of different cells on DLC can also be found in review articles [7,8].

When a material is implanted into the body, in a first step, depending on the chemical situation at the surface, proteins will adsorb onto the surface. These protein

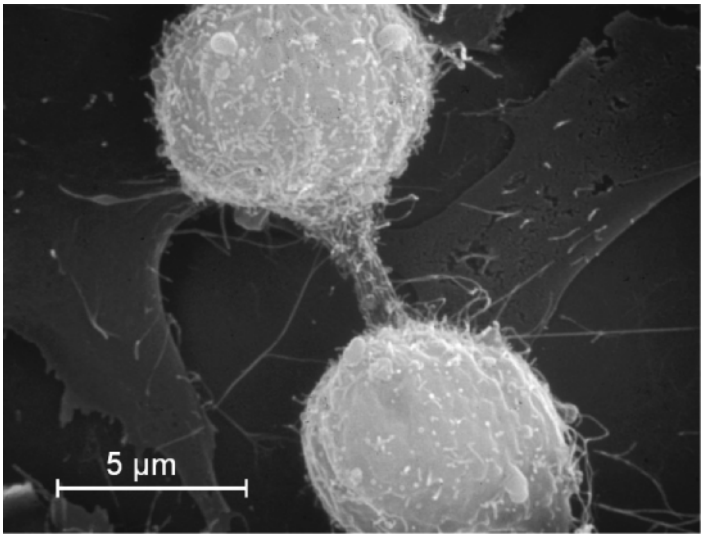

Fig. 1 SEM image of two mouse fibroblast cells after mitosis on a DLC substrate. The intense contact of the cells to the underlying cell layer by their filopodiae, as well as the high density of microvilli at the cell surfaces demonstrate the cell-compatibility of the DLC surface

distributions will then interact with the different cells and strongly influence cell attachment, cell proliferation, and cell differentiation. Additionally, on articulating surfaces of artificial joints, the wetting angle as well as the ability of a surface to attract biomolecules present in the synovial fluid (e.g., phospholipids, glycoproteins such as lubricin, albumin, hyaluronic acid) influence the biotribological behavior of the joint.

The surface chemical behavior of DLC can be easily tuned by the addition of different elements into the DLC film. This can be done by ion-beam implantation or by alloying DLC with other elements, which must also be biocompatible. By varying the alloy element concentration, it should be possible to tailor the biological reactions to any desired point between the properties of DLC and those of the added element. However, it has to be guaranteed that the alloyed DLC is also biocompatible. In the past years a few papers have presented experiments where the biological reactions on DLC have been changed by alloying. Especially the addition of SiO_x to DLC seems to result in a reduction of inflammatory reactions. Scheerder et al. [9] report on DLC-coated and DLN-coated or Dylyn (diamond-like nanocomposite, a Si:O containing DLC)-coated stainless-steel stents, which were implanted in pigs for 6 weeks. Their histopathological observation on the explanted stents showed that the inflammatory reactions, monitored by the number of inflammatory cells on the stent surface, were significantly higher on DLC than on DLN. Similarly, some companies (Sulzer CarboMedics and St. Jude Medical) use silicon-alloyed pyrolytic carbons (Pyrolite), a material that proved to be resistant to blood clotting, also

indicating an improved biocompatibility by the addition of Si. Dorner-Reisel et al. [10] demonstrated that the addition of Ca-O to DLC decreased the film hardness, the wetting angle, and the fraction of sp^3/sp^2-bonded carbon. Cell tests with mouse fibroblast showed an increased number of cells, when compared to pure DLC, as well as improved cell viability for the Ca-O-DLC films. DLC samples containing different concentrations of titanium have also been examined in vitro to obtain a biocompatible surface that is hard, preventing abrasion and scratching. When Ti-DLC is exposed to a biological environment, the adsorption of different proteins could be altered as a function of the Ti content in the DLC film [11]. The adsorbed proteins will subsequently influence cell attachment, cell proliferation, and cell differentiation and probably even the tribological behavior. Bone marrow cell culture experiments on these Ti-DLC coatings demonstrated that the differentiation of bone marrow cells into bone resorbing cells, i.e. osteoclasts, is inhibited by the addition of Ti into the DLC [12].

When introducing a coating into the body, the long-term adhesion has to be guaranteed. Additionally, in the worst case of total film delamination, the generated particles should not have any harmful effects. It is known that materials that are tolerated well in bulk form are able to induce toxic reaction if present in particulate form, such as asbestos or quartz dust. Therefore, particles have been deliberately delaminated from a 500-nm-thick DLC film deposited on polyethylene foil as can be seen in Fig. 2 (left). From the average area of the particles of about $20\,\mu m^2$, a total film delamination in a hip joint would generate around 5×10^7 DLC particles. To investigate the biological reactions induced by delaminated DLC particles, bone marrow cell cultures have been incubated in vitro with these particles. The cells were able to internalize most of the particles within a few days, as displayed in Fig. 2 (right). Furthermore, the appearance of the cells was not different from the control cultures with no particles after 7 days. The addition of particles did not have any effect either on the cell viability or on the proliferation or differentiation, indicating that no toxic or inflammatory reaction of the body to

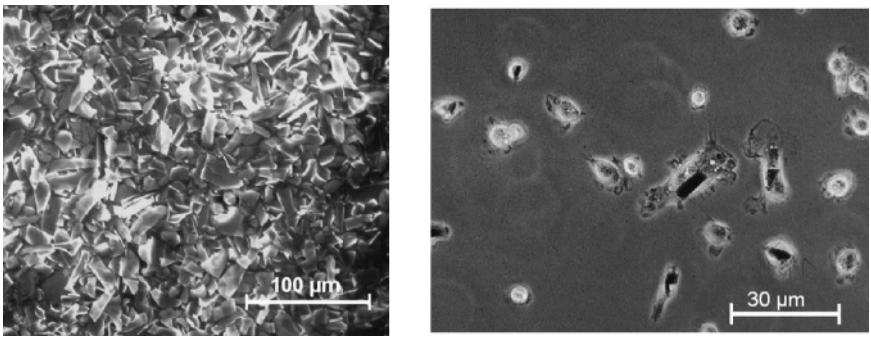

Fig. 2 (*Left*) SEM picture of deliberately delaminated particles from a 500-nm-thick DLC film. (*Right*) Phase contrast microscopy after 3 days in culture, bone marrow cells internalized the particles [13]

delaminated DLC particles may be expected [13]. Similarly, Aspenberg et al. showed that diamond or SiC particles, introduced into implanted bone harvest chambers in rabbits, did not cause any decrease in bone formation, whereas polyethylene, cobalt-chromium or bone cement particles caused inflammatory reaction and reduced bone ingrowth [14].

3 Blood-Contacting Applications

The excellent tribological properties of DLC are usually not of prime interest for blood-contacting applications; however, for some applications such as blood pumps and heart valves (friction in the hinges) the combination of the good haemocompatibility and excellent tribological behavior is required. For a more detailed description see Ref. [4] and other references therein.

For implants in direct contact with blood, a key issue is the ability of the implant surface to prevent thrombus formation. It is generally known that increased platelet adhesion, activation and aggregation on implant surfaces exposed to blood precede the formation of a thrombus. Therefore, in vitro analysis of these properties is usually performed as a first test of the haemocompatibility of a surface. Several papers of in vitro assays on DLC surfaces indicate that this material may have the ability to suppress thrombus formation similar to, or even better than, glassy carbon, a material widely used for heart valves. Maguire et al. describe the beneficial properties of Si-doped DLC for applications on stents and guidewires. By using Si doping, the mechanical barrier properties, and the in vitro response of DLC coatings have been improved [15]. Only a few papers present in vivo results of DLC-coated implants. In his Ph.D. thesis [16], Yang studied the haemocompatibility of different surfaces implanted for 2 h into the intrathoracic venae cavae of Swedish native sheep. The results showed that there were significantly more blood platelets on pyrolytic carbon and methylated titanium than on titanium, cobalt-chromium and DLC [16]. A DLC-coated centrifugal ventricular blood pump device (made by SunMedical Technology Research Corporation, Nagano, Japan) coated with DLC was implanted in calves and, even without postoperative anticoagulation, only minor evidence of thrombosis was found on the DLC-coated surfaces after explantation. Due to the good haemocompatibility of DLC, a few companies have DLC-coated implants already commercially available or in the state of development. The company Sorin Biomedica produces heart valves, annuloplasty rings, and stents that are coated by a so-called Carbofilm. A clinical study on the coated stents, implanted in 122 patients, showed a low restenosis rate of 11% after 6 months [17], whereas another medical follow-up did not show any difference in the restenosis rate between Carbofilm-coated and Carbofilm-uncoated stainless-steel stents [18]. Annuloplasty rings (used for heart valve repair) coated with Carbofilm have been implanted in sheep for 2–4 months and the explants showed an excellent biocompatibility and no thrombosis [19].

4 Tribology of DLC in Load-bearing Implants and the Influence of Lubricants

It is known that DLC shows a very low wear and also a low friction in atmosphere against most materials, except some polymers, and as shown in the last paragraph DLC can be expected to be biocompatible in in vivo applications. Furthermore, DLC has, when sliding in ambient atmosphere against certain materials, the ability to form a transfer layer on the softer counterpart, protecting it from wear. All this makes DLC a promising candidate for application on the articulating surfaces of orthopedic implants. For illustration, one of our own DLC-coated femoral heads is displayed in Fig. 3. A comparison of the potential of different coatings in hip replacement can be found in Ref. [20].

Many papers reporting on biotribological experiments involve either a ball-on-disk setup or a hip simulator to determine friction and wear of DLC-coated hip joint balls sliding against UHMWPE or of metal/metal joints with one or both sides coated with DLC. Depending on the test setup and especially the liquid lubricant used, different results can be found in the literature.

Fig. 3 DLC-coated femoral head of a hip joint

4.1 DLC-coated Femoral Heads Articulating Against UHMWPE Cups

As described in the introduction, in prosthetic implants consisting of a steel head sliding against UHMWPE, the polyethylene wear particles produced are the main cause for implant loosening. Making the steel surface harder with a DLC coating will probably protect it from scratches and corrosive attack (as with ceramic heads) but to lower the wear of the softer UHMWPE counterpart, the buildup of a transfer layer may be required. Additionally, it has to be considered that the adsorption of lubricating biomolecules on DLC may be different than on steel, which will also influence the tribological behavior. However, it is questionable if the buildup of a transfer layer on the polymeric cup can take place in a joint where body fluids are capable of reacting with wear products and of removing wear products out of the tribological contact area.

In the literature, experiments with different setups, especially different lubricants, are described. In cases where water or aqueous NaCl (aqNaCl) are used as lubricants, a reduction of the UHMWPE wear is usually obtained. Tetrahedral amorphous carbon (ta-C)-coated metal hip joint balls tested in 1 wt % aqNaCl with ball-on-disk and in a hip joint simulator showed a reduced wear of the UHMWPE cup by a factor of 10–100, compared to the uncoated samples [21,22]. A decrease of a factor of 5 in wear of the UHMWPE was obtained by coating the cobalt-chromium counterface with DLC when tested in a knee wear simulator using distilled water as a lubricant [23]. Different coatings have been tested with a ball-on-disk, also using distilled water as a lubricant, and a large decrease in UHMWPE wear was obtained with all the coatings. However, under these conditions, the thermally oxidized Ti6Al4V surface still performed about 8 times better than the DLC coating [24]. Analogously, DLC-coated stainless-steel femoral heads have been tested against UHMWPE cups in a hip joint simulator using distilled water as a lubricant. A decrease of the UHMWPE wear by a factor of 6 was obtained with the DLC coating. The same low wear rate of the UHMWPE was also obtained when using a zirconia femoral head under the same test conditions [25].

The setups described in this paragraph used diluted bovine serum. Saikko et al. [26] compared the wear of UHMWPE cups operated against CoCr, alumina, and DLC-coated CoCr hip joint balls in a biaxial hip wear simulator in the presence of diluted bovine serum. For all three combinations tested, they obtained wear rates of the UHMWPE cups between 48 and 57 mg/million cycles. Thus, they observed no significant difference in the wear due to the DLC coating and all wear values obtained are in the range known from clinical observations with CoCr and alumina hip joint balls. Similar results have also been obtained by Affatato et al. [27]. Femoral heads made from 316L stainless steel, alumina, CoCrMo, and DLC-coated TiAlV were tested in a hip joint simulator using bovine serum as a lubricant. They obtained wear rates of the UHMWPE cups between 25 and 37 mg/ million cycles for all four material used as femoral heads.

From the results shown above, it can be seen that, depending on setup and the lubricant used, different results on the wear of DLC sliding against UHMWPE are obtained. It was shown that, depending on the tribological conditions, DLC is able to form a transfer layer on the counterpart when using distilled water as a lubricant [28], which may explain the low wear results found when tested in water and aqNaCl. In the cases where bovine serum and synovial fluid are used as lubricant, the different biomolecules, especially phospholipids, glycoproteins, albumin, and hyaluronic acid adsorbed on the articulating surfaces, are able to strongly influence the tribological behavior in the joints. The transfer of polymer to the metallic surface and also the amount and size of particles produced are influenced by the biomolecular composition [29–33]. Analogous to Ref. [29], it was also shown that long polyethylene glycol chains attached in a brush-like arrangement on a surface are able to trap water in between their chains resulting in about 20-nm-thick fluid film (with increased viscosity of water) and a lower friction.

In joint simulators, it was shown that when the protein concentration is too low, the results may show a nonclinically relevant wear morphology [31] and variations in the serum protein concentrations produce different wear results [30]. Additionally, in a tribological setup, it has to be considered that a change of the conformational state of adsorbed biomolecules due to local overheating (thermal denaturation) can change the tribological outcome [31]. The surface texture also has a decisive influence on the wear behavior of a joint. Even single scratches, which may not be detected by an average surface roughness measurement, are capable of increasing the wear rate of UHMWPE by a factor of 30–70 [32].

In summary, it can be stated that wear tests on load-bearing implants having a polymer as a counterpart should be made with an adequate tribological setup such as an implant joint simulator. As a lubricant, a supply of a solution containing an adequate distribution of tribologically relevant biomolecules (such as serum or synovial liquid), has to be maintained to compensate for the proteins decomposed in the test due to high pressures between contact spots of the bearing [33]. From the different experiments shown above, it seems that no transfer layer is formed on the UHMWPE when sliding against DLC in biological media and the UHMWPE wear could not be lowered.

4.2 DLC-coated Femoral Heads Articulating Against Metal or Against DLC-coated Cups

Lappalainen et al. reported very low wear rates in metal/metal hip joints, with both sides coated with hydrogen-free DLC made by filtered pulsed plasma arc discharge (85% sp^3 bonding). The long-duration wear tests of 15,000,000 cycles (corresponding to about 15 years of implant use) with a hip joint simulator using bovine serum as a lubricant, which was replaced regularly to compensate for depleted proteins, showed extremely low wear below 10–4 mm^3/year [34]. Similarly, Tiainen investigated hip joints with both sides having an approximately 100-µm-thick layer of

hydrogen-free DLC also made by filtered pulsed plasma arc discharge. Using a hip joint simulator and aqNaCl as a lubricant, a reduction of the wear rates, by a factor of about 10,000, corresponding to wear rates of 10^{-3} to 10^{-4} mm^3/year, have been reported [21]. Shi et al. tested steel, ceramic, and a 2-µm-thick DLC (a-C:H)-coated steel ball sliding against a flat steel plate and using bovine serum as lubricant. They found a large reduction of the ball wear by about a factor of 100, as well as reduced wear rate in the stainless-steel plate [35].

The clinically relevant tests made on a hip simulator in bovine serum did lead to very low wear rates; however, the tests performed in aqNaCl or with a pin on disk setup also led to comparable low wear values. It seems that in the case where DLC is articulating against DLC, the biotribological behavior does not change dramatically in the presence of proteins or that the buildup of a transfer layer may not be a key requirement for low wear (analogous to DLC/sapphire in atmosphere [36]).

4.3 DLC-coated Joint Replacements Articulating Against UHMWPE Implanted in Humans

To my knowledge, none of the global implant manufacturing companies sell DLC-coated load-bearing implants today. Dearnley [3] states in his review article, published in 1999, that he is unaware of any commercially available DLC-coated bearing surfaces for joint replacements. However, in recent years some materials and coating companies have offered DLC-coated implants. For example, the company Morgan Technical Ceramics offers in its news release (No. 4 July–December 2005) hip joints coated with Diamonex DLC. Until 2005, the French company M.I.L. SA (Matériels Implants du Limousin SA) commercially offered DLC-coated titanium shoulder joint balls and ankle joints with both parts (the tibial and the talar component) made from a nitrided AISI Z5 CNMD 21 steel and coated with DLC, but there is no published medical follow-up on the in vivo behavior of these implants.

In the two cases described below, DLC-coated knee and hip joints have been implanted, and in both cases a high rate of implant failure required revision surgery.

Up to 2001, the company Implant Design AG sold knee joints under the trade name Diamond Rota Gliding with the sliding area of the femur component coated with DLN (diamond-like nanocomposite, a SiO_x containing DLC described in reference [37]) that was sliding against a UHMWPE counterpart. Within a short time many of the ~190 implanted joints showed increased wear, partial coating delamination, as well as implant loosening. In July 2001, the implantation of this knee joint was forbidden by the Swiss Federal Office of Public Health (SFOPH).

A medical follow-up on 101 patients with DLC-coated femoral heads articulating against polyethylene was published in 2003 by Teager et al. [38]. The DLC-coated femoral heads with the trade name Adamante had been obtained from the company Biomecanique, France, and consisted of a 2–3-µm-thick DLC coating on

a Ti6Al4V alloy ball, made by ion-beam deposition. While the DLC-coated implants showed no sign of problems within the first 1.5 years, thereafter more and more DLC implants showed aseptic loosening, requiring revision of the implant. The cause for aseptic loosening is the large amount of polyethylene wear particles, generated from the prosthesis, that initiate a macrophage-mediated inflammatory response, leading to osteoclast cells activation and resulting in bone resorption in the vicinity of the implant and finally implant loosening. Within 8.5 years, 45% of the implanted DLC-coated joints had to be replaced. The DLC coating on the retrieved joint heads showed numerous, mostly round, pits of complete film delamination whereas the remaining DLC film seemed to be undamaged.

In my opinion, the cause for the adhesive failure at the interface has to be attributed to the chemical stability of the DLC/Ti6Al4V interface. When a DLC coating is deposited onto a metallic substrate, usually about 1-nm-thick metal–carbide reaction layer is formed at the interface, which is responsible for good adhesion. Depending on the precleaning and the conditions at the very beginning of the DLC deposition process, the interface reaction layer may also consist of metal-oxy-carbide. On implantation, the long-term chemical stability of this interface reaction layer toward body fluids has to be guaranteed. That aqueous fluids, particularly phosphate buffered saline solution (PBS), can penetrate the coating through pinholes and slowly corrode the interface between DLC and a-Si: H/DLC is described in Ref. [39]. An example of oxygen containing instable interface, leading to ongoing interface corrosion and delamination, even during storage in ambient atmosphere, is given in Ref. [40]. In vivo interface corrosion involves the chemistry at the interface and probably also residual stress, the load pattern applied, and electrochemical aspects, and is not fully understood today.

5 The DLC Substrate Interface

As described above, the coating/substrate interface, in connection with the internal stress of the film and the applied load pattern during use, may be critical in determining the long-term coating adhesion. Therefore, an exact determination of the chemistry at the interface is required. Since the carbidic reaction layer at the interface usually has a thickness in the range of 1 nm, angle-resolved x-ray photoelectron spectroscopy (XPS) or XPS and Auger electron spectroscopy (AES) sputter depth profiling can be used to analyze the interface.

During depth profiling, the argon ion energies are usually between 500 and 5000 eV, which is more than the energy of chemical bonds and, therefore, depth profiling may alter the chemistry originally present at the interface [41]. On the other hand, the DLC films are deposited by ion-assisted processes, with the ions having energies between 20 and 200 eV, which is also higher than the energy of chemical bonds. Therefore, the interface chemistry observed during depth profiling of a DLC/metal interface displays the ability of the interface to form a reaction layer, but this is about the same interface chemistry as observed by nondestructive

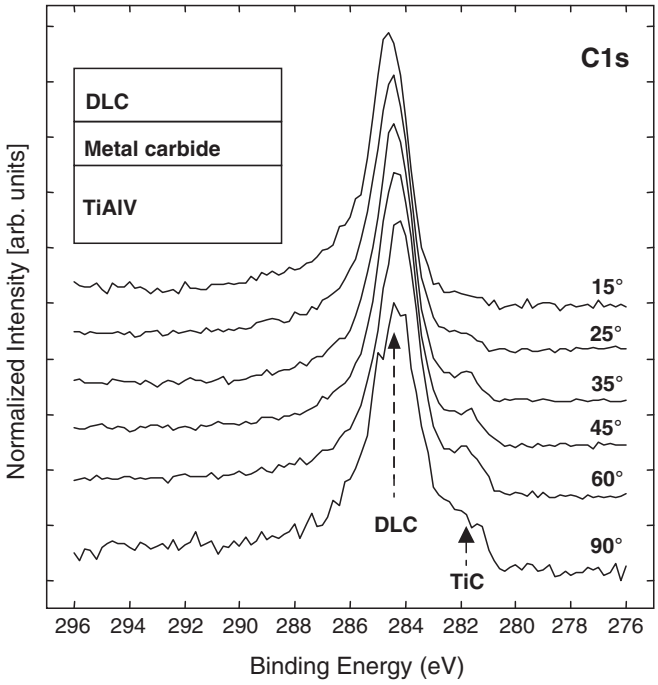

Fig. 4 Angle-resolved XPS analysis of a 5-nm DLC film on medical TiAlV. At high observation angle (perpendicular to the surface) the carbidic state of the interface can be seen

angle-resolved XPS. One main difference is that the carbidic interface reaction layer seen in depth profiles is usually thicker than the original interlayer determined by angle-resolved XPS [42]. Figure 4 displays an angle-resolved XPS analysis through a 5-nm-thick DLC film on TiAlV surgical alloy. The angles are given with respect to the surface. At high angles the carbidic nature of the interface can be observed by the appearance of the carbidic C1's contribution (mainly TiC) at 282-eV binding energy. From the analysis of the Ti, Al, and V electrons, we can determine that they are all in a carbidic state at the interface. Unfortunately, neither XPS nor AES can determine hydrogen, which, therefore, may or may not be present in the interface reaction layer.

The chemistry at an interface can be influenced or improved by the deposition of interlayers. In many industrial processes, ~50-nm-thick chromium, titanium interlayers or even multilayers are used. For implant materials, tantalum [43] and niobium interlayers are biocompatible and may show good interface properties. Additional, graded interfaces may also h ave some beneficial effects, since the grading allows an adaptation of the mechanical properties. On the other hand, the use of interlayers between the substrate and the DLC generates two interfaces, which both must adhere and be stable in the long term in vivo.

6 Other DLC Applications Connected to Tribology

There are other biomedical applications under development which may, depending on the success of research, be commercially available in some years. A few examples are given below. The torque used to insert or remove stainless-steel bone screws could be reduced by 50% with an amorphous diamond (AD) coating on the screws [44]. The DLC coating of medical guidewires could reduce the friction upon advancement by up to 33% and also particle generation and corrosion resistance could be improved [15]. Similarly, the DLC and F-DLC coatings on stainless-steel guidewires, tested in vitro under vascular conditions, resulted in a 30% reduction of the load, depending on the setup [45]. The University of Bonn reported that DLC-coated urinary tract catheters and ureter stents can prevent bacterial growth and incrustation. On the tribological side (inserting and replacing the catheter), the coated catheters are easier to insert and additionally the patients described the procedure with DLC-coated urinary tract catheters as substantially less unpleasant [46].

In dental correction, orthodontic archwires and brackets, usually made of stainless steel or NiTi, are used. The two main disadvantages of these alloys are the release of Ni ions, with the prevalence of allergic reactions, as well as a high coefficient of friction between the wire and the brackets. The archwire is designed to impose a force perpendicular to the wire (or along the radius of curvature) on the tooth, but a high coefficient of static friction will introduce unwanted tangential forces. It was shown by in vitro tests that the nickel ion release could be drastically reduced by a DLC coating [47,48]. Additionally, the coefficient of friction between the archwire and the brackets could be reduced, as shown by in vitro tests, with DLC-coated stainless steel and TiAlV archwires and brackets [49]. In humid air (75% R.H.) the static friction of steel against steel was measured to be 0.21 and it was reduced to 0.16 for DLC against steel [50] and to 0.15 for Si-DLC against steel [51]. On repeat experiments at the same positions the static coefficient of friction on steel against steel starts to scatter between 0.22 and 0.7 whereas it stays stable for the DLC and Si-DLC samples. For future successful applications, in vivo tests have to be performed on, for example, the adhesion of deposits by biomineralization and by bacteria, and its influence on the static friction.

7 Summary

In all the in vitro and in vivo cell culture experiments on DLC, no adverse effect of the coating on the cells has been observed and, therefore, DLC can be expected to be biocompatible in most in vivo applications. However, as DLC is a class of material, it has to be noticed that with altered deposition conditions, different biological reactions may be obtained. Therefore, any biological results on DLC should be correlated with an exact description of the deposition conditions, including pretreatment and a detailed characterization of the coating.

The different studies presented demonstrate that DLC has the ability to reduce wear, more or less independently of the lubricant used, in load-bearing implants when sliding against metals or against DLC. However, when DLC slides against UHMWPE in the presence of serum, the good tribological properties which DLC shows in air or vacuum cannot be obtained in load-bearing implants. The in vitro experiments of DLC sliding against UHMWPE showed different results, due to the different experimental setups (ball-on-disk, hip or knee simulator, surface roughness) and especially the different liquids used as lubricants.

In implant technology, issues like biocompatibility, long-term adhesion, corrosion stability, allergic reactions to corrosion products, and possible toxicity of delaminated particles have to be considered. In biotribology, additionally, the tribochemistry plays a crucial role and the adhesion of lubricating molecules to the surface, the reaction of wear products with lubricating molecules or biomolecules, the deposition of reaction products or biomolecules on the implant surface, as well as any cell reaction to wear products have to be considered. Furthermore, the applied load pattern, the amount of different lubricating molecules generated by the body, the cell reaction to wear products, etc. may also differ from patient to patient. Biotribology is a system property, involving the complex interaction of many factors and cannot be viewed as a sum of independent properties.

In some applications such as guidewires and orthodontic archwires, the in vitro experiments on DLC-coated parts showed an improved tribological performance. When implanting a DLC-coated material, it has to be considered that even the reaction layer at the DLC/substrate interface has to be chemically durable under in vivo conditions to guarantee lifetime adhesion.

Acknowledgement Special thanks to Rowena Crockett for carefully reading the manuscript, to Ulrich Müller and Philipp Leibacher for preparing and analyzing the DLC/TiAlV interface, and to Günther Hobi for solving many technical problems.

References

1. A. U. Daniels, F. H. Barnes, S. J. Charlebois, and R. A. Smith, J. Biomed. Mat. Res. 49, 469–478 (2000).
2. D. Dowson, Wear 190, 171–183 (1995).
3. P. A. Dearnley, Proceedings of the Institution of Mechanical Engineers. Part H. J. Eng. Med. 213, 107–135 (1999).
4. R. Hauert, Diamond Relat. Mater. 12, 583–589 (2003).
5. M. Allen, B. Myer, and N. Rushton, J Biomed. Mater. Res. 58, 319–328 (2000).
6. M. Mohanty, T. V. Anilkumar, P. V. Mohanan, C. V. Muraleedharan, G. S. Bhuvaneshwar, F. Derangere, Y. Sampeur, and R. Suryanarayanan, Biomol. Eng. 19, 125–128 (2002).
7. F. Z. Cui and D. J. Li, Surf. Coat. Technol. 131, 481–487 (2000).
8. R. S. Butter and A. H. Lettington, J Chem. Vapor Deposition 3, 182 (1995).
9. I. De Scheerder, M. Szilard, H. Yanming, X. B. Ping, E. Verbeken, D. Neerinck, E. Demeyere, W. Coppens, and F. Van de Werf, J. Invasive Cardiol. 12/8, 389–394 (2000).
10. A. Dorner-Reisel, C. Schürer, C. Nischan, O. Seidel, and E. Müller, Thin Solid Films 420–421, 263–268 (2002).

11. R. Hauert, L. Knoblauch-Meyer, G. Francz, A. Schroeder, and E. Wintermantel, Surf. Coat. Technol. 120–121, 291–296 (1999).
12. A. Schroeder, G. Francz, A. Bruinink, R. Hauert, J. Mayer, and E. Wintermantel, Biomaterials 21, 449–456 (2000).
13. A. Bruinink, A. Schroeder, G. Francz, and R. Hauert, Biomaterials 26, 3487–3494 (2005).
14. P. Aspenberg, A. Anttila, Y. T. Konttinen, R. Lappalainen, S. B. Goodman, L. Nordsletten, and S. Santavirta, Biomaterials 17, 807–812 (1996).
15. P. D. Maguire, J. A. McLaughlin, T. I. T. Okpalugo, P. Lemoine, P. Papakonstantinou, E. T. McAdams, M. Needham, A. A. Ogwu, M. Ball, and G. A. Abbas, Diamond Relat. Mater. 14, 1277–1288 (2005).
16. Yanqi Yang, Linköping University Medical Dissertation. No 539, Sweden, ISBN 91-7219-084-1 Linköping (1997).
17. D. Antoniucci et al. Am. J. Cardiol. 85/7, 821–825 (2000).
18. P. B. Sick, G. Gelbrich, U. Kalnins, A. Erglis, R. Bonan, W. Aengevaeren, D. Elsner, B. Lauer, M. Woinke, O. Brosteanu, and G. Schuler, Am. J. Cardiol. 93, 1351–1356 (2004).
19. M. D. Barbera, F. Laborde, G. Thiene, V. Arata, E. Pettenazzo, E. Pasquino, L. Behr, and M. Valente, Cardiovasc. Pathol. 14, 96–103 (2005).
20. R. Lappalainen and S. S. Santavirta, Clin. Orthopaedics Relat. Res. 430, 72–79 (2005).
21. V.-M. Tiainen, Diamond Relat. Mater. 10, 153–160 (2001).
22. R. Lappalainen, H. Heinonen, A. Anttila, and S. Santavirta, Diamond Relat. Mater. 7, 482–485 (1998).
23. J. I. Oñate, M. Comin, I. Braceras, A. Garcia, J. L. Viviente, M. Brizuela, N. Garagorri, J. L. Peris, and J. I. Alava, Surf. Coat. Technol. 142–144, 1056–1062 (2001).
24. H. Dong, W. Shi, and T. Bell, Wear 225–229, 146–153 (1999).
25. D. P. Dowling, P. V. Kola, K. Donelly T. C. Kelly, K. Brumitt, L. Lloyd, R. Eloy, M. Therin, and N. Weill, Diamond Relat. Mater. 6, 390–393 (1997).
26. V. Saikko, T. Ahlroos, O. Calonius, and J. Keränen, Biomaterials 22, 1507–1514 (2001).
27. S. Affatato, M. Frigo, and A. Toni, J. Biomed. Mater. Res. 53, 221–226 (2000).
28. H. Ronkainen, S. Varjus, and K. Holmberg, Wear 249, 267–271 (2001).
29. M. Müller, S. Lee, H. A. Spikes, and N. D. Spencer, Tribol. Lett. 15, 395–405 (2003).
30. I. C. Clarke, F. W. Chan, A. Essner, V. Good, C. Kaddick, R. Lappalainen, M. Laurent, H. McKellop, W. McGarry, D. Schroeder, et al., Wear 250, 188–198 (2001).
31. M. P. Heuberger, M. R. Widmer, E. Zobeley, R. Glockshuber, and N. D. Spencer, Biomaterials 26, 1165–1170 (2005).
32. J. Fisher, P. Firkins, E. A. Reeves, J. L. Hailey, and G. H. Isaac, Proceedings of the Institution of Mechanical Engineers. Part H. J. Eng. Med. 209, 263–264 (1995).
33. M. A. Wimmer, J. Loos, R. Nassutt, M. Heitkemper, and A. Fischer, Wear 250, 129–139 (2001).
34. R. Lappalainen, M. Selenius, A. Anttila, Y. T. Konttinen, and S. S. Santavirta, J. Biomed. Mat. Res. Part B: Appl. Biomater. 66B, 410–413 (2003).
35. B. Shi, O. O. Ajayi, G. Fenske, A. Erdemir, and H. Liang, Wear 255, 1015–1021 (2003).
36. H. Ronkainen, J. Likonen, J. Koskinen, and S. Varjus, Surf. Coat. Technol. 79, 87–94 (1996).
37. D. Neerinck, P. Persoone, M. Sercu, A. Goel, C. Venkatraman, D. Kester, C. Halter, P. Swab, and D. Bray, Thin Solid Films 317, 402–404 (1998).
38. G. Taeger, L. E. Podleska, B. Schmidt, M. Ziegler, and D. Nast-Kolb, Mat.-wiss. u. Werkstofftech. 34, 1094–1100 (2003).
39. L. Chandra, M. Allen, R. Butter, N. Rushton, A. H. Lettington, and T. W. Clyne, J. Mater. Sci. Mat. Med. 6, 581–589 (1995).
40. U. Müller, R. Hauert, B. Oral, and M. Tobler, Surf. Coat. Technol. 71, 233–238 (1995).
41. R. Zehringer and R. Hauert, Surf. Sci. 262, 21–24 (1992).
42. R. Hauert, J. Patscheider, M. Tobler, and R. Zehringer, Surf. Sci. 292, 121–129 (1993).
43. M. Kiuru, Ph.D. Thesis HU-P-D115, University of Helsinki (2004).

44. A. Koistinen, S. S. Santavirta, H. Kröger, and R. Lappalainen, Biomaterials 26, 5687–5694, (2005).
45. T. Hasebe, Y. Matsuoka, H. Kodama, T. Saito, S. Yohena, A. Kamijo, N. Shiraga, M. Higuchi, S. Kuribayashi, K. Takahashi, and T. Suzuki, Diamond Relat. Mater. 15, 129–132 (2006).
46. N. Laube, University of Bonn, public press release, 18 November 2004.
47. Y. Ohgoe, S. Kobayashi, K. Ozeki, H. Aoki, H. Nakamori, K. K. Hirakuri, and O. Miyashita, Thin Solid Films 497, 218–222 (2006).
48. S. Kobayashi, Y. Ohgoe, K. Ozeki, K. Sato, T. Sumiya, K. K. Hirakuri, and H. Aoki, Diamond Relat. Mater. 14, 1094–1097 (2005).
49. Manfred Kiser, Diploma work, LSST-ETH Zürich (2000).
50. R. Hauert and U. Müller, Surf. Coat. Technol. 174–175, 421–426 (2003).
51. R. Hauert and U. Müller, Surf. Coat. Technol. 177–178, 552–557 (2004).

Nanotribology of Ultrathin and Hard Amorphous Carbon Films

B. Bhushan

Abstract One of the best materials to use in applications that require very low wear and reduced friction is diamond, especially in the form of a diamond coating. Unfortunately, true diamond coatings can only be deposited at high temperatures and on selected substrates, and they require surface finishing. However, hard amorphous carbon – commonly known as diamond-like carbon (DLC) coating – has similar mechanical, thermal, and optical properties to those of diamond. It can also be deposited at a wide range of thicknesses using a variety of deposition processes on various substrates at or near room temperature. The coatings reproduce the topography of the substrate removing the need for finishing. The friction and wear properties of some DLC coatings make them very attractive for some tribological applications. The most significant current industrial application of DLC coatings is in magnetic storage devices.

In this chapter, the state of the art in the chemical, mechanical, and tribological characterization of ultrathin amorphous carbon coatings is presented.

Electron energy loss spectroscopy (EELS) and Raman spectroscopy can be used to characterize amorphous carbon coatings chemically. The prevailing atomic arrangement in the DLC coatings is amorphous or quasi-amorphous, with small diamond (sp^3), graphite (sp^2), and other unidentifiable micro- or nanocrystallites. Most DLC coatings, except for those produced using a filtered cathodic arc (FCA), contain from a few to about 50 at. % hydrogen (H). Sometimes, H is deliberately incorporated into the sputtered and ion-plated coatings in order to tailor their properties.

Amorphous carbon coatings deposited by different techniques exhibit different mechanical and tribological properties. Thin coatings deposited by FCA, ion beam, and ECR-CVD hold much promise for tribological applications. Coatings of 5 nm or even less provide wear protection. A nanoindenter can be used to measure DLC-coating hardness, elastic modulus, fracture toughness, and fatigue life. Microscratch and microwear tests can be performed on the coatings using either a nanoindenter or an atomic force microscopy (AFM), and along with accelerated wear testing, can be used to screen potential industrial coatings. For the examples shown in this chapter, the trends observed in such tests were similar to those found in functional tests.

Nanotribology Laboratory for Information Storage and MEMS/NEMS,
The Ohio State University, 210 W 19th Avenue, Columbus, OH 43210, USA

C. Donnet and A. Erdemir (eds.), *Tribology of Diamond-Like Carbon Films: Fundamentals and Applications*.

Keywords ultra thin DLC films, nanotribology, nanomechanical characterization, head disk interface

1 Introduction

Carbon exists in both crystalline and amorphous forms and exhibits both metallic and nonmetallic characteristics [26, 18, 23]. Crystalline carbon includes graphite, diamond, and a family of fullerenes (Fig. 1). The graphite and diamond are infinite periodic network solids with a planar structure, whereas the fullerenes are a molecular form of pure carbon with a finite network with a nonplanar structure. Graphite has a hexagonal, layered structure with weak interlayer bonding forces, and exhibit excellent lubrication properties. The graphite crystal may be visualized as infinite parallel layers of hexagons stacked 0.34 nm apart with a 0.1415 nm interatomic distance between the carbon atoms in the basal plane. The atoms lying in the basal planes are trigonally coordinated and closely packed with strong σ (covalent)-bonds to its three carbon neighbors using the hybrid sp^2 orbitals. The fourth electron lies in a p_z orbital lying normal to the σ-bonding plane and forms a weak π-bond by overlapping side to side with a p_z orbital of an adjacent atom to which carbon is attached by a σ-bond. The layers (basal planes) themselves are relatively

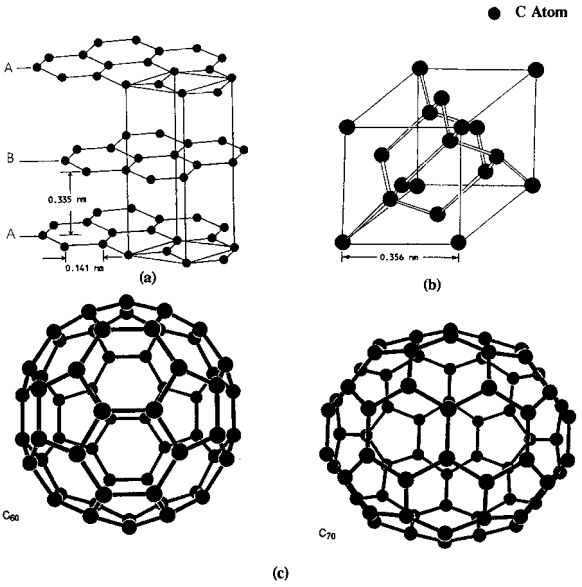

Fig. 1 The structure of three known forms of crystalline carbon (a) hexagonal structure of graphite, (b) modified face-centered cubic (fcc) structure, two interpenetrating fcc lattices displaced by one one-quarter of the cube diagonal, of diamond (each atom is bonded to four others that form the corners of the pyramidal structure called tetrahedron), and (c) the structure of two most common forms of fullerenes – soccer ball C_{60} and rugby ball C_{70} molecules

far apart and the forces that bond them are weak van der Waals forces. These layers can align themselves parallel to the direction of the relative motion and slide over one another with relative ease, thus providing low friction. Strong interatomic bonding and packing in each layer is thought to help reduce wear. Operating environment has a significant influence on lubrication, i.e., low friction and low wear, properties of graphite. It lubricates better in humid environment than a dry one which results from adsorption of water vapor and other gases from the environment which further weakens the interlayer bonding forces, resulting in easy shear and transfer of the crystallite platelets to the mating surface. Thus transfer plays an important role in controlling friction and wear. Graphite oxidizes at high operating temperatures and can be used up to about 430°C.

One of the fullerene molecule is C_{60}, commonly known as Buckyball. Since the C_{60} molecules are very stable and do not require additional atoms to satisfy chemical bonding requirements, they are expected to have low adhesion to the mating surface and low surface energy. Since C_{60} molecules with a perfect spherical symmetry are weakly bonded to other molecules, C_{60} clusters get detached readily, similar to other layered lattice structures, and either get transferred to the mating surface by mechanical compaction or are present as loose wear particle which may roll like tiny ball bearings in a sliding contact, resulting in low friction and wear. The wear particles are expected to be harder than as-deposited C_{60} molecules because of their phase transformation at high asperity contact pressures present in a sliding interface. The low surface energy, spherical shape of C_{60} molecules, weak intermolecular bonding, and high load-bearing capacity offer potential for various mechanical and tribological applications. The sublimed C_{60} coatings and fullerene particles as an additive to mineral oils and greases, have been reported to be good solid lubricants comparable to graphite and MoS_2 [31, 65, 62].

Diamond crystallizes in the modified face-centered cubic (fcc) structure with an interactomic distance of 0.154 nm. The diamond cubic lattice consists of two interpenetrating fcc lattices displaced by one quarter of the cube diagonal. Each carbon atom is tetrahedrally coordinated, making strong σ (covalent) bonds to its four carbon neighbors using the hybrid sp^3 atomic orbitals which accounts for its highest hardness (80–104 GPa) and thermal conductivity (900–2,100 W/mK, on the order of five times that of copper) of any known solid, and a high electrical resistivity, optical transmission, and a large optical band gap. It is relatively chemically inert, and exhibits poor adhesion with other solids with consequent low friction and wear. Its high thermal conductivity allows dissipation of frictional heat during sliding and protects the interface and the dangling carbon bonds on the surface react with the environment to form hydrocarbons which act as good lubrication films. These are some of the reasons for low friction and wear of the diamond. Diamond and its coatings find many industrial applications: tribological applications (low friction and wear), optical applications (exceptional optical transmission, high abrasion resistance), and thermal management or heat sink applications (high thermal conductivity). The diamond can be used to high temperatures and it starts to graphitize at about 1,000°C in ambient air and at about 1,400°C in vacuum. Diamond is an attractive material for cutting tools, as an abrasive for grinding wheels and lapping compounds, and other extreme wear applications.

The natural diamond particularly in large sizes is very expensive and its coatings, a low cost alternative, are attractive. The true diamond coatings are deposited by chemical vapor deposition (CVD) processes at high substrate temperatures (on the order of 800°C). They adhere best on a silicon substrate and require an interlayer for other substrates. A major roadblock to the widespread use of true diamond films in tribological, optical, and thermal management applications is the surface roughness. Growth of the diamond phase on a nondiamond substrate is initiated by nucleation either at randomly seeded sites or at thermally favored sites due to statistical thermal fluctuation at the substrate surface. Based on growth temperature and pressure conditions, favored crystal orientations dominate the competitive growth process. As a result, the grown films are polycrystalline in nature with relatively large grain size (>1 μm), and terminate in very rough surfaces with RMS roughness ranging from few tenth of a micron to tens of microns. Techniques for polishing these films have been developed. It has been reported that the laser polished films exhibit friction and wear properties almost comparable to that of bulk polished diamond [32, 33].

Amorphous carbon has no long-range order and the short-range order of carbon atoms can have one or more of three bonding configurations – sp^3 (diamond), sp^2 (graphite), or sp^1 (with two electrons forming strong σ-bonds and the remaining two electrons left in orthogonal p_y and p_z orbitals to form weak π-bonds). Short-range order controls the properties of amorphous materials and coatings. Hard amorphous carbon (a-C) coatings, commonly known as diamond-like carbon (DLC) (implying high hardness) coatings, are a class of coatings which are mostly metastable amorphous materials but include a micro- or nanocrystalline phase. The coatings are random network of covalently bonded carbon in hybridized tetragonal (sp^3) and trigonal (sp^2) local coordination, with some of the bonds terminated by H. These coatings have been successfully deposited by a variety of vacuum deposition techniques on a variety of substrates at or near room temperature. These coatings generally reproduce substrate topography and do not require any post-finishing. However, these coatings mostly adhere best on silicon substrates. Best adhesion is obtained on substrates that form carbides, e. g., Si, Fe, and Ti. Based on depth profile analyses using Auger and XPS of DLC coatings deposited on silicon substrates, it has been reported that substantial amount of silicon carbide (on the order of 5–10 nm in thickness) is present at the carbon–silicon interface for the coatings with good adhesion and high hardness (e.g., [92]). For good adhesion of DLC coatings to other substrates, in most cases, an interlayer of silicon is required except for cathodic arc-deposited coatings.

There is significant interest in DLC coatings because of their unique combination of desirable properties. These properties include high hardness and wear resistance, chemical inertness to acids and alkalis, lack of magnetic response, and an optical band gap ranging from zero to a few electron volts, depending upon the deposition conditions. These are used in a wide range of applications including tribological, optical, electronic, and biomedical applications [84, 26, 71]. The high hardness, good friction and wear properties, versatility in deposition and

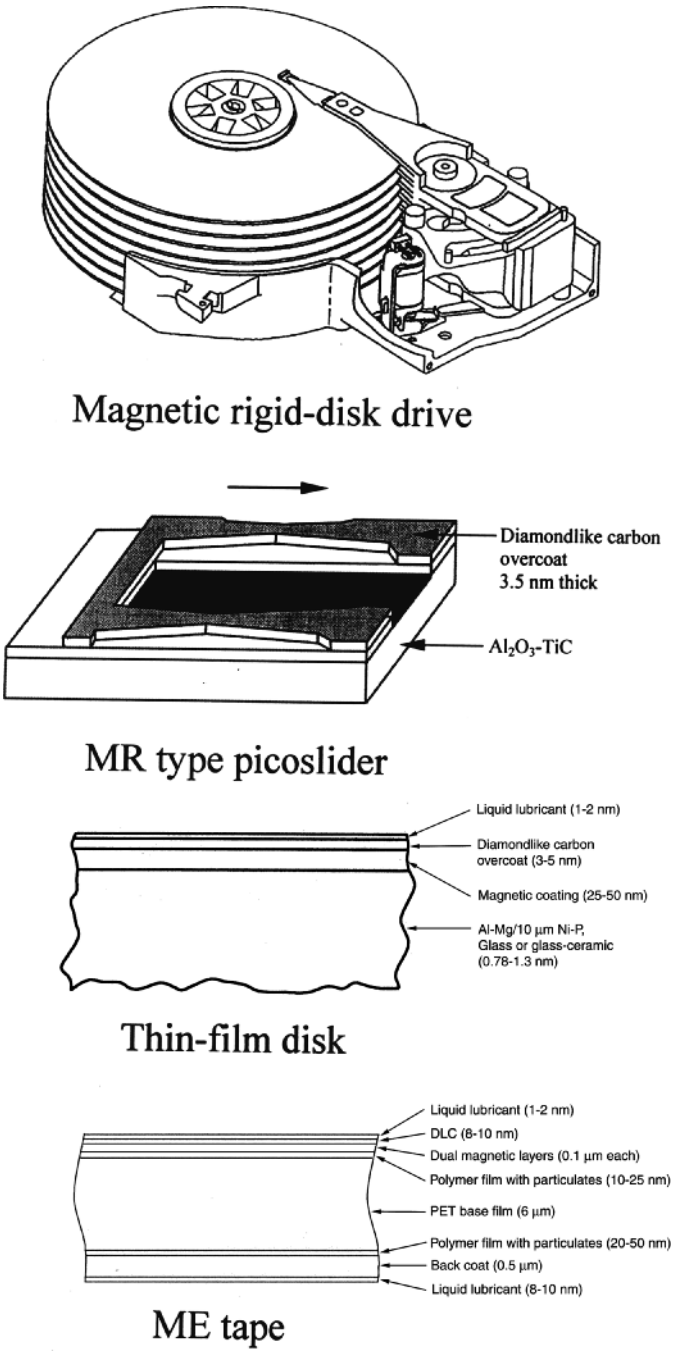

Fig. 2 Schematic of a magnetic rigid disk drive and MR type picoslider and cross-sectional schematics of a magnetic thin-film rigid disk and a metal evaporated (ME) tape

substrates, and no requirements of post-finishing make them very attractive for tribological applications. Two primary examples include overcoats for magnetic media (thin-film disks and ME tapes) and MR-type magnetic heads for magnetic storage devices, Fig. 2 [63, 14, 20, 21, 36, 112, 97, 98, 99] and the emerging field of microelectromechanical systems, Fig. 3 [15, 16, 17, 22]. The largest industrial application of the family of amorphous carbon coatings, typically deposited by DC/RF magnetron sputtering, plasma-enhanced chemical vapor deposition (PECVD), or ion beam deposition (IBD) techniques, is in magnetic storage devices. These are employed to protect against wear and corrosion, magnetic coatings on thin-film rigid disks and metal evaporated tapes, and the thin-film head structure of a read/write disk head (Fig. 2). To maintain low physical spacing between the magnetic element of a read/write head and the magnetic layer of a media, the thicknesses ranging from 3 to 10 nm are employed. Mechanical properties affect friction wear and these need to

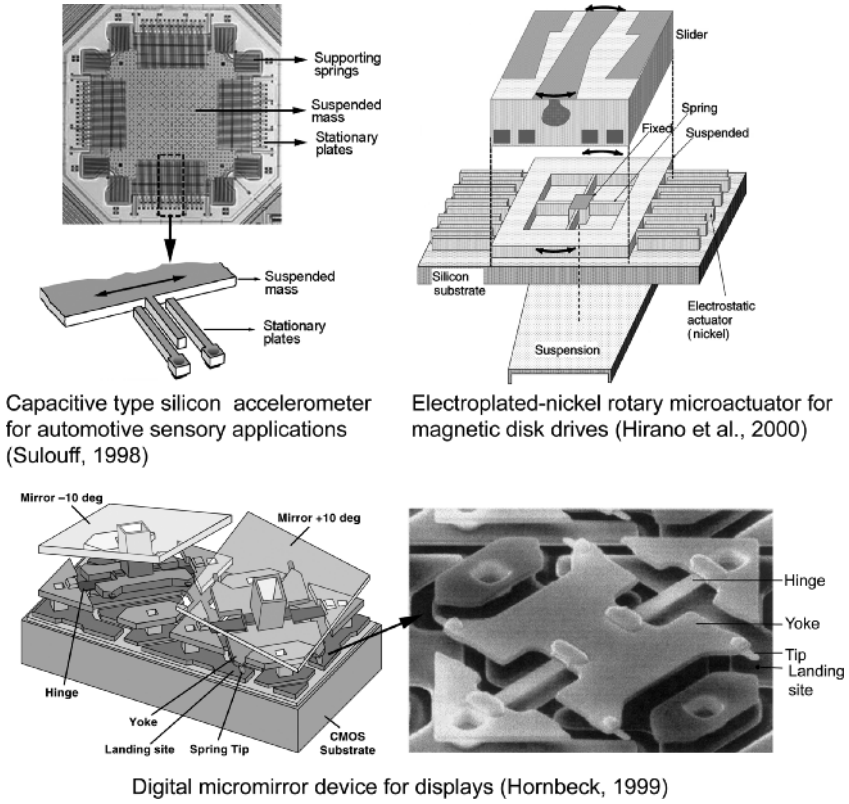

Fig. 3 Schematics of a capacitive type silicon accelerometer for automotive sensory applications, digital micrometer devices for high-projection displays, and polysilicon rotary microactuator for magnetic disk drives

be optimized. In 1998, Gillette introduced Mach 3 razor blades with ultrathin DLC coatings which have the potential of being a very large industrial application. DLC coatings are also used in other commercial applications such as glass windows of supermarket laser barcode scanners and sunglasses. These coatings are actively pursued in microelectromechanical systems (MEMS) components [17].

In this chapter, a state-of-the-art review of recent developments in the chemical, mechanical, and tribological characterization of ultrathin amorphous carbon coatings is presented. An overview of most commonly used deposition techniques is presented next followed by typical chemical and mechanical characterization data, and typical tribological data both from coupon-level testing and functional testing.

2 Description of Commonly Used Deposition Techniques

The first hard amorphous carbon coatings were deposited by a beam of carbon ions produced in an argon plasma on room-temperature substrates as reported by Aisenberg and Chabot [3]. Subsequent confirmation by Spencer et al. [100] led to explosive growth of this field. Following the first work, several alternative techniques have been developed. The amorphous carbon coatings have been prepared by a variety of deposition techniques and precursors, including evaporation, DC, RF, or ion beam sputtering, RF or DC PECVD, electron cyclotron resonance chemical vapor deposition (ECR-CVD), direct IBD, and pulsed laser vaporization and vacuum arc, from a variety of carbon-bearing solids or gaseous source materials [58, 26]. Coatings with both graphitic and diamond-like properties have been produced. Evaporation and ion plating techniques have been used to produce coatings with graphitic properties (low hardness, high electrical conductivity, very low friction, etc.) and all techniques have been used to produce coatings with diamond-like properties.

Structure and properties of a coating are dependent upon the deposition technique and the deposition parameters. High-energy surface bombardment has been used to produce harder and denser coatings. It is reported that sp^3/sp^2 fractions are in the decreasing order for cathodic arc deposition, pulsed laser vaporization, direct IBD, PECVD, ion beam sputtering, and DC/RF sputtering [42, 44, 63]. A common feature of these techniques is that the deposition is energetic, that is, carbon species arrive with energy significantly greater than that represented by the substrate temperature. The resultant coatings are amorphous in structure, with H content up to 50%, and display a high degree of sp^3 character. From the results of previous investigations, it has been proposed that deposition of sp^3-bonded carbon requires the depositing species to have kinetic energies on the order of 100 eV or higher, well above those obtained in thermal processes like evaporation (0–0.1 eV). The species must then be quenched into the

metastable configuration via rapid energy removal. Excess energy, such as that provided by substrate heating, is detrimental to the achievement of a high sp^3 fraction. In general, a high fraction of the sp^3-bonded carbon atoms in an amorphous network results in a higher hardness [9, 10, 56, 43, 44, 8, 30, 89]. The mechanical and tribological properties of a carbon coating depend on the sp^3/sp^2-bonded carbon ratio, the amount of H in the coating, and adhesion of the coating to the substrate, which are influenced by the precursor material, kinetic energy of the carbon species prior to deposition, deposition rate, substrate temperature, substrate biasing, and the substrate itself [94, 11, 88, 43, 91, 108, 44, 45, 30, 87, 96, 48, 57]. The kinetic energies and deposition rates involved in selected deposition processes used in the deposition of DLC coatings are compared in Table 1 [42, 26].

In the studies by Gupta and Bhushan [63, 64], Li and Bhushan [74, 75] and Sundararajan and Bhushan [102], DLC coatings, ranging in thickness typically from 3.5 to 20 nm, were deposited on single-crystal silicon, magnetic Ni–Zn ferrite and Al_2O_3–TiC substrates (surface roughness ≈ 1–3 nm RMS) by FCA deposition, (direct) IBD, ECR-CVD, PECVD, and DC/RF planar, magnetron sputtering (SP) deposition techniques [19]. In this chapter, we will limit the presentation of data of coatings deposited by FCA, IBD, ECR-CVD, and SP deposition techniques.

Table 1 Summary of most commonly used deposition techniques and the kinetic energy of depositing species and deposition rates

Deposition technique	Process	Kinetic energy (eV)	Deposition rate (nm/s)
Filtered cathodic arc (FCA)	Energetic carbon ions produced by a vacuum arc discharge between a graphite cathode and grounded anode	100–2500	0.1–1
Direct ion beam (IB)	Carbon ions produced from methane gas in an ion source and accelerated towards a substrate	50–500	0.1–1
Plasma enhanced chemical vapor deposition (PECVD)	Hydrocarbon species, produced by plasma decomposition of hydrocarbon gases (e.g., acetylene) are accelerated towards a DC-biased substrate	1–30	1–10
Electron cyclotron resonance plasma chemical vapor deposition (ECR-CVD)	Hydrocarbon ions, produced by plasma decomposition of ethylene gas in the presence of a plasma in electron cyclotron resonance condition, are accelerated towards an RF-biased substrate	1–50	1–10
DC/RF sputtering	Sputtering of graphite target by argon ion plasma	1–10	1–10

2.1 Filtered Cathodic Arc Deposition Technique

In the FCA deposition of carbon coating [44, 2, 85, 80, 39, 55, 4, 5, 6], a vacuum arc plasma source is used to form a carbon film. In the FCA technique used by Bhushan and coworkers (e.g., [63]), energetic carbon ions are produced by a vacuum arc discharge between a planar graphite cathode and grounded anode (Fig. 4(a)). The cathode is a 6 mm diameter high density graphite disk mounted on a water-cooled copper block. The arc is driven at an arc current of 200 A, arc duration of 5 ms, and arc repetition rate of 1 Hz. The plasma beam is guided by a magnetic field that transports current between the electrodes to form tiny, rapidly moving spots on the cathode surface. The source is coupled to a 90° bent magnetic filter to remove the macroparticles produced concurrently with the plasma in the cathode spots. The ion current density at the substrate is in the range of 10–50 mA/cm^2. The base pressure is less than 10^{-4} Pa. Compared with electron beam evaporation with auxiliary discharge, much higher plasma density is achieved with the aid of powerful arc discharge. In this process, the cathodic material suffers a complicated transition from the solid phase to an expanding, nonequilibrium plasma via liquid and dense, equilibrium nonideal plasma phases [5]. The carbon ions in the vacuum arc plasma have a direct kinetic energy of 20–30 eV. The high voltage pulses are applied to the substrate mounted on a water-cooled sample holder, ions are accelerated through the sheath and arrive at the substrate with an additional energy given by the potential difference between the plasma and the substrate. The substrate holder is pulse biased to a negative voltage up to −2 kV with a pulse duration of 1 μs. The negative biasing of −2 kV corresponds to 2 keV kinetic energy of the carbon ions. The use of a pulse bias instead of a DC bias has advantages of applying a much higher voltage and building a surface potential on a nonconducting film. The energy of the ions is varied during the deposition. For the first 10% of the deposition the substrates are pulsed biased to −2 keV with a pulse duty cycle of 25%, that is, for 25% of the time the energy is 2 keV, for the remaining 75% time it is 20 eV which is the "natural" energy of carbon ions in a vacuum discharge. For the last 90% of the deposition the pulsed bias voltage is reduced to −200 eV with a pulse bias duty cycle of 25%, that is, the energy is 200 eV for 25% and 20 eV for 75% of the deposition. The high energy at the beginning leads to a good intermixing and good adhesion of the films whereas the lower energy at later stage leads to hard films. Under the conditions described, the deposition rate at the substrate is about 0.1 nm/s which is slow. As compared with most gaseous plasma, the cathodic arc plasma is nearly fully ionized and the ionized carbon atoms have high kinetic energy of carbon ions help achieving a high fraction of sp^3-bonded carbon ions which in turn result into a high hardness and higher interfacial adhesion. Cuomo et al. [45] have reported that based on electron energy loss spectroscopy (EELS) analysis, the sp^3-bonded carbon fraction of cathodic arc coating is 83% as compared with 38% for the ion beam sputtered carbon. These coatings are reported to be *nonhydrogenated*.

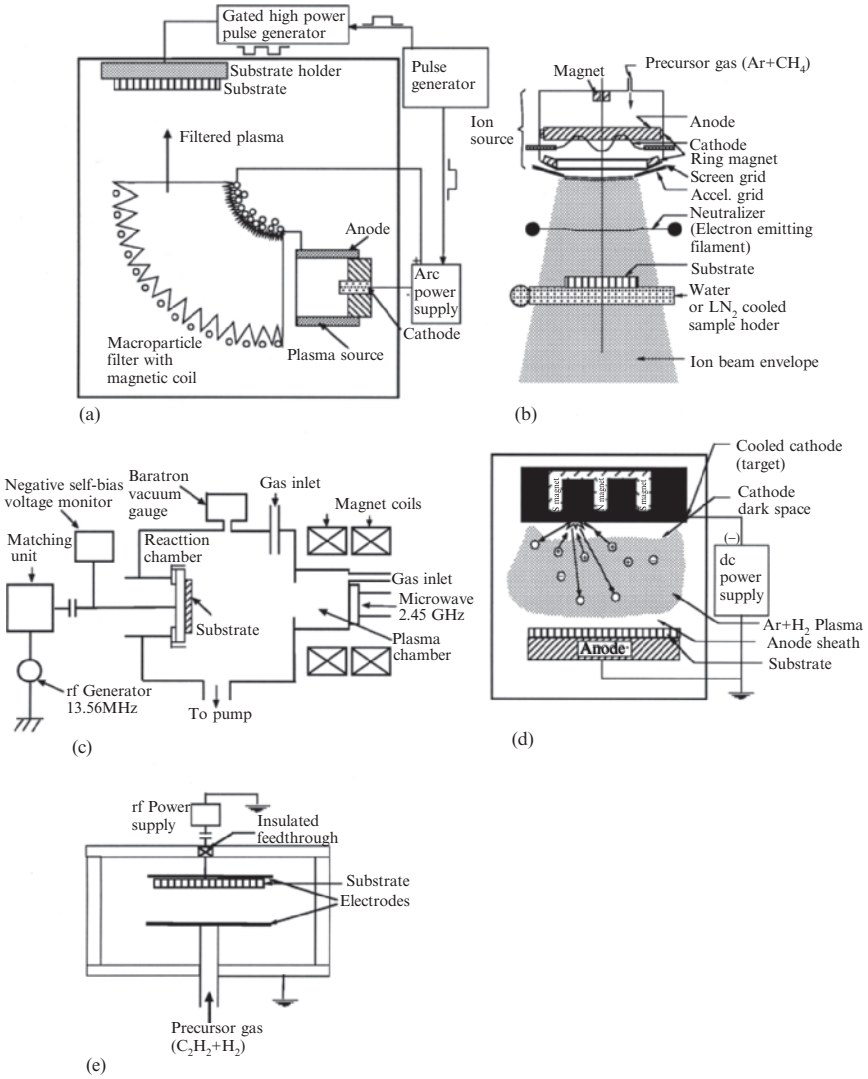

Fig. 4 Schematic diagrams of deposition by (a) filtered cathodic arc (FCA) deposition, (b) ion beam deposition (IBD), (c) electron cyclotron resonance chemical vapor deposition (ECR-CVD), (d) DC planar magnetron sputtering, and (e) plasma enhanced chemical vapor deposition (PECVD)

This technique does not require an adhesion underlayer for nonsilicon substrates. However, adhesion of the DLC coatings on the electrically insulating substrate is poor as negative pulse biasing forms an electrical sheath which accelerates depositing ions to the substrate and enhances the adhesion of the coating to the substrate with associated ion implantation. It is difficult to build potential on an insulating substrate and lack of biasing results in poor adhesion.

2.2 Ion Beam Deposition Technique

In the direct IBD of carbon coating [106, 52, 53, 109, 51], as used by Bhushan and coworkers (e.g. [63]) (deposition carried out by Ion Tech Inc., Fort Collins, Colorado), the carbon coating is deposited from an accelerated carbon ion beam. The sample is precleaned by ion etching. For the case of nonsilicon substrates, 2–3 nm thick amorphous silicon adhesion layer is deposited by ion beam sputtering using an ion beam of a mixture of methane and argon at 200 V. For the carbon deposition, chamber is pumped to about 10^{-4} Pa and methane gas is fed through the cylindrical ion source and is ionized by energetic electrons produced by a hot-wire filament (Fig. 4(b)). Ionized species then pass through as grid with a bias voltage of about 50 eV where they gain a high acceleration energy and reach a hot-wire filament, emitting thermionic electons that neutralize the incoming ions. Discharging of ions is important when insulating ceramics are used as substrates. The species are then deposited on a water-cooled substrate. Operating conditions are adjusted to give an ion beam with an acceleration energy of about 200 eV and a current density of about 1 mA/cm^2. At this operating condition, the deposition rate is about 0.1 nm/s which is slow. Incidentally, for deposition of tough and soft coatings, these are deposited at high acceleration energy of about 400 eV at a deposition rate of about 1 nm/s. The ion beam deposited carbon coatings are reported to be hydrogenated (30–40 at. % H).

2.3 Electron Cyclotron Resonance Chemical Vapor Deposition Technique

The lack of electrodes and its ability to create high densities of charged and excited species at low pressures ($\leq 10^{-4}$ Torr) in ECR plasma, make it an attractive processing discharge in the coating depositions [12]. In the ECR-CVD deposition process of carbon coating described by Suzuki and Okada [105] and used by Li and Bhushan [74, 75] and Sundararajan and Bhushan [102], microwave power is generated by a magnetron operating in continuous mode at a frequency of 2.45 GHz (Fig. 4(c)). The plasma chamber functions as a microwave cavity resonator. The magnetic coils arranged around the plasma chamber generate a magnetic field of 875 G necessary for electron cyclotron resonance condition. The substrate is placed on a stage which is capacitively connected to a 13.56 MHz RF generator. The process gas is introduced into the plasma chamber and the hydrocarbon ions generated are accelerated by a negative self-bias voltage, which is generated by applying RF power to the substrate. Both the substrate stage and plasma chamber are water-cooled. The process gas used is 100% ethylene and its flow rate is held constant at 100 sccm. The microwave power is 100–900 W. The RF power is 30–120 W. The pressure during deposition is kept

close to the optimum value of 5.5×10^{-3} Torr. Before the deposition, the substrates are cleaned using Ar ions generated in the ECR plasma chamber.

2.4 Sputtering Deposition Technique

In DC planar magnetron sputtered carbon coating [13, 110, 46, 94, 43, 91, 34, 35, 14], the carbon coating is deposited by the sputtering of graphite target with Ar ion plasma. In the glow discharge, positive ions from the plasma strike the target with sufficient energy to dislodge the atoms by momentum transfer which are intercepted by the substrate. First an about 5 nm thick amorphous silicon adhesion layer is deposited by sputtering if the deposition is to be carried out on a nonsilicon surface. In the process used by Bhushan and coworkers (e.g., [63]), the coating is deposited by sputtering of graphite target with Ar ion plasma, at 300 W power for 200 mm diameter target and pressure of about 0.5 Pa (6 mTorr), Fig. 4(d). Plasma is generated by applying a DC potential between the substrate and a target. Bhushan et al. [30] reported that sputtered carbon coating contain about 35 at. % H. Hydrogen comes from the hydrocarbon contaminants present in the deposition chamber. To produce hydrogenated carbon coating with a larger concentration of H, deposition is carried out in Ar and H plasma.

2.5 Plasma-enhanced Chemical Vapor Deposition Technique

In the RF-PECVD deposition of carbon coating as used by Bhushan and coworkers (e.g., [63]), carbon coating is deposited by adsorption of most free radicals of hydrocarbon to the substrate and chemical bonding to other atoms on the surface. The hydrocarbon species are produced by the RF plasma decomposition of hydrocarbon precursors such as acetylene (C_2H_2), Fig. 4(e) [66, 7, 40, 46, 60, 61,58]. Instead of requiring thermal energy in thermal CVD, the energetic electrons in the plasma (at pressures ranging from 1 to 5×10^2 Pa, typically less than 10 Pa) can activate almost any reaction among the gases in the glow discharge at relatively low substrate temperatures ranging from 100°C to 600°C (typically less than 300°C). To deposit the coating on nonsilicon substrates, about 4 nm thick amorphous silicon adhesion layer, used to improve adhesion, is first deposited under similar conditions from a gas mixture of 1% silane in argon [59]. In the process used by Bhushan and coworkers [63], the plasma is sustained in a parallel-plate geometry by a capacitive discharge at 13.56 MHz, at a surface power density on the order of 100 mW/cm^2. The deposition is performed at a flow rate on the order of 6 sccm and a pressure on the order of 4 Pa (30 mTorr) on a cathode-mounted substrate maintained at a substrate temperature of 180°C.

The cathode bias held fixed at on the order of −120 V with external DC power supply attached to substrate (powered electrode). The carbon coatings deposited by PECVD usually contain H up to 50% [61, 30].

3 Chemical Characterization and Effect of Deposition Conditions on Chemical

3.1 Characteristics and Physical Properties

The chemical structure and properties of amorphous carbon coatings are a function of deposition conditions. It is important to understand the relationship of the chemical structure of amorphous carbon coatings to the properties in order to define useful deposition parameters. Amorphous carbon films are metastable phases formed when carbon particles are condensed on a substrate. The prevailing atomic arrangement in the DLC coatings is amorphous or quasi-amorphous with small diamond (sp^3), graphite (sp^2), and other unidentifiable micro- or nanocrystallites. The coatings dependent upon the deposition process and its conditions contain varying amounts of sp^3/sp^2 ratio and H. The sp^3/sp^2 ratio of DLC coatings ranges typically from 50% to 100% with an increase in hardness with sp^3/sp^2 ratio. Most DLC coatings except those produced by FCA contain from a few to about 50 at. % H. Sometimes, H and nitrogen are deliberately added to produce hydrogenated (a-C:H) and nitrogenated amorphous carbon (a-C:N) coatings, respectively. H helps to stabilize sp^3 sites (most of the carbon atoms attached to H have a tetrahedral structure); therefore, the sp^3/sp^2 ratio for hydrogenated carbon is higher [9]. Optimum sp^3/sp^2 in random covalent network composed of sp^3 and sp^2 carbon sites (N_{sp^2} and N_{sp^3}) and H is [9],

$$\frac{N_{sp^3}}{N_{sp^2}} = \frac{6X_H - 1}{8 - 13X_H} \tag{1}$$

where X_H is the atom fraction of H. The hydrogenated carbon has a larger optical band gap, higher electrical resistivity (semiconductor), and has a lower optical absorption or high optical transmission. The hydrogenated coatings have a lower density probably because of reduction of cross-linking due to H incorporation. However, hardness decreases with an increase of the H even though the proportion of sp^3 sites increases (i.e., as the local bonding environment becomes more diamond-like) [67,68]. It is speculated that the high H content introduces frequent terminations in the otherwise strong three-dimensional network and H increases the soft polymeric component of the structure more than it enhances the cross-linking sp^3 fraction.

A number of investigations have been performed to identify the microstructure of amorphous carbon films using a variety of techniques such as Raman spectroscopy, EELS, nuclear magnetic resonance, optical measurements, transmission electron microscopy, and x-ray photoelectron spectroscopy [43]. The structure of diamond-like amorphous carbon is amorphous or quasi-amorphous with small graphitic (sp^2) and tetrahedrally coordinated (sp^3), and other unidentifiable nanocrystallites (typically on the order of 2 nm, randomly oriented) [107, 82, 43]. These studies indicate that the chemical structure and physical properties of the coatings are quite variable, depending on the deposition techniques and film growth conditions. It is clear that both sp^2 and sp^3-bonded atomic sites are incorporated in diamond-like amorphous carbon coatings and that the physical and chemical properties of the coatings depend strongly on their chemical bonding and microstructure. Systematic studies have been conducted to carry out chemical characterization and to investigate how the physical and chemical properties of amorphous carbon coatings vary as a function of deposition parameters (e.g., [43, 91, 30]). EELS and Raman spectroscopy are commonly used to characterize the chemical bonding and microstructure. H concentration of the coatings is obtained by means of forward recoil spectrometry (FRS). A variety of physical properties of the coatings relevant to tribological performance are measured.

To present the typical data obtained for characterization of typical amorphous carbon coatings and their relationships to physical properties, we present data on several sputtered, one RF-PECVD amorphous carbon and one microwave-PECVD (MPECVD) diamond coatings [43, 91, 30]. The sputtered coatings were DC magnetron sputtered at a chamber pressure of 10 mTorr, under sputtering power densities of 0.1 and 2.1 W/cm^2 in a pure Ar plasma, labeled as W1 and W2, respectively; and prepared at a power density of 2.1 W/cm^2 with various H fractions of 0.5, 1, 3, 5, 7, and 10% of Ar/H the gas mixtures labeled as H1, H2, H3, H4, H5, and H6, respectively.

3.1.1 EELS and Raman Spectroscopy

EELS and Raman spectra of four sputtered (W1, W2, H1, and H3) and one PECVD carbon samples were obtained. Figure 5 shows the EELS spectra of these carbon coatings. EELS spectra for bulk diamond and polycrystalline graphite in an energy range up to 50 eV are also shown in Fig. 5. One prominent peak is seen at 35 eV in diamond, while two peaks are seen at 27 eV and 6.5 eV in graphite, which are called ($\pi + \sigma$) and (π) peaks, respectively. These peaks are produced by the energy loss of transmitted electrons to the plasmon oscillation of the valence electrons. The $\pi + \sigma$ peak in each coating is positioned at a lower energy region than that of graphite. The π-peaks in the W series and PECVD samples are also seen at a lower energy region than that of the graphite; however, the π-peaks in the H-series are comparable to or higher than that of graphite (see Table 2). The plasmon oscillation frequency is proportional to the square root of the corresponding electron density to a first

Table 2 Experimental results from EELS and Raman spectroscopy [30]

Sample	EELS peak position		Raman peak position		Raman FWHM[a]		
	π (eV)	$\pi + \sigma$ (eV)	G -band[b] (cm^{-1})	D-band[c] (cm^{-1})	G-band (cm^{-1})	D-band (cm^{-1})	I_D/I_G[d]
Sputtered a-C coating (W1)	5.0	24.6	1541	1368	105	254	2.0
Sputtered a-C coating (W2)	6.1	24.7	1560	1379	147	394	5.3
Sputtered a-C:H coating (H1)	6.3	23.3	1542	1334	95	187	1.6
Sputtered a-C:H coating (H3)	6.7	22.4	[e]	[e]	[e]	[e]	[e]
PECVD a-C:H coating	5.8	24.0	1533	1341	157	427	1.5
Diamond coating	–	–	1525[f]	1333[g]	–	8[g]	–
Graphite (for reference)	6.4	27.0	1580	1358	37	47	0.7
Diamond (for reference)	–	37.0	–	1332[g]	–	2[g]	–

[a]Full width at half maximum width

[b]Peak associated with sp^2 "graphite" carbon

[c]Peak associated with sp^2"disordered" carbon (not sp^3-bonded carbon)

[d]Intensity ratio of the D-band to the G-band

[e]Fluorescence

[f]Includes D- and G-band, signal too weak to analyze

[g]Peak position and width for diamond phonon

approximation. Therefore, the samples in the H-series most likely have a higher density of π-electrons than the other samples.

Amorphous carbon coatings contain (mainly) a mixture of sp^2- and sp^3-bonds even though there is some evidence for the presence of sp-bonds as well [47]. The PECVD coatings and the H-series coatings in this study have nearly the same mass density as seen in Table 4, to be presented later, but the former have a lower concentration of H (18.1%) than the H-series (35–39%), as seen in Table 3, to be presented later. The relatively low energy position of π-peaks of PECVD coatings, compared to those of the H-series, indicates that the PECVD coatings contain a higher fraction of sp^3-bonds than the sputtered hydrogenated carbon coatings (H-series).

Figure 5(b) shows the EELS spectra associated with the inner-shell (K-shell) ionization. Again, the spectra for diamond and polycrystalline graphite are included for comparisons. Sharp peaks are observed at 285.5 and 292.5 eV in graphite, while no peak is seen at 285.5 eV in diamond. The general features of the K-shell EELS spectra for the sputtered and PECVD carbon samples resemble the features of graphite, but with the higher energy features smeared. The observation of the peak

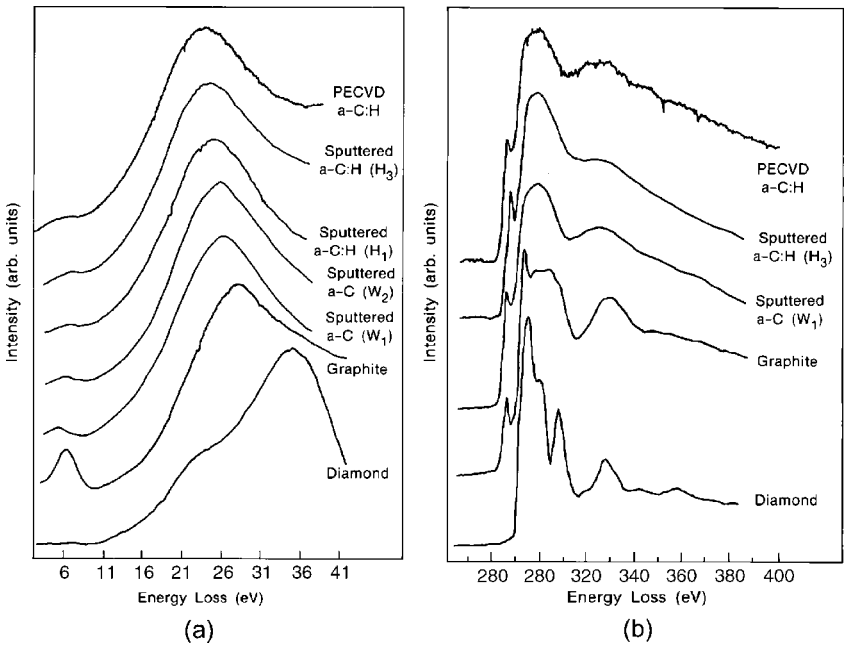

Fig. 5 (a) Low energy, and (b) high energy EELS of DLC coatings produced by DC magnetron sputtering and RF-PECVD techniques, Data for bulk diamond and polycrystalline graphite are included for comparisons [30]

Table 3 Experimental results of FRS analysis [30]

Sample	Ar/H ratio	C (at. % ± 0.5)	H (at. % ± 0.5)	Ar (at. % ± 0.5)	O (at. % ± 0.5)
Sputtered a-C coating (W2)	100/0	90.5	9.3	0.2	–
Sputtered a-C:H coating (H2)	99/1	63.9	35.5	0.6	–
Sputtered a-C:H coating (H3)	97/3	56.1	36.5	–	7.4
Sputtered a-C:H coating (H4)	95/5	53.4	39.4	–	7.2
Sputtered a-C:H coating (H5)	93/7	58.2	35.4	0.2	6.2
Sputtered a-C:H coating (H6)	90/10	57.3	35.5	–	7.2
PECVD a-C:H coating	99.5% CH_4	81.9	18.1	–	–
Diamond coating	H_2 – 1 mole % CH_4	94.0	6.0	–	–

Table 4 Experimental results of physical properties [30]

Sample	Mass density (g/cm^3)	Nano-hardness (GPa)	Elastic modulus (GPa)	Electrical resistivity (Ohm-cm)	Compressive residual stress (GPa)
Sputtered a-C coating (W1)	2.1	15	141	1300	0.55
Sputtered a-C:H coating (W2)	1.8	14	136	0.61	0.57
Sputtered a-C:H coating (H1)	–	14	96	–	>2
Sputtered a-C:H coating (H3)	1.7	7	35	$>10^6$	0.3
PECVD a-C:H coating	1.6–1.8	33–35	~200	$>10^6$	1.5–3.0
Diamond coating	–	40–75	370–430	–	–
Graphite (for reference)	2.267	Soft	9–15	5×10^{-5}[a], 4×10^{-3}[b]	0
Diamond (for reference)	3.515	70–102	900–1,050	10^7–10^{20}	0

[a]Parallel to layer planes

[b]Perpendicular to layer planes

at 285.5 eV in the sputtered and PECVD coatings also indicates the presence of sp^2-bonded atomic sites in the coatings. These spectra peak at 292.5 eV, similar to the spectra of graphite, but the peak in graphite is sharper.

Raman spectra from samples W1, W2, H1, and PECVD are shown in Fig. 6. Raman spectra could not be observed in specimens H2 and H3 due to high flourescence signals. The Raman spectra of single crystal diamond and polycrstalline graphite are also shown for comparison in Fig. 6. The results of the spectral fits are summarized in Table 2. We will focus on the G-band position, which has been shown to be related to the fraction of sp^3-bonded sites. Increasing the power density in the amorphous carbon coatings (W1 and W2) results in a higher G-band frequency, implying a smaller fraction of sp^3-bonding in W2 than in W1. This is consistent with higher density of W1. H1 and PEVCD have still lower G-band positions than W1, implying an even higher fraction of sp^3-bonding, which is presumable caused by the incorporation of H atoms into the lattice. The high hardness of H3 might be attributed to efficient sp^3 cross-linking of small, sp^2-ordered domains.

The Raman spectrum of a MPECVD diamond coating is shown in Fig. 6. The diamond Raman peak is at 1,333 cm^{-1} with a line width of 7.9 cm^{-1}. There is a small broad peak around 1525 cm^{-1}, which is attributed to a small amount of a-C:H. This impurity peak is not intense enough to fit to separate G- and D-bands. The diamond peak frequency is very close to that of natural diamond (1332.5 cm^{-1}, e.g., Fig. 6), indicating that the coating is not under stress [69]. The large line width compared to that of natural diamond (2 cm^{-1}) indicates that the microcrystallites likely have a high concentration of defects [1].

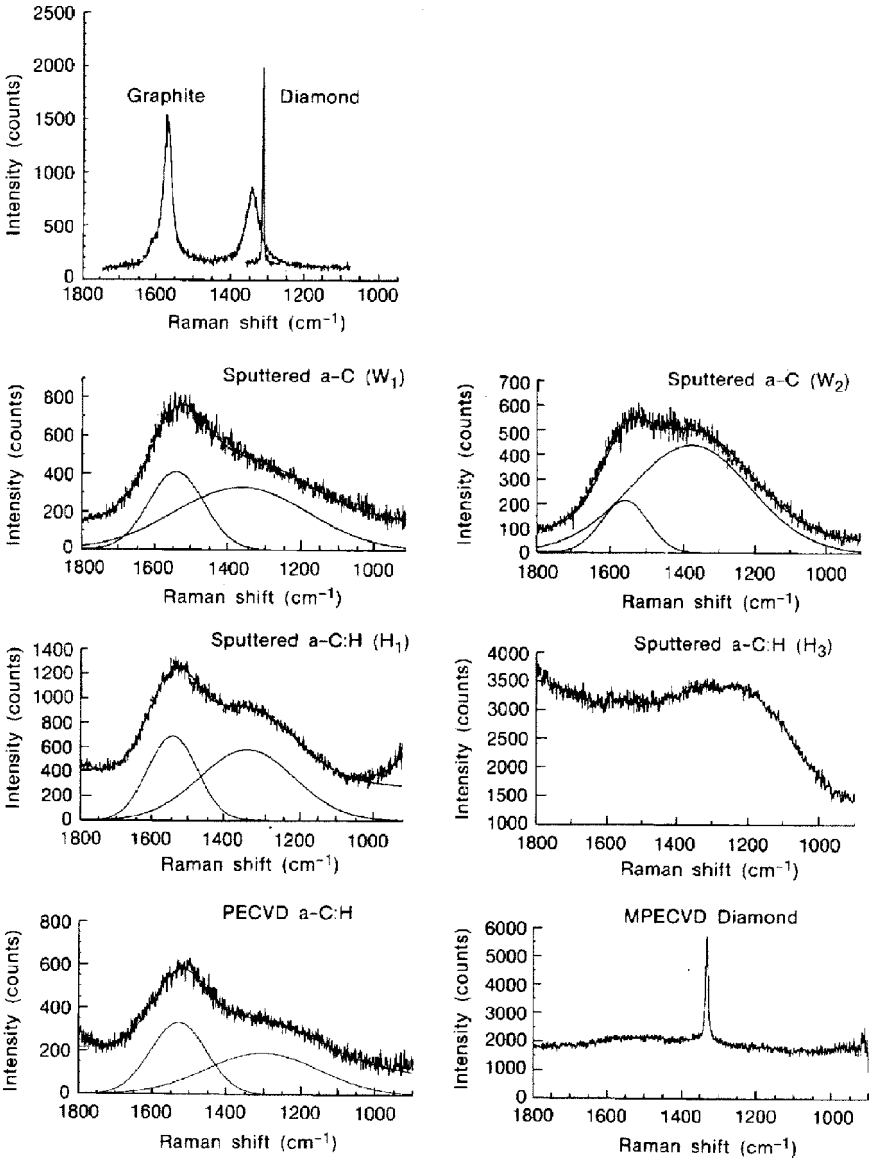

Fig. 6 Raman spectra of DLC coatings produced by DC magnetron sputtering and RF-PECVD techniques and a diamond film produced by MPECVD technique. Data for bulk diamond and microcrystalline graphite are included for comparison. [30]

3.1.2 Hydrogen Concentrations

FRS analysis of six sputtered (W2, H2, H3, H4, H5, and H6) coatings, one PECVD coating, and one diamond coating was performed. Figure 7 shows an overlay of the spectra from the six sputtered samples. Similar spectra were obtained from the

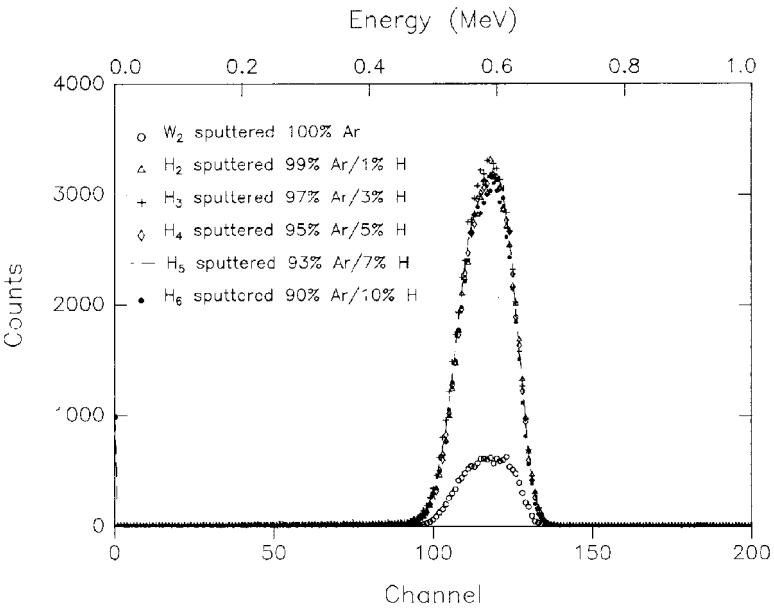

Fig. 7 FRS spectra of six DLC coatings produced by DC magnetron sputtering [30]

PECVD and the diamond films. Table 3 shows the H and C fractions as well as the amount of impurities (Ar and O) in the films in atomic percentage. Most apparent is the large fraction of H in the sputtered films. Regardless of how much H_2 is in the Ar sputtering gas, the H content of the coatings is about the same, ~35 at. %. Interestingly, there is still ~10% H present in the coating sputtered in pure Ar (W2). It is interesting to note that Ar is present only in coatings grown under low (<1%) H content in the Ar carrier gas. The presence of O in the coatings, combined with the fact that the coatings were prepared approximately 9 months before the FRS analysis, caused suspicion that they had absorbed water vapor, and that this may be the cause for the H peak in specimen W2.

All samples were annealed for 24 h at 250°C in a flowing He furnace and then reanalyzed. Surprisingly, the H content of all coatings measured increased slightly, even though the O content decreased, and W2 still had a substantial amount of H_2. This slight increase in H concentration is not understood; however, since H concentration did not decrease with the oxygen as a result of annealing, it suggests that high H concentration is not due to adsorbed water vapor. The PECVD film has more H (~18%) than the sputtered films initially, but after annealing it has the same fraction as specimen W2, the film sputtered in pure Ar. The diamond film has the smallest amounts of H, as seen in Table 3.

3.1.3 Physical Properties

Physical properties of the four sputtered (W1, W2, H1, and H3) coatings, one PECVD coating, one diamond coating, coatings and bulk diamond, and graphite are presented in Table 4. The hydrogenated carbon and the diamond coatings have very high resistivity compared to unhydrogenated carbon coatings. It appears that unhydrogenated carbon coatings have a higher density than the hydrogenated carbon coatings, although both groups are less dense than graphite. The density depends on the deposition technique and the deposition parameters. It appears that unhydrogenated sputtered coatings deposited at low power exhibit the highest density. Nanohardness of hydrogenated carbon is somewhat lower than that of the unhydrogenated carbon coatings. PECVD coatings are significantly harder than sputtered coatings. The nanohardness and modulus of elasticity of the diamond coatings are very high compared to that of DLC coatings even though the H content is similar. The compressive residual stresses of the PECVD coatings are substantially higher than those of sputtered coatings, which is consistent with the hardness results.

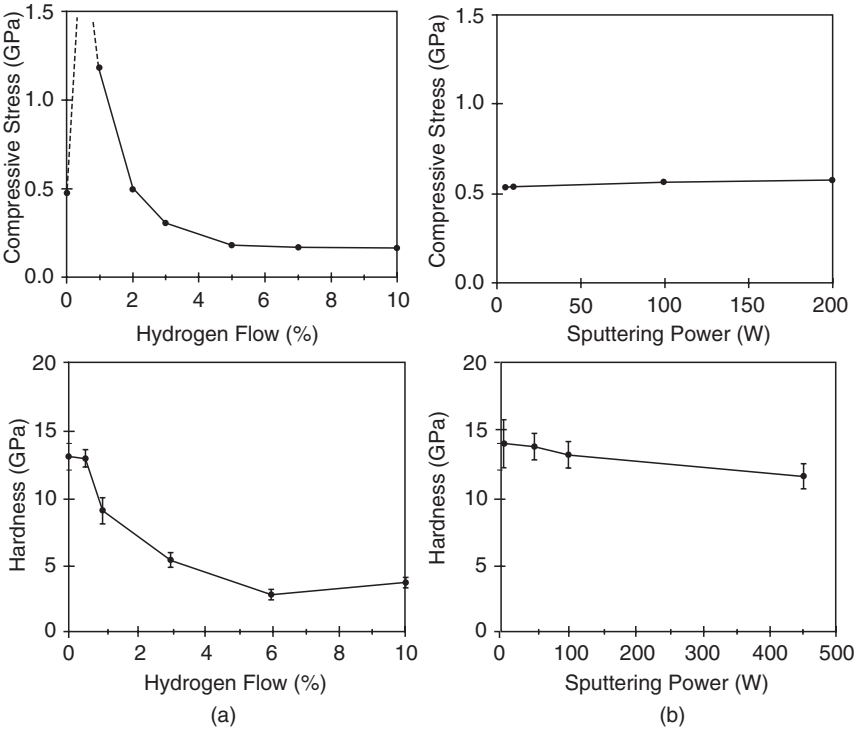

Fig. 8 Residual compressive stresses and nanohardness (a) as a function of hydrogen flow rate; sputtering power is 100 W and target diameter is 75 mm (power density = 2.1 W/cm^2), and (b) as a function of sputtering power over a 75 mm diameter target with no hydrogen added in the plasma [91]

Figure 8(a) shows the effect of H in the plasma on the residual stresses and the nanohardness for sputtered coatings W2 and H1–H6. The coatings made with H_2 flow between 0.5% and 1.0% delaminate very quickly, even when only a few tens of nanometers thick. In pure Ar and at H_2 flows greater than 1%, the coatings appear to be more adhesive. The tendency of some coatings to delaminate can be caused by intrinsic stress in the coating, which is measured by substrate bending. All of the coatings in the figure are in compressive stress. The maximum stress occurs between 0% and 1% H_2 flow, but the stress cannot be quantified in this range because the coatings instantly delaminate upon exposure to air. At higher H concentrations the stress gradually diminishes. A generally decreasing trend is observed in the hardness of the coatings as H content increased. The hardness decreases slightly, going from 0% to 0.5% H_2, and then decreases sharply. These results are probably lower than the true values because of local delamination around the indentation point. This is especially likely for the 0.5% and 1.0% coatings where delamination is visually apparent, but may also be true to a lesser extent for the other coatings. Such an adjustment would bring the hardness profile into closer correlation with the stress profile. Weissmantel et al. [110] and Scharff et al. [95] observed a downturn in hardness for high bias and low pressure of hydrocarbon gas in ion-plated carbon coating and therefore presumably low H content in support of the above contention.

Figure 8(b) shows the effect of sputtering power (with no H added in the plasma) on the residual stresses and nanohardness for various sputtered coatings. As the power decreases, compressive stress does not seem to change while nanohardness slowly increases. The rate of change becomes more rapid at very low power levels.

Addition of H_2 during sputtering of carbon coatings increases H concentration in the coating. H causes the character of the C–C bonds to shift from sp^2 to sp^3, and the rising number of C–H bonds which ultimately relieves stress and produces a softer "polymer-like" material. Low power deposition, like the presence of H, appears to stabilize the formation of sp^3 C–C bonds, increasing hardness. These coatings have relieved stress and better adhesion. An increase in temperature during deposition at high power density results in graphitization of the coating material, responsible for a decrease in hardness with an increase in power density. Unfortunately, low power also means impractically low deposition rates.

3.1.4 Summary

Based on the EELS and Raman data, all DLC coatings have both sp^2- and sp^3-bondings. sp^2/sp^3-bonding ratio depends on the deposition techniques and parameters. The DLC coatings deposited by sputtering and PECVD contain significant concentrations of H while the diamond coating contains only small amounts of H impurity. Sputtered coatings with no deliberate addition of H in the plasma contain a significant amount of H. Regardless of how much H is in the Ar sputtering gas, the H content of the coatings increases initially with no further increase.

H flow and sputtering power density affect the mechanical properties of these coatings. Maximum compressive residual stress and hardness occur between 0% and 1% H flow, resulting in rapid delamination. Low sputtering power moderately increases hardness while relieving residual stress.

4 Micromechanical and Tribological Characterizations of Coatings Deposited

4.1 Various Techniques

4.1.1 Micromechanical Characterization

Common mechanical characterizations include measurement of hardness and elastic modulus, fracture toughness, fatigue life, and scratch and wear testing. Nanoindentation and atomic force microscopy (AFM) are used for mechanical characterization of ultrathin films.

Hardness and elastic modulus are calculated from the load displacement data obtained by nanoindentation at loads ranging typically from 0.2 to 10 mN using a commercially available nanoindenter [17, 28]. This instrument monitors and records the dynamic load and displacement of the three-sided pyramidal diamond (Berkovich) indenter during indentation. For fracture toughness measurement of ultrathin films ranging from 100 nm to few microns, a nanoindentation-based technique is used in which through-thickness cracking in the coating is detected from a discontinuity observed in the load–displacement curve and energy released during the cracking is obtained from the curve [79, 73, 76]. Based on the energy released, fracture mechanics analysis is then used to calculate fracture toughness. An indenter with a cube corner tip geometry is preferred because the through-thickness cracking of hard films can be accomplished at lower loads. In fatigue measurement, a conical diamond indenter having a tip radius of about 1 μm is used and load cycles of a sinusoidal shape are applied [77, 78]. The fatigue behavior of coatings is studied by monitoring the change in contact stiffness which is sensitive to the damage formation.

Hardness and Elastic Modulus

For materials which undergo plastic deformation, high hardness and elastic modulus are generally needed for low friction and wear, whereas for brittle materials, high fracture toughness is needed [15, 18, 23]. DLC coatings used for many applications are hard and brittle and values of hardness and fracture toughness need to be optimized.

Representative load–displacement plots of indentations made at 0.2 mN peak indentation load on 100 nm thick DLC coatings deposited by the four deposition

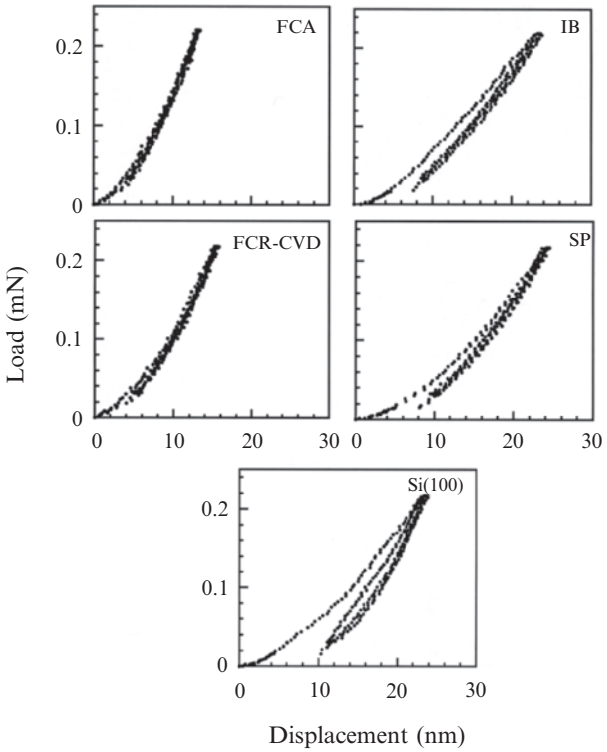

Fig. 9 Load versus displacement plots for various 100 nm thick amorphous carbon coatings on single-crystal silicon substrate and bare substrate

techniques on single-crystal silicon substrate are compared in Fig. 9. The indentation depths at the peak load range from about 18–26 nm, smaller than that of the coating thickness. Many of the coatings exhibit a discontinuity or pop-in marks in the loading curve, which indicate a sudden penetration of the tip into the sample. A nonuniform penetration of the tip into a thin coating possibly results due to either formation of cracks in the coating, formation of cracks at the coating–substrate interface, or debonding or delamination of the coating from the substrate.

The hardness and elastic modulus values at a peak load of 0.2 mN on the various coatings and single-crystal silicon substrate are summarized in Table 5 and Fig. 10 [64, 75, 76, 77]. Typical values for the peak and residual indentation depths ranged from 18 to 26 nm and from 6 to 12 nm, respectively. The FCA coatings exhibit the highest hardness of 24 GPa and elastic modulus of 280 GPa of various coatings, followed by the ECR-CVD, IB, and SP coatings. Hardness and elastic modulus have been known to vary over a wide range with sp^3/sp^2 bonding ratio, which depends on the kinetic energy of the carbon species and amount of H [9, 90, 62, 64, 41]. The high hardness and elastic modulus of the FCA coatings are attributed to the high kinetic energy of carbon species involved in the FCA deposition [63, 64].

Table 5 Hardness, elastic modulus, fracture toughness, fatigue life, critical load during scratch, coefficient of friction during accelerated wear testing, and residual stresses of various DLC coatings on single-crystal silicon substrate

Coating	Hardness[a] (Li and Bhushan, 1999a) (GPa)	Elastic modulus[a] (Li and Bhushan, 1999a) (GPa)	Fracture toughness[a] (Li and Bhushan, 1999c) (MPa $m^{1/2}$)	Fatigue life[b], Nf[d] (Li and Bhushan, 2002a) ($x10^4$)	Critical load during scratch[b] (Li and Bhushan, 1999a) (mN)	Coefficient of friction during accelerated wear testing[b] (Li and Bhushan, 1999a)	Compressive residual stress[c] (Gupta and Bhushan, 1995b) (GPa)
Cathodic arc carbon coating (a-C)	24	280	11.8	2.0	3.8	0.18	12.5
Ion beam carbon coating (a-C:H)	19	140	4.3	0.8	2.3	0.18	1.5
ECR-CVD carbon coating (a-C:H)	22	180	6.4	1.2	5.3	0.22	0.6
DC sputtered carbon coating (a-C:H)	15	140	2.8	0.2	1.1	0.32	2.0
Bulk graphite (for comparison)	Very soft	9–15	–	–	–	–	–
Diamond (for comparison)	80–104	900–1050	–	–	–	–	–
Si(100) substrate	11	220	0.75	–	0.6	0.55	0.02

[a]Measured on 100 nm thick coatings

[b]Measured on 20 nm thick coatings

[c]Measured on 400 nm thick coatings

[d]Nf was obtained at a mean load of 10 μN and a load amplitude of 8 μN

Anders et al. [4] also reported a high hardness, measured by nanoindentation, of about 45 GPa for cathodic arc carbon coatings. They observed a change in hardness from 25 to 45 GPa with pulsed bias voltage and bias duty cycle. The high hardness of cathodic arc carbon was attributed to the high percentage (more than 50%) of sp^3 bonding. Savvides and Bell [93] reported an increase in hardness from 12 to 30 GPa

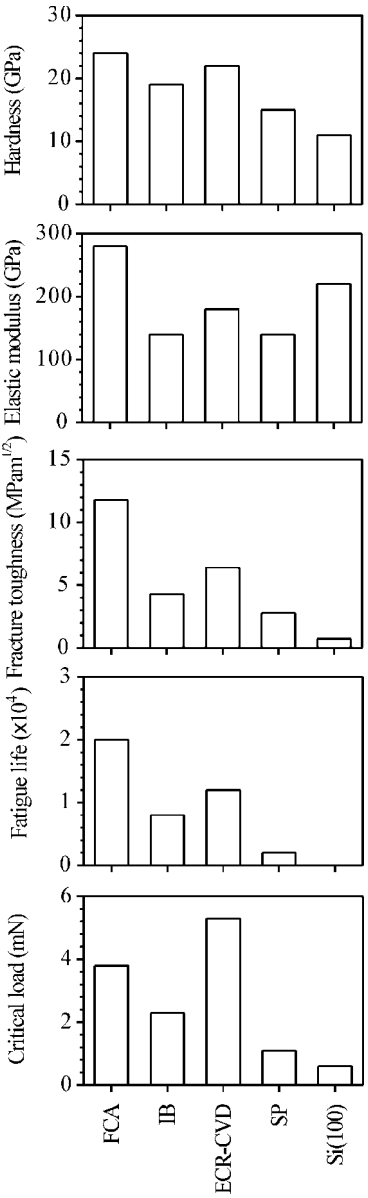

Fig. 10 Bar charts summarizing the data of various coatings and single-crystal silicon substrate. Hardness, elastic modulus, and fracture toughness were measured on 100 nm thick coatings, and fatigue life and critical load during scratch were measured on 20 nm thick coatings

and in elastic modulus from 62 to 213 GPa with an increase of sp^3/sp^2 bonding ratio, from 3 to 6, for a C:H coating deposited by low-energy ion-assisted unbalanced magnetron sputtering of a graphite target in an Ar–H_2 mixture.

Bhushan et al. [30] reported hardnesses of about 15 and 35 GPa and elastic moduli of about 140 and 200 GPa, measured by nanoindentation, for a-C:H coatings deposited by DC magnetron sputtering and RF-PECVD techniques, respectively. The high hardness of RF-PECVD a-C:H coatings is attributed to a higher concentration of sp^3 bonding than in a sputtered hydrogenated a-C:H coating. H is believed to play a crucial role in the bonding configuration of carbon atoms by helping to stabilize tetrahedra-coordination (sp^3 bonding) of carbon species. Jansen et al. [67] suggested that the incorporation of H efficiently passivates the dangling bonds and saturates the graphitic bonding to some extent. However, a large concentration of H in the plasma in sputter deposition is undesirable. Cho et al. [43] and Rubin et al. [91] observed that hardness decreased from 15 to 3 GPa with increased H content. Bhushan and Doerner [24] reported a hardness of about 10–20 GPa and an elastic modulus of about 170 GPa, measured by nanoindentation, for 100 nm thick DC-magnetron sputtered a-C:H on the silicon substrate.

Residual stresses measured using a well-known curvature measurement technique is also presented in Table 5. The DLC coatings are under significant compressive internal stresses. Very high compressive stresses in FCA coatings are believed to be partly responsible for their high hardness. However, high stresses result in coating delamination and buckling. For this reason, the coatings thicker than about 1 μm have a tendency to delaminate from the substrates.

Fracture Toughness

Representative load–displacement curves of indentations on the 400 nm thick cathodic arc carbon coating on silicon at various peak loads are shown in Fig. 11. Steps are found in all curves as shown by arrows in Fig. 11(a). In the 30 mN SEM micrograph, in addition to several radial cracks, ring-like through-thickness cracking is observed with small lips of material overhanging the edge of indentation. The step at about 23 mN in the loading curves of indentations made at 30 and 100 mN peak indentation loads results from the ring-like through-thickness cracking. The step at 175 mN in the loading curve of indentation made at 200 mN peak indentation load is caused by spalling and second ring-like through-thickness cracking.

Based on Li et al. [79], the fracture process progresses in three stages: (1) first ring-like through-thickness cracks form around the indenter by high stresses in the contact area, (2) delamination and buckling occur around contact area at the coating/substrate interface by high lateral pressure, (3) second ring-like through-thickness cracks and spalling are generated by high bending stresses at the edges of the buckled coating, see Fig. 12(a). In the first stage, if the coating under the indenter is separated from the bulk coating via the first ring-like through-thickness cracking, a corresponding step will be present in the loading curve. If discontinuous cracks form and the coating under the indenter is not separated from the remaining coating, no step appears in the loading curve

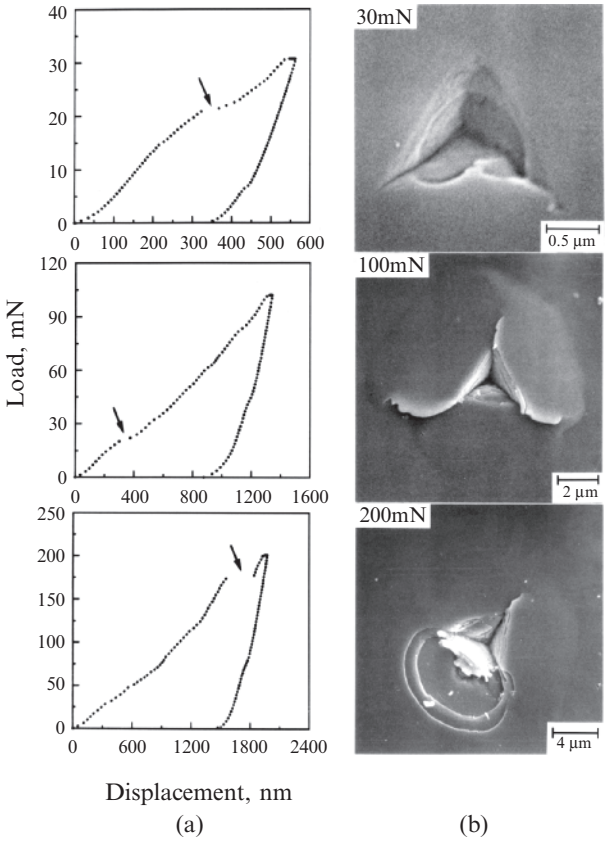

Fig. 11 (a) Load–displacement curves of indentations made at 30,100 and 200 mN peak indentation loads using the cube corner indenter, and (b) the SEM micrographs of indentations on the 400 nm thick cathodic arc carbon coating on silicon. Arrows indicate steps during loading portion of the load–displacement curve [79]

because the coating still supports the indenter and the indenter cannot suddenly advance into the material. In the second stage, for the coating used in the present study, the advances of the indenter during the radial cracking, delamination, and buckling are not big enough to form steps in the loading curve because the coating around the indenter still supports the indenter, but generate discontinuities which change the slope of the loading curve with increasing indentation loads. In the third stage, the stress concentration at the end of the interfacial crack cannot be relaxed by the propagation of the interfacial crack. With an increase in indentation depth, the height of the bulged coating increases. When the height reaches a critical value, the bending stresses caused by the bulged coating around the indenter will result in the second ring-like through-thickness crack formation and spalling at the edge of the buckled coating as shown in Fig. 12(a), which leads

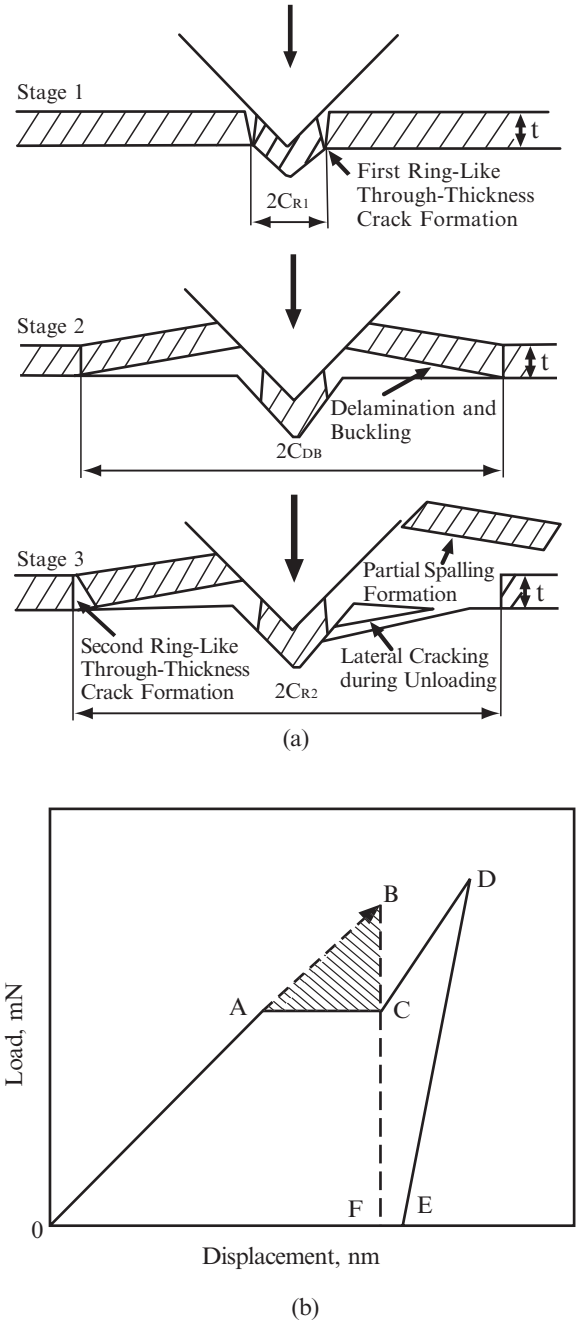

Fig. 12 (a) Schematic of various stages in nanoindentation fracture for the coatings/substrate system, and (b) schematic of a load–displacement curve, showing a step during the loading cycle and associated energy release

to a step in the loading curve. This is a single event and results in the separation of the part of the coating around the indenter from the bulk coating via cracking through coatings. The step in the loading curve is totally from the coating cracking and not from the interfacial cracking or the substrate cracking.

The area under the load–displacement curve is the work performed by the indenter during elastic–plastic deformation of the coating/substrate system. The strain energy release in the first/second ring-like cracking and spalling can be calculated from the corresponding steps in the loading curve. Figure 12(b) shows a modeled load–displacement curve. OACD is the loading curve and DE is the unloading curve. Since the first ring-like through-thickness crack should be considered. It should be emphasized that the edge of the buckled coating is far from the indenter, therefore, it does not matter if the indentation depth exceeds the coating thickness or if deformation of the substrate occurs around the indenter when we measure fracture toughness of the coating from the released energy during the second ring-like through-thickness cracking (spalling). Suppose that the second ring-like through-thickness cracking occurs at AC. Now, let us consider the loading curve OAC. If the second ring-like through-thickness crack does not occur, it can be understood that OA will be extended to OB to reach the same displacement as OC. This means that the crack formation changes the loading curve OAB into OAC. For point B, the elastic–plastic energy stored in the coating/substrate system should be OBF. For point C, the elastic–plastic energy stored in the coating/substrate system should be OACF. Therefore, the energy difference before and after the crack generation is the area of ABC, that is, this energy stored in ABC will be released as strain energy to create the ring-like through-thickness crack. According to the theoretical analysis by Li et al. [79], the fracture toughness of thin films can be written as

$$K_{Ic} = \left[\left(\frac{E}{\left(1-\nu^2\right) 2\pi C_R} \right) \left(\frac{U}{t} \right) \right]^{1/2} \tag{2}$$

where E is the elastic modulus, ν is the Poisson's ratio, $2\pi C_R$ is the crack length in the coating plane, t is the coating thickness, and U is the strain energy difference before and after cracking,

Using Eq. 2, the fracture toughness of the coatings is calculated. The loading curve is extrapolated along the tangential direction of the loading curve from the starting point of the step up to reach the same displacement as the step. The area between the extrapolated line and the step is the estimated is estimated strain energy difference before and after cracking. C_R is measured from SEM micrographs or AFM images of indentations. Second ring-like crack is where the spalling occurs. For example, for the 400 nm thick cathodic arc carbon coating data presented in Fig. 11, U of 7.1 nNm is assessed from the steps in Fig. 11(a) at the peak indentation loads of 200 mN. For C_R of 7.0 μm from Fig. 11(b), E = 300 GPa measured using nanoindenter and an assumed value of 0.25 for ν, fracture toughness values is calculated as 10.9 MPa $\sqrt{\text{m}}$ [79, 73]. The fracture toughness and

related data for various 100 nm thick DLC coatings are presented in Fig. 10 and Table 5.

Nanofatigue

Delayed fracture resulting from extended service is called fatigue [104]. Fatigue fracturing progresses through a material via changes within the material at the tip of a crack, where there is high stress intensity. There are several situations: cyclic fatigue, stress corrosion, and static fatigue. Cyclic fatigue results from cyclic loading of machine components. In a low-flying slider in a magnetic head-disk interface, isolated asperity contacts occur during use and the fatigue failure occurs in the multilayered thin-film structure of the magnetic disk [14]. In many MEMS components, impact occurs and the failure mode is cyclic fatigue. Asperity contacts can be simulated using a sharp diamond tip in an oscillating contact with the component.

Figure 13 shows the schematic of a fatigue test on a coating/substrate system using a continuous stiffness measurement (CSM) technique. Load cycles are applied to the coating, resulting in a cyclic stress; P is the cyclic load, P_{mean} is the mean load, P_0 is the oscillation load amplitude, and ω is the oscillation frequency. The following results can be obtained: (1) endurance limit; i.e., the maximum load

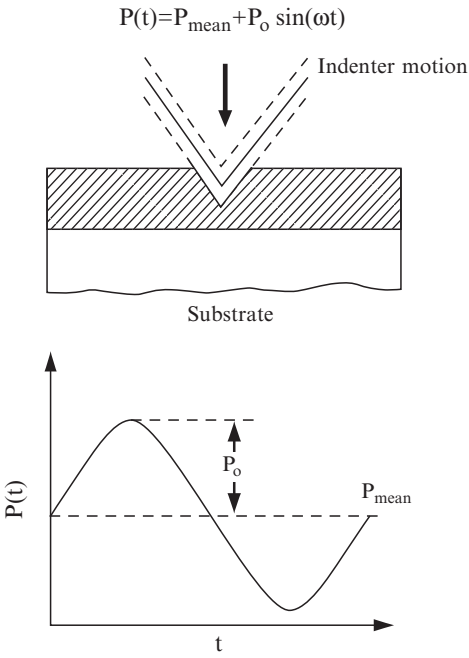

Fig. 13 Schematic of a fatigue test on a coating/substrate system using the continuous stiffness measurement technique

below which there is no coating failure for a preset number of cycles; (2) number of cycles at which the coating failure occurs; and (3) changes in contact stiffness measured by using the unloading slope of each cycle which can be used to monitor the propagation of the interfacial cracks during cyclic fatigue process.

Figure 14(a) shows the contact stiffness as a function of the number of cycles for 20 nm thick FCA coatings cyclically deformed by various oscillation load amplitudes with a mean load of 10 μN at a frequency of 45 Hz. At 4 μN load amplitude,

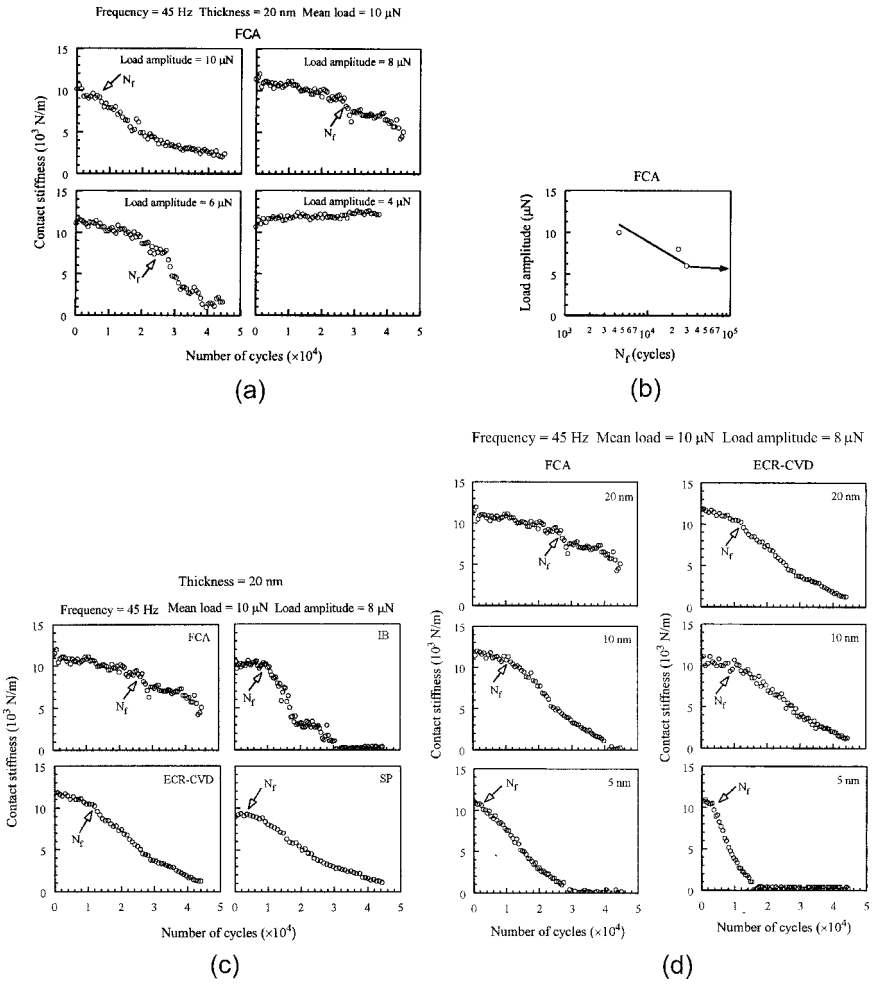

Fig. 14 (a) Contact stiffness as a function of the number of cycles for 20 nm thick FCA coatings cyclically deformed by various oscillation load amplitudes with a mean load of 10 μN at a frequency of 45 Hz; (b) plot of load amplitude versus N_f; (c) contact stiffness as a function of the number of cycles for four different 20 nm thick coatings; and (d) contact stiffness as a function of the number of cycles for two coatings of the different thicknesses

no change in contact stiffness was found for all coatings. This indicates that 4 μN load amplitude is not high enough to damage the coatings. At 6 μN load amplitude, an abrupt decrease in contact stiffness was found at a certain number of cycles for each coating, indicating that fatigue damage has occurred. With increasing load amplitude, the number of cycles to failure, N_f, decreases for all coatings. Load amplitude versus N_f, a so-called S–N curve, is plotted in Fig. 14(b). The critical load amplitude below which no fatigue damage occurs (an endurance limit) was identified for each coating. This critical load amplitude together with mean load is of critical importance to the design of head-disk interfaces or MEMS/NEMS device interfaces.

To compare the fatigue lives of different coatings studied, the contact stiffness as a function of the number of cycles for 20 nm thick FCA, IB, ECR-CVD, and SP coatings cyclically deformed by an oscillation load amplitude of 8 μN with a mean load of 10 μN at a frequency of 45 Hz is shown in Fig. 14(c). FCA coating has the longest N_f, followed by ECR-CVD, IB, and SP coatings. In addition, after the N_f, the contact stiffness of the FCA coating shows a slower decrease than the other coatings. This indicates that after the N_f, the FCA coating had less damage than others. The fatigue behavior of FCA and ECR-CVD coatings of different thicknesses is compared in Fig. 14(d). For both coatings, N_f decreases with decreasing coating thickness. At 10 nm, FCA and ECR-CVD have almost the same fatigue life. At 5 nm, ECR-CVD coating shows a slightly longer fatigue life than FCA coating. This indicates that even for nanometer thick DLC coatings, their microstructure and residual stresses are not uniform across the thickness direction. Thinner coatings are more influenced by interfacial stresses than thicker coating.

Figure 15(a) shows the high magnification SEM images of 20 nm thick FCA coatings before, at, and after N_f. In the SEM images, the net-like structure is the gold film coated on the DLC coating, which should be ignored in analyzing the indentation fatigue damage. Before the N_f, no delamination or buckling was found except the residual indentation mark at magnifications up to 1,200,000x using SEM. This suggests that only plastic deformation occurred before the N_f. At the N_f, the coating around the indenter bulged upwards, indicating delamination and buckling. Therefore, it is believed that the decrease in contact stiffness at the N_f results from the delamination and buckling of the coating from the substrate. After the N_f, the buckled coating was broken down around the edge of the buckled area, forming a ring-like crack. The remaining coating overhung at the edge of the buckled area. It is noted that the indentation size increases with increasing number of cycles. This indicates that deformation, delamination and buckling, and ring-like crack formation occurred over a period of time.

The schematic in Fig. 15(b) shows various stages in the indentation fatigue damage for a coating/substrate system. Based on this study, three stages in the indentation fatigue damage appear to exist: (1) indentation induced compression; (2) delamination and buckling; and (3) ring-like crack formation at the edge of the buckled coating. Residual stresses are often induced in coatings by the deposition process. The model shown in Fig. 15(b) considers a coating with a uniform biaxial

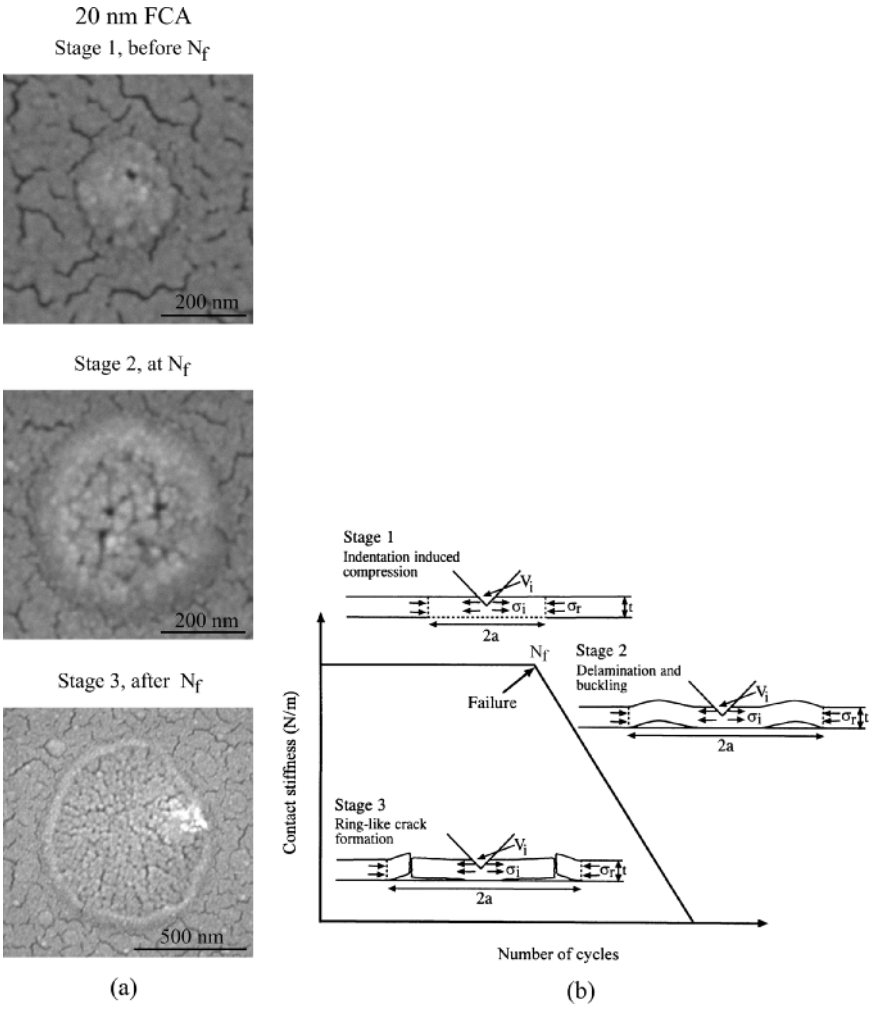

Fig. 15 (a) High magnification SEM images of a coatings before, at, and after N_f, and (b) schematic of various stages in the indentation fatigue damage for a coating/substrate system [77]

residual compression σ_r. In the first stage, indentation induces elastic/plastic deformation, exerting an outward acting pressure on the coating around the indenter. Interfacial defects like voids and impurities act as original cracks. These cracks propagate and link up as the indentation compressive stress increases. At this stage, the coating, which is under the indenter and above the interfacial crack (with a crack length of $2a$), still maintains a solid contact with the substrate; the substrate still fully supports the coating. Therefore, this interfacial crack does not lead to an abrupt decrease in contact stiffness, but gives a rise to a slight decrease in contact

stiffness as shown in Fig. 14. The coating above the interfacial crack is treated as a rigidly clamped disk. We assume that the crack radius (a) is large compared with the coating thickness (t). Since the coating thickness ranges from 20 to 5 nm, this assumption is easily satisfied in this study (radius of the delaminated and buckled area, shown in Fig. 15(a) is on the order of 100 nm). The compressive stress caused by indentation is given as [83]

$$\sigma_i = \frac{E}{(1-\nu)}\varepsilon_i = \frac{EV_i}{2\pi t a^2(1-\nu)} \tag{3}$$

where ν and E are the Poisson's ratio and elastic modulus of the coating, V_i is the indentation volume, t is the coating thickness, and a is the crack radius. With increasing number of cycles, the indentation volume V_i increases. Therefore, the indentation compressive stress σ_i increases accordingly. In the second stage, buckling occurs during the unloading segment of fatigue testing cycle when the sum of indentation compressive stress σ_i and the residual stress σ_r exceed the critical buckling stress σ_b for the delaminated circular section as given by [54]

$$\sigma_b = \frac{\mu^2 E}{12\left(1-\nu^2\right)}\left(\frac{t}{a}\right)^2 \tag{4}$$

where the constant μ equals 42.67 for a circular clamped plate with a constrained centerpoint and 14.68 when the center is unconstrained. The buckled coating acts as a cantilever. In this case, the indenter indents a cantilever rather than a coating/substrate system. This ultrathin coating cantilever has much less contact stiffness than the coating/substrate system. Therefore, the contact stiffness shows an abrupt decrease at the N_f. In the third stage, with increasing the number of cycles, the delaminated and buckled size increases, resulting in a further decrease in contact stiffness since the cantilever beam length increases. On the other hand, a high bending stress acts at the edge of the buckled coating. Larger the buckled size, higher is the bending stress. The cyclically bending stress causes fatigue damage at the end of the buckled coating, forming a ring-like crack. The coating under the indenter is separated from the bulk coating (caused by the ring-like crack at the edge of the buckled coating) and the substrate (caused by the delamination and buckling in the second stage). Therefore, the coating under the indenter is not constrained but is free to move with the indenter during fatigue testing. At this point, the sharp nature of the indenter is lost because the coating under the indenter gets stuck on the indenter. The indentation fatigue experiment results in the contact of a relative huge blunt tip with the substrate. This results in a low contact stiffness value.

Compressive residual stresses result in delamination and buckling. A coating with higher adhesion strength and a less compressive residual stress is required for

a higher fatigue life. Interfacial defects should be avoided in coating deposition process. We know that the ring-like crack formation occurs in the coating. Formation of fatigue cracks in the coating depends upon the hardness and fracture toughness. Cracks are more difficult to form and propagate in the coating with higher strength and fracture toughness.

It is now accepted that long fatigue life in a coating/substrate almost always involves "living with crack," that the threshold or limit condition is associated with the nonpropagation of exiting cracks or defects, even though these cracks may be undetectable [104]. For all coatings studied, at 4 μN, contact stiffness does not change much. This indicates that delamination and buckling did not occur within the number of cycles tested in this study. This is probably because the indentation induced compressive stress was not high enough to allow the cracks to propagate and link up under the indenter or the sum of indentation compressive stress σ_i and the residual stress σ_r did not exceed the critical buckling stress σ_b.

Figure 10 and Table 5 summarize the hardness, elastic modulus, fracture toughness, and fatigue life of all coatings studied. A good correlation exists between fatigue life and other mechanical properties. Higher mechanical properties result in a longer fatigue life. The mechanical properties of DLC coatings are controlled by the sp^3/sp^2 ratio. The sp^3-bonded carbon exhibits the outstanding properties of diamond [19]. A higher deposition kinetic energy will result in a larger fraction of sp^3-bonded carbon in an amorphous network. Thus, the higher kinetic energy for the FCA could be responsible for its better carbon structure and higher mechanical properties [74, 75, 102, 103]. Higher adhesion strength between the FCA coating and substrate makes the FCA coating more difficult to delaminate from the substrate.

4.1.2 Microscratch and Microwear Studies

For microscratch studies, a conical diamond indenter (e.g., having a tip radius of about 1 μm and included angle of 60°) is drawn over the sample surface, and the load is ramped up (typically from 2 to 25 mN), until substantial damage occurs. The coefficient of friction is monitored during scratching. Scratch-induced damage of coating, specifically fracture or delamination, can be monitored by in situ friction force measurements and by optical and SEM imaging of the scratches after tests. A gradual increase in friction is associated with plowing and abrupt increase in friction is associated with fracture or catastrophic failure [25]. The load, corresponding to the abrupt increase in friction or an increase in friction above a certain value (typically $2x$ of initial value), provides a measure of scratch resistance or adhesive strength of a coating and is called "critical load." Depth of scratches with increasing scratch length or normal load is measured by using an AFM, typically with an area of 10×10 μm [72, 74, 75].

The microscratch and microwear studies are also conducted using an AFM [27, 70, 17, 102, 103]. A square pyramidal diamond tip (tip radius ~100 nm) or a three-sided pyramidal diamond (Berkovich) tip, with an apex angle of 60° and a

tip radius of about 100 nm, mounted on a platinum-coated, rectangular stainless steel cantilever of stiffness of about 40 N/m, is scanned orthogonal to the long axis of the cantilever to generate scratch and wear marks. During the scratch test, the normal load is either kept constant or is increased (typically from 0 to 100 μN), until damage occurs. Topography images of the scratch are obtained in situ with the AFM at a low load. By scanning the sample during scratching, wear experiments can be conducted. Wear at a constant load is monitored as a function of number of cycles. Normal loads ranging from 10 to 80 μN are typically used.

Microscratch

Scratch test conducted with a sharp diamond tip simulate a sharp asperity contact. In a scratch test, the cracking or delamination of a hard coating is signaled by a sudden increase in the coefficient of friction [17]. The load associated with this event is called the "critical load."

Wu [111], Bhushan et al. [34], Gupta and Bhushan [63, 64], and Li and Bhushan [72, 74, 75] have used a nanoindenter to perform microscratch studies (mechanical durability) of various carbon coatings. The coefficient of friction profiles as a function of increasing normal load and AFM surface height maps of regions over scratches at the respective critical loads (indicated by the arrows in the friction profiles and AFM images), made on the various coatings of different thicknesses and single-crystal silicon substrate using a conical tip are compared in Figs. 16 and 17. Bhushan and Koinkar [27], Koinkar and Bhushan [70], Bhushan [17], and Sundararajan and Bhushan [102, 103] have used an AFM to perform microscratch studies. Data for various coatings of different thicknesses and silicon substrate using a Berkovich tip are compared in Figs. 18 and 19. Critical loads for various coatings tested using nanoindenter and AFM are summarized in Fig. 20. The selected data for 20 nm thick coatings obtained using nanoindenter, are also presented in Fig. 10 and Table 5.

It can be seen that there exists a well-defined critical load for each coating. The AFM images clearly show that below the critical loads the coatings were plowed by the scratch tip, associated with the plastic flow of materials. At and after the critical loads, debris (chips) or buckling were observed on the sides of scratches. Delamination or buckling can be observed around or after the critical loads which suggests that the damage starts from delamination and buckling. For the 3.5 and 5 nm thick FCA coatings, before the critical loads small debris is observed on the sides of scratches. This suggests that the thinner FCA coatings are not so durable. It is obvious that for a given deposition method, the critical loads increase with increasing coating thickness. This indicates that the critical load is determined not only by the adhesion strength to the substrate but also by the coating thickness. We note that the debris generated on the thicker coatings is larger than that generated on the thinner coatings. For a thicker coating, it is more difficult to be broken; the broken coating chips (debris) for a thicker coating are larger than those for the

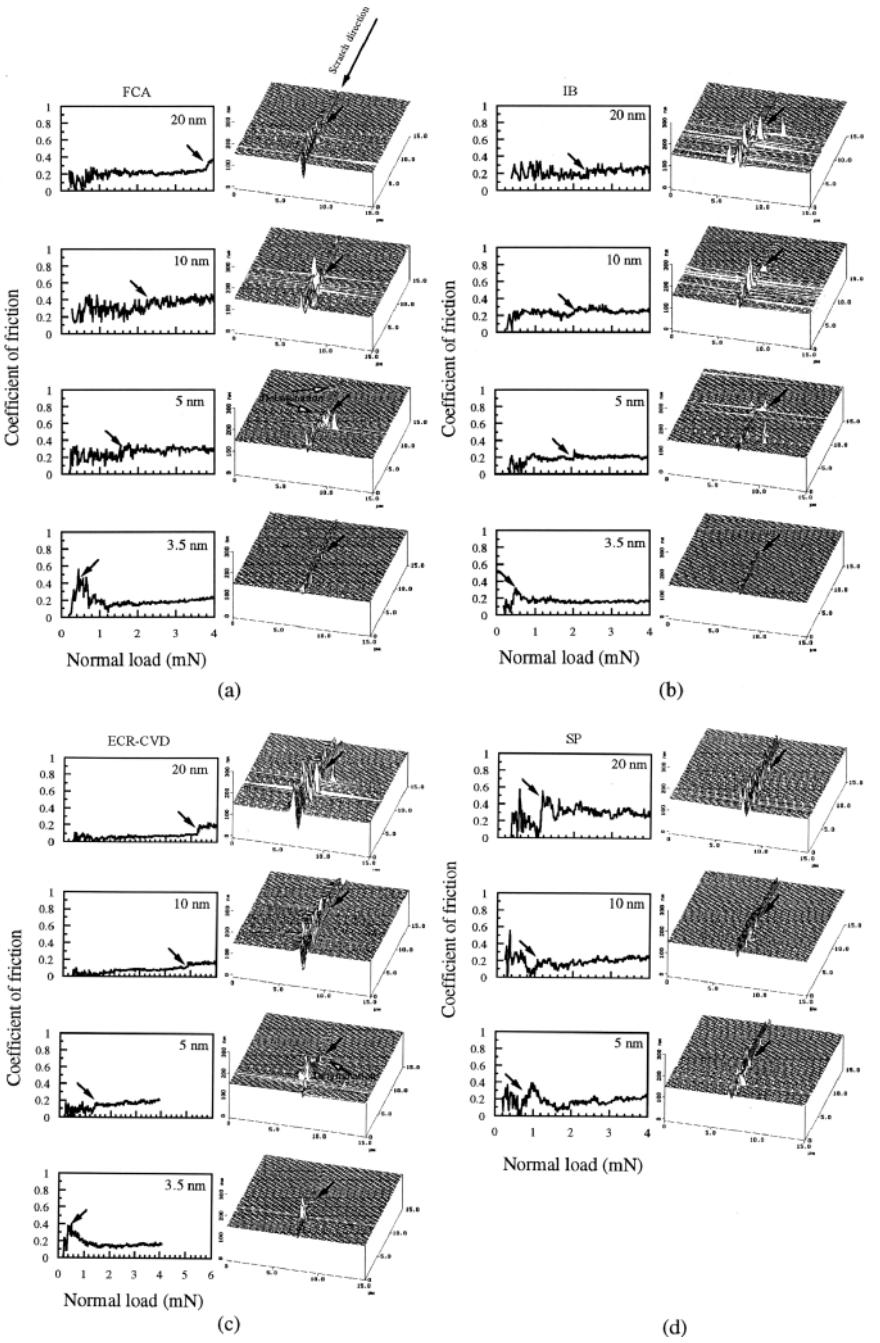

Fig. 16 Coefficient of friction profiles as a function of normal load and corresponding AFM surface height maps of regions over scratches at the respective critical loads (indicated by the arrows in the friction profiles and AFM images) for coatings of different thicknesses deposited by various deposition techniques: (a) FCA, (b) IB, (c) ECR-CVD, (d) SP

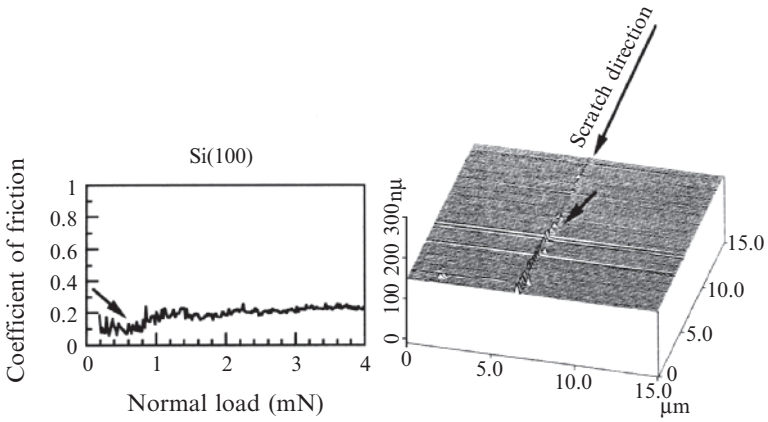

Fig. 17 Coefficient of friction profiles as a function of normal load and corresponding AFM surface height maps of regions over scratches at the respective critical loads (indicated by the arrows in the friction profiles and AFM images) for Si(100)

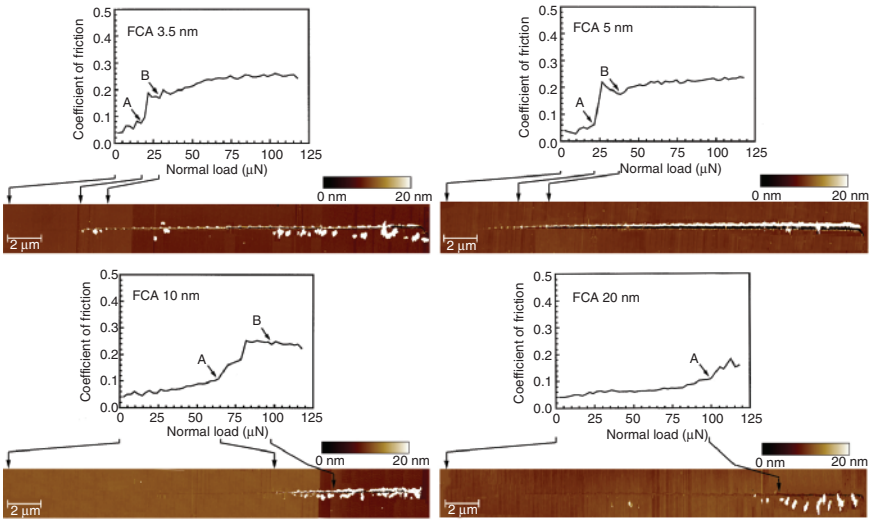

(a)

Fig. 18 Coefficient of friction profiles during scratch as a function of normal load and corresponding AFM surface height maps for (a) FCA, (b) ECR-CVD, and (c) SP coatings [103]

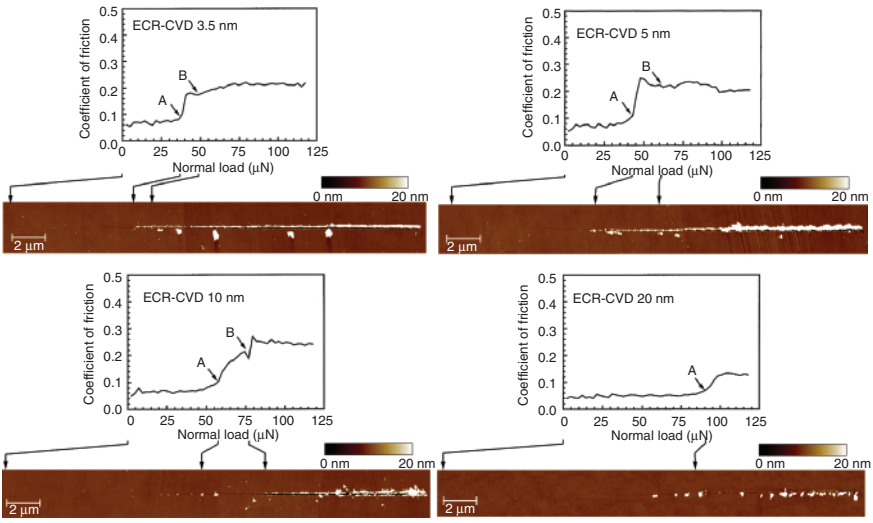

(b)

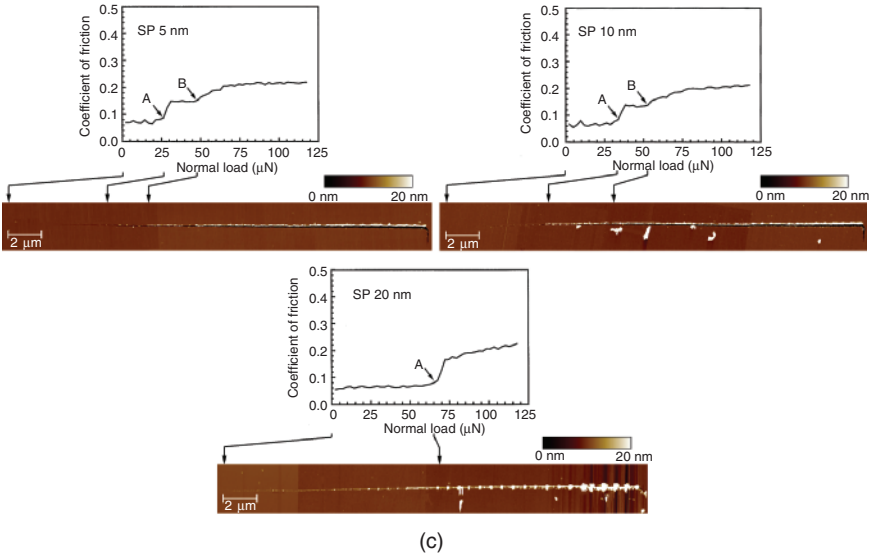

(c)

Fig. 18 (continued)

thinner coatings. The difference in the residual stresses of the coatings of different thicknesses could also affect the size of debris. The AFM image shows that the silicon substrate was damaged by plowing, associated with the plastic flow of materials. At and after the critical load, small and uniform debris is observed and the amount of debris increases with increasing normal load.

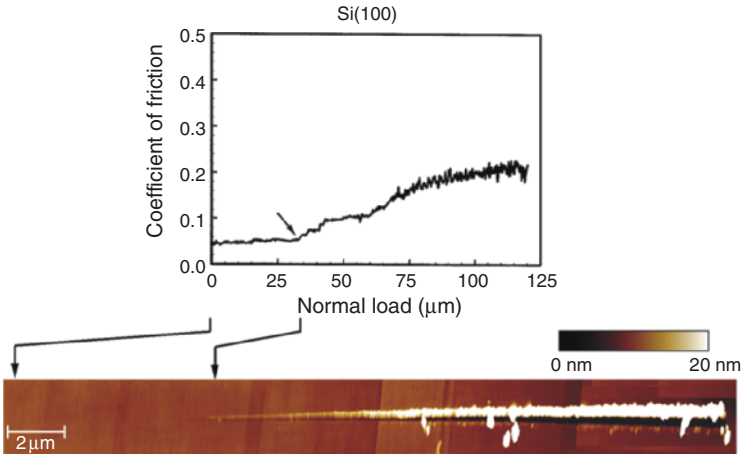

Fig. 19 Coefficient of friction profiles during scratch as a function of normal load and corresponding AFM surface height maps for Si(100) [103]

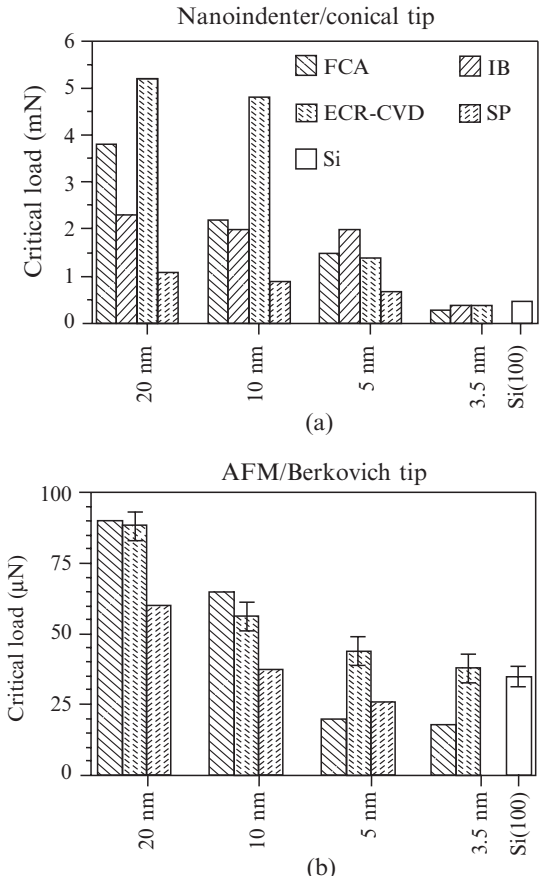

Fig. 20 Critical loads estimated from the coefficient of friction profiles from (a) nanoindenter and (b) AFM tests for various coatings of different thicknesses and Si(100) substrate

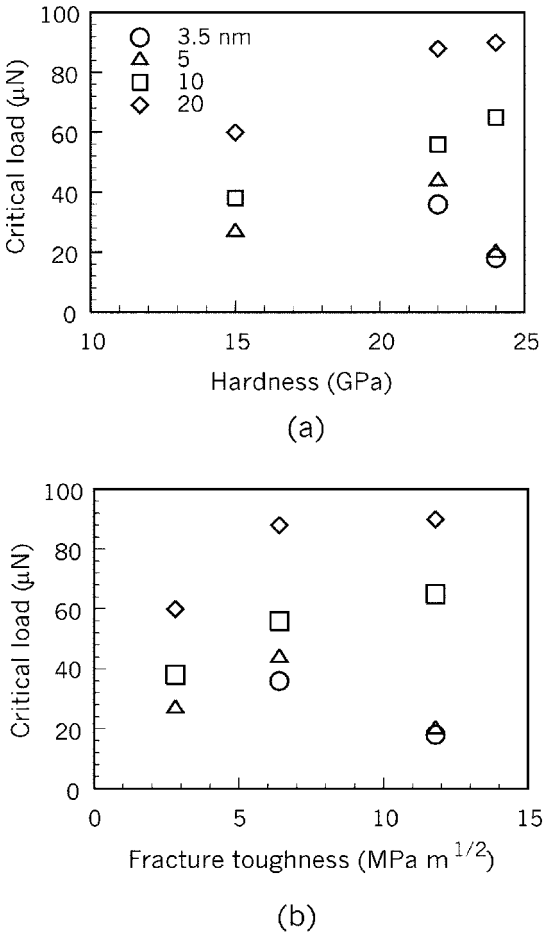

Fig. 21 Measured critical loads estimated from the coefficient of friction profiles from AFM tests as a function of (a) coating hardness and (b) fracture toughness. Coating hardness and fracture toughness values were obtained using a nanoindenter on 100 nm thick coatings (Table 5)

As the damage mechanism appears to be onset of plowing at the critical load, higher hardness and fracture toughness of a coating will result in higher load required for deformation and hence higher critical load. Figure 21 shows critical loads of the various coatings, obtained with AFM tests, as a function of the coating hardness and fracture toughness (from Table 5). It can be seen that, in general, higher coating hardness and fracture toughness result in higher critical load. The only exceptions are the FCA coatings at 5 and 3.5 nm coating thickness, which show the lowest critical loads despite their high hardness and fracture toughness.

The brittleness of the thinner FCA coatings may be one reason for their low critical loads. The mechanical properties of coatings that are less than 10 nm thick are unknown. The FCA process may result in coatings with low hardness at such low thickness due to differences in coating stoichiometry and structure as compared to the coatings of higher thickness. Also, at these thicknesses stresses at the coating/substrate interface may affect adhesion and load-carrying capacity of the coatings.

Based on the experimental results, a schematic of scratch damage mechanisms of the DLC coatings used in this study is shown in Fig. 22. Below the critical load, if a coating has a good combination of strength and fracture toughness, plowing associated with the plastic flow of materials is responsible for the damage of coating (Fig. 22(a)). Moreover, if a coating has a lower fracture toughness, cracking could occur during plowing, associated with the formation of small debris (Fig. 22(b)). When normal load increases up to the critical load, delamination or buckling will occur at the coating/substrate interface (Fig. 22(c)). Further increase in normal load will result in breakdown of coating via through-coating thickness cracking, as shown in Fig. 22(d). Therefore, adhesion strength plays a crucial role in the determination of critical load. If a coating has stronger adhesive strength with the substrate, the coating is more difficult to be delaminated, which will result in a higher critical load. The interfacial and residual stresses of a coating could greatly affect the delamination and buckling [26]. The coating with higher interfacial and residual stresses is more easily delaminated and buckled, which will result in a low critical load. It has been reported earlier that the FCA coatings have higher residual stresses than the other coatings [64]. Interfacial stresses play a more important role when a coating gets thinner. A large mismatch in elastic modulus between the FCA coatings and the silicon substrate may cause large interfacial stresses. This may be why the thinner FCA coatings show relatively low critical loads compared with the thicker FCA coatings, even though the FCA coatings have higher hardness and elastic modulus. The brittleness of the thinner FCA coatings may be another reason for the lower critical loads. The strength and fracture toughness of a coating also affect the critical load. Higher strength and fracture toughness will make the coating more difficult to be broken after delamination and buckling. The high scratch resistance/adhesion of FCA coatings is attributed to an atomic intermixing at the coating/substrate interface because of high kinetic energy (2 keV) plasma formed during the cathodic-arc deposition process [4]. The atomic intermixing at the interface provides a graded compositional transition between the coating and the substrate materials. In all other coatings used in this study, the kinetic energy of the plasma was insufficient for atomic intermixing.

Gupta and Bhushan [63, 64] and Li and Bhushan [74, 75] measured scratch resistance of DLC coatings deposited on Al_2O_3–TiC, Ni–Zn ferrite, and single-crystal silicon substrates. For good adhesion of DLC coating to other substrates, in most cases, an interlayer of silicon is required except for cathodic-arc deposited coatings. The best adhesion with cathodic arc carbon coating is obtained on electrically conducting substrates such as Al_2O_3–TiC and silicon as compared to Ni–Zn ferrite.

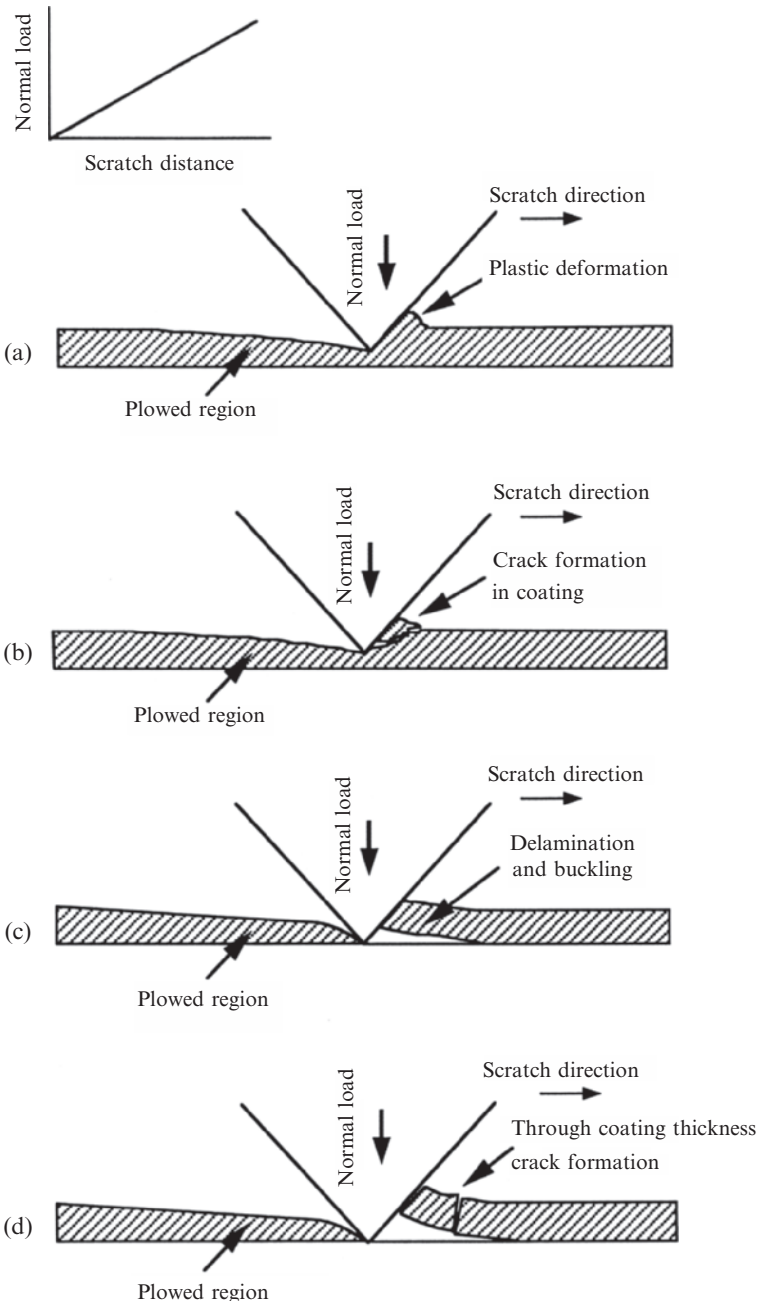

Fig. 22 Schematic of scratch damage mechanisms of the DLC coatings, (a) plowing associated with the plastic flow of materials, (b) plowing associated with the formation of small debris, (c) delamination and buckling at the critical load, and (d) breakdown via through coating thickness cracking at and after the critical load [74]

Microwear

Microwear studies can be conducted using an AFM [17]. For microwear studies, a three-sided pyramidal single-crystal natural diamond tip with an apex angle of about 80° and a tip radius of about 100 nm is used at relatively high loads of 1–150 μN. The diamond tip is mounted on a stainless steel cantilever beam with a normal stiffness of about 30 N/m. The sample is generally scanned in a direction orthogonal to the long axis of the cantilever beam (typically at a rate of 0.5 Hz). The tip is mounted on the beam such that one of its edges is orthogonal to the beam axis. For wear studies, typically an area of $2 \times 2\,\mu m$ is scanned for a selected number of cycles.

Microwear studies of various types of DLC coatings have been conducted [27, 70, 102]. Figure 23(a) shows a wear mark on uncoated Si(100). Wear occurs uniformly and material is removed layer by layer via plowing from the first cycle, resulting in the constant friction force seen during the wear (Fig. 24(a)). Figure 23(b) shows AFM images of the wear marks on all 10 nm coatings. It is seen that the coatings wear nonuniformly. Coating failure is sudden and accompanied by a

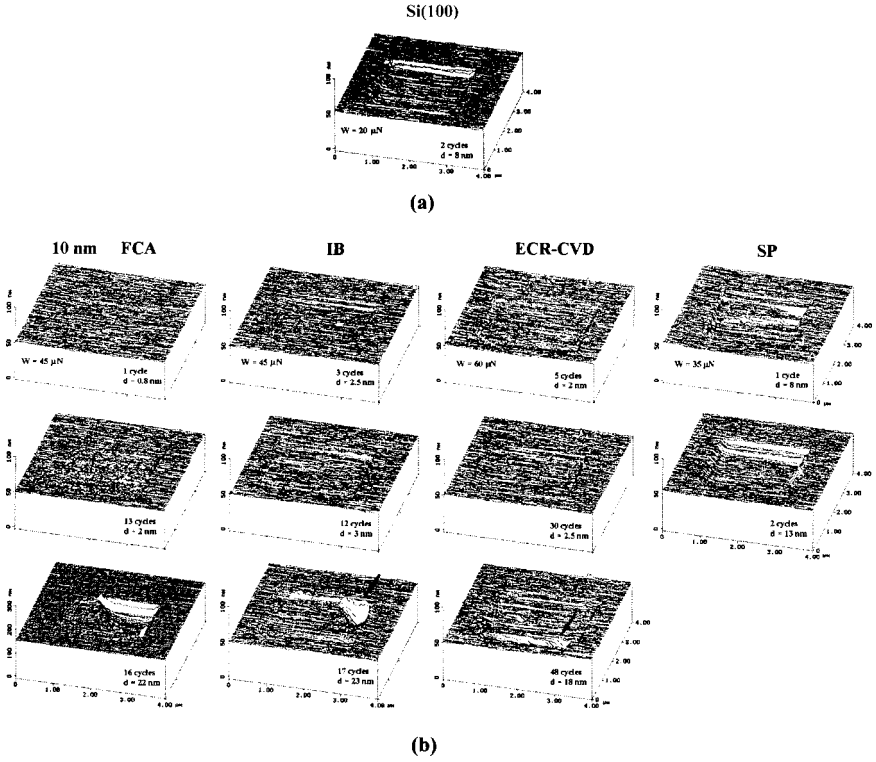

Fig. 23 AFM images of wear marks on (a) bare Si(100), and (b) all 10 nm thick DLC coatings [102]

sudden rise in the friction force (Fig. 24(b)). Figure 24 shows the wear depth of Si(100) substrate and various DLC coatings at two different loads. FCA and ECR-CVD, 20 nm thick coatings show excellent wear resistance up to 80 µN, the

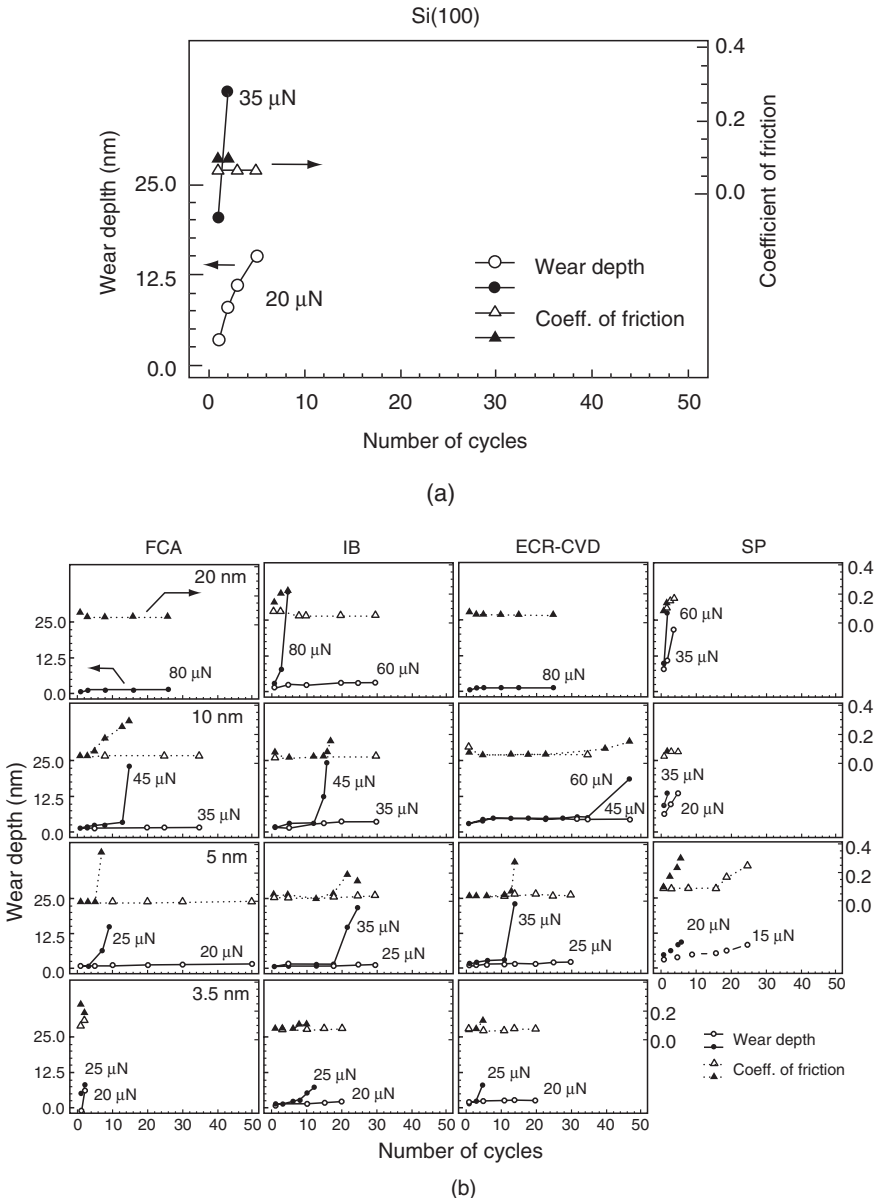

Fig. 24 Wear data of (a) bare Si(100) and (b) all DLC coatings. Coating thickness is constant along each row in Fig. (b). Both wear depth and coefficient of friction during wear for a given cycle are plotted [102]

load that is required for the IB 20 nm coating to fail. In these tests, "failure" of a coating results when the wear depth exceeds the quoted coating thickness. The SP 20 nm coating fails at the much lower load of 35 μN. At 60 μN, the coating hardly provides any protection. Moving onto the 10 nm coatings, ECR-CVD coating requires about 45 cycles at 60 μN to fail as compared to IB and FCA which fail at 45 μN. The FCA coating exhibits slight roughening in the wear track after the first few cycles, which leads to an increase in the friction force. The SP coating continues to exhibit poor resistance, failing at 20 μN. For the 5 nm coatings, the load required to fail the coatings continue to decrease. But IB and ECR-CVD still provide adequate protection as compared to bare Si(100) in that order, failing at 35 μN compared to FCA at 25 μN and SP at 20 μN. Almost all the 20, 10, and 5 nm coatings provide better wear resistance than bare silicon. At 3.5 nm, FCA coating provides no wear resistance, failing almost instantly at 20 μN. The IB and ECR-CVD coating show good wear resistance at 20 μN compared to bare Si(100). Moreover, IB lasts only about 10 cycles and ECR-CVD about 3 cycles at 25 μN.

The wear tests highlight the differences in the coatings more vividly than the scratch tests. At higher thicknesses (20 and 10 nm), the ECR-CVD and FCA coating appear to show the best wear resistance. This is probably due to higher hardness of the coatings (see Table 5). At 5 nm, IB coating appears to be the best. FCA coatings show poorer wear resistance with decreasing coating thickness. This suggests that the trends in hardness seen in Table 5 no longer hold at low thicknesses. SP coatings showed consistently poor wear resistance at all thicknesses. The IB 3.5 nm coating does provide reasonable wear protection at low loads.

4.1.3 Macroscale Tribological Characterization

So far data on mechanical characterization and microscratch and microwear studies using a nanoindenter and an AFM have been presented. Mechanical properties affect tribological performance of the coatings and microwear studies simulate a single asperity contact which helps in the development of fundamental understanding of the wear process. These studies are useful in screening various candidates as well as to understand the relationships between deposition conditions and properties of various samples. As a next step, macroscale friction and wear tests need to be conducted to measure tribological performance of the coatings.

Macroscale-accelerated friction and wear tests to screen a large number of candidates and functional tests on selected candidates have been conducted. An accelerated test is designed to accelerate the wear process such that it does not change the failure mechanism. The accelerated friction and wear tests are generally conducted using a ball-on-flat tribometer under reciprocating motion [34]. Typically, a diamond tip with 20 μm tip radius or a sapphire ball with 3 mm diameter and surface finish of about 2 nm RMS is slid against the coated substrates at selected loads. Coefficient of friction is monitored during the tests.

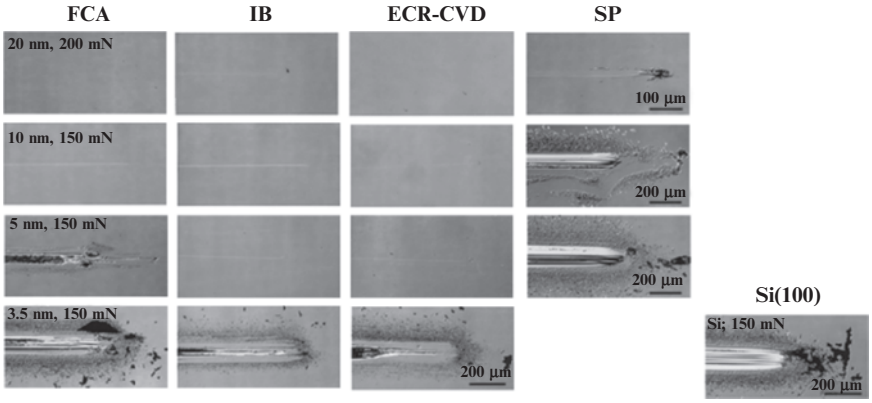

Fig. 25 Optical micrographs of wear tracks and debris formed on the various coatings of different thicknesses and silicon substrate when slid against a sapphire ball after sliding distance of 5 m. The end of the wear track is on the right hand side of the image

Functional tests are conducted using an actual machine under close to actual operating conditions for which coatings is developed. Generally, the tests are accelerated somewhat to fail the interface in a short time.

Accelerated Friction and Wear Tests

Li and Bhushan [74] conducted accelerated friction and wear tests on DLC coatings deposited by various deposition techniques, using a ball-on-flat tribometer. Average values of coefficient of friction are presented in Table 5. The optical micrographs of wear tracks and debris formed on all samples when slid against a sapphire ball after sliding distance of 5 m are presented in Fig. 25. The normal load used for the 20 and 10 nm thick coatings is 200 mN and the normal load used for the 5 and 3.5 nm thick coatings and silicon substrate is 150 mN.

Among the 20 nm thick coatings, the SP coating exhibits a higher coefficient of friction of about 0.3 than the other coatings which have comparable values of coefficient of friction of about 0.2. The optical micrographs show that the SP coating has a larger wear track and more debris than the IB coatings. No wear track and debris were found on the 20 nm thick FCA and ECR-CVD coatings. The optical micrographs of 10 nm thick coatings show that the SP coating was severely damaged showing a large wear track with scratches and lots of debris. The FCA and ECR-CVD coatings show smaller wear tracks and less debris than the IB coatings.

For the 5 nm thick coatings, the wear tracks and debris of the IB and ECR-CVD coatings are comparable. The bad wear resistance of the 5 nm thick FCA coating is in good agreement with the low scratch critical load, which may be due to the higher interfacial and residual stresses as well as brittleness of the coating.

At 3.5 nm, all coatings exhibit wear. The FCA coating provides no wear resistance, failing instantly like the silicon substrate. Large block-like debris is observed on the sides of the wear track of the FCA coating. This indicates that large region delamination and buckling occurred during sliding, resulting in large block-like debris.

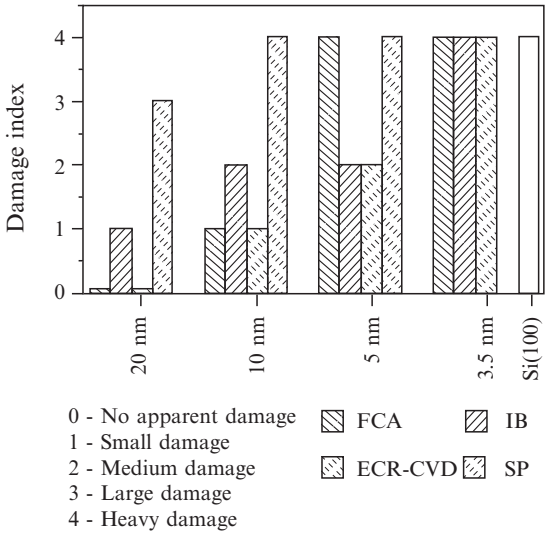

Fig. 26 Wear damage index bar chart of the various coatings of different thicknesses and Si(100) substrate based on optical examination of the wear tracks and debris

This block-like debris, in turn, scratches the coating, making the coating damage even more severe. The IB and ECR-CVD coatings are able to provide some protection against wear at 3.5 nm.

In order to better evaluate the wear resistance of various coatings, based on the optical examination of the wear tracks and debris after tests, the wear damage index bar chart of the various coatings of different thicknesses and an uncoated silicon substrate is presented in Fig. 26. Among the 20 and 10 nm thick coatings, the SP coatings show the worst damage, followed by and FCA/ECR-CVD. At 5 nm, the FCA and SP coatings show the worst damage, followed by IB and ECR-CVD coatings. All 3.5 nm thick coatings show as the same heavy damage as the uncoated silicon substrate.

The wear damage mechanisms of thick and thin DLC coatings studied are believed to be as illustrated in Fig. 27. At the early stages of sliding, deformation zone and Herztian and wear fatigue cracks formed beneath the surface extend within the coating upon subsequent sliding [26]. Formation of fatigue cracks depend upon the hardness and subsequent cycles. These are controlled by the sp^3/sp^2 ratio. For thicker coating, the cracks generally do not penetrate the coating. While for a thinner coating, the cracks easily propagate down to the interface with the aid of the interfacial stresses, they get diverted along the interface just enough to cause local delamination of the coating. When this happens, the coating experiences excessive plowing. At this point, the coating fails catastrophically, resulting in a sudden rise in the coefficient of friction. All 3.5 nm thick coatings, failed much quicker as compared to the thicker coatings. It appears that these thin coating have very low load-carrying capacity and therefore the substrate undergoes deformation almost immediately. This generates

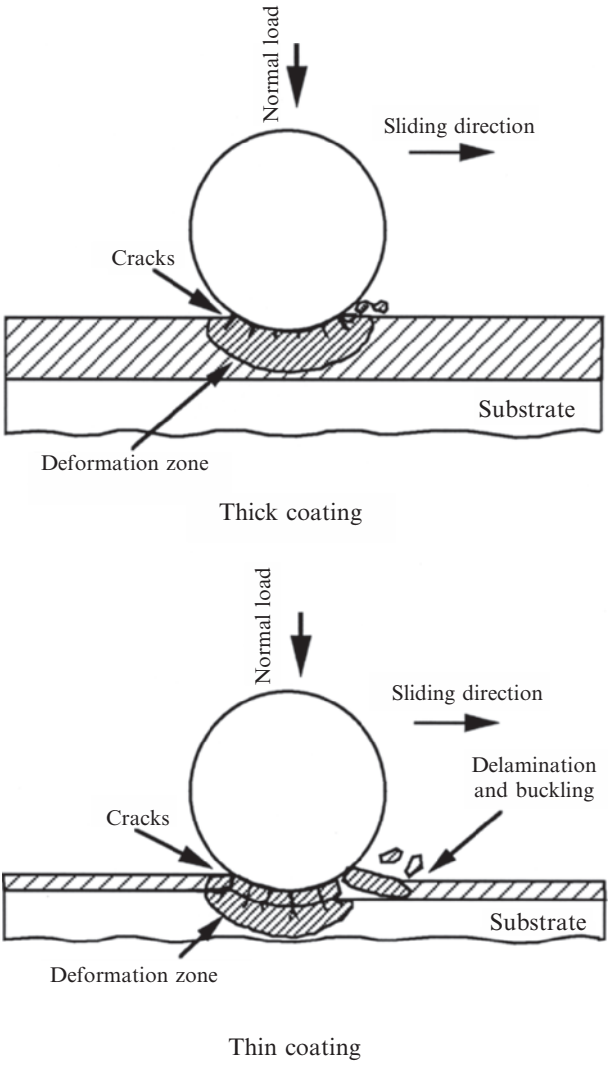

Fig. 27 Schematic of wear damage mechanisms of thick and thin DLC coatings [74]

stresses at the interface that weaken the coating adhesion and lead to delamination of the coating. Another reason may be that the thickness is insufficient to produce a coating comprised of the DLC structure. Instead, the bulk may be made up of a matrix characteristic of the interface region where atomic mixing occurs with the substrate and/or any interlayer used. This would also result in poor wear resistance and silicon-like behavior of the coating, especially in the case of FCA coatings, which show the worst performance at 3.5 nm. In contrast to the other coatings, all SP coatings show the worst wear performance at any thicknesses

(Fig. 25). This may be due to their poor mechanical properties, such as lower hardness and scratch resistance compared to the other coatings.

Comparison of Figs 20 and 26 shows a very good correlation between the wear damage and scratch critical loads. Less wear damage corresponds to higher scratch critical load. Based on the data, thicker coatings do show better scratch and wear resistance than thinner coatings. This is probably due to better load-carrying capacity of the thick coatings as compared to the thinner ones. For a given coating thickness, higher hardness and fracture toughness and better adhesion strength are believed to be responsible for the superior wear performance.

Effect of Environment

Friction and wear performance of amorphous carbon coatings are found to be strongly dependent on the water vapor content and partial gas pressure in the test environment. The friction data for an amorphous carbon film on the silicon substrate sliding against steel are presented as a function of the partial pressure of water vapor in Fig. 28 [46, 86, 14, 26, 49]. Friction increases dramatically above a

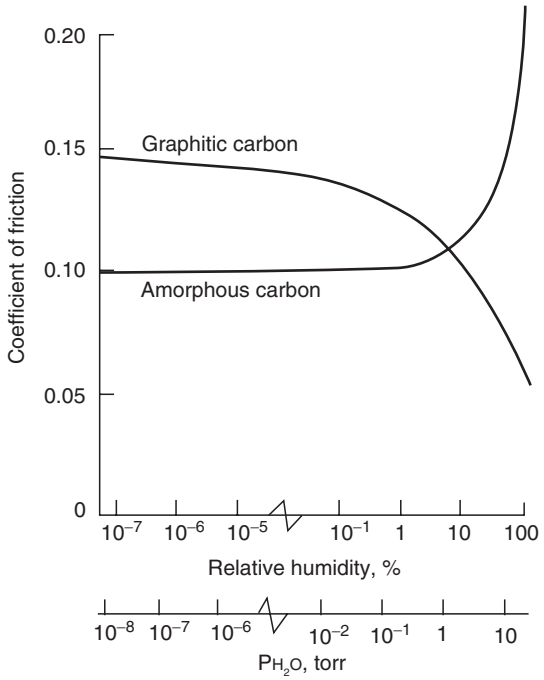

Fig. 28 Coefficient of friction as a function of relative humidity and water vapor partial pressure of RF-plasma deposited amorphous carbon coating and bulk graphitic carbon coating sliding against a steel ball

relatively humidity of about 40%. At high relatively humidity, condensed water vapor forms meniscus bridges at the contacting asperities and the meniscii result in an intrinsic attractive force which is responsible for an increase in friction. For completeness, the data for the coefficient of friction of bulk graphitic carbon are also presented in Fig. 28. Note that friction decreases with an increase in the relative humidity [38]. Graphitic carbon has a layered lattice crystal structure. Graphite absorbs polar gases (H_2O, O_2, CO_2, NH_3, etc.) at the edges of the crystallites, which weakens the interlayer bonding forces facilitating interlayer slip and results in lower friction [26].

To better study the effect of environment for carbon-coated magnetic disks, a number of tests have been conducted in controlled environments. Marchon et al. [81] conducted tests in alternating environments of oxygen and nitrogen gases (Fig. 29). The coefficient of friction increases as soon as oxygen is added to test environment whereas in a nitrogen environment the coefficient of friction reduces slightly. Tribochemical oxidation of the DLC coating in the oxidizing environment is responsible for an increase in the coefficient of friction implying wear. Dugger et al. [50], Strom et al. [101], Bhushan and Ruan [29], and Bhushan et al. [35] conducted tests with DLC-coated magnetic disks (with about 2 nm thick of perfluoropolyether lubricant film) in contact with Al_2O_3–TiC sliders, in different gaseous environments including a high vacuum of 2×10^{-7} Torr (Fig. 30). The wear lives are shortest in high vacuum and the longest in most atmospheres of nitrogen and argon with the following order (from best to worst): argon or nitrogen, Ar + H_2O, ambient, Ar + O_2, and Ar + H_2O, vacuum. From this sequence of wear performance, we can see that having oxygen and water in an operating environment worsen wear performance of the coatings, but having nothing in it (vacuum) is the worst of all. Indeed, failure mechanisms differ in various environments. In high vacuum, intimate contact between disk and slider surfaces results in significant wear. In ambient air, Ar + O_2, and Ar + H_2O, tribochemical oxidation of the carbon

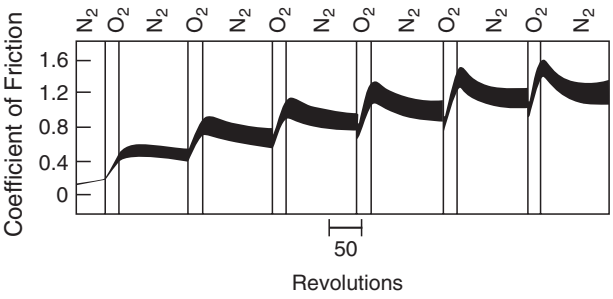

Fig. 29 Coefficient of friction as a function of sliding distance for a ceramic slider against a magnetic disk coated with 20 nm thick DC magnetron sputtered DLC coating, measured at a speed of 0.06 m/s and 10 g load. The environment is alternated between oxygen and nitrogen gases [81]

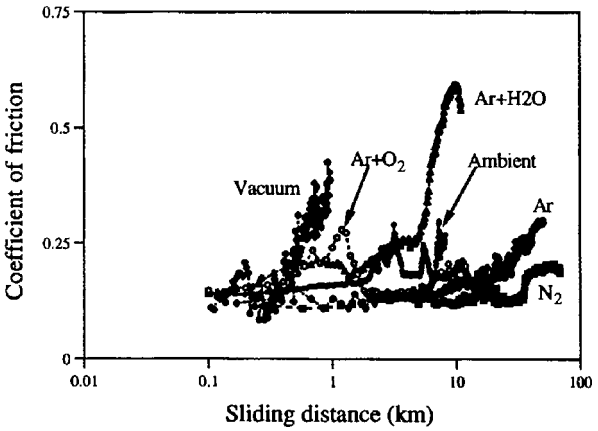

Fig. 30 Durability measured by sliding a Al_2O_3–TiC magnetic slider against a magnetic disk coated with 20 nm thick DC sputtered amorphous carbon coating and 2 nm thick perfluoropolyether film, measured at a speed of 0.75 m/s and 10 g load. Vacuum refers to 2×10^{-7} Torr [35]

overcoat is responsible for interface failure. For experiments performed in pure argon and nitrogen, mechanical shearing of the asperities cause the formation of debris which is responsible for the formation of scratch marks on the carbon surface as could be observed with an optical microscope [35].

Functional Tests

Magnetic thin-film heads made with Al_2O_3–TiC substrate are used in magnetic storage applications [14]. Multilayered thin-film pole-tip structure present on the head surface wears more rapidly than the Al_2O_3–TiC substrate which is much harder. Pole-tip recession (PTR) is a serious concern in magnetic storage [36, 37, 112, 97, 98, 99]. Two of the DLC coatings superior in mechanical properties – ion beam and cathodic arc carbon – were deposited on the air bearing surfaces of Al_2O_3–TiC head sliders [36]. The functional tests were conducted by running a metal–particle (MP) tape in a computer tape drive. Average PTR as a function of sliding distance data are presented in Fig. 31. We note that PTR increases for the uncoated head, whereas for the coated heads there is a slight increase in PTR in early sliding followed by little change. Thus, coatings provide protection.

Micromechanical and accelerated and functional tribological data presented here clearly suggest that there is a good correlation between the scratch resistance and wear resistance measured using accelerated tests and functional tests. Thus, scratch tests can be successfully used to screen coatings for wear applications.

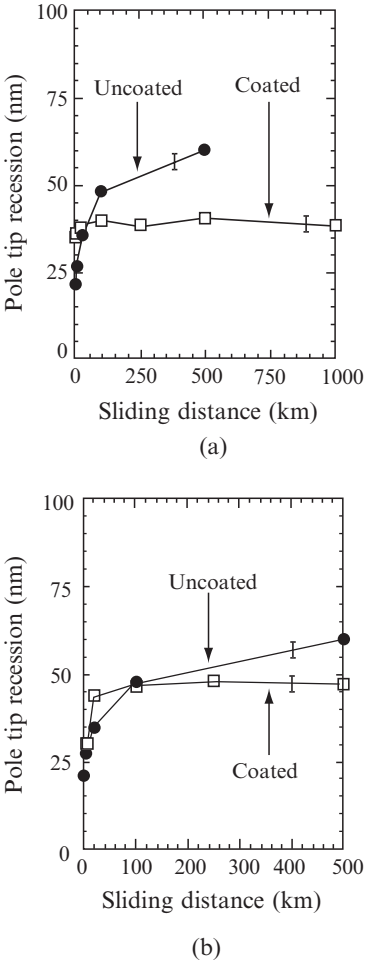

Fig. 31 Pole tip recession as a function of sliding distance as measured with an AFM for (a) uncoated and 20 nm thick ion beam carbon coated, and (b) uncoated and 20 nm thick cathodic arc carbon coated Al_2O_3–TiC heads run against MP tapes [36]

4.1.4 Coating Continuity Analysis

Ultrathin coatings less than 10 nm may not uniformly coat the sample surface. In other words, coating may be discontinuous and deposited in the form of islands on the microscale. A possible reason for poor wear protection and the nonuniform failure of the coatings may be due to poor coverage of the thin coatings on the

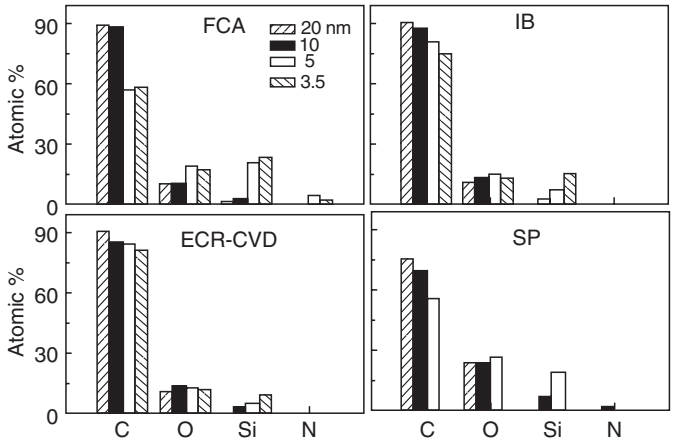

Fig. 32 Quantified XPS data for various DLC coatings on Si(100) substrate [102]. Atomic concentrations are shown

substrate. Coating continuity can be studied by using surface analytical techniques such as Auger and/or XPS analyses. Any discontinuity with coating thickness less than sampling depth of the instrument will detect locally the substrate species [27, 75, 102].

The results of XPS analysis on various coatings, deposited on Si(100) substrates, over a 1.3 mm^2 region (single point measurement with spot diameter 1,300 μm) are shown in Fig. 32. The sampling depth is about 2–3 nm. The poor SP coatings show much less carbon content (<75% atomic concentration) as does the poor 5 nm and 3.5 nm FCA coatings (<60%) as compared to the IB and ECR-CVD coatings. Silicon is detected in all 5 nm coatings. From the data it is hard to say if the Si is from the substrate or from exposed regions due to coating discontinuity. Based on the sampling depth any Si detected in 3.5 nm coatings would likely be from the substrate. The other interesting observation is that all poor coatings (all SP and FCA 5 and 3.5 nm) show almost twice the oxygen content than that of the other coatings. Any oxygen present may be due to leaks in the deposition chamber and is present in the form of silicon oxides.

AES measurements, averaged over a scan area of 900 μm^2, were conducted on FCA and SP 5 nm coatings at six different regions on each sample. Very little silicon was detected on this scale and the detected peaks were characteristic of oxides. The oxygen levels were comparable to that seen for the good coatings by XPS. These contrast the XPS measurements at a larger scale suggest that the coating possesses discontinuities only at isolated areas and that the 5 nm coatings are generally continuous on the microscale. Figure 33 shows representative XPS and AES spectra of selected samples.

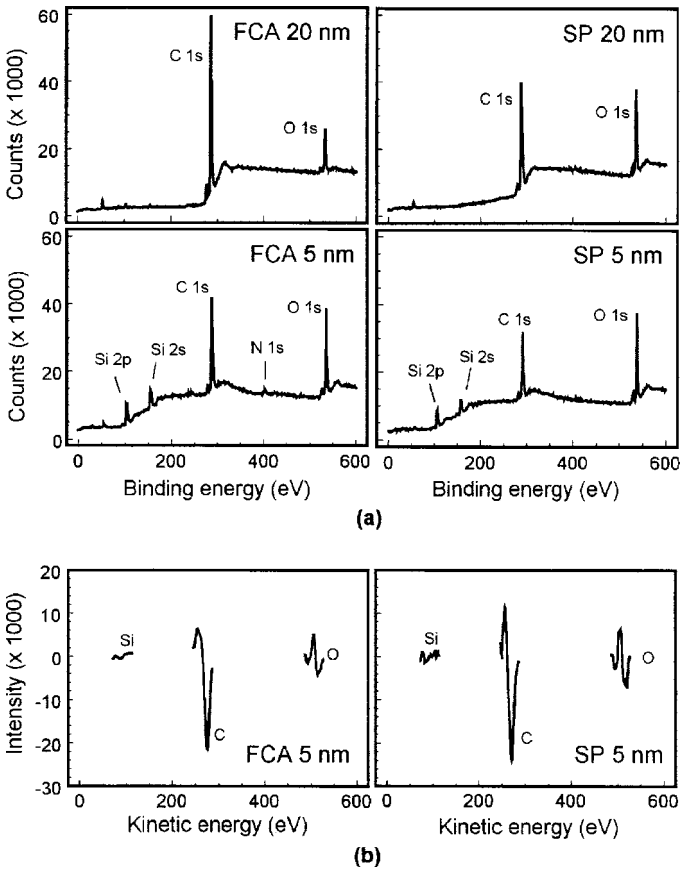

Fig. 33 (a) XPS spectra for FCA and SP coatings of 5 nm and 20 nm coating thicknesses on Si(100) substrate, and (b) AES spectra for FCA and SP coatings at 5 nm thickness on Si(100) substrate [102]

5 Closure

Diamond material and its smooth coatings are used for very low wear and relatively low friction. Major limitations of the true diamond coatings are that they need to be deposited at high temperatures, can only be deposited on selected substrates, and require surface finishing. Hard amorphous carbon (a-C), commonly known as DLC coatings exhibit mechanical, thermal, and optical properties close to that of diamond. These can be deposited with a large range of thicknesses by using a variety of deposition processes, on variety of substrates at or near room temperature. The coatings reproduce substrate topography, avoiding the need of postfinishing. Friction and wear properties of some DLC coatings can be very attractive for tribological applications.

The largest industrial application of these coatings is in magnetic storage devices. They are expected to be used in MEMS/NEMS.

EELS and Raman spectroscopies can be successfully used for chemical characterization of amorphous carbon coatings. The prevailing atomic arrangement in the DLC coatings is amorphous or quasi-amorphous with small diamond (sp^3), graphite (sp^2) and other unidentifiable micro- or nanocrystallites. Most DLC coatings except those produced by FCA contain from a few to about 50 at. % H. Sometimes, H is deliberately incorporated in the sputtered and ion-plated coatings to tailor their properties.

Amorphous carbon coatings deposited by various techniques exhibit different mechanical and tribological properties. The nanoindenter can be successfully used for measurement of hardness, elastic modulus, fracture toughness, and fatigue life. Microscratch and microwear experiments can be performed using either a nanoindenter or an AFM. Thin coatings deposited by FCA, ion beam, and ECR-CVD hold a promise for tribological applications. Coatings as thin as 5 nm or even thinner in thickness provide wear protection. Microscratch, microwear, and accelerated wear testing, if simulated properly can be successfully used to screen coating candidates for industrial applications. In the examples shown in this chapter, trends observed in the microscratch, microwear, and accelerated macrofriction wear tests are similar to that found in functional tests.

References

1. Ager, J. W., Veirs, D. K., and Rosenblatt, C. M. (1991), Spatially resolved Raman studies of diamond films grown by chemical vapor deposition, Phys. Rev. B43, 6491–6499.
2. Aksenov, I. I. and Strel'Nitskii, V. E. (1991), Wear resistance of diamond-like carbon coatings, Surf. Coat. Technol. 47, 252–256.
3. Aisenberg, S. and Chabot, R. (1971), Ion beam deposition of thin films of diamond like carbon, J. Appl. Phys. 49, 2953–2958.
4. Anders, S., Anders, A., Brown, I. G., Wei, B., Komvopoulos, K., Ager III, J. W., and Yu, K. M. (1994a), Effect of vacuum arc deposition parameters on the properties of amorphous carbon thin films, Surf. Coat. Technol. 68–69, 388–393.
5. Anders, S., Anders, A., Brown, I. G., Dickinson, M. R., and MacGill, R. A. (1994b), Metal plasma immersion ion implantation and deposition using arc plasma sources, J. Vac. Sci. *Technol*. B12, 815–820.
6. Anders, S., Anders, A., and Brown, I. G. (1995), Transport of vacuum arc plasma through magnetic macroparticle filters, Plasma Sources Sci. 4, 1–12.
7. Andersson, L. P. (1981), A review of recent work on hard i-C films, Thin Solid Films 86, 193–200.
8. Angus, J. C. (1992), Diamond and diamondlike films, Thin Solid Films 216, 126–133.
9. Angus, J. C. and Hayman, C. C. (1988), Low pressure metastable growth of diamond and diamondlike phase, Science 241, 913–921.
10. Angus, J. C. and Jensen, F. (1988), Dense diamondlike hydrocarbons as random covalent networks, J. Vac. Sci. Technol. A6, 1778–1782.
11. Angus, J. C., Koidl, P., and Domitz, S. (1986), Carbon thin films, in J. Mort and F. Jensen, (eds.) Plasma Deposited Thin Films, CRC Press, Boca Raton, FL, pp. 89–127.

12. Asmussen, J. (1989), Electron cyclotron resonance microwave discharges for etching and thin-film deposition, J. Vac. Sci. Technol. A7, 883–893.
13. Banks, B. A. and Rutledge, S. K. (1982), Ion beam sputter deposited diamond like films, J. Vac. Sci. Technol. 21, 807–814.
14. Bhushan, B. (1996a), Tribology and Mechanics of Magnetic Storage Devices, 2nd edn., Springer, New York.
15. Bhushan, B. (1996b), Nanotribology and nanomechanics of MEMS devices, Proc. Ninth Annual Workshop on Micro Electro Mechanical Systems, IEEE, New York, pp. 91–98.
16. Bhushan, B. (ed.) (1998), Tribology Issues and Opportunities in MEMS, Kluwer Academic, Dordrecht, The Netherlands.
17. Bhushan, B. (1999a), Handbook of Micro/Nanotribology, 2nd edn., CRC Press, Boca Raton, FL.
18. Bhushan, B. (1999b), Principles and Applications of Tribology, Wiley, New York.
19. Bhushan, B. (1999c), Chemical, mechanical, and tribological characterization of ultra-thin and hard amorphous carbon coatings as thin as 3.5 nm: recent developments, Diam. Relat. Mater. 8, 1985–2015.
20. Bhushan, B. (2000), Mechanics and Reliability of Flexible Magnetic Media, 2nd edn., Springer, New York.
21. Bhushan, B. (2001a), Macro- and microtribology of magnetic storage devices, in B. Bhushan, (ed.) Modern Tribology Handbook, Vol. 2: Materials, Coatings, and Industrial Applications, CRC Press, Boca Raton, FL, pp. 1413–1513.
22. Bhushan, B. (2001b), Macro- and microtribology of MEMS materials, in B. Bhushan, (ed.) Modern Tribology Handbook, Vol. 2: Materials, Coatings, and Industrial Applications, CRC Press, Boca Raton, FL, pp. 1515–1548.
23. Bhushan, B. (2002), Introduction to Tribology, Wiley, New York.
24. Bhushan, B. and Doerner, M. F. (1989), Role of mechanical properties and surface texture in the real area of contact of magnetic rigid disks, ASME J. Tribol. 111, 452–458.
25. Bhushan, B. and Gupta, B. K. (1995), Micromechanical characterization of ni-p coated aluminum-magnesium, glass and glass-ceramic substrates and finished magnetic thin-film rigid disks, Adv. Info. Storage Syst. 6, 193–208.
26. Bhushan, B. and Gupta, B. K. (1997), Handbook of Tribology: Materials, Coatings, and Surface Treatments, McGraw-Hill, New York, 1991, reprint ed., Krieger, Malabar, FL, 1997.
27. Bhushan, B. and Koinkar, V. N. (1995), Microscale mechanical and tribological characterization of hard amorphous coatings as thin as 5 nm for magnetic disks, Surf. Coat. Technol. 76–77, 655–669.
28. Bhushan, B. and Li, X. (2003), Nanomechanical characterization of solid surfaces and thin films, Int. Mater. Rev. 48, 125–164.
29. Bhushan, B. and Ruan, J. (1994), Tribological performance of thin film amorphous carbon overcoats for magnetic recording rigid disks in various environments, Surf. Coat. Technol. 68/69, 644–650.
30. Bhushan, B., Kellock, A. J., Cho, N. H., and Ager III, J. W. (1992), Characterization of chemical bonding and physical characteristic of diamond-like amorphous carbon and diamond films, J. Mater. Res. 7, 404–410.
31. Bhushan, B., Gupta, B. K., VanCleef, G. W., Capp, C., and Coe, J. V. (1993a), Fullerene (C_{60}) films for solid lubrication, Tribol. Trans. 36, 573–580.
32. Bhushan, B., Subramaniam, V. V., Malshe, A., Gupta, B. K., and Ruan, J. (1993b), Tribological properties of polished diamond films, J. Appl. Phys. 74, 4174–4180.
33. Bhushan, B., Gupta, B. K., and Subramaniam, V. V. (1994), Polishing of diamond films, Diam. Films Technol. 4, 71–97.
34. Bhushan, B., Gupta, B. K., and Azarian, M. H. (1995a), Nanoindentation, microscratch, friction and wear studies for contact recording applications, Wear 181–183, 743–758.
35. Bhushan, B., Yang, L., Gao, C., Suri, S., Miller, R. A., and Marchon, B. (1995b), Friction and wear studies of magnetic thin-film rigid disks with glass-ceramic, glass and aluminum-magnesium substrates, Wear 190, 44–59.

36. Bhushan, B., Patton, S. T., Sundaram, R., and Dey, S. (1996), Pole tip recession studies of hard carbon-coated thin-film tape heads, J. Appl. Phys. 79, 5916–5918.
37. Bhushan, B., Theunissen, G. S. A. M., and Li, X. (1997) Tribological studies of chromium oxide films for magnetic recording applications, Thin Solid Films 311, 67–80.
38. Bowden, F. P. and Young, J. E. (1951), Friction of diamond, graphite and carbon and the influence of surface films, Proc. R. Soc. Lond. 208, 444–455.
39. Brown, I. G., Anders, A., Anders, S., Dickinson, M. R., Ivanov, I. C., MacGill, R. A., Yao, X. Y., and Yu, K. M. (1993), Plasma synthesis of metallic and composite thin films with atomically mixed substrate bonding, Nucl. Instrum. Meth. Phys. Res. B80–B81, 1281–1287.
40. Bubenzer, A., Dischler, B., Brandt, B., and Koidl, P. (1983), R.F. plasma deposited amorphous hydrogenated hard carbon thin films, preparation, properties and applications, J. Appl. Phys. 54, 4590–4594.
41. Bull, S. J. (1995), Tribology of carbon coatings: DLC, diamond and beyond, Diam. Relat. Mater. 4, 827–836.
42. Catherine, Y. (1991), Preparation techniques for diamond-like carbon, in R. E. Clausing, L. L. Horton, J. C. Angus, and P. Koidl (eds.) Diamond and Diamond-like Films and Coatings, Plenum, New York, pp. 193–227.
43. Cho, N. H., Krishnan, K. M., Veirs, D. K., Rubin, M. D., Hopper, C. B., Bhushan, B., and Bogy, D. B. (1990), Chemical structure and physical properties of diamond-like amorphous carbon films prepared by magnetron sputtering, J. Mater. Res. 5, 2543–2554.
44. Cuomo, J. J., Pappas, D. L., Bruley, J., Doyle, J. P., and Seagner K. L. (1991), Vapor deposition processes for amorphous carbon films with sp^3 fractions approaching diamond, J. Appl. Phys. 70, 1706–1711.
45. Cuomo, J. J., Pappas, D. L., Lossy, R., Doyle, J. P., Bruley, J., Di Bello, G. W., and Krakow, W. (1992), Energetic carbon deposition at oblique angles, J. Vac. Sci. Technol. A10, 3414–3418.
46. Dimigen, H. and Hubsch, H. (1983–1984), Applying low-friction wear-resistant thin solid films by physical vapor deposition, Philips Tech. Rev. 41, 186–197.
47. Dischler, B., Bubenzer, A., and Koidl, P. (1983), Hard carbon coatings with low optical-absorption, Appl. Phys. Lett. 42, 636–638.
48. Donnet, C. and Grill, A. (1997), Friction control of diamond-like carbon coatings, Surf. Coat. Technol. 94–95, 456.
49. Donnet, C., Le Mogne, T., Ponsonnet, L., Belin, M., Grill, A., and Patel, V. (1998), The respective role of oxygen and water vapor on the tribology of hydrogenated diamond-like carbon coatings, Tribol. Lett. 4, 259.
50. Dugger, M. T., Chung, Y. W., Bhushan, B., and Rothschild, W. (1990), Friction, wear, and interfacial chemistry in thin film magnetic rigid disk files, ASME J. Tribol. 112, 238–245.
51. Erdemir, A. and Donnet, C. (2001), Tribology of diamond, diamond-like carbon, and related films, in B. Bhushan (ed.) Modern Tribology Handbook, Vol. 2: Materials, Coatings, and Industrial Applications, CRC Press, Boca Raton, FL, pp. 871–908.
52. Erdemir, A., Switala, M., Wei, R., and Wilbur, P. (1991), A tribological investigation of the graphite-to-diamond-like behavior of amorphous carbon films ion beam deposited on ceramic substrates, Surf. Coat. Technol. 50, 17–23.
53. Erdemir, A., Nicols, F. A., Pan, X. Z., Wei, R., and Wilbur, P. J. (1993), Friction and wear performance of ion-beam deposited diamond-like carbon films on steel substrates, Diam. Relat. Mater. 3, 119–125.
54. Evans, A. G. and Hutchinson, J. W. (1984), On the mechanics of delamination and spalling in compressed films, Int. J. Solids Struct. 20, 455–466.
55. Fallon, P. J., Veerasamy, V. S., Davis, C. A., Robertson, J., Amaratunga, G. A. J., Milne, W. I., Koskinen, J. (1993), Properties of filtered-ion-beam-deposited diamond-like carbon as a function of ion energy, Phys. Rev. B48, 4777–4782.
56. Green, D. C., McKenzie, D. R., and Lukins, P. B. (1989), The microstructure of carbon thin films, Mater. Sci. Forum 52–53, 103–124.

57. Grill, A. (1997), Tribological properties of diamondlike carbon and related materials, Surf. Coat. Technol. 94–95, 507.
58. Grill, A. and Meyerson, B. S. (1994), Development and status of diamondlike carbon, in K. E. Spear and J. P. Dismukes (eds.) Synthetic Diamond: Emerging CVD Science and Technology, Wiley, New York, pp. 91–141.
59. Grill, A., Meyerson, B. S., and Patel, V. V. (1988), Interface modification for improving the adhesion of a-C:H to metals, J. Mater. Res. 3, 214.
60. Grill, A., Meyerson, B. S., and Patel, V. V. (1990a), Diamond-like carbon films by RF plasma-assisted chemical vapor depostion from acetylene, IBM J. Res. Develop. 34, 849–857.
61. Grill, A., Patel, V. V., and Meyerson, B. S. (1990b), Optical and tribological properties of heat-treated diamond-like carbon, J. Mater. Res. 5, 2531–2537.
62. Gupta, B. K. and Bhushan, B. (1994), Fullerene particles as an additive to liquid lubricants and greases for low friction and wear, Lub. Eng. 50, 524–528.
63. Gupta, B. K. and Bhushan, B. (1995a), Mechanical and tribological properties of hard carbon coatings for magnetic recording heads, Wear 190, 110–122.
64. Gupta, B. K. and Bhushan, B. (1995b), Micromechanical properties of amorphous carbon coatings deposited by different deposition techniques, Thin Solid Films 270, 391–398.
65. Gupta, B. K., Bhushan, B., Capp, C., and Coe, J. V. (1994), Material characterization and effect of purity and ion implantation on the friction and wear of sublimed fullerene films, J. Mater. Res. 9, 2823–2838.
66. Holland, L. and Ojha, S. M. (1976), Deposition of hard and insulating carbonaceous films of an RF target in butane plasma, Thin Solid Films 38, L17–L19.
67. Jansen, F., Machonkin, M., Kaplan, S., and Hark, S. (1985), The effect of hydrogenation on the properties of ion beam sputter deposited amorphous carbon, J. Vac. Sci. Technol. A3, 605–609.
68. Kaplan, S., Jansen, F., and Machonkin, M. (1985), Characterization of amorphous carbon-hydrogen films by solid-state nuclear magnetic resonance, Appl. Phys. Lett. 47, 750–753.
69. Knight, D. S. and White, W. B. (1989), Characterization of diamond films by Raman spectroscopy, J. Mater. Res. 4, 385–393.
70. Koinkar, V. N. and Bhushan, B. (1997), Microtribological properties of hard amorphous carbon protective coatings for thin-film magnetic disks and heads, Proc. Inst. Mech. Eng., Part J 211, 365–372.
71. Lettington, A. H. (1998), Applications of diamond-like carbon thin films, Carbon 36, 555–560.
72. Li, X. and Bhushan, B. (1998a), Micromechanical and tribological characterization of hard amorphous carbon coatings as thin as 5 nm for magnetic recording heads, Wear 220, 51–58.
73. Li, X. and Bhushan, B. (1998b), Measurement of fracture toughness of ultra-thin amorphous carbon films, Thin Solid Films 315, 214–221.
74. Li, X. and Bhushan, B. (1999a), Micro/nanomechanical and tribological characterization of ultra-thin amorphous carbon coatings, J. Mater. Res. 14, 2328–2337.
75. Li, X. and Bhushan, B. (1999b), Mechanical and tribological studies of ultra-thin hard carbon overcoats for magnetic recording heads, Z. Metallkd. 90, 820–830.
76. Li, X. and Bhushan, B. (1999c), Evaluation of fracture toughness of ultra-thin amorphous carbon coatings deposited by different deposition techniques, Thin Solid Films 355–356, 330–336.
77. Li, X. and Bhushan, B. (2002a), Development of a nanoscale fatigue measurement technique and its application to ultrathin amorphous carbon coatings," Scripta Mater. 47, 473–479.
78. Li, X. and Bhushan, B. (2002b), Nanofatigue studies of ultrathin hard carbon overcoats used in magnetic storage devices, J. Appl. Phys. 91, 8334–8336.
79. Li, X., Diao, D., and Bhushan, B. (1997), Fracture mechanisms of thin amorphous carbon films in nanoindentation, Acta Mater. 45, 4453–4461.
80. Lossy, R., Pappas, D. L., Roy, R. A., and Cuomo, J. J. (1992), Filtered arc deposition of amorphous diamond, Appl. Phys. Lett. 61, 171–173.

81. Marchon, B., Heiman, N., and Khan, M. R. (1990), Evidence for tribochemical wear on amorphous carbon thin films, IEEE Trans. Magn. 26, 168–170.
82. Marchon, B., Salmeron, M., and Siekhaus, W. (1989), Observation of graphitic and amorphous structures on the surface of hard carbon films by scanning tunneling microscopy, Phys. Rev. B 39, 12907–12910.
83. Marshall, D. B. and Evans, A. G. (1984), Measurement of adherence of residual stresses in thin films by indentation. I. Mechanics of interface delamination, J. Appl. Phys. 15, 2632–2638.
84. Matthews, A. and Eskildsen, S. S. (1994), Engineering applications for diamond-like carbon, Diam. Relat. Mater. 3, 902–911.
85. McKenzie, D. R., Muller, D., Pailthorpe, B. A., Wang, Z. H., Kravtchinskaia, E., Segal, D., Lukins, P. B., Martin, P. J., Amaratunga, G., Gaskell, P. H., and Saeed, A. (1991), Properties of tetrahedral amorphous carbon prepared by vacuum arc deposition, Diam. Relat. Mater. 1, 51–59.
86. Memming, R., Tolle, H. J., and Wierenga, P. E. (1986), Properties of polymeric layers of hydrogenated amorphous carbon produced by plasma-activated chemical vapor deposition: tribological and mechanical properties, Thin Solid Films 143, 31–41.
87. Pappas, D. L., Saegner, K. L., Bruley, J., Krakow, W., and Cuomo, J. J. (1992), Pulsed laser deposition of diamondlike carbon films, J. Appl. Phys. 71, 5675–5684.
88. Robertson, J. (1986), Amorphous carbon, Adv. Phys. 35, 317–374.
89. Robertson, J. (1992), Properties of diamond-like carbon, Surf. Coat. Technol. 50 185–203.
90. Robertson, J. (1993), Deposition of diamond-like carbon, Philos. Trans. R. Soc. London A342, 277–286.
91. Rubin, M., Hooper, C. B., Cho, N. H., and Bhushan, B. (1990), Optical and mechanical properties of DC sputtered carbon films, J. Mater. Res. 5, 2538–2542.
92. Sander, P., Kaiser, U., Altebockwinkel, M., Wiedmann, L., Benninghoven, A., Sah, R. E., and Koidl, P. (1987), Depth profile analysis of hydrogenated carbon layers on silicon by x-ray photoelectron spectroscopy, Auger electron spectroscopy, electron energy-loss spectroscopy, and secondary ion mass spectrometry, J. Vac. Sci. Technol. A5, 1470–1473.
93. Savvides, N. and Bell, T. J. (1992), Microhardness and Young's modulus of diamond and diamondlike carbon films, J. Appl. Phys. 72, 2791–2796.
94. Savvides, N. and Window, B. (1985), Diamondlike amorphous carbon films prepared by magnetron sputtering of graphite, J. Vac. Sci. Technol. A3, 2386–2390.
95. Scharff, W., Hammer, K., Stenzel, O., Ullman, J., Vogel, M., Frauenheim, T., Eibisch, B., Roth, S., Schulze, S., and Muhling, I. (1989), Preparation of amorphous i-C films by ion-assisted methods, Thin Solid Films 171, 157–169.
96. Scheibe, H. J. and Schultrich, B. (1994), DLC film deposition by laser-arc and study of properties, Thin Solid Films 246, 92–102.
97. Scott, W. W. and Bhushan, B. (2000a), Corrosion and wear studies of uncoated and ultra-thin DLC coated magnetic tape-write heads and magnetic tapes, Wear 243, 31–42.
98. Scott, W. W. and Bhushan, B. (2000b), Loose debris and head stain generation and pole tip recession in modern tape drives, J. Info. Storage Proc. Syst. 2, 221–254.
99. Scott, W. W., Bhushan, B., and Lakshmikumaran, A. V. (2000), Ultrathin diamond-like carbon coatings used for reduction of pole tip recession in magnetic tape heads, J. Appl. Phys. 87, 6182–6184.
100. Spencer, E. G., Schmidt, P. H., Joy, D. C., and Sansalone, F. J. (1976), Ion beam deposited polycrystalline diamond-like films, Appl. Phys. Lett. 29, 118–120.
101. Strom, B. D., Bogy, D. B., Bhatia, C. S., and Bhushan, B. (1991), Tribochemical effects of various gases and water vapor on thin film magnetic disks with carbon overcoats," ASME J. Tribol. 113, 689–693.
102. Sundararajan, S. and Bhushan, B. (1999), Micro/nanotribology of ultra-thin hard amorphous carbon coatings using atomic force/friction force microscopy, Wear 225–229, 678–689.

103. Sundararajan, S. and Bhushan, B. (2001), Development of a continuous microscratch technique in an atomic force microscope and its application to study scratch resistance of ultrathin hard amorphous carbon coatings, J. Mater. Res. 16, 437–445.
104. Suresh, S. (1991), Fatigue of materials, Cambridge University Press, Cambridge.
105. Suzuki, J. and Okada, S. (1995), Deposition of diamondlike carbon films using electron cyclotron resonance plasma chemical vapor deposition from ethylene gas, Jpn. J. Appl. Phys. 34, L1218–L1220.
106. Swec, D. M., Mirtich, M. J., and Banks, B. A. (1989), Ion beam and plasma methods of producing diamondlike carbon films, Report No. NASATM102301, NASA, Cleveland, OH.
107. Tsai, H. C., Bogy, D. B., Kundmann, M. K., Veirs, D. K., Hilton, M. R., and Mayer, S. T. (1988), Structure and properties of sputtered carbon overcoats on rigid magnetic media disks, J. Vac. Sci. Technol. A6, 2307–2315.
108. Vandentop, G. J., Kawasaki, M., Nix, R. M., Brown, I. G., Salmeron, M., and Somorjai, G. A. (1990), Formation of hydrogenated amorphous carbon films of controlled hardness from a methane plasma, Phys. Rev. B41, 3200–3210.
109. Wei, R., Wilbur, P. J., and Liston, M. J. (1993), Effects of diamond-like hydrocarbon films on rolling contact fatigue of bearing steels, Diam. Relat. Mater. 2, 898–903.
110. Weissmantel, C., Bewilogua, K., Breuer, K., Dietrich, D., Ebersbach, U., Erler, H. J., Rau, B., and Reisse, G. (1982), Preparation and properties of hard i-C and i-BN coatings, Thin Solid Films 96, 31–44.
111. Wu, T. W. (1991), Microscratch and load relaxation tests for ultra-thin films, J. Mater. Res. 6, 407–426.
112. Xu, J. and Bhushan, B. (1998) Pole tip recession studies of thin-film rigid disk head sliders II: effects of air bearing surface and pole tip region designs and carbon coating, Wear 219, 30–41.

Laser Processing of Tribological DLC Films: An Overview

G. Dumitru

Abstract The chapter deals with the multifaceted interrelations between the laser processing and the diamond-like carbon (DLC) films.

After presenting the most relevant optical, electrical, and mechanical properties of DLC films, the use of laser beams in producing such coatings on different substrates is briefly exposed. The dissimilarities between nanosecond (ns) and femtosecond (fs) pulsed laser deposition are also referred to. This is followed by a discussion on the direct and the indirect laser processing of tribological films.

Section 3 commences with a discussion on their optical absorption properties and on the processes occurring when laser pulses of different durations and energy densities impinge on such films. The ablation characteristics and the structure changes in laser-treated DLC coatings are presented for short (ns, UV) and ultrashort (fs, IR) pulses.

Section 4 explains that the indirect laser processing of tribological films relies on the high productivity laser machining of substrates, using robust diode pumped solid-state lasers. It discusses the main factors governing the laser processing of substrates and their cross-correlations and also presents particular results on hard metal and tool steel – both processed with ns pulses (wavelengths: 1,064 nm, 355 nm).

Results of oscillation–friction–wear tribological tests, which were performed on indirectly laser-processed DLC films (deposited on tool steel substrates), some concluding remarks and a list of 64 references complete this chapter.

Keywords laser texturation, pulsed laser deposition, direct machining, indirect machining

University of Applied Sciences Northwestern Switzerland, School of Engineering, Institute for Product and Production Engineering (IPPE), Steinackerstrasse 5, 5210 Windisch, Switzerland.
E-mail: gabriel.dumitru@fhnw.ch

C. Donnet and A. Erdemir (eds.), *Tribology of Diamond-Like Carbon Films: Fundamentals and Applications*.

1 Introduction

The use of lasers in the machining of advanced hard-brittle protective films, which embed value-adding functional features or components, nowadays, undergoes a continuous growth. The increased market value of the resulted parts counterbalances the high production costs, which the laser processing usually involves. Furthermore, numerous research studies and industrial applications showed that the surface characteristics of such coatings depend not only on their chemical composition, but also on their topography [1–3]. Structures on hard-brittle materials (e.g., arrays of dots, holes, lines, or grooves) can be fabricated by means of different manufacturing processes: deposition techniques, lithography processes, adapted ultrafine polishing, etc. [4–6]. These procedures are advantageous for mass production; however, they require huge and expensive facilities and are not always suitable for a flexible production. In such situations, the laser machining may be the technique of choice.

The interconnections between lasers and diamond-like carbon (DLC) films are tight and multifaceted. On the one hand, certain carbon films are fabricated by means of pulsed laser deposition: a focused laser beam impinges on a carbon-containing target, an ablation plume is generated, and the DLC film results upon the deposition of the ablated material onto a suitable positioned substrate. On the other hand, certain properties of DLC films can be modified through laser processing: surface shape or material structure changes are induced through the laser treatment of DLC films. The latter facets are discussed here, whereas the former are only briefly reviewed.

2 General Considerations

2.1 Properties and Applications of DLC Films

DLC films belong to value-adding hard-brittle materials and their distinctive electrical, chemical, and physical properties enable their spread in optical, electronic, mechanical, and biotechnological areas [7–9]. Structurally, these films are amorphous and are composed of short-range-ordered domains of sp^3 and sp^2 bonds. These carbon bonds show their Raman peaks between 800 and 2,000 cm^{-1} [10,11]: (i) The G-peak is due to the bond stretching of all pairs of sp^2 atoms in both rings and chains and lies around 1,560 cm^{-1}. (ii) The D-peak is due to the breathing modes of sp^2 atoms in rings and is situated at approximately 1,360 cm^{-1}. (iii) The T-peak is commonly assigned to the vibrations of sp^3 atoms and is roughly located at 1,060 cm^{-1}. The G- and D-peaks are visible for VIS excitation and the T-peak is visible only for UV excitation.

The laser processing bears on the absorption of the incident photons, hence the optical properties of DLC films are central for the laser–film interactions. These films are typically transparent in the IR (except for the 3.4 μm CH absorption band), they absorb weakly in the VIS spectrum, and are increasingly absorbing in UV, with decreasing wavelength. The band gap of DLC films, which determines the one-photon absorption properties, was found to be dependent on the deposition system: band gap values between

0.38 and 2.72 eV were reported for films obtained under similar conditions [12]. The band gap value was found to decrease strongly for films deposited above 250°C.

Although exhibiting typical band gaps in the 1–3 eV domain, DLC films do not behave like typical semiconductors, since their electrical properties can vary from that of a semimetal to that of a wide band gap insulator [12]. The electrical resistivity of DLC films can be strongly reduced (orders of magnitude), by doping them with metals or nitrogen [10]. However, the doping efficiency is very low and no p-n DLC junction has yet been evidenced. A decrease of electrical resistivity was also obtained by laser-induced graphitization, which may enable the production of conductive lines on DLC films [13].

Further distinguishing properties of DLC films are their low friction and high wear resistance. Friction stems from the chemical and physical interactions between the sliding surfaces, whereas deformation and third-body interactions may also play a significant role. As a result, high friction is generated by large chemical or adhesive interactions between the sliding surfaces or by rough surfaces. Through controlling their deposition processes, DLC films can be obtained mechanically very hard (values as high as 90 GPa, depending on the amount of sp^3 bonds [14]), physically very smooth, and chemically very inert (no open corrosion paths up to 800°C [15]). They can be extremely wear resistant and exhibit outstanding friction properties: a friction coefficient below 0.01 was measured for DLC sliding against steel in 10^{-1} Pa vacuum [16].

This unique combination of properties makes the DLC films an ideal coating for tribological, optical, and medical applications. Among the already "classical" utilizations, one can enumerate thin-film magnetic rigid discs [17], low-pressure tribological systems [18], or parts in aggressive tribological environments (e.g., metal chipping tools). In addition, DLC films also have interesting optics-related applications: antireflective and scratch-resistant wear-protective coatings for Ge, ZnS, or ZnSe IR-optics [19], or abrasion protection coatings for polycarbonate sunglass lenses [20].

2.2 DLC Films by Pulsed Laser Deposition

DLC films can be produced through various techniques: cathodic arc deposition, direct ion beam deposition, plasma-enhanced chemical vapor deposition, ion beam sputtering, DC/RF sputtering, pulsed laser deposition (PLD). The latter technique involves low deposition temperatures and has the advantage of enabling the deposition of high purity non-hydrogenated DLC films with a predominance of sp^3 hybridization [21]. The sp^3/sp^2 ratio can be varied by tuning the deposition parameters, such as energy and degree of ionization of the ablated species, target materials, laser wavelength, pulse repetition frequency, gas chamber pressure, and additional substrate heating [22]. Upon optimization, PLD may yield DLC films superior to those obtained by filtered cathodic vacuum arc deposition and mass selected ion-beam deposition techniques. PLD-fabricated DLC films showed good mechanical properties and hardness values ranging between 20 and 70 GPa were reported [23,24].

The PLD-fabrication of DLC films involves – according to the duration of the utilized laser pulses – two classes of lasers: nanosecond (ns) and femtosecond (fs) systems. The pulse duration has a direct influence on the physical processes occurring in the carbon-containing target and, as a consequence, on the ablation plume properties (e.g., ionization grade, kinetic energy, spatial distribution). Because sp^3 is a nonequilibrium structure, the particles arriving onto the substrate must be able to deliver their excess energy to the substrate rapidly (quenching). Otherwise, the energetic species can thermalize to the equilibrium state (sp^2), since they have enough energy to get over the activation barrier between these two structures [25]. As a result, the formation of sp^3 carbon is favored by highly energetic plasma particles and completely ionized plasma is required to achieve high concentration of sp^3 bonds [26]. The background gas also influences the particle energy: at higher pressures in the PLD chamber, the ablated particles are progressively more scattered, they lose kinetic energy and this raises the sp^2 amount in the deposited film [27].

In the case of ns PLD, the ablation plume consists mainly of lower energy carbon species, but due to the higher pulse energy, the particle flow is higher than in fs PLD. With more and more reliable fs lasers, the fs PLD experienced a rapid development during the last few years. Its advantages, as compared with ns PLD, were exposed in several recent works [23,24]. For instance (150 fs, laser fluences between 1 and 6 J/cm^2), DLC films with compressive stresses below 3 GPa were fabricated by fs PLD. The DLC films exhibited wear resistances in the 10^{-8} mm^3 N^{-1} m^{-1} range and hardness values in the range 20–30 GPa. Predominantly (>70%) sp^3 bonds were found and the nanohardness and Young's modulus were rather moderate, as compared to ns PLD [24].

2.3 Laser Processing of Tribological Films: Two Approaches

The field of laser tribology (i.e., the laser-based surface engineering of tribological surfaces) underwent an exponential growth in the recent years and a large variety of lab reports, as well as concrete industrial applications (combustion engines, metal forming tools, pumps, etc.) are available [28]. Briefly, these applications bear on arrays of conveniently distributed laser-induced pores, which can play different roles: (i) They can serve as lubricant reservoirs, capable of feeding the lubricant directly into the contact zone of the sliding surfaces. (ii) They can trap wear particles and to remove them from the tribocontact area. (iii) They can promote the occurrence of hydrostatic or hydrodynamic lubrication conditions [29]. Mainly depending on pore dimensions and on application-related conditions (e.g., contact pressure, sliding velocity, and oil viscosity), the effects of one of the aforementioned mechanism may prevail; however, all of them contribute to improving the tribological properties of laser-patterned surfaces.

The laser tribology is a field of great potential, but it is still in the development phase. On the other hand, the coating of sliding surfaces with wear-resistant thin films is a well-established method to minimize wear and the occurrence of debris particles.

These methods are to be combined, in order to obtain ultralow wear surfaces [30,31]. Under this viewpoint, the ratio between the film thickness and the dimensions of the needed tribological structures becomes very important, and it may determine the choice of the laser-processing method. Typical laser tribology elements may exhibit diameters between a few microns and 100 µm and depths from a few 100 nm to several 10 µm, whereas film thicknesses lie in the range 1–5 µm. In certain cases, the needed pore depths exceed the film thickness and such surfaces can be obtained either by the laser processing of already coated parts (direct processing) or by the coating of already laser-patterned substrates (indirect processing).

These two approaches (Fig. 1) have different technological requirements, their optimization paths are also dissimilar, and they may involve different laser sources. For instance, the highest priority in direct processing is gentle laser machining, without any collateral film damages. The wavelength and the pulse duration of the processing laser are an important factor for the occurring absorption processes and they must match the thermal and optical properties of the processed coating. In this case, small (<1 J/cm^2) incident fluences are used, UV or fs lasers have certain advantages, and the material removal rates are rather of secondary importance. On the other hand, indirect processing is to be optimized for a rapid and versatile material removal from metallic substrates (e.g., steel, hard metal) and it can be performed efficiently with IR ns lasers. Here, large (20–100 J/cm^2) laser fluences are involved,

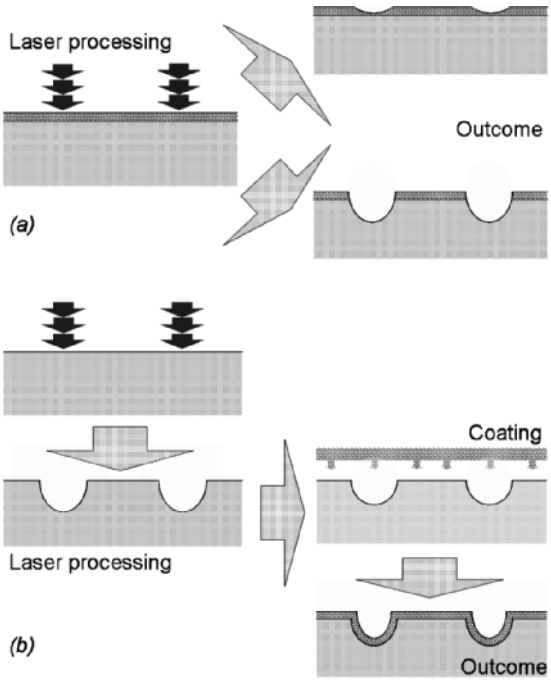

Fig. 1 Direct (*a*) and indirect (*b*) laser processing of thin tribological films (e.g., DLC)

high ablation rate and patterning felxibility are required, and a soft mechanical polishing is usually needed before the coating procedure.

3 Direct Processing

In the case of the direct processing approach, the laser machining is the last link of the process chain and a laser treatment with no or minimal damage of surrounding and underlying material is the most important requirement here. The incident laser energy must be adequately dosed, and the extension of the absorption volume should be carefully considered. To meet these precision demands in the case of DLC films, two major ways are available. On the one hand, the optical absorption depth in DLC films diminishes if UV lasers are used. The use of excimer lasers [13,32] and the rising utilization of novel, frequency-converted solid-state lasers in the direct processing of DLC films rely on this approach. On the other hand, the thermal diffusion length in DLC can be minimized to values comparable with the optical absorption depth, if the duration of the processing laser pulses is reduced to ps or even fs.

The absorbed laser energy represents the energy source of the processes occurring in the DLC film and it can yield – mainly depending on incident fluence – structural modifications (e.g., crystallization of the original amorphous matrix), spallation, film melting, or film vaporization [33,34]. The structural modifications (usually graphitization) are accompanied by significant changes of DLC physical properties (mass density, optical absorption, thermal conductivity). Furthermore, at high laser fluences, the evaporation is the predominant material removal mechanism, whereas at fluences between the ablation and the damage thresholds, the laser direct processing is rather less effective than O_2-assisted plasma etching [35]. At fluences below the damage threshold and for the multiple pulse approach, an incubation phenomenon was evidenced. This effect stems from the phase changes that are induced by each pulse, and which cumulatively changes the optical properties of the processed film: the optical absorptivity increases and the ablation threshold decreases [36]. Incubation effects were also evidenced in metals [37], semiconductors [38], and ceramics [39].

The most important phase change occurring in the direct-processed DLC film is its graphitization and this depends both on the incident laser fluence and on the duration of the processing pulses. The decrease of the pulse duration in the nanosecond range yields a reduction of the thermal diffusion length and leads to a noticeable reduction of the graphitized layer thickness. Below a certain pulse length (sub-ns pulses), the thermal diffusion length becomes comparable to the optical penetration depth and further decrease of the pulse duration does not affect the graphitized layer thickness. The graphitized layer thickness increases with the irradiation doze at fixed low laser fluences and it is almost independent of the laser fluence above the evaporation threshold [40].

At laser fluences near the threshold region (0.1–0.2 J/cm^2), the spallation of laser-treated DLC films may occur. The film spallation was observed for a wide

range of laser parameters and the film split thickness can vary from 10 to 200 nm, depending on the pulse duration and on the wavelength [41]. This phenomenon is reproducible only to a certain extent and is therefore to some extent inconvenient for the direct processing. Reproducible spallation was noticed for the first laser pulse that impinges onto the original DLC film, but for the subsequent pulses, the process becomes rather stochastic. The spallation of DLC films is most likely generated by the fast laser-induced "graphitization wave," which propagates from the film surface into the bulk and causes a sudden decrease in material density [41]. The film spallation was used in specific cases to laser micromachine Al/DLC microcantilever structure [42].

3.1 UV Lasers, ns Pulses

Excimer lasers have been used since early 1990s to produce patterns on DLC films [43]. These first tries were related to lithography purposes, then geometrical goals were also involved. For instance, the KrF excimer laser ablation ensures extremely efficient patterning of thick DLC coatings. In this case, it was found that the damage threshold is situated at 0.06–0.07 J/cm^2 and that the ablation threshold lies at 0.13 J/cm^2. Ablation rates exceeding 100 nm/pulse were found at laser fluences above 1 J/cm^2 [32]. In the case of the third harmonic (355 nm) of a pulsed Nd:YAG laser, the damage threshold of DLC films is in the range 0.06–0.08 J/cm^2 and film graphitization occurred at fluences above the damage threshold [44].

In other approach, exicmer laser beams with fluences slightly exceeding 0.1 J/cm^2 were used to irradiate DLC films, in order to use them as resists in lithography. The DLC film was graphitized only in the exposed regions and no material is being removed. Therefore, less chemical-resistant DLC surface structures were delineated and these were subsequently developed by etching in an O_2 plasma [13].

The mask-related problems, the poor focusabilty and their small pulse repetition rates are the main drawbacks of the excimer laser systems. The novel UV solid-state lasers, which exhibit good focusability, and which allow pulse repetition rates up to 100 kHz, may give the UV laser direct processing of DLC films new dimensions. The following estimation may illustrate these considerations: In a specific application, 25 μm dots are to be produced on a DLC film with a spatial frequency of 20 mm^{-1}. With a pulse repetition rate of 100 kHz and in single pulse technique, the patterning of 1 cm^2 would last 0.8 s. Considering a fluence of 0.1 J/cm^2 (graphitization) or even 1 J/cm^2 (evaporation), an average laser power below 1 W would be sufficient for this purpose.

3.2 Ultrashort Pulses

Experiments on the interaction between fs laser pulses and different carbon phases (mostly diamond) have been reported in literature since the mid-1990s [45] and

theoretical interaction models based on molecular dynamics were developed. In the case of sp^3 bonds, it was shown [46] that fs pulses induce a nonequilibrium transition to sp^2 bonds that evolves on a timescale below 100 fs. Simulation studies, which investigated the influence of the pulse duration on the graphitization process, demonstrated that for fs pulses a layer-by-layer graphitization occurs, whereas for ns pulses the graphitization propagates vertically into bulk [47]. This model results also give a deeper insight into the aforementioned spallation process.

In DLC direct processing by fs laser pulses, both photo-ablation (photon absorption – bond breaking – material removal) and thermal ablation (absorbed energy – heat transfer – vaporization) processes play a role in the laser–film interactions and in the material removal [48,49]. Depending on incident laser fluence, one of these mechanisms may become dominant: the photo-ablation prevails at low fluences (<2 J/cm^2), whereas the thermal effects may become predominant at high fluences [50].

The damage threshold in the fs laser processing of a hydrogenated DLC was found to be 0.16 J/cm^2, for other DLC films values between 0.1 and 0.15 J/cm^2 are reported [51,52]. After a complete film penetration, the laser ablation of the substrate can occur without collateral damages of the surrounding DLC coating. The ablation rate can be calculated as the ratio between the film thickness and the number of laser pulses needed to complete the film penetration, and a set of specific values is represented in Fig. 2. The deviation from the linear slope corresponding to the low fluences is associated with an intensification of the thermal effects, as the incident laser fluence increases towards 4 J/cm^2.

The fs direct processing (100 fs, fluences <4 J/cm^2)-induced small expansions of the irradiated surface were after each first incident pulse. This volume increase may be explained by the graphitization of the laser-treated films and phase transformation associated with a mass density decrease. In all investigated cases, the second pulse tensed the surface protuberance and initiated the material removal; the following incoming pulses induced a uniform material removal process. However,

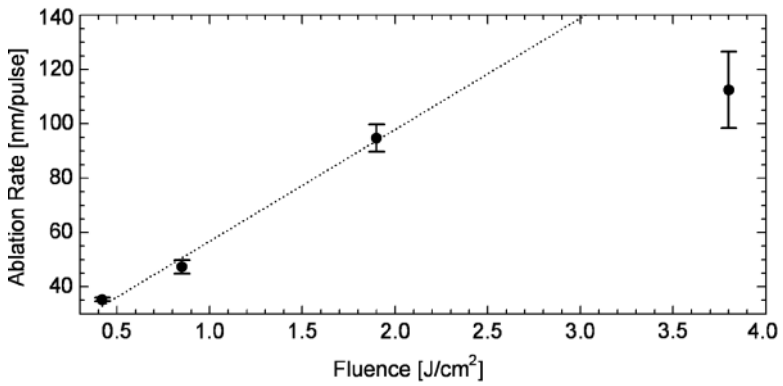

Fig. 2 Ablation rates in DLC at different incident laser fluences

in order to determine the thickness of the graphitized layers, the DLC film was chemically etched. Using depth profiles measured by white light interferometry measurements before and after etching, these thicknesses could be calculated. Depending on the incident fluence (higher fluences yielded broader layers), values between 100 and 350 nm were found in spot centers. Such depth profiles from spots irradiated with 1, 2, and 3 pulses at 1.9 J/cm^2 and are shown in Fig. 3.

The occurrence of periodic surface structures is also a characteristic of the fs laser direct processing of DLC films and this occurs at incident fluences below 1 J/cm^2. The ripples depicted in Fig. 4 have a spatial period of 0.6 µm and in that case, their maximal extension occurred at around 0.3 J/cm^2. Such ripples originate [48] from the interference between the incident and reflected waves, which yields inhomogeneities of the energy distribution and may cause periodic surface instabilities. In addition to this kind of ripples, another type of surface structures were evidenced on DLC surfaces structured by means of fs laser pulses, at fluences slightly above the ablation threshold. The size of these surface structures was 1/10–1/5 of the used laser wavelength. They were produced only by the linearly polarized beams, while the circularly polarized light formed fine-dot structures [51,52]. The classical ripple formation model [48] does not describe the observed periodic nanostructure, because the structure size observed was much smaller than that predicted by the model. The morphology changes in nanometer size may be associated with the coherent production of electron-hole plasma and with the resulting ultrafast change in bonding

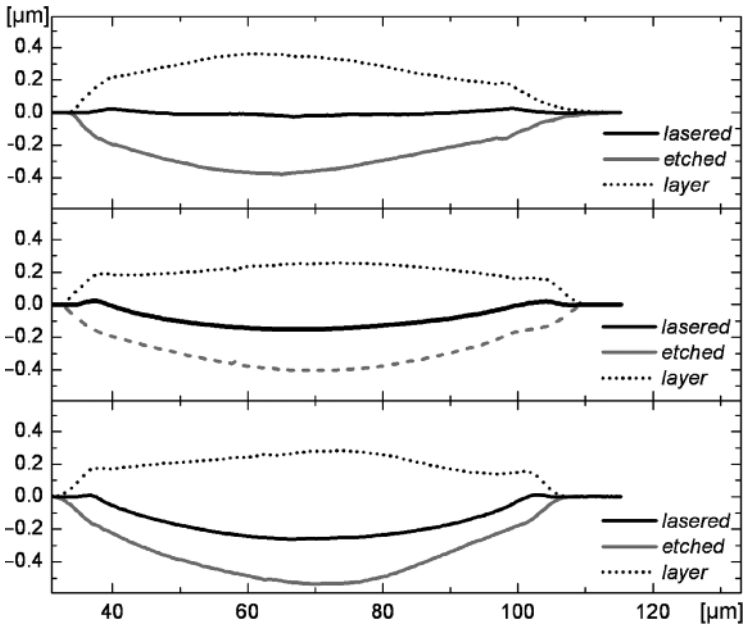

Fig. 3 WLI depth profiles after laser processing (solid), after etching (solid gray), and calculated thicknesses of the graphitized layers (dotted) after 1, 2, and 3 pulses (100 fs, 1.9 J/cm^2)

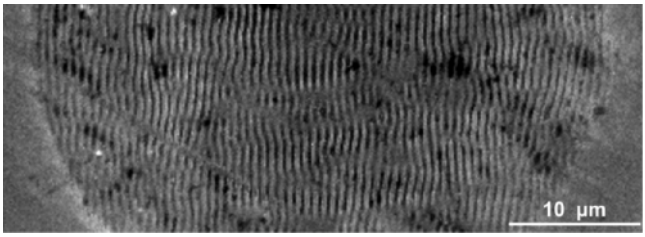

Fig. 4 Ripples on a laser-processed DLC film (20 pulses, 0.2 J/cm^2)

structure in DLC [51]. The nonequilibrium transition of bonding structure, from DLC to glassy carbon, takes place in the 0.1–0.2 J/cm^2 region and plays an important role in the formation of these nanostructures on the film surface. The glassy carbon layer that resulted through direct processing is expected to have physical and chemical properties, similar to those of the bulk glassy carbon [53].

Raman investigations were carried out [42,50] to study the structure changes induced by fs laser irradiation and spectra corresponding to the untreated film and to central zones of spots after irradiation with 1 and 2 pulses, respectively, are shown in Fig. 5. Raman analyses were also carried out for spots treated with more than two laser pulses, but the resulted spectra did not vary significantly from the curve depicted in Fig. 5c [50]. The first fs pulse yield narrower D and G lines, as compared with the Raman spectrum of the as-deposited films, these lines are slightly broadened after the second laser pulse, and subsequent pulses produced only minor changes in the Raman spectra. An upward shift of the G-line was observed and this, combined with its narrowing, indicates the decreasing of the sp^3 fraction. This agrees with the increasing of I(D)/I(G) ratio [10,11].

3.3 Summary

The phase changes in the surface layer by the first (ns or fs) pulse causes a rise of the film optical absorption and, as a result, the surface layer in the second pulse absorbs a large amount of energy. The boundary of the modified layer shifts deeper into the DLC film, but its thickness reaches a stable level after a certain number of shots. The accumulation of the structural changes in several successive pulses is also possible, if the incident fluence remains below the ablation threshold or just slightly exceeds. Laser-induced evaporation of DLC film yields progressive rise of the crater depth and the ablation rate rises quickly with the incident laser fluence and becomes close to the thickness of the graphitized layer. This means that the graphitized layer is completely vaporized and is renewed by each new laser shot.

Raman investigations carried out on DLC films after their direct processing with ns and fs laser pulses evidenced mostly similarities, but also a few dissimilarities. In both cases, the D and G lines became narrower and an upward shift of the G-peak

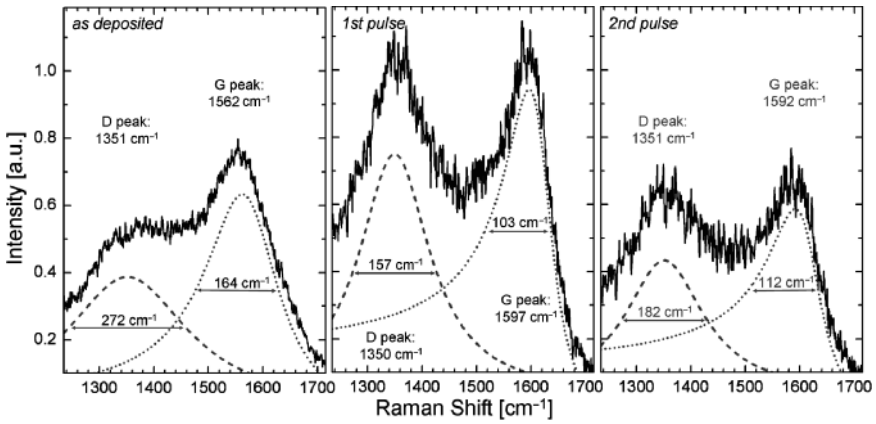

Fig. 5 Raman spectra and the deconvoluted D and G lines (100 fs, 1.9 J/cm^2)

occurred. This indicates the presence of a more ordered and less dense phase and an increased sp^2 fraction, as compared with the initial film [11]. The I(D)/I(G) ratio, which is related to the clustering degree of the laser-irradiated DLC films, increased in both cases, however stronger in the case of ns. The band-coupling parameter, which can be used as measure of in-plane graphitic order, was also calculated. Values towards zero of this parameter correspond to complete in-plane ordering, [54], although DLC films with small band-coupling parameters and with no in-plane order were reported by other authors [55]. In the case of fs pulses, the coupling parameter increased, whereas for ns pulses, small coupling parameters were calculated. According to these similarities and dissimilarities, one can state that the direct laser processing without complete film penetration (both fs and ns) induces an increase of sp^2 fraction and a growth of the clustering degree. Moreover, one might suggest that the ns-laser treatment increases the in-plane order, whereas fs-laser irradiation lowers it, which is consistent with the abovementioned observation of glassy carbon after fs-laser direct processing.

4 Indirect Processing

The energy source of the material removal processes, on which the indirect processing is based on, is the laser energy absorbed by the machined substrate. The extent of the ablation processes is correlated with the incident laser fluence: more intense surface energy sources yield increased enthalpies, that is, larger temperature increases and enough energy to induce phase changes. According to the incident fluence, superficial materials property changes (surface hardening, quenching), accurate material removal (microstructuring), or substantial material removal (cutting, drilling) can be induced [47]. It has to be mentioned that the laser fluence

on the machined substrate can be adjusted by means of properly chosen delivery optics (e.g., filters, beam expanders, focusing objectives). In addition, the focused spot diameter is proportional to the laser wavelength [48]: a three times smaller wavelength (e.g., from 1,064 nm to 355 nm) yields a three times smaller spot diameter and therefore a nine times larger fluence.

There is a strong connection between the laser-processing wavelength and the actual part of incident laser energy absorbed by the machined substrate. Depending on their electronic structure, materials exhibit specific absorption behaviors at different incident wavelengths. A common rule, frequently valid for metallic and ceramic surfaces is that, the shorter the wavelength (from IR to UV), the higher the absorption. The duration of the processing pulses plays also an important role in the ablation mechanisms and to understand it, the specific times of laser–matter interactions should be considered. A laser beam that is incident on a surface generates an intense electric field, localized under the irradiated surface. Electrons are accelerated by this field and gain kinetic energy, they collide with lattice atoms and transfer their energy to them. This energy is macroscopically mirrored in material heating and in phase changes. The energy transfer chain: photons–electrons–phonons needs about 1 ps in metals [56] and slightly more in ceramics [57]. Therefore, the thermalization of the laser energy occurs during the pulse for ns processing and after the pulse for the fs processing.

The influence and the simultaneous interdependences of the laser- and the substrate-related parameters are synthesized in Fig. 6, where the primary parameters are depicted as grey rectangles, the derivate parameters are indicated as white rectangles, and the arrows mark causal dependencies. For example, the primary laser parameter "wavelength" has an impact on the chain: wavelength → beam diameter → processing width → machining precision, but also on the chain: wavelength → surface reflectivity → processing energy density → machining efficiency. In addition to these considerations on machining precision and

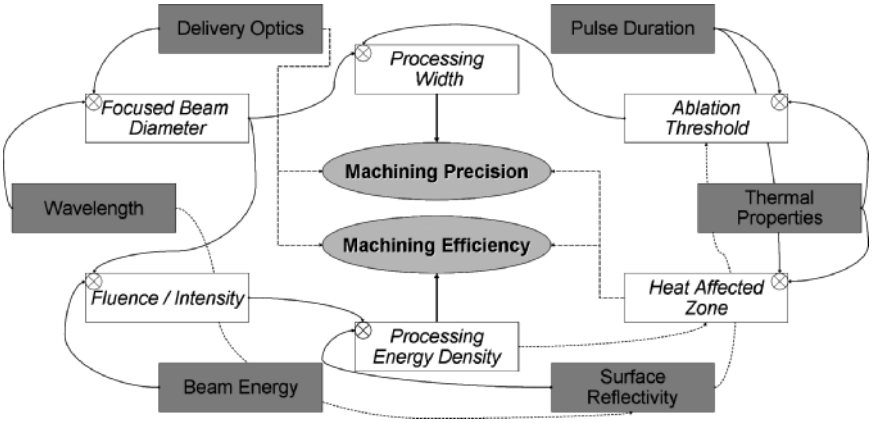

Fig. 6 Interdependencies between the laser-processing parameters

collateral affected zones, the overall material removal efficiency must also be considered. Melt-driven processes at longer pulses (sub-μs) yield a more efficient material removal than short and ultrashort pulses and may be more effective in patterning bulk substrates, but they yield rather extended (>10 μm) thermally affected zones.

4.1 Steel

The laser microstructuring of steel substrates with both ns and fs is extensively treated in the recent literature [28]. It can be efficiently carried out with Q-switched IR lasers and in this case, the melt rims can usually not be avoided. It can however be minimized through process optimization. Good results were reported for a configuration, in which the ratio between the peak irradiation fluence and the ablation threshold was 7.5. In this case, the high-peak energy density yielded a rapidly forming ablation channel and the expulsion of material through the vapor pressure occurred in a quasi-normal direction to the surface. The melt rims were still present, but they were minimized and due to their extent (thinner than 0.5 μm), they could easily be removed by gentle mechanical polishing [58].

The surface depicted in Fig. 7 (ball bearing steel) was laser patterned with 150 ns pulses, at the wavelength of 1,064 nm. Pores of 10 μm diameter, 8 μm depth, and with a spatial frequency of 33 mm^{-1} were produced on the considered substrate. Rims of resolidified melt were present around the induced pores, but their extent

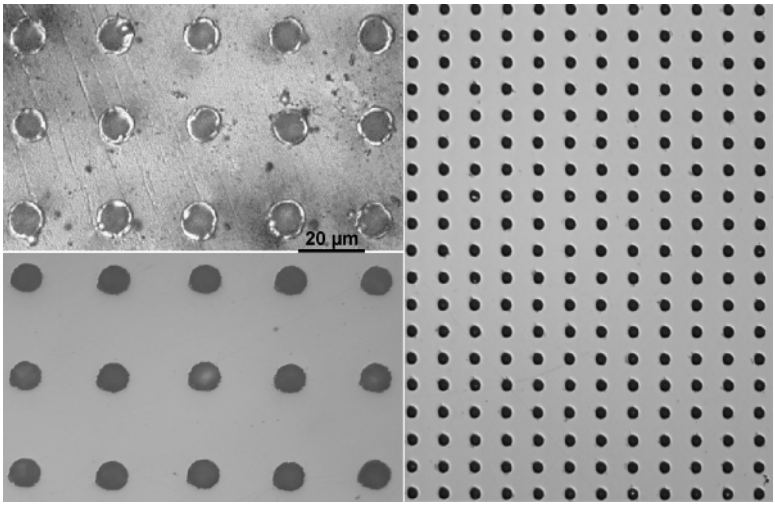

Fig. 7 Indirect processing of a steel substrate: melt rims after laser machining (*top left*), substrate after gentle polishing (*bottom left*), overview (*right*)

could be minimized and they were easily removed by a gentle polishing procedure. Regarding the rims extension, the occurring thermal collateral phenomena can be described, in a first rough calculation, by the thermal diffusion length. In this case, the value of this length can be estimated at almost 1.0 µm [59] – corresponding to the observed melt rims dimensions.

4.2 Hardmetal

Hardmetals (cemented WC-Co) are not easily machinable by chip-removal techniques and laser machining is a very effective technique in this case. The fine laser machining of hardmetal parts came into prominence at the end of the1990s, connected with the development of rugged laser sources that met both physical and industrial requirements. Laser beams (UV, ns pulses) with fluences around 2.5 J/cm^2 were reported to be suitable for a selective removal of the Co binder, which increased the adhesion of subsequent diamond films [60]. For effective machining of forms for microembossing, values in the range 10–20 J/cm^2 were reported to yield good results. WC-Co machining with a fs laser at fluences of 2 J/cm^2 led to a complete absence of collateral affected zones [61].

For ns pulses, the laser–matter energy transfer takes place during the pulse, under thermal equilibrium conditions and in this case, the thermal properties of the WC grains and of the Co binder play an important role. According to these specific features, the Co phase first melts and vaporizes and the material ablation occurs mainly by selective binder removal [61,62]. This allows WC grains to be removed in the solid phase (WC "dust") either by the ejected Co melt or by the Co vapors (Fig. 8). At higher energy densities, temperatures surpassing the melting point of WC can be reached and in this case larger WC grains can grow (locally, over a few microns) from the melt [30]. The thermal diffusion length for 100 ns laser pulses can be calculated at 1.3 µm for the WC grains and at 1.4 µm for the Co binder. The thermal penetration depths are therefore comparable, and only the large difference between the melting points of Co and WC dictates their different laser ablation behavior in ns regime.

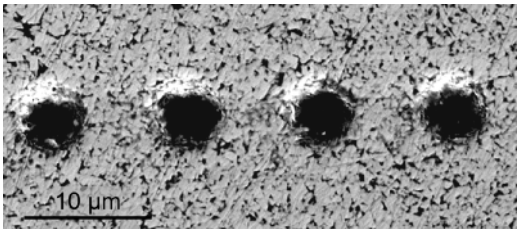

Fig. 8 Hardmetal substrate patterned by 355 nm solid-state laser

5 Tribological Tests

Tests simulating conditions that occur in the metal forming demonstrated that the combination between laser micropatterning and coating techniques represents a gain in increasing surface functionality: laser-patterned TiCN-coated surfaces have notably increased (by a factor of 15) lifetimes [31]. Beside TiN and TiCN, also laser-paterned DLC-coated substrates were fabricated and tribologically tested. In particular, high-precision patterns created on DLC surfaces by excimer lasers have been shown to improve the tribological properties of these films under boundary lubricated sliding conditions [31,63].

The tribological characteristics of hard coatings have been considerably improved by means of laser-based three-dimensional (3D)-design, permitting solid lubricant refill inside the sliding contacts. A functionally gradient Ti-TiC-TiC/DLC coating with an upper layer of tough nanocrystalline/amorphous composite was used for load support, crack prevention, and stress equalization. Grooves were produced by direct laser processing on this coating and they were then filled with MoS_2, to provide a solid lubricant reservoir in the lateral dimension of the coating. The 3D coating was tested in long-duration sliding tests at fixed and variable humidity [64].

In a particular case [59], steel substrates were laser patterned with pores 25 µm diameter and 15–20 µm depth, having a spatial frequency of 13 mm^{-1}. DLC films were deposited on the polished substrates, both unpatterned and laser patterned (Fig. 9). Before deposition, the steel substrates were kept for 10 min in Ar plasma. For the deposition process, a classical diode discharge with a hot filament was used, with

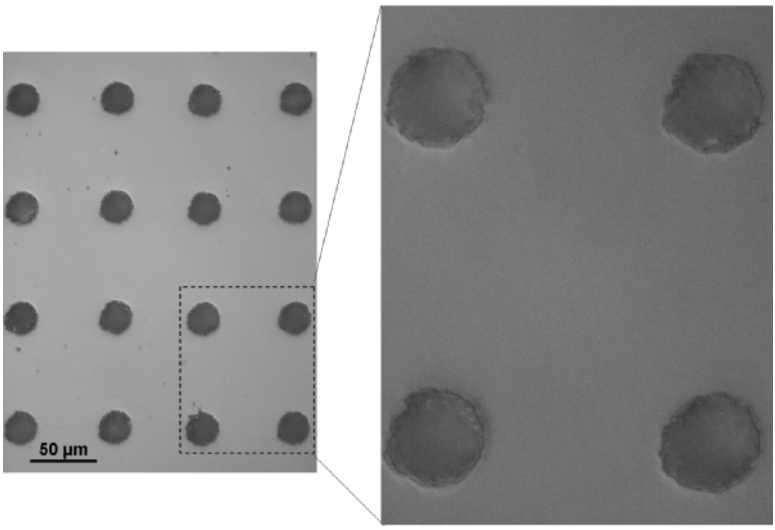

Fig. 9 Indirectly processed DLC film on steel substrate

the potential of 1.76 MHz and 250–500 V being applied to substrate. The deposition temperature was 120°C, given by the plasma heating.

The resulted DLC surfaces were tested using the oscillation–friction–wear method. In this method, the investigated surface is fixed and a hard probe body (placed under a controllable load) oscillates on it with given amplitude. The friction coefficient between the probe and the tested surface is continuously monitored. Tests can be carried out in dry-lubrication or in low-lubrication regime and can be stopped after a given time or if the friction coefficient exceeds a certain limit. The tests were performed with a starting load of 50 N that was increased to 200 N after 50 s, with oscillation amplitude of 4 mm and a probe ball of 6 mm diameter. Averaged test results are depicted in Fig. 10.

Analyzing the friction curves, one sees that both structured and unstructured DLC-coated surfaces showed similar friction coefficients in the beginning phase (50 N). Furthermore, the measured friction coefficient (0.13, rather high value for steel on DLC) may suggest some problems in the film deposition. After increasing the applied load, friction coefficient increases were evidenced for both patterned and unpatterned surfaces. This can be associated with damages produced to the DLC film (delamination), leading to additional hard debris particles with an abrasive effect. In the case of the unstructured surface, the friction coefficient showed significant instabilities and the tribological breakdown occurred. On the other hand, the structured DLC coated surfaces were not destabilized: the pores trapped the debris (the decay of the small peak in Fig. 10), and the tribological system functioning remained functional.

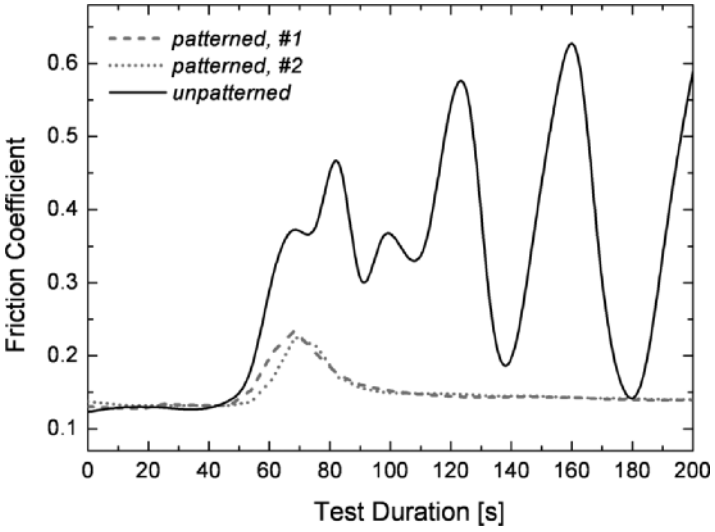

Fig. 10 Results of tribological tests performed on patterned and unpatterned DLC-coated steel substrates

6 Conclusions

The advantages of laser tribology and the mature and, nowadays, very effective DLC-deposition techniques can be combined to obtained low wear surfaces. Under these circumstances, the relation between the sizes of the needed tribological structures and DLC film thicknesses becomes central and determines the choice of the processing method: such patterned surfaces can be obtained either by the laser processing of already coated parts (direct processing) or by the coating of already laser-patterned substrates (indirect processing).

These approaches have different technological requirements and may involve different laser sources. The highest priority in the direct processing is a gentle laser machining, without any film damages, whereas indirect processing is optimized for a fast material removal by smallest collateral heat affected zones.

Through direct processing of tribological DLC films both topography modifications (evaporation, material removal) and material structure changes (sp^3/sp^2 bonds, graphitization) can be obtained; UV lasers with ns pulses and ultrashort pulse lasers can be utilized. The indirect processing yields only film shape changes and it can be effectively carried out with Q-switched solid-state lasers (IR or frequency converted). Some tribological tests have already demonstrated the potential of the laser surface engineered DLC tribological films.

References

1. Kupka R. K., Bouamrane F., Cremers C., Megtert S.: Microfabrication: LIGA-X and applications, Appl. Surf. Sci. 164 (2000) 97–110.
2. Frost F., Rauschenbach B.: Nanostructuring of solid surfaces by ion-beam, Appl. Phys. A 77 (2003) 1–9.
3. Evans C. J., Bryan J. B.: Structured, textured or engineered surfaces, Ann. CIRP 48/2 (1999) 541–556.
4. Narayan R. J., Jin C., Doraiswamy A., Mihailescu I. N., Jelinek M., Ovsianikov B., Chichkov B., Chrisey D. B.: Laser processing of advanced bioceramics, Adv. Eng. Mater. 7 (2005) 1083–1098.
5. Yoshino M., Matsumura T., Umeharac U., Akagamid Y., Aravindan S., Ohno T.: Engineering surface and development of a new DNA micro array chip, Wear 260 (2006) 274–286.
6. Masuzawa T.: State of the art of micromachining, Ann. CIRP 49/2 (2000) 473–488.
7. Erdemir A., Donnet C.: Tribology of diamond-like carbon films: recent progresses and future prospects, J. Phys. D: Appl. Phys. 39 (2006) R311-R327.
8. Grill A.: Diamond-like carbon coatings as biocompatible materials: an overview, Diamond Relat. Mater. 12 (2003) 166–170.
9. Hauert R., Müller U.: An overview on tailored tribological and biological behavior of diamond-like carbon, Diamond Relat. Mater. 12 (2003) 171–177.
10. Robertson J.: Diamond-like amorphous carbon, Mater. Sci. Eng. R 37 (2002) 129–281.
11. Ferrari A. C., Robertson J.: Interpretation of Raman spectra of disordered and amorphous carbon, Phys. Rev. B 61 (2000) 14095–14107.
12. Grill A.: Electrical and optical properties of diamond-like carbon, Thin Solid Films 355–356 (1999) 189–193.

13. Seth J., Babu S. V., Ralchenko V. G., Kononenko T. V., Ageev V. P., Strelnitsky V. E.: Lithographic application of diamond-like carbon films, Thin Solid Films 254 (1995) 92–95.
14. Lee E. H., Hembree D. M., Rao G. R., Mansur L. K.: Raman scattering from ion-implanted diamond, graphite, and polymers, Phys. Rev. B 48 (1993) 15540–15551.
15. Narayan R. J.: Laser processing of diamond-like carbon–metal composites, Appl. Surf. Sci. 245 (2005) 420–430.
16. Erdemir A., Eryilmaz O. L., Fenske G.: Synthesis of diamondlike carbon films with superlow friction and wear properties, J. Vac. Sci. Technol. A 18 (2000) 1987–1992.
17. Kohira H., Prabhakaran V., Talke F.E.: Effect of air bearing design on wear of diamond-like carbon coated proximity recording sliders, Tribol. Inter. 33 (2000) 315–321.
18. Gao F., Erdemir A., Tysoe W. T.: The tribological properties of low-friction hydrogenated diamond-like carbon measured in ultrahigh vacuum, Tribol. Lett. 20 (2005) 221–227.
19. Lettington A. H.: Applications of diamond-like carbon thin films, Carbon 36 (1998) 555–560.
20. Kimock F. M., Knapp B. J.: Commercial applications of ion beam deposited diamond-like carbon (DLC) coatings, Surf. Coat. Technol. 56 (1993) 273–279.
21. Akita N., Konishi Y., Ogura S., Imamura M., Hu Y. H., Shi X.: Comparison of deposition methods for ultra thin DLC overcoat film for MR head, Diamond Relat. Mater. 10 (2001) 1017–1023.
22. Van Rompay P. A., Nantel M., Pronko P. P.: Carbon ion charge states and energy distributions for DLC ablation plumes from 100-fs 780 nm laser pulses, Surf. Coat. Technol. 100–101 (1998) 496–499.
23. Garrelie F., Loir A. S., Donnet C., Rogemond F., Le Harzic R., Belin M., Audouard E., Laporte P.: Femtosecond pulsed laser deposition of diamond-like carbon thin films for tribological applications, Surf. Coat. Technol. 163–164 (2003) 306–312.
24. Loir A. S., Garrelie F., Donnet C., Belin M., Forest B., Rogemond F., Laporte P.: Deposition of tetrahedral diamond-like carbon thin films by femtosecond laser ablation for applications of hip joints, Thin Solid Films 453–454 (2004) 531–536.
25. Jung H. S., Park H. H., Pang S. S., Lee S. Y.: The investigation of thermal effect on the properties of pulsed laser deposited diamond-like carbon films, Thin Solid Films 332 (1998) 103–108.
26. Witke T., Schuelke T., Berthold J., Meyer C. F., Schultrich B.: Deposition of hard amorphous carbon coatings by laser and arc methods, Surf. Coat.Technol. 116–119 (1999) 609–613.
27. Ossi P. M., Bottani C. E., Miotello A.: Pulsed laser deposition of nano-glassy carbon films, Appl. Surf. Sci. 248 (2005) 334–339.
28. Etsion I.: State of the art in laser surface texturing, J. Tribol. 127 (2005) 248–253.
29. Bech J., Bay N., Eriksen M.: Entrapment and escape of liquid lubricant in metal forming, Wear 232 (1999) 134–139.
30. Dumitru G., Romano V., Gerbig Y., Weber H. P., Haefke H.: Femtosecond laser processing of nitride-based thin films to improve their tribological performance, Appl. Phys. A 80 (2005) 283–287.
31. Erdemir A.: Review of engineered tribological interfaces for improved boundary lubrication, Tribol. Int. 38 (2005) 249–256.
32. Danyi R., Szörényi T.: KrF excimer laser processing of thick diamond-like carbon films, Appl. Phys. A 79 (2004) 1373–1376.
33. Prawer S., Kalish R., Adel M., Richter V.: Ion beam induced conductivity and structural changes in diamondlike carbon coatings, Appl. Phys. Lett. 49 (1986) 1157–1159.
34. Nistor L. C., Landuyt J., Ralchenko V. G., Kononenko T. V., Obraztsova E. D., Strelnitsky V. E.: Direct observation of laser-induced crystallization of a-C:H films, Appl. Phys. A 58 (1994) 137–144.
35. Ralchenko V. G., Kononenko T. V., Foursova T., Loubnin E. N., Strelnitsky V. E., Seth J., Babu S. V.: Comparison of laser and O_2 plasma etching of diamond-like carbon films, Diamond Relat. Mater. 2 (1993) 211–217.

36. Vouagner D., Beleznai C., Girardeau-Montaut J. P., Templir C., Gonnord H.: A new method to determine laser damage threshold for thin diamond-like carbon films on silicon, Diamond Relat. Mater. 9 (2000) 786–791.
37. Güdde J., Hohlfeld J. Müller J. G., Matthias E.: Damage threshold dependence on electron-phonon coupling in Au and Ni films, Appl. Surf. Sci. 127–129 (1998) 40–45.
38. Dong Y., Molian P.: Femtosecond pulsed laser ablation of 3CSiC thin film on silicon, Appl. Phys. A 77 (2003) 839–846.
39. Bonse J., Rudolph P., Krüger J., Baudach S., Kautek W.: Femtosecond pulse laser processing of TiN on silicon, Appl. Surf. Sci. 154–155 (2000) 659–663.
40. Kononenko T. V., Pimenov S. M. Kononenko V. V., Zavedeev E. V., Konov V. I., Dumitru G., Romano, V.: Laser-induced spallation in diamond-like carbon films, Appl. Phys. A 79 (2004) 543–549.
41. Kononenko T. V., Kononenko V. V., Pimenov S. M., Zavedeev E. V., Konov V. I., Romano V., Dumitru G.: Effects of pulse duration in laser processing of diamond-like carbon films, Diamond Rel. Mater. 14 (2005) 1368–1376.
42. Fu Y. Q., Luo J. K., Flewitt A. J., Ong S. E., Zhang S., Milne W. I.: Laser micromachining of sputtered DLC films, Appl. Surf. Sci. 252 (2006) 4914–4918.
43. Malshe A. P., Ogale S. B., Kshirsagar S. T., Chari K. S.: Excimer laser-induced etching of non-hydrogenated (a-C) and hydrogenated (a-C:H) diamond-like carbon films: a comparative study, Mater. Lett. 11 (1991) 175–179.
44. Nakamiya T., Aoqui S., Ebihara K.: Experimental and numerical study on pulsed-laser annealing process of diamond-like carbon thin films, Diamond Relat. Mater. 10 (2001) 905–909
45. Preuss S., Stuke M.: Subpicosecond ultraviolet laser ablation of diamond: Nonlinear properties at 248 nm and time-resolved characterization of ablation dynamics, Appl. Phys. Lett. 67 (1995) 338–340.
46. Jeschke H. O., Garcia M. E., Bennemann K. H.: Theory for laser-induced ultrafast phase transitions in carbon, Appl. Phys. A 69 (1999) S49–S53.
47. Wang C. Z., Ho K. M., Shirk M. D., Molian P. A.: Laser-Induced Graphitization on a Diamond (111) Surface, Phys. Rev.Lett. 85 (2000) 4092–4095.
48. Bäuerle D.: Laser processing and chemistry (Springer, Berlin 2000).
49. Shirk M. D., Molian P. A.: Ultra-short pulsed laser ablation of highly oriented pyrolytic graphite, Carbon 39 (2001) 1183–1193.
50. Dumitru G., Romano V., Weber H. P., Pimenov S., Kononenko T., Sentis M., Hermann J., Bruneau S.: Femtosecond laser ablation of diamond-like carbon films, Appl. Surf. Sci. 222 (2004) 226–233.
51. Miyazaki K., Maekawa N., Kobayashi W., Kaku M., Yasumaru N., Kiuchi J.: Reflectivity in femtosecond-laser-induced structural changes of diamond-like carbon film, Appl. Phys. A 80 (2005) 17–21.
52. Yasumaru N., Miyazaki K., Kiuchi J.: Femtosecond-laser-induced nanostructure formed on hard thin films of TiN and DLC, Appl. Phys. A 76 (2003) 983–985.
53. Yasumaru N., Miyazaki K., Kiuch J.: Glassy carbon layer formed in diamond-like carbon films with femtosecond laser pulses, Appl. Phys. A 79 (2004) 425–427.
54. McGulloch D. G., Prawer S., Hoffman A.: Structural investigation of xenon-ion-beam-irradiated glassy carbon, Phys. Rev. B 50 (1994) 5905–5917.
55. Prawer S., Nugent K. W., Lifshitz Y., Lempert G. D., Grossman E., Kulik J., Avigal I., Kalish R.: Systematic variation of the Raman spectra of DLC films as a function of sp^2:sp^3 composition, Diamond Relat. Mater. 5 (1996) 433–438.
56. Chichkov B. N., Momma C., Nolte S., von Alvensleben F., Tünnermann A.: Femtosecond, picosecond and nanosecond laser ablation of solids, Appl Phys A 63 (1996) 109–115.
57. Von Allmen M.: Laser-beam interactions with materials (Springer, Berlin 1987).
58. Dumitru G., Romano V., Weber H. P., Haefke H., Gerbig Y., Pflüger, E.: Laser microstructuring of steel surfaces for tribological applications, Appl. Phys. A 70 (2000) 485–487.
59. Dumitru G., Romano V., Weber H. P., Pimenov S., Kononenko T., Hermann J., Bruneau S., Gerbig Y., Shupegin M.: Laser treatment of tribological DLC films, Diamond Rel. Mater. 12 (2003) 1034–1040.

60. Heyl P., Olschewski T., Wijnaendts R.: Manufacturing of 3D structures for micro-tools using laser ablation, Microelectr. Eng. 57 (2001) 775–80.
61. Dumitru G., Lüscher B., Krack, M., Bruneau S., Hermann J., Gerbig, Y.: Laser processing of hardmetals: Physical basics and applications, Int. J. Refract. Met. Hard Mater. 23 (2005) 278–286.
62. Li T., Lou Q., Dong J., Wie Y., Liu J.: Phase transformation during surface ablation of cobalt-cemented tungsten carbide with pulsed UV laser, Appl Phys A 73 (2001) 391–396.
63. Podgornik B., Hren D., Vizintin J.: Low-friction behaviour of boundary-lubricated diamond-like carbon coatings containing tungsten, Thin Solid Films 476 (2005) 92–100.
64. Voevodin A. A., Bultman J., Zabinski J. S.: Investigation into three-dimensional laser processing of tribological coatings, Surf. Coat. Technol. 107 (1998) 12–19.

New Trends in Boundary Lubrication of DLC Coatings

M. I. De Barros Bouchet* and J. M. Martin

Abstract Fuel economy and reduction of harmful elements in lubricants are becoming important issues in the automotive industry. An approach to respond to these requirements is the potential use of low friction coatings in engine components exposed to boundary lubrication conditions. Diamond-like carbon (DLC) coatings present a wide range of tribological behavior, including friction coefficients in ultrahigh vacuum below 0.02. The engine oil environment which provides similar favorable air-free conditions might lead to such low friction levels.

In this work, the friction and wear properties of DLC coatings in boundary lubrication conditions have been investigated as a function of the hydrogen content in the carbon coating. First, their interactions with usual additives like zinc dialkyldithiophosphates (ZDDP) which is the exclusive antiwear agent in most automotive lubrication blends and friction-modifier additive molybdenum dithiocarbamate (MoDTC) have been studied. Other kinds of friction-modifier additives were examined including amine, amide, and ester, when blended to a poly-alpha-olefin (PAO)-based oil. We found that the best tribological performance is obtained for tetrahedral hydrogen-free DLC (ta-C) in the presence of environment friendly additive Glycerol Mono-Oleate (GMO), which we focus on here.

Keywords boundary lubrication, DLC Coatings, OH-containing lubricants, tribochemistry

1 Introduction

In the new millennium, the long-term impact of lubricants and additive components will become design and marketing issues based on such concerns as the environment, toxicity, and fuel economy. Development of lubricant additives directly from renewable natural materials and new mechanical components for combustion engine

Ecole Centrale de Lyon, UMR CNRS 55 13, 69134 Ecully, France

*Corresponding author, e-mail: maria-isabel.de-barros@ec-lyon.fr, Fax: 00 33 (0)4 78 43 33 83.

C. Donnet and A. Erdemir (eds.), *Tribology of Diamond-Like Carbon Films: Fundamentals and Applications*.

(light-weight body structures, direct-injection systems for gasoline engines) [1–3] will play a far more important role than in the past for improving fuel economy and environment protection. However, the replacement of antiwear additives such as zinc dialkyldithiophosphates (ZDDP) will present a challenge in terms of being found in nature and the development of mechanical components has several disadvantages such as its high cost and design limitations.

Another approach to respond to these economical and environmental requirements is the potential use of low friction and wear resistant coatings in mechanical components submitted to boundary lubrication conditions. DLC coatings which have been extensively studied as surface films to protect hard brittle materials from cracking [4] and ductile metal surfaces from adhesion [5] may fulfill this role. Depending on their properties which are in turn dependent on the deposition procedure, these coatings present a wide range of tribological behaviors, including superlow friction coefficients (below 0.02) in ultrahigh vacuum [6–8]. Under boundary lubrication, the engine oil environment which provides similar favorable air-free conditions may lead to such low friction levels.

In this chapter, we present the new trends in the boundary lubrication of DLC coatings. First, we are especially interested in the issue such as the coupling of usual engine oil additives with DLC materials, without compromising long-term engine durability by the formation of unacceptable wear debris. In this way, we tested both low-cost multifunctional additive ZDDP, used for over 50 years in the lubricant industry in engine oils, and friction modifier molybdenum dithiocarbamate (MoDTC) later introduced into automotive crankcase lubricants to improve the fuel efficiency.

Another issue receiving increased attention is the release of sulfur and phosphorous from the engine oil additives in order to preserve the catalyst's function. As it is to promote more complete combustion of the fuel, anything that upsets the efficiency of the catalyst is likely to cause environmental deterioration and limit energy efficiency. In this new area which is certain to become a major issue in the future, biodegradable organic compounds were investigated.

2 Methods

2.1 DLC Materials Preparation

Different kinds of DLC materials were deposited on polished AISI 52100 steel substrates, including hydrogenated DLC (a-C:H), titanium-containing hydrogenated DLC (Ti-C:H), and hydrogen-free DLC (ta-C) coatings. The surface roughness of polished AISI 52100 steel substrates before deposition was about 10 nm in Ra. Hydrogenated DLC (a-C:H_1) and Ti-C:H were prepared by hybrid technique of magnetron sputtering and d.c. plasma-assisted chemical vapor deposition (PACVD) performed in the same reactor. Substrates were cleaned by a bias etching at −200 V for 10 min prior to film deposition. The substrate temperature during the deposition

Table 1 Composition and properties of the different DLC films

Coating	Thickness (μm)	Surface roughness (Ra) (nm)	Hardness (GPa)	Young modulus (GPa)	Hydrogen content (at. %)	Ti content (at. %)
a-C:H_1	3	20–40	≈16	≈150	≈50	0
Ti-C:H	3	20–40	≈10	≈80	≈35	Ti ≈ 2
ta-C	0.7	20–40	≈65	≈650	<1	0
a-C:H_2	1	20–40	≈15	≈140	≈20	0

process was maintained lower than 200°C. The tetrahedral hydrogen-free DLC coating (so-called ta-C) was applied to the polished carburized steel substrate from a graphite target by arc-ion plating, a physical vapor deposition (PVD) process, and it did not contain hydrogen [9]. Another kind of hydrogenated DLC coating (a-C:H_2) containing less hydrogen was applied by a PACVD process from hydrocarbon gas. The thicknesses of the different DLC-based films are reported in Table 1 with other characteristics like surface roughness and mechanical properties. All kinds of coatings display a surface roughness varying in the 20–40 nm range. The coatings a-C:H_1 and Ti-C:H were respectively characterized by Forward Recoil Elastic Scattering (FRES) and Rutherford Back-Scattering Spectroscopy (RBS) to determine their composition. For the coating a-C:H_2, the hydrogen content was estimated by SIMS analysis and compared with a hydrogen content from a well-known standard sample [9]. The film thicknesses were measured by cross-sectional micrographs. The mechanical properties were determined by nanoindentation.

2.2 Lubricants

Lubricants comprise a base fluid and additives. The base fluid was a mixture of synthetic poly-alpha-olefin (PAO) 4 and 6. In the case of the interactions study between usual additives and DLC materials, ZDDP was added to the base fluid to enhance its oxidation resistance and to impart antiwear performance. The ZDDP is a C3/C6 secondary zinc di-alkyl dithiophosphate. MoDTC was also added to the base fluid to reduce the friction and make smooth transition from static to dynamic conditions. The MoDTC is mainly composed of di-sulfide-bis [oxo(dialkyldithiocarbamate)] molybdenum. It contains impurities consisting of 10% atomic thiuram disulfide. The alkyl chains are C8 (2-ethylhexyl) and C13. The S/Mo ratio (weight %) is equal to 1.3. The two additives were obtained from Asahi Denka Kogyo (Japan). The tribological properties of coatings under base fluid lubrication were first investigated and then additivated MoDTC and ZDDP + MoDTC lubricants were studied. Previous works [10] have shown that an equi-molar concentration of ZDDP and MoDTC in base fluid yields optimum friction-reduction results. Therefore, the lubricant concentration of MoDTC and ZDDP was adjusted to that value which corresponds to 700 ppm of zinc and 200 ppm of molybdenum in base oil.

For the organic additives, friction-modifier additive Glycerol Mono-Oleate (GMO) was added to PAO-base oil at about 1% by weight. Pure glycerol (from Merck) was also studied as a lubricant for DLC materials.

2.3 Tribological Tests

A Cameron–Plint friction machine with a reciprocating cylinder-on-flat configuration shown in the Fig. 1 was used to generate a relatively large area of tribofilms in mild/severe tribological conditions. The DLC coatings were systematically deposited on the plane counterface. The films were also deposited on the AISI 52100 steel cylinder counterface to check whether or not the tribological behavior depends on the lubricant interaction with coatings, in comparison with the deposition on the plane only. The diameter and length of the steel cylinders were 6 and 5 mm, respectively. The DLC-coated steel flat was immersed in the lubricant solution. The friction tests were performed at 363 K (100°C) with a sliding speed of 0.2 m s^{-1} under a normal load of 350 N (maximum initial contact pressure 0.6 GPa) and for 1 h duration. The normal load was increased progressively up to 50 N and maintained to this value during 5 min for a run-in period. Then, the load was increased to 350 N. The solid tribochemical film (tribofilm) formed during the tests covers a rectangular area of $5 \times 8\,mm^2$. After the tribological experiments, the worn surfaces were examined by optical microscopy. The final worn volumes of the flat and the cylinder were evaluated from cross-sectional images of the wear tracks, and from the width of the wear scars, respectively.

The pin-on-disc sliding tests were conducted in the following manner. The pins, measuring 5 mm in diameter and 5 mm in length, were made of hardened bearing steel (AISI 52100) and polished to a surface roughness of Ra 0.05 µ. The disc measured 35 mm in diameter and 2.5 mm in thickness and was made of carburized steel. The three pins were secured to prevent them from rotating and were pressed against

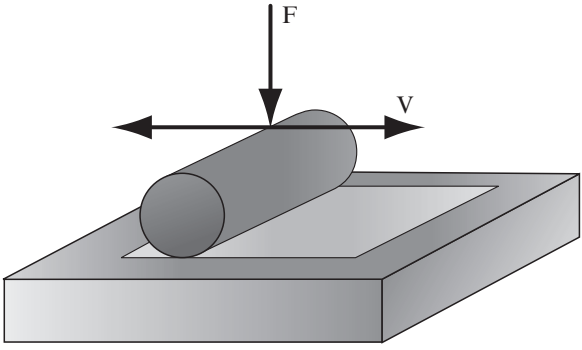

Fig. 1 Cameron–Plint tribometer with a reciprocating cylinder-on-flat configuration

the toric sliding surface of the rotating disc at a position that was 20 mm in diameter from the center of the disc. Contact at the sliding interfaces was in the shape of lines under high Hertzian pressure of 700 MPa due to a normal force of 500 N, as shown in Fig. 2. Lubrication was provided by an oil bath heated to 353 K. The sliding speed was varied in a range of 0–1 m s^{-1} for the tribological experiments and the sliding time was 60 min.

The SRV sliding tests were performed with a reciprocating needle-pin-on-flat-disc tribometer that was lubricated before the test by wetting it with several droplets (5 cc) of the test oil heated to 353 K. The pins, measuring 18 mm in diameter and 22 mm in length, were made of hardened steel and polished to a surface roughness of Ra 0.05 μ. The disc measured 24 mm in diameter and 7.9 mm in thickness and was made of carburized steel. The reciprocating pins were pressed against the stationary disc by a force of 400 N that generated 270 MPa of pressure as shown in Fig. 3. The length of the track was 3.0 mm and the reciprocating time was 15 min at 50 Hz.

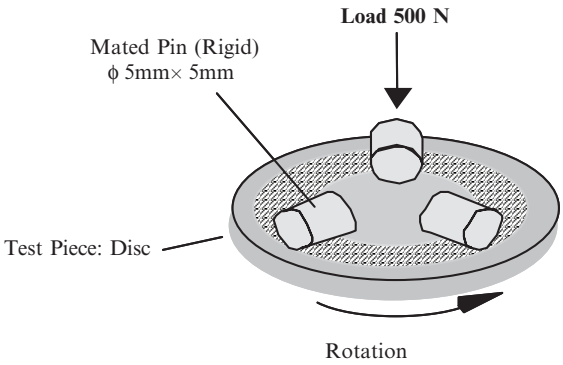

Fig. 2 Pin-on-disc test rig

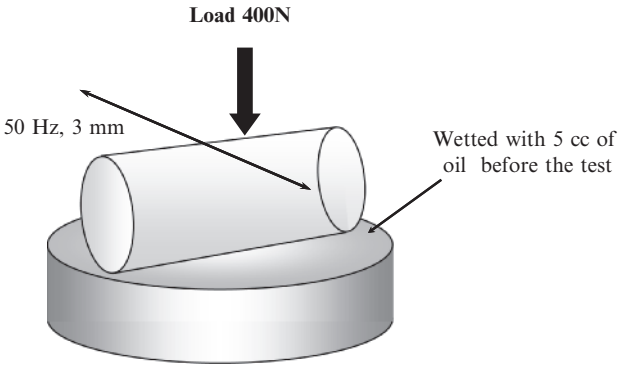

Fig. 3 SRV sliding test rig

For each kind of tribometer, the friction experiment was repeated a few times under the same conditions in order to check the reproducibility of the measurements. At the end of the tests, the flat samples were washed in n-heptane to eliminate all the residual oil, gel-like species and contaminants and permit accurate surface analyses.

2.4 Engine Tests

The valvetrain system is a significant source of mechanical friction loss in an automobile engine, especially at low speeds where fuel economy is most important. Friction at the sliding interfaces between the cam and follower (Fig. 4) accounts for about 80% of all valvetrain system friction and 20% of the total engine friction. Therefore, the DLC coating for obtaining a superlow friction level was first applied to the engine cam and follower lubricated with standard 5 W-30 engine oil. A cam and follower pair was tested, with the test cam made of chilled cast iron fitted to a shaft driven by a variable speed DC motor while the follower was pressed against the cam by a load spring, as shown in Fig. 5 which presents the single cam and follower test rig. Friction torque was measured with a torque sensor.

2.5 Mechanical Measurements

Several tests of indentation have been made on the DLC coatings in order to measure their mechanical properties (hardness and Young's modulus). Experiments were performed using a nanoindenter with a Berkovich indenter (three-sided pyramid, angle between arête: 115°12). Thus, the imposed deformation is about 7%. The system has load and displacement amplitudes of 500 mN and 100 µm respectively

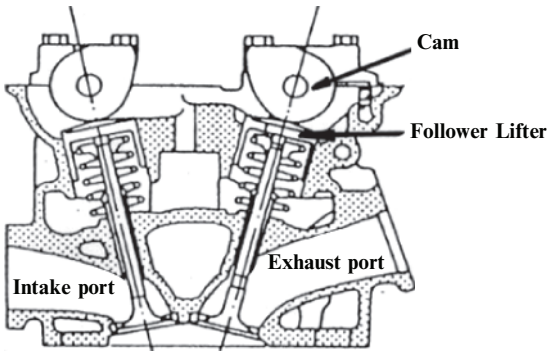

Fig. 4 Valvetrain system

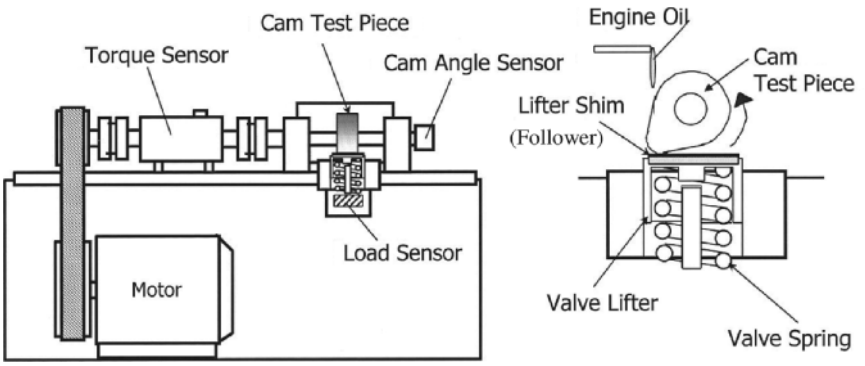

Fig. 5 Single cam and follower test rig

and load and displacement resolution of 10 mN and 0.5 nm respectively. Continuous stiffness measurement is used: this means that a small oscillation is superimposed to the large-scale DC loading. The excitation amplitude is continuously adjusted such that the corresponding displacement amplitude remains constant at 3 nm. The displacement and force amplitudes, as well as the phase angle between the two, are monitored using a lock-in amplifier (frequency specific amplification). By observing the resultant displacement amplitude and the phase shift between the force and the displacement, we can thus infer that the stiffness S at all displacements can be measured. Thus, the elastic modulus and the hardness as a continuous function of indenter displacement can be obtained. The frequency of the sinusoidal motion ranges from 5.10–3 to 60 Hz. In the experiments reported in this paper, a 32 Hz frequency is used.

2.6 Surface Analyses Techniques

Different surface analytical tools are coupled to obtain complementary information on the nature of the studied DLC coatings and on the chemical species of the tribofilms formed during the friction on the DLC surface.

XANES spectra at the C K-edge were recorded in order to characterize the DLC materials. Details on physical aspects of XANES spectroscopy can be found elsewhere [11]. X-ray absorption spectra were obtained at CSRF (Canadian Synchrotron Radiation Facility) using the 1 GeV Aladdin storage ring, University of Wisconsin, Madison, USA. The Grasshopper soft x-ray beamline which covers the photon region of 40–1000 eV was used to record the C K-edge spectra with an energy resolution of 0.1 eV and an analyzed area of $5 \times 1\,mm^2$. The assignment of the fine structure in XANES spectra was obtained by using the spectra of model compounds. The maximum sampling depth probed by XANES at C K-edge is about 10 nm. XANES measurement did not induce any significant irradiation

damage to the specimen, and other analysis can be carried out on the same surface with good confidence.

X-ray Photoelectron Spectroscopy (XPS) and Auger Electron Spectroscopy (AES) data were obtained using a VG 220I apparatus. AES spectra were recorded with the $0.5 \times 0.5\,\mu m^2$-focused electron beam which permits a high spatial resolution. Special attention has been paid to the Auger C KLL line to obtain information on the structure of the DLC coating with a good signal/noise ratio. Interestingly, the thickness probed in AES is about 5 nm,with the exponential decay leading to an extreme surface information. XPS was also performed with a nonmonochromatized AlKα x-ray source. The size of the analyzed area was set at 500 µm so that spatially resolved analysis can be achieved inside the tribofilm on the flat specimen. XPS is also a very surface-sensitive technique probing from monolayer to a few nanometers (5 nm). Before etching, such a surface is generally contaminated with carbon and possibly oxygen but this does not hinder the detection of the additive elements. Argon etching (Ar^+, 5 keV) was not performed because of possible irradiation damage to species before XPS analysis. Then the thickness of the tribofilms formed during the friction tests has not been accurately estimated.

Time-of-Flight Secondary Ion Mass Spectroscopy (ToF-SIMS) experiments were performed with a ToF-SIMS V apparatus from ION-TOF. For static SIMS analysis (SSIMS), Au + pulsed ion beam of 25 keV energy was used for scanning an area of $100 \times 100\,\mu m^2$ on the surface. The diameter of the spot was smaller than 1 µm in order to obtain average information. In SSIMS, chemical information is coming from a depth of 0.1–1 nm below the surface. This is much more near-surface information than the ones obtained with XANES and AES techniques. For dynamic SIMS (DSIMS), depth profiles were obtained combining depth profiling with secondary ion analysis. Sputter erosion was achieved using O_2^+ ions low energy beam of 0.5 keV. Analysis of the crater center was performed using Ga^+ ions high energy beam of 15 keV.

2.7 Microstructural Analysis Technique

Direct determination and imaging of physical properties of DLC coatings were obtained using energy filtering transmission electron microscopy (EFTEM) combined with valence electron energy-loss spectroscopy (VEELS). This was carried out on a cross-section TEM specimen of a thin DLC film deposited on steel substrate produced by focused ion beam (FIB) processing. The microscope is a Leo 912 fitted with a built-in Omega filter which is linked to an image analysis system. The microscope is fitted with a LaB_6 cathode and was operating at an accelerating voltage of 120 kV. EFTEM has been used to map the sp^3 and sp^2 phase composition based on plasmon ratio images.

In addition, elementary composition of the wear particles formed during the friction tests which are related to the tribofilm composition can also be obtained. Then at the end of the tests, some wear particles were picked up with care from the

flat samples. They were rinsed in the n-heptane and deposited on a copper grid, covered by a very thin carbon film, approximately 5 nm thick, for the TEM observations. The wear particles were observed in an analytical Transmission Electron Microscope (PHILIPS 420EM) equipped with Electron Energy Loss Spectroscopy (PEELS GATAN 666).

3 Results and Discussion

3.1 Coupling of DLC Materials with Usual ZDDP and MoDTC Additives

We evaluated the friction properties under boundary lubrication conditions with usual additives for DLC-coating materials, including: hydrogenated DLC (a-C:H_1), Ti-C:H, and ta-C.

3.1.1 Steel/DLC Tribological System

Figure 6a shows the steady-state friction coefficients of the DLC/steel couples under different lubricated conditions obtained with the Cameron–Plint tribometer. With PAO alone, all the DLC coatings exhibit a similar low steady-state friction coefficient lying in the 0.08–0.1 range. The friction tests performed with MoDTC and ZDDP additivated base oil show lower friction coefficients ranging between 0.05 and 0.06 for hydrogenated DLC coatings (a-C:H_1 and Ti-C:H), a highest value, 0.08, is obtained with the hydrogen-free DLC ta-C. This coating causes also the higher wear of the steel counterface as shown by the Fig. 6b which reports the final wear rates measured in the steel cylinders.

No significant wear is observed on the flat. It should be noted that similar wear rates are obtained under PAO and additivated PAO-lubricated conditions for all

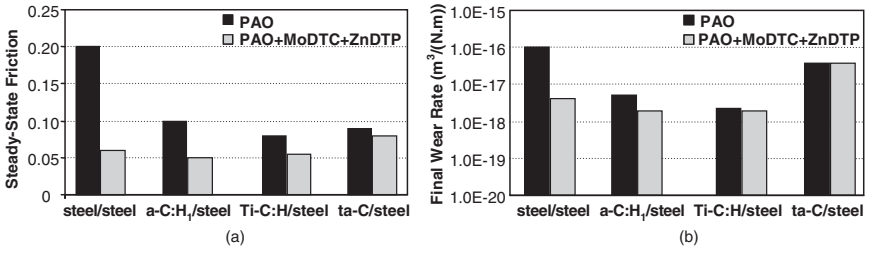

Fig. 6 Tribological performances of the DLC-coated flat/steel cylinder couples tested under different lubricated conditions: a) steady-state friction coefficient; and b) final wear rate of the steel cylinder. Steel/steel couple is reported for the comparison

DLC coatings. To conclude for the steel/DLC tribological system, the lubrication by usual additives of hydrogenated DLC coatings (a-C:H_1 and Ti-C:H) does not provide significant improvement of friction and wear in comparison with steel/steel couple in the same conditions.

3.1.2 DLC/DLC Tribological System

Tests with the films deposited on both the plane and the cylinder were also performed for the hydrogenated DLC coatings. In this configuration, the lubrication with MoDTC-additivated fluid base was also investigated. As shown in Fig. 7a, the additional coating deposition on the cylinder slightly decreases the steady-state friction level, in comparison with the coating deposited only on the plane. Figures 8a and 8b show details of the evolution of the average friction coefficients in the different lubricated conditions, versus the sliding distance, and for the a-C:H_1 and Ti-C:H coatings respectively. First of all, we observe that the influence of additives appears much more significant on the friction behavior of the highly hydrogenated coating a-C:H_1. However, the friction level during the running-in period stays higher for the a-C:H_1 coating, say in the 0.08–0.2 range, than for the Ti-C:H coating, in the 0.05–0.08 range, and this whatever the lubrication conditions may be. As shown in Figs. 8a and 8b, the friction-modifier additive MoDTC provides the better running-in effect, whatever be the coating. No significant production of wear debris was observed from the wear tracks of both the plane and the cylinder after the friction tests with MoDTC and ZDDP additivated lubricant, contrary to the case of PAO which led to scratches formation on the plane and severe wear on the cylinder. For the MoDTC-additivated lubricant, the Ti-C:H coating do not present significant wear in comparison to the a-C:H_1 coating which displays some scratches. The final wear rates measured in the DLC-coated cylinders are presented on Fig. 7b.

As shown in Figs. 6b and 7b, the additional deposition of the coating on the cylinder improves significantly the antiwear behavior of the tribological system coatings under MoDTC and ZDDP additivated lubrication, in comparison with the film deposited only on the plane.

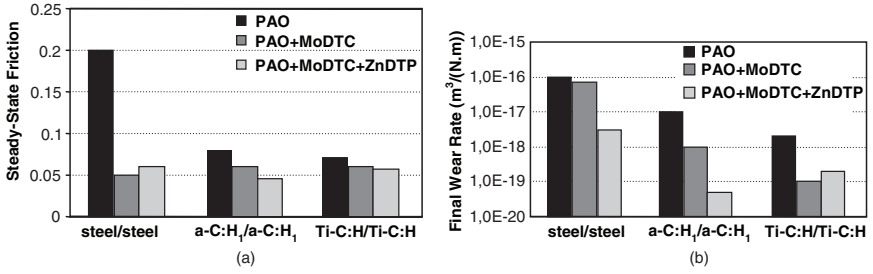

Fig. 7 Tribological performances of the DLC/DLC couples tested under different lubricated conditions: (a) steady-state friction coefficient; and (b) final wear rate of the DLC-coated steel cylinder. Steel/steel couple is reported for the comparison

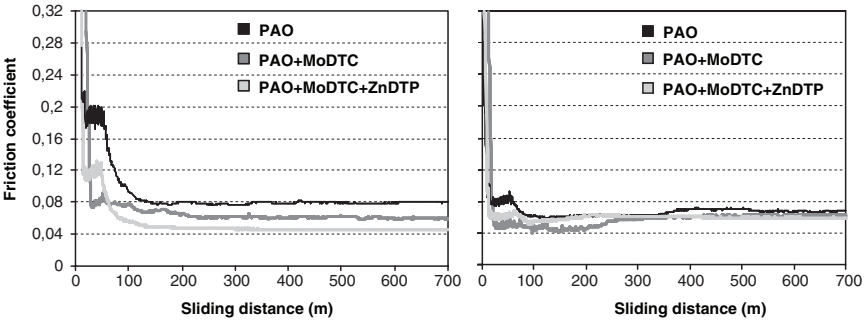

Fig. 8 Evolution of the friction coefficient versus sliding distance under different lubricated conditions: (a) a-C:H_1/a-C:H_1 couple; and (b) Ti-C:H/Ti-C:H couple

3.1.3 XPS Analyses and TEM Observations

Steel/DLC System

After friction experiments, TEM/EELS observations and XPS surface analyses were performed on the surface of the complete set of films to elucidate the origin of the friction improvement by hydrogenated DLC coatings (a-C:H_1 and Ti-C:H) under MoDTC + ZDDP lubrication, in comparison with the hydrogen-free DLC coating (ta-C). The advantage of XPS is to provide semiquantitative elementary analysis, which permits to calculate the stoichiometry of the tribofilm compounds. XPS analyses were also carried out outside the tribofilms to clarify the material change occurring under the friction process. Table 2 shows the elemental composition of the MoDTC + ZDDP tribofilms (wear track) formed on the hydrogenated DLC (a-C:H_1) and hydrogen-free DLC (ta-C)-coatings surfaces after the friction tests against steel counterfaces. First of all, it can be noticed that zinc, molybdenum, and sulfur elements derived from MoDTC and ZDDP additives were detected on both DLC surfaces but in low proportion, typically a few atomic percent. No iron is found in both tribofilms indicating that the DLC films were not delaminated during the test and that no major wear debris was transferred from the pin. As shown in Table 2, both tribofilms are strongly depleted in phosphorous when compared with the initial ZDDP molecule which presents a P/Zn ratio of 2. The Zn2p XPS spectra obtained from these two surfaces look broader than those of the standard compounds ZnO, ZnS, and $ZnSO_4$, and then it is difficult to correctly assign the zinc to chemical speciation. The S2p photopeaks show only one contribution at 162 eV indicating that sulfur is essentially involved in metal sulfide (molybdenum sulfide and/or zinc sulfide). From the study of Mo3d photopeaks, molybdenum sulfide might be present in the whole tribofilms. The decomposition of Mo3d photopeaks in spectra from the top surfaces analysis was compared with pure MoS_2 (229.7 eV) and MoO_3 (232.7 eV) in Fig. 9. As reported in Table 2, the MoS_2/MoO_3 ratio for the hydrogenated DLC is greater than the one obtained for the

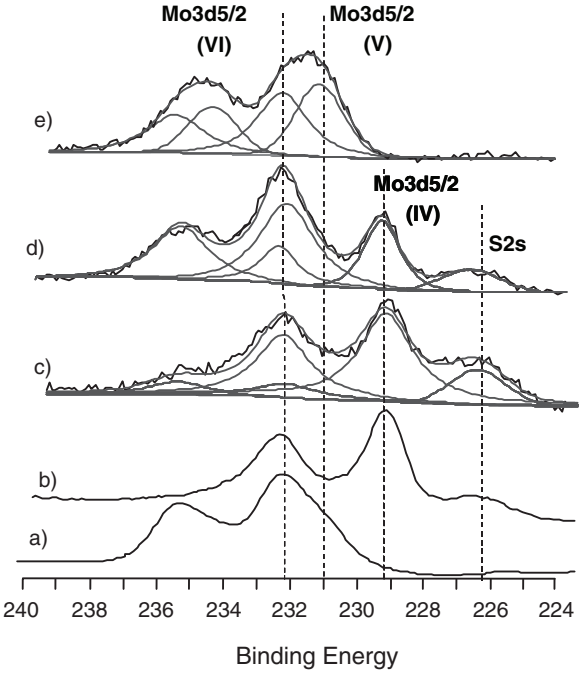

Fig. 9 Friction-induced MoS_2 with steel cylinder against DLC-coated flat friction test. XPS Mo3d peak recorded on: (a) pure MoO_3 powder; (b) pure cleaved MoS_2crystal; (c) MoDTC + ZDDP tribofilm on the a-C:H_1 coating; (d) MoDTC + ZDDP tribofilm on the ta-C coating; and (e) outside the MoDTC + ZDDP tribofilm on the a-C:H_1 coating

Table 2 Chemical composition of ZDDP + MoDTC tribofilms formed on DLC coatings

		Elemental composition (at. %)	
Elements	Energy (eV)	a-C:H_1	ta-C
C1s	284.8–285.5–287.6	94.6	92.5
O1s	531.0–532.8	3.1	5.0
S2p (sulfide)	162	0.8	0.9
Mo3d (Mo(IV))	229	0.4	0.4
Mo3d (Mo(VI))	232	0.1	1
P2p	133.2	≈ 0	≈ 0
Zn2p	1022.4	1.0	0.2

nonhydrogenated DLC. It is also interesting to compare the spectrum recorded inside the tribofilm formed on a-C:H_1 coating with the one recorded outside the tribofilm (Fig. 9e). Results show the presence of the MoO_3 compound and a new contribution which can be attributed either to Mo(V) (331 eV) which is effectively present in the MoDTC molecule, and/or to oxi-sulfide species like $MoS_xO_{(2-x)}$.

It appears more reasonable to assume that some residual MoDTC stays on the surface of the DLC coatings.

No nitrogen is detected in the N1s photopeak, but it has to be noticed that interferences may exist between the N1s and Mo3p lines, so that a few percent of nitrogen would be hardly visible in these conditions. The comparison of Mo3d XPS photopeaks obtained inside and outside tribofilm clearly demonstrates that molybdenum disulfide was only in situ generated by the friction process between DLC-coated surfaces and steel counterfaces.

DLC/DLC System

To verify that the build-up of molybdenum sulfide interfacial material takes place directly on the surface of hydrogenated amorphous carbon coatings, without any transfer from a steel counterface, XPS analyses were carried out on the hydrogenated DLC-coated flats which have been tested against hydrogenated DLC-coated cylinders. No iron was found in these tribofilms formed on DLC surfaces, indicating that no delamination and/or excessive wear of carbon material occured. Figures 10a and 10b present Mo3d photopeaks recorded inside the tribofilms formed on the highly hydrogenated DLC coating a-C:H_1 after the friction tests carried out with MoDTC + ZDDP additivated lubricant and MoDTC additive, respectively.

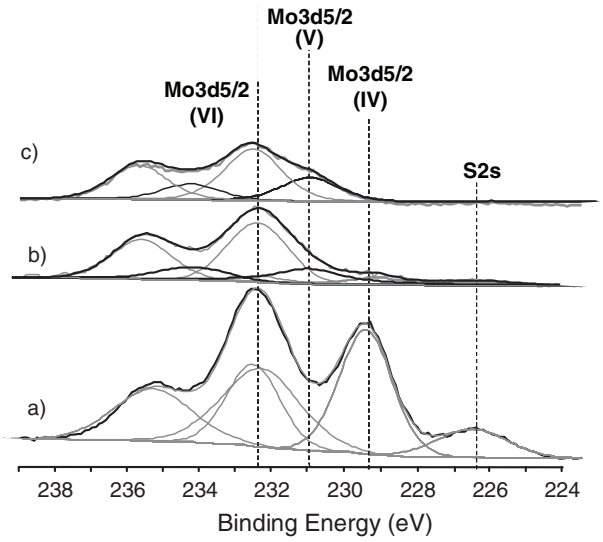

Fig. 10 Friction-induced MoS_2 with DLC-coated cylinder against DLC-coated flat friction test. XPS Mo3d peak recorded on the a-C:H_1 coating: (a) inside MoDTC + ZDDP tribofilm; b) inside MoDTC tribofilm; and (c) outside the MoDTC + ZDDP tribofilm

For binary mixture, the Mo3d XPS spectrum shows two main contributions MoS_2 (Mo (IV)) and MoO_3 (Mo (VI)) unlike the Mo3d XPS spectrum obtained with only MoDTC additive which displays a third peak at about 231 eV (Mo(V)). This Mo3d photopeak clearly indicates the incomplete decomposition of the MoDTC molecule during friction and the strong contribution of molybdenum oxide in comparison with molybdenum sulfide (1.3 at. % of MoO_3 and 0.4 at. % of MoS_2) for MoDTC additive. Also, the S2s photopeak at 226 eV is very weak in this case. The presence of MoS_2 bonding is strongly visible on the MoDTC + ZDDP-derived surface (2.5 at. % of MoS_2 and 2.5 at. % of MoO_3) and this is corroborated by the sulfide form of sulfur (S2p at 162.3 eV) and a quantitative ratio S/Mo of about 2.1. This data clearly indicates that the presence of ZDDP is to promote the formation of MoS_2 in the tribofilm. Moreover, the comparison of Mo3d XPS photopeaks obtained inside (Fig. 10a) and outside (Fig. 10c) the tribofilm clearly shows that molybdenum sulfide material was only in situ generated by the friction process between two hydrogenated amorphous carbon surfaces. These two results were already observed, but only on steel substrates [12,13].

The TEM micrographs of typical fragments of the tribofilms obtained on the a-C:H_1 coating after the friction tests carried out with MoDTC + ZDDP additivated lubricant and MoDTC additive are shown in Figs. 11a and 11b, respectively. For the binary mixture, X-ray analysis (not shown) revealed few phosphate zones containing phosphorous, oxygen, and zinc. Dispersed inside this phosphate matrix, we can observe a few MoS_2 single sheets which have already been formed. These sheets are recognized as MoS_2 because of the basal plane distance of h-MoS_2 crystal lamellar structure (0.7 nm) which can be observed in some places. The length of the sheets is variable, from 2 to 10 nm, and they appear in a very dispersed and diluted form (Fig. 11a) contrary to that observed in the case of MoDTC additive in Fig. 11b where the MoS_2 sheets form bundles. These bundles are embedded in a carbon, oxygen, and iron-rich matrix.

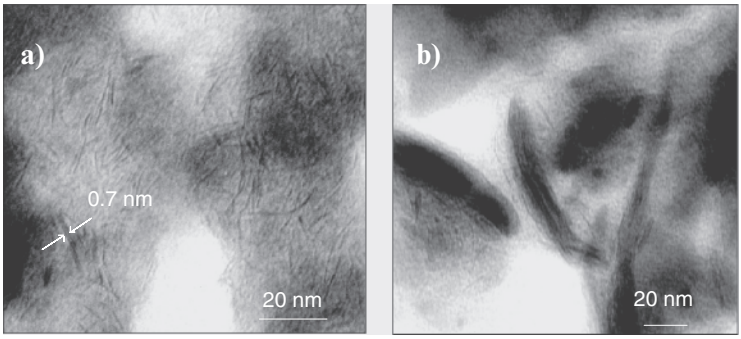

Fig. 11 TEM micrograph of wear particles obtained after the friction tests of a-C:H_1/a-C:H_1 couples: (a) MoDTC + ZDDP lubrication; and (b) MoDTC lubrication

3.1.4 Conclusions on the Coupling of DLC Materials with Usual ZDDP and MoDTC Additives

The present study shows that selected hydrogenated amorphous carbon surfaces can be lubricated by usual MoDTC and ZDDP additivated lubricants. The tribochemical reactions between amorphous carbon coatings and usual lubrication additives depend on the coating properties. Relationships between hydrogen content and improvement of tribological behavior under lubricated conditions needs more research. In particular, more work is needed to understand the interactions between MoS_2 and carbonaceous surfaces. At the moment, only assumptions can be made on the basis of the chemical hardness approach (HSAB principle) [14]. During the friction process, hydrogen-terminated surface of DLC coatings is disrupted and the species present in the lubricant can react with the dangling bonds of the nascent carbon surface. From the chemical hardness point of view, hydrogenated carbon materials are soft bases and will preferentially interact with soft acids, like Mo^{4+}, involved in the formation of MoS_2. Hydrogenated-free carbon materials might be "intermediate bases" which also react with hard acids, like Mo^{6+}, involved in the formation of MoO_3 compound. This can explain why hydrogen-containing carbon materials promote the MoS_2 formation to the detriment of MoO_3.

On the other hand, in the light of both XPS and TEM investigations and previous works on the tribochemistry of additives on steel surfaces which show that ZDDP additive increases the formation of MoS_2 [12,13], we can suggest the mechanisms described in Fig. 12 for the in situ tribochemical formation of MoS_2, in the presence of MoDTC and ZDDP binary lubricant mixture. The MoS_2 units come from degradation of MoDTC in the contact by the tribochemical reaction. From a chemical point of view, electron transfer occurs on the Mo-S chemical bonding in MoDTC molecule, which leads under *friction mechanical process* to the formation of free radicals, one oxysulfide corresponding to the core of MoDTC molecule and the others to the chain ends. Chain-end radicals then recombine to form thiuram disulfide, whereas the oxysulfide decomposes into MoS_2, which crystallizes into sheets, and MoO_2. These sheets can oxidize in the presence of O_2. The role of ZDDP is principally to provide the sulfur atoms to complete the sulfuration of the oxysulfide. If the concentration in ZDDP is sufficient, then a lot of MoS_2 units are formed and can diffuse in the phosphate matrix. These units can easily meet together and a two-dimensional lamellar sheet can progressively grow and cover the asperity tip and then reduce efficiently the friction. In these conditions, MoS_2 sheets are present in the contact with a few molybdenum oxides. If the ZDDP concentration is low, the sulfuration is reduced and also the presence of molybdenum oxide is predominant in the contact. In this last case, the MoS_2 sheets form isolated and compact bundles in a carbon-rich and oxygen-rich matrix which can easily be ejected from the contact and then do not reduce efficiently the friction.

To summarize, MoDTC and ZDDP additives react directly with amorphous carbon surfaces. The role of antiwear ZDDP agent is to principally enhance the

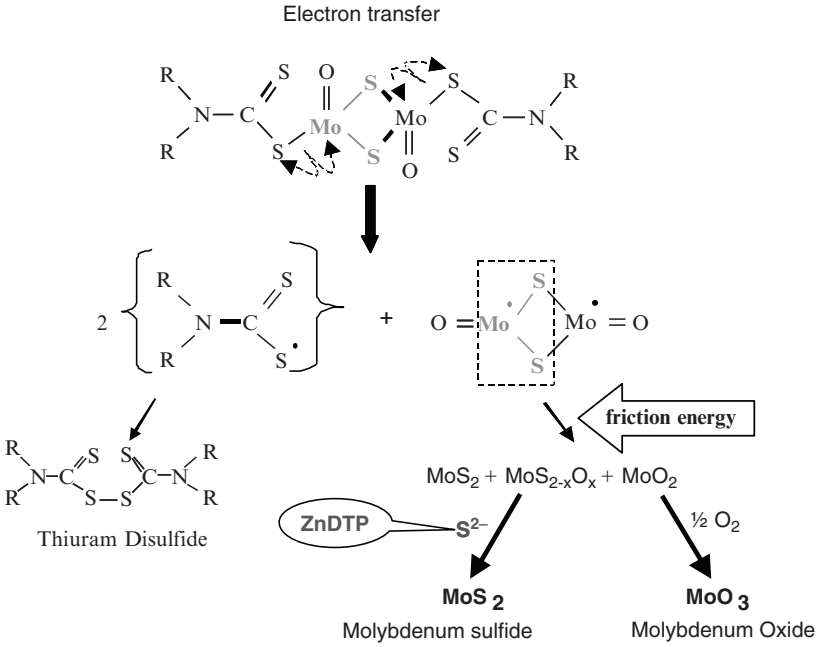

Fig. 12 Chemical process of the MoS_2 formation from MoDTC + ZDDP binary mixture

formation of MoS_2 sheets. The composition of tribofilm appears close to that of tribofilm obtained on steel surfaces in the same lubrication conditions despite depletion in phosphorous and zinc [15]. It is interesting to notice that tribochemical reactions can occur without the presence of iron catalyst element in the tribological system. Unfortunately, the energy efficiency of the usual additives ZDDP and MoDTC is not significantly increased by the use of DLC coatings even when the concentration of additives is not reduced in comparison to the standard steel system. These observations lead us to provide increasing attention in developing *new oil additives* for *selected DLC materials* to promote energy efficiency, to reduce fuel consumption, and environmental contamination.

3.2 New trends in Lubrication of DLC Materials

We evaluated the friction properties under boundary lubrication conditions for more than 50 different kinds of DLC-coating materials, including: hydrogen-containing DLC (a-C:H), metal-containing DLC (Me-C:H), and hydrogen-free DLC (a-C and ta-C). We found that the best performance is for hydrogen-free DLC (ta-C), which we focus on here.

3.2.1 Full Characterization of ta-C–DLC Material

Extreme surface characterizations are suitable for describing surface properties, such as adhesion, which are primordial in friction. XANES spectra performed on the ta-C and a-C:H_2 coatings are shown in the Fig. 13. The comparison with the XANES spectra of diamond and graphite compounds also reported on this figure clearly showed that the surface (a few nanometers thick) of the ta-C coating is mostly composed of carbon with sp^3 hybridization. The hydrogenated coating a-C:H_2 contains more sp^2 carbon than the ta-C coating as clearly demonstrated by the strong pic at about 285 eV.

AES experimentations performed on the ta-C coating confirm its strong sp^3 hybridization. Indeed, its AES-derivated spectrum shows a fine structure that is assigned to KVV transitions involving $p\pi$ electrons (Fig. 14). The distance D between the maximum of the positive-going excursion and the minimum of the negative-going excursion in the derivative AES spectrum, which is characteristic of the different carbon atoms arrangement as shown previously by Mizokawa et al. [16,17], indicates a percentage of sp^3 sites of about 70%.

Besides the surface sensitive application of AES and XANES, other techniques available for gaining direct imaging and information about changes in the cross section of the sample were carried out. The EFTEM image at 180-eV energy-loss with 7-eV-slit width obtained on the FIB cross section of the ta-C-coated steel sample is presented in the Fig. 15. This energy loss permits to decrease the contrast of the image due to the difference between the iron and carbon atomic numbers as well as thickness fluctuations. This leads to a better visualization of the steel structure and chromium-based interlayer used here to improve the ta-C-coating adhesion on the steel substrate. The metal W layer located above the ta-C coating was necessary for applying the focused ion beam technique.

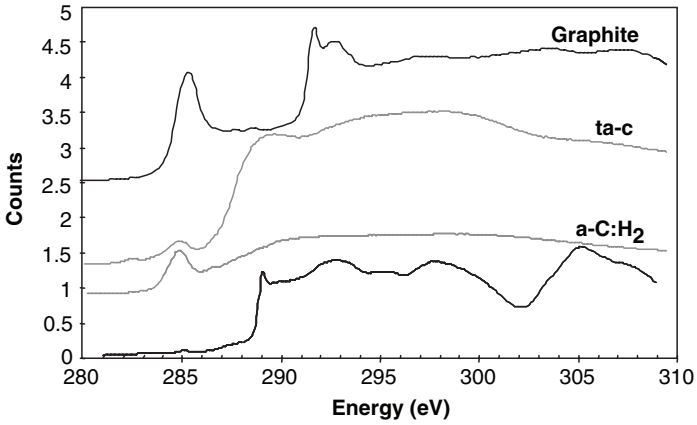

Fig. 13 XANES spectra recorded on ta-C and a-C:H_2 materials. XANES spectra of diamond and graphite materials are also reported on the figure for the comparison

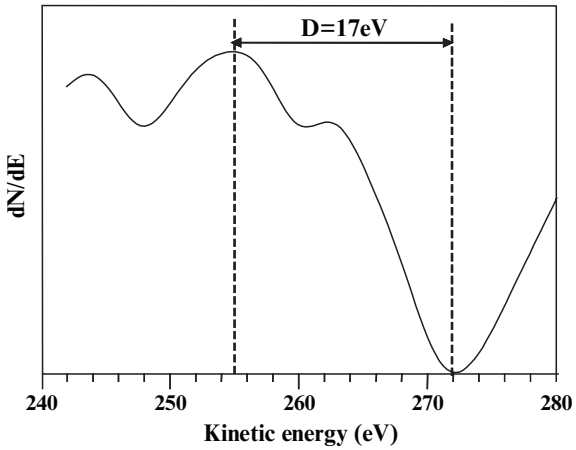

Fig. 14 Derivated dN/dE XAES spectrum of ta-C coating

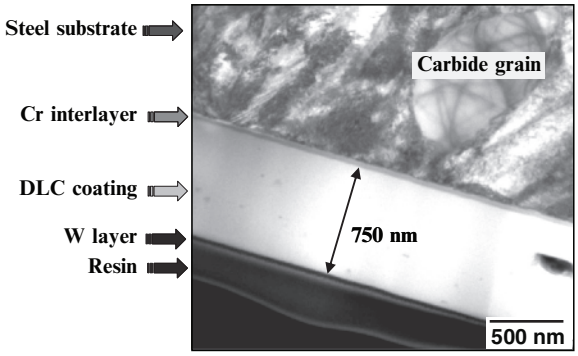

Fig. 15 EFTEM image at 180 eV energy-loss with 7 eV slit width of a cross-sectioned ta-C coating deposited on a steel substrate

The distribution of the carbon sp^3 bonding through the FIB cross section was visualized using π and σ bond imaging by EFTEM. The Figs. 16a and 16b show respectively the EFTEM images performed at 6 eV and 30 eV energy-loss, regions mapping respectively only the sp^2-bonded carbon and both sp^3/sp^2 carbon hybridizations. In the 6 eV energy-loss image corresponding to π/π^* transition, a 1–2 nm thick brighter layer which is closer to the ta-C coating surface (near to the W layer) has more graphite-like character (sp^2) while the bottom darker area has more diamond-like character (sp^3) as confirmed by the 30-eV energy-loss image. This means that there is a chemical heterogeneity of the ta-C coating towards the surface region coupled probably with a gradient of mechanical properties.

Unfortunately, it is very difficult to determine this gradient of mechanical properties since it concerns an outermost layer of less than 5 nm in thickness. Nevertheless, nanoindentation permits to evaluate the hardness and Young's modulus

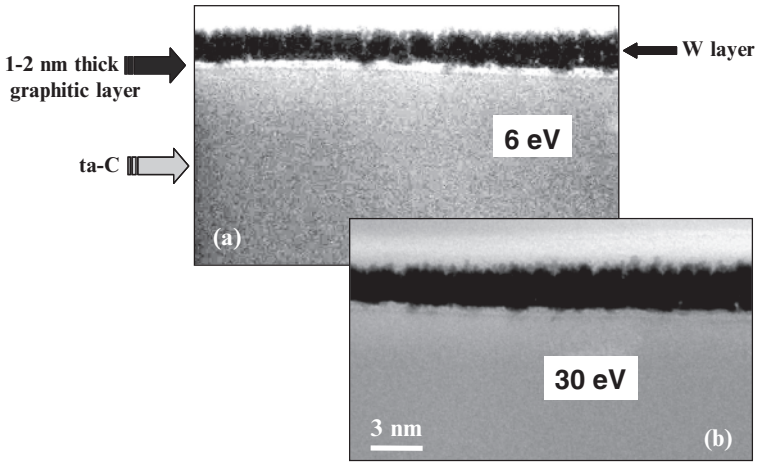

Fig. 16 (a) EFTEM image at 6 eV energy-loss with 4 eV slit width and (b) EFTEM image at 30 eV energy-loss with 4 eV slit width

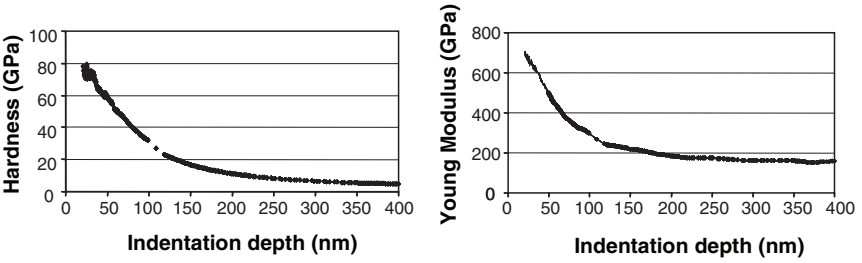

Fig. 17 Evolution of hardness and Young's modulus versus indentation depth for hydrogen-free DLC coating ta-C

of the bulk ta-C material. Figure 17 reveals a hardness of about 65 GPa and a Young's modulus of about 650 GPa for the ta-C material. For comparison, nanoindentation measurements were performed on the a-C:H_2 coating. The hydrogen-containing DLC presents a low hardness of about 15 GPa and a Young's modulus of about 140 GPa confirming its strong sp^2 hybridization.

To fully characterize our ta-C material from the extreme surface towards the deeper layers, DSIMS profiling experiments were also performed. They showed no hydrogen in the ta-C coating (Fig. 18). The metallic chromium-based interlayer used to improve the adhesion of the coating to the steel substrate is clearly seen. No oxygen is detected in the interfacial region confirming the strong adherence of the ta-C coating on the steel substrate.

To summarize, our material would be denoted as tetrahedral amorphous hydrogen-free carbon (or ta-C) in the C–H phase diagram terminology of Robertson [18], closed to the diamond material. However, the upper surface region (<5 nm) of the

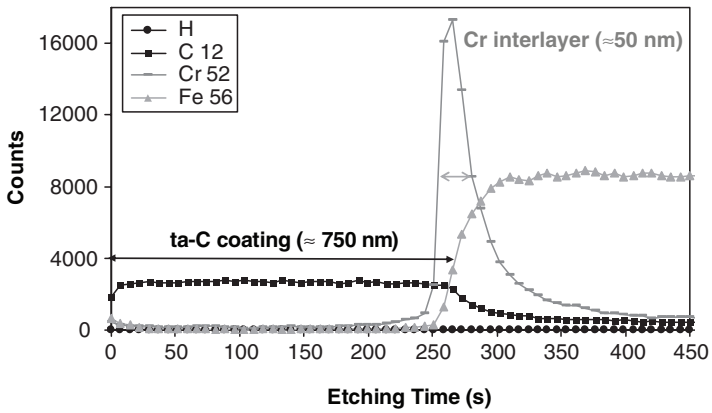

Fig. 18 DSIMS profiles of H, C, Cr, and Fe elements obtained on the ta-C coated steel

ta-C coating, which has a determinant role in the friction behavior, consists predominantly of graphite-like carbon (sp^2).

3.2.2 Steel/ta-C Tribological Systems Lubricated by Glycerol Mono-Oleate (GMO)

As automotive engine oil contains many kinds of additives, it was difficult to identify the specific interactions occurring between friction modifiers and the ta-C coating. Many kinds of friction-modifier additives were examined, including amine, amide, and ester. We evaluated the effect of the GMO friction-modifier additive on the friction property of ta-C, when blended to a PAO-based oil. First, tribological tests were conducted using a cylinder-on-disc type machine consisting of three fixed cylinders sliding on a rotating disc. Different tests were performed with steel/steel, ta-C/steel, and a-C:H_2/steel friction pairs and different lubricants: 5 W 30 engine oil, PAO and PAO + GMO (1% by weight of GMO). Results are shown in Fig. 19. When lubricated with typical API SG 5 W-30 engine oil, friction coefficient of ta-C/steel combination was 0.08 compared to 0.125 for the steel/steel pair, which is a 40% reduction. Interestingly, friction of a-C:H_2/steel lubricated with engine oil showed a higher value of 0.105. As shown in Fig. 19, when GMO is used as additive in PAO it was found the ta-C/steel friction pair gave an ultralow friction coefficient of 0.02 instead of 0.07 with pure PAO. On the contrary, a-C:H_2/steel and steel/steel pairs displayed a much higher friction coefficient of 0.09 and 0.1 in the same conditions. In previous studies, it was found that the lower the hydrogen content of DLC, the lower is the friction coefficient of this combination [6].

Generally, a tribofilm is known to form on sliding steel surfaces as a result of complex tribochemical reactions, and shearing of the tribofilm which often increases the friction level [19–21]. Therefore, it is thought that a low-shear-strength tribofilm resulting from reactions with the friction modifiers contained in the

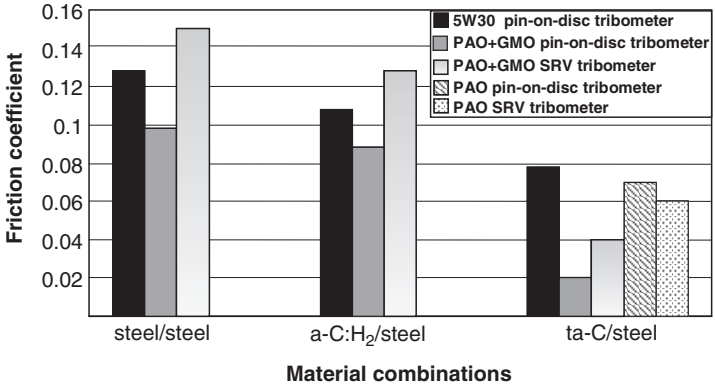

Fig. 19 Friction coefficients of steel counterpart on tested materials lubricated with different oils measured in pin-on-disc sliding tests and SRV sliding tests. The sliding speed was 0.03 m/s and the sliding time was 60 min for the pin-on-disc tribometer. The friction coefficient was measured at 60 min. Oil temperature was 80°C for both test machines. 5 W-30 was API SG standard engine oil. PAO was a PAO oil that had the same viscosity at 80°C as 5 W-30 oil. PAO + GMO contained 1 mass % of GMO

engine oil is presumably formed on the hydrogen-free ta-C surface and is responsible for the ultralow friction coefficient observed for this material in Fig. 19.

To confirm this ultralow friction property, the ta-C/steel friction pair lubricated with PAO + GMO was evaluated using another sliding test rig, the SRV test machine, which is commonly used to evaluate the boundary lubrication properties of engine oil. The ta-C/steel couple showed a friction coefficient of 0.04 compared with the value of 0.02 measured in the pin-on-disc test as shown in Fig. 19. The reason for this discrepancy is that the SRV value was actually averaged with those measured during reciprocating motion, including the high values at the reciprocating points. Nevertheless, friction of ta-C/steel was much lower than the friction coefficient exhibited by the a-C:H_2/steel couple and the steel/steel one, both of which showing a higher friction level than the pin-on-disc-test results in Fig. 19. So, ultralow friction property of the ta-C/steel couple lubricated with PAO + GMO was observed in the two different testing machines.

As a final step, friction properties were evaluated in a pin-on-disc test as a function of the sliding speed for the ta-C/steel pair lubricated with PAO + GMO and compared with those of the a-C:H_2/steel pair. Moreover, the sliding friction data were compared with the results found for a needle bearing lubricated with 5 W-30 engine oil. The results are shown in Fig. 20.

Data show that friction coefficients of the ta-C/steel pairs are much lower than those of the a-C:H_2/steel pairs. The most notable result here is that the ta-C/steel pair lubricated with PAO + GMO exhibited a superlow friction coefficient of 0.006 at sliding speeds over 0.1 m s^{-1} (100 rpm), which was comparable to the friction coefficient of the needle bearing (pure rolling). This superlow friction performance demonstrates for the first time that the rolling contact friction level of needle bearings can be obtained in sliding contact under a boundary lubrication condition.

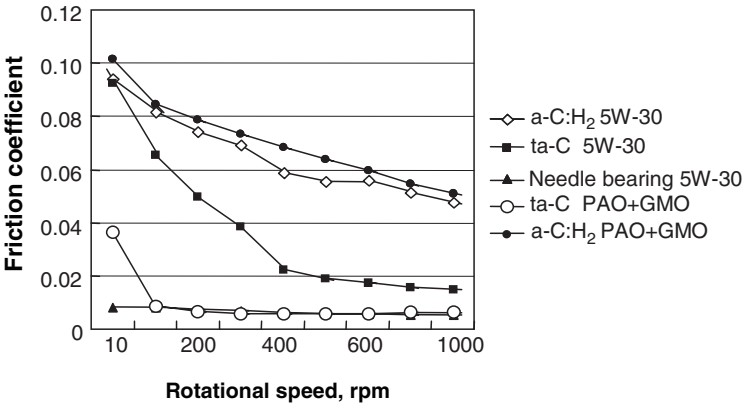

Fig. 20 Friction properties of the ta-C/steel pair lubricated with PAO + GMO as a function of the sliding speed compared with those of a needle bearing

3.2.3 Ta-C/ta-C Tribological Systems Lubricated by Glycerol and GMO

Friction tests with the DLC films deposited on both the flat and the pin were also performed with the SRV machine in the presence of PAO + GMO lubricant to clarify the origin for ultralow friction. Figure 21 shows the friction coefficients of different kinds of material combinations lubricated with PAO + GMO and pure glycerol. Amazing results were obtained for the ta-C/ta-C combination. The friction coefficients of the ta-C couples were substantially lower than for a-C:H_2/a-C:H_2 and for the ta-C/steel combination (see Fig. 19). These results suggest strongly that the ultralow friction phenomenon involves the interaction between the ta-C coating and the ester-containing oil due to the formation of a very thin and low-shear-strength tribofilm on the ta-C sliding surface.

In addition, these outstanding characteristics of vanishing friction and zero-wear behavior were obtained for the ta-C/ta-C combination lubricated with pure glycerol at 80°C. As shown in Fig. 21, the friction coefficient was below 0.01, but the exact value could not be measured with the available equipment at hand. Indeed, the wear scar is not visible by optical microscopy. This result suggests that superlubricity is related to the alcohol chemical function (OH), which is common to both GMO and glycerol molecules.

3.2.4 Superlubricity Mechanism as Studied by Surface Analyses

To study the origin of the superlow friction observed for glycerol lubricated ta-C coatings in boundary lubrication, surface sensitive chemical and molecular analysis techniques XPS and ToF-SIMS were used to investigate the nature of the tribofilm generated at the sliding surfaces of ta-C couples. In order to understand the

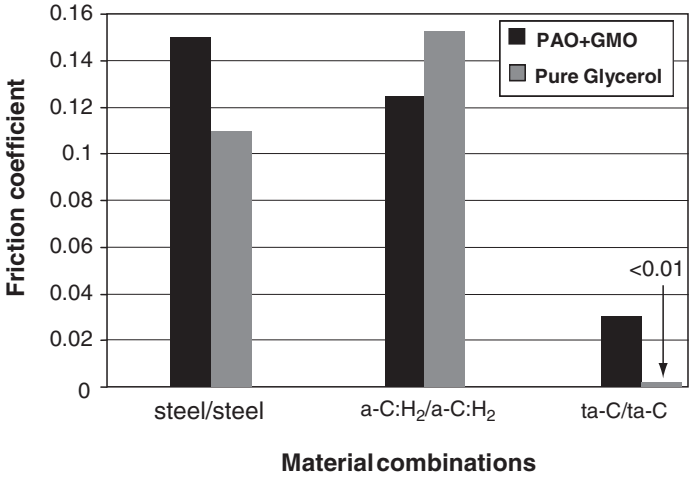

Fig. 21 Friction coefficients obtained with steel/steel and DLC/DLC couples lubricated with PAO + GMO oil and pure glycerol in SRV tests

tribochemical reactions which lead to the tribofilm (wear track), we used pure ^{13}C glycerol (13C G) and deuterated glycerol (^{2}H G-containing) lubricants. For the ^{13}C glycerol, we substituted ^{13}C for all carbon atoms and in the case of deuterated glycerol only the hydrogen atom of hydroxyl group was substituted. The friction results obtained with these specific products on ta-C material are very similar to those obtained with standard glycerol. First, XPS spectra were recorded inside and outside the tribofilm area to clarify the material change on the ta-C surface after the superlow friction tests with glycerol. XPS analyses revealed the presence of C and O elements both inside and outside the tribofilm area. The C–OH and C = O bonds were clearly detected inside the tribofilm as shown by the Fig. 22 which compares the C1s photopeaks obtained on the ta-C virgin surface with the C1s photopeaks obtained inside and outside the tribofilm. These contributions are present in lower proportion outside the tribofilm area than inside. This seems to indicate that some glycerol molecules were adsorbed on the ta-C surface before the friction process. The O1s photopeaks (not shown here) are in good agreement with this suggestion.

The molecular transformations of glycerol under friction were further investigated by SSIMS. The negative ion spectra recorded inside and outside the tribofilm formed on ta-C coating after the ^{13}C glycerol lubricated friction test are compared in the Fig. 23 to the spectrum of the virgin ta-C surface. They clearly show the presence of the 13C glycerol molecule ($^{13}C3H7O3$-) and their characteristic ion fragments ($^{13}C2H3O2$-, ^{13}CHO-, $^{13}CH2$-, $^{13}CH2O$-,) on the ta-C surface after the friction experiment. No higher molecular masses containing ^{13}C obtained by polymerization of glycerol were found; thus the hypothesis that superlow friction results are due to long chain molecules lubrication is not probable in our case. Also, no new species created by the friction were detected inside the tribofilm in comparison with outside.

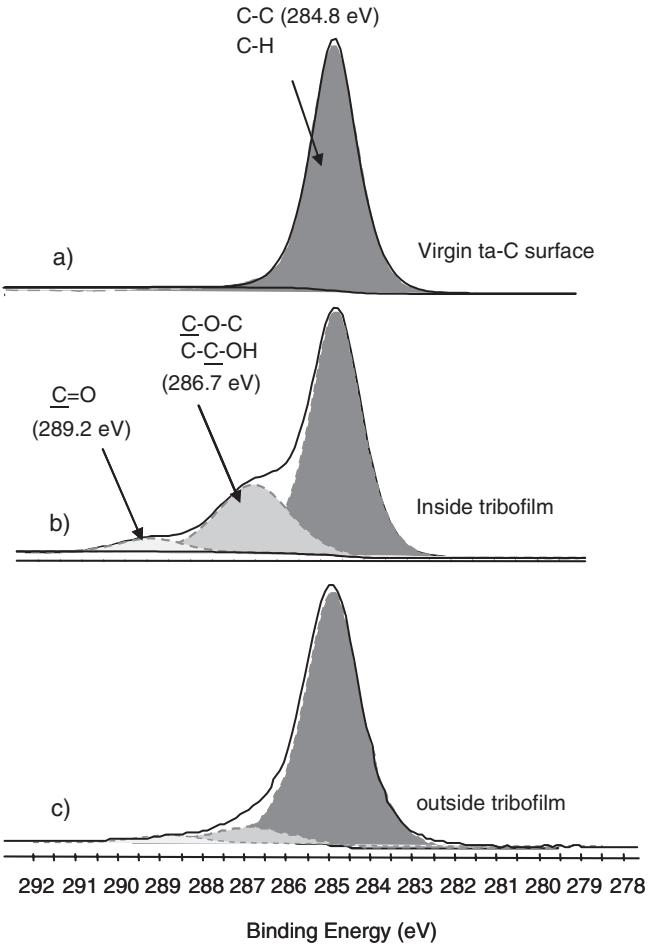

Fig. 22 C1s photopeaks recorded: a) on ta-C virgin surface; b) inside the tribofilm; and c) outside the tribofilm formed on ta-C coating after ta-C/ta-C friction test lubricated with glycerol

Table 3 reports the relative intensities of the 13C glycerol molecule (13C3H7O3-) and their characteristic ion fragments (13C2H3O2-, 13CHO-, 13CH2-, 13CH2O-,) versus the sum of the cluster ion Cn (with $n \geq 5$) intensities which are mostly characteristic of ta-C material. The relative intensities of the 13C components were found nearly twice higher inside the wear scar than outside indicating the possible adsorption of glycerol fragments on ta-C surface. Table 3 also reports the relative intensity of the alcohol group (OH). No significant increase was observed for OH group after the friction experiment in comparison with virgin ta-C surface probably due to a tribofilm screening effect and to the strong presence of this species in the ambient air contamination. However, the superlow friction experiments performed with deuterated glycerol (2H G) lubricant on ta-C coating showed a significant

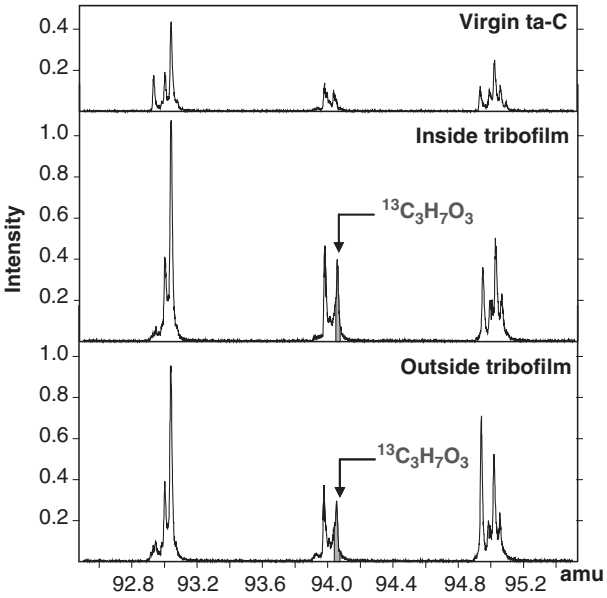

Fig. 23 ToF-SIMS surface analyses. The negative ion spectrum of virgin ta-C surface is compared with spectra obtained inside the wear track and outside the wear track after the friction test lubricated with 13C glycerol

increase in 2H and O2H species inside the tribofilm in comparison with outside as shown by the negative ions spectra displayed on the Fig. 24.

3.2.5 Engine Test Results and Application

The results for the friction torque measurement at the single cam–follower interface are shown in Fig. 25 as a function of the cam–follower composite surface roughness after the test under the boundary lubrication condition with the standard gasoline engine oil. The results indicate that friction torque decreased as the composite surface roughness was reduced. The ta-C coating is below a line drawn in relation to the composite roughness. This result confirms the findings of the preliminary pin-on-disc tests.

The effect of the ta-C coating on valve train friction torque has been measured as a function of engine speed by motoring test using the actual engine valvetrain. The ta-C coating reduced friction torque by 45% compared with the result for a conventional phosphate coating at an engine speed of 2000 rpm. This advanced DLC-coating technology will be applied shortly to valve lifters (Fig. 26) lubricated with a newly formulated engine oil in actual mass-produced gasoline engines. A larger friction reduction of more than 45% is expected to be obtained at an engine speed of 2000 rpm.

Table 3 The relative intensities of the 13C glycerol molecule (13C3H7O3-) and their characteristic ion fragments (13C2H3O2-, 13CHO-, 13CH2-, 13CH2O-,) versus the sum of the cluster ion Cn (with n ≥ 5) intensities. The relative intensity of the alcohol group (OH) is also reported

	OH	$^{13}CH_2$	^{13}CHO	$^{13}CH_2O$	$^{13}C_2H_3O_2$	$^{13}C_3H_7O_3$	$\sum_{n\geqslant 5} C_n$
Virgin ta-C	883,479	NM	NM	NM	NM	NM	100%
Inside tribofilm on ta-C	63,579	1,055	155	118	1,488	208	100%
Outside tribofilm on ta-C	54,534	609	103	69	987	107	100%

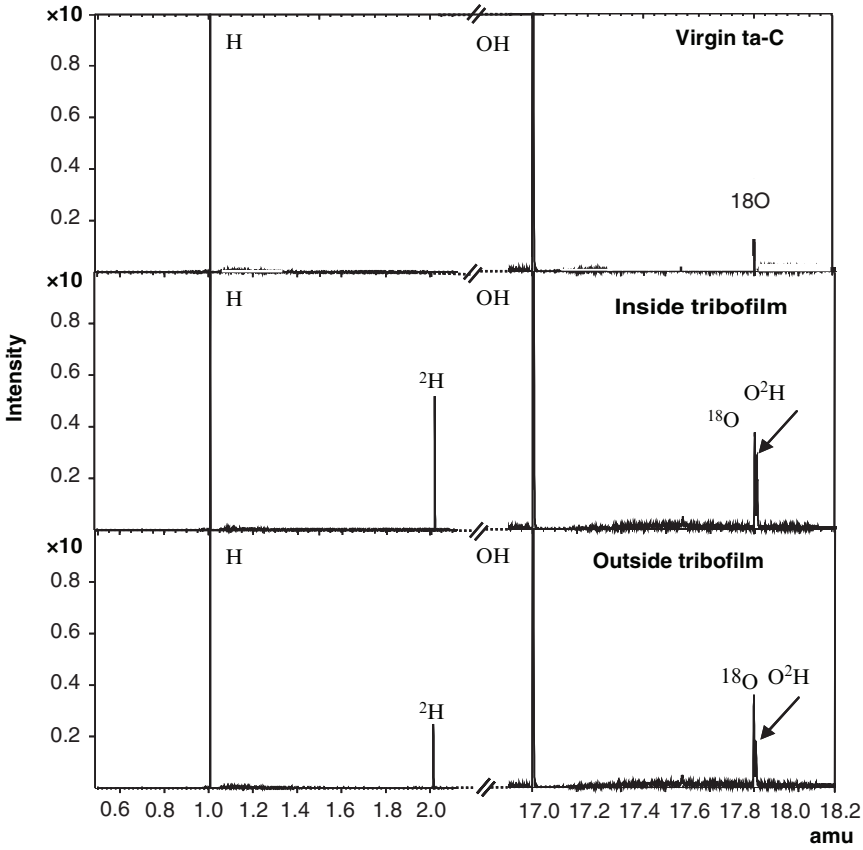

Fig. 24 ToF-SIMS surface analyses. The negative ion spectrum of virgin ta-C surface is compared with spectra obtained inside the wear track and outside the wear track after the friction test lubricated with deuterated glycerol

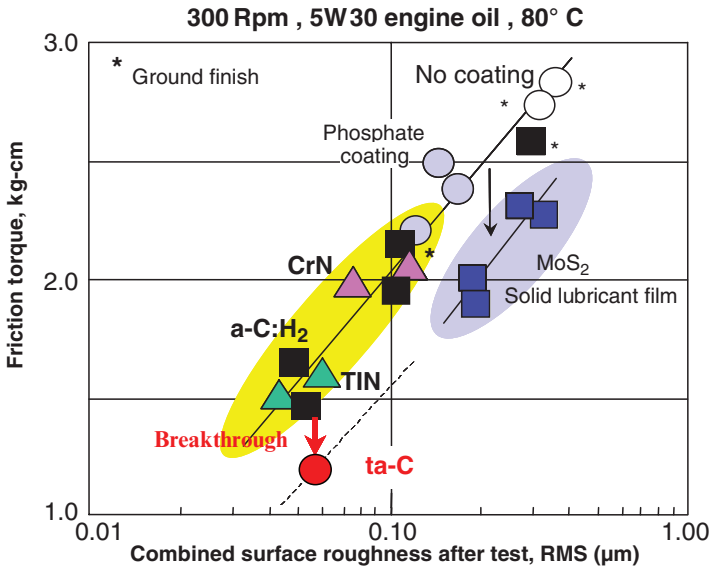

Fig. 25 Reduction in cam/follower friction torque

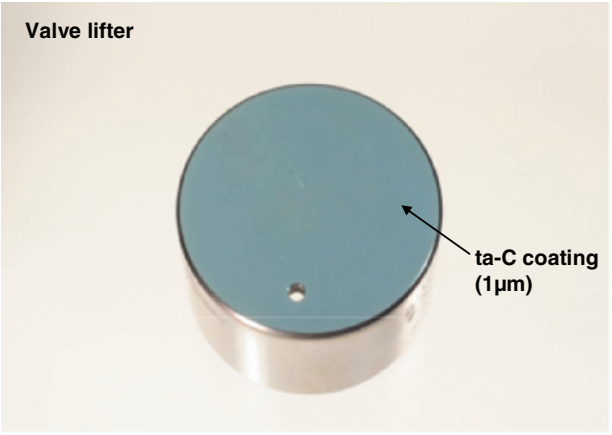

Fig. 26 ta-C coated valve lifter

3.2.6 Conclusion on Lubrication of ta-C Material by GMO and Glycerol

Summarizing, superlubricity was obtained by sliding the ta-C/ta-C friction pair in the presence of pure glycerol as a lubricant at 353 K in boundary lubrication conditions. The mechanism of friction vanishing was studied experimentally by performing

XPS and ToF-SIMS analyses inside and outside wear scar and by using deuterated glycerol and 13C glycerol. SIMS experiments provide an atomic-level explanation for the superlubricity in terms of the formation of a low friction tribofilm involving first hydroxylation of surface carbon atoms, preferentially the sp^2-hybridized carbon atoms, that occurs upon beginning of the sliding. Second, the attachment of glycerol molecules to OH groups by hydrogen bonds is certainly an additional benefit.

4 Summary

Previous sections have focused on engine lubrication issue currently receiving considerable attention. It is clear that boundary lubrication of DLC coatings can be a promising alternative for reducing or even removing the sulfur and phosphorous compounds from engine oil without compromising long-term engine durability and performance. Very promising results were obtained with hydrogen-free DLC material in presence of some organic additives, for example GMO blended to PAO or pure glycerol. It appears that tribological performance deeply depends on the nature of *both DLC material and additive and on the contact parameters*.

Depending on the application, various additives combinations can be used to meet the required performance level. Frequently, combinations of two or more additives show different performance compared to individual components. Whether a carbon-based material is used in a drivetrain system or another application, the lubricant must be *adapted* to ensure the formation of necessary lubricant films and the adequate lubrication of components.

Acknowledgments The authors would like to thank C. Héau and J. P. Terrat from Hydromecanique et Frottement, Andrézieux-Bouthéon France, for providing hydrogenated amorphous coatings and A. Miyashita from ASAHI DENKA Co. Ltd., ,Tokyo 16–8553, Japan for supplying base solution and additives.

References

1. M. Hoshi, Reducing friction losses in automobile engines, Tribol. Int. 1984; 17 (4): 185.
2. R. C. Rosenberg, General Friction Considerations for Engine design, SAE Paper 821576, 1982.
3. A. Katoh and Y. Yasuda, An Analysis of Friction Techniques for the Direct-Acting Valve train System of a New-Generation Lightweight 3-Liter V6 Nissan Engine, SAE Paper 940992, 1994.
4. S. Miyake, S. Takahashi, I. Watanabe, and H. Yoshihara, Friction and wear behavior of hard carbon films, ASLE Trans.1987; 30 (1):121.
5. S. Miyake, Tribological improvement of carbon films due to other material additions, J. Tribol. 1996; 41: 754.

6. C. Donnet, Recent progress on the tribology of doped diamond-like and carbon alloy coatings: a review, Surf. Coat. Technol. 1998; 100/101: 180.
7. C. Donnet, J. Fontaine, T. Le-Mogne, M. Belin, C. Héau, J. P. Terrat, F. Vaux, and G. Pont, Diamond-like carbon-based functionally gradient coatings for space tribology, Surf. Coat. Technol. 1999; 100/101: 548.
8. J. Fontaine, C. Donnet, A. Grill, and T. Le-Mogne, Tribochemistry between hydrogen and diamond-like carbon films, Surf. Coat. Technol. 2001; 146/147: 286.
9. Socoliuc, et al. PRL, 92 (2004) 134301.
10. M. Muraki and H. J. Wada, Frictional properties of organo molybdenum compounds in the presence of ZDTP under sliding conditions (Part 1): frictional properties of MoDTC and MoDTP, Japanese J. Tribol. 1993; 38: 1348.
11. Y. Zhanfeng, M. Kasrai, M. Fuller, G. Michael Bancroft, K. Fyfe, and K. H. Tan, Application of soft X-ray absorption spectroscopy in chemical characterization of antiwear films generated by ZDDP, Wear, 202 (1997) 172–201.
12. C. Grossiord, K. Varlot, J.M. Martin, Th. Le-Mogne, C. Esnouf, and K. Inoue, MoS2 single sheet lubrication by molybdenum dithiocarbamate (MoDTC), Tribol. Int. 1998; 31 (12): 737.
13. M. I. De Barros, J. Bouchet, I. Raoult, Th. Le-Mogne, J. M. Martin, M. Kasrai, and Y. Yamada, Friction reduction by metal sulfides in boundary lubrication studied by XPS and XANES analyses, Wear 254 (2003) 863.
14. G. Pearson, Chemical hardness, Wiley-VCH, GmbH, 1996.
15. M. I. De Barros Bouchet, T. Le Mogne, J. M. Martin, and B. Vacher, Lubrication of carbon coatings with MoS2 single sheet formed by MoDTC and ZDDP lubricants, Proceedings of 4th AIMETA International Tribology Conference, 14/09/2004–17/09/2004, Roma, Italia. Published also in Lubrication Science 18 (2006) 141.
16. Y. Mizokawa, T. Miyasato, S. Nakamura, K. M. Geib, and C. W. Wilmsen, Surf. Sci., 182 (1987), 431.
17. A. A. Galuska, H. H. Madden, and R.E. Allred, Appl. Surf. Sci., 32 (1988), 253.
18. J. Robertson, Amorphous Carbon: State of the Art, (eds.) Silva S.R.P., Robertson J., Milne W. and Amaratunga G.A, (Wold Scientific, Singapore, 1998) 32.
19. M. Chhowalla and G. A. J. Amaratunga, Thin films of fullerene-like MoS2 nanoparticles with ultra-low friction and wear, Nature, 407 (2000) 164–167.
20. J. A. Heimberg, K. J. Wahl, I. L. Singer, and A. Eldemir, Superlow friction behaviour of diamond-like carbon coatings: Time and speed effects, Appl. Phys. Lett., 78, 17 (2001) 2449.
21. J. Fontaine, C. Donnet, A. Grill and T. Le Mogne, Tribochemistry between hydrogen and diamond-like carbon films, Surf. Coat. Technol. 146–147 (2001) 286.

Fullerene-like Carbon Nitride: A New Carbon-based Tribological Coating

E. Broitman[1], J. Neidhardt[2,3] and L. Hultman[3]

Abstract In 1994, researchers at Linköping University discovered the *fullerene-like* allotrope of carbon nitride (FL-CN_x) by using reactive magnetron sputtering in a nitrogen-containing atmosphere at rather low ion energy assistance. FL-CN_x is a predominantly sp^2-hybridized material with nitrogen structurally incorporated either substitutionally in a graphite sheet or in a pyridine-like manner, which initiates bending by formation of pentagons and cross-linking, respectively. The assumed nitrogen-induced cross-linkage between the sheets contributes considerably to the strength of FL-CN_x by preventing interplanar slip. This results in an extremely fracture tough, elastic, and compliant material, which deforms by reversible bond rotation and bond angle deflection rather than slip and bond breaking.

In Section 1, we show that, depending on the growth conditions, FL-CN_x thin films can exhibit a large variation in basal plane curvature and, hence, extension and alignment of sheets. In Section 2, we show how the mechanical and tribological properties can be correlated to the film microstructure. The superior resiliency to deformation in FL-CN_x films makes asperities in a tribological contact more likely to deform elastically. Furthermore, the low modulus dissipates the contact stresses over large volumes making adhesive failures of the film-substrate system less likely. The above-mentioned conditions lead to a reduced wear compared to amorphous CN_x or pure carbon. This in combination with the rather low coefficient of friction makes fullerene-like CN_x a promising candidate for tribological applications, while the process control provides for tailoring the mechanical properties. In Section 3, we discuss the possible applications in the areas of biomaterials and the hard disk industry.

Keywords carbon nitride, C_3N_4, CN_x, fullerene-like, thin films, magnetron sputtering

[1] Department of Chemical Engineering, Carnegie Mellon University, Pittsburgh, PA 15213, USA

[2] Christian Doppler Laboratory for Advanced Hard Coatings, Department of Physical Metallurgy and Materials Testing, University of Leoben, 8700 Leoben, Austria

[3] Thin Film Physics Division, Department of Physics, Chemistry and Biology (IFM), Linköping University, 58183 Linköping, Sweden

C. Donnet and A. Erdemir (eds.), *Tribology of Diamond-Like Carbon Films: Fundamentals and Applications*.

1 Introduction

The appearance of reports on carbon nitrides can be backdated to the beginning of the nineteenth century. In 1816 Guy-Lussac observed that cyanogen C_2N_2 (N≡C–C≡N), which is a gas at room temperature, can polymerize to form solid paracyanogen – $(CN)_n$ [1]. The first reference in the literature to the compound C_3N_4 was given by Franklin in 1921 [2]. The author suggested that graphitic C_3N_4 could be the final product after a series of deammonation of ammono carbonic acids. A voluminous solid residue close in composition to C_3N_4 was reported, though containing 0.6–2.4% hydrogen. The author called this product *carbonic nitride*, but did not study its structure and properties. In 1937, Pauling and Sturdivant were the first to make quantum mechanical calculations and to suggest the possible structure of new C–N and C–N–H compounds [3]. On the basis that the graphitic C_3N_4 proposed by Franklin might be converted to a hard form, analogous to the graphite–diamond relationship, a substantial effort in the 1970s was devoted without success at GE Research Laboratory to the synthesis of possible new C–N phases [4].

The first attempt to produce carbon nitride in the form of a thin film was reported by Cuomo et al. in 1979 [5]. The authors used an r.f. diode sputtering system to deposit CN_x films which they identified to be a paracyanogen-like material, with a composition of 49% C, 48% N, and 3% O. Two other reports on the electrical and optical properties of amorphous CN_xH_y films deposited by CVD were published in the late eighties [6,7]

In 1984, C.M. Sung predicted in an unpublished patent disclosure letter at the Diamond Technology Center of Norton Company that C_3N_4 may be harder than diamond, the hardest material known [8]. In order to estimate the hardness of these hypothetical materials, the author contracted Marvin Cohen to calculate the theoretical values of their bulk moduli. In 1985 Cohen published an empirical formula relating the bulk modulus of tetrahedrally coordinated materials to the length and ionicity of their chemical bonds [9]. From this relationship, he predicted that a material made of carbon and nitrogen should exhibit a bulk modulus higher than diamond due to the short length and high covalency of the C–N bond. Subsequently, Liu and Cohen predicted that β-C_3N_4, a material isostructural with β-Si_3N_4 possesses a bulk modulus approaching that of diamond [10,11]. It should be noted here that in none of Cohen's publications the term *harder than diamond* appears [9–11]. As it was pointed by Teter some years later [12], the shear modulus rather than the bulk modulus is a good predictor for hardness. Nevertheless, it appears that Cohen's papers are the beginning of a remarkable stimulation of interest in the system C–N as the possible source of a material harder than diamond. This excitement within the scientific community was also reflected by divulging articles in the general press [13–17].

Many deposition methods and techniques have been employed in the quest for the elusive superhard crystalline phase β-C_3N_4 (see, for instance, the reviews from Muhl [18] Wang [19], and Kroke [20]). DeVries counted in 1997 more than 400 papers on

carbon nitride: 16% claimed the synthesis of β-C_3N_4, 4% were skeptical of its synthesis, and about 65% reported synthesizing other types of carbon nitride [21]. Figure 1 is an updated analysis of the literature using only the keyword "C_3N_4" in the American Chemical Society database "SciFinder". As on August 30, 2007, 824 papers (including a few patents) can be ascribed to this material. The data shows that the predictions of Liu and Cohen [9–11] sparked off intense theoretical and experimental activity worldwide with a view to realize experimentally the new C–N superhard material. We can also see that the activity started to decrease after 1999, a probable consequence from the publication of critical reviews that have speculated about the impossibility of fabricating the *"harder than diamond"* β-C_3N_4 single crystal film [21].

Since 1990 many investigators have claimed the formation of crystalline carbon nitride. But, to date, no satisfactory evidence has been presented. In a recent review, Malkow has shown that researchers had failed to use complementary techniques to support their claim about the formation of crystalline β-C_3N_4 [22]. Most of claims are based in the analysis of electron diffraction patterns. However, diffraction patterns alone have proven not to be suitable to identify carbon nitride crystalline phases because the strong peaks of *lonsdaleite* (hexagonal diamond) do match with the predicted electron diffraction pattern of hypothetical β-C_3N_4 [23]. Also, it has been shown that FeO(OH) which forms during TEM specimen preparation, matches almost exactly with the predicted patterns of β-C_3N_4. Furthermore, the elemental compositions in the obtained crystals were not always reported, or only overall N/C ratios were given and mostly impurities such as oxygen and hydrogen or silicon (from the substrate) were not considered or if at all considered, their exact concentrations were not given [22,23].

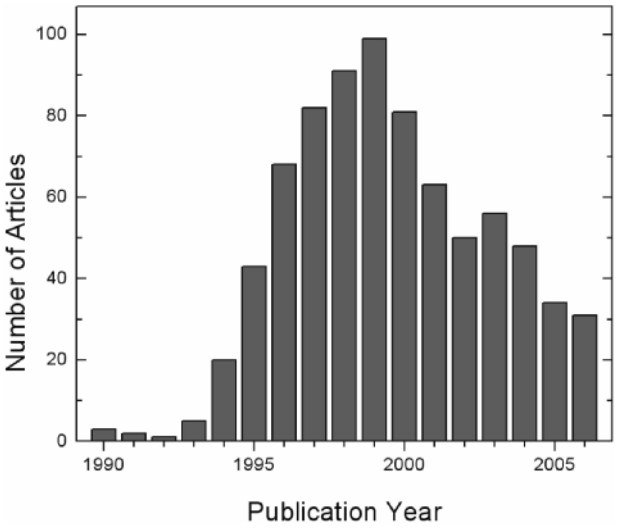

Fig. 1 Estimation of the number of articles on carbon nitride published since 1990. Numbers were determined by searching "C_3N_4" in the database SciFinder, August 30, 2007

Difficulties to synthesize C_3N_4 films arise primarily from the inherent drive of nitrogen to form strongly covalent-bonded N_2 with the consequence that as-deposited films are deficient in nitrogen which readily desorbs [24]. In order to incorporate the required 57% of nitrogen the focus was mainly on high energetic deposition techniques to provide for pronounced nonequilibrium growth conditions. These high energies, however, suppressed any structure evolution by displacing film atoms via knock-on collisions. Despite these efforts, the nitrogen content in the resulting amorphous CN_x material rarely surpasses 30 at. % (see Section 2.3) and any nitrogen concentration exceeding this limit seems to be due to N_2 gas trapped in a porous film structure.

If, on the other hand, alternative deposition techniques such as reactive magnetron sputtering of carbon in a nitrogen-containing atmosphere are employed, the energy per deposited particle is rather low. This is mainly due to the low ion-to-neutral arrival rate ratio inherent to the technique. Therefore, most film-forming particles carry thermal energies, which allows for the evolution of structured films. Reactive magnetron sputtering with rather low ion-assist energies was employed by Sjöström et al., which led to the discovery of the *fullerene-like* allotrope of carbon nitride (FL-CN_x) in Linköping in 1994 [25,26]. This nanostructured CN_x ($0 < x < 0.25$) thin film material was found to be much more interesting from a materials research and applications point of view as its amorphous counterpart. By using nitrogen as a reactive gas a film structure consisting of bent and frequently intersecting planes evolves at elevated temperatures, whereas pure carbon films sputtered under the same conditions result in a porous underdense soot-like material [27].

2 Fullerene-like Carbon Nitride Films

Fullerene-like materials are characterized as compound materials, by the effect of the structural incorporation of odd-membered rings, with heavily bent and intersecting hexagonal basal planes. These structures are besides CN_x observed in, e.g., C [28], BN:C [29], BN [30], MoS_2 [31], TiO [32], NbS_2 [33], and WS_2 [34]. Out of these material systems only C, CN_x and BC:N exhibit cross-linking, which enables the material to extend the strength of the covalent-bonded two-dimensional hexagonal network into three dimensions.

Fullerene-like CN_x consists of, upon substitution of nitrogen for carbon, bent, intersecting, and cross-linked graphite sheets, as seen in the high-resolution transmission electron microscopy plan-view image in Fig. 2. This implies that the majority of carbon is incorporated in a three-coordinated planar sp^2-hybridized state. The double bond between sp^2-hybridized carbon as in graphite, is with a bond energy of 6.3 eV compared to 3.6 eV, actually stronger than the single bond sp^3-hybride bond of diamond [36]. However, the overall strength of graphite is limited by its two-dimensional structure of hexagonal planes and, thus, the rather weak interplanar van der Waals-type bonding. Hence, graphite deforms easily by gliding of basal planes. If on the other hand nitrogen is incorporated during growth

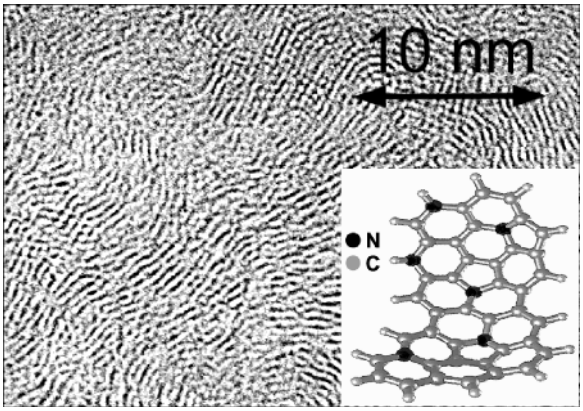

Fig. 2 Plan-view high-resolution transmission electron micrograph of the curved and intersecting fullerene-like sheets in CN_x for a film grown at 450°C with an N_2 fraction of 0.5 and a bias voltage of −25 V. The inset illustrates the buckling of the graphene sheets by pentagon-incorporation obtained from ab-initio calculations [35]

the energy required to form pentagons is considerably lowered and thus the graphitic sheets curve and buckle (inset Fig. 2) [37]. This enables the material to extend the extraordinary strength of a planar sp^2-coordinated carbon network in three dimensions.

The assumed nitrogen-induced cross-linkage between the sheets contributes considerably to the strength of fullerene-like CN_x by preventing interplanar slip (see Section 2.2 for a more detailed description). This results in an extremely fracture tough, elastic, and compliant material, which deforms by reversible bond rotation and bond angle deflection rather than slip and bond breaking [38]. Diamond-like carbon films for instance also exhibit properties beneficial for many applications, such as high hardness due to a high fraction of sp^3 carbon bonding and favorable tribological behavior. However, contrary to fullerene-like CN_x, the application of DLC films suffers mostly from the inherently higher brittleness of the material.

Depending on the growth conditions, fullerene-like CN_x thin films exhibit a large variation in basal plane curvature and, hence, extension and alignment of sheets. Thus, due to the variation in microstructure it denotes a material with a large spread in properties, e.g., elastic modulus, elasticity, and electrical resistance [27,39,40], all having in common an extraordinary mechanical strength. This provides for tailoring of the properties to given applications, e.g., wear protective coatings.

2.1 Bonding Configuration

Fullerene-like CN_x is a compound material where nitrogen is incorporated in a carbon matrix. The effect of impurities such as hydrogen might also be of importance,

as it is known to improve the properties of, e.g., DLC films [41]. However, the very low concentrations of impurities such as hydrogen and oxygen in the magnetron sputtered CN_x films should not have any significant effect upon the film structure. On the other hand Hellgren et al. studied the effect of intentional hydrogen addition to the discharge during CN_x deposition [42]. It was shown that hydrogen terminates potential bonding sites for CN precursors and, thus, the formation of a fullerene-like structure is hindered. Additionally, hydrogen is enhancing the etching process by formation of, not only volatile C_2N_2 molecules (see Section 2.2), but also NH_3 and volatile C_xH_y species.

Carbon is an excellent constituent in the synthesis of hard compounds, since it fulfills both requirements of a small atomic size and the ability to form strong bonds. The four valence electrons of carbon ([He] $2s^2\ 2p^2$) are able to form three hybridization states enabling three major bond configurations; the sp^3 tetrahedral bonds like in diamond, the sp^2 planar graphite-like bonds and the sp bonds like in alkynes. In Fig. 3 it is depicted that for sp^3-hybridized carbon, all four electrons are able to form σ-bonds pointing towards the corners of a tetrahedron enabling for a strong three-dimensional network. In a sp^2-bonded network, only three electrons form three planar bonds, while the fourth forms a π-orbital perpendicular to the plane of the three σ-bonds. The electron in the π-orbital can be delocalized to strengthen the bonds by forming a resonance structure of single and double bonds in an appropriate matrix. Sp-hybridized carbon, for instance, forms two linear, but very strong bonds due to the possible overlap of two orthogonal π-orbitals. The strength of carbon compounds is easily envisioned by the example of diamond, still the hardest material known, due to the strong C–C bond, the high three-dimensional coordination, and the small atomic size. However, the overlap of the π-orbitals for the sp and sp^2 C–C bonds, commonly referred to as double and triple bonds, results in bond energies of 6.3 and 8.7 eV, which are much higher bond energy compared to 3.6 eV for the single bond as in the sp^3 hybrid. This gives graphite and polymers their extraordinary in-plane/chain strength.

Nitrogen, like carbon, predominantly forms covalent bonds. Its valence electrons ([He] $2s^2\ 2p^3$) exhibit, despite the additional electron, bond hybridizations similar

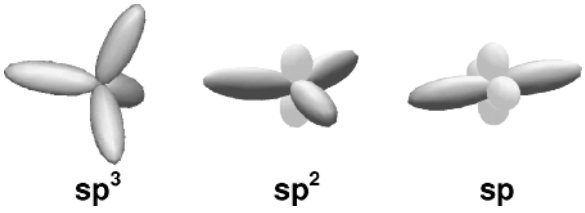

Fig. 3 Schematic of the three different valence electron hybridization states of carbon; sp^3 as in diamond, sp^2 as in graphite and alkenes and sp as for alkynes. The elongated orbitals represent the hybrids able to form σ-type molecular bonds, while the smaller round orbitals are the remaining 2p electron(s) that can form π-type bonds

to carbon. However, the extra valence electron implies some differences. In the case of sp^3-hybridized nitrogen, four hybrid orbitals are formed just like in carbon, while the extra electron forms a nonbonding lone pair with an electron in a hybrid orbital leaving only three σ-bonding orbitals (Fig. 4). The bond angle is slightly deflected to 109° instead of 107° compared to diamond due to the effect of the more spacious lone pair. There are two possibilities for the sp^2-hybridized bond configuration. First, the extra electron is able to form a nonbonding lone pair with a sp-hybrid orbital leaving the atom with two nonlinear σ-bonds and the possibility to participate in π-resonance structures with the electron in the remaining 2p orbital. Second, the extra electron forms the lone pair with the remaining 2p orbital leaving the atom with three planar σ-bonds and no possibility to contribute to a π-resonance structure, due to the filled, nonbonding 2p orbital. Sp-hybridization of nitrogen is also common, whereas the atom can form one σ-bond and two π-bonds, while the 5th valence electron forms a lone pair with the second sp-hybrid orbital.

Due to the inherently disordered structure of CN_x compounds, it has been difficult to determine the exact bonding structure of carbon and nitrogen in the material. Thus, complementary spectroscopic techniques have to be used to investigate the local bonding environment of fullerene-like CN_x. It has been shown that the bonding structure can be readily analyzed by X-ray photoelectron spectroscopy (XPS) [43,44]. The N1s core level peak has typically two strong components (Fig. 5) P1 at ≈400.7 eV and P2 at 398–399 eV, and at least two smaller ones P3 positioned at ≈402 eV and P4 at ≈399.5 eV. The assignment of these peaks has been widely divergent in literature [45]. However, strong support can be found for the following peak interpretation by comparing the XPS results of a wide range of films with other spectroscopic techniques, such as X-ray absorption/emission spectroscopy (XANES, XES) [46], nuclear magnetic resonance spectroscopy (NMR) [47], electron energy loss spectroscopy (EELS) [48], and theoretical calculations [46].

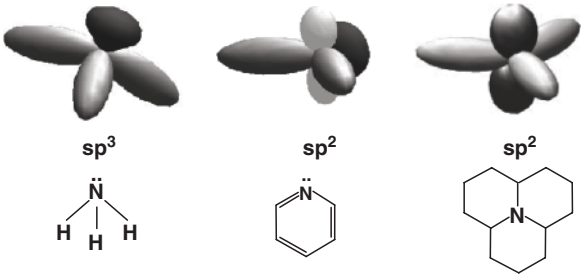

Fig. 4 Schematic of different electron hybridization states for nitrogen; sp^3 like in ammonia, sp^2 twofold coordinated like in pyridine and threefold coordinated as in a substitutional graphite site. The difference in coordination is due to the location of the nonbonding electron pair

- P1 (400.7 eV) corresponds to threefold coordinated sp^2-hybridized nitrogen bonded to three carbon atoms, substitutional in a predominantly sp^2-coordinated graphite network (see inset Fig. 5), while a sp^3-hybridized carbon as neighbor cannot be ruled out. N–H bonding originating from reactions with ambient air might also have contributions in this region.
- P2 (398.0–399.0 eV) has initially been assigned to nitrogen bonded to an at least partially sp^3-hybridized carbon matrix, but has rather to be seen as nitrogen in a pyridine-like structure (see inset Fig. 5), where a twofold coordinated sp^2-hybridized nitrogen forms two bonds to an otherwise graphitic structure. This bonding configuration may occur along edges of planes or next to defects and is essential for eventual cross-linking.
- P3 (402.5 eV) is normally assigned to N–O bonds formed after air exposure [45]. However, recent results from in situ XPS in a UHV environment show no such correlation. Instead P3 scales with the intensity of P1, suggesting that it originates from a similar substitutional graphite structure, where nitrogen donates an electron to the structure leaving it with a virtual positive charge and thus increasing the binding energy [49].

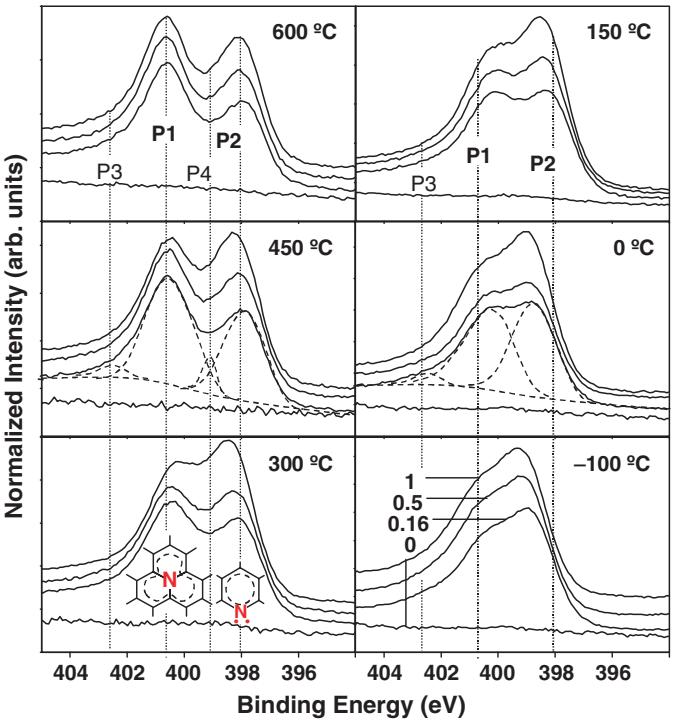

Fig. 5 XPS N1s photoelectron spectra of CN_x films synthesized at various N_2 fractions, a bias voltage of −25 V and substrate temperatures from 600°C down to −100°C. P1–P4 indicate the 3–4 spectral contributions. The insets illustrate the associated major bonding configurations [44]

- P4 (399.5 eV) is a minor contribution and most likely corresponds to sp-hybridized nitrogen in a nitrile structure. Raman spectroscopy is a more suited technique for the detection of residual nitriles [50] and has indicated that a minor fraction is present in fullerene-like CN_x films. N–H bonding configurations due to contamination or surface reactions may also contribute in this region [49].

In [44] it is shown by combining XPS and HRTEM (SAED) the N1s core-level P1/P2 intensity ratio reflects the structural arrangement of CN_x films. A decreasing extension of the fullerene-like sheets implies a decreasing number of nitrogen in a substitutional site (P1) and in turn more nitrogen bonded along edges and defects (P2). Hence, a pronounced fullerene-like microstructure consisting of extended planar domains is characterized by a large P1/P2 ratio, where the peaks are well separated (≈2 eV) and P1 is dominating the spectra. If, on the other hand, the fullerene-like structure is disrupted the P1/P2 ratio is decreasing.

Detailed analysis based on the XPS C1s photoelectron peak is impractical, since it is typically broad and its contributions cannot be extracted separately. Still, the C1s peak is observed to broaden towards higher binding energies as soon as nitrogen is incorporated. This is consistent with the above-mentioned distribution in bonding environments and the broadening is correspondingly more pronounced at lower growth temperatures [48].

The information extracted from XPS and XANES (NEXAFS) are in many aspects complementary, while the latter assesses the electronic structure of a compound at a much superior resolution. Using this technique, the bonding structure of CN_x – in particular the fullerene-like allotrope – was analyzed in detail by Gago et al. [51]. As seen in Fig. 6 the C1s spectra consists of two broad major peaks

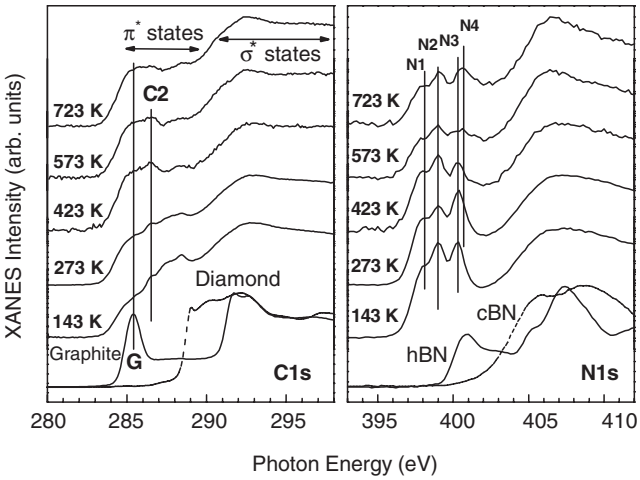

Fig. 6 XANES spectra at the C1s and N1s edge for CN_x films grown at a N_2 fraction of 0.16, −25 V bias and various substrate temperatures. The spectra of graphite and diamond as well as hexagonal and cubic BN are shown as a reference for sp^2 and sp^3 hybridizations [51]

around 284 and 290 eV corresponding to $1s \Rightarrow \pi^*$ and $1s \Rightarrow \sigma^*$ transitions, respectively. The intensity of the π^* peak and the position of the σ^* absorption edge indicate the dominance of sp^2 hybrids, as compared to the reference spectra of graphite and diamond. The states below the graphite peak (G) are attributed to defects in the graphitic network [52], while the formation of various CN bonds is revealed by peaks in the 290–294 eV region. The small (C2) peak indicates the existence of a minor fraction of nitrile bonding configurations regardless of the substrate temperature [53]. This is not surprizing given the large number of preformed CN species in the deposition flux (see Section 2.2). The graphitization occurring at higher temperatures can be seen by an increasing (G) peak. A complete deconvolution and peak assignment for the C1s spectra is, as for XPS, very complex due to the multitude of bonding configurations.

Similar to XPS, more direct information can be extracted from the N1s spectra, where four distinctively different peaks in the π^* can be resolved (Fig. 6). Nitrogen also seems to be predominantly sp^2-hybridized as indicated by the pronounced π^* region. The peaks N1, N2, and N4 are assigned to nitrogen bonded in a pyridine, nitrile, and graphite-like configuration (comparable to P2, P4, and P1 in the XPS spectra), whereas N3 is still under discussion.

The development of the peak N2 as a function of the deposition temperature as analyzed by XANES (see Fig. 6) indicates that the nitrile configuration C≡N is most pronounced at lower temperatures. This is due to the fact that the triple bond, present in most of the preformed CN species in the flux, stays intact upon partial nonaligned incorporation due to a decreased reactivity at lower temperatures (see Section 2.3). At higher temperature, however, these species are incorporated along edges of sheets and thus the electron of the triple bond forms a third bond or a lone pair, as it is the case for a graphite or pyridine-like configuration. In addition, the remaining nitrile groups react to form C_2N_2, which desorbs by the chemical desorption process described above.

In congruence with XPS, the incorporation of nitrogen in a graphite-like configuration (N4) is preferred at elevated temperatures and lower N_2 fractions. This alongside with lower number of nitrogen incorporated in a pyridine (N1) or nitrile (N2) configuration is the fingerprint of an evolving fullerene-like microstructure, which is even more pronounced at lower N_2 fractions. However, these bonding states are still present especially while the pyridine-like configuration might play an important role for interplanar cross-linking.

2.2 The Role of Nitrogen

The substitution of nitrogen for carbon in the graphite basal planes affects both curvature of planes and their reactivity, which is one of the key processes for the formation of fullerene-like CN_x solid films at elevated temperatures. For comparison, pure carbon films grown under the same conditions result in an amorphous underdense structure consisting of aromatic disordered fragments. It is only upon introducing

of even small fractions of nitrogen in the discharge that dense and structured films form. Three major roles were assigned to nitrogen and will be described in the following sections.

2.2.1 Evolution of Curvature

The first role is that nitrogen incorporation induces curvature. This is evident from the fingerprint-like appearance of basal planes of a fullerene-like CN_x film in Fig. 2. The highly corrugated and curved basal planes imply a radius of curvature in the nanometer range. This curvature is induced for all nitrogen fractions of a N_2/Ar magnetron sputter discharge, while its degree can be controlled by the N_2 fraction [27]. Thus, nitrogen plays an essential role for inducing spherical curvature. For pure carbon structures, curvature is known to be due to the incorporation of odd-member rings in an otherwise hexagonal structure. Twelve pentagons thus yield the spherical appearance of closed caged carbon fullerenes, such as C60. Experimental results as well as calculations actually suggest that isostructures to C60 might exist in fullerene-like CN_x thin solid films [54]. The corresponding so called nano-onions (Fig. 7) form under certain deposition conditions, such as elevated temperatures (Ts = 450°C) and low N_2 fractions (0.1–0.16).

These experimental findings were, furthermore, verified by total energy calculations, which show that nitrogen stabilizes pentagons in aromatic carbon structures [55]. However, the structures are shown to be less stable if more than one carbon is substituted in a ring and/or nitrogen is incorporated next to each other, from which geometrical conditions explains the apparent saturation in maximum nitrogen concentration of approximately 20–25 at. %.

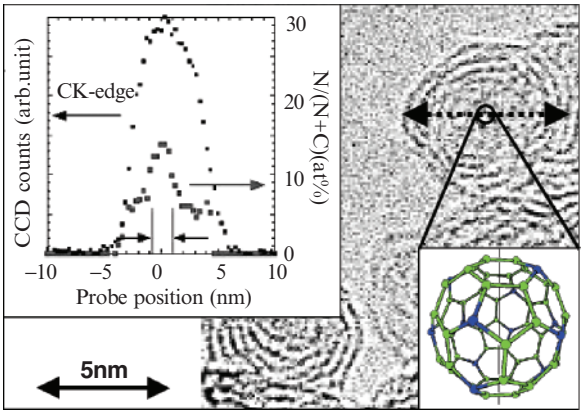

Fig. 7 Spatially resolved electron energy-loss spectroscopy showing the CCD counts and relative nitrogen concentration scanned across a CN_x nano-onion as indicated in the respective high-resolution electron transmission microscopy plan-view image. The inset shows the energetically most favorable structure of $C_{48}N_{12}$ and the space it would occupy if existing in the center of the nano-onion [54]

In summary, both experiments and theoretical calculations suggest that nitrogen triggers the evolution of curvature by stabilizing the required pentagons at much lower energies as compared to pure carbon structures, while the incorporation of more than one nitrogen atom in a carbon ring structure seems to be energetically less favorable [55].

2.2.2 Formation of Interplanar Cross-linking

The second role of nitrogen is the promotion of interplanar cross-linking. The combination of mechanical properties, such as elasticity and hardness of fullerene-like carbon nitride is superior to most carbon-only materials (see Section 3.1). The mechanical strength of graphite, for instance, is limited by its easily activated slip system along the graphite basal planes. On the other hand, this weakening interplanar slip also holds the key for the extremely low friction. Carbon fullerene cages, instead, are known to be extremely resilient and to withstand severe deformation without any plastic yield via broken C–C bonds [56]. However, the mechanical properties of crystalline compounds formed from fullerenes – so called fullerites – still suffer from the rather weak intermolecular bonding. It has also been shown that temperature treatment can initiate intermolecular covalent cross-linking or polymerization, which improves the mechanical strength [57,58]. The other extreme of hard carbon-only materials is represented by diamond, where the highest degree of three-dimensional cross-linking is provided by a 100% sp^3 hybridization. Also DLC thin films synthesized by various techniques exhibit a significant fraction of sp^3-hybridized carbon that give the material an outstanding hardness, while still retaining favorable low friction properties. However, these superhard materials have only a limited tolerance to deformation and overloading results in imminent brittle fracture and, thus, mechanical failure of the substrate-coating system.

Fullerene-like CN_x compared to common superhard thin film materials (c-BN, DLC) has a low to moderate resistance to penetration (hardness), as probed by nanoindentation [38]. Still, the indentation response surpasses crystalline graphite by far, which implies the existence of strong interplanar cross-links or interlocking of sheets. The most striking property, however, is its outstanding resistance to plastic deformation (see Section 3.1). In fact, fullerene-like CN_x deforms predominantly elastically, which combined with its compliance results in a resilient and fracture tough material [27,38]. Nitrogen plays a crucial role, since pure carbon materials grown under similar conditions have a soot-like appearance, which is in conjunction with a deficient cohesion and strength.

The precise nature of the cross-linking mechanisms is, however, still under discussion. A first explanation for cross-linking mechanisms was established by total energy calculations performed in [55]. The presented results suggest that, upon nitrogen incorporation in a hexagon, it is for the adjacent carbon atom energetically more favorable to change from a sp^2-hybridized to a sp^3-hybridized state, which could provide for the required out-of-plane bond. For that reason, nitrogen-doped hetero fullerenes also known as aza-fullerenes, e.g., $C_{59}N$ instantaneously dimerize

upon synthesis via a C–C bond next to the substituted nitrogen atom [59]. Experimental results, however, indicate that fullerene-like CN_x is predominantly sp^2-bonded (see [60] and the references therein, and [47]) and the existence of significant numbers of sp^3-hybridized carbon remains to be affirmed. On the other hand only a few interplanar cross-links are needed to increase the stiffness significantly and any low fraction of sp^3-hybridized carbon might pass undetected due to experimental limitations of, e.g., NMR.

Cross-linking at the nitrogen site on the other hand is rather unlikely. First, it was shown by total energy calculations in [55] that the structure is more stable if two incorporated nitrogen atoms in a graphite fragment are separated by at least two carbon atoms. Second, chemical synthesis of, e.g., aza-fullerene dimmers indicates that the cross-linking is initiated at the carbon next to an incorporated nitrogen atom and not at the nitrogen site itself [59].

The high stiffness of fullerene-like carbon nitride, in contrast to planar graphite, can also be explained by the 3D interlocking of curved meandering fullerene-like sheets. In addition, purely sp^2-based cross-linking mechanisms might also be present, such as branching of sheets and/or C–C bond rotation as suggested in references [28,43,47,60,61]. For the latter, the electron lone pair in the 2p orbital of substitutional incorporated nitrogen or the formation of pentagons disturbs locally the π-resonance structure. Therefore, the double bond resonance structure between two neighbor carbon atoms is disrupted and, thus, the C–C bond is free to rotate due to a missing 2p–2p orbital coupling. This might result in an out-of-plane rotation of the subsequently growing structures and hence enables cross-linking leading to a multitude of possible configurations. This is most likely if one considers also the disruption of the continuous sheet-structure by the incorporation of two-coordinated, pyridine-like-bonded nitrogen that is present in significant numbers as suggested by spectroscopy-based techniques.

Most recent computational studies corroborated the existence of out-of-plane bond deflection and rotation in the presence of multiatomic precursors [62]. Figure 8 exemplifies two of the energetically stable structures exhibiting cross-linking obtained by simulated (synthetic) growth.

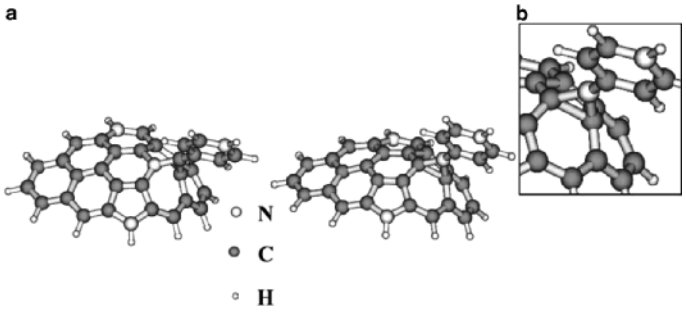

Fig. 8 Stable cross-linked structures with cross-linking bridge (enlarged in the inset) [62].

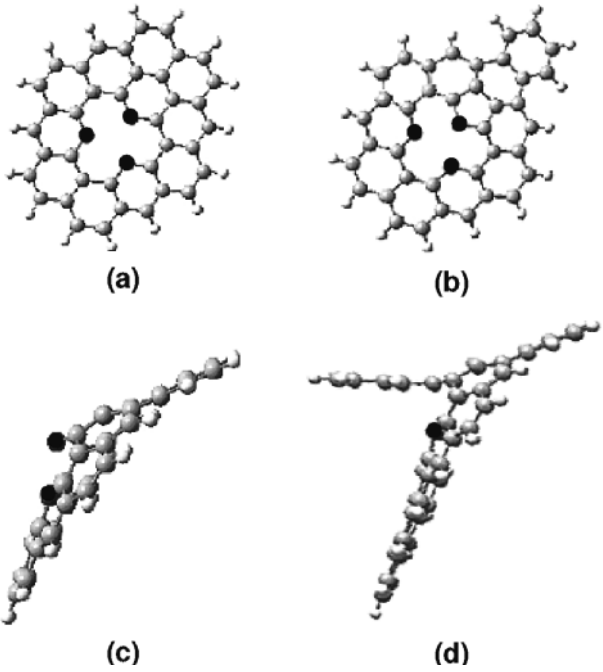

Fig. 9 Alternative sp^2-based cross-linking mechanisms via a nitrogen-induced vacancy (a) and pentagon formation (b), which results in out-of-plane bending (c) and finally provides a nucleation site for out-of-plane growth (d) [47]. The gray-shaded atoms represent carbon and the black nitrogen; the hydrogen (white) atoms are terminating the fullerene-like fragment

Another potential sp^2-based cross-linking mechanism is branching of fullerene-like sheets. It was shown in Section 2.1 that nitrogen is bonded primarily in two different configurations; substitutional at carbon sites, which does not affect continuous planar growth or in a pyridine configuration, where one of the three σ-bonds is terminated by the electron lone pair. The latter implies the existence of vacancy defects as depicted in Fig. 9a. Additionally, nitrogen induces pentagon formation, which provides for spherical curvature at the vacancy site (Fig. 9b). This presented configuration results in out-of-plane nucleation sites (Fig. 9c), where three-dimensional growth can be initiated (Fig. 9d). These ideas were confirmed by initial calculations [47].

2.2.3 Formation of C_xN_y ($x,y \leq 2$) Species

The third major role of nitrogen is the formation of C_xN_y ($x,y \leq 2$) species. Carbon nitride thin films are commonly grown by plasma-activated deposition techniques, where carbon is prone to react with activated nitrogen originating from the discharge. This reactivity of nitrogen is considered to be the dominant compound

forming reaction on surfaces for most PVD nitride films, due to the rather low probability of gas phase reactions under the subatmospheric pressures. However, the experimentally established existence of a low-mass gaseous compound in the carbon–nitride system, namely C_2N_2 [63], adds numerous degrees of freedom to the formation mechanisms of fullerene-like CN_x films as compared to other nitrides forming from single atomic precursors.

As a consequence the deposition flux from a carbon target sputtered in a N_2-containing atmosphere consists to a large extent of multiatomic species. They form via reaction between the carbon atoms in the target and the vast number of nitrogen ions implanted into the top surface layers during sputtering [63]. In turn C_2N_2 and fragments thereof are emitted whereas their number scales with the nitrogen fraction in the discharge [63].

The presence of nitrogen-containing species in the deposition flux leads to various effects also on the substrate site. One important process is that they partially react upon adsorption to form volatile gases such as N_2 and C_2N_2, which subsequently desorb. This results in a film-surface etching commonly referred to as chemical sputtering [64]. This process is observed for various CN_x deposition techniques especially those utilizing hyperthermal species to assist the growth [65–68]. It was first established for ion beam-assisted deposition, where a deficiency of carbon and nitrogen in the film was detected compared to the calibrated fluxes of both elements [69]. The extent of the chemical desorption is determined by the reaction probability to form a volatile gas and, thus, depends on type and mobility of adsorbed species. The overall process can therefore be seen as a preferential etching of less favorably bonded adsorbates and, thus, results in dense and smooth films. Prevailing CN precursors bonded in an aligned manner along edges of sheets are more resilient to concurrent etching and therefore play an important role for the evolution of fullerene-like planes (see Section 3). The chemical desorption process also accounts for the apparent maximum of incorporated nitrogen at ≈25 at. %, due to its higher desorption probability.

2.3 Structure Evolution Mechanisms

For magnetron sputtering, the presence of nitrogen in the discharge gas leads to complex chemical reactions at the target and substrate surface [60]. The intense high-energy ion bombardment at the target results in sputtered target constituents, whereas most of the nitrogen ions are implanted during the process. The implanted nitrogen radicals react readily with the carbon atoms in the target. Thus, the composition of the target surface is altered substantially, especially if one considers the initially rather low sputter yield of pure C. Hence, predominantly C_xN_y ($x,y \leq 2$) molecules are emitted from such a dynamically self-modified target surface, due to the relatively high strength of the C≡N bond, alongside with desorbing gases like N_2 and C_2N_2. The extent of these processes scale with the availability of N_2 in the discharge and therefore lead to a strong increase in flux of preformed CN species at higher N_2 fractions, while the carbon flux only plays a minor role [63].

Although low ion-assist energies (≈20–50 eV) are generally beneficial for film growth by enhancing ad-atom mobility at relatively low substrate temperatures, it has been shown that they are not the dominant structure-determining factor in case of fullerene-like CN_x films. Instead the flux and type of preformed CN species carrying only thermal energy is crucial for the evolution of fullerene-like structures. These molecules might be stabilized against desorption in an evolving sheet by multiple bonding on the C and N side upon aligned incorporation and, thus, promoting the evolution of planar structures. Gueorguiev et al. has corroborated the energetic advantage of this process using step-by-step ab initio approaches in reference [70]. Furthermore, the formation of C_2N_2 as volatile gas is also active on the substrate site and provides for selective etching of misaligned molecules by reaction with adsorbed CN and their subsequent desorption. This process accounts for the apparent saturation in nitrogen content at approximately 25 at. % nitrogen incorporated into the films, which is in congruence with the theoretical established most stable structures [54,62]. The incorporated nitrogen seems to originate predominantly from the already bonded nitrogen in the preformed molecules arriving at the substrate, while the extensive low energetic nitrogen ion bombardment from the discharge plasma readily reacts upon adsorption to form volatile N_2. Thus, the evolution of the fullerene-like microstructure has to be seen as a delicate interplay of adsorbing preformed molecules, which are either incorporated in a stabilized and, thus, aligned manner or desorb via the formation of C_2N_2 if they are less favorably bonded [60].

These requirements of low to moderate energy input during growth via ion bombardment or substrate heating and in particular the existence of a predominant number of preformed molecules in the film forming flux are not only inherent to reactive magnetron sputtering, but can also be found for pulsed laser deposition [68]. Both techniques result in fullerene-like CN_x films, whereas the structured domains are much larger for magnetron sputtered films. On the other hand, if no preformed species are present in the deposition flux no structure evolution is observed as it is the case for low-energy ion beam-assisted deposition [71]. For magnetron sputtering the growth parameters such as substrate temperature, N_2 fraction, and bias voltage strongly affect the fullerene-like structure evolution in terms of extension, alignment, and cross-linking. All of the mentioned parameters primarily concern the magnitude of the chemical desorption and, thus, the selectivity incorporation sites either by influencing the ad-atom (molecule) mobility (bias, temperature) or by changing the number and type of film forming species (N_2 fraction).

The general trends in terms of deposition parameters and resulting structures are summarized in Fig. 10. According to HRTEM [44] and XPS (Fig. 5), films grown at higher temperatures (Ts > 300°C) and intermediate bias ($V_s \approx -25$ V) are all fullerene-like, since both parameters provide sufficient selectivity to incorporate most of the arriving species in an aligned fashion, regardless of the N_2 fraction. The availability of N_2, however, determines the extension and alignment of the sheets, since the dominance of preformed species at higher N_2 fractions promotes the growth of extended, well-aligned sheets resulting in an almost graphite-like appearance.

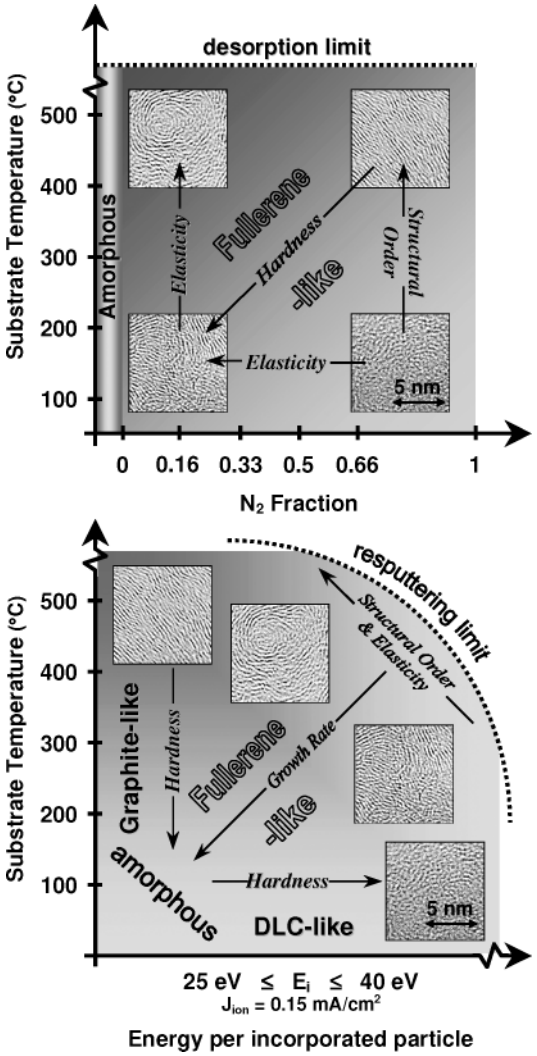

Fig. 10 Structure zone diagrams of structures and properties observed for magnetron sputtered fullerene-like CN_x thin films depending on the substrate temperature, the degree of ion bombardment, comprising the ion to neutral ratio and ion energy and the N_2 fraction in the discharge. The HRTEM plan-view inserts should be seen as representatives only [60]

At lower N_2 fractions the flux of carbon atoms becomes relevant instead and the complexity and total number of the preformed species is decreasing, which in turn leads to shorter heavily bent fullerene-like fragments. This is an effect of a lower selectivity of incorporation sites via more complex reaction pathways for the formation of C_2N_2.

If the temperature is decreased ($T < 300°C$) the ad-atom (molecule) mobility is reduced and an increasing number of preformed molecules are incorporated in an

out-of-plane orientation due to a decreased efficiency of the chemical desorption process.

This results in the amorphisation of the otherwise graphitic nature of the films grown at higher N_2 fractions. The smaller number of species arriving at lower N_2 fractions is, however, still effectively incorporated in an aligned fashion into short fragments down to a deposition temperature of 150°C.

A higher bias or ion energy, exceeding the displacement energy of carbon ($E > 30\,eV$), on the other hand induces an increasing number of defects into the growing sheets and thus decreases the fullerene-like fragment size. This is most pronounced at higher N_2 fractions, most likely due to a high sensitivity of the aligned incorporation process towards energy input (Fig. 10).

3 Mechanical and Tribological Properties

3.1 Indentation Hardness and Modulus

The mechanical properties, such as hardness and modulus, of macroscopic materials are easily determined by, e.g., tensile testing and purely plastic indentation methods [72]. These properties are also of vital importance for thin film materials. Their evaluation is, however, not straight forward mainly due to limitations in lateral dimensions and the rather small volume of the analyzed thin film material. The problem is partially overcome by depth sensing indentation techniques, where load and displacement of a sharp indenter penetrating a thin film on a substrate can be recorded on μN and nm scale [73]. In the past, however, the extreme elasticity of fullerene-like CN_x made the straightforward application of this technique rather ambiguous in terms of quantification [74,75]. In order to overcome these problems, the elastic-plastic behavior of the material was investigated in detail in [38]. The so-gained understanding allowed for the numerical evaluation of fullerene-like CN_x by novel adaptation of existing techniques [27]. However, these methods could not be applied to the extremely thin films and, thus, purely elastic indents accompanied by Hertzian modelling had to be employed [40].

Fullerene-like CN_x denotes a new class of superelastic material, due to its unique microstructure of bent and cross-linked basal planes, which extends the extraordinary strength of the sp^2-hybridized planar network in three dimensions. The detailed studies mentioned above provide the analytical tool to study the correlation between the microstructure and mechanical properties in [27]. Here, the influence of the growth conditions, such as N_2 fraction and ion energy, were investigated and it was shown that the resistance to penetration (hardness) can be varied over a wide range by increasing the number of cross-linking sites between the fullerene-like sheets by, e.g., increasing the ion energy.

Figure 11 shows two typical examples of load displacement curves for CN_x films grown at a N_2 fraction of 0.5, but for two different bias voltages. $CN_{0.18}$ grown

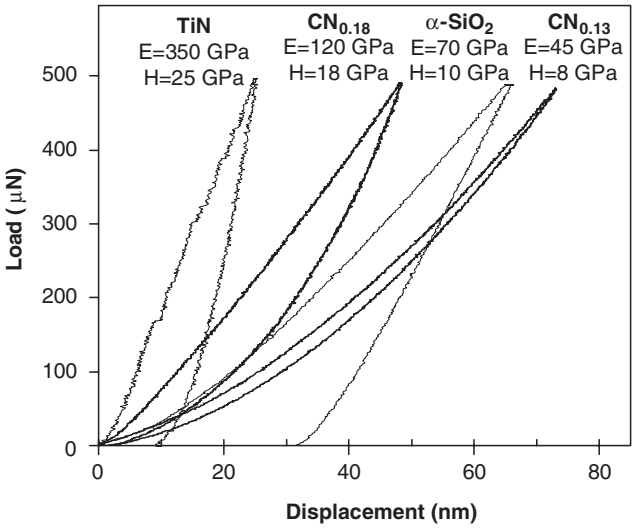

Fig. 11 Load displacement curves of two CN_x films grown at −25 V bias ($CN_{0.13}$), −40 V bias ($CN_{0.18}$), and at a N_2 fraction of 0.5 in comparison to TiN and fused silica (a-SiO_2) as reference materials [49]

at −40 V bias has a higher degree of cross-linkage and therefore exhibits a higher resistance to penetration (smaller maximum displacement) while the more graphitic-like appearance of $CN_{0.13}$ with its extended, well-aligned sheets (Fig. 10) has a fairly low resistance to penetration, due to the weak interplanar interactions via cross-links. These differences also manifest itself in lower modulus and hardness numbers. Remarkably, both films, despite their different compliance, show no or only very little tendency to plastic deformation and the indentation energy is exclusively stored elastically and released upon unload. This high elasticity is readily appreciated by comparing the residual displacement of the load displacement curves of fullerene-like CN_x to depicted reference materials such as TiN and fused silica (a-SiO_2).

Similar tendencies are observed for the dependence of H and E on the ion energy for a change in substrate temperature (Table 1). Both growth parameters basically influence the number of defects and, thus, the number of potential cross-linking sites. A lower substrate temperature increases H and E significantly; presumably by increasing the number of cross-linking sites via incorporation of out-of-plane aligned preformed species (see Section 2.3). However, this increase in cross-linking sites goes hand in hand with a decrease in extension of fullerene-like planes. This implies restrictions for elastic buckling and compression of inter planar spacing. Thus, the more resistant films grown at higher bias and lower temperatures commonly exhibit a reduced relative elastic recovery [27].

Furthermore, the microstructure and, thus, the properties of fullerene-like CN_x are also influenced by the N_2 fraction, see Fig. 10 and [27]. A pronounced fullerene-like structure synthesized at lower N_2 fraction (0.16) and a moderate bias (−25 V)

Table 1 Hardness and Modulus values determined by elastic-plastic indentations with a diamond indenter of cube corner geometry for various growth conditions. Films considered fullerene-like are underlined

		Hardness (GPa)			Modulus (GPa)		
T_s (°C)	N_2 fraction	−10 V	−25 V	−40 V	−10 V	−25 V	−40 V
	0		7			115	
150	**0.16**		**15**			**166**	
	1		10			91	
	0		**0.3**			**11**	
450	**0.16**		**10**	**18**		**75**	**120**
	1	**5**	**6**	**12**	**43**	**50**	**135**

consists of heavily bent sheets (Fig. 2), which by curling restrict their size and extension as compared to more elongated sheet structures grown at higher N_2 fractions. This implies a higher cross-linking density and thus a higher resistance to indentation, but lower relative elastic recovery.

The detailed analysis of the mechanical response of fullerene-like CN_x characterizes a new class of extremely resilient materials, where deformation energy is predominantly stored elastically. This can be understood by the cross-linked planar structure of fullerene-like CN_x, where the sheet-like domains wrap and buckle under load, while the presumed strong C–C cross-links prevent gliding. Thus, plastic deformation by mechanisms similar to graphite is inhibited. Additionally, the interplanar strength of a predominantly sp^2-hybridized material is considerable, which in turn makes plastic yielding by cracking or bond-breaking less likely. On the other hand, the rather weak intraplanar van-der-Waals forces and the large lattice spacing provides for a high compressibility, which explains the observed low to moderate resistance to penetration. Therefore fullerene-like CN_x deforms by bond angle deflection rather than breaking providing for the compression of the intraplanar lattice spacing, much like in a "superhard rubber". A similar behavior is also inherent to C60 Fullerenes, which are known to withstand extreme deformation down to 20% of their original size without yielding [76]. However, the strength in fullerene solids (fullerites) is limited due to the weak cross-linking between the molecules. This is not the case for fullerene-like CN_x where the curved sheets extend throughout the material providing for its elasticity on a macroscopic scale.

3.1.1 The Concept of Hardness for Carbon Nitride

According to [12] "Hardness is not difficult to measure, it is difficult to define." In a more general sense, hardness is defined as resistance of a material to deformation under external load, which permanently affects the surface by plastic deformation. Thus, the conventional hardness concept has to be applied with great care for extremely elastic materials, such as fullerene-like CN_x. For instance, TiN is perceived as a

hard material with a low tendency to plastic deformation, due to its much higher hardness number compared to CN_x (Fig. 11). Contrary to TiN, CN_x leaves no residual imprint and can therefore be considered much tougher, since it exhibits a lower tendency to plastic deformation, despite its higher compliance. This leads to ambiguities in the common understanding of "hardness" and, therefore, the indentation response of fullerene-like CN_x is best seen, as the one of a superhard elastomer, whereas the hardness number becomes less meaningful [38].

3.2 Tribology of Carbon Nitride

Since the beginning of the 1990s carbon nitrides have been discussed as a potential material for many tribological uses because of their particular mechanical properties [19,77,78]. Although the synthesis of single-phase crystal films remains an open challenge, amorphous CN_x with low concentrations are already industrially applied [79] and many patents of products using CN_x films have been claimed [80].

There are several studies on the wear rate and friction coefficient of CN_x films, as reviewed recently by Broitman et al. [79]. Although many researchers have accounted for improved properties in terms of wear resistance in comparison to DLC films, there is an apparent contradiction in the results published by different authors regarding an increase, no change, or decrease of the friction coefficient with the incorporation of nitrogen in the films [79]. Furthermore, a large spread of friction values for CN_x films ($x > 0$) has been reported, from 0.08 up to 0.45 or more (see [79] and references therein). These apparently contradictory results arise from the difficulty to correlate the published properties of CN_x films with their tribological behavior, due to differences in microstructure (generally the structural characterization of the materials has been lacking) and the lack of standardization of tribological tests.

3.2.1 Tribological Properties of Fullerene-like Carbon Nitride

The outstanding mechanical properties, in particular the high compliance, predict fullerene-like CN_x to be a promising candidate as a tribological coating [79]. Its high hardness-to-modulus ratio is descriptive for a superelasticity (Table 2) and is as such the delimiting factor in the so-called plasticity index describing the compliance of a material [81]. The extremely high H/E ratio suggests that asperities in a tribological contact are likely to behave elastic [38,82]. This is of crucial importance; since microscopic asperities are present for all technological surfaces and as such bear the load in a tribological contact. Their total area, however, is only a fraction of the nominal contact area, which results locally in extreme pressures. Under these conditions, commonly used hard thin film materials are likely to behave in a brittle manner, which might result in abrasive wear debris. Fullerene-like CN_x on the other hand is highly compliant (see Section 3.2) and, thus, the contact pressure is dissipated.

Table 2 Moduli and hardness numbers of some reference materials compared to two CN_x films grown at 25 eV ($CN_{0.13}$) and 40 eV ($CN_{0.18}$) alongside with their H/E ratio. A ratio exceeding 0.15 indicates a superelastic behavior

	Hard and Brittle			Plastic	Elastic	Super Elastic	
	Diamond[a)]	Al_2O_3[b)]	TiN thin film[b)]	HSS*[)a)]	DLC thin film[b)]	$CN_{0.18}$[b)]	$CN_{0.13}$[b)]
H (GPa)	80	23	25	9	10–20	18	7
E (GPa)	1050	320	350	250	100–200	120	37
H/E	**0.076**	**0.072**	**0.071**	**0.036**	**≈ 0.1**	**0.15**	**0.19**

[a]taken from [83]; [b]measured data; *high speed steel

Furthermore, the rather low modulus (E < 200 GPa) of fullerene-like CN_x suggests that the macroscopic contact stresses are dissipated over larger volumes compared to hard coatings with higher moduli (250 GPa < E < 450 GPa). This in turn reduces stress discontinuities along the film-substrate interface and, thus, prevents substrate deformation. Additionally, the shear stresses along the interface plane for a strained substrate-coating system are also reduced, which might be beneficial for the adhesion of the film under load [84].

3.2.2 Friction and Wear of Fullerene-like CN_x

The friction and wear rate of fullerene-like CN_x films have been tested and benchmarked to the behavior of amorphous CN_x as well as graphitic and diamond-like carbon films by different authors [79, 85–87].

A pin-on-disk equipment with ball-bearing steel balls has been used by Broitman et al. to measure the friction coefficient in ambient atmosphere (22°C and a relative humidity of 35%) [79]. The friction coefficient, $\propto$, as a function of sliding cycles has been studied for a-CN_x (Fig. 12) and FL-CN_x (Fig. 13). While the friction coefficient of Si is around 0.75, those of the films prepared at low temperature (amorphous) have an increasing value of $\propto$ from 0.19 (for pure C) to 0.45 (for $CN_{0.35}$). When the films are deposited at higher temperature (fullerene-like structure), the friction coefficient increases from 0.24 to 0.27. In both cases, friction coefficient tends to increase as the nitrogen content in the film is increased. It was found that the friction coefficient as a function of sliding cycles is characterized by two stages: an initial stage of high friction followed by a second steady-state stage of reduced friction coefficient (Figs. 12 and 13). In the initial stage, the friction coefficient is controlled by film roughness and the build-up of a transfer layer (tribolayer) and in the second stage the friction and wear are controlled by the nature of the tribolayer [79]. The extent of the first stage and the variation of the friction coefficient depend on the amount of nitrogen in the film. In the case of C films, the first stage takes only some few revolutions, but for the films containing nitrogen, the first stage takes more revolutions because the lower roughness and higher hardness of the films make it more difficult to generate enough material to

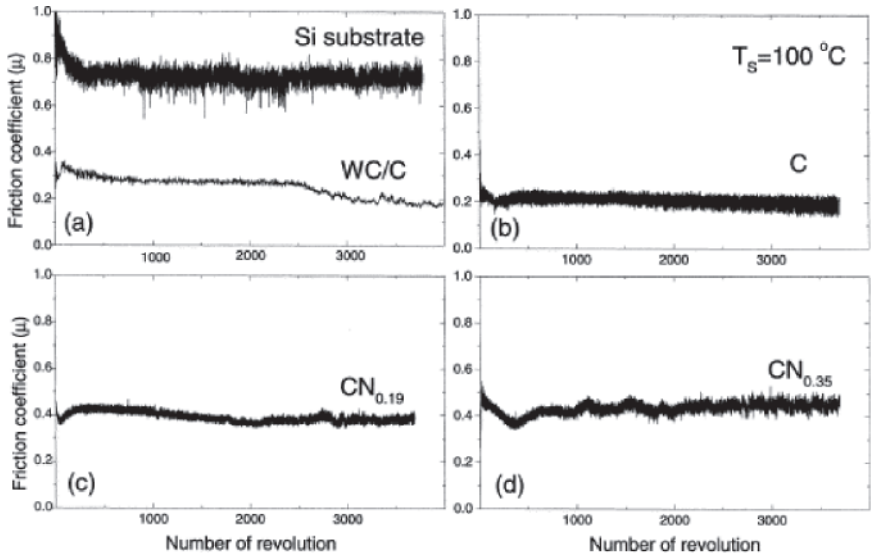

Fig. 12 Friction coefficient (μ) against ball bearing steel versus number of sliding cycles for a-CN_x films deposited on Si at T_S = 100°C. The friction coefficient for the Si substrate and a commercial WC/C coating are also indicated [79]

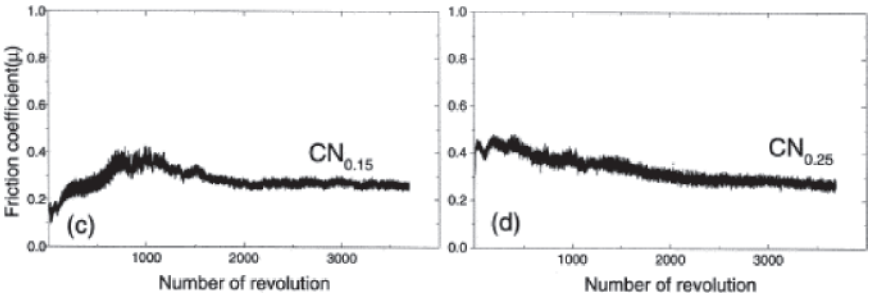

Fig. 13 Friction coefficient (μ) against ball bearing steel versus number of sliding cycles for FL-CN_x films deposited on Si at T_S = 350°C [79]

form a tribolayer. Furthermore, the slight increase of the steady-state friction coefficient with the incorporation of nitrogen in the film can also be related to the decrease in roughness [79].

The coating wear rates of amorphous and fullerene-like carbon nitride films were also measured and compared to a commercial WC/C coating. The wear rate was determined from the wear groves of the pin-on-disk experiments by an optical profilometer. Fig. 14 shows that CN_x films grown at low temperature (amorphous) have an apparently lower wear rate than the FL-CN_x films. However, SEM analysis of the wear tracks exhibits a different appearance. The amorphous carbon film

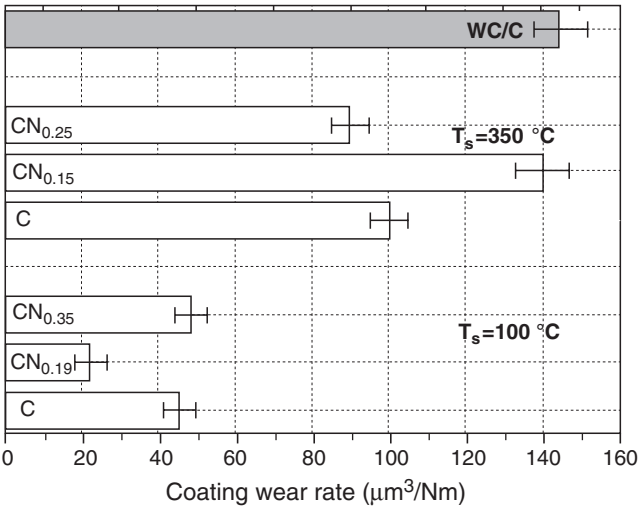

Fig. 14 Coating wear rate for a-CN_x films (T_s = 100°C) and FL-CN_x films (T_s = 350°C). The coating wear rate of a commercial WC/C film is also indicated [79]

appears mechanically damaged, with the presence of pits, while the wear track of the FL-CN_x has a very flat surface with no apparent damages. The presence of N in the films inhibits the formation of extended cracks and pits; As a consequence, the comparison of wear rates reported in Fig. 14 among films with and without nitrogen are not relevant. Recently Voevodin et al. have also informed the presence of mirror-polished wear tracks for FL-CN_x films grown by pulsed-laser deposition [87].

A different approach was done by Neidhardt et al. [86]. Reciprocal sliding was chosen as contact geometry, where a coated substrate moves relative to a sapphire counterpart. The transparent sapphire sphere allowed for in situ visualization and Raman spectroscopy in order to elucidate the eventual formation of transfer layers. The tribochemistry between two counterparts in respect to the formation of debris and transfer layers depends strongly on the composition of the surrounding gas and the dissipated energy in the contact [88,89]. The friction coefficient, defined as the tangential/normal force ratio, was recorded by a lateral force sensor.

The coefficient of friction for fullerene-like CN_x for the above-described setup and under an average contact pressure of 0.7 GPa is with approximately 0.2 ± 0.05 slightly higher than the values for pure carbon films (0.15 ± 0.02), while no difference is observed for amorphous CN_x (Fig. 15). These values can be considered low in comparison to the friction coefficient of, e.g., Si (0.6) and TiN (0.7) under similar conditions. A low coefficient of friction is desired for a tribological contact not only because it increases the system effectiveness, but most importantly it also reduces the thermal energy dissipated in the asperities, which prevents them from, e.g., oxidizing [90]. Furthermore, a dependence on the humidity of the surrounding atmosphere is observed (Fig. 15), while no correlation in between the friction coefficient and hardness (resistance to penetration) can be detected [86]. This alongside with the

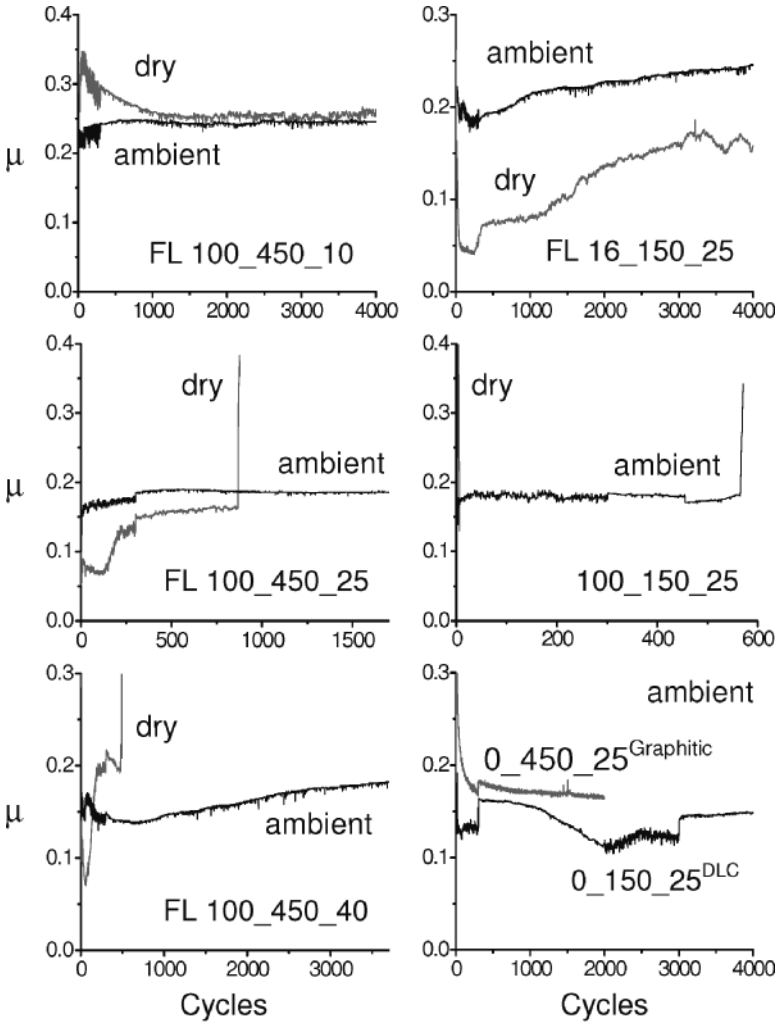

Fig. 15 Friction curves of fullerene-like (FL) and amorphous CN_x compared to pure carbon films tested in dry and ambient air. The nomenclature as in e.g., 100_450_25 reads [N_2(%)_Ts(°C)_VB(V)] [86]

unsteady friction traces as seen in Fig. 15 indicates the formation of third bodies in the tribological contact [91].

In ambient air, the wear rate of fullerene-like CN_x is significantly lower compared to amorphous CN_x (100_150_25) and carbon films (0_150_25, 0_450_25) (Fig. 16). Most remarkably the wear rates of fullerene-like CN_x in ambient air are almost constant despite the dramatic difference in hardness ranging from 5 to 15 GPa depending on the synthesis conditions. For dry conditions, the wear rates are higher, and scale with the hardness of the films (Fig. 16). This indicates that for

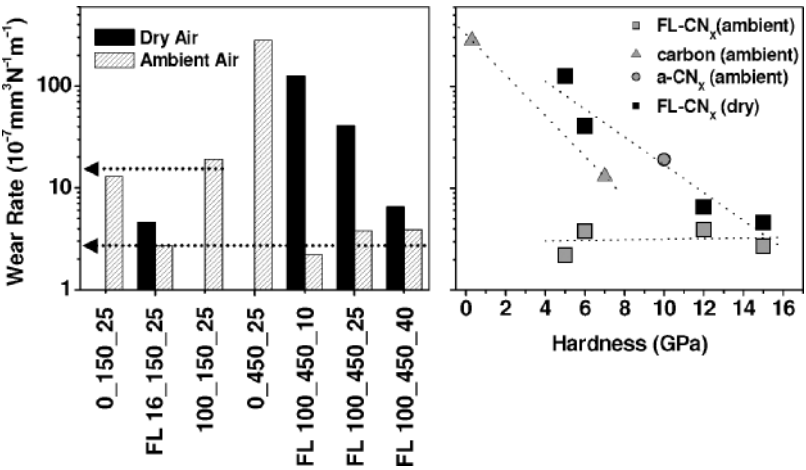

Fig. 16 Wear rates of various fullerene-like (FL) and amorphous CN_x as well as carbon films for sliding in dry and ambient air. In the right graph the relation to the hardness is plotted for the three groups of films. The hardness independent wear rate for ambient sliding of fullerene-like CN_x is indicated by the horizontal line (guide to the eye only) [86]

ambient sliding either thin transfer layers might have formed or that the reactive surface sites of CN_x were passivated by reactions with ambient moisture. Both effects result in the separation of the two bulk counterparts and, thus, the wear rate is not solely based on the mechanical properties of the film anymore. During dry sliding, however, eventually formed transfer layers break up and the initially low coefficient of friction is increasing and wear accelerates as seen by the unsteady friction traces for dry sliding in Fig. 15.

The tribological properties of fullerene-like CN_x films deposited on orthopedic substrates have also been studied by Broitman et al. [85]. The effect on the coating and substrates of immersion in biological fluids was investigated in three different solutions. Specimens were incubated for 16 days at a temperature of 50°C in:

- *W: distilled H_2O + NaN_3 (1.6×10^{-3}%)*
- *H: Hanks balanced buffer + NaN_3 (1.6×10^{-3}%)*
- *S: 50% human serum + Hanks balanced buffer + NaN_3 (1.6×10^{-3}%)*

Nanoindentation studies after the three aqueous treatments have shown a change in the mechanical properties of the films (Table 3). The maximum penetration depth and the elastic recovery decrease, with the smaller change in the solution W and the bigger variation in the solution H. These changes were correlated to changes in the composition (decrease of nitrogen concentration) suggesting that some N is lost from the sp^3-coordinated carbon. To our knowledge, there are no other reported studies on the change of mechanical properties or chemical composition of DLC or CN_x films due to reaction with aqueous solutions. Furthermore, no results on the probable degradation of carbon-based thin films on biological solutions can be found in the literature.

Table 3 Nanoindentation results, showing the maximum penetration depth h_{max} (nm)at 5 mN maximum load, and the elastic recovery %R (%)for the as-deposited films and after treatment in three solutions: water (W); Hanks buffer (H); and human serum (S). The data of the substrates are also indicated [85]

		As-deposited	After treatment in			Substrate
			W	S	H	
CN_X/Ti	h_{max}	144	151	165	169	284
	%*R*	81	78	74	73	30
CN_X/ZrO_2	h_{max}	116	140	170	195	119
	%*R*	79	65	62	59	59

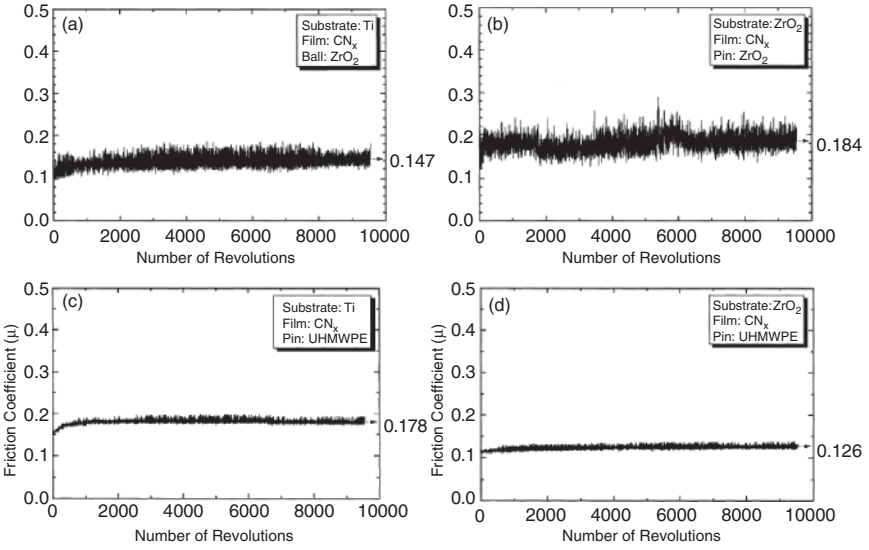

Fig. 17 Friction coefficient (μ) versus number of sliding cycles (wet testing human serum) for FL-CN_x films: (a) Ti substrate, ZrO_2 ball; (b) ZrO_2 substrate, ZrO_2 ball; (c) Ti substrate, UHMWPE ball; (d) ZrO_2 substrate, UHMWPW ball [85]

Broitman et al. measured the friction coefficients of FL-CN_x films by a pin-on-disk equipment using high speed steel (HSS), ZrO_2 and ultrahigh molecular weight polyethylene (UHMWPE) balls [85]. The films were deposited on two different substrates: Ti and ZrO_2. The evaluation of the friction coefficient with human serum as lubricant was carried out for samples treated with solution *S*. In the case of wet sliding against a ZrO_2 ball, the steady state friction coefficient values are 0.15 on a coated Ti substrate and 0.18 on a coated ZrO_2 substrate (Fig. 17 a, b). When an UHMWPE ball is used, friction coefficient values are 0.18 for the coated Ti and 0.13 for the coated ZrO_2 substrate (Fig. 17 c, d). There are no other reported studies on the friction coefficient of carbon-based materials with human serum as lubricant; the values from Fig. 17 could be considered acceptable for orthopedic applications [92].

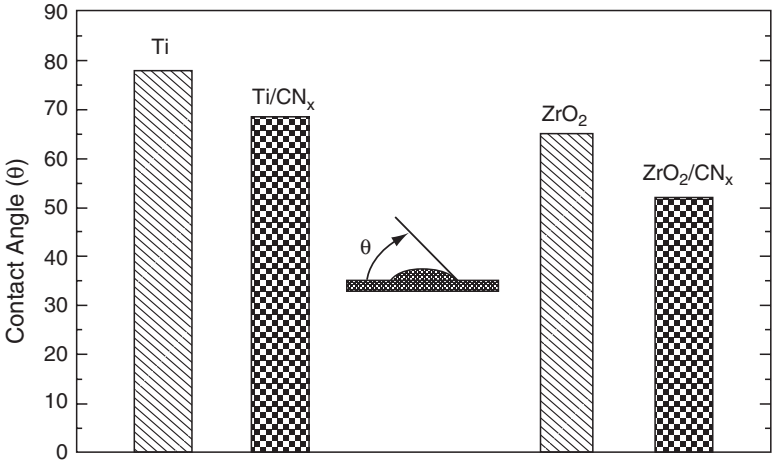

Fig. 18 Contact angle of human serum for FL-CN_x films deposited on Ti and ZrO_2 substrates [85]

Figure 18 shows the decrease in the contact angle (θ) of human plasma for FL-CN_x films compared to Ti and ZrO_2 substrates. When a Ti substrate is coated, the contact angle decreases from 77° to 68° and when ZrO_2 substrate is coated, θ decreases from 65° to 52°. The difference in contact angle between the two coated surfaces may be attributed to the difference in surface roughness. The increase in wettability on coated FL-CN_x bearing surfaces, due probably to a change in the polar part of the surface energy [85], can help to enhance the retention of synovial fluid on those surfaces, improving the lubrication of the bearings of total joint arthroplasty components during function. With increased wettability of the surfaces, the retention of fluid-film or hydrodynamic lubrication in the articulating area would be improved and the onset of boundary lubrication and other less favorable bearing conditions would be delayed.

Amorphous carbon nitride has replaced DLC as protective coating on hard disks and recorder heads, which is an indication of its advantageous mechanical and tribological properties [26,49]. Recently, it has been proposed to use FL-CN_x films on hard magnetic storage media [93]. A quartz crystal microbalance was used to probe the adsorption of water on DLC, a-CN_x, and FL-CN_x films.

Figure 19 shows the adsorption of water versus the water vapor pressure for films deposited under different conditions (a-C_{sp2} denotes an amorphous carbon film with a high content of sp^2 bonds) [93]. For comparison, the adsorption of water on a commercial overcoat (a-CH_y) is also indicated. All films show a characteristic dependence of water coverage on the H_2O vapor pressure. There are, however, differences in the amounts of the adsorbed water. We can classify the films into three different groups. A first group of films, FL-CN_x and a-C_{sp2}, show the lower adsorption rate. Taking into consideration one monolayer coverage is roughly 30 ng/cm^2 (cf. Section 3.2.1) and that at room temperature 1.33×10^3 Pa of H_2O vapor pressure is equivalent to 50% RH, these films adsorb less than 2 ML of water

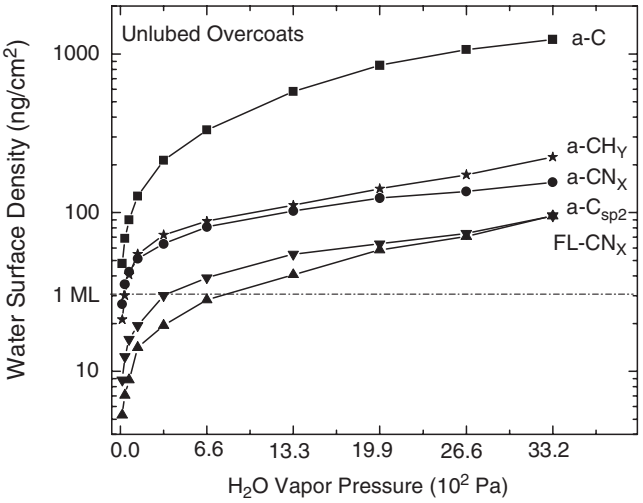

Fig. 19 The mass of water adsorbed on the surface of quartz crystal with unlubricated carbon overcoats at 50°C versus pressure. The dotted line indicates the value of 1 ML of H_2O on the surface [93]

on their surface at that pressure. A second group of films, a-CN_x and the commercial a-CH_y, have adsorbed roughly 2–3 times more water than the first group. Finally, the film a-C adsorbs more than 14 times the amount adsorbed by FL-CN_x. Similar results have been found for films lubricated with Z-tetraol, a lubricant used in hard disk devices. The results have demonstrated that water adsorption of fullerene-like carbon nitride films is lower than carbon-based films used in magnetic media. Taking into consideration their superior tribological properties, FL-CN_x overcoats have a potential application in the hard disk industry.

4 Concluding Remarks

Fullerene-like CN_x is shown to be an inherently nanostructured material consisting of bent and cross-linked predominantly sp^2-hybridized graphene planes. The incorporation of sp^2-hybridized nitrogen, either substitutional for carbon in a graphene network or in a pyridine-like manner, induces bending by formation of pentagons and initiates cross-linking, while a cross-linking mechanism on the C sp^3 site still cannot be ruled out. Although low ion-assist energies are generally beneficial for film growth by enhancing ad-atom mobility at relatively low substrate temperatures, it has been shown that it is not the structure-determining factor in case of fullerene-like CN_x films. Instead the flux of preformed C_xN_y ($x,y \leq 2$) species, originating from a self-modified C target surface that acts as a virtual CVD source under N-ion bombardment, is a crucial aspect for understanding the evolution of fullerene-like structures. That is because these species are stabilized by multiple bonding on the

C and N side upon aligned incorporation during growth and, thus, contribute directly to the evolution of sheet structures. Furthermore, the formation of volatile CN species namely C_2N_2 is also active on the substrate side and provides for selective etching of misaligned molecules by reaction with adsorbed CN and subsequent desorption. Thus, the evolution of the fullerene-like microstructure has to be seen as a delicate interplay of adsorbing preformed molecules, which are either incorporated in a stabilized and, thus, aligned manner or desorb via the formation of C_2N_2 if they are less favorably bonded.

The mechanical deformation of fullerene-like CN_x thin films is in general determined by, the rather weak van-der-Waals interactions between the planes and interplanar cross-links. The fairly large (0.35 nm) interplanar spacing is easily compressed under stress, whereas interplanar slip, as it is limiting the strength of graphite, is hindered due to the strong alleged C–C cross-linking and mechanical interlocking. Hence, fullerene-like CN_x is an extremely resilient material where deformational stresses are dissipated over large volumes. The likeliness of bond breaking and slip is reduced enabling the structure to recover after unload. Therefore, one can imagine the deformation mechanism like the reaction of a nanostructured polymeric sponge of great intraplanar strength upon compression, where the walls buckle without rupturing or breaking. It is concluded that on a macroscopic scale, fullerene-like CN_x exhibits a fairly low resistance to indentation (high compliance) combined with a comparatively low modulus. It also shows very little tendency to plastic deformation.

This superior resiliency to deformation makes asperities in a tribological contact more likely to deform elastic. Hence, brittle fracture is hampered giving rise to possible applications in especially abrasive environments. Furthermore, the low modulus might be also of importance for thin film applications, since it dissipates the contact stresses over large volumes making adhesive failures of the film-substrate system less likely, due to reduced stress gradients at the interface. The above-mentioned facts lead to a reduced wear compared to amorphous CN_x or pure carbon. This in combination with the rather low coefficient of friction makes fullerene-like CN_x a promising candidate for tribological applications, while the process control provides for tailoring the mechanical properties.

Acknowledgements E. Broitman acknowledges the National Science Foundation, Award Nr. 0408574 "Vapor Lubrication of Magnetic Data Storage". J. Neidhardt and L. Hultman acknowledge the European Commission and The Swedish Foundation for Strategic Research (SSF), Center in Materials Science for Nanoscale Surface Engineering. The authors acknowledge Isabell Arce-Garcia, Steven J. Bull, Zsolt Czigány, Raul Gago, Andy Gellman, Niklas Hellgren, Brian Holloway, Hans Sjöström, Sven Stafström, Jan-Eric Sundgren, Jon Molina-Aldareguia, Irwin Singer for valuable discussions.

References

1. Hellgren, N., Sputtered Carbon Nitride Thin Films, in Thesis, IFM, Linköping University, Sweden (1999).
2. Franklin, E. C., The Ammono Carbonic Acids. J. Am. Chem. Soc. (1922), 44: 486–509.

3. Pauling, L. and Sturdivant, J. H., The Structure of Cyameluric Acid, Hydromelonic Acid, and Related Substances. Proc. Natl. Acad. Sci. (1937), 23: 615–620.
4. DeVries, R. C., Inventory on Innovative Research: The Case of C3N4. Mat. Res. Innovat. (1997), 1: 161–162.
5. Cuomo, J. J., Leary, P. A., Yu, D., Reuter, W., and Frisch, M., Reactive Sputtering of Carbon and Carbide Targets in Nitrogen. J.Vac. Sci. Technol. (1979), 16(2): 299–302.
6. Han, H. X. and Feldman, B. J., Structural and optical properties of amorphous carbon nitride. Sol. State Commun. (1988), 65(9): 921–923.
7. Han, H. X. and Feldman, B. J., Structural, optical, and electrical properties of amorphous hydrogenated carbon nitride. Materials Research Society Symposium Proceedings (1987), 95: 347–352.
8. Sung, C. M. and Sung, M., Carbon nitride and other speculative superhard materials. Mater. Chem. Phys. (1996), 43(1): 1–28.
9. Cohen, M. L., Calculation of bulk moduli of diamond and zinc-blende solids. Phys. Rev. B (1985), 32: 7988–7991.
10. Liu, A. Y. and Cohen, M. L., Prediction of new low compressibility solids. Science (1989), 245(4920): 841–842.
11. Liu, A. Y. and Cohen, M. L., Structural properties and electronic structure of low-compressibility materials: β-Si_3N_4 and hypothetical β-C_3N_4. Phys. Rev. B (1990), 41(15): 10727–10734.
12. Teter, D. M., Computational alchemy: the search for new superhard materials. MRS Bull. (1998), 23(1): 22–27.
13. Carbon nitride seen out-muscling diamonds. American Metal Market, June 10, 1992.
14. Diamonds may no longer be hardest substance – carbon nitride. American Metal Market, July 28, 1993.
15. As hard as diamond? Tracking the elusive carbon nitride. Science News, July 11, 1998.
16. A new route to a superhard material? Science News, June 5, 1999.
17. Harder Than Diamond Is Not Faster Than Light. Discover (1993), 14(11): 132–133.
18. Muhl, S. and Mendez, J. M., A review of the preparation of carbon nitride films. Diamond Relat. Mater. (1999), 8(10): 1809.
19. Wang, E. G., Research on carbon nitrides. Prog. Mater. Sci. (1997), 41(5): 241.
20. Kroke, E. and Schwarz, M., Novel group 14 nitrides. Coord. Chem. Rev. (2004), 248: 493–532.
21. DeVries, R. C., Inventory on Innovative Research: The Case of C_3N_4. Mater. Res. Innovations (1997), 1(3): 161.
22. Malkow, T., Critical observations in the research of carbon nitride. Mater. Sci. Eng. A (2001), 302(2): 311.
23. Matsumoto, S., Xie, E. Q., and Izumi, F., On the validity of the formation of crystalline carbon nitrides, C_3N_4. Diamond and Relat. Mater. (1999), 8(7): 1175.
24. Badzian, A., Badzian, T., Roy, R., and Drawl, W., Silicon carbonitride, a new hard material and its relation to the confusion about "harder than diamond" C_3N_4. Thin Solid Films (1999), 354: 148–153.
25. Sjostrom, H., Stafstrom, S., Boman, M., and Sundgren, J. E., Superhard and elastic carbon nitride thin films having fullerene-like microstructure. Phys.l Rev. Lett. (1995), 75(7): 1336.
26. Neidhardt, J., Broitman, E., and Hultman, L., Fullerene-Like Carbon Nitride: A New Thin Film Material. Wide bandgap materials and new developments, (ed.) M. Syväjärvi and R. Yakimova. October 2006, Singapore: Research Signpost.
27. Neidhardt, J., Czigany, Z., Brunell, I. F., and Hultman, L., Growth of fullerene-like carbon nitride thin solid films by reactive magnetron sputtering; role of low-energy ion irradiation in determining microstructure and mechanical properties. J Appl. Phys. (2003), 93(5): 3002.
28. Alexandrou, I., Scheibe, H.-J., Kiely, H.-J., Papworth, C. J., G. A., A., and Schultrich, B., Carbon films with an sp2 network structure. Phys. Rev. B (2003), 60: 10903–10907.
29. Johansson, M. P., Sjostrom, H., and Hultman, L., HREM and nanoindentation studies of BN: C films deposited by reactive sputtering from a B4C target. Vacuum (1999), 53(3–4): 451.

30. Strout, D. L., Structure and Stability of Boron Nitrides: Isomers of $B_{12}N_{12}$. J. Phys. Chem. A (2000), 104: 3364–3366.
31. Chhowalla, M. and Amaratunga, G. A. J., Thin films of fullerene-like MoS2 nanoparticles with ultra-low friction and wear. Nature (2000), 407: 164–167.
32. Avivi, S., Mastai, Y., and Gedanken, A., A New Fullerene-like Inorganic Compound Fabricated by the Sonolysis of an Aqueous Solution of $TlCl_3$. J. Am. Chem. Soc. (2000), 122: 4331–4334.
33. Seifert, G., Terrones, H., Terrones, M., and Frauenheim, T., Novel NbS_2 metallic nanotubes. Sol. State Commun. (2000), 115: 635–638.
34. Rothschild, A., Sloan, J., and Tenne, R., Growth of WS_2 Nanotubes Phases. J. Am. Chem. Soc. (2000), 122: 5169–5179.
35. Johansson, A., Charge Dinamics and Electronic Structure of pi-Conjugated Systems, in thesis, IFM, Linköping University, Sweden (2002).
36. Porterfield, W. W., Inorganic Chemistry - A Unnified Approach (1993), London: Academic Press.
37. Stafstrom, S., Reactivity of curved and planar carbon–nitride structures. Appl. Phys. Lett. (2000), 77: 3941–3943.
38. Garcia, I. A., G.-Berasategui, E., Bull, S. J., Page, T. F., Neidhardt, J., Hultman, L., and Hellgren, N., How hard is fullerene-like CN_x Some observations from the nanoindentation response of a magnetron-sputtered coating. Philos. Mag. A ()2002), 82(10 SPEC): 2133.
39. Broitman, E., Hellgren, N., Neidhardt, J., Brunell, I., and Hultman, L., Electrical Properties of Carbon Nitride Thin Films: Role of Morphol. Hydrogen Content (2002), 31(9): L11-L15.
40. Neidhardt, J., Hogberg, H., and Hultman, L., Cryogenic deposition of carbon nitride thin solid films by reactive magnetron sputtering; suppression of the chemical desorption processes. Thin Solid Films (2004), 478(1–2): 34–41.
41. Robertson, J., Diamond-like amorphous carbon. Mater. Sci. Eng. R (2002), 37: 129–153.
42. Hellgren, N., Johansson, M. P., Hjorvarsson, B., Broitman, E., Ostblom, M., Liedberg, B., Hultman, L., and Sundgren, J. E., Growth, structure, and mechanical properties of CN_xH_y films deposited by dc magnetron sputtering in $N_2/Ar/H_2$ discharges. J. Vac. Sci. and Technol. A (2000), 18(5): 2349.
43. Gammon, W. J., Kraft, O., Reilly, A. C., and Holloway, B. C., Experimental comparison of N(1s) X-ray photoelectron spectroscopy binding energies of hard and elastic amorphous carbon nitride films with reference organic compounds. Carbon (2003), 41(10): 1917–1923.
44. Neidhardt, J., Hultman, L., and Czigany, Z., Correlated high resolution transmission electron microscopy and X-ray photoelectron spectroscopy studies of structured CNx ($0 < x < 0.25$) thin solid films. Carbon (2004), 42(12–13): 2729.
45. Rodil, S. E., Bonding structure in carbon nitride films. Rec. Res. Dev. Appl. Phys. (2003), 6(1): 391–426.
46. Hellgren, N., Guo, J., Sathe, C., Agui, A., and Nordgren, J., Nitrogen bonding structure in carbon nitride thin films studied by soft x-ray spectroscopy. Appl. Phys. Lett. (2001), 79(26): 4348–4350.
47. Gammon, W. J., Hoatson, G. L., Holloway, B. C., Vold, R. L., and Reilly, A. C., Bonding in hard and elastic amorphous carbon nitride films investigated using 15N, 13C, and 1H NMR spectroscopy. Phys. Rev. B (2003), 68(19): 195401.
48. Hellgren, N., Nian, L., Broitman, E., Serin, V., Grillo, S. E., Twesten, R., Petrov, I., Colliex, C., Hultman, L., and Sundgren, J. E., Thermal stability of carbon nitride thin films. Journal of Mater. Res. (2001), 16(11): 3188.
49. Hultman, L., Neidhardt, J., Hellgren, N., Sjostrom, H., and Sundgren, J. -E., Fullerene-like carbon nitride: A resilient coating material. MRS Bulletin (2003), 28(3): 194.
50. Ferrari, A. C., E., R. S., and Robertson, J., Interpretation of infrared and Raman spectra of amorphous carbon nitrides. Phys. Rev. B (2003), 67: 155306.
51. Gago, R., Jiménez, I., Neidhardt, J., Abendroth, B., Caretti, I., Hultman, L., and Moller, W., Correlation between bonding structure and microstructure in fullerene-like carbon nitride thin films. Phys. Rev. B (2005), 71: 125414.

52. Gago, R., Jiménez, I., Albella, J. M., Climent-Font, A., Caceres, D., Vergara, I., Banks, J. C., Doyle, B. L., and Terminello, L. J., Bonding and hardness in nonhydrogenated carbon films with moderate sp3 content. J. Appl. Phys. (2000). 87(11): 8174–8180.
53. Jimenez, I., Gago, R., Albella, J. M., and Terminello, L. J., X-Ray absorption studies of bonding environments in graphitic carbon nitride. Diamond Relat. Mater (2001), 10(3–7): 1170–1174.
54. Hultman, L., Stafstrom, S., Czigany, Z., Neidhardt, J., Hellgren, N., Brunell, I. F., Suenaga, K., and Colliex, C., Cross-linked nano-onions of carbon nitride in the solid phase: existence of a novel $C_{48}N_{12}$ aza-fullerene. Phys. Rev. Lett. (2001), 87(22): 225503.
55. Stafstrom, S., Reactivity of curved and planar carbon-nitride structures. Appl. Phys. Lett. (2000), 77(24): 3941.
56. Kerford, M. and Webb, R. P., Desorption of molecules by cluster impact: A preliminary molecular dynamics study. Nucl. Instrum. Methods Phys. Res., Sect. B (2001), 180: 44–52.
57. Soifer, Y. M., Kobelev, N. P., and Levin, V. M., Internal friction and elastic properties of the high pressure-induced phases of solid C_{60}. J. Alloys Compd. (2000), 310(1–2): 292–299.
58. Talyzin, A. V., Dubrovinsky, L. S., Oden, M., and Jansson, U., Superhard and superelastic films of polymeric C60. Diamond Relat. Mater. (2000), 10(11): 2044–2048.
59. Brown, C. M., Cristofolini, L., Kordatos, K., Prassides, K. B., C., Gonzalez, R., M., K.-K., Wudl, F., and Cheetham, A. K., Crystal Structure of Azafullerene ($C_{48}N_{12}$). Chem. Mater. (1996), 8(11): 2548–2550.
60. Neidhardt, J., Fullerene-Like Carbon Nitride Thin Solid Films, in Ph.D. thesis, IFM, Linköping University, Sweden (2004).
61. Townsend, S. J., Lenosky, T. J., Muller, D. A., Nichols, C. S., and Elser, V., Negatively curved graphitic sheet model of amorphous carbon. Phys. Rev. Lett.,69(6): 921–924.
62. Gueorguiev, G. K., Neidhardt, J., Stafstrom, S., and Hultman, L., First-principles calculations on the curvature evolution and cross-linkage in carbon nitride. Chemical Phys. Lett. (2005), 410(4–6): 228.
63. Neidhardt, J., Hultman, L., Abendroth, B., Gago, R., and Moller, W., Diagnostics of a N_2/Ar direct current magnetron discharge for reactive sputter deposition of fullerene-like carbon nitride thin films. J. Appl. Phys. (2003), 94(11): 7059.
64. Boyd, K. J., Marton, B., Todorov, S. S., Al-Bayati, A. H., Kulik, J., Zuhr, R. A., and Rabalais, J. W., Formation of C-N thin films by ion beam deposition. J.Vac. Sci. Technol. A (1995), 13(4): 2110–2122.
65. Vlcek, J., Rusnak, K., Hajek, V., and Martinu, L., Reactive magnetron sputtering of CNx films: Ion bombardment effects and process characterization using optical emission spectroscopy. J. Appl. Phys. (1999), 86(7): 3646–3654.
66. Hellgren, N., Johansson, M. P., Broitman, E., Sandstrom, P., Hultman, L., and Sundgren, J. -E., Effect of chemical sputtering on the growth and structural evolution of magnetron sputtered CNx thin films. Thin Solid Films (2001), 382(1–2).
67. Kaltofen, R., Sebald, T., and Weise, G., Plasma diagnostic studies to the carbon nitride film deposition by reactive r.f. magnetron sputtering. Thin Solid Films (1996), 290–291: 112–119.
68. Voevodin, A. A., Jones, J. G., Zabinski, J. S., and Hultman, L., Plasma characterization during laser ablation of graphite in nitrogen for the growth of fullerene-like CNx films. J. Appl. Phys. (2002), 92(2): 724.
69. Todorov, S. S., Marton, D., Boyd, K. J., H., A.-B. A., and Rabalais, J. W., Computer simulation of the ion beam deposition of binary thin films: carbon nitride and boron carbide. J.Vac. Sci. Technol. A (1994), 12(6): 3192–3199.
70. Gueorguiev, G. K., Neidhardt, J., StafstrAm, S., and Hultman, L., First-principles calculations on the role of CN precursors for the formation of fullerene-like carbon nitride. Chemical Phys. Lett. (2005), 401(1–3): 288.
71. Gago, R., Neidhardt, J., Vinnichenko, M., Kreissig, U., Czigany, Z., Kolitsch, A., Hultman, L., and Moller, W., Synthesis of carbon nitride thin films by low-energy ion beam assisted evaporation: On the mechanisms for fullerene-like microstructure formation. Thin Solid Films (2005), 483(1–2): 89–94.

72. Shackelford, J. F., Introduction to Materials Science for Engineers (2000), Prentice-Hall, New York.
73. Bunshah, R. F., Handbook of Hard Coatings (2001), Noyes Publications, New Jersey.
74. Sjostrom, H., Hultman, L., Sundgren, J. -E., Hainsworth, S. V., Page, T. F., and Theunissen, G. S. A. M., Structural and mechanical properties of carbon nitride CNx ($0.2 < x < 0.35$) films. J. Vac. Sci. Technol. A (1996), 14(1): 56–62.
75. Hellgren, N., Johansson, M. P., Broitman, E., Hultman, L., and Sundgren, J. -E., Role of nitrogen in the formation of hard and elastic CNx thin films by reactive magnetron sputtering. Phys. Rev. B (1999), 59(7): 5162–5169.
76. Webb, R. P. and Kerford, M., The computer simulation of the scattering of fullerenes from a graphite surface. Energy partitioning and vibrational spectra. Nucl. Instrum. Methods Phys. Res., Sect. B (2001), 180: 32–36.
77. Bull, S. J., Tribology of carbon coatings: DLC, diamond and beyond. Diamond Relat. Mater. (1995), 4(5–6): 827.
78. Grill, A. and Patel, V., Tribological properties of diamond-like carbon and related materials. Diamond Relat. Mater. (1993), 2(5–7): 597–605.
79. Broitman, E., Hellgren, N., Wanstrand, O., Johansson, M. P., Berlind, T., Sjostrom, H., Sundgren, J. E., Larsson, M., and Hultman, L., Mechanical and tribological properties of CNx films deposited by reactive magnetron sputtering. Wear (2001), 248(1–2): 55.
80. See for example, US04664976, US05630275, US5232570, US05855746, and JP61174377A2.
81. Greenwood, J. A. and Williamson, J. B. P., Contact of nominally flat surfaces. Proc. Roy. Soc. Lond. A (1966), 295(1442): 300–319.
82. Palacio, J. F., Bull, S. J., Neidhardt, J., and Hultman, L., Nanoindentation response of high performance fullerene-like CNx. Thin Solid Films (2006), 494(1–2): 63.
83. Molina-Aldareguia, J. M., Lloyd, S. J., Oden, M., Joelsson, T., Hultman, L., and Clegg, W. J., Deformation structures under indentations in TiN/NbN single-crystal multilayers deposited by magnetron sputtering at different bombarding ion energies. Philos. Mag. A (2002), 82(10): 1983–1992.
84. Schwarzer, N., Coating design due to analytical modelling of mechanical contact problems on multilayer systems. Surf. Coat. Technol. (2000), 133–134: 397–402.
85. Broitman, E., Macdonald, W., Hellgren, N., Radnoczi, G., Czigany, Z., Wennerberg, A., Jacobsson, M., and Hultman, L., Carbon nitride films on orthopedic substrates. Diamond Relat. Mater. (2000), 9(12): 1984.
86. Neidhardt, J., Hultman, L., Broitman, E., Scharf, T. W., and Singer, I. L., Structural, mechanical and tribological behavior of fullerene-like and amorphous carbon nitride coatings. Diamond and Relat. Mater. (2004), 13(10): 1882.
87. Voevodin, A. A., Jones, J. G., Back, T. C., Zabinski, J. S., Strel'nitzki, V. E., and Aksenov, I. I., Comparative study of wear-resistant DLC and fullerene-like CNx coatings produced by pulsed laser and filtered cathodic arc depositions. Surf. Coat. Technol. (2005), 197(1): 116.
88. Sanchez-Lopez, J. C., Belin, M., Donnet, C., Quiros, C., and Elizalde, E., Friction mechanisms of amorphous carbon nitride films under variable environments: a triboscopic study. Surf. Coat. Technol. (2002), 160(2–3): 138–144.
89. Singer, I. L., How third-body processes affect friction and wear. MRS Bull. (1998), 23(6): 37–40.
90. Hutchings, I. M., Friction and Wear of Engineering Materials. (1992), London: Edward Arnold.
91. Singer, I. L., Dvorak, S. D., Wahl, K. J., and Scharf, T. W., Role of third bodies in friction and wear of protective coatings. J. Vac. Sci. Technol. A (2003), 21(5, Suppl.): S232–S240.
92. Fisher, J., Dowson, D., Hamdzah, H., and Lee, H. L., The effect of sliding velocity on the friction and wear of UHMWPE for use in total artificial joints. Wear (1994), 175(1–2): 219–225.
93. Broitman, E., Pushkarev, V. V., Gellman, A. J., Novotny, V., Furlan, A., and Hultman, L., Water Adsorption on Lubricated Fullerene-like CNx Films. Thin Solid Films (2006), 513(3): 970–983.

Index

C

S